Energy, Environment, and Sustainability

Santanu De
Avinash Kumar Agarwal
Swetaprovo Chaudhuri
Swarnendu Sen *Editors*

Modeling and Simulation of Turbulent Combustion

Springer

Energy, Environment, and Sustainability

Series editors

Avinash Kumar Agarwal, Department of Mechanical Engineering, Indian Institute of Technology, Kanpur, Uttar Pradesh, India
Ashok Pandey, Distinguished Scientist, CSIR-Indian Institute of Toxicology Research, Lucknow, India

This books series publishes cutting edge monographs and professional books focused on all aspects of energy and environmental sustainability, especially as it relates to energy concerns. The Series is published in partnership with the International Society for Energy, Environment, and Sustainability. The books in these series are editor or authored by top researchers and professional across the globe. The series aims at publishing state-of-the-art research and development in areas including, but not limited to:

- Renewable Energy
- Alternative Fuels
- Engines and Locomotives
- Combustion and Propulsion
- Fossil Fuels
- Carbon Capture
- Control and Automation for Energy
- Environmental Pollution
- Waste Management
- Transportation Sustainability

More information about this series at http://www.springer.com/series/15901

Santanu De · Avinash Kumar Agarwal
Swetaprovo Chaudhuri · Swarnendu Sen
Editors

Modeling and Simulation of Turbulent Combustion

Springer

Editors
Santanu De
Department of Mechanical Engineering
Indian Institute of Technology Kanpur
Kanpur, Uttar Pradesh
India

Swetaprovo Chaudhuri
Department of Aerospace Engineering
Indian Institute of Science
Bangalore, Karnataka
India

Avinash Kumar Agarwal
Department of Mechanical Engineering
Indian Institute of Technology Kanpur
Kanpur, Uttar Pradesh
India

Swarnendu Sen
Department of Mechanical Engineering
Jadavpur University
Kolkata, West Bengal
India

ISSN 2522-8366 ISSN 2522-8374 (electronic)
Energy, Environment, and Sustainability
ISBN 978-981-10-7409-7 ISBN 978-981-10-7410-3 (eBook)
https://doi.org/10.1007/978-981-10-7410-3

Library of Congress Control Number: 2017959165

© Springer Nature Singapore Pte Ltd. 2018, corrected publication 2018
This work is subject to copyright. All rights are reserved by the Publisher, whether the whole or part of the material is concerned, specifically the rights of translation, reprinting, reuse of illustrations, recitation, broadcasting, reproduction on microfilms or in any other physical way, and transmission or information storage and retrieval, electronic adaptation, computer software, or by similar or dissimilar methodology now known or hereafter developed.
The use of general descriptive names, registered names, trademarks, service marks, etc. in this publication does not imply, even in the absence of a specific statement, that such names are exempt from the relevant protective laws and regulations and therefore free for general use.
The publisher, the authors and the editors are safe to assume that the advice and information in this book are believed to be true and accurate at the date of publication. Neither the publisher nor the authors or the editors give a warranty, express or implied, with respect to the material contained herein or for any errors or omissions that may have been made. The publisher remains neutral with regard to jurisdictional claims in published maps and institutional affiliations.

Printed on acid-free paper

This Springer imprint is published by Springer Nature
The registered company is Springer Nature Singapore Pte Ltd.
The registered company address is: 152 Beach Road, #21-01/04 Gateway East, Singapore 189721, Singapore

Foreword

Turbulent combustion is a fascinating research field with major societal implications: more than eighty per cent of the energy produced on earth is obtained by combustion, and in most cases by turbulent combustion. In most energy scenarios, combustion will continue to be the major source of energy for a very long time because the drastic increase of renewable energies is not enough to cover the overall growth of the world energy consumption. At the same time, combustion is a major source of pollutants as well as the main contributor to climate change. In this context, optimizing combustion systems is obviously the first task to tackle and combustion science is at the forefront of this work. This task, however, is a daunting one because turbulent combustion combines the complexities of turbulence and of chemical kinetics, two fields of research where our fundamental knowledge remains largely insufficient. Studying turbulent combustion and disseminating this research in the community are crucial actions, and this book contributes to both by presenting the latest results obtained in this field and organizing them in such a way that students, professors and engineers will have a general overview of the domain and an easy, detailed access to each topic.

Combustion systems have been improved over more than a century. Today, improving turbulent combustion in piston engines, furnaces, boilers, aircraft, helicopter, rockets, etc., beyond state-of-the-art technologies cannot be done without a deep understanding of the mechanisms controlling turbulence-chemistry interaction (TCI). Performing experiments in turbulent flames is a difficult task, and the last couple of decades have seen an impressive revolution taking place where numerical simulations, based on new theoretical approaches and on massively parallel computers, have progressively become the basic tools used by most teams to analyse the structure of turbulent flames and understand how to master turbulent combustion. In the present book, the world leaders of research in turbulent combustion give detailed and exhaustive overviews of all simulation methods used today for turbulent flames, starting from classical methods (such as RANS for Reynolds-averaged Navier–Stokes simulations, used today in many companies) to very advanced techniques (such as DNS for direct numerical simulations, which can offer extremely high precision when computations can be performed on the world's

largest computers). The different contributions of the book describe all aspects of these simulation methods, covering the derivation of subgrid TCI models but also methods to include realistic descriptions of complex chemistry in turbulent combustion simulations. Most presentations focus on subsonic gaseous flames (deflagrations), but extensions to more complex cases such as spray flames or detonations are also presented. Since high-performance computations (HPC) have become mandatory to simulate turbulent flames, the book also discusses numerical techniques and multiple HPC aspects specifically linked to combustion. As such, this book will be a valuable source for all researchers and engineers who want to understand turbulent combustion and master the numerical tools which are used and developed today in this crucial field for our planet.

Toulouse, France

Thierry Poinsot
Professor and Research Director
Institut de Mécanique des Fluides de Toulouse
CNRS, Université de Toulouse

Preface

Energy demand has been rising remarkably due to increasing population and urbanization. Global economy and society are significantly dependent on the energy availability because it touches every facet of human life and its activities. Transportation and power generation are the major examples of energy. Without the transportation by millions of personalized and mass transport vehicles and availability of 24 × 7 power, human civilization would not have reached contemporary living standards.

First International Conference on 'Sustainable Energy and Environmental Challenges' (SEEC-2017) was organized under the auspices of 'International Society for Energy and Environmental Sustainability' (ISEES) by the 'Center of Innovative and Applied Bioprocessing' (CIAB), Mohali, from 26–28 February 2017. ISEES was founded at IIT Kanpur in January 2014 with the aim of spreading knowledge in the fields of energy, environment, sustainability and combustion. The society's goal is to contribute to the development of clean, affordable and secure energy resources and a sustainable environment for the society and to spread knowledge in the above-mentioned areas and spread awareness about the environmental challenges, which the world is facing today. ISEES is involved in various activities such as conducting workshops, seminars, conferences in the domains of its interests. The society also recognizes the outstanding works done by the young scientists and engineers for their contributions in these fields by conferring them awards under various categories.

This conference provided a platform for discussions between eminent scientists and engineers from various countries including India, USA, South Korea, Norway, Malaysia and Australia. In this conference, eminent speakers from all over the world presented their views related to different aspects of energy, combustion, emissions and alternative energy resource for sustainable development and a cleaner environment. The conference started with four mini-symposiums on very topical themes, which included (i) New Fuels and Advanced Engine Combustion, (ii) Sustainable Energy, (iii) Experimental and Numerical Combustion and (iv) Environmental Remediation and Rail Road Transport. The conference had 14 technical sessions on the topics related to energy and environmental sustainability

and panel discussions on 'Challenges, Opportunities and Directions of Technical Education & Research in the Area of Energy, Environment and Sustainability' to wrap up the 3-day technical extravaganza. The conference included 2 plenary talks, 12 keynote talks, 42 invited talks from prominent scientists, 49 contributed talks and 120 posters. A total of 234 participants and speakers attended this three-day conference, which hosted Dr. V. K. Saraswat, Member NITI Ayog, India, as a chief guest for the award ceremony of ISEES. This conference laid out the road map for technology development, opportunities and challenges in this technology domain. The technical sessions in the conference included Advances in IC Engines and Fuels; Conversion of Biomass to Biofuels; Combustion Processes; Renewable Energy: Prospects and Technologies; Waste to Wealth–Chemicals and Fuels; Energy Conversion Systems; Numerical Simulation of Combustion Processes; Alternate Fuels for IC Engines; Sprays and Heterogeneous Combustion of Coal/Biomass; Biomass Conversion to Fuels & Chemicals—Thermochemical Processes; Utilization of Biofuels and Environmental Protection and Health. All these topics are very relevant to the country and the world in the present context. The society is grateful to Prof. Ashok Pandey for organizing and hosting this conference, which led to the germination of this series of monographs, which included 16 books related to different aspects of energy, environment and sustainability. This is the first time that such voluminous and high-quality outcome has been achieved by any society in India from one conference.

The editors would like to express their sincere gratitude to the authors for submitting their work in a timely manner and revising it appropriately at short notice. We would like to express our special thanks to Prof. Nilanjan Chakraborty, Prof. Amitava Datta, Prof. Ashoke De, Prof. Ranjan Ganguly, Prof. Hong Im, Dr. Hemanth Kolla, Prof. Neeraj Kumbhakarna, Prof. K. N. Lakshmisha, Prof. Joseph Mathew, Prof. Achnitya Mukhopadhyay, Dr. Sishendu Mondal, Dr. Vineeth Nair, Prof. Krithika Narayanaswamy, Prof. Salvador Navarro-Martinez, Prof. Abhishek Saha, Prof. Sreedhara Seshadri, Prof. Pallab Sinha Mahapatra and Prof. Peng Zhao, who reviewed various chapters of this monograph and provided their valuable suggestions to improve the manuscripts. We acknowledge the support received from various funding agencies and organizations for the successful conduct of the first ISEES conference SEEC-2017, where these monographs germinated. These include Department of Science and Technology, Government of India (special thanks to Dr. Sanjay Bajpai); TSI, India (special thanks to Dr. Deepak Sharma); Tesscorn, India (special thanks to Sh. Satyanarayana); AVL India; Horiba, India; Springer (special thanks to Swati Meherishi); CIAB (special thanks to Dr. Sangwan).

Design and development of practical combustion systems require extensive investigation of multi-scale and multi-physics processes, such as fuel injection, spray atomization, evaporation of injected droplets, mixing of fuel and air, chemical reactions, formation of NOx, soot and unburnt hydrocarbons. Gaining fundamental insights on these complex processes via experimental investigations is not only expensive but sometimes impossible due to lack of optical access, complex flows and extremely fast combustion reactions. Numerical simulations of these complex

multi-scale and multi-physics phenomena are more easily and conveniently carried out using efficient numerical algorithms designed for massively parallel computers. However, the complex multi-scale and nonlinear interaction between chemistry and turbulence pose a significant modelling challenge of turbulent reactive flows encountered in modern combustion systems. Notwithstanding the significant progress in the last couple of decades, the modelling and numerical simulations of turbulent combustion remain in the forefront of research due to its inherent complexity, significant modelling difficulties and industrial relevance. Besides changing the existing design of combustion systems, application of different alternate fuels such as biofuels, renewable fuels, alcohols and other synthetic fuels is being explored in the context of sustainable energy and environmental issues.

In this monograph, comprehensive reviews of the state-of-the-art models are presented for turbulent premixed and nonpremixed combustion with a specific focus on the theory, development of combustion models and applications in laboratory and practical combustion systems. This book is envisaged to benefit a relatively broad audience, including beginners, graduate students in engineering, seasoned researchers, practicing combustion system developers, computational fluid dynamics code developers and users, and provides a holistic approach of turbulent combustion in terms of fundamentals, modelling and numerical simulations.

The topics are organized into five different sections: (i) fundamentals, methodology and architecture of turbulent combustion computations, (ii) turbulent premixed combustion, (iii) turbulent nonpremixed combustion, (iv) probability density function methods and (v) recent applications of turbulent combustion.

Kanpur, India — Santanu De
Kanpur, India — Avinash Kumar Agarwal
Bangalore, India — Swetaprovo Chaudhuri
Kolkata, India — Swarnendu Sen

Contents

Editors and Contributors

About the Editors

Dr. Santanu De is an Assistant Professor in the Mechanical Engineering, IIT Kanpur, since December 2014. He received a Bachelor of Engineering from the North Bengal University in 2002 and an M.Tech. from the IIT Kanpur in 2004, both in Mechanical Engineering. He received his Ph.D. in Aerospace Engineering from the Indian Institute of Science, Bangalore, in 2012. Prior to his joining at IIT Kanpur, he served 2 years at the Michigan Technological University as a postdoctoral research associate and 1 year at the Institute of Combustion Technology (ITV), University of Stuttgart. He also worked as a Scientist at the Liquid Propulsion Systems Center, Indian Space Research Organization, between 2004 and 2005. His primary areas of research are numerical modelling of turbulent combustion, spray atomization and combustion, coal gasification and combustion. He is a member of the editorial board of 'Journal of Energy, Environment and Sustainability.'

Prof. Avinash Kumar Agarwal joined IIT Kanpur in 2001 and is currently a Poonam and Prabhu Goyal Endowed Chair Professor. He was at ERC, University of Wisconsin, Madison, USA, as a Postdoctoral Fellow (1999–2001). His areas of interest are IC engines, combustion, alternative fuels, hydrogen, conventional fuels, lubricating oil tribology, optical diagnostics, laser ignition, HCCI, emission and particulate control and large bore engines. He has published more than 160 peer-reviewed international journals and conference papers. He is an Associate Editor of ASME Journal of Energy Resources Technology and International Journal of Vehicle Systems Modelling and Testing. He has edited 'Handbook of Combustion' (5 volumes; 3168 pages), published by Wiley VCH, Germany. He is a Fellow of SAE (2012), Fellow of ASME (2013) and a Fellow of INAE (2015). He is recipient of several

prestigious awards such as NASI-Reliance Industries Platinum Jubilee Award-2012; INAE Silver Jubilee Young Engineer Award-2012; Dr. C. V. Raman Young Teachers Award-2011; SAE International's Ralph R. Teetor Educational Award-2008; INSA Young Scientist Award-2007; UICT Young Scientist Award-2007; INAE Young Engineer Award-2005. He is the recipient of Prestigious Shanti Swarup Bhatnagar Award-2016 in Engineering Sciences. He is the first combustion/IC engine researcher to get this honour.

Dr. Swetaprovo Chaudhuri is an Assistant Professor at the Department of Aerospace Engineering, Indian Institute of Science, since June 2013. Prior to this appointment, he was a Research Staff at the Department of Mechanical and Aerospace Engineering, Princeton University. He earned his Ph.D. from the University of Connecticut in 2010 and B.E. from Jadavpur University in 2006, both in Mechanical Engineering. His research interests and contributions span over fundamental and applied aspects of turbulent combustion and functional droplets. Important contributions of him include but are not limited to: resolving the blowoff mechanism of bluff-body stabilized flames using laser diagnostics, scaling laws of turbulent flame speed, fundamental mechanisms involved in generation and annihilation of turbulent premixed flames, mitigating instability by actuating the swirler in a combustor and nanoparticle-laden droplet stacking. So far, he has authored/co-authored more than 70 articles disseminated through top journals and conference proceedings. Recently, he was selected as the Recipient of the Young Scientist Medal by the Indian National Science Academy and as an Associate of the Indian Academy of Sciences. His earlier contributions have been recognized by American Society of Mechanical Engineers and by the University of Connecticut.

Dr. Swarnendu Sen is a Professor at the Department of Mechanical Engineering, Jadavpur University, and he is teaching there since November 1989. He earned his Bachelor and Masters in Mechanical Engineering as well as Ph.D. (Engineering) from Jadavpur University. He worked in University of Illinois at Chicago and Virginia Tech as Visiting Research Scholar. He has also worked in Technical University of Munich as a DAAD Fellow. His research interests and contributions span over fundamental and applied aspects of reacting and multi-phase flows, heat transfer augmentation and carbon nanostructure synthesis. So far, he has authored/co-authored more than 200 articles disseminated through top journals and conference proceedings.

Contributors

V'yacheslav (Slava) B. Akkerman Department of Mechanical and Aerospace Engineering, West Virginia University, Morgantown, WV, USA

Muhsin M. Ameen Argonne National Laboratory, Lemont, IL, USA

Shokri Amzin Western Norway University of Applied Sciences, Bergen, Norway

Xue-Song Bai Division of Fluid Mechanics, Department of Energy Science, Lund University, Lund, Sweden

Kedar G. Bhide IC Engines and Combustion Laboratory, Mechanical Engineering Department, Indian Institute of Technology Bombay, Mumbai, India

Nilanjan Chakraborty School of Mechanical and Systems Engineering, Newcastle University, Newcastle-upon-Tyne, UK

Saugata Chakravorty Indian Institute of Science, Bangalore, India; Honeywell, Bangalore, India

Swetaprovo Chaudhuri Department of Aerospace Engineering, Indian Institute of Science, Bangalore, India

Jacqueline H. Chen Reacting Flow Research, Sandia National Laboratories, Livermore, CA, USA

Matthew J. Cleary School of Aerospace, Mechanical and Mechatronic Engineering, The University of Sydney, Sydney, Australia; Department of Mechanical and Aerospace Engineering, Princeton University, Princeton, USA

Amitava Datta Department of Power Engineering, Jadavpur University, Kolkata, India

Ashoke De Department of Aerospace Engineering, Indian Institute of Technology Kanpur, Kanpur, India

Santanu De Department of Mechanical Engineering, Indian Institute of Technology Kanpur, Kanpur, India

Ranjan Ganguly Department of Power Engineering, Jadavpur University, Kolkata, India

Sanjeev Kumar Ghai Department of Mechanical Engineering, Indian Institute of Technology Kanpur, Kanpur, India

Prakash Ghose Department of Power Engineering, Jadavpur University, Kolkata, India

Hong G. Im Clean Combustion Research Center, King Abdullah University of Science and Technology, Thuwal, Saudi Arabia

Hemanth Kolla Scalable Modeling and Analysis, Sandia National Laboratories, Livermore, CA, USA

Prithwish Kundu Argonne National Laboratory, Lemont, IL, USA

Jiawei Lai School of Mechanical and Systems Engineering, Newcastle University, Newcastle-upon-Tyne, UK

Andrei N. Lipatnikov Chalmers University of Technology, Gothenburg, Sweden

Joseph Mathew Indian Institute of Science, Bangalore, India

Sirshendu Mondal Indian Institute of Technology Madras, Chennai, India

Achintya Mukhopadhyay Department of Mechanical Engineering, Jadavpur University, Kolkata, India

S. Navarro-Martinez Imperial College London, London, UK

V. A. Sabelnikov ONERA–The French Aerospace Laboratory, Palaiseau, France; TsAGI, Moscow Region, Russia

Rohit Saini Department of Aerospace Engineering, Indian Institute of Technology Kanpur, Kanpur, India

Swarnendu Sen Department of Mechanical Engineering, Jadavpur University, Kolkata, India

Sibendu Som Argonne National Laboratory, Lemont, IL, USA

S. Sreedhara IC Engines and Combustion Laboratory, Mechanical Engineering Department, Indian Institute of Technology Bombay, Mumbai, India

Jeroen A. van Oijen Mechanical Engineering, Eindhoven University of Technology, MB, Eindhoven, The Netherlands

V. V. Vlasenko TsAGI, Moscow Region, Russia

Konstantina Vogiatzaki School of Computing, Engineering and Mathematics, University of Brighton, Brighton, UK

Peng Zhao Department of Mechanical Engineering, Oakland University, Rochester, MI, USA

Part I
Fundamentals, Methodology and Architecture of Turbulent Combustion Computations

Chapter 1
Mechanics and Modelling of Turbulence–Combustion Interaction

Santanu De and Swetaprovo Chaudhuri

Abstract Engineering applications of combustion for aviation, automotive and power generation invariably encounter an underlying turbulent flow field. A proper understanding of the complex turbulence–combustion interactions, flame structure and dynamics is indispensable towards the optimal design and systematic evolution of these applications. A predictive solution of turbulent combustion phenomenon in a practical combustion system where all scales of turbulence are fully resolved is extremely difficult with currently available computational facilities. The urgent requirement for the solution of fluid engineering problems has led to the emergence of turbulence models. The turbulence models could be systematically derived based on the Navier–Stokes equations up to a certain point; however, they require closure hypotheses that depend on dimensional arguments and empirical input. Over the past several decades, turbulence models based on Reynolds-averaged Navier–Stokes (RANS) and large eddy simulation (LES) framework have been developed and used for engineering applications. The success of turbulence models for non-reactive flows has encouraged similar approaches for turbulent reactive flows which consequently led to the development of turbulent combustion models. Modelling of the chemical source term remains the central issue of turbulent combustion simulations. In this introductory chapter, we will review the basics of turbulent flows and multiscale interactions between turbulence and combustion, and proceed towards a brief discussion on the state-of-the-art turbulent combustion models.

Keywords Turbulence–chemistry interaction · RANS · LES
Turbulent premixed combustion · Turbulent non-premixed combustion

Santanu De (✉)
Department of Mechanical Engineering, Indian Institute of Technology Kanpur, Kanpur, India
e-mail: sde@iitk.ac.in

S. Chaudhuri
Department of Aerospace Engineering, Indian Institute of Science, Bangalore, India
e-mail: schaudhuri@iisc.ac.in

© Springer Nature Singapore Pte Ltd. 2018

S. De et al. (eds.), *Modeling and Simulation of Turbulent Combustion*, Energy, Environment, and Sustainability, https://doi.org/10.1007/978-981-10-7410-3_1

Nomenclature

ρ	Density
u	Velocity
R_u	Universal gas constant
p	Pressure
τ_{ij}	Viscous stress tensor
μ	Dynamic viscosity
υ	Kinematic viscosity
Y	Mass fraction
D	Mass diffusivity
Sc	Schmidt number
Pr	Prandtl number
Le	Lewis number
Re	Reynold's number
λ	Thermal conductivity
α	Thermal diffusivity
X	Mole fraction
W	Molecular weight
E_a	Activation energy
T	Temperature
h	Enthalpy
$\overrightarrow{\dot{q}}$	Heat flux
Q	Conditional mean
C_χ	Scalar dissipation constant
Z	Mixture fraction
$\boldsymbol{J}$	Flux
τ_L	Mixing timescale
Δ	Filter width
T_a	Activation temperature
$k^{(f)}$, $k^{(r)}$	Forward and reverse reaction rates
n_r	Number of reactions
n_s	Number of species
χ	Scalar dissipation
ε	Dissipation rate
k	Turbulent kinetic energy
$\dot{\omega}$	Chemical source term
η	Sample space
P	Probability density function
C_s	Smagorinsky model constant
$\mathcal{T}_{ij}$	Residual stress tensor
$\mathcal{L}_{ij}$	Leonard term
$\mathcal{M}_{ij}$	Modelled term
η	Kolmogorov length scale

Overbar Symbols

– Average, ensemble or time average depending on context
~ Favre average
″ Fluctuations with respect to conditional mean
′ Fluctuations with respect to unconditional mean

Indices

J Reaction number
I Species

1.1 Introduction

Intense turbulence–combustion interactions are ubiquitous in nature and in engineering devices. Due to the impressive energy density of the liquid hydrocarbons, combustion processes will certainly continue to power aero transportation and power generation in the foreseeable future. Despite the advent of electric land vehicles and renewable power sources, its role in automotive and power industries will remain dominant. However, in the devices which follow the principles of a thermodynamic cycle, work/thrust can only be extracted after heat addition occurs at a high pressure in a combustor. High pressure means high density of the working fluid (e.g., air in air-breathing engines) which along with high flow velocities makes combustion processes in all practical engines invariably turbulent. For example, aero-engines operate at turbulence Reynolds numbers of few tens of thousands and the carbon–oxygen flame preceding a supernova Ia explosion propagates in turbulence Reynolds numbers of a few hundreds of thousands. While turbulence still remains one of the most important unresolved problems in classical physics, conversion of chemical to thermal energy through a myriad of chemical reactions in fluid turbulence renders turbulent combustion as a problem of unparalleled complexity in the context of fundamental understanding or predictive modelling. In case of non-premixed combustion where fuel and oxidizer are separated before combustion, turbulence greatly assists in fuel–air mixing and hence in the overall combustion process. In case of premixed flames where fuel and air are mixed at a molecular level before combustion, turbulence stretches, wrinkles, and folds a flame at a multitude of length and timescales and the resulting evolutionary topology and state of the turbulent premixed flame lead to its much faster than laminar propagation rate. With recent advances in computational technologies at both hardware and software levels, turbulent combustion is now amenable to numerical experiments to explore and enhance new physical understanding as well as modelling of engine relevant combustion phenomena that could be used towards faster and rigorous development of new generation engines. In the present day, scientific

computing offers a competing approach along with research tools of experiments/theory to gather multiscale information (Bilger 1976). Computational fluid dynamics (CFD) has become an integral part of the design procedure followed by combustion engineers. However, owing to a multitude complex processes involved in turbulent combustion with or without associated phase change, use of modern CFD techniques is yet to sufficiently mature. Typical difficulties encountered in numerical modelling of turbulent combustion include, but are not limited to (1) the richness of spatio-temporal scales, (2) a high degree of nonlinearities, (3) the stochastic nature of turbulence, and (4) strong interaction between the different subprocesses (Peters 2000; Libby and Williams 1994).

In this chapter, we discuss the rudiments of turbulent combustion which includes discussion of the fundamental mechanics of non-reacting and reacting turbulences to proceed into an overview of the different modelling strategies for turbulent combustion presently adopted in industry and research labs around the world. The remainder of this chapter is arranged as follows. In the next section, fundamental principles of turbulence are reviewed. The instantaneous transport equations for turbulent reactive flows are presented in Sect. 1.3 along with a brief description of transport properties and chemical reaction term. In Sects. 1.4 and 1.5, turbulence models based on Reynolds-averaged Navier–Stokes (RANS) and large eddy simulation (LES) frameworks are briefly reviewed. A brief overview of some state-of-the-art turbulence models is provided in Sect. 1.6.

1.2 Fundamentals of Turbulence and Turbulence–Premixed Flame Interaction

In this introductory chapter, first, we describe the energetics and kinematics of non-reacting turbulence to proceed into those for turbulent combustion. Also, in this first part of the chapter, we will consider the mechanics of fully developed turbulence in the very high turbulence Reynolds number limit (Pope 2000), unless otherwise mentioned. It is well accepted that the mechanics of incompressible turbulent flow is fully described by the Navier–Stokes equation (Eqs. 1.1–1.3) written as mass per unit volume times acceleration = force per unit volume:

$$\rho \frac{Du_j}{Dt} = \frac{\partial \tau_{ij}}{\partial x_i}, \tag{1.1}$$

where

$$\tau_{ij} = -p\delta_{ij} + \mu\left(\frac{\partial u_i}{\partial x_j} + \frac{\partial u_j}{\partial x_i}\right) \tag{1.2}$$

The material derivative on the LHS could be expanded into

$$\rho\left[\frac{\partial u_j}{\partial t}+u_i\frac{\partial u_j}{\partial x_i}\right]=-\frac{\partial p}{\partial x_j}+\mu\left[\frac{\partial^2 u_j}{\partial x_i\partial x_i}\right] \tag{1.3}$$

Of course, this must be supplemented with the continuity equation which for constant density flows stands as $\partial u_j/\partial x_j=0$. As such, it is possible to numerically solve the above equations with appropriate boundary and initial conditions to simulate a turbulent flow at given Reynolds number. However, one of the hallmarks of turbulence is its multiscale structure where eddies are formed all the way from the size of flow domain say L to some small microscales which will eventually be defined as Kolmogorov length scale η. This separation of the large and small length scales (similar situation arises for timescales also) implies that the computations must be performed on a grid which spans the entire range of scales, i.e. the size of the domain L to the smallest length scales η. Fully developed turbulence is inherently a three-dimensional phenomenon (2D turbulence is a special case); hence, the simulation grid requires a large number of grid points on all three dimensions which often leads to prohibitively expensive computational costs for many practical flow situations of interest. However, a great many numbers of such computationally intensive Direct Numerical Simulation (DNS) have been performed till date for both non-reacting and reacting flows for idealized configurations. If one wants to avoid such computationally expensive direct simulation, the other possibility is to simulate an averaged or a filtered flow field using an averaged/filtered form of the Navier–Stokes equation. These are known as Reynolds-averaged Navier–Stokes (RANS) simulation and Large Eddy Simulation (LES), respectively, and will be described in detail in the second part of this chapter. To these ends, the non-linearity arising from the second term on the LHS of Eq. (1.3) is the most difficult term towards modelling statistical features of turbulence. Of course, RANS or LES cannot yield complete features of turbulence as the variables that are solved for are not the actual velocities but rather averaged or filtered velocities, respectively. This may not be the problem since most often we are interested in statistical features of turbulence and in the following, we will see how the dynamics of turbulence emerges from such averaged equations.

Defining ensemble averaged quantities from the corresponding probability density functions (PDF) as

$$\overline{u_1}\equiv\int_{-\infty}^{+\infty}V_1 f(V_1)dV_1, \tag{1.4}$$

where V_1 is the sample space variable of a velocity component u_1, and f is the PDF of V_1.

One can write $u_1=\overline{u_1}+u_1^{'}$, where $u_1^{'}$ is fluctuating part of velocity u_1.

Averaging the LHS of Eq. (1.3), we get

$$\begin{aligned}\overline{\frac{Du_j}{Dt}} &= \frac{\partial \overline{u_j}}{\partial t} + \overline{u_i}\frac{\partial \overline{u_j}}{\partial x_i} + \frac{\partial \overline{u_i' u_j'}}{\partial x_i} \\ &= \frac{\overline{D}\,\overline{u_j}}{\overline{D}t} + \frac{\partial \overline{u_i' u_j'}}{\partial x_i}\end{aligned} \tag{1.5}$$

$\overline{u_i' u_j'}$ appearing in the second term of the last RHS is called the Reynolds stress though they emerge upon averaging the convective part of the acceleration. These are unclosed term and have historically posed a serious modelling challenge. In fact, it is the Reynolds stress term (or its equivalent subgrid-scale stress term) and the modelling uncertainties it entails makes RANS or LES intrinsically less reliable than a corresponding DNS.

Averaging both sides of Eq. (1.3) yields the following RANS equations:

$$\frac{\overline{D}\,\overline{u_j}}{Dt} = \nu \nabla^2 \overline{u_j} - \frac{\partial \overline{u_i' u_j'}}{\partial x_i} - \frac{1}{\rho}\frac{\partial \overline{p}}{\partial x_j} \tag{1.6}$$

Next, we move on to the transfer and conversion between different forms of kinetic energies involved in turbulence. In a given turbulent flow, the total kinetic energy per unit mass, typically referred to as only kinetic energy, is given by $E(\vec{x}, t) = \frac{1}{2} u_i(\vec{x}, t) u_i(\vec{x}, t)$. Just like velocity, the kinetic energy could be averaged. Upon averaging, it yields a kinetic energy of the mean flow, given by the first term on the RHS of the following equation: $\overline{E}(\vec{x}, t) = \overline{\overline{E}}(\vec{x}, t) + k(\vec{x}, t)$. The averaging also yields the second term of the RHS, called the turbulent kinetic energy (TKE). Here, the kinetic energy of the mean flow is given by $\overline{\overline{E}}(\vec{x}, t) = \frac{1}{2}\overline{u_i} \cdot \overline{u_i}$ and the TKE is given by $k(\vec{x}, t) = \frac{1}{2}\overline{u_i' u_i'}$. Next, we briefly show how TKE is produced at the cost of $\overline{\overline{E}}(\vec{x}, t)$ in the presence of mean velocity gradients and Reynolds stresses. To that end, the transport equation for $\overline{\overline{E}}(\vec{x}, t)$ and $k(\vec{x}, t)$ can be derived after algebraic manipulations of the Navier–Stokes equation (Eq. 1.3) and RANS equations (Eq. 1.6). See Pope (1988) for further details.

The transport equations for $\overline{E}(\vec{x}, t)$ and $k(\vec{x}, t)$ are given by

$$\frac{\overline{D}\,\overline{\overline{E}}}{\overline{D}t} + \nabla \cdot \overline{T} = -P - \overline{\varepsilon} \tag{1.7}$$

$$\frac{\overline{D}k}{\overline{D}t} + \nabla \cdot T' = P - \varepsilon \tag{1.8}$$

The equations are written together for reasons which will be clarified immediately.

Here, a transport term appearing on the LHS of Eq. 1.7 is given by $\overline{T_i} = \overline{u_j}\,\overline{u_i' u_j'} + \overline{u_i}\frac{\bar{p}}{\rho} - 2\nu\overline{u_j}\,\overline{S_{ij}}$ and $\bar{\varepsilon}$ is the dissipation due to the mean flow.

Equation (1.7) describes the transport of the kinetic energy of the mean flow with $\overline{\overline{E}}(\vec{x}, t)$ as the mean kinetic energy. By Eq. (1.5), the mean substantial derivative is the rate of change along the trajectory of a point moving with mean velocity $\overline{\vec{u}}(\vec{x}, t)$. The mean substantial derivative operator is given by $\frac{\overline{D}}{\overline{D}t} = \frac{\partial}{\partial t} + \overline{u_i}\frac{\partial}{\partial x_i}$.

The first term of the RHS of Eqs. (1.7) and (1.8), $P = -\overline{u_i' u_j'}\frac{\partial \overline{u_i}}{\partial x_j}$ is the production of turbulent kinetic energy. Clearly, it depends on two critical but dissimilar quantities: (i) Reynolds stresses $\overline{u_i' u_j'}$ and (ii) Mean velocity gradients given by $\frac{\partial \overline{u_i}}{\partial x_j}$.

The last term on RHS of Eq. (1.7) is dissipated due to mean flow given by $\bar{\varepsilon} = 2\nu\overline{S}_{ij}\overline{S}_{ij}$. Here, $\overline{S}_{ij} = \frac{1}{2}\left(\frac{\partial \overline{u_i}}{\partial x_j} + \frac{\partial \overline{u_j}}{\partial x_i}\right)$ is the mean strain rate.

Coming to the transport equation of $k(\vec{x}, t)$ in Eq. (1.8), first, we encounter a mean substantial derivative of $k(\vec{x}, t)$ followed by the fluctuating transport term on the LHS. The second term on the RHS of Eq. (1.8) is the mean dissipation rate of turbulent kinetic energy given by $\varepsilon = 2\nu\overline{s_{ij}' s_{ij}'}$. Here, $s_{ij}' = S_{ij} - \overline{S_{ij}}$ is the fluctuating strain rate.

Now, let us arrive at the most outstanding feature of this set of Eqs. (1.7) and (1.8).

As mentioned earlier, we find the same production term P appearing as the first term of the RHS of both Eqs. (1.7) and (1.8) but with opposite signs. Typically, in turbulent shear flows the sign of the production term by $P = -\overline{u_i' u_j'}\frac{\partial \overline{u_i}}{\partial x_j}$ is positive. Therefore, it is clear that it serves as a sink term in Eq. (1.7) and in the exact same magnitude, it serves as a source term in Eq. (1.8). It is, therefore, reasonable to conclude that the production term extracts kinetic energy of the mean flow and deposits the same as turbulent kinetic energy. In fact, this is the source of turbulent kinetic energy and hence turbulence which justifies the name *production*. So, clearly, the production of turbulence requires the presence of mean velocity gradients which are essentially large-scale features of a given turbulent flow. Once produced, the TKE $k(\vec{x}, t)$ is transported and eventually dissipated by $\varepsilon = 2\nu\overline{s_{ij}' s_{ij}'}$ which requires the presence of kinematic viscosity and fluctuating strain rates. It turns out that fluctuating strain rates, s_{ij}', are essentially small-scale features of a flow. So, the turbulent kinetic energy that is produced by production, P, at large scales is dissipated at small scales after being transported by the LHS of Eq. (1.8). So, from Eq. (1.8) we arrive at the concept of scale separation: TKE is produced at large scales and is dissipated at small scales. However, the LHS does not yield an intuitive picture of the mechanics of the process. Now that we understand how TKE enters into turbulence to drive it, we will take a step back and look into the hypotheses on turbulent kinetic energy cascade which qualitatively describes the mechanics of how TKE produced at the large scales is dissipated at the small scales.

Kolmogorov's hypotheses state that at high turbulence Reynolds number, Re_t, the statistics of the small-scale turbulent motions are inherently isotropic, i.e. PDFs are invariant upon rotation and reflection of the coordinate system and that the small-scale motions near the smallest scales of turbulence, η, are universal and only determined by ε and ν. Furthermore, there is an intermediate range of scales smaller than the largest scales, L, yet larger than η where the turbulent motions are universal but only governed by ε, independent of ν. As such it can be shown that $\eta/L \sim Re_t^{-3/4}$. This range of intermediate scales $L > l > \eta$ is called the inertial range. An immediate question may arise that if ε is itself a small-scale quantity how does it control the turbulent motion in the inertial range? This can be understood by introducing a quantity called the turbulent kinetic energy transfer rate $\mathcal{T}(l) = u'(l)^2/t(l)$. Here, u' and t are the characteristic velocity and eddy turnover timescales at a length scale l within the inertial range. The cascade picture suggests that the TKE entering into turbulence at the large scales by production mechanism is transferred into the smaller and smaller scales within the inertial range by breakup or stretching of eddies. While this is happening, the TKE transfer rate $\mathcal{T}(l)$ remains constant across all scales within the inertial range, i.e. $\mathcal{T}(l_0) = \mathcal{T}(l_1) = \mathcal{T}(l_2) = \cdots = \mathcal{T}(l_N)$, where $L > l_0 > l_1 > l_2 > \cdots > l_N > \eta$. This TKE transfer rate remains constant as the entire cascade process is inertial and happens in the absence of dissipative frictional forces arising from viscosity. Now that the TKE has arrived at the small scales l_N which is at the junction of inertial and dissipative ranges, it can be dissipated, i.e. transformed into thermal energy by viscosity and small-scale strain rates in the fluid through ε. Therefore, we can again write the above TKE transfer rate equation as $\mathcal{T}(l_0) = \mathcal{T}(l_1) = \mathcal{T}(l_2) = \cdots = \mathcal{T}(l_N) = \varepsilon$. So, it is indeed true that ε is active only at small scales but since it appears at the end of the cascade process, it determines the motion in the inertial range as the TKE transfer rate at all scales within the inertial range must be equal to ε. This constant transfer rate of $\mathcal{T}(l) = u'(l)^2/t(l)$ which can also be expressed as $\mathcal{T}(l) = u'(l)^3/l = \varepsilon$ gives rise to the following exact equation written in terms of separation vector $\vec{r}$: Kolmogorov's 4/5th law for constant density, homogeneous isotropic turbulence, given by (Kolmogorov 1941) :

$$\overline{\left\{\left(\vec{u}(\vec{r},t) - \vec{u}(0,t)\right)\cdot\frac{\vec{r}}{r}\right\}^3} = -\frac{4}{5}\varepsilon r \tag{1.9}$$

Here, $\vec{r}$ is the separation vector between two points in the flow. The 2/3rd law and its spectral equivalence in the form of −5/3 sloped TKE spectrum in wavenumber space also were obtained by Kolmogorov and Obukhov, respectively. The well-known energy spectrum function is given by

$$E(K) = f(\varepsilon, K) = C\varepsilon^{2/3}k^{-5/3} \tag{1.10}$$

C is a universal Kolmogorov constant = 1.5 from experimental data (Sreenivasan 1995).

Similar relationships and cascade ideas have been developed for passive scalar fluctuations as well. The question remains on how does the cascade happen physically?

As such, there are several viewpoints on this topic and in the following, we will present the vortex stretching mechanism where strain rates, stretch vortices and reduce their characteristic length scale. Ashurst et al. (1987) obtained the eigenvalues and eigenvectors of the strain rate tensor S_{ij} from DNS solutions of homogeneous isotropic turbulence in a box as well as from a shear flow. Then, the alignment between the unit vorticity vector $\widehat{\omega}$ and the unit eigenvectors of S_{ij} given by $\widehat{\alpha},\widehat{\beta},\widehat{\gamma}$ were studied. Here, $\widehat{\alpha},\widehat{\beta},\widehat{\gamma}$ corresponded to the directions of the largest, intermediate, and least principal strain rates, respectively. As such the eigenvalues are distributed on average as 3:1:−4 such that the sum should be equal to 0 to satisfy $\partial u_i/\partial x_i = 0$. It was found that on average $\widehat{\omega}$ was most strongly aligned with $\widehat{\beta}$, i.e. along the intermediate principal strain direction. So, it was suggested that the intermediate principal strain rate aligns the vorticity vector along its direction and by virtue of its most extensive nature; it stretches the vortex into a thinner yet elongated vortex tube. All this happens while angular momentum is conserved; therefore, the turbulent kinetic energy is transferred to a smaller scale vortex in accordance to the energy cascade in inertial range hypothesis. This is similar to the dynamics of an ice skater who folds his/her arms around the body to reduce the moment of inertia, thereby increasing the rotational speed, while angular momentum remains nearly constant in the absence of an external force/torque field. However, if vortex stretching is indeed the mechanism that drives the cascade, why do the weaker intermediate principal strain rate and not the most extensive principal strain rate gets aligned with the vorticity? Recent studies by Hamlington et al. (2008) and Xu et al. (2011) have shed light on the solution of this issue through non-local approaches. The former established the spatial non-locality of straining action on the vorticity, while the latter used non-locality in time. Using DNS, Hamlington et al. (2008) decomposed the strain rate field into local and non-local components by calculating the local velocity and strain rate field induced by the local vorticity, using Biot–Savart law. The non-local or the background strain rate field S_{ij}^B was obtained by removal of this local strain rate field from the total strain rate field. It was found that $\widehat{\omega}$ aligned best along the direction of the most extensive principal component of S_{ij}^B despite its alignment with the intermediate principal component direction of the complete strain rate field S_{ij}. Xu et al. (2011) used experiments and DNS to track several sets of four Lagrangian particles initially located at vertices of a tetrahedron and showed that the most extensive principal component of strain rate forces vorticity to align with itself. However, this alignment takes some time to develop; hence, the most extensive principal component $\widehat{\alpha}(t=0)$ aligns vorticity to itself with a characteristic time delay implying the vortex tube is being stretched while it is being aligned to the most extensive principal component.

Historically, development of analysis and understanding of passive scalar fluctuations in turbulence immediately followed that of the turbulent kinetic energy and

the analysis for reactive scalars followed those of their passive counterparts, albeit with significant points of departure in terms of results. As such Ashurst et al. (1987) also showed that the unit vector along the direction of the scalar gradient $\widehat{g}$ was mostly aligned with the $\widehat{\gamma}$, i.e. along the direction of the most compressive (negative) principal strain. If so, it is reasonable to conclude that turbulence cascade of a passive scalar is rather peculiar. For a blob of a passive scalar in turbulence, the turbulence compresses it along the normal (gradient) direction and stretches it along the transverse (tangential) direction. These further increase the gradient magnitude and decrease the scale concomitantly with strain vorticity alignment, to finally dissipate the gradient at smallest scales by molecular diffusivity. Here, the scalar dissipation rate controls the scalar variance transfer rate from a large-scale inhomogeneity to the large gradients at smaller scales. This discussion was for a passive scalar. What happens if there is a scalar source to support the gradient as it happens in turbulent combustion?

This question was first addressed by Swaminathan and Grout (2006) and then by Chakraborty and Swaminathan (2007) and Kim and Pitsch (2007). Description of turbulent combustion involves wider timescales emerging from chemical reactions and hence the need for an additional non-dimensional number like Damköhler number defined as $Da = t_{Flow}/t_{Flame}$. Here, the t_{Flow} typically corresponds to the integral timescale and t_{Flame} corresponds to a flame timescale which for a premixed flame can be the flame crossing time given by $t_{Flame} = l_I/S_L$, where l_I is the integral length scale and S_L is the planar laminar flame speed. For a non-premixed flame, an inverse of the scalar dissipation rate at stoichiometric conditions could be selected as the appropriate flame timescale $t_{Flame} = \chi_{st}^{-1}$. Clearly, large Da imply a flame that is oblivious to the surrounding turbulence and its structure remains almost unperturbed behaving like a wrinkled laminar flame. A small Da flame implies intense turbulence–flame interaction which can approach a passive scalar in turbulence behaviour in certain circumstances. It was found that for large Da premixed flames, much unlike the passive scalar behaviour described above, the most extensive component of the principal strain rate aligns with the scalar gradient or the flame surface normal (Swaminathan and Grout 2006). This could be attributed to the strong flow acceleration effects opposite to the flame normal direction from heat release rates inducing $\partial u_j/\partial x_j \neq 0$. However, it was also showed that for small Da flames, the most extensive component of principal strain rate aligns with the tangents and the most compressive principal strain rate aligns with the normal (Xu et al. 2011; Chakraborty and Swaminathan 2007). Thus, at small Da, the passive scalar like behaviour is restored at least in terms of the strain rate–scalar gradient alignments. The alignment issues are important not only for the cascade which continuously removes large-scale inhomogeneity by preferential alignments and eventually through scalar dissipation rate but also the alignment leads to straining of the flame surface which increases the flame surface area and the mass flow rate of reactants that can pass and be consumed through the surface.

As discussed above, most of the investigations in the fundamental understanding of turbulent combustion followed a Eulerian approach, whereas modelling

approaches developed by Pope (1985) have utilized Lagrangian viewpoint, extensively. In a seminal paper, Pope (1988) laid down the rigorous foundations for analysing propagating surfaces using the concept of surface points. He defined (Pope 1988) "A *surface point* is defined, first, by its location on the surface at a reference initial time t_0; and, second, by the specification that it remains on the surface by moving relative to the fluid (if at all) in the direction of the local normal to the surface". This led to in-depth analysis in non-reacting turbulence in the early 90s which could be found in Girimaji and Pope (1992, 1990) and Yeung et al. (1990). To understand the fundamentals of turbulence–premixed flame interaction, Chaudhuri (2015a) introduced a Lagrangian viewpoint called Flame Particle Tracking (FPT) as a computational diagnostic on DNS data. Flame particles are surface points (Pope 1988; Hamlington et al. 2008) that always remain embedded on, by co-moving with a given iso-scalar surface within a premixed flame. Tracking flame particles allows one to study the fate of propagating surface locations uniquely identified throughout their evolution with time and to explore turbulence–flame interaction from the viewpoint of an observer roaming in turbulence, but locally attached to a reacting, propagating front. In particular, using forward and backward Flame Particle Tracking (FPT), the following are being explored: From where and how does the complex, convoluted structure of a turbulent flame generate and evolve in time? It has shown that despite flame particles and fluid particles being very different concepts, a modified Batchelor scaling law holds for flame particle pair dispersion (Chaudhuri 2015b). It has also shown how generalized flame speed versus stretch rate (Uranakara et al. 2016) and unified extinction characteristics could be obtained over a range of Reynolds and Damköhler numbers, from this Lagrangian viewpoint (Uranakara et al. 2017). Lagrangian diagnostic has revolutionized our understanding of fluid turbulence (Toschi and Bodenschatz 2009) and these recent works show that Lagrangian techniques like FPT can emerge as a powerful technique towards analysing turbulence–combustion interaction.

1.3 Simulation of Reactive Flows

In the foregoing, the gas-phase equations are expressed in the limit of low Mach number to remove the strong coupling between pressure and density fluctuations. The chemically reacting flows can be completely described by a set of coupled partial differential equations describing conservation of mass, momentum, species mass fractions and enthalpy (or internal energy or temperature). Here, we use the conservative form of the governing equations. For variable density flows, the instantaneous conservation equations for mass and momentum may be written as

$$\frac{\partial \rho}{\partial t} + \frac{\partial \left(\rho u_j\right)}{\partial x_j} = 0, \tag{1.11}$$

$$\frac{\partial (\rho u_i)}{\partial t} + \frac{\partial}{\partial x_j}\left(\rho u_i u_j\right) = -\frac{\partial p}{\partial x_i} + \frac{\partial \tau_{ij}}{\partial x_j}. \tag{1.12}$$

In Eq. (1.12), conservative form of the momentum equations is presented which is slightly different for momentum equations (c.f. Eq. (1.3)) for constant density incompressible flows. Also, the molecular diffusion terms are rewritten in terms of viscous stresses. The first term on the LHS of Eq. (1.12) is the local rate of change of momentum, while the second term represents the momentum advection. The first and second terms on the RHS represent the pressure gradient and viscous stress, respectively. The body force term is neglected in the momentum equation. For Newtonian fluids, the viscous stress tensor τ_{ij} can be represented as

$$\tau_{ij} = \mu\left(\frac{\partial u_i}{\partial x_j} + \frac{\partial u_j}{\partial x_i} - \frac{2}{3}\frac{\partial u_k}{\partial x_k}\delta_{ij}\right). \tag{1.13}$$

In the above equation, δ_{ij} is the kronecker delta ($\delta_{ij} = 1$ if $i = j$, 0 otherwise) and μ is the molecular viscosity.

For multicomponent reacting system, the transport equation for the mass fraction of the I-th species, Y_I, may be written as

$$\frac{\partial}{\partial t}(\rho Y_I) + \frac{\partial \left(\rho u_j Y_I\right)}{\partial x_j} = -\frac{\partial J_{I,j}}{\partial x_j} + \dot{\omega}_I. \tag{1.14}$$

In Eq. (1.14), the diffusional flux of species I is $J_{I,j} = -\rho \mathcal{D}_{Y_I} \frac{\partial Y_I}{\partial x_j}$, where $\mathcal{D}_{Y_I}$ is the diffusion coefficient of species I into the rest of the gas mixture. It is convenient to assume that diffusion coefficients of all species are equal ($\mathcal{D}_{Y_I} = \mathcal{D}$). Readers please note that diffusion coefficients are different for different species and lighter gas molecules diffuse faster than heavier molecules. Also, $\dot{\omega}_I$ is the volumetric reaction rate of the I-th species. Note that the diffusional flux of species is modelled based on molecular diffusion only. Species can also diffuse due to the gradients of temperature (Soret effect) and pressure (pressure diffusion) and forced diffusion. However, for most practical combustion systems, these effects are usually small and often neglected.

Multiple forms of energy equations are possible based on total internal energy, total enthalpy, internal energy, enthalpy, sensible enthalpy, sensible energy, etc. (c.f. Table 1.7 of Poinsot and Veynante 2012). In the foregoing, we only present transport equation for enthalpy:

$$\frac{\partial}{\partial t}(\rho h) + \frac{\partial(\rho u_j h)}{\partial x_j} = \frac{Dp}{Dt} + \tau_{ij}\frac{\partial u_i}{\partial x_j} - \frac{\partial J_{q,j}}{\partial x_j} + \dot{Q}. \tag{1.15}$$

The first term on the RHS is the total derivative of pressure, which can be neglected for open flames. For flows with small Mach number, spatial gradients of pressure vanish in the temperature equations. For reciprocating engines, the unsteady change of pressure is important and the term is retained. Here, $\dot{Q}$ is the heat source term due to electrical spark, laser or radiation flux, and $J_{q,j} = -\lambda\frac{\partial T}{\partial x_j} + \sum_{I=1}^{n_s} h_I J_{I,j}$ is the energy flux. Here, λ is the thermal conductivity of the gas mixture. Note that for most practical applications involving combustion, the heat flux due to the species mass fraction gradients (Dufour effect) is small and hence neglected. The energy transport equation may be simplified assuming unity Lewis number. Lewis number for species I is defined as the ratio of the thermal diffusivity and the mass diffusivity of species I:

$$Le_I = \frac{\alpha}{\mathcal{D}_I} = \frac{\lambda}{\rho c_p \mathcal{D}_I}. \tag{1.16}$$

Assuming unity Lewis number for all species, the enthalpy flux becomes $J_{q,j} = -\rho\mathcal{D}\frac{\partial h}{\partial x_j}$.

In addition to mass, momentum, species transport, and energy transport equations, a thermodynamic equation of state that gives density as a function of other thermodynamic variables is required to completely describe the system:

$$\rho = \frac{p}{R_u T}\left(\sum_{I=1}^{n_s}\frac{Y_I}{W_I}\right)^{-1}, \tag{1.17}$$

where R_u is the universal gas constant and W_I is the molecular weight of the I-th species.

In a chemically reacting system, the temperature may typically vary from 300 K (non-reacting mixture) to as high as up to 2500 K (reacting mixture). The transport properties, e.g. viscosity, thermal conductivity and mass diffusivity, vary over the entire temperature range. The molecular viscosity as a function of temperature may be obtained using Sutherland's law:

$$\mu = \mu_0\left(\frac{T}{T_0}\right)^{3/2}\frac{T_0 + S}{T + S}. \tag{1.18}$$

In the above expression, μ is the dynamic viscosity corresponding to the static temperature T. For air at moderate temperatures and pressures, $\mu_0 = 1.7894 \times 10^{-5}$ kg/m-s is the viscosity at reference temperature $T_0 = 273.11$ K and $S = 110.56$ K is an effective temperature. The variation in the specific heat, c_p, with temperature can be calculated from the JANAF tables which can be easily accessed from any standard combustion textbook (Turns 2012).

1.3.1 Chemical Reaction Rates

Chemical mechanisms for combustion often involve multiple reactions and multiple species. Consider a multistep chemical mechanism with n_s species reacting through n_r number of chemical reactions. A compact notation for this complex chemical mechanism may be written as

$$\sum_{I=1}^{n_s} \nu_{IJ}^{'} M_I \underset{k_J^{(r)}}{\overset{k_J^{(f)}}{\rightleftharpoons}} \sum_{I=1}^{n_s} \nu_{IJ}^{''} M_I \text{ for } J = 1, \ \ldots, \ n_r. \tag{1.19}$$

Here, M_I is the symbol for I-th chemical species, while $\nu_{IJ}^{'}$ and $\nu_{IJ}^{''}$ are the stoichiometric coefficients for the reactant and product side of the elementary reaction, respectively. The chemical reaction rate, $\dot{\omega}_I$, which is primarily a function of concentration and temperature of the contributing species is expressed by the following equation:

$$\dot{\omega}_I = W_I \sum_{J=1}^{n_r} \left(\nu_{IJ}^{''} - \nu_{IJ}^{'}\right) \left(k_J^{(f)} \prod_{I=1}^{n_s} \left(\frac{X_I p}{R_u T}\right)^{\nu_{IJ}^{'}} - k_J^{(r)} \prod_{I=1}^{n_s} \left(\frac{X_I p}{R_u T}\right)^{\nu_{IJ}^{''}} \right), \text{ where } J = 1, \ \ldots, \ n_r. \tag{1.20}$$

In Eq. (1.20), $k_J^{(f)}$ and $k_J^{(r)}$ are the forward and reverse reaction rate constants for the J-th reaction in a multistep chemical mechanism, respectively. Also, the mole fraction of I-th species is $X_I = \frac{Y_I W_{\text{mix}}}{W_I}$, and the molecular weight of the mixture is $W_{\text{mix}} = \left(\sum_{I=1}^{n_s} \frac{Y_I}{W_I}\right)^{-1}$. The Arrhenius rate laws are used for the elementary reaction rate constant:

$$k_J^{(f)}(T) = A_J^{(f)} T^{b_J} \exp\left(- \frac{E_{a,J}^{(f)}}{R_u T} \right). \tag{1.21}$$

Here, $A_J^{(f)}$ is the pre-exponential factor, b_J is the temperature exponent and $E_{a,J}^{(f)}$ is the activation energy. The elementary reaction rates for the reverse reaction are calculated from reaction rates of the forward reactions and equilibrium constants:

$$k_J^{(r)} = \frac{k_J^{(f)}}{K_{c_J}}, \tag{1.22}$$

where K_{c_J} is the equilibrium constant, which is a function of temperature.

1.4 Reynolds-Averaged Navier–Stokes of Reactive Flows

Unfortunately, the full solution of the instantaneous balance equations (Eqs. 1.11, 1.12, 1.14 and 1.15) is restricted to very simple and canonical flow configurations, where the number of timescales and length scales present are very few. Direct solution of instantaneous balance equations is referred to as DNS, where no modelling is required as the smallest scales of the flow are resolved. However, DNS becomes computationally prohibitive for engineering applications due to the requirement of high CPU time. Therefore, averaging techniques and simplifications become necessary to reduce the computational costs. However, averaging leads to several new or 'unclosed' terms. Special models are then developed to close the problem. Reynolds-averaged (or Favre-averaged) Navier–Stokes (RANS) method describes the time-averaged (or density-weighted averaged) quantities of the flow field. In RANS approach, the effects of the fluctuating variables are usually modelled either by a turbulent viscosity model or by Reynolds stress model (RSM). Among the turbulent viscosity models, the k-ε model (Launder and Spalding 1974) is most widely used.

1.4.1 Averaging and Averaged Equations

In RANS approach, any scalar, vector or tensor field $\phi(\mathbf{x};t)$ is decomposed into its mean and fluctuating components. The mean field may be determined by averaging the field $\phi(\mathbf{x};t)$ over a sufficiently long time interval, or by defining an ensemble of statistically equivalent realizations of a stochastic process. When averaging is performed over a sufficiently long time interval, the mean field $\overline{\phi}(\mathbf{x}) = \lim_{(t_2-t_1)\to\infty} \frac{1}{(t_2-t_1)} \sum_{t=t_1}^{t_2} \phi(x;t)$ does not vary with time. Taking average over time is most convenient because time averages are simple to visualize and have a clear physical interpretation. Time averaging is applicable only for a statistically stationary process. However, they are meaningful only if the turbulence is statistically steady. There are other types of averages commonly used, namely the ensemble average and the volume average. For transient and spatially non-uniform mean flows, such as combustion in piston engine undergoing cyclic variation, ensemble averaged quantities are commonly used. In such a case, mean field $\phi(\mathbf{x};t) = \lim_{N\to\infty} \frac{1}{N} \sum_{i=1}^{N} \phi(\mathbf{x};t)$ denotes an ensemble of fields, where N is the number of experiments. The ensemble average at any spatial location may vary with time. Under certain conditions, if the averaging methods (time and ensemble) described above are applied to the same field $\phi(\mathbf{x};t)$ or the same ensemble of fields, the mean field remains the same. Even when a time average is not meaningful, the ensemble average can still be defined, e.g. non-stationary or periodic flow. Only ensemble averages will be used in the development of the turbulence equations here unless otherwise stated. Another type of averaging is based on spatial average. Spatial averaging is most suitable for a statistically 1D process, e.g. a

spherical flame in homogeneous turbulence observed after spark ignition. In such a case, mean field depends on the radial coordinate only.

In RANS approach, the averaged quantities of the flow field are solved and the scales smaller than the grid size are modelled. Transport equations for the mean flow variable are obtained after applying ensemble averaging or density-weighted (or Favre) averaging to the instantaneous transport equations. In Reynolds averaging, a quantity ϕ of the flow field is split into a mean $\overline{\phi}$ and a fluctuation from the mean, ϕ' as $\phi = \overline{\phi} + \phi'$ with $\overline{\phi'} = 0$. The transport equations for the mean quantity $\overline{\phi}$ may be obtained by applying ensemble average to the instantaneous balance equations with the above decomposition to the instantaneous variables. For flows with large density variations, the concept of density (or mass) weighted average, called the Favre average $\widetilde{\phi} = \overline{\rho\phi}/\overline{\rho}$, is often preferred over the conventional Reynolds averaging technique. In Favre averaging, any instantaneous quantity ϕ is decomposed into its Favre average ($\widetilde{\phi}$) and fluctuations about the Favre average (ϕ'') as $\phi = \widetilde{\phi} + \phi''$ with a requirement of $\overline{\rho\phi''} = 0$.

Favre averaging is often preferred over the conventional Reynolds averaging as the former offers considerable advantages in simplifying the derivation of the averaged Navier–Stokes equations for flows with large density change. The nonlinear advection terms appearing in the transport equations for momentum, energy and chemical species contain products of density, velocity and the dependent variables. Favre averaging is often preferred for these terms. For instance, the classical Reynolds averaging technique, widely used in the non-reacting fluid mechanics, brings terms with unclosed correlations:

$$\overline{\rho u\phi} = \overline{\rho}\,\overline{u}\,\overline{\phi} + \overline{\rho}\overline{u'\phi'} + \overline{\rho' u'}\,\overline{\phi} + \overline{\rho'\phi'}\,\overline{\mathrm{u}} + \overline{\rho' u'\phi'}. \tag{1.23}$$

While using Favre average, one gets

$$\overline{\rho u\phi} = \overline{\rho(\tilde{u} + u'')\left(\widetilde{\phi} + \phi''\right)} = \overline{\rho}\tilde{\mathrm{u}}\widetilde{\phi} + \widetilde{\rho u''\phi''}. \tag{1.24}$$

Note that in Eq. (1.24) density fluctuations do not appear explicitly. This expression is simpler than the one written in terms of time averages in Eq. (1.23). Moreover, the expression appearing in Eq. (1.24) retains the familiar form of the conventional average of $u\phi$ for constant density flows: $\overline{u\phi} = \overline{u}\,\overline{\phi} + \overline{u'\phi'}$.

With the usual notation, the Favre-averaged conservation equations for variable density, reactive flows are provided in this section.

Mass conservation equation:

$$\frac{\partial \overline{\rho}}{\partial t} + \frac{\partial\left(\overline{\rho}\widetilde{u_j}\right)}{\partial x_j} = 0 \tag{1.25}$$

Momentum conservation equation:

$$\frac{\partial \overline{\rho}\widetilde{u}_i}{\partial t} + \frac{\partial \overline{\rho}\widetilde{u}_i\overline{u}_j}{\partial x_j} = -\frac{\partial \overline{p}}{\partial x_i} + \frac{\partial}{\partial x_j}\left(\overline{\tau}_{ij}\right) - \frac{\partial\left(\overline{\rho}\widetilde{u_i^{''}u_j^{''}}\right)}{\partial x_j} \tag{1.26}$$

Species transport equation:

$$\frac{\partial}{\partial t}\left(\overline{\rho}\widetilde{Y}_I\right) + \frac{\partial}{\partial x_j}\left(\overline{\rho}\widetilde{u}_j\widetilde{Y}_I\right) = \frac{\partial}{\partial x_j}\left(\overline{\rho\mathcal{D}\frac{\partial Y_I}{\partial x_j}}\right) - \frac{\partial\left(\overline{\rho}\widetilde{u_j^{''}Y_I^{''}}\right)}{\partial x_j} + \overline{\dot{\omega}_I} \tag{1.27}$$

Enthalpy transport equation:

$$\frac{\partial}{\partial t}\left(\overline{\rho}\widetilde{h}\right) + \frac{\partial}{\partial x_j}\left(\overline{\rho}\widetilde{u}_j\widetilde{h}\right) = \frac{D\overline{p}}{Dt} + \frac{\partial}{\partial x_j}\left(\overline{\rho\mathcal{D}\frac{\partial h}{\partial x_j}}\right) - \frac{\partial\left(\overline{\rho}\widetilde{u_j^{''}h^{''}}\right)}{\partial x_j} + \overline{u_j\frac{\partial \tau_{ij}}{\partial x_j}} + \overline{\dot{Q}} \tag{1.28}$$

In the above equations, mean pressure is $\overline{p}$ and mean density is $\overline{\rho}$. The mean viscous stress tensor is given by

$$\overline{\tau}_{ij} = \mu\left(\frac{\partial \widetilde{u}_i}{\partial x_j} + \frac{\partial \widetilde{u}_j}{\partial x_i} - \frac{2}{3}\frac{\partial \widetilde{u}_k}{\partial x_k}\delta_{ij}\right). \tag{1.29}$$

There are several unclosed terms in the above equations (Eqs. 1.26–1.28) which require modelling. The last term on the RHS of Eq. (1.26) is Reynold's stress term $(\overline{\rho}\widetilde{u_i^{''}u_j^{''}})$ that requires a closure model. The Favre-averaged species and enthalpy transport equations also contain unclosed turbulent transport terms of species and enthalpy fluxes, $\overline{\rho}\widetilde{u_j^{''}Y_I^{''}}$ and $\overline{\rho}\widetilde{u_j^{''}h^{''}}$. The closure of the turbulent transport terms of scalars is discussed in Sect. 1.4.2. The last term on the RHS of Eq. (1.27) is the mean source term due to chemical reactions. This term is a highly nonlinear function of temperature and species mass fractions, and poses the greatest difficulty in developing closure models. In Sect. 1.6, various turbulent combustion models are briefly discussed.

1.4.2 Turbulence Model

Following the turbulence viscosity assumption proposed by Boussinesq (Hinze 1975), the Reynolds stresses $\overline{\rho}\widetilde{u_i^{''}u_j^{''}}$ are generally described using the viscous stress tensor τ_{ij} as

$$\overline{\rho}\widetilde{u_i^{''}u_j^{''}} = -\mu_t\left(\frac{\partial \widetilde{u}_i}{\partial x_j} + \frac{\partial \widetilde{u}_j}{\partial x_i} - \frac{2}{3}\delta_{ij}\frac{\partial \widetilde{u}_k}{\partial x_k}\right) + \frac{2}{3}\overline{\rho}\widetilde{k}\delta_{ij}, \tag{1.30}$$

where $\widetilde{k} = \frac{1}{2}\widetilde{u_k'' u_k''}$ is the Favre-averaged turbulent kinetic energy. The unknown terms appearing in the Favre-averaged momentum equations (Reynolds stress terms) pose the well-known closure problem of turbulence. In RANS approach, the turbulent viscosity μ_t may be obtained either by solving an algebraic relation or by solving modelled transport equations for turbulent quantities such as turbulent kinetic energy and its dissipation rate. In RSM, the modelled transport equations are solved for each component of the Reynolds stress $\overline{\rho}\widetilde{u_i'' u_j''}$ and for the dissipation rate of turbulent kinetic energy $\widetilde{\varepsilon}$, which provides the information related to the length and timescales of turbulence (Pope 2000).

Turbulent viscosity μ_t appearing in Eq. (1.30) needs to be evaluated. In literature, three different approaches exist for the closure of turbulent viscosity term: algebraic equations or zero-equation model, one-equation model and two-equation model. Zero-equation model does not need solution of additional transport equation. It is based on Prandtl's mixing length model $\mu_t = \rho l_m^2 |\widetilde{\tau}|$, where the mixing length l_m depends on the flow geometry which is obtained from the empirical relations. In one-equation model, additional transport equation for turbulent kinetic energy is solved and turbulent viscosity is modelled as $\mu_t = \rho C_\mu l_{pk} \sqrt{k}$. Here, l_{pk} is a characteristic length scale which is evaluated using empirical relationship and $C_\mu = 0.09$ is a model constant. Here, most widely used two-equation model (Jones and Launder 1972), namely k-ε turbulence model is discussed briefly. In k-ε model, the turbulent viscosity is modelled in terms of turbulent kinetic energy $\widetilde{k}$ and its dissipation rate $\widetilde{\varepsilon}$ as $\mu_t = \overline{\rho} C_\mu \frac{\widetilde{k}^2}{\widetilde{\varepsilon}}$. Additional transport equations for $\widetilde{k}$ and $\widetilde{\varepsilon}$ are solved (Jones and Launder 1972).

Turbulent kinetic energy equation:

$$\frac{\partial \overline{\rho}\widetilde{k}}{\partial t} + \frac{\partial\left(\overline{\rho}\widetilde{u_j}\widetilde{k}\right)}{\partial x_j} = \frac{\partial}{\partial x_j}\left[\left(\mu + \frac{\mu_t}{\sigma_k}\right)\frac{\partial \widetilde{k}}{\partial x_j}\right] + P - \overline{\rho}\widetilde{\varepsilon} \tag{1.31}$$

Dissipation rate of turbulent kinetic energy equation:

$$\frac{\partial \overline{\rho}\widetilde{\varepsilon}}{\partial t} + \frac{\partial\left(\overline{\rho}\widetilde{u_j}\widetilde{\varepsilon}\right)}{\partial x_j} = \frac{\partial}{\partial x_j}\left[\left(\mu + \frac{\mu_t}{\sigma_\varepsilon}\right)\frac{\partial \widetilde{\varepsilon}}{\partial x_j}\right] + C_{\varepsilon 1}\frac{\widetilde{\varepsilon}}{\widetilde{k}}P - C_{\varepsilon 2}\overline{\rho}\frac{\widetilde{\varepsilon}^2}{\widetilde{k}} \tag{1.32}$$

The production of the turbulent kinetic energy due to the mean velocity gradient is defined as

$$P = -\overline{\rho}\widetilde{u_i'' u_j''}\frac{\partial \widetilde{u_i}}{\partial x_j} \tag{1.33}$$

The k–ε model involves several model constants. Standard values of these model constants are provided below (Pope 1988; Jones and Launder 1972):

$$C_\mu = 0.09,\ \sigma_k = 1,\ \sigma_\varepsilon = 1.3,\ C_{\varepsilon 1} = 1.44,\ C_{\varepsilon 2} = 1.92.$$

Turbulent fluxes of scalars (e.g. $\overline{\rho} \widetilde{u_j'' Y_I''}, \overline{\rho} \widetilde{u_j'' h''}$) are usually calculated using the classical gradient assumption:

$$\overline{\rho} \widetilde{u_j'' Y_I''} = -\frac{\mu_t}{Sc_t} \frac{\partial \widetilde{Y}_I}{\partial x_j}, \tag{1.34}$$

$$\overline{\rho} \widetilde{u_j'' h} = -\frac{\mu_t}{Pr_t} \frac{\partial \widetilde{h}}{\partial x_j}, \tag{1.35}$$

where Sc_t and Pr_t are the turbulent Schmidt number and Prandtl number, generally taken as 0.7.

1.4.3 Transport of Non-reactive Scalars

In turbulent combustion, transport of an inert scalar is often needed to describe the mixing between streams. In this section, transport equations of mean and variance of an inert scalar, namely mixture fraction, are presented. Mixture fraction is a conserved scalar, which has been routinely used for simulations of turbulent non-premixed combustion based on presumed PDF approach. The mixture fraction may be defined as the fraction of mass of material having its origin in the fuel stream (Bilger 1976; Peters 1984). Statistical description of turbulent combustion is possible by using a presumed shape of PDF. In turbulent non-premixed combustion, the PDF of mixture fraction $\widetilde{P}(Z)$ is commonly used. Standard β-function parametrized by the mean and variance of mixture fraction ($\widetilde{Z}, \widetilde{Z''^2}$) is used for $\widetilde{P}(Z)$. Additional balance equations for $\widetilde{Z}, \widetilde{Z''^2}$ need to be solved at all physical locations at all time in order to fully describe the mixing field.

Starting from the instantaneous transport equation of mixture fraction

$$\frac{\partial(\rho Z)}{\partial t} + \frac{\partial(\rho u_j Z)}{\partial x_j} = \frac{\partial}{\partial x_j}\left(\rho \mathcal{D} \frac{\partial Z}{\partial x_j}\right), \tag{1.36}$$

and using the decomposition $Z = \widetilde{Z} + Z''$, one can obtain the transport equation for the Favre mean mixture fraction as follows:

$$\frac{\partial(\bar{\rho}\widetilde{Z})}{\partial t}+\frac{\partial(\bar{\rho}\tilde{u}_j\widetilde{Z})}{\partial x_j}=\frac{\partial}{\partial x_j}\left(\bar{\rho}\widetilde{\mathcal{D}}\frac{\partial\widetilde{Z}}{\partial x_j}\right)-\frac{\partial}{\partial x_j}\left(\bar{\rho}\widetilde{u_j''Z''}\right). \tag{1.37}$$

The scalar flux ($\widetilde{\overline{\rho}u_j''Z''}$) term arising out of the averaging process is usually modelled using the standard gradient transport assumption for non-reacting scalars: $\widetilde{\overline{\rho}u_j''Z''}=-\bar{\rho}\widetilde{\mathcal{D}}_t\frac{\partial\widetilde{Z}}{\partial x_j}$ Here, the turbulent diffusivity is modelled by analogy to the eddy viscosity as $\mathcal{D}_t=\frac{\mu_t}{\mathrm{Sc}_t}$. A transport equation for $\widetilde{Z''^2}$ may be derived by algebraic manipulations as

$$\frac{\partial(\bar{\rho}\widetilde{Z''^2})}{\partial t}+\frac{\partial(\bar{\rho}\tilde{u}_j\widetilde{Z''^2})}{\partial x_j}=\frac{\partial}{\partial x_j}\left(\bar{\rho}\widetilde{\mathcal{D}}\frac{\partial\widetilde{Z''^2}}{\partial x_j}\right)-\frac{\partial}{\partial x_j}\left(\bar{\rho}\widetilde{u_j''Z''^2}\right)-2\bar{\rho}\widetilde{u_j''Z''}\frac{\partial\widetilde{Z}}{\partial x_j}-\bar{\rho}\tilde{\chi}. \tag{1.38}$$

The first and second terms on the RHS are the molecular diffusion and the turbulent transport term of $\widetilde{Z''^2}$, respectively. The turbulent transport of mixture fraction variance is modelled using the standard gradient transport assumption. The third term on the RHS is the production term of the mixture fraction variance. The production term after substitution of the scalar flux becomes $-\bar{\rho}\widetilde{u_j''Z''}\frac{\partial\widetilde{Z}}{\partial x_j}=\bar{\rho}\widetilde{\mathcal{D}}_t\left(\frac{\partial\widetilde{Z}}{\partial x_j}\right)^2$. The last term of Eq. (1.38) is the scalar dissipation rate which is $\tilde{\chi}=2\widetilde{\mathcal{D}\left(\frac{\partial Z}{\partial x_j}\right)^2}$, which measures the decay of the mixture fraction fluctuations. The scalar dissipation rate term may be modelled by assuming the mixing timescale $\tau_Z=\frac{\widetilde{Z''^2}}{\tilde{\chi}}$ is proportional to the turbulence timescale $\tau_t=c_\chi\tau_Z$, where the turbulence timescale may be modelled as $\tau_t=\widetilde{k}/\widetilde{\varepsilon}$ within the RANS framework. These relationships yield $\bar{\chi}=c_\chi\frac{\widetilde{\varepsilon}}{\widetilde{k}}\widetilde{Z''^2}$. The value of the scalar dissipation rate constant c_χ is often taken as 2.

1.4.4 Transport of Reactive Scalars

In many premixed combustion systems, combustion takes place in a thin flame sheet. In premixed combustion model, the reacting flow field is subdivided into regions of burnt and unburnt mixtures, separated by the flame sheet. The progress of the flame is, therefore, the same as the progress of the flame front. The flame front propagation may be modelled by solving a transport equation of a reactive scalar, namely reaction progress variable c. Different definitions of c are used in the literature, such as $c=(T-T_u)/(T_b-T_u)$, where T_u and T_b are temperatures of the unburnt and burnt gas mixtures, respectively. Also, $c=Y_P/Y_{P,eq}$ is used, where 'P'

denotes product species (CO_2, H_2O, CO and H_2) and '*eq*' denotes equilibrium composition. Based on this definition, we have $c = 0$ for the unburnt mixture and $c = 1$ for the burnt mixture. The balance equation of instantaneous reaction progress variable may be written as

$$\frac{\partial}{\partial t}(\rho c) + \frac{\partial(\rho u_j c)}{\partial x_j} = \frac{\partial}{\partial x_j}\left(\rho \mathcal{D} \frac{\partial c}{\partial x_j}\right) + \dot{\omega}_C = \rho S_d \left|\frac{\partial c}{\partial x_j}\right|. \tag{1.39}$$

Note that two different forms of c equation are possible. Here, S_d denotes the flame front displacement speed. Starting from Eq. (1.39) and using the decomposition $c = \widetilde{c} + c''$, one can obtain the transport equations for the Favre mean and variance of reaction progress variable ($\widetilde{c}, \widetilde{c''^2}$) as

$$\frac{\partial \overline{\rho}\widetilde{c}}{\partial t} + \frac{\partial\left(\overline{\rho}\widetilde{u}_j\widetilde{c}\right)}{\partial x_j} = \frac{\partial}{\partial x_j}\left(\overline{\rho}\widetilde{\mathcal{D}}\frac{\partial \widetilde{c}}{\partial x_j}\right) - \frac{\partial}{\partial x_j}\left(\overline{\rho}\widetilde{u_j'' c''}\right) + \overline{\dot{\omega}_c} = \overline{\rho S_d \left|\frac{\partial c}{\partial x_j}\right|}, \tag{1.40}$$

$$\begin{aligned}
&\frac{\partial \overline{\rho}\widetilde{c''^2}}{\partial t} + \frac{\partial\left(\overline{\rho}\widetilde{u}_j\widetilde{c''^2}\right)}{\partial x_j} \\
&= \frac{\partial}{\partial x_j}\left(\overline{\rho}\widetilde{\mathcal{D}}\frac{\partial \widetilde{c''^2}}{\partial x_j}\right) - \frac{\partial}{\partial x_j}\left(\overline{\rho}\widetilde{u_j'' c''^2}\right) - 2\overline{\rho}\widetilde{u_j'' c''}\frac{\partial \widetilde{c}}{\partial x_j} \\
&+ \overline{2c'' \frac{\partial}{\partial x_j}\left(\rho \mathcal{D}\frac{\partial c}{\partial x_j}\right)} + 2\overline{c'' \dot{\omega}_c}.
\end{aligned} \tag{1.41}$$

In Eq. (1.41), the first two terms on the RHS are molecular diffusion and the turbulent transport of reaction progress variable, respectively. The scalar flux may be again modelled using the standard gradient transport assumption. The third term on the RHS is the production term of the reaction progress variable.

The spatial and temporal resolutions needed for the RANS approach are lesser than those needed for the LES and DNS, which has allowed widespread use of RANS for the industrial applications on turbulent reacting flows. Unfortunately, many unsteady phenomena, such as flame extinction, re-ignition cannot be captured by the RANS approach. Moreover, the accuracy of numerical predictions depends largely on the validity of the model employed and varies from one problem to another.

1.5 Large Eddy Simulation of Reactive Flows

LES falls in between RANS and DNS approaches. It does not resolve all the length scales of a turbulent flow; it only resolves a fraction of the energy-containing scales within the inertial subrange and models the smaller unresolved or subgrid scales,

which contain only a small fraction of turbulent kinetic energy (Pitsch 2006). Direct effects of the small-scale fluctuations are removed by applying a spatial filter to the instantaneous governing equations. The effects of small-scale fluctuations are indirectly modelled using subgrid-scale closures. LES is less demanding in terms of requirement of computational resources in comparison with DNS, as the latter attempts to resolve all length scales of a turbulent flow. The application of LES for practical combustion problems is yet difficult as it is computationally expensive. However, it has been successfully applied for turbulent flames (Mahesh et al. 2006). With an increase in the hardware and software capability over the last decades, LES is finding more and more applications in combustion simulations of real engines.

1.5.1 Filtering Operation

In LES, variables are filtered in the spectral or in the physical space. For variable density case, a density-weighted filter is introduced:

$$\overline{\rho}\widetilde{\phi}(\mathbf{x},t) = \int_{-\infty}^{+\infty} \rho\phi(\mathbf{x}',t)F(\mathbf{x}'-\mathbf{x})d\mathbf{x}', \tag{1.42}$$

where the unfiltered quantity is $\phi = \widetilde{\phi} + \phi''$. The filtered quantity $\widetilde{\phi} = \overline{\rho\phi}/\overline{\rho}$ is resolved in numerical simulations, whereas ϕ'' corresponds to the unresolved (i.e. the subgrid-scale) part. The LES filter should have the following three qualities:

(i) Consistency: the filter function F (appearing in Eq. 1.42) should satisfy the following requirement:

$$\int_{-\infty}^{+\infty} \rho(\mathbf{x}',t)F(\mathbf{x}'-\mathbf{x})d\mathbf{x}' = \overline{\rho}(x,t); \tag{1.43}$$

(ii) Linearity: $\overline{\phi_1+\phi_2} = \overline{\phi_1} + \overline{\phi_2}$, which is satisfied by the convolution form of filtering;

(iii) Commutation with differentiation: $\frac{\overline{\partial\phi}}{\partial\mathbf{x}} = \frac{\partial\bar{\phi}}{\partial\mathbf{x}}, \frac{\overline{\partial\phi}}{\partial t} = \frac{\partial\bar{\phi}}{\partial t}$.

Balance equations for the filtered variables are obtained by filtering the instantaneous balance equations. In LES, the filtered value of a LES perturbation is not zero, i.e. $\widetilde{\phi''} \neq 0$ and $\widetilde{\widetilde{\phi}} \not\approx \widetilde{\phi}$. Strictly speaking, the derivation of transport equations for the filtered quantity requires the exchange of filter and derivative operators, which is applicable only when the filter size which corresponds to the mesh size does not change spatially and temporally. However, the uncertainties associated

with the operator exchange are usually neglected and their effects are assumed to be reflected via subgrid-scale models.

1.5.2 Filtered Navier–Stokes Equations

The filtered Navier–Stokes equations can be written as

$$\frac{\partial \overline{\rho}}{\partial t} + \frac{\partial \left(\overline{\rho}\widetilde{u_j}\right)}{\partial x_j} = 0, \tag{1.44}$$

$$\frac{\partial \overline{\rho}\widetilde{u_i}}{\partial t} + \frac{\partial}{\partial x_j}\left(\overline{\rho}\widetilde{u_i}\widetilde{u_j}\right) = -\frac{\partial \overline{\rho}}{\partial x_i} + \frac{\partial}{\partial x_j}\left(2\overline{\mu}\widetilde{\tau}_{ij}\right) - \frac{\partial \tau_{ij}^{\text{sgs}}}{\partial x_j}. \tag{1.45}$$

In the above equations, the density-weighted filtered velocity is $\widetilde{u_i}$, and the filtered density and pressure are $\overline{\rho}$ and $\overline{p}$, respectively. In the filtered momentum equation (Eq. 1.45), the filtered strain rate tensor is given as $\widetilde{\tau}_{ij} = \frac{1}{2}\left(\frac{\partial \widetilde{u_j}}{\partial x_i} + \frac{\partial \widetilde{u_i}}{\partial x_j}\right)$ and sub-filter stresses are denoted as $\tau_{ij}^{\text{sgs}} = \overline{\rho u_i u_j} - \overline{\rho}\widetilde{u_i}\widetilde{u_j}$. The sub-filter stresses need a closure model. For closure of τ_{ij}^{sgs}, again an eddy viscosity type subgrid-scale (SGS) model is used: $\tau_{ij}^{\text{sgs}} = -2\mu_{\text{sgs}}\widetilde{\tau}_{ij}$. The eddy viscosity is modelled as the product of a characteristic length scale $l = \Delta$ (which represents the largest size of the unresolved scales) and a characteristic velocity scale, $q = l||\widetilde{\tau}_{ij}||$, where $||\widetilde{\tau}_{ij}|| = \sqrt{2\widetilde{\tau}_{ij}\widetilde{\tau}_{ij}}$. This leads to $\mu_{\text{sgs}} = \overline{\rho}(C_S\Delta)^2||\widetilde{\tau}_{ij}||$.

1.5.2.1 Smagorinsky Model

The Smagorinsky model contains a dimensionless empirical parameter, C_S, and the SGS stress tensor becomes

$$\tau_{ij}^{\text{sgs}} = -2\overline{\rho}(C_S\Delta)^2||\widetilde{\tau}_{ij}||\widetilde{\tau}_{ij}. \tag{1.46}$$

which typically has a value 0.1–0.2. This model is known as Smagorinsky–Lilly model, which assumes that the energy production and dissipation of the small scales are in equilibrium. The classical model predicts many flows reasonably well. However, problems are encountered during determination of an optimum value for C_S, which varies with flow type, e.g. for isotropic flows at high Reynolds number, $C_S \approx 0.16$ is typically used, whereas for the shear flows $C_S \approx 0.065$ is used. Moreover, difficulty is encountered for definition of length scale for an anisotropic filter. Typically, the length scale is modelled either as $(\Delta_1\Delta_2\Delta_3)^{1/3}$ or $\left(\Delta_1^2 + \Delta_2^2 + \Delta_3^2\right)^{1/2}$. The above problems may be overcome either by dynamically

determining the value of $C_S = C_S(\mathbf{x}, t)$, or by solving transport equations for relevant quantities, say subgrid kinetic energy k_{sgs}. In particular, solving the transport equation for k_{sgs} allows a much better estimation of the velocity scale for the SGS fluctuations.

1.5.2.2 Dynamic Smagorinsky Model

Dynamic Smagorinsky model of Germano et al. (1991) for sub-filter stresses are briefly discussed in this section. In the case of filtered Navier–Stokes and LES, the Germano identity (Germano et al. 1991) is usually written as $T_{ij} = \mathcal{L}_{ij} + \widehat{\tau}_{ij}$, where the resolved turbulent stress (often known as Leonard stress) tensor is $\mathcal{L}_{ij} = \widehat{\overline{\rho}\widetilde{u}_i\widetilde{u}_j} - \frac{1}{\widehat{\overline{\rho}}}\left(\widehat{\overline{\rho}\widetilde{u}_i}\widehat{\overline{\rho}\widetilde{u}_j}\right)$ and the residual stress tensor for the test filter scale is $T_{ij} = \widehat{\overline{\rho u_i u_j}} - \frac{1}{\widehat{\overline{\rho}}}\left(\widehat{\overline{\rho u_i}}\,\widehat{\overline{\rho u_j}}\right)$. The Germano identity is exact and holds at every point in the flow at all times. The dynamic Smagorinsky model is based on the Germano identity. Assuming scale invariance, i.e. C_S, is the same at the grid filter Δ and at the test filter levels $\widehat{\Delta}$ and that C_S does not change rapidly in directions over which the test filter acts, the following relationship may be obtained from Germano identity after expressing the tensors τ and T using Eq. 1.46 at scales Δ and $\widehat{\Delta}$:

$$C_s^2 \mathcal{M}_{ij} = \mathcal{L}_{ij}, \text{ where } \mathcal{M}_{ij} = -2\left(\widehat{\Delta}^2\widehat{\overline{\rho}}\left\|\widehat{\widetilde{\tau}}_{ij}\right\|\widehat{\widetilde{\tau}}_{ij} - \Delta^2\overline{\rho}\widehat{\|\widetilde{\tau}_{ij}\|\widetilde{\tau}_{ij}}\right). \tag{1.47}$$

The ratio of test filter size to grid filter size is proposed as $\kappa = \frac{\widehat{\Delta}}{\Delta} = 2$ by Germano (1989), and $\kappa = \sqrt{5}$ is proposed by Vreman et al. (1997). Lilly (1992) used a minimum least-square error method, which leads to an equation for C_S:

$$C_S^2 = \frac{\mathcal{L}_{ij}\mathcal{M}_{ij}}{\mathcal{M}_{ij}\mathcal{M}_{ij}}. \tag{1.48}$$

However, when the numerator becomes negative, this procedure becomes numerically unstable and large fluctuations in C_S are often observed. An additional averaging for the minimization of the error is often performed, which leads to

$$C_S^2 = \frac{\langle \mathcal{L}_{ij}\mathcal{M}_{ij} \rangle}{\langle \mathcal{M}_{ij}\mathcal{M}_{ij} \rangle}. \tag{1.49}$$

In order to prevent numerical instability caused by negative values of C_s^2, the numerator and denominator are averaged (angular brackets represent averaging) over homogeneous flow directions (Germano et al. 1991). In the absence of a homogeneous flow direction, some form of local averaging may be used. Meneveau et al. (1996) proposed an averaging method based on the fluid imaginary particle trajectory following a Lagrangian framework. This approach is particularly suitable

for complex geometries. One assumption in the formulation above is that variations of C_S on the scale of the test filter are small.

1.5.3 Transport Equations for Filtered Reactive Scalars

The transport equations for filtered species mass fractions and enthalpy may be obtained by applying density-weighted filtering to the instantaneous transport equations for species mass fractions and enthalpy:

$$\frac{\partial \overline{\rho}\widetilde{Y}_I}{\partial t} + \frac{\partial\left(\overline{\rho}\widetilde{u}_i\widetilde{Y}_I\right)}{\partial x_j} = \frac{\partial}{\partial x_j}\left(\overline{\rho}\widetilde{\mathcal{D}}\frac{\partial \widetilde{Y}_I}{\partial x_j}\right) - \frac{\partial q_{Y_I}}{\partial x_j} + \overline{\omega}_{Y_i}, \tag{1.50}$$

$$\frac{\partial \overline{\rho}\widetilde{h}}{\partial t} + \frac{\partial\left(\overline{\rho}\widetilde{u}_i\widetilde{h}\right)}{\partial x_j} = \frac{\partial}{\partial x_j}\left(\overline{\rho}\widetilde{\mathcal{D}}\frac{\partial \widetilde{h}}{\partial x_j}\right) - \frac{\partial q_h}{\partial x_j}. \tag{1.51}$$

The second terms on the RHS of Eqs. 1.50 and 1.51 are the subgrid scalar fluxes. For scalar $\phi = \left\{\widetilde{Y}_I, \widetilde{h}\right\}$, the subgrid scalar flux may be modelled as

$$q_\phi = \overline{\rho}\widetilde{u_j\phi} - \overline{\rho}\widetilde{u}_j\widetilde{\phi} = -\overline{\rho}\mathcal{D}_{t,\phi}\frac{\partial \widetilde{\phi}}{\partial x_j}, \tag{1.52}$$

where the SGS diffusivity $\mathcal{D}_{t,\phi} = C_\phi \Delta^2 ||\widetilde{\tau}_{ij}||$. The constant C_ϕ may be determined following the dynamic Smagorinsky model. The closure of the filtered chemical source term $(\overline{\omega}_{Y_i})$ requires numerical model.

1.5.4 Subgrid-Scale Model for Turbulent Mixing

We present here a simple SGS model proposed to describe unresolved fluctuations in mixture composition. In LES, a subgrid-scale model for turbulent mixing is needed to describe mixing and chemical reactions. Similar to RANS for non-premixed combustion, a β-function, parameterized by the first two moments of mixture fraction, is usually used for the marginal filtered density function (FDF) of mixture fraction, $\widetilde{P}(Z;\mathbf{x},t)$. The filtered mixture fraction $\widetilde{Z}$ is determined by the solution of a transport equation, whereas the sub-filter scalar variance $\widetilde{Z''^2}$ is determined either by using an algebraic model or by solving a transport equation.

Starting from the transport equation for the instantaneous mixture fraction (Eq. 1.36), the transport equation for the density-weighted filtered mixture fraction may be derived as

$$\frac{\partial \overline{\rho}\widetilde{Z}}{\partial t}+\frac{\partial}{\partial x_j}\left(\overline{\rho}\widetilde{u_i}\widetilde{Z}\right)=\frac{\partial}{\partial x_j}\left(\overline{\rho}\widetilde{\mathcal{D}}\frac{\partial \widetilde{Z}}{\partial x_j}\right)-\frac{\partial q_Z}{\partial x_j}, \tag{1.53}$$

where the SGS flux of mixture fraction q_Z is modelled as

$$q_Z=\overline{\rho}\widetilde{u_jZ}-\overline{\rho}\widetilde{u_j}\widetilde{Z}=-\overline{\rho}\mathcal{D}_{t,Z}\frac{\partial \widetilde{Z}}{\partial x_j}, \tag{1.54}$$

where the turbulent diffusivity $\mathcal{D}_{t,Z}=C_Z\Delta^2\left\|\widetilde{\tau}_{ij}\right\|$. The constant C_Z is obtained using the dynamic Smagorinsky model. In LES, most often the subgrid variance of mixture fraction $\widetilde{Z''^2}$ is approximated by an algebraic relationship $\widetilde{Z''^2}=C_{V,Z}\Delta^2\left(\nabla\widetilde{Z}\right)^2$, where $C_{V,Z}=2\frac{C_Z^2}{C_\phi}$. The constant C_ϕ is the ratio of timescales. Alternative models for LES, where a transport equation for the scalar variance is solved, have also been used (Jimenez et al. 2001).

For turbulent premixed combustion, the filtered reaction progress variable $\widetilde{c}$ is determined by the solution of a transport equation, whereas the sub-filter variance of reaction progress variable $\widetilde{c''^2}$ is determined either by using an algebraic model or by solving a transport equation. Starting from the instantaneous equation of reaction progress variable (Eq. 1.39) and applying filter, we obtain balance equation for the density-weighted filtered reaction progress variable:

$$\frac{\partial \overline{\rho}\widetilde{C}}{\partial t}+\frac{\partial}{\partial x_j}\left(\overline{\rho}\widetilde{u_i}\widetilde{c}\right)=\frac{\partial}{\partial x_j}\left(\overline{\rho}\widetilde{\mathcal{D}}\frac{\partial \widetilde{c}}{\partial x_j}\right)-\frac{\partial q_c}{\partial x_j}, \tag{1.55}$$

where the SGS flux of reaction progress variable q_c is modelled as

$$q_c=\overline{\rho}\widetilde{u_jc}-\overline{\rho}\widetilde{u_j}\widetilde{c}=-\overline{\rho}\mathcal{D}_{t,c}\frac{\partial \widetilde{c}}{\partial x_j}, \tag{1.56}$$

where the turbulent diffusivity $\mathcal{D}_{t,c}=C_c\Delta^2||\widetilde{S}_{ij}||$. The constant C_c is obtained using the dynamic Smagorinsky model. In LES, most often the subgrid variance of reaction progress variable $\widetilde{c''^2}$ is approximated by an algebraic relationship $\widetilde{c''^2}=C_{V,c}\Delta^2(\nabla\widetilde{c})^2$, where $C_{V,c}=2\frac{C_c^2}{C_\phi}$. Alternately, a transport equation for $\widetilde{c''^2}$ needs to be solved.

LES offers considerable advantages for simulation of turbulent combustion over RANS approach. In LES, large-scale information of velocity and scalar fields are captured, which helps us to ascertain the role of large flow structures on mixing and combustion. Capturing the interaction between the inherently unsteady large-scale flow structures and combustion chemistry is important in many practical

applications involving combustion in internal combustion engines, gas turbine combustors, etc. LES is also suitable for multiscale applications, where subgrid-scale model is implemented within LES to describe the contributions from all relevant scales. Applications of LES are very much needed for flows with strong swirl and recirculation zones, transient phenomena involving flame blow-off and liftoff, more complex geometries, and flows with cycle-to-cycle variations. Dynamics of transient phenomena can hardly be captured by unsteady RANS. LES is less demanding in computer resources in comparison to DNS. However, the application of LES for practical combustion problems is yet difficult as it is computationally expensive. However, it has been successfully applied for various lab-scale (De and Kim 2013) as well as industrial applications of turbulent combustion (Mahesh et al. 2006; Patel and Menon 2008).

1.6 Modelling of Turbulence–Chemistry Interaction

In turbulent combustion, the mixing of reactants (fuel and oxidizer) is initially done by turbulent advection before the reactants are mixed at the molecular level. Once a range of different size eddies has developed, shear and strain at the interface between eddies promote the mixing. Shear and strain increase during the breakup of eddies and formation of smaller eddies, which results in an increase in the concentration gradients at the interface between reactants. The increased concentration gradients cause an increase in molecular mixing between the reactants at the interface between small eddies.

In the RANS or LES approach for the solution of flow equations, the transport equations of species mass fractions have a mean chemical reaction rate terms (last term of Eqs. 1.27 and 1.50), which is a nonlinear function of temperature and species concentrations. Due to the nonlinearities, the so-called 'direct closure' approach (Magnussen and Hjertager 1977), presented in Sect. 1.6.1 is known to lead to erroneous values of mean chemical source terms. Closure of the mean chemical reaction rate term has been the primary issue in RANS and LES of reacting flows. Several turbulent combustion models have been proposed in the recent past, which modelled the complex turbulence–chemistry interaction either by assuming it is primarily controlled by turbulent mixing (e.g. eddy breakup (EBU), eddy dissipation models (EDM), etc.) or via statistical approaches using a PDF (Pope 1985; Dopazo 1994). If the joint composition PDF $\widetilde{P}(\rho, Y_1, Y_2, ..., Y_N, T; \mathbf{x}, t)$ is known, the mean reaction rate for I-th species may be written as

$$\overline{\dot{\omega}_{Y_I}}(\mathbf{x}, t) = \int_{\rho,\, Y_1, Y_2,\, ...,\, Y_N,\, T} \dot{\omega}_{Y_i}(\rho,\, Y_1,\, Y_2,\, \ldots,\, Y_N,\, T)\widetilde{P}(\rho,\, Y_1, Y_2,\, \ldots,\, Y_N,\, T;\, \mathbf{x},\, t)\mathrm{d}\rho\mathrm{d}Y_1\mathrm{d}Y_2 \ldots \mathrm{d}Y_N\mathrm{d}T, \tag{1.57}$$

where the instantaneous reaction rates $\dot{\omega}_{Y_i}(\rho, Y_1, Y_2, ..., Y_N, T)$ are directly provided by the Arrhenius rate laws. However, the major challenge lies in the estimation of the joint PDF. The joint PDF of species and temperature may be determined either by presumed PDF method (Peters 1984) or transported PDF method (Pope 1985).

1.6.1 Direct Closure of Chemical Source Term

The direct closure of the chemical source term based on series expansion is discussed in this section along with the difficulties arising due to the nonlinear nature of the chemical source term. For a simple irreversible reaction between fuel (F) and oxidizer (O) leading to products (P): F + sO $\rightarrow$ (s + 1) P, the instantaneous rate of reaction for fuel using Arrhenius law may be written as

$$\dot{\omega}_F = -A\rho^2 T^b Y_F Y_O \exp\left(-\frac{T_A}{T}\right), \tag{1.58}$$

where A is the pre-exponential constant, b is the exponent of temperature and T_A is the activation temperature. The direct closure for the averaged reaction rate $\overline{\dot{\omega}_F}$ as a function of the mean fuel and oxidizer mass fractions $\widetilde{Y}_F$ and $\widetilde{Y}_O$, mean density $\overline{\rho}$ and mean temperature $\widetilde{T}$ is not trivial. Expanding the mean reaction rate as a Taylor series, we have (Veynante and Vervisch 2002)

$$\bar{\dot{\omega}}_F = -A\bar{\rho}^2\tilde{T}^b\tilde{Y}_F\tilde{Y}_O \exp\left(-\frac{T_A}{\tilde{T}}\right)\left[1 + \frac{\widetilde{Y_F''Y_O''}}{\tilde{Y}_F\tilde{Y}_O} + (P_1+Q_1)\left(\frac{\widetilde{Y_F''T''}}{\tilde{Y}_F\tilde{T}} + \frac{\widetilde{Y_O''T''}}{\tilde{Y}_O\tilde{T}}\right)\right.$$
$$\left. + (P_2+Q_2+P_1Q_1)\left(\frac{\widetilde{Y_F''T''^2}}{\tilde{Y}_F\tilde{T}^2} + \frac{\widetilde{Y_O''T''^2}}{\tilde{Y}_O\tilde{T}^2}\right) + \ldots\right]. \tag{1.59}$$

The above equation leads to several difficulties. Closure of the new quantities involving second-order correlation, e.g. $\widetilde{Y_F''T''}$, $\widetilde{Y_O''T''}$ may be obtained either using algebraic expressions or solving additional transport equations. The chemical reaction term represented by the Arrhenius expression is highly nonlinear. Large errors will be incurred when only the first few terms of the series expansion are retained. The complicated expression for the mean reaction rate term (Eq. 1.59) is only valid for a single-step irreversible reaction, and its direct extension to a multistep chemical mechanism is difficult. First-order closure of mean reaction rate leads to error. Therefore, direct closure of reaction rates is not used. This approach is particularly suitable for simulations of supersonic reacting flows or to describe the reaction in atmospheric boundary layer where the temperature T may be

assumed to be constant and the first two terms of Eq. 1.59 are only retained. A segregation factor,

$$\alpha_{FO} = -\frac{\widetilde{Y_F'' Y_O''}}{\tilde{Y}_F \tilde{Y}_O} = -\left(1 - \frac{\widetilde{Y_F Y_O}}{\tilde{Y}_F \tilde{Y}_O}\right), \tag{1.60}$$

is often used to characterize mixing between fuel and oxidizer streams. In case of perfect mixing ($\widetilde{Y_F'' Y_O''} = 0$), $\alpha_{FO} = 0$, whereas $\alpha_{FO} = -1$ for the perfectly separated streams ($\widetilde{Y_F'' Y_O''} = 0$). The mean reaction rate becomes

$$\overline{\dot{\omega}} = -A(1 + \alpha_{FO})\bar{\rho}^2 \tilde{T}^b \tilde{Y}_F \tilde{Y}_O \exp\left(-\frac{T_A}{\tilde{T}}\right). \tag{1.61}$$

The segregation factor α_{FO} is either postulated or provided by a balance equation.

1.6.2 Eddy Breakup and Eddy Dissipation Model

Under the assumption of large Damköhler number $Da \gg 1$, the chemical timescales are much shorter than the turbulent timescales, and reaction rates are controlled by the turbulent mixing rates. The remaining challenge is based on the suitable closure model for the turbulent mixing rates, generally represented in terms of scalar dissipation rates.

Spalding (1971) provided one of the early closures for the chemical source term. He argued that turbulent mixing may be viewed as a cascade process from the integral scale down to the molecular scales. For flows where mixing and not the chemical reaction is the rate-limiting process, the cascade process also controls the chemical reactions. This model is known as the EBU model. It is based on phenomenological analysis of turbulent combustion for high Reynolds number ($\mathrm{Re} \gg 1$) and Damköhler number ($\mathrm{Da} \gg 1$). The turbulent mean reaction rate is mainly controlled by a characteristic turbulent mixing time and the fluctuation of fuel mass fraction $\widetilde{Y_F''^2}$ as

$$\overline{\dot{\omega}_F'''} = -\rho C_{EBU} \frac{\tilde{\varepsilon}}{\tilde{k}} \left(\widetilde{Y_F''^2}\right)^{1/2}, \tag{1.62}$$

where C_{EBU} is the eddy break up model constant. The turbulent mixing time is modelled as the ratio of turbulent kinetic energy $\widetilde{k}$ and its dissipation rate $\widetilde{\varepsilon}$. The mean reaction rate of a turbulent premixed flame based on EBU model is written as

$$\overline{\dot{\omega}_c'''} = \rho C_{EBU} \frac{\tilde{\varepsilon}}{\tilde{k}} \left(\widetilde{c''^2} \right)^{1/2}. \tag{1.63}$$

For a bimodal progress variable c (i.e. $c = 0$ or $c = 1$), $\widetilde{c''^2} = \tilde{c}(1 - \tilde{c})$. Subsequently, in the eddy dissipation model (EDM), Magnussen and Hjertager (1977) replaced $\left(\widetilde{Y_F''^2} \right)^{1/2}$ simply by the mean mass fraction of the deficient species, i.e. fuel for lean mixture or oxidizer for rich mixtures. The model takes the minimum of three reaction rates of fuel, oxidizer and products in order to calculate the mean chemical source term:

$$\overline{\dot{\omega}_F'''} = -\rho A \frac{\tilde{\varepsilon}}{\tilde{k}} \min \left(\tilde{Y}_F, \frac{\tilde{Y}_{O_2}}{s}, B \frac{\tilde{Y}_P}{(1+s)} \right). \tag{1.64}$$

In the above equations, A and B are the modelling constants and s is the stoichiometric oxygen-to-fuel mass ratio.

The EBU and EDM models are based on intuitive arguments, where the chemical timescale of a single-step irreversible reaction is replaced by the turbulent timescale, $\tau = \tilde{k}/\tilde{\varepsilon}$. These models eliminate the effect of finite-rate chemistry by representing the fast chemistry limit only. The modelling constants C_{EBU} or A and B are specific to a particular problem and they need to be adjusted within a wide range in order to achieve reasonable results.

1.6.3 Flame Surface Density Model

The flame surface density model is a typical topological, finite-rate combustion model applied to premixed combustion. In this type of model, one considers that the heat release in a given volume is the product of the heat release per unit flame surface, times the total flame surface present in this volume. The idea is to get the increased exchange surface available for combustion where the flame is highly contorted by turbulence. In this formalism, reaction rates are modelled as $\overline{\dot{\omega}_I} = \langle \dot{\omega}_I \rangle \Sigma$, where $\langle \dot{\omega}_I \rangle$ is the mean reaction rate of species I per unit of flame area, generally represented by the Arrhenius reaction rate expression. The model is based on available flame surface per unit volume, commonly referred as flame surface density Σ. Under flamelet assumptions, this approach separates complex chemistry features incorporated in $\langle \dot{\omega}_I \rangle$ through flamelet libraries from flame/turbulence interactions described by Σ. The flame surface density Σ may be obtained from an algebraic equation $\Sigma = g\tilde{c}(1 - \tilde{c})/(\sigma_y L_y)$, where g is a model constant, L_y is the length scale associated with flame wrinkling and σ_y is an orientation factor. Also, additional transport equation for Σ may be solved (Veynante and Vervisch 2002; Trouve and Poinsot 1994).

$$\frac{\partial \Sigma}{\partial t} + \frac{\partial \left(\widetilde{u}_j \Sigma\right)}{\partial x_j} = \frac{\partial}{\partial x_j}\left(\rho \mathcal{D} \frac{\partial \Sigma}{\partial x_j}\right) + C_1 \frac{\varepsilon}{k}\Sigma - C_2 s_L \frac{\Sigma^2}{1-\widetilde{c}}. \tag{1.65}$$

The first term on the RHS is the turbulent transport term, whereas the second and third terms correspond to production due to stretching of the flame and flame annihilation, respectively.

1.6.4 Transported PDF Methods

In transported PDF method, the turbulent flow is described by the transport equation of joint scalar or joint scalar/velocity PDF. The transport equation of joint PDF can be derived from Navier–Stokes equations and conservation equation for scalars (Pope 1985). The transported PDF method does not require any closure model for the nonlinear chemical source term. Theoretically, this method can treat arbitrary complex chemistry without any assumption. Since the joint scalar PDF depends on space, time and all independent scalars, the PDF transport equation cannot be solved using conventional finite-volume or finite-difference methods. The joint scalar PDF is usually represented by a collection of notional particles, which are evolved by solving a set of ordinary differential equations describing particle location, velocity, temperature or enthalpy, and species mass fractions.

However, it needs closure models for the molecular mixing or micromixing term in reactive scalar space, and PDF transport in velocity space by viscous stresses and fluctuating pressure term (Peters 2000; Pope 2000). The performance of the transported PDF method largely relies on the accuracy of associated submodels for these unknown terms (Subramaniam and Pope 1999). Several molecular mixing models, namely interaction by exchange with the mean (IEM) (Celis and da Silva 2015), linear mean-square estimation (LMSE) (Dopazo and Obrien 1974), modified curl (MC) (Janicka et al. 1979) and Euclidean minimum spanning tree (EMST) (Subramaniam and Pope 1998) model are available in literature. However, they could not adequately provide a physically realistic representation of scalar dissipation rate, which is crucial for capturing unsteady flame dynamics observed during local flame extinction and re-ignition (Bilger 2000). The accuracy of the method scales with the square root of the number of notional particles per CFD cell. It is common to use 100 particles per cell to achieve an error on the order of 10% of the r.m.s. In LES, typically a large number of CFD cells are used, which requires more number of notional particles. Computation and storage of chemical source terms $\dot{\omega}_{Y_i}(\rho, Y_1, \ldots, Y_N, T)$ thus become an enormously difficult task for current computers. The in situ adaptive tabulation (ISAT) method (Pope 1997) proposed for the chemical source term integration has demonstrated substantial reduction of integration times. Part IV of the book extensively covers transported PDF method.

1.6.5 Presumed PDF Approach

In the presumed PDF method, a given shape of the PDF, e.g. β-function is assumed. The shape of the PDF can be fully represented in terms of the local physical conditions described at each physical location based on the balance equations of the first and second moments, i.e. mean and variance of the random variable. The presumed PDF method is usually based on a single variable, as it becomes difficult to model more than one variable with a presumed joint PDF. For problems with more than one variable, the joint PDF is simplified by assuming that the variables are statistically independent: $P(\psi_1, \psi_2, \ldots, \psi_N) \approx P(\psi_1)P(\psi_2)\ldots P(\psi_{N.})$, and the PDF $P(\psi_N)$ is modelled using a presumed shape. Here, $\psi = \{Y_1, Y_2, \ldots\ldots, Y_N, T\}$ signifies the composition space.

Besides this, significant efforts have been taken to simplify the expression of the joint PDF $P(Y_1, Y_2, \ldots, Y_N, T; \mathbf{x}, t)$. For instance, the entire composition space $\{Y_1, Y_2, \ldots\ldots, Y_N, T\}$ is replaced with a scalar variable, whose PDF is known a priori or presumed to have some known distribution. For non-premixed combustion, the joint PDF $P(Y_1, Y_2, \ldots, Y_N, T; \mathbf{x}, t)$ is greatly simplified using a chemistry-independent conserved scalar, namely mixture fraction, Z. The presumed PDF model allows the formation of intermediate species, dissociation and turbulence–chemistry coupling. For non-premixed combustion, only the first two moments of mixture fraction are solved, and species mass fractions, temperature are obtained from the state relationships. Hypotheses are formulated to construct different models such as (1) infinitely fast chemistry model, (2) flamelet models and (3) conditional moment closure (CMC) method. First two models are applicable in the limit of high Damköhler number $(Da \gg 1)$, where it is assumed that the chemical reaction occurs in thin layers between fuel and oxidizer. The reaction zone is viewed as a collection of laminar flamelets. Similar concepts have been extended to coherent flamelet and flame surface density models for turbulent premixed combustion (Peters 2000; Veynante and Vervisch 2002). Peters (2000) provided a detailed review of these modelling approaches of turbulent combustion, which are briefly discussed in this section. Recent developments in this subject have been reviewed by Bilger et al. (2005) and Pitsch (2006).

1.6.5.1 Flamelet Model

William (1975) viewed a turbulent diffusion flame as an ensemble of thin, one-dimensional, stretched laminar flamelets embedded within an underlying turbulent flow. The inherent assumption behind the flamelet theory is that the thickness of the reaction zone is sufficiently small compared to the Kolmogorov length scale. The internal structure of the reaction zone can be determined by molecular diffusion without the influence of turbulence. In case of intense turbulence, Kolmogorov eddies become sufficiently smaller than the flame thickness and penetrate the reaction zone, and thereby destroying the local, laminar flame structure. Under

these conditions, the entire flame is likely to extinguish. This model has been developed both for non-premixed (Peters 1984; Bray and Peters 1994) and premixed combustion (Peters 1999) and considers the coupling between the turbulence and non-equilibrium chemistry.

Flamelet concept focuses on the location of the flame surface and not on the reactive scalars themselves. The flame is defined as an isosurface of a known scalar quantity, e.g. mixture fraction Z for non-premixed combustion or the location of the flame surface G or reaction progress variable c for premixed combustion. The profiles of the reactive scalars (temperature and species mass fractions) normal to the surface are obtained by solving the flamelet equations. These profiles are assumed to remain attached to the flame surface and are convected by the underlying turbulent flow field. Transport equations describing statistical moments (mean and variance) for Z in case of non-premixed combustion or G (or c) for premixed combustion are solved. Finally, the mean and variance of the reactive scalars are obtained from the statistical distribution of the scalar quantities Z and G (or c) via a known or presumed PDF.

For non-premixed combustion, the coupling between turbulence and non-equilibrium chemistry is achieved using the statistical description in terms of mixture fraction Z and the scalar dissipation rate χ. The mean value of any scalar (ϕ), e.g. temperature and compositions, is obtained by convoluting the state relationships $\phi = \phi(Z,\chi)$ with the joint PDF $\widetilde{P}(Z,\chi;\mathbf{x},t)$ of the mixture fraction Z and the scalar dissipation rate χ:

$$\widetilde{\phi}(\mathbf{x},t) = \int_0^1 \int_0^\infty \phi(Z,\chi)\widetilde{P}(Z,\chi;\mathbf{x},t)\mathrm{d}\chi\mathrm{d}Z. \tag{1.66}$$

For simplification purpose, often these two parameters are assumed to be statistically independent, i.e. $\widetilde{P}(Z,\chi;\mathbf{x},t) = \widetilde{P}_Z(Z;\mathbf{x},t) \times \widetilde{P}_\chi(\chi;\mathbf{x},t)$. Two different probability density functions are used. The standard β-function parameterized by the mean and variance of the mixture fraction is used for the PDF of the mixture fraction $\widetilde{P}_Z$, whereas a log-normal distribution is used for the PDF of the scalar dissipation rate $\widetilde{P}_\chi$. A look-up table containing temperature, species mass fractions and density is generated from the pre-calculated laminar flamelet library in terms of the mean and variance of mixture fraction and scalar dissipation rate for non-premixed combustion. Similar approaches exist for the statistical description of turbulent premixed combustion.

1.6.5.2 Bray–Moss–Libby (BML) Model

The Bray–Moss–Libby model (BML) is introduced as a model for turbulent premixed combustion. In this model, the PDF of c at a given location $\mathbf{x}$ is described as $P(c;\mathbf{x},t) = \alpha(\mathbf{x},t)\delta(c) + \beta(\mathbf{x},t)\delta(1-c)$, where α and β are the probabilities of

finding unburnt, fully burnt mixtures, respectively, at location, **x,** and δ is the Dirac function. The Favre mean value of any quantity is directly given by

$$\phi = \int_0^1 \phi(c) P(c; \mathbf{x}, t) dc = \alpha \overline{\phi^u} + \beta \overline{\phi^b}, \tag{1.67}$$

where $\overline{\phi}$ denote the conditional averages, superscripts 'b' and 'u' denote burnt and fresh gases, respectively. Also, applying Eq. (1.67) to $c, \rho c$ and ρ gives

$$\bar{c} = \beta; \quad \overline{\rho c} = \overline{\rho}\widetilde{c} = \rho_b \bar{c}; \quad \overline{\rho} = (1-\beta)\rho_u + \beta \rho_b. \tag{1.68}$$

Introducing heat release factor $\gamma = \frac{\rho_u - \rho_b}{\rho_b} = \frac{T_b - T_u}{T_u}$, from relations provided in Eq. (1.68), we have

$$\alpha = \frac{1-\widetilde{c}}{1+\gamma\widetilde{c}}; \quad \beta = \frac{(1+\gamma)\widetilde{c}}{1+\gamma\widetilde{c}}. \tag{1.69}$$

In another variant of BML model, joint PDF of reaction progress variable and velocity is considered. A detailed discussion on BML model is available in Chap. 6 of this monograph.

1.6.5.3 G-Equation Model

The flame front may be regarded as a geometrical entity. The flame brush in RANS or the resolved flame front in LES may be described as a surface propagating with a turbulent flame speed s_T. The turbulent flame is then identified as a isosurface G^* of a scalar G, leading to the so-called G-equation (Kerstein 1988; Kerstein et al. 1988):

$$\frac{\partial G}{\partial t} + u_j \frac{\partial G}{\partial x_j} = S_d |\nabla G|, \tag{1.70}$$

where S_d is the local flame displacement speed. Starting from the instantaneous equation of G, transport equations for Favre mean $\widetilde{G}$ and variance $\widetilde{G''^2}$ may be obtained by applying decomposition. The detailed derivation of these equations is available in Peters (1999).

Several other presumed PDF-based models are available for turbulent premixed combustion. Theoretical background of one such model, namely flamelet-generated manifold (FGM) model, and its application are discussed in Chap. 7 of this monograph. The multi-dimensional manifolds may be created based on control variables, such as reaction progress variable, mixture fraction, enthalpy, etc. Usually, the joint PDF of these control variables is written in terms of product of the marginal PDFs of individual control variables assuming statistical independence.

1.6.6 Conditional Moment Closure Method

In the conditional moment closure (CMC) method, it is assumed that most of the fluctuations in the reactive scalars are inherently associated with the fluctuations in one key quantity. Mixture fraction and reaction progress variables serve as these key quantities for non-premixed and premixed combustion, respectively. For non-premixed combustion, where there is mixing between fuel and oxidizer streams, the reactive scalars within the mixing field strongly depend on the local and instantaneous value of mixture fraction $Z(\mathbf{x}, t)$. The Favre conditional mean of the I-th chemical species $Y_I(\mathbf{x}, t)$, conditioned on the associated value $Z(\mathbf{x}, t)$ taking a specific value η, is defined as,

$$Q_I(\eta,\ \mathbf{x},\ t) = \langle \rho Y_I(\mathbf{x}, t) | Z(\mathbf{x}, t) = \eta \rangle / \rho_\eta. \tag{1.71}$$

Here, η is the reference or sample space for mixture fraction $Z(\mathbf{x}, t)$ and the conditional density $\rho_\eta = \rho_\eta(\mathbf{x}, t)$ is obtained from Eq. (1.17) after replacing the instantaneous pressure, temperature and species mass fractions by mean pressure, conditional mean temperature $Q_T(\eta, \mathbf{x}, t)$ and conditional mean species mass fractions Q_I, respectively. In Eq. (1.71), the angular brackets indicate that the average is taken upon those members of the ensemble which obey the condition to the right of the vertical bar. The local and instantaneous value of species mass fraction is decomposed into its Favre conditional mean and fluctuations around the Favre conditional mean $Y_I(\mathbf{x}, t) = Q_I(\eta; \mathbf{x}, t) + Y_I^{''}(\eta; \mathbf{x}, t)$. In the CMC model, the transport equations for the conditional scalars, e.g. conditional temperature $Q_T(\eta; \mathbf{x}, t)$ or conditional enthalpy $Q_H(\eta; \mathbf{x}, t)$, and conditional species mass fractions $Q_I(\eta; \mathbf{x}, t)$ are derived either from the joint PDF method (Klimenko 1990) or decomposition method (Bilger 1993). These transport equations are solved in the sample space (η) for mixture fraction at all physical locations. When transport equation for Q_H is solved, conditional temperature Q_T may be obtained from the computed values of Q_H and Q_I. The unconditional or Favre mean values of reactive scalars are recovered from the conditional scalars (temperature and species mass fractions) by convoluting it with the PDF of mixture fraction $\widetilde{P}(\eta)$ over the reference space for mixture fraction:

$$\widetilde{T} = \int_0^1 Q_T(\eta; x, t)\widetilde{P}(\eta; x, t)d\eta, \quad \widetilde{Y}_I = \int_0^1 Q_I(\eta; \mathbf{x}, t)\widetilde{P}(\eta; \mathbf{x}, t)\mathrm{d}\eta. \tag{1.72}$$

A β-function is used for PDF of mixture fraction $\widetilde{P}(\eta; \mathbf{x}, t)$. In the first-order CMC, the mean chemical source term is modelled at the first moment level by using the computed conditional mean values of the reactive scalars and thereby neglecting the conditional fluctuations:

$$\langle \dot{\omega}_I^{'''}(\rho, T, Y_1, Y_2, .., Y_N) | \eta \rangle = \dot{\omega}_I^{'''}\left(\rho_\eta, Q_T, Q_{Y_1}, Q_{Y_2}, \ldots, Q_{Y_N}\right). \tag{1.73}$$

The Arrhenius reaction rate expression is used for the chemical source term. For a fully coupled CMC-CFD solver, the CMC equations are solved in the mixture fraction space in tandem with the flow field at all physical locations. At every time step, the flow solver provides the mixing field ($\widetilde{Z}, \widetilde{Z''^2}$) to the CMC equations, which in turn provides the unconditional or mean density ($\overline{\rho}$) to the flow solver.

For flames exhibiting extinction and re-ignition, the conditional scalar fluctuations about the conditional mean become significant. Such flames require closure at the second-moment level. In the second-order CMC model (Sreedhara and Lakshmisha 2002), additional transport equations for conditional fluctuations are solved. Sometimes, another variable such as sensible enthalpy is used as second conditioning variable (Kronenburg 2004). In the past decades, CMC model has found applications in several turbulent combustion problems (Patwardhan et al. 2009). However, it requires huge computational efforts mainly due to the additional dimension of the mixture fraction space. More details on the CMC model and its applications for turbulent premixed and non-premixed combustion are available in Chaps. 8 and 9, respectively.

However, CMC model has some limitations for predictions of transient flame phenomena involving extinction and re-ignition. The method also suffers setback for cases with partial premixing, spray combustion with pre-evaporation. The model fails to capture strong spatial inhomogeneity of the conditional moments and fast changes in conditional moments. Nonetheless, the CMC model captures spatio-temporal evolution of reactive scalars, which is not possible in flamelet model.

1.6.7 Multiple Mapping Conditioning Approach

Multiple mapping conditioning (Klimenko and Pope 2003) (MMC) approach is a relatively new turbulent combustion model. This method integrates the advantages of mapping closure, PDF and CMC methods. Much similar to the CMC method, the concept of reference space is used in MMC method, whose PDF is known in advance. Usually, a single reference variable is used, although the choice of more than one reference variable is possible. In case of non-premixed combustion, a single reference variable is usually used whose mapping function represents mixture fraction. The small-scale mixing and turbulent fluctuations are described by mapping of physical space with the reference space. Both deterministic (Vogiatzaki et al. 2009) and stochastic versions (Straub et al. 2016; Vogiatzaki et al. 2015) of MMC are available. For LES of turbulent reactive flows, the sparse Lagrangian version of MMC is preferred. Recently, the MMC method has been used for different turbulent non-premixed combustion problems. However, there are only limited applications of this method to premixed combustion (Sundaram and Klimenko 2017).

1.6.8 Summary of Turbulent Combustion Models

A brief overview of different turbulent combustion models is presented. Most of these models are applicable in one of the regimes, either premixed or non-premixed combustion. The underlying closure of these models is based on certain assumptions and they often have some adjustable parameters. For certain combustion problem, more and more detailed chemistry is required for an accurate representation. The inherently low computational cost of flamelet-type models has made it popular and these models are routinely used for engineering applications. These models are available in most commercial CFD packages for turbulent combustion. However, need for more accurate description of turbulent combustion has fuelled development of advanced combustion models, such as PDF, CMC and MMC models. These models are developed for both RANS and LES frameworks and require closure models with adjustable parameters. Future research should be directed towards the development of a combustion model which is universally applicable to all burner configurations, such as pilot-stabilized, hot-coflow stabilized and bluff-body stabilized flames. Also, more general combustion models are needed to bridge the gap between premixed and non-premixed combustion.

1.7 Concluding Remarks

The complex multiscale and nonlinear interaction between chemistry and turbulence poses a significant modelling challenge of turbulent reactive flows encountered in modern combustion systems. Notwithstanding the significant progress in the last couple of decades, the modelling and numerical simulations of turbulent combustion remain in the forefront of research due to its inherent complexity, significant modelling difficulties and industrial relevance. In this chapter, a brief description of theory and modelling challenges of turbulence–chemistry interactions is provided. Over the last few decades, significant progress has been made to understand the complex multiscale and multi-physics processed involving turbulent combustion.

Besides reviewing the theory and fundamental modelling of turbulent reactive flows, this book attempts to highlight recent progress made in the modelling and simulation of turbulent combustion. Comprehensive reviews of the state-of-the-art models are presented for turbulent premixed and non-premixed combustion with a specific focus on the theory, development of combustion models and applications in practical combustion systems. The book is arranged into four parts. In Part I, Methodology and Architecture of Turbulent Combustion Computations, besides the present introductory chapter on Fundamentals and Modelling of Turbulence—Chemistry Interactions, optimization and reduction of complex chemical kinetics are presented. Rapid advances in computer hardware and algorithms have made it possible to use LES for engineering applications and provide direct solutions of

many unresolved physics of turbulent reactive flows using high-fidelity simulations. Role of high-performance computing in DNS of turbulent reactive flows are discussed in Chaps. 3 and 4.

Part II emphasizes on modelling of turbulent premixed combustion. It starts with DNS of turbulent premixed combustion and its relevance and applications to engineering computational analyses (Chap. 5). In Chap. 6, different modelling strategies of RANS of turbulent premixed combustion are discussed. Application of flamelet-generated manifold method and the CMC method for turbulent premixed combustion are covered in Chaps. 7 and 8, respectively.

Numerical models on turbulent non-premixed combustion are presented in Part III of this book. It starts with the CMC method for turbulent non-premixed combustion (Chap. 9), followed by DNS of auto-ignition in turbulent non-premixed combustion (Chap. 10). Modelling of soot formation is an important aspect for hydrocarbon flames. Semi-empirical models and method of moments on soot formation are covered in Chap. 11 followed by modelling of soot formation in a kerosene spray flame using flamelet model (Chap. 12). We tried to provide details on state-of-the-art turbulent combustion models in Parts II and III; however, we could only provide details of a very few turbulent combustion models. Parts II and III are somewhat incomplete but it provides a flavour of current state-of-the-art and trends in development and applications of models for turbulent combustion.

In Part IV, PDF and stochastic methods of turbulent combustion are presented. This part presents the theory and recent applications of transported PDF method (Chap. 13), filtered mass density function (FMDF) approach (Chap. 14) and MMC approach (Chap. 15).

In Part V, different applications of combustion are presented. This includes turbulent spray combustion (Chap. 16), applications of turbulent combustion in internal combustion engine (Chap. 17), characterization of turbulent combustion using dynamical systems theory (Chap. 18). Finally, advanced topics, such as theory and modelling of deflagration to detonation transition (DDT) and scramjet combustion, are presented in Chaps. 19 and 20.

References

Ashurst WT, Kerstein A, Kerr R, Gibson C (1987) Alignment of vorticity and scalar gradient with strain rate in simulated Navier-Stokes turbulence. Phys Fluids 30:2343–2353

Bilger RW (1976) Turbulent jet diffusion flames. Prog Energy Combust Sci 1:87–109

Bilger RW (1993) Conditional moment closure for turbulent reacting flow. Phys Fluids a-Fluid Dyn 5:436–444

Bilger RW (2000) Future progress in turbulent combustion research. Prog Energy Combust Sci 26:367–380

Bilger RW, Pope SB, Bray KNC, Driscoll JF (2005) Paradigms in turbulent combustion research. Proc Combust Inst 30:21–42

Bray KNC, Peters N (1994) Laminar flamelet in turbulent flames. In: Libby PA, Williams FA (ed) Turbulent reacting flows. Academic Press, London

Celis C, da Silva LFF (2015) Lagrangian mixing models for turbulent combustion: review and prospects. Flow Turbul Combust 94:643–689
Chakraborty N, Swaminathan N (2007) Influence of the Damköhler number on turbulence-scalar interaction in premixed flames. I. Physical insight. Phys Fluids 19:045103
Chaudhuri S (2015a) Life of flame particles embedded in premixed flames interacting with near isotropic turbulence. Proc Combust Inst 35:1305–1312
Chaudhuri S (2015b) Pair dispersion of turbulent premixed flame elements. Phys Rev E 91:021001
De S, Kim SH (2013) Large eddy simulation of dilute reacting sprays: droplet evaporation and scalar mixing. Combust Flame 160:2048–2066
Dopazo C (1994) Recent developments in PDF methods. In: Libby PA, Williams FA (ed) Turbulent reacting flows. Academic, London
Dopazo C, Obrien EE (1974) Approach to autoignition of a turbulent mixture. Acta Astronaut 1:1239–1266
Germano M (1989) The dean equations extended to a helical pipe-flow. J Fluid Mech 203:289–305
Germano M, Piomelli U, Moin P, Cabot WH (1991) A dynamic subgrid-scale eddy viscosity model. Phys Fluids a-Fluid 3:1760–1765
Girimaji S, Pope S (1990) Material-element deformation in isotropic turbulence. J Fluid Mech 220:427–458
Girimaji S, Pope S (1992) Propagating surfaces in isotropic turbulence. J Fluid Mech 234:247–277
Hamlington PE, Schumacher J, Dahm WJ (2008) Local and nonlocal strain rate fields and vorticity alignment in turbulent flows. Phys Rev E 77:026303
Hinze JO (1975) Turbulence. McGraw-Hill, New york
Janicka J, Kolbe W, Kollmann W (1979) Closure of the transport-equation for the probability density-function of turbulent scalar fields. J Non-Equilib Thermodyn 4:47–66
Jimenez C, Valino L, Dopazo C (2001) A priori and a posteriori tests of subgrid scale models for scalar transport. Phys Fluids 13:2433–2436
Jones WP, Launder BE (1972) The prediction of laminarization with a two-equation model of turbulence. Int J Heat Mass Transf 15:301–314
Kerstein AR (1988) Simple derivation of Yakhots turbulent premixed flamespeed formula. Combust Sci Technol 60:163–165
Kerstein AR, Ashurst WT, Williams FA (1988) Field equation for interface propagation in an unsteady homogeneous flow field. Phys Rev A 37:2728–2731
Kim SH, Pitsch H (2007) Scalar gradient and small-scale structure in turbulent premixed combustion. Phys Fluids 19:115104
Klimenko AY (1990) Multicomponent diffusion of various admixtures in turbulent flow. Fluid Dyn 25:327–334
Klimenko AY, Pope SB (2003) The modeling of turbulent reactive flows based on multiple mapping conditioning. Phys Fluids 15:1907–1925
Kolmogorov AN (1941) The local structure of turbulence in incompressible viscous fluid for very large Reynolds numbers. Dokl Akad Nauk SSSR 299–303
Kronenburg A (2004) Double conditioning of reactive scalar transport equations in turbulent nonpremixed flames. Phys Fluids 16:2640–2648
Launder BE, Spalding DB (1974) The numerical computation of turbulent flows. Comput Methods Appl Mech Eng 3:269–289
Libby PA, Williams FA (1994) Fundamental aspects and review. In: Libby PA, Williams FA (eds) Turbulent reacting flows. Academic Press, London
Lilly DK (1992) A proposed modification of the germano-subgrid-scale closure method. Phys Fluids a-Fluid 4:633–635
Magnussen BF, Hjertager BH (1977) On mathematical modeling of turbulent combustion with special emphasis on soot formation and combustion. Symp (Int) Combust 16:719–729
Mahesh K, Constantinescu G, Apte S, Iaccarino G, Ham F, Moin P (2006) Large-eddy simulation of reacting turbulent flows in complex geometries. J Appl Mech-T Asme 73:374–381

Meneveau C, Lund TS, Cabot WH (1996) A Lagrangian dynamic subgrid-scale model of turbulence. J Fluid Mech 319:353–385
Patel N, Menon S (2008) Simulation of spray-turbulence-flame interactions in a lean direct injection combustor. Combust Flame 153:228–257
Patwardhan SS, De S, Lakshmisha KN, Raghunandan BN (2009) CMC simulations of lifted turbulent jet flame in a vitiated coflow. Proc Combust Inst 32:1705–1712
Peters N (1984) Laminar diffusion flamelet models in non-premixed turbulent combustion. Prog Energy Combust Sci 10:319–339
Peters N (1999) The turbulent burning velocity for large-scale and small-scale turbulence. J Fluid Mech 384:107–132
Peters N (2000) Turbulent combustion. Cambridge University Press, Cambridge
Pitsch H (2006) Large-eddy simulation of turbulent combustion. Annu Rev Fluid Mech 38:453–482
Poinsot T, Veynante D (2012) Theoretical and numerical combustion, 3rd edn. Toulouse Cedex
Pope SB (1985) PDF methods for turbulent reactive flows. Prog Energy Combust Sci 11:119–192
Pope S (1988) The evolution of surfaces in turbulence. Int J Eng Sci 26:445–469
Pope SB (1997) Computationally efficient implementation of combustion chemistry using in situ adaptive tabulation. Combust Theoret Model 1:41–63
Pope SB (2000) Turbulent flows. Cambridge University Press
Spalding DB (1971) Mixing and chemical reaction in steady confined turbulent flames. Symp (Int) Combust 13:649–657
Sreedhara S, Lakshmisha KN (2002) Assessment of conditional moment closure models of turbulent autoignition using DNS data. Proc Combust Inst 29:2069–2077
Sreenivasan KR (1995) On the universality of the Kolmogorov constant. Phys Fluids 7:2778–2784
Straub C, De S, Kronenburg A, Vogiatzaki K (2016) The effect of timescale variation in multiple mapping conditioning mixing of PDF calculations for Sandia Flame series D–F. Combust Theory Model 1–19
Subramaniam S, Pope SB (1998) A mixing model for turbulent reactive flows based on Euclidean minimum spanning trees. Combust Flame 115:487–514
Subramaniam S, Pope SB (1999) Comparison of mixing model performance for nonpremixed turbulent reactive flow. Combust Flame 117:732–754
Sundaram B, Klimenko AY (2017) A PDF approach to thin premixed flamelets using multiple mapping conditioning. Proc Combust Inst 36:1937–1945
Swaminathan N, Grout R (2006) Interaction of turbulence and scalar fields in premixed flames. Phys Fluids 18:045102
Toschi F, Bodenschatz E (2009) Lagrangian properties of particles in turbulence. Annu Rev Fluid Mech 41:375–404
Trouve A, Poinsot T (1994) The evolution equation for the flame surface-density in turbulent premixed combustion. J Fluid Mech 278:1–31
Turns SR (2012) An Introduction to combustion, 3rd edn. Tata McGraw hill, New York
Uranakara HA, Chaudhuri S, Dave HL, Arias PG, Im HG (2016) A flame particle tracking analysis of turbulence–chemistry interaction in hydrogen–air premixed flames. Combust Flame 163:220–240
Uranakara HA, Chaudhuri S, Lakshmisha K (2017) On the extinction of igniting kernels in near-isotropic turbulence. Proc Combust Inst 36:1793–1800
Veynante D, Vervisch L (2002) Turbulent combustion modeling. Prog Energy Combust Sci 28:193–266
Vogiatzaki K, Cleary MJ, Kronenburg A, Kent JH (2009) Modeling of scalar mixing in turbulent jet flames by multiple mapping conditioning. Phys Fluids 21
Vogiatzaki K, Navarro-Martinez S, De S, Kronenburg A (2015) Mixing modelling framework based on multiple mapping conditioning for the prediction of turbulent flame extinction. Flow Turbul Combust 95:501–517

Vreman B, Geurts B, Kuerten H (1997) Large-eddy simulation of the turbulent mixing layer. J Fluid Mech 339:357–390

William FA (1975) Recent advances in theoretical descriptions of turbulent diffusion flames. In: Murthy SNB (ed) Turbulent mixing in nonreactive and reactive flows. Plenum Press, New York, pp 189–208

Xu H, Pumir A, Bodenschatz E (2011) The pirouette effect in turbulent flows. Nat Phys 7:709

Yeung P, Girimaji S, Pope S (1990) Straining and scalar dissipation on material surfaces in turbulence: implications for flamelets. Combust Flame 79:340–365

Chapter 2
Detailed Kinetics in Combustion Simulation: Manifestation, Model Reduction, and Computational Diagnostics

Peng Zhao

Abstract In this chapter, the essential feature of realistic combustion chemistry is first introduced. Manifestations of nonlinear detailed chemistry in homogeneous combustion systems as well as convective–diffusive systems are demonstrated, with useful insights on turbulent combustion and guidance for the adoption of detailed chemistry in combustion modeling. Recent progress on premixed and non-premixed counterflow cool flamelets is systematically discussed, shedding light on the local behavior of detailed chemistry in turbulent reacting flows. In addition, an overview covering model reduction, stiffness removal, and other computational methods to facilitate chemistry integration is provided to show the feasibility to accommodate realistic chemistry in laminar and turbulent combustion modeling. Last but not the least, typical methods of computational diagnostics are reviewed to show the necessity and capability of probing and understanding combustion modeling results in general.

Keywords Detailed chemistry · NTC · Model reduction · Stiffness removal Cool flame · Computational diagnostics

2.1 Intrinsic Complexities in Detailed Chemical Kinetics

A modern combustion researcher has at least five major tasks in chemical kinetics, including identification of the species involved, identification of the reactions between the species, determination of the parameters involved in the rate constants, solving the ordinary differential equations (ODE) for the chemistry source term, and understanding the coupled behavior of chemistry and fluid flow described by the governing partial differential equations (PDE). Clearly, the first three tasks are

P. Zhao (✉)
Department of Mechanical Engineering, Oakland University, Rochester, MI 48309, USA
e-mail: pengzhao@oakland.edu; zhaodbustc@gmail.com

© Springer Nature Singapore Pte Ltd. 2018

S. De et al. (eds.), *Modeling and Simulation of Turbulent Combustion*, Energy, Environment, and Sustainability, https://doi.org/10.1007/978-981-10-7410-3_2

responsibilities of the chemists, while the last two should be accomplished by those who work on combustion physics and modeling. The number one challenge in chemical kinetics is that thermal pyrolysis and oxidation of fuels constantly involve many intermediate species and elementary reactions, leading to the high dimensionality of all combustion problems. Consequently, extensive efforts have been spent on the development of chemical kinetic models over the past few decades, focusing on increasingly complex fuel molecules and blends. Unsurprisingly, the size of the chemical mechanisms significantly grows with increasing fuel molecular size (Lu and Law 2009). Given the molecular structure of the fuel, the numbers of species and reactions can be up to a few thousands and tens of thousands, respectively. Such features directly lead to immense difficulties in the computation and understanding combustion including subproblems of *uncertainty quantification* (*UQ*) (Wang and Sheen 2015), *model reduction* (Lam and Goussis 1994), and *stiffness removal* (Lu et al. 2009a, b).

Through the combined approach of quantum chemistry calculations and laser spectroscopy techniques, the transition state, rate constant, and other information on many elementary reactions can be acquired quite satisfactorily (Miller et al. 2005; Pilling 2009). However, quantifying the elementary reaction rates one by one is extremely time-consuming, and is strongly limited by the computational cost for complex fuels. Consequently, kinetic modelers first try to identify all possible elementary reaction pathways based on existing knowledge, and then either obtain known reaction rate constants based on available calculations and measurement (usually a small portion) or estimate those where the related calculations or measurements are not feasible. This eventually leads to the construction of detailed reaction mechanisms (Westbrook et al. 2009). In these reaction mechanisms, pre-calculated or measured reaction rates inevitably have uncertainties in the rate constants, and estimated rates are associated with larger uncertainties. It is also highly possible that there could be an incomplete physical understanding or missing reaction pathways in the model construction, as in the case of a recently discovered low-temperature reaction pathway (Jalan et al. 2013). The uncertainties in the model description and reaction rate constants would eventually be reflected in the modeling results such as ignition delay time and laminar flame speed, generating biased comparison against experimental measurements, and hence necessitating *UQ* in combustion systems. While it is relatively straightforward to evaluate uncertainty for homogeneous and laminar combustion systems, uncertainty induced by chemical kinetics in turbulent combustion modeling is still under investigation (Mueller et al. 2013). A crucial question that could be raised for chemists and combustion modelers is: which reaction rates do we need accurately, which reaction rates do we only need their order of magnitude, and which reaction is the "rate controlling" reaction of a reacting system? The answer relies on the understanding of combustion chemistry and the utilization of computational diagnostics.

Another major problem resulting from the high dimensionality of the kinetic model is the unaffordable computational cost, in that even if all the elementary

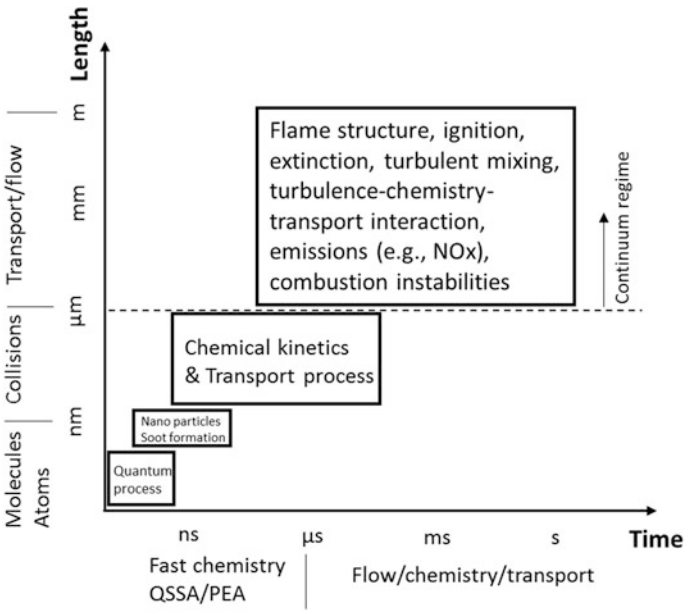

Fig. 2.1 Multi-length and timescale nature of combustion process

reaction rates are known and accurate, the computational cost of solving so many species and reactions in any reacting flow simulation is too much to be practically useful. Such complexity includes the large number of species conservation equations, multicomponent diffusivity, and limited length and time scales required to resolve the physical–chemical process for the combustion field both locally and instantaneously. As shown in Fig. 2.1, the chemical timescale in a combustion process ranges from O(ns) to O(s) and the length scale involved ranges from O(µm) to O(m), and consequently, combustion phenomena can occur across more than six orders of magnitude for both length and time domains. With computational power increasing exponentially following the Moore's law (Waldrop 2016), direct numerical simulation (DNS) of a turbulent flame in a simple geometry resolving all turbulent scales can nevertheless only track about 50 species using one of the most powerful computational resources available (Chen 2011). Recognizing that the number of species allowed in combustion computations in complex geometries is even significantly less, substantial reduction of the kinetic model in terms of its size is necessary, while maintaining reasonable accuracy. This is the major motivation for extensive methods developed for *model reduction*.

Even a reduced mechanism with sufficiently small size might still be unsuitable for DNS. Besides the large number of species, additional complexity exists due to the broad range of timescales corresponding to each species' lifetime ($\tau_i = -\frac{1}{J_{ii}}$, the

magnitude of the reciprocal of diagonal terms of chemical Jacobian $\boldsymbol{J}$. When the timescale of the fastest species is much shorter compared to the integration time step of interest, the difficulty of *chemical stiffness* occurs. The short timescales associated with those highly reactive radicals and fast reversible reactions can be in the order of nanoseconds or shorter, placing strong constrain on the direct usage of explicit combustion CFD solvers. Species with short timescales can be largely eliminated by skeletal model reduction, further facilitated by the proper implementation of classical quasi-steady-state assumption (QSSA) for species and partial equilibrium assumption (PEA) for reactions, in many cases.

The second feature of the complexity in chemical kinetics is the high nonlinearity, through the functional dependence of the rate constant, reaction rate, and the interaction among elementary reactions. For an elementary reaction, e.g., $v_A A + v_B B \rightarrow v_P P + v_Q Q$, the *Law of Mass Action* states that the reaction rate ω has the following dependence on concentration: $\omega = k[A]^{v_A}[B]^{v_B}$, where $[A]$ and $[B]$ are the mole concentrations for species A and B, respectively (mole/unit volume); v_A and v_B are stoichiometric coefficients for species A and B, respectively. As such the pressure dependence of the reaction rate could be quite nonlinear through the non-unity reaction order. Furthermore, strong nonlinearities are associated with the Arrhenius dependence on temperature of the reaction rate constant k as $k = AT^b \exp\left(-\frac{E_a}{RT}\right)$, where A is the pre-exponential factor, b is the temperature power exponent, T is the temperature, E_a is the activation energy that represents the minimum energy barrier required for a successful collision, and R is the universal gas constant. It should be noted that these reaction rate coefficients usually have different dimensions because the reactions have different molecularities. So a direct comparison of the order of magnitude of such rate coefficients is *meaningless* to tell which reaction is faster, the answer to which is then vigorously provided in (Lam 2013). Due to the strong sensitivity of k to T, a reaction hardly proceeds when $T \ll T_a$, while it initiates rapidly with depletion of the reactants as T approaches T_a. The higher the activation energy, the more sensitive this process to temperature. This explains why many combustion phenomena either occur in a very short period of time or within a very limited spatial domain, and explains the abrupt nature of ignition and extinction. The large activation energy assumption actually brings significant convenience for theoreticians to conduct analytical combustion research using asymptotic analysis (Law 2006), by assuming one-step overall or a few steps semi-global reactions. It should be noted that asymptotic method is useful in capturing the leading order physics in certain simplified theoretical problems, but not so useful in modern reacting flow research where the finite rate chemistry is crucial in determining the local thermal–chemical structure and emission generation. In unsteady and turbulent flows, where local temperature fluctuation presents, the induced reaction rate fluctuation could be large enough to cause leading order change in the local thermal expansion and therefore the flow field, which is a fundamental difficulty in resolving *turbulent–chemistry interaction* (Meier et al. 2000).

In addition to temperature, pressure can also lead to nonlinear behavior in a chemical reaction, such as in the cases of unimolecular reaction and three-body recombination reaction, which could be explained using Lindemann theory. It is straightforward to obtain the distinctive pressure dependence of k in the low- and high-pressure limits for such reactions, and interpolate for the other conditions using the pressure fall-off curve (Troe and Ushakov 2011).

Moreover, the global behavior of a kinetic-controlled system could be quite nonlinear as well, due to the coordination and competition of the chain mechanism, for which the simplified one-step overall reaction is inadequate even to be qualitatively correct. Two examples are given here as a demonstration of such intricacies in realistic kinetic systems: the H_2/air explosion limits and the negative temperature coefficient (NTC) phenomena, both of which have attracted considerable research efforts and could demonstrate the necessity of using realistic detailed chemistry for combustion research.

2.2 Necessity of Adopting Realistic Chemistry in Combustion

2.2.1 Representative Non-monotonic Kinetic Behaviors in Homogeneous Reacting Systems

The well-known Z-shaped curve describing the explosion limits of H_2/air mixtures (Law 2006) is shown in Fig. 2.2a. Basically, at a given moderate temperature, the mixture becomes explosive, nonexplosive, and explosive again as it traverses the first, second, and third explosion limits by gradually increasing the system pressure.

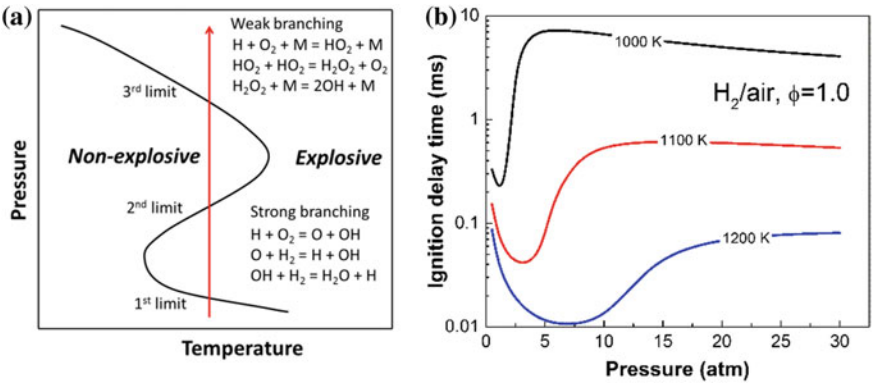

Fig. 2.2 **a** Schematic of the three explosion limits of homogeneous H_2/air mixtures, demonstrating the non-monotonic Z-curve response (left) and **b** Non-monotonic ignition delay time of H_2/air as a function of pressure—the negative pressure coefficient (NPC) behavior (right)

It is well established that the first explosion limit is controlled by the competition of strong chain branching reactions involving H, O, and OH radicals, as represented by (H1): $H + O_2 = O + OH$, versus wall destruction. As such, as pressure increases, H1 dominants and the system becomes explosive. However, with increasing pressure, the mixture crosses the second limit where the three-body termination reaction (H9): $H + O_2 + M = HO_2 + M$ becomes more important due to the enhanced collision frequency, competing with (H1) for the highly reactive H atom, and producing less reactive HO_2 radical. This weakens the overall reactivity and consequently suppresses the explosion, causing the second limit. With further increase in pressure, the accumulation of the HO_2 eventually facilitates the formation of H_2O_2 and triggers the strong chain branching $H_2O_2 + M = OH + OH + M$, forming reactive radical OH above the third explosion limit. Therefore, the mixture is nonexplosive on the left of Z-curve, while explosive on its right. A hidden parameter in Fig. 2.2a is actually the threshold residence time for explosion observation. In other words, the Z-curve itself is an iso-contour of ignition delay. The non-monotonic Z-curve of H_2/air could lead to the non-monotonic response of ignition delay time in terms of pressure. As pressure increases, the ignition delay of H_2/air system decreases, increases, and decreases again, leading to the negative pressure coefficient (NPC) phenomena as in Fig. 2.2b, using the mechanism from (Li et al. 2007).

Another example is the non-monotonic explosion limit and autoignition delay of general large hydrocarbons and certain oxygenated fuels, affected by the low-temperature chemistry (LTC). Take one of the primary reference fuels (PRF) *n*-heptane as an example. As indicated by the arrow in Fig. 2.3a, for a given pressure and with increasing initial temperature, the mixture transits from nonexplosive, explosive, nonexplosive, and explosive again. Similar to the H_2/O_2 system, the longer the residence time allowed for the observation, the wider the

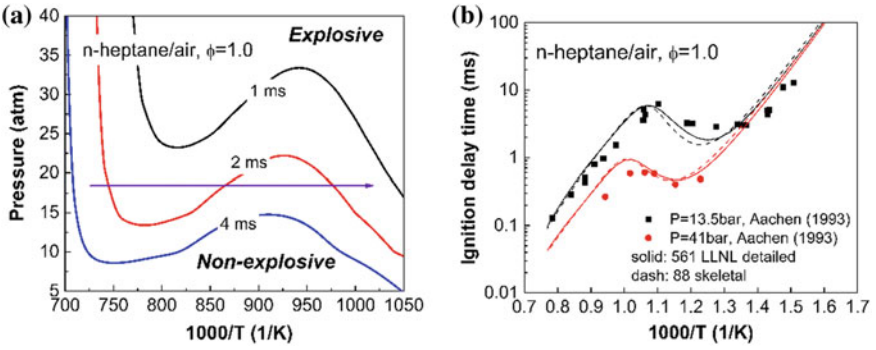

Fig. 2.3 **a** Explosion limit of stoichiometric n-heptane/air mixture (left) and **b** Experimental and modeled ignition delay of stoichiometric n-heptane/air mixture as a function of temperature (right), demonstrating NTC

thermodynamic regime for the mixture to be explosive. In Fig. 2.3b, the ignition delay for the homogeneous stoichiometric *n*-heptane/air mixture obtained from both shock tube experiments from Aachen (Ciezki and Adomeit 1993) and simulated by detailed (Curran et al. 1998) and skeletal kinetic models (Yoo et al. 2011) are compared, for a wide range of temperatures under two pressure conditions.

There are three major observations in Fig. 2.3: first, for both pressures, there is a low-to-intermediate temperature regime where the ignition delay time actually increases with initial temperature, implying reduced reactivity. This is the fingerprint negative temperature coefficient (NTC) phenomena for many fuels, indicating a non-monotonic change of the overall chemical reactivity with initial temperature; second, under both low and high temperatures beyond NTC, the ignition delay exhibits an Arrhenius behavior, meanwhile with the low-temperature ignition delay only slightly depending on pressure; third, as pressure increases, NTC shifts to higher temperatures, and the extent of NTC becomes less pronounced. Such shifting feature is systematically studied in two sequential works on the kinetics of upper and lower NTC turning points (Ji et al. 2016, 2017). If the ignition history is further investigated, it is seen that in the intermediate temperature regime, the autoignition includes two stages, with the first stage controlled by LTC and the second stage controlled by H_2O_2 decomposition. Recent modeling and experimental work (Zhao and Law 2013; Zhang et al. 2016) also shows that the first-stage ignition delay exhibits an NTC behavior itself.

Taking n-heptane as an example, major reaction pathways of oxidation are shown in Fig. 2.4 for both low- and high-temperature chemistry. For LTC, following the H abstraction reaction, the alkyl radical (R) generated first combines an oxygen molecule to form alkyl peroxide (RO_2) and isomerizes to alkyl hydroperoxy (QOOH, where Q has one less H atom than R), which then combines with another oxygen molecule to form ($QOOHO_2$) and further forms ketohydroperoxide and an OH radical. The decomposition of ketones then produces aldehydes, carbonyls, and additional OH radical, resulting in the low-temperature chain branching. At the end of this stage, a certain amount heat release occurs to rise the system temperature by

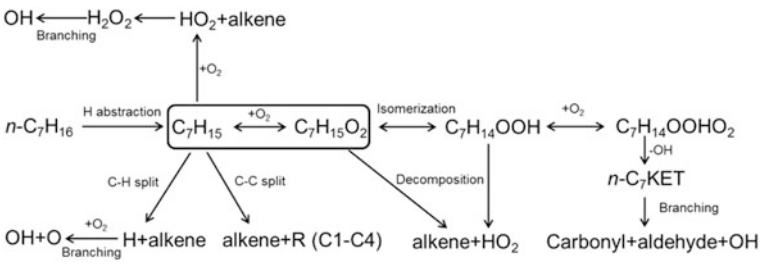

Fig. 2.4 Map of combustion chemistry, represented by n-heptane

a few hundred degrees, which is known as the cool flame phenomenon. The oxygen combination reaction forming RO_2 as boxed in Fig. 2.4 is referred as the heart of combustion chemistry (Tomlin et al. 1997). Due to its exothermic nature, the chemical equilibrium shifts backward when cool flame occurs and consequently LTC is suppressed, the alkyl radicals generated hence continue thermal pyrolysis via *C-C* and *C-H* splitting rule forming smaller fragments. Together with the low-temperature product decomposition (e.g., QOOH), substantial amounts of HO_2 and H_2O_2 can be formed which eventually branch into OH radicals and drive ignition. This understanding is essential in the working mechanism of early lead-based antiknock additives, where their abilities of destroying HO_2 and retarding H_2O_2 branching could effectively help to increase ignition delay and thereby suppress engine knock (Benson 1988). With very high initial temperatures, it is also possible that H(1) could be the dominant chain branching in ignition. The detailed low-temperature chemical kinetics are extensively reviewed in (Battin-Leclerc 2008; Zádor et al. 2011), which are closely related to cool flames and engine knock.

Knowing about the map of combustion chemistry, NTC is fundamentally induced by the transition from low- to high-temperature chemistry, via two-stage ignition. Specifically, at very low temperature, there is no apparent delay between the first-stage ignition and the subsequent main ignition, and hence the observed single-stage ignition; as initial temperature increases, the duration of the first-stage ignition becomes shorter while the corresponding cool flame temperature rise at the end of the first stage is also lower, indicating decreasing amount of heat release in the low-temperature chain branching, and consequently the lower initial temperature for the second stage leads to a longer second-stage ignition delay and the overall ignition delay from low-to-intermediate temperature regimes; with further increase in initial temperature, the ignition reverts back to a single stage and the overall ignition delay decreases again. The non-monotonic change of the total ignition delay time with initial temperature then constitutes the NTC effect. The quasi-linear response in cool flame temperature rise also brings useful convenience in modeling other more complex behaviors, for example, the NTC-affected combustion phasing in homogeneous charge compression ignition conditions (Pan et al. 2016; Tao et al. 2017).

In general, the global nonlinearity of a kinetic system could be induced by either the competition of different chain branching and termination reactions or the equilibrium shift of certain critical reactions. For either case, a kinetic model with a qualitatively complete set of reactions and quantitatively accurate thermal–chemical parameters are needed for a reasonable description even in a purely homogeneous kinetics-controlled system. A combustion system involving large hydrocarbons needs both low- and high-temperature kinetics for reasonable and accurate description.

2.2.2 Manifestations of Non-monotonic Kinetic Behaviors in Reacting Flows

Out of the high dimensionality of chemical kinetics, combustion systems always involve multiple components. The collisions among different molecules fundamentally lead to the transport phenomena of mass diffusion, which needs accurate characterizations of binary diffusion coefficients between each pair of species, and more importantly, the diffusion velocity of an individual component in the local mixture. Neglecting pressure, temperature gradients, and body forces, the multicomponent diffusivity (Lam 2006) can be derived from the Boltzmann equation through the Maxwell–Stefan model:

$$\nabla X_i = \sum_{j=1}^{N} \frac{X_i X_j}{D_{i,j}} \left(V_j - V_i\right),$$

where X_i and V_i are the molar fraction and diffusion velocity of species i, respectively; and $D_{\mathrm{i,j}}$ is the binary diffusion coefficient between species i and j. For an N component mixture, V_i can be solved from matrix inversion with a computational complexity of $\mathrm{O}(N^3)$. This model has good accuracy and ensures mass conservation, and is recommended in high-fidelity combustion simulations, which is nevertheless limited by its nonlinearity and prohibitive computational cost. In most combustion modeling, a simplified mixture-average diffusion model or even constant non-unity Lewis number assumption (Burali et al. 2016) is hence applied to replace the multicomponent diffusivity. Recently, there has been work on multicomponent diffusivities reduction via species grouping (Xin et al. 2015), and an accurate non-iterative algorithm with computational complexity O(N) to calculate the multicomponent diffusion velocities (Ambikasaran and Narayanaswamy 2017), both of which achieve reasonable accuracy and much lower computational cost. When there is diffusion, the diffusion matrix of the species in reacting flow problems is modified by reduced chemistry, which is addressed in (Lam 2007).

Flows are complex by nature, reflected by essential nonlinearity rooted in the Navier–Stokes (N–S) equations, regardless of potential complex geometry. When a chemical reaction occurs in turbulent flow, timescales of the local eddies are involved to further constrain the chemistry, which hence leads to nonlinear couplings between chemistry and transport. When nonuniformities and unsteadiness exist, the divergence or convergence of the local flow field could change the local residence time tangential or normal to the flame surface, resulting in combined effects such as the displacement of the flame surface, distortion of the flame structure, and modification of the flame temperature and burning rate. Wrinkles could also be generated on the flame surface via hydrodynamic and thermal-diffusive instabilities (Matalon 2007), which in turn affect the burning flux significantly. Furthermore, practical combustion processes could occur in boundary

layers, turbulence, supersonic and multiphase flows, causing more ambiguities in measuring, simulating, and understanding chemistry-flow coupling. For such reasons, laboratory burners are usually laminar and have simple configurations, such as the bunsen burner, spherical bomb, counterflow, and stagnation flow. However, it should be realized that a major goal for those well-defined studies is to eventually extrapolate the insights to complex turbulent combustion scenarios, at least locally.

In Sect. 2.1, the H_2 explosion limit exhibits the well-known Z-curve behavior in a homogeneous system; however, it is expected that in a spatially nonuniform system, the characteristic flow time can fundamentally affect the ignition event. Such an influence becomes especially significant for a non-premixed system due to the intrinsic needs for mixing. By using numerical modeling with detailed chemistry and transport, Kreutz and Law (1998) computed the S-curve for the forced ignition in a non-premixed counterflow configuration, in which a jet of H_2 diluted with N_2 impinges against an opposed jet of heated air. It is shown in Fig. 2.5a that, at higher strain rate, the ignition limits retain its Z-shaped explosion response, which nevertheless shift to elevated temperature and pressure along the backbone of the extended second limit. This demonstrates that while the system retains its chemical kinetic feature, the reduced residence time modifies the reactivity progressively. In case of premixed flame propagation, where the role of transport is no less important but the temperature and radical pool concentration are much higher, the calculated laminar burning flux of a lean hydrogen–air mixture as a function of pressure does show a non-monotonic behavior as well, consistent with the transition of chemistry in the Z-curve effect, as shown in Fig. 2.5b (Lu and Law 2008). Recognizing the relative simplicity of H_2 as well as the central role that it plays in the combustion process of all hydrocarbons, the retaining of the non-monotonic

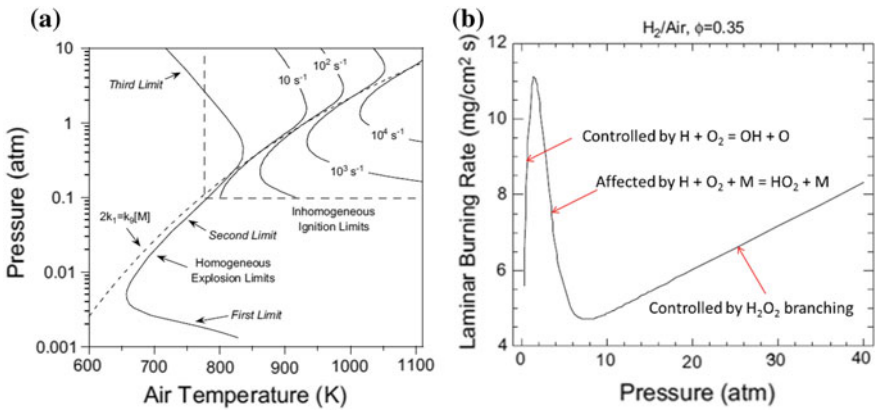

Fig. 2.5 **a** Ignition temperatures at various pressures for counterflowing 60% H_2 in N_2 vs. heated air for different pressure-weighted strain rates, superimposed on the curve for the homogeneous explosion limits (left). **b** The calculated laminar burning flux of H_2/air mixtures ($\phi = 0.35$) with non-monotonic response to pressure (right)

Z-curve effect on ignition and flame propagation in convective–diffusive environments further accentuates the inherent necessity of accommodating realistic chemistry in describing combustion phenomena.

Similarly, different counterpart phenomena of NTC have been identified in non-premixed combustion systems. In a non-premixed system, the S-curve concept is frequently adopted to describe the global response, for example, in a plot of maximum system temperature versus hot air boundary temperature. In particular, Zhao and Law (2012, 2013) have demonstrated that with sufficient low strain rates and/or high pressures, the low-temperature chemistry can strongly couple with transport process with substantial thermal feedback and induce a secondary S-curve on the lower branch of the primary S-curve, which includes distinct ignition and extinction states, shown as Regime II in Fig. 2.6a. For even higher strain rate/lower pressure conditions, the LTC-induced secondary S-curve becomes stretched with disappeared non-monotonicity (Regime I), while for even lower strain rate/higher pressure, the LTC-induced secondary S-curve becomes more pronounced and can directly transition to hot flame (Regime III). As such, the manifestation of LTC in a convective–diffusive system is identified for the first time, which is subsequently observed experimentally using infrared and ultraviolet (UV) detection in the non-premixed counterflow at atmospheric and elevated pressures (Deng et al. 2014, 2017). As shown in Fig. 2.6b, the LTC-induced secondary S-curve corresponds to a

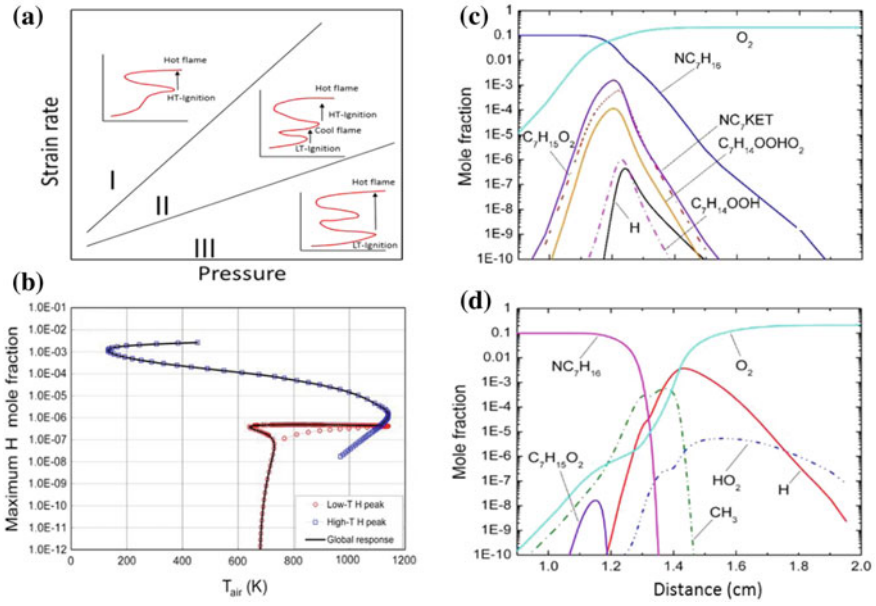

Fig. 2.6 **a** Regime boundary of NTC-affected ignition in a non-premixed counterflow; **b** A typical NTC-affected S-curve response in non-premixed counterflow; **c** Chemical structure for a typical cool diffusion flame; **d** Chemical structure for a typical hot diffusion flame

unique radical peak in a lower temperature region and the double S-curve response is indeed the combined effects from both low- and high-temperature chemistry occurring at regions with different temperatures. A novel class of flame, referred as the diffusion cool flame or the NTC flame, occurs along the upper branch of the secondary S-curve, for which the distinctive chemical structures for a diffusion cool flame of n-heptane in counterflow are demonstrated in Fig. 2.6c, with the counterpart structure for a regular n-heptane/air diffusion flame shown in Fig. 2.6d.

It is seen that unlike the regular diffusion flame featured by steep consumption of fuel and oxidizer as well as reactive radicals (e.g., H) in the flame, such a diffusion cool flame exhibits much lower heat release and flame temperature, spans in a much broader flame zone, and is characterized by the low-temperature intermediates as products, as discussed in Fig. 2.4. The fuel is reformed by the LTC and leaked through the flame zone, instead of being completely consumed to form CO_2 and H_2O. The diffusion cool flame has also been suggested to explain experimental results on microgravity droplet combustion (Nayagam et al. 2012; Farouk and Dryer 2014) and plasma-assisted combustion (Won et al. 2015).

While in a premixed system, the coupling between LTC and convective–diffusive transport can lead to the existence of a novel LTC-controlled propagating flame front. It should be first noted that the concepts of "a 1-D steady planar premixed cool flame" and "cool flame speed" are fundamentally not well-defined compared to the classical regular laminar premixed flames. Specifically, the downstream of a cool flame is at *quasi* or the *rate-constrained* chemical equilibrium such that with long enough residence time, it can eventually evolve to the chemical equilibrium state with adiabatic flame temperature. Recognizing such failures, there are at least two approaches for the establishment of a steadily propagating, planar cool flame. The first is to freeze the downstream chemistry by involving radiative heat loss, rendering it to be asymptotically non-reactive (Ju 2017). The problem is similar to that of the cold boundary difficulty in the conventional premixed flame analysis, in that given infinite time any chemistry with a finite temperature can achieve complete reaction, even with radiative loss. The second scenario is more realistic, where a steady self-sustained cool flame is established by truncating the downstream flow time in order to prevent transition from cool flame to the state of chemical equilibrium such that the downstream is constrained in cool flame quasi-chemical equilibrium state. This can be readily accomplished by aerodynamically straining the flow, as observed both computationally and experimentally in the counterflow system (Zhao et al. 2016). It is seen that a strain rate window exists for the steady self-sustaining premixed cool flame, out of which a cool flame either cannot be initiated or transitions to a hot flame, as shown in Fig. 2.7a. It is shown in Fig. 2.7b that the laminar premixed cool flame has a much lower flame speed and very different equivalence ratio dependence for its temperature, compared to the regular laminar premixed flame. Unique dependence of flame speed on the cool flame temperature is also observed. It is also worth noting that the LTC effect could be generally significant in IC engines even for flame propagation, as shown by a recent

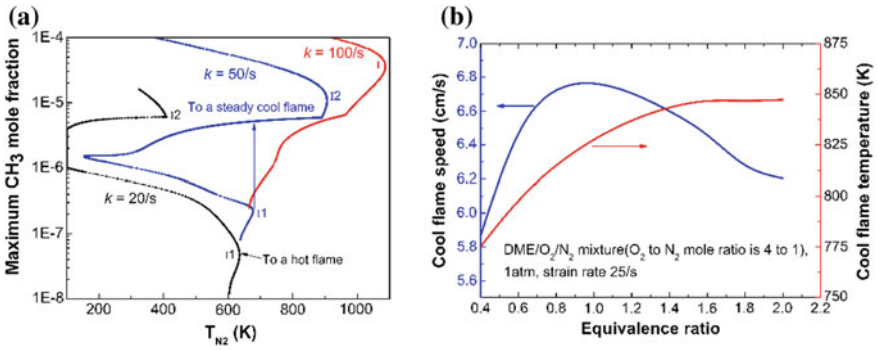

Fig. 2.7 **a** S-curve response of stoichiometric DME/O_2 mixture with 15.8% N_2 versus hot N_2 at different strain rates 20/s, 50/s, and 100/s. **b** Flame speeds and temperatures for the cool flames under various equivalence ratios of DME/O_2/N_2 mixtures with 15.8% N_2, in a counterflow twin-flame configuration at 300 K and 1 atm, with local strain rate fixed at 25/s

study (Pan et al. 2016), a flame could propagate faster under lower upstream temperature conditions than higher ones due to the fuel reforming and feeding of reactive intermediates via LTC.

So far, the manifestations of two typical non-monotonic kinetic behaviors have been shown in a representative convective–diffusive system—counterflow. Actually, the results bear relevance to practical situations due to the fact that a local laminar flamelet within a turbulent flame structure is frequently positively stretched. Therefore, it is strongly recommended that the flamelet model used in large eddy simulation (LES) must be comprehensive enough to capture the exact solution for chemistry-flow coupling. In light of flame modeling, some recent progress on the autoignition-affected flame propagation (Martz et al. 2011), stabilization (Deng et al. 2015b), and combustion mode transition (Pan et al. 2016) is worth noting, where the flame dynamics and transition could be fundamentally affected by ignition chemistry and heat release occurs upstream of the flame.

As an example, the steady laminar flame propagation in stoichiometric n-heptane/air mixture at elevated inlet temperatures and 40 atm calculated using PREMIX is presented in Fig. 2.8a, which shows the non-monotonic trend affected by upstream LTC reactivity. Namely, the flame speed increases, decreases, and increases again with elevated inlet temperature, similar to NTC for ignition delay. Different from normal flames, the flame speed with partially reactive upstream boundary quantitatively depends on the length of computational domain from the upstream inlet to the flame front. From the classical laminar flame theory, the laminar burning flux is usually considered an eigenvalue of the energy or species conservation equation, and could be uniquely determined by imposing proper boundary conditions. Note that the cold boundary difficulty is avoided by setting zero reaction rate at upstream boundary for temperature below a threshold value, so that no reaction occurs in the preheat zone. In the current cases, such dilemma from

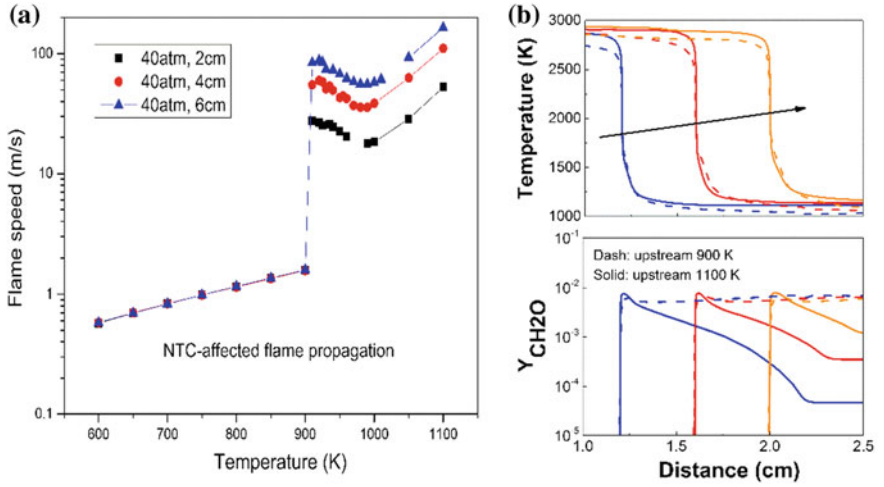

Fig. 2.8 **a** NTC-affected laminar flame propagation for stoichiometric n-heptane/air mixture at 40 atm and elevated upstream temperatures, exhibiting non-monotonic flame speed. **b** Enhanced flame propagation through low-temperature intermediates feeding, e.g., formaldehyde

the severe cold boundary difficulty is nevertheless inevitable due to more pronounced partial oxidation and chemical reactivity from autoignition under elevated thermodynamic conditions, and consequently the flame burning flux cannot be uniquely determined anymore. This shows the essential unsteady nature of the autoignitive upstream boundary and the crucial role of residence time for the autoignition-affected flame propagation, similar to the laminar premixed cool flame (Zhao et al. 2016). The non-monotonic NTC behavior of the laminar flame propagation nevertheless holds qualitatively for different domain lengths in NTC regime. To further demonstrate the thermal and chemical effect on the NTC behavior of flame speed, profiles of flame temperature and formaldehyde are shown in Fig. 2.8b (Pan et al. 2016) for two cases during the transient development of flame propagation with upstream temperature 900 K and 1100 K, respectively. It is seen that although the 900 K case has a lower upstream temperature, the more pronounced LTC upstream leads to much higher HCHO concentration and reactive intermediate feeding, eventually rendering a higher flame speed from its dominant chemical effects. This is also very relevant to practical combustors where elevated temperature and pressure inevitably exist, and could result in severe abnormal combustion, such as engine knock in spark-ignition engines (Wang et al. 2017), and flashback in gas turbines (Benim and Syed 2014). It should be realized that the new features of LTC and transport coupling not only shed light on the physics of local behavior in general turbulent–chemistry–transport coupling, but also place new constrains on the integration time step and spatial refinement for combustion modeling.

In addition to the Z-curve and NTC phenomena, there are more examples inherently controlled by nonlinear chemical kinetics and hence require the proper accommodation of detailed chemistry, which include but not limited to flammability limits (Law and Egolfopoulos 1992), NO_x (Turns 1995) and soot (Frenklach 2002) formation, and combustion phasing in compression ignition engines (Tao et al. 2017). It should be fairly clear now that although the one-step overall kinetic mechanism has been used for some combustion applications, it is both physically and chemically insufficient for general reacting flow and turbulent combustion research.

2.3 Methods to Accommodate Detailed Kinetics in Combustion Modeling

Now, it is clear that chemical kinetics are complex by nature and are essential in predicting combustion and flame processes. A large number of strongly coupled species and reactions are invariably included as aforementioned, which not only require high computational cost for validation and prediction but also impose considerable difficulty in identifying the controlling physical and chemical entities. Consequently, considerable interest has been attracted in the developing computational tools for the reduction of the size of detailed reaction mechanisms, and for the diagnostics of the processes and phenomena of interest.

2.3.1 Model Reduction and Stiffness Removal

A major approach for mechanism reduction is the skeletal reduction, in which unimportant species and the corresponding reactions are eliminated from detailed mechanisms. As such, mechanism reduction is by nature an optimization process, and hence compromise has to be achieved between the number of species remained and the relative error caused by the species eliminated. Obviously, a larger size of the skeletal mechanism usually has a smaller error. Skeletal reduction can be achieved using methods such as sensitivity analysis (Rabitz et al. 1983), detailed reduction (Wang and Frenklach 1991), principal component analysis (Vajda et al. 1985), Jacobian analysis (Turanyi 1990), directed relation graph (DRG) (Lu and Law 2005; Luo et al. 2010), and other DRG-based methods such as DRG-aided sensitivity analysis (DRGASA) (Zheng et al. 2007), DRG with error propagation (DRGEP) (Pepiot-Desjardins and Pitsch 2008), DRGEP with sensitivity analysis (DRGEPSA) (Niemeyer et al. 2010), path flux analysis (PFA) (Sun et al. 2010), and transport flux-based DRG (Tosatto et al. 2011). These methods, especially DRG and its extensions, have resulted in substantial simplifications in reducing the size of kinetic mechanisms and the subsequent application in combustion modeling.

Compared with DRG, DRGEP assumes that the reduction error decays geometrically along the graph searching paths. In path flux analysis (PFA), the direct relation between each pair of species pair in DRG was redefined, where the creation and consumption reactions of a species are considered separately. A systematic review of the DRG-based methods can be found in (Tosatto et al. 2013), and many of them have already been integrated in commercial software, such like ANSYS, CONVERGE, etc. Recently, some new tools for model reduction are also developed, such as the betweenness centrality (BC)-based method to evaluate how close a certain species serves as hub in effectively connecting other species (Zhao et al. 2015), element flux analysis (He et al. 2010), and global pathway selection (GPS) method (Gao et al. 2016) to account for the elemental flux in a reaction network. A common feature for all these methods is that different criteria are used to rank species based on the sampling of a wide range of representative reaction states including intense burning, ignition, and extinction. The species ranking obtained is subsequently used to guide the elimination of species. In general, model reduction for large kinetic mechanisms is not a problem anymore and could be easily performed with user-preferred size and good error control.

While the skeletal mechanisms could be sufficiently small, many of them are still inaccessible for large-scale combustion modeling. The additional obstacle comes from chemical stiffness induced by the highly reactive radicals and fast reversible reactions. Consequently, beyond skeletal level, a mechanism could be further reduced by timescale reduction. Based on the understanding that fast chemical modes typically are not self-sustained and could lead to algebraic relations when exhausted, systematic approaches such as intrinsic low-dimensional manifold (ILDM) (Maas and Pope 1992) and computational singular perturbation (CSP) (Lam and Goussis 1989, 1994; Lam 2013) were developed. However, both involve time-consuming evaluation and manipulation of Jacobian matrices, especially with large mechanisms. As direct and intuitive methods to further reduce a mechanism especially the corresponding stiffness, QSSA species and PEA reactions are frequently implemented in theoretical analysis and computation of reacting systems. A species can be considered as QSS when its production and consumption rates are both fast, such that the net reaction rate is much smaller compared to either. CSP is particularly useful in identifying fast species, and a systematic and vigorous way of identifying QSS species based on CSP is demonstrated (Lu and Law 2008). On the other hand, in the case of a fast reversible reaction, both forward and backward reaction rates are so fast that the net reaction rate is much smaller compared to either. It should be noted that these approximations are simple to apply; however, rigorous classification of these two types of fast processes in a kinetic system, PEA in particular, is still not straightforward and requires user expertise. By taking the advantage of QSS and PEA, methods with dynamic stiffness removal have been demonstrated for 2D turbulent combustion DNS with moderate stiffness, and an integration timescale of 5–10 ns is achieved (Lu et al. 2009).

Figure 2.9 shows the comparison of the ignition history of stoichiometric n-heptane/air mixture under 800 K and 20 atm. Three different levels of chemical

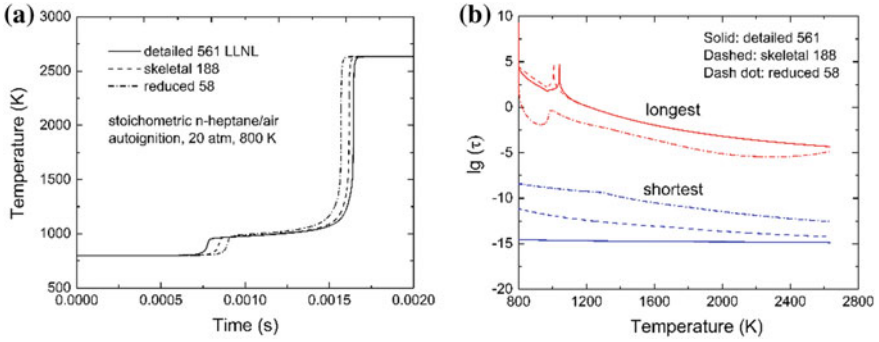

Fig. 2.9 **a** Temperature history of stoichiometric n-heptane/air autoignition under 800 K and 20 atm. **b** species lifetime span calculated using the detailed (LLNL V2 with 561 species), skeletal (188 species), and reduced (58 species) mechanisms

kinetics have been utilized, including the detailed mechanism with 561 species from LLNL (Curran et al. 1998), a skeletal mechanism with 188 species using DRG, and a reduced mechanism with 58 species further accommodating sensitivity analysis and QSSA assumptions (Yoo et al. 2011). The two-stage ignition behavior is both qualitatively and quantitatively captured by the three mechanisms, with the reduced mechanism causing the largest deviation compared to the detailed mechanism. The lifetime of the fastest and slowest species is calculated based on the reciprocal of the diagonal terms of the Jacobian. A span of lifetime up to 15 orders of magnitude is observed for the most detailed mechanism, and the range shrinks with reduced mechanism size. But still, even the most reduced mechanism with 58 species leads to the fastest species time around 1 ns or shorter, demonstrating remained stiffness for the application of explicit CFD solvers. It should be noted that the O(10^{-15} s) timescale is even shorter than that of molecule vibration and is potential induced by empirical rate rules (chen et al. 2017), special attention therefore has to be paid on the species timescales and chemical stiffness for kinetic modelers.

2.3.2 *Methods to Accelerate Chemistry Integration*

With chemical stiffness as a remained challenge, the characteristic chemical time of the fastest species constrains the time step allowed for explicit chemistry integration, which is typically around or below 10^{-9} s depending on the system and thermodynamic conditions. Recently, an analytical formulation for the efficient implementation of computational singular perturbation (CSP) has been theoretically constructed by Lam (2017), in which insights have been made on the fastest species based on its timescale and the corresponding QSS value could be accurately predicted across the thin transition layer at each time step. As a result, tedious explicit integration to resolve the apparent exponential transition layer of the fastest species is avoided and the

integration time step could be extended. However, the computational cost using explicit solvers can be hardly affordable if severe chemical stiffness exists, especially when there is no gap in the species timescale. Implicit time integration involving chemical Jacobian evaluation and factorization is widely adopted in practical reacting flow simulations, such as the legacy ODE solvers VODE (Brown et al. 1989) or DASAC (Caracotsios and Stewart 1985), which allow for longer time steps usually limited to 10^{-8}–10^{-6} s by the spatial resolution and the flow Courant–Friedrichs–Lewy (CFL) condition. The computational overhead of implicit solvers is primarily attributed to the Jacobian evaluation and *LU* decomposition. For small to moderate mechanisms, the computational cost is typically $O(N^2)$ and dominated by Jacobian evaluation through numerical perturbations; while for large mechanisms, the computational cost is instead $O(N^3)$ and controlled by *LU* decomposition. The performance of an implicit solver could be substantially improved by incorporating recent developments. For example, evaluation of the Jacobian matrix can be expedited through analytic techniques (Perini et al. 2012; Niemeyer et al. 2017), and *LU* decomposition can be enhanced by preconditioning (McNenly et al. 2015) and sparse matrix techniques (Schwer et al. 2002). These advantages should be taken whenever possible for a combustion modeler.

For multidimensional reacting flow simulation, neither fully explicit nor fully implicit integration schemes are applicable, due to the large number of integration time steps or spatial grid points, respectively. Therefore, implicit and explicit discretizations are usually applied separately to different terms in the governing equation via operator-splitting schemes. Specifically, implicit solvers are utilized for the integration of chemistry, while the explicit solvers are employed to integrate the transport terms. It is worth noting that the Strang splitting (Strang 1968) is among the most widely used operator-splitting schemes for combustion simulations, which has second-order accuracy for sufficiently small integration time step and is rather straightforward to implement. However, recent studies have shown that large error might be introduced by Strang splitting when there is strong coupling between chemistry and diffusion, especially for limiting phenomena approaching ignition and extinction (Lu et al. 2017). Therefore, cautions should be taken when splitting scheme is applied in general turbulent combustion modeling.

One idea of particular interest to facilitate combustion simulation is the dynamic adaptive chemistry (DAC). The basic idea is to have an on-the-fly mechanism reduction scheme with minor computational cost, such that an adaptively reduced mechanism is rigorously produced based on the local and instantaneous thermochemical state as CFD proceeds. DAC has been realized based on primarily DRGEP (Liang et al. 2009; Shi et al. 2010) and DRG (Yang et al. 2013) with both noticeable reduction of CPU time and satisfactory accuracy. During implementation of DAC, the eliminated species are typically treated as chemically frozen, such that the conservation of element and mass is automatically satisfied. To further exploit the relative fastness of species in chemistry integration, another dynamic adaptive hybrid integration method (Gao et al. 2015; Xu et al. 2016) is constructed by implicitly integrating the chemistry of fast species, while explicitly integrating the slow chemical process and transport. This method, however, needs to be further

improved to account for the diffusion terms, which might not be necessarily slow compared to the chemical process. A few other representative advances in the development of explicit solvers for stiff chemistry include the dynamic multi-timescale (MTS) method by grouping and integrating species with similar timescales (Gou et al. 2010), which can be further coupled with dynamic adaptive chemistry (Sun et al. 2015), and an extended robustness-enhanced numerical algorithm (ERENA) based on an analytical solution of QSSA species with enhanced mass conservation (Morii et al. 2016). A crucial point to evaluate these algorithms is the most fundamental principle—mass conservation, which should always be guaranteed.

In addition to algorithms and software, the development in hardware-based reacting flow simulation tool is equally alluring. In the past, one could just wait for the next generation of CPUs to enable previously unaffordable calculations. However, due to aggravated power consumption and heat generation, the pace of decrease in transistor size slows down, so does the increase in computation power. To keep up with Moore's Law, parallelism technique is largely adopted by processor manufacturers. Graphics processing units (GPUs) consist of thousands of fairly simple processing cores, compatible with the level of parallelism of large clusters with CPUs. With explosive growth in processing capabilities and diminishing cost, GPUs with massive parallelism are becoming popular in general scientific computation (Niemeyer and Sung 2013). For reacting flow simulation, by taking the advantage of operator splitting, the chemistry integration can be performed on the GPUs with transport calculations done on the CPUs simultaneously, such that no portion of the computation waits for the other to accomplish.

2.4 Analyze and Understand Combustion Simulation Results Through Computational Diagnostics

Reacting flow simulation not only takes expensive computational cost but also generates huge amount of data, up to hundreds of terabytes (TB) or larger. Compared to the simulation itself, it is more valuable to mine the massive data and detect critical combustion features, such that general insights and guidance could be obtained; otherwise, one cannot learn much by just looking at those simulated colorful contours. Contrary to the direct response shown in the S-curve in laminar flow, ignition and extinction in turbulent environment could be difficult to detect and model, especially when embedded in spatial nonuniformities. Such a difficulty is further complicated by the complex fuel chemistry and various combustion modes, where one or several scalars, such as temperature, concentration, or mixture fraction, are usually inadequate. Similar to the development of laser-based diagnostics for turbulent flames, more can be learned through the computational diagnostics of flame simulations, especially recognizing the rapidly enhanced computational and physical–chemical fidelity of such simulations.

Sensitivity analysis (SA) (Turanyi 1990) has been extensively used in homogeneous and simple laminar combustion systems to identify important species and reactions for global and local responses. This method is performed by perturbing the parameters of interest, e.g., reaction rate constant, activation energy, etc., by a small percentage and observing the corresponding change in the target, e.g., ignition delay, flame speed, etc. By its trial-and-error nature, it is not practical to perturb a certain reaction rate constant and redo the simulation to obtain the sensitivity coefficients in turbulent combustion modeling.

Chemical explosive mode analysis (CEMA) (Lu et al. 2010; Shan et al. 2012), as an extension to CSP, has been developed as a post-processing tool to computationally identify key species and reactions, as well as critical flame response including ignition and extinction. In this method, CEM is a chemical property associated with the positive eigenvalues of the local chemical Jacobian, indicating the propensity of the mixture to ignite. It has been shown in the above references that the zero-crossing of the CEM is able to correlate with homogeneous autoignition, ignition and extinction turning points in a perfectly stirred reactor, propagation premixed flame front controlled by diffusion and autoignition, compression ignition for stratified charge, local extinction, and re-ignition in premixed and non-premixed jet flame. Another unique feature of CEMA is that radical explosion pointer and reaction participation index could be further defined to identify the contribution from each species and reaction to the explosive mode.

In recent works by Deng et al. (2015a, b), to understand the stabilization mechanism of a non-premixed jet in practical systems, direct numerical simulation has been conducted for dimethyl ether in a coflow configuration of air ambient with elevated temperature and pressure. Multi-brachial flame structure is observed as shown by the heat release rate profile in Fig. 2.10. It is expected some of the reaction fronts are regular flames, while the rest could be autoignition-induced

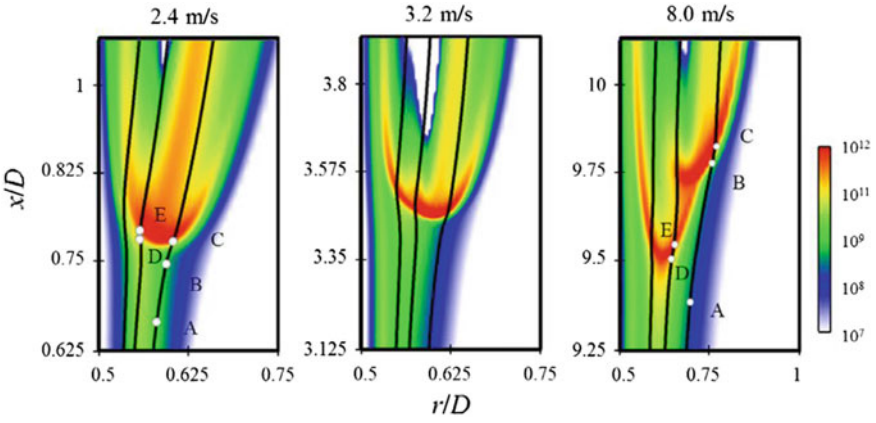

Fig. 2.10 Heat release rate (W/m^3) profiles. The mixture fraction iso-contours of Z_{st}, Z = 0.2, and Z = 0.3 are outlined from right to left, respectively. The CEMA sampling points for 2.4 and 8.0 m/s cases are marked along the iso-contours

reaction fronts. A question naturally raised is how to distinguish those different fronts and therefore combustion modes in such a partially premixed region? Representative points along different mixture fraction iso-contours have been selected to identify the key species and reactions using CEMA. From the radical and reaction participation index calculated at the sampled points, the reaction fronts are easy to distinguish: a normal flame front is found to have (H1): $H + O_2 = O+OH$ as the major chain branching, while autoignition reacting front is instead dominated by $H_2O_2 + M = OH + OH + M$ chain branching in this case. In addition, the active role of low-temperature chemistry is also demonstrated, characterized by reactions involving RO_2 radicals upstream to the multi-brachial structure.

The above example shows the usefulness of CEMA as a computational diagnostic tool during post-processing. It is worth noting that the exclusion of transport in the definition of CEMA should not be confused with the misunderstanding that diffusion is insignificant in flames. Although chemistry is strongly coupled with transport in most flames, the complex interaction between them eventually results in the changes in the chemical properties of the local mixture, which could be readily diagonalized via CEMA.

2.5 Concluding Remarks

This monograph focuses on the characteristics of combustion chemistry and its manifestation in reacting flows. Problems and potential solutions to accommodate, accelerate, and analyze the effect of detailed chemistry in combustion modeling are also discussed in detail. It is hoped that the readers of this chapter could have a brief taste of the key fundamental knowledge and challenges of chemical kinetics, as well as relevant cutting-edge application on the kinetic and numerical aspects of laminar and turbulent combustion modeling. The key message from the author is that detailed chemistry is essential for combustion research, for which the key kinetic features must be understood and utilized in combustion modeling to generate meaningful and predictive numerical results. Due to the length limit of this chapter, the readers are encouraged to dig into the reference for more details whenever necessary.

Acknowledgements PZ would like to thank Professors S. H. Lam, C. K. Law, F. L. Dryer, Y. Ju, M. E. Mueller at Princeton University, T. F. Lu at University of Connecticut, and many other colleagues for stimulating discussions and learning experiences over the years. Help from Mingyuan Tao and Yufeng Liu during the preparation of this chapter is also highly appreciated.

References

Ambikasaran S, Narayanaswamy K (2017) An accurate, fast, mathematically robust, universal, non-iterative algorithm for computing multi-component diffusion velocities. Proc Combust Inst 36(1):507–515. https://doi.org/10.1016/j.proci.2016.05.055

Battin-Leclerc F (2008) Detailed chemical kinetic models for the low-temperature combustion of hydrocarbons with application to gasoline and diesel fuel surrogates. Prog Energy Combust Sci 34:440–498. https://doi.org/10.1016/j.pecs.2007.10.002

Benim AC, Syed KJ (2014) Flashback mechanisms in lean premixed gas turbine combustion. https://doi.org/10.1016/C2013-0-18847-2

Benson SW (1988) The mechanism of inhibition of knock by lead additives, a chain debranching reaction. J Phys Chem 92:1531–1533

Brown PN, Byrne GD, Hindmarsh AC (1989) VODE, a variable coefficient ODE solver. SIAM J Sci Stat Comput 10:1038–1051. https://doi.org/10.1137/0910062

Burali N, Lapointe S, Bobbitt B, Blanquart G, Xuan Y (2016) Assessment of the constant non-unity Lewis number assumption in chemically-reacting flows. Combust Theor Model 20 (4):632–657. https://doi.org/10.1080/13647830.2016.1164344

Caracotsios M, Stewart WE (1985) Sensitivity analysis of initial value problems with mixed ODEs and algebraic equations. Comput Chem Eng 9(4):359–365. https://doi.org/10.1016/0098-1354(85)85014-6

Chen JH (2011) Petascale direct numerical simulation of turbulent combustion—fundamental insights towards predictive models. Proc Combust Inst 33(1):99–123. https://doi.org/10.1016/j.proci.2010.09.012

Chen D, Wang K, Wang H (2017) Violation of collision limit in recently published reaction models. Combust. Flame (186):208–210. https://doi.org/10.1016/j.combustflame.2017.08.005

Ciezki HK, Adomeit G (1993) Shock-tube investigation of self-ignition of N-heptane-air mixtures under engine relevant conditions. Combust Flame 93(4):421–433. https://doi.org/10.1016/0010-2180(93)90142-P

Curran HJ, Gaffuri P, Pitz WJ, Westbrook CK (1998) A comprehensive modeling study of N-heptane oxidation. Combust Flame 114(1–2):149–177. https://doi.org/10.1016/S0010-2180(97)00282-4

Deng S, Zhao P, Zhu D, Law CK (2014) NTC-affected ignition and low-temperature flames in nonpremixed DME/air counterflow. Combust Flame 161(8):1993–1997. https://doi.org/10.1016/j.combustflame.2014.01.020

Deng S, Zhao P, Mueller ME, Law CK (2015a) Autoignition-affected stabilization of laminar nonpremixed DME/air coflow flames. Combust Flame 162(9). https://doi.org/10.1016/j.combustflame.2015.06.007

Deng S, Zhao P, Mueller ME, Law CK (2015b) Stabilization of laminar nonpremixed DME/air coflow flames at elevated temperatures and pressures. Combust Flame 162(12):4471–4478. https://doi.org/10.1016/j.combustflame.2015.08.019

Deng S, Han D, Law CK (2017) Ignition and extinction of strained nonpremixed cool flames at elevated pressures. Combust Flame 176:143–150. https://doi.org/10.1016/j.combustflame.2016.10.015

Farouk TI, Dryer FL (2014) Isolated N-heptane droplet combustion in microgravity: 'cool flames'—two-stage combustion. Combust Flame 161(2):565–581. https://doi.org/10.1016/j.combustflame.2013.09.011

Frenklach M (2002) Reaction mechanism of soot formation in flames. Phys Chem Chem Phys 4 (11):2028–2037. https://doi.org/10.1039/b110045a

Gao X, Yang S, Sun W (2016) A global pathway selection algorithm for the reduction of detailed chemical kinetic mechanisms. Combust Flame 167:238–247. https://doi.org/10.1016/j.combustflame.2016.02.007

Gao Y, Liu Y, Ren Z, Tianfeng L (2015) A dynamic adaptive method for hybrid integration of stiff chemistry. Combust Flame 162(2):287–295. https://doi.org/10.1016/j.combustflame.2014.07.023

Gou X, Sun W, Chen Z, Ju Y (2010) A dynamic multi-timescale method for combustion modeling with detailed and reduced chemical kinetic mechanisms. Combust Flame 157(6):1111–1121. https://doi.org/10.1016/j.combustflame.2010.02.020

He K, Androulakis IP, Ierapetritou MG (2010) Multi-element flux analysis for the incorporation of detailed kinetic mechanisms in reactive simulations. Energy Fuels 24:309–317. https://doi.org/10.1021/ef900803q

Jalan A, Alecu IM, Meana-Pañeda R, Aguilera-Iparraguirre J, Yang KR, Merchant SS, Truhlar DG, Green WH (2013) New pathways for formation of acids and carbonyl products in low-temperature oxidation: the Korcek decomposition of γ-Ketohydroperoxides. J Am Chem Soc 135(30):11100–11114. https://doi.org/10.1021/ja4034439

Ji W, Zhao P, He T, He X, Farooq A, Law CK (2016) On the controlling mechanism of the upper turnover states in the NTC regime. Combust Flame 164:294–302. https://doi.org/10.1016/j.combustflame.2015.11.028

Ji W, Zhao P, Zhang P, Ren Z, He X, Law CK (2017) On the crossover temperature and lower turnover state in the NTC regime. Proc Combust Inst 36(1):343–353. https://doi.org/10.1016/j.proci.2016.05.046

Ju Y (2017) On the propagation limits and speeds of premixed cool flames at elevated pressures. Combust Flame 178:61–69. https://doi.org/10.1016/j.combustflame.2017.01.006

Kreutz TG, Law CK (1998) Ignition in nonpremixed counterflowing hydrogen versus heated air: computational study with skeletal and reduced chemistry. Combust Flame 114(3–4):436–456. https://doi.org/10.1016/S0010-2180(97)00318-0

Lam SH (2006) Multicomponent diffusion revisited. Phys Fluids 18(7):73101. https://doi.org/10.1063/1.2221312

Lam SH (2007) Reduced chemistry-diffusion coupling. Combust Sci Technol 179(4):767–786. https://doi.org/10.1080/00102200601093498

Lam SH, Goussis DA (1994) The CSP method for simplifying kinetics. Int J Chem Kinet 26(4):461–486. https://doi.org/10.1002/kin.550260408

Lam SH, Goussis DA (1989) Understanding complex chemical kinetics with computational singular perturbation. Symp (Int) Combust 22(1):931–941. https://doi.org/10.1016/S0082-0784(89)80102-X

Lam SH (2013) Model reductions with special CSP data. Combust Flame 160(12):2707–2711. https://doi.org/10.1016/j.combustflame.2013.06.013

Lam SH (2017) An efficient implementation of CSP. Combust Sci Tech. http://dx.doi.org/10.1080/00102202.2017.1379512

Law CK, Egolfopoulos FN (1992) A unified chain-thermal theory of fundamental flammability limits. Proc Combust Inst 24(1):137–144. https://doi.org/10.1016/S0082-0784(06)80021-4

Law CK, Zhao P (2012) NTC-affected ignition in nonpremixed counterflow. Combust Flame 159(3):1044–1054. https://doi.org/10.1016/j.combustflame.2011.10.012

Law CK (2006) Combustion physics. Cambridge University Press

Li J, Zhao Z, Kazakov A, Chaos M, Dryer FL (2007) A comprehensive kinetic mechanism for CO, CH_2O, and CH_3OH combustion. Int J Chem Kinet 39:109–136. https://doi.org/10.1002/kin.20218

Liang L, Stevens JG, Farrell JT (2009) A dynamic adaptive chemistry scheme for reactive flow computations. Proc Combust Inst 32(1):527–534. https://doi.org/10.1016/j.proci.2008.05.073

Lu TF, Yoo CS, Chen JH, Law CK (2010) Three-dimensional direct numerical simulation of a turbulent lifted hydrogen jet flame in heated coflow: a chemical explosive mode analysis. J Fluid Mech 652(6):45–64. https://doi.org/10.1017/S002211201000039X

Lu T, Law CK (2005) A directed relation graph method for mechanism reduction. Proc Combust Inst 30(1):1333–1341. https://doi.org/10.1016/j.proci.2004.08.145

Lu T, Law CK (2008) A criterion based on computational singular perturbation for the identification of quasi steady state species: a reduced mechanism for methane oxidation with NO chemistry. Combust Flame 154(4):761–774. https://doi.org/10.1016/j.combustflame.2008.04.025

Lu T, Law CK (2009) Toward accommodating realistic fuel chemistry in large-scale computations. Progress Energy Combust Sci 35(2):192–215. https://doi.org/10.1016/j.pecs.2008.10.002

Lu T, Law CK, Yoo CS, Chen JH (2009) Dynamic stiffness removal for direct numerical simulations. Combust Flame 156(8):1542–1551. https://doi.org/10.1016/j.combustflame.2009.02.013

Lu Z, Zhou H, Li S, Ren Z, Tianfeng L, Law CK (2017) Analysis of operator splitting errors for near-limit flame simulations. J Comput Phys 335:578–591. https://doi.org/10.1016/j.jcp.2017.01.044

Luo Z, Tianfeng L, MacIaszek MJ, Som S, Longman DE (2010) A reduced mechanism for high-temperature oxidation of biodiesel surrogates. Energy Fuels 24(12):6283–6293. https://doi.org/10.1021/ef1012227

Maas U, Pope SB (1992) Simplifying chemical kinetics: intrinsic low-dimensional manifolds in composition space. Combust Flame 88(3–4):239–264. https://doi.org/10.1016/0010-2180(92)90034-M

Martz JB, Kwak H, Im HG, Lavoie GA, Assanis DN (2011) Combustion regime of a reacting front propagating into an auto-igniting mixture. Proc Combust Inst 33(2):3001–3006. https://doi.org/10.1016/j.proci.2010.07.040

Matalon M (2007) Intrinsic flame instabilities in premixed and nonpremixed combustion. Annu Rev Fluid Mech 39(1):163–191. https://doi.org/10.1146/annurev.fluid.38.050304.092153

McNenly MJ, Whitesides RA, Flowers DL (2015) Faster solvers for large kinetic mechanisms using adaptive preconditioners. Proc Combust Inst 35(1):581–587. https://doi.org/10.1016/j.proci.2014.05.113

Meier W, Barlow RS, Chen YL, Chen JY (2000) Raman/Rayleigh/LIF measurements in a turbulent $CH_4/H_2/N_2$ jet diffusion flame: experimental techniques and turbulence chemistry interaction. Combust Flame 123(3):326–343

Miller JA, Pilling MJ, Troe J (2005) Unravelling combustion mechanisms through a quantitative understanding of elementary reactions. Proc Combust Inst 30(1):43–88. https://doi.org/10.1016/j.proci.2004.08.281

Morii Y, Terashima H, Koshi M, Shimizu T, Shima E (2016) ERENA: A fast and robust jacobian-free integration method for ordinary differential equations of chemical kinetics. J Comput Phys 322:547–558. https://doi.org/10.1016/j.jcp.2016.06.022

Mueller ME, Iaccarino G, Pitsch H (2013) Chemical kinetic uncertainty quantification for large eddy simulation of turbulent nonpremixed combustion. Proc Combust Inst 34(1):1299–1306. https://doi.org/10.1016/j.proci.2012.07.054

Nayagam V, Dietrich DL, Ferkul PV, Hicks MC, Williams FA (2012) Can cool flames support quasi-steady alkane droplet burning? Combust Flame 159(12):3583–3588. https://doi.org/10.1016/j.combustflame.2012.07.012

Niemeyer KE, Curtis NJ, Sung CJ (2017) pyJac: Analytical jacobian generator for chemical kinetics. Comput Phys Commun 215:188–203. https://doi.org/10.1016/j.cpc.2017.02.004

Niemeyer KE, Sung CJ, Raju MP (2010) Skeletal mechanism generation for surrogate fuels using directed relation graph with error propagation and sensitivity analysis. Combust Flame 157(9):1760–1770. https://doi.org/10.1016/j.combustflame.2009.12.022

Niemeyer KE, Sung C-J (2013) Recent progress and challenges in exploiting graphics processors in computational fluid dynamics. J Supercomput 528–564. https://doi.org/10.1007/s11227-013-1015-7

Pan J, Zhao P, Law CK, Wei H (2016) A predictive Livengood-Wu correlation for two-stage ignition. Int J Engine Res 17(8):825–835. https://doi.org/10.1177/1468087415619516

Pepiot-Desjardins P, Pitsch H (2008) An efficient error-propagation-based reduction method for large chemical kinetic mechanisms. Combust Flame 154(1–2):67–81. https://doi.org/10.1016/j.combustflame.2007.10.020

Perini F, Galligani E, Reitz RD (2012) An analytical Jacobian approach to sparse reaction kinetics for computationally efficient combustion modeling with large reaction mechanisms. Energy Fuels 26(8):4804–4822. https://doi.org/10.1021/ef300747n

Pilling MJ (2009) From elementary reactions to evaluated chemical mechanisms for combustion models. Proc Combust Inst 32:27–44. https://doi.org/10.1016/j.proci.2008.08.003

Rabitz H, Kramer M, Dacol D (1983) Sensitivity analysis in chemical kinetics. Annu Rev Phys Chem 34(1):419–461. https://doi.org/10.1146/annurev.pc.34.100183.002223

Schwer DA, Tolsma JE, Green WH, Barton PI (2002) On upgrading the numerics in combustion chemistry codes. Combust Flame 128(3):270–291. https://doi.org/10.1016/S0010-2180(01)00352-2

Shan R, Yoo CS, Chen JH, Tianfeng L (2012) Computational diagnostics for N-heptane flames with chemical explosive mode analysis. Combust Flame 159(10):3119–3127. https://doi.org/10.1016/j.combustflame.2012.05.012

Shi Y, Liang L, Ge HW, Reitz RD (2010) Acceleration of the chemistry solver for modeling DI engine combustion using dynamic adaptive chemistry (DAC) schemes. Combust Theor Model 14(1):69–89. https://doi.org/10.1080/13647830903548834

Strang G (1968) On the construction and comparison of difference schemes. SIAM Journal on Numerical Analysis 5(3):506–517. https://doi.org/10.1137/0705041

Sun W, Gou X, El-Asrag HA, Chen Z, Yiguang J (2015) Multi-timescale and correlated dynamic adaptive chemistry modeling of ignition and flame propagation using a real jet fuel surrogate model. Combust Flame 162(4):1530–1539. https://doi.org/10.1016/j.combustflame.2014.11.017

Sun W, Chen Z, Gou X, Yiguang J (2010) A path flux analysis method for the reduction of detailed chemical kinetic mechanisms. Combust Flame 157(7):1298–1307. https://doi.org/10.1016/j.combustflame.2010.03.006

Tao M, Han D, Zhao P (2017) An alternative approach to accommodate detailed ignition chemistry in combustion simulation. Combust Flame 176:400–408. https://doi.org/10.1016/j.combustflame.2016.11.009

Tao M, Tong W, Ge H, DelVescovo D, Zhao P (2017) A kinetic modeling study on octane rating and fuel sensitivity in advanced compression ignition engines. Combust Flame 185(11):234–244. https://doi.org/10.1016/j.combustflame.2017.07.020

Tomlin AS, Turányi T, Pilling MJ (1997) Low-temperature combustion and autoignition. Compr Chem Kinet 35. https://doi.org/10.1016/S0069-8040(97)80019-2

Tosatto L, Bennett BA, Smooke MD (2011) A transport-flux-based directed relation graph method for the spatially inhomogeneous instantaneous reduction of chemical kinetic mechanisms. Combust Flame 158(5):820–835. https://doi.org/10.1016/j.combustflame.2011.01.018

Tosatto L, Bennett BAV, Smooke MD (2013) Comparison of different DRG-based methods for the skeletal reduction of JP-8 surrogate mechanisms. Combust Flame 160(9):1572–1582. https://doi.org/10.1016/j.combustflame.2013.03.024

Troe J, Ushakov VG (2011) Revisiting falloff curves of thermal unimolecular reactions. J Chem Phys 135(5):054304. https://doi.org/10.1063/1.3615542

Turanyi T (1990) Sensitivity analysis of complex kinetic systems. Tools and applications. J Math Chem 5:203–248. https://doi.org/10.1007/bf01166355

Turns SR (1995) Understanding NOx formation in nonpremixed flames: experiments and modeling. Prog Energy Combust Sci 21(5):361–385. https://doi.org/10.1016/0360-1285(94)00006-9

Vajda S, Valko P, Turanyi T (1985) Principal component analysis of kinetic models. Int J Chem Kinet 17(1):55–81. https://doi.org/10.1002/kin.550170107

Waldrop M Mitchell (2016) The chips are down for Moore's law. Nature 530(7589):144–147. https://doi.org/10.1038/530144a

Wang H, Frenklach M (1991) Detailed reduction of reaction mechanisms for flame modeling. Combust Flame 87(3–4):365–370. https://doi.org/10.1016/0010-2180(91)90120-Z

Wang H, Sheen DA (2015) Combustion kinetic model uncertainty quantification, propagation and minimization. Prog Energy Combust Sci 47:1–31. https://doi.org/10.1016/j.pecs.2014.10.002
Wang Z, Liu H, Reitz RD (2017) Knocking combustion in spark-ignition engines. Prog Energy Combust Sci 61:78–112. https://doi.org/10.1016/j.pecs.2017.03.004
Westbrook CK, Pitz WJ, Herbinet O, Curran HJ, Silke EJ (2009) A comprehensive detailed chemical kinetic reaction mechanism for combustion of n-Alkane hydrocarbons from n-Octane to n-Hexadecane. Combust Flame 156:181–199
Won SH, Jiang B, Dievart P, Sohn CH, Yiguang J (2015) Self-sustaining n-Heptane cool diffusion flames activated by Ozone. Proc Combust Inst 35(1):881–888. https://doi.org/10.1016/j.proci.2014.05.021
Xin Y, Liang W, Liu W, Tianfeng L, Law CK (2015) A reduced multicomponent diffusion model. Combust Flame 162(1):68–74. https://doi.org/10.1016/j.combustflame.2014.07.019
Xu C, Gao Y, Ren Z, Tianfeng L (2016) A sparse stiff chemistry solver based on dynamic adaptive integration for efficient combustion simulations. Combust Flame 172:183–193. https://doi.org/10.1016/j.combustflame.2016.07.009
Yang H, Ren Z, Tianfeng L, Goldin GM (2013) Dynamic adaptive chemistry for turbulent flame simulations. Combust Theor Model 17(1):167–183. https://doi.org/10.1080/13647830.2012.733825
Yoo CS, Tianfeng L, Chen JH, Law CK (2011) Direct numerical simulations of ignition of a lean N-heptane/air mixture with temperature inhomogeneities at constant volume: parametric study. Combust Flame 158(9):1727–1741. https://doi.org/10.1016/j.combustflame.2011.01.025
Zador J, Taatjes CA, Fernandes RX (2011) Kinetics of elementary reactions in low-temperature autoignition chemistry. Prog Energy Combust Sci 37:371–421. https://doi.org/10.1016/j.pecs.2010.06.006
Zhang P, Ji W, He T, He X, Wang Z, Yang B, Law CK (2016) First-stage ignition delay in the negative temperature coefficient behavior: experiment and simulation. Combust Flame 167:14–23. https://doi.org/10.1016/j.combustflame.2016.03.002
Zhao P, Law CK (2013) The role of global and detailed kinetics in the first-stage ignition delay in NTC-affected phenomena. Combust Flame 160(11):2352–2358. https://doi.org/10.1016/j.combustflame.2013.06.009
Zhao P, Liang W, Deng S, Law CK (2016) Initiation and propagation of laminar premixed cool flames. Fuel 166:477–487. https://doi.org/10.1016/j.fuel.2015.11.025
Zhao P, Nackman SM, Law CK (2015) On the application of betweenness centrality in chemical network analysis: computational diagnostics and model reduction. Combust Flame 162:2991–2998. https://doi.org/10.1016/j.combustflame.2015.05.011
Zheng XL, Lu TF, Law CK (2007) Experimental counterflow ignition temperatures and reaction mechanisms of 1,3-Butadiene. Proc Combust Inst 31:367–375. https://doi.org/10.1016/j.proci.2006.07.182

Author Biography

Professor Peng Zhao has been an Assistant Professor of Mechanical Engineering at Oakland University since he obtained his Ph.D. in Mechanical and Aerospace Engineering from Princeton University in June 2015. He has extensive research experience in both computational and experimental fundamental combustions as well as combustion process in practical systems, especially internal combustion engines. Previously, he has systematically investigated low-temperature flames in nonhomogeneous reacting systems with computational and experimental approaches. A novel class of premixed and non-premixed cool flame has been discovered, manifesting the general features of low-temperature fuel kinetics in flows. The insights gained have then been utilized in subsequent mechanistic studies on engine knock, where he has further

found that the low-temperature chemistry could significantly affect the flame propagation, combustion mode evolution, and knock tendency in engine combustion. He has published extensively on the topics of combustion modeling, fuel performance, cool flames, engine knock, model reduction, and computational diagnostics with more than 20 journal papers so far in top journals *Combust. Flame*, *Proc. Combust. Inst.*, *Fuel*, and *Int. J. Engine Res*. and many conference presentations. He has also been invited to review more than 200 journal papers and awarded outstanding review contribution by many journals.

Chapter 3
Turbulent Combustion Simulations with High-Performance Computing

Hemanth Kolla and Jacqueline H. Chen

Abstract Considering that simulations of turbulent combustion are computationally expensive, this chapter takes a decidedly different perspective, that of high-performance computing (HPC). The cost scaling arguments of non-reacting turbulence simulations are revisited and it is shown that the cost scaling for reacting flows is much more stringent for comparable conditions, making parallel computing and HPC indispensable. Hardware abstractions of typical parallel supercomputers are presented which show that for design of an efficient and optimal program, it is essential to exploit both *distributed memory parallelism* and *shared-memory parallelism*, i.e. *hierarchical parallelism*. Principles of efficient programming at various levels of parallelism are illustrated using archetypal code examples. The vast array of numerical methods, particularly schemes for spatial and temporal discretization, are examined in terms of tradeoffs they present from an HPC perspective. Aspects of data analytics that invariably result from large feature-rich data sets generated by combustion simulations are covered briefly.

Keywords Direct numerical simulation · High performance computing · Parallel computing · Hierarchical parallelism

3.1 Introductory Remarks

Arguably, the *raison d'être* of turbulent combustion simulations has been to inform the design of energy conversion devices, predominantly those in the power generation and transportation sectors (reciprocating and air-breathing engines). While combustion simulations have addressed alternative applications (e.g. atmospheric chemistry, chemical engineering and manufacturing processes), the overwhelming

H. Kolla (✉)
Scalable Modeling and Analysis, Sandia National Laboratories, Livermore, CA, USA
e-mail: hnkolla@sandia.gov

J. H. Chen
Reacting Flow Research, Sandia National Laboratories, Livermore, CA, USA
e-mail: jhchen@sandia.gov

© Springer Nature Singapore Pte Ltd. 2018

S. De et al. (eds.), *Modeling and Simulation of Turbulent Combustion*, Energy, Environment, and Sustainability, https://doi.org/10.1007/978-981-10-7410-3_3

majority of simulation efforts have been devoted to this endeavour due to the obvious technological incentives and imperatives. Given such a scenario, a question that arises at the outset is

What is the role of direct numerical simulations (DNS) of turbulent combustion?

This question is pertinent since the largest, state-of-art, DNS to date are still in domains that are orders of magnitude smaller in scale (device size) or conditions (Reynolds, Damköhler numbers) compared to real devices. The answer to this question establishes the scope and ambition of combustion DNS and, more importantly, its envelope of feasibility.

This chapter is structured in the hope that the reader will arrive, step-by-step, at a comprehensive and nuanced answer to this question. The first section will discuss, using simple dimensional scaling arguments, the computational cost of combustion DNS. The next section will cover aspects of parallel high-performance computing (HPC) and the choices available to exploit multiple levels of parallelism in a typical supercomputer. These choices are invariably interlinked to the governing equations and numerical aspects, which can guide the design of a high-fidelity combustion code which will be the focus of the following section. The final section will cover aspects of data analytics which are essential in making sense of the large volumes of data generated by combustion DNS.

3.2 Computational Cost of Combustion DNS

It is perhaps prudent to establish what the term "direct numerical simulations" means in the context of turbulent combustion. DNS, as has come to be accepted by convention, may best be described

a simulation methodology where all the relevant scales in the continuum regime are sufficiently resolved on the computational grid.

Note the carefully worded qualifiers. The scales that are resolved are in the 'continuum regime' and not anything smaller such as, for instance, those described by the kinetic theory of gases (e.g. mean free paths). Note also that the scales being resolved on the computational grid implies that the spatial grid resolution is smaller than the smallest (continuum scales) of motion. These thumb rules for what qualifies as DNS can be attributed to early simulations of non-reacting turbulent flow when DNS was pioneered as a means to understand and quantify multiscale statistics of turbulence. For reactive flows, the definition of DNS extends to all scales, or more aptly spatial gradients, relevant to fluid motion (velocity) and reacting scalars (temperature and species mass fractions). It is worth pointing out that many practical devices of interest have flows that defy such an easy characterization. The most prominent examples, relevant to combustion devices, are turbulent spray flames and flames with soot. Mutliphase turbulent flows, whether reacting or non-reacting, introduce scales of interaction between the liquid and gas phases that are prohibitively expensive to resolve. Likewise, the physical processes governing soot straddle the continuum

regime. Soot formation occurs at molecular scales with soot precursors understood to be a few aromatic molecules, while they can grow, by agglomeration, to sizes that are larger than the smallest continuum flow scales (Raman and Fox 2016).

With this context, let us revisit some scaling arguments that determine the computational cost of DNS. The cost scaling is simply determined by the ratio of the largest to smallest spatio-temporal scales and the requirement that the computational domain be at least as large as the largest length scale, the so-called integral length scale Λ, while the grid resolution has to be at least as small as the smallest length scale, the Kolmogorov length scale η. This ratio dictates the minimum number of grid points required per spatial dimension, N, which scales with the Reynolds number, Re, as

$$N \sim \frac{\Lambda}{\eta} \sim \mathrm{Re}^{3/4}. \tag{3.1}$$

The total number of grid points for a three-dimensional simulation thus scales as

$$N^3 \sim \mathrm{Re}^{9/4}. \tag{3.2}$$

Combustion exacerbates the cost scaling in two principal ways. First, chemical reactions introduce spatial scales which, under most conditions of practical interest, are finer than turbulent flow scales. Consider, for illustrative purposes, the somewhat benign conditions of an atmospheric pressure methane–air turbulent flame at a Reynolds number of 10,000 and an integral length scale of 0.1 m (10 cm). The Kolmogorov scale $\eta = \Lambda/\mathrm{Re}^{3/4} = 10^{-4}$ m. A reasonable estimate for a chemical length scale, δ, is the ratio of thermal diffusivity to kinematic viscosity which, under these conditions, is $\delta \sim 10^{-5}$ m. The grid points requirement must now be revised to account for the fact that grid resolution must be smaller than δ,

$$N \sim \frac{\Lambda}{\eta}\frac{\eta}{\delta} \implies N^3 \sim \mathrm{Re}^{9/4}\left(\frac{\eta}{\delta}\right)^3. \tag{3.3}$$

Second, combustion considerably increases the number of solution variables and associated number of partial differential equations (PDEs). For non-reacting turbulent flows, the solution state comprises five variables: three components of velocity and any two of energy/enthalpy, pressure and density, and these are obtained as solutions of five PDEs governing conservation of mass, momentum and energy. The thermodynamic equation of state provides the additional constraint. For turbulent reacting flows, the solution state must be expanded to include details of the chemical composition in the form of species mass fractions, Y_i. For the simplest fuel, hydrogen, nine species sufficiently describe the oxidation mechanism (Burke et al. 2012), whereas for hydrocarbons this number is much larger. For the simplest hydrocarbon, methane, the mechanisms can be, depending on the conditions, as small as involving 13 species (Sankaran et al. 2007) or as large as 53 species (GRI-Mech 2017). Hence, for the methane–air turbulent flame example considered above, for the widely used GRI-Mech mechanism, the additional cost factor due to chemical reactions, assuming the cost scales linearly with number of PDEs, is

$$\left(\frac{\eta}{\delta}\right)^3 \times \frac{53+5}{5} \approx 1.16 \times 10^4. \tag{3.4}$$

These cost considerations dictate that turbulent combustion DNS is only feasible with high-performance parallel computing. For the same reasons, combustion DNS have, up to now, only been possible for small 'postage-stamp-sized' computational domains and are unable to approach sizes anywhere close to real devices. Only in recent years, thanks to the exponential growth in computing power, have DNS begun to approach laboratory-scale flames. Figure 3.1 shows a historical trend of DNS simulations performed with the Sandia code S3D (Chen et al. 2009) for five representative simulations. Plotted on the y-axis is the computational problem size in logarithmic scale, defined as the product of the total number of grid points and the number of solution variables, and the x-axis shows the year when each simulation was performed. The figure shows a trend where the computational problem size has increased exponentially with time, indicating that state-of-art DNS simulations have kept pace with the increase in computational power. In spite of requiring such massive computational resources, the largest DNS simulations have only been able to approach Re $\sim O(10^4)$, whereas the Re values in practical devices are at least an order of magnitude higher, suggesting that DNS is still quite some way away from approaching real device conditions.

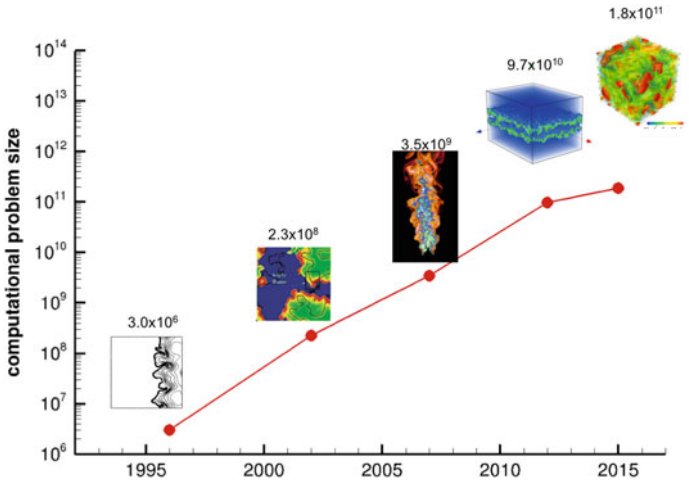

Fig. 3.1 Historical trend showing five representative simulations performed with the DNS code S3D over the last 20 years. The computational problem size is shown on a logarithmic scale on the Y-axis and the year corresponding to each simulation is on the X-axis. From left to right, the simulations correspond to **a** 2D turbulent premixed methane–air flame (Echekki and Chen 1996), **b** 2D turbulent auto-igniting stratified hydrogen–air flame (Echekki and Chen 2002), **c** 3D rectangular slot-jet turbulent Bunsen premixed methane–air flame (Sankaran et al. 2007), **d** 3D temporally evolving rectangular jet turbulent premixed hydrogen–air flame, and **e** a 3D reactivity controlled compression ignition (RCCI) flame of primary reference fuel (Treichler et al. 2018)

3.3 HPC and Hierarchical Parallelism

Having established that turbulent combustion simulations are infeasible without large computational resources, it is necessary to examine the intersection of HPC and CFD simulations. In particular, it is critical to appreciate that achieving efficiency in HPC and parallel computing requires, unfortunately, that one pay attention to numerous aspects of modern parallel computers. In an ideal world, principles governing parallel computing are simple, flexible, robust and mature enough that a programmer requires little or no knowledge of the hardware or software architecture details to write an efficient program, allowing him/her to focus efforts on the algorithmic and physics aspects of the computer program. In reality, however, the situation is the opposite and writing an efficient and performant parallel program involves a careful structuring and organization of the code within the confines and constraints imposed by the system. The payoff, or conversely the penalty, is that a carefully optimized code can often be orders of magnitude faster than a naively written one. It is also worth pointing out that even LES and URANS simulations are tackling problems large enough as to require HPC resources and the principles outlined in this section apply to these as well.

Just by considering an abstract model of typical parallel supercomputer, it becomes apparent that a program has to expose various levels of parallelism, i.e. *hierarchical parallelism*. Without being simplistic, at a high level, a parallel computer can be thought of as a set of inter-connected computing nodes that can communicate with each other through a network. Each node comprises some memory that is private to it and some computing elements that share this memory. Accessing data from the memory of another node requires communicating via the network. This picture establishes the concepts of *distributed* versus *shared-memory parallelism*.[1] The detail to bear in mind is that it is much quicker and more efficient to access shared node-local memory than accessing the memory of another node via network communication.

3.3.1 Distributed Memory Parallelism

At the highest level, utilizing a set of nodes requires decomposing a computational problem into subsets that can each be assigned to a different node. Each node can make progress on its respective subset, communicating with other node(s) to share data as and when necessary. The chief principles guiding the design for distributed memory parallelism are as follows:

1. **Balanced computational load**: It is desirable to decompose the problem such that the computational load is divided as equitably as possible among the nodes.

[1] This distinction is also referred to sometimes as internode versus intra-node or node-level parallelism.

If the load is not balanced, the progress on the overall problem might be limited by the node(s) with the largest load.

2. **Maximize computation-to-communication ratio**: It is desirable to decompose the problem such that the computational load associated with the subset on each node is much larger than the amount of communication that need be performed with other nodes.
3. **Minimize global communication**: It is desirable to devise the algorithms such that the need for global communication, i.e. data aggregation involving all nodes, is minimized or even eliminated if possible.

These principles reflect the constraint that network communication is an expensive proposition and both the number of messages and their sizes must be reduced to the extent possible.

For illustration, consider a general prototype 1D PDE of form

$$\dot{u} = F(u', u''), \tag{3.5}$$

where the dot denotes a time derivative and the single and double primes denote first and second spatial derivatives, respectively. This PDE, with suitable initial and boundary conditions, is to be solved on a discretised 1D computational domain of N grid points. Considering the computational cost arises mainly due to N being large, the most natural choice for decomposing this problem is to divide the grid points among the available nodes (P), an approach commonly referred to as *domain decomposition*. Each node is then responsible for solving the equation over N/P grid points, as shown schematically in Fig. 3.2. The computational work at each grid point involves evaluating the spatial derivatives and assembling them to advance the solution in time. The spatial derivative evaluation will necessarily require information from neighbouring grid points and for grid points at the edges of each subset N/P, these grid points reside on the adjacent node, which have to be exchanged by internode communication. The grid points that need to be exchanged are referred to as *ghost points*, and the number of ghost points and the direction of internode exchange are stipulated by the specifics of the spatial discretization scheme such as

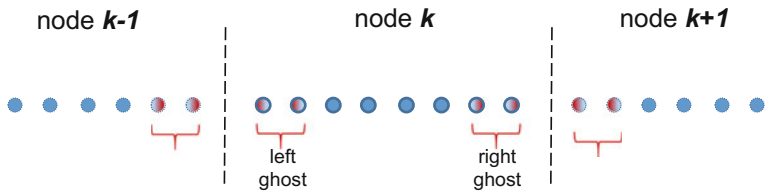

Fig. 3.2 Schematic showing a typical domain decomposition of a 1D computational domain. The dashed line denotes node boundaries and each node is assigned a subset of the computational grid points. The grid points at the edge of the node boundaries, ghost points, need to be communicated. On node k, the left ghost points are required by node $k-1$ while the right ghost points by $k-1$. Conversely, node k requires the right ghost points of $k-1$ and left ghost points of $k+1$

the stencil width and whether it is central or one-sided differencing. The principles listed above translate to the following:

- If the same computations are performed at each grid point, balanced computational load translates to the condition that N is exactly divisible by P. If it is not, then some nodes end up with a larger subset of the domain, and greater load, than others.
- Maximizing computation-to-communication ratio translates to the condition that the ratio of the number of ghost points to the number N/P be minimized. In the example depicted in Fig. 3.2, $N/P = 8$ while the number of ghost points on each node is 4 (2 at either edges). It is easy to conceive of a situation where the number of ghost points is greater than N/P, which is undesirable since each node might have to communicate with more than one adjacent node in each direction, increasing the number of communication messages.
- Minimizing global communication translates to the condition that for advancing the solution on its share of grid points each node needs to communicate only with a small subset of the other nodes, and not all.

An example of an algorithm that requires global communication arises in early DNS codes which transformed the Navier–Stokes equations from physical space to the wavenumber space and solved for the Fourier modes of the velocity components. The nonlinear convective term poses a problem since it represents a multiplication in the physical space and hence a convolution in the wavenumber space, which requires an integral over all the Fourier modes, or information over all the grid points.

In many circumstances, it becomes possible to optimize beyond these three principles and, in particular, for each node to completely hide the apparent cost of, or delay due to, communication with a fairly simple rearranging of the computational work. For node k in Fig. 3.2, it is possible to further distinguish the grid points as *interior* (blue) points versus the ghost points (blue-red). Recognizing that computations for the interior points require data that is completely local to node k, an algorithm could start the computations on the interior points without waiting on the messages from the neighbouring nodes to arrive. If N/P is large enough relative to the number of ghost points, these computations take longer than the time it takes for the messages to arrive and the computations on the ghost points can begin as soon as those on the interior points are completed. With such a rearrangement each node is kept busy doing computational work all the time. This principle is generally referred to as *hiding communication latency* and is an aspirational goal of all distributed networked systems, of which parallel computers are just one example. However, from a programmer's perspective, designing for these principles requires a protocol that enables all types of internode communications and, more importantly, a robust implementation of the protocol which can be accessed from within common programming languages (e.g. C, C++ and Fortran). The most popular and widely used communication protocol for parallel scientific computing is the *Message Passing Interface* (MPI) (Gropp et al. 1994). MPI is, strictly speaking, a community standard (MPI Forum 2017) for an interface that provides a communication protocol for parallel computing, but it is

not the only one. It just is the most successful standard and has become synonymous with parallel computing and is supported by all major vendors of supercomputers.

3.3.2 Node-Level Parallelism

In some respects, distributed memory parallelism is easy to reason about and design for since the basic architecture of distributed supercomputers at the system level have changed very gradually over the decades. On the other hand, node architectures have been continuously and rapidly changing, making node-level parallelism much harder to expose in a program. Recall that we defined a computational node, rather loosely, as an entity containing some private memory which is shared among certain computational elements. This definition is simplistic and in reality a typical computational node has a rather complex *memory hierarchy*, ranging from *main memory* (also known as *random access memory* or RAM), *cache memory* and *processor registers*. The computational element is typically a processor core that performs the computational operations on data accessed from said memory hierarchy. Registers are smallest in capacity (often large enough to hold only a handful of numbers), closest to the core and fastest to access, whereas main memory is largest in capacity, farthest from the core and the slowest to access. Node architectures have gradually progressed in complexity from containing single-core CPUs, multicore (10s) CPUs, multiple multicore CPUs, to a hybrid multicore CPU together with many-core (100s) CPUs and GPUs. The memory hierarchy, complexity and management have also increased with the growing number of units on each node, although the memory-to-core ratio is decreasing. This makes optimizing for node-level parallelism arduous but necessary.

The performance of a program in a shared-memory environment hinges almost entirely on optimal utilization of the memory hierarchy, so some context is necessary. The purpose of main memory is to provide storage for the entire duration of a running program. Hence, it is usually large, but accessing it is time-consuming (compared to the speed with which arithmetic operations can be performed by the processor). This is ameliorated by cache memory whose purpose is to provide storage for frequently accessed variables by a program. Cache memory is comparatively much faster to access but has limited capacity which is usually not large enough to provide storage for an entire program.[2] In that regard, cache memory acts as an intermediate buffer, but the cache access patterns of a program have an outsized impact on its performance. And finally registers are the memory locations that hold the actual variables feeding the arithmetic operations of the processor and the results. As a consequence, the design of an efficient program must pay careful attention to the following:

[2]Early computer architectures had just a single level of cache between the processor and main memory. However, with the number of processors and their speed, increasing dramatically the current architecture has multiple (upto 3) cache levels. Furthermore, in multicore architectures, some levels of caches are not shared amongst all cores on a node, but subsets of them.

- **Data storage and layout in memory**: Most scientific codes operate on arrays of numbers. Practically, in all programming languages, these arrays are stored in contiguous memory.[3] However, multidimensional arrays are also stored as though they were 1D arrays (vectors) by stretching out the dimensions successively. The scheme depends on whether the arrays are stored in row- or column-major order which can be different for different programming languages, e.g. Fortran is column-major order, while C/C++ are row-major order.
- **Memory access**: Since most scientific programs spend a bulk of the time performing operations on loops over arrays, knowledge of data layout in memory can be leveraged to significantly improve their performance. This arises from a concept known as *locality of reference* (Denning 2005) which establishes that when a memory location, an element `i` of a multidimensional array, is accessed (referenced) in a program, it is highly likely that it will be accessed again in the near future (temporal locality) and highly likely that nearby memory locations—array elements close to `i`—will be accessed in the near future (spatial locality). Hence, aligning the access pattern of the array elements in the program with the underlying memory layout significantly improves performance.

These considerations inform the principles for designing a program for optimal performance. The principles, which are not necessarily mutually exclusive and sometimes even conflicting, can be organized along the various levels of the memory hierarchy as described below. This discussion is kept simple so as to be accessible to someone without a background in computer science. An interested reader will readily find, upon even a cursory search, a wealth of articles that expound these topics in greater depth and nuance.

3.3.2.1 Vectorization

Vectorization pertains to the fact that modern processor architectures are primed to execute an instruction on multiple data elements (vectors) very efficiently, a concept known as *Single Instruction Multiple Data* (SIMD). Consider an example Fortran code that adds two arrays `a` and `b`, and stores the results in array `c`:

```
do i = 1,N
   c(i) = a(i) + b(i)
enddo
```

Behind the scenes, this code is transformed by the compiler to a set of instructions on the processor that comprise a sequence involving reading the elements of `a` and `b` from memory, performing the addition operation and storing the result element `c` in memory. This sequence can be sped up significantly if it is performed on blocks

[3] This is a bit of an illusion. What a program addresses is not directly the physical location of memory but what is known as virtual memory. All arrays are stored contiguously in virtual memory, i.e. the memory addresses of successive elements of an array are contiguous in the virtual address space. The translation of the virtual address space to physical memory addresses is handled by memory management layer of an operating system.

of the arrays being operated on, rather than one element at a time. This is enabled by a combination of processor registers that are large enough to hold multiple data elements and processor instruction sets that support simultaneous execution of the instruction on all elements held in the register.

Modern compiler technology is sophisticated enough that if the loops are straightforward to vectorize, and the corresponding instruction set is supported on a given architecture, compilers can automatically vectorize relevant portions of the code.[4] However, even simple missteps can prevent loops from being vectorized, resulting in significant performance penalty. Consider, instead, the case of adding 2D arrays in the following example:

```
do i = 1,N
  do j = 1,M
    c(i,j) = a(i,j) + b(i,j)
  enddo
enddo
```

Because of the way Fortran arrays are stored in memory, array elements along the first index `i` will be contiguous. However, the inner loop in this example is over the index `j` and successive elements of `j`, not being contiguous in memory, do not constitute blocks of vectors that can be fetched from memory efficiently. A compiler will attempt and fail to vectorize this code. Just by reordering the loops, making the `j` loop as the outer and `i` loop as the inner, the code can be vectorized without affecting correctness. There are other common pitfalls, e.g. placing conditional statements (e.g. `if`, `while`) inside the nested loops, introducing data dependencies on successive elements of the vectors, etc., that prevent a straightforward vectorization. The Intel compiler user guide has a very useful and explanatory page on tips for writing vectorizable codes (Programming Guidelines for Vectorization 2017). Vectorization as a programming practice was pioneered in the early decades of parallel computing (1970s–1990s) when the architecture of supercomputers was dominated by *vector processors*. In subsequent decades, with the changing complexion of computing and the rise of personal desktop computers, vector processors gave way to *scalar processors* and vectorization was not as critical for performance. The architectures are changing once again and with increasing number of computing elements on a given node, it has become necessary once again to optimize for data parallelism through vectorization.

[4]The Intel compiler suite has a very useful compiler option that generates a detailed vectorization report. When turned on, it generates output to a file that lists every portion of the code that was attempted to be vectorized by the compiler, whether the vectorization was successful and what, if anything, prevented a loop from being vectorized.

3.3.2.2 Cache Utilization

As described earlier, caches are memory layers that provide fast access of data to the processor cores to operate on. Most scientific computing applications, and certainly CFD codes, suffer from having low *computational intensity* which is defined as the ratio of number of arithmetic operations performed per units of memory accessed per operation. This would not be an issue if *memory bandwidth*—the rate at which memory can be accessed or transferred—outpaces the rate of performing operations, i.e. FLOPS. Unfortunately, the opposite is true and the performance of virtually all scientific codes is memory bandwidth limited. The purpose of cache is to relieve the bandwidth pressure on main memory by providing an intermediate location that stores the variables frequently accessed by a program. Accordingly, memory access patterns within a program can benefit greatly by optimizing the utilization of cache resulting in improved performance.

Consider a simple example of performing an outer product of two vectors `a` and `b`, of lengths `N` and `M`, respectively, resulting in an $\texttt{N} \times \texttt{M}$ matrix `c`:

```
do j = 1,M
  do i = 1,N
    c(i,j) = a(i) * b(j)
  enddo
enddo
```

At the point of execution of these loops, all the elements for the innermost-`i`-loop will be fetched from main memory to cache. Even accounting for the fact that these elements are contiguous in memory, if `N` is too large, the cache might not be large enough to hold all the elements, resulting in poor *cache reuse*. Each block of `a` that fits in cache will be fetched from main memory, operated on and purged before moving on to the next block.

Accordingly, optimizing the code for cache reuse requires a modification using a concept called *cache blocking*. Effectively, reorganizing loops and breaking them down further into blocks large enough to fit in cache, and reusing the block sized data as much as possible while it resides in cache, pays dividends. In the above example, let us assume that it is known that the cache is large enough to hold `B` elements of a vector. With this knowledge, rearranging the loops and having the inner most loop span blocks of size B, as shown below,

```
do j = 1, M, B
  do i = 1, N
    do jj = j, j+B-1
      c(i,jj) = a(i) * b(jj)
    enddo
  enddo
enddo
```

ensures that (1) the chunk of vector `b` accessed in the inner most `jj` loop fits in cache and (2) this chunk is reused for each evaluation of the `i` loop, increasing cache reuse. A careful reader will notice in the above example that, in the process of reordering nested loops for cache blocking, we have reintroduced an inefficiency. The inner-

most loop index `jj` is not the fastest varying dimension for the matrix `c` and the above code will result in *cache write misses*. A reordering of the loops that respects both contiguous memory access and does cache blocking for this example can be performed as follows:

```
do i = 1, N, B
  do j = 1, M
    do ii = i, i+B-1
      c(ii,j) = a(ii) * b(j)
    enddo
  enddo
enddo
```

This is a somewhat simplistic example illustrating the principle of cache blocking. For operations on multidimensional arrays, e.g. matrix–matrix multiplication, cache blocking can be done in one or two dimensions and the code with reordered loops becomes considerably larger (and less easy to read).

3.3.2.3 Shared-Memory Multiprocessing

At the highest level of a node virtually all computing platforms, and even most desktops, have multicore processors (and often multiples of them). While vectorization and cache utilization can be seen as optimizations necessary at a per-core level, at the node level it becomes necessary to fully utilize the multiple cores for good performance. Usually, multicore architectures have multiple cache levels, with at least one level of cache that is closest to each individual core, and at least one level that is shared by the multiple cores.[5] This allows a programmer to divide computational work among the multiple cores and have them execute in parallel.

By far the most common programming model for shared-memory multiprocess parallelism, and certainly the most accessible for common programming languages, is *Open Multiprocessing* (OpenMP) (Open Multi-Processing 2017). OpenMP provides a simple and easy way to extract parallelism by allowing a programmer to view the multiple cores as a set of *threads* that can each work on independent subsets of a problem concurrently. It extends the concept of *multi-threading* to multicore architectures and provides a core set of constructs that enable the creation of multiple threads, specifying a block of work for each thread, providing access to data variables which may be private to each thread or shared amongst the threads and synchronizing threads. To illustrate the use of OpenMP, consider the earlier example of

[5]The term *multiprocessing* is itself very general, simply referring to a system with multiple processors. The multicore nodes commonly found today may be thought to belong a subset known as *symmetric multiprocessors* (SMP) which strictly means that all the processors share all the memory and I/O resources equally and are orchestrated by one instance of an operating system kernel. The reality may be somewhere in between. Most modern node architectures have multiple sets of multicore CPUs, and they are not all exactly equal since at least one or more layers of memory hierarchy are not equally shared by all the cores. They are better described by a category known as *non-uniform memory access* (NUMA) nodes.

adding two arrays. This example code can be parallelized using OpenMP *directives* as follows:

```
!$OMP PARALLEL DO
do i = 1,N
   c(i) = a(i) + b(i)
enddo
!$OMP END PARALLEL DO
```

To speed up this portion of the code, one compiles the program by providing a compiler flag that ensures the spawning of multiple threads, launching each one on a separate processor at runtime. Each thread/processor executes this loop on the subset of the `i` index range assigned to it, thereby speeding up the program.

While this simple example illustrates the principle, the speedup achievable by such a multi-threading model is often hampered by other aspects. Behind the scenes, OpenMP follows a fork-join model. Typically, a program has a single master thread running which then spawns multiple worker threads upon encountering the directive `OMP PARALLEL DO`. The worker threads execute the block of code that follows and are destroyed at the directive `OMP END PARALLEL DO` with control passing back to the single master thread from thereon. There is a cost associated with the spawning and destroying of multiple threads by the master thread and this cost may not outweigh the benefits if the portion of the multi-threaded code is too lightweight. Moreover, the speedup of an overall larger program might still be limited by the portions of it that cannot be parallelized over multiple threads (so-called serial portion of a code), a phenomenon known as *Amdahl's law*. Also, OpenMP provides constructs for having variables shared amongst all threads versus keeping them private to each thread. The lifetime of a variable is clearly defined by such attributes and ignoring these rules can easily lead to erroneous code. In the above example, the subsets of the arrays `a`, `b` and `c` which fall within the index range for each thread are private to it and no other threads read/modify them. If a variable needs to be accessed by all threads, e.g. a global constant, then it needs to be declared as a shared variable and multiple copies of it are made, one for each thread. If shared variables are created indiscriminately, then this can cause an undue increase in memory footprint. At the same time, one needs to be careful about modifying the values of shared variables inside the multi-threaded portion of the code. Since each thread runs in parallel, the exact order in which the threads finish is undetermined. As a result, if more than one thread modifies the value of a shared variable differently, the final value might depend on whichever threads finishes last, a phenomenon known as *data race*. In general, OpenMP places the heavy burden of ensuring correctness on the application programmer. As a result, getting appreciable speedup in large programs without disrupting correctness proves challenging.

Of course no discussion on multiprocessing is complete without covering *Graphics Processing Units* (GPUs), the latest class of computing processors that are having a large impact on scientific computing. GPUs are best described as an array of *streaming multiprocessors* where each multiprocessor is designed to efficiently execute a large number of threads. Each multiprocessor further organizes the large num-

ber of threads into smaller thread groups that can execute one common instruction.[6] By efficiently switching context between multiple thread groups, a multiprocessor can ensure apparent concurrent progress on a rather large number of threads. Conceptually, this may be seen as extending the principle of SIMD to *Single Instruction Multiple Thread* (SIMT), although from the perspective of a programmer this is purely a matter of nuance. For efficient use of GPUs, it is desirable to organize the computational kernels into a hierarchy of thread groups such that at the finest level of this hierarchy, all the threads are performing the same computation. Often the starting point for such an organization is to transform loop computations into thread groups/blocks. However, the level of parallelism required to get the most out of a GPU is rather large ($\sim$1000s of threads) and one might be hard pressed to express such large loops for a majority of a program. Moreover, the available memory on a GPU is smaller on a per-thread basis making the efficient use of its capacity difficult. This requires going beyond simple 'data-level parallelism', which is the subject of the next subsection.

Finally, while the concepts listed above are illustrative, using them in concert for a complex program requires considerable effort, often using trial and error. A pragmatic approach is to identify the portions of a code that may be the most time-consuming, and reasoning about how they could be improved for a given platform. The solution could involve some combination of the approaches above and at different levels. For instance, one could employ multi-threading at a high level and get further speed up by vectorizing or cache blocking the lower levels of nested loops. This effort is made further challenging by the fact that a solution that works best for one platform might not carry over easily to a different platform due to a slight difference in the node-level architecture. The best programs parametrize their codes for the various levels of parallelism such that the parameters reflect the specifics of the architecture. But such a straightforward solution might elude all but the simplest codes.

3.3.3 Data, Task and Hybrid Parallelism

The entire preceding discussion, starting from distributed memory parallelism using domain decomposition to shared-memory parallelism using multiprocessing, was illustrated using examples of *data-level parallelism*, i.e. computations that can be performed in parallel on multiple data elements, which in the case of CFD invariably become solution variables at the computational grid points. As the discussion on GPUs illustrated, with the increasingly complex node-level architectures, data parallelism is no longer sufficient to fully utilize HPC computing resources. An alter-

[6] NVIDIA, which has pioneered use of GPUs for scientific computing, has developed a full-fledged programming model—CUDA—that provides constructs for the thread hierarchy. The smallest group of threads that execute a common instruction is called a *warp* and from a performance perspective having all threads in a warp do the same computation without diverging is critical.

native paradigm, *task parallelism*, is becoming increasingly important. Simply put, task parallelism is orthogonal to data parallelism and can be thought of as independent sets of computation that can be performed on the same data element. The term independent here refers to concept that the sets of computation have inputs and outputs that do not depend on each other. An example from a combustion perspective would be the computations of viscosity, thermal conductivity and species diffusivities. These quantities are required for different conservation equations, and their computations are independent and can be performed in parallel. Yet, it is fairly common for programmers to express these operations in sequence in a code since that is what all the widely used programming languages enable. Programming languages/models that allow expressing task parallelism are far less common. As the GPU discussion illustrates, to get the best performance, one might be required to exploit both data and task parallelism, i.e. *hybrid parallelism*. For the GPU example, this maybe accomplished by launching, on each multiprocessor, separate thread groups for independent tasks but have each thread within a group perform the same task on multiple data elements.

A fairly recent, and radical, development in parallel computing is the concept of *asynchronous many-task* (AMT) programing models and runtimes (Bennett et al. 2015). In this paradigm, a programmer is not required to manually reason about, and order, computational kernels in a program for parallel execution of independent tasks. Rather, the programmer is required only to specify tasks and their inputs and output dependencies. The *runtime* does the analysis of determining when a certain task is ready to be executed, based on whether its input dependencies are satisfied, and issues the task for execution on the next available resource. In such a paradigm, there is no notion of synchronous or 'in-order' execution, as would happen in common programming languages like C/C++/Fortran, and the actual order of execution only respects the data dependencies of the tasks as specified by the programmer. Treichler et al. (2018) describe the implementation of a combustion DNS code in one such AMT runtime "legion" (Legion 2017). Bennett et al. (2015) report a systematic comparative study of a few state-of-art AMT runtimes.

3.4 Physics and Numerical Aspects

A discussion on the physics and numerical aspects of computational combustion was deliberately set to follow the section on HPC aspects. Historically, combustion codes have been developed based on the classes of problems one was interested in solving, which establishes the framework for the set of physics and associated numerics. Considerations of HPC usually follow later. In inverting the perspective, we hope to give an appreciation for what implications the physics/numerics choices have on parallel computing and in particular which choices are conducive for HPC and which might be inhibiting. It is not the intent of this section to be a comprehensive survey of numerical methods for CFD of reacting flows, which would be a vast undertaking. Rather, we intend to present step-by-step the choices confronted as viewed through

the lens of HPC. In the discussion to follow, we limit ourselves to gas-phase turbulent reacting flows and do not consider aspects of multiphase reacting flows.

3.4.1 Governing Equations and Constitutive Laws

As mentioned in Sect. 3.2, a reacting flow system is described by a set of variables that are governed by conservation laws in the form of PDEs. These are typically the conservation of mass, momentum, energy, species concentrations and a thermodynamic equation of state. The governing equations are complemented by constitutive laws for molecular transport (mass diffusion for species concentrations, thermal diffusion and viscosity), thermodynamic quantities (specific heat at constant pressure/volume) and chemical kinetics. Within this framework, there is some flexibility, depending on the conditions, in choosing the form of governing equations one wishes to solve. For instance, the energy equation could be transformed into an equation for enthalpy or temperature. Likewise, for species concentrations one could choose mass fractions or mole fractions. Poinsot and Veynante (2012) give an excellent overview of the governing equations for reacting flows, various equivalent forms and simplifications.

The first choice to be made is the size of the chemical system. As mentioned in Sect. 3.2, this has a direct bearing on the size of the resulting system of equations and the computational cost. For higher hydrocarbons, as may be relevant for transportation systems, the number of species in a mechanism can be extremely large, e.g. 2885 species (11754 elementary reaction steps) for a diesel surrogate mechanism (Pei et al. 2015), so as to be prohibitively expensive. Large chemical mechanisms also involve a relatively large fraction of intermediate species that are extremely shortlived (fast chemical timescales) which makes the PDEs very stiff, compounding the problem. Hence, some sort of mechanism reduction is almost always necessary, and a reduced mechanism must be judiciously chosen such that it includes the chemical pathways relevant for the phenomenon under study, and it remains valid for the conditions (pressure, temperature and equivalence ratios) of the simulation. As an example, the RCCI simulation (Treichler et al. 2018) of a primary reference fuel (a blend of isooctane and n-heptane) targeted the study of ignition timing in a turbulent mixture undergoing piston compression. The mechanism, chosen to be valid under the range of pressures and mixture stratifications expected in the simulation and retain the key elementary steps governing ignition chemistry, contained 116 transported species, 55 species treated with a quasi-steady-state assumption (QSSA) and 861 elementary reaction steps (Luong et al. 2013), itself reduced from a much larger detailed mechanism with 874 species and 3796 elementary steps (Curran et al. 2002).

For engineering simulations—LES or RANS—such detailed mechanisms may be unnecessary and they could be significantly reduced while still preserving the fidelity required to predict engineering quantities of interest. An excellent example of this is a two-step reduced six species chemical mechanism for kerosene–air premixed combustion by Franzelli et al. (2010). Even for DNS, the purpose is sometimes to for-

mulate, test and validate models for *turbulence–chemistry interactions* and a simple description of the combustion chemistry suffices. For premixed combustion, under certain assumptions (Bray and Libby 1976), global single-step irreversible reaction mechanism; unity Lewis numbers of reactant and product species; and adiabatic flow and constant pressure combustion, it is possible to represent the entire thermochemical system by a single reacting scalar, a progress variable. DNS of turbulent premixed flames using just a progress variable-based description have made major contributions to the understanding and modelling of turbulence–chemistry interactions, as detailed in chapter [refer Prof. Nilanjan Chakraborty].

For thermodynamic quantities, the widely accepted practice, established by the authors of the CHEMKIN package (Kee et al. 1990), is to evaluate them as polynomials of temperature. This may seem like the more expensive approach compared to the simplification of assuming these quantities to be temperature-independent. However, this is one example where, from the perspective of computational cost, such a simplification may be unnecessary. Univariate polynomial evaluations have a high computational intensity, i.e. they require a lot of FLOPS per byte of data accessed and they are generally favourable from the perspective of easing memory bandwidth pressure. As a result, opting for the more compute-intensive option of temperature polynomials might incur no penalty on computational performance. The same argument applies to transport properties. Evaluating them as polynomials of temperature, as established by the TRANSPORT package (Kee et al. 1986), might not incur significant penalty on the computational cost. However, for multi-species mixtures, there still is a choice between evaluating the transport properties using a mixture-averaged or a full multicomponent formulation for the molecular transport coefficients. The mixture-averaged formulation is effectively a weighted sum of the transport coefficients of the individual components, evaluated as polynomials of temperature, weighted by their concentrations. The full multicomponent formulation requires inverting a matrix of dimensions equal to the number of components, which can be extremely expensive. While it is well known that for laminar flames the two formulations yield considerably different results, a recent DNS of a temporally evolving turbulent stratified jet flame (Bruno et al. 2015) observed that, statistically, the quantitative differences between a mixture-averaged and multicomponent diffusion formulation were negligible in the turbulent flame. While this may be encouraging, it is not conclusive and it is fair to expect the differences between the two formulations to be regime dependent and greater for systems with a large number of species.

3.4.2 Compressible Versus Low-Mach Formulations

A large subset of turbulent combustion applications occur in low-speed subsonic flows. Under such conditions, the timescales pertaining to advection are much larger compared to that of acoustic propagation and yet stability considerations of time advancement schemes will dictate that the time step be limited by the acoustic timescale. Even though the density is varying in the domain, its change arises to

leading order due to the temperature change from combustion and not due to thermodynamic compression/expansion. Representing such a system by a conventional compressible formulation will require needlessly small time steps.

An elegant solution that takes advantage of the separation of the acoustic and advective timescales is the low-Mach formulation for reactive flows (Tomboulides et al. 1997; Najm and Knio 2005; Nonaka et al. 2012), which filters out the acoustic waves by decomposing pressure into a thermodynamic and a hydrodynamic part

$$p(x,t) = p_{therm}(t) + p_{hydro}(x,t). \tag{3.6}$$

The equation of state involves only the thermodynamic pressure, p_{therm}, which is assumed to equilibrate in the whole domain instantly and hence is a function only of time, while the momentum equation involves only the gradient of the hydrodynamic pressure, p_{hydro}. In terms of the formulation, this decomposition transforms the continuity equation and the equation of state into a constraint on velocity divergence that requires solving an elliptic equation with spatially variable coefficients. From an HPC perspective, this maybe seen as a drawback of this approach. An elliptic PDE has the attribute that the solution at every point in the domain is influenced by every other point. Solving such a PDE, in a distributed memory setting, requires an all-to-all exchange of information which is communication intensive. In practice, sophisticated algorithms are used to solve elliptic PDEs in an efficient way but effectively the global information exchange has to happen in one form or another. In contrast, this is avoided in a compressible formulation since the flow of information by acoustic propagation is resolved and the domain of influence for the PDE solution at any grid point is localized. The choice then is between a compressible formulation that restricts the time steps and increases the time to solution but with a simpler algorithm (and code) versus the low-Mach formulation that allows large time steps but at the expense of a much more complicated numerical algorithm and code.

3.4.3 Spatial and Temporal Discretizations

The most consequential design choice for any CFD program, the one that establishes the entire numerical, algorithmic and computational framework for a code, is the choice of spatial and associated temporal discretizations for the PDEs. Here too, the landscape is vast and we do not attempt an exhaustive discussion. Rather, we focus on the prominent classes of numerical methods that have emerged for reactive flow problems and assess their pros and cons from an HPC perspective.

The choice of the spatial discretization is guided first and foremost by what kind of simulations one wishes to perform and what accuracy is required. For simulations that are fundamentaly of academic interest and whose aim to investigate and quantify the multiscale nature of turbulence–chemistry interactions, the computational domains can be kept simple but a high accuracy is desired for spatial derivatives.

Finite-difference schemes are a natural choice. Early DNS codes for incompressible turbulence were based on *spectral* or *pseudo-spectral* methods[7] which solve the Fourier modes of velocity. The transformation of Navier–Stokes equations to the Fourier space allows one to precisely control the range of wavenumbers that can be resolved and hence the Reynolds numbers that are affordable, but these methods are limited to periodic spatial domains. High-order accurate spatial finite-difference schemes (Lele 1992; Kennedy and Carpenter 1994) emerged from this need to perform DNS in physical space but with targeted spectral-like accuracy. These schemes are simple to implement and offer a high order of accuracy at relatively modest computational expense and combustion DNS codes have successfully implemented schemes that are up to tenth-order accurate (Jenkins and Cant 1999). But the main concern is that the formulation of these schemes is not mathematically conservative and choosing a scheme of modest-order accuracy might violate domain-wide global conservation laws. Finite-volume discretization, on the other hand, is conservative by construction and preserves domain-wide conservation. However, finite-volume schemes become increasingly difficult to formulate for higher order accuracy and require large stencil widths increasing the computational cost. Of a secondary concern is the ability to handle irregular geometry domains. The finite-difference approach, being of the method of lines mould, is restricted to only simple computational domains, purely rectangular domains with structured meshes. The finite-volume method, in principle, can handle complex geometries with tetrahedral mesh elements, but the difficulties in formulating high-order accurate schemes for tetrahedral elements become more severe. Multi-block body-fitted curvilinear meshes also allow one to handle modestly complex geometries but these are usually preferred for engineering, as opposed to academic simulations and finite-volume methods are a better choice since ensuring conservation is more important than resolving spatial gradients with high fidelity.

From an HPC perspective, the choice of temporal discretization and the overall time advancement scheme has a much larger bearing. The main issue confronting turbulent combustion simulations is that there are four relevant timescales governed by the distinct physical processes: convection, acoustics, diffusion and chemistry, and they can be different by orders of magnitude. The choice of which timescales to resolve explicitly, which to handle implicitly and how to couple them all consistently determines the overall temporal discretization framework. The previous section already elucidated the choice between resolving and filtering acoustic timescales when they are much smaller than convective timescales. For convective–diffusive–reactive flows, three classes of temporal schemes are apparent: fully explicit schemes, coupled implicit–explicit (IMEX) schemes and decoupled operator splitting schemes:

- Fully explicit schemes represent the brute force approach and the time step is chosen to be smaller than the smallest relevant timescale. These schemes are relatively

[7] The difference between *spectral* and *pseudo-spectral* methods lie in how the nonlinear convective term was handled. In the spectral method, all computations were in the wavenumber space, but pseudo-spectral methods use an intermediate step to transform the velocity Fourier modes to physical space, compute the convective term in the physical space and transform it back to the Fourier space.

straightforward to implement and the spatial domain of influence is nearest neighbour, i.e. advancing the solution in time at a grid point requires information only from the grid points in the immediate vicinity. From a distributed memory perspective, this is extremely attractive since the time advancement algorithm for a set of grid points assigned to a node requires communication only with a handful of other nodes that contain the adjacent grid points. Widely used classes of explicit methods (e.g. Runge–Kutta and Adams–Bashforth) differ in terms of the number of stages involved in an overall time step and the storage required for the intermediate solution. The former determines the computational cost of the scheme and the latter determines the memory footprint.

- Coupled implicit–explicit schemes (IMEX) schemes allow one to choose much larger time steps, by treating the fast processes implicitly. The low-Mach formulation can be construed as being explicit for convective and implicit for acoustic processes. The term coupled refers to the fact that all the physical processes are considered together in time advancing each PDE, which makes it easier to reason about the temporal order of accuracy, compared to the decoupled schemes (see below). However, the implicit treatment incurs the cost that the spatial domain of influence is no longer nearest neighbour and this manifests itself as a global linear system of form $\mathrm{A}\phi^{n+1} = \mathrm{B}\phi^{n} + \mathrm{d}$, where ϕ is the solution vector at all the grid points with superscript n denoting the time, A and B are matrices (usually sparse) that contain the coefficients of the discretization, and d is the vector containing the spatial boundary conditions. Solving such systems requires sophisticated linear system solvers (e.g. multi-grid methods and Krylov methods) whose implementation is fairly involved.
- Operator split methods (Strang 1968) also use a combination of implicit and explicit schemes, but they decouple physical processes and consider the time advancement due to the various processes one at a time. A typical implementation for reacting flow (Najm and Knio 2005) involves advancing the solution state by the diffusion terms for one half time step, followed by a full time step advancement by the reaction terms and finally another half step advancement by the diffusion terms. This offers the advantage that a different solver, best suited for the relevant terms, can be used for each stage. The terms treated implicitly will still require sophisticated solvers and in addition operator split methods introduce splitting errors requiring special numerical treatment to preserve consistency across the physical processes. The end result is a temporal scheme that requires a fairly complicated algorithm even for guaranteeing modest orders of temporal accuracy (Descombes et al. 2014).

On a concluding note, the choice of temporal scheme should be guided by the separation of the timescales, if any, in the target simulation. If all the timescales are comparable, it is best to use fully explicit methods due to their simplicity, ease of implementation and desirability from a distributed memory perspective. If the timescales are disparate, the combined implicit–explicit schemes may be a better option for reasons described above. Moreover, a fairly elaborate set of linear system solvers, which are usually required for the implicit schemes, are available as open libraries which have

been designed and specifically optimized for HPC (PETSC 2017; Trilinos Home Page 2017).

3.4.4 An Exemplar Combustion DNS Code: S3D

The preceding discussion highlights the various factors, by no means exhaustive, that guide the design of a combustion code. To illustrate how they are all put together we present an exemplar code S3D (Chen et al. 2009), developed at the Combustion Research Facility, Sandia National Laboratories. S3D is a massively parallel solver developed for performing DNS of multi-species gas-phase turbulent reacting flows. It employs explicit high-order accurate central difference schemes for spatial discretization and explicit multi-stage low storage Runge–Kutta scheme for temporal discretization (Kennedy and Carpenter 1994). It interfaces with the CHEMKIN and TRANSPORT library routines for incorporating detailed finite-rate chemical kinetics and mixture-averaged molecular transport properties. The longstanding version of the code, written in Fortran 90, uses MPI-based distributed domain decomposition. More recently, it has been refactored for heterogeneous architectures using a hybrid MPI+OpenACC implementation and also a radical task-based programing model called Legion (Treichler et al. 2018). Over the years, S3D has performed turbulent combustion DNS simulations of remarkable scale and chemical complexity. Due to its simplicity and ease of use, it has been ported to a variety of supercomputer architectures with excellent parallel scalability and performance. Moreover, it has served as a vehicle that enabled various other facets of HPC research: data analytics and visualization (Ye et al. 2016), data compression (Austin et al. 2016), large-scale parallel I/O (Schendel et al. 2012) and HPC resilience (Gamell et al. 2017).

3.5 Data Analyses

While performing massive turbulent combustion simulations is challenging in its own right, the effort does not end there. Turbulent combustion is the classic multiscale multi-physics scientific application and accordingly its simulations generate large volumes of data rich in information. Extracting insight buried in these data sets is also often a large computational undertaking. The recent S3D simulation shown in Fig. 3.1 has a computational problem size of 1.8×10^{11}. If the data are represented by double-precision floating-point numbers (8 bytes), this translates to each snapshot of this data set having a file size of 1.44 TB! Considering a few hundred time snapshots are required for capturing the temporal evolution, the total data size approaches PetaBytes, which is well beyond the capacity of even modest computing clusters, let alone desktop computers.

The only pragmatic approach for analysing such volumes of data is to perform the analysis *in place*, i.e. the same computing resource where the data is generated. This

dictates the use parallel computing for the analyses as well and domain decomposition serves as a good strategy for distributed parallelism. Below are some commonly recurring motifs for combustion data analyses:

- **Descriptive statistics**: Statistical moments (mean, variance, covariance, etc.) gathered over ensembles in the 'homogeneous' dimensions. For temporally evolving simulations, homogeneous dimensions are the spatial dimensions that are periodic while for statistically stationary simulations time is a homogeneous dimension. In either case, gathering statistics requires global communication and aggregation of data in space and/or time.
- **Feature-based analyses**: Often, it is of interest to hone in on specific features of the turbulent flames (ignition kernels, extinction regions, iso-surfaces/iso-volumes of reacting scalars, strain-/vorticity-dominated regions, etc.). Feature identification, extraction and tracking is a broad topic requiring specialized algorithms for different types of features (e.g. Marching cubes algorithm for iso-surface construction) and these need to be further implemented in a parallel setting. An example of an iso-surface based analysis is the geometric flame thickness studied in Chaudhuri et al. (2017).
- **Phase-space analyses**: It is sometimes required to transform from a space–time domain to the solution variables domain (phase-space). Examples of analyses in such transformed domains include constructing joint/conditional/marginal probability distribution functions (PDFs), trajectories in phase space, empirical low-dimensional chemical manifolds, etc.
- **Fourier spectral analyses**: Assessing classical hypotheses borne out of the spectral view of the turbulence energy cascade requires constructing energy (Kolla et al. 2014) and dissipation spectra (Kolla et al. 2016) of velocities and reactive scalars. Fast Fourier transforms are integral to this which are challenging in a distributed data set since they are communication intensive and extremely expensive.
- **Filtering and multiscale analyses**: In multiscale settings, it is sometimes desirable to extract scale-specific features and statistics. Examples of such analyses include wavelet transforms, bandpass filtering, explicit spatial filtering in the vein of LES, etc.

It is obvious that the space for analyses is rather broad and in some sense more diverse, in terms of algorithmic needs and implementations, compared to the PDE solution algorithms. Another concept, which takes the idea of in-place analyses even further, is in-situ analysis which refers to a paradigm where the analyses and solver are much more tightly integrated and the data is being analysed as it is generated. Looking towards the future, and extrapolating the rate at which the scale of combustion simulations is growing, generating and saving such volumes of data seems unsustainable. It appears that in-situ analyses will play a much bigger role in the overall workflow and the final data sets generated will have to be reduced by orders of magnitude. A good example of what such a workflow might look like is presented by Bennett et al. (2012).

Acknowledgements This work was supported by Sandia National Laboratories, a multi-mission laboratory managed and operated by National Technology and Engineering Solutions of Sandia, LLC., a wholly owned subsidiary of Honeywell International, Inc., for the U.S. Department of Energys National Nuclear Security Administration under contract DE-NA-0003525. The authors acknowledge the support of the Exascale Computing Project (ECP), Project Number: 17-SC-20-SC, a collaborative effort of two DOE organizations—the Office of Science and the National Nuclear Security Administration—responsible for the planning and preparation of a capable exascale ecosystem including software, applications, hardware, advanced system engineering and early testbed platforms to support the nations exascale computing imperative. Helpful comments and inputs from Dr. Xinyu Zhao (University of Connecticut), Dr. Giulio Borghesi (Sandia National Labs) and Dr. Aditya Konduri (Sandia National Labs) are gratefully acknowledged.

References

GRI-Mech 3.0. http://www.me.berkeley.edu/gri_mech
Legion: a data-centric parallel programming system. http://legion.stanford.edu
MPI forum. http://mpi-forum.org
Open multi-processing. http://www.openmp.org
PETSc web page. http://www.mcs.anl.gov/petsc
Programming guidelines for vectorization. https://software.intel.com/en-us/node/695829
Trilinos home page. https://trilinos.org
Austin W, Ballard G, Kolda T (2016) Parallel tensor compression for large-scale scientific data. In: IPDPS'16: Proceedings of the 30th IEEE international parallel and distributed processing symposium, pp 912–922. https://doi.org/10.1109/IPDPS.2016.67
Bennett J, Abbasi H, Bremer PT, Grout R, Gyulassy A, Jin T, Klasky S, Kolla H, Parashar M, Pascucci V, Pebay P, Thompson D, Yu H, Zhang F, Chen J (2012) Combining in-situ and in-transit processing to enable extreme-scale scientific analysis. In: International conference on high performance computing, networking, storage and analysis (SC)
Bennett J, Clay R, Baker G, Gamell M, Hollman D, Knight S, Kolla H, Sjaardema G, Slattengren N, Teranishi K, Wilke J, Bettencourt M, Bova S, Franko K, Lin P, Grant R, Hammond S, Olivier S, Kale L, Jain N, Mikida E, Aiken A, Bauer M, Lee W, Slaughter E, Treichler S, Berzins M, Harman T, Humphrey A, Schmidt J, Sunderland D, McCormick P, Gutierrez S, Schulz M, Bhatele A, Boehme D, Bremer PT, Gamblin T (2015) ASC ATDM Level 2 Milestone #5325: asynchronous many-task runtime system analysis and assessment for next generation platforms. Technical report SAND2015-8312, Sandia National Laboratories, Albuquerque, NM
Bray K, Libby PA (1976) Interaction effects in turbulent premixed flames. Phys Fluids 19(11):1687–1701
Bruno C, Sankaran V, Kolla H, Chen J (2015) Impact of multi-component diffusion in turbulent combustion using direct numerical simulations. Combust Flame 162:4313–4330
Burke M, Chaos M, Ju Y, Dryer F, Klippenstein S (2012) Comprehensive H_2/O_2 kinetic model for high-pressure combustion. Int J Chem Kinet 44:444–474
Chaudhuri S, Kolla H, Dave H, Hawkes E, Chen J, Law C (2017) Flame thickness and conditional scalar dissipation rate in a premixed temporal turbulent reacting jet. Combust Flame 184:273–285
Chen JH, Choudhary A, de Supinski B, DeVries M, Hawkes ER, Klasky S, Liao WK, Ma KL, Mellor-Crummey J, Podhorszki N, Sankaran R, Shende S, Yoo CS (2009) Terascale direct numerical simulations of turbulent combustion using S3D. Comput Sci Discov 2:015001
Curran H, Gaffuri P, Pitz W, Westbrook C (2002) A comprehensive modeling study of iso-octane oxidation. Combust Flame 129:253–280
Denning P (2005) The locality principle. Commun ACM 48(7):19–24

Descombes S, Duarte M, Dumont T, Laurent F, Louvet V, Massot M (2014) Analysis of operator splitting in the non-asymptotic regime for nonlinear reaction-diffusion equations. Application to the dynamics of premixed flames. SIAM J Numer Anal 52:1311–1334
Echekki T, Chen J (1996) Unsteady strain rate and curvature effects in turbulent premixed methane-air flames. Combust Flame 106:184–202
Echekki T, Chen J (2002) High-temperature combustion in autoigniting non-homogeneous hydrogen/air mixtures. Proc Combust Inst 29:2061–2068
Franzelli B, Riber E, Sanjose M, Poinsot T (2010) A two-step chemical scheme for kerosene-air premixed flames. Combust Flame 157:1364–1373
Gamell M, Teranishi K, Mayo J, Kolla H, Heroux M, Chen J, Parashar M (2017) Modeling and simulating multiple failure masking enabled by local recovery for stencil-based applications at extreme scales. IEEE Trans Parallel Distrib Syst
Gropp W, Lusk E, Skjellum A (1994) Using MPI: portable parallel programming with the message-passing interface. Scientific and engineering computation series. MIT Press
Jenkins K, Cant R (1999) Direct numerical simulation of turbulent flame kernels. In: Knight D, Sakell L (eds) Proceedings of the second AFOSR conference on DNS and LES. Kluwer
Kee R, Rupley F, Miller J (1990) The CHEMKIN thermodynamic data base. Technical report SAND-87-8215B, Sandia National Laboratories
Kee RJ, Dixon-Lewis G, Warnatz J, Coltrin ME, Miller JA (1986) A Fortran computer code package for the evaluation of gas-phase multicomponent transport properties. Technical report SAND86-8246, Sandia National Laboratories
Kennedy C, Carpenter M (1994) Several new numerical methods for compressible shear-layer simulations. Appl Numer Math 14:397–433
Kolla H, Hawkes E, Kerstein A, Chen J (2014) On velocity and reactive scalar spectra in turbulent premixed flames. J Fluid Mech 754:456–487
Kolla H, Zhao XY, Chen J, Swaminathan N (2016) Velocity and reactive scalar dissipation spectra in turbulent premixed flames. Combust Sci Technol 188:1424–1439
Lele S (1992) Compact finite-difference schemes with spectral like resolution. J Comput Phys 103:16–42
Luong M, Luo Z, Lu T, Chung S, Yoo C (2013) Direct numerical simulations of the ignition of lean primary reference fuel/air mixtures under HCCI condition. Combust Flame 160:2038–2047
Najm H, Knio O (2005) Modeling low Mach number reacting flow with detailed chemistry and transport. J Sci Comput 25:263–287
Nonaka A, Bell J, Day M, Gilet C, Almgren A, Minion M (2012) A deferred correction coupling strategy for low Mach number flow with complex chemistry. Combust Theory Model
Pei Y, Mehl M, Liu W, Lu T, Pitz W, Som S (2015) A multi-component blend as a diesel fuel surrogate for compression ignition engine applications. J Eng Gas Turbines Power (GTP-15-1057)
Poinsot T, Veynante D (2012) Theoretical and numerical combustion, chapter 1. Edwards
Raman V, Fox RO (2016) Modeling of fine-particle formation in turbulent flames. Annu Rev Fluid Mech 48:159–190
Sankaran R, Hawkes E, Chen J, Lu T, Law C (2007) Structure of a spatially developing turbulent lean methane-air Bunsen flame. Proc Combust Inst 31:1291–1298
Schendel ER, Pendse SV, Jenkins J, Boyuka II DA, Gong Z, Lakshminarasimhan S, Liu Q, Kolla H, Chen J, Klasky S, Ross R, Samatova NF (2012) ISOBAR Hybrid compression-I/O interleaving for large-scale parallel I/O optimization. In: Proceedings of the 21st international symposium on high-performance parallel and distributed computing, HPDC '12. ACM, New York, NY, USA, pp 61–72. https://doi.org/10.1145/2287076.2287086. http://doi.acm.org/10.1145/2287076.2287086
Strang G (1968) On the construction and comparison of difference schemes. SIAM J Numer Anal 5:503–517
Tomboulides A, Lee J, Orszag S (1997) Numerical simulation of Low-Mach number reactive flows. J Sci Comput 12:139–167

Treichler S, Bauer M, Bhagatwala A, Borghesi G, Sankaran R, Kolla H, McCormick P, Slaughter E, Lee W, Aiken A, Chen J (2018) S3D-Legion: an exascale software for direct numerical simulation (DNS) of turbulent combustion with complex multicomponent chemistry. In: Straatsma T, Williams KAT (eds) Exascale scientific applications scalability and performance portability, chapter 12. CRC Press

Ye Y, Neuroth T, Sauer F, Ma KL, Borghesi G, Konduri A, Kolla H, Chen J (2016) In situ generated probability distribution functions for interactive post hoc visualization and analysis. In: IEEE sixth symposium on large data analysis and visualization (LDAV)

Chapter 4
Direct Numerical Simulations for Combustion Science: Past, Present, and Future

Hong G. Im

Abstract Direct numerical simulations (DNS) of turbulent combustion have evolved tremendously in the past decades, thanks to the rapid advances in high performance computing technology. Today's DNS is capable of incorporating detailed reaction mechanisms and transport properties, with physical parameter ranges approaching laboratory scale flames, thereby allowing direct comparison and cross-validation against laser diagnostic measurements. While these developments have led to significantly improved understanding of fundamental turbulent flame characteristics, there are increasing demands to explore combustion regimes at higher levels of turbulent Reynolds (Re) and Karlovitz (Ka) numbers, with a practical interest in new combustion engines driving towards higher efficiencies and lower emissions. This chapter attempts to provide a brief historical review of the progress in DNS of turbulent combustion during the past decades. Major scientific accomplishments and contributions towards fundamental understanding of turbulent combustion will be summarized and future challenges and research needs will be proposed.

Keywords Direct numerical simulations · Turbulent combustion
High performance computing · Flame-flow interaction · Extreme combustion

4.1 Introduction

It has been nearly three decades since direct numerical simulations (DNS) were used in combustion research. First, a disclaimer on terminology is warranted. The word "direct" herein refers to the absence of closure submodels in the context of traditional turbulent flow simulations, such as the statistical average of the Reynolds stress terms (in case of Reynolds-averaged Navier–Stokes, RANS) or the subgrid stress terms (in

H. G. Im (✉)
Clean Combustion Research Center, King Abdullah University of Science and Technology, Thuwal 23955, Saudi Arabia
e-mail: Hong.Im@kaust.edu.sa

© Springer Nature Singapore Pte Ltd. 2018

S. De et al. (eds.), *Modeling and Simulation of Turbulent Combustion*, Energy, Environment, and Sustainability, https://doi.org/10.1007/978-981-10-7410-3_4

case of large eddy simulation, LES). The same cannot be said for the chemical reaction source terms appearing in the conservation equations for reacting flows, as essentially all reaction source terms represented in the current DNS are a continuum representation of the chemical reaction events that result from inter-molecular collisions. As such, the "DNS" designation is only valid in multi-dimensional, turbulent flow simulations in which all relevant continuum scales, including the Kolmogorov scale eddies and flame structures, are fully resolved.

The role of DNS in combustion research continues to expand with the advances in computing power, which allows large DNS simulations approaching the parametric conditions relevant to realistic laboratory conditions. Given that the thermochemical and transport properties of individual reactive scalars are well known, and that the computational solution algorithm is robust and all scales are sufficiently resolved, the solution fields generated by DNS are spatially and temporally accurate. Contributions of DNS in fundamental combustion science are twofold. First, the solutions provide detailed information of flow–chemistry interaction for highly localized phenomena, such as flame structure changes, quenching, re-ignition, and edge flame formation. Second, the simulations that are run in a sufficiently large domain size and a long physical time serve as a useful benchmark for validating turbulent combustion submodels by allowing statistical information of key observables. In this chapter, some major accomplishments of DNS in these two aspects will be reviewed in chronological order. Emphasis will be on the first contributions, the scientific discoveries, while detailed description of the latter will be left for other dedicated chapters.

4.2 A Brief History of Early Combustion DNS

4.2.1 From Nonreacting to Reacting Flow DNS

Historical aspects of DNS of turbulent flows can be found in excellent review articles by Rogallo and Moin (1984) and Moin and Mahesh (1998). The first successful attempt to solve full Navier–Stokes equations in three-dimensional flows was accomplished by a pseudo-spectral method for *incompressible* isotropic turbulence in the presence of a mean shear (Rogallo 1981). Subsequently, DNS of wall-bounded channel flows was demonstrated with the advances in the supercomputing power (Kim et al. 1987). These simulations involved a few million grid points for which pseudo-spectral method for spatial discretization and semi-implicit time integration was employed. The study was the first demonstration of DNS in turbulent boundary layer flows and provided tremendous insights into our fundamental understanding of the origin of boundary layer turbulence by unraveling the temporally and spatially resolved development of the vorticity generation. Subsequent simulations incorporated additional aspects of the specific configuration, and the database was used to extract various statistical quantities for validation and comparison with experimental measurements.

In comparison, DNS of *compressible* turbulent flows came out almost a decade later (Lee et al. 1991, Sarkar et al. 1991), investigating the interaction of turbulence, shock, and boundary layers. As discussed in the previous chapter, computational solution algorithm for compressible Navier–Stokes equations is made in a simple form of the method of lines solving a system of ordinary equations, in contrast to the incompressible counterpart (Bell et al. 1989) which involves iterative solutions of the pressure Poisson equation, but at the expense of smaller time steps due to the need to resolve acoustic timescales. The pros and cons of the compressible versus low-Ma solution algorithms will continue to be debated. While the latter approach clearly has an advantage of using a larger time step (at the expense of increased computational cost per time step), the argument becomes less evident in modern DNS in which a large number of species and chemical reactions are considered, whose timescales are often comparable or even shorter than the corresponding acoustic timescales. Note that around this time, computation of simple laminar flames with detailed chemistry was being established through the framework of Chemkin (Kee et al. 1989), providing the combustion community with various flame application codes to compute one-dimensional flame structures involving tens of major and minor reactive species. However, employing the detailed chemistry into multi-dimensional DNS had to wait nearly a decade due to computational hardware limitation, and thus the first multi-dimensional simulations in this era were mainly limited to simple one-step Arrhenius chemistry model.

While not directly considering real turbulent flow fields or detailed chemistry, the first DNS of multi-dimensional flame–flow interaction was realized around the same time in the late 1980s using both compressible and low-Ma approaches, in the study of flame–vortex interaction. Although this configuration does not literally qualify for the definition of DNS stated in the introduction, these were the first studies that utilized the same computational framework, while a single vortex represents an elementary unit of turbulent eddy motion interacting with the flame front. In the compressible formulation, Poinsot et al. (1991) conducted parametric studies of two-dimensional (2D) planar flames subjected to an impinging vortex at various strengths, and the results were used to provide theoretical basis to modify the turbulent premixed combustion regime diagram as shown in Fig. 4.1. One of the main conclusions was that the laminar flamelet regime boundary defined by $\mathrm{Ka} = 1$ needs to be modified if the unsteady aspects are accounted for. In other words, the smaller eddies that are likely to penetrate into the laminar flame structures also have timescales that are too short to have any meaningful effects to perturb the flames, such that the laminar flame structure remains intact. An empirical fit for the "inner cut-off" length scale, the size of turbulent eddies below which the flame is not affected, was derived. This was argued as a justification that the validity of the laminar flamelet regime may be wider than predicted in the original Borghi diagram. A similar conclusion was also drawn from theoretical (Im et al. 1995) and computational (Egolfopoulos and Campbell 1996) studies of laminar counterflow flames.

As for the first DNS using the low-Ma algorithm, Rutland and Ferziger (1991) also conducted simulations of 2D flame–vortex interaction, which quantitatively demonstrated the flame-generated vorticity through the well-known baroclinic

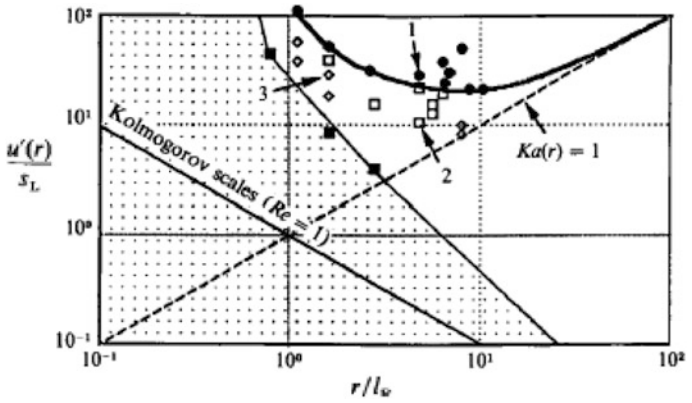

Fig. 4.1 A revised turbulent premixed combustion regime diagram accounting for unsteadiness of turbulent eddies (taken from Poinsot et al. 1991)

torque involving the density and pressure gradients across the flame. As such, it was shown that the magnitude of the flame-generated vorticity depends strongly on the amount of heat release and the resulting density variation across the flame.

Subsequent development in combustion DNS in the 1990s evolved either (a) to increase spatial complexity by incorporating three-dimensional (3D) turbulent field using simple chemistry, or (b) to increase chemical complexity by solving for detailed reactive species in 2D configurations. It took almost another decade for 3D DNS with detailed chemistry to emerge, thanks to terascale computing hardware.

4.2.2 Premixed Combustion

4.2.2.1 3D DNS with Simple Chemistry

In the 3D simulations, a rectangular Cartesian domain was commonly adopted and turbulent premixed flames propagating in the streamwise direction with transverse periodic conditions with simple chemistry have been simulated, again by the low-Ma (Rutland and Cant 1994) and by the compressible formulation (Trouve and Poinsot 1994). Common in the two simulations, a steady 1D laminar flame profile with a one-step chemistry with a unity Lewis number was mapped into the 3D domain as the initial condition. A homogeneous and isotropic turbulent flow field as an instantaneous snapshot was generated in a 3D periodic cube by the Fourier transform converted from a prescribed turbulent kinetic energy spectrum (Lee et al. 1991; Baum et al. 1994). The 3D static turbulent flow field (usually at constant density and temperature) was fed at the inflow boundary surface, translated into the streamwise direction at a prescribed speed, such that the flame stays within the computational domain while the turbulence–flame interaction is fully established.

As such, the turbulent kinetic energy level decays from the initial condition by the time the flow interacts with the flame. Nevertheless, a rich database was obtained that can provide valuable insights into validating many existing RANS combustion modeling approaches.

These earlier 3D DNS studies were limited to a lower level of turbulent Reynolds number and simple chemistry; hence, all the conditions were considered in the classical laminar flamelet regime in which the flame structure is only wrinkled or stretched by the turbulent eddies. Under the obvious limitations, the data field was still found to be useful in identifying the statistical distribution of flame topology. For example, by defining the flame surface as an iso-surface of a chosen scalar variable (e.g., isotherm), the flame speed relative to the local flow velocity, namely the displacement speed (Echekki and Chen 1998), the local flame surface curvature, and the flow strain rate can be computed by a kinematic analysis. Compiling the data on the entire flame surface has yielded the statistical distribution of the flame stretch and curvature, which are important in determining the local displacement speed according to the laminar flame theory (Williams 1985), namely

$$S_L(\kappa) = S_L^0 - \mathcal{L}\kappa\,, \tag{4.1}$$

where $\kappa = (1/A)\,dA/dt$ is the flame stretch (Matalon 1983) defined as the normalized Lagrangian time rate of change of the flame surface, consisting of the contributions from the flame curvature and tangential strain rate. $\mathcal{L}$ is referred to as the Markstein length, a proportionality constant that is a function of thermochemical parameters of the reactant mixture such as the Lewis number and the heat release ratio. In the laminar flamelet regime, the turbulent burning velocity is, in the first approximation, the integral of the local flame speed on the entire flame surface, and thus the distribution of the flame speed and stretch on the flame surface is important.

Another valuable contribution of the earlier 3D DNS analysis was the validation of existing turbulent combustion models. For example, Fig. 4.2 shows the comparison of the two DNS data discussed above, at different normalized turbulence intensities: $u'/S_L^0 = 1$ for Rutland and Cant (1994) and 10 for Trouve and Poinsot (1994). In particular, the Favre-averaged transport equation for the reaction progress variable $\tilde{c}$ generates the flux term to be modeled as (see Chap. 5 for detailed derivation):

$$\bar{\rho}\widetilde{u_i'' c''} = -D_t \frac{\partial \tilde{c}}{\partial x_i} \tag{4.2}$$

which is called the gradient transport model, and the Bray–Moss–Libby (BML) model:

$$\bar{\rho}\widetilde{u_i'' c''} = \bar{\rho}\tilde{c}(1-\tilde{c})(\bar{u}_{ib} - \bar{u}_{iu})\,, \tag{4.3}$$

where $\bar{u}_{iu}$ and $\bar{u}_{ib}$ are the conditional average velocities in the unburned and burned gases, respectively. For a typical passive scalar variable, the flame propagates from

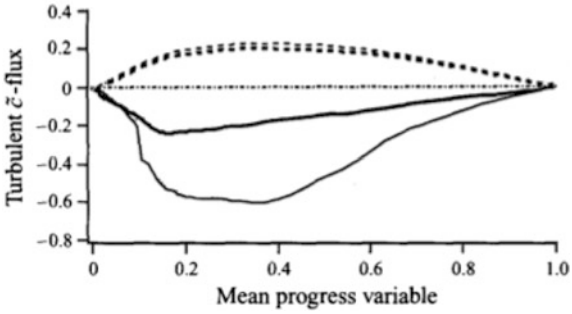

Fig. 4.2 Comparison between the DNS data for $\frac{u'}{S_L^0} = 10$ (solid; Trouve and Poinsot 1994) and $\frac{u'}{S_L^0} = 1$ (dashed; Rutland and Cant 1994). The bold lines denote the turbulent flux terms directly computed from the DNS data, and the thin lines the corresponding BML model evaluation per Eq. (4.3)

$\tilde{c} = 1$ to $\tilde{c} = 0$ with $\bar{u}_{ib} - \bar{u}_{iu} < 0$, and hence $\widetilde{\bar{\rho} u_i'' c''} > 0$ according to Eq. (4.3). This contradicts the gradient transport model, Eq. (4.2), which requires the flux to be negative in order for the turbulent diffusivity, D_t, to be positive. This is the well-known "counter-gradient diffusion" problem in combustion modeling. Considering that the problem arises from the presence of the flames, it is anticipated that the effect may be attenuated as the turbulence intensity increases.

3D DNS data serve as an excellent benchmark to validate this hypothesis. The transverse periodicity of the simulation allows an approximate evaluation of the statistical averaging conditional on the mean progress variable, $\tilde{c}$, by averaging one or multiple instantaneous solution fields of the simulation. Figure 4.2 shows the actual turbulent flux term (LHS of Eq. (4.3)) and the BML term per Eq. (4.3) (RHS of Eq. (4.3)), for the two DNS data at high and low turbulence intensities. The positive values across the entire range of $\tilde{c}$ indicate counter-gradient diffusion (dashed lines for $u'/S_L = 1$), and the negative gradient diffusion is observed for $u'/S_L = 10$, confirming that the counter-gradient diffusion effect vanishes as the turbulence intensity increases.

3D turbulent flame simulations have since been extensively used in validation of various turbulent combustion models, an excellent summary of which can be found in the book by Poinsot and Veynante (2005). Even today, 3D DNS with simple chemistry is being studied at higher Reynolds and Karlovitz number conditions in favor of their advantages in computational cost. One must bear in mind that the simple chemistry model is perfectly valid approximation depending on science questions under investigation.

4.2.2.2 2D DNS with Detailed Chemistry

Toward mid-90s for about a decade, high fidelity DNS with full consideration of detailed chemistry emerged. Even with the simplest fuel like hydrogen/air combustion, the total number of species is increased to nine and nineteen elementary

reaction steps, making 3D computations prohibitive during the gigaflops era. While some would argue that 2D turbulence is not realistic due to the absence of the critical vortex stretching mechanism, the value of 2D DNS can be justified provided that the data are used wisely. That is, it may be questionable to extract the kinetic energy spectrum and transfer which are distinct in 3D, but 2D data provide useful information by reproducing a large number of interaction incidents between the turbulent eddies and flames. In other words, it is inappropriate to analyze the distribution of the scales of turbulent eddies and their evolution over time (which is often in reverse direction in 2D), but capturing the moment of eddy action in corrugating and disrupting the flame structure bears physical relevance. Further justification of 2D turbulence analysis has also been based on the observation of 3D homogeneous isotropic turbulent flow simulations (Ashurst et al. 1987), showing that the vortical structures are more likely cylindrical than spherical.

2D DNS of turbulent premixed flames in a channel has been undertaken with a hydrogen–air detailed mechanism (Baum et al. 1994; Chen and Im 2000), with a methane–air skeletal mechanism (Echekki and Chen 1996; Chen and Im 1998; Chen et al. 1998), and later with propane–air skeletal mechanism (Haworth et al. 2000; Jimenez et al. 2002). Since 2D turbulence does not evolve in a physical manner over time, most of these simulations started with superimposing a 2D slice of 3D turbulent flow onto the initial planar premixed flame, and observed the flame–turbulence interaction while the turbulence was decaying in time. Again, this was not an ideal data set to investigate turbulent kinetic energy statistics, but nonetheless was able to capture the details of the flame and eddy structures during the interaction. Figure 4.3 shows an example of instantaneous images of the hydrogen (H_2) consumption rates for hydrogen–air premixed flames at different mixture equivalence ratios (Chen and Im 2000). Consistent with the diffusive-thermal instabilities based on the laminar flame theory (Williams 1985), it is seen that the local attenuation/quenching of the fuel consumption rate was noticeable at the trough region with negative flame curvature towards unburned gas for the fuel lean mixture (Fig. 4.3b), while the opposite trend was observed for the fuel rich mixture condition (Fig. 4.3c).

Since the 2D DNS provides a large collection of different flame–eddy interaction incidents in terms of the magnitude and signs of the flame stretch and curvature, the data have been analyzed to assess the laminar flame theory as in Eq. (4.1), by plotting the correlation between the local flame displacement speed versus the stretch, as shown in Fig. 4.4. While the linear correlation was found to be reasonable for moderate stretch values, some data points are seen to deviate significantly from the correlation line. These points were found to be predominantly at the flame locations where the curvature is large; it has been often the case that some extremely large stretch is more likely experienced by the curvature effect rather than the tangential straining. These types of 2D DNS data have been used to extract the Markstein length for different hydrogen/air mixtures (Baum et al. 1994; Chen and Im 2000) for comparison with existing experimental measurements. While the quantitative agreement was difficult to achieve due to the large scatters in the turbulent simulation data and experimental uncertainties, a qualitative observation was noted

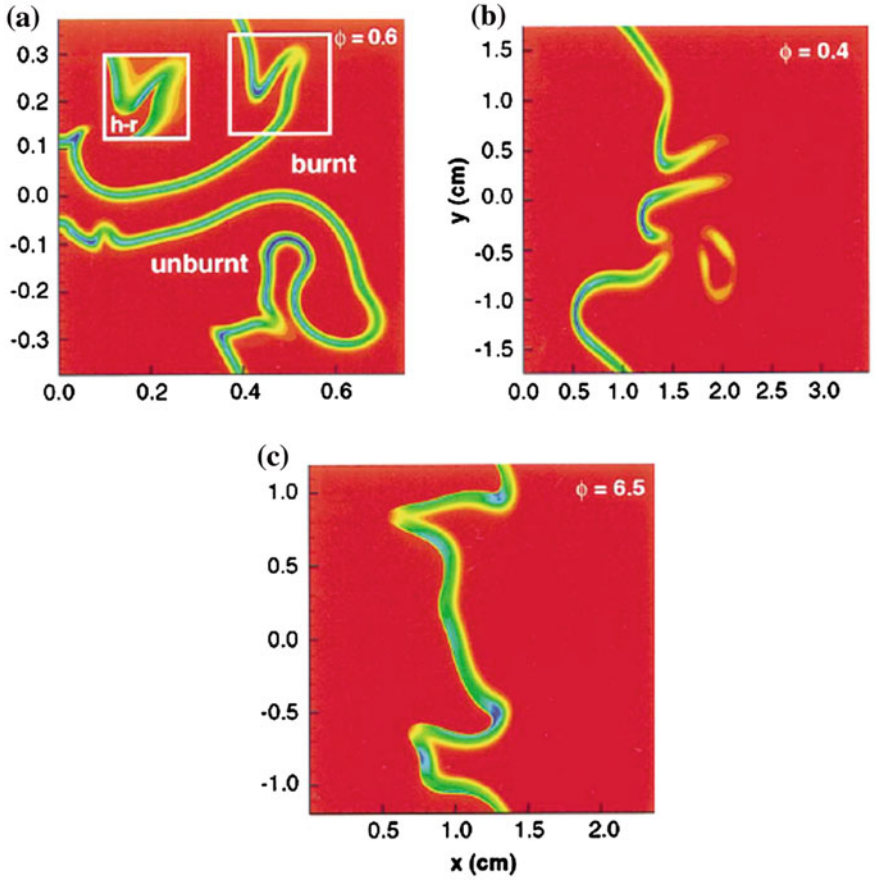

Fig. 4.3 Iso-contours of the hydrogen consumption rate (strong in blue) in hydrogen/air premixed flames interacting with 2D turbulent flow fields, for three different equivalence ratio conditions: $\phi = 0.6$, 0.4, and 6.5 (Chen and Im 2000)

that the Markstein length tends to be attenuated as the turbulence intensity increases (Chen and Im 2000). This was attributed to the increased unsteadiness of small and fast eddies, limiting the extent to modify the flame structure.

DNS data complement experimental diagnostics by allowing access to spatially and temporally resolved information of all major and minor reactive species considered in the simulation. This offers an opportunity to determine some experimental observables by measuring alternative quantities. For example, heat release rate is an important quantity to determine combustion behavior but is difficult to measure. DNS with full consideration of detailed chemical pathways allows such alternative methods through the analysis of different chemical species and reaction signature and setting up proper correlations. Najm et al. (1998) have conducted DNS simulations of methane–air premixed flames interacting with vortices, and suggested various

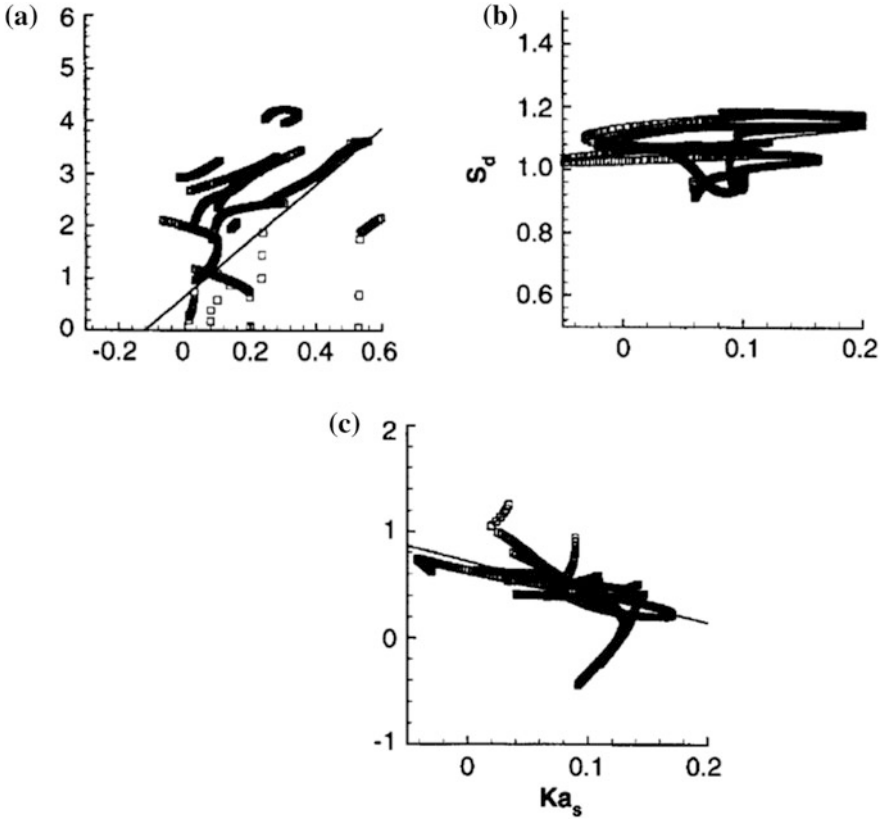

Fig. 4.4 Correlation of normalized displacement speed versus normalized tangential strain rate for the three simulation cases corresponding to Fig. 4.3 (Chen and Im 2000)

possible flame diagnostics in terms of cross-products of different species concentrations. For the methane–air premixed flames, the peak value of the product of OH and CH_4 or OH and CO were found to yield excellent correlations with the heat release rate with little systematic effects due to mixture composition or flow disturbances.

4.2.3 Nonpremixed Combustion and Ignition Studies

In contrast to a long list of 2D and 3D DNS for turbulent premixed flames, studies of the nonpremixed flame counterpart are relatively scarce. This is mainly because statistically steady nonpremixed flames are difficult to establish in a similar rectangular domain. Even if the solution field is initialized by a fuel versus air mixing layer, the mixing thickness continues to grow due to molecular transport unless a mean tangential strain rate is imposed to the flame, similar to the opposed-jet flames

in 1D studies. More realistic geometries like nonpremixed jet flames require a very long computational domain and were cost-prohibitive. Indeed, only a few studies are available in the literature on DNS of nonpremixed flames with growing thickness and decaying turbulence (Mahalingam et al. 1995; Bedat et al. 1999). With a one-step chemistry model, these limited studies attempted to compare the flame structure with the theoretical laminar flames in the mixture fraction space.

For a nonpremixed combustion condition, a more commonly studied DNS configuration is ignition of a mixing layer subjected to a superimposed turbulent flow field. One of the first DNS works with simple chemistry was by Mastorakos et al. (1997), in the study of cold air facing hot air for autoignition source. The effects of the imposed turbulent flows were investigated. When the 2D solution field was mapped in the mixture fraction space, the "most reactive" mixture fraction, $Z_{MR} = 0.1$, was identified as the preferred spot for autoignition, and the temporal evolution of the reaction progress during the ignition process was monitored. From this finding, a modeling framework based on the conditional moment closure (CMC) was proposed, emphasizing the significance of the conditionally averaged reaction rate and scalar dissipation rates near Z_{MR}. Subsequent studies using detailed hydrogen/air chemistry have followed (Im et al. 1998; Hilbert and Thevenin 2002; Hilbert et al. 2002) with consistent results. For consideration of detailed hydrogen chemistry and transport, it was found that the net ignition delay time showed a non-monotonic response to the increase in the turbulence intensity (Im et al. 1998), in that the ignition delay time slightly increases with turbulence level and then decreases as the turbulence intensity increases further. Considering that the ignition is inherently a local event, the overall ignition behavior was found to be insensitive to the level of turbulence.

4.2.4 Partially Premixed Combustion

One of the highly active theoretical combustion research subjects at the turn of the century was the structure and dynamics of the partially premixed combustion. When a segment of nonpremixed flames becomes extinguished by an excessive local straining, as encountered at the base of the lifted jet flames, just ahead of the extinguished flame *edge* there is instant mixing of fuel and oxidizer, creating a *tribrachial* or *triple flames* whose edge propagates along the stoichiometric mixture fraction line, as shown in Fig. 4.5. The bow shape of the frontal part of the flame behaves like a premixed flame front propagating onto a mixture with a transverse gradient in the equivalence ratio, and its propagation velocity (may be positive or negative) is found to be a strong function of the neighboring flow field and mixture distribution, such as the scalar dissipation rate. The specific edge flame dynamics determines whether the nonpremixed flame *hole* will be healed or will lead to the total extinction, and the subsequent stabilization of the lifted nonpremixed flames. While there had been a number of theoretical studies available in conceptualizing the edge flame dynamics, as summarized by Buckmaster (2002), high fidelity DNS

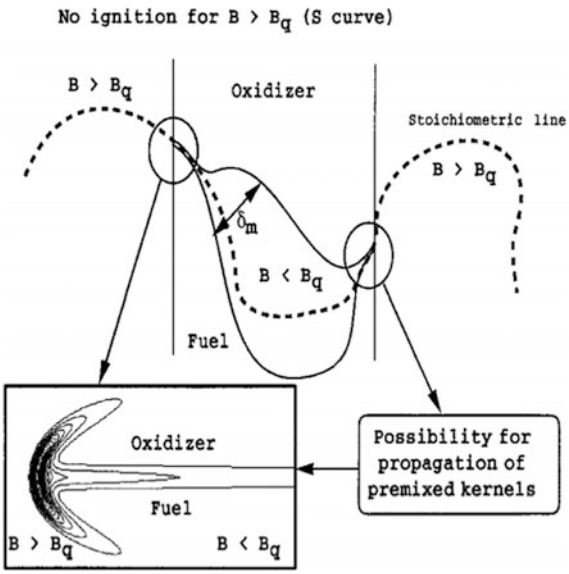

Fig. 4.5 Schematic of nonpremixed flame quenching and the structure and mechanism of the edge flame formation (Domingo and Vervisch 1996)

simulations further advanced our fundamental understanding by reproducing the formation of the edge flames in realistic flow field (Domingo and Vervisch 1996) and their temporal evolution. Simulations of edge flames with detailed chemistry (Echekki and Chen 1998; Im and Chen 1999) have further provided detailed structure of major and minor species distributions in asymmetric edge flames, and the evolution of the flame speed as it propagates along the mixing layer was analyzed in detail. The existence of *negative edge displacement speed* in the presence of strong tangential straining has also been demonstrated and the transient dynamics have been investigated (Favier and Vervisch 2001; Im and Chen 2001; Yoo and Im 2005). These detailed simulations provided insights into the development of modeling framework for partially premixed combustion in turbulent flows (Peters 2000).

4.3 Recent Advances in DNS—Tera-, Petascale, and Beyond

At the turn of the new millennium, supercomputing power at teraflops (10^{12} floating point operations per second) scale became available, thereby allowing for the first time some serious levels of 3D DNS simulations with detailed chemistry at the physical scale and parameter ranges approaching those of laboratory flames (Chen 2011). These studies opened a new avenue in the way scientific questions are answered on turbulence–chemistry interactions and their implications in turbulent combustion modeling. This section attempts to give an overview of some notable science achievements made by large-scale DNS simulations.

4.3.1 Premixed Combustion

4.3.1.1 Scientific and Computational Considerations

Turbulent burning velocity has long been a key observable quantity with practical significance, as it directly determines the performance of premixed combustion systems. A large number of review papers are available with continual updates on the progress in our fundamental understanding of the subjects (Pope 1987; Bradley 1992; Poinsot et al. 1995; Poinsot 1996; Bradley 2002; Bradley et al. 2011; Ronney 1995; Lipatnikov et al. 2002, 2005, 2010; Driscoll 2008). Advances in the laser diagnostics and computational capabilities enabled even deeper investigations into the important issue by analyzing spatial and temporal details of the instantaneous flame structures at unprecedented resolution and fidelity.

More recent articles give a good overview of some mainstream developments and specific computational aspects of turbulent combustion studies (Hilbert et al. 2004; Chen 2011; Im et al. 2016). The increase in the computing power in the recent decades rapidly expanded the roles of DNS as an essential tool to provide insights into the intricate dynamics of the turbulence–chemistry interaction with more details of real fuel chemistry and at parametric conditions approaching those realized in the laboratory. In fact, typical spatial resolutions employed in modern DNS range from a few to tens of microns, with temporal resolution at a few to tens of nanoseconds. Thus, provided that the thermochemical properties and rate constants are accurate and the numerical schemes robust, DNS yields the detailed information about the small scale physics much better than the state-of-the-art experimental counterpart.

The latest landmark DNS cases commonly involve a few to tens of billion grid points, and with tens of reacting species with usually less than a hundred elementary reaction steps. A typical simulation case requires a few to tens of million CPU hours on the latest supercomputing hardware with the MPI (message passing interface) protocol. A caveat must be noted on the CPU hour requirements: note that temporal evolution of unsteady dynamics is critical in DNS but cannot be parallelized. Therefore, the physical time duration of the problem directly affects the total computational cost; two simulation cases at seemingly comparable physical scales and chemical complexities may take 1 week or 1 year depending on the timescales of observation. This has an important implication in the selection of the DNS cases for various combustion problems. For example, a turbulent channel flame propagation in a 1 cm^3 volume with a few large eddy turnover times may require a simulation up to a few tens of milliseconds in the physical time. For the same physical scale of simulations involving autoignition events, the total length of the simulation time depends entirely on the overall ignition delay times, which can easily vary by more than orders of magnitude depending on the bulk temperature and pressure even for practically relevant conditions. One must be keenly aware that the CPU requirement of any types of DNS simulations can quickly become cost-prohibitive by pushing the envelope of the physical conditions of the problem

under study. For this reason, there are only a few canonical computational geometries adopted for 3D DNS of turbulent premixed flames. These will be briefly reviewed in the following.

4.3.1.2 Rectangular Periodic Channels

Due to the many practical limitations discussed above, by far the most commonly employed configuration is a rectangular channel with inflow/outflows in one direction and periodic on four sides. This is an excellent reference geometry to study the basic flame–turbulence interaction to validate the theoretical predictions which are mostly based on the homogeneous and isotropic turbulence. Such an ideal turbulent flow field is generated either by using a prescribed spectrum (Baum et al. 1994), mapped onto the 3D physical domain by the fast fourier transform. Alternatively, a similar homogeneous and isotropic turbulent flow field may be generated efficiently by solving an incompressible spectral solver (e.g., Rogallo 1981). An instantaneous snapshot of the 3D flow field is then fed into the inflow rectangular surface at a prescribed inflow velocity following the Taylor's hypothesis (Taylor 1938). The inflow mean velocity may be fixed or varied over time to ensure that the propagating flame remains inside the computational domain. This approach has an issue that turbulence intensity decays over the distance as the eddies at the inflow travel the domain to reach the flame front. To alleviate this problem, recent DNS simulations employed various types of kinetic energy forcing. The forcing may be imposed in the spectral or physical space, and it may be applied only in the upstream unburned region or throughout the entire domain. The many subtle points regarding the specifics of different turbulence forcing schemes are beyond the scope of this book, and readers are referred to relevant publications (Eswaran and Pope 1988; Aspden et al. 2008; Lapointe et al. 2015). With an effective use of the turbulence forcing schemes, the channel DNS simulations were able to push the parametric range further into higher Ka and Re conditions.

In determining the parametric conditions for the DNS simulations, the most important consideration is the position on the turbulent combustion regime diagram, namely the Borghi diagram (Peters 2000), where different combustion regimes are distinguished in terms of the nondimensional length scales, ℓ_I/ℓ_f, and the velocity scales, u'/S_L. Figure 4.6 shows a compilation of conditions covered by recent DNS simulations (Tanahashi et al. 2002; Minamoto et al. 2011; Shim et al. 2013; Aspden et al. 2011a, 2011b, 2015; Hawkes et al. 2012; Chatakonda et al. 2013; Hamlington et al. 2011, 2012; Carlsson et al. 2014, 2015; Savard and Blanquart 2015; Savard et al. 2015; Nikolaou and Swaminathan 2015; Minamoto et al. 2014), which needs to be updated as more new simulation data continue to be reported. A great majority of the simulations shown here employed hydrogen/air or methane/air flames with detailed chemistry, and some limited amount of studies are available with other higher hydrocarbon flames (Aspden et al. 2011c; Savard and Blanquart 2015; Savard et al. 2015).

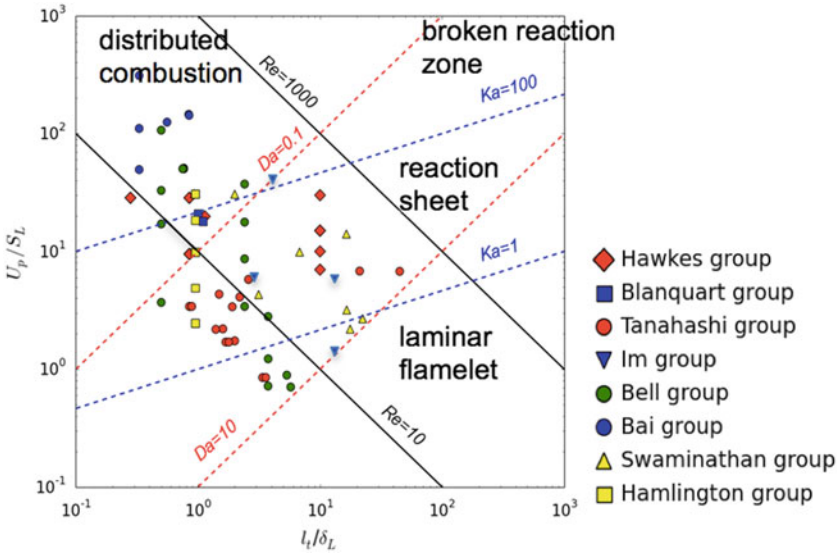

Fig. 4.6 The Borghi diagram and the data points representing recent DNS simulation cases (figure adapted from Im et al. 2016)

The most important nondimensional parameter that determines the combustion regime is the turbulent Karlovitz number (Peters 2000):

$$Ka = \frac{\tau_c}{\tau_K} = \left(\frac{\ell_K}{\ell_f}\right)^2, \tag{4.4}$$

where τ_c and ℓ_f are the flame time and length scales, respectively, and τ_K and ℓ_K denote the Kolmogorov turbulent eddy time and length scales, respectively. According to Peters (2000), the conventional laminar flamelet regime is expected for $Ka < 1$, the reaction sheet regime for $1 < Ka < 100$, and broken or distributed combustion regime for $Ka > 100$. Figure 4.7 shows instantaneous solution fields for two cases at $Ka = 14$ and 126 based on the inflow conditions (Im et al. 2016). Constant temperature iso-surfaces were rendered as the flame front, with the color denoting the heat release rate intensity. As expected from the Borghi diagram, the $Ka = 14$ case shows highly wrinkled laminar flamelet structure, while the $Ka = 126$ case does not show distinct and contiguous flame surface, suggesting that a nearly distributed combustion regime was achieved.

While the numerical simulations confirmed the general flame topologies consistent with the theoretical predictions, the true distributed combustion regime has yet to be experimentally observed. Figure 4.8 shows recent experimental results of the reaction zones denoted by the OH-LIF measurements (Wabel et al. 2017) for two cases of turbulence intensities at three different locations. While the broadening of the thermal thickness was noted, there is no clear evidence that a significant

Fig. 4.7 Instantaneous images of the heat release rate isocontours for statistically stationary turbulent premixed hydrogen–air flames at Ka = 14 (left) and 126 (right), representing the corrugated laminar flamelet and distributed combustion regimes, respectively (Im et al. 2016)

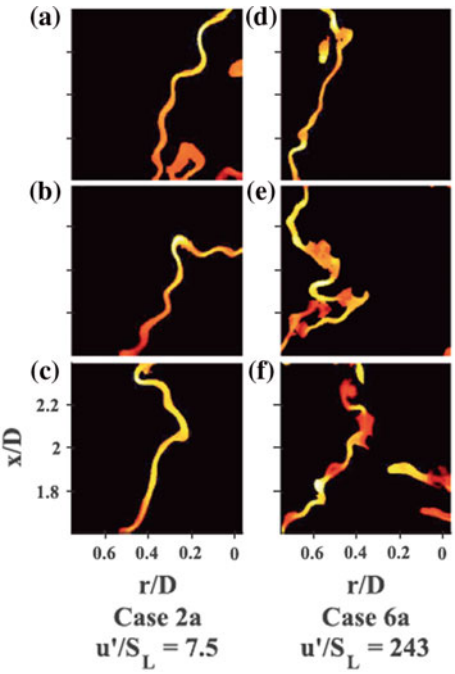

Fig. 4.8 Experimental measurements of highly turbulent methane–air premixed flames at two different conditions of turbulence intensities (Wabel et al. 2017)

portion of the flames shows distributed combustion regime, even for $u'/S_L = 243$. This is an open question today and needs to be investigated further.

The majority of the DNS results fall in the laminar flamelet regime and the 3D data were used to assess various issues investigated in the previous 3D DNS with simple chemistry or 2D DNS with detailed chemistry, in terms of the flame

topology, statistical distribution of the curvature and tangential strain rate on the flame surface, the turbulent burning velocity—S_T/S_L versus u'/S_L (Nikolaou and Swaminathan 2015). Most of these results were found to be largely consistent with the findings from the simple chemistry DNS results, with a few notable exceptions:

- For the hydrogen/air flames, the location of the main heat release, which is associated with HO_2 and H_2O_2 reaction steps, is much further ahead in the lower temperature preheat zone, and thus shows a larger deviation in the flame structure compared to the reference laminar premixed flame (Tanahashi 2002; Carlsson et al. 2014, 2015; Im et al. 2016).
- The diffusive-thermal instability mechanism is evident as expected from the laminar flame theory (most notably for lean and rich hydrogen–air flames), although the *effective* Lewis number of the mixture is not as obvious due to the existence of a number of radical species (such as H or H_2 as an intermediate generated in hydrocarbon flames) whose direction of diffusion is opposite to the direction of the fuel (Chen and Im 2000; Carlsson et al. 2015).
- The preferential diffusion effect for hydrogen or higher hydrocarbon flames arises due to the large imbalance in the molecular weight among different major and minor species. The effect, however, gradually vanishes as the turbulence intensity increases, so that the turbulent flames approach the behavior of equi-diffusive (Le = 1) flames (Aspden et al. 2011c; Savard et al. 2015).
- The attempt to obtain the quantitative prediction of the S_T/S_L versus u'/S_L curve was difficult. This is in part due to the difficulties in extensive parametric simulations for the size of expensive 3D simulations, and in part due to the relatively small domain size that limits the growth and energy transfer from large-scale turbulent eddies. This is an area of active research today (O'Brien et al. 2017), with the help of the peta- and exascale computing infrastructure that allows 3D simulations at significantly large scales.
- The effect of flames on topology of turbulent eddies and their breakdown in the enstrophy transport equations have recently been studied (Hamlington et al. 2011, 2012; Bobbit and Blanquart 2016; Wacks et al. 2016). The overarching conclusion is that the flame-generated turbulence resulting from the baroclinic torque mechanism is diminished as the turbulence intensity increases. Therefore, the significance of flame-generated turbulence in determining the overall turbulent flame dynamics and propagation is still not clearly understood.
- There are a few unique turbulent combustion conditions explored in the same rectangular geometry. Minamoto et al. (2014) studied the DNS of syngas–air flames at MILD condition, at which the mixture is significantly preheated above the ignition temperature. A kinematic analysis of the flame topology revealed a much richer spectrum of different types of flame structures, including an increasing preponderance of distributed combustion-like regimes. This finding may be an opportunity to represent the possible practical conditions where the distributed combustion regime is relevant. This is a new area of research to be further investigated.

4.3.1.3 Spherically Expanding Flames

Another relatively simple computational domain to explore turbulent premixed flame dynamics is a spherically expanding flame. This configuration is of practical interest considering many experimental studies (Abdel-Gayed et al. 1987; Liu et al. 2012; Chaudhuri et al. 2012) of turbulent flame propagation have been conducted in a spherical combustion chamber. The computational geometry can be set up as a cubic domain with uniform mesh, and a flame kernel can be placed at the center to initiate flame propagation. While the computational setup is simple, there are a number of obvious difficulties including the initial transients, the limitations in the flame growth due to the domain size, the mean flame curvature that can bias the results and interpretations, and the difficulty in maintaining the level of turbulence intensity after the start of the simulations. The first 3D spherical DNS simulations were reported by Jenkins et al. (2002, 2006), and the simulations with detailed chemistry have been recently conducted (Tomboulides 2013). Despite the limitations, the configuration is still attractive in capturing a more realistic turbulent expanding flame encountered in the laboratory, and with careful analysis of the data can provide important fundamental understanding.

4.3.1.4 Flame–Wall Interaction

All combustion devices have solid walls. How the propagating flames interact with the wall and boundary layers is an important practical issue, as it is often a primary source of pollutant emission due to the flame quenching by wall heat losses. The first DNS study of turbulent premixed flames impinging on a solid wall, in the form of head-on collision, was conducted with simple chemistry and 2D geometry (Poinsot et al. 1993). With the modest scale of simulation data, the standard RANS submodels, such as the law of the wall, were refined to incorporate the effect of the flame–wall interaction. Subsequent DNS studies followed for a channel flow (Bruneaux et al. 1996; Alshaalan and Rutland 1998), and DNS of hydrogen–air flames impinging on inert walls and the transient history of the wall heat fluxes was investigated (Dabireau et al. 2003).

More recently, the rectangular channel flames with transverse periodicity have been modified to investigate another important practical issue as encountered in the flame flashback. The top and bottom surfaces of the computational domains are specified to be solid walls with no-slip and impermeable boundary conditions. The thermal condition of the wall can be made adiabatic or with some conductive heat losses. The hydrogen–air turbulent premixed flames between two parallel walls have been investigated by Gruber et al. (2010, 2012). As shown in Fig. 4.9, a notable finding from the simulation was that, due to the slow flow velocity at the wall boundary layers, where the leading edge of the flame front is located, the diffusive-thermal instability mechanism for lean hydrogen–air flames produces

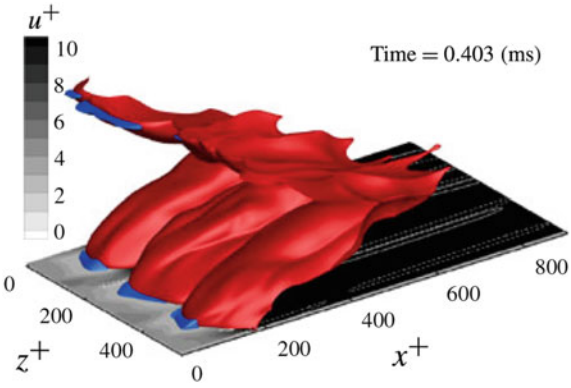

Fig. 4.9 Premixed flame iso-surface (red) and the streamwise velocity in the viscous sublayer (u^+) in an instantaneous image of the unsteady simulation of hydrogen–air premixed flame propagation in parallel walls (Gruber et al. 2012)

lateral flame bulges, leading to intricate three-dimensional dynamics of the flame–wall interaction. Considering that this is the critical location that governs the flame flashback conditions, detailed understanding of the overall flame propagation behavior as a function of various system parameters is needed.

4.3.1.5 Temporally Evolving Shear Layer

Hawkes et al. (2012, 2013) conducted a series of DNS simulations of turbulent premixed flames in a unique configuration. As an attempt to achieve a high level of turbulence intensity, a 3D rectangular domain was set up such that a fuel–air mixture strip is sandwiched between the burned product gases, thus forming parallel premixed flames propagating onto each other. The center fuel strip is initially superimposed with an isotropic broadband turbulent flow field, and the entire strip is then moved at a given velocity in parallel to the flame front, generating a strong shear layer which serves as a source of turbulent kinetic energy. This configuration is often referred to as the *temporally evolving jet* or shear layer due to the nature of streamwise periodicity. Despite a drawback that the turbulent flows continue to change the kinetic energy level throughout the simulation, which typically increases first due to kinetic energy generation by the shear and decreases later due to the flame propagation and resulting thermal expansion, the configuration is an easy way to achieve a long time monitoring of flame–turbulence interaction without a large domain size. Three different simulation cases were analyzed for the assessment of the unresolved wrinkling factor for an a priori study of LES subgrid model (Hawkes et al. 2012), and subsequently the fractal dimension of the low Damkohler number flames was determined to be 8/3 (Chatakonda et al. 2013), in contrast to the prevailing theoretical prediction of 7/3 as well as a previous channel DNS study which reported a numerical value of 2.3–2.5 (Shim et al. 2011).

4.3.1.6 Turbulent Jet Premixed Flames

From the standpoint of relevance to laboratory flames, perhaps the most desirable DNS configuration is the turbulent Bunsen flame, where the fuel/air mixture stream is supplied to form the inner cylindrical or slot jet, surrounded by the external air which is quiescent. While the configuration is attractive in that it closely resembles the laboratory conditions, a typical length of the flames at significantly large jet velocities requires the computational domain length to be an order of magnitude larger than the other dimensions, making the computational cost drastically high. The longer domain size in the streamwise direction also implies a long flow-through time and thus a higher computational cost. Due to this consideration, existing DNS studies were all done for a slot jet configuration with periodic boundary conditions in the lateral direction with a minimal length. While it may not exactly coincide with the laboratory burner geometry, it is computationally easier for grid generation and, more importantly, statistical average quantities can be readily obtained by averaging the solution field in the lateral direction. This way the limited physical time duration for simulation can be compensated for. In distinction from the temporally evolving jet, this geometry is also referred to as the *spatially evolving jet* configuration.

Thus far, two research groups have produced large-scale slot jet turbulent premixed flames with methane–air skeletal/reduced mechanisms (Sankaran et al. 2007; Bell et al. 2007). The main issues investigated were the effects of turbulence on the local flame structure as well as the turbulent flame brush thickness. Subsequent studies (Sankaran et al. 2015; Wang et al. 2017) included additional and larger simulation cases to explore the thin reaction zone regime, and found that the preheat zone was thickened due to the turbulence action, while the reaction zone thickness remains largely unaffected.

4.3.1.7 Bluff-Body Stabilized Flames

Another configuration of practical interest is premixed flames stabilized around a solid object, often called the bluff body. This is a typical way to achieve stable combustion in premixed combustors in gas turbines. Many engineering problems related to the bluff-body flame stabilization and associated acoustic instability issues have been extensively studied in the past decades but DNS of such configurations are scarce and remain computational challenge, not only due to the large computational cost to capture the dimension but also the need to embed a solid object in high fidelity numerical algorithm.

Vervisch et al. (2004) conducted simulations of a V-flame, where the premixed flame is anchored by a *numerical wire*, represented by a small kernel of burned gases with a Gaussian distribution, and turbulence was generated by a separate spectral solver and fed from the inflow. After a statistically steady state was reached, the simulation data were used to investigate various flame statistics such as average progress variable or scalar fluxes.

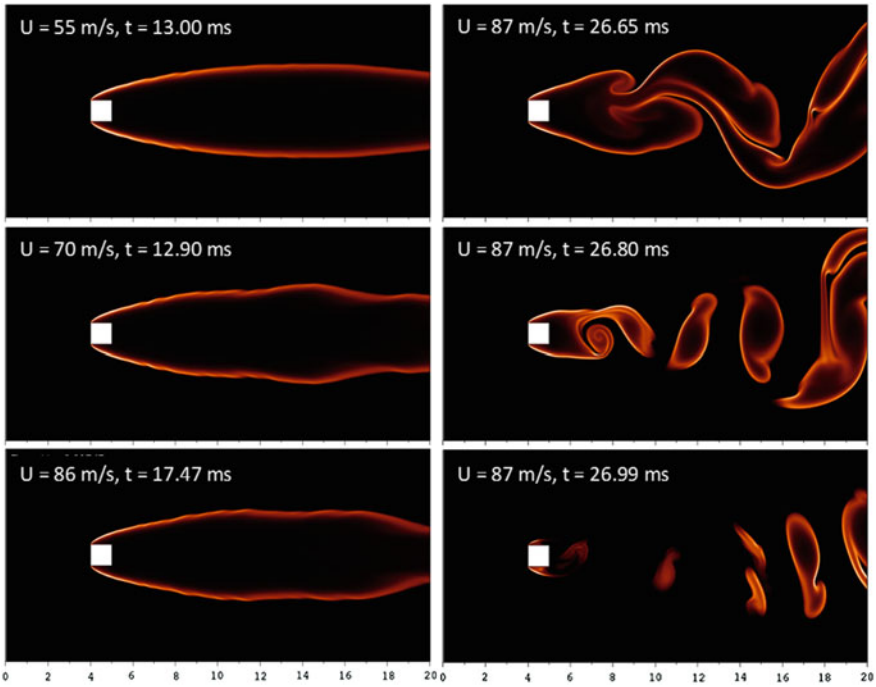

Fig. 4.10 Instantaneous snapshots of heat release rate for hydrogen/air premixed flames anchored around a square bluff body at different inflow velocities (Kim et al. 2017)

Figure 4.10 shows a recent study (Kim et al. 2017) of 2D hydrogen/air premixed flames stabilized by a square bluff body in a reduced domain size of 2 cm × 2 cm, with the bluff-body size of 1 mm × 1 mm. An embedded boundary method was employed to represent a solid object in a finite difference grid structure. While the physical dimension is much smaller than a realistic combustor and thus the flame condition is inherently laminar, the unsteady flame response exhibits a wide spectrum of dynamical behavior as the inflow velocity is increased, from mild fluctuations to symmetric and asymmetric vortex shedding, and eventually forming a vortex street pattern before the total blowout. The high fidelity simulation data provide fundamental insights into the mechanisms for flame blow-off in practical combustors.

4.3.2 Nonpremixed Combustion

Relative to the diverse simulation work on turbulent premixed combustion, fewer studies are found for turbulent nonpremixed flames. As briefly discussed in Sect. 4.2.3, any statistically steady nonpremixed flames require a finite amount of

mean strain rate, either in the form of counterflow or shear layers that would occur in jet flames. Either way, the computational domain needs to capture a large physical scale that is characteristic of the burner system, such as the distance between the nozzle and the jet diameter. Therefore, the usual dimension required for the simulation is much larger than a few integral scale eddies, which is a usual practice in the channel premixed flames, making a typical turbulent nonpremixed flame simulation a larger computational challenge. This is why the 3D DNS of nonpremixed flames with detailed chemistry have been conducted some years later than the premixed counterpart. With the advances in HPC hardware, however, simulations at remarkably large scales are being conducted and reported today.

Some canonical configurations for turbulent nonpremixed flame study can be found in the Turbulent Nonpremixed Flame (TNF) Workshop (http://www.sandia.gov/TNF), a community research forum launched in 1996 with the leadership of Sandia National Laboratories. The experimental data archives show that the predominant geometry is the jet flame configuration, with or without the pilot depending on the level of difficulties in stabilizing the flames. There are some experimental setups for turbulent counterflow nonpremixed flames (Coppola et al. 2009) using elaborate turbulence generation mechanism at the nozzle inlet. However, DNS at this scale is still expensive and no 3D simulations of this system have been reported to date.

4.3.2.1 Turbulent Jet Flames

Despite the computational challenge, the first landmark 3D DNS of turbulent nonpremixed flames with detailed hydrogen/air chemistry was conducted by Mizobuchi et al. (2002, 2005). A hydrogen jet was injected from a cylindrical nozzle at a diameter of 2 mm, at a velocity of 660 m/s into the surrounding quiescent air, yielding the Reynolds number based on the nozzle diameter at 13,600. Due to the high jet velocity, the nonpremixed flame is lifted from the burner, such that the flame stabilization mechanism and partial premixing of the reactants in the flame base region were extensively investigated. These studies are also highly cited for the assessment of the *Takeno Index*, defined as the product of the local fuel and oxidizer gradients, such that the positive and negative values of the index indicate the combustion mode being premixed and nonpremixed, respectively. Figure 4.11 shows a snapshot image of the lifted flame, with the premixed and nonpremixed combustion regimes color-coded.

Shortly after, the Sandia group also conducted a slot jet lifted nonpremixed flames with preheated coflow air for hydrogen–air (Lu et al. 2010; Yoo et al. 2011) and ethylene–air (Yoo et al. 2011) flames, at Reynolds numbers comparable to the work by Mizobuchi et al. (2002, 2005). A rectangular slot jet of a width of 2 mm and the jet velocity of 204 m/s was used, resulting in the Reynolds number of 10,000 based on the nozzle width, compared to the study by Mizobuchi et al. (2002, 2005). Main differences were that the air coflow velocity was imposed at 20 m/s, and highly preheated to 1550 K. The coflow preheating was a pragmatic

Fig. 4.11 Global structure of the hydrogen jet lifted flame. Surface color shows the combustion mode: red (rich premixed), blue (lean premixed), and green (nonpremixed) (Mizobuchi 2005)

computational choice to stabilize the flame, but it also shifted the focus of the scientific study as the mechanism for the flame stabilization at the lifted base was changed to autoignition of the preheated reactants rather than the conventional edge flame propagation. The autoignitive stabilization behavior was manifested by the saw-toothed shape of the flame base trajectory in time, where the slow downstream movement was followed by a rapid upstream movement.

4.3.2.2 Temporally Evolving Shear Layer

These simulations are marked as the largest scale HPC simulations of turbulent combustion DNS to date, while a few other simulations are being presented at technical conferences. Considering the large computational cost, as in the premixed flame simulations, reduced size nonpremixed combustion DNS was also conducted in the temporally evolving shear layer configuration. Hawkes et al. (2009) conducted 3D DNS of temporally evolving shear layer, similar to that discussed in

Sect. 4.3.1 (Hawkes et al. 2012), except that the inner layer was a fuel strip and the outer layers were oxidizer stream. The parallel shear flow created by the imposed lateral velocity field yielded a significantly larger level of the scalar dissipation rates on the spatially periodic dual nonpremixed flame surfaces, thereby allowing an excellent database to analyze the true 3D turbulence effects on the probability density function (pdf) statistics of the scalar dissipation rate on the flame surface, which is an important quantity for accurate combustion submodels for LES and RANS simulations. A new theoretical relationship was developed for the joint pdf of the scalar dissipation rate and other scalar quantities. The same computational setting was also used to study the dynamics of the sooting flames with skeletal ethylene–air chemistry and semi-empirical soot models in 2D and 3D configurations (Lignell et al. 2007, 2008).

4.3.2.3 Turbulent Counterflow Flames

Despite the advantages of compact configurations, 3D DNS of turbulent counterflow flames, either premixed or nonpremixed, have not been conducted at full scale for high Reynolds number conditions. 2D DNS of counterflow nonpremixed flames has been conducted for the edge flame dynamics for hydrogen–air flames (Yoo and Im 2005), 2D turbulent sooting flames with simple ethylene and soot chemistry (Yoo and Im 2007), and 2D turbulent ethylene flames with a skeletal mechanism (Arias et al. 2011) which also added a Lagrangian droplet transport to investigate the flame extinction by fine water mist. A 3D laminar counterflow nonpremixed hydrogen–air flame with detailed chemistry was conducted by Lee et al. (2010), investigating the effect of NO on extinction and re-ignition induced by vortex injection, in comparison with experimental data. The re-ignition is characterized by the positive edge flame propagation after the quenching of the flame center. The effects of NO concentration and the vortex strength on the flame recovery were investigated.

4.3.2.4 Jet in Cross-Flow

The jet in cross-flow (JICF) configuration is highly relevant in high-speed vehicles. The fuel jet injected normal to the air stream serves as a bluff body for the upcoming cross-flows, so that the subsequent flame development and stabilization is facilitated by the vortices generated in the wake of the flow behind the fuel jet. While there is a long history of studying the hydrodynamic aspects—the vortex structure, breakdown, and recirculation—realistic 3D simulation of reacting JICF is rare. Grout et al. (2012) conducted a large-scale 3D DNS of JICF with hydrogen–air detailed chemistry. Figure 4.12 shows an instantaneous image of the iso-surfaces of various scalar quantities. For the physical dimension of approximately 8 cm^3, 1.6 billion grid points were used and the simulation was run on Cray XT5 for 5M CPU hours. The realistic 3D solution field was examined in detail to provide fundamental

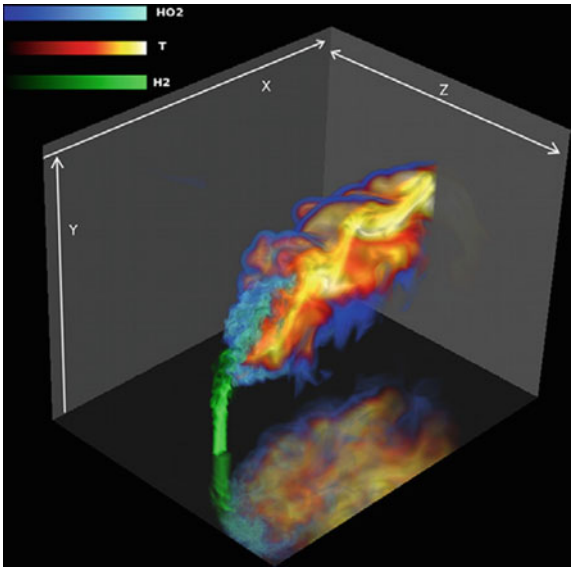

Fig. 4.12 Volume rendering of temperature, HO_2, and H_2 concentrations around a nitrogen-diluted hydrogen jet in a heated turbulent air cross-flow (Grout et al. 2012)

understanding of the flame stabilization mechanism downstream of the transverse fuel jet. It was found that the coherent vortical structures originating from the jet shear layer interaction have a strong effect in determining the upstream portion of the flames.

4.4 Future Research Opportunities in Modeling and Science

This chapter attempted to provide a historical review of the advances in combustion DNS in both physical scale and the complexities of problems investigated. The past decade has seen the role of DNS from an extended reduced model to validate a smaller subset of combustion problems to a serious research tool that can directly complement or even guide laboratory experiments. It is hoped that the comparison of Sects. 4.2 and 4.3 in this chapter would highlight such a dramatic progress in computational combustion research.

The HPC hardware will continue to advance, still keeping up with the Moore's law, such that the academic community worldwide is preparing for the exascale era. It is anticipated that the next decade will lead us into even more impressive breakthroughs in the way combustion modeling can be utilized in answering both long-standing fundamental questions and overcoming real-life engineering design

challenges for future combustion systems, which must explore vastly different designs and fuel diversities in order to keep up with emerging alternative power systems in terms of energy efficiency and environmental impact. The advances in these alternative transportation and stationary power generation systems in recent times have been truly remarkable. It is obvious that combustion of conventional and alternative fuels will continue to play a key role in the next decades and beyond in favor of its energy density and existing supply infrastructure. Combustion research will remain viable for the future generation, and advanced predictive computational tools will play a vital role in achieving the goal.

For DNS to utilize the future exascale architecture successfully, there are a number of research challenges in both computational and physical modeling capabilities. It is important to keep in mind that the fidelity of simulations is satisfied only if the underlying physical and chemical submodels are correct and reliable at the thermochemical conditions under study, and if the embedded numerical algorithms and schemes are stable and accurate with sufficient spatial and temporal resolution. If any one of these factors is not adequate, the simulation results cannot be trusted. Another important challenge is that the specific problem configuration and physical conditions for the large-scale simulations need to be carefully chosen to address the most critical fundamental issues that will have strongest impact in future combustion systems. In the following, the research challenges in both aspects toward successful exascale DNS will be discussed and summarized.

4.4.1 New Models and Computational Capabilities

4.4.1.1 Physical Models

As the computational power increases, DNS will be able to enhance the fidelity by adding more details of the underlying physical and chemical submodels. Provided that the physics models are compatible with the computational solution algorithms, the enhanced submodels will increase the realism and quantitative prediction of the simulation results. In general, the submodels must be carefully validated under controlled parametric conditions against experimental data or with a more detailed model prediction in lower dimensional conditions for efficient computation prior to their implementation into the 3D production runs.

First, the **detailed chemical reaction mechanism** must be able to predict the needed observables (e.g., ignition delay times, flame speed, and maximum temperature) accurately over the thermodynamic conditions under study. Ideally, the detailed kinetic mechanism should include all major and minor reactive species and relevant chemical pathways with accurate rate constants. However, this exercise becomes quickly unmanageable for practical fuels with large and complex molecular structures. Even if the rate constants for each elementary reaction step can be accurately determined, such detailed mechanisms would become too big to

be employed in 3D DNS due to the large number of reactive scalars and reaction source term evaluations. Furthermore, the wide range of characteristic timescales among various reactions introduces temporal stiffness which will significantly increase the computational cost. Therefore, the mechanism development should be done judiciously by retaining the minimal number of species and reactions, while ensuring that there are no unphysical short timescales. As such, today's kinetic mechanism development for real fuels has become a large collaborative effort among the experts in quantum chemistry, experiments and laser diagnostics, and computational method for optimization and dynamical analysis toward the development of the minimal reaction mechanism. For each species considered, it is also equally important to determine the relevant transport properties in the multicomponent system.

Quantitative prediction of **particulate formation** (soot or other combustion-generated particles) needs further advancement in the ability to determine not only the total mass and number of the particulates but also the particle size distribution which is critical in meeting various environmental regulations. Today's state of the art is higher order hybrid method of moments (Mueller et al. 2009; Salenbauch et al. 2017), for which a variety of refinements are available. Sectional methods dealing with the number density variable for each of a finite number of size classes have been considered a more advanced detailed approach in the aerosol modeling community but has been computationally prohibitive for today's combustion DNS applications. With the exascale computing hardware, however, it is foreseeable that the sectional approach becomes a standard practice in soot prediction in 3D DNS. Note also that accurate soot prediction is also contingent on reliable heterogeneous kinetic mechanisms to describe the soot nucleation, growth/agglomeration, and oxidation processes.

Combustion product gases are commonly at higher temperature and a number of gaseous species are highly absorptive and emissive in thermal radiation. Furthermore, a significant level of soot production will further participate in the radiative heat transfer process. Therefore, reliable **radiative heat transfer** models for relevant combustion conditions are necessary. Today's DNS largely neglects the detailed radiation effects by resorting to gray gas assumption (in the spectral space) and optically thin gas approximation (in the physical space). Some DNS studies incorporated optically thick gas conditions and solve radiative transfer equations (RTE). Stochastic photon Monte Carlo method (Modest 2013) is being explored as a viable method that can incorporate spectral resolution of the radiative properties. To move beyond the gray approximation, at the 3D DNS level some scaled or correlated approaches such as full spectrum correlated-k (FSCK) or scaled-k (FSSK) methods are available in the literature (Modest 2013).

Many real combustion devices deal with direct injection of liquid fuels into the combustion chamber. Depending on the injection timing, the combustion process may become extremely complex with full interactions among spray breakup, evaporation, mixing, and combustion in the surrounding air flows. The liquid spray itself contains a wide spectrum of the droplet size distribution with complex secondary breakup, collision, and agglomeration, and interaction with the solid walls.

DNS to resolve the details of such **multiphase flows** is an extremely challenging task. A common practice in high fidelity simulations is to use the Lagrangian particle-in-cell method (Mashayek 1998) for far-field spray dynamics, and the Eulerian volume-of-fluid method for near-field spray close to or inside the nozzle (Desjardins et al. 2008; Lebas et al. 2009). Full-scale Eulerian spray DNS for the entire injector throughout the combustion process has yet to be demonstrated and more work needs to be done in order to accomplish this goal efficiently.

Modern combustion devices are pushing the operating conditions toward higher pressure for efficiency enhancement. For internal combustion engines, some engine cycle concepts demand combustion at 300 bar conditions. At such pressure conditions, many existing kinetic mechanisms and transport properties no longer work. Furthermore, the multiphase flow reaches supercritical conditions, and the entire interface dynamics and multiphase mixing process becomes totally different. DNS of **supercritical combustion** is still a wide open area and much work is needed.

4.4.1.2 Computational Capabilities

The exascale supercomputers will further extend the realizable range of physical parameters to close the gap between the simulations and practical systems. To successfully utilize the new HPC hardware, however, extensive modifications of the software program and the solution algorithms are needed. It is projected that the upcoming leadership computing hardware (e.g., https://www.olcf.ornl.gov/summit/) will likely utilize a large fraction of the system equipped with multi-core accelerators, such as graphical processing units (GPU) or Intel Xeon Phi, demanding the DNS code to be optimized for the **hybrid MPI + X architecture**, where X refers to various types of multi-core accelerators, in order to achieve the maximum scalability as well as per-core speedup.

While the computational power increases rapidly, permanent disk and archival tape storage are not expected to grow proportionately. Even with the state-of-the-art visualization and analysis tools, common analysis tasks require substantial computing resources. Consequently, the exascale era will also demand innovations in the use of large datasets for scientific discovery. It is thus expected that such discoveries will be made through **in situ/in-transit analytics** (Bennett et al. 2012). That is, simulations have to be instrumented for data reduction and feature extraction to selectively reduce the volume of data that needs to be processed immediately and/or sent to archival disks and tapes. Most of today's visualization and analysis tools and workflows only process the raw data through the storage, and are not capable of such efficient data-mining and analysis.

Furthermore, one of the common difficulties in data extraction and analysis of the massive DNS data is that the parameters of the analysis themselves have uncertainties. For example, for highly turbulent premixed flames, it is unclear which scalar variable at what iso-contour value serves as the best metric to determine the overall burning velocity. As such, the current practice of analyzing the DNS data is extremely time-consuming with a large number of trials and errors. The definitions

of geometrical features, statistical measures, and correlations have an associated uncertainty that makes the analysis process iterative and highly dependent on the availability of massive storage capacity. As a practical implementation, the initial phases of data analysis are often highly exploratory with several subsets of data through reduction that provides the most useful information with a high degree of confidence. Performing such analysis in situ will remain a major challenge and require a new paradigm in data management infrastructure combined with **real-time data streaming and post-processing** (Pascucci et al. 2012).

Landmark DNS simulations at maximum achievable scales and parameter ranges have been attempted within the reach of available computing power. While these simulations provided tremendous insights into understanding of underlying physical mechanisms of critical phenomena under consideration, such simulations can only be undertaken for a few realizations at limited parametric conditions. Therefore, they are not well suited for systematic statistical analysis. To this end, another important role of DNS is to create a large ensemble of well-defined canonical DNS simulations. Exascale HPC will enable hundreds to thousands of petascale **ensemble simulations** for statistically converged data analysis over a wide range of parametric conditions along with quantifiable uncertainties.

The ability to perform a large number of simulations comes with the associated difficulties in choosing the most effective way to conduct the computational parametric studies includes the massive data management and interrogation. Therefore, there is a strong demand for automation and **machine learning** in the selection and prioritization of cases, their scheduling, and subsequent data management. Such optimal learning techniques are employed in many other fields such as meteorology, biology, drug discovery, and combustion kinetics (Huan and Marzouk 2013). The optimal learning techniques start with an initial belief on the output characteristics of the simulations. The aforementioned in situ and in-transit analysis capability allows a comparative visualization to guide the selection of the next simulation case. To this end, **uncertainty quantification** (UQ) (Le Maître and Knio 2010) plays a crucial role in the decision-making process through global analysis, parameter inference, model calibration, and Bayesian optimal design techniques.

4.4.2 Research Questions

With the best DNS capabilities in the exascale era with the state-of-the-art data analytics, time is ripe to tackle some important science and engineering questions for future combustion systems. Here is a list of research topics that are currently being investigated as critical issues for modern combustion systems. As discussed before, many of the research questions are closely tied to the fact that modern combustion systems are being designed at extreme thermodynamic and physical conditions that have not been explored in the past. The following list is by no means comprehensive and is only intended to spawn many more new ideas.

- What are the prevailing combustion characteristics at strongly turbulent conditions, represented by high Ka, Re, and Da? Does the postulated distributed combustion regime really exist in practical engines?
- What are the distinct characteristics of turbulent combustion at higher pressure? That is, provided that the basic responses of chemistry and transport processes to pressure are well understood, can the turbulent combustion behavior be predicted as an extension of our existing knowledge, or are there a significant nonlinear effect associated with turbulence–flame interaction?
- What are the most critical features (e.g., phase relation, transport properties) that need to be captured for accurate prediction of multiphase combustion at supercritical conditions? What are the proper predictive simulation strategies?
- Is the low-temperature chemistry, also referred to as the cool flame phenomena, important in high pressure and high Re turbulent combustion? What is its most significant impact on the combustion performance?
- What are the distinct characteristics of pollutant formation (NOx and soot) at such extreme conditions? What are the adequate strategies to mitigate the pollutant emissions?
- How can we develop a unified combustion closure models that are applicable for mixed mode (both premixed and nonpremixed) turbulent combustion?

Acknowledgements The author was sponsored by King Abdullah University of Science and Technology (KAUST).

References

Abdel-Gayed RG, Bradley D, Lawes M (1987) Turbulent burning velocities: a general correlation in terms of straining rates. Proc R Soc London A 1847:389–413

Alshaalan TM, Rutland CJ (1998) Turbulence, scalar transport, and reaction rates in flame-wall interaction. Proc Combust Inst 27:793–799

Arias PG, Im HG, Narayanan P, Trouvé A (2011) A Computational study of nonpremixed flame extinction by water spray. Proc Combust Inst 33:2591–2597

Ashurst WT, Kerstein AR, Kerr RM, Gibson CH (1987) Alignment of vorticity and scalar gradient with strain in simulated Navier-Stokes turbulence. Phys Fluids 30:2343–2353

Aspden AJ, Bell JB, Day MS, Woosley SE, Zingale M (2008) Turbulence-flame interactions in type Ia supernovae. Astrophys J 689(2)

Aspden AJ, Day MS, Bell JB (2011a) Characterization of low Lewis number flames. Proc Combust Inst 33:1463–1471

Aspden AJ, Day MS, Bell JB (2011b) Turbulence–flame interactions in lean premixed hydrogen: transition to the distributed burning regime. J Fluid Mech 680:287–320

Aspden AJ, Day MS, Bell JB (2011c) Lewis number effects in distributed flames. Proc Combust Inst 33:1473–1480

Aspden AJ, Day MS, Bell JB (2015) Turbulence-chemistry interaction in lean premixed hydrogen combustion. Proc Combust Inst 35:1321–1329

Baum M, Poinsot T, Haworth D, Darabiha N (1994) Using direct numerical simulations to study H2/O2/N2 flames with complex chemistry in turbulent flows. J Fluid Mech 281:1–32

Bedat B, Egolfopoulos F, Poinsot T (1999) Direct numerical simulation of heat release and NOx formation in turbulent non premixed flames. Combust Flame 119:69–83
Bell JB, Collela P, Glaz HM (1989) A second-order projection method for the incompressible Navier-Stokes equations. J Comput Phys 85:257–283
Bell JB, Day MS, Grcar JF, Lijewski MJ, Driscoll JF, Filatyev SA (2007) Numerical simulation of a laboratory-scale turbulent slot flame. Proc Combust Inst 27:1299–1307
Bennett JC, Abbasi H, Bremer P-T, Grout R, Gyulassy A, Jin T, Klasky S, Kolla H, Parashar M, Pascucci V, Pebay P, Thompson D, Yu H, Zhang F, Chen JH (2012) Combining in-situ and in-transit processing to enable extreme-scale scientific analysis. In: Proceedings of the international conference on high performance computing, networking, storage and analysis, SC '12, pp 49:1–49:9, Los Alamitos, CA, USA. IEEE Computer Society Press
Bobbitt B, Blanquart G (2016) Vorticity isotropy in high Karlovitz number premixed flames. Phys Fluids 28:105101
Bradley D (1992) How fast can we burn? Proc Combust Inst 24:247–262
Bradley D (2002) Problems of predicting turbulent burning rates. Combust Theory Model 6 (2):361–382
Bradley D, Lawes M, Mansour MS (2011) The problems of the turbulent burning velocity. Flow Turbul Combust 87:191–204
Bruneaux G, Akselvoll K, Poinsot T, Ferziger JH (1996) Flame-wall interaction simulation in a turbulent channel flow. Combust Flame 107:27–44
Buckmaster J (2002) Edge flames. Prog Energy Combust Sci 28:435–475
Carlsson H, Yu R, Bai XS (2014) Direct numerical simulation of lean premixed CH4/air and H2/air flames at high Karlovitz numbers. Int J Hydrogen Energy 39:20216–20232
Carlsson H, Yu R, Bai XS (2015) Flame structure analysis for categorization of lean premixed CH4/air and H2/air flames at high Karlovitz numbers: direct numerical simulation studies. Proc Combust Inst 35:1425–1432
Chatakonda O, Hawkes ER, Aspden AJ, Kerstein AR, Kolla H, Chen JH (2013) On the fractal characteristics of low Damköhler number flames. Combust Flame 160:2422–2433
Chaudhuri S, Wu F, Zhu D, Law CK (2012) Flame speed and self-similar propagation of expanding turbulent premixed flames. Phys Rev Lett 108:044503
Chen JH (2011) Petascale direct numerical simulation of turbulent combustion—fundamental insights towards predictive models. Proc Combust Inst 33:99–123
Chen JH, Echekki T, Kollman W (1998) The mechanism of two-dimensional pocket formation in lean premixed methane air flames with implications for turbulent combustion. Combust Flame 116:15–48
Chen JH, Im HG (1998) Correlation of flame speed with stretch in turbulent premixed methane/air flames. In: 27th international symposium on combustion, vol 27, The Combustion Institute, pp 819–826
Chen JH, Im HG (2000) Stretch effects on the burning velocity of turbulent premixed hydrogen-air flames. Proc Combust Inst 28:211–218
Coppola G, Coriton B, Gomez A (2009) Highly turbulent counterflow flames: a laboratory scale benchmark for practical systems. Combust Flame 156:1834–1843
Cuenot B, Poinsot T (1994) Effects of curvature and unsteadiness in diffusion flames. Implications for turbulent diffusion combustion. In: 25th proceedings of the symposium (international) on combustion, Irvine, pp 1383–1390
Dabireau F, Cuenot B, Vermorel O, Poinsot T (2003) Interaction of flames of H2 + O2 with inert walls. Combust Flame 135:123–133
Desjardins O, Moureau V, Pitsch H (2008) An accurate conservative level set/ghost fluid method for simulating turbulent atomization. J Comput Phys 18:8395–8416
Domingo P, Vervisch L (1996) Triple flames and partially premixed combustion in autoignition of non-premixed mixtures. In: 26th symposium (international) on combustion, The Combustion Institute, Pittsburgh, pp 233–240
Driscoll JF (2008) Turbulent premixed combustion: flamelet structure and its effect on turbulent burning velocities. Prog Energy Combust Sci 34:91–134

Echekki T, Chen JH (1996) Unsteady strain rate and curvature effects in turbulent premixed methane-air flames. Combust Flame 106:184–202
Echekki T, Chen JH (1998) Structure and propagation of methanol-air triple flames. Combust Flame 114:231–245
Egolfopoulos FN, Campbell CS (1996) Unsteady counterflowing strained diffusion flames: diffusion-limited frequency response. J Fluid Mech 318:1–29
Eswaran V, Pope S (1988) An examination of forcing in direct numerical simulations of turbulence. Comput Fluids 16(3):257–278
Favier V, Vervisch L (2001) Edge flames and partially premixed combustion in diffusion flame quenching. Combust Flame 125:788–803
Grout RW, Gruber A, Kolla H, Bremer P-T, Bennett JC, Gyulassy A, Chen JH (2012) A direct numerical simulation study of turbulence and flame structure in transverse jets analysed in jet-trajectory based coordinates. J Fluid Mech 706(10):351–383
Gruber A, Sankaran R, Hawkes ER, Chen JH (2010) Turbulent flame-wall interaction: a direct numerical simulation study. J Fluid Mech 658:5–32
Gruber A, Chen JH, Valiev D, Law CK (2012) Direct numerical simulation of premixed flame boundary layer flashback in turbulent channel flow. J Fluid Mech 709:516–542
Hamlington PE, Poludnenko AY, Oran ES (2011) Interactions between turbulence and flames in premixed reacting flows. Phys Fluids 23:125111
Hamlington PE, Poludnenko AY, Oran ES (2012) Intermittency in premixed turbulent reacting flows. Phys Fluids 24:075111
Hawkes ER, Chatakonda O, Kolla H, Kerstein AR, Chen JH (2012) A petascale direct numerical simulation study of the modelling of flame wrinkling for large-eddy simulations in intense turbulence. Combust Flame 159:2690–2703
Hawkes ER, Sankaran R, Chen JH, Kaiser SA, Frank JH (2009) An analysis of lower-dimensional approximations to the scalar dissipation rate using direct numerical simulations of plane jet flames. Proc Combust Inst 32:1455–1463
Haworth D, Cuenot B, Poinsot T, Blint R (2000) Numerical Simulation of turbulent propane-air combustion with non homogeneous reactants. Combust Flame 121:395–417
Hilbert R, Thevenin D (2002) Autoignition of turbulent non-premixed flames investigated using direct numerical simulations. Combust Flame 128:22–37
Hilbert R, Tap F, El-Rabii H, Thévenin D (2004) Impact of detailed chemistry and transport models on turbulent combustion simulations. Prog Energy Combust Sci 30:61–117
Huan X, Marzouk YM (2013) Simulation-based optimal Bayesian experimental design for nonlinear systems. J Comput Phys 232(1):288–317
Im HG, Arias PG, Chaudhuri S, Uranakara H (2016) Direct numerical simulations of statistically stationary turbulent premixed flames. Combust Sci Technol 188(8):1182–1198
Im HG, Bechtold JK, Law CK (1995) Counterflow diffusion flames with unsteady strain rates. Combust Sci Technol 106:345–361
Im HG, Chen JH, Law CK (1998) Ignition of hydrogen/air mixing layer in turbulent flows. In: 27th international symposium on combustion, The Combustion Institute, vol 27, pp 1047–1056
Im HG, Chen JH (1999) Structure and propagation of triple flames in partially premixed hydrogen/air mixtures. Combust Flame 119:436–454
Im HG, Chen JH (2001) Effects of flow strain on triple flame propagation. Combust Flame 126:1384–1392
Jenkins KW, Cant RS (2002) Curvature effects on flame kernels in a turbulent environment. Proc Combust Inst 29:2023–2029
Jenkins KW, Klein M, Chakraborty N, Cant RS (2006) Effects of strain rate and curvature on the propagation of a spherical flame kernel in the thin-reaction-zones regime. Combust Flame 145:415–434
Jimenez C, Cuenot B, Poinsot T, Haworth D (2002) Numerical simulation and modeling for lean stratified propane-air flames. Combust Flame 128:1–21
Kee RJ, Rupley FM, Miller JA (1989) Chemkin-II: a Fortran chemical kinetics package for the analysis of gas-phase chemical kinetics, Sandia Report SAND-89-8009

Kim J, Moin P, Moser RD (1987) Turbulence statistics in fully-developed channel flow at low Reynolds number. J Fluid Mech 177:133–166
Kim, Y.J., Lee, B.J., Im, H.G. 2017. Scale effect on dynamics of meso-scale bluff-body-stabilized flames in lean premixed hydrogen-air and syngas-air mixtures. In: Fourteenth international conference on flow dynamics, Sendai, Japan, 1–3 Nov, 2017
Lapointe S, Savard B, Blanquart G (2015) Differential diffusion effects, distributed burning, and local extinctions in high Karlovitz premixed flames. Combust Flame 162(9):3341–3355
Le Maître OP, Knio OM (2010) Spectral methods for uncertainty quantification: with applications to computational fluid dynamics. Springer
Lebas R, Menard T, Beau PA, Berlemont A, Demoulin FX (2009) Numerical simulation of primary break-up and atomization: DNS and modelling study. Int J Multiph Flow 35:247–260
Lee ED, Yoo CS, Chen JH, Frank JH (2010) Effect of NO on extinction and re-ignition of vortex-perturbed hydrogen flames. Combust Flame 157:217–229
Lee S, Lele SK, Moin P (1991) Simulations of spatially decaying compressible turbulence. Center for Turbulence Research, NASA Ames/Stanford University, Manuscript 126
Lignell DO, Chen JH, Smith PJ, Lu T, Law CK (2007) The effect of flame structure on soot formation and transport in turbulent nonpremixed flames using direct numerical simulation. Combust Flame 151:2–28
Lignell DO, Chen JH, Smith PJ (2008) Three-dimensional direct numerical simulation of soot formation and transport in a temporally evolving nonpremixed ethylene jet flame. Combust Flame 155:316–333
Lipatnikov AN, Chomiak J (2002) Turbulent flame speed and thickness: phenomenology, evaluation, and application in multi-dimensional simulations. Prog Energy Combust Sci 28:1–74
Lipatnikov AN, Chomiak J (2005) Molecular transport effects on turbulent flame propagation and structure. Prog Energy Combust Sci 31:1–73
Lipatnikov AN, Chomiak J (2010) Effects of premixed flames on turbulence and turbulent scalar transport. Prog Energy Combust Sci 36:1–102
Liu CC, Shy SS, Peng MW, Chiu CW, Dong Y-C (2012) High-pressure burning velocities measurements for centrally-ignited premixed methane/air flames interacting with intense near-isotropic turbulence at constant Reynolds numbers. Combust Flame 159:2608–2619
Lu TF, Yoo CS, Chen JH, Law CK (2010) Three-dimensional direct numerical simulation of a turbulent lifted hydrogen jet flame in a heated coflow: a chemical explosive mode analysis. J Fluid Mech 652:45–64
Mahalingam S, Chen JH, Vervisch L (1995) Finite-rate chemistry and transient effects in simulations of turbulent non-premixed flames. Combust Flame 102:285
Mastorakos E, Baritaud TA, Poinsot TJ (1997) Numerical simulations of autoignition in turbulent mixing flows. Combust Flame 109:198–223
Matalon M (1983) On flame stretch. Combust Sci Technol 31:169–181
Mashayek F (1998) Droplet-turbulence interactions in low Mach number homogeneous shear two-phase flows. J Fluid Mech 367:163–203
Minamoto Y, Fukushima N, Tanahashi M, Miyauchi T, Dunstan TD, Swaminathan N (2011) Effect of flow-geometry on turbulence-scalar interaction in premixed flames. Phys Fluids 23:125107
Minamoto Y, Swaminathan N, Cant RS, Leung T (2014) Reaction zones and their structure in MILD combustion. Combust Sci Technol 186(8):1075–1096
Mizobuchi Y, Tachibana S, Shinjo J, Ogawa S, Takeno T (2002) A numerical analysis of the structure of a turbulent hydrogen jet lifted flame. Proc Combust Inst 29:2009–2015
Mizobuchi Y, Shinjo J, Ogawa S, Takeno T (2005) A numerical study on the formation of diffusion flame islands in a turbulent hydrogen jet lifted flame. Proc Combust Inst 30:611–619
Modest MF (2013) Radiative heat transfer, 3rd edn. Academic Press
Moin P, Mahesh K (1998) Direct numerical simulation: a tool in turbulence research. Annu Rev Fluid Mech 40:539–578

Mueller ME, Blanquart G, Pitsch H (2009) Hybrid method of moments for modeling soot formation and growth. Combust Flame 156:1143–1155
Najm HN, Knio OM, Paul PH, Wyckoff PS (1998) A study of flame observables in premixed methane-air flames. Combust Sci Technol 140:369–403
Nikolaou ZM, Swaminathan N (2015) Direct numerical simulation of complex fuel combustion with detailed chemistry: physical insight and mean reaction rate modeling. Combust Sci Technol 187:1759–1789
O'Brien J, Towery CAZ, Hamlington PE, Ihme M, Poludnenko AY, Urzay J (2017) The cross-scale physical-space transfer of kinetic energy in turbulent premixed flames. Proc Combust Inst 36:1967–1975
Pascucci V, Scorzelli G, Summa B, Bremer PT, Gyulassy A, Christensen C, Philip S, Kumar S (2012) The ViSUS visualization framework, Chapter 19. Chapman & Hall/CRC Computational Science, pp 401–414
Peters N (2000) Turbulent combustion. Cambridge University Press
Poinsot T (1996) Using direct numerical simulations to understand premixed turbulent combustion. Proc Combust Inst 26:219–232
Poinsot T, Candel S, Trouvé A (1995) Applications of direct numerical simulation to premixed turbulent combustion. Prog Energy Combust Sci 21:531–576
Poinsot T, Veynante D (2005) Theoretical and numerical combustion. 2nd edn. RT Edwards, Inc.
Poinsot T, Veynante D, Candel S (1991) Quenching processes and premixed turbulent combustion diagrams. J Fluid Mech 228:561–606
Poinsot T, Haworth DC, Bruneaux G (1993) Direct simulation and modeling of flame-wall interaction for premixed turbulent combustion. Combust Flame 95:118–132
Pope SB (1987) Turbulent premixed flames. Annu Rev Fluid Mech 19:237–270
Rogallo RS (1981) Numerical experiments in homogeneous turbulence. NASA TM-81315
Rogallo RS, Moin P (1984) Numerical simulation of turbulent flows. Annu Rev Fluid Mech 16:99–137
Ronney PD (1995) Modeling in combustion science. Lect Notes Phys 449:1–22
Rutland CJ, Ferziger JH (1991) Simulations of flame-vortex interactions. Combust Flame 84:343–360
Rutland CJ, Cant RS (1994) Turbulent transport in premixed flames. In Proceedings of the summer program center for turbulence research, NASA Ames/Stanford University
Salenbauch S, Sirignano M, Marchisio D, Pollack M, D'Anna A, Hasse C (2017) Detailed particle nucleation modeling in a sooting ethylene flame using a conditional quadrature method of moments (CQMOM). Proc Combust Inst 36:771–779
Sankaran R, Hawkes ER, Chen JH, Lu TF, Law CK (2007) Structure of a spatially developing turbulent lean methane-air Bunsen flame. Proc Combust Inst 27:1291–1298
Sankaran R, Hawkes ER, Yoo CS, Chen JH (2015) Response of flame thickness and propagation speed under intense turbulence in spatially developing lean premixed methane-air jet flames. Combust Flame 162:3294–3306
Sarkar S, Erlebacher G, Hussaini MY (1991) Direct simulation of compressible turbulence in a shear flow. Theor Comput Fluid Dyn 2:291–305
Savard B, Blanquart G (2015) Broken reaction zone and differential diffusion effects in high Karlovitz n-C7H16 premixed turbulent flames. Combust Flame 162:2020–2033
Savard B, Bobbitt B, Blanquart G (2015) Structure of a high Karlovitz n-C7H16 premixed turbulent flame. Proc Combust Inst 35:1377–1384
Shim YS, Fukushima N, Shimura M, Nada Y, Tanahashi M, Miyauchi T (2013) Radical fingering in turbulent premixed flame classified into thin reaction zones. Proc Combust Inst 34:1383–1391
Tanahashi M, Nada Y, Ito Y, Miyauchi T (2002) Local flame structure in the well-stirred reactor regime. Proc Combust Inst 29:2041–2049
Taylor GI (1938) The spectrum of turbulence. Proc R Soc London 164(919):476–490
Tomboulides A (2013) DNS of Flame Propagation Phenomena, ERCOFTAC Spring Festival, Toulon

Trouve A, Poinsot T (1994) The evolution equation for the flame surface density in turbulent premixed combustion. J Fluid Mech 278:1–31

Vervisch L, Hauguel R, Domingo P, Rullaud M (2004) Three facets of turbulent combustion modelling: DNS of premixed V-flame, LES of lifted nonpremixed flame and RANS of jet-flame. J Turbul 5:004

Wabel TM, Skiba AW, Temme JE, Driscoll JF (2017) Measurements to determine the regimes of premixed flames in extreme turbulence. Proc Combust Inst 36:1809–1816

Wacks DH, Chakraborty N, Klein M, Arias PG, Im HG (2016) Flow topologies in different regimes of premixed turbulent combustion: a direct numerical simulation analysis. Phys Rev Fluids 1:083401

Wang H, Hawkes ER, Chen JH (2017) A direct numerical simulaiton study of flame structure and stabilization of an experimental high Ka CH4/air premixed jet flame. Combust Flame 180:110–123

Williams FA (1985) Combustion theory, 2nd edn. Westview Press

Yoo CS, Im HG (2005) Transient dynamics of edge flames in a laminar nonpremixed hydrogen-air counterflow. Proc Combust Inst 30:349–356

Yoo CS, Im HG (2007) Transient soot dynamics in turbulent nonpremixed ethylene-air counterflow flames. Proc Combust Inst 31:701–708

Yoo CS, Richardson ES, Sankaran R, Chen JH (2011) A DNS study on the stabilization mechanism of a turbulent lifted ethylene jet flame in highly heated coflow. Proc Combust Inst 33:1619–1627

Part II
Turbulent Premixed Combustion

Chapter 5
Direct Numerical Simulations of Premixed Turbulent Combustion: Relevance and Applications to Engineering Computational Analyses

Nilanjan Chakraborty and Jiawei Lai

Abstract Analysis of turbulent flows is one of the most difficult and challenging topics in physical sciences because of the nonlinearity of the governing equations, which is manifested by a large range of length and time scales. Resolution of this large range of scales is difficult to address using both experimental and numerical means. This problem is further exacerbated in turbulent reacting flows due to the nonlinearity of the temperature dependence of burning rate in typical combustion processes. Moreover, the interaction of flow and chemistry in turbulent premixed combustion (where reactants are homogeneously mixed prior to the combustion process) necessitates simultaneous measurements of fluid velocity and flame propagation in three dimensions with adequate spatial resolution. Such an experimental analysis is either impossible in most configurations or extremely expensive to carry out. The advances in high-performance computing have made it possible to carry out three-dimensional Direct Numerical Simulations (DNS) of turbulent premixed combustion by resolving all the relevant length and time scales of turbulent reacting flows without any recourse to physical approximations. The cost of DNS for non-reacting flows is immense where one only has to resolve the Kolmogorov scale, and it is more expensive for premixed combustion because it requires additional resolution of the internal flame structure. It can be shown that for simulating homogeneous non-reacting turbulence the number of grid points varies with Reynolds number as $Re_t^{9/4}$, where Re_t is the large-scale turbulent Reynolds number, which is why DNS is limited by computer capacity and the application of DNS remains limited to research problems in simple configurations for moderate turbulent Reynolds numbers. However, the data obtained from DNS circumvents the aforementioned limitations of experimental data and can be considered as an equivalent to experimental data with a spatial resolution up to the Kolmogorov length scale (i.e. the smallest significant length scale of turbulence). Although DNS

N. Chakraborty (✉) · J. Lai
School of Mechanical and Systems Engineering, Newcastle University,
Claremont Road, Newcastle-upon-Tyne NE1 7RU, UK
e-mail: s.navarro@imperial.ac.uk

© Springer Nature Singapore Pte Ltd. 2018

S. De et al. (eds.), *Modeling and Simulation of Turbulent Combustion*, Energy, Environment, and Sustainability, https://doi.org/10.1007/978-981-10-7410-3_5

does not require turbulence and combustion modelling (and thus avoids physical inaccuracies associated with them), the chemical aspect of premixed combustion is often simplified for the sake of computational economy in order to conduct a detailed parametric analysis. The simplification of chemistry and the specification of 'soft' boundary conditions often significantly affect the results and determine the aspects which can be analysed using DNS data. In spite of these constraints, DNS data can be explicitly Reynolds-averaged/filtered to extract the 'exact' behaviour of the unclosed terms in the Reynolds-averaged/ filtered transport equations of momentum, energy and species. This makes it possible to compare the predictions of existing models with respect to the 'exact' unclosed terms extracted from DNS data and propose either model modifications or new models, wherever necessary, in the light of physical insights obtained from DNS data. Thus, even though the DNS of premixed combustion remains mostly limited to canonical configurations, the physical insights obtained from it contribute significantly to the development of the high-fidelity models for Reynolds-Averaged Navier–Stokes (RANS) and Large Eddy Simulations (LES), which are used for engineering calculations for designing industrial burners. As an example, this chapter will illustrate how DNS data can contribute to the model development for the Reynolds flux of sensible enthalpy in head-on quenching of statistically planar turbulent premixed flames by an inert isothermal wall.

Keywords DNS · Turbulent combustion · Premixed combustion

5.1 Introduction

Combustion is a physical phenomenon with much importance and relevance from household applications to energy generation processes in industry. Yet, the understanding of the phenomenon of combustion is incomplete in many respects. Deep understanding of the basic phenomena of combustion is essential to improve the efficiency, reliability, safety and environmental pollution control aspects of combustion systems. In many practical combustion devices like gas turbines and Spark Ignition (SI) engines, the combustion takes place in a turbulent environment in such a manner that fuel and oxidiser are fully homogeneously mixed before being burnt in the device. Recent pollution control regulations have further increased the importance of premixed combustion.

In addition to the complexity of reacting flows, the inherent difficulty in analysing turbulent transport makes 'turbulent combustion' a very challenging subject. The evaluation and estimation of combustion performance with the help of Computational Fluid Dynamics (CFD) has become a necessary task for the automotive, gas turbine and manufacturing industries all over the world. It is instructive to consider an example in which CFD could be used an effective design tool in the industry. Stricter requirements for NO_x emission in energy production have prompted industrial gas turbine manufacturers to develop "Lean Premixed Prevaporised" (LPP) combustors. The LPP combustors operate under globally lean

fuel–air mixture. For the increased amount of air mass flow, the peak temperature drops down compared to that in a combustion situation without LPP, so thermal NO_x production is reduced. Unfortunately, these systems are susceptible to damage-causing dynamic oscillating conditions. Prediction and prevention of these oscillations are primary considerations for combustor designers. The internal conditions of gas turbine combustors are not amenable to detailed experimental investigation. Current trial and error methods for combustor development are expensive. CFD, on the other hand, can offer a detailed understanding of the processes involved in the instability mechanisms, enabling the design of active or passive control strategies.

Due to the advancement in computational power, it has now become possible to resolve all the relevant length and time scales of turbulence without any physical approximation regarding the underlying turbulent flow. However, strong assumptions are often invoked for the purpose of simplification of chemistry, droplet atomisation, and particle–fluid interactions. The advancement in high-performance computing offers the opportunity to tackle some of the outstanding challenges in the analysis of turbulent reacting flows by carrying out numerical simulations and obtaining fundamental physical insights by post-processing the simulation results. One such simulation technique is Direct Numerical Simulation (DNS), which resolves all the length and time scales to reveal the underlying physics without recourse to any closure models. DNS data can, in principle, be considered equivalent to time-resolved experimental data with resolution up to the smallest length and time scales. DNS is computationally one of the most expensive approaches, and it is still not possible to simulate combustion systems of practical interest which involve complex geometries. Engineering simulations, therefore, rely upon techniques where a suitably averaged/filtered flow field is obtained. The averaging/filtering procedure gives rise to unclosed terms, which are approximated using turbulence and combustion models. These simulations are computationally cheaper than DNS, but the fidelity of the simulation predictions are strongly dependent on the accuracy of the turbulent combustion models. One of these methodologies is Reynolds-Averaged Navier–Stokes (RANS) simulations, where all the governing equations are solved in an averaged sense, and all the pertinent turbulent processes take place at the sub-grid level and thus need to be modelled. As a result, the performance of RANS simulations is strongly influenced by the accuracy of the models. A further technique known as LES solves the filtered governing equations and resolves the turbulent processes, which are associated with length scales greater than the computational grid spacing. However, the physical processes occurring at the unresolved sub-grid scale still need to be modelled. Since part of the turbulence is resolved in LES, the implications of the turbulence modelling inaccuracy are less serious in LES than in RANS, although LES is more computationally expensive than RANS. For the foreseeable future, RANS and LES will continue to be used for engineering simulations of practical problems, with LES likely to play an increasingly important role in the future with the increased affordability and deployment of HPC.

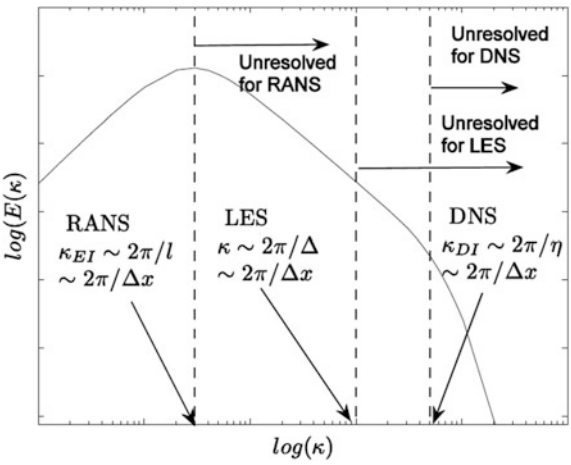

Fig. 5.1 Grid resolution requirements of different computational methodologies

The grid spacing and extent of resolution for DNS, LES and RANS are summarised in Fig. 5.1 in terms of turbulent kinetic energy spectrum $E(\kappa)$ where κ is the wave number (which is inversely proportional to the length scale of turbulent eddies), and $k = \int_0^\infty E(\kappa)d\kappa$ is the turbulent kinetic energy (Pope 2000). The grid size of DNS needs to be either smaller than or comparable to the Kolmogorov length scale. Thus, the physical processes associated with the length scale smaller than the Kolmogorov length scale η remain unresolved but turbulent fluctuations decay rapidly under viscous action for length scales smaller than η, and thus one does not miss much information in terms of turbulent fluid motion by not resolving these length scales. Using the aforementioned reasoning one can assume that $k = \int_0^\infty E(\kappa)d\kappa \approx \int_0^{\pi/\eta} E(\kappa)d\kappa$ (Pope 2000), and almost 100% of turbulent kinetic energy is resolved on DNS grid. In RANS, the grid size Δx remains comparable to the integral length scale l, and thus all the physical processes associated with length scales smaller than the integral length scale remain unresolved. The sub-grid-level physics needs to be modelled (i.e. approximated) with the help of closures proposed for turbulence and combustion modelling. The turbulent kinetic energy can be approximated as $k = \int_0^\infty E(\kappa)d\kappa \approx \int_{2\pi/l}^{\pi/\eta} E(\kappa)d\kappa$ (Pope 2000), and thus almost 100% of kinetic energy remains unresolved for RANS simulations. In the case of LES, the grid spacing Δx is either equal to or closely linked with the filter width Δ, and the filter width remains $\eta < \Delta < l$ for LES calculations. Thus, LES resolves a part of turbulent kinetic energy spectrum but the physical processes occurring at the length scale smaller than Δ remain unresolved and need modelling. For non-reacting flows, the implications of modelling inaccuracies are comparatively less severe for LES than in RANS but this is not fully true for reacting flows. The reaction zone often remains smaller than the Kolmogorov length scale in turbulent flames and thus combustion takes place at the sub-grid level. This effectively indicates that the sub-grid modelling of combustion in LES is as important as in RANS. Figure 5.2

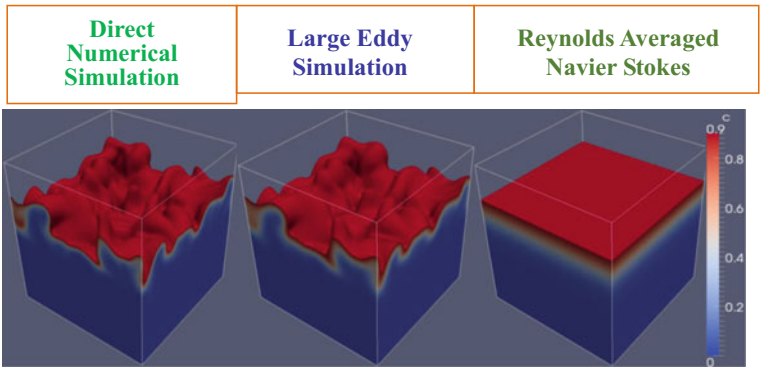

Fig. 5.2 Instantaneous realisations of reaction progress variable field (increasing from blue to red) for a statistically planar flame from DNS, LES and RANS calculations

shows instantaneous realisations from RANS, LES and DNS for a given statistically planar freely propagating turbulent premixed flame. In the case of RANS all the information regarding flame wrinkles is accounted for by sub-grid combustion models, whereas some of the wrinkles are resolved for LES grid. However, a comparison of the outputs of LES and DNS reveals that the surface is less wrinkled for LES than in DNS and the closures of LES combustion model needs to account for the sub-grid level wrinkling.

5.2 Computational Requirements of DNS and Its Implications

For the benefit of the discussion in this chapter, it is now necessary to estimate the computational cost of DNS. From the foregoing discussion, it is evident that for non-reacting flows the grid size needs to be smaller than the Kolmogorov length scale (i.e. $\Delta x \leq \eta$). However, it is worth considering that DNS of passive scalar mixing of fluids with $Sc > 1$ needs a resolution of the Batchelor length scale $\eta_B = \eta/Sc^{0.5}$ (Fox 2003) where Sc is the Schmidt number. However, this is not a major issue in turbulent premixed flames because gaseous species have Schmidt numbers of the order of unity. If one considers that n_l number of integral eddies needs to be accommodated in the computational domain, the length of a cubic computational domain becomes $L = n_l l$, where one needs $n_l > 3-4$ to have meaningful statistics. This, suggests that the number of grid points in one-direction scales as $N \sim L/\Delta x \geq n_l l/\eta = n_l Re_t^{3/4}$ using the well-known scaling $l/\eta = Re_t^{3/4}$ where $Re_t = u' l/\nu$ is the turbulent Reynolds number with u', l and ν being the Root Mean Square (rms) turbulent velocity fluctuation, integral length scale and the

kinematic viscosity, respectively. This suggests that the grid size for three-dimensional DNS can be scaled as $N^3 \sim n_l^3 Re_t^{9/4}$. Moreover, the time step size Δt needs to be either equal or smaller than the lifetime of the smallest eddy in turbulent flows (which is the Kolmogorov time scale τ_η), whereas the simulation needs to be carried out for at least for a few integral eddy turn-over times (i.e. $t_e \sim l/u^{'}$) so that the simulation remains independent of initial condition which is often taken to be a synthetically produced fluctuating velocity field. Thus, the number of time steps from the point of view of resolving temporal statistics of turbulent flows is given by: $N_t = n_t t_e/\Delta t \geq n_t t_e/\tau_\eta \sim n_t Re_t^{0.5}$ where n_t is the number of integral eddy turn-over times and n_t is typically 2–4 for simulations under decaying homogeneous isotropic turbulence. Thus, the computational cost w for non-reacting flows with $Sc \sim 1$ is given by

$$w \sim N^3 N_t \sim n_l^3 n_t Re_t^{11/4} \tag{5.1}$$

It is worth noting that for explicit time marching in compressible turbulent flows needs to consider Courant number criterion, which dictates $\Delta t \leq \Delta x/(u \pm a)$. This can alternatively be written as $\Delta t \leq \eta/l \times l/u^{'} \times u^{'}/a \sim Ma/Re_t^{0.75} t_e$, where $Ma = u^{'}/a$ is the Mach number based on RMS turbulent velocity fluctuation with a being the acoustic velocity. Thus, the computational cost w for non-reacting compressible flows with $Sc \sim 1$ for explicit time marching is given by

$$w \sim N^3 N_t \sim n_l^3 n_t Re_t^3/Ma \tag{5.2}$$

In DNS of reacting flows, one needs to resolve the thermal flame thickness $\delta_{th} = (T_{ad} - T_0)/Max\left|\nabla \widehat{T}\right|_L$ where $\widehat{T}, T_{ad}$ and T_0 are the instantaneous, adiabatic flame and unburned gas temperatures, respectively, by Q number of grid points where Q varies from 10 for simple chemical mechanisms and can go up to 20 for detailed chemical mechanisms. Thus, the grid spacing for turbulent premixed combustion DNS can be given as

$$\Delta x < \min\left(\eta, \frac{\delta_{th}}{Q}\right) = \min\left(\eta, \frac{Ka^{0.5}}{Q}\right) \tag{5.3}$$

where $Ka \sim (\delta_{th}/\eta)^2$ is the Karlovitz number. Thus, the computational cost for compressible DNS of turbulent premixed combustion in the case of explicit time marching is given by

$$w \sim N^3 N_t \sim Q^3 n_l^3 n_t Re_t^3/\left(Ka^{1.5} Ma\right) \tag{5.4}$$

A comparison between Eqs. (5.1) and (5.4) reveals that DNS of subsonic turbulent premixed combustion DNS is more expensive than non-reacting flow DNS for $Ka < 100$ and $Q = 10$. It is worth noting that the density may change by a factor

of 7 in the case of premixed turbulent combustion even though the Mach number remains small and thus it is not appropriate to ignore the compressibility in premixed combustion DNS. Furthermore, the information related to flame–acoustics interaction becomes completely unavailable for incompressible calculations. It is worth noting that the computational cost estimated by Eq. (5.4) does not include the effects of walls and the necessity of resolving viscous sub-layer increases the computational cost of DNS further. It is worthwhile to consider premixed combustion regimes in order to understand the implication of the computational cost given by Eq. (5.4). Broadly, a premixed flame is made up of three zones. There is a mostly chemically inert preheat zone which is followed by a thin reaction layer, and finally the oxidation layer where the products are formed. In many premixed turbulent combustion applications, turbulent time scales are long compared to chemical time scales (Bray 1980). The implication is that the chemical reaction is confined to thin propagating surfaces, with a typical thickness of about 1 mm. Thus, the species field tends to be composed of packets of unburned reactants and completely burned products, separated by thin reacting interfaces called flamelets. This is the basic assumption of the flamelet concept. The flamelet assumption reduces the modelling of the entire turbulent combustion analysis to a more tractable two-fluid problem. The analysis reduces to a description of the flow variables in the fresh and burnt gases, the flame surface and the burning rate. Further simplifications can be made, if it is assumed that the local structure of the reacting interfaces resembles a strained and curved laminar flame. In this situation, the reactant consumption rate can be approximated by that found in a laminar flame. This effectively decouples the effects of chemistry and turbulence. Chemical effects work to modify the local laminar flame speed, which may be obtained from separate laminar flame calculations (Cant and Bray 1988). The primary effect of the turbulence is to wrinkle and strain these laminar flamelets. Much controversy has been centred on the limits of applicability of flamelet assumptions. The different regimes of turbulent combustion are traditionally expressed on a phase diagram as a function of non-dimensional parameters. Here, the approach taken by Peters (2000) is taken to demonstrate the principles.

The turbulent Damköhler number is given by the ratio of turbulent time scale t_e to the chemical time scale t_{chem}. This is defined as

$$Da = t_e / t_{chem} \tag{5.5}$$

where $t_e = l/u^{'}$ is the eddy turn-over time and $t_{chem} = D/S_L^2$ is the chemical time scale where D is the diffusivity and S_L is the unstrained laminar burning velocity. If it is assumed that the Kolmogorov scale eddies are responsible for most of the flame stretch on account of their large velocity gradients, the Karlovitz number is given by

$$Ka = t_{chem}/\tau_\eta \sim \delta_{th}^2/\eta^2 \sim v_\eta^2/S_L^2 \tag{5.6}$$

where v_η is the Kolmogorov velocity scale. A second Karlovitz number Ka_δ can be defined in terms of reaction zone thickness δ_r as

$$Ka_\delta = \delta_r^2/\eta^2 \tag{5.7}$$

Typically, the reaction zone thickness remains 1/10 of the overall thermal thickness and thus Ka_δ/Ka scales as $Ka_\delta/Ka \sim 1/100$. Under the Klimov–William criterion (Peters 2000) the laminar flamelet exists in a turbulent flow when the flame stretch is smaller than a critical value. Under some assumptions, this is equivalent to $Ka < 1$ (Peters 2000). Another way of stating the above criterion is that the laminar flamelet will not be observed if the Kolmogorov scale η is less than the thermal flame thickness δ_{th}. This regime of combustion is known as the corrugated flamelet regime (Peters 2000).

When the Damköhler number is much less than unity, the turbulent time scales are small compared to the chemical time scale and the combustion behaviour is characterised as a well-stirred reaction. The zone given by the combination of $Re_t > 1, Ka > 1$ and $Ka_\delta > 1$ is termed as broken reaction zones regime. In this regime, the smallest eddies can penetrate the flame structure, causing a thickening effect and possibly leading to local extinction. The above concepts are illustrated in the combustion diagram presented in Fig. 5.3 after Peters (2000).

Analysis Poinsot et al. (1990, 1991) has indicated that the Klimov–Williams criterion underestimates the flamelet regime by more than one order of magnitude. It is thought that the Kolmogorov eddies can penetrate the flame front but they are not energetic enough to affect the flame stretch significantly. Poinsot et al. (1990, 1991) suggested that flamelet regime could be extended to accommodate the flames whose internal structure may be somewhat altered by small-scale turbulence, without quenching of the flamelets.

A comparison of computational cost (i.e. Eq. (5.4)) and the criteria for different combustion regimes reveals that the computational cost of turbulent premixed

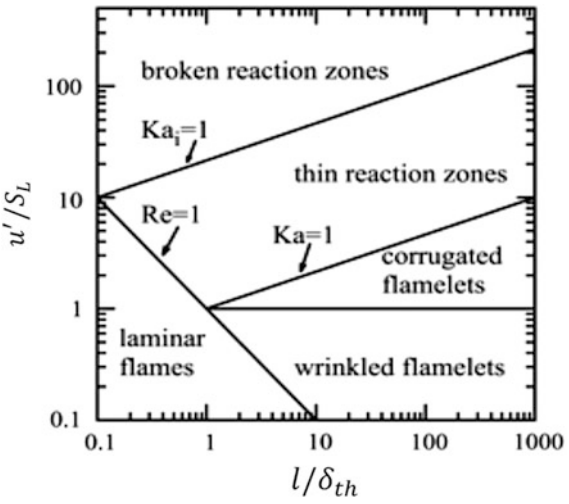

Fig. 5.3 Regime diagram by Peters (2000) for turbulent premixed combustion

combustion DNS approaches to that of non-reacting flow DNS in the broken reaction zones regime. The computational cost for conducting DNS becomes progressively expensive with the drop in Karlovitz number Ka. Thus, premixed combustion DNS in the thin reaction zones (corrugated flamelets) regime is more expensive than in the broken reaction zones (thin reaction zones) regime of combustion. Thus, until now most premixed combustion DNS studies (Haworth and Poinsot 1992; Rutland and Trouvé 1993; Baum et al. 1994; Echekki and Chen 1996; Boger et al. 1998; Echekki and Chen 1999; Im and Chen 2002; Chakraborty and Cant 2004; Hawkes and Chen 2004; Chakraborty et al. 2007, 2011; Han and Huh 2008; Chakraborty et al. 2009; Poludnenko and Oran 2010; Aspden et al. 2011; Dopazo et al. 2015; Im et al. 2016) have been carried out in the thin reaction zones and broken reaction zones regimes and most DNS databases for $Ka < 1$ sacrificed the compressibility aspect to adopt implicit time marching to reduce the computational cost (Rutland and Cant 1994; Zhang and Rutland 1995).

In order to address the combustion performance in engineering combustion devices, it is necessary to address the chemical aspects of the reacting flow together with the associated transport mechanisms. In real-life combusting flows, transport properties like viscosity, mass diffusivity and thermal conductivity change with temperature, which result in a complex nature of momentum, heat and mass transfer behaviour in reacting turbulent flows. Very often in DNS studies one of the above (if not more) aspects is simplified. With the present computational storage capacity, it is extremely expensive to address both the three-dimensional nature of turbulence and the detailed chemistry of the reaction concerned. For this reason, most combustion DNS are carried out either in three dimensions with single step chemistry (e.g. Rutland and Trouvé 1993; Boger et al. 1998; Chakraborty and Cant 2004; Chakraborty et al. 2007; Han and Huh 2008; Chakraborty et al. 2009; Poludnenko and Oran 2010; Chakraborty et al. 2011; Dopazo et al. 2015; Rutland and Cant 1994; Zhang and Rutland 1995; Nishiki et al. 2006; Dunstan et al. 2012) or in two dimensions with complex chemistry (e.g. Baum et al. 1994; Echekki and Chen 1996, 1999; Im and Chen 2002; Hawkes and Chen 2004). Frequently, the variation of transport properties is either neglected or simplified. It is now possible to carry out to carry out three-dimensional premixed combustion DNS (Aspden et al. 2011; Im et al. 2016; Sankaran et al. 2007; Hawkes et al. 2012; Gruber et al. 2010, 2012; Wang et al. 2017) in the presence of detailed chemical mechanism and transport but such simulations are often limited to simple fuels (e.g. H_2 and CH_4) and the computational cost still remains extremely high to afford a detailed parametric analysis (Chen et al. 2009). Moreover, most engineering combustion devices have complex geometry but almost all DNS studies are done for simple domain geometry. Recently, a few premixed combustion DNS studies (Dunstan et al. 2012; Sankaran et al. 2007; Hawkes et al. 2012; Gruber et al. 2010; Gruber et al. 2012; Wang et al. 2017) have been carried out for relatively complex configurations, which can be realised in laboratory-scale experiments, but these simulations remain extremely expensive and a detailed parametric analysis is not possible to carry out in these configurations at the present time.

For hydrocarbon-air combustion, the unstrained laminar burning velocity S_L decreases with pressure P. For example, S_L in methane-air flames varies with pressure P as $S_L \sim P^{-0.5}$ (Turns 2011), whereas dynamic viscosity μ does not change with pressure but gas density ρ in isobaric combustion increases with pressure as $\rho \propto P$. This implies that the thermal flame thickness $\delta_{th} = (T_{ad} - T_0)/\max|\nabla T|_L$ (where T, T_0 and T_{ad} are the instantaneous dimensional, unburned gas and adiabatic flame temperatures respectively) scales as $\delta_{th} \sim \mu/(\rho S_c S_L) \sim P^{-0.5}$. Thus, for a given set of values of u' and l, the turbulent Reynolds number $Re_t = u' l/\nu \sim \left(u'/S_L\right)(l/\delta_{th}) \sim P$ increases with pressure. Thus, most premixed combustion DNS analyses have been carried out at atmospheric pressure (because the computational cost of DNS is strongly dependent on Re_t, see Eq. (5.4)) in spite of the fact that combustion processes in IC engines and gas turbines take place at elevated pressures.

Apart from these physical aspects, there are practical aspects of DNS which inhibits its use for common engineering applications. The computational storage capacity and CPU time for DNS with a Reynolds number typical of engineering applications are immense. Haworth (Haworth 2003) presented the estimated computational time for in-cylinder aero-thermochemical processes using a skeletal propane-air mechanism (27 species, 73 reactions (Haworth 2003; Haworth et al. 2000)). The simulation of this process would require 1000000 time steps. With present algorithms, such a computation would take 500 CPU years on a teraflop computer and 1000 terabytes of memory. IC engines will be of historical interest by the time such computers are available. In this context, it is useful to mention that the full chemical mechanism of iso-octane–air mixture requires more than 800 species and 3500 chemical reactions which are impossible to address taking the three-dimensional nature of turbulence into account, even with the present highest computational storage available.

Apart from detailed chemistry, computational storage and simplified geometry, the boundary condition specification for DNS studies poses an important challenge. The simplified boundary conditions based on statistical sampling, i.e. symmetry boundary condition, axisymmetric boundary conditions which greatly simplify problems in RANS simulations cannot be used in DNS. Lack of complete theoretical background makes boundary condition specification for Navier–Stokes equations a difficult task. Exact boundary conditions ensuring well-posedness for Euler equations can be derived, but this becomes much more complex for Navier–Stokes equations (Poinsot and Veynante 2001). DNS of unsteady compressible flows requires accurate control over wave reflections from the boundaries of the computational domain. When acoustic waves are allowed, the solution depends strongly on appropriate boundary conditions. It is well known that for gas turbine applications combustion instability can result from an interaction between combustion and acoustic waves. Thus, if the boundary conditions are not treated consistently with the acoustic wave propagation, erroneous results may be obtained. A reflective outflow boundary would not allow any escape of acoustic energy

therefore often predicts overestimated interaction phenomena. In addition to acoustic waves, numerical waves are generated due to the discrete treatment of the boundaries. These numerical waves can lead to a coupling between inlet and outlet boundaries, in some cases leading to unphysical oscillations as discussed in Poinsot and Lele (Poinsot and Lele 1992). The Navier–Stokes Characteristic Boundary Conditions (NSCBC) formulation is an attempt to provide precise boundary conditions to avoid numerical instabilities and spurious wave reflection at the boundary.

The boundary conditions used for the solution of compressible Navier–Stokes equations can be classified into two broad categories. The first consists of physical boundary conditions, which are boundary conditions dictated by the original non-discretised problem, for example, inlet velocities in the present case. The second consists of 'soft' conditions, which are required by the discretised system to close the equations. These can be viewed as compatibility relations required by the numerical method, and not as actual physical conditions. In order to achieve this, extrapolation from inside the domain is used in many studies but the approach is inherently arbitrary and often leads to over-constrained boundary conditions. This approach cannot handle acoustic wave reflection correctly. The NSCBC approach removes the necessity of ad hoc extrapolation.

The NSCBC approach (Poinsot and Lele 1992) provides guidelines for providing the specification of numerical and physical boundary conditions. The physical conditions are specified according to the well-posedness of the Euler equations. Viscous conditions are added to the inviscid Euler conditions to obtain the correct number of boundary conditions for the Navier–Stokes equations. 'Soft' boundary conditions are constructed using a Local One-Dimensional Inviscid (LODI) approximation (Thompson 1987) for the wave crossing the boundary in either direction. The amplitude variations of the outgoing waves are dependent only on the solution internal to the domain according to Thomson (1987). These are estimated using the internal solution from an analysis of the LODI scheme. Incoming waves cannot be estimated from the internal solution and where necessary, the incoming wave amplitudes are estimated by the specification of physical boundary conditions. The amplitude variations are then used to construct a reduced set of conservation equations to determine any variables that were not specified by the physical boundary conditions. The LODI scheme is used for specifying numerically soft boundary conditions in order to ensure well-posedness the numerical problem in a consistent manner. Numerical 'soft' boundary conditions are required to evaluate the derivatives normal to the boundary. These could be calculated using an extrapolation scheme or by imposing a physical condition, for example setting the external pressure to a constant. The NSCBC formulation replaces these derivatives with their equivalents in terms of wave amplitude variations L_i. Each of the wave amplitude variations can be identified with different characteristic physical waves crossing the boundary in inviscid flow situations. If x_1 is the normal direction to the boundary the wave amplitude variations L_i's are given by Thompson (1987):

$$L_1 = \lambda_1 \left(\frac{\partial P}{\partial x_1} - \rho a \frac{\partial u_1}{\partial x_1} \right) \tag{5.8}$$

$$L_2 = \lambda_2 \left(a^2 \frac{\partial \rho}{\partial x_1} - \frac{\partial P}{\partial x_1} \right) \tag{5.9}$$

$$L_3 = \lambda_3 \frac{\partial u_2}{\partial x_1} \tag{5.10}$$

$$L_4 = \lambda_4 \frac{\partial u_3}{\partial x_1} \tag{5.11}$$

$$L_5 = \lambda_5 \left(\frac{\partial P}{\partial x_1} + \rho a \frac{\partial u_1}{\partial x_1} \right) \tag{5.12}$$

Here, λ_i are characteristic wave velocities associated with $L_i^{'}s$ and a is the sonic speed. The characteristic velocities are given by (Thompson 1987):

$$\lambda_1 = u_1 - a \tag{5.13}$$

$$\lambda_2 = \lambda_3 = \lambda_4 = u_1 \tag{5.14}$$

$$\lambda_5 = u_1 + a \tag{5.15}$$

The wave amplitude variation L_1 corresponds to the wave travelling towards the negative x_1 direction, L_5 corresponds to the wave travelling in the positive x_1 direction, L_2 is the entropy wave, whilst L_3 and L_4 correspond to advection in transverse directions x_2 and x_3 respectively. NSCBC is specified for a variety of boundary conditions. The various waves entering and leaving the computational domain at the inflow and outflow boundary are illustrated in Fig. 5.4.

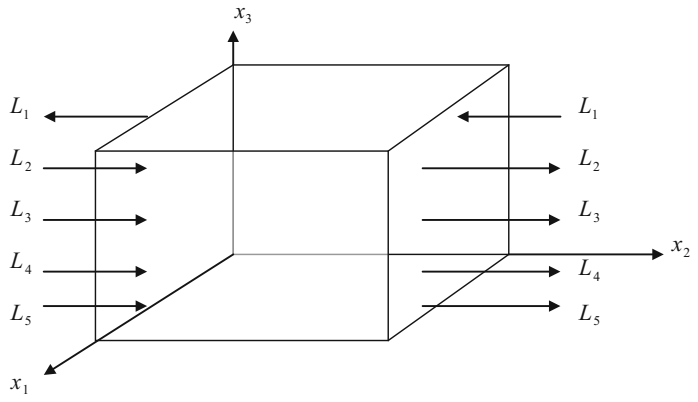

Fig. 5.4 Wave amplitude variations into and out of the domain at the inflow and outflow boundaries

Table 5.1 Number of physical boundary conditions required well posedness (three-dimensional flow). N is the number of reacting species

Boundary type	Euler (Non-reacting)	Navier–Stokes (Non-reacting)	Navier–Stokes (Reacting)
Supersonic Inflow	5	5	5+N
Subsonic inflow	4	5	5+N
Supersonic outflow	0	4	4+N
Subsonic outflow	1	4	4+N

The boundary condition specification in terms of $L_i s$ provides the required number of boundary conditions for Euler equations. In the framework of the Navier–Stokes equations, extra viscous boundary conditions are needed in order to ensure a problem is numerically well-posed. The NSCBC scheme proposed by Poinsot and Lele (1992) specifies the required number of boundary conditions for well-posed problems and prescribes the viscous conditions in the light of a previous work (Dutt 1988). The required number of boundary conditions for different kinds of boundaries is presented in Table 5.1 after Poinsot and Lele (1992). Thus, it is not straightforward to specify realistic boundary conditions except when the boundaries are periodic or impenetrable walls. In addition to that, in combustion DNS the associated acoustic activity requires non-reflecting inlet and outlet boundary conditions but with present-day formulations of the same, there is plenty of scope for improvement (Sutherland and Kennedy 2003; Yoo and Im 2007; Prosser 2007). The techniques that are used for specifying non-reflecting boundary conditions are relatively easier in simple geometry but they are not very straightforward in the case of complex geometries encountered in engineering problems.

5.3 Engineering Relevance of DNS

In spite of these difficulties, DNS has become an indispensable part of the analysis of turbulent combustion. Even with several assumptions, DNS can capture the correct trends, which are verified in experiments and are sometimes able to predict important quantities like displacement speed, and scalar dissipation rate, which are difficult to measure in experiments. The statistics obtained from DNS can be used for the modelling for RANS and LES studies (Boger et al. 1998; Han and Huh 2008; Zhang and Rutland 1995; Hawkes et al. 2012; Veynante et al. 1997; Swaminathan and Bilger 2001; Swaminathan et al. 2001; Charlette et al. 2002a, b; Chakraborty and Swaminathan 2007, 2010; Chakraborty et al. 2008; Chakraborty and Klein 2008; Chakraborty and Cant 2007, 2009a, b, c, 2011; Kolla et al. 2009; Katragadda et al. 2011; Chakraborty et al. 2011; Chakraborty and Swaminathan 2011; Gao et al. 2014, 2015a, b; Klein et al. 2015; Gao et al. 2016; Gao and

Chakraborty 2016; Lai and Chakraborty 2016a, b, c; Sellmann et al. 2017; Lai et al. 2017), and this approach which has contributed a lot to the analysis of turbulent combustion in the past decade. It is possible to reduce a real engineering problem to a generic problem in order to concentrate on a particular aspect of the practical problem for better understanding. DNS of statistically planar freely propagating turbulent premixed flames can be regarded as a generic problem for studying a small element of flow in gas turbine combustors. Likewise, DNS studies carried out for a premixed flame kernel in the turbulent environment is a generic problem of flame propagation in SI engines (Chakraborty et al. 2007). In the present scenario, DNS is limited to a small range of turbulent Reynolds number and Damköhler number as shown in Fig. 5.5 after Poinsot and Veynante (Poinsot and Veynante 2001). With the increase in computational storage and power, DNS will continue to address more problems of engineering significance. Interested readers can refer to Cant (1999) for a comprehensive review of DNS applications in the modelling of turbulent premixed combustion.

At the present stage, the state of art of DNS is far from being used for practical engineering problems. The detailed information that can be extracted from DNS forms a huge dataset, which can be used effectively for improved LES and RANS model. Thus, in this way, DNS can contribute positively to industrial requirements. As an example, it will be shown next in this chapter that how DNS data can be used for closure of the terms of the turbulent sensible enthalpy flux transport equation in the context of head-on quenching of turbulent premixed flames. Thus, the modelling of the unclosed terms of the transport equation of turbulent flux of sensible enthalpy the will be discussed next in this chapter.

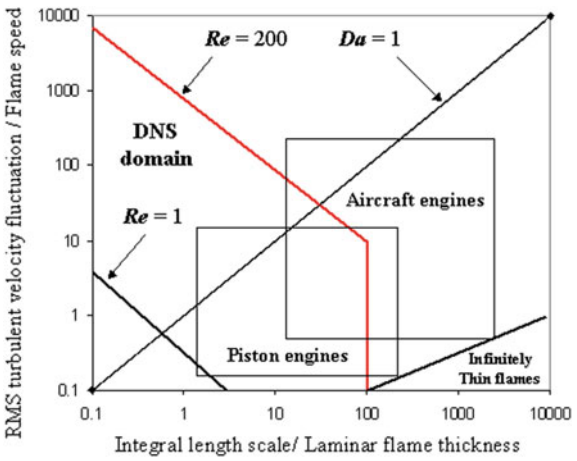

Fig. 5.5 DNS domain is shown with the thick red line in relation to engineering applications in reciprocating engines and aircraft engines on the combustion diagram after Poinsot and Veynante (2001)

5.3.1 An Example of DNS-Based Modelling: Closure of Unclosed Terms of Transport Equation of Turbulent Flux of Sensible Enthalpy

The transport equation-based closure of turbulent scalar flux of enthalpy has received limited attention in combustion literature Chakraborty and Cant (2009b, 2015). However, in principle, a transport equation-based closure accounts for all the necessary physical mechanisms, which can affect the statistical behaviour of the turbulent flux of enthalpy. Moreover, it is often necessary to solve transport equations of turbulent scalar flux components in the context of a second-moment closure approach Lindstedt and Vaos (1999), and interested readers are referred to Lindstedt and Vaos (1999) and Lindstedt (2011) for more detailed discussion on this.

The transport equation of c takes the following form:

$$\frac{\partial(\rho c)}{\partial t} + \frac{\partial\left(\rho u_j c\right)}{\partial x_j} = \frac{\partial}{\partial x_j}\left(\rho D \frac{\partial c}{\partial x_j}\right) + \dot{w} \tag{5.16}$$

where c is reaction progress variable which is defined based on a suitable reactant mass fraction Y_R as

$$c = \frac{Y_{R0} - Y_R}{Y_{R0} - Y_{R\infty}} \tag{5.17}$$

where the subscripts 0 and ∞ refer to values in unburned reactants and fully burned products respectively and $\rho, u_j, \dot{w}$ and D are the density, jth component of velocity, reaction rate and progress variable diffusivity respectively. On Reynolds averaging Eq. (5.16) one obtains

$$\frac{\partial(\bar{\rho}\tilde{c})}{\partial t} + \frac{\partial\left(\bar{\rho}\tilde{u}_j\tilde{c}\right)}{\partial x_j} = \overline{\frac{\partial}{\partial x_j}\left(\rho D \frac{\partial c}{\partial x_j}\right)} + \overline{\dot{w}} - \overline{\frac{\partial\left(\rho u_j^{''} c^{''}\right)}{\partial x_j}} \tag{5.18}$$

where $\bar{q}, \tilde{q} = \overline{\rho q}/\bar{\rho}, q^{'} = q - \bar{q}$ and $q^{''} = q - \tilde{q}$ are the Reynolds-averaged, Favre-averaged Reynolds fluctuation and Favre fluctuation of a general quantity q respectively. The last two terms on the right-hand side of Eq. (5.18) are unclosed and need modelling. The molecular diffusion term $\overline{\nabla \cdot (\rho D \nabla c)}$ can be neglected in comparison to the value of $\nabla \cdot \overline{\rho \vec{u}^{''} c^{''}}$ for large values of turbulent Reynolds number. The reaction–diffusion imbalance term $\bar{\dot{w}} + \overline{\nabla \cdot (\rho D \nabla c)}$ can be modelled as $\overline{(\rho S_d)}_s \Sigma$ in the context of Flame Surface Density (FSD) based closure, where $S_d = (Dc/Dt)/|\nabla c|$ is the displacement speed, $\Sigma = \overline{|\nabla c|}$ is the generalised FSD, and $\overline{(q)}_s = \overline{q|\nabla c|}/\Sigma$ indicates the surface averaged value of a general variable q (Boger et al. 1998). The modelling of the last term on the right-hand side of Eq. (5.18)

represents the turbulent transport of reaction progress variable and its modelling depends on the closure of turbulent scalar flux components $\overline{\rho u_j'' c''}$. Modelling of $\overline{\rho u_j'' c''}$ and $\bar{\dot{w}}$ for head-on quenching of turbulent premixed flames has been addressed elsewhere (Lai and Chakraborty 2016a, c, d) so only the modelling of the Reynolds flux of enthalpy $\overline{\rho u_j'' h''}$ (where h is the specific sensible enthalpy) will be addressed in this chapter. In RANS, the Favre-averaged sensible enthalpy transport can be written as the following form:

$$\frac{\partial\left(\bar{\rho}\tilde{h}\right)}{\partial t}+\frac{\partial\left(\bar{\rho}\tilde{u}_j\tilde{h}\right)}{\partial x_j}=\overline{\frac{\partial}{\partial x_j}\left(\lambda\frac{\partial h}{\partial x_j}\right)}+\bar{\dot{w}}_T-\frac{\partial\overline{\left(\rho u_j'' h''\right)}}{\partial x_j} \tag{5.19i}$$

In Eq. (5.19i), $\bar{\dot{w}}_T$ is the heat release due to combustion, it can be written as

$$\bar{\dot{w}}_T=H\bar{\dot{w}} \tag{5.19ii}$$

where H. is the heat of combustion. The exact transport equation of $\overline{\rho u_i'' h''}$ can be derived based on momentum and reaction progress variable transport equations as (Chakraborty and Cant 2009b; Chakraborty and Cant 2015):

$$\begin{aligned}\frac{\partial\left(\bar{\rho}\widetilde{u_i'' h''}\right)}{\partial t}+\frac{\partial\left(\bar{\rho}\tilde{u}_j\widetilde{u_i'' h''}\right)}{\partial x_j}=&\underbrace{-\frac{\partial\overline{\rho u_i'' u_j'' h''}}{\partial x_j}}_{T_1}\underbrace{-\overline{\rho u_i'' u_j''}\frac{\partial\tilde{h}}{\partial x_j}}_{T_2}\underbrace{-\overline{\rho u_j'' h''}\frac{\partial\tilde{u}_i}{\partial x_j}}_{T_3}\underbrace{-\overline{h''}\frac{\partial\bar{P}}{\partial x_i}}_{T_4}\underbrace{-\overline{h''\frac{\partial P'}{\partial x_i}}}_{T_5}\\&+\underbrace{\left[\overline{u_i''\frac{\partial}{\partial x_k}\left(\lambda\frac{\partial\hat{T}}{\partial x_k}\right)}\right]}_{T_6}+\underbrace{\left[\overline{h''\frac{\partial\tau_{ik}}{\partial x_k}}\right]}_{T_7}+\underbrace{\overline{u_i''\dot{w}_T}}_{T_8}.\end{aligned} \tag{5.20}$$

where P is the pressure, $\tau_{ik}=\mu[\partial u_i/\partial x_k+\partial u_k/\partial x_i]-(2\mu/3)\delta_{ik}(\partial u_l/\partial x_l)$ is the component of viscous stress in tensor where μ is the dynamic viscosity. The terms on the left-hand side are the transient and mean advection terms. The term T_1 represents the turbulent transport of $\widetilde{u_i'' h''}$, whereas T_2 and T_3 represent the turbulent scalar flux transport due to mean scalar and velocity gradients respectively. The terms T_4 and T_5 are responsible for the turbulent scalar flux transport by mean and fluctuating pressure gradients respectively. The terms T_6 and T_7 originate due to mass diffusion and viscous stress respectively, and these terms act to reduce the magnitude of $\widetilde{u_i'' h''}$ irrespective of the nature of scalar flux transport. Thus, these terms are often referred to as the dissipation terms. The last term on the right-hand side T_8 originates from the correlation between heat release rate and enthalpy fluctuations. The terms T_1, T_4, T_5, T_6, T_7 and T_8 are the unclosed terms and need modelling, whereas the terms T_2 and T_3 are closed because modelled transport

equations for $\overline{\rho u_i'' u_j''}$ and $\overline{\rho u_j'' h''}$ are solved in the context of second-moment closure (Lindstedt and Vaos 1999; Lindstedt 2011). In order to analyse the statistical behaviours of T_1, T_4, T_5, T_6, T_7 and T_8, a DNS dataset of head-on quenching of statistically planar turbulent flames has been considered. A schematic diagram of head-on quenching of a statistically planar flame is shown in Fig. 5.6a which shows that the flame propagation direction is perpendicular to the inert isothermal wall in this configuration. For this purpose, a simple chemistry DNS database of head-on

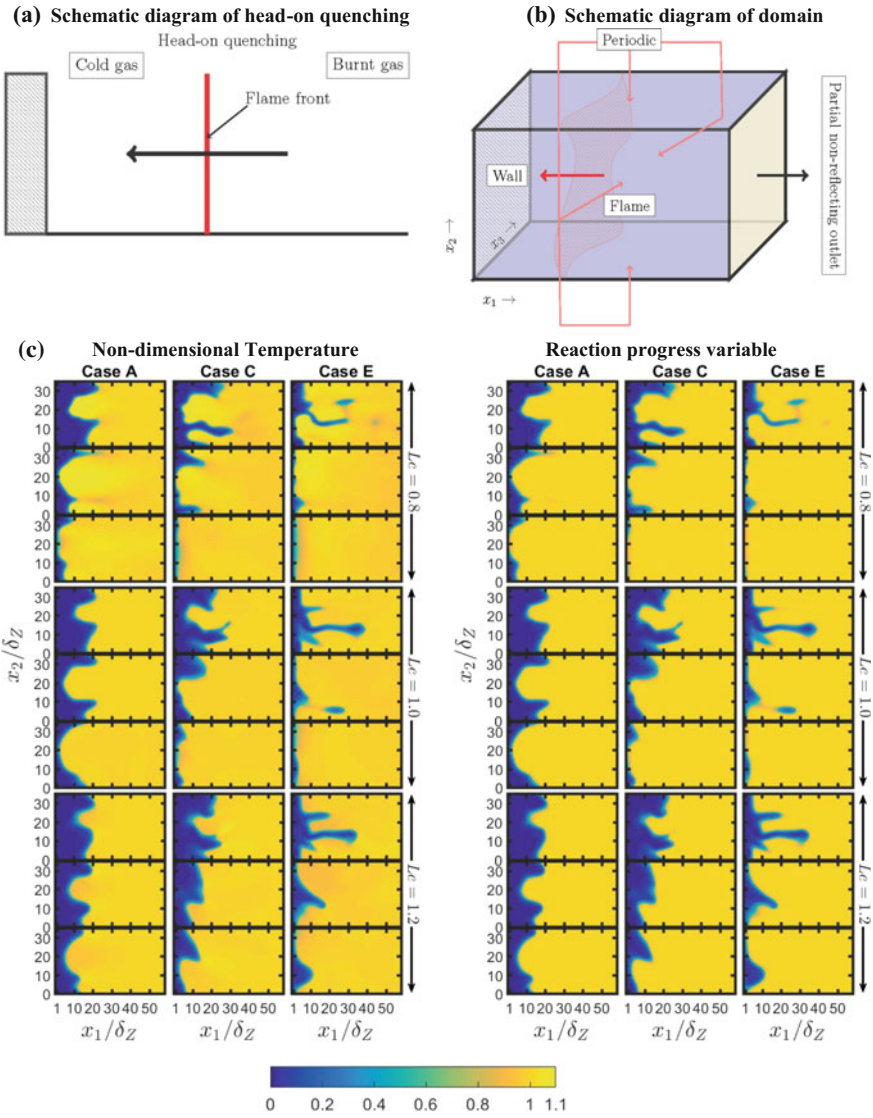

Fig. 5.6 **a** Schematic diagram of head-on quenching of a statistically planar flame, **b** schematic diagram of the computational domain, **c** Instantaneous c and T fields for cases A, C and E (first–third column) at $t = 2\delta_z/S_L, 4\delta_z/S_L$ and $6\delta_z/S_L$ (1st–3rd row)

quenching of turbulent premixed flames by an isothermal wall for different values of Damköhler and Karlovitz numbers (i.e. Da and Ka) has been considered. Chakraborty and Cant (2009b, c) demonstrated that global Lewis number Le can have significant influences on statistical behaviour and modelling of turbulent scalar flux and the terms of its transport equation even when the flow remains away from the wall. Thus, all head-on quenching simulations in this analysis have been carried out for three different values of global Lewis number (i.e. $Le = 0.8,\ 1.0$ and 1.2). For this DNS database the simulation domain has been taken to be $70.6\delta_Z \times 35.2\delta_Z \times 35.2\delta_Z$ (where $\delta_Z = \alpha_{T_0}/S_L$ is the Zel'dovich flame thickness with α_{T0} being the thermal diffusivity of unburned gas) with the largest side aligned with the mean direction of flame propagation (i.e. *-ve* x_1-direction here). The simulation domain is discretised using a uniform Cartesian grid of size $512 \times 256 \times 256$, which ensures 10 grid points across the thermal flame thickness δ_{th}. A no-slip isothermal inert wall with temperature $T_w = T_0$ is specified for the left-hand side boundary in the x_1 -direction, and the boundary opposite to the wall is considered to be partially non-reflecting. The wall normal mass flux is considered to be zero at the wall. The boundaries in x_2 and x_3 directions are considered to be periodic. The schematic diagram of the domain is shown in Fig. 5.6b. A tenth-order central difference scheme is used for spatial differentiation for the internal grid points but the order of differentiation gradually drops to a one-sided second-order scheme at the non-periodic boundaries (Jenkins and Cant 1999). A low-storage third-order Runge–Kutta scheme (Wray 1990) has been adopted for explicit time marching.

A steady unstrained planar laminar premixed flame solution is used to initialise the reactive field. The flame is initially placed away from the wall so that $T = \left(\hat{T} - T_0\right)/\left(T_{ad} - T_0\right) = 0.9$ isosurface remains at a distance $20\delta_Z$ away from the wall. The distance ensures that the flame gets enough time to evolve before interacting with the wall. The velocity field is initialised using a homogeneous isotropic field of turbulent velocity fluctuations, which is generated using a pseudo-spectral method (Rogallo 1981) following the Batchelor–Townsend spectrum (Bachelor and Townsend 1948), but the velocity components at the wall u_1, u_2 and u_3 are specified to be zero to ensure the no-slip condition. This field is allowed to evolve for an initial eddy turn-over time before interacting with the flame.

The initial values of normalised rms turbulent velocity fluctuation u'/S_L, the ratio of longitudinal integral length scale to thermal flame thickness L_{11}/δ_{th} for the turbulent velocity field away from the wall are listed in Table 5.2 along with the

Table 5.2 List of initial simulation parameters away from the wall for each of the Lewis number cases for the DNS database used for the analysis of $\overline{\rho u_i'' h''}$ transport

Case	A	B	C	D	E
u'/S_L	5.0	6.25	7.5	9.0	11.25
L_{11}/δ_{th}	1.67	1.44	2.5	4.31	3.75
Da	0.33	0.23	0.33	0.48	0.33
Ka	8.65	13.0	13.0	13.0	19.5
Re_t	22.0	23.5	49.0	100	110

corresponding values of Damköhler number $Da = L_{11}S_L/\delta_{th}u^{'}$, Karlovitz number $Ka = (u^{'}/S_L)^{3/2}(L_{11}/\delta_{th})^{-1/2}$ and turbulent Reynolds number based on L_{11} (i.e. $\mathrm{Re_t} = \rho_0 u^{'} L_{11}/\mu_0$). One will get an increase in the numerical value of $\mathrm{Re_t}$ by a factor of almost 2.35 if the integral length scale $l_T = \tilde{k}^{\frac{3}{2}}/\tilde{\varepsilon}$ is used. It can be seen from Table 5.2 that the cases A, C and E (B, C and D) have same values of Da(Ka). Three different global Lewis numbers (i.e. $Le = 0.8, 1.0$ and 1.2) have been considered for each set of turbulence parameters considered here. Standard values are chosen for Prandtl number Pr and ratio of specific heats γ (i.e. $Pr = 0.7$ and $\gamma = 1.4$). For the present analysis, both the heat release parameter $\tau = (T_{ad} - T_0)/T_0$, and Zel'dovich number $\beta = E_{ac}(T_{ad} - T_0)/RT_{ad}^2$ are taken to be 6.0 (i.e. $\tau = 6.0$ and $\beta = 6.0$). The values $\beta = 6.0$ and $\tau = 6.0$ are representative of an iso-octane–air mixture with unburned gas temperature $T_0 \approx 325.0K$ and equivalence ratio of 1.10 under atmospheric pressure. The gaseous mixture is assumed to follow the ideal gas law. The simulations for turbulent cases have been carried out until a time when the maximum and minimum values of wall heat flux become identical values following the flame quenching. The simulation time remains different for different cases, but the simulations for all cases were continued for $t \geq 12\delta_Z/S_L$ where $12\delta_Z/S_L$ corresponds to 21, 30, 21, 15 and 21 initial eddy turn-over times (i.e. $t_e = L_{11}/u^{'}$) for cases A–E respectively. The non-dimensional grid spacing next to the wall $y^+ = u_\tau \Delta x/\nu$ remains smaller than unity for all turbulent cases (the maximum value of y^+ has been found to be 0.93 during the course of the simulation), where $u_\tau = \sqrt{\tau_w/\rho}$, τ_w and ν are the friction velocity, mean wall shear stress, and kinematic viscosity respectively. For $y^+ = u_\tau \Delta x/\nu \approx 0.93$, the minimum normalised wall normal distance $u_\tau x_1/\nu$ of $T = \left(\hat{T} - T_0\right)/(T_{ad} - T_0) = 0.9$ isosurface has been found to be about 15.0 for the quenching flames considered here. Further information on this database can be obtained from Refs. (Lai and Chakraborty 2016a, b, c, d; Sellmann et al. 2017; Lai et al. 2017).

For the purpose of extracting Reynolds/Favre-averaged quantities, the DNS data has been ensemble averaged on the transverse plane (i.e. x_2 and x_3 direction as these are statistically homogeneous directions in this configuration) at a given x_1 location at a given instant of time (Zhang and Rutland 1995; Veynante et al. 1997; Swaminathan and Bilger 2001; Swaminathan et al. 2001; Charlette et al.2002a, b; Chakraborty and Swaminathan 2007, 2010, 2011; Chakraborty and Cant 2007, 2009a, b, c, 2011; Chakraborty et al. 2008, 2011; Kolla et al. 2009; Katragadda et al. 2011; Lai and Chakraborty 2016a, b, c, d; Sellmann et al. 2017; Lai et al. 2017).

5.3.1.1 Global Features of Flame–Wall Interaction

The distributions of reaction progress variable c, non-dimensional temperature $T = \left(\hat{T} - T_0\right)/(T_{ad} - T_0)$ in the central $x_1 - x_3$ plane for $Le = 0.8, 1.0$ and 1.2 are shown in Fig. 5.6c for case E. For unity Lewis number flames, c and T are identical

to each other under adiabatic low Mach number conditions. This can be observed when the flame is away from the wall before the initiation of flame quenching. However, the adiabatic condition is not maintained in the case of isothermal boundary condition, and the equality between c and T does not hold during flame quenching. In the non-unity Lewis number flames, the equality between c and T does not hold even when the flame is away from the wall. The regions with $T > c$ in the $Le = 0.8$ flame are associated with the regions where the flame surface is convex towards the reactants whereas $T < c$ are associated with flame surface concave to the reactants. Just the opposite behaviour has been observed for the $Le = 1.2$ flame and thus $T > c(T < c)$ is associated with the flame wrinkles which are concave (convex) to the reactants. This behaviour is consistent with several previous findings (Rutland and Trouvé 1993; Im and Chen 2002; Lai and Chakraborty 2016d; Chakraborty and Cant 2005). Figure 5.6c further suggests that flame starts to interact with the wall and quenching initiates at an earlier time in the case of $Le = 0.8(Le = 1.0)$ than in the $Le = 1.0(Le = 1.2)$ cases because of faster flame propagation for flames with smaller values of Lewis number. Faster diffusion of reactants into the reaction zone than the thermal diffusion rate out of it gives rise to the simultaneous presence of high reactant concentration and high temperature, which leads to a faster flame propagation in the $Le < 1$ flames than the corresponding unity Lewis number flame. Just the opposite mechanism gives rise to smaller rate of flame propagation and burning in turbulent $Le < 1$ flames than the corresponding turbulent unity Lewis number flame. Fast flame propagation and earlier initiation of flame quenching for small Lewis number flames can be seen from the normalised turbulent flame speed S_T/S_L (where $S_T = \left(\rho_0 A_p\right)^{-1} \int_V \dot{w} dV$, and A_p is the projected area in the direction of flame propagation), and normalised flame surface area A_T/A_L (where flame surface area has been evaluated using the volume integral $A = \int_V |\nabla c| dV$, and turbulent and laminar values are shown with subscripts T and L respectively) values reported in Table 5.3, which also shows that the rate of flame propagation is faster for higher values of $u^{'}/S_L \sim Re_t^{1/4} Ka^{1/2} \sim Re_t^{1/2} Da^{-1/2}$ when the flame is away from the wall and thus flame quenching starts at an earlier time instant for higher values of $u^{'}/S_L$. The reactants diffuse into the reaction zone at a faster rate than the rate of thermal diffusion out of it in the case of $Le < 1$, which in turn leads to the simultaneous strong focusing of reactants and defocusing of heat in the positively stretched zones. This gives rise to simultaneous occurrence of high reactant concentration and temperature in positively stretched zones in turbulent $Le < 1$ flames, which augments the rate of burning, magnitude of dilatation rate and thereby strengthens the flame normal acceleration in comparison to unity Lewis number flames with statistically similar unburned gas turbulence (see e.g. Chakraborty et al. (2007); Han and Huh (2008); Chakraborty and Cant (2005, 2009b, c); Chakraborty and Swaminathan (2010) and references therein). By contrast, thermal diffusion rate supersedes the mass diffusion rate in $Le > 1$ flames and thus a combination of simultaneous strong defocusing of heat and weak focusing of reactants in the positively stretched zones leads to the weakening of the rate of burning, magnitude of dilatation rate and flame normal acceleration in comparison to unity

Table 5.3 List of normalised flame surface area A_T/A_L and turbulent flame speed S_T/S_L at different stages of flame quenching for all cases considered here

		Case A		Case B		Case C		Case D		Case E	
	tS_L/δ_Z	A_T/A_L	S_T/S_L	A_T/A_L	S_T/S_L	A_T/A_L	S_T/S_L	A_T/A_L	S_T/S_L	A_T/A_L	S_T/S_L
$Le = 0.8$	1	1.62	1.61	1.69	1.68	3.50	3.47	3.26	3.23	5.33	5.29
	2	2.49	2.48	2.63	2.63	4.05	4.05	5.74	5.73	6.71	6.70
	4	2.64	2.62	2.36	2.35	2.69	2.67	2.32	2.30	1.50	1.48
	6	1.90	1.88	1.70	1.68	0.44	0.43	0.28	0.28	0.15	0.15
	8	0.94	0.93	1.07	1.06	0.04	0.04	0.03	0.03	0.02	0.02
	10	0.17	0.17	0.19	0.19	0.01	0.01	0.01	0.01	0.01	0.01
$Le = 1.0$	1	1.57	1.55	1.59	1.57	2.79	2.78	2.91	2.90	4.18	4.17
	2	1.67	1.66	1.60	1.59	2.99	2.99	3.95	3.93	4.77	4.76
	4	1.77	1.76	1.73	1.71	2.34	2.31	2.39	2.37	2.03	2.01
	6	1.64	1.62	1.68	1.66	1.43	1.41	0.74	0.74	0.68	0.67
	8	1.51	1.49	1.53	1.51	0.50	0.49	0.20	0.19	0.12	0.12
	10	0.86	0.85	0.85	0.84	0.09	0.09	0.03	0.03	0.03	0.03
$Le = 1.2$	1	1.29	1.28	1.22	1.21	1.92	1.91	2.04	2.02	2.68	2.66
	2	1.38	1.37	1.33	1.32	2.01	2.00	2.75	2.74	3.43	3.43
	4	1.31	1.30	1.28	1.27	1.82	1.81	1.98	1.96	1.57	1.55
	6	1.30	1.29	1.29	1.28	1.60	1.59	1.51	1.49	1.23	1.22
	8	1.23	1.22	1.24	1.23	1.12	1.11	0.60	0.60	0.47	0.46
	10	1.15	1.14	1.14	1.13	0.60	0.60	0.18	0.18	0.10	0.10

Lewis number flames with statistically similar unburned gas turbulence. Interested readers are referred to Lai and Chakraborty (2016a, b, c, d); Sellmann et al. (2017); Lai et al. (2017) for further discussion on Lewis number effects on wall heat flux and flame wrinkling in the current configuration.

5.3.1.2 Statistical Behaviour of Turbulent Scalar Flux $\overline{\rho u_1^{''} h^{''}}$

The variations of $\widetilde{h^+} = \left(\tilde{h} - h_0\right)/(h_{ad} - h_0)$, $\overline{\rho u_1^{''} h^{''}}/[\rho_0 S_L (h_{ad} - h_0)]$ and $\overline{\rho u_1^{''} h^{''}} \times \left(\partial \tilde{h}/\partial x_1\right) \times \delta_{th}/\left[\rho_0 S_L (h_{ad} - h_0)^2\right]$ (where h_0 and h_{ad} are specific sensible enthalpies in the unburned gas and at the adiabatic flame temperature respectively) with x_1/δ_Z at three time instants $t = 2\delta_z/S_L, 6\delta_z/S_L$ and $10\delta_z/S_L$ are shown in Figs. 5.7, 5.8 and 5.9, respectively, for cases A, C and E. Cases B and D are not shown due to their qualitative similarities with cases A and E. A comparison between Figs. 5.7 and 5.8 reveals that $\overline{\rho u_1^{''} h^{''}}/[\rho_0 S_L (h_{ad} - h_0)]$ assumes predominantly positive values within the flame brush, and its magnitude decreases with time as the quenching progresses. A comparison between Figs. 5.7, 5.8 and 5.9 reveals that both $\overline{\rho u_1^{''} h^{''}}/[\rho_0 S_L (h_{ad} - h_0)]$ and $\overline{\rho u_1^{''} h^{''}} \times \left(\partial \tilde{h}/\partial x_1\right) \times \delta_{th}/\left[\rho_0 S_L (h_{ad} - h_0)^2\right]$ exhibit same signs for the major part of the flame brush suggesting a predominance of counter-gradient transport, because the gradient and flux are expected to be of opposite sign for gradient transport:

$$\overline{\rho u_j^{''} h^{''}} = -\bar{\rho} D_t \frac{\partial \tilde{h}}{\partial x_j} \tag{5.21}$$

Equation (5.21) suggests that $\overline{\rho u_1^{''} h^{''}} \times \left(\partial \tilde{h}/\partial x_1\right) \times \delta_{th}/\left[\rho_0 S_L (h_{ad} - h_0)^2\right]$ is expected to assume a positive (negative) value for counter-gradient (gradient) transport. According to the Bray–Moss–Libby (BML) analysis, the probability density function (pdf) of T is presumed to have a bi-modal distribution with impulses at $T = 0$ and $T = 1.0$ which leads to $\overline{\rho u_j^{''} h^{''}} = \bar{\rho}(h_{ad} - h_0)\left[\overline{(u_j)}_P - \overline{(u_j)}_R\right]\tilde{T}\left(1 - \tilde{T}\right) + O(\gamma_T)$. It can be elucidated from this relationship that a counter-gradient (gradient) transport is obtained for $\overline{(u_j)}_P > \overline{(u_j)}_R \left(\overline{(u_j)}_P < \overline{(u_j)}_R\right)$. Veynante et al. (1997) expressed the slip velocity $\overline{(u_1)}_P - \overline{(u_1)}_R$ as $\left[-\alpha_E u^{'} + \tau S_L\right]$, where α_E is an appropriate efficiency function. It leads to a non-dimensional number known as the Bray number N_B which is proportional to $\tau S_L/u^{'}$ (i.e. $N_B \propto \tau S_L/u^{'}$) (Veynante et al. 1997; Chakraborty and Cant 2009b, c, 2015) so that a counter-gradient (gradient) transport is obtained for $N_B \gg 1 (N_B \ll 1)$. This indicates that the effects of gradient transport are expected to be stronger in case E (case C) than case C (case A). By contrast, case A (case C) is expected to show stronger counter-gradient transport than case C (case E). These

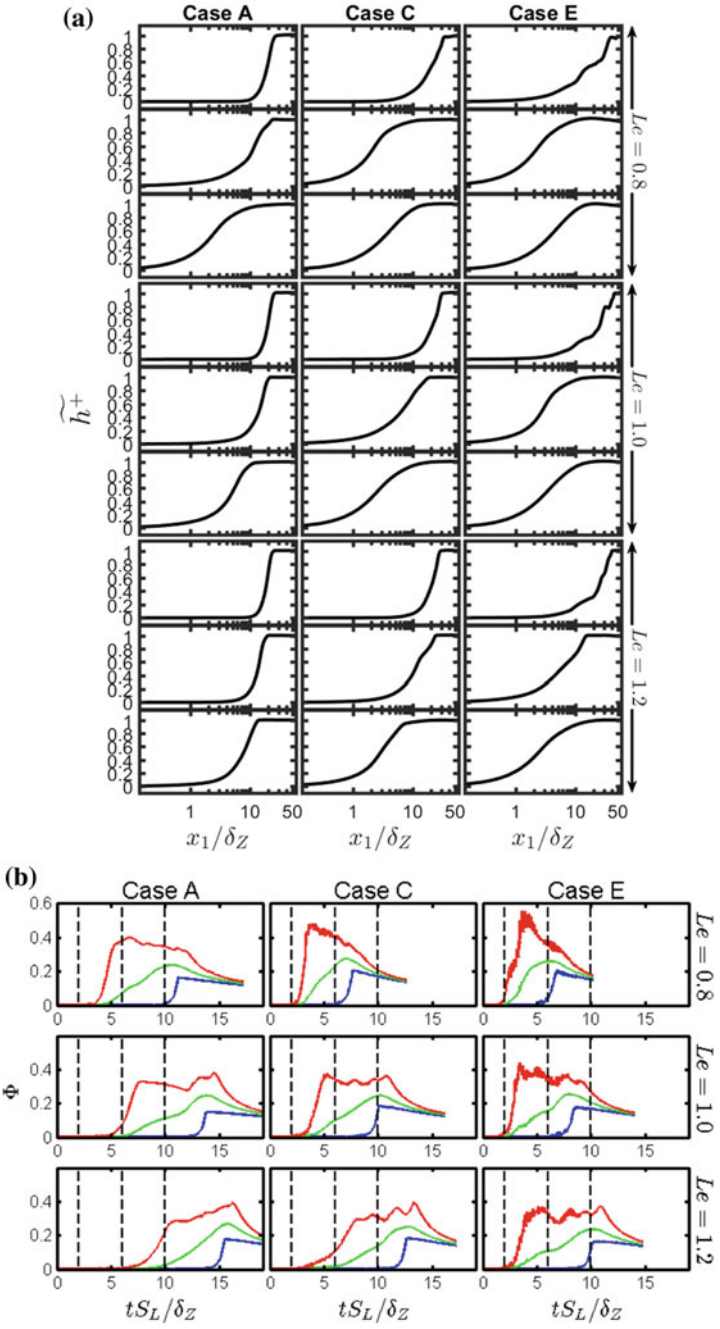

Fig. 5.7 **a** Variation of $\widetilde{h^+} = \left(\widetilde{h} - h_0\right)/(h_{ad} - h_0)$ with $\mathbf{x}_1/\boldsymbol{\delta}_\mathbf{Z}$ (log scale) for cases A, C and E (1st–3rd column) at $t = 2\boldsymbol{\delta}_z/S_L, 6\boldsymbol{\delta}_z/S_L$ and $10\boldsymbol{\delta}_z/S_L$ (first–third row). **b** Temporal evolution of the maximum, mean and minimum values of non-dimensional wall heat flux $\boldsymbol{\Phi}_w$ for cases A, C and E (1st–3rd column). Vertical black broken lines are indicating $t = 2\boldsymbol{\delta}_\mathbf{Z}/S_L, 6\boldsymbol{\delta}_\mathbf{Z}/S_L$ and $8\boldsymbol{\delta}_\mathbf{Z}/S_L$ (left to right)

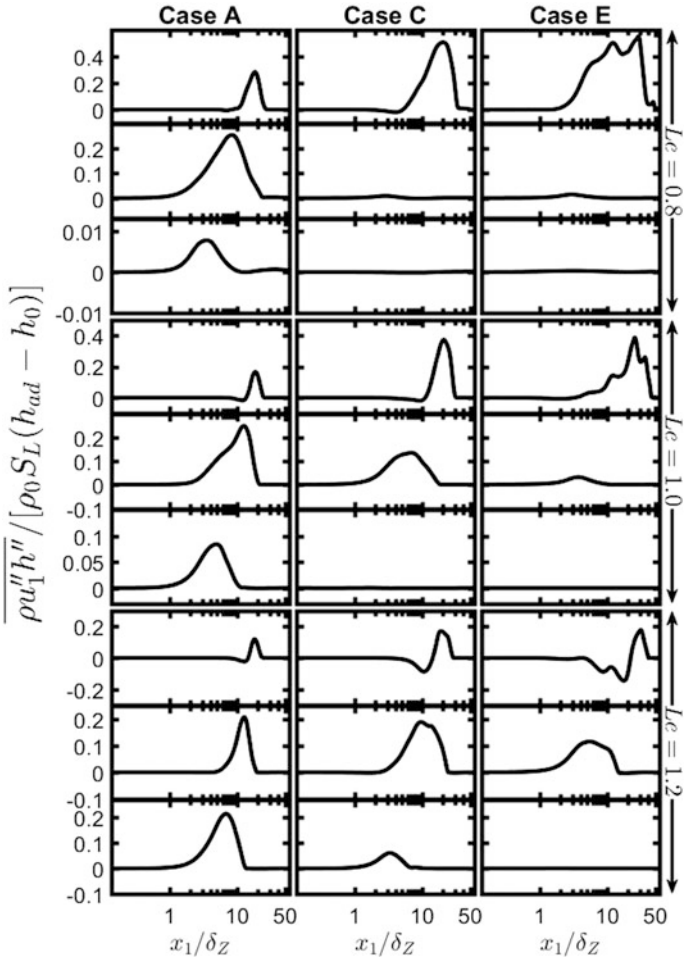

Fig. 5.8 Variation of $\overline{\boldsymbol{\rho} u_1^{''} h^{''}}/[\boldsymbol{\rho}_0 S_L(h_{ad} - h_0)]$ with $\mathbf{x_1/\delta_Z}$ (log scale) for cases A, C and E (first–third column) at $t = 2\boldsymbol{\delta}_z/S_L, 6\boldsymbol{\delta}_z/S_L$ and $10\boldsymbol{\delta}_z/S_L$ (1st–3rd row)

expectations are consistent with the observations made from Fig. 5.8, which shows greater extent of gradient transport for cases C and E than in case A. Furthermore, the gradient transport is predominant towards the unburned gas side of the flame brush where the effects of flame normal acceleration due to thermal expansion arising from chemical heat release are weak. The spatial distributions of $u^{'}/S_L = \sqrt{2\tilde{k}/3}/S_L$ and the integral length scale where $l = (\tilde{k}^{3/2}/\tilde{\epsilon})/\delta_{th}$ are shown in Fig. 5.9. It can be seen from Fig. 5.9 that the magnitudes of $\sqrt{2\tilde{k}/3}/S_L$ and

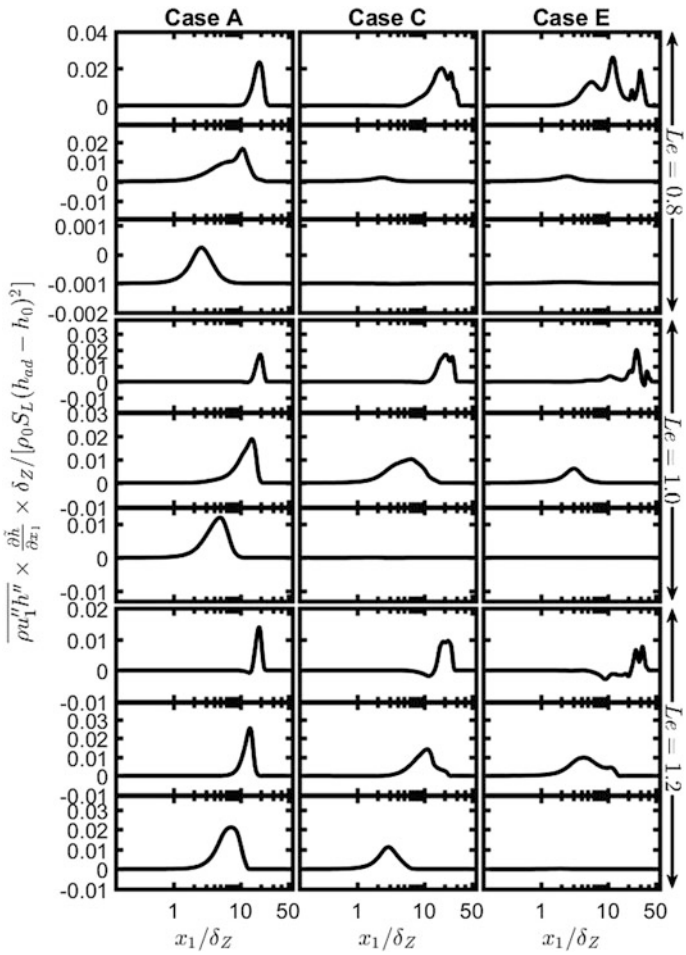

Fig. 5.9 Variation of $\overline{\rho u_1'' h''} \times (\partial \tilde{h}/\partial x_1) \times \boldsymbol{\delta}_Z / \left[\rho_0 S_L (h_{ad} - h_0)^2\right]$ with $\mathbf{x_1/\delta_Z}$ (log scale) for cases A, C and E (first–third column) at $t = 2\boldsymbol{\delta}_z/S_L, 6\boldsymbol{\delta}_z/S_L$ and $10\boldsymbol{\delta}_z/S_L$ (1st–3rd row)

$l/\delta_{th} = (\tilde{k}^{3/2}/\tilde{\epsilon})/\delta_{th}$ decrease with time but these values remain non-negligible for the time instants shown here so that these snapshots capture different stages of flame movement (i.e. from away from the wall to flame–wall interaction to flame quenching). Furthermore, a comparison between Figs. 5.7a and 5.9 reveals that the relatively high values of $\sqrt{2\tilde{k}/3}$ are obtained ahead of the flame but it decreases both across the flame brush and in the vicinity of the isothermal inert wall. A combination of high values of $\sqrt{2\tilde{k}/3}$ and weak effects of heat release and flame normal acceleration at the leading edge of the flame brush gives rise to a gradient-type transport in cases C and E.

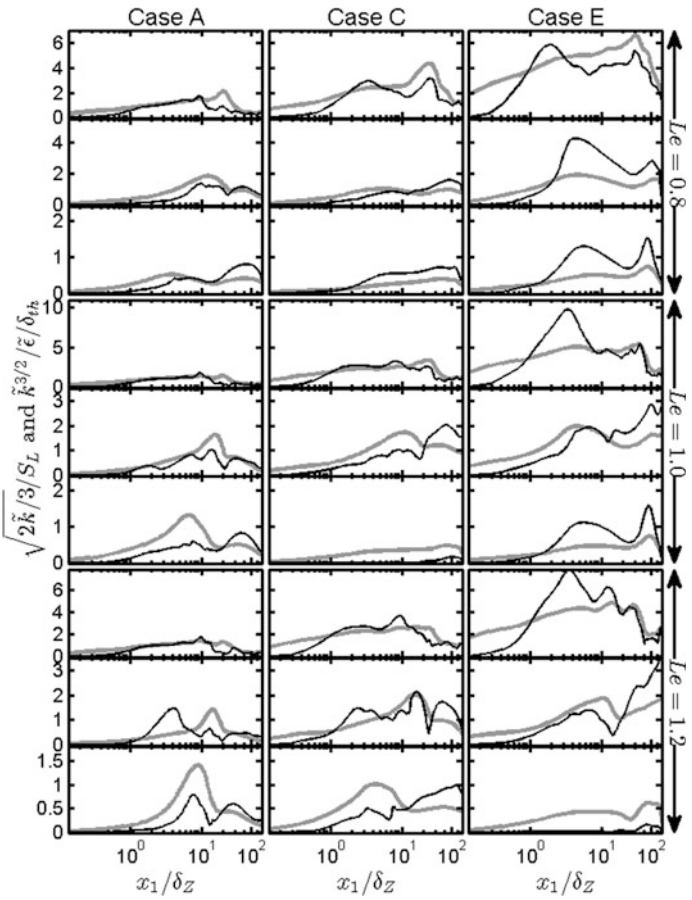

Fig. 5.10 Variation of $\sqrt{2\tilde{k}/3}/S_L$ (——) and $\tilde{k}^{3/2}/\tilde{\epsilon}/\boldsymbol{\delta}_{th}$ (▬▬) with $\mathbf{x}_1/\boldsymbol{\delta}_\mathbf{Z}$ (log scale) for cases A, C and E (1st–3rd column) at $t = 2\boldsymbol{\delta}_z/S_L, 6\boldsymbol{\delta}_z/S_L$ and $10\boldsymbol{\delta}_z/S_L$ (first–third row)

5.3.2 *Statistical Behaviours of the Terms in Turbulent Scalar Flux Transport Equation*

The variations of $T_1 - T_8$ for the $\overline{\rho u_1^{''} h^{''}}$ transport equation with normalised wall normal distance x_1/δ_Z for cases A, C and E are shown in Fig. 5.10 for different time instants. The positive contributions in Fig. 5.10 act to promote a counter-gradient transport, whereas negative contributions tend to induce a gradient transport. It can be seen from Fig. 5.11 that the reaction contribution T_8 assumes predominantly assumes positive values, whereas both T_6 and T_7 exhibit negative values at all times. The pressure gradient terms T_4 and T_5 play important roles in the transport of $\overline{\rho u_1^{''} h^{''}}$ for all cases when the flame is away from the wall. The mean pressure

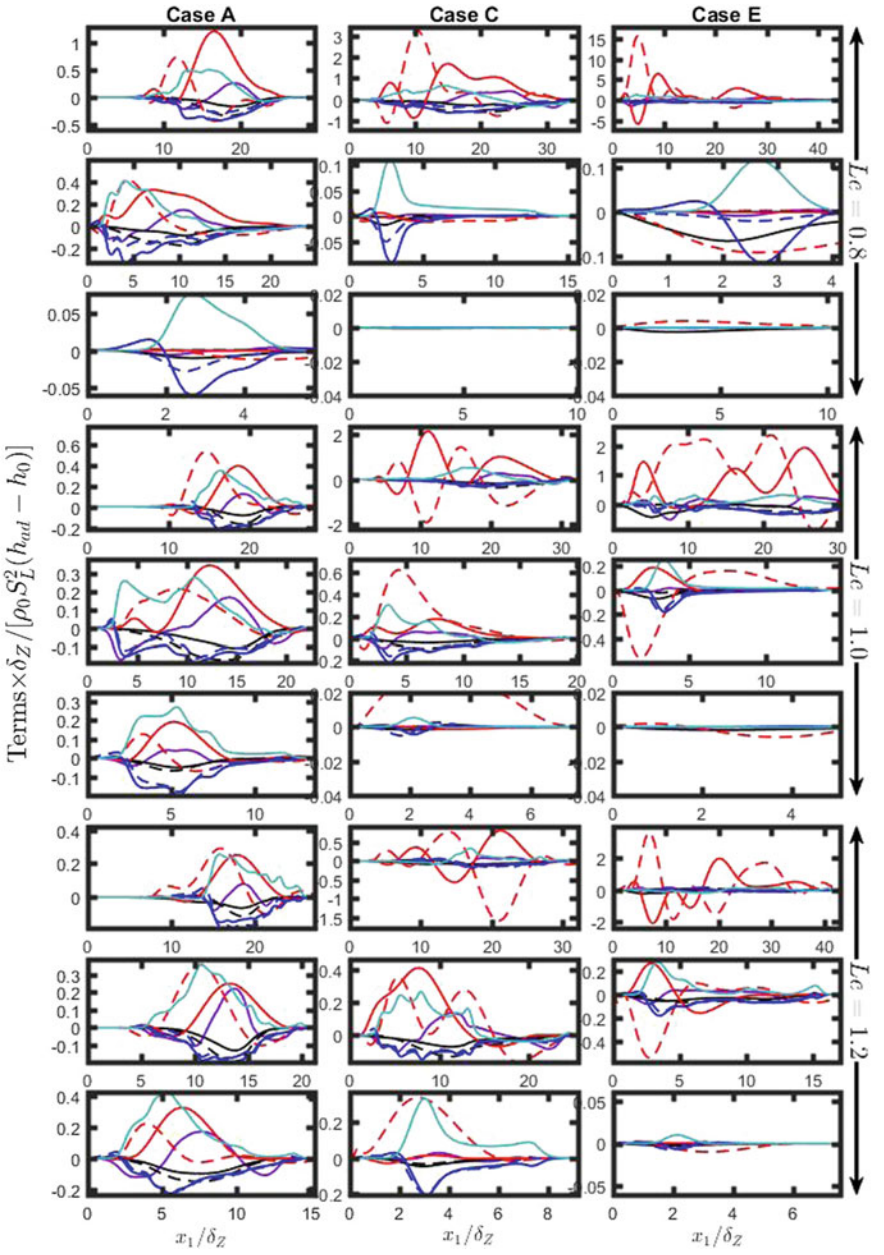

Fig. 5.11 Variations of the terms T_1 (——), T_2 (——), T_3 (— —), T_4 (——), T_5 (— —), T_6 (——), T_7 (— —) and T_8 (——) with $\mathbf{x_1/\delta_Z}$ for cases A, C and E (1st–3rd column) at $t = 2\boldsymbol{\delta}_z/S_L, 6\boldsymbol{\delta}_z/S_L$ and $10\boldsymbol{\delta}_z/S_L$ (first–third row). All terms are non-dimensionalised by $\boldsymbol{\rho}_0 S_L^2(h_{ad} - h_0)/\boldsymbol{\delta}_Z$

gradient term T_4 assumes positive values for the major part of the flame brush although local negative values of T_4 are also obtained within the flame brush when the flame is away from the wall. The fluctuating pressure gradient term T_5 also exhibits both positive and negative values within the flame brush. The contributions of T_2 and T_3 remain negative, whereas the turbulent transport term T_1 exhibits both positive and negative values. The relative magnitudes of T_1, T_2 and T_3 in comparison to the pressure gradient terms T_4 and T_5 decrease with increasing Re_t (i.e. from case A to case E). The magnitudes of $T_1 - T_8$ decrease considerably as the quenching progresses and they eventually vanish altogether.

The terms $T_1 - T_8$ can be scaled in the following manner (Chakraborty and Cant 2015):

$$T_1 \sim \left(\rho_0 S_L^2/\delta_{th}\right)\left(\overline{\rho u_1^{''} h^{''}}/\rho_0 S_L\right)^2 Da^{-0.5} Re_t^{-0.5}/(h_{ad} - h_0) \tag{5.22i}$$

$$T_2 \sim \left(\rho_0 S_L^2/\delta_{th}\right) Da^{-1.5} Re_t^{0.5} (h_{ad} - h_0) \tag{5.22ii}$$

$$T_3 \sim \left(\rho_0 S_L^2/\delta_{th}\right)\left(\overline{\rho u_1^{''} h^{''}}/\rho_0 S_L\right)\left(U_{ref}/S_L\right) Da^{-0.5} Re_t^{-0.5} \tag{5.22iii}$$

$$T_4 \sim \left(\rho_0 S_L^2/\delta_{th}\right) Da^{-1.5} Re_t^{0.5} (h_{ad} - h_0) \tag{5.22iv}$$

$$T_5 \sim \left(\rho_0 S_L^2/\delta_{th}\right)\left(\overline{\rho u_1^{''} h^{''}}/\rho_0 S_L\right)^2/(h_{ad} - h_0) \tag{5.22v}$$

$$T_6 \sim \left(\rho_0 S_L^2/\delta_{th}\right)\left(\overline{\rho u_1^{''} h^{''}}/\rho_0 S_L\right) \tag{5.22vi}$$

$$T_7 \sim \left(\rho_0 S_L^2/\delta_{th}\right)\left(\overline{\rho u_1^{''} h^{''}}/\rho_0 S_L\right) \tag{5.22vii}$$

$$T_8 \sim \left(\rho_0 S_L^2/\delta_{th}\right)\left(\overline{\rho u_1^{''} h^{''}}/\rho_0 S_L\right) \tag{5.22viii}$$

Here, the gradients of the mean quantities are scaled using l and the quantities $\overline{\rho u_1^{''} u_1^{''} h^{''}}$ and $\overline{\rho u_1^{''} u_1^{''}}$ are scaled with respect to $\left(\overline{\rho u_1^{''} h^{''}}\right)^2/[\rho_0 (h_{ad} - h_0)]$ and $\rho_0 u^{'2}$ respectively. The mean pressure gradient can be taken to scale as $\partial \bar{P}/\partial x_1 \sim \partial\left(\overline{\rho u_1^{''} u_1^{''}}\right)/\partial x_1$ for flows with $u^{'}$ either greater than or comparable to $\tilde{u}_1$, as in the cases considered here. For terms $T_5 - T_8$, the scalings of the key quantities may be taken as $\partial P^{'}/\partial x_1 \sim \left(\rho u_1^{''} h^{''}\right)^2/[\rho_0 \delta_{th} (h_{ad} - h_0)^2]$, $u_1^{''} \sim \rho u_1^{''} h^{''}/[\rho_0 (h_{ad} - h_0)]$ and $\partial \tau_{ik}/\partial x_k \sim \left(\rho u_1^{''} h^{''}\right) S_L/[(h_{ad} - h_0)\delta_{th}]\big)$. The molecular diffusion rate and reaction rate in T_7 and T_8 have been scaled with respect to $\rho_0 S_L (h_{ad} - h_0)/\delta_{th}$ (i.e. $\dot{w}_T \sim \rho_0 S_L (h_{ad} - h_0)/\delta_{th}$ and $\nabla \cdot \left(\lambda \nabla \hat{T}\right) \sim \rho_0 S_L (h_{ad} - h_0)/\delta_{th}\big)$. Moreover, both $\tilde{h}$ and $h^{''}$ are scaled with respect to $(h_{ad} - h_0)$. The scaling estimates given by Eq. (5.22) indicate that the terms $T_2, T_4 - T_8$ are expected to be the leading order

contributors for $Da<1$, whereas the contributions of T_1 and T_3 are expected to become progressively less important with increasing Re_t. This is consistent with the observations made from Fig. 5.11. The terms T_2 and T_3 are closed in the context of second-moment closure, as the closures are employed for Reynolds stresses $\overline{\rho u_i'' u_j''}$ and the solution of Eq. (5.20) provides the Reynolds flux components of enthalpy $\overline{\rho u_i'' h''}$. Thus, the modelling of T_1 and T_4 to T_8 will be discussed next.

5.3.3 Modelling of the Turbulent Transport Term T_1

The turbulent transport term is given by $T_1=\partial(\overline{\rho u_j'' u_i'' h''})/\partial x_j$, and therefore modelling of this term depends on $\overline{\rho u_j'' u_i'' h''}$. The model (referred to as the TDH model) by Daly and Harlow (1970) is one of the widely used models for $\overline{\rho u_j'' u_i'' h''}$ closure for passive scalars:

$$\overline{\rho u_i'' u_j'' h''} = -C_{CS}\frac{\tilde{k}}{\tilde{\varepsilon}}\overline{\rho u_j'' u_k''}\frac{\partial\left(\overline{\rho u_i'' h''}/\bar{\rho}\right)}{\partial x_k} \tag{5.23}$$

where $\tilde{\varepsilon}=\overline{\mu\left(\partial u_i''/\partial x_j\right)\left(\partial u_i''/\partial x_j\right)}/\bar{\rho}$ is the dissipation rate of kinetic energy $\tilde{k}$, and $C_{CS}\approx 0.22$ is the model constant. The predictions of the TDH model are compared to $\overline{\rho u_1'' u_1'' h''}$ extracted from DNS data in Fig. 5.12. The TDH model fails to capture the quantitative and qualitative behaviour of the DNS data, for cases A–C. However, for high values of $u'/S_L \sim Re_t^{\frac{1}{4}} Ka^{\frac{1}{2}} \sim Re_t^{\frac{1}{2}} Da^{-\frac{1}{2}}$ (e.g. cases D and E), the TDH model exhibits slightly improved agreement with DNS data at $t\le 6\delta_Z/S_L$ but this model fails to predict the near-wall behaviour of $\overline{\rho u_1'' u_1'' h''}$ at $t\ge 8\delta_Z/S_L$. The TDH model is proposed for non-reacting flow based on gradient hypothesis, and it does not take into account for the effect of chemical reaction. According to the BML analysis (i.e. subject to the assumption of bi-modal pdf of T (i.e. $P(T)$) with impulses at $T=0$ and $T=1$) the Favre-average velocity component takes the following form: $\tilde{u}_j=\overline{(u_j)}_P\tilde{T}+\left(1-\tilde{T}\right)\overline{(u_j)}_R+O(1/Da)$, which once used in $\overline{\rho u_i'' u_j'' h''}=(h_{ad}-h_0)\int_{-\infty}^{\infty}\int_{-\infty}^{\infty}\int_0^1 \rho(u_i-u_i)\left(u_j-\tilde{u}_j\right)P\left(u_i;u_j;T\right)du_i du_j dT$ yields (Bray et al. 1985; Chakraborty and Lipatnikov 2013):

$$\begin{aligned}\overline{\rho u_1'' u_1'' h''} \approx \Big\{&\bar{\rho}\left[\overline{(u_1)}_P-\overline{(u_1)}_R\right]^2\tilde{T}\left(1-\tilde{T}\right)\left(1-2\tilde{T}\right)-\bar{\rho}\,\overline{\left(u_1'u_1'\right)}_R\tilde{T}\left(1-\tilde{T}\right)+\bar{\rho}\,\overline{\left(u_1'u_1'\right)}_P\tilde{T}\left(1-\tilde{T}\right)\\&+O(1/Da)\Big\}(h_{ad}-h_0)\end{aligned} \tag{5.24}$$

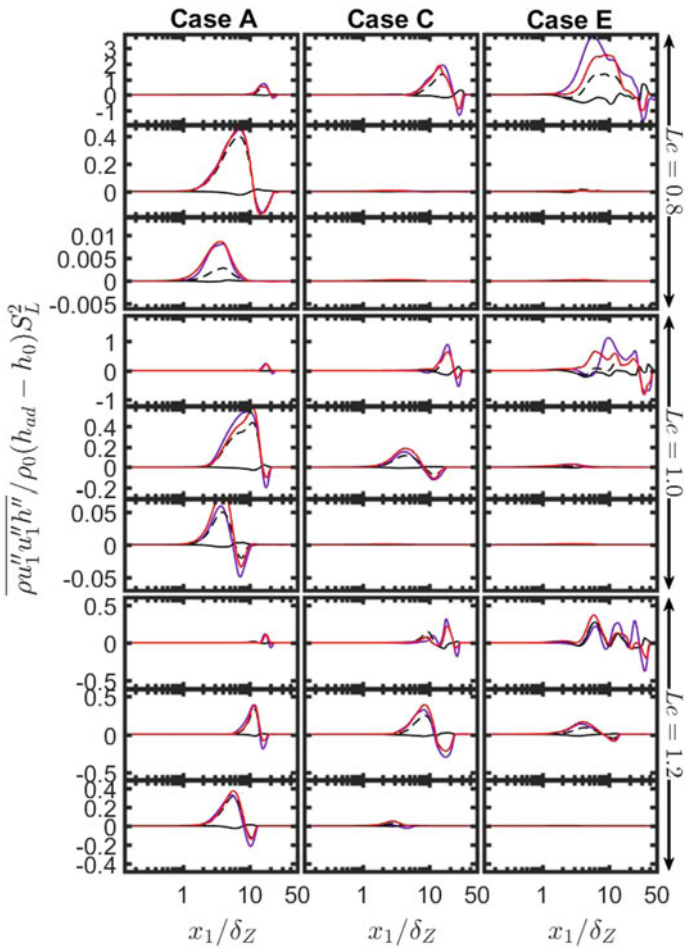

Fig. 5.12 Variation of terms $\overline{\boldsymbol{\rho} u_1'' u_1'' h''}/\boldsymbol{\rho}_0(h_{ad} - h_0)S_L^2$ from DNS data (——), TDH(——), CC (— —) and New model (i.e. Equation (26i)) (——) with $\mathbf{x}_1/\boldsymbol{\delta}_\mathbf{Z}$ for cases A, C and E (1st–3rd column) at $t = 2\boldsymbol{\delta}_z/S_L, 6\boldsymbol{\delta}_z/S_L$ and $10\boldsymbol{\delta}_z/S_L$ (first–third row)

The first term on the right-hand side represents the reacting contribution to $\overline{\rho u_1'' u_1'' h''}$, whereas the combined action of second and third terms represent the effects of turbulence on $\overline{\rho u_1'' u_1'' h''}$. The last term $O(1/Da)$ originates from the interior of the flame and this contribution becomes negligible for $Da \gg 1$. The pdf of T cannot be approximated by a bi-modal distribution in the near-wall region and especially at the wall where it shows a monomodal behaviour at $T = 0$. The departure from a bi-modal distribution is often quantified in terms of a segregation factor $g = \overline{\rho T''^2}/\bar{\rho}\tilde{T}(1 - \tilde{T})$. Chakraborty and Cant (2009b, 2015) utilised the TDH model for the turbulent contribution part in Eq. (5.24) and utilised the segregation

factor to propose a model (referred to as the CC model here) based on a-priori DNS analyses for the flames without any influence of walls in the following manner:

$$\overline{\rho u_1'' u_1'' h''} = -C_{CS}\frac{\tilde{k}}{\tilde{\varepsilon}}\overline{\rho u_1'' u_1''}\frac{\partial\left(\overline{\rho u_1'' h''}/\bar{\rho}\right)}{\partial x_1} + \bar{\rho}(h_{ad}-h_0)\left[\frac{\overline{\rho u_1'' h''}}{\bar{\rho}\tilde{T}(1-\tilde{T})(h_{ad}-h_0)} + \alpha_3\sqrt{\overline{\rho u_1'' u_1''}/\bar{\rho}}\right]^2 \tilde{T}(1-\tilde{T})(1-2\sqrt{g}\tilde{T}) \tag{5.25}$$

where $\left[\overline{\rho u_1'' h''}/\left\{\bar{\rho}\tilde{T}(1-\tilde{T})(h_{ad}-h_0)\right\} + \alpha_3\sqrt{\overline{\rho u_1'' u_1''}/\bar{\rho}}\right]$ represents $\left[\overline{(u_j)}_P - \overline{(u_j)}_R\right]$ in Eq. (5.25) where $\alpha_3 = 0.2 + 0.3\mathrm{erf}(Re_L/20)$ is a model parameter with $Re_L = \rho_0\tilde{k}^2/\mu_0\tilde{\epsilon}$ is the local turbulent Reynolds number. The predictions of the CC model (Eq. (5.25)) are also shown in Fig. 5.12, which indicates that the CC model is more successful in capturing the behaviour of $\overline{\rho u_1'' u_1'' h''}$ than the TDH model when the flame is away from the wall, where the CC model reasonably captures both the quantitative and qualitative behaviours of $\overline{\rho u_1'' u_1'' h''}$. However, $\tilde{T}$ approaches 0.0 close to the wall (and is identically zero at the wall), and as a result the second term on the right-hand side of Eq. (5.25) disappears and thus the CC model prediction approaches that of the TDH model in the near-wall region. Thus, the CC model does not adequately capture the near-wall behaviour of $\overline{\rho u_1'' u_1'' h''}$. Here the CC model has been modified in the following manner:

$$\overline{\rho u_1'' u_1'' h''} = -C_{CS}\left(\frac{\tilde{k}}{\tilde{\varepsilon}}\right)\overline{\rho u_1'' u_1''}\frac{\partial\left(\overline{\rho u_1'' h''}/\bar{\rho}\right)}{\partial x_1} + \bar{\rho}(h_{ad}-h_0)\tilde{T}(1-\tilde{T})\left(1-2g^{0.5(1-\tilde{c}_W)}\tilde{T}\right) \times\left[A_w\left(\frac{\overline{\rho u_1'' h''}}{\bar{\rho}\tilde{T}(1-\tilde{T})(h_{ad}-h_0)} + \alpha_{3W}\sqrt{\frac{\overline{\rho u_1'' u_1''}}{\bar{\rho}}}\right)\right]^2 \tag{5.26i}$$

where

$$\alpha_{3W} = 0.2[3(1-\tilde{c}_W)]^{\eta_1} + 0.3erf(Re_L/20); \eta_1 = 0.5erf\left[-0.5\left(x_1/\delta_Z - 5(Pe_{min})_L\right)\right] \tag{5.26ii}$$

$$A_w = exp\left[-\frac{\tilde{c}_W - \tilde{T}_W}{Le}\eta_2\right]; \eta_2 = 0.5erf\left[-0.5\left(x_1/\delta_Z - (Pe_{min})_L\right)\right]; \tag{5.26iii}$$

where $\tilde{c}_W$ and $\tilde{T}_W$ are the Favre-averaged values of reaction progress variable and non-dimensional temperature at a given instant of time. In Eq. (5.26iii) $(Pe_{min})_L$ is the minimum Peclet number (where $Pe = X/\delta_Z$ is the wall Peclet number with the wall normal distance X of the $T = 0.9$ isosurface Poinsot et al. 1993) for head-on

quenching of laminar premixed flames. For the present thermochemistry $(Pe_{min})_L = 3.09$, 2.83 and 2.75 for $Le = 0.8$, 1.0 and 1.2 respectively (Lai and Chakraborty 2016d). The minimum Peclet number $(Pe_{min})_L$ values can be interpreted as the flame quenching distance normalised by the Zel'dovich flame thickness. These normalised flame quenching distances have been found to be consistent with several previous experimental (Huang et al. 1986; Jarosinsky 1986; Vosen et al. 1984) and computational (Poinsot et al. 1993) analyses.

The model parameter α_{3W} is modified form of α_3 in the CC model, and this modification accounts for the dampening of turbulence close to the wall. The magnitude of $\overline{\rho u_1'' u_1'' h''}$ drops during flame quenching, especially in near-wall region, and the presence of flame close to the wall is sensed by A_w due to an increase in the value of $\left(\tilde{c}_W - \tilde{T}_W\right)$ during flame quenching, and this damps the contribution arising from velocity jump across the flame brush due to the thermal expansion. The extent of velocity jump across the flame brush is dependent on Le, and thus the damping factor A_w is dependent on Le. Both TDH and CC models do not adequately predict the negative values of $\overline{\rho u_1'' u_1'' h''}$ close to the wall but this behaviour cannot be captured by $\left(1 - 2\sqrt{g\tilde{T}}\right)$ because $\overline{\rho T''^2}/\bar{\rho}$ (and thus g) drops drastically during flame quenching and vanishes at the isothermal wall at all times. However, the modification $g^{0.5(1-\tilde{c}_W)}$ allows the term $\left(1 - 2g^{0.5(1-\tilde{c}_W)}\tilde{T}\right)$ to assume negative values during flame quenching when $\tilde{c}_W$ approaches unity (i.e. $\tilde{c}_W \to 1.0$). It can be seen from Fig. 5.12 that the model given by Eq. (5.26i) (referred to as the new model) is capable of predicting both qualitative and quantitative behaviours of $\overline{\rho u_1'' u_1'' h''}$ satisfactorily for both far from and near to the wall for all cases considered here.

The model parameters which are given by Eqs. (5.26ii) and (5.26iii) involve empiricism but their functional forms are proposed in such a manner that Eq. (5.26i) asymptotically approaches previously proposed model for unbounded flows (see Eq. (5.25)) away from the wall. The numerical values of the model parameters in Eqs. (5.26ii) and (5.26iii) have been calibrated using explicitly Reynolds-averaged DNS data. The involvements of the exponential function and Re_L in the empirical functions are similar to the van Driest's damping function (Durbin and Pettersson Reif 2001). Moreover, Eqs. (5.26ii) and (5.26iii) are taken to be functions of $(Pe_{min})_L, \tilde{c}_W$ and $\left(\tilde{c}_W - \tilde{T}_W\right)$. The involvement of $(Pe_{min})_L$ implicitly ensures quenching information is included into the model, whereas the $\left(\tilde{c}_W - \tilde{T}_W\right)$ dependence of the model parameter ensures that the effects of enthalpy loss due to wall heat transfer are accounted for. As the value of $\tilde{c}_W$ changes with time (it remains 0 when the flame is away from the wall but it increases from 0 and approaches 1.0 with the advancement of quenching (Lai and Chakraborty 2016a, b, c,d; Sellmann et al. 2017; Lai et al. 2017) so the dependence of $\tilde{c}_W$ in the model parameters acts as the sensor of flame position from the wall. Similar modelling approaches were previously adopted by Bruneaux et al. (1997) and Alshaalan and Rutland (1998) in the context of FSD closures for wall-bounded turbulent premixed flames.

5.3.4 Modelling of the Pressure Gradient Terms $(T_4 + T_5)$

Both the mean and fluctuating pressure terms are often modelled in a combined manner due to their similar origin (Durbin and Pettersson Reif 2001). There are several available models for the closure of $(T_4 + T_5)$. Three of these models take the following form by combining conventional closures of slow and rapid terms (Durbin and Pettersson Reif 2001):

$$T_4 + T_5 = -C_{1c}\frac{\tilde{\varepsilon}}{\tilde{k}}\overline{\rho u_i'' h''} + C_{2c}\overline{\rho u_k'' h''}\frac{\partial \widetilde{u_i}}{\partial x_k} + C_{3c}\overline{\rho u_k'' h''}\frac{\partial \widetilde{u_k}}{\partial x_i} + C_{4c}\overline{\rho u_i'' u_k''}\frac{\partial \tilde{h}}{\partial x_k} \quad (5.27)$$

where the slow part is represented by $-C_{1c}\left(\tilde{\varepsilon}/\tilde{k}\right)\overline{\rho u_i'' h''}$ and the rapid part is given by: $C_{2c}\overline{\rho u_k'' h''}\left(\partial \widetilde{u_i}/\partial x_k\right) + C_{3c}\overline{\rho u_k'' h''}\left(\partial \widetilde{u_k}/\partial x_k\right) + C_{4c}\overline{\rho u_i'' u_j''}\left(\partial \tilde{h}/\partial x_j\right)$ with C_{1c}, C_{2c}, C_{3c} and C_{4c} being the model parameters. Launder (1989) suggested that $C_{1c} = 3.0, C_{2c} = 0, C_{3c} = 0$ and $C_{4c} = 0.4$, and this model will henceforth be referred to the PL model. Craft (1993) adopted a similar model (referred to as the PC model) with $C_{1c} = 3.0, C_{2c} = 0.5, C_{3c} = 0$ and $C_{4c} = 0$. Durbin (1993) suggested an alternative model (PD model) where $C_{1c} = 2.5, C_{2c} = 0, C_{3c} = 0$ and $C_{4c} = 0.45$. In addition, Jones (1994) and Bradley et al. (1994) proposed alternative models for $(T_4 + T_5)$ in the following manner:

$$T_4 + T_5 = -\overline{h''}\frac{\partial \bar{P}}{\partial x_i} - C_{\phi 1}\frac{\tilde{\varepsilon}}{\tilde{k}}\overline{\rho u_i'' h''} + C_{\phi 2}\overline{\rho u_k'' h''}\frac{\partial \overline{u_i}}{\partial x_k} \quad (5.28)$$

Jones (1994) considered $C_{\phi 1} = 3.0$ and $C_{\phi 2} = 0.5$ for this (PJ model) model. By contrast, Bradley et al. (1994) chose $C_{\phi 1} = 3.0$ and $C_{\phi 2} = 0$ for their model (PB model). Another alternative model (PLV model) was proposed by Lindstedt and Vaos (1999):

$$T_4 + T_5 = -\overline{h''}\frac{\partial \bar{P}}{\partial x_i} + \overline{\rho u_l'' h''}G_{il} + C_{As}\overline{h''}\frac{\partial \bar{P}}{\partial x_i} \quad (5.29)$$

where $C_{As} = 1/3$ and G_{il} is the generalised Langevin coefficient which is a function of Reynolds stress $\overline{\rho u_i'' u_i''}$ and the mean velocity gradient $\partial \overline{u_i}/\partial x_j$ (Lindstedt and Vaos 1999). Domingo and Bray (2000) proposed a model expression (PDB model) for the strict flamelet burning of premixed turbulent flames:

$$T_4 + T_5 = \left\{\frac{\tilde{T}(1-\tilde{T})}{(1+\tau\tilde{T})}\left[-\frac{\partial \bar{P}_R}{\partial x_i} + (1+\tau)\frac{\partial \bar{P}_P}{\partial x_i}\right] - 0.5\left(\overrightarrow{\vec{N}.\overrightarrow{M_i}}\right)\tau.\rho_0 S_L^2(0.7-\tilde{T})\Sigma\right\}(h_{ad} - h_0) \quad (5.30)$$

where $\bar{P}_R$ and $\bar{P}_P$ represent the conditional mean pressure in reactants and products, respectively, $\vec{N} = -\nabla c/|\nabla c|$ is the local flame normal vector and $\overrightarrow{M_i}$ is the unit

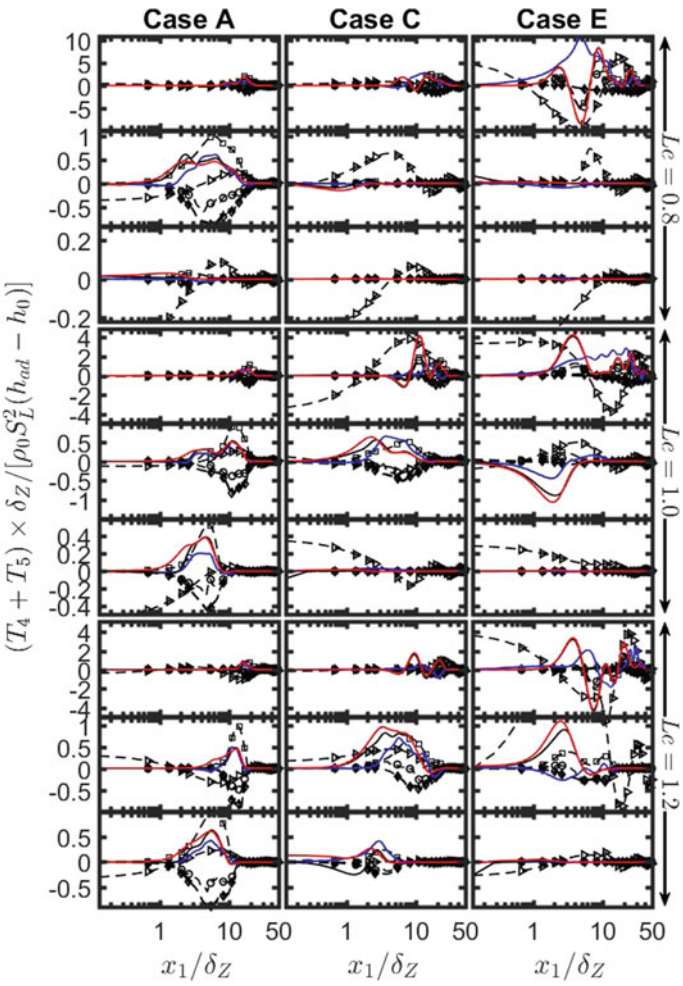

Fig. 5.13 Variation of terms $(T_4+T_5)\times\boldsymbol{\delta}_Z/\left[\boldsymbol{\rho}_0 S_L^2(h_{ad}-h_0)\right]$ from DNS data (——), PN (——), PC (—+—), PD (—◊—), PJO (—□—), PLV (—○—), PDB(—▷—), modified PN model (——) with $\mathbf{x}_1/\boldsymbol{\delta}_\mathbf{Z}$ for cases A, C and E (1st–3rd column) at $t=2\boldsymbol{\delta}_z/S_L$, $6\boldsymbol{\delta}_z/S_L$ and $10\boldsymbol{\delta}_z/S_L$ (1st–3rd row)

vector in the x_i -direction. Nishiki et al. (2006) proposed the following model (PN model) based on a-priori DNS analysis:

$$T_4+T_5=-C_D\frac{\bar{\rho}}{\rho_0}(h_{ad}-h_0)\tilde{T}(1-\tilde{T})\tau\frac{\partial\bar{P}}{\partial x_i}-C_{E1}\frac{\tilde{\varepsilon}}{\tilde{k}}\overline{\rho u_i'' h''}+C_{E2}\tau.S_L\overline{w_T}(1-\tilde{T})^{1.7} \tag{5.31}$$

where $C_D = 0.8$, $C_{E1} = 0.38$ and $C_{E2} = 0.66$ are the model constants. In the context of BML analysis $\overline{h''}$ can be expressed as $\overline{h''} = (\bar{\rho}/\rho_0)(h_{ad} - h_0)\tilde{T}(1-\tilde{T})\tau$ when the pdf of T can be assumed to follow a bi-modal distribution with impulses at $T = 0$ and $T = 1.0$ (Bray 1980). Thus, the first term on the right-hand side of Eq. (5.31) accounts for the contribution of $T_4 = -\overline{h''}\partial\bar{P}/\partial x_i$.

The predictions of all these model are compared to $(T_4 + T_5)$ extracted from DNS data for cases A, C and E in Fig. 5.13 for different time instants. It is clear from Fig. 5.13 that each of the PL, PC and PD models exhibits negative values for all cases, and fails to capture both the qualitative and quantitative behaviours of $(T_4 + T_5)$ extracted from DNS data. These models (i.e. PL, PC and PD models) were originally proposed for incompressible non-reacting flows (Launder 1989; Craft et al. 1993; Durbin 1993; Jones 1994) where the contribution of $-\overline{h''}\partial\bar{P}/\partial x_i$ was ignored. However, it can be seen from Fig. 5.12 that T_4 plays a key role in turbulent scalar flux transport in turbulent premixed flames, and thus the PL, PC and PD models do not adequately capture the behaviour of $(T_4 + T_5)$. The PJ model predicts positive values of $(T_4 + T_5)$ but overpredicts the magnitude obtained from DNS data in case A. The quantitative agreement between the PJ model and DNS data in case C is better than case A. However, the prediction of the PJ model does not adequately capture the behaviour of $(T_4 + T_5)$ for high values of $u'/S_L \sim Re_t^{1/4} Ka^{1/2} \sim Re_t^{1/2} Da^{-1/2}$ (e.g. case E) and at some time instants (e.g. $t \geq 6\delta_Z/S_L$) this model also does not even predict the correct qualitative behaviour. The PB model satisfactorily captures the qualitative behaviour of $(T_4 + T_5)$ with some underprediction for case A until $t \leq 8\delta_Z/S_L$. However, the PB model locally overpredicts $(T_4 + T_5)$ at the later times (see $t > 10\delta_Z/S_L$). The PB model shows some qualitative agreement with DNS data in cases C and E at early times when the flame is away from the wall (e.g. $t = 4\delta_Z/S_L$), whereas both the qualitative and quantitative agreement remain poor at later times when the flame quenching is in progress.

The PLV model captures the qualitative behaviour of DNS in case A, but it overpredicts the magnitude of $(T_4 + T_5)$ for all time instants shown here. For cases with high $u'/S_L \sim Re_t^{\frac{1}{4}} Ka^{\frac{1}{2}} \sim Re_t^{\frac{1}{2}} Da^{-\frac{1}{2}}$ (e.g. cases C and E) the PLV model overpredicts the DNS data for $t \leq 6\delta_Z/S_L$ when the flame is away from the wall. As the flame approaches the wall the PLV models fails to capture both quantitative and qualitative behaviours obtained from DNS data. Whilst the PDB model captures the qualitative behaviour but overpredicts the magnitude of $(T_4 + T_5)$ for case A when the flame is away from the wall (e.g. $t = 4\delta_Z/S_L$), as the flame starts to approach the wall the PDB model predicts negative values whereas $(T_4 + T_5)$ remains positive. The predictions of the PDB model do not perform satisfactorily for high $u'/S_L \sim Re_t^{1/4} Ka^{1/2} \sim Re_t^{1/2} Da^{-1/2}$ cases (e.g. cases C and E) and the predictions show large extent of noise. This noise originates due to limited sample size in the evaluation of conditional mean pressures $\bar{P}_R$ and $\bar{P}_P$. This spiky behaviour was also reported in the original paper by the proponents of the model (Domingo and Bray 2000) and previous analyses (Chakraborty and Cant 2009b, 2015) which dealt with

this model. The PDB model was originally proposed for the strict flamelet regime (i.e. $Ka<1$ and $Da>1$) where the pdf of T can be approximated by a bi-modal distribution with impulses at $T=0$ and 1.0 but such an assumption is not valid for the flames (where $Ka>1$ and $Da<1$) considered here. Furthermore, it has been discussed earlier that the pdf of T does not show bi-modality in the near-wall region at any stage of head-on quenching so it is not surprising that the PDB model does not adequately capture the behaviour of (T_4+T_5) during flame quenching.

Finally, the PN model captures both the qualitative and quantitative behaviours of (T_4+T_5) better than the other alternative models. However, for high values of $u^{'}/S_L \sim Re_t^{1/4}Ka^{1/2} \sim Re_t^{1/2}Da^{-1/2}$, the PN model overpredicts the behaviour of (T_4+T_5). The agreement with the PN model prediction and (T_4+T_5) from DNS data deteriorates at later times during flame quenching for all cases.

The models (e.g. PL, PC, PD models) which neglected the leading contribution of $T_4=-\overline{h''}\partial\bar{P}/\partial x_i$ are not successful in predicting the behaviour obtained from DNS data. However, the PJ, PB and PN models, which account for $T_4=-\overline{h''}\partial\bar{P}/\partial x_i$ are more successful in capturing the behaviour of (T_4+T_5) than the PL, PC, PD models which ignore this contribution. However, some near-wall corrections are needed to account for the behaviour of (T_4+T_5) during flame quenching. Here the following near-wall modification has been suggested for the PN model:

$$T_4+T_5=-C_D\frac{\bar{\rho}}{\rho_0}.\tilde{T}(1-\tilde{T})\tau\frac{\partial\bar{P}}{\partial x_i}(h_{ad}-h_0)-C_{E1}^{*}\frac{\tilde{\varepsilon}}{\tilde{k}}\overline{\rho u_i^{''}h^{''}}+C_{E2}^{*}\tau.S_L[\rho_0 S_L\Sigma(h_{ad}-h_0)](1-\tilde{T})^{1.7} \tag{5.32}$$

where $C_{E1}^{*}=0.38\eta_3 5^{1-0.5[\mathrm{erf}(x_1/\delta_Z-\Phi)+1]}$, $C_{E2}^{*}=0.66\eta_3^{1-0.5[\mathrm{erf}(5(\tilde{c}_W-0.5))+1]}$ and $\eta_3=0.5\left[\mathrm{erf}\left(x_1/\delta_Z-0.5(Pe_{min})_L\right)+1\right]$ are the model parameters and $\Phi=0.5(Pe_{min})_L(\mathrm{erf}(8Le-6)+1)$ is the parameterisation of minimum Peclet number for turbulent flames as proposed earlier by Lai and Chakraborty (2016d). This parameterisation accounts for the finding by Lai and Chakraborty (2016d) that the minimum wall Peclet number Pe_{min} for turbulent flames remains comparable to the corresponding laminar flame value $(Pe_{min})_L$ for Le = 1.0 and 1.2 cases, but for Le = 0.8 cases, Pe_{min} assumes a smaller magnitude than the corresponding $(Pe_{min})_L$. Interested readers are referred to Lai and Chakraborty (2016d) for further discussion on wall Peclet number behaviour in head-on quenching of turbulent premixed flames. The involvement of error functions in the model parameters C_{E1}^{*} and C_{E2}^{*} ensure that they approach asymptotically to $C_{E1}=0.38$ and $C_{E2}=0.66$ away from the wall in the absence of flame quenching. The involvement of $\Sigma=\overline{|\nabla c|}$ in the third term on right-hand side of Eq. (5.32) allows for a non-zero prediction at the wall which is identically zero in the PN model because $\overline{w}_T$ vanishes at the wall due to flame quenching in the context of simplified thermochemistry used here. The involvement of $(Pe_{min})_L$ and Φ in C_{E1}^{*} and η_3 implicitly includes flame quenching information into the revised model, whereas $\tilde{c}_W$ dependence of C_{E2}^{*} senses the flame quenching and modifies the value accordingly. It can be seen from Fig. 5.13 that

the modified PN model (Eq. (5.32)) captures the near-wall behaviour of $(T_4 + T_5)$ during flame quenching better than any other available models.

5.3.5 *Modelling of the Molecular Dissipation Terms* $(T_6 + T_7)$

The terms T_6 and T_7 tend to reduce the magnitude of the scalar flux (i.e. behaves as a sink), and are usually modelled together. The most common model for $(T_6 + T_7)$ is the one which was proposed in the context of BML analysis (Bray 1980; Bray et al. 1985) (i.e. referred to as the DBML model in this analysis):

$$T_6 + T_7 = -K_1 \overline{\rho u_i'' h''} \frac{\overline{w}_T}{\left[\bar{\rho}\tilde{T}\left(1-\tilde{T}\right)(h_{ad}-h_0)\right]} \tag{5.33}$$

where $K_1 \approx 0.85$ is the model parameter. An alternative model was proposed by Nishiki et al. (2006) (i.e. DN model) in the following manner:

$$T_6 + T_7 = -C_F \tau S_L \overline{w_T} \tag{5.34}$$

where $C_F \approx 0.4$ is the model parameter. However, Eq. (5.34) is only valid for counter-gradient transport and thus Chakraborty and Cant (2015) suggested a combination of DBML and DL model, which was shown previously to model $(T_6 + T_7)$ satisfactorily even for low Damköhler number combustion without the influence of walls. The expression proposed by Chakraborty and Cant (2009b), (2015) (i.e. DC model) is given by

$$T_6 + T_7 = -0.5 C_F \tau S_L \overline{w_T} - 0.5 K_1 \overline{\rho u_i'' h''} \times \frac{\overline{w}_T}{\left[\bar{\rho}\tilde{T}\left(1-\tilde{T}\right)(h_{ad}-h_0)\right]} \tag{5.35}$$

The predictions of the DBML, DN and DC models are compared to $(T_6 + T_7)$ extracted from DNS data in Fig. 5.14. It can be seen from Fig. 5.14 that the DBML model captures the correct qualitative behaviour of $(T_6 + T_7)$ but it underestimates the negative contribution of $(T_6 + T_7)$ in cases C–E. For cases A and B, the DBML model underpredicts both negative (away from the wall) and positive (when the flame is close to the wall) contribution of $(T_6 + T_7)$. The DN model provides a satisfactory qualitative prediction of $(T_6 + T_7)$ for all cases but this model overpredicts (underpredicts) the magnitude of negative (positive) contribution of $(T_6 + T_7)$ for $t \geq 6\delta_Z/S_L$ in cases A and B. In other cases the DN model exhibits overprediction of the magnitude of the negative contribution of $(T_6 + T_7)$. The agreement between the DC model prediction and DNS data remains better than the DBML and DN models. However, the DC model still underpredicts (overpredicts) the magnitude of positive (negative) contribution of $(T_6 + T_7)$ for all cases

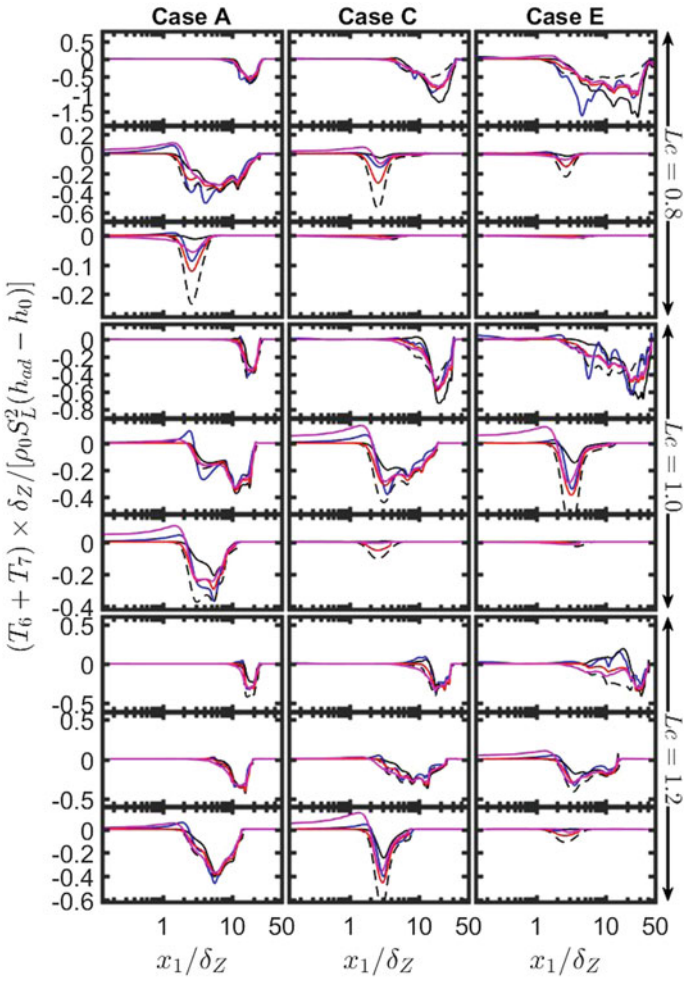

Fig. 5.14 Variation of $(T_6 + T_7) \times \boldsymbol{\delta}_Z / \left[\boldsymbol{\rho}_0 S_L^2 (h_{ad} - h_0)\right]$ from DNS data (——), DBML (——), DN (— —) and DC (——) and New model (——) with $\mathbf{x_1}/\boldsymbol{\delta_Z}$ for cases A, C and E (first–third column) at $t = 2\boldsymbol{\delta}_z/S_L, 6\boldsymbol{\delta}_z/S_L$ and $10\boldsymbol{\delta}_z/S_L$ (first–third row)

considered here, but this modelling inaccuracy is much smaller in extent in comparison to the DN model. It can further be seen from Fig. 5.14 that all the available models (i.e. DBML, DN and DC models) cannot predict the non-zero contributions of $(T_6 + T_7)$ in the near-wall region (and at the wall) because T_7 exhibits non-zero values even when the flame is quenched (i.e. $\overline{\dot{w}_T} = 0$). To avoid this problem, the following modification to the DN model is proposed here (referred to here as the new model):

$$(T_6+T_7) = -0.5C_F\tau S_L[\rho_0 S_L \Sigma Q^p(h_{ad}-h_0)] - 0.5K_1\overline{\rho u_i^{''} h^{''}} \times \frac{\overline{\dot{w}_T}}{\left[\bar{\rho}\tilde{T}\left(1-\tilde{T}\right)(h_{ad}-h_0)\right]} \tag{5.36i}$$

where

$$Q = \mathrm{erf}[2(\tilde{c}_W - 0.5)] \text{and} \, p = 0.5\left[\mathrm{erf}\left(x_1/\delta_Z - 0.7(Pe_{\min})_L\right)+1\right] \tag{5.36ii}$$

The involvement of $\Sigma = \overline{|\nabla c|}$ allows for a non-zero prediction at the wall which was not possible by the other alternative models. At the beginning of quenching, a positive value of (T_6+T_7) is obtained at the wall but it becomes negative at later stages. The model parameter Q accounts for the change of sign of (T_6+T_7) depending on the value of Favre-averaged progress variable at the wall $\tilde{c}_W$, whereas p ensures that Q^p modifies the magnitude of Eq. (5.36i) to predict (T_6+T_7) extracted from DNS data. Here, $(Pe_{\min})_L$ dependence of p implicitly accounts for the reacting boundary layer information and the error functions in Eq. (5.36ii) ensure that Eq. (5.36i) reduces to Eq. (5.35) for $x_1/\delta_Z \gg (Pe_{\min})_L$. It is evident from Fig. 5.14 that Eq. (5.36i) satisfactorily captures both qualitative and quantitative behaviours of (T_6+T_7) both away from and close to the wall.

5.3.6 Modelling of the Reaction Rate Velocity Correlation Term T_8

The model proposed for the reaction rate velocity correlation term $T_8 = \overline{u_i^{''}\dot{w}_T}$ in the context of BML analysis (referred to as the RB model here) takes the form (Bray 1980; Bray et al. 1985):

$$T_8 = C_R\left(\varphi_m - \tilde{T}\right)\overline{\dot{w}_T}\frac{\overline{\rho u_i^{''} h^{''}}}{\overline{\rho h^{''2}}}(h_{ad}-h_0) \tag{5.37}$$

where the model parameters are given by $C_R \approx 1$ and $\varphi_m \approx 0.5$. A-priori DNS analysis by Chakraborty and Cant (2015) showed that the RB model captures the qualitative behaviour of T_8 even for low Damköhler number (i.e. $Da < 1$) combustion, but revealed some turbulent Reynolds number dependence of φ_m and the following parameterisation was proposed for φ_m:

$$\varphi_m = 0.57 + 0.6 erfc[(Re_L+1)/10] \tag{5.38}$$

Equation (5.37) with φ_m parameterisation given by Eq. (5.38) will henceforth be referred to as the RB-M model. The predictions of the RB and RB-M models are compared to T_8 extracted from DNS data in Fig. 5.15 for cases A, C and E for

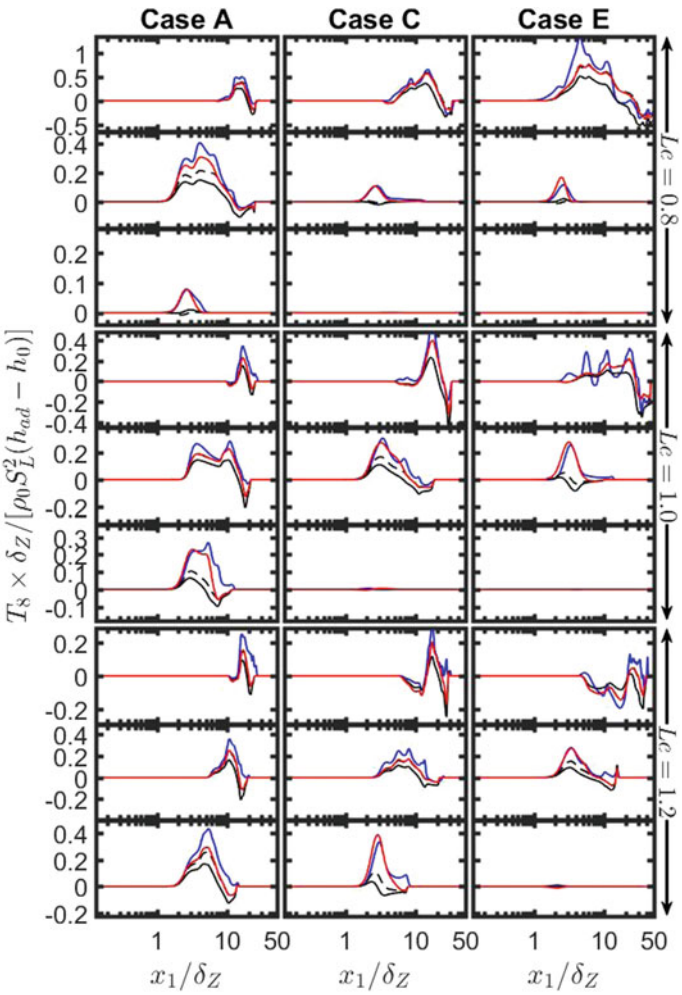

Fig. 5.15 Variation of $T_8 \times \boldsymbol{\delta}_Z / \left[\rho_0 S_L^2 (h_{ad} - h_0)\right]$ from DNS data (——), RB (▬▬), RBM (▬ ▬) and New model (——) with $\mathbf{x}_1/\boldsymbol{\delta}_\mathbf{Z}$ for cases A, C and E (1st–3rd column) at $t = 2\boldsymbol{\delta}_z/S_L, 6\boldsymbol{\delta}_z/S_L$ and $10\boldsymbol{\delta}_z/S_L$ (first–third row)

different time instants. Figure 5.15 shows that the RB model captures quantitative and qualitative behaviours of T_8 for cases A before the initiation of flame quenching in this case (i.e. $t \leq 6\delta_Z/S_L$). However, this model overpredicts the magnitude of positive and negative values of T_8 close to the wall and away from the wall respectively for case A at $t > 6\delta_Z/S_L$. For cases C–E, the RB model overpredicts of both negative (away from wall region) and positive (near-wall region) values of T_8. As the flame propagates towards the wall and the flame starts to quench, the RB model fails to predict the reaction rate velocity correlation term T_8, as shown in

Fig. 5.15. By contrast, the RB-M model captures both quantitative and qualitative behaviour of reaction rate–velocity correlation term T_8 more satisfactorily than the RB model in spite of slight underprediction of T_8 for cases with high values of $u^{'}/S_L \sim Re_t^{\frac{1}{4}} Ka^{\frac{1}{2}} \sim Re_t^{\frac{1}{2}} Da^{-\frac{1}{2}}$ (e.g. cases D and E). The prediction of T_8 can further be improved by modifying the RB-M model in the following manner (i.e. new model):

$$T_8 = C_R\left(\varphi_m exp\left[2\left(\tilde{c}_W - \tilde{T}_W\right)\xi\right] - \tilde{T}\right)\overline{\dot{w}_T} \times \frac{\overline{\rho u_i^{''} h^{''}}}{\overline{\rho h^{''2}}}\left(h_{ad} - h_0\right) \tag{5.39i}$$

where

$$\xi = 1 - 0.5\left[\mathrm{erf}\left(x_1/\delta_Z - \left(Pe_{min}\right)_L\right) + 1\right] \tag{5.39ii}$$

The factor $\left(\varphi_m exp\left[2\left(\tilde{c}_W - \tilde{T}_W\right)\xi\right] - \tilde{T}\right)$ approaches $\left(\varphi_m - \tilde{T}\right)$ for $x_1/\delta_Z \gg \left(Pe_{min}\right)_L$. A comparison between the predictions of the RB-M and the new model indicates that $\left(\varphi_m exp\left[2\left(\tilde{c}_W - \tilde{T}_W\right)\xi\right] - \tilde{T}\right)$ in Eq. (5.39) modifies the RB-M model close to the wall depending on the value of $\left(\tilde{c}_W - \tilde{T}_W\right)$ to yield better agreement with model prediction with T_8 extracted from DNS data than the other available models especially in the vicinity of the wall.

5.4 Final Remarks and Conclusions

From the foregoing discussion, it should be evident that DNS data can be suitably processed to assess the performance of the existing models and these models can be modified and model parameters can be extracted from DNS data so that models can accurately predict the unclosed terms and capture the underlying physics. Here, an example is provided in the context of RANS but a similar analysis can be done for LES modelling as well where DNS data needs to be explicitly filtered (i.e. convolution operation is performed) to assess LES closures. This type of analysis is known as a-priori DNS analysis, which plays a key role in the existing model assessment and new model development in the context of both RANS and LES. Although DNS can significantly contribute to the high-fidelity modelling in engineering simulations using RANS and LES, the results of a-priori DNS analysis need to be treated with caution. For example, models for T_1 and $(T_4 + T_5)$ are functions of turbulent kinetic energy $\tilde{k}$ and its dissipation rate $\tilde{\varepsilon}$ but both $\tilde{k}$ and $\tilde{\varepsilon}$ are unclosed. In RANS simulations, $\tilde{k}$ and $\tilde{\varepsilon}$ are modelled and thus their evaluations involve inaccuracies whereas in a-priori analysis exact values of $\tilde{k}$ and $\tilde{\varepsilon}$ are extracted from explicitly Reynolds-averaged DNS data. Thus, it is not possible to predict how the inaccuracies involved in the modelling of $\tilde{k}$ and $\tilde{\varepsilon}$ are going to affect the closure of $\overline{\rho u_i^{''} h^{''}}$ solely based on a-priori analysis. Thus, the models proposed based on a-priori analysis need to be implemented in actual RANS and LES simulations (i.e.

for a-posteriori assessment) as appropriate, to assess if they perform satisfactorily while interacting with other numerical and modelling errors. Moreover, DNS data often represents the flow conditions with moderate values of turbulent Reynolds number and for simple configurations and that is why the models developed using a-priori DNS analysis need to perform well also in a-posteriori assessments based on practical burners involving high Reynolds number and complex flow configurations. It is possible for a model to perform well fortuitously in actual RANS and LES simulations, if two modelling inaccuracies cancel each other or due to the interaction of modelling inaccuracies with numerical errors. Thus, a robust model needs to perform satisfactorily both for a-priori and a-posteriori assessments.

The advancements of high-performance computing will expand the capability of DNS which will increasingly remove the limitations related to moderate values of turbulent Reynolds number, simplification of chemical mechanism and simplicity of flow configuration. This will enable DNS and a-priori analysis to play an increasingly important role in the developments of high-fidelity closures for both RANS and LES in the future. This, in turn, will enable CFD simulations to become a viable tool for the design of combustors and also to play a pivotal role in the development of the future generation of energy-efficient and environment-friendly combustors.

Acknowledgements The authors are grateful to Engineering and Physical Sciences Research Council (EPSRC) and ARCHER for financial and computational supports.

References

Alshaalan TM, Rutland CJ (1998) Turbulence, scalar transport, and reaction rates in flame-wall interaction. Proc Combust Inst 27:793–800

Aspden AJ, Day MS, Bell JB (2011) Turbulence-flame interactions in lean premixed hydrogen: transition to the distributed burning regime. J Fluid Mech 680:287–320

Bachelor GK, Townsend AA (1948) Decay of turbulence in final period. Proc R Soc Lond A194:527–543

Baum, T., Haworth, D., Poinsot, T., and Darabiha, N., (1994), Direct Numerical Simulation of H_2/O_2 /N_2 flames with complex chemistry in two-dimensional turbulent flows. J Fluid Mech 284:1–32

Boger M, Veynante D, Boughanem H, Trouvé A (1998) Direct Numerical Simulation analysis of flame surface density concept for Large Eddy Simulation of turbulent premixed combustion. Proc Combust Inst 27:917–925

Bradley D, Gaskell PH, Gu XJ (1994) Application of a Reynolds stress, stretched flamelet, mathematical model to computations to turbulent burning velocities and comparison with experiments. Combust Flame 96:221–248

Bray KNC (1980) Turbulent flows with premixed reactants. In Libby PA, Williams FA (eds) Turbulent reacting flows. Springe Heidelburg, pp 115–183

Bray KNC, Libby PA, Moss JB (1985) Unified modelling approach for premixed turbulent combustion—part I: general formulation. Combust Flame 61:87–102

Bruneaux G, Poinsot T, Ferziger JH (1997) Premixed flame–wall interaction in a turbulent channel flow: budget for the flame surface density evolution equation and modelling. J Fluid Mech 349:191–219

Cant RS (1999) Direct numerical simulation of premixed turbulent flames. Phil Trans R Soc Lond A 357:3583–3604
Cant RS, Bray KNC (1988) Strained laminar flamelet calculations of premixed turbulent combustion in a closed vessel. Proc Combust Inst 22:791–799
Chakraborty N, Cant S (2004) Unsteady effects of strain rate and curvature on turbulent premixed flames in an inlet-outlet configuration. Combust Flame 137:129–147
Chakraborty N, Cant RS (2005) Influence of Lewis Number on curvature effects in turbulent premixed flame propagation in the thin reaction zones regime. Phys Fluids 2005:105105
Chakraborty N, Cant RS (2007) A-priori analysis of the curvature and propagation terms of the flame surface density transport equation for large eddy simulation. Phys Fluids 19:105101
Chakraborty N, Cant RS (2009a) Direct numerical simulation analysis of the flame surface density transport equation in the context of large eddy simulation. In: Proceedings of the Combustion Institute, vol 32, pp 1445–1453
Chakraborty N, Cant RS (2009b) Effects of Lewis number on turbulent scalar transport and its modelling in turbulent premixed flames. Combust Flame 156:1427–1444
Chakraborty N, Cant RS (2009c) Physical insight and modelling for Lewis number effects on turbulent heat and mass transport in turbulent premixed flames. Numer Heat Trans A 55:762–779
Chakraborty N, Cant RS (2011) Effects of lewis number on flame surface density transport in turbulent premixed combustion. Combust Flame 158:1768–1787
Chakraborty N, Cant RS (2015) Effects of turbulent Reynolds number on the modelling of turbulent scalar flux in premixed flames. Numer Heat Trans A 67(11):1187–1207
Chakraborty N, Klein M (2008) A priori direct numerical simulation assessment of algebraic flame surface density models for turbulent premixed flames in the context of large eddy simulation. Phys Fluids 20:085108
Chakraborty N, Lipatnikov AN (2013) Conditional velocity statistics for high and low Damköhler number turbulent premixed combustion in the context of Reynolds Averaged Navier Stokes simulations. Proc Combust Inst 34(2013):1333–1345
Chakraborty N, Swaminathan N (2007) Influence of Damköhler number on turbulence-scalar interaction in premixed flames, part ii: model development. Phys Fluids 19:045104
Chakraborty N, Swaminathan N (2010) Effects of Lewis number on scalar dissipation transport and its modelling implications for turbulent premixed combustion. Combust Sci Technol 182:1201–1240
Chakraborty N, Swaminathan N (2011) Effects of Lewis number on scalar variance transport in turbulent premixed flames. Flow Turb Combust 87:261–292
Chakraborty N, Klein M, Cant RS (2007) Stretch rate effects on displacement speed in turbulent premixed flame kernels in the thin reaction zones regime. Proc Combust Inst 31:1385–1392
Chakraborty N, Rogerson JW, Swaminathan N (2008) A-priori assessment of closures for scalar dissipation rate transport in turbulent premixed flames using direct numerical simulation. Phys Fluids 20:045106
Chakraborty N, Klein M, Swaminathan N (2009) Effects of Lewis number on reactive scalar gradient alignment with local strain rate in turbulent premixed flames. Proc Combust Inst 32:1409–1417
Chakraborty N, Klein M, Cant RS (2011a) Effects of turbulent Reynolds number on the displacement speed statistics in the thin reaction zones regime turbulent premixed combustion. J. Combust. 2011:473679
Chakraborty N, Katragadda M, Cant RS (2011b) Effects of Lewis number on turbulent kinetic energy transport in turbulent premixed combustion. Phys Fluids 23:075109
Charlette F, Meneveau C, Veynante D (2002a) A power law wrinkling model for LES of premixed turbulent combustion, part i: Non dynamic formulation and initial tests. Combust Flame 131:159–180
Charlette F, Meneveau C, Veynante D (2002b) A power law wrinkling model for LES of premixed turbulent combustion, part ii: dynamic formulation. Combust Flame 131:181–197

Chen JH, Choudhary A, De Supinski D, Hawkes ER, Klasky S, Liao WK, Ma KL, Mellor-Crummey J, Podhorski N, Sankaran R, Shende S, Yoo CS (2009) Terascale direct numerical simulations of turbulent combustion using S3D. Comput Sci Discov 2(1):015001

Craft T, Graham L, Launder B (1993) Impinging jet studies for turbulence model assessment –II. An examination of the performance of four turbulence models. Int J Heat Mass Trans 36:2687–2697

Daly BJ, Harlow FH (1970) Transport equations of turbulence. Phys Fluids A 13:2634–2649

Domingo P, Bray KNC (2000) Laminar flamelet expressions for pressure fluctuation terms in second moment models of premixed turbulent combustion. Combust Flame 121:555–574

Dopazo C, Cifuentes L, Martin J, Jimenez C (2015) Strain rates normal to approaching isoscalar surfaces in a turbulent premixed flame. Combust Flame 162:1729–1736

Dunstan TD, Swaminathan N, Bray KNC (2012) Influence of flame geometry on turbulent premixed flame propagation: A DNS investigation. J Fluid Mech 709:191–222

Durbin PA (1993) A Reynolds stress model for near-wall turbulence. J Fluid Mech 249:465–493

Durbin PA, Pettersson Reif BA (2001) Statistical theory and modelling for turbulent flows. Willey

Dutt P (1988) Stable boundary conditions and difference schemes for Navier Stokes equations. J Num Anal 25:245–267

Echekki T, Chen JH (1996) Unsteady strain rate and curvature effects in turbulent premixed methane-air flames. Combust Flame 106:184–202

Echekki T, Chen JH (1999) Analysis of the contribution of curvature to premixed flame propagation. Combust Flame 118:303–311

Fox RO (2003) Computational models for turbulent reacting flows. Cambridge University Press, Cambridge

Gao Y, Chakraborty N (2016) Modelling of Lewis Number dependence of Scalar dissipation rate transport for Large Eddy Simulations of turbulent premixed combustion. Numer Heat Trans A 69:1201–1222

Gao Y, Chakraborty N, Swaminathan N (2014) Algebraic closure of Scalar Dissipation Rate for Large Eddy Simulations of turbulent premixed combustion. Combust Sci Technol 186:1309–1337

Gao Y, Chakraborty N, Swaminathan N (2015a) Scalar dissipation rate transport and its modelling for Large Eddy Simulations of turbulent premixed combustion. Combust Sci Technol 187:362–383

Gao Y, Chakraborty N, Swaminathan N (2015b) Dynamic scalar dissipation rate closure for Large Eddy Simulations of turbulent premixed combustion: a direct numerical Simulations analysis. Flow Turb Combust. 95:775–802

Gao Y, Chakraborty N, Klein M (2016) Assessment of sub-grid scalar flux modelling in premixed flames for Large eddy simulations: a-priori direct Numerical Simulation. Eur J Mech Fluids-B 52:97–108

Gruber A, Sankaran R, Hawkes ER, Chen JH (2010) Turbulent flame-wall interaction: a direct numerical simulation study. J Fluid Mech 658:5–32

Gruber A, Chen JH, Valiev D, Law CK (2012) Direct numerical simulation of premixed flame boundary layer flashback in turbulent channel flow. J Fluid Mech 709:516–542

Han I, Huh KH (2008) Roles of displacement speed on evolution of flame surface density for different turbulent intensities and Lewis numbers for turbulent premixed combustion. Combust Flame 152:194–205

Hawkes ER, Chen JH (2004) Direct numerical simulation of hydrogen-enriched lean premixed methane–air flames. Combust Flame 138:242–258

Hawkes ER, Chatakonda O, Kolla H, Kerstein AR, Chen JH (2012) A petascale direct numerical simulation study of the modelling of flame wrinkling for large-eddy simulations in intense turbulence. Combust Flame 159:2690–2703

Haworth DC (2003) Applications of turbulent combustion modelling. In: Turbulent combustion, lecture series 2003–04. von Karman Institute for Fluid Dynamics, 17–21 March 2003

Haworth DC, Poinsot TJ (1992) Numerical simulations of Lewis number effects in turbulent premixed flames. J Fluid Mech 244:405–436

Haworth DC, Cuenot B, Blint RJ, Poinsot TJ (2000) Numerical simulations of turbulent Propane-Air combustion with non homogeneous reactants. Combust Flame 121:395–417

Huang WM, Vosen SR, Greif R (1986) Heat transfer during laminar flame quenching. Proc Combust Inst 21:1853–1860

Im HG, Chen JH (2002) Preferential diffusion effects on the burning rate of interacting turbulent premixed Hydrogen-Air flames. Combust Flame 126:246–258

Im HG, Arias PG, Chaudhuri S, Uranakara HA (2016) Direct numerical simulations of statistically stationary turbulent premixed flames. Combust Sci Technol 188:1182–1198

Jarosinsky J (1986) A survey of recent studies on flame extinction. Combust Sci Technol 12:81–116

Jenkins KW, Cant RS (1999) DNS of turbulent flame kernels. In: Knight D, Sakell T (eds) Proceedings of the second AFOSR conference on DNS and LES. Rutgers University, Kluwer Academic Publishers, pp 192–202

Jones WP (1994) Turbulence modelling and numerical solution methods for variable density and combusting flows. In: Libby A, Williams FA (eds) Turbulent Reacting Flows (P. Academic Press, London, pp 309–374

Katragadda M, Malkeson SP, Chakraborty N (2011) Modelling of the tangential strain rate term of the Flame Surface Density transport equation in the context of Reynolds Averaged Navier Stokes Simulation. Proc Combust Inst 33:1429–1437

Klein M, Kasten C, Gao Y, Chakraborty N (2015) A-priori Direct Numerical Simulation assessment of sub-grid scale stress tensor closures for turbulent premixed combustion. Comput Fluids 122:1–11

Kolla H, Rogerson J, Chakraborty N, Swaminathan N (2009) Prediction of turbulent flame speed using scalar dissipation rate. Combust Sci Technol 181:518–535

Lai J, Chakraborty N (2016a) Statistical behaviour of scalar dissipation rate for head on quenching of turbulent premixed flames: a direct numerical simulation analysis. Combust Sci Technol 188:250–276

Lai J, Chakraborty N (2016b) A-priori Direct Numerical Simulation modelling of scalar dissipation rate transport in head-on quenching of turbulent premixed flames. Combust Sci Technol 188:1440–1471

Lai J, Chakraborty N (2016c) Modelling of progress variable variance transport in head on quenching of turbulent premixed flames: a direct numerical simulation analysis. Combust Sci Technol 188:1925–1950

Lai J, Chakraborty N (2016d) Effects of Lewis number on head on quenching of turbulent premixed flame: a direct numerical simulation analysis. Flow Turb Combust 96:279–308

Lai J, Moody A, Chakraborty N (2017) Turbulent kinetic energy transport in head-on quenching of turbulent premixed flames in the context of Reynolds Averaged Navier Stokes simulations. Fuel 199:456–477

Launder BL (1989) Second-moment closure: present… and future. Int J Heat Fluid Flow 10:282–300

Lindstedt RP (2011) Transported probability density function methods for turbulent premixed flames with second moment methods. In: Swaminathan N, Bray KNC eds Turbulent premixed flames. Cambridge University Press, pp 102–130

Lindstedt RP, Vaos EM (1999) Modelling of premixed turbulent flames with second moment methods. Combust Flame 116:461–485

Nishiki S, Hasegawa T, Borghi R, Himeno R (2006) Modelling of turbulent scalar flux in turbulent premixed flames based on DNS databases. Combust Theor Model 10:39–55

Peters N (2000) Turbulent combustion. Cambridge University Press, Cambridge

Poinsot T, Lele SK (1992) Boundary conditions for direct simulation of compressible viscous flows. J. Comp. Phys. 101:104–129

Poinsot T, Veynante D (2001) Theoretical and numerical combustion. R.T. Edwards Inc., Philadelphia, USA

Poinsot T, Veynante D, Candel S (1990) Diagrams of premixed turbulent combustion based on direct simulation. Proc Combust Inst 23:613–619

Poinsot T, Veynante D, Candel S (1991) Quenching processes and premixed turbulent combustion diagrams. J Fluid Mech 228:561–606
Poinsot T, Haworth D, Bruneaux G (1993) Direct simulation and modeling of flame-wall interaction for premixed turbulent combustion. Combust Flame 95:118–132
Poludnenko AY, Oran ES (2010) The interaction of high-speed turbulence with flames: Global properties and internal flame structure. Combust Flame 157:995–1011
Pope SB (2000) Turbulent flows. Cambridge University Press, Cambridge
Prosser R (2007) Towards improved boundary conditions for the DNS and LES turbulent subsonic flows. J Comp Phys 222:469–474
Rogallo RS (1981) Numerical experiments in homogeneous turbulence, NASA technical memorandum 81315. NASA Ames Research Center, California
Rutland CJ, Cant RS (1994) Turbulent transport in premixed flames. In: Proceedings of the summer program. Center for Turbulence Research, pp 75–94
Rutland C, Trouvé A (1993) Direct simulations of premixed turbulent flames with nonunity Lewis numbers. Combust Flame 94:41–57
Sankaran R, Hawkes ER, Chen JH, Lu T, Law CK (2007) Structure of a spatially developing turbulent lean methane–air Bunsen flame. In: Proceedings of the Combustion Institute, vol 31, pp 1291–1298
Sellmann J, Lai J, Chakraborty N, Kempf AM (2017) Flame Surface Density based modelling of head-on quenching of turbulent premixed flames. Proc Combust Inst 36:1817–1825
Sutherland JC, Kennedy CA (2003) Improved boundary conditions for viscous, reacting, compressible flows. J Comp Phys 191:502–524
Swaminathan N, Bilger RW (2001) Analyses of conditional moment closure for turbulent premixed flames. Combust Theor Model 5:1–20
Swaminathan N, Bilger RW, Cuenot B (2001) Relationship between turbulent scalar flux and conditional dilatation in premixed flames with complex chemistry. Combust Flame 126:1764–1779
Thompson KW (1987) Time dependent boundary conditions for hyperbolic systems. J. Comp. Phys 68:1–24
Turns SR (2011) An introduction to combustion: concepts and applications, 3rd edn. McGraw Hill
Veynante D, Trouvé A, Bray KNC, Mantel T (1997) Gradient and counter-gradient scalar transport in turbulent premixed flames. J Fluid Mech 332:263–293
Vosen SR, Greif R, Westbrook C (1984) Unsteady heat transfer in laminar quenching. Proc Combust Inst 20:76–83
Wang H, Hawkes ER, Chen JH, Zhou B, Li Z, Alden M (2017) Direct numerical simulations of a high Karlovitz number laboratory premixed jet flame- an analysis of flame stretch and flame thickening. J Fluid Mech 815:511–536
Wray AA (1990) Minimal storage time advancement schemes for spectral methods. Unpublished report, NASA Ames Research Center, California
Yoo CS, Im HG (2007) Characteristic boundary conditions for simulations of compressible reacting flows with multi-dimensional, viscous and reaction effects. Combust Theor Model 11:259–286
Zhang S, Rutland CJ (1995) Premixed flame effects on turbulence and pressure related terms. Combust Flame 102:447–461

Chapter 6
RANS Simulations of Premixed Turbulent Flames

Andrei N. Lipatnikov

Abstract While Reynolds-Averaged Navier-Stokes (RANS) simulations are widely used in applied research into premixed turbulent burning in spark ignition piston engines and gas-turbine combustors, fundamental challenges associated with modeling various unclosed terms in the RANS transport equations that describe premixed flames have not yet been solved. These challenges stem from two kinds of phenomena. First, thermal expansion due to heat release in combustion reactions affects turbulent flow and turbulent transport. Such effects manifest themselves in the so-called counter gradient turbulent transport, flame-generated turbulence, hydrodynamic instability of premixed combustion, etc. Second, turbulent eddies wrinkle and stretch reaction zones, thus, increasing their surface area and changing their local structure. Both the former effects, i.e. the influence of combustion on turbulence, and the latter effects, i.e. the influence of turbulence on combustion, are localized to small scales unresolved in RANS simulations and, therefore, require modeling. In the present chapter, the former effects, their physical mechanisms and manifestations, and approaches to modeling them are briefly overviewed, while discussion of the latter effects is more detailed. More specifically, the state-of-the-art of RANS modeling of the influence of turbulence on premixed combustion is considered, including widely used approaches such as models that deal with a transport equation for the mean Flame Surface Density or the mean Scalar Dissipation Rate. Subsequently, the focus of discussion is placed on phenomenological foundations, closed equations, qualitative features, quantitative validation, and applications of the so-called Turbulent Flame Closure (TFC) model and its extension known as Flame Speed Closure (FSC) model.

Keywords Turbulent combustion · Premixed turbulent flames · Modelling RANS simulations · validation

A. N. Lipatnikov (✉)
Chalmers University of Technology, 41296 Gothenburg, Sweden
e-mail: lipatn@chalmers.se

© Springer Nature Singapore Pte Ltd. 2018

S. De et al. (eds.), *Modeling and Simulation of Turbulent Combustion*, Energy, Environment, and Sustainability, https://doi.org/10.1007/978-981-10-7410-3_6

6.1 Introduction

In this chapter, the problem of unsteady multidimensional numerical simulations of premixed turbulent combustion is stated, transport equations that describe variations of mean (Favre-averaged) mixture and flow characteristics in turbulent flames are introduced, and fundamental challenges associated with applications of these equations are discussed. Various approaches to modeling unknown terms in the Favre-averaged transport equations are briefly overviewed, followed by a detailed discussion of foundations, equations, qualitative features, quantitative validation, and engine applications of the so-called Turbulent Flame Closure (TFC) model, which is implemented into most commercial CFD codes, as well as its extension known as Flame Speed Closure (FSC) model.

6.2 Mathematical Background

The goal of this section is to introduce transport equations that RANS models of premixed turbulent combustion deal with.

6.2.1 General Transport Equations

A general set of transport equations that model reacting flows is discussed in detail elsewhere (Williams 1985). When modeling premixed turbulent combustion, a less general set of transport equations is commonly used by invoking the following simplifications (Libby and Williams 1994)

- The molecular mass and heat fluxes are approximated by Fick's and Fourier's laws, respectively.
- The Soret and Dufour effects, pressure gradient diffusion, and bulk viscosity are negligible.
- There is no body force.
- The Mach number is much less than unity.
- The mixture is an ideal gas, i.e.,

$$pM = \rho R^o T, \tag{6.1}$$

where p, ρ, and T are the pressure, density, and temperature, respectively, M is the molecular weight of the mixture, and R^o is the universal gas constant.

Under the above assumptions, combustion of gases is modeled by the following transport equations.

Mass conservation (continuity) equation reads

$$\frac{\partial \rho}{\partial t} + \frac{\partial}{\partial x_j}\left(\rho u_j\right) = 0, \tag{6.2}$$

where t is the time, x_j and u_j are the spatial coordinates and flow velocity components, respectively. Henceforth, the summation convention applies for a repeated index that indicates the coordinate axis, e.g., the repeated index j in Eq. (6.2), if the opposite is not stated.

Momentum conservation (Navier–Stokes) equation reads

$$\frac{\partial}{\partial t}\left(\rho u_i\right) + \frac{\partial}{\partial x_j}\left(\rho u_i u_j\right) = \frac{\partial \tau_{ij}}{\partial x_j} - \frac{\partial p}{\partial x_i}, \tag{6.3}$$

where

$$\tau_{ij} = \mu\left(\frac{\partial u_i}{\partial x_j} + \frac{\partial u_j}{\partial x_i} - \frac{2}{3}\frac{\partial u_l}{\partial x_l}\delta_{ij}\right) \tag{6.4}$$

is the viscous stress tensor, δ_{ij} is the Kronecker delta, and the dynamic molecular viscosity μ depends on pressure, temperature, and mixture composition. Methods for evaluating the viscosity and other molecular transport coefficients (e.g., the mass diffusivity D_k of species k in a mixture or the heat diffusivity κ of the mixture) are discussed elsewhere (Giovangigli 1999; Hirschfelder et al. 1954). In the present chapter, these transport coefficients are considered to be known functions of pressure and temperature for each particular mixture.

Species mass conservation equations read

$$\frac{\partial}{\partial t}\left(\rho Y_k\right) + \frac{\partial}{\partial x_j}\left(\rho u_j Y_k\right) = \frac{\partial}{\partial x_j}\left(\rho D_k \frac{\partial Y_k}{\partial x_j}\right) + \dot{\omega}_k, \tag{6.5}$$

where Y_k is the mass fraction of species k, $\dot{\omega}_k$ is the mass rate of creation ($\dot{\omega}_k > 0$) or consumption ($\dot{\omega}_k < 0$) of the species k, and the summation convention does not apply for the species index k. If N species $\mathscr{S}_k$ ($k = 1, \ldots, N$) participate in M reactions

$$\sum_{k=1}^{N} a_{km}\mathscr{S}_k \rightleftharpoons \sum_{k=1}^{N} b_{km}\mathscr{S}_k, \tag{6.6}$$

where $m = 1, \ldots, M$, then, the rate

$$\dot{\omega}_k = \sum_{m=1}^{M} \dot{\omega}_{km}, \tag{6.7}$$

where

$$\dot{\omega}_{km} = a_{km} k_{b,m} \rho^{b_m} \prod_{n=1}^{N} Y_n^{b_{nm}} - b_{km} k_{f,m} \rho^{a_m} \prod_{n=1}^{N} Y_n^{a_{nm}}, \tag{6.8}$$

$a_m = \sum_{k=1}^{N} a_{km}$ and $b_m = \sum_{k=1}^{N} b_{km}$ are orders of the forward and backward reactions m, respectively, and the forward and backward reaction rates $k_{f,m}$ and $k_{b,m}$, respectively, have dimensions of $(\mathrm{kg/m^3})^{a_m - 1}\mathrm{s}^{-1}$ and $(\mathrm{kg/m^3})^{b_m - 1}\mathrm{s}^{-1}$, respectively. The reaction rates are commonly modeled as follows:

$$k_{f,m} = B_{f,m} T^{n_{f,m}} \exp\left(-\frac{\Theta_{f,m}}{T}\right), \qquad k_{b,m} = B_{b,m} T^{n_{b,m}} \exp\left(-\frac{\Theta_{b,m}}{T}\right), \tag{6.9}$$

where $B_{f,m}, n_{f,m}$ and $B_{b,m}, n_{b,m}$ are constants of the forward and backward reactions m, respectively, $\Theta_{f,m}$ and $\Theta_{b,m}$ are their activation temperatures, with a ratio of $\Theta_{f,m}/T$ being large for many important combustion reactions.

In premixed flames, energy conservation can be modeled using a transport equation for specific mixture enthalpy h, specific mixture internal energy $e = h - p/\rho$, or temperature. For instance, the enthalpy conservation equation reads

$$\frac{\partial}{\partial t}(\rho h) + \frac{\partial}{\partial x_j}\left(\rho u_j h\right) = \frac{\partial p}{\partial t} + \frac{\partial}{\partial x_j}\left[\frac{\mu}{Pr}\frac{\partial h}{\partial x_j} + \mu \sum_{k=1}^{N}\left(\frac{1}{Sc_k} - \frac{1}{Pr}\right) h_k \frac{\partial Y_k}{\partial x_j}\right] - q_R, \tag{6.10}$$

where $Pr = \mu/\rho\kappa = \nu/\kappa$ and $Sc_k = \mu/\rho D_k$ are the Prandtl and Schmidt numbers, respectively, $\nu = \mu/\rho$ is the molecular kinematic viscosity, q_R is radiative heat loss,

$$h_k = \int_{T_0}^{T} c_{p,k} dT + \Delta h_k \tag{6.11}$$

is the specific enthalpy of species k per unit mass,

$$h = \sum_{k=1}^{N} Y_k h_k = \sum_{k=1}^{N} \int_{T_0}^{T} c_{p,k} dT + \sum_{k=1}^{N} Y_k \Delta h_k = \int_{T_0}^{T} c_p dT + \sum_{k=1}^{N} Y_k \Delta h_k \tag{6.12}$$

is the specific mixture enthalpy per unit mass, Δh_k is the enthalpy of species k at a reference temperature T_0, and $c_p = \sum_{k=1}^{N} c_{p,k}$ is the specific heat of the mixture at constant pressure. In the rest of this chapter, adiabatic burning will be considered, i.e., $q_R = 0$ if the opposite is not specified.

If the specific heats $c_{p,k}$ are equal to the same c_p for all species, then, the following temperature transport equation

$$c_p \frac{\partial}{\partial t}(\rho T) + c_p \frac{\partial}{\partial x_j}\left(\rho u_j T\right) = \frac{\partial p}{\partial t} + \frac{\partial}{\partial x_j}\left(\lambda \frac{\partial T}{\partial x_j}\right) - \sum_{k=1}^{N} (\Delta h_k \dot{\omega}_k) \tag{6.13}$$

can be obtained by substituting Eq. (6.12) into Eq. (6.10) and using Eq. (6.5). Here, $\lambda = \rho c_p \kappa$ is the heat conductivity of the mixture. For simulations of turbulent combustion, Eq. (6.10) is more suitable than Eq. (6.13), because the latter equation involves highly nonlinear source term $\sum_{k=1}^{N} (\Delta h_k \dot{\omega}_k)$, whose magnitude fluctuates strongly in a premixed turbulent flame.

Equations (6.1)–(6.12) can be integrated numerically to study a 1D laminar flame. Such a research method is routinely used today and a number of advanced software packages are available on the market.

If Eqs. (6.1)–(6.12) are numerically solved to simulate a 3D turbulent flame, such computations should be performed using a fine mesh that resolves both the smallest turbulent eddies and spatial variations of species within thin reaction zones. Such a research method is known as Direct Numerical Simulation (DNS).

DNS is an expensive numerical tool and its applications are mainly limited to simple model problems. Even in a constant-density non-reacting case, the size of a numerical mesh required for 3D DNS study of a turbulent flow is on the order of Re_t^3 (Pope 2000), because (i) a ratio of length scales of the largest and smallest eddies in such a flow is on the order of $\mathrm{Re}_t^{3/4}$ and (ii) time step Δt is typically proportional to the mesh step $\Delta x \propto \mathrm{Re}_t^{3/4}$ in such simulations. Therefore, a DNS of a flow characterized by a really high turbulent Reynolds number $\mathrm{Re}_t = u'L/\nu$ is still a challenging task. Here, u' and L designate rms velocity and an integral length scale of turbulence, respectively.

In the case of premixed combustion, the main challenge consists not only of a significant increase in a number of transport equations to be solved, i.e., $O(N)$ Eq. (6.5), but also (and mainly) in extension of the range of spatial scales to be resolved. Accordingly, the majority of contemporary DNS studies of premixed turbulent flames deal with moderate Re_t (typically, well below 1000) and with comparable values of L and laminar flame thickness in order for ranges of spatial scales associated with combustion and turbulence to well overlap. A 3D DNS study of a turbulent premixed flame characterized by a large (when compared to the laminar flame thickness) length scale L and, hence, by $\mathrm{Re}_t = O(1000)$ or higher is still an unfeasible task. Accordingly, such flames are numerically modeled invoking simplified approaches such as Reynolds-Averaged Navier Stokes (RANS) or Large Eddy Simulation (LES). The former research tool will be discussed in the rest of the present chapter.

6.2.2 *Favre-Averaged Transport Equations for First Moments*

RANS approach is based on the decomposition of any (scalar, vector, tensor, etc.) field $q(\mathbf{x}, t)$ into mean $\bar{q}(\mathbf{x}, t)$ and fluctuating $q'(\mathbf{x}, t) \equiv q(\mathbf{x}, t) - \bar{q}(\mathbf{x}, t)$ fields. By definition $\overline{\bar{q}(\mathbf{x}, t)} = \bar{q}(\mathbf{x}, t)$ and, hence, $\overline{q'(\mathbf{x}, t)} = \bar{q}(\mathbf{x}, t) - \overline{\bar{q}(\mathbf{x}, t)} = 0$. The mean field $\bar{q}(\mathbf{x}, t)$ can be determined by averaging the field $q(\mathbf{x}, t)$ over a sufficiently long time interval, surface, or an ensemble of statistically equivalent realizations of a stochastic process. Taking average over time is most suitable in the case of a statistically stationary process, e.g., burning behind a flame-holder. In such a case, $\bar{q}$ does not depend on time. Taking average over a surface is most suitable in the case of a statistically 1D process, e.g., a statistically planar 1D flame addressed in a DNS or a spherical flame kernel growing in homogeneous turbulence after spark ignition. In

such a case, $\bar{q}$ depends on a single spatial coordinate, distance x normal to the mean flame position or radial coordinate r, respectively. Ensemble-averaged quantities are commonly used in investigations of transient and spatially nonuniform mean flows, e.g., combustion in a chamber of a piston engine. In such a case, $q(\mathbf{x}, t)$ is an ensemble of fields. These three methods of taking an average are considered to be fundamentally equivalent, i.e., if the two or three methods can be applied to the same field $q(\mathbf{x}, t)$ or the same ensemble of fields, the obtained mean fields $\bar{q}(\mathbf{x}, t)$ should be the same.

If $\rho(\mathbf{x}, t) = \bar{\rho}(\mathbf{x}, t) + \rho'(\mathbf{x}, t)$ and $\mathbf{u}(\mathbf{x}, t) = \bar{\mathbf{u}}(\mathbf{x}, t) + \mathbf{u}'(\mathbf{x}, t)$ are substituted into Eq. (6.2) and the obtained transport equation is averaged, then, we arrive at

$$0 = \frac{\partial \bar{\rho}}{\partial t} + \frac{\partial}{\partial x_j}\left(\bar{\rho}\bar{u}_j + \overline{\rho' u_j'}\right), \tag{6.14}$$

because $\overline{ab} = \overline{(\bar{a} + a')(\bar{b} + b')} = \bar{a}\bar{b} + \overline{a'}\bar{b} + \overline{b'}\bar{a} + \overline{a'b'} = \bar{a}\bar{b} + \overline{a'b'}$ for arbitrary quantities a and b. In the following, dependencies of various flow and mixture characteristics on the spatial coordinates $\mathbf{x}$ and time t will often be skipped for brevity. Nevertheless, when introducing new flame characteristics, such dependencies will sometimes be specified in the beginning and, then, will be skipped.

Equation (6.14) involves a second moment $\overline{\rho' u_j'}$, i.e., a correlation of fluctuating density and velocity fields, which should be modeled. This problem can be circumvented by introducing Favre-averaged mass-weighted quantities as follows; $\tilde{q} \equiv \overline{\rho q}/\bar{\rho}$ and $q'' \equiv q - \tilde{q}$. By definition, $\tilde{q''} = \overline{\rho q''} = 0$. If $\mathbf{u} = \tilde{\mathbf{u}} + \mathbf{u}''$ is substituted into Eq. (6.2) and the obtained transport equation is averaged using the Reynolds method, then, we arrive at

$$\frac{\partial \bar{\rho}}{\partial t} + \frac{\partial}{\partial x_j}\left(\bar{\rho}\tilde{u}_j\right) = 0, \tag{6.15}$$

because $\overline{\rho \mathbf{u}} = \bar{\rho}\tilde{\mathbf{u}}$ by definition. The Favre-averaged transport Eq. (6.15) involves less number of terms when compared to the Reynolds-averaged transport Eq. (6.14) and a similar result can be obtained by averaging other transport equations. For this reason, RANS models of turbulent combustion deal with the Favre-averaged transport equations.

Substitution of $u_i = \tilde{u}_i + u_i''$ and $u_j = \tilde{u}_j + u_j''$ into the Navier–Stokes Eq. (6.3), followed by averaging, yields

$$\frac{\partial}{\partial t}\left(\bar{\rho}\tilde{u}_i\right) + \frac{\partial}{\partial x_j}\left(\bar{\rho}\tilde{u}_i\tilde{u}_j\right) = -\frac{\partial}{\partial x_j}\overline{\rho u_i'' u_j''} + \frac{\partial \bar{\tau}_{ij}}{\partial x_j} - \frac{\partial \bar{p}}{\partial x_i}, \tag{6.16}$$

because $\overline{\rho ab} = \overline{\rho(\tilde{a} + a'')(\tilde{b} + b'')} = \bar{\rho}\tilde{a}\tilde{b} + \overline{\rho a''}\tilde{b} + \overline{\rho b''}\tilde{a} + \overline{\rho a'' b''} = \bar{\rho}\tilde{a}\tilde{b} + \overline{\rho a'' b''}$ for arbitrary quantities a and b.

Using a similar method, we arrive at the following Favre-averaged transport equations for species mass fractions

$$\frac{\partial}{\partial t}\left(\bar{\rho}\tilde{Y}_k\right)+\frac{\partial}{\partial x_j}\left(\bar{\rho}\tilde{u}_j\tilde{Y}_k\right)=-\frac{\partial}{\partial x_j}\overline{\rho u_j'' Y_k''}+\frac{\partial}{\partial x_j}\left(\overline{\rho D_k\frac{\partial Y_k}{\partial x_j}}\right)+\bar{\dot{\omega}}_k \tag{6.17}$$

and specific mixture enthalpy

$$\frac{\partial}{\partial t}\left(\bar{\rho}\tilde{h}\right)+\frac{\partial}{\partial x_j}\left(\bar{\rho}\tilde{u}_j\tilde{h}\right)=-\frac{\partial}{\partial x_j}\overline{\rho u_j'' h''}+\frac{\partial\bar{p}}{\partial t}$$
$$+\frac{\partial}{\partial x_j}\left[\frac{\mu}{Pr}\frac{\partial h}{\partial x_j}+\mu\sum_{k=1}^{N}\left(\frac{1}{Sc_k}-\frac{1}{Pr}\right)h_k\frac{\partial Y_k}{\partial x_j}\right]. \tag{6.18}$$

Finally, the Favre-averaged ideal gas state Eq. (6.1) reads

$$\overline{pM}=R^o\bar{\rho}\tilde{T}. \tag{6.19}$$

If the Mach number is much less than unity, then, fluctuations and spatial variations in the pressure may be neglected in Eq. (6.19) when compared to the mean pressure (Majda and Sethian 1985). Therefore, symbol p in Eq. (6.19) designates pressure averaged over the entire combustion chamber. Accordingly, Eq. (6.19) reads $p\overline{M}=R^o\bar{\rho}\tilde{T}$ and allows us to evaluate the mean density, e.g., if the molecular wight M is assumed to be constant.

6.3 Challenges of and Approaches to Premixed Turbulent Combustion Modeling Within RANS Framework

Equations (6.15)–(6.18) involve (i) terms that can be determined by solving these equations, e.g., the first moments $\bar{\rho}$, $\tilde{u}_i$, $\tilde{Y}_k$, and $\tilde{h}$ of the density, velocity, mass fraction, and enthalpy fields, and (ii) the so-called unclosed terms that cannot be determined by solving the transport Eqs. (6.15)–(6.18), e.g., turbulent Reynolds stresses $\overline{\rho u_i'' u_j''}$, turbulent scalar fluxes $\overline{\rho u_j'' Y_k''}$ and $\overline{\rho u_j'' h''}$ or the mean reaction rates $\bar{\dot{\omega}}_k$. Accordingly, the number of unknowns is larger than the number of equations and the latter terms should be modeled. Model equations invoked for these purposes are commonly called closure relations.

The present section aims at briefly reviewing (i) various approaches to modeling the aforementioned unclosed terms and (ii) associated challenges. However, before considering such approaches and challenges, it is worth substantially simplifying the problem, because an analysis of $O(N)$ transport Eq. (6.17) is difficult if $N \gg 1$. This goal is commonly reached using the so-called combustion progress variable, as discussed in the next section.

6.3.1 Combustion Progress Variable

The vast majority of models for RANS simulations of premixed turbulent flames are based on an assumption that the state of the mixture in a premixed flame can be characterized with a single combustion progress variable c in the adiabatic iso-baric[1] case (e.g., an open flame) or by two variables c and h if heat losses are substantial or/and the pressure depends on time (e.g. combustion in piston engines). For simplicity, in the rest of the present chapter, we will address the former (adiabatic iso-baric) case if the opposite is not stated.

The aforementioned assumption can be justified by invoking one of the following three approximations: (i) single-step chemistry and equidiffusive mixture, (ii) flamelet combustion regime, (iii) two-fluid flow. Each approximation offers an opportunity to significantly simplify the problem, but retain the basic physics of flame–turbulence interaction in the focus of consideration. Let us consider these three approximations in a more detailed manner.

6.3.1.1 Single-Step Chemistry Approximation

If combustion chemistry is reduced to a single reaction

$$\Phi \mathrm{F} + St\mathrm{O} \rightarrow \mathrm{P}$$

and the Lewis number $Le_k = \kappa/D_k$ is equal to unity for fuel F and oxidant O, then, Eq. (6.5) reads

$$\frac{\partial}{\partial t}\left(\rho Y_F\right) + \frac{\partial}{\partial x_j}\left(\rho u_j Y_F\right) = \frac{\partial}{\partial x_j}\left(\rho D \frac{\partial Y_F}{\partial x_j}\right) - \dot{\omega} \tag{6.20}$$

and

$$\frac{\partial}{\partial t}\left(\rho Y_O\right) + \frac{\partial}{\partial x_j}\left(\rho u_j Y_O\right) = \frac{\partial}{\partial x_j}\left(\rho D \frac{\partial Y_O}{\partial x_j}\right) - St\dot{\omega} \tag{6.21}$$

for the fuel and oxidant, respectively. Here, St is the mass stoichiometric coefficient and Φ is the equivalence ratio. A transport equation for the mass fraction of product P is not required, because $Y_P = Y_{F,u} - Y_F + St(Y_{O,u} - Y_O)$ due to mass conservation. Here, subscripts u and b designate fresh mixture and equilibrium combustion products, respectively.

If $Y_F = Y_{F,b} + y_F(Y_{F,u} - Y_{F,b})$ and $Y_O = Y_{O,b} + y_O(Y_{O,u} - Y_{O,b})$ are substituted into Eqs. (6.20) and (6.21), respectively, then, the transport equations for the normalized mass fractions of the fuel, y_F, and oxidant, y_O, are identical, because

[1] It is worth remembering that the pressure in a turbulent flow always fluctuates with time, but the magnitude of such fluctuations is much smaller than the mean pressure if the Mach number is low. Here, term "iso-baric case" means that the mean pressure does not depend on time.

$Y_{O,u} - Y_{O,b} = St(Y_{F,u} - Y_{F,b})$. The boundary conditions for y_F and y_O are also identical, i.e., $y_{F,u} = y_{O,u} = 1$ and $y_{F,b} = y_{O,b} = 0$. Consequently, the solutions $y_F(\mathbf{x}, t)$ and $y_O(\mathbf{x}, t)$ to the two equations should be the same in a general unsteady 3D case. Accordingly, if a combustion progress variable is defined as follows:

$$c = \frac{Y_F - Y_{F,u}}{Y_{F,b} - Y_{F,u}} = \frac{Y_O - Y_{O,u}}{Y_{O,b} - Y_{O,u}}, \tag{6.22}$$

then, the following transport equation

$$\frac{\partial}{\partial t}(\rho c) + \frac{\partial}{\partial x_j}\left(\rho u_j c\right) = \frac{\partial}{\partial x_j}\left(\rho D \frac{\partial c}{\partial x_j}\right) + \dot{\omega}_c \tag{6.23}$$

results from Eq. (6.20) or (6.21). Here, $\dot{\omega}_c = \dot{\omega}_F/(Y_{F,b} - Y_{F,u})$. By definition $c = 0$ and 1 in the unburned and burned gas, respectively.

Thus, the mixture composition is solely controlled by c. The temperature can be evaluated using Eq. (6.12), because the transport equation for the enthalpy simply reads

$$\frac{\partial}{\partial t}(\rho h) + \frac{\partial}{\partial x_j}\left(\rho u_j h\right) = \frac{\partial}{\partial x_j}\left(\lambda \frac{\partial h}{\partial x_j}\right) \tag{6.24}$$

and has a trivial solution of $h(\mathbf{x}, t) = \text{const}$ in the considered adiabatic, iso-baric, equidiffusive case. Furthermore, if the mixture specific heat c_p is constant, as widely assumed when modeling premixed turbulent combustion, then, Eqs. (6.12) and (6.22) result straightforwardly in

$$c = \frac{T - T_u}{T_b - T_u}. \tag{6.25}$$

The mean molecular weight of the mixture is equal to

$$\overline{M} = \left(\frac{\overline{Y}_F}{M_F} + \frac{\overline{Y}_O}{M_O} + \frac{\overline{Y}_P}{M_P}\right)^{-1}, \tag{6.26}$$

where M_F, M_O, and M_P are molecular weights of the fuel, oxidant, and product, respectively.

Thus, the combustion progress variable fully characterizes the mixture state in an arbitrary unsteady 3D flow provided that the invoked simplifications (single-step chemistry, $Le_F = Le_0 = 1$, $q_R = 0$, and the mean pressure p does not depend on time) hold.

The Favre-averaged transport Eq. (6.23) reads

$$\frac{\partial}{\partial t}(\bar{\rho}\tilde{c}) + \frac{\partial}{\partial x_j}\left(\bar{\rho}\tilde{u}_j\tilde{c}\right) = -\frac{\partial}{\partial x_j}\overline{\rho u_j'' c''} + \frac{\partial}{\partial x_j}\overline{\left(\rho D \frac{\partial c}{\partial x_j}\right)} + \overline{\dot{\omega}_c} \tag{6.27}$$

To conclude this section, it is worth stressing the following points. The major goal of premixed turbulent combustion modeling consists in predicting the burning rate, which is commonly quantified by evaluating turbulent burning velocity U_t, i.e., burning rate per unit area of a mean flame surface, normalized using partial density of an appropriate reactant in unburned mixture. In various flames, this goal may be reached invoking a single-step chemistry and characterizing the mixture state in the flame with a single combustion progress variable provided that the used values of ρ_b, T_b, the laminar flame speed S_L and thickness δ_L have been obtained in experiments or in simulations that dealt with detailed combustion chemistry.

For instance, Burluka et al. (2009) experimentally investigated expansion of various statistically spherical premixed turbulent flames in the well-known Leeds fan-stirred bomb. These authors studied not only burning of commonly used hydrocarbon–air mixtures, but also flames of di-t-butyl-peroxide (DTBP) decomposition, with such flames being associated with a much simpler chemistry when compared to combustion of hydrocarbons in the air. Nevertheless, similar dependencies of U_t on the rms turbulent velocity u' were obtained from both the hydrocarbon–air and DTBP flames, provided that they were characterized by approximately the same laminar flame speeds. These experimental data imply a minor effect of combustion chemistry on U_t.

Moreover, in a recent DNS study of premixed flames propagating in intense small-scale turbulence, Lapointe and Blanquart (2016) found that neither fuel formula nor chemical mechanism substantially affected computed turbulent burning velocity. Accordingly, they have concluded that "fuel consumption can be predicted with the knowledge of only a few global laminar flame properties" (Lapointe and Blanquart 2016). In another recent DNS study of lean methane–air turbulent flames under conditions relevant to Spark Ignition (SI) engines, Wang et al. (2017) compared results simulated using a single-step and a 13-species-reduced chemical mechanism. These authors have also concluded that the single-step "mechanism is adequate for predicting flame speed" (Wang et al. 2017).

Thus, in many cases, the use of a single combustion progress variable and a single-step chemistry appears to be basically adequate for analyzing the fundamentals of flame–turbulence interaction even if complex chemistry introduces new local effects, e.g., see Dasgupta et al. (2017). Nevertheless, combustion chemistry appears to play an important role under conditions associated with local combustion quenching e.g. due to heat losses, inflammable local mixture composition, strong local perturbations caused by turbulent eddies, etc.

6.3.1.2 Flamelet Approximation

In the previous section, characterization of mixture state with a single combustion progress variable was obtained by considering an arbitrary flow, but significantly simplifying combustion chemistry and molecular transport model. The same result can also be obtained in the opposite case of complex combustion chemistry and an advanced model of molecular transport, but significantly simplified flow.

Indeed, the simplest paradigm of the influence of turbulence on premixed combustion consists in reducing this influence to wrinkling the surface of a thin inherently laminar flamelet whose structure is assumed to be close to the structure of the unperturbed planar 1D laminar flame (Bilger et al. 2005; Bray 1980, 1996; Lipatnikov 2012; Peters 2000; Poinsot and Veynante 2005). Accordingly, within the framework of such a paradigm, (i) the 1D laminar flame can be simulated using detailed chemistry and molecular transport models and (ii) results of such simulations can be tabulated in a form of $Y_k(c)$, $T(c)$, $\rho(c)$, etc., e.g., see a recent review paper by van Oijen et al. (2016). Subsequently, the state of the mixture in a premixed turbulent flame can be characterized with a single combustion progress variable c and the aforementioned tables.

Such an approach was used in certain recent RANS studies of premixed turbulent combustion and is widely used in LES research into turbulent flames. However, it is worth remembering that the assumption that reaction zones retain the structure of weakly perturbed 1D laminar flames in a turbulent flow is very demanding and does not seem to hold even in weakly turbulent flames, e.g., see results (Lipatnikov et al. 2015b, 2017; Sabelnikov et al. 2016, 2017) of processing DNS data obtained from weakly turbulent flames that are well associated (Lipatnikov et al. 2015a) with the flamelet combustion regime. In the present author's opinion, this assumption distorts the basic physics of flame–turbulence interaction much stronger when the assumption of single-step chemistry does.

6.3.1.3 Two-Fluid Approximation and BML Approach

To the best of the present author's knowledge, two-fluid approximation was introduced into the combustion literature by Prudnikov (1960, 1964). It is based on an assumption that unburned and burned gases are separated by an infinitely thin interface that propagates at the laminar flame speed S_L with respect to the unburned mixture. Accordingly, the mean value of any mixture characteristic q can be evaluated as follows:

$$\bar{q}(\mathbf{x}, t) = q_u \mathbb{P}_u(\mathbf{x}, t) + q_b \mathbb{P}_b(\mathbf{x}, t), \tag{6.28}$$

where $\mathbb{P}_u(\mathbf{x}, t)$ or $\mathbb{P}_b(\mathbf{x}, t)$ is the probability of finding the unburned or burned mixture, respectively, in point $\mathbf{x}$ at instant t and q_u or q_b is the value of q in the unburned or burned mixture, respectively. The latter value can be found by calculating the temperature and composition of the adiabatic equilibrium combustion products. In such calculations, the product composition may consist of a number of different species such as H_2O, CO_2, CO, O_2, H_2, N_2, OH, O, H, etc.

If we (i) introduce an indicator variable I, which is equal to zero and unity in the unburned and burned mixtures, respectively, and (ii) apply Eq. (6.28) to I, $(1 - I)$, ρI, and $\rho(1 - I)$, then, we obtain

$$\bar{I} = \mathbb{P}_b, \qquad 1 - \bar{I} = \mathbb{P}_u, \qquad \bar{\rho}\tilde{I} = \overline{\rho I} = \rho_b \mathbb{P}_b, \qquad \bar{\rho}(1 - \tilde{I}) = \overline{\rho(1 - I)} = \rho_u \mathbb{P}_u, \tag{6.29}$$

respectively. Subsequently, the application of Eqs. (6.28) and (6.29) to ρY_R and ρT yields

$$\bar{\rho}\tilde{Y}_R = \bar{\rho}(1 - \tilde{I})Y_{R,u} + \bar{\rho}\tilde{I}Y_{R,b}, \qquad \bar{\rho}\tilde{T} = \bar{\rho}(1 - \tilde{I})T_u + \bar{\rho}\tilde{I}T_b, \tag{6.30}$$

where subscript R designates a reactant, e.g., fuel, oxygen, or product species. Consequently,

$$\tilde{I} = \frac{\tilde{Y}_F - Y_{F,u}}{Y_{F,b} - Y_{F,u}} = \frac{\tilde{Y}_O - Y_{O,u}}{Y_{O,b} - Y_{O,u}} = \frac{\tilde{T} - T_u}{T_b - T_u}, \tag{6.31}$$

i.e., the Favre-averaged value of the indicator function is equal to the Favre-averaged value of the combustion progress variable c defined by Eq. (6.22) or (6.25). Finally, application of Eqs. (6.28) and (6.29) to c and $(1 - c)$ yields

$$\bar{c} = \mathbb{P}_b = \bar{I}, \qquad 1 - \bar{c} = \mathbb{P}_u = 1 - \bar{I}, \tag{6.32}$$

i.e., the Reynolds-averaged value of the combustion progress variable is equal to the probability of finding combustion products and the indicator function I can be substituted with c in Eqs. (6.29)–(6.31).

In the particular case of single-step chemistry, the two-fluid approximation is associated with the limit of the infinitely fast reaction. Accordingly, the two-fluid approximation might be claimed to invoke an extra simplification when compared to the approximation of single-step chemistry. However, the former approximation offers an opportunity to use the temperature, density, and species mass fractions calculated for the equilibrium combustion products in the case of detailed chemistry.

Therefore, if the sum of the probabilities $\mathbb{P}_u$ and $\mathbb{P}_b$ is close to unity everywhere in a real flame, the two-fluid approach is capable of predicting mean mixture characteristics whose values within the reaction zones are of the same order or less than their values in the unburned or burned gas. However, the approach cannot be used to predict mean mass fractions of intermediate species, e.g., radicals, whose concentration is very low both in the unburned and burned mixtures. At first glance, this limitation of the two-fluid approximation appears to be a substantial drawback when compared to the flamelet approximation, which offers an opportunity to compute the mean mass fractions of intermediate species. However, to compute does not mean to predict. The use of the assumption of weak perturbations of the local flamelet structure when compared to the counterpart 1D laminar flame may yield wrong values of the mean mass fractions of the intermediate species if perturbations of the local flamelet structure are strong enough, as occurs in various flames. Accordingly, the present author cannot claim that the flamelet approximation is superior to the two-fluid approximation, at least within the RANS framework.

A bridge between the two-fluid and flamelet approximations was built by Bray (1980), Bray and Moss (1977), Bray et al. (1985) and Libby and Bray (1977, 1981) who developed the well-known BML approach by introducing the following Probability Density Function (PDF)

$$P(c,t,\mathbf{x}) = \alpha(t,\mathbf{x})\delta(c) + \beta(t,\mathbf{x})\delta(1-c) + \gamma(t,\mathbf{x})P_f(c,t,\mathbf{x}) \tag{6.33}$$

for the combustion progress variable defined using Eq. (6.22) written for the mass fraction of the deficient reactant, i.e., fuel in a lean mixture or oxygen in a rich mixture. Here, $\delta(c)$ and $\delta(1-c)$ are Dirac delta functions, $P_f(c,t,\mathbf{x})$ is an unknown PDF for $0 < c < 1$, i.e., $P_f(0,t,\mathbf{x}) = P_f(1,t,\mathbf{x}) = 0$, $\alpha(t,\mathbf{x})$ and $\beta(t,\mathbf{x})$ are the probabilities of finding unburned ($c = 0$) and burned ($c = 1$) mixture, respectively, while the probability $\gamma(t,\mathbf{x})$ of finding intermediate states ($0 < c < 1$) of the mixture is assumed to be much less than unity at any point $\mathbf{x}$ at any instant t. If $\gamma = 0$, the BML approach reduces to the two-fluid approximation. Alternatively, if $\gamma > 0$, a model for the intermediate PDF P_f may be developed invoking the flamelet approximation (Bray et al. 2006).

Using Eq. (6.33), one can easily obtain Eqs. (6.29) and (6.30), where I is substituted with c and small terms on the order of $O(\gamma)$ are added on the RHSs of each equation. Moreover,

$$\bar{\rho} = (1-\bar{c})\rho_u + \bar{c}\rho_b + O(\gamma) = \rho_u - (\sigma-1)\rho_b\bar{c} + O(\gamma) = \rho_u - (\sigma-1)\bar{\rho}\tilde{c} + O(\gamma) \tag{6.34}$$

and, hence,

$$\bar{\rho} = \frac{\rho_u}{1+\tau\tilde{c}} + O(\gamma), \tag{6.35}$$

where $\sigma = \rho_u/\rho_b$ is the density ratio and $\tau = \sigma - 1$ is a heat-release factor.

The domain of validity of the BML approach is commonly characterized using the segregation factor

$$g = \frac{\overline{\rho c''^2}}{\bar{\rho}\tilde{c}(1-\tilde{c})}, \tag{6.36}$$

i.e., the closer g to unity, the more accurate the BML approach is considered to be. Indeed, using Eq. (6.33), we have

$$\begin{aligned}\overline{\rho c''^2} &= \overline{\rho(c-\tilde{c})^2} = (1-\bar{c})\rho_u\tilde{c}^2 + \bar{c}\rho_b(1-\tilde{c})^2 + O(\gamma)\\ &= \bar{\rho}\left[(1-\tilde{c})\tilde{c}^2 + \tilde{c}(1-\tilde{c})^2\right] + O(\gamma) = \bar{\rho}\tilde{c}(1-\tilde{c}) + O(\gamma).\end{aligned} \tag{6.37}$$

Therefore, when $\overline{\rho c''^2} \to \bar{\rho}\tilde{c}(1-\tilde{c})$ and $g \to 1$, the magnitude of $O(\gamma)$-terms is asymptotically decreased and such unknown terms may be neglected if $g \approx 1$ and $\gamma \ll 1$. It is worth noting that Eqs. (6.34)–(6.37) can also be derived within the framework of the two-fluid approximation, but $O(\gamma)$-terms vanish in such a case.

In addition to the c-PDF given by Eq. (6.33), the BML approach deals with the following joint PDF

$$P(c,\mathbf{u},t,\mathbf{x}) = \alpha(t,\mathbf{x})P_u(\mathbf{u},t,\mathbf{x})\delta(c) + \beta(t,\mathbf{x})P_b(\mathbf{u},t,\mathbf{x})\delta(1-c) + \gamma(t,\mathbf{x})P_f(c,\mathbf{u},t,\mathbf{x}) \tag{6.38}$$

for the flow velocity vector $\mathbf{u}$ and the combustion progress variable c at point $\mathbf{x}$ at instant t. Here, $P_u(\mathbf{u},t,\mathbf{x})$ and $P_b(\mathbf{u},t,\mathbf{x})$ are velocity PDFs conditioned on either the unburned or the burned mixture, respectively. Using Eq. (6.38), one can easily obtain the following equations:

$$\bar{\mathbf{u}} = \bar{\mathbf{u}}_u(1-\bar{c}) + \bar{\mathbf{u}}_b\bar{c} + O(\gamma), \tag{6.39}$$

$$\tilde{\mathbf{u}} = \bar{\mathbf{u}}_u(1-\tilde{c}) + \bar{\mathbf{u}}_b\tilde{c} + O(\gamma), \tag{6.40}$$

$$\overline{\rho\mathbf{u}''c''} = \overline{\rho(\mathbf{u}-\tilde{\mathbf{u}})(c-\tilde{c})} = (1-\bar{c})\rho_u(\bar{\mathbf{u}}_u-\tilde{\mathbf{u}})(-\tilde{c}) + \bar{c}\rho_b(\bar{\mathbf{u}}_b-\tilde{\mathbf{u}})(1-\tilde{c}) + O(\gamma)$$
$$= \bar{\rho}\left[-(1-\tilde{c})\tilde{c}(\bar{\mathbf{u}}_u-\tilde{\mathbf{u}}) + \tilde{c}(1-\tilde{c})(\bar{\mathbf{u}}_b-\tilde{\mathbf{u}})\right] + O(\gamma) = \bar{\rho}\tilde{c}(1-\tilde{c})\left(\bar{\mathbf{u}}_b-\bar{\mathbf{u}}_u\right) + O(\gamma), \tag{6.41}$$

$$\begin{aligned}\rho_u\overline{\mathbf{u}''} = \rho_u\overline{(\mathbf{u}-\tilde{\mathbf{u}})} &= (1-\bar{c})\rho_u(\bar{\mathbf{u}}_u-\tilde{\mathbf{u}}) + \bar{c}\rho_u(\bar{\mathbf{u}}_b-\tilde{\mathbf{u}}) + O(\gamma)\\ &= (1-\tilde{c})\bar{\rho}\tilde{c}(\bar{\mathbf{u}}_u-\bar{\mathbf{u}}_b) + \tilde{c}\sigma\bar{\rho}(1-\tilde{c})(\bar{\mathbf{u}}_b-\bar{\mathbf{u}}_u) + O(\gamma)\\ &= (\sigma-1)\bar{\rho}\tilde{c}(1-\tilde{c})(\bar{\mathbf{u}}_b-\bar{\mathbf{u}}_u) + O(\gamma) = \tau\overline{\rho\mathbf{u}''c''} + O(\gamma),\end{aligned} \tag{6.42}$$

$$\overline{\rho\mathbf{u}''\mathbf{u}''} = \bar{\rho}(1-\tilde{c})(\overline{\mathbf{u}'\mathbf{u}'})_u + \bar{\rho}\tilde{c}(\overline{\mathbf{u}'\mathbf{u}'})_b + \bar{\rho}\tilde{c}(1-\tilde{c})(\bar{\mathbf{u}}_b-\bar{\mathbf{u}}_u)(\bar{\mathbf{u}}_b-\bar{\mathbf{u}}_u) + O(\gamma). \tag{6.43}$$

Here, $\bar{\mathbf{u}}_u$ and $\bar{\mathbf{u}}_b$ are the velocity vectors conditioned to the unburned and burned mixture respectively, i.e.

$$\begin{aligned}\bar{\mathbf{u}}_u(\mathbf{x},t) &= \int_0^{\varepsilon}\left[\iiint \mathbf{u}P(c,\mathbf{u},\mathbf{x},t)d\mathbf{u}\right]dc,\\ \bar{\mathbf{u}}_b(\mathbf{x},t) &= \int_{1-\varepsilon}^{1}\left[\iiint \mathbf{u}P(c,\mathbf{u},\mathbf{x},t)d\mathbf{u}\right]dc,\end{aligned} \tag{6.44}$$

where $\varepsilon \ll 1$ is a small number. Because the probabilities $P_u(\mathbf{u},t,\mathbf{x})$ and $P_b(\mathbf{u},t,\mathbf{x})$ are unknown, the conditioned velocities $\bar{\mathbf{u}}_u$ and $\bar{\mathbf{u}}_b$ are also unknown and require modeling.

Equation (6.35) is widely used as a state equation in RANS simulations of premixed turbulent flames. Equations (6.39)–(6.43) are widely used when interpreting experimental data and discussing the influence of combustion on turbulence, as will be demonstrated in the next section. In the rest of the present chapter, all the BML equations are considered to be valid and $O(\gamma)$-terms will be neglected if the opposite is not stated.

The same equations can be derived within the framework of the two-fluid approximation. In this case, the conditioned velocities are defined as follows

$$(1-\bar{c})\tilde{\mathbf{u}}_u = \overline{(1-c)\mathbf{u}}, \qquad \bar{c}\tilde{\mathbf{u}}_b = \overline{c\mathbf{u}}. \tag{6.45}$$

If the state of a mixture in a flame is characterized with a single combustion progress variable, then, within the RANS framework, the adiabatic and iso-baric combustion process is modeled using a single specific transport Eq. (6.27) in addition to the Favre-averaged continuity and Navier–Stokes equations, i.e., Eqs. (6.15) and (6.16), respectively. To close the problem, all terms on the RHS of Eq. (6.27) and the Reynolds stresses $\overline{\rho u_i'' u_j''}$ in Eq. (6.16) should be modeled.

The first, molecular transport, term on the RHS of Eq. (6.27) is often neglected when compared to other terms if turbulent Reynolds number is sufficiently large. Modeling of the turbulent scalar flux $\overline{\rho \mathbf{u}'' c''}$ and the mean reaction rate $\overline{\dot{\omega}_c}$ is addressed in the next two Sects. 6.3.1 and 6.3.2, respectively.

To conclude the present section, it is worth noting that the approximation of a single-step chemistry appears to be the best tool (i) for qualitatively discussing most important local effects associated with flame–turbulence interaction and (ii) for developing closure relations for $\overline{\rho \mathbf{u}'' c''}$ and, especially, $\overline{\dot{\omega}_c}$. However, when applying these closure relations in CFD research, it is better to invoke two-fluid or BML approach, because it offers an opportunity to use values of ρ_b, T_b, and species mass fractions $Y_{k,b}$, which are calculated for a mixture of H_2O, CO_2, CO, O_2, H_2, OH, O, H, etc.

6.3.2 *Effects of Combustion on Turbulence and Model Challenges*

The problems of modeling the flux $\overline{\rho \mathbf{u}'' c''}$ and the Reynolds stresses $\overline{\rho u_i'' u_j''}$ are not specific to turbulent combustion and were thoroughly investigated in studies of (i) turbulent mixing in constant-density flows and (ii) turbulent flows, respectively. However, due to significant density variations localized to thin zones, combustion generates variety of new effects and makes the problem much more difficult, as briefly discussed in the present section. The reader interested in a more detailed discussion of these effects and approaches to modeling them is referred to recent review papers (Lipatnikov and Chomiak 2010; Sabelnikov and Lipatnikov 2017) and monograph (Lipatnikov 2012).

6.3.2.1 Transport Equations for Second Moments

At first glance, the problem of modeling the second moments $\overline{\rho u_i'' c''}$ and $\overline{\rho u_i'' u_j''}$ of turbulent fields $\mathbf{u}(\mathbf{x}, t)$ and $c(\mathbf{x}, t)$ might be solved by deriving appropriate transport equations, as such a derivation is straightforward. For instance, let us, first, (i) use the continuity Eq. (6.2) to move ρ and ρu_j outside the time and spatial derivatives on the Left Hand Side (LHS) of Eq. (6.3) or (6.23), (ii) multiply the two equations with c and u_i, respectively, and sum them, (iii) use the continuity Eq. (6.2) to move ρ and ρu_j inside the time and spatial derivatives on the LHS of the obtained equation. Then, we arrive at

$$\frac{\partial}{\partial t}\left(\rho u_i c\right) + \frac{\partial}{\partial x_j}\left(\rho u_i u_j c\right) = c\frac{\partial \tau_{ij}}{\partial x_j} - c\frac{\partial p}{\partial x_i} + u_i \frac{\partial}{\partial x_j}\left(\rho D \frac{\partial c}{\partial x_j}\right) + u_i \dot{\omega}_c. \tag{6.46}$$

Second, application of a similar algorithm to the Favre-averaged Eqs. (6.16) and (6.27) results in

$$\begin{aligned}\frac{\partial}{\partial t}\left(\bar{\rho}\tilde{u}_i\tilde{c}\right) + \frac{\partial}{\partial x_j}\left(\bar{\rho}\tilde{u}_i\tilde{u}_j\tilde{c}\right) = &-\tilde{c}\frac{\partial}{\partial x_j}\overline{\rho u_i'' u_j''} - \tilde{u}_i \frac{\partial}{\partial x_j}\overline{\rho u_j'' c''} \\ &+\tilde{u}_i \frac{\partial}{\partial x_j}\left(\overline{\rho D \frac{\partial c}{\partial x_j}}\right) + \tilde{c}\frac{\partial \bar{\tau}_{ij}}{\partial x_j} - \tilde{c}\frac{\partial \bar{p}}{\partial x_i} + \tilde{u}_i \overline{\dot{\omega}_c}.\end{aligned} \tag{6.47}$$

Third, the Favre-averaged Eq. (6.46) reads

$$\begin{aligned}&\frac{\partial}{\partial t}\left(\bar{\rho}\tilde{u}_i\tilde{c}\right) + \frac{\partial}{\partial t}\overline{\rho u_i'' c''} + \frac{\partial}{\partial x_j}\left(\bar{\rho}\tilde{u}_i\tilde{u}_j\tilde{c}\right) + \frac{\partial}{\partial x_j}\left(\tilde{u}_j\overline{\rho u_i'' c''}\right) \\ &= -\frac{\partial}{\partial x_j}\left(\tilde{u}_i\overline{\rho u_j'' c''} + \tilde{c}\overline{\rho u_i'' u_j''}\right) - \frac{\partial}{\partial x_j}\overline{\rho u_i'' u_j'' c''} + \tilde{c}\frac{\partial \bar{\tau}_{ij}}{\partial x_j} + \overline{c''\frac{\partial \tau_{ij}}{\partial x_j}} \\ &-\tilde{c}\frac{\partial \bar{p}}{\partial x_i} - \overline{c''\frac{\partial p}{\partial x_i}} + \tilde{u}_i \frac{\partial}{\partial x_j}\left(\overline{\rho D \frac{\partial c}{\partial x_j}}\right) + \overline{u_i''\frac{\partial}{\partial x_j}\left(\rho D \frac{\partial c}{\partial x_j}\right)} + \tilde{u}_i\overline{\dot{\omega}_c} + \overline{u_i''\dot{\omega}_c},\end{aligned} \tag{6.48}$$

because $\overline{\rho a b c} = \overline{\rho(\tilde{a}+a'')(\tilde{b}+b'')(\tilde{c}+c'')} = \bar{\rho}\tilde{a}\tilde{b}\tilde{c} + \overline{\rho a''}\tilde{b}\tilde{c} + \overline{\rho b''}\tilde{a}\tilde{c} + \overline{\rho c''}\tilde{a}\tilde{b} + \overline{\rho a'' b''}\tilde{c} + \overline{\rho a'' c''}\tilde{b} + \overline{\rho b'' c''}\tilde{a} + \overline{\rho a'' b'' c''} = \bar{\rho}\tilde{a}\tilde{b}\tilde{c} + \overline{\rho a''}\tilde{b}\tilde{c} + \overline{\rho a'' c''}\tilde{b} + \overline{\rho b'' c''}\tilde{a} + \overline{\rho a'' b'' c''}$ for arbitrary quantities a, b, and c.

Finally, subtraction of Eq. (6.47) from Eq. (6.48) yields

$$\begin{aligned}\frac{\partial}{\partial t}\overline{\rho u_i'' c''} + \frac{\partial}{\partial x_j}\left(\tilde{u}_j\overline{\rho u_i'' c''}\right) = &\underbrace{-\overline{\rho u_i'' u_j''}\frac{\partial \tilde{c}}{\partial x_j} - \overline{\rho u_j'' c''}\frac{\partial \tilde{u}_i}{\partial x_j}}_{\text{i}} \underbrace{-\frac{\partial}{\partial x_j}\overline{\rho u_i'' u_j'' c''}}_{\text{ii}} \\ &\underbrace{+\overline{c''\frac{\partial \tau_{ij}}{\partial x_j}}}_{\text{iii}} \underbrace{+\overline{u_i''\frac{\partial}{\partial x_j}\left(\rho D \frac{\partial c}{\partial x_j}\right)}}_{\text{iv}} \underbrace{-\overline{c''\frac{\partial p'}{\partial x_i}}}_{\text{v}} \underbrace{-\overline{c''}\frac{\partial \bar{p}}{\partial x_i}}_{\text{vi}} \underbrace{+\overline{u_i''\dot{\omega}_c}}_{\text{vii}}.\end{aligned} \tag{6.49}$$

Using a similar method, the following transport equation for the Reynolds stresses

$$\frac{\partial}{\partial t}\overline{\rho u_i'' u_j''} + \frac{\partial}{\partial x_l}\left(\tilde{u}_l \overline{\rho u_i'' u_j''}\right) = \underbrace{-\overline{\rho u_j'' u_l''}\frac{\partial \tilde{u}_i}{\partial x_l} - \overline{\rho u_i'' u_l''}\frac{\partial \tilde{u}_j}{\partial x_l}}_{\text{I}} \tag{6.50}$$

$$\underbrace{-\frac{\partial}{\partial x_l}\overline{\rho u_i'' u_j'' u_l''}}_{\text{II}} \underbrace{+\overline{u_j''\frac{\partial \tau_{il}}{\partial x_l}} + \overline{u_i''\frac{\partial \tau_{jl}}{\partial x_l}}}_{\text{III}} \underbrace{-\overline{u_j''\frac{\partial p'}{\partial x_i}} - \overline{u_i''\frac{\partial p'}{\partial x_j}}}_{\text{IV}} \underbrace{-\overline{u_j''}\frac{\partial \bar{p}}{\partial x_i} - \overline{u_i''}\frac{\partial \bar{p}}{\partial x_j}}_{\text{V}}$$

can be derived.

The transport Eqs. (6.49) and (6.50) do not resolve the problem of closing the turbulent scalar flux $\overline{\rho u_i'' c''}$ and the Reynolds stresses $\overline{\rho u_i'' u_j''}$, because these transport equations involve a number of new unclosed terms, i.e., terms (ii)–(vii) on the RHS of Eq. (6.49) and terms (II)–(V) on the RHS of Eq. (6.50). It is worth stressing that some of these unclosed terms are specific to turbulent combustion. Indeed, application of the two transport equations to a constant-density non-reacting flow results in

$$\frac{\partial}{\partial t}\overline{u_i' c'} + \frac{\partial}{\partial x_j}\left(\overline{u_j u_i' c'}\right) = \underbrace{-\overline{u_i' u_j'}\frac{\partial \bar{c}}{\partial x_j} - \overline{u_j' c'}\frac{\partial \bar{u}_i}{\partial x_j}}_{\text{i}'} \underbrace{-\frac{\partial}{\partial x_j}\overline{u_i' u_j' c'}}_{\text{ii}'}$$

$$\underbrace{+\nu\overline{c'\frac{\partial^2 u_i'}{\partial x_j^2}}}_{\text{iii}'} \underbrace{+D\overline{u_i'\frac{\partial^2 c'}{\partial x_j^2}}}_{\text{iv}'} \underbrace{-\frac{1}{\rho}\overline{c'\frac{\partial p'}{\partial x_i}}}_{\text{v}'} \tag{6.51}$$

and

$$\frac{\partial}{\partial t}\overline{u_i' u_j'} + \frac{\partial}{\partial x_l}\left(\overline{u_l u_i' u_j'}\right) = \underbrace{-\overline{u_j' u_l'}\frac{\partial \bar{u}_i}{\partial x_l} - \overline{u_i' u_l'}\frac{\partial \bar{u}_j}{\partial x_l}}_{\text{I}'}$$

$$\underbrace{-\frac{\partial}{\partial x_l}\overline{u_i' u_j' u_l'}}_{\text{II}'} \underbrace{+\nu\left(\overline{u_j'\frac{\partial^2 u_i'}{\partial x_l^2}} + \overline{u_i'\frac{\partial^2 u_j'}{\partial x_l^2}}\right)}_{\text{III}'} \underbrace{-\frac{1}{\rho}\left(\overline{u_j'\frac{\partial p'}{\partial x_i}} - \overline{u_i'\frac{\partial p'}{\partial x_j}}\right)}_{\text{IV}'}. \tag{6.52}$$

Equation (6.51) does not contain counterparts of terms (vi) and (vii) on the RHS of Eq. (6.49), with an important role played by these terms in premixed turbulent flames being documented in DNS studies reviewed elsewhere (Lipatnikov and Chomiak 2010). Similarly, Eq. (6.52) does not contain a counterpart of term V on the RHS of Eq. (6.50), with this term also playing an important role in premixed turbulent flames (Lipatnikov and Chomiak 2010).

Because transport equations for the considered second moments are substantially different in the cases of a non-reacting constant-density turbulent flow and a premixed turbulent flame, we could expect that closure relations developed for $\overline{u_i' c'}$ and $\overline{u_i' u_j'}$ may be inappropriate in the latter case.

6.3.2.2 Countergradient Turbulent Transport

For instance, when modeling turbulent mixing in constant-density flows, the following gradient diffusion closure relation

$$\overline{\mathbf{u}'' c''} = -D_t \nabla \tilde{c} \tag{6.53}$$

is widely used. Here, $D_t > 0$ is the turbulent diffusivity given by an invoked model of turbulence and it is worth remembering that $\bar{q} = \tilde{q}$ and $q'' = q'$ in the case of a constant density. However, as well documented in various experiments reviewed elsewhere (Bray 1995; Lipatnikov and Chomiak 2010; Sabelnikov and Lipatnikov 2017), the scalar product of $\overline{\mathbf{u}'' c''} \cdot \nabla \tilde{c}$ may be positive in premixed flames, contrary to Eq. (6.53). This phenomenon is known as countergradient turbulent transport. It was predicted by Clavin and Williams (1979) and Libby and Bray (1981) and was first documented in experiments by Moss (1980) and by Yanagi and Mimura (1981).

The simplest explanation of the countergradient turbulent transport in premixed flames is as follows. Equation (6.41) shows that $(\bar{\mathbf{u}}_b - \bar{\mathbf{u}}_u) \cdot \nabla \tilde{c} > 0$ in the case of the countergradient turbulent transport. In particular, $\bar{u}_b > \bar{u}_u$ within a statistically planar 1D turbulent flame brush[2] sketched in Fig. 6.1. This difference in $\bar{u}_b$ and $\bar{u}_u$ may stem from the following two physical mechanisms.

First, the mean pressure gradient $\nabla \bar{p}$ induced within the mean flame brush due to thermal expansion accelerates lighter products stronger than denser unburned gas (Libby and Bray 1981; Scurlock and Grover 1953), because $\partial \mathbf{u}/\partial t \propto \rho^{-1} \nabla p$ due to Navier–Stokes equations. For instance, the axial velocity in point A′ in Fig. 6.1 is larger than the axial velocity in point A or B, because the burned gas is significantly accelerated by the mean pressure gradient when moving from point A to A′, whereas such an acceleration is weak in the unburned gas and even negligible if $\rho_u \gg \rho_b$

Second, due to thermal expansion, the normal gas velocity increases from unburned to burned edges of a laminar premixed flame (Zel'dovich et al. 1985) and similar jumps in $|\mathbf{u} \cdot \mathbf{n}|$ occur locally at flame fronts in turbulent flows, e.g., in point A or B in Fig. 6.1. Here, $\mathbf{n} = -\nabla c/|\nabla c|$ is a unit vector that is locally normal to the flamelet and points to the unburned gas.

In a turbulent flow, the two aforementioned mechanisms associated with thermal expansion are counteracted by velocity fluctuations, which yield turbulent diffusion in constant-density flows. Accordingly, depending on conditions, both the counter-

[2]Premixed turbulent flame brush is a spatial volume where the probabilities of finding $c = 0$ and $c = 1$ are both less than unity.

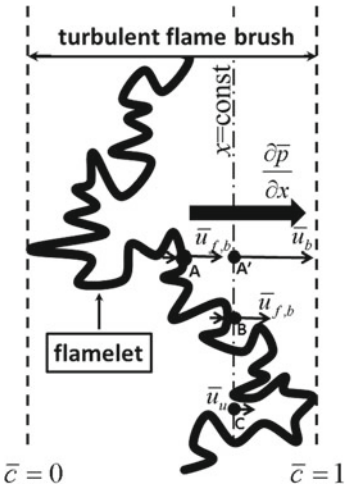

Fig. 6.1 Preferential acceleration of burned gas due to thermal expansion

gradient turbulent transport and gradient diffusion associated with $\overline{\rho \mathbf{u}'' c''} \cdot \nabla \tilde{c} < 0$ can occur in premixed turbulent flames. It is widely accepted that the countergradient turbulent transport dominates if the Bray number (Bray 1995) defined as follows:

$$N_B = \frac{\tau S_L}{u'} \tag{6.54}$$

is substantially larger than unity, whereas the gradient diffusion is often associated with a low N_B. It is worth stressing, however, that the sign of $\overline{\rho \mathbf{u}'' c''} \cdot \nabla \tilde{c}$ depends also on other flow and mixture characteristics, as discussed in detail elsewhere (Lipatnikov and Chomiak 2010). For instance, the sign of the flux $\overline{\rho \mathbf{u}'' c''}$ may change its direction during premixed turbulent flame development (Lipatnikov 2011b), but the Bray number does not involve flame-development time.

Over the first two decades, since the discovery of the countergradient turbulent transport in premixed flames (Clavin and Williams 1979; Libby and Bray 1981; Moss 1980; Yanagi and Mimura 1981), the sole approach to modeling this phenomenon within the RANS framework consisted in developing closure relations for various terms in Eq. (6.49). However, as discussed in detail elsewhere (Lipatnikov and Chomiak 2010), such efforts have not yet yielded a model whose predictive capabilities were well documented against a representative set of experimental or DNS data obtained from substantially different flames under substantially different conditions.

Accordingly, over the past years, alternative approaches were developed by placing the focus of modeling on the conditioned velocities $\tilde{\mathbf{u}}_u$ and $\tilde{\mathbf{u}}_b$. The reader interested in a review of such models is referred to (Sabelnikov and Lipatnikov 2017). At the moment, there is no model that is widely recognized to be able to predict the flux $\overline{\rho \mathbf{u}'' c''}$ under substantially different conditions, including transition from $\overline{\rho \mathbf{u}'' c''} \cdot \nabla \tilde{c} > 0$ to $\overline{\rho \mathbf{u}'' c''} \cdot \nabla \tilde{c} < 0$. Nevertheless, certain progress in validation of

recently proposed models was made. For instance, the following simple closure relation (Lipatnikov et al. 2015c; Sabelnikov and Lipatnikov 2011)

$$(1-\bar{c})\nabla\cdot\tilde{\mathbf{u}}_u \approx (-0.18+0.35\sigma)\frac{(1-\bar{c})^{1/2}}{(1+u'/S_L)^{1/2}}\frac{u'}{S_L}\overline{\dot{\omega}_c} \tag{6.55}$$

was validated against experimental and DNS data associated with the countergradient turbulent transport in premixed flames, see Figs. 6.2, 6.3 and 6.4, respectively.

Numerical results reported in Figs. 6.2, 6.3 and 6.4 were obtained by simulating flames described by statistically 1D transport equations. In such a case, a single scalar Eq. (6.55) allows us to evaluate a single conditioned velocity $\tilde{u}_u$, followed by calculation of a single component of the turbulent flux vector $\overline{\rho u'' c''}$ using Eq. (6.41). However, a single scalar Eq. (6.55) is not sufficient to obtain two or three components of the conditioned vector $\tilde{\mathbf{u}}_u$ in a statistically 2D or 3D case, respec-

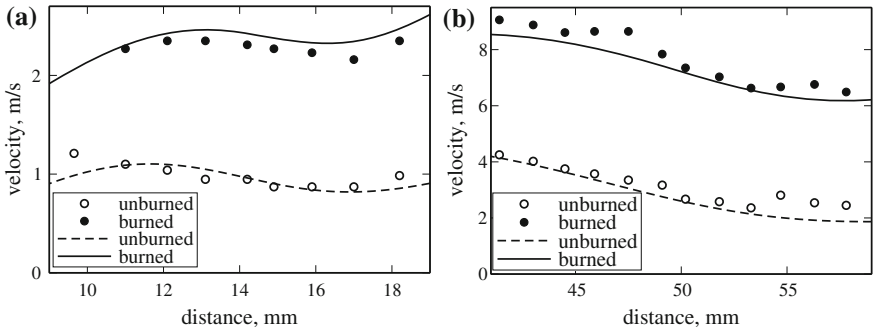

Fig. 6.2 Velocities conditioned to unburned (open symbols or dashed lines) and burned (filled symbols or solid lines) gases. Circles show experimental data obtained by **a** Cho et al. (1988) and **b** Cheng and Shepherd (1991) from impinging-jet flames. Solid lines show results computed by Lipatnikov et al. (2015c) using Eq. (6.55)

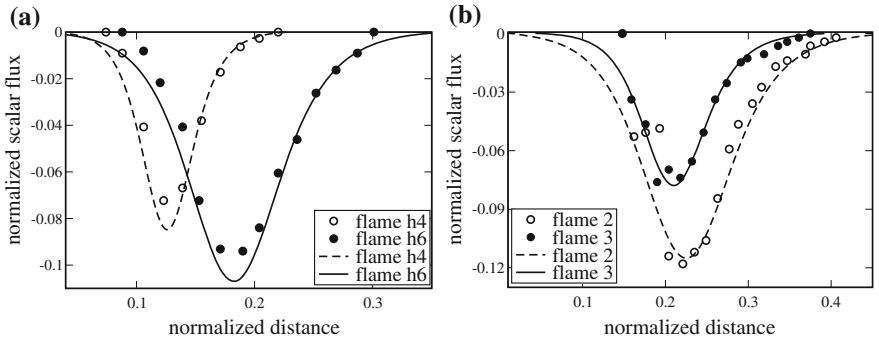

Fig. 6.3 Turbulent scalar fluxes measured (symbols) by **a** Li et al. (1994) and **b** Stevens et al. (1998) and computed (lines) by Lipatnikov et al. (2015c) using Eqs. (6.41) and (6.55)

tively. In recent 2D RANS simulations (Yasari and Lipatnikov 2015) of open conical rim-stabilized (Bunsen) methane–air flames that were experimentally investigated by Frank et al. (1999) and Pfadler et al. (2008), the problem was resolved by invoking the gradient diffusion closure of the tangential (to the mean flame brush) component of the flux vector $\overline{\rho \mathbf{u}'' c''}$, i.e., the tangential flux vanished in that model. In line with the former measurements (Frank et al. 1999), the simulations (Yasari and Lipatnikov 2015) yielded reduction of the magnitude of the countergradient flux followed by transition to gradient diffusion at $\Phi = 0.7$ when Φ was decreased from $\Phi = 1$ to 0.6. In line with the latter measurements (Pfadler et al. 2008), the simulations (Yasari and Lipatnikov 2015) yielded the countergradient flux in the radial (almost normal to the mean flame brush) direction in all studied flames, with the magnitude of the flux being weakly decreased with increasing the inlet mass flow rate, but being significantly increased by the equivalence ratio in the lean flames.

Thus, the aforementioned RANS tests of Eq. (6.55) yielded encouraging results, but further studies aimed at validating and applying this simple model are definitely required.

6.3.2.3 Flame-Generated Turbulence

The problem of flame-generated turbulence was raised by Karlovitz (1951) and by Scurlock and Grover (1953) and was studied in many subsequent papers reviewed elsewhere (Lipatnikov and Chomiak 2010). This problem is commonly considered to be of paramount importance, because turbulence eventually generated due to thermal expansion in a premixed flame was hypothesized to significantly increase the burning rate (Karlovitz et al. 1951).

In principle, both countergradient turbulent flux and flame-generated turbulence are caused by the same physical mechanisms. First, the jump in the locally normal velocity at a flamelet contributes not only to an increase in $|\tilde{\mathbf{u}}_b|$ when compared to

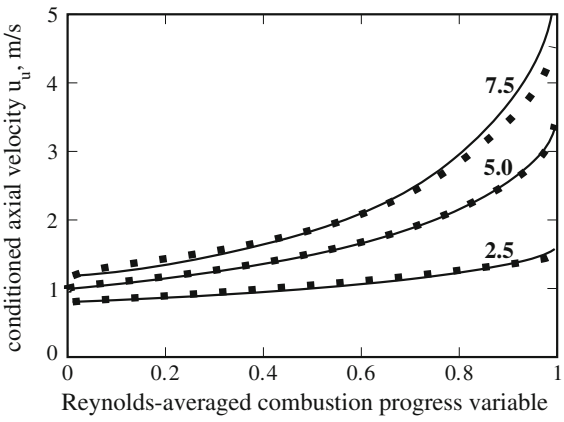

Fig. 6.4 Turbulent scalar fluxes obtained by processing DNS data (symbols) and computed (lines) using Eq. (6.55) (Lipatnikov et al. 2015c). Three different flames characterized by three different density ratios specified near lines and symbols

$|\bar{\mathbf{u}}_u|$, as discussed in the previous section, see points A and B in Fig. 6.1, but also to an increase in the magnitude of velocity fluctuations due to fluctuations in the direction of the normal vector $\mathbf{n}$ and, hence, in the direction of the local velocity jump. This physical mechanism was highlighted by Karlovitz et al. (1951).

Second, preferential acceleration of the burned gas by combustion-induced pressure gradient not only contributes to an increase in $|\bar{\mathbf{u}}_b|$ when compared to $|\bar{\mathbf{u}}_u|$, as discussed in the previous section, but also generates a shear flow behind flamelets, because some product volumes, e.g., see point A′ in Fig. 6.1, are accelerated during a longer time interval when compared to other product volumes, see point B. Subsequently, the shear flow generates turbulence. This physical mechanism was highlighted by Scurlock and Grover (1953).

Although both the countergradient turbulent transport and flame-generated turbulence are governed by basically the same mechanisms, as discussed above, models of the latter phenomenon have yet been developed substantially worse when compared to models of the former phenomenon. In particular, within the RANS framework, flame-generated turbulence is still addressed mainly using Eq. (6.50) and developing closure relations for various terms on the RHS. However, such efforts have not yet yielded a widely recognized model whose predictive capabilities were well documented against a representative set of experimental or DNS data obtained from substantially different flames under substantially different conditions. Accordingly, in RANS simulations of premixed turbulent flames, the problem of flame-generated turbulence is often ignored by invoking a turbulence model, e.g., the k-ε one (Launder and Spalding 1972), that was developed and validated in the non-reacting constant-density case.

6.3.2.4 Can We Properly Characterize Turbulence in a Flame?

It is also worth stressing that appropriateness of the Reynolds stresses $\overline{\rho u_i'' u_j''}$ for characterizing turbulence in premixed flames may be put into question (Lipatnikov 2009a, 2011a; Lipatnikov and Chomiak 2010; Sabelnikov and Lipatnikov 2017). For instance, Eq. (6.43) clearly shows that $\overline{\rho u_i'' u_j''}$ is controlled not only by the Reynolds stresses $(\overline{u_i' u_j'})_u$ and $(\overline{u_i' u_j'})_b$ conditioned to unburned and burned mixtures, respectively, but also by the unburned–burned intermittency term, which involves differences in velocities conditioned to the unburned and burned mixtures, see the last term on the RHS. If this difference is on the order of τS_L, then, the last term on the RHS scales as $(\tau S_L)^2$ and can be much larger than two other terms in the case of a weak turbulence, i.e., $u'/S_L = O(1)$. However, this term is not associated with turbulence, because the local normal velocity jump at a flamelet is controlled by the local combustion-induced pressure gradient and, therefore, does not change the local vorticity[3] $\nabla \times \mathbf{u}$. On the contrary, turbulence is considered to be inherently rotational

[3]If the curl operator is applied to the Navier–Stokes equations, then, the pressure gradient term vanishes, because $\nabla \times \nabla q \equiv 0$ for any scalar quantity q.

3D flow. Therefore, the irrotational velocity jump and the local turbulence generation appear to be two fundamentally different phenomena, which should be characterized by different quantities.

Accordingly, the conditioned Reynolds stresses $(\overline{u_i'u_j'})_u$ and $(\overline{u_i'u_j'})_b$ are often considered to be fundamentally more proper characteristics of turbulence in the unburned and burned gases, respectively, within a premixed flame brush. For instance, the physical mechanism highlighted by Scurlock and Grover (1953), i.e., generation of turbulence by shear caused by the preferential acceleration of light products by the combustion-induced bulk pressure gradient, is clearly associated with generation of turbulence in the burned gas. However, a physical mechanism of eventual influence of turbulence generated behind flamelets on the flamelet propagation into the unburned reactants has not yet been revealed.

Local variations in turbulence characteristics just upstream of flamelets appear to be of much more importance when discussing eventual self-acceleration of premixed flames due to combustion-induced turbulence. From this perspective, the Reynolds stresses $(\overline{u_i'u_j'})_u$ conditioned to the unburned mixture appear to be the best turbulence characteristics within a premixed flame brush at first glance and such a standpoint is shared by many experts. Nevertheless, this standpoint can be disputed. Due to random motion of an interface that separates two fluids, a statistical sub-ensemble over that a conditional average is taken depends on $\mathbf{x}$ and t, as is well known in the theory of intermittent flows (Kuznetsov and Sabelnikov 1990; Libby 1975; Townsend 1976). Consequently, the conditioned second moments differ from their mean counterparts even in the case of self-propagation of a passive interface in a constant-density flow, whereas it is the mean moments that characterize turbulence that is not affected by the interface propagation.

For combustion applications, this feature of conditionally averaged second moments follows straightforwardly from Eq. (6.43), which shows that $(\overline{u_i'u_j'})_u$ differs from $\overline{u_i'u_j'}$ even in the constant-density case, but it is the latter quantity that properly characterizes turbulence in such a case. The same feature of conditionally averaged second moments was also demonstrated by analyzing simple model problems (Lipatnikov 2009a, 2011a) and was recently shown in a 3D DNS study of self-propagation of an infinitely thin and dynamically passive interface in constant-density turbulence (Yu et al. 2014, 2015). The DNS also indicated that quantities controlled by velocity gradients were significantly less sensitive to averaging method. In particular, the mean and conditioned total strains $S^2 = S_{ij}S_{ij}$ or enstrophies $\omega^2 = (\nabla \times \mathbf{u})^2$ were almost equal to one another in all simulated cases, thus, implying that $(\overline{S^2})_u$ or $(\overline{\omega^2})_u$ is a proper characteristic of turbulence in reactants at least in the case of a constant density. Here, $S_{ij} = (\partial u_i/\partial x_j + \partial u_j/\partial x_i)/2$ is the rate-of-strain tensor.

All in all, the problem of characterizing turbulence within a premixed turbulent flame brush strongly requires further research. It is worth noting that this unresolved fundamental problem reduces the importance of another unresolved problem, i.e., modeling of $\overline{\rho u_i'' u_j''}$ and $(\overline{u_i'u_j'})_u$ or $(\overline{u_i'u_j'})_b$ in premixed turbulent flames. Indeed, if

neither of these second moments properly characterizes flame-turbulence interaction, then, modeling of these second moments appear to be of secondary importance.

6.3.2.5 Flow Perturbations Upstream of a Flame. Hydrodynamic Instability

As already noted, perturbations of the incoming flow of unburned reactants appear to be required in order for thermal expansion effects cause self-acceleration of the flame. Such a kind of flow perturbations is well known in the theory of laminar combustion and causes the hydrodynamic instability of laminar premixed flames, which was theoretically discovered by Darrieus (1938) and Landau (1944). In honor of these two scientists, the instability is often called the DL instability.

As discussed in many combustion textbooks (Law 2006; Lipatnikov 2012; Poinsot and Veynante 2005; Williams 1985; Zel'dovich et al. 1985), the physical mechanism of the DL instability is as follows. Due to flow acceleration in the direction normal to a laminar flame, the flow velocity vector changes its direction when crossing the flame, with the magnitude of $\mathbf{u} \cdot \mathbf{n}/|\mathbf{u}|$ being larger on the burned side of the flame (or $|\mathbf{u} \cdot \mathbf{n}|/|\mathbf{u}| = 1$ on both sides of the flame if the vectors $\mathbf{u}$ and $\mathbf{n}$ are parallel to one another). Such a change in the flow velocity vector direction is illustrated in insert associated with point B in Fig. 6.5. Accordingly, if the flame surface is subject to infinitesimal perturbations, see solid line in Fig. 6.5, then, the flame induces divergence (convergence) of the unburned (burned) mixture flow upstream (downstream) of convex (toward the unburned gas, see arc AB) elements of the flame surface, see fluid tubes bounded by flow lines A′A and B′B (AA″ and BB″, respectively). Consequently, the flow velocity of unburned gas at the convex flame surface decreases, whereas the flame speed S_L is assumed to be constant within the framework of the DL theory. Similarly, the flame induces convergence (divergence) of the unburned (burned) mixture flow upstream (downstream) of concave elements (arc BC) of the flame surface, see fluid tubes bounded by flow lines C′C and B′B (CC″ and BB″, respectively), and the flow velocity of unburned gas at the concave flame surface increases. As a result, convex (arc AB) and concave (arc BC) bulges are characterized by $|\mathbf{u}_u \cdot \mathbf{n}| < S_L$ and $|\mathbf{u}_u \cdot \mathbf{n}| > S_L$, respectively. Therefore, the bulges grow, the amplitude of the flame surface perturbation increases, and the flame becomes unstable. This instability is the classical example of self-acceleration of a flame due to perturbations of the incoming flow of unburned reactants, caused by thermal expansion in the flame.

Flamelets in a turbulent flow may also be subject to such a local DL instability, which results in increasing flamelet surface area and, hence, turbulent burning rate. However, such effects appear to be of substantial importance only in weak turbulence, i.e., if a ratio of $u'/S_L = O(1)$ (Boughanem and Trouvé 1998; Chaudhuri et al. 2011; Fogla et al. 2017; Lipatnikov and Chomiak 2005c). Nevertheless, the governing physical mechanism of the DL instability, i.e., acceleration of unburned mixture flow due to combustion-induced pressure gradient, may manifest itself in other phenomena, e.g., the growth of the so-called unburned mixture fingers that deeply

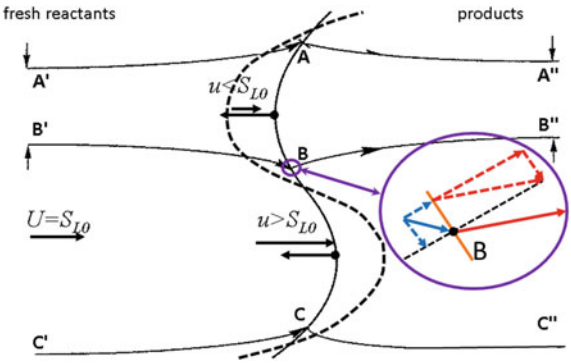

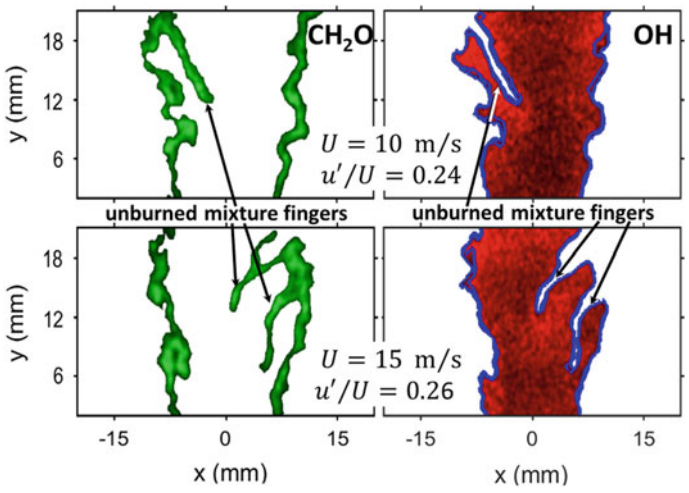

Fig. 6.5 Physical mechanism of the DL instability

Fig. 6.6 Unburned mixture fingers in bluff body stabilized conical lean premixed turbulent flames. Adapted from the paper by Chowdhury and Cetegen (2017)

intrude into combustion products (Lipatnikov et al. 2015b). A recent image of such fingers is shown in Fig. 6.6. The latter manifestation of the DL mechanism differs from the hydrodynamic instability of laminar flames, caused by the same mechanism, because the magnitude of pressure gradient within a premixed turbulent flame brush may be much larger than the magnitude of pressure gradient in unburned gas in the vicinity of a weakly wrinkled laminar premixed flame.

Moreover, pressure perturbations induced due to thermal expansion in flamelets may rapidly propagate upstream of the flame brush and change the incoming velocity field (Sabelnikov and Lipatnikov 2017). Such effects require thorough investigation.

6.3.2.6 Summary

Modeling of the influence of premixed combustion on turbulence and turbulent transport is the weakest point of the contemporary theory of turbulent combustion. While certain promising approaches to modeling turbulent transport in premixed flames were recently put forward, other fundamental issues such as

- selection of proper turbulence characteristics in flames,
- modeling of these turbulence characteristics, and
- eventual self-acceleration of premixed flames due to combustion-induced perturbations of the incoming flow of unburned reactants

have not yet been resolved even in a first approximation.

In applied CFD research into turbulent combustion, these fundamental issues are commonly disregarded and turbulence is modeled invoking methods developed and validated in studies on non-reacting constant-density flows.

While such a practical solution appears to be justified unless the aforementioned issues are resolved, it is still unclear why results of such applied simulations agreed with experimental data in a number of studies.

One possible answer consists in (i) highlighting a crucial role played by the leading edge of a premixed turbulent flame brush in its propagation and (ii) assuming that effects of combustion on turbulence are weak at the leading edge. However, this subject is beyond the scope of the present chapter and the interested reader is referred to a review paper (Lipatnikov and Chomiak 2005c), a monograph (Lipatnikov 2012), and recent papers (Kha et al. 2016; Kim 2017; Sabelnikov and Lipatnikov 2013, 2015; Venkateswaran et al. 2015).

6.3.3 *Effects of Turbulence on Combustion: Problems, Physical Mechanisms, and Models*

A major challenge of premixed turbulent combustion modeling within the RANS framework stems from (i) highly nonlinear dependencies of the rates of reactions that control heat release on the temperature and (ii) large magnitude of the temperature fluctuations in a turbulent flow. Accordingly, $\dot{\omega}_c$ depends on c in a highly nonlinear manner and is subject to large fluctuations in c, from zero to unity and back.

To illustrate the problem, let us compare $\overline{\exp\left(-\Theta/T\right)}$ and $\exp\left(-\Theta/\overline{T}\right)$ in a point where the probabilities of finding unburned and burned mixtures are equal to 0.5, i.e., the probability of finding the intermediate temperatures is assumed to be negligible in the considered example. In the case of $T_u = 300$ K, $T_b = 2200$ K, and $\Theta = 20000K$, we have $\overline{T} = 1250$ K and $\exp\left(-\Theta/\overline{T}\right) = 1.1 \times 10^{-7}$, whereas $\overline{\exp\left(-\Theta/T\right)} \approx 0.5\overline{\exp\left(-\Theta/T_b\right)} = 5.6 \times 10^{-5}$, i.e., the former exponential term is lower than the latter term by a factor os 500!

Obviously, such a huge difference cannot be modeled by expanding $\exp(-\Theta/T)$ into the Taylor series with respect to $T'/\overline{T}$, followed by averaging, e.g.,

$$\overline{\exp\left(-\frac{\Theta}{T}\right)} = \overline{\exp\left\{-\frac{\Theta}{\overline{T}}\left[1-\frac{T'}{\overline{T}}+\left(\frac{T'}{\overline{T}}\right)^2-\left(\frac{T'}{\overline{T}}\right)^3+\left(\frac{T'}{\overline{T}}\right)^4\right\}+\cdots\right]}$$
$$= \exp\left(-\frac{\Theta}{\overline{T}}\right)\left[1+\frac{3}{2}\overline{\left(\frac{T'}{\overline{T}}\right)^2}-\frac{13}{6}\overline{\left(\frac{T'}{\overline{T}}\right)^3}+\frac{73}{22}\overline{\left(\frac{T'}{\overline{T}}\right)^4}+\ldots\right]. \quad (6.56)$$

In the considered example ($\bar{c}=0.5$, $T_u=300$ K, $T_b=2200$ K, $\overline{T}=1250$ K, and $\Theta=20000K$), the odd moments $\overline{(T'/\overline{T})^{2n+1}}$ vanish, whereas the even moments $\overline{(T'/\overline{T})^{2n}}$ are equal to $[(T_b-T_u)/2\overline{T}]^{2n}=0.76^{2n}$. Here, $n\geq 1$ is an integer number. Consequently, the use of the first-order terms in the above Taylor series does not allow us to increase $\overline{\exp(-\Theta/T)}$ by a required factor of 500 when compared to $\exp\left(-\Theta/\overline{T}\right)$. Thus, standard perturbation methods cannot be used to predict the influence of strong turbulent fluctuations in the temperature (or the combustion progress variable c) on reaction rates that depend on T (or c) in a highly nonlinear manner, e.g. $\dot{\omega}_c(c)$. To resolve the problem, RANS models of premixed turbulent combustion are commonly developed by highlighting a few of many physical mechanisms of flame–turbulence interaction.

6.3.3.1 Physical Mechanisms

When discussing physical mechanisms of the influence of turbulence on premixed combustion, there are several levels of simplifications, which are illustrated in Fig. 6.7.

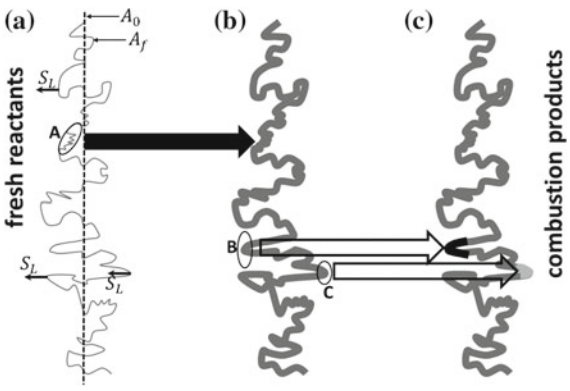

Fig. 6.7 Various effects associated with the influence of turbulence on premixed combustion

At the first, simplest level, the influence of turbulence on premixed combustion is solely reduced to wrinkling an infinitely thin flame front by turbulent eddies, see Fig. 6.7a, with the front speed with respect to the unburned gas being assumed to be constant and equal to S_L. The first models of that kind were put forward by Damköhler (1940) and Shelkin (1943) and, since that, this physical mechanism is taken into account by the vast majority of premixed turbulent combustion models. At this level of simplifications, turbulent burning velocity is solely controlled by an increase in the mean area $\overline{A}_f$ of the flame-front surface (wrinkled solid line in Fig. 6.7a) when compared to the area A_0 of a mean flame surface (dashed straight line), i.e.,

$$U_t = S_L \frac{\overline{A}_f}{A_0}. \tag{6.57}$$

An increase in u' results in increasing the mean dissipation rate $\overline{\varepsilon} \propto u'^3/L$, decreasing the Kolmogorov length $\eta = (\nu^3/\overline{\varepsilon})^{1/4}$ and time $\tau_\eta = (\nu/\overline{\varepsilon})^{1/2}$ scales, and increasing the magnitude τ_η^{-1} of the highest local stretch rate, which is generated by the Kolmogorov eddies (Pope 2000). Because the local area of the flame-front surface is increased by the local turbulent stretch rates, an increase in u' results in increasing $\overline{A}_f$ and U_t. A recent DNS study (Yu et al. 2015) of propagation of an infinitely thin interface in constant-density turbulence characterized by $0.5 \le u'/S_L \le 10$ showed a linear dependence of U_t on u', in line with pioneering predictions by Damköhler (1940) and Shelkin (1943).

At the second, more sophisticated level, the local burning rate is still assumed to be unperturbed[4] and controlled by S_L, but finite thickness of flamelets is taken into account, see Fig. 6.7b, thus, introducing several new effects. In particular, the smallest scale wrinkles of an infinitely thin interface are smoothed out in the case of a flamelet of a finite thickness, cf. ellipse A in Fig. 6.7a and its counterpart in Fig. 6.7b. A recent DNS study (Yu and Lipatnikov 2017a) showed that such a smoothing mechanism results in decreasing U_t and bending of the computed $U_t(u')$-curves, with the magnitudes of both effects being increased with decreasing L/δ_L.

Moreover, if heat losses play a role, a flamelet of a finite thickness may be quenched by strong turbulent stretching (Bradley et al. 1992). Such effects are often taken into account by multiplying the RHS of Eq. (6.57) with a stretch factor $G_s = 1 - \mathbb{P}_q$, where $\mathbb{P}_q$ is the probability of local combustion quenching by turbulent stretching. The reader interested in modeling this probability is referred to Bradley et al. (2005).

Furthermore, if the rms turbulent velocity u' is increased, the Kolmogorov length scale η is decreased and the Kolmogorov eddies may penetrate into the flamelet

[4] In the case of a single-step chemistry, the local burning rate in an adiabatic laminar premixed flame is not affected by the flame curvature or the local strain rate if (i) the activation temperature of the combustion reaction is asymptotically high, i.e., $\Theta/T_b \gg 1$, and (ii) the mixture is equidiffusive, i.e., $D_F = D_O = \kappa$, e.g., see a review paper by Clavin (1985).

preheat[5] zones and perturb their structure, thus, making the flamelet approximation wrong in such a case. If u' is further increased, the Kolmogorov eddies may become very small and may be able to penetrate even into the reaction zones, thus, intensifying mixing in these zones. By considering the case of $L/\delta_L \ll 1$, Damköhler (1940) assumed that the influence of turbulence on premixed combustion might solely be reduced to an increase in the diffusivity within the flame. Accordingly, turbulent burning velocity may be determined using results of the thermal laminar flame theory (Zel'dovich et al. 1985) and substituting the molecular diffusivity with the turbulent one, i.e.,

$$U_t = S_L \sqrt{\frac{D_t}{\kappa}} \propto S_L \sqrt{\mathrm{Re}_t} \tag{6.58}$$

This scaling is supported by recent DNS data (Yu and Lipatnikov 2017b) obtained from a number of premixed turbulent flames characterized by high Karlovitz and low Damköhler numbers.

On the contrary, if flamelet thickness is sufficiently large, the smallest turbulent eddies may disappear in the flamelet preheat zones due to increased viscous dissipation and dilatation (Poinsot et al. 1991; Roberts et al. 1993). In such a case, the smallest eddies do not affect U_t, i.e., the considered dissipation and dilatation effects are somehow similar to the smoothing effect discussed earlier.

Finally, if flamelets of a finite thickness are convected close to one another, they preheated zones may overlap, thus, heating the unburned gas and, subsequently, increasing the local burning rate (Poludnenko and Oran 2011).

Thus, even this brief overview shows that, if a finite thickness of flamelets is taken into account, various physical mechanisms of flame–turbulence interaction may be highlighted. Accordingly, in the literature, a number of different expressions for U_t and the mean rate $\overline{\dot{\omega}_c}$ may be found, as will be illustrated later.

When compared to models that address an infinitely thin flame front, the following feature of models that allow for a finite flamelet thickness appears to be of paramount importance, especially for engine applications. Even if the former models yield different expressions for U_t, all these expressions may be subsumed to $U_t = u' f(S_L/u')$ for dimensional reasoning, because these models consider S_L to be a single dimensional combustion characteristic. Here, f is an arbitrary function with its derivative $f' \geq 0$ in order for an increase in S_L to result in increasing or constant U_t. Therefore, if the pressure is increased and u' retains the same value, then, these models yield a decreasing or constant U_t, because S_L is decreased with increasing p for a typical hydrocarbon–air mixture.

However, as reviewed elsewhere (Lipatnikov 2012; Lipatnikov and Chomiak 2002, 2010), there is a large body of experimental data that cogently show an increase in U_t by p. This well-documented effect may play an important role in pis-

[5] Within the framework of the classical thermal theory of laminar premixed combustion (Zel'dovich et al. 1985), a laminar flame consists of a preheat zone, where the reaction rate vanishes, and a significantly thinner reaction zone which heat release is localized to.

ton engines where the pressure strongly varies during the combustion phase, but, as argued above, this effect cannot be predicted by a model that deals with infinitely thin flame fronts.

On the contrary, a model that allows for a finite flamelet thickness and yields an increase in U_t by L/δ_L may predict the increase in U_t by the pressure. Indeed, $\delta_L \propto \kappa/S_L \propto p^{-1}/p^{-s}$ is decreased with increasing pressure, because the power exponent s in $S_L \propto p^{-s}$ is significantly smaller than unity, e.g. $s \approx 0.5$ or 0.25 for methane or heavier paraffins, respectively. Thus, dependence of turbulent burning rate on flamelet thickness is of substantial importance, especially for CFD research into burning in piston engines.

At the third level of simplification, see Fig. 6.7c, not only a finite flamelet thickness, but also differences in (i) D_F and D_O (the so-called preferential diffusion effects) and (ii) *Le* and unity (the so-called Lewis number effects) are taken into account. Discussion of such effects is beyond the scope of the present chapter and the interested reader is referred to review paper (Lipatnikov and Chomiak 2005c) and monograph (Lipatnikov 2012). Here, it is worth noting that, if the molecular diffusivity of the deficient reactant, e.g. hydrogen in a lean H_2/air mixture, is significantly higher than the diffusivity of another reactant, then, local burning rate in positively curved[6] flamelets may be significantly increased by the preferential diffusion and Lewis number effects, cf. ellipse B and its counterpart in Figs. 6.7b and 6.7c, respectively. The opposite change in the local burning rate is observed (in the considered case of a lean H_2/air mixture) in negatively curved flamelets, cf. ellipse C and its counterpart in Figs. 6.7b and 6.7c, respectively.

As reviewed elsewhere (Kuznetsov and Sabelnikov 1990; Lipatnikov 2012; Lipatnikov and Chomiak 2005c), the preferential diffusion and Lewis number effects play a very important role in premixed turbulent combustion even at high u'/S_L and Re_t. In particular, such effects appear to be of great importance when burning renewable fuels such as syngas (Venkateswaran et al. 2011, 2013, 2015).

An important role played by molecular transport even at $D_F/D_t \propto \mathrm{Re}_t^{-1} \ll 1$ might appear to be surprising at first glance. However, it is worth remembering that combustion is localized to thin reaction zones, where a small molecular diffusivity, e.g. D_F, is multiplied with a large spatial gradient, e.g., ∇Y_F. Accordingly, in these zones, the molecular transport and reaction terms are of the same order, in line with the thermal theory of laminar premixed combustion (Zel'dovich et al. 1985). Consequently, the preferential diffusion and Lewis number effects may substantially change the local temperature and mixture composition in reaction zones, thus, strongly affecting the local $\dot{\omega}_c$. In the Favre-averaged transport Eq. (6.27), the mean molecular transport term may be significantly smaller than the mean reaction term, because flamelet preheat zones do not contribute to the latter term, but contribute to the former term, with the reaction and preheat zone contributions to the mean molecular transport term counterbalancing one another to the leading order. Nevertheless, the mean reaction rate may straightforwardly depend on D_F/D_O and/or

[6]Curvature is considered to be positive or negative if the curvature center is in burned or unburned gas, respectively.

Le, because molecular transport plays an important role in the reaction zones, as noted above.

Finally, it is worth noting that, in the case of single-step chemistry, a single combustion progress variable does not allow us to characterize mixture composition if $D_F \neq D_O$ or $Le \neq 1$. At least two (if $D_F \neq D_O$ and $Le = 1$ or $D_F = D_O$ and $Le \neq 1$) or three (if $D_F \neq D_O$ and $Le \neq 1$) scalar quantities are required to properly characterize the mixture composition in such a case. However, if $\bar{c}$ is considered to be the probability of finding combustion products, a single combustion progress variable and a single transport Eq. (6.27) may be used to simulate premixed turbulent combustion by invoking the two-fluid or BML approximation. In order for such simulations to allow for the preferential diffusion and Lewis number effects, these effects should be properly addressed by the invoked closure relation for $\overline{\dot{\omega}_c}$. An example of such a model will be given in Sect. 6.4.2.

6.3.3.2 Some Approaches to Modeling

The contents of this section are restricted to models developed to obtain a closure relation solely for the source term $\overline{\dot{\omega}_c}$ in Eq. (6.27), whereas a closure relation for the scalar flux $\overline{\rho \mathbf{u}'' c''}$ is assumed to be provided by another model. The most widely used models of the mean rate $\overline{\dot{\omega}_c}$ belong to one of the following three groups; (i) algebraic models, (ii) models that deal with an extra transport equation for the mean Flame Surface Density (FSD) $\overline{|\nabla c|}$, (iii) models that deal with an extra transport equation for the mean Scalar Dissipation Rate (SDR) $\tilde{\chi} = 2\bar{\rho}^{-1}\overline{\rho D \nabla c'' \cdot \nabla c''}$.

Algebraic Models

In the literature, there is a number of different algebraic closure relations for $\overline{\dot{\omega}_c}$, which were obtained invoking different assumptions. All such models may be subsumed to

$$\overline{\dot{\omega}_c} = \frac{\bar{\rho}\Omega}{\tau_f}, \tag{6.59}$$

where a flame time scale τ_f is introduced for dimensional reasoning and $\Omega = \Omega(\tilde{c}, \bar{\rho}/\rho_u)$ is a function of the normalized density and the mean combustion progress variable $\tilde{c}$ or $\bar{c}$. Since such models usually invoke the BML approach and, in particular, $\bar{\rho}\tilde{c} = \sigma^{-1}\rho_u \bar{c}$, the knowledge of $\bar{\rho}/\rho_u$ and $\tilde{c}$ is equivalent to the knowledge of $\bar{\rho}/\rho_u$ and $\bar{c}$ within the framework of these models.

Examples of expressions for the time scale τ_f and function $\Omega(\tilde{c}, \bar{\rho}/\rho_u)$, associated with various models, are given in Table 6.1, where $\tau_t = L/u'$ is a turbulence time scale, $Da = \tau_t/\tau_c$ is the Damköhler number, $\tau_c = \delta_L/S_L$ is the laminar flame time scale, C_1, C_2, and C_3 are model constants (values of C_1 are different for different models) provided in the cited papers, and the functions $\Gamma(u'/S_L, L/\delta_L)$, $I_0(\mathrm{Re}_t^{1/2}/Da)$, and $\mathscr{F}(\mathrm{Re}_t)$ are also provided in the cited papers, as well as the length scale $\hat{L}_y$.

Table 6.1 Algebraic models

τ_f^{-1}	Ω	References
$C_1\Gamma\tau_t^{-1}$	$\bar{c}(1-\bar{c})$	Bailly et al. (1997)
$C_1\tau_t^{-1}$	$\bar{\rho}\tilde{c}(1-\tilde{c})/\rho_u$	Bray (1980)
$C_1 l_0 S_L/\hat{L}_y$	$\bar{c}(1-\bar{c})$	Bray (1990)
$\mathscr{F}\frac{S_L}{u'}\tau_t^{-1}$	$\bar{c}(1-\bar{c})$	Lindstedt and Váos (1999)
$C_1\left[S_L/u' + \left(1+Da^{-2}\right)^{-1/4}\right]^2\tau_t^{-1}$	$\bar{\rho}\tilde{c}(1-\tilde{c})/\rho_u$	Schmidt et al. (1998)
$C_1\left(1+C_2 S_L/u'\right)\left(C_3 Da^{-1}+1\right)\tau_t^{-1}$	$\bar{\rho}\tilde{c}(1-\tilde{c})/\rho_u$	Swaminathan and Bray (2005)

Table 6.1 clearly shows that different model expressions are associated with different levels of simplifications. For instance, one of the oldest expressions for τ_f, see the second row in Table 6.1, involves neither laminar flame speed nor the laminar flame thickness. This model is based on an assumption that burning rate is controlled by turbulent mixing rate and, therefore, τ_f scales as τ_t. However, such a model cannot predict the well-documented and practically important increase in turbulent burning velocity by the pressure (provided that u' and L are not affected by p).

Certain models yield an increase in the burning rate by S_L, but do not involve the thickness δ_L, e.g., see the fourth row in Table 6.1. Other models involve both S_L and δ_L, but the influence of the thickness of $\overline{\dot{\omega}_c}$ vanishes if $Da \gg 1$, e.g., see the fifth and sixth rows in Table 6.1. Consequently, at high Damköhler numbers, these models yield a decrease in the burning rate with increasing pressure (due to a decrease in S_L), contrary to a large amount of experimental data that show an increase in U_t by p (Lipatnikov 2012; Lipatnikov and Chomiak 2002).

As far as capability for predicting the increase in U_t by p is concerned, the expressions listed in the first and third rows in Table 6.1 do yield the correct trend. Therefore, these expressions appear to be most promising. Nevertheless, it is worth stressing that neither of the algebraic models has yet been validated in a solid manner, i.e., by retaining the model constant(s) unchanged, against a wide set of experimental data obtained from substantially different flames under substantially different conditions. While the model addressed in the second row in Table 6.1 was applied to simulating various experiments, significant changes in the model constant C_1 were required to reach an agreement with data obtained from different flames.

Flame Surface Density Models

The most FSD models are based on assumptions that (i) the mass rate $\overline{\dot{\omega}_c}$ of product creation per unit volume is equal to a product of the mean flamelet surface area per this unit volume, i.e., the mean flame surface density $\overline{\Sigma}$, and the mean mass rate $\rho_u \bar{u}_c$ of product creation per the unit area of the flame surface, and (ii) the latter mass rate is approximately equal to $\rho_u S_L$. The former assumption neglects eventual correlations between Σ and $\rho_u u_c$. The latter assumption neglects perturbations of the local flamelet structure and the local burning rate by turbulent eddies and, therefore, may be valid in sufficiently weak turbulence only.

The foundations of the FSD approach can be illustrated by rewriting Eq. (6.23) as follows:

$$\frac{\partial}{\partial t}(\rho c) + \nabla \cdot (\rho \mathbf{u} c) = \rho S_d |\nabla c| \tag{6.60}$$

where S_d defined as follows:

$$S_d \equiv \frac{\nabla \cdot (\rho D \nabla c) + \dot{\omega}_c}{\rho |\nabla c|} \tag{6.61}$$

is the so-called displacement speed in the case of a finite flamelet thickness.[7] The displacement speed is the speed of motion of an iso-scalar surface with respect to the local flow. Indeed, using Eq. (6.2), Eq. (6.60) reads

$$\frac{\partial c}{\partial t} = \left(S_d + \mathbf{n} \cdot \mathbf{u}\right) |\nabla c| \tag{6.62}$$

in the case of a finite flamelet thickness.

The Favre-averaged Eq. (6.60) reads

$$\frac{\partial}{\partial t}(\bar{\rho}\tilde{c}) + \nabla \cdot (\bar{\rho}\tilde{\mathbf{u}}\tilde{c}) = -\nabla \cdot \overline{\rho \mathbf{u}'' c''} + \overline{\rho S_d |\nabla c|}. \tag{6.63}$$

Subsequently, if we assume that equality of $\rho S_d = \rho_u S_L$ holds not only in the unperturbed laminar flame, but also in turbulent flames, then, we arrive at

$$\frac{\partial}{\partial t}(\bar{\rho}\tilde{c}) + \nabla \cdot (\bar{\rho}\tilde{\mathbf{u}}\tilde{c}) = -\nabla \cdot \overline{\rho \mathbf{u}'' c''} + \rho_u S_L \overline{|\nabla c|}. \tag{6.64}$$

Comparison of Eqs. (6.27) and (6.64) shows

$$\overline{\nabla \cdot (\rho D \nabla c) + \dot{\omega}_c} = \rho_u S_L \overline{|\nabla c|} \tag{6.65}$$

or

$$\overline{\dot{\omega}_c} \approx \rho_u S_L \overline{|\nabla c|} \tag{6.66}$$

if the molecular transport term is neglected at high Reynolds numbers. Equation (6.66) is the cornerstone of the FSD approach, as the straightforward relation between FSD Σ and $|\nabla c|$ is well established, as reviewed elsewhere (Poinsot and Veynante 2005; Veynante and Vervisch 2002).

Transport equations for Σ were derived using different methods (Candel and Poinsot 1990; Pope 1988; Trouvé and Poinsot 1994; Vervisch et al. 1995; Zimont 2015). After averaging such equations involve a set of unclosed terms that should be modeled. There are different models of that kind, but all of them may be subsumed

[7] A product of $\rho|\nabla c|$ is mathematically meaningless in the case of an infinitely thin flame front, because both ρ and $|\nabla c|$ are discontinuous at the front.

Table 6.2 Flame surface density models

Source term $\mathscr{P}$	Sink term $\mathscr{D}$	Model
$C_1 \left(\frac{\tilde{\varepsilon}}{\nu}\right)^{1/2} \overline{\Sigma}$	$C_2 S_L \frac{2+e^{-C_3 R}}{3(1-\bar{c})} \overline{\Sigma}^2$, where $R = \frac{(1-\bar{c})\tilde{\varepsilon}}{S_L \overline{\Sigma}\tilde{k}}$	Cant et al. (1990)
$C_1 \frac{\tilde{\varepsilon}}{\tilde{k}} \overline{\Sigma}$	$C_2 \frac{S_L}{1-\bar{c}} \overline{\Sigma}^2$	CFM (Candel et al. 1990; Fichot et al. 1993)
$C_1 \frac{\tilde{\varepsilon}}{\tilde{k}} \overline{\Sigma}$	$C_2 \frac{S_L + C_3 u'}{1-\bar{c}} \overline{\Sigma}^2$	CFM1 (Candel et al. 1990; Duclos et al. 1993)
$C_1 \Gamma \frac{\tilde{\varepsilon}}{\tilde{k}} \overline{\Sigma}$	$C_2 \frac{S_L + C_3 u'}{1-\bar{c}} \overline{\Sigma}^2$	CFM2a (Boudier et al. 1992)
$C_1 \Gamma \frac{\tilde{\varepsilon}}{\tilde{k}} \overline{\Sigma}$	$C_2 \frac{S_L + C_3 u'}{\bar{c}(1-\bar{c})} \overline{\Sigma}^2$	CFM2b (Duclos et al. 1993)
$C_1 \frac{\tilde{\varepsilon}}{\tilde{k}} \overline{\Sigma}$ if $Da \geq C_2$	$C_3 \frac{S_L}{1-\bar{c}} \overline{\Sigma}^2$	Cheng and Diringer (1991)
$C_1 \left(\frac{\tilde{\varepsilon}}{\nu}\right)^{1/2} \overline{\Sigma}$	$C_2 \frac{\rho_u S_L}{\bar{\rho}\bar{c}(1-\bar{c})} \overline{\Sigma}^2$	Choi and Huh (1998)
$C_1 \frac{u'}{l_r} \overline{\Sigma}$	$C_2 \frac{\rho_u S_L}{\bar{\rho}\bar{c}(1-\bar{c})} \overline{\Sigma}^2$	Lee et al. (1998)

to

$$\frac{\partial \overline{\Sigma}}{\partial t} + \nabla \cdot \left(\tilde{\mathbf{u}} \overline{\Sigma}\right) = \nabla \cdot \left(\frac{\nu_t}{Sc_t} \nabla \overline{\Sigma}\right) + \mathscr{P} - \mathscr{D}, \tag{6.67}$$

with the source $\mathscr{P}$ and consumption $\mathscr{D}$ terms being specified in Table 6.2. Here, Sc_t and C_j are constants, which may be different for different models, $\tilde{k}$ and $\tilde{\varepsilon}$ are the Favre-averaged turbulent kinetic energy and its dissipation rate, respectively, ν_t is the turbulent viscosity given by a turbulence model, $\Gamma = \Gamma(u'/S_L, L/\Delta_L)$ is the so-called efficiency function[8] introduced by Meneveau and Poinsot (1991), and l_r is a dimensional constant (a length scale).

While the FSD models are widely used in applied CFD research into premixed turbulent combustion in engines, there is a need for thoroughly validating such models against a wide set or representative experimental data obtained from various well-defined simple flames under substantially different conditions.

Moreover, the FSD models suffer from fundamental limitations. In particular, first, the validity of the cornerstone Eq. (6.65) and its simplified version given by Eq. (6.66) may be put into question even in weakly turbulent flames commonly associated with the flamelet combustion regime and minor perturbations of local flamelet structure and burning rate ρu_c by turbulent eddies. For instance, dashed line in Fig. 6.8 shows that a ratio of $\overline{\dot{\omega}_c}/(\rho_u S_L |\overline{\nabla c}|)$ is significantly increased by $\bar{c}$ at $\bar{c} < 0.2$ and $0.8 < \bar{c}$. At low $\bar{c}$, variations in a ratio of $\overline{(\nabla \cdot (\rho D \nabla c) + \dot{\omega}_c)}/(\rho_u S_L |\overline{\nabla c}|)$, see solid line, are less pronounced, but they are still substantial at $0.8 < \bar{c}$. Therefore, neither Eq. (6.65) nor Eq. (6.66) holds under conditions of this DNS study (Lipat-

[8] There is the same function in Table 6.1 also.

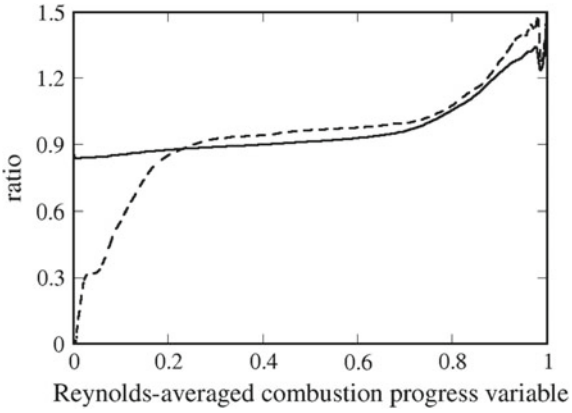

Fig. 6.8 Ratios of $\overline{\dot{\omega}_c}/(\rho_u S_L|\overline{\nabla c}|)$ (dashed line) and $\overline{(\nabla\cdot(\rho D\nabla c)+\dot{\omega}_c)}/(\rho_u S_L|\overline{\nabla c}|)$ (solid line) obtained in a DNS study (Lipatnikov et al. 2017) of weakly turbulent premixed burning associated with the flamelet combustion regime (Peters 2000)

nikov et al. 2017) in spite of the facts that (i) these conditions are well associated with the flamelet regime of premixed turbulent combustion and (ii) at least one of the two aforementioned equations is commonly assumed to be valid in the flamelet combustion regime.

Second, closure relations summarized in Table 6.2 involves the unperturbed laminar flame speed S_L, but do not allow for the influence of local flamelet perturbations on the balance of the mean FSD within a premixed turbulent flame brush. However, the already cited DNS study (Lipatnikov et al. 2017) shows that such an influence is of substantial importance and should be addressed properly.

Scalar Dissipation Rate Models

The SDR models are based on the following linear relation:

$$\overline{\dot{\omega}_c} = \frac{\bar{\rho}\tilde{\chi}}{2c_m - 1}, \tag{6.68}$$

where

$$c_m = \frac{\overline{c\dot{\omega}_c}}{\overline{\dot{\omega}_c}} \tag{6.69}$$

is commonly assumed to be a constant larger than 0.5.

Within the framework of the BML approach, Eqs. (6.68) and (6.69) can be derived straightforwardly (Bray 1979). First, multiplication of Eq. (6.23) with c yields

$$\frac{\partial}{\partial t}\left(\rho c^2\right) + \nabla\cdot\left(\rho\mathbf{u}c^2\right) = 2c\nabla\cdot(\rho D\nabla c) + 2c\dot{\omega}_c \tag{6.70}$$

using Eq. (6.2). Second, the Favre-averaged Eq. (6.70) reads

$$\frac{\partial}{\partial t}\left(\bar{\rho}\tilde{c}^2\right)+\frac{\partial}{\partial t}\left(\overline{\rho c''^2}\right)+\nabla\cdot\left(\bar{\rho}\tilde{\mathbf{u}}\tilde{c}^2\right)+\nabla\cdot\left(\tilde{\mathbf{u}}\overline{\rho c''^2}\right)+2\nabla\cdot\left(\tilde{c}\overline{\rho\mathbf{u}''c''}\right)$$
$$+\nabla\cdot\overline{\rho\mathbf{u}''c''^2}=2\tilde{c}\nabla\cdot\overline{(\rho D\nabla c)}+2\overline{c''\nabla\cdot(\rho D\nabla c)}+2\tilde{c}\overline{\dot{\omega}_c}+2\overline{c''\dot{\omega}_c}. \quad (6.71)$$

Third, multiplication of Eq. (6.27) with $\tilde{c}$ yields

$$\frac{\partial}{\partial t}\left(\bar{\rho}\tilde{c}^2\right)+\nabla\cdot\left(\bar{\rho}\tilde{\mathbf{u}}\tilde{c}^2\right)+2\tilde{c}\nabla\cdot\overline{\rho\mathbf{u}''c''}=2\tilde{c}\nabla\cdot\overline{(\rho D\nabla c)}+2\tilde{c}\overline{\dot{\omega}_c}. \quad (6.72)$$

Fourth, subtraction of Eq. (6.72) from Eq. (6.71) results in

$$\frac{\partial}{\partial t}\left(\overline{\rho c''^2}\right)+\nabla\cdot\left(\tilde{\mathbf{u}}\overline{\rho c''^2}\right)$$
$$=-2\overline{\rho\mathbf{u}''c''}\cdot\nabla\tilde{c}-\nabla\cdot\overline{\rho\mathbf{u}''c''^2}+2\overline{c''\nabla\cdot(\rho D\nabla c)}+2\overline{c''\dot{\omega}_c}. \quad (6.73)$$

Fifth, within the framework of the BML approach, we have

$$\begin{aligned}\overline{\rho\mathbf{u}''c''^2}&=\rho_u(1-\tilde{c})\left(\tilde{\mathbf{u}}_u-\tilde{\mathbf{u}}\right)\tilde{c}^2+\rho_b\tilde{c}\left(\tilde{\mathbf{u}}_b-\tilde{\mathbf{u}}\right)(1-\tilde{c})^2\\&=\bar{\rho}\tilde{c}(1-\tilde{c})\left[\tilde{c}\left(\tilde{\mathbf{u}}_u-\tilde{\mathbf{u}}\right)+(1-\tilde{c})\left(\tilde{\mathbf{u}}_b-\tilde{\mathbf{u}}\right)\right]\\&=\bar{\rho}\tilde{c}(1-\tilde{c})\left[\tilde{c}\tilde{\mathbf{u}}_u+(1-\tilde{c})\tilde{\mathbf{u}}_b-\tilde{\mathbf{u}}\right]\\&=\bar{\rho}\tilde{c}(1-\tilde{c})\left[\tilde{c}\tilde{\mathbf{u}}_u+(1-\tilde{c})\tilde{\mathbf{u}}_b-(1-\tilde{c})\tilde{\mathbf{u}}_u-\tilde{c}\tilde{\mathbf{u}}_b\right]\\&=\bar{\rho}\tilde{c}(1-\tilde{c})\left(\tilde{\mathbf{u}}_b-\tilde{\mathbf{u}}_u\right)(1-2\tilde{c})=\overline{\rho\mathbf{u}''c''}(1-2\tilde{c}).\end{aligned} \quad (6.74)$$

Sixth, substitution of Eqs. (6.37), (6.41), (6.69) and (6.74) into Eq. (6.73) yields

$$(1-2\tilde{c})\frac{\partial}{\partial t}(\bar{\rho}\tilde{c})+(1-2\tilde{c})\nabla\cdot(\bar{\rho}\tilde{\mathbf{u}}\tilde{c})$$
$$=-(1-2\tilde{c})\nabla\cdot\overline{\rho\mathbf{u}''c''}+2\overline{c''\nabla\cdot(\rho D\nabla c)}+2(c_m-\tilde{c})\overline{\dot{\omega}_c} \quad (6.75)$$

using Eq. (6.15). Seventh, subtraction of Eq. (6.27) multiplied with $(1-2\tilde{c})$ from Eq. (6.75) results in

$$\begin{aligned}\left(2c_m-1\right)\overline{\dot{\omega}_c}&=-2\overline{c''\nabla\cdot(\rho D\nabla c)}+(1-2\tilde{c})\nabla\cdot\overline{(\rho D\nabla c)}\\&=2\overline{\rho D\nabla c\cdot\nabla c''}-2\nabla\cdot\overline{(\rho c''D\nabla c)}+(1-2\tilde{c})\nabla\cdot\overline{(\rho D\nabla c)}\\&=\bar{\rho}\tilde{\chi}+2\overline{\rho D\nabla c''}\cdot\nabla\tilde{c}-2\nabla\cdot\overline{(\rho c''D\nabla c)}+(1-2\tilde{c})\nabla\cdot\overline{(\rho D\nabla c)}.\end{aligned} \quad (6.76)$$

At $\mathrm{Re}_t\gg 1$ and $Da\gg 1$, instantaneous variations in c are localized to thin flamelets characterized by large (when compared to $|\nabla\tilde{c}|$) spatial gradients $|\nabla c|$. Consequently, the first term on the RHS of Eq. (6.76) scales as δ_L^{-2} and dominates, whereas other terms scale as $\delta_t^{-1}\delta_L^{-1}$. Therefore, by neglecting $O(\delta_t^{-1}\delta_L^{-1})$-order terms, we arrive at Eq. (6.68).

Equations (6.68) and (6.69) offer an opportunity to evaluate the mean rate $\overline{\dot{\omega}_c}$ by studying a transport equation for the Favre-averaged scalar dissipation rate $\tilde{\chi}$. Such an approach was pioneered by Borghi (1990) who derived a transport equation for $\bar{\chi}$ in the case of a constant density. Subsequently, Swaminathan and Bray (2005) derived a transport equation for $\tilde{\chi}$ in the case of variable density. In both cases, the transport equations involve a number of terms that require closure relations.

Models of these terms were developed by a few research groups, as reviewed elsewhere (Chakraborty et al. 2011). In all applications of these models, c_m was assumed to retain the same value in the entire flame brush and this assumption was supported in a recent DNS study (Lipatnikov et al. 2015a). However, c_m is not a constant and may depend e.g. on the choice of a combustion progress variable (Lipatnikov et al. 2015a).

The discussed SDR approach definitely requires more validation studies. In particular, capabilities of the SDR models for predicting an increase in U_t by the pressure should be tested. The point is that equations written in the bottom row in Table 6.1 were obtained using a SDR model (Swaminathan and Bray 2005), but these equations appear to yield a wrong trend, i.e., a decrease in U_t with increasing p, if $Da \gg 1$.

Moreover, since Eq. (6.68) was derived within the framework of the BML paradigm, the SDR approach seems to be best justified in the flamelet combustion regime. However, DNS data obtained from weakly turbulent flames associated with the flamelet combustion regime (Lipatnikov et al. 2015a) and plotted in Fig. 6.9a show that a ratio of $\overline{\dot{\omega}_c}/(\bar{\rho}\tilde{\chi})$ is increased by $\bar{c}$, whereas c_m evaluated using Eq. (6.69) is close to 0.9 in the largest parts of all three flame brushes, see Fig. 6.9b. Therefore, Fig. 6.9 does not support Eq. (6.68), with the differences between the model and DNS results being most pronounced at the trailing and, especially, leading edge of the mean flame brush. Inability of Eq. (6.68) to yield the correct value of the mean rate $\overline{\dot{\omega}_c}$ at $\bar{c} \ll 1$ is a serious limitation, because the leading edge of a premixed turbulent flame brush may play a crucial role in the flame propagation, as discussed in detail elsewhere (Kuznetsov and Sabelnikov 1990; Lipatnikov 2012; Lipatnikov and Chomiak 2005c; Sabelnikov and Lipatnikov 2013, 2015; Zel'dovich et al. 1985).

Thus, as far as models that invoke an extra transport equation for $\overline{\Sigma}$ or $\tilde{\chi}$ are concerned, a basic weak point of such models consists of the fact that neither the linear Eq. (6.66) nor the linear Eq. (6.68) is a sufficiently precise closure relation even under conditions that are well associated with its derivation.

Alternatively, transport equations for $\dot{\omega}_c$ and $\overline{\dot{\omega}_c}$ can be derived straightforwardly. Such an approach was recently put forward and already yielded encouraging results (Sabelnikov et al. 2016, 2017). Nevertheless, discussion of this new approach is beyond the scope of the present chapter, because a completely closed transport equation for $\overline{\dot{\omega}_c}$ has not yet been elaborated.

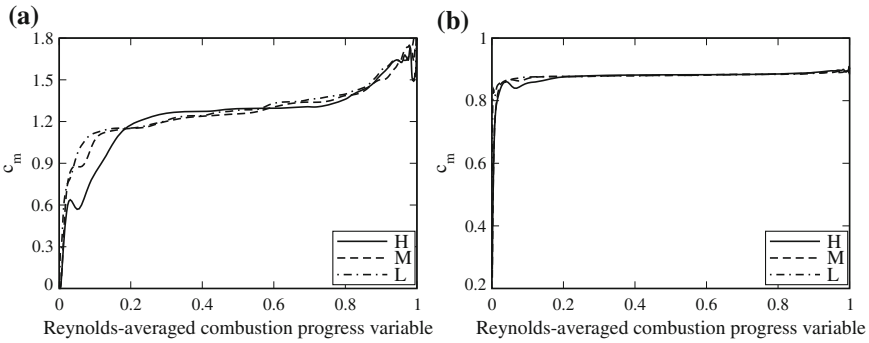

Fig. 6.9 **a** Ratios of $\overline{\dot{\omega}_c}/(\bar{\rho}\tilde{\chi})$ and **b** c_m obtained from three statistically planar 1D flames in a DNS study (Lipatnikov et al. 2015a) of weakly turbulent premixed burning associated with the flamelet combustion regime (Peters 2000). Flames H, M, and L are characterized by the density ratio $\sigma = 7.53$, 5.0, and 2.5, respectively

6.4 Turbulent Flame Closure and Flame Speed Closure Models

The goal of the present section is to discuss (i) the so-called Turbulent Flame Closure (TFC) model of the influence of turbulence on premixed burning and (ii) its extension known as Flame Speed Closure (FSC) model. These models are selected for a more detailed discussion, because they have yet been validated using a significantly wider set of experimental data obtained from well-defined simple cases when compared to any competing model developed for RANS simulations of premixed turbulent combustion.

6.4.1 Equations

TFC Model

The foundations of the TFC model were laid in the pioneering work by Prudnikov (1960, 1964). Subsequently, the model was developed by Zimont (1979). The final version of the TFC model, which is implemented in various commercial CFD codes, was presented by Karpov et al. (1996) and Zimont and Lipatnikov (1995).

The TFC model deals with the following closed transport equation

$$\frac{\partial}{\partial t}\left(\bar{\rho}\tilde{c}\right) + \nabla \cdot \left(\bar{\rho}\tilde{\mathbf{u}}\tilde{c}\right) = \nabla \cdot \left[\bar{\rho}(\kappa + D_t)\nabla\tilde{c}\right] + \rho_u U_t \left|\nabla\tilde{c}\right|, \tag{6.77}$$

i.e., the model provides the following joint closure relation

$$-\nabla\cdot\overline{\rho\mathbf{u}''c''}+\overline{\dot{\omega}_c}=\nabla\cdot[\bar{\rho}(\kappa+D_t)\nabla\tilde{c}]+\rho_u U_t\,|\nabla\tilde{c}| \tag{6.78}$$

for the two terms on the RHS of Eq. (6.27). The molecular heat diffusivity κ of the mixture is commonly neglected when compared to the turbulent diffusivity D_t when using the TFC model.

Equation (6.77) was in fact introduced into the combustion literature by Prudnikov (1960, 1964), but he wrote it in another form and applied it solely to statistically planar 1D flame that propagated in frozen turbulence. In the same 1D case, Eq. (6.77) was derived by Lipatnikov and Chomiak (2005a, b) by assuming that the mean structure of a developing premixed turbulent flame was self-similar,[9] in line with various experimental data analyzed elsewhere (Lipatnikov 2012; Lipatnikov and Chomiak 2000b, 2001, 2002, 2004; Prudnikov 1964).

Equation (6.77) yields permanent growth of the mean thickness δ_t of the statistically planar 1D flame, whereas turbulent burning velocity does not depend on time to the leading order (Prudnikov 1964). Such an intermediately asymptotic regime of premixed turbulent combustion pointed out by Prudnikov (1964), Kuznetsov (1975), Clavin and Williams (1979), and Zimont (1979) was later called "intermediate steady propagation (ISP) flames" (Zimont 2000).

In order to be consistent with this basic peculiarity of Eq. (6.77), a model for the turbulent burning velocity U_t, required to close the approach, should also address the ISP flames. To the best of the present author's knowledge, the sole model that satisfies this basic requirement has yet been developed by Zimont (1979), who has theoretically obtained the following expression:

$$U_{t,ISP}=Au'Da^{1/4}=Au'\left(\frac{\tau_t}{\tau_c}\right)^{1/4}=Au'^{3/4}S_L^{1/2}L^{1/4}\kappa_u^{-1/4}, \tag{6.79}$$

with $U_t=U_{t,ISP}$ being substituted into the second term on the RHS of Eq. (6.77) within the framework of the TFC model. Here, A is a single model constant. Equation (6.79) was derived under the following constraints (Zimont 1979, 2000); (i) the turbulent Reynolds number $\mathrm{Re}_t=u'L/\nu_u\gg 1$, (ii) the Damköhler number $Da\gg 1$, (iii) the Karlovitz number $Ka\propto(u'/S_L)^2\mathrm{Re}_t^{-1/2}>1$, and (iv) the flame-development time $\tau_t<t_{fd}\ll\tau_t Da^{3/2}$. Subsequent tests of the TFC model have shown that it works well in a wider range of conditions, e.g., (ii′) $Da>1$ and (iii′) $u'>S_L$.

The reader interested in further discussion of the foundations of the TFC model is referred to Lipatnikov (2012), Lipatnikov and Chomiak (2002) and Zimont (2000).

To the best of the present author's knowledge, in all RANS applications of the TFC model, (i) the turbulent diffusivity D_t in the first term on the RHS of Eq. (6.77) was associated with the fully developed turbulent diffusivity $D_{t,\infty}$ yielded by a turbulence model, e.g.

$$D_{t,\infty}=\frac{C_\mu}{Sc_t}\frac{\tilde{k}^2}{\tilde{\varepsilon}} \tag{6.80}$$

[9] This feature of premixed turbulent burning will be discussed in Sect. 6.4.4.

if the k-ε model (Launder and Spalding 1972) is invoked, and (ii) the mean density was evaluated using Eq. (6.35). Here, $C_\mu = 0.09$ is a constant of the k-ε model (Launder and Spalding 1972) and Sc_t is a turbulent Schmidt number. Note that Eq. (6.35) is valid not only within the framework of the BML paradigm, but also in a general case provided that $c = (T - T_u)/(T_b - T_u)$, $\rho T = \rho_u T_u$, and, therefore, $1 + (\sigma - 1)c = \rho_u/\rho$. Indeed, Favre averaging of the latter equality results in Eq. (6.35).

FSC Model

The FSC model is strongly based on the TFC model and involves Eqs. (6.77)–(6.79). In addition, the FSC model extends the TFC model in order to simulate an early stage of premixed turbulent flame development and weakly turbulent flames, as discussed in the rest of the present section.

Within the framework of the FSC model, growth of turbulent diffusivity and burning velocity during an early stage of premixed flame development is addressed following the classical theory of turbulent mixing by Taylor (1935), which yields the following well-known expression (Brodkey 1967; Hinze 1975)

$$D_t = D_{t,\infty}\left[1 - \exp\left(-\theta_{fd}\right)\right] \equiv D_{t,\infty} f_1(\theta_{fd}) \tag{6.81}$$

for developing turbulent diffusivity in the simple case of a single point source of admixture. Subsequently, the following expression

$$U_t = U_{t,ISF}\left\{1 + \theta_{fd}^{-1}\left[\exp\left(-\theta_{fd}\right) - 1\right]\right\}^{1/2} \equiv U_{t,ISF} f_2(\theta_{fd}) \tag{6.82}$$

for developing turbulent burning velocity was derived (Lipatnikov and Chomiak 1997) by combining the Taylor theory and the aforementioned model of $U_{t,ISF}$ by Zimont (1979). Here, $\theta_{fd} = t_{fd} u'^2/D_{t,\infty} = t_{fd}/\tau_L$ is the normalized flame-development time t_{fd}, τ_L is the Lagrangian time scale of the turbulence, while $U_{t,ISF}$ and $D_{t,\infty}$ are modeled using Eqs. (6.79) and (6.80), respectively.

The two extra terms $f_1(\theta_{fd})$ and $f_2(\theta_{fd})$, which pertain to the FSC model and describe the development of turbulent diffusivity and burning velocity, respectively, do not involve an empirical or tuning parameter. Both time-dependent terms tend to unity as $\theta_{fd} \to \infty$, i.e., the FSC Eqs. (6.81) and (6.82) reduce to the TFC Eqs. (6.80) and (6.79), respectively, in this limiting case.

The flame-development time can easily be determined in the case of unsteady combustion initiated by a single spark. In such a case, t_{fd} is simply counted from the ignition instant. When modeling a statistically stationary premixed turbulent flame, t_{fd} is still a meaningful quantity. Indeed, a statistically stationary flow can be a developing process, with the development occurring as a fluid particle is convected by the mean flow. Statistically stationary turbulence behind a grid develops, i.e., decays in the direction of the mean flow. A statistically stationary mixing layer develops, i.e., grows in the direction of the mean flow. Similarly, a statistically stationary premixed turbulent flame develops, i.e., both flame speed and mean flame brush thick-

ness grow in the direction of the mean flow. In these cases, the turbulence (layer, or flame, respectively) development time is a meaningful quantity, which is equal to the time required in order for a fluid particle to be convected from the grid (cross section associated with start of the mixing, or cross section where the flame is stabilized, respectively) to the considered point.

It is worth noting that development of turbulent burning velocity can also be of importance for thermoacoustic applications, e.g., (Lipatnikov and Sathiah 2005).

In the simplest case of a statistically planar, 1D flow with frozen turbulence characteristics, the burning velocity U_t yielded by the TFC model scales as $u'Da^{1/4}$ and vanishes as $u' \to 0$. Accordingly, the source term on the RHS of Eq. (6.77) also vanishes in this limiting case, i.e., the TFC model cannot be applied to such a weakly turbulent flame. To resolve the problem, the following laminar-like source term

$$Q_L = \frac{\bar{\rho}(1-\tilde{c})}{t_{ch}(1+D_t/\kappa_b)} \exp\left(-\frac{\Theta}{\tilde{T}}\right) \tag{6.83}$$

was incorporated (Lipatnikov and Chomiak 1997, 2000a, 2002) into the RHS of Eq. (6.77), which reads

$$\frac{\partial}{\partial t}(\bar{\rho}\tilde{c}) + \nabla \cdot (\bar{\rho}\tilde{\mathbf{u}}\tilde{c}) = \nabla \cdot [\bar{\rho}(\kappa + D_t)\nabla \tilde{c}] + \rho_u U_t |\nabla \tilde{c}| + Q_L \tag{6.84}$$

within the framework of the FSC model. Here, t_{ch} and Θ are the time scale and activation temperature, respectively, of a single reaction that combustion chemistry is reduced to, and the Favre-averaged temperature can easily be evaluated using the ideal gas state equation, e.g., $\bar{\rho}\tilde{T} = \rho_u T_u$. In intense turbulence associated with $\mathrm{Re}_t \to \infty$, a ratio of $D_t/\kappa_b \to \infty$ and, therefore, Q_L vanishes. In this limiting case, the sole difference between the FSC and TFC models is associated with the two time-dependent terms on the RHSs of Eqs. (6.81) and (6.82).

If the laminar flame speed is known, then, the extra source term Q_L given by Eq. (6.83) does not involve a tuning parameter, because the time scale t_{ch} can easily be determined within the framework of the FSC model before running simulations of turbulent combustion. Indeed, if a value of Θ is set, then, t_{ch} can be evaluated by (i) applying the FSC model to a planar 1D flame in the case of $u' = 0$ and (ii) finding t_{ch} such that the computed flame speed is equal to S_L, which is the key input parameter of both the TFC and FSC models. Because the computed flame speed scales as $(\kappa_u/t_{ch})^{1/2}$ (Zel'dovich et al. 1985) if $u' = 0$, the pre-calculation of t_{ch} based on a known S_L requires only two iterations.

If (i) the simplest case of a statistically planar, 1D flame that propagates in frozen turbulence is addressed, (ii) the problem is considered in a coordinate framework that moves at a speed equal to U_t in the direction from the burned to the unburned gas, and (iii) $\kappa + D_t$ and $t_{ch}(1 + D_t/\kappa_b)$ are substituted with κ' and t'_{ch}, respectively, then, Eqs. (6.83) and (6.84) reduce to the basic equation of the thermal laminar flame theory (Zel'dovich et al. 1985). Consequently, the flame speed is equal to S_L in that coordinate framework (Lipatnikov and Chomiak 1997, 2002). Coming back to the

coordinate framework attached to the mean flow of the unburned gas, we see that the flame speed is equal to $U_t + S_L$ and tends to S_L as $u' \to 0$. Moreover, when $u' \to 0$, the turbulent diffusivity $D_t \to 0$ and the FSC Eq. (6.84) reduces to a well-known simple balance equation that models a laminar premixed flame in the case of a single-step chemistry (Zel'dovich et al. 1985). Thus, the extra source term Q_L results solely from the linear interpolation between the latter balance equation valid at $u' = 0$ and the TFC balance equation valid at $Ka > 1$ or at least $u' > S_L$.

It is worth noting that the use of the extra source term Q_L allows us not only apply the FSC model to weakly turbulent combustion, but also resolves the following problem, which may be of substantial importance in applications. The point is that Eq. (6.77) admits a trivial solution of $\tilde{c}(\mathbf{x}, t)$ =const if boundary conditions are set using $\nabla\tilde{c}$. Accordingly, in order for simulations to yield $\tilde{c} = 1$ somewhere at each instant, at least one boundary condition should be $\tilde{c} = 1$. On the contrary, due to the extra source Q_L, Eq. (6.84) is compatible with both types of boundary conditions.

Side by side with the advantages discussed above, the use of $Q_L > 0$ has disadvantages. First, the RHS of Eq. (6.83) is a highly nonlinear function of the mean temperature $\tilde{T}$. Accordingly, if the term Q_L plays a substantial role, it should be resolved using a significantly finer mesh when compared to a mesh required to numerically solve Eq. (6.77).

Second, as discussed in Sect. 6.4.3, the TFC Eq. (6.77) admits an exact analytical solution in a statistically planar 1D case if D_t and U_t are assumed to be constant. This exact solution allows us to easily reveal certain basic features of the TFC model. Such a method of a qualitative analysis cannot be applied straightforwardly to Eq. (6.84) with $Q_L > 0$. Nevertheless, because numerical simulations indicate that the basic features of the TFC and FSC models are similar (with a single exception discussed later), investigation of the basic features of the TFC model sheds some light on the basic features of the FSC model also.

Finally, it is worth noting that the influence of the extra source term Q_L on the computed heat-release rate and mean flame brush thickness is reduced with increasing u'. Accordingly, this term may be skipped in simulations of sufficiently intense turbulence provided that the boundary conditions involve $\tilde{c} = 1$ somewhere.

6.4.2 Extensions

When performing the first tests of the TFC model (Karpov et al. 1996; Zimont and Lipatnikov 1993, 1995), it was extended by invoking submodels of two well-documented effects that are not addressed by the TFC model. Such a method allowed those researchers to extend the domain of applicability of the TFC model and to test it against a significantly wider set of experimental data. The same two submodels may also be incorporated into the FSC model. It is worth stressing, however, that the two submodels invoked to extend the TFC or FSC model are totally independent and may be either switched on or switched off when necessary.

Local Flame Quenching

In order to address local combustion quenching by intense turbulent stretching, which is discussed in detail elsewhere (Abdel-Gayed et al. 1984; Bradley 1992, 2002; Bradley et al. 1992; Bray 1987; Bray and Cant 1991; Lipatnikov 2012; Lipatnikov and Chomiak 2005c), a stretch factor $G_s = (1 - \mathbb{P}_q)$ may be incorporated into Eq. (6.79), which reads

$$U_{t,ISP} = Au'^{3/4} S_L^{1/2} L^{1/4} \kappa_u^{-1/4} (1 - \mathbb{P}_q), \tag{6.85}$$

where

$$\mathbb{P}_q = 1 - \frac{1}{2} \mathrm{erfc} \left\{ -\frac{1}{\sqrt{2}\sigma_\varepsilon} \left[\ln \frac{\varepsilon_q}{\tilde{\varepsilon}} + \frac{\sigma_\varepsilon^2}{2} \right] \right\} \tag{6.86}$$

is the probability of local combustion quenching by turbulent strains, erfc is the complementary error function, $\sigma_\varepsilon^2 = 0.26 \ln(L/\eta)$, $\eta = (\nu_u^3/\varepsilon)^{1/4}$ is the Kolmogorov length scale, $\varepsilon_q = 15 \nu_u \dot{s}_q^2$, and $\dot{s}_q$ is a critical stretch rate associated with the local combustion quenching. Equation (6.86) was invented by Bray (1987).

Due to strong sensitivity of a stretched laminar premixed flame to the flame topology and transient effects (Lipatnikov and Chomiak 2005c), a model capable for predicting $\dot{s}_q$ in turbulent flows has not yet been developed. Accordingly, the critical stretch rate is in fact an unknown input parameter of the quenching submodel given by Eq. (6.86). Therefore, the use of that submodel makes simulation results dependent on a tuned value of $\dot{s}_q$, whereas the original TFC model involves a single unknown input parameter, i.e., the constant A in Eq. (6.79), which may be set equal to the same value $A = 0.5$ for various significantly different flames. In all simulations discussed in the following, $\mathbb{P}_q = 0$ unless the opposite is stated.

Preferential Diffusion and Lewis Number Effects

Discussion of effects that stem from differences in molecular transport coefficients of fuel, oxygen, and heat is beyond the scope of the present chapter and the interested reader is referred to books (Kuznetsov and Sabelnikov 1990; Lipatnikov 2012), a review article (Lipatnikov and Chomiak 2005c), and recent papers (Goulier et al. 2017; Venkateswaran et al. 2011, 2013, 2015). Here, it is worth only noting that such effects could be addressed by the TFC or FSC model by substituting the standard chemical time scale τ_c in Eq. (6.79) with a time scale that characterizes local burning rate in critically perturbed laminar flames. Following Kuznetsov and Sabelnikov (1990), Zimont and Lipatnikov (1993, 1995) used a time scale that characterized burning rate in critically strained planar laminar flames. Subsequently, Karpov and Lipatnikov (1995, 1997) suggested to use another time scale that characterized burning rate in critically curved spherical laminar flames. In particular, that time scale was invoked in a validation study by Karpov et al. (1996), which will be discussed later.

6.4.3 Features

Let us consider a statistically planar 1D flame that propagates in homogeneous turbulence from left to right and does not affect the turbulence, i.e., u', L, and D_t are assumed to be independent of the spatial coordinate x. Then, one can easily check by substitution (Lipatnikov 2009b) that Eqs. (6.34) and (6.77) have the following exact analytical solution for the Reynolds-averaged combustion progress variable

$$\bar{c} = \frac{1}{2}\,\mathrm{erfc}\left(\xi\sqrt{\pi}\right) = \sqrt{\frac{1}{\pi}}\int_{\xi\sqrt{\pi}}^{\infty} e^{-\zeta^2} d\zeta, \tag{6.87}$$

where

$$\xi = \frac{x - x_f(t)}{\delta(t)}, \tag{6.88}$$

$$x_f(t) = x_{f,0} + \int_0^t U_t d\zeta, \tag{6.89}$$

$x_{f,0}$ is an initial flame position,

$$\delta_t^2 = 4\pi \int_0^t D_t d\zeta, \tag{6.90}$$

and the mean flame brush thickness is defined using the maximum gradient method, i.e.,

$$\delta_t \equiv \frac{1}{\max\left\{\left|\partial\bar{c}/\partial x\right|\right\}}. \tag{6.91}$$

Indeed, substitution of Eq. (6.87) into the state Eq. (6.34) and the mass balance Eq. (6.15) results in

$$-\frac{1}{\rho_u - \rho_b}\frac{d\bar{\rho}}{d\xi} = \frac{\bar{\rho}^2}{\rho_u\rho_b}\frac{d\tilde{c}}{d\xi} = \frac{d\bar{c}}{d\xi} = -\mathrm{e}^{-\pi\xi^2} \tag{6.92}$$

and

$$\frac{d}{d\xi}(\bar{\rho}\tilde{u}) = \left(U_t + \xi\frac{d\delta_t}{dt}\right)\frac{d\bar{\rho}}{d\xi}, \tag{6.93}$$

respectively. Integrating the latter equation from ξ to infinity and using Eq. (6.92), we obtain

$$-\bar{\rho}\tilde{u} = U_t(\rho_u - \bar{\rho}) + \frac{d\delta_t}{dt}\int_{\xi}^{\infty}\zeta\frac{d\bar{\rho}}{d\zeta}d\zeta = U_t(\rho_u - \bar{\rho}) + \frac{d\delta_t}{dt}\frac{\rho_u - \rho_b}{2\pi}\mathrm{e}^{-\pi\xi^2} \tag{6.94}$$

in the framework linked with the unburned gas, i.e., $\tilde{u}(\xi \to \infty) \to 0$. Substitution of Eqs. (6.87) and (6.94) into Eq. (6.77) yields

$$-\bar{\rho}\xi\frac{d\delta_t}{dt}\frac{d\tilde{c}}{d\xi}-\rho_u U_t\frac{d\tilde{c}}{d\xi}-\frac{d\delta_t}{dt}\frac{\rho_u-\rho_b}{2\pi}\mathrm{e}^{-\pi\xi^2}\frac{d\tilde{c}}{d\xi}$$
$$=\frac{D_t}{\delta_t}\frac{d}{d\xi}\left(\bar{\rho}\frac{d\tilde{c}}{d\xi}\right)-\rho_u U_t\frac{d\tilde{c}}{d\xi}. \tag{6.95}$$

Using Eq. (6.92), we obtain

$$\frac{1}{2}\frac{d\delta_t^2}{dt}\frac{\rho_b}{\bar{\rho}^2}\frac{d\bar{c}}{d\xi}\left(-\bar{\rho}\xi+\frac{\rho_u-\rho_b}{2\pi}\frac{d\bar{c}}{d\xi}\right)$$
$$=D_t\frac{d}{d\xi}\left(\frac{\rho_b}{\bar{\rho}}\frac{d\bar{c}}{d\xi}\right)=D_t\frac{\rho_b}{\bar{\rho}^2}\left[(\rho_u-\rho_b)\frac{d\bar{c}}{d\xi}-2\pi\xi\bar{\rho}\right]\frac{d\bar{c}}{d\xi}, \tag{6.96}$$

which is valid if Eq. (6.90) holds. Thus, Eqs. (6.87)–(6.90) satisfy Eq. (6.77) supplemented with the state Eq. (6.35) and the mass balance Eq. (6.15).

It is worth noting that, in the above equations, the burning velocity U_t may be evaluated using either Eq. (6.79) within the framework of the TFC model or Eq. (6.82) associated with the FSC model. Similarly, the diffusivity D_t may either be constant within the framework of the TFC model or depend on flame-development time, e.g. see Eq. (6.81) associated with the FSC model.

This analytical solution reveals three important features of the TFC model. First, different terms on the RHS of Eq. (6.77) control different flame characteristics. The second spatial derivative in the turbulent diffusion term controls the shape of the spatial profile of $\bar{c}$. The turbulent diffusivity in the same term controls the growth of the mean flame brush thickness δ_t, but does not affect the flame propagation speed, which is solely controlled by the gradient source term. On the contrary, the source term affects neither the mean flame structure nor the thickness δ_t.

Second, the TFC model predicts self-similarity of the mean structure of a developing premixed turbulent flame, i.e., spatial profiles of $\bar{c}(x,t)$ collapse to the same curve $\bar{c}(\xi)$ if the spatial distance is normalized using the growing mean flame brush thickness, see Eq. (6.88).

Third, Eq. (6.90) yields a permanently growing mean flame brush thickness.

6.4.4 Validation

Let us begin with assessing the analytical results given by Eqs. (6.87) and (6.90). The self-similarity of the mean structure of a developing premixed turbulent flame is well documented in various experiments analyzed elsewhere (Lipatnikov and Chomiak 2000b, 2001, 2002, 2004), see also recent papers (Tamadonfar and Gülder 2014, 2015), with the measured self-similar profiles of $\bar{c}(\xi)$ being well fitted with Eq. (6.87), e.g., see Fig. 6.10.

As far as development of mean flame brush thickness is concerned, substitution of a constant $D_t \propto u'L$ associated with the TFC model into Eq. (6.90) yields

$$\delta_t \propto \sqrt{u'Lt}, \tag{6.97}$$

whereas substitution of Eq. (6.81) associated with the FSC model into Eq. (6.90) results in

$$\frac{\delta_t^2}{4\pi u'^2 \tau_L^2} = \theta_{fd}\left[1 - \frac{1}{\theta_{fd}}\left(1 - \mathrm{e}^{-\theta_{fd}}\right)\right] \tag{6.98}$$

and, hence, $\delta_t \propto u' t_{fd}$ at $\theta_{fd} = t_{fd}/\tau_L = t_{fd} u'^2 / D_{t,\infty} \ll 1$ and $\delta_t = 2u'\tau_L\sqrt{\pi\theta_{fd}} \propto \sqrt{u' L t_{fd}}$ at $\theta_{fd} \gg 1$. Consequently, the former model yields a significantly larger δ_t during an earlier stage of the flame development, but the mean flame brush thicknesses obtained using the two models are almost equal to one another at large θ_{fd}, cf. solid and dashed lines in Fig. 6.11a.

Figure 6.11b indicates that results calculated using Eq. (6.98), see solid line, agree with various experimental data, see symbols, substantially better than results calculated using Eq. (6.97), see dashed line. Qualitatively, the TFC model yields square-root dependence of the mean flame brush thickness on the flame-development time, whereas the FSC model predicts the linear dependence of $\delta_t \propto u' t_{fd}$ at $t_{fd} \ll \tau_L$. The latter prediction is validated not only by the data plotted in Fig. 6.11b, but also by numerous other data obtained from various flames, e.g., see recent papers (Chowdhury and Cetegen 2017; Kheirkhah and Gülder 2013, 2014, 2015; Sponfeldner et al. 2015; Tamadonfar and Gülder 2014, 2015). Indeed, those data show (i) the linear dependence of δ_t on the distance from the flame-holder and, hence, on the flame-development time and (ii) and an almost linear increase in δ_t by u'.

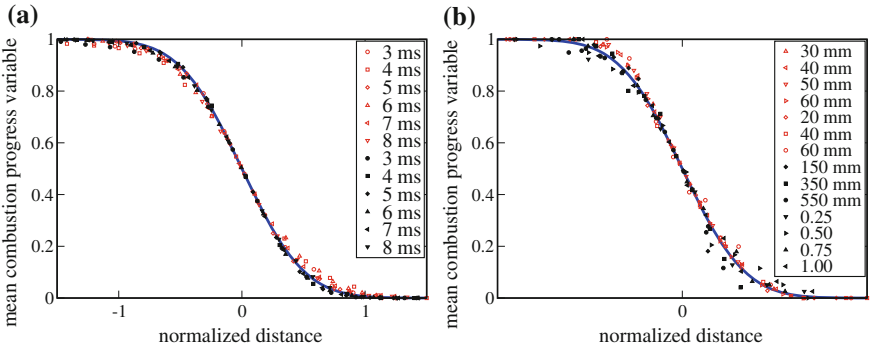

Fig. 6.10 Self-similar profiles of the mean combustion progress variable. **a** Data obtained by Renou et al. (2002) from expanding statistically spherical lean ($\Phi = 0.27$) H_2-air (open symbols) and stoichiometric C_3H_8-air (filled symbols) flames under the room conditions at different instants after spark ignition, specified in legends. Curve shows results computed using Eq. (6.87). **b** Data obtained by Gouldin and Miles (1995) from lean ($\Phi = 0.68$) C_2H_6-air V-shaped flames (open triangles), by Namazian et al. (1986) from lean ($\Phi = 0.8$) C_2H_6-air V-shaped flames (open squares, diamonds, and circles), by Sjunnesson et al. (1992) from lean ($\Phi = 0.6$) C_3H_8-air confined flames stabilized with a bluff body (filled squares, diamonds, and circles), and by Wu et al. (1990) from lean ($\Phi = 0.8$) H_2-air jet flames (filled triangles). Dimensional or normalized distances from flame stabilization points are specified in legends. Curve shows results computed using Eq. (6.87)

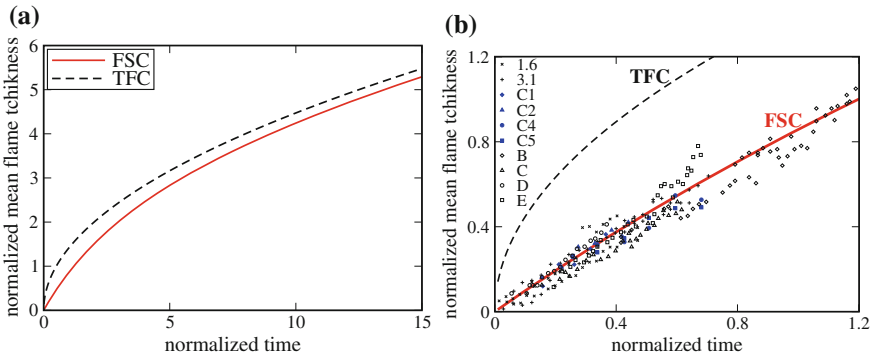

Fig. 6.11 Normalized mean flame brush thickness $\delta_t/\sqrt{2\pi L}$ versus normalized flame-development time θ_{fd}. **a**, **b** Dashed and solid lines show results calculated using Eqs. (6.97) and (6.98) associated with the TFC and FSC models, respectively. **b** Crosses and pluses show data obtained by Atashkari et al. (1999) from expanding statistically spherical CH_4-air flames at two different values of u'/S_L specified in legends. Filled diamonds, triangles, circles and squares show data obtained by Renou et al. (2002) from expanding statistically spherical stoichiometric CH_4-air (C2, $u'/S_L = 0.92$ and C5, $u'/S_L = 1.38$) and C_3H_8-air (C1, $u'/S_L = 0.85$ and C4, $u'/S_L = 1.28$) flames. Open diamonds, triangles, circles, and squares show data obtained by Goix et al. (1990) from open V-shaped lean ($\Phi = 0.2$) H_2-air flames B, C, D, and E stabilized in different turbulent flows

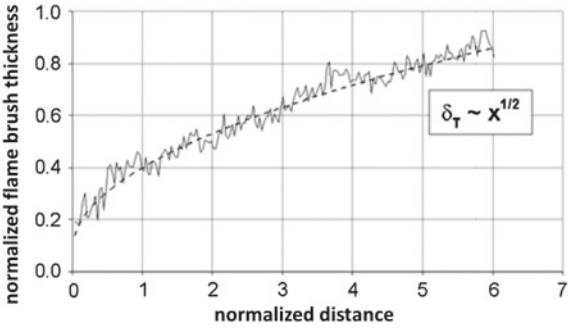

Fig. 6.12 Growth of the normalized mean flame brush thickness with the normalized distance from the combustor inlet. Reprinted from the paper by Griebel et al. (2007)

It is worth noting that certain data obtained from V-shaped (Kheirkhah and Gülder 2013, 2014, 2015) or Bunsen (Tamadonfar and Gülder 2014, 2015) statistically stationary flames indicate an increase in a flame thickness Δ_t by S_L, with Δ_t being measured along a normal to the burner axis, rather than along a normal to the mean flame position. Since U_t is increased by S_L, an acute angle φ between the aforementioned axis and the mean flame surface is also increased by S_L. This effect can result in increasing $\Delta_t \approx \delta_t/\cos\varphi$ even if δ_t is constant.

Experimental data obtained from long flames and associated with a long flame-development time show the square-root dependence of δ_t on the distance from the flame-holder, e.g., see Fig. 6.12, in line with the TFC Eq. (6.97) or the FSC Eq. (6.98).

Let us consider results of testing the TFC and FSC models in RANS simulations of well-defined simple cases.

The TFC model has been shown to predict;

- The effects of mixture composition (the equivalence ratio and various fuels such as methane, ethane, propane, etc.) on turbulent burning velocities obtained from statistically spherical, premixed turbulent flames expanding in a fan-stirred bomb at various u', e.g., see Fig. 6.13a. Comparison of curves shown in dashed ($\mathbb{P}_q = 0$) and solid ($0 < \mathbb{P}_q < 1$) lines in Fig. 6.13a indicates that the submodel for the quenching probability $\mathbb{P}_q$ given by Eq. (6.86) affects the computed results only at high u'. As far as the increasing branches of the measured and computed curves, associated with moderate turbulence, are concerned, the obtained good agreement between the experimental and the numerical data does not result from tuning of $\dot{s}_q$ in Eq. (6.86). In the case of the stoichiometric C_3H_8-air mixture, results computed either setting $\mathbb{P}_q = 0$ or using Eqs. (6.85) and (6.86) are almost the same. Accordingly, solely the former results are shown in a dashed line in this case.
- Mean structure of an open, Bunsen, premixed turbulent flame (Dinkelacker 2002).
- Profiles of the mean combustion progress variable in two open, swirl-stabilized flames (Dinkelacker 2002).
- Burning velocities obtained from slightly lean ($\Phi = 0.9$) CH_4-air Bunsen flames under normal and elevated pressures provided that a ratio of u'/S_L is markedly lager than unity, cf. filled and open symbols at $(u'/S_L)(p_0/p) \geq 0.6$ in Fig. 6.13b. If the ratio of u'/S_L is low, the TFC model underpredicts the measured data, because $U_{t,ISP}$ given by Eq. (6.79) tends to zero at $u' \to 0$.
- Mean structure of a statistically stationary, oblique, confined, lean ($\Phi = 0.8$) CH_4-air turbulent flame stabilized by a hot jet in intense turbulence (Ghirelli 2011; Yasari et al. 2015; Zimont et al. 2001), cf. dashed lines and symbols in Fig. 6.15d.
- Mean shape of open, V-shaped, lean ($\Phi = 0.5$, 0.58, and 0.7) CH_4-air turbulent flames (Dinkelacker and Hölzler 2000; Ghirelli 2011; Moreau 2009).
- Influence of bulk flow velocity, turbulence generation method, and pressure, on the mean axial length and the mean axial thickness of confined preheated ($T_u = 673$ K) lean ($\Phi = 0.5$) CH_4-air turbulent flames stabilized due to abrupt expansion of a channel at elevated pressures, cf. symbols and dashed lines in Fig. 6.13c and d.
- Axial profile of the Reynolds-averaged combustion progress variable in such a flame, see Fig. 6.13e.
- Mean shape of a lean ($\Phi = 0.7$) CH_4-air V-shaped flame, see Fig. 6.13f.

Moreover, the TFC model was successfully applied to RANS simulations of premixed and partially premixed turbulent combustion in engines, e.g., see (Polifke et al. 2002; Zimont et al. 1998).

Thus, the predictive capabilities of the TFC model were quantitatively validated by several independent research groups in RANS simulations of a wide set of substantially different, well-defined, simple premixed turbulent flames. Nevertheless, certain experimental results were not predicted in the numerical studies cited above.

First, to obtain a decrease in U_t by u' in intense turbulence, Eqs. (6.85) and (6.86) with unknown input parameter $\dot{s}_q$ were invoked, with $\dot{s}_q$ being tuned. Accordingly,

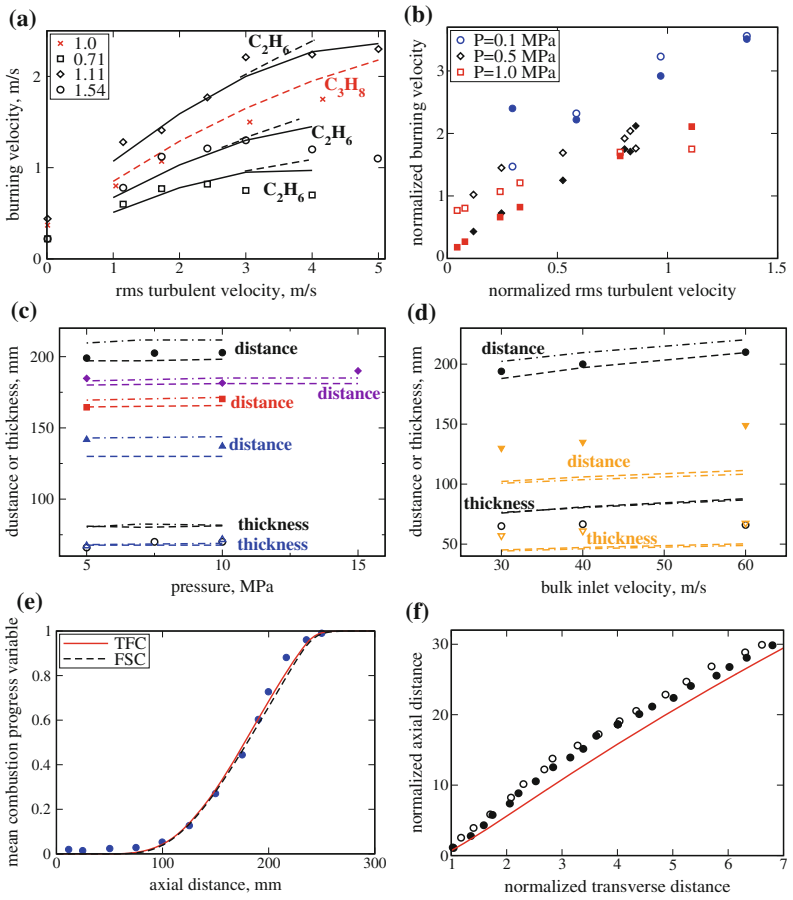

Fig. 6.13 Some examples of validation of the TFC model with $A = 0.5$ in RANS simulations of various experiments. **a** Dependencies of turbulent burning velocity U_t on the rms turbulent velocity u' measured (symbols) by Karpov and Severin (1980) and computed (curves) by Karpov et al. (1996). Crosses show data obtained from C_3H_8-air flames. Other symbols show data obtained from C_2H_6-air flames. Equivalence ratio is specified in figure legends. Solid and dashed lines show results computed invoking Eq. (6.85) with a tuned $\dot{s}_q$ and Eq. (6.79), respectively. **b** Normalized turbulent burning velocities measured (open symbols) by Kobayashi et al. (1996) and computed (filled symbols) by Muppala and Dinkelacker (2004) at three different pressures specified in the legends. Both U_t/S_L and u'/S_L are multiplied with p_0/p in order for the scales of the data obtained at different pressures to be comparable. $p_0 = 0.1$ MPa. **c**, **d** The mean centerline flame position (filled symbols) and the mean centerline flame brush thickness (open symbols) versus pressure and inlet bulk velocity, respectively. Different symbols show experimental data obtained by Siewert (2006) utilizing different grids in order to generate turbulence. Results computed by Yasari et al. (2015) using the TFC and FSC models are shown in dashed and dotted-dashed lines, respectively. **e** Centerline profiles of the Reynolds-averaged combustion progress variable, measured (symbols) by Siewert (2006) and computed by Yasari et al. (2015) using either the TFC (solid line) or FSC (dashed line) model. **f** Mean surface of a V-shaped flame. Open and filled symbols show experimental data obtained by Kheirkhah and Gülder (2013) from the left and right, respectively, branches of the flame. Line show results computed by Verma and Lipatnikov (2016)

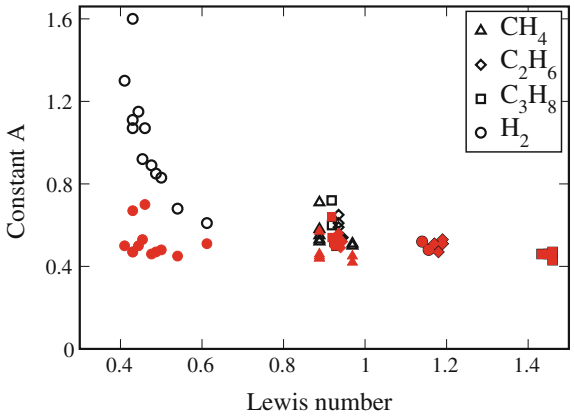

Fig. 6.14 Values of A tuned in RANS simulations (Karpov et al. 1996; Zimont and Lipatnikov 1995) of experiments by Karpov and Severin (1980) versus the Lewis number. Open symbols show results obtained using the original TFC model. Filled symbols show results obtained substituting the standard chemical time scale τ_c in Eq. (6.79) with a chemical time that characterizes local burning rate in extremely curved laminar flames

the so-extended TFC model cannot predict the decrease in U_t by u' in intense turbulence, but this phenomenon challenges all combustion models to the best of the present author's knowledge.

Second, the TFC model underpredicts U_t in weak turbulence, e.g., see Fig. 6.13b. Moreover, Yasari et al. (2015) were not able to obtain reasonable agreement between numerical and measured data when applying the TFC model to RANS simulations of experiments with weakly turbulent Bunsen flames (Cohé et al. 2009; Pfadler et al. 2008), whereas the FSC model performs much better in these cases, as will be discussed later.

Third, in simulations of the flames investigated by Siewert (2006), the TFC model (i) underpredicted the influence of variations in Φ on the mean flame axial length and (ii) yielded too narrow radial profiles of $\bar{c}(r)$ when compared to the measured data (Yasari et al. 2015). In the cited paper, the observed difference between the measured and computed results was attributed to the influence of heat release on the turbulence and to eventual local combustion quenching.

Finally, it is worth noting that the original TFC model significantly underpredicts turbulent burning velocities obtained by Karpov and Severin (1980) from expanding, statistically spherical lean hydrogen flames. In particular, when the TFC model was applied to RANS simulations of similar flames propagating in hydrocarbon–air mixtures (Karpov et al. 1996; Zimont and Lipatnikov 1995), a reasonably good agreement with the experimental data was obtained using the same $A = 0.5$ for various mixtures, but the agreement could be improved by slightly tuning the value of A in certain cases. However, the values of A tuned in similar simulations of lean hydrogen flames are significantly larger than 0.5 and are increased with decreasing the Lewis number, see open symbols in Fig. 6.14. This trend vanishes if the standard

chemical time scale τ_c in Eq. (6.79) is substituted with a chemical time that characterizes local burning rate in extremely curved laminar flames, see filled symbols. The reader interested in further discussion and substantiation of such a method is referred to books (Kuznetsov and Sabelnikov 1990; Lipatnikov 2012) and a review paper (Lipatnikov and Chomiak 2005c).

The FSC model has been shown to predict;

- Dependence of the mean growth rate of a statistically spherical flame kernel on mixture composition, e.g. see Fig. 6.15a and b.
- Dependence of the mean growth rate of a statistically spherical flame kernel on the rms turbulent velocity, e.g., see Fig. 6.15a and b.
- An increase in the observed turbulent flame speed as the flame kernel grows, e.g., see Fig. 6.15c.
- An increase in the observed turbulent flame speed by pressure, e.g., see Fig. 6.15c.
- Mean structure of a statistically stationary, oblique, confined, lean ($\Phi = 0.8$) CH_4-air turbulent flame stabilized by a hot jet in intense turbulence, e.g., see Fig. 6.15d, which also shows that results computed using the FSC model agree with the experimental data better than results computed using the TFC model, cf. solid and dashed lines, respectively.
- Mean shape of open, V-shaped, lean ($\Phi = 0.5$, 0.58, and 0.7) CH_4-air turbulent flames, e.g., see Fig. 6.15e, which also shows that results computed using the FSC model agree with the experimental data better than results computed using the TFC model, cf. solid and dotted-dashed lines, respectively.
- Influence of bulk flow velocity, turbulence generation method, and pressure on the mean axial length and the mean axial thickness of confined preheated ($T_u = 673$ K) lean ($\Phi = 0.5$) CH_4-air turbulent flames stabilized due to abrupt expansion of a channel at elevated pressures, cf. symbols and dotted-dashed lines in Fig. 6.13c and d. When simulating these experiments, the TFC and FSC models yielded very close results, cf. dashed and dotted-dashed lines, respectively.
- Axial profile of the Reynolds-averaged combustion progress variable in such a flame, see Fig. 6.13e.
- Mean structure of confined lean ($\Phi = 0.61$) C_3H_8-air flames stabilized by a bluff body, e.g. see Fig. 6.15f, which also shows that results computed using the FSC model agree with the experimental data better than results computed using the TFC model, cf. solid and dashed lines, respectively.
- Mean axial heights of the leanest CH_4-air weakly turbulent Bunsen flames, measured by Pfadler et al. (2008) at various equivalence ratios or inlet mass flow rates, with the TFC model yielding unsatisfactory results in this case (Yasari et al. 2015).
- Axial profiles of $\bar{c}(x)$ obtained by Cohé et al. (2009) from axisymmetric weakly turbulent CH_4/CO_2/air Bunsen flames stabilized within a cylindrical high pressure combustion chamber using an annular laminar stoichiometric methane–air pilot flame, with the TFC model yielding unsatisfactory results in this case (Yasari et al. 2015).

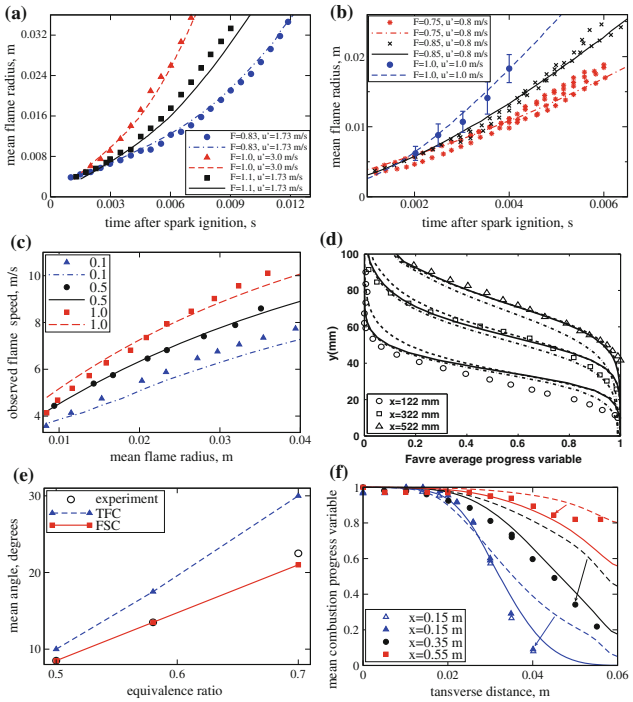

Fig. 6.15 Some examples of validation of the FSC model with $\mathbb{P}_q = 0$ in RANS simulations of various experiments. **a** Increase in the mean radii of expanding statistically spherical CH_4-air turbulent flames. Symbols show Leeds experimental data (Bradley et al. 1994b) obtained at $L = 20$ mm and $T_u = 328$ K. Lines show results computed using the FSC model (Lipatnikov and Chomiak 1997; Lipatnikov et al. 1998). Equivalence ratio and u' are specified in the legends. **b** Increase in the mean radii of expanding statistically spherical C_3H_8-air turbulent flames. Symbols show Rouen experimental data (Mouqallid et al. 1994) obtained at $L = 5$ mm and $T_u = 295$ K. Lines show results computed using the FSC model (Lipatnikov and Chomiak 1997; Lipatnikov et al. 1998). Equivalence ratio and u' are specified in the legends. **c** Observed speeds $d\bar{R}_f/dt$ of expanding, statistically spherical, stoichiometric iso-octane/air turbulent flames versus the mean flame radius $\bar{R}_f$. Symbols show Leeds experimental data (Bradley et al. 1994a) obtained at $u' = 2$ m/s, $L = 20$ mm, and $T_u = 400$ K. Lines show results computed using the FSC model (Lipatnikov and Chomiak 1997). Pressure is specified in MPa in the legends. **d** Transverse profiles of $\tilde{c}(y)$, computed by Yasari et al. (2015) using the TFC model (dashed lines), the FSC model (solid lines), and the FSC model with $Q_L = 0$ (dotted-dashed lines). Symbols show experimental data obtained by Moreau (1977) at various distances x from the inlet, specified in legends. Circles, squares, and triangles show data obtained from flames with $\Phi = 0.83$, 0.85, and 0.87, respectively. **e** Circles show an angle between the mean flame surface and the burner axis, averaged over $15 \le x \le 45$ mm in the experiments by Dinkelacker and Hölzler (2000). Triangles and squares show the mean angle computed by Yasari et al. (2015) using the TFC and FSC model, respectively. **f** Transverse profiles of the normalized Reynolds-averaged temperature. Symbols show experimental data (Sjunnesson et al. 1992) obtained from preheated ($T_u = 600$ K) lean ($\Phi = 0.61$) C_3H_8-air flames at different distances from a bluff body, specified in the legends. Data measured in the up and down halves of the channel are plotted in open and filled symbols, respectively. Dashed and solid lines show results (Sathiah and Lipatnikov 2007) computed using the TFC and FSC models, respectively

Thus, predictive capabilities of the FSC model were quantitatively validated in RANS simulations of a wide set of substantially different, well-defined, simple premixed turbulent flames. Nevertheless, certain experimental results were not predicted in the numerical studies cited above.

First, as already noted, in the simulations of the flames investigated by Siewert (2006), the FSC model (i) underpredicted the influence of variations in Φ on the mean flame axial length and (ii) yielded too narrow radial profiles of $\bar{c}(r)$ when compared to the measured data (Yasari et al. 2015). In the cited paper, the observed difference between the measured and computed results was attributed to the influence of heat release on the turbulence and to eventual local combustion quenching.

Second, in the simulations of the Bunsen flames investigated by Pfadler et al. (2008), the FSC model substantially underpredicted the axial flame height at $\Phi > 0.8$ and underpredicted the axial flame thickness in all studied cases (Yasari and Lipatnikov 2015). In the cited paper, the observed difference between the measured and computed results was also attributed to the influence of heat release on the turbulence.

It is also worth noting that the aforementioned RANS simulations of expanding and statistically stationary flames were performed using the FSC model with $A = 0.4$ and 0.5, respectively. In the former case, the value of A was reduced, because the use of the extra term Q_L was expected to result in increasing computed turbulent flame speed. Moreover, in the simulations by Sathiah and Lipatnikov (2007), the extra term Q_L was skipped, but such a simplification appears to be justified in the case of a large ratio of u'/S_L associated with that study.

Finally, it is worth noting that the FSC model was successfully applied to RANS simulations of stratified turbulent combustion in research optical SI engines (Huang et al. 2016; Wallesten et al. 2002).

6.5 Concluding Remarks

As shown in the present chapter, there are sufficiently advanced models, e.g., the TFC or FSC one, of the influence of turbulence on combustion that allow us to reasonably well predict mean turbulent burning rate, mean flame thickness and structure in various turbulent flows, for various fuels and equivalence ratios, at various pressures, etc.

Nevertheless, even the most advanced models cannot predict a decrease in turbulent burning velocity with increasing u' in intense turbulence characterized by $u'/S_L \gg 1$ or $Ka > 1$. Such effects could be of great importance for burning of lean mixtures characterized by a low S_L.

Moreover, the influence of combustion-induced thermal expansion on turbulence in flames is not yet well studied and this issue strongly challenges the combustion community.

Furthermore, simulation of emissions from turbulent flames is a very important subject, which has been attracting paramount attention. However, it is worth stressing that the mean heat-release rate and the mean flame structure should be well pre-

dicted in order for simulations of emissions to yield satisfactory results. Therefore, at the present level of model development, the best way of attacking this problem appears to consist in (i) computation of fields of the mean temperature, density, etc., by invoking an advanced model that does not address emissions, but can predict the aforementioned fields, and (ii) subsequent simulation of emissions invoking another model at a post-processing stage. The choice of an appropriate emission model is beyond the scope of the present chapter.

Acknowledgements This work was supported by Swedish Research Council (VR), Swedish Energy Agency (EM), Swedish Gas Turbine Center (GTC), Chalmers Areas of Advance Transport and Energy, and Combustion Engine Research Center (CERC). The author is grateful to Profs. Chomiak, Karpov, Sabelnikov, and Zimont for valuable discussions.

References

Abdel-Gayed RG, Al-Khishali KJ, Bradley D (1984) Turbulent burning velocities and flame straining in explosions. Proc R Soc Lond A 391:391–414

Atashkari K, Lawes M, Sheppard CGW, Woolley R (1999) Towards a general correlation of turbulent premixed flame wrinkling. In: Rodi W, Laurence D (eds) Engineering turbulence modelling and measurements 4. In: Proceedings of 4th International Symposium on Engineering Turbulence Modelling and Measurements, Ajaccio, Corsica, France, 24–26 May, 1999, pp 805–814

Bailly P, Champion M, Garreton D (1997) Counter-gradient diffusion in a confined turbulent premixed flame. Phys Fluids 9:766–775

Bilger RW, Pope SB, Bray KNC, Driscoll JF (2005) Paradigms in turbulent combustion research. Proc Combust Inst 30:21–42

Borghi R (1990) Turbulent premixed combustion: further discussions of the scales of fluctuations. Combust Flame 80:304–312

Boudier P, Henriot S, Poinsot T, Baritaud T (1992) A model for turbulent flame ignition and propagation in spark ignition engines. Proc Combust Inst 24:503–510

Boughanem H, Trouvé A (1998) The domain of influence of flame instabilities in turbulent premixed combustion. Proc Combust Inst 27:971–978

Bradley D (1992) How fast can we burn? Proc Combust Inst 24:247–262

Bradley D (2002) Problems of predicting turbulent burning rates. Combust Theory Model 6:361–382

Bradley D, Lau AKC, Lawes M (1992) Flame stretch rate as a determinant of turbulent burning velocity. Philos Trans R Soc Lond A 338:359–387

Bradley D, Lawes M, Sheppard CGW (1994a) Study of turbulence and combustion interaction: measurement and prediction of the rate of turbulent burning. Report, University of Leeds

Bradley D, Lawes M, Scott MJ, Mushi EMJ (1994b) Afterburning in spherical premixed turbulent explosions. Combust Flame 99:581–590

Bradley D, Gaskell PH, Gu XJ, Sedaghat A (2005) Premixed flamelet modelling: factors influencing the turbulent heat release rate source term and the turbulent burning velocity. Combust Flame 143:227–245

Bray KNC (1979) The interaction between turbulence and combustion. Proc Combust Inst 17:223–233

Bray KNC (1980) Turbulent flows with premixed reactants. In: Libby PA, Williams FA (eds) Turbulent reacting flows. Springer, Berlin

Bray KNC (1987) Methods of including realistic chemical reaction mechanisms in turbulent combustion models. In: Warnatz J, Jager W (ed) Complex chemical reaction systems. Mathematical modelling and simulation. Springer, Heidelberg

Bray KNC (1990) Studies of the turbulent burning velocity. Proc R Soc Lond A 431:315–335
Bray KNC (1995) Turbulent transport in flames. Proc R Soc Lond A 451:231–256
Bray KNC (1996) The challenge of turbulent combustion. Proc Combust Inst 26:1–26
Bray KNC, Moss JB (1977) A unified statistical model for the premixed turbulent flame. Acta Astronaut 4:291–319
Bray KNC, Cant RS (1991) Some applications of Kolmogorov's turbulence research in the field of combustion. Proc R Soc Lond A 434:217–240
Bray KNC, Libby PA, Moss JB (1985) Unified modeling approach for premixed turbulent combustion—Part I: General formulation. Combust Flame 61:87–102
Bray KNC, Champion M, Libby PA, Swaminathan N (2006) Finite rate chemistry and presumed PDF models for premixed turbulent combustion. Combust Flame 146:665–667
Brodkey RS (1967) The phenomena of fluid motions. Addison-Wesley Publishing Company, London
Burluka AA, Griffiths JF, Liu K, Orms M (2009) Experimental studies of the role of chemical kinetics in turbulent flames. Combust Explos Shock Waves 45:383–391
Candel S, Poinsot T (1990) Flame stretch and the balance equation for the flame area. Combust Sci Technol 170:1–15
Candel S, Veynante D, Lacas F, Maistret E, Darabiha N, Poinsot T (1990) Coherent flame model: applications and recent extensions. In: Larrouturou BE (ed) Advances in combustion modeling. World Scientific, Singapore
Cant RS, Pope SB, Bray KNC (1990) Modelling of flamelet surface-to-volume ratio in turbulent premixed combustion. Proc Combust Inst 23:809–815
Chakraborty N, Champion M, Mura A, Swaminathan N (2011) Scalar-dissipation-rate approach. In: Swaminathan N, Bray KNC (eds) Turbulent premixed flames. Cambridge University Press, Cambridge
Chaudhuri S, Akkerman V, Law CK (2011) Spectral formulation of turbulent flame speed with consideration of hydrodynamic instability. Phys Rev E 84:026322
Cheng RK, Shepherd IG (1991) The influence of burner geometry on premixed turbulent flame propagation. Combust Flame 85:7–26
Cheng WK, Diringer JA (1991) Numerical modelling of SI engine combustion with a flame sheet model. SAE Paper 910268
Cho P, Law CK, Cheng RK, Shepherd IG (1988) Velocity and scalar fields of turbulent premixed flames in stagnation flow. Proc Combust Inst 22:739–745
Choi CR, Huh KY (1998) Development of a coherent flamelet model for spark-ignited turbulent premixed flame in a closed vessel. Combust Flame 114:336–348
Chowdhury BR, Cetegen BM (2017) Experimental study of the effects of free stream turbulence on characteristics and flame structure of bluff-body stabilized conical lean premixed flames. Combust Flame 178:311–328
Clavin P (1985) Dynamical behavior of premixed flame fronts in laminar and turbulent flows. Prog Energy Combust Sci 11:1–59
Clavin P, Williams FA (1979) Theory of premixed-flame propagation in large-scale turbulence. J Fluid Mech 90:589–604
Cohé C, Chauveau C, Gökalp I, Kurtuluş DF (2009) CO_2 addition and pressure effects on laminar and turbulent lean premixed CH_4 air flames. Proc Combust Inst 32:1803–1810
Damköhler G (1940) Der einfuss der turbulenz auf die flammengeschwindigkeit in gasgemischen. Z Electrochem 46:601–652
Darrieus G (1938) Propagation d'un front de flamme. Presented at La Technique Moderne (Paris) and in 1945 at Congrés de Mećanique Appliqueé (Paris)
Dasgupta D, Sun W, Day M, Lieuwen T (2017) Effect of turbulence-chemistry interactions on chemical pathways for turbulent hydrogen-air premixed flames. Combust Flame 176:191–201
Dinkelacker F (2002) Numerical calculation of turbulent premixed flames with an efficient turbulent flame speed closure model. In: Breuer M, Durst F, Zenger C (eds) High-performance scientific and engineering computing. Lecture notes in computational science and engineering, vol 21, pp 81–88

Dinkelacker F, Hölzler S (2000) Investigation of a turbulent flame speed closure approach for premixed flame calculations. Combust Sci Technol 158:321–340
Duclos JM, Veynante D, Poinsot T (1993) A comparison of flamelet models for premixed turbulent combustion. Combust Flame 95:101–117
Fichot F, Lacas F, Veynante D, Candel S (1993) One-dimensional propagation of a premixed turbulent flame with a balance equation for the flame surface density. Combust Sci Technol 90:35–60
Fogla N, Creta F, Matalon M (2017) The turbulent flame speed for low-to-moderate turbulence intensities: Hydrodynamic theory vs. experiments. Combust Flame 175:155–169
Frank JH, Kalt PAM, Bilger RW (1999) Measurements of conditional velocities in turbulent premixed flames by simultaneous OH PLIF and PIV. Combust Flame 116:220–232
Ghirelli F (2011) Turbulent premixed flame model based on a recent dispersion model. Comput Fluids 44:369–376
Giovangigli V (1999) Multicomponent flow modeling. Springer, Berlin
Goix P, Paranthoen P, Trinité M (1990) A tomographic study of measurements in a V-shaped H_2-air flame and a Lagrangian interpretation of the turbulent flame brush thickness. Combust Flame 81:229–241
Gouldin FC, Miles PC (1995) Chemical closure and burning rates in premixed turbulent flames. Combust Flame 100:202–210
Goulier J, Comandini A, Halter F, Chaumeix N (2017) Experimental study on turbulent expanding flames of lean hydrogen/air mixtures. Proc Combust Inst 36:2823–2832
Griebel P, Siewert P, Jansohn P (2007) Flame characteristics of turbulent lean premixed methane/air flames at high-pressure: turbulent flame speed and flame brush thickness. Proc Combust Inst 31:3083–3090
Hinze JO (1975) Turbulence, 2nd edn. McGraw Hill, New York
Hirschfelder JO, Curtiss CF, Bird RB (1954) Molecular theory of gases and liquids. Wiley, New York
Huang C, Yasari E, Johansen LCR, Hemdal S, Lipatnikov AN (2016) Application of flame speed closure model to RANS simulations of stratified turbulent combustion in a gasoline direct-injection spark-ignition engine. Combust Sci Technol 188:98–131
Karlovitz B, Denniston DW, Wells FE (1951) Investigation of turbulent flames. J Chem Phys 19:541–547
Karpov VP, Severin ES (1980) Effects of molecular-transport coefficients on the rate of turbulent combustion. Combust Explos Shock Waves 16:41–46
Karpov VP, Lipatnikov AN (1995) An effect of molecular thermal conductivity and diffusion on premixed combustion. Doklady Phys Chemistry 341:83–85
Karpov VP, Lipatnikov AN, Zimont, (1996) A test of an engineering model of premixed turbulent combustion. Proc Combust Inst 26:249–257
Karpov VP, Lipatnikov AN, Zimont (1997) Flame curvature as a determinant of preferential diffusion effects in premixed turbulent combustion. In: Sirignano WA, Merzhanov AG, De Luca L (eds) Advances in combustion science: In honor of Ya.B. Zel'dovich. Prog Astronaut Aeronaut 173:235-250
Kha KQN, Robin V, Mura A, Champion M (2016) Implications of laminar flame finite thickness on the structure of turbulent premixed flames. J Fluid Mech 787:116–147
Kheirkhah S, Gülder ÖL (2013) Turbulent premixed combustion in V-shaped flames: characteristics of flame front. Phys Fluids 25:055107
Kheirkhah S, Gülder ÖL (2014) Influence of edge velocity on flame front position and displacement speed in turbulent premixed combustion. Combust Flame 161:2614–2626
Kheirkhah S, Gülder ÖL (2015) Consumption speed and burning velocity in counter-gradient and gradient diffusion regimes of turbulent premixed combustion. Combust Flame 162:1422–1439
Kim SH (2017) Leading points and heat release effects in turbulent premixed flames. Proc Combust Inst 36:2017–2024
Kobayashi H, Tamura T, Maruta K, Niioka T, Williams FA (1996) Burning velocity of turbulent premixed flames in a high-pressure environment. Proc Combust Inst 26:389–396

Kuznetsov VR (1975) Certain peculiarities of movement of a flame front in a turbulent flow of homogeneous fuel mixtures. Combust Explos Shock Waves 11:487–493
Kuznetsov VR, Sabelnikov VA (1990) Turbulence and combustion. Hemisphere Publ Corp, New York
Landau LD (1944) On the theory of slow combustion. Acta Psysicochim USSR 19:77–85
Lapointe S, Blanquart G (2016) Fuel and chemistry effects in high Karlovitz premixed turbulent flames. Combust Flame 167:294–307
Launder BE, Spalding DB (1972) Mathematical models of turbulence. Academic Press, London
Law CK (2006) Combustion physics. Cambridge University Press, Cambridge
Lee B, Choi CR, Huh KY (1998) Application of the coherent flamelet model to counterflow turbulent premixed combustion and extinction. Combust Sci Technol 138:1–25
Li SC, Libby PA, Williams FA (1994) Experimental investigation of a premixed flame in an impinging turbulent stream. Proc Combust Inst 25:1207–1214
Libby PA (1975) On the prediction of intermittent turbulent flows. J Fluid Mech 68:273–295
Libby PA, Bray KNC (1977) Variable density effects in premixed turbulent flames. AIAA J 15:1186–1193
Libby PA, Bray KNC (1981) Countergradient diffusion in premixed turbulent flames. AIAA J 19:205–213
Libby PA, Williams FA (1994) Fundamental aspects and a review. In: Libby PA, Williams FA (eds) Turbulent reactive flows. Academic Press, London
Lindstedt RP, Váos EM (1999) Modeling of premixed turbulent flames with second moment methods. Combust Flame 116:461–485
Lipatnikov AN (2009a) Can we characterize turbulence in premixed flames? Combust Flame 156:1242–1247
Lipatnikov AN (2009b) Testing premixed turbulent combustion models by studying flame dynamics. Int J Spray Combust Dyn 1:39–66
Lipatnikov AN (2011a) Conditioned moments in premixed turbulent reacting flows. Proc Combust Inst 33:1489–1496
Lipatnikov AN (2011b) Transient behavior of turbulent scalar transport in premixed flames. Flow Turbul Combust 86:609–637
Lipatnikov AN (2012) Fundamentals of premixed turbulent combustion. CRC Press, Boca-Raton, Florida
Lipatnikov AN, Chomiak J (1997) A simple model of unsteady turbulent flame propagation. SAE Paper 972993
Lipatnikov AN, Chomiak J (2000a) Transient and geometrical effects in expanding turbulent flames. Combust Sci Technol 154:75–117
Lipatnikov AN, Chomiak J (2000b) Dependence of heat release on the progress variable in premixed turbulent combustion. Proc Combust Inst 28:227–234
Lipatnikov AN, Chomiak J (2001) Developing premixed turbulent flames: Part I. A self-similar regime of flame propagation. Combust Sci Technol 162:85–112
Lipatnikov AN, Chomiak J (2002) Turbulent flame speed and thickness: phenomenology, evaluation, and application in multi-dimensional simulations. Prog Energy Combust Sci 28:1–74
Lipatnikov AN, Chomiak J (2004) Comment on "Turbulent burning velocity, burned gas distribution, and associated flame surface definition" Bradley D, Haq MZ, Hicks RA, Kitagawa T, Lawes M, Sheppard CGW, Woolley R, Combust Flame, 133:415 (2003). Combust Flame 137:261–263
Lipatnikov AN, Chomiak J (2005a) A theoretical study of premixed turbulent flame development. Proc Combust Inst 30:843–850
Lipatnikov AN, Chomiak J (2005b) Self-similarly developing, premixed, turbulent flames: a theoretical study. Phys Fluids 17:065105
Lipatnikov AN, Chomiak J (2005c) Molecular transport effects on turbulent flame propagation and structure. Prog Energy Combust Sci 31:1–73
Lipatnikov AN, Sathiah P (2005) Effects of turbulent flame development on thermoacoustic oscillations. Combust Flame 142:130–139

Lipatnikov AN, Chomiak J (2010) Effects of premixed flames on turbulence and turbulent scalar transport. Prog Energy Combust Sci 36:1–102
Lipatnikov AN, Wallesten J, Nisbet J (1998) Testing of a model for multi-dimensional computations of turbulent combustion in spark ignition engines. In: Proc Fourth Int Symp Diagnostics and modeling of combustion in internal combustion engines—COMODIA98. JSME, Kyoto, pp 239–44
Lipatnikov AN, Nishiki S, Hasegawa T (2015a) DNS assessment of relation between mean reaction and scalar dissipation rates in the flamelet regime of premixed turbulent combustion. Combust Theory Model 19:309–328
Lipatnikov AN, Chomiak J, Sabelnikov VA, Nishiki S, Hasegawa T (2015b) Unburned mixture fingers in premixed turbulent flames. Proc Combust Inst 35:1401–1408
Lipatnikov AN, Sabelnikov VA, Nishiki S, Hasegawa T, Chakraborty N (2015c) DNS assessment of a simple model for evaluating velocity conditioned to unburned gas in premixed turbulent flames. Flow Turbul Combust 94:513–526
Lipatnikov AN, Sabelnikov VA, Nishiki S, Hasegawa T (2017) Flamelet perturbations and flame surface density transport in weakly turbulent premixed combustion. Combust Theory Model 21:205–227
Majda A, Sethian J (1985) The derivation and numerical solution of the equations for zero Mach number combustion. Combust Sci Technol 42:185–205
Meneveau C, Poinsot T (1991) Stretching and quenching of flamelets in premixed turbulent combustion. Combust Flame 86:311–332
Moreau P (1977) Turbulent flame development in a high velocity premixed flow. AIAA paper 77/49
Moreau V (2009) A self-similar premixed turbulent flame model. Appl Math Model 33:835–851
Moss JB (1980) Simultaneous measurements of concentration and velocity in an open premixed turbulent flame. Combust Sci Technol 22:119–129
Mouqallid M, Lecordier B, Trinité M (1994) High speed laser tomography analysis of flame propagation in a simulated internal combustion engine—applications to nonuniform mixture. SAE paper 941990
Muppala SRP, Dinkelacker F (2004) Numerical modelling of the pressure dependent reaction source term for turbulent premixed methane-air flames. Prog Comp Fluid Dyn 4:328–336
Namazian M, Shepherd IG, Talbot L (1986) Characterization of the density fluctuations in turbulent V-shaped premixed flames. Combust Flame 64:299–308
van Oijen JA, Donini A, Bastiaans RJM, ten Thije Boonkkamp JHM, de Goey LPH (2016) State-of-the-art in premixed combustion modeling using flamelet generated manifolds. Prog Energy Combust Sci 57:30–74
Peters N (2000) Turbulent combustion. The University Press, Cambridge
Pfadler S, Leipertz A, Dinkelacker F (2008) Systematic experiments on turbulent premixed Bunsen flames including turbulent flux measurements. Combust Flame 152:616–631
Poinsot T, Veynante D (2005) Theoretical and numerical combustion, 2nd edn. Edwards, Philadelphia
Poinsot T, Veynante D, Candel S (1991) Quenching processes and premixed turbulent combustion diagrams. J Fluid Mech 228:561–606
Polifke W, Flohr P, Brandt M (2002) Modeling of inhomogeneously premixed combustion with an extended TFC model. ASME J Eng Gas Turbines Power 124:58–65
Poludnenko AY, Oran ES (2011) The interaction of high-speed turbulence with flames: turbulent flame speed. Combust Flame 158:301–326
Pope SB (1988) The evolution of surface in turbulence. Int J Eng Sci 26:445–469
Pope SB (2000) Turbulent flows. The University Press, Cambridge
Prudnikov AG (1960) Hydrodynamics equations in turbulent flames. In: Prudnikov AG (ed) Combustion in a turbulent flow. Oborongiz, Moscow (in Russian)
Prudnikov AG (1964) Burning of homogeneous fuel-air mixtures in a turbulent flow. In: Raushenbakh BV (ed) Physical principles of the working process in combustion chambers of jet engines. Mashinostroenie, Moscow (in Russian; translated from Russian by the Translation Division, For-

eign and Technology Division, Wright Patterson AFB, Clearing House for Federal Scientific & Technical Information, Ohio, 1967, pp 244–336)
Renou B, Mura A, Samson E, Boukhalfa A (2002) Characterization of the local flame structure and flame surface density for freely-propagating premixed flames at various Lewis numbers. Combust Sci Technol 174:143–179
Roberts WL, Driscoll JF, Drake MC, Goss LP (1993) Images of the quenching of a flame by a vortex—to quantify regimes of turbulent combustion. Combust Flame 94:58–69
Sabelnikov VA, Lipatnikov AN (2011) A simple model for evaluating conditioned velocities in premixed turbulent flames. Combust Sci Technol 183:588–613
Sabelnikov VA, Lipatnikov AN (2013) Transition from pulled to pushed premixed turbulent flames due to countergradient transport. Combust Theory Model 17:1154–1175
Sabelnikov VA, Lipatnikov AN (2015) Transition from pulled to pushed fronts in premixed turbulent combustion: theoretical and numerical study. Combust Flame 162:2893–2903
Sabelnikov VA, Lipatnikov AN (2017) Recent advances in understanding of thermal expansion effects in premixed turbulent flames. Annu Rev Fluid Mech 49:91–117
Sabelnikov VA, Lipatnikov AN, Chakraborty N, Nishiki S, Hasegawa T (2016) A transport equation for reaction rate in turbulent flows. Phys Fluids 28:081701
Sabelnikov VA, Lipatnikov AN, Chakraborty N, Nishiki S, Hasegawa T (2017) A balance equation for the mean rate of product creation in premixed turbulent flames. Proc Combust Inst 36:1893–1901
Sathiah P, Lipatnikov AN (2007) Effects of flame development on stationary premixed turbulent combustion. Proc Combust Inst 31:3115–3122
Schmidt HP, Habisreuther P, Leuckel W (1998) A model for calculating heat release in premixed turbulent flames. Combust Flame 113:79–91
Scurlock AC, Grover JH (1953) Propagation of turbulent flames. Proc Combust Inst 4:645–658
Shelkin KI (1943) On combustion in a turbulent flow. J Tech Phys 13:520–530. Transl NACA, 1967, in NACA TM 1110:1–18 (from Russian)
Siewert P (2006) Flame front characteristics of turbulent lean premixed methane/air flames at high-pressure. PhD thesis, ETHZ Zürich
Sjunnesson A, Henrikson, Löfström C (1992) CARS measurements and visualization of reacting flows in a bluff body stabilized flame. AIAA paper 92/3650
Sponfeldner T, Soulopoulos N, Beyrau F, Hardalupas Y, Taylor AMKP, Vassilicos JC (2015) The structure of turbulent flames in fractal- and regular-grid-generated turbulence. Combust Flame 162:3379–3393
Stevens EJ, Bray KNC, Lecordier B (1998) Velocity and scalar statistics for premixed turbulent stagnation flames using PIV. Proc Combust Inst 27:949–955
Swaminathan N, Bray KNC (2005) Effect of dilatation on scalar dissipation in turbulent premixed flames. Combust Flame 143:549–565
Taylor GI (1935) Statistical theory of turbulence. IV. Diffusion in a turbulent air stream. Proc R Soc Lond A 151:465–478
Tamadonfar P, Gülder ÖL (2014) Flame brush characteristics and burning velocities of premixed turbulent methane/air Bunsen flames. Combust Flame 161:3154–3165
Tamadonfar P, Gülder ÖL (2015) Effects of mixture composition and turbulence intensity on flame front structure and burning velocities of premixed turbulent hydrocarbon/air Bunsen flames. Combust Flame 162:4417–4441
Townsend AA (1976) The structure of turbulent shear flow, 2nd edn. Cambridge University Press, Cambridge
Trouvé A, Poinsot T (1994) Evolution equation for flame surface density in turbulent premixed combustion. J Fluid Mech 278:1–31
Venkateswaran P, Marshall A, Shin DH, Noble D, Seitzman J, Lieuwen T (2011) Measurements and analysis of turbulent consumption speeds of H_2/CO mixtures. Combust Flame 158:1602–1614
Venkateswaran P, Marshall A, Seitzman J, Lieuwen T (2013) Pressure and fuel effects on turbulent consumption speeds of H_2/CO blends. Proc Combust Inst 34:1527–1535

Venkateswaran P, Marshall A, Seitzman J, Lieuwen T (2015) Scaling turbulent flame speeds of negative Markstein length fuel blends using leading points concepts. Combust Flame 162:375–387

Verma S, Lipatnikov AN (2016) Does sensitivity of measured scaling exponents for turbulent burning velocity to flame configuration prove lack of generality of notion of turbulent burning velocity? Combust Flame 173:77–88

Vervisch L, Bidaux E, Bray KNC, Kollmann W (1995) Surface densiuty function in premixed turbulent combustion modeling, similarities between probability density function and flame surface approaches. Phys Fluids 7:2496–2503

Veynante D, Vervisch L (2002) Turbulent combustion modeling. Prog Energy Combust Sci 28:193–266

Wallesten J, Lipatnikov AN, Chomiak J (2002) Modeling of stratified combustion in a DI SI engine using detailed chemistry pre-processing. Proc Combust Inst 29:703–709

Wang Z, Magi V, Abraham J (2017) Turbulent flame speed dependencies of lean methane-air mixtures under engine relevant conditions. Combust Flame 180:53–62

Williams FA (1985) Combustion theory, 2nd edn. Benjamin/Cummings, Menlo Park, California

Wu MS, Kwon A, Driscoll G, Faeth GM (1990) Turbulent premixed hydrogen/air flames at high Reynolds numbers. Combust Sci Technol 73:327–350

Yanagi T, Mimura Y (1981) Velocity-temperature correlation in premixed flame. Proc Combust Inst 18:1031–1039

Yasari E, Lipatnikov AN (2015) Assessment of a recent model of turbulent scalar flux in RANS simulations of premixed Bunsen flames. In: Hanjalic K, Miyauchi T, Borello D, Hadžiabdić M, Venturini P (eds) THMT15, Proceedings of the International Symposium Turbulence, Heat and Mass Transfer 8, Sarajevo, Bosnia and Herzegovina, September 15–18, 2015. ICHMT

Yasari E, Verma S, Lipatnikov AN (2015) RANS simulations of statistically stationary premixed turbulent combustion using flame speed closure model. Flow Turbul Combust 94:381–414

Yu R, Lipatnikov AN (2017a) A direct numerical simulation study of statistically stationary propagation of reaction wave in homogeneous turbulence. Phys Rev E 95:063101

Yu R, Lipatnikov AN (2017b) DNS study of dependence of bulk consumption velocity in a constant-density reacting flow on turbulence and mixture characteristics. Phys Fluids 29:065116

Yu R, Lipatnikov AN, Bay XS (2014) Three-dimensional direct numerical simulation study of conditioned moments associated with front propagation in turbulent flows. Phys Fluids 26:085104

Yu R, Bay XS, Lipatnikov AN (2015) A direct numerical simulation study of interface propagation in homogeneous turbulence. J Fluid Mech 772:127–164

Zel'dovich YaB, Barenblatt GI, Librovich VB, Makhviladze GM (1985) The mathematical theory of combustion and explosions. Consultants Bureau, New York

Zimont VL (1979) Theory of turbulent combustion of a homogeneous fuel mixture at high Reynolds number. Combust Explos Shock Waves 15:305–311

Zimont VL (2000) Gas premixed combustion at high turbulence. Turbulent flame closure combustion model. Exp Thermal Fluid Sci 21:179–186

Zimont VL (2015) Unclosed Favre-averaged equation for the chemical source and an analytical formulation of the problem of turbulent premixed combustion in the flamelet regime. Combust Flame 162:874–875

Zimont VL, Lipatnikov AN (1993) Calculation of the rate of heat release in a turbulent flame. Doklady Phys Chem 332:440–443

Zimont VL, Lipatnikov AN (1995) A numerical model of premixed turbulent combustion. Chem Phys Rep 14:993–1025

Zimont VL, Biagioli F, Syed K (2001) Modelling turbulent premixed combustion in the intermediate steady propagation regime. Prog Comput Fluid Dyn 1:14–28

Zimont VL, Polifke W, Bettelini M, Weisenstein W (1998) An efficient computational model for premixed turbulent combustion at high Reynolds number based on a turbulent flame speed closure. J Eng Gas Turbines Power 120:526–532

Chapter 7
Modeling of Turbulent Premixed Flames Using Flamelet-Generated Manifolds

Jeroen A. van Oijen

Abstract Efficient and reliable numerical models have become important tools in the design and optimization process of modern combustion equipment. For accurate predictions of flame stability and pollutant emissions, the use of detailed comprehensive chemical models is required. This accuracy, unfortunately, comes at a very high computational cost. The flamelet-generated manifold (FGM) method is a chemical reduction technique which lowers this burden drastically, but retains most of the accuracy of the comprehensive model. In this chapter, the theoretical background of FGM is briefly reviewed. Its application in simulations of premixed and partially premixed flames is explained. Extra attention is given to the modeling of preferential diffusion effects that arise in lean premixed methane–hydrogen–air flames. The effect of preferential diffusion on the burning velocity of stretched flames is investigated and it is shown how these effects can be included in the FGM method. The impact of preferential diffusion on flame structure and turbulent flame speed is analyzed in direct numerical simulations of premixed turbulent flames. Finally, the application of FGM in large-eddy simulations is briefly reviewed.

Keywords Tabulated chemistry · Flame stretch · Preferential diffusion · Lewis number effects · Hydrogen

7.1 Introduction

Numerical models of turbulent reacting flows have become important tools for the development of combustion equipment. For accurate and reliable predictions of flame stability and pollutant emissions, detailed descriptions of chemistry, flow, and their interaction are required. The use of comprehensive chemical reaction mechanisms is, however, extremely costly from a computational point of view. The large number of species and chemical reactions leads to a large system of equations with

J. A. van Oijen (✉)
Mechanical Engineering, Eindhoven University of Technology, 70, De Rondom, 5612 AP, Eindhoven, The Netherlands
e-mail: j.a.v.oijen@tue.nl

© Springer Nature Singapore Pte Ltd. 2018

S. De et al. (eds.), *Modeling and Simulation of Turbulent Combustion*, Energy, Environment, and Sustainability, https://doi.org/10.1007/978-981-10-7410-3_7

a wide range of timescales, which makes it very stiff and hard to solve without dedicated numerical solvers. The cost of flame simulations can be lowered by using chemical reduction techniques. Making use of the fact that many chemical timescales are very small, reduced order chemical models can be constructed. Fast chemical processes are assumed in steady state and the chemical state becomes a function of only a few slowly varying control variables. This defines a so-called manifold in composition space. As a result, all variables can be stored in a database as a function of the control variables and during run time only the equations for the control variables are solved. In this way, not only the number of equations to be solved is reduced, but also the stiffness of the problem is reduced.

Another approach to reduce computational cost of combustion simulations is the use of flamelet models. In laminar flamelet models, it is assumed that the wildly moving flame in a combustion application can be regarded locally as a one-dimensional idealized flame front (flamelet). The complex chemical structure of the flamelet is described by one or two parameters (e.g., mixture fraction and scalar dissipation). A flame in a combustion system is then composed of a superposition of such flamelets, which live on the aerodynamic structure of the flow. In 1986, Peters (1986) developed the basis of these flamelet models, which are still very popular in the combustion community.

The flamelet-generated manifold (FGM) method combines these two modeling approaches and has been applied successfully in many combustion studies, e.g., (Bekdemir et al. 2014; Bongers et al. 2005; Delhaye et al. 2008; Donini et al. 2015; van Oijen 2002; van Oijen and de Goey 2000, 2002; van Oijen et al. 2001; Vreman et al. 2008, 2009a). The FGM method is more accurate in colder parts of the flame than reduction techniques based on chemistry, because FGM also takes the main transport effects into account, which are essential for the correct prediction of flame dynamics and propagation speed. The FGM method is based on a detailed analysis of (partially) premixed flames in the laminar flamelet and thin reaction zones regime. The basis is a set of flamelet equations, which describes the internal structure and dynamics of the flame. Solutions of these flamelet equations are used to construct a manifold, which is applied in flame simulations in a similar way as chemistry-based reduction methods.

The theoretical background of FGM and its application in simulations of laminar flames are explained in Sect. 7.2. In Sect. 7.3, extra attention is given to the modeling of preferential diffusion effects. These effects are very important in flames with highly diffusive fuel components such as hydrogen. The large interest in hydrogen as a fuel, possibly blended with natural gas or other conventional fuels, makes this topic very relevant.

Since turbulent flows are characterized by large range of length scales, the direct numerical simulation (DNS) of turbulent flows, in which all scales are resolved, is computationally very demanding. This means that DNS is not applicable to high Reynolds number flows without the use of super computing facilities. Large-eddy simulation (LES) is much cheaper than DNS and still resolves most of the turbulent length scales. This gives it a superior accuracy compared to Reynolds-Averaged Navier–Stokes (RANS) models, in which all fluctuations are modeled. Though LES

is more expensive than RANS, the continuous increase in computing power has made LES affordable and the method of choice in many applications. In Sect. 7.4, the use of FGM in LES of turbulent flames is discussed. Finally, this chapter ends with conclusions in Sect. 7.5.

7.2 Flamelet-Generated Manifolds

In the FGM method, a low-dimensional manifold is created by solving a set of one-dimensional equations describing the internal structure of a flame front. In the following section, this set of flamelet equations is derived by rewriting the conservation equations in a flame-adapted coordinate system. How the solutions of this set of equations are used to construct a manifold and stored as a lookup table is explained in the subsequent Sects. 7.2.2 and 7.2.3. Finally, the use of this lookup table in a flame simulation is discussed in Sect. 7.2.4.

7.2.1 Flamelet Equations

In this section, the flamelet description for premixed flames introduced by De Goey and Ten Thije Boonkkamp (1999) is briefly reviewed. A more comprehensive review is given in (van Oijen et al. 2016). The flamelet description has been derived in a systematic way by decomposing the system of combustion equations in three parts: (1) a flow and mixing part without chemistry, (2) a kinematic equation for the flame motion, including internal flame dynamics, and (3) a flamelet part describing the inner structure and propagation speed of the flame structure. The flame, including internal structure, is described in terms of iso-surfaces of a progress variable $\mathscr{Y}$, which can be any linear combination of species mass fractions for which $\nabla\mathscr{Y} \neq 0$ in the flame zone. The motion of each iso-surface of $\mathscr{Y}$, to which we will refer as flame surfaces, is described by the kinematic equation (Matalon 1983)

$$\frac{\partial \mathscr{Y}}{\partial t} + \mathbf{v}_\mathrm{f} \cdot \nabla\mathscr{Y} = \frac{\partial \mathscr{Y}}{\partial t} + \mathbf{v} \cdot \nabla\mathscr{Y} - s_\mathrm{d}|\nabla\mathscr{Y}| = 0, \tag{7.1}$$

where $\mathbf{v}_\mathrm{f}$ is the local velocity of a flame surface. The kinematic equation expresses that a flame surface is advected by the fluid flow with velocity $\mathbf{v}$ and, in addition, propagates normal to itself with the displacement speed $s_\mathrm{d}\mathbf{n}$ (see Fig. 7.1). The unit normal vector $\mathbf{n}$ on the flame surface is defined as $\mathbf{n} = -\nabla\mathscr{Y}/|\nabla\mathscr{Y}|$ and is directed toward the unburnt mixture. Note that (7.1) is introduced for each iso-surface in the complete flame region where $\mathscr{Y}_\mathrm{u} < \mathscr{Y} < \mathscr{Y}_\mathrm{b}$, with $\mathscr{Y}_\mathrm{u}$ and $\mathscr{Y}_\mathrm{b}$ the values of $\mathscr{Y}$ in the unburnt and burnt mixture, respectively. As a result $\mathbf{v}_\mathrm{f}$ and s_d are field variables, which vary throughout the flame region (Poinsot and Veynante 2011).

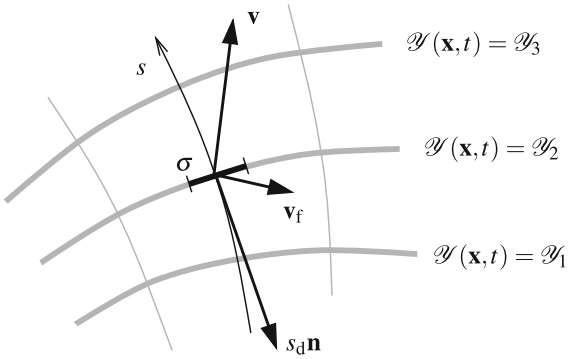

Fig. 7.1 Flame-adapted coordinate system (van Oijen 2002)

The iso-surfaces of $\mathscr{Y}$ can be used to introduce a flame-adapted coordinate system as shown in Fig. 7.1. In this coordinate system, s is the coordinate locally perpendicular to the flame surfaces and σ is the local flame surface area, which is related to flame curvature κ as

$$\kappa = \nabla \cdot \mathbf{n} = -\sigma^{-1} \partial\sigma/\partial s. \tag{7.2}$$

De Goey and Ten Thije Boonkkamp (1997) proposed the flame stretch rate K as the relative rate of change of the mass in an infinitesimal small control volume moving in the flame with velocity $\mathbf{v}_\mathrm{f}$. By applying Reynolds' transport theorem to this control volume, they derived an equation for the stretch rate

$$\rho K = \frac{\partial \rho}{\partial t} + \nabla \cdot (\rho \mathbf{v}_\mathrm{f}), \tag{7.3}$$

with ρ the density.

Let us now consider the transport equation for the progress variable

$$\frac{\partial(\rho\mathscr{Y})}{\partial t} + \nabla \cdot (\rho \mathbf{v} \mathscr{Y}) - \nabla \cdot \left(\frac{1}{\mathrm{Le}_\mathscr{Y}} \frac{\lambda}{c_p} \nabla \mathscr{Y} \right) = \omega_\mathscr{Y}, \tag{7.4}$$

where we introduced the chemical source term ω_i and the Lewis number $\mathrm{Le}_i = \lambda/\rho D_i c_p$ with λ the conductivity, c_p the specific heat capacity at constant pressure, and D_i the diffusion coefficient of scalar i. If this equation is combined with the kinematic Eq. (7.1) and expression (7.3) for ρK, the following quasi-one-dimensional equation is obtained rigorously

$$\frac{\partial}{\partial s}(\sigma m \mathscr{Y}) - \frac{\partial}{\partial s} \left(\sigma \frac{1}{\mathrm{Le}_\mathscr{Y}} \frac{\lambda}{c_p} \frac{\partial \mathscr{Y}}{\partial s} \right) = \sigma \left(\omega_\mathscr{Y} - \rho K \mathscr{Y} \right), \tag{7.5}$$

where the mass burning rate $m = \rho s_\mathrm{d}$ is introduced. Equation (7.5) describes the convection–diffusion–reaction balance of $\mathscr{Y}$ along the flamelet path coordinate s. It

contains an additional source term $-\rho K\mathscr{Y}$ describing the gain or loss of mass due to flow along the flame surfaces.

The same procedure can be applied to the conservation equations for mass, species mass fractions Y_i, and enthalpy h. This yields the following set of quasi-one-dimensional differential equations, to which we will refer as the flamelet equations:

$$\frac{1}{\sigma}\frac{\partial}{\partial s}(\sigma m) = -\rho K Y_i \tag{7.6a}$$

$$\frac{1}{\sigma}\frac{\partial}{\partial s}\left(\sigma m Y_i - \sigma\frac{1}{\mathrm{Le}_i}\frac{\lambda}{c_p}\frac{\partial Y_i}{\partial s}\right) - \omega_i = -\rho K Y_i + Q_{Y_i} - \rho\frac{\partial Y_i}{\partial \tau} \tag{7.6b}$$

$$\frac{1}{\sigma}\frac{\partial}{\partial s}\left(\sigma m h - \sigma\frac{\lambda}{c_p}\frac{\partial h}{\partial s} - \sigma\mathbf{J}_h\cdot\mathbf{n}\right) = -\rho K h + Q_h - \rho\frac{\partial h}{\partial \tau}, \tag{7.6c}$$

where $\mathbf{J}_h = \frac{\lambda}{c_p}\sum\left(\frac{1}{\mathrm{Le}_i} - 1\right)h_i\nabla Y_i$ is the preferential diffusion flux of enthalpy. Note that Eqs. (7.5) and (7.6a) are steady, but that the other equations have a time derivative $\partial/\partial\tau$ indicating the unsteady behavior of the variable in the flame-adapted coordinate system. Furthermore, so-called Q-terms arise which describe the transport if Y_i and h along the flame surfaces. They are given by $Q_{Y_i} = \nabla_\mathrm{t}\left(\rho D_i\nabla_\mathrm{t}Y_i\right)$ and a similar expression for Q_h, with ∇_t the gradient operator restricted to the flame surfaces. The set of flamelet equations is derived from the full 3D equations without assumptions about the magnitude of the terms. However, it can be shown that the stretch terms, Q-terms, and unsteady terms are all negligible in the corrugated flamelet regime (Oijen et al. 2016). This assumption will be used in the following to compute one-dimensional flamelets for the construction of an FGM.

7.2.2 Flamelet Solutions

In the FGM method, representative flamelets are computed by solving the set of flamelet Eq. (7.6) for conditions that are appropriate for the combustion system to which the FGM will be applied. For a premixed flame, this means that the boundary conditions of (7.6) correspond to an inflow of reactants at one side ($s \to -\infty$) and an outflow of reaction products at the other side. When we furthermore assume that $\sigma = 1$, $K = 0$, $Q_i = 0$, and that the time derivatives ($\partial/\partial\tau$) are zero, the equations describe the most elementary 1D premixed flamelet: an adiabatic, flat, stretchless, steady flame. Specialized 1D flame codes can solve the flamelet equations numerically employing detailed chemistry and transport models. The solution consists of the profiles of mass burning rate m, enthalpy h, and species mass fractions Y_i as functions of the spatial coordinate s. So the 1D flamelet solution yields the thermochemical variables φ parameterized by one variable: the spatial coordinate, $\varphi = \varphi(s)$. In fact, this 1D solution defines a 1D FGM in composition space, which can be parameterized by a single control variable: $\varphi = \varphi(y_1)$. When more degrees of freedom

are required, e.g., to account for changes in element mass fractions Z_j, enthalpy h, and pressure p, multiple flamelets have to be computed.

For instance, when the reactants are not purely premixed, variations in the element mass fractions Z_j occur and a series of flamelets with different equivalence ratios has to be computed (see, e.g., (Oijen and Goey 2004)). Another example is heat loss to the walls of a combustion chamber, which decreases the enthalpy h in the computational domain. In order to take this into account in the FGM tabulation process, laminar flamelets have to be solved for different values of enthalpy, introducing enthalpy as an additional degree of freedom. The enthalpy in an adiabatic premixed flame is constant and equal to the enthalpy of the burnt mixture, h_b, apart from small local changes due to non-unity Lewis number effects. The enthalpy of the flamelets can be reduced by lowering the temperature of the reactants, dilute them with cold combustion products, computing burner-stabilized flames, by adding a radiation source term, or by rescaling the heat release source term. These different approaches are explained in (van Oijen and de Goey 2000, 2002; Oijen et al. 2001; Proch and Kempf 2015; Trisjono et al. 2014). With enthalpy as an additional parameter, the thermochemical state is parameterized by two variables: $\varphi = \varphi(s, h_\mathrm{b})$. In general, an M-dimensional FGM can be generated from a series of one-dimensional flamelets with $M - 1$ parameters π:

$$\varphi = \varphi(s, \pi_1, \ldots, \pi_{M-1}). \tag{7.7}$$

7.2.3 Storage and Retrieval

In order to use a manifold in flame calculations, it is parameterized by control variables y_i and stored as a database or lookup table. Therefore, a transformation needs to be performed:

$$\varphi(s, \pi_1, \ldots, \pi_{M-1}) \rightarrow \varphi'(y_1, \ldots, y_M), \tag{7.8}$$

or more specifically for the example with heat loss

$$\varphi(s, h_\mathrm{b}) \rightarrow \varphi'(y_1, y_2), \tag{7.9}$$

in which the control variables y_i are linear combinations of the original variables $(Y_1, \ldots, Y_N, h)$. A straightforward choice for (y_1, y_2) is $(\mathscr{Y}, h)$. The reaction progress variable is usually chosen as a linear combination of species mass fractions

$$\mathscr{Y} = \sum_{i=1}^{N} \alpha_i Y_i, \tag{7.10}$$

with α_i the weight factor of the mass fraction of species i. This choice should result in a monotonic function $\mathscr{Y}(s)$ for all h_b in order to have a non-singular mapping.

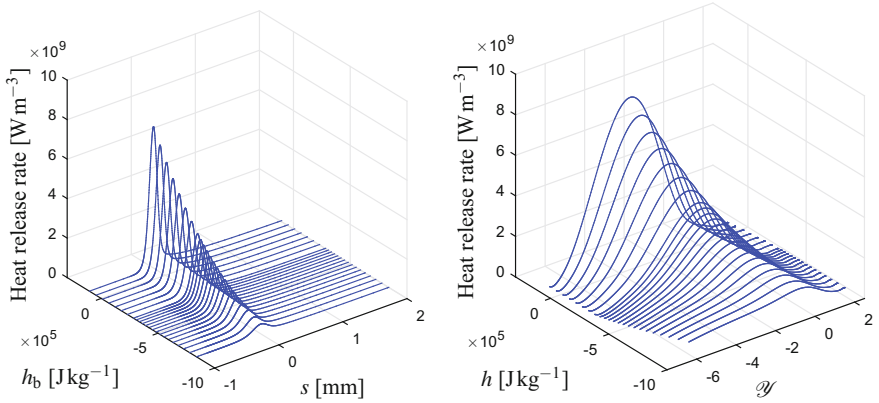

Fig. 7.2 Chemical heat release rate as a function of the original parameters s and burnt enthalpy h_b (left) and after transformation as a function of the control variables $y_1 = \mathscr{H}$ and $y_2 = h$ (right) (Oijen et al. 2016)

Therefore, linear combinations of reactants or products are commonly used. In the example shown in Fig. 7.2, we have chosen a combination of carbon dioxide and oxygen,

$$\mathscr{H} = \alpha_{CO_2} Y_{CO_2} + \alpha_{O_2} Y_{O_2}, \tag{7.11}$$

with $\alpha_{CO_2} = 22.7$ and $\alpha_{O_2} = -31.3$. This choice results in a monotonous progress variable for the case studied here. Note that this choice is not unique; many other choices that result in a monotonous progress variable are possible. Although theoretically the exact choice is not important, it can be optimized to reduce numerical interpolation errors of the retrieval procedure (see e.g. (Ihme et al. 2012; Niu et al. 2013)). Apart from monotonicity and numerical resolution, it is also relevant that all chemical processes in the flame are covered.

As an example, the chemical heat release rate is shown in Fig. 7.2 as a function of the original parameters s and h_b and as a function of $y_1 = \mathscr{H}$ and $y_2 = h$ after transformation. The heat release rate decreases with decreasing enthalpy. Below a certain enthalpy level, the flame temperature is too low to sustain a steady flame. Since steady flamelets can not be computed for lower T_b, the tabulated data ends at this level. In the application of the manifold, lower enthalpy levels might occur, which requires an extrapolation of the data in Fig. 7.2. Often linear extrapolation is employed, but a more accurate extrapolation is described in (van Oijen and de Goey 2000).

A multitude of methods has been used to store the data and to retrieve values from it, e.g., artificial neural networks (Christo et al. 1996), in situ adaptive tabulation (Pope 1997), k-d trees (Shunn 2009) and orthogonal polynomials (Turanyi 1994), each with its own merits. The most common and straightforward method, however, is to store a discrete representation of the function $\varphi = f(y_1, \ldots, y_M)$ on a structured mesh and using multidimensional linear interpolation for retrieval. In

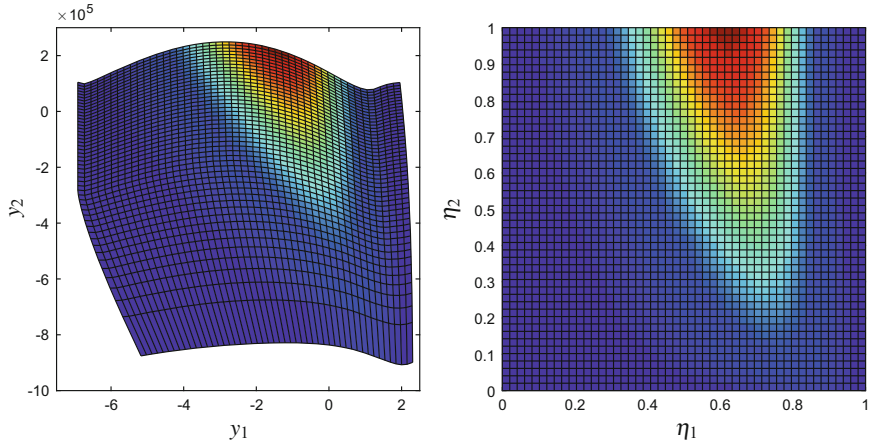

Fig. 7.3 Chemical source term of the progress variable as a function of the control variables $y_1 = \mathscr{Y}$ and $y_2 = h$ (left) and as a function of η_1 and η_2 after transformation to the unit square (right) (Oijen et al. 2016)

this case, the thermochemical variables are interpolated to a curvilinear mesh in $(y_1, \ldots, y_M)$ space. The mesh for the present example is shown in the left plot of Fig. 7.3. The curved mesh lines follow the boundaries given by the flamelets with the highest and lowest enthalpy h_b. Note that the enthalpy in these flamelets changes because of preferential diffusion effects. Subsequently, the curvilinear mesh is mapped onto an M-dimensional unit domain, viz.

$$f(y_1, \ldots, y_M) \rightarrow f'(\eta_1, \ldots, \eta_M) \quad \text{with} \quad \eta_i \in [0, 1]. \tag{7.12}$$

An equidistant mesh with $n_1 \times n_2 \cdots \times n_M$ mesh points is used to discretize f' on this unit domain and the function values at the mesh points are stored in an M-dimensional array. This array is stored in a file, which can be read by the CFD code. The right plot of Fig. 7.3 shows the source term of progress variable on an equidistant mesh in the unit domain. To retrieve data from the table at an entry $(y_1^\star, \ldots, y_M^\star)$, the corresponding coordinates $(\eta_1, \ldots, \eta_M)$ in the unit domain are determined first. After that, it is straightforward to find the enclosing mesh points and to interpolate the values.

The main advantages of this method are its simplicity, fast retrieval, and the fact that one has full control over inter- and extrapolation errors. The large memory requirement is its main—and probably its only—drawback. A 3D table of 15 variables stored with double precision at 100 points in each dimension, results in $15 \times 100^3 \times 8 = 12 \times 10^7$ bytes or approximately 120 MB. A 4D table would result in approximately 12 GB, which is more than the memory of a single CPU in many computer clusters. A higher order interpolation procedure or local mesh refinement could reduce the required number of grid points, but it increases complexity and

computational cost to retrieve a value from the table. A method to reduce the memory requirements by using a memory abstraction layer was introduced by Weise et al. (2013).

7.2.4 Coupling with a Flow Solver

After the manifold is stored in a lookup table, it can be linked to a standard CFD code. First, in the initialization phase, the database is loaded into memory. Then, the CFD code must solve transport equations for the control variables, together with the momentum and continuity equations. In manifold methods, the conservation equations for the control variables are derived by a projection of the full system onto the manifold (see, e.g., (Maas and Pope 1994; Pope 2013)). The projection determines how processes that drive the composition of the manifold, are forced back to the manifold by the fast chemical processes. In flamelet-based methods, this projection is usually not considered. It was shown by van Oijen and de Goey (2000, 2002) that the projection has only a small contribution in the FGM method and can be ignored. However, this omission causes that the final result of an FGM calculation depends on the choice of control variables.

Ignoring the projection, the transport equations for the control variables can be derived by taking the proper linear combinations of the original balance equations. For the progress variable, this yields

$$\frac{\partial}{\partial t}\left(\rho \sum_{i=1}^{N} \alpha_i Y_i\right) + \nabla \cdot \left(\rho \mathbf{v} \sum_{i=1}^{N} \alpha_i Y_i\right) = \nabla \cdot \left(\frac{\lambda}{c_p} \sum_{i=1}^{N} \frac{\alpha_i}{\mathrm{Le}_i} \nabla Y_i\right) + \sum_{i=1}^{N} \alpha_i \omega_i, \quad (7.13)$$

which can be rewritten as

$$\frac{\partial (\rho \mathscr{Y})}{\partial t} + \nabla \cdot (\rho \mathbf{v} \mathscr{Y}) - \nabla \cdot \left(\frac{\lambda}{c_p} \nabla \mathscr{Y}\right) = \nabla \cdot \left[\frac{\lambda}{c_p} \sum_{i=1}^{N} \alpha_i \left(\frac{1}{\mathrm{Le}_i} - 1\right) \nabla Y_i\right] + \omega_{\mathscr{Y}}, \quad (7.14)$$

with $\omega_{\mathscr{Y}} = \sum_{i=1}^{N} \alpha_i \omega_i$ the progress variable source term. The first term on the right-hand side of (7.14) represents the fluxes due to preferential diffusion. In case of unity Lewis numbers, this term is zero. By applying the chain rule,

$$\nabla Y_i = \sum_{j=1}^{M} \frac{\partial Y_i}{\partial y_j} \nabla y_j, \quad (7.15)$$

this term can be rewritten in terms of the gradients of the control variables ∇y_i. This can be simplified by assuming that the gradients of the control variables are not independent but are correlated as in the 1D flamelets:

$$\nabla y_i = c_i \nabla \mathscr{Y}, \tag{7.16}$$

with c_i a coefficient that is a function of the control variables. The transport equation then reads (van Oijen 2002; van Oijen and de Goey 2000; de Swart 2009).

$$\frac{\partial(\rho\mathscr{Y})}{\partial t} + \nabla\cdot(\rho\mathbf{v}\mathscr{Y}) - \nabla\cdot\left(\frac{\lambda}{c_p}\nabla\mathscr{Y}\right) = \nabla\cdot\left(\mathscr{D}_{\mathscr{Y}}\nabla\mathscr{Y}\right) + \omega_{\mathscr{Y}}. \tag{7.17}$$

The preferential diffusion coefficient $\mathscr{D}_{\mathscr{Y}}$ is stored in the FGM table. In a similar way, transport equations for the other control variables can be derived. For the enthalpy, it reads

$$\frac{\partial(\rho h)}{\partial t} + \nabla\cdot(\rho\mathbf{v}h) - \nabla\cdot\left(\frac{\lambda}{c_p}\nabla h\right) = \nabla\cdot\left(\mathscr{D}_h\nabla\mathscr{Y}\right), \tag{7.18}$$

with $\mathscr{D}_h$ the preferential diffusion coefficient (van Oijen and de Goey 2000).

The transport equations for the control variables are solved during run time together with the momentum and continuity equations, while all other parameters (e.g., ρ, c_p, λ, $\omega_{\mathscr{Y}}$, $\mathscr{D}_{\mathscr{Y}}$, $\mathscr{D}_h$, T) are retrieved from the FGM database. For low-Mach, pressure-based solvers, ρ and T can be taken directly from the manifold. For density-based solvers, however, an energy equation should be solved that includes acoustic terms (contrary to Eq. (7.18)). The temperature can then be computed from the energy equation and the pressure follows from the gas law. The implementation of FGM in fully compressible solvers is described in detail by de Swart et al. (2009) and Vicquelin et al. (2011).

Since the progress variable is a combination of species mass fractions, the boundary conditions for $\mathscr{Y}$ are straightforward to implement and follow from the definition in (7.10). The boundary conditions for h are somewhat more cumbersome because they are often not defined in terms of enthalpy itself but in terms of temperature. Therefore, an iterative procedure might be needed to obtain the enthalpy at a boundary. To find the enthalpy at a wall with constant temperature T_{wall}, one has to solve

$$T(\mathscr{Y}, h) = T_{\text{wall}} \tag{7.19}$$

for h with $\mathscr{Y}$ given at the wall. Since T is a nearly linear function of h, this equation can be solved with only a few iterations. Alternatively, one can solve (7.19) in a preprocessing step for a given T_{wall} and store the solution h_{wall} as a function of $\mathscr{Y}$. This has also been studied by Ketelheun et al. (2013).

In the method described here, the species mass fractions are not required to solve the equations and they are only retrieved from the database during postprocessing and visualization of the results. Several alternative methods to couple the manifold with a flow solver, in which all or major species are transported, were compared by Jha and Groth (2012).

7.3 Preferential Diffusion Effects

In turbulent flames, the flame fronts are stretched and curved by turbulent flow structures. It is well known that flame stretch affects the burning velocity of premixed flame fronts. Moreover, flame stretch and curvature in combination with non-unity Lewis number mixtures give rise to differential diffusion effects. The difference in diffusion of mass and heat results in local changes in enthalpy, leading to changes in temperature and burning rates. In case of unequal Lewis numbers of the species, $\mathrm{Le}_i \neq \mathrm{Le}_j$, differential diffusion occurs leading to an imbalance of the fluxes of elements, which gives rise to variations in element mass fractions. In Sect. 7.3.1, these preferential diffusion effects in stretched 1D flames and the modeling of these effects with FGM are discussed. In Sect. 7.3.2, DNS of premixed turbulent flames are presented and the effects of preferential diffusion on flame behavior are discussed.

7.3.1 Modeling Preferential Diffusion Effects with FGM

In de Goey and ten Thije Boonkkamp (1999), it was shown that the combined effect of flame stretch and preferential diffusion leads to changes in the enthalpy $\Delta h_\mathrm{b} = h_\mathrm{b} - h_\mathrm{b}^0$ and element mass fractions $\Delta Z_{j,\mathrm{b}} = Z_{j,\mathrm{b}} - Z_{j,\mathrm{b}}^0$ at the burnt side of the flame. The superscript ^{0} indicates a property of a flame with zero stretch. In Fig. 7.4, the changes in element mass fractions, $\Delta Z_{j,\mathrm{b}}$, are shown for steady planar 1D flames in a flow with a constant strain rate a, such that the flame stretch rate $K = a$. The strain rate is made dimensionless by the thermal flame thickness and the laminar burning velocity. The fuel mixture consists of 60% methane and 40% hydrogen by volume and is premixed with air at an equivalence ratio of $\phi = 0.7$. It can be observed that the mass fractions of C and H are increasing while O is decreasing with increasing strain rate. This means that the mixture at the burnt side of the flame, close to the reaction zone, is getting richer. For this lean flame, this implies it will have a higher burning rate.

The variations in element mass fraction and enthalpy affect the mass burning rate. De Goey and ten Thije Boonkkamp (1999) derived an expression for the mass burning rate m_b of stretched flames that takes these effects into account. For not too large variations, it reads

$$\frac{m_\mathrm{b}}{m_\mathrm{b}^0} = 1 - \mathrm{Ka}_\mathrm{b} + \Delta h_\mathrm{b} \frac{\partial \left(\ln m_\mathrm{b}^0\right)}{\partial h_\mathrm{b}^0} + \sum_{j=1}^{N_\mathrm{e}} \Delta Z_{j,\mathrm{b}} \frac{\partial \left(\ln m_\mathrm{b}^0\right)}{\partial Z_{j,\mathrm{b}}^0} + hot \tag{7.20}$$

with

$$\mathrm{Ka}_\mathrm{b} = \frac{1}{m_\mathrm{b}^0} \int_{s_\mathrm{u}}^{s_\mathrm{b}} \rho K \tilde{\mathscr{Y}} \, \mathrm{d}s \tag{7.21}$$

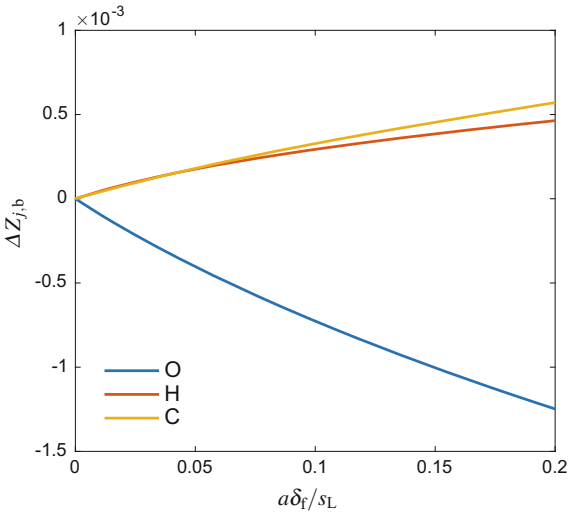

Fig. 7.4 Change in element mass fractions $\Delta Z_{j,\mathrm{b}}$ of strained methane–hydrogen–air flames ($X_{\mathrm{H_2}} = 0.4$) versus dimensionless strain rate $a\delta_\mathrm{f}/s_\mathrm{L}$

the Karlovitz integral. The second term on the right-hand side of (7.20) represents the direct effect of stretch on the mass burning rate, while the third and fourth terms represent the preferential diffusion effects. The derivatives $\partial(\ln m_\mathrm{b}^0)/\partial h_b^0$ and $\partial(\ln m_\mathrm{b}^0)/\partial Z_{j,b}^0$ are the sensitivity coefficients of changes in m_b^0 with respect to changes in h_b and $Z_{j,\mathrm{b}}^0$, which can be numerically determined as explained in (Swart et al. 2006). In order to model these preferential diffusion effects on the mass burning rate, the changes in h_b and $Z_{j,\mathrm{b}}$ should be included in the FGM method.

The variations in h_b and $Z_{j,\mathrm{b}}$ can be incorporated in the manifold by solving the flamelet equations including a stretch term. Here two different methods are compared. In the first method, the flamelet equations are solved including a constant stretch term with $K = K_\mathrm{u}$. By applying a range of stretch rates $K_\mathrm{u} = -200, -175, \ldots, 950\,\mathrm{s}^{-1}$, a 2D manifold is generated: FGM A. In the second method, a 2D manifold is generated by solving the flamelet equations assuming constant curvature $\kappa = \kappa_\mathrm{u}$ (or equivalently $\sigma = \exp(\kappa_\mathrm{u} s)$) and a stretch term related to constant curvature, i.e., $K = \kappa m^0/\rho_\mathrm{u}$. By computing a series of flamelets with different curvatures $\kappa_u = -300, -290, \ldots, 300\,\mathrm{m}^{-1}$, a 2D manifold, FGM B, is generated. These ranges of K_u and κ_u are taken to span a manifold that covers the range of variations in element mass fractions expected in the application.

Both manifolds are parameterized by two control variables. The first control variable is the progress variable, which is here chosen as $\mathscr{Y} = \phi_{\mathrm{CO_2}} + \phi_{\mathrm{H_2O}} - 0.6\phi_{\mathrm{CH_4}} - 0.4\phi_{\mathrm{H_2}}$ with $\phi_i = Y_i/M_i$. The second control variable is chosen as a combination of element mass fractions $\mathscr{Z} = \frac{1}{2}Z_\mathrm{C} + Z_\mathrm{H}$. This set of control variables results in a monotonic parametrization of both 2D manifolds. The chemical source term of the progress variable in FGM A is shown in Fig. 7.5. The source term increases for higher values of $\mathscr{Z}$, which corresponds to an increased burning rate at richer

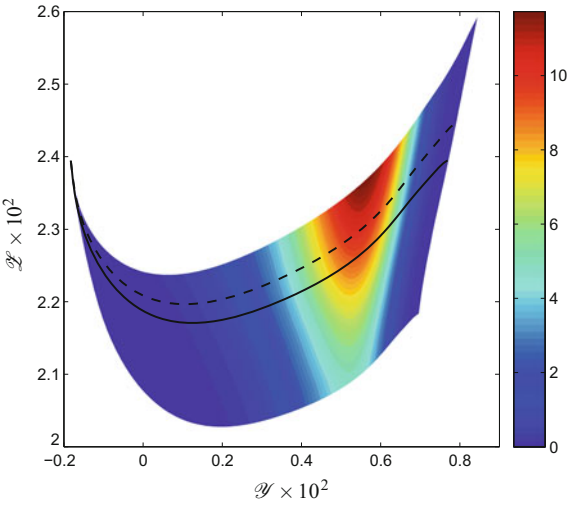

Fig. 7.5 Chemical source term of progress variable $\omega_{\mathscr{Y}}$ [kg/m^{3}s] in the two-dimensional FGM A generated by assuming constant stretch rates. The solid and dashed curves correspond to flamelets with $K = 0\,\mathrm{s}^{-1}$ and $K = 200\,\mathrm{s}^{-1}$, respectively (Oijen et al. 2016)

conditions. The two flamelet curves demonstrate that a positive stretch rate leads to an increase in $\mathscr{Z}$ which is in agreement with the results in Fig. 7.4.

Both 2D manifolds are used to compute strained flames. The results obtained with the 2D manifolds are compared with results of calculations using detailed chemistry (GRI-Mech 3.0 (Smith et al. 2017)) and a 1D FGM. In Fig. 7.6, the mass burning rate is plotted versus Karlovitz integral for methane blended with 40% hydrogen as fuel ($X_{\mathrm{H_2}} = 0.4$), but also for pure methane as a reference. ($X_{\mathrm{H_2}} = 0$) demonstrate that the mass burning rate decreases almost linearly with strain rate. Furthermore, it can be seen that a 1D FGM results agree very well with the detailed chemistry calculations. This can be explained by the fact that the effective Lewis number of methane–air mixtures is close to one, which causes the preferential diffusion effects to be negligible (Oijen et al. 2016).

For the methane–hydrogen blend, the results computed using detailed chemistry show a strong effect of preferential diffusion. The 1D FGM cannot predict the preferential diffusion effects because it does not include changes in h_{b} and $Z_{j,\mathrm{b}}$. Both 2D FGMs, however, predict the correct trend in mass burning rate. This good agreement and the small difference between the two 2D FGMs indicate that one degree of freedom is sufficient to describe the changes in enthalpy and element mass fractions, and that it is not very important how they are imposed.

7.3.2 *Application in Direct Numerical Simulations*

The 2D FGM A introduced in the previous section is used in DNS of an expanding flame kernel and compared with results obtained using the 1D FGM and the

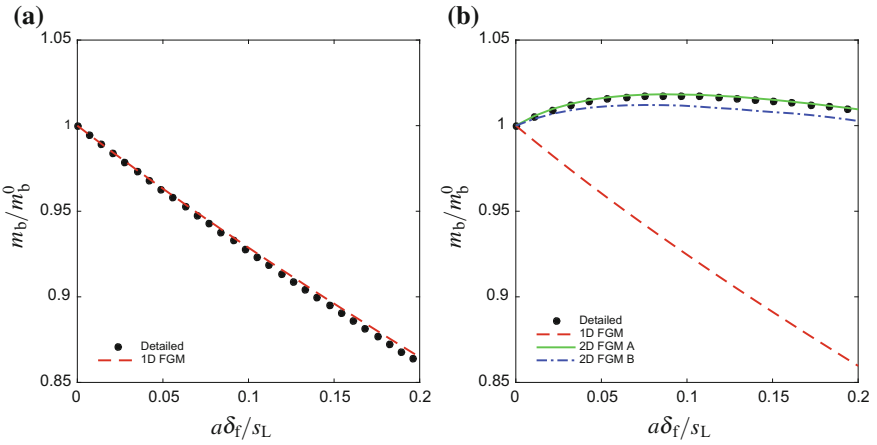

Fig. 7.6 Mass burning rate m_b/m_b^0 of strained methane–hydrogen–air flames versus dimensionless strain rate $a\delta_f/s_L$ for a) $X_{H_2} = 0$ and b) $X_{H_2} = 0.4$

detailed GRI 3.0 mechanism (Smith et al. 2017). Premixed flame kernels in homogeneous isotropic turbulence were simulated. Further details of these simulations can be found in (van Oijen et al. 2010). Snapshots of the mass fraction of the hydrogen radical, which is an important intermediate in hydrocarbon oxidation and an indicator for the fuel consumption rate, are shown in Fig. 7.7. The detailed result shows the increased mass fraction of H in parts of the flame front that are curved outward. These parts of the flame are positively stretched and become richer due to preferential diffusion effects. This local increase in stoichiometry leads to an increase in mass burning rate, which attributes to the cellular instability of lean flames with Le < 1 (Law and Sung 2000). While the 1D FGM cannot predict the change in Z_j, the 2D FGM reproduces the detailed chemistry results very well. The increased H mass fractions in the outward curved parts are very well predicted. At closer inspec-

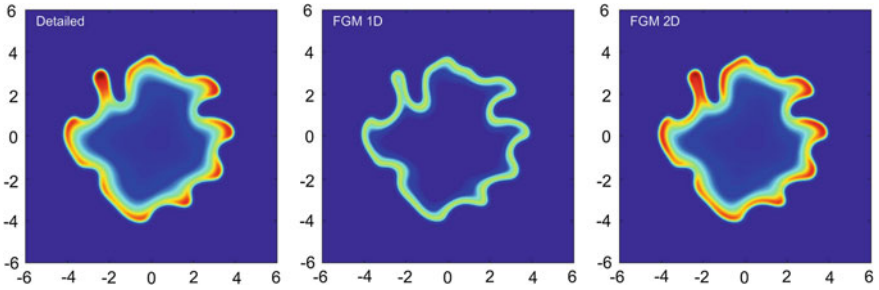

Fig. 7.7 Contour plots of the mass fraction of hydrogen radicals computed with detailed chemistry (left), 1D FGM (middle), and 2D FGM (right) at $t = 0.3$ ms (van Oijen et al. 2010). Spatial dimensions are in millimeters

tion, however, one can still find differences. Due to the variations of species mass fractions along isocontours of the progress variable, diffusion in this direction starts to play a role. Delhaye (2009) performed a quantitative analysis of all terms in the flamelet equations for a similar DNS of a lean methane–air mixture. He found that the Q-terms are mostly much smaller than the stretch and curvature terms, but in the part with the highest curvature, where the curvature radius is comparable to the thickness of the reaction layer δ_r, the Q-terms become comparable in magnitude. Since Delhaye investigated a methane flame with a near unity Lewis number, the variations in Z_j along the flame front are not as large as in the present methane–hydrogen mixture. Therefore, the Q-terms are expected to be larger for the present case. For an accurate representation of these tangential diffusion fluxes, additional degrees of freedom have to be added to the manifold.

The local variations in Z_j and h lead to a change in mass burning rate m_b, which on its turn affects the propagation of the flame front. This effect is not clearly visible in Fig. 7.7 because only one eddy turnover time was simulated and in this time span the movement of the flame front is mainly determined by the velocity of the gas. The effect of preferential diffusion on the dynamics of the flame was investigated by Vreman et al. (2009a) by using FGM in DNS. Premixed turbulent flames of lean methane–hydrogen–air mixtures were simulated on a slot burner geometry that was based on the experiments of Filatyev et al. (2005) and that was used in earlier FGM-DNS studies of methane combustion (Vreman et al. 2009, b). In this study, the preferential diffusion effects were demonstrated by comparing a 1D FGM without changes in Z_j and h, with a 2D FGM that does account for these changes. In Fig. 7.8, instantaneous contours of the progress variable source term are shown for both cases.

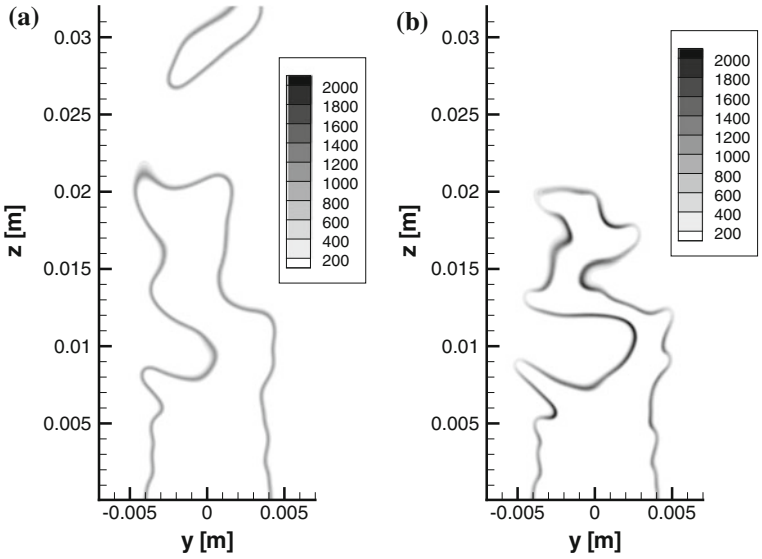

Fig. 7.8 Contours of instantaneous $\omega_{\mathscr{Y}}$ (kgm^{-3}s^{-1}) in the vertical plane $x = 0$m, for a 1D FGM **a** and a 2D FGM **b**. Adapted from (Vreman et al. 2009a)

The FGM model with preferential diffusion effects (Fig. 7.8b) shows an increase of the source term in regions of the flame front that are convex with respect to the unburnt mixture and vice versa. Therefore, the flame front becomes more wrinkled than in case of the 1D FGM (Fig. 7.8a). This increase in flame surface density leads to an increase in the averaged burning rate and a shorter averaged flame length. In Vreman et al.(2009a), the turbulent burning velocity was found to increase by 30% when preferential diffusion was included. The change in local equivalence ratio does not only affect the mass burning rate but it also alters the NO production rate, because the flame temperature changes. The NO mass fraction was found to increase by approximately a factor two at the burnt side of the convex flame front in Fig. 7.8b. Variations in equivalence ratio at the flame front are not only caused by preferential diffusion, but they also arise often due to imperfect premixing of fuel and oxidizer. The effect of such a fuel stratification on the dynamics of the flame was investigated in a similar numerical setup with DNS-FGM by Ramaekers et al. (2012).

7.4 Large-Eddy Simulation with FGM

In the previous section, it was shown that the use of FGM in DNS yields results close to results of detailed chemistry calculations, but at a fraction of the computational cost. This makes it possible to perform DNS of high Reynolds number flows in real burners (see e.g., (Moureau et al. (2011)). In practice, however, a DNS is still too costly for most applications and RANS or LES approaches have to be used. Typically, two types of models are required in order to close the first moment equations of turbulent reacting flows with flamelet-based tables. First, a fluid mechanical model must describe the unresolved stress and flux terms. Usually, eddy viscosity and gradient transport assumptions are employed to close these terms (Poinsot and Veynante 2011). Second, a closure method is needed for the mean values of the highly nonlinear chemical terms, such as the averaged source term, density, temperature, and species mass fractions.

7.4.1 Modeling Unresolved Fluctuations

First implementations of FGM in RANS of premixed turbulent flames are described in (Fiorina et al. 2005; Albrecht et al. 2008). In these studies, 3D manifolds with $\mathscr{Y}$, Z and h as control variables are used and the chemical closure problem is tackled by describing the control variables in a stochastic way. It is assumed that locally the probability of occurrence of a certain state is described by a presumed shape probability density function (PDF). Usually, the joint PDF of the control variables is written as a product of the marginal PDFs assuming statistical independence of the variables. Beta functions parameterized by the first two Favre-averaged moments (mean and variance) are used to describe the marginal PDFs. The combination of

a tabulated premixed flamelet with a beta PDF for RANS modeling of turbulent combustion was already introduced by Bradley et al. (1988) in 1988. Cook and Riley (1994) proposed to use the beta PDF for the modeling of unresolved terms in the context of LES. Since then it has become a standard closure technique in both LES and RANS, although various other PDF shapes have been proposed and used successfully as well (Floyd et al. 2009; Olbricht et al. 2012).

In LES, usually Favre-filtered conservation equations are solved. For a scalar variable f, the filtered equation reads (Vreman et al. 2008)

$$\frac{\partial \overline{\rho}\widetilde{f}}{\partial t} + \frac{\partial}{\partial x_j}\left(\overline{\rho}\widetilde{u}_j\widetilde{f}\right) = \frac{\partial}{\partial x_j}\left[\left(\overline{\rho}\widetilde{D} + \frac{\mu_t}{\mathrm{Sc}_t}\right)\frac{\partial \widetilde{f}}{\partial x_j}\right] + \overline{\rho}\widetilde{\Omega} \tag{7.22}$$

with diffusion coefficient D and chemical source term $\Omega = \omega/\rho$. The unresolved fluxes are modeled here with a standard gradient approach, in which the turbulent viscosity μ_t and Schmidt number Sc_t are used. An overline is used to indicate Reynolds filtering, while a tilde indicates Favre-filtered quantities. The modeling of the filtered source term with a presumed PDF method is described in the following.

In case of a one-dimensional FGM, $\varphi = \varphi(\mathscr{Y})$ and the presumed PDF model for the source term of the progress variable $\Omega_{\mathscr{Y}}$ reads

$$\widetilde{\Omega}_{\mathscr{Y}} = \int_0^1 \Omega_{\mathscr{Y}}(c)P(c)\mathrm{d}c, \tag{7.23}$$

where we have introduced the normalized progress variable $c = (\mathscr{Y} - \mathscr{Y}_\mathrm{u})/(\mathscr{Y}_\mathrm{b} - \mathscr{Y}_\mathrm{u})$. The (sub-filter) probability distribution $P(c)$ is modeled with the above mentioned β-function:

$$P(c) = \frac{\Gamma(a+b)}{\Gamma(a)\Gamma(b)}c^{a-1}(1-c)^{b-1}, \tag{7.24}$$

where Γ is the gamma function. The two parameters a and b are given by

$$a = \widetilde{c}\left(\frac{\widetilde{c}(1-\widetilde{c})}{\widetilde{c''^2}} - 1\right) \quad \text{and} \quad b = \left(\frac{a}{\widetilde{c}}\right) - a. \tag{7.25}$$

Note that this PDF is based on the first two moments of c: the mean $\widetilde{c}$ and the variance $\widetilde{c''^2}$. Therefore, the filtered quantities become a function of both variables, $\widetilde{\varphi} = \widetilde{\varphi}(\widetilde{c}, \widetilde{c''^2})$ and the dimension of the lookup table increases by one.

In many situations, the progress variable is not enough to describe the chemical state and additional variables are used to parameterize the manifold. For instance, when fuel and oxidizer are not perfectly premixed, the mixture fraction Z is required as additional degree of freedom and $\varphi = \varphi(\mathscr{Y}, Z)$. In this case, the turbulence–chemistry interaction needs to be considered for both progress variable $\mathscr{Y}$ and mixture fraction Z. The unresolved local state in composition space is then described

by the joint PDF $P(c, Z)$. As an example, the filtered source term of the progress variable $\mathscr{Y}$ is now given by

$$\widetilde{\Omega}_{\mathscr{Y}} = \int_0^1 \int_0^1 \Omega_{\mathscr{Y}}(c, Z)\, P(c, Z)\, \mathrm{d}c\, \mathrm{d}Z. \tag{7.26}$$

By assuming that the normalized progress variable c and mixture fraction Z are statistically independent, $P(c, Z)$ can be reduced to the product of two marginal PDFs:

$$P(c, Z) = P(c)\, P(Z). \tag{7.27}$$

This allows to adopt the presumed β-PDF model separately to the two marginal PDFs. As previously described, the β-PDF shape is described by the first two moments

$$P(c) = P(c; \widetilde{c}, \widetilde{c''^2}) \quad \text{and} \quad P(Z) = P(Z; \widetilde{Z}, \widetilde{Z''^2}). \tag{7.28}$$

With this model, the source term of the progress variable $\mathscr{Y}$ is given by

$$\widetilde{\Omega}_{\mathscr{Y}} = \int_0^1 \int_0^1 \Omega_{\mathscr{Y}}(c, Z)\, P(c; \widetilde{c}, \widetilde{c''^2})\, P(Z; \widetilde{Z}, \widetilde{Z''^2})\, \mathrm{d}c\, \mathrm{d}Z. \tag{7.29}$$

The filtered source term is now a function of 4 parameters $\widetilde{\Omega}_{\mathscr{Y}}(\widetilde{c}, \widetilde{c''^2}, \widetilde{Z}, \widetilde{Z''^2})$, which has to be stored in a 4D lookup table. The moments of the normalized progress variable have to be determined from the values of $\widetilde{\mathscr{Y}}$ and $\widetilde{\mathscr{Y}''^2}$. Since the range of $\mathscr{Y}$ depends on Z, this conversion is not straightforward and the scaling factors become functions of $\widetilde{Z}$ and $\widetilde{Z''^2}$. This effect can be important for large unresolved variances as in RANS. In most LES, it is negligible. Further details of this transformation can be found in (Albrecht et al. 2008; Fiorina et al. 2005).

To close the system, models for the sub-filter variances are required. Various models have been proposed in the literature. The simplest model (apart from neglecting the variance) is probably the algebraic closure based on the gradient of the average $\widetilde{f}$:

$$\widetilde{f''^2} = \frac{a\Delta^2}{12} |\nabla \widetilde{f}|^2 \tag{7.30}$$

with Δ the filter width and a a model coefficient, which should lie between 1 and 2 Vreman et al. (2009b). Usually a constant value is chosen, but it can also be determined dynamically. The sub-filter variance can also be modeled by solving a transport equation for it (see, e.g., (Domingo et al. 2005)).

FGM and other tabulated chemistry models have been combined with many other approaches to close the unresolved or sub-grid scale terms in LES. An overview of various approaches to couple flamelet tabulated chemistry with LES is given in a

review by Fiorina et al. (2015). A non-exhaustive list of recently used methods for premixed flames features: The level set or *G*-equation formalism (Knudsen et al. 2010; Moureau et al. 2009), presumed PDF methods (Hernández-Pérez et al. 2011; Vreman et al. 2009b), flame surface density methods (Boger et al. 1998; Vermorel et al. 2009), thickened flame models (Ketelheun et al. 2013; Kuenne et al. 2011), and filtered flamelet methods (Duwig 2007; Fiorina et al. 2010; Mukhopadhyay et al. 2015a, b; Vreman et al. 2009b). Several of these LES approaches have been used recently by various groups to simulate the turbulent stratified flame experiments performed at TU Darmstadt (Seffrin et al. 2010; Kuenne et al. 2012). A comparison of these LES results is described in a joint paper (Fiorina et al. 2015). Good predictions were found for all the models that were based on premixed flamelet tables that included mixture fraction and enthalpy as additional degrees of freedom. Since the premixed flamelet models performed well, it is expected that the diffusion fluxes tangential to the flame front (Q-terms in (7.6)) are relatively small for this mild stratified flame, although a quantitative analysis was not given in Fiorina et al. (2015). Including heat loss by adding enthalpy as a control variable was necessary to quench the flame near the cold burner tip leading to a lifted flame as it was observed in the experiments.

7.4.2 Application in LES of a Gas Turbine Combustor

As an example, we discuss here the application of FGM in LES of a turbulent swirling flame in a laboratory-scale gas turbine combustor developed at DLR. This modified version of a practical gas turbine combustor has been extensively investigated by Weigand et al. (2006) and Meier et al. (2006). This burner setup provides a suitable test case for verification and validation of combustion models, given the challenging complexity of the flow and the availability of a comprehensive set of experimental measurements. Donini et al. (2016) applied the FGM method in combination with a presumed PDF approach in an LES of this setup. Since the fuel (methane) is injected separately from the air, the mixture fraction has to be used as additional control variable. Additionally, enthalpy is used as control variable to account for heat losses due to gas radiation and convective cooling at the combustor walls. The manifold is stored in a five-dimensional table with $120 \times 30 \times 40 \times 10 \times 10$ grid points for $\tilde{\mathscr{Y}}$, $\tilde{h}$, $\tilde{Z}$, $\widetilde{\mathscr{Y}''^2}$, $\widetilde{Z''^2}$, respectively. The grid points are equidistantly distributed for the means, while for the variances the points are clustered near zero in a quadratic way. More details about the numerical setup can be found in (Donini et al. 2016).

The complex flow behavior characterized by inner and outer recirculation zones and a precessing vortex core, as well as the average location of the flame are accurately predicted by the numerical model. A detailed discussion of the flow pattern and a comparison with measurements is given in (Donini et al. 2016). In Fig. 7.9, the computed instantaneous and time-averaged distributions of the control variables are shown. High turbulence levels in the shear layers near the inlet lead to fast mixing

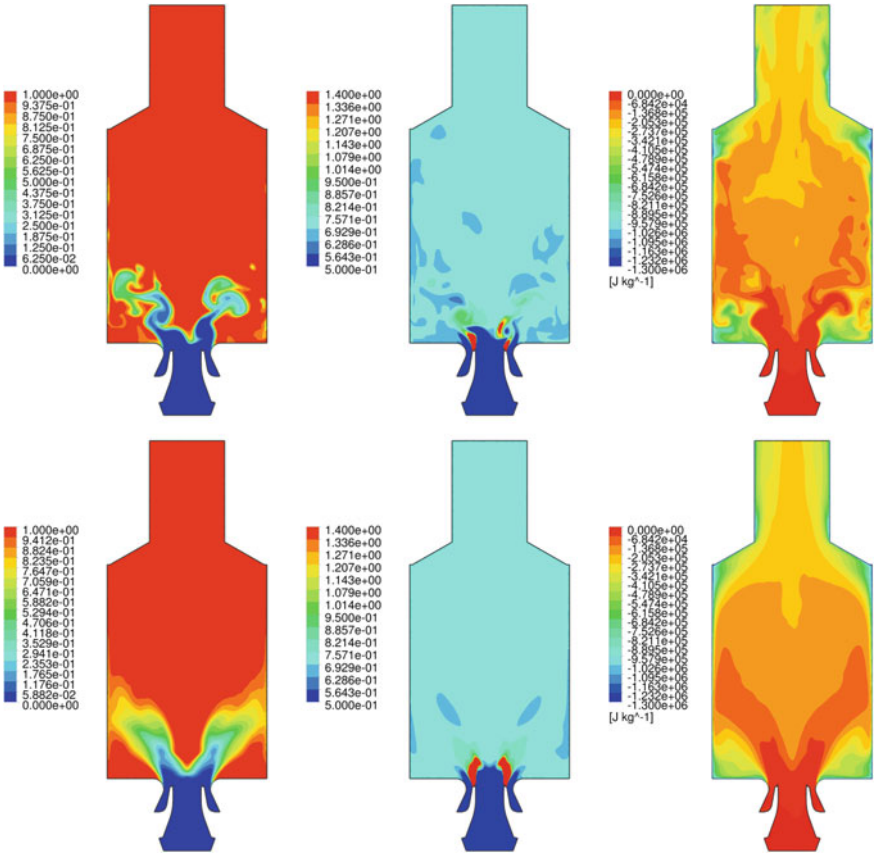

Fig. 7.9 Iso-contour representations of instantaneous (*top*) and time-averaged (*bottom*) distributions of normalized progress variable (*left*), local equivalence ratio (*middle*) and enthalpy deficit [J kg^{-1}] (*right*) at the mid-plane of the combustor. Adapted from Donini et al. (2016)

of fuel and air. At the location of the flame front, they are almost completely premixed and burn in a premixed mode. This is confirmed by an analysis of the resolved scalar dissipation rate χ, which drops from approximately $10^3\ s^{-1}$ near the inlet to values below $1\ s^{-1}$ at the flame front. The scalar dissipation rate in the flame surface, is therefore much smaller than the premixed flame timescale s_L/δ_f. This low scalar dissipation rate indicates that the related Q-terms in the flamelet equations can be ignored. In the enthalpy plots, it can be observed that heat loss to the combustor walls leads to a significant enthalpy deficit in the outer recirculation, but that the region where the flame stabilizes is nearly adiabatic. Strong enthalpy gradients in the flame front can therefore be neglected in the FGM modeling of this case. However, when the flame front comes close to the wall, local quenching may occur and the enthalpy gradients will have the same length scale as the flame thickness. In that case, large Q-terms are expected, which may have to be accounted for in the manifold.

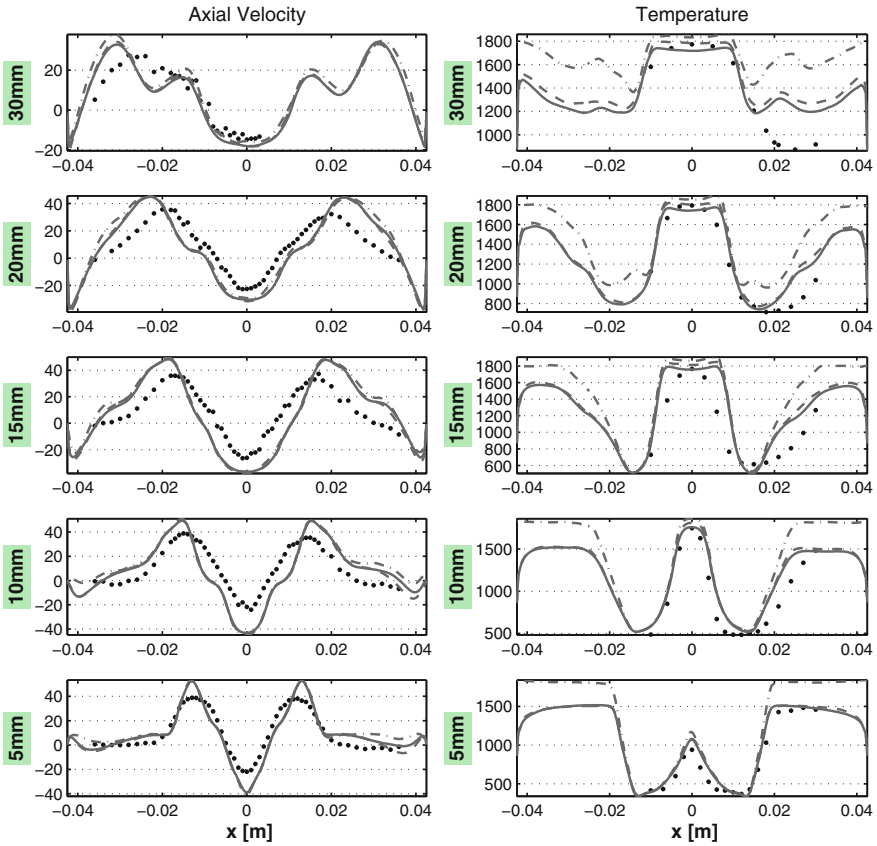

Fig. 7.10 Radial profiles of time-averaged axial velocity (left, in m s^{-1}) and temperature (right, in K) at different axial distances from the nozzle. Measurements (symbols), adiabatic model results (dash-dotted), model results with radiation heat loss (dashed) and model results with radiation and wall heat loss (solid) are compared. Adapted from (Donini et al. 2016)

Figure 7.10 compares measurements and model predictions of time-averaged axial velocity and temperature at different axial distances from the nozzle. Three different model predictions are shown. The first model result is from a simulation without heat loss. This means that radiation is neglected and the walls are adiabatic. The second model includes an optically thin gas radiation model and the third model includes both gas radiation and nonadiabatic walls. By giving special attention to the generation of the turbulent inlet velocity and the mesh refinement near the inlet ducts, flame front and walls, good agreement is obtained between model predictions and measurements. The recirculation zones and other flow features are well predicted by the different models. Larger differences between the model predictions are found for the temperature profiles. Although the location of the flame is predicted rather well, the temperature of the burnt gas is significantly overpredicted when heat loss

to the walls is ignored. A more detailed comparison of measurements and simulation results can be found in (Donini et al. 2016).

The FGM model was also used to predict NO concentrations in this combustor by solving a transport equation with the NO source term obtained from the lookup table. The predicted NO level in the exhaust of the combustor was in excellent agreement with the measured value of 6 ppm. The influence of gas radiation on the NO emission was found to be small, but ignoring heat loss to the walls resulted in an overprediction of 50% due to an overestimation of the flame temperature.

7.5 Conclusions

In this chapter, the numerical modeling of premixed turbulent flames by using the FGM method has been explained. In the FGM method, a low-dimensional manifold in composition space is created by solving 1D flamelet equations. In this way, a reduced chemical model is constructed, in which a few control variables describe the thermochemical state. The 1D flamelet equations can be regarded as steady-state relations that not only balance chemical production and consumption rates, but also include the main parts of convection and diffusion. The manifold is stored as a lookup table and is linked to a flow solver, which does not have to solve transport equations for all species, but only for the control variables. In order to include changes in enthalpy, element mass fractions, and pressure, these variables have to be added to the manifold as extra dimension by solving a series of flamelets. The changes in enthalpy and element mass fractions can be caused for example by heat loss to cooled reactor walls and imperfect mixing of fuel and oxidizer, but also by the combined effect of flame stretch and preferential diffusion. It was shown that these preferential diffusion effects can be significant for fuels with Lewis numbers that are very different from unity. For lean methane–hydrogen–air mixtures, positive flame stretch leads to an increase in local equivalence ratio. This leads to a higher reactivity and hence a higher mass burning rate. The increased burning rate causes positively stretched bulges in the flame front to grow further into the reactants. This local instability was shown to increase the flame surface area and average mass burning rate of a premixed turbulent flame by 30%. A 2D FGM, which includes the changes in h and Z_j, is able to predict these effects.

For the use in LES, the FGM method needs to be coupled with a turbulence model that accounts for the unresolved terms in the governing equations. The presumed beta PDF approach is probably the most commonly used method, but more advanced methods are gaining interest. The use of FGM in an LES of a gas turbine combustor was discussed. The results obtained for this case, demonstrate the large potential of FGM in combination with LES for the modeling of turbulent combustion in real devices.

References

Albrecht BA, Zahirovic S, Bastiaans RJM, van Oijen JA, de Goey LPH (2008) A premixed flamelet-PDF model for biomass combustion in a grate furnace. Energy Fuels 22(3):1570–1580

Bekdemir C, Somers B, de Goey P (2014) DNS with detailed and tabulated chemistry of engine relevant igniting systems. Combust Flame 161(1):210–221

Boger M, Veynante D, Boughanem H, Trouvé A (1998) Direct numerical simulation analysis of flame surface density concept for large eddy simulation of turbulent premixed combustion. Proc Combust Inst 27:917–925

Bongers H, van Oijen JA, Somers LMT, de Goey LPH (2005) The flamelet-generated manifold method applied to steady planar partially premixed counterflow flames. Combust Sci Technol 177(12):2373–2393

Bradley D, Kwa LK, Lau AKC, Missaghi M (1988) Laminar flamelet modeling of recirculating premixed methane and propane-air combustion. Combust Flame 71:109–122

Christo FC, Masri AR, Nebot EM (1996) Artificial neural network implementation of chemistry with PDF simulation of H_2/CO_2 flames. Combust Flame 106:406–427

Cook AW, Riley JJ (1994) A subgrid model for equilibrium chemistry in turbulent flows. Phys Fluids 6(8):2868–2870

Delhaye S (2009) Incorporating unsteady flow-field effects in flamelet-generated manifolds. PhD thesis, Eindhoven University of Technology

Delhaye S, Somers LMT, van Oijen JA, de Goey LPH (2008) Incorporating unsteady flow-effects in flamelet-generated manifolds. Combust Flame 155:133–144

Domingo P, Vervisch L, Payet S, Hauguel R (2005) DNS of a premixed turbulent V flame and LES of a ducted flame using a FSD-PDF subgrid scale closure with FPI-tabulated chemistry. Combust Flame 143(4):566–586

Donini A, Bastiaans RJM, van Oijen JA, de Goey LPH (2015) Differential diffusion effects inclusion with flamelet generated manifold for the modeling of stratified premixed cooled flames. Proc Combust Inst 35:831–837

Donini A, Bastiaans RJM, van Oijen JA, de Goey LPH (2016) A 5-d implementation of fgm for the large eddy simulation of a stratified swirled flame with heat loss in a gas turbine combustor. Flow Turbul Combust 68(3):887–922

Duwig C (2007) Study of a filtered flamelet formulation for large eddy simulation of premixed turbulent flames. Flow Turbul Combust 79:433–454

Filatyev SA, Driscoll JF, Carter CD, Donbar JM (2005) Measured properties of turbulent premixed flames for model assessment, including burning velocities, stretch rates, and surface densities. Combust Flame 141:1–21

Fiorina B, Gicquel O, Vervisch L, Carpentier S, Darabiha N (2005) Approximating the chemical structure of partially premixed and diffusion counterflow flames using FPI flamelet tabulation. Combust Flame 140(3):147–160

Fiorina B, Mercier R, Kuenne G, Ketelheun A, Avdić A, Janicka J, Geyer D, Dreizler A, Alenius E, Duwig C, Trisjono P, Kleinheinz K, Kang S, Pitsch H, Proch F, Marincola FC, Kempf A (2015) Challenging modeling strategies for LES of non-adiabatic turbulent stratified combustion. Combust Flame 162:4262–4282

Fiorina B, Veynante D, Candel S (2015) Modeling combustion chemistry in large eddy simulation of turbulent flames. Flow Turbul Combust 94(3):3–42

Fiorina B, Vicquelin R, Auzillon P, Darabiha N, Gicquel O, Veynante D (2010) A filtered tabulated chemistry model for LES of premixed combustion. Combust Flame 157(3):465–475

Floyd J, Kempf AM, Kronenburg A, Ram RH (2009) A simple model for the filtered density function for passive scalar combustion LES. Combust Theory Modelling 13(4):559–588

de Goey LPH, ten Thije Boonkkamp JHM (1997) A mass-based definition of flame stretch with finite thickness. Combust Sci Technol 122:399–405

de Goey LPH, ten Thije Boonkkamp JHM (1999) A flamelet description of premixed laminar flames and the relation with flame stretch. Combust Flame 119:253–271

Hernández-Pérez FE, Yuen FTC, Groth CPT, Gülder OL (2011) LES of a laboratory-scale turbulent premixed Bunsen flame using FSD, PCM-FPI and thickened flame models. Proc Combust Inst 33:1365–1371

Ihme M, Shunn L, Zhang J (2012) Regularization of reaction progress variable for application to flamelet-based combustion models. J Comput Phys 231:7715–7721

Jha PK, Groth CP (2012) Tabulated chemistry approaches for laminar flames: evaluation of flame-prolongation of ILDM and flamelet methods. Combust Theory Modelling 16(1):31–57

Ketelheun A, Kuenne G, Janicka J (2013) Heat transfer modeling in the context of large eddy simulation of premixed combustion with tabulated chemistry. Flow Turbul Combust 91:867–893

Knudsen E, Kim SH, Pitsch H (2010) An analysis of premixed flamelet models for large eddy simulation of turbulent combustion. Phys Fluids 22:115109

Kuenne G, Ketelheun A, Janicka J (2011) LES modeling of premixed combustion using a thickened flame approach coupled with FGM tabulated chemistry. Combust Flame 158:1750–1767

Kuenne G, Seffrin F, Fuest F, Stahler T, Ketelheun A, Geyer D, Janicka J, Dreizler A (2012) Experimental and numerical analysis of a lean premixed stratified burner using 1D Raman/Rayleigh scattering and large eddy simulation. Combust Flame 159:2669–2689

Law CK, Sung CJ (2000) Structure, aerodynamics, and geometry of premixed flamelets. Prog Energy Combust Sci 26:459–505

Maas U, Pope SB (1994) Laminar flame calculations using simplified chemical kinetics based on intrinsic low-dimensional manifolds. Proc Combust Inst 25:1349–1356

Matalon M (1983) On flame stretch. Combust Sci Technol 31:169–181

Meier W, Duan XR, Weigand P (2006) Investigations of swirl flames in a gas turbine model combustor II. turbulence/chemistry interactions. Combust Flame 144:225–236

Moureau V, Domingo P, Vervisch L (2011) From large-eddy simulation to direct numerical simulation of a lean premixed swirl flame: filtered laminar flame-PDF modeling. Combust Flame 158:1340–1357

Moureau V, Fiorina B, Pitsch H (2009) A level set formulation for premixed combustion LES considering the turbulent flame structure. Combust Flame 156:801–812

Mukhopadhyay S, Bastiaans RJM, van Oijen JA, de Goey LPH (2015a) Analysis of a filtered flamelet approach for coarse DNS of premixed turbulent combustion. Fuel 144:388–399

Mukhopadhyay S, van Oijen JA, de Goey LPH (2015b) A comparative study of presumed PDFs for premixed turbulent combustion modeling based on progress variable and its variance. Fuel 159:728–740

Niu YS, Vervisch L, Taoa PD (2013) An optimization-based approach to detailed chemistry tabulation: automated progress variable definition. Combust Flame 160:776–785

van Oijen JA (2002) Flamelet-generated manifolds: development and application to premixed laminar flames. PhD thesis, Eindhoven University of Technology

van Oijen JA, Bastiaans RJM, de Goey LPH (2010) Modelling preferential diffusion effects in premixed methane-hydrogen-air flames by using flamelet-generated manifolds. In: Sequeira A, Pereira JCF (eds) Fifth European conference on computational fluid dynamics. Lisbon, Portugal

van Oijen JA, Donini A, Bastiaans RJM, ten Thije Boonkkamp JHM, de Goey LPH (2016) State-of-the-art in premixed combustion modeling using flamelet generated manifolds. Prog Energy Combust Sci 57:30–74

van Oijen JA, de Goey LPH (2000) Modelling of premixed laminar flames using flamelet-generated manifolds. Combust Sci Technol 161:113–138

van Oijen JA, de Goey LPH (2002) Modelling of premixed counterflow flames using the flamelet-generated manifold method. Combust Theory Model 6:463–478

van Oijen JA, de Goey LPH (2004) A numerical study of confined triple flames using a flamelet-generated manifold. Combust Theory Model 8:141–163

van Oijen JA, Lammers FA, de Goey LPH (2001) Modelling of complex premixed premixed burner systems using flamelet-generated manifolds. Combust Flame 127:2124–2134

Olbricht C, Stein OT, Janicka J, van Oijen JA, Wysocki S, Kempf AM (2012) LES of lifted flames in a gas turbine model combustor using top-hat filtered PFGM chemistry. Fuel 96:100–107

Peters N (1986) Laminar flamelet concepts in turbulent combustion. Proc Combust Inst 21:1231–1250
Poinsot T, Veynante D (2011) Theoretical and numerical combustion, 3rd edn
Pope SB (1997) Computationally efficient implementation of combustion chemistry using in situ adaptive tabulation. Combust Theory Model 1:41–63
Pope SB (2013) Small scales, many species and the manifold challenges of turbulent combustion. Proc Combust Inst 34:1–31
Proch F, Kempf AM (2015) Modeling heat loss effects in the large eddy simulation of a model gas turbine combustor with premixed flamelet generated manifolds. Proc Combust Inst 35:33373345
Ramaekers WJS, van Oijen JA, de Goey LPH (2012) Stratified turbulent bunsen flames: flame surface analysis and flame surface density modelling. Combust Theory Model 16(6):943–975
Seffrin F, Fuest F, Geyer D, Dreizler A (2010) Flow field studies of a new series of turbulent premixed stratified flames. Combust Flame 157:384–396
Shunn L (2009) Large-eddy simulation of combustion systems with convective heat-loss. PhD thesis, Stanford University
Smith GP, Golden DM, Frenklach M, Moriarty NW, Eiteneer B, Goldenberg M, Bowman CT, Hanson RK, Song S, Gardiner WC, Lissianski VV, Qin Z (2017) GRI-Mech 3.0 reaction mechanism. http://www.me.berkeley.edu/gri_mech/
de Swart JAM (2009) Modeling and analysis of flame stretch and preferential diffusion in premixed flames. PhD thesis, Eindhoven University of Technology
de Swart JAM, Groot GRA, van Oijen JA, ten Thije Boonkkamp JHM, de Goey LPH (2006) Detailed analysis of the mass burning rate of stretched flames including preferential diffusion effects. Combust Flame 145:245–258
Trisjono P, Kleinheinz K, Kang S, Pitsch H (2014) Large eddy simulation of stratified and sheared flames of a premixed turbulent stratified flame burner using a flamelet model with heat loss. Flow Turbul Combust 92:201–235
Turanyi T (1994) Parameterization of reaction mechanisms using orthogonal polynomials. Comp Chem 18(1):45–54
Vermorel O, Richard S, Colin O, Angelberger C, Benkenida A, Veynante D (2009) Towards the understanding of cyclic variability in a spark ignited engine using multi-cycle LES. Combust Flame 156:1525–1541
Vicquelin R, Fiorina B, Payet S, Darabiha N, Gicquel O (2011) Coupling tabulated chemistry with compressible cfd solvers. Proc Combust Inst 33:1481–1488
Vreman AW, Albrecht BA, van Oijen JA, de Goey LPH, Bastiaans RJM (2008) Premixed and non-premixed generated manifolds in large-eddy simulation of Sandia flame D and F. Combust Flame 153:394–416
Vreman AW, Bastiaans RJM, Geurts BJ (2009) A similarity subgrid model for premixed turbulent combustion. Flow Turbul Combust 82:233–248
Vreman AW, van Oijen JA, de Goey LPH, Bastiaans RJM (2009) Direct numerical simulation of hydrogen addition in turbulent premixed Bunsen flames using flamelet generated manifold reduction. Int J Hydrogen Energy 34:2778–2788
Vreman AW, van Oijen JA, de Goey LPH, Bastiaans RJM (2009) Subgrid scale modeling in large-eddy simulation of turbulent combustion using premixed flamelet chemistry. Flow Turbul Combust 82:511–535
Weigand P, Meier W, Duan XR, Stricker W, Aigner M (2006) Investigation of swirl flames in a gas turbine model combustor I. flow/field, structures, temperature and species distributions. Combust Flame 144:205–224
Weise S, Messig D, Meyer B, Hasse C (2013) An abstraction layer for efficient memory management of tabulated chemistry and flamelet solutions. Combust Theory Model 17(3):411–430

Chapter 8
Conditional Moment Closure for Turbulent Premixed Flames

Shokri Amzin

Abstract The conditional moment closure (CMC) is a well-established method for the modelling of turbulent non-premixed combustion, but its suitability when applied to turbulent premixed combustion is still a topic of research. Recently, the method has been improved and implemented with encouraging results. The method is used as a closure for the mean reaction rate, which includes the averaged species transport equation. Unlike the flamelet-based methods, its transport equations are derived with no explicit assumptions about the effect of turbulent vortices on the flame front structure. Hence, the CMC is expected to capture the finite-rate chemistry effects and thus predicts species with slow chemical time scales more efficiently. Most importantly, the method would apply to all regimes in turbulent premixed combustion. In this chapter, the method is described comprehensively along with its numerical implementation and some selected results.

Keywords Lean premixed combustion · Conditional moment closure · Dissipation rate · Pollutants

8.1 Introduction

The evolution of control measures towards reducing the impact of combustion on our environment has led to more, yet better, emissions legislation. This stringent legislation is the driving force behind the development of efficient and less polluting combustion systems. Consequently, scientists and engineers have been focusing on the fuel lean premixed combustion because it has the potential to meet efficiency and environmental demands satisfactorily. Lean premixed combustion reduces the combustion temperature and accordingly significantly reduces the level of thermal NOx emissions generated from combustion. However, it is susceptible to combustion oscillations and incurs stability issues associated with pressure fluctuations; both of

S. Amzin (✉)
Department of Mechanical & Marine Engineering, Western Norway University of Applied Sciences, Inndalsveien 28, 5063 Bergen, Norway
e-mail: shokri.amzin@hvl.no

© Springer Nature Singapore Pte Ltd. 2018

S. De et al. (eds.), *Modeling and Simulation of Turbulent Combustion*, Energy, Environment, and Sustainability, https://doi.org/10.1007/978-981-10-7410-3_8

which are undesirable aspects of lean premixed and have an impact on the life and efficiency of combustion systems (Brewster et al. 1999; Correa 1993; Lieuwen et al. 2001; Swaminathan and Bray 2011). Also, its application to practical combustors is restricted by the lean flammability limit. For example, operating very close to the lean flammability limit elevates the level of CO or leads to a flame extinction. In addition to the restrictions above, from a modelling point of view, the interactions between turbulence, chemical reaction, and diffusion are stronger in lean flames, and a suitable numerical model must include their influences. These restrictions make modelling of turbulent lean premixed flames quite challenging, and hence, sophisticated models are required in the design and development of the next generation of low emissions combustion systems.

Based on the CMC hypothesis discussed in Sect. 8.2, the method is capable of capturing the interaction between turbulence and chemical reactions in premixed combustion efficiently. Thus, the method is expected to predict the generated emissions with a reasonable computational cost. However, the successful application of the method is predominately influenced by the accuracy of its sub-models.

Flamelets methods (Bray 2011; Veynante and Vervisch 2002) and transported probability density function (PDF) (OBrien 1980; Pope 1985) are common methods used for simulating turbulent premixed flames. In recent studies (Amzin and Swaminathan 2013; Amzin et al. 2012), the RANS-CMC method has been implemented and used with encouraging results. It was validated using turbulent premixed stoichiometric CH_4-air (Amzin et al. 2012) and turbulent premixed lean CH_4-air flames (Amzin and Swaminathan 2013). The stoichiometric flames are located in the corrugated flamelets and thin reaction zones. While, the lean flames are located in the distributed combustion regime and are thus substantially difficult to model. These two independent studies show that the strength of the CMC method is significantly influenced by the assumptions used to derive its sub-models. Amongst these sub-models, the conditional scalar dissipation rate, the turbulence model, the turbulent transport of conditional fluxes and the differential diffusion effects require further investigation.

The outline of this chapter is as follows. In the next section, the CMC method for premixed combustion is presented. In Sect. 8.3, a brief description of selected test flames are made in conjunction with significant features applicable to this method. The computational details are discussed in Sect. 8.4 followed by the results and a discussion in Sect. 8.5. A concise summary of this chapter is presented in the final section.

8.2 Conditional Moment Closure (CMC) Method

The argument of the CMC method is based on the hypothesis that oscillations of the scalars of interest (such as species mass fractions, temperature and enthalpy) in turbulent flames are related with the oscillation of core scalars (Bilger 1993; Klimenko and Bilger 1999). These fundamental scalars are the mixture fraction, Z, for

turbulent non-premixed combustion and the progress variable, c, for turbulent premixed combustion. The mixture fraction is a nonreactive scalar, which represents the stoichiometry of the reactants and measures the fuel-oxidiser ratio. It is normalised to maintain $Z = 0$ in the oxidiser stream and $Z = 1$ in the fuel stream. The progress variable c, is a reactive scalar, and it can be defined based on temperature or fuel mass fraction (Veynante and Vervisch 2002). It is also possible to define c using the sensible enthalpy (Klimenko and Bilger 1999). When the Lewis number, which is defined as the ratio of the thermal diffusivity to the mass diffusivity of the mixture, is unity then $c_f = c_T$ (Poinsot and Veyante 2005). Here, the progress variable c is used as the conditioning variable and is defined based on the fuel mass fraction as

$$c = Y_f / Y_f^u, \tag{8.1}$$

where Y_f^u denotes the fuel mass fraction in the unburnt side. This choice has been made because the test flame described in Sect. 8.3 has a unity Lewis number based on the deficient reactant. The instantaneous progress variable equation is given by

$$\rho \frac{\partial c}{\partial t} + \rho u_i \frac{\partial c}{\partial x_i} = \frac{\partial}{\partial x_i}\left(\rho \mathscr{D}_c \frac{\partial c}{\partial x_i}\right) + \dot{\omega}_c, \tag{8.2}$$

where the source term, $\dot{\omega}_c$, is the ratio between the instantaneous reaction rate of the fuel and the fuel mass fraction in the unburnt side and is given by

$$\dot{\omega}_c = \dot{\omega}_f / Y_f^u. \tag{8.3}$$

A transport equation for the instantaneous mass fraction of species α in the conventional notation is given by

$$\rho \frac{\partial Y}{\partial t} + \rho u_i \frac{\partial Y}{\partial x_i} = \frac{\partial}{\partial x_i}\left(\rho \mathscr{D}_\alpha \frac{\partial Y}{\partial x_i}\right) + \dot{\omega}_\alpha, \tag{8.4}$$

where $\dot{\omega}_\alpha$ and $\mathscr{D}_\alpha$ are the reaction rate and the molecular diffusivity of species α, respectively.

In the CMC method, the instantaneous mass fraction of species, Y_α, is decomposed into a conditional mean, Q_α, and a conditional fluctuation, y_α'', as

$$Y_\alpha(x,t) = Q_\alpha(c;\mathbf{x},t) + y_\alpha''(\mathbf{x},t), \tag{8.5}$$

where the conditional mean scalar is defined as

$$Q_\alpha(\zeta;\mathbf{x},t) \equiv \langle Y_\alpha(\mathbf{x},t) | c = \zeta(\mathbf{x},t)\rangle. \tag{8.6}$$

The angled brackets in Eq. (8.6) indicate an ensemble averaging subject to the condition $c = \zeta$. Transport equations for the conditional mean scalar values, Q_α, are derived by substituting Eq. (8.5) in Eq. (8.4) (Klimenko and Bilger 1999).

A density weighted conditional averaging is used to derive the CMC transport equation. An alternative derivative using the velocity-scalar joint probability density function (PDF) is also suitable (Klimenko and Bilger 1999). These techniques essentially produce the same transport equation for the conditional mean, Q_α, which is written as (Klimenko and Bilger 1999; Swaminathan and Bilger 2001)

$$\langle\rho|\zeta\rangle\frac{\partial Q_\alpha}{\partial t}+\langle\rho u_i|\zeta\rangle\frac{\partial Q_\alpha}{\partial x_i}-\frac{\mathrm{Le}_c}{\mathrm{Le}_\alpha}\langle\rho N_c|\zeta\rangle\frac{\partial^2 Q_\alpha}{\partial\zeta^2}=\langle\dot{\omega}_\alpha|\zeta\rangle-\langle\dot{\omega}_c|\zeta\rangle\frac{\partial Q_\alpha}{\partial\zeta}-\frac{1}{\widetilde{p}(\zeta)}\frac{\partial}{\partial x_i}\left[\langle\rho u_i'' Y_\alpha''|\zeta\rangle\widetilde{p}(\zeta)\right]+e_{Q_\alpha},\tag{8.7}$$

where Le is the Lewis number of species, α, and $\tilde{p}$ is the Favre PDF of c. The physical meaning of each term in Eq. (8.7) is as follows. The first and second terms denote the unsteady and convective changes of the conditional mean, respectively. The third term represents the diffusion of the conditional mean in the sample space ζ. The fourth term is the conditional mean chemical reaction rate for species α. The fifth term signifies the effect of the conditioning variable, c, (reactive scalar) on the evolution of Q_α. The sixth term represents the influence of the conditional fluctuation, Y_α'', on the evolution of Q_α. The last term, eQ_α, represents contributions of molecular diffusion of Q_α in physical space and the effects of differential diffusion of mass and heat, and it is given by

$$e_{Q_\alpha}\equiv\left\langle\frac{\partial}{\partial x_i}\left(\rho D_\alpha\frac{\partial Q_\alpha}{\partial x_i}\right)\Big|\zeta\right\rangle+\left\langle\rho D_\alpha\frac{\partial\zeta}{\partial x_i}\frac{\partial}{\partial x_i}\left(\frac{\partial Q_\alpha}{\partial\zeta}\right)\Big|\zeta\right\rangle+\left\langle\frac{\partial Q_\alpha}{\partial\zeta}\frac{\partial}{\partial x_i}\left[\left(1-\frac{\mathrm{Le}_\alpha}{\mathrm{Le}_c}\right)\rho D_\alpha\frac{\partial\zeta}{\partial x_i}\right]\Big|\zeta\right\rangle.\tag{8.8}$$

The molecular diffusion is negligible for high Reynolds number flows and the differential diffusion remains as the dominant term (Swaminathan and Bilger 2001) and is modelled as

$$e_{Q_\alpha}\approx\frac{1}{\tilde{p}(\zeta)}\left(1-\frac{\mathrm{Le}_\alpha}{\mathrm{Le}_c}\right)\frac{\partial Q_\alpha}{\partial\zeta}\frac{\partial N_c\tilde{p}}{\partial\zeta}.\tag{8.9}$$

eQ_α becomes zero when $Le_\alpha/Le_c=1$ signifying that there is no differential diffusion of mass and heat.

The quantities $\langle\rho u_i'' Y_\alpha''|\zeta\rangle$, $\widetilde{p}$, $\langle\rho u_i|\zeta\rangle$, $\langle\dot{\omega}_\alpha|\zeta\rangle$, $\langle\dot{\omega}_c|\zeta\rangle$ and $\langle N_c|\zeta\rangle$ require suitable models along with appropriate initial and boundary conditions to solve Eq. (8.7). The turbulent flux term is modelled using the gradient transport hypothesis as

$$\langle u_i'' Y_\alpha''|\zeta\rangle=-\frac{\mu_t}{Sc_\alpha}\frac{\partial Q_\alpha}{\partial x_i},\tag{8.10}$$

where Sc_α is the turbulent Schmidt number for species α and μ_t is turbulent viscosity. It is also possible for this conditional flux to be a counter-gradient

(Richardson et al. 2007). For high Reynolds number flows, the gradient flux model is adequate. This justification was judged from the computational results in Sect. 8.5. However, it is worthwhile to test the method with a counter-gradient assumption.

In turbulent combustion, the coupling between turbulence and chemical reaction is strong. This interaction creates a complex fluid structure, which makes simulating such complex flow fields accurately a challenging task. For years, modelling of turbulent fluctuations in RANS context has been an active research area. Accordingly, a considerable number of turbulence models are proposed and are available in the literature with diverse degrees of complexity. Often, these models are applicable only to particular kinds of flow (Jeffrey et al. 2001). Thus, it is desirable for turbulence models to be able to predict the boundary layers and the free shear flows simultaneously.

One common choice to close the turbulent dynamic viscosity, μ_t, which appears in the Boussinesq approximation for the stress tensors introduced by the Reynolds averaging Eq. (8.10), is the standard turbulence $k-\epsilon$ model. The model links the turbulent viscosity, μ_t, to the mean turbulent kinetic, $\widetilde{k}$, and dissipation rate, $\widetilde{\epsilon}$. This model is numerically stable and it converges relatively quickly. It can be used with large geometries and thus, is an attractive choice for engineering applications. The standard $k-\epsilon$ model is suitable for high Reynolds number and free shear flows. It predicts quite accurately the velocity fields of plan jets (Jeffrey et al. 2001). However, its prediction of flows near wall boundary or axisymmetric round jets is inaccurate where the spreading rate is commonly overestimated. This overprediction can be slightly improved by modifying the constants in $k-\epsilon$ transport equations. The turbulent dynamic viscosity, μ_t, is given as follows:

$$\mu_t = \overline{\rho} C_\mu((\widetilde{k^2}/\widetilde{\epsilon}). \tag{8.11}$$

Two transport equations for the mean $\widetilde{k}$ and $\widetilde{\epsilon}$ are solved and written as

$$\frac{\partial}{\partial t}(\overline{\rho}\widetilde{k}) + \frac{\partial}{\partial x_i}(\overline{\rho}\widetilde{u_i k}) = \frac{\partial}{\partial x_i}\left[\left(\mu + \frac{\mu_t}{\sigma_k}\right)\frac{\partial \widetilde{k}}{\partial x_i}\right] + \overline{\rho}\tau_{ij}\frac{\partial \widetilde{u}_j}{\partial x_i} - \overline{\rho}\widetilde{\epsilon}, \tag{8.12}$$

and

$$\frac{\partial}{\partial t}(\overline{\rho}\widetilde{\epsilon}) + \frac{\partial}{\partial x_i}(\overline{\rho}\widetilde{u_i \epsilon}) = \frac{\partial}{\partial x_i}\left[\left(\mu + \frac{\mu_t}{\sigma_\epsilon}\right)\frac{\partial \widetilde{\epsilon}}{\partial x_i}\right] + C_{\epsilon_1}\frac{\widetilde{\epsilon}}{k}\overline{\rho}\tau_{ij}\frac{\partial \widetilde{u}_j}{\partial x_i} - C_{\epsilon_2}\overline{\rho}\frac{\epsilon^2}{\widetilde{k}}. \tag{8.13}$$

The standards model constants are $C_\mu = 0.09$, $\sigma_k = 1.0$, $\sigma_\epsilon = 1.30$, $C_{\epsilon_1} = 1.44$, and $C_{\epsilon_2} = 1.92$. In the modified $k-\epsilon$ model, the closure coefficient $C_{\epsilon 1} = 1.44$ is modified to 1.6 to justify the round jet anomaly (Pope 1978). The PDF of the progress variable is modelled using a presumed shape with a beta function as follows,

$$\widetilde{p}(\zeta) = C\,\zeta^{a-1}\,(1-\zeta)^{b-1}, \tag{8.14}$$

where,

$$C = \frac{1}{\beta(a,b)}, \quad a = \tilde{c}\left(\frac{1-g}{g}\right), \quad b = (1-\tilde{c})\left(\frac{1-g}{g}\right), \tag{8.15}$$

the variance parameter is $g = \widetilde{c''^2}/\tilde{c}(1-\tilde{c})$ and $\beta(a,b) = \int_0^1 \zeta^{a-1}\,(1-\zeta)^{b-1}\,d\zeta$.

The CMC hypothesis states that the fluctuations of conditional reactive scalars and temperature over the mean are smaller when compared with the unconditional ones. Therefore, the conditional mean reaction rate has the functional dependence on the conditional mean as the instantaneous reaction rate has on the instantaneous scalar values. Hence, the conditional mean reaction rate, $\langle\dot{\omega}_\alpha|\zeta\rangle$, for species α in Eq. (8.7) is closed using a first-order CMC closure (Klimenko and Bilger 1999).

$$\langle\dot{\omega}_\alpha(\rho, Y_\alpha, T)|\zeta\rangle = \dot{\omega}_\alpha(\langle\rho|\zeta\rangle, \mathbf{Q}_\alpha, Q_T), \tag{8.16}$$

where Q_T is the conditional temperature and $\langle\rho|\zeta\rangle$ is the conditional density. A closure for $\langle\dot{\omega}_c|\zeta\rangle$ can be obtained based on the definition of c. In this study, c is defined based on the fuel mixture fraction, thus $\langle\dot{\omega}_c|\zeta\rangle$ is given by

$$\langle\dot{\omega}_c|\zeta\rangle = \frac{\langle\dot{\omega}_f|\zeta\rangle}{Y_f^u}. \tag{8.17}$$

The conditional mean scalar dissipation rate, $\langle N_c|\zeta\rangle$, is a key term in CMC method linked to the unconditional mean scalar dissipation rate, $\overline{\rho}\,\widetilde{\epsilon}_c = \overline{\rho\mathscr{D}_c(\partial c''/\partial x_i)(\partial c''/\partial x_i)}$, through

$$\widetilde{\epsilon}_c = \int_0^1 \langle N_c|\zeta\rangle\,\widetilde{p}\,d\zeta. \tag{8.18}$$

In premixed flames, the scalar gradients are produced predominately by chemical reactions. Also, it is observed that the turbulent stretch influences the local reaction rates. Thus, the local scalar gradients will also be influenced by the stretch rate. The local flame front can be considered as an ensemble of strained laminar flamelets, so the conditional dissipation rate can be written as (Kolla and Swaminathan 2010)

$$\langle N_c|\zeta\rangle = \int_0^1 N_c(\zeta, a)\,p(a)da, \tag{8.19}$$

where $N_c(\zeta, a)$ is the scalar dissipation rate in the flamelet subject to a strain rate a. The strain rate predominantly influences the gradient of c in the inner reaction zone, ζ^* (Libby and Williams 1982). This zone corresponds to the location of the peak heat release rate when fuel molecules are attacked by a hydrogen atom. Hence, $N_c(\zeta, a)$ can be written as (Kolla and Swaminathan 2010)

$$N_c(\zeta; a) = N_c(\zeta^*; a)\,f(\zeta), \tag{8.20}$$

where ζ^* is the location of inner reaction zone in ζ space and f is nearly a single curve which can be obtained using an unstrained laminar flame (Kolla and Swaminathan 2010). This approximation is examined by Kolla and Swaminathan (2010) using three laminar premixed flames: lean and stoichiometric methane–air flames, and a lean propane air flame for different values of a. Using this approximation in Eqs. (8.19) and (8.18), one obtains

$$\widetilde{\epsilon}_c = \int_0^1 \langle N_c|\zeta^*\rangle\, f(\zeta)\tilde{p}(\zeta)d\zeta, \tag{8.21}$$

and

$$\langle N_c|\zeta\rangle = \frac{\widetilde{\epsilon}_c\, f(\zeta)}{\int_0^1 f(c)\,\widetilde{p}(c)\,\mathrm{d}c}. \tag{8.22}$$

This approach maintains the consistency between the conditional and unconditional mean dissipation rate while maintaining the strong coupling of reaction and diffusion in a premixed flame front. This strong coupling has been recognised in earlier studies using the transported PDF approach (Mura et al. 2003; Pope and Anand 1987).

The Favre mean scalar dissipation rate, $\widetilde{\epsilon}_c$, is modelled using a simple algebraic model developed in Kolla et al. (2009) and it is given by

$$\widetilde{\epsilon}_c = \frac{1}{\beta'}\left[\left(2K_c^* - \tau C_4\right)\frac{S_L^0}{\delta_L^0} + C_3\frac{\tilde{\epsilon}}{\tilde{k}}\right]\widetilde{c''^2}, \tag{8.23}$$

where $\beta' = 6.7$, $K_c^* = 0.85\tau$ for hydrocarbon–air flames, $C_4 = 1.1/(1 + \mathrm{Ka})^{0.4}$ and $C_3 = 1.5$. The Karlovitz number is $\mathrm{Ka} = (\delta/\eta_k)^2$, where η_k is the Kolmogorov length scale and δ is the Zeldovich thickness. The unstrained laminar flame speed is S_L^o and its thermal thickness is δ_L^o. The heat release parameter is $\tau = (T_b - T_u)/T_u$ (with the subscripts b and u respectively denote burnt and unburnt mixtures). The Favre-averaged turbulent kinetic energy and its dissipation rate are denoted by $\widetilde{k}$ and $\widetilde{\epsilon}$ respectively. Other models for the mean scalar dissipation available in the literature are reviewed by Chakraborty et al. (2011) and the model in Eq. (8.23) is chosen for this study because it is systematically obtained using the transport equation for $\widetilde{\epsilon}_c$. The models in Eqs. (8.22) and (8.23) can be used for flamelets and distributed combustion regimes as long as the local Damköhler number is high.

The conditional mean velocity $\langle u_i|\zeta\rangle$ can be closed by using either a linear (Klimenko and Bilger 1999) or gradient (Colucci et al. 1998) models. A detailed assessment of both models using DNS data showed (Swaminathan and Bilger 2001) that they were equally realistic for turbulent premixed flames. Thus, the linear model is chosen to close the conditional mean velocity Eq. (8.7). This model is given by

$$\langle u_i|\zeta\rangle = \tilde{u}_i + \frac{\widetilde{u_i'' c''}}{\widetilde{c''^2}}(\zeta - \tilde{c}), \tag{8.24}$$

where $\tilde{u}_i$ is the unconditional mean velocity, $\widetilde{u_i'' c''}$ is the correlation between the velocity and progress variable fluctuations, and $\widetilde{c''^2}$ is the variance of the progress variable fluctuations. Equation (8.24) indicates that the selected model for the turbulent scalar flux has an effect on the conditional mean velocity.

The conditional density is obtained using the state equation and the conditional temperature, Q_T, as

$$P = RQ_T \langle \rho | \zeta \rangle, \tag{8.25}$$

where R is the gas constant.

The CMC transport equations are to be solved with appropriate initial and boundary conditions. The Favre average quantities are then obtained using

$$\widetilde{Y}_\alpha = \int_0^1 Q_\alpha \, \widetilde{p}(\zeta) \; d\zeta. \tag{8.26}$$

An arbitrarily complex chemistry can be used in the CMC equation to obtain $\langle \dot{\omega}_\alpha | \zeta \rangle$ and $\langle \dot{\omega}_c | \zeta \rangle$ (Eq. (8.7)). The various unclosed terms noted above are common for both the CMC and transported PDF approaches. However, in the transported PDF approach, the reaction rate appears in a closed form and thus no modelling is required for it. The conditional dissipation rate and velocities need modelling in both approaches.

8.3 Selected Experimental Measurements

The selected test flames are the piloted lean premixed flames of Dunn et al. (2007). These flames are shown schematically in Fig. 8.1 along with the computational domain and the specified boundary conditions Fig. 8.2. The burner consists of three streams surrounded by ambient air. The fuel jet has an inner diameter of 4 mm and it contains a lean premixed methane–air mixture with an equivalence ratio, ϕ, of 0.5 with an initial temperature of 300 K. A pilot encircles the fuel jet and it contains a hot product of a stoichiometric premixed methane–air with an average temperature of 2280 K with an inner diameter of 23.5 mm. A third stream encircles the pilot stream and it contains a lean premixed laminar H_2-air flame with ϕ of 0.43 and has an inner diameter of 197 mm. The pilot and the hot co-flow streams flow with uniform low velocities of 0.8 and 0.7 m/s, respectively (Dunn et al. 2007). A uniform velocity of 0.2 m/s is specified to account for ambient air entrainment.

Four flames are designated as PM1-50, PM1-100, PM1-150 and PM1-200 which were studied experimentally with an axial fuel jet mean velocities, U_0, at the exit of the fuel nozzle of 50, 100, 150 and 200 m/s, respectively. These flames have a Reynolds number of 12,500, 25,000, 37,000 and 50,000, respectively. The PM1-50 and PM1-200 flames, which have the lowest and highest Reynolds numbers, respectively are selected in this study. The physical and chemical features of these streams are shown in Table 8.1.

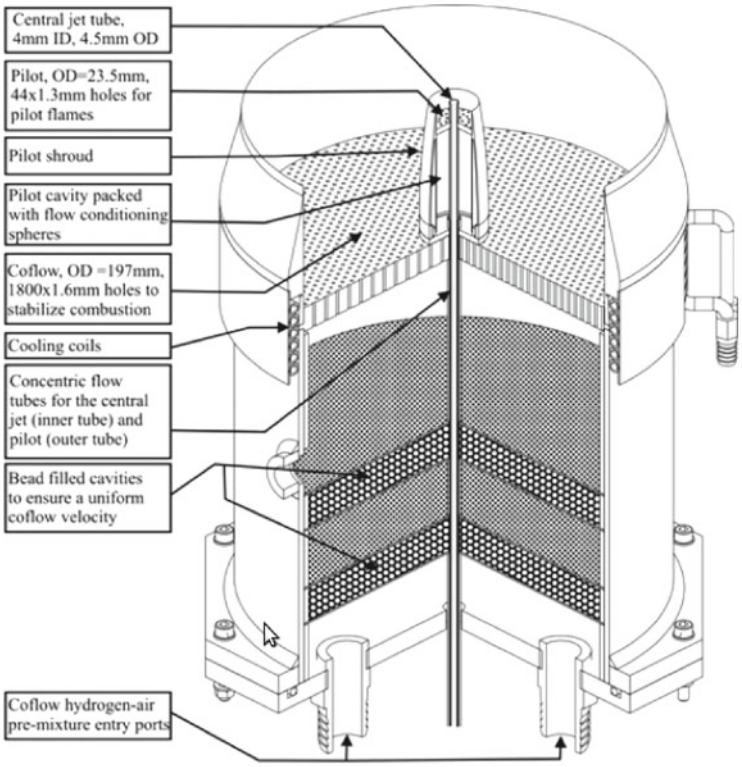

Fig. 8.1 Schematic diagram of the premixed Bunsen burner from (Dunn et al. 2007)

The turbulence conditions of these flames are measured using a Laser Doppler Velocimetry (Dunn et al. 2010) at axial and radial locations of $x/D = 15$ and $r/D = 0.53$, respectively. The conditions of these lean flames are located in the distributed combustion regime as shown in the turbulent combustion regime diagram Fig. 8.3. In this regime, the characteristic chemical length and time scales of the flame are larger than the turbulence length and time scales, and hence turbulent eddies are expected to penetrate the reaction zones causing local extinction.

The values of Λ/δ for the flames PM1-50 and PM1-200 are 2.4 and 1.8, respectively with corresponding values of u'' which are 15 and 54 as reported by Dunn et al. (2007). The laminar flame speed is $S_L^o = 0.051$ m/s. These values yield significantly smaller than unity Damköhler numbers, i.e. 0.05. Accordingly, the finite-rate chemistry effects are likely to be stronger in the lean flames. Thus, using the flamelet-based method proves to be incompatible. These flames have been used in earlier studies to validate premixed turbulent combustion models such as a transported PDF model (Dunn et al. 2009; Rowinski and Pope 2011) and large eddy simulation (Duwig et al. 2011).

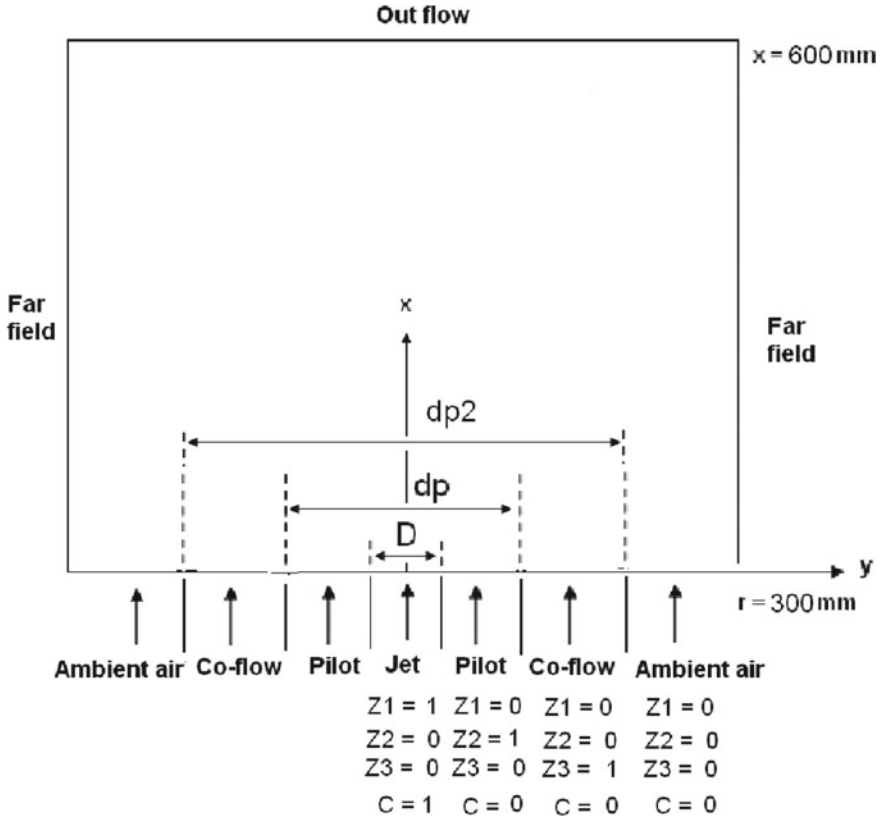

Fig. 8.2 Schematic diagram of the burner set-up and the computational domain accompanying with boundary conditions (Amzin and Swaminathan 2013)

Table 8.1 The properties of the streams of the flames PM1-50 and PM1-200

Stream	D (mm)	U_0 (m/s)	T(K)	ϕ	Mixture
Jet	4	50, 200	300	0.5	CH_4 – air (reactant)
Pilot	23.5	0.8	2280	0.5	CH_4 – air (products)
Co-flow	197	0.7	1500	0.43	H_2 – air (products)

On the other hand, the CMC transport equations Eq. (8.7) are derived without any explicit assumptions on the influence of turbulent eddies on the flame front structure. Hence, the CMC is expected to capture the finite-rate chemistry effects and thus predicts species with slow chemical time scales. Based on this argument, the CMC method would be applicable to all regimes in turbulent premixed combustion. However, the useful application of the method is predominately influenced by the assumptions used to derive its sub-models. The computational capability of the RANS-CMC

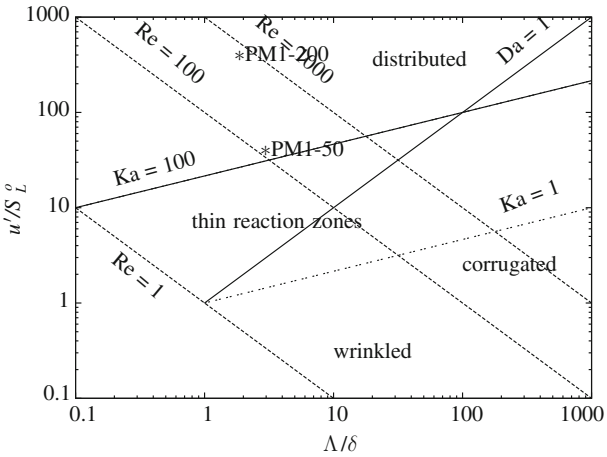

Fig. 8.3 The premixed combustion regime diagram showing PM1-200 and PM1-50 flames (Amzin and Swaminathan 2013)

was explored in recent studies by Amzin et al. in two different regimes, namely thin reaction (Amzin et al. 2012) and disturbed (Amzin and Swaminathan 2013). Its prediction was observed to be consistent with those results using other combustion modelling methods such as flamelets and joint scalar PDFs. Nevertheless, the reported results were observed to show discrepancies when compared with the experimental data. As recommended by Amzin et al., several issues should be investigated in future studies, among them are turbulence models.

8.4 RANS-CMC Approach

The RANS-CMC computer code, Fig. 8.4 is used in this study solves transport equations for the Favre-averaged mass, momentum, turbulence, total enthalpy, along with transport equations for the progress variable, $\tilde{c}$, with its variance, $\widetilde{c''^2}$, and the mixture fraction, $\tilde{Z}$. These equations are solved on the RANS physical domain and are integrated with a CMC solver which computes the conditional averaged quantities, Q_α and Q_T, Eq. (8.7) in ζ space as shown in the schematic diagram Fig. 8.4. This computational tool has been validated in earlier studies for turbulent premixed (Amzin and Swaminathan 2013; Amzin et al. 2012) and non-premixed flames (Rogerson et al. 2007). The implementations of these equations and their sub-models are discussed comprehensively in Amzin et al. (2012) and Amzin and Swaminathan (2013).

Transport equations for the progress variable and its variance are written as

$$\frac{\partial(\overline{\rho}\widetilde{c})}{\partial t} + \frac{\partial(\overline{\rho}\widetilde{u_i}\widetilde{c})}{\partial x_i} = \frac{\partial}{\partial x_i}\left(\overline{\rho D_c \frac{\partial c}{\partial x_i}} - \overline{\rho u_i'' c''}\right) + \overline{\dot{\omega}}_c, \tag{8.27}$$

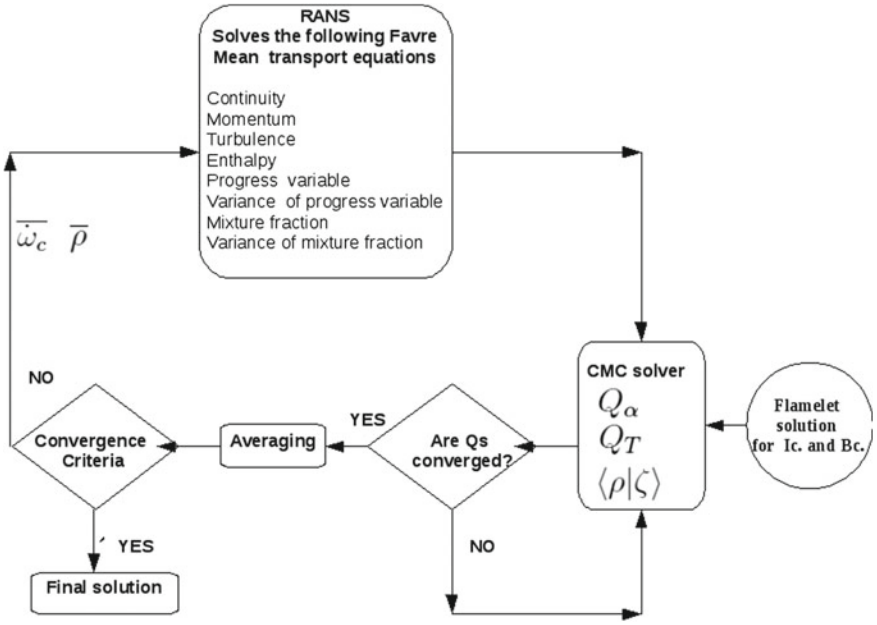

Fig. 8.4 The computational sequence in the RANS-CMC program (Amzin and Swaminathan 2013)

and

$$\frac{\partial(\overline{\rho}\widetilde{c''^2})}{\partial t}+\frac{\partial(\overline{\rho}\widetilde{u}_i\widetilde{c''^2})}{\partial x_i}=\frac{\partial}{\partial x_i}\left(\overline{\rho D_c\frac{\partial c''^2}{\partial x_i}}-\overline{\rho u_i'' c''^2}\right)-2\overline{\rho u_i'' c''}\frac{\partial\tilde{c}}{\partial x_i}-2\overline{\rho}\tilde{\epsilon}_c+2\overline{c''\dot{\omega}_c}. \tag{8.28}$$

The mean density, $\overline{\rho}$, and the source terms $\overline{\dot{\omega}}_c$, and $\overline{c''\dot{\omega}_c}$ are modelled in a manner consistent with CMC method as

$$\overline{\rho}=\int_0^1\langle\overline{\rho}|\zeta\rangle\, p(\zeta,x)\, d(\zeta), \tag{8.29}$$

$$\overline{\dot{\omega}}_c=\int_0^1\langle\dot{\omega}_c|\zeta\rangle\, p(\zeta,x)\, d(\zeta), \tag{8.30}$$

$$\overline{c''\dot{\omega}_c}=\int\zeta\langle\dot{\omega}_c|\zeta\rangle\, p\, d\zeta-\tilde{c}\int\langle\dot{\omega}_c|\zeta\rangle\, p\, d\zeta. \tag{8.31}$$

It is of significance that, the progress variable, $\tilde{c}$, is defined based on the fuel mass fraction Eq. (8.1) and thus is quantified to be *one* in the fuel stream and *zero* in the other streams.

It should be noted that the three streams have different composition and equivalence ratios as given in Table 8.1, and thus more than one passive scalar (fluid marker variable) is required to account for the mixing of these streams. Thus, three transport equations for $\widetilde{Z}_1, \widetilde{Z}_2$ and $\widetilde{Z}_3$ are included in the simulation. Their values are set to be unity at the inlet of these streams as shown in Fig. 8.2. These equations are solved in the physical space and the general form is written as

$$\frac{\partial(\overline{\rho}\widetilde{Z}_k)}{\partial t} + \frac{\partial(\overline{\rho}\widetilde{u}_i\widetilde{Z}_k)}{\partial x_i} = \frac{\partial}{\partial x_i}\left(\overline{\rho D_{Z_k}\frac{\partial Z_k}{\partial x_i}} - \overline{\rho u_i'' Z_k''}\right). \tag{8.32}$$

and

$$\frac{\partial(\overline{\rho}\widetilde{Z_k''^2})}{\partial t} + \frac{\partial(\overline{\rho}\widetilde{u}_i\widetilde{Z_k''^2})}{\partial x_i} = \frac{\partial}{\partial x_i}\left(\overline{\rho D_{Z_k}\frac{\partial Z_k''^2}{\partial x_i}} - \overline{\rho u_i'' Z_k''^2}\right) - 2\overline{\rho u_i'' Z_k''}\frac{\partial \tilde{Z}_k}{\partial x_i} - 2\overline{\rho}\tilde{\epsilon}_{Z_k}. \tag{8.33}$$

The dissipation rate, $\widetilde{\epsilon_c}$, in Eqs. (8.28) and (8.33) is modelled using Eq. (8.23). The mixture fraction transport equations serve as a marker to track the fluids emerging from the hot pilot, hot co-flow streams and to account for the effects of mixing of these streams with the main jet and with the entrained air. These markers are used in the following manner to obtain the average temperature $\widetilde{T}$. The total enthalpy computed using its transport equation at a given grid point in the physical space is written as

$$\widetilde{h} = h^s + \Delta h^o_{f,\mathrm{mix}}, \tag{8.34}$$

$$= \sum_\alpha \left[\widetilde{Z}_1\widetilde{Y_\alpha} + \widetilde{Z}_2\widetilde{Y_{\alpha,2}} + \widetilde{Z}_3\widetilde{Y_{\alpha,3}} + \left(1 - \widetilde{Z}_1 - \widetilde{Z}_2 - \widetilde{Z}_3\right)\widetilde{Y_{\alpha,air}}\right] c_{p_i}(\widetilde{T} - T_0) + \sum_\alpha \left(\widetilde{Z}_1\widetilde{Y_\alpha} + \widetilde{Z}_2\widetilde{Y_{\alpha,2}} + \widetilde{Z}_3\widetilde{Y_{\alpha,3}}\right)\Delta h^o_{f_\alpha}, \tag{8.35}$$

where $\widetilde{Y_\alpha}$ is the mass fraction of species α at the grid point. $\widetilde{Y_{\alpha,2}}$ and $\widetilde{Y_{\alpha,3}}$ are the mass fractions of species α in the streams 2 and 3 at the inlet. $\Delta h^o_{f_\alpha}$ is the enthalpy of formation for species α and the enthalpy of formation for air is taken to be zero. From the above equation, one can easily verify that the temperature of the incoming streams is recovered by using the boundary values for $\widetilde{Z}_1, \widetilde{Z}_2$ and $\widetilde{Z}_3$ marked in Fig. 8.2.

The initial mean velocity at the inlet is specified as a profile given by

$$u(r)/U_0 = (1 - \frac{r}{R})^{1/7}, \tag{8.36}$$

where R is the radius of the main jet port. Low uniform velocities of 0.8 and 0.7 m/s are specified at the inlet of the pilot and co-flow streams, respectively. A low uniform velocity of 0.2 m/s is assumed to account for the ambient air entrainment.

The turbulence is modelled using the standard and the modified $k - \epsilon$ turbulence model. The initial value of the variance of the progress variable in all the streams entering the computational domain is set to be zero. A uniform value for the mean turbulent kinetic energy, $\widetilde{k}_o$, at the centre line of the fuel nozzle exit, is obtained from $I = u'/U_0 = \sqrt{2k/3}/U_0$. The axial rms velocity, u', for the cold and reacting flows for both selected flames is reported in the experiment (Dunn et al. 2007). The initial value for dissipation rate, $\widetilde{\epsilon}_o$, at the centre line of the fuel nozzle exit, is obtained using $\widetilde{\epsilon}_o = C_u \widetilde{k}_o^{3/2}/\Lambda$.

Previous investigations (Amzin and Swaminathan 2013; Amzin et al. 2012; Swaminathan and Bilger 2001) recommend that the influence of eQ_α is comparatively insignificant compared with the contributions from other terms in Eq. (8.7) and hence this term is neglected in this study. A thorough sensitivity analysis of eQ_α is described in Amzin et al. (2012), Amzin and Swaminathan (2013) and Swaminathan and Bilger (2001).

The stationary CMC equations are discretised by finite volume methodology using the power law scheme of Patankar (1980) for spatial derivatives. A simpler approach (Patankar 1980) is used to couple the velocity and pressure fields inside the computational domain. The power law scheme is used to discretise the physical and ζ space derivatives in the CMC equation Eq. (8.7). These discretised equations are solved using an iterative algorithm to obtain the conditional mean quantities, eQ_α. The mean density, $\overline{\rho}$, $\overline{\dot{\omega}}_c$, and $\overline{c''\dot{\omega}_c}$ are calculated using their conditional means computed in the CMC solver Eqs. (8.29), (8.30) and (8.31) and are fed back to the fluid dynamics solver. The mean flow and turbulence quantities computed in this solver are passed to the CMC solver. This inter-exchange process iterates until convergence criteria are satisfied for all quantities of interest as shown in Fig. 8.4.

A computational domain spans 600 mm in the axial direction, x, and 300 mm in the radial direction, r. The RANS physical computational domain has 150×100×100 cells in y, z, and x directions. The grid is refined near the fuel and the pilot exit with the smallest cell size of 1×1.6 mm.

The conditional averages vary slowly in the physical space and hence, two cells in each physical direction of the RANS domain are combined to create the physical space grid for the CMC equations. The sensitivity of the CMC method to the grid refinement is tested and these provided solutions with negligible sensitivity to any further changes in the physical or CMC grids. The CMC computational domain in ζ space has 500 nonuniform cells.

The conditional mean reaction rate term is closed using a first-order CMC closure in conjunction with the GRI-3.0 (Smith et al. 2011) chemical mechanism to represent the chemical kinetics of methane–air mixture. The initial and boundary conditions for the CMC equations in ζ space are specified using planar unstrained laminar flame solution obtained from the Premix code of Chemkin (1985).

8.5 Results and Discussion

The computed mean axial velocity from the nonreacting and reacting flows is compared with the experimental measurements to assess the boundary conditions and the $k - \epsilon$ turbulence model. These results are shown in Figs. 8.5 and 8.6 for the flames PM1-200 and flames PM1-50, respectively. The mean values are normalised using the bulk mean velocity, U_0, at the jet exit. The letters N and R in Figs. 8.5 and 8.6 denote the nonreacting and reacting flow fields, respectively. The agreement shown for the mean axial velocity suggests that the spread rate of the jet is well captured in the simulations and the boundary conditions used are representative of the experimental conditions.

To ensure a complete convergence and minimal computational errors, the terms in the CMC transport equations Eq. (8.7) are also examined. The balance of the steady CMC transport equation can be simply stated as

$$\text{Conv.} - \text{Diff.} - \text{reac.} + \text{reac}_c. - \text{e}_{Q_\alpha} = \text{Imb.} \tag{8.37}$$

The results are shown for some selected representative species from the flame PM1-200 at $\tilde{c} = 0.55$ and $x/D = 4.5$. These values do not include the algebraic sign in Eq. (8.37) thus, a positive value indicates a source and a negative value indicates a sink. The selected species are produced by the chemical reactions in methane–air flames, implies that the term 'reac.' is positive. The reactive nature of the conditioning variable makes a sink contribution to these scalars through the term 'reac_c'.

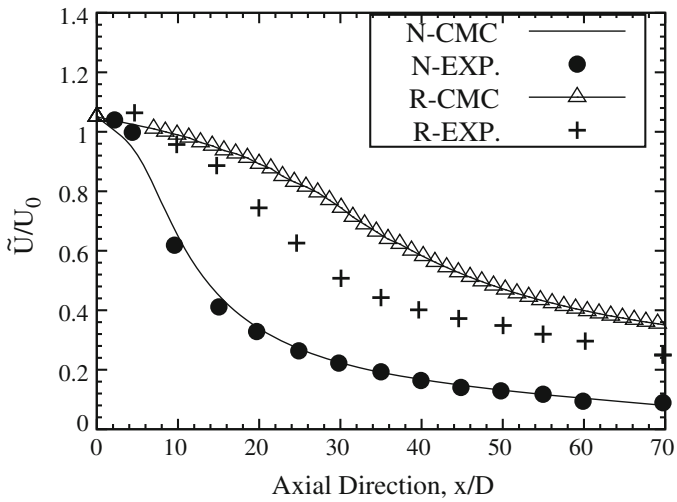

Fig. 8.5 The calculated (lines) normalised mean axial velocity from nonreacting and reacting flows are compared with experimental data (symbols) for the flame PM1-200 (Amzin and Swaminathan 2013)

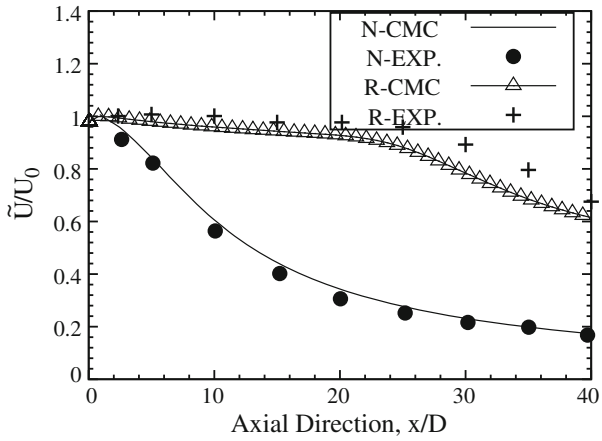

Fig. 8.6 The calculated (lines) normalised mean axial velocity from nonreacting and reacting flows are compared with experimental data (symbols) for the flame PM1-50 (Amzin and Swaminathan 2013)

Also as observed in Fig. 8.7, there is a predominant balance between the convective and the diffusive terms. The reaction rate of species α is balanced by the 'reac$_c$' and e_{Q_α} terms in the reactive zone. The magnitude of e_{Q_α} is dictated by $\partial Q_\alpha/\partial\zeta$ and the value of Lewis number for species α, see Eq. (8.9). However, if Le$_\alpha$ is close to unity then one observes that $e_{Q_\alpha} = 0$, unless $\partial Q_\alpha/\partial\zeta$ is singular. The Lewis number for the conditioning variable is unity. The negligible value of e_{Q_α} is noted in Fig. 8.7 for CO, since Le$_{CO} = 1.084$. The contribution of e_{Q_α} for H_2O is smaller than the reactive terms, but it is nonnegligible because Le$_{H_2O} = 0.78$. However, for atomic and molecular hydrogen, the contribution of e_{Q_α} is as big as the reactive term in Eq. (8.37) since the Lewis number for these species are small (Le$_H = 0.172$, Le$_{H_2} = 0.293$). Finally, the numerical error represented by the 'imb.' in Eq. (8.37) is observed to be very close to zero in Fig. 8.7 indicating that the equations are solved with very small numerical errors.

The variation of the conditional mean mass fractions, Q_α with the sample space, ζ shown in Fig. 8.8 is obtained by solving the CMC equation, Eq. (8.7). The results are shown for $\tilde{\theta} = 0.55$ and at axial location $x/D = 4.5$, where $\zeta = 0$ is the product side and $\zeta = 1$ is the reactant side. It should be noted that the values of H_2 and OH are multiplied by 40 and 20, respectively. The unstrained laminar premixed flame is computed using Chemkin-II package (Kee et al. 1985) along with GRI-mechanism (Smith et al. 2011). The computed conditional averages of major species obtained by the CMC are in good agreement with those obtained by the unstrained laminar flame. The same agreement applies for the minor species except for H_2. The computed conditional mean H_2 shows a peak near $\zeta = 0.4$ while, the laminar varies slowly with sharp drops near $\zeta = 0$ and $\zeta = 1$. Similar behaviour is observed at other axial locations.

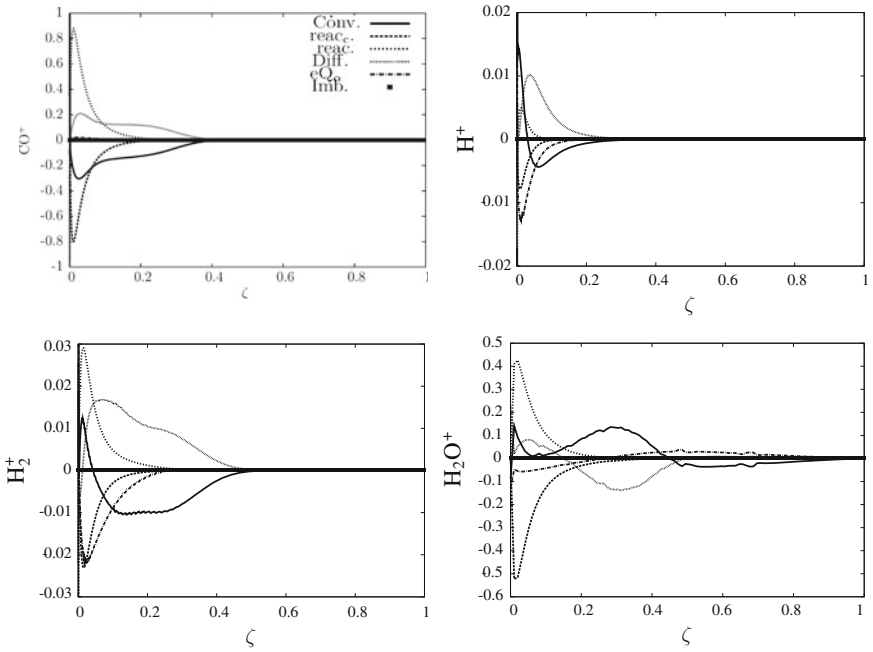

Fig. 8.7 Typical variation of different terms in the CMC transport equation, Eq. (8.37), with ζ in the flame PM1-200 at $\tilde{c} = 0.55$. The results are shown for four representative scalars (Amzin and Swaminathan 2013)

The typical variation of the $\langle N_\theta | \zeta \rangle$ for the flames PM1-200 and PM1-50 is shown in Fig. 8.9 at $\tilde{\theta} = 0.55$ and axial location $x/D = 4.5$. As mentioned earlier, the flame PM1-200 has a higher axial velocity and Reynolds number; thus, a higher variation of $\langle N_\theta | \zeta \rangle$ is expected. The chemical reactions are expected to be strong near $\zeta \approx 0.8$ for hydrocarbon flames because of the large activation energy and so $\langle N_\theta | \zeta \rangle$ peaks around this ζ value as shown in Fig. 8.9.

The marginal PDF of the progress variable, obtained using the presumed Beta function for the given Favre mean and variance, is shown in Fig. 8.10 for the flame PM1-200. The Favre mean, $\widetilde{\theta}$, and variance, $\widetilde{\theta''^2}$, are obtained from their implemented transport equations. These PDFs are shown for seven different radial locations, denoted by $\widetilde{\theta}$, at a given axial location $x/D = 4.5$. In such a combustion regime, the flames are expected to have mono-modal shape. A similar variation is observed for the flame PM1-50.

The computed radial variation of the mean mass fractions of CO is shown in Figs. 8.11 and 8.12 for the flames PM1-50 and PM1-200, receptively. It should be noted that these values are multiplied by 10^3 for plotting purpose. Despite some discrepancies, the general agreement is observed to be consistent with the experimental measurements close to the fuel exit for both flames and the trend is well captured. For the PM1-200 flame, the peak value of Y_{CO} at axial location $x/D = 2.5$ is located

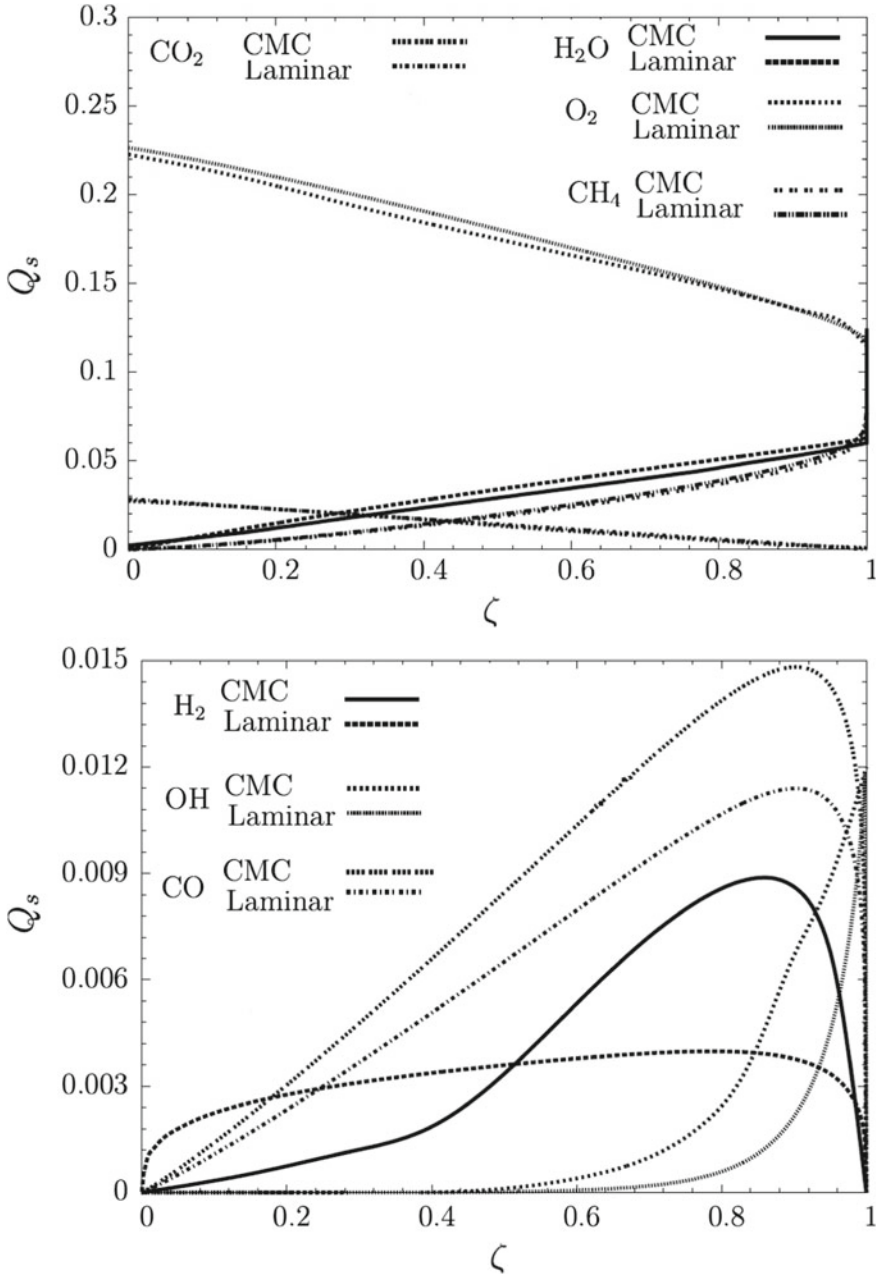

Fig. 8.8 The variation of the conditional mean mass fraction with ζ for major and minor species for the flame PM1-200 at $\tilde{\theta} = 0.55$ and $x/D = 4.5$ (Amzin and Swaminathan 2013)

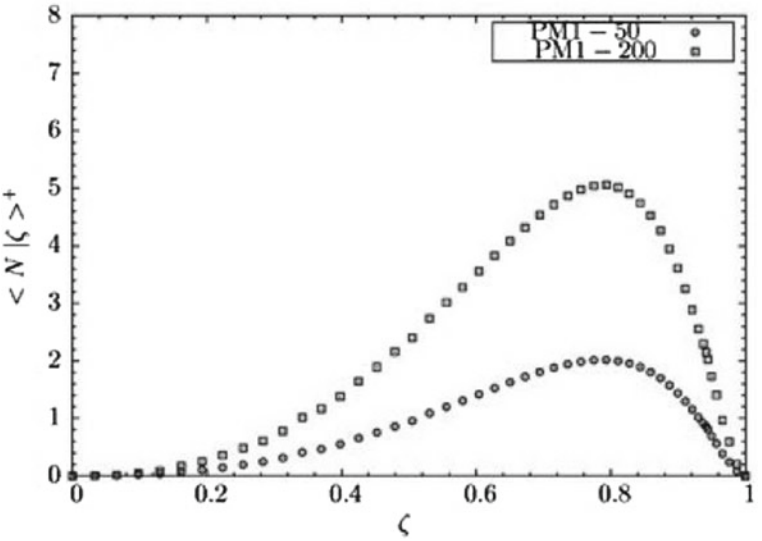

Fig. 8.9 The variation of the conditional scalar dissipation rate,$\langle N_\theta^+|\zeta\rangle$, obtained in the CMC calculation for the flame PM1-50 and PM1-200 at $\tilde{\theta} = 0.55$, $x/D = 4.5$. The values are nondimensionalised using S_L^o and δ_L^o (Amzin and Swaminathan 2013)

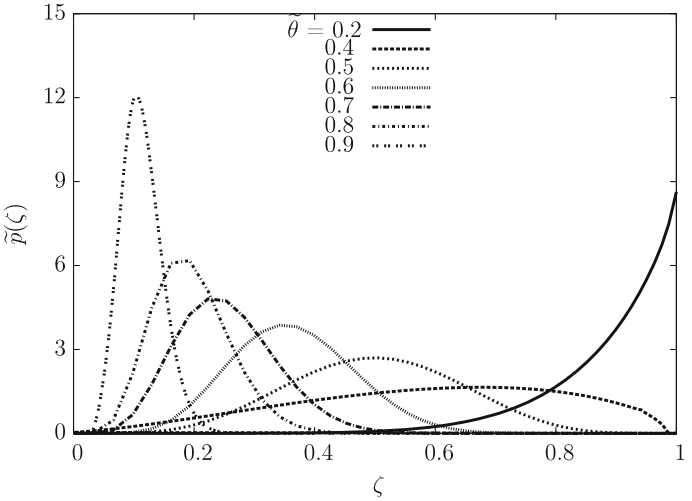

Fig. 8.10 The variation of the Favre PDF of the regress variable, $\tilde{p}(\zeta)$, at selected locations of the flame brush of PM1-200 flame (Amzin and Swaminathan 2013)

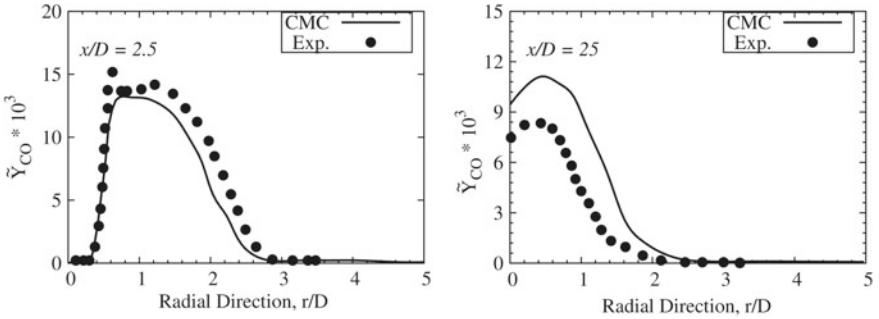

Fig. 8.11 The variation of $\widetilde{Y_{CO}}$ at some selected axial locations for the PM1-50 (Amzin and Swaminathan 2013)

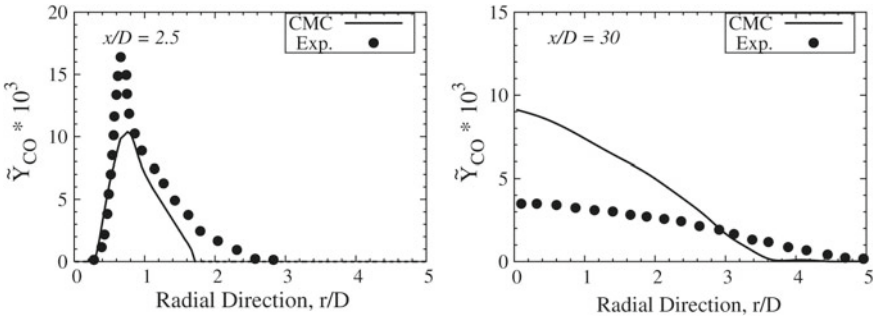

Fig. 8.12 The variation of $\widetilde{Y_{CO}}$ at some selected axial locations for the PM1-200 (Amzin and Swaminathan 2013)

inside the flame brush and is slightly under-predicted by the CMC. For the flame PM1-50 and in the upstream region at the axial location, $x/D = 25$ a relatively high under-prediction is observed, but the general trend is captured quite well by the CMC. This is because flame PM1-50 has a relatively lower Reynolds number compared with the flame PM1-200. It is interesting to mention the similar behaviour of the reactive scalars was observed by the other combustion models (Rowinski and Pope 2011).

8.6 Summary and Conclusion

An accurate closure for the mean reaction rate of species α which is included in the species transport equations can be difficult to obtain using the conventional moment method. This is because the fluctuations of various scalar concentrations and temperature over the mean are very large. This large fluctuation, along with the strong nonlinearity in the reaction rate, mainly renders the moment method to be ineffec-

tive. On the other hand, the CMC reduces these large fluctuations by associating the reactive scalars of interest, such as Y_α or T, with the fluctuations of a key scalar. The progress variable, c, is chosen for turbulent premixed combustion. It should be noted that c is a reactive scalar and it can be defined based on temperature, fuel mass fraction or alternatively using the enthalpy.

The CMC is a well-established method for turbulent non-premixed combustion, but its suitability to turbulent premixed combustion is ongoing research. Unlike flamelet-based methods, the CMC transport equation is derived with no explicit assumptions about the effect of turbulent vortices on the flame front structure. Hence, the CMC is expected to capture efficiently the finite-rate chemistry effects and thus predicts species with slow chemical time scales. Most importantly, the method would apply to all regimes in turbulent premixed combustion.

Recently, the method was improved and validated in two independent studies with some promising outcomes. However, these studies show that the strength of the method in turbulent premixed combustion is significantly affected by the assumptions used to derive its sub-models. Some of these issues, the conditional scalar dissipation rate, turbulent transport of conditional fluxes, differential diffusion effects and turbulence models, require additional investigations (Amzin and Swaminathan 2013; Amzin et al. 2012).

In this chapter, the CMC method was described comprehensively along with its numerical implementation and some selected results.

Acknowledgements This work was supported by EPSRC, Siemens, Cambridge European Trust and the University of Cambridge. The generous support and assistance of Prof. Nedunchezhian Swaminathan is acknowledged.

References

Amzin S, Swaminathan N (2013) Conditional Moment Closure for turbulent lean premixed flames. Combust Theory Model 17:1125–1153

Amzin S, Swaminathan N, Rogerson J, Kent JH (2012) Conditional Moment Closure for turbulent premixed flames. Combust Sci Tech 184:1–25

Bilger RW (1993) Conditional Moment Closure for turbulent reacting flow. Phys Fluids A 5(2): 436–444

Bray KNC (2011) Laminar flamelets and the Bray, Moss, and Libby model. In: Swaminathan N, Bray KNC (ed) Turbulent premixed flames, 1st edn. Cambridge University Press, Cambridge, UK, pp 41–60

Brewster BS, Cannon SM, Farmer JR, Meng F (1999) Modeling of lean premixed combustion in stationary gas turbines. Prog Energy Combust Sci 25(4):353–385

Chakraborty N, Champion M, Mura A (2011) Scalar dissipation rate approach. In: Swaminathan N, Bray KNC (eds) Turbulent premixed flames, 1st edn. Cambridge University Press, Cambridge, UK, pp 1–33

Colucci PJ, Jaberi FA, Pope SB (1998) Filtered density function for large eddy simulation of turbulent reacting flows. Phys Fluids 10:499–515

Correa SM (1993) A review of NO_x formation under gas turbine combustion conditions. Combust Sci Tech 87(1–6):329–362

Dunn MJ, Masri AR, Bilger RW (2007) A new piloted premixed jet burner to study strong finite-rate chemistry effects. Combust Flame 151(1–2):46–60
Dunn MJ, Masri AR, Bilger RW, Barlow RS, Wang GH (2009) The compositional structure of highly turbulent piloted premixed flames issuing into a hot co-flow. Proc Combust Inst 32(2):1779–1786
Dunn MJ, Masri AR, Bilger RW, Barlow RS (2010) Finite rate chemistry effects in highly sheared turbulent premixed flames. Flow Turb Combust 85:621–648
Duwig C, Nogenmyr KJ, Chan CK, Dunn MJ (2011) Large Eddy Simulations of a piloted lean premix jet flame using finite-rate chemistry. Combust Theory Model 15(4):537–568
Jeffrey L, Christopher J, Steven JA (2001) comparison of turbulent models for a supersonic jet in transonic cross-flow. AIAA (1):1048
Kee RJ, Grcar JF, Smooke MD, Miller JA, Meeks E (1985) A fortran program for modelling steady laminar one-dimensional premixed flames. Sandia National Laboratories, Livermore, CA
Klimenko AY, Bilger RW (1999) Conditional moment closure for turbulent combustion. Prog. Energy Combust. Sci. 25:595–687
Kolla H, Swaminathan N (2010) Strained flamelets for turbulent premixed flames I: formulation and planar flame results. Combust Flame 157:943–954
Kolla H, Rogerson JW, Chakraborty N, Swaminathan N (2009) Scalar dissipation rate modelling and its validation. Combust Sci Tech 181(3):518–535
Libby PA, Williams FA (1982) Structure of laminar flamelets in premixed turbulent flames. Combust Flame 44(1–3):287–303
Lieuwen T, Torres H, Johnson C, Zinn BT (2001) A mechanism of combustion instability in lean premixed gas turbine combustors. J Eng Gas Turb Power 123(1):182–189
Mura A, Galzin F, Borghi R (2003) A unified PDF-flamelet model for turbulent premixed combustion. Combust Sci Technol 175:1573–1609
OBrien EE (1980) The probability density function PDF approach to reacting turbulent flows. In: Turbulent reacting flows, pp 185–218
Patankar SV (1980) Numerical heat transfer and fluid flow. Hemisphere Publishing Corporation, Washington, USA
Poinsot T, Veyante D (2005) Theoretical and numerical combustion, 2nd edn. Westview Press, Philadelphia, USA
Pope SB (1978) An explanation of the turbulent round-jet/plane-jet anomaly. AIAA J 16(3):279–281
Pope SB (1985) PDF methods for turbulent reactive flows. Prog Energy Combust Sci 11(2):119–192
Pope SB, Anand MS (1987) Calculations of premixed turbulent flames by PDF methods. Combust Flame 67:127–142
Richardson ES, Chakraborty N, Mastorakos E (2007) Analysis of Direct Numerical Simulations of ignition fronts in turbulent non-premixed flames in the context of Conditional Moment Closure. Proc Combust Inst 31(1):1683–1690
Rogerson JW, Kent JH, Bilger RW (2007) Conditional moment closure in bagasse-fired boiler. Proc Combust Ins 31:2805–2811
Rowinski DH, Pope SB (2011) Pdf calculations of piloted premixed jet flames. Combust Theory Model 15(2):245–266
Smith GP, Golden DM, Frenklach M, Moriarty NW, Eiteneer B, Goldenberg M, Bowman CT, Hanson RK, Song S, Gardiner WC, Lissianski VV, Qin Z (2011) Gri-mech 3.0. In: The Gas research institute. http://www.me.berkeley.edu/grimech
Swaminathan N, Bilger RW (2001) Analysis of Conditional Moment Closure for turbulent premixed flames. Combust Theory Model 5:241–260
Swaminathan N, Bray KNC (2011) Turbulent premixed flames. Cambridge University Press, Cambridge, UK
Veynante D, Vervisch L (2002) Turbulent combustion modelling. Prog Energy Combust Sci 28(3):193–266

Part III
Turbulent Non-premixed Combustion

Chapter 9
Conditional Moment Closure Methods for Turbulent Non-premixed Combustion

S. Navarro-Martinez

Abstract Computational models for engineering applications need to be both accurate and computationally efficient. Turbulent flows with combustion cannot be directly solved due to the wide range of spatial scales and the large number of reactive scalars. In non-premixed systems, strong correlations exist between the value reactive scalar and the mixing between the fuel and oxidiser. Conditional moment closure (CMC) methods assumed that conditional fluctuations around a single scalar (in non-premixed flows the mixture fraction) are small. Using this assumption, CMC models derive Eulerian transport equations for the conditioned scalars that can be solved efficiently. This chapter will introduce the CMC method in non-premixed combustion and its formulations in RANS and LES, with the modelling of the unclosed terms and relevant algorithms. Next, the chapter will review recent progress in CMC modelling of auto-ignition, flame stabilisation and extinction; including recent applications in engines and gas turbine combustion, as well as theoretical developments on double conditioning, differential diffusion and spray combustion.

Keywords Non-premixed combustion · Conditional moment · Closure method · Large eddy simulation · RANS

9.1 Introduction

Modelling *turbulence–chemistry interactions* in combustion is a long-standing challenge in computational engineering. Pollutants such as NO_x, SO_x, soot emissions are relatively slow chemical reactions (compared to CO to oxidation for example). These *finite-rate* process are far from chemical equilibrium and the associated Damköhler numbers (ratio of flow to chemical timescale) can be low. Turbulent fluctuations increase mixing and promote combustion but can also disrupt the chemical reactions. This can happen in combustion ignition or in flame extinction or blow-out.

S. Navarro-Martinez (✉)
Department of Mechanical Engineering, Imperial College London, South Kensington Campus, Exhibition Rd., SW7 2AZ, London, UK
e-mail: s.navarro@imperial.ac.uk

© Springer Nature Singapore Pte Ltd. 2018

S. De et al. (eds.), *Modeling and Simulation of Turbulent Combustion*, Energy, Environment, and Sustainability, https://doi.org/10.1007/978-981-10-7410-3_9

In non-premixed combustion with fast chemistry, reaction rates are proportional to the rate of mixing, controlled by the scalar dissipation. The rate of mixing vary spatially and therefore the turbulence–chemistry interaction also changes in space. For example, in jet flames, the scalar dissipation is large in the fuel inlet and chemistry reactions are locally inhibited. Further downstream, the dissipation is low and the chemical reactions rates increase. In turbulent flows, time and spatial variations of scalar dissipation exist; and interaction between chemistry and turbulence is in-homogenous.

Turbulence combustion modellers have been concerned for several decades with the accurate representation of the turbulence–chemistry interaction. Ever-increasing sophisticated models have been developed, see reviews Bilger et al. (2005), Pitsch (2006), Pope (2013). These models aim to capture the physics and make the problem tractable without *solving* directly all relevant scales. These models faces a dual challenge: First, the number of degrees of freedom to solve all turbulence scales with $Re^{9/4}$. Second, the cost of integrate the chemistry scales with the square of the number of species considered, N^2, and to N^3, if molecular properties are to be considered Lu and Law (2009). The turbulence problem can be partially alleviated by the use of Reynolds-Averaged Navier–Stokes (RANS) or better large eddy simulation (LES) models. These techniques can predict turbulent flows relatively well and form the basis of modern turbulent computational fluid dynamics (CFD) solvers. However, their behaviour in the presence of reacting flows is markedly different as most of the turbulent-chemistry interaction occurs at scales that need to be modelled. The chemistry cost has been partially mitigated by the use of reduced chemistry mechanisms and tabulation techniques. However, there is still large uncertainties in the cost-efficient representation of large hydrocarbons typical of diesel and gasoline combustion and detailed chemistry CFD is too expensive. Moreover, there is also a lack of experimental data to validate chemistry sub-models under a wide range of conditions. For example, pressure effects on pollutant formation have barely been investigated, however, they are of large importance in gas turbine emissions. There is a need of intermediate models that can represent the turbulent-chemistry interaction accurately, while at the same time reduce the cost of integrating complex chemistry. Conditional moment closure (CMC) is one of these models.

The combustion characteristics of a system depends on its thermodynamic state and the reactive scalars, $\mathbf{Y}(\mathbf{x}, t) = (Y_1, Y_2, \ldots Y_N)$, in it. However, the combustion characteristics will depend *strongly* on a reduced set of scalars $\xi(\mathbf{x}, t) = \xi_1, \xi_2 \ldots, \xi_{Nr}$, where $N_r << N$. The major assumption in CMC-type models is that variables *condition* on the reduced set have small fluctuations. This is formally generalised in multiple mapping conditioning (MMC) approaches Klimenko and Pope (2003). In non-premixed combustion, a single variable, the local state of the mixture (indicated by the *mixture fraction*, ξ) can be used as the conditioning variable. In adiabatic flames at chemical equilibrium, the reactive scalars composition depends only on the mixing state.

The fundamental assumption is that fluctuations around conditional means (or conditional fluctuations) of reactive scalars on mixture fraction are small, compared to unconditional fluctuations. Or, in other words, turbulent fluctuations in a reactive

scalar are primarily associated with fluctuations in the mixture fraction. This simplifies the problem, as mixture fraction (at least in gaseous flames) is a conserved bounded scalar and relatively easy to solve. Under these assumptions, Bilger (1993) and Klimenko (1990) derived separately equations for the conditional variables for turbulent-reactive flows. Large reviews on the CMC methodology exist (Klimenko and Bilger 1999; Kronenburg and Mastorakos 2010) and the reader is pointed to them for the full details of the derivations and rationale behind the methodology. This chapter presents the CMC formulations in RANS and LES context, including implementation and recent developments and application for non-premixed turbulent combustion.

9.2 Formulation

The Navier–Stokes equations are

$$\frac{\partial \rho}{\partial t} + \nabla \cdot \rho \mathbf{v} = 0 \tag{9.1}$$

$$\frac{\partial \rho \mathbf{v}}{\partial t} + \nabla \cdot \rho \mathbf{v}\mathbf{v} = -\nabla p + \nabla \cdot \tau. \tag{9.2}$$

The variable ρ denotes density, $\mathbf{v}$ is the velocity field (u, v, w), p is the pressure and τ is the viscous stress which may be written as a function of the strain rate tensor, S_{ij},

$$\tau_{ij} = \mu \left[2S_{ij} - \frac{2}{3}\delta_{ij} \frac{\partial u_k}{\partial x_k} \right], \tag{9.3}$$

where μ is the dynamic viscosity that depends on temperature. The strain rate tensor is

$$S_{ij} = \frac{1}{2} \left(\frac{\partial u_i}{\partial x_j} + \frac{\partial u_j}{\partial x_i} \right), \tag{9.4}$$

where Newtonian approximations have been used and the bulk viscosity is assumed to be 0 (Kuo 1986). The reactive scalar transport equation for the mass fraction of i-specie is

$$\rho \frac{\partial Y_i}{\partial t} + \rho \mathbf{v} \cdot \nabla Y_i = \nabla \cdot \left(\rho D_i \nabla Y_i \right) + \rho \dot{\omega}_i. \tag{9.5}$$

Fick's law has been assumed and Soret effects (diffusion of species due to temperature gradients) have been neglected. D_i is the diffusion coefficient of species i into the mixture and $\dot{\omega}_i$ stands for the reaction rate of species i. The transport equation of a conserved scalar ξ (e.g. mixture fraction) is given by

$$\rho \frac{\partial \xi}{\partial t} + \rho \mathbf{v} \cdot \nabla \xi = \nabla \cdot (\rho D \nabla \xi), \tag{9.6}$$

where D is the mixture fraction diffusion coefficient. The energy equation for the enthalpy h is

$$\rho\frac{\partial h}{\partial t}+\rho\mathbf{v}\cdot\nabla h=\frac{\partial p}{\partial t}+\mathbf{v}\cdot\nabla p+\Phi_v+q_R-\nabla\cdot\mathbf{q}. \tag{9.7}$$

q_R is the radiative heat transfer and $\Phi_v=\tau_{ij}(\partial u_i/\partial x_j)$ is the viscous heating term. In constant pressure flames at low Mach numbers, the first two terms on the right-hand side of Eq. (9.7) and the viscous heating term Φ_v can be neglected (see Poinsot and Veynante (2001)). For small Dufour effects, the heat diffusion flux can be expressed as (Peters 2000)

$$\mathbf{q}=-\rho D_T\nabla h+\rho\sum h_i(D_T-D_i)\nabla Y_i, \tag{9.8}$$

where D_T is the thermal diffusivity, which may be obtained from the molecular viscosity as $D_T=\nu/Pr$ (Kuo 1986). The kinematic molecular viscosity ν is defined by $\nu\equiv\mu/\rho$, and the Prandtl number for simple gases can be set to $Pr=0.72$. In most combustion applications, air acts as the oxidiser and all species are assumed to diffuse at the same speed. Therefore, the diffusion coefficients are equivalent to the thermal diffusivity, $D_i=D\approx D_T$ (Lewis numbers are unity) and the second term on the RHS of Eq. (9.8) vanishes. An equation of state is required to close the system of equations. In combustion, the ideal gas law is commonly used $p=\rho RT$; where R is the gas constant (universal gas constant divided by mean molecular weight). The chemical source term $\dot{\omega}_i$ is the sum of all rates produced by all chemical reaction involved, where the rate constants for the particular reactions are in the form of Arrhenius expressions $AT^{\beta}\exp(-T_a/T)$.

9.2.1 RANS-CMC Formulation

In RANS modelling, the following Reynolds decomposition is introduced

$$Y_i(\mathbf{x},t)=\langle Y_i(\mathbf{x})\rangle+Y_i'(\mathbf{x},t), \tag{9.9}$$

where $\langle\cdot\rangle$ indicates a time-average operation. The nonlinearity of the chemical source term implies that

$$\left\langle\dot{\omega}_i(\underline{Y},T)\right\rangle\neq\dot{\omega}_i(\left\langle\underline{Y}\right\rangle,\langle T\rangle) \tag{9.10}$$

The errors associated with the above closure can be very large, due to the exponential term in the Arrhenius expression $\langle\exp[-T_a/T]\rangle\neq\exp[-T_a/\langle T\rangle]$. In CMC, a new decomposition is introduced

$$Y_i(x,t)=Q_i(\mathbf{x};\eta)+Y_i''|\eta(\mathbf{x},t), \tag{9.11}$$

where $Q_i(\mathbf{x};\eta) \equiv \langle Y_i|\xi=\eta\rangle$ is the conditional average. Following the above decomposition, the equation for the steady-state conditional average scalars is obtained (Bilger 1993):

$$< \mathbf{v}|\eta > \cdot\nabla Q_i = \frac{\langle\chi|\eta\rangle}{2}\frac{\partial^2 Q_i}{\partial\eta^2} + \langle\dot{\omega}_i|\eta\rangle + e_Y + e_D \tag{9.12}$$

The term e_Y relates to scalar transport by turbulent fluctuations and is expressed as

$$e_Y = \frac{\nabla\cdot\langle\rho|\eta\rangle\left\langle\mathbf{v}''Y_i''|\eta\right\rangle}{\langle\rho|\eta\rangle P(\eta)} \tag{9.13}$$

The term e_D is a scalar diffusion term, that scales with $\mathcal{O}(Re^{-1})$.

$$e_D = \nabla\cdot\rho D\nabla Q_i + \left\langle\rho D\nabla\xi\nabla\frac{\partial Q_i}{\partial\eta}|\eta\right\rangle \tag{9.14}$$

The variable $\chi = 2D|\nabla\xi|^2$ is the scalar dissipation rate and $P(\eta) \equiv P(\mathbf{x};\eta)$ is the probability density function (PDF) of the mixture fraction. A similar equation to (9.12) is obtained by using a PDF transport approach as proposed by Klimenko (1995). Under the assumption of high Reynolds numbers; $e_D \to 0$ and both formulations revert to the same expression (9.12). The details of the derivation are lengthy and the reader is pointed to Klimenko and Bilger (1999). The terms in Eq. (9.12) involve convective transport of the conditional averages; diffusion over scalar space; chemical source term and transport due to conditional fluctuations. In homogenous flows, the CMC equations reduce to a balance between chemical reaction and diffusion along scalar space:

$$\frac{\langle\chi|\eta\rangle}{2}\frac{\partial^2 Q_i}{\partial\eta^2} = -\langle\dot{\omega}_i|\eta\rangle \tag{9.15}$$

The solution $Q_i(\mathbf{x},\eta) \approx Q_i(\eta)$ is the same as a steady flamelet (Peters 1984) although the derivation and assumptions behind it are fundamentally different. This solution is often referred in the literature as 0D-CMC.

The conditional energy equation is derived in analogous manner to the species equation. For unity Lewis number flows at low Mach number, the steady conditional enthalpy equation simplifies to

$$< \mathbf{v}|\eta > \cdot\nabla Q_h = \frac{\langle\chi|\eta\rangle}{2}\frac{\partial^2 Q_h}{\partial\eta^2} + e_h + e_D \tag{9.16}$$

$Q_h \equiv \langle h|\xi=\eta\rangle$ is the conditional average enthalpy and the term e_h is the same as e_Y, just replacing Y_i by h. Alternatively, an equation for the conditional temperature can be used, where a conditional heat release source term should be added to the equation.

9.2.2 RANS Closures

Under the assumption of small conditional fluctuations $Y'' << Y'$, the conditional source term can be approximated using first-order closure

$$\langle \dot{\omega}_i | \eta \rangle \approx \dot{\omega} \left(\mathbf{Q}, \langle T | \eta \rangle \right) \tag{9.17}$$

Alternative closures have been proposed, to account for large conditional fluctuations; for example extinction or ignition. Second-order closure was proposed by Mastorakos and Bilger (1998); where the effect of temperature fluctuations was included by a series expansion of the exponential term in the Arrhenius expression truncated to second order. Species fluctuations were still neglected and a transport equation was required for the conditional temperature variance $< (T'')^2 | \eta >$. Expansions were introduced to add the effects of species covariances $< Y_i'' Y_j'' | \eta >$ (Klimenko and Bilger 1999), however, the complexity of these formulations and the need to solve more variables have limited their use. Kronenburg (2004) proposed conditioning in two variables (mixture fraction and enthalpy) effectively reducing the conditional fluctuations. The conditional source term is then

$$\langle \dot{\omega}_i | \eta_1, \eta_2 \rangle \approx \dot{\omega} \left(\mathbf{Q}, \langle T | \eta_1, \eta_2 \rangle \right) \tag{9.18}$$

The results show very good agreement with DNS data of non-premixed flames with extinction. However, there are large uncertainty in how to model double-conditioning convective terms and double-conditioning models are not very extended.

The conditional scalar dissipation $\langle \chi | \eta \rangle$, often represented in the CMC literature by $N|\eta$, is modelled as $\langle \chi | \eta \rangle = \langle \chi \rangle F(\eta)$. The average scalar dissipation $\langle \chi \rangle$ is obtained from the mixing field; for example in RANS is

$$\langle \chi \rangle = C_\chi \frac{k}{\varepsilon} \left\langle \xi''^2 \right\rangle, \tag{9.19}$$

where k is the turbulent kinetic energy and ε the energy dissipation. Both can be obtained from conventional turbulent RANS models. The dissipation constant, C_χ, is often 2 (Beguier et al. 1978). The functional dependence on the mixture fraction $F(\eta)$ can be approximated by the amplitude mapping closure (AMC) (O'Brien and Jiang 1991).

$$F^*(\eta) = \exp \left[-2 \mathrm{erf}^{-1} (2\eta - 1)^2 \right], \tag{9.20}$$

where $F(\eta) = F^*(\eta) / \int F^*(\eta) P(\eta) d\eta$. The shape of the conditional scalar dissipation depends on the shape of the scalar PDF, $P(\eta)$ as both variables are closely linked through the PDF transport equation (Klimenko and Bilger 1999). Passive scalar mixing has been largely studied in the literature. Experiments and DNS show that a

two-parameter PDF, the β-PDF, is able to represent mixing characteristics. The β-PDF is given by (in the interval $0 \leq \eta \leq 1$)

$$P(\eta) = \frac{\eta^{a-1}(1-\eta)^{b-1}}{\beta(a,b)}, \tag{9.21}$$

where $\beta(a,b) = \Gamma(a)\Gamma(b)/\Gamma(a+b)$ and Γ is the Gamma function. a and b are related to the scalar mean $\langle\xi\rangle$ and variance $\left\langle \xi''^2 \right\rangle$through:

$$a = \langle\xi\rangle \left(\langle\xi\rangle \frac{1-\langle\xi\rangle}{\langle\xi'^2\rangle} - 1 \right) \quad b = a\frac{1-\langle\xi\rangle}{\langle\xi\rangle} \tag{9.22}$$

The β-PDF is smooth and tends to a Gaussian at low variance. Girimaji (1992) showed that the PDF corresponding to the AMC model in a quasi-steady process is the β-PDF. However, despite its flexibility, the β-PDF cannot describe turbulent intermittency where unmixed mixture exist. In these cases, a clipped or composite PDF can be used (Klimenko and Bilger 1999) Kuznetsov and Sabel'nikov (1990) assume that the joint PDF of the velocity and mixture fraction is Gaussian, and therefore the conditional velocity can be written as

$$\langle \mathbf{v}|\eta\rangle = \mathbf{v} + \frac{\langle \mathbf{v}''\xi''\rangle}{\langle\xi''\rangle^2}(\eta - \langle\xi\rangle) \tag{9.23}$$

where the transport flux is modelled using a gradient approach as $\mathbf{v}''\xi'' = -D_t\nabla\langle\xi\rangle$. This model has found to agree well with DNS (Swaminathan and Bilger 2001). Similarly, the conditional fluctuations are modelled using a gradient approach

$$\left\langle \mathbf{v}''Y_i''|\eta \right\rangle = -D_t\nabla Q_i \tag{9.24}$$

with the closures (9.20), (9.21), (9.23) and (9.24) the system of CMC equations (9.12) is closed and if appropriate boundary conditions are employed the conditional moments Q_i can be obtained (see Sect. 9.2.5) The unconditional averages are recovered by convolution with the scalar PDF

$$\langle Y_i\rangle = \int_0^1 Q_i P(\eta)d\eta \tag{9.25}$$

The conditional ideal equation of state is

$$\langle p|\eta\rangle = \langle\rho|\eta\rangle \langle R|\eta\rangle \langle T|\eta\rangle, \tag{9.26}$$

where $\langle R|\eta\rangle \approx R(\mathbf{Q})$ and the conditional pressure is often taken as a constant in low-Mach number flows. The conditional temperature can be obtained from the conditional enthalpy, Q_h, by an iterative method.

9.2.3 LES-CMC Formulation

The LES-CMC methodology solves equations for the conditionally filtered variables instead of conditional average. Conditionally filtered variables are defined with the fine-grained PDF $\psi_\eta \equiv \delta[\eta - \xi(\mathbf{x}, t)]$ of the mixture fraction, where δ stands for a Dirac delta function. ψ_η is a generalised function and its properties are defined by convolution with a continuous function (see details in Klimenko and Bilger (1999)). The conditional filtering operation on a variable f was introduced by Bushe and Steiner (1999) as

$$\overline{f(\mathbf{x}, t)|\eta} \equiv \frac{\int_V f(\mathbf{x}, t)\psi_\eta G(\mathbf{x} - \mathbf{x}'; \Delta)dV'}{\bar{P}(\eta)}, \tag{9.27}$$

where $\bar{P}(\eta)$ is the sub-grid or filtered density function (FDF), which is obtained from ψ_η through

$$\bar{P}(\mathbf{x}, t; \eta) = \int_V \psi_\eta G(\mathbf{x} - \mathbf{x}'; \Delta)dV'. \tag{9.28}$$

If the LES filter kernel G is positive definite, then $\bar{P}(\eta)$ has the properties of a PDF (Colucci et al. 1998). Analogous to density weighting in RANS, a Favre-filtered density function is defined by $\bar{\rho}\widetilde{P}(\eta) = \bar{\rho}|\eta\bar{P}(\eta)$. The conditionally and unconditionally filtered values are related through integration over sample space:

$$\tilde{f}(\mathbf{x}, t) = \int_0^1 \widetilde{f(\mathbf{x}, t)|\eta}\widetilde{P}(\mathbf{x}, t; \eta)\, d\eta. \tag{9.29}$$

The transport equations for the conditionally filtered scalars are given by Navarro-Martinez et al. (2005),

$$\frac{\partial Q_i}{\partial t} + \hat{\mathbf{v}} \cdot \nabla Q_i = \frac{\hat{\chi}}{2}\frac{\partial^2 Q_i}{\partial \eta^2} + \hat{\omega}_i + \nabla \cdot (\widehat{D} + \widehat{D}_{sgs})\nabla Q_i + \frac{\widehat{D}_{sgs}}{\bar{\rho}\tilde{P}(\eta)}\nabla\bar{\rho}\tilde{P}(\eta), \tag{9.30}$$

where for clarity the conditional moments such as velocity, dissipation, diffusion and chemical source term are written as $\widehat{f}(\mathbf{x}, t; \eta) \equiv \widetilde{f(\mathbf{x}, t)|\eta}$ and $Q_i \equiv \widehat{Y}_i$. The last term is normally neglected since gradients of the PDF are assumed to be small compared to other contributions (Devaud and Bray 2003). The contribution of the conditional fluctuations is modelled using a conventional gradient approach similar to RANS and added as sub-grid turbulent diffusion to form an effective diffusion, $D_e = \widehat{D} + \widehat{D}_{sgs}$, term of conditional moments. In LES, unlike RANS, the e_D is retained and added to the unclosed e_Y term.

9.2.4 LES Closures

The main advantage of LES-CMC is that conditional fluctuations are smaller than their RANS-CMC counterparts, mostly due to the better representation of the unsteady mixing field. Based on the same arguments than in RANS, same closures can be directly applied and in most cases simplified. For example, the first-order closure of the conditional source term $\widehat{\omega_k} = \dot{\omega}_k(\mathbf{Q}, \tilde{T}|\eta)$ is more accurate in LES than RANS. As conditional fluctuations are small, conditional filtered values change slowly in space. This allows two grids to be defined: a fine grid (hereafter $\mathbf{x}^{LES}$ of average size Δ) for the discretisation of the filtered velocities $\widetilde{\mathbf{v}}$ and mixture fraction $\widetilde{\xi}$; and a coarse grid ($\mathbf{x}^{CMC}$, average size Δ_{CMC}) for the solution of the conditional scalar Q_i. This dual-grid greatly reduces the computational cost, which is limited by the amount of chemistry calculations in the coarse mesh.

Nevertheless, Δ_{CMC}, limits the size of the region with chemistry fluctuations. For example, combustion extinction pockets will be always greater than Δ_{CMC}. Extinction, ignition or combustion phenomena with large conditional fluctuations will not be able to be captured at scales below Δ_{CMC}. Large CMC cell may also hide scalar dissipation fluctuations that could be important for prediction of slow-chemistry species (Navarro-Martinez et al. 2005). In principle, $\Delta_{CMC} \sim \ell$; where ℓ is the turbulent integral scale. However, it is possible to use homogenous directions to further reduce the number of CMC cells and therefore the cost of the simulations.

Most closures of the LES-CMC (Triantafyllidis et al. 2009) use the same AMC model (9.20) as RANS for the conditional filtered scalar dissipation $\hat{\chi} = \tilde{\chi}F(\eta)$. The conditional velocity is assumed uncorrelated with the scalar $\widehat{\mathbf{v}} \approx \mathbf{v}$ (see for example Ayache et al. 2011; Triantafyllidis et al. 2009) Alternatively, the conditionally *filtered* values can be approximated by the conditional *average* of filtered values over one CMC cell (see Navarro-Martinez et al. 2005), i.e.

$$\widehat{\chi} \approx \langle \tilde{\chi}|\eta\rangle \qquad \widehat{\mathbf{v}} \approx \langle \tilde{\mathbf{v}}|\eta\rangle \qquad \widehat{D}_e \approx \langle D_e|\eta\rangle\,, \tag{9.31}$$

where interpolation is used to extend $\widehat{\chi}$, $\widehat{\mathbf{u}}$ and $\widehat{D}_e$ over the whole range of η. This implementation produces noisy instantaneous profiles in scalar space. Smoothing techniques filter-out spatial fluctuations of the order of Δ and therefore neglect small-scale fluctuations.

Similarly to RANS, the unconditionally filtered reactive species are obtained by integration over mixture fraction space

$$\widetilde{Y}_i(\mathbf{x}^{LES}; t) = \int_0^1 Q_i(\mathbf{x}^{LES}; t; \eta)\widetilde{P}(\mathbf{x}^{LES}; t; \eta)d\eta, \tag{9.32}$$

where the sub-grid PDF is assumed to have a β-PDF distribution (9.21) reconstructed from the calculated mean $\tilde{\xi}$ and sub-grid variance $\widetilde{\xi''^2_{sgs}}$. It has to be noted that in LES, the sub-grid scalar variance is much smaller than turbulent scalar variance and faster integration techniques can be used (Floyd et al. 2009). The conditional values on the

LES grid, $\mathbf{x}^{LES}$, are interpolated from values on the CMC grid $Q(\mathbf{x}^{CMC})$ using trilinear interpolation techniques. In LES, the mean mixture fraction $\tilde{\xi}$ is transported and the sub-grid variance can be modelled using equilibrium approaches (Branley and Jones 2001)

$$\widetilde{\xi_{sgs}^2} = C_\xi \Delta^2 |\nabla \tilde{\xi}|^2 \tag{9.33}$$

The sub-grid scalar dissipation and variance are linked through

$$\chi_{sgs} = \frac{C_\chi}{2\tau_{sgs}} \widetilde{\xi''^2_{sgs}}, \tag{9.34}$$

where τ_{sgs} is a LES sub-grid timescale (the inverse of the filtered strain rate). The value of C_χ can be obtained through calibration with experimental data and a value of 42 is often used (Ayache et al. 2011). Unlike RANS, the scalar dissipation has a *resolved* and a *sub-grid* component, i.e. $\chi = D|\nabla\tilde{\xi}|^2 + \chi_{sgs}$.

9.2.5 Implementation

Equation (9.30) is not written in conservative form and therefore cannot be directly used in finite volume formulations. In the finite difference formulation (9.30), the conditional source term $\widehat{\dot{\omega}_k}$ can be non-zero in regions of very low probability, $\tilde{P}(\eta) \approx 0$. The unrealistic generated moments can be transported to physical regions by conditional dissipation and velocity. This can be mitigated by forcing $\widehat{\dot{\omega}_k} \to 0$ when $\tilde{P}(\eta) \approx 0$; although this may cause 'jumps' in Q between neighbouring CMC cells of near-zero and non-zero probabilities. Full conservative CMC formulations were developed to prevent these discontinuities in Q. The finite volume discretisations for the two-dimensional CMC equations were first implemented in RANS by Cleary and Kent (2005) and in LES by Siwaborworn and Kronenburg (2013). In the LES context (similarly for RANS), the conservative equations can be obtained by multiplying (9.30) by $\gamma \equiv \bar{\rho}\tilde{P}(\eta)$

$$\gamma \frac{\partial Q_i}{\partial t} + \nabla \cdot \gamma \hat{\mathbf{v}} Q_i = Q_i \nabla \cdot \gamma \hat{\mathbf{v}} + \gamma \frac{\hat{\chi}}{2} \frac{\partial^2 Q}{\partial \eta^2} + \gamma \widehat{\dot{\omega}_I} + \gamma \nabla \cdot \hat{D}_e \nabla Q_i \tag{9.35}$$

This form of the equation is fully conservative and, by including the probability in the convective term, prevents the spatial propagation of information in low probability regions. Alternatively, the system of Eq. (9.30) formulation can be rearranged (Garmory and Mastorakos 2015),

$$\frac{\partial Q_i}{\partial t} + \nabla \cdot \hat{\mathbf{v}} Q_i = Q_i \nabla \cdot \hat{\mathbf{v}} + \frac{\hat{\chi}}{2} \frac{\partial^2 Q_i}{\partial \eta^2} + \hat{\omega}_i + \nabla \cdot \hat{D}_e \nabla Q_i \tag{9.36}$$

and integrated over a CMC cell $V_{CMC} \sim \Delta^3_{CMC}$ where Q_i is assumed constant

$$\frac{\partial Q_i}{\partial t} + \frac{1}{V_{CMC}} \oint \hat{\mathbf{v}} Q_i dS = \frac{Q_i}{V_{CMC}} \oint \hat{\mathbf{v}} dS + \frac{\hat{\chi}}{2} \frac{\partial^2 Q_i}{\partial \eta^2} + \widehat{\dot{\omega}_k} + \frac{1}{V_{CMC}} \oint \hat{D}_e \nabla Q_i dS \tag{9.37}$$

The above finite volume formulation allows to compute CMC-type fluxes $\hat{\mathbf{v}} Q$ across the CMC cell boundaries, where the conditional velocity can be reconstructed from the filtered velocity. The finite volume formulation (9.38) allows to use generic unstructured solvers, with their added flexibility, and extend the applicability of LES-CMC to complex geometries (Garmory and Mastorakos 2015; Zhang et al. 2016). The communication between CMC and CFD solver is sketched in Fig. 9.1, where the evaluation of conditional integrated values is

$$\hat{f} = \frac{\int_{V_{CMC}} \bar{\rho} \tilde{f} \widetilde{P}(\eta) dV}{\int_{V_{CMC}} \bar{\rho} \widetilde{P}(\eta) dV} \tag{9.38}$$

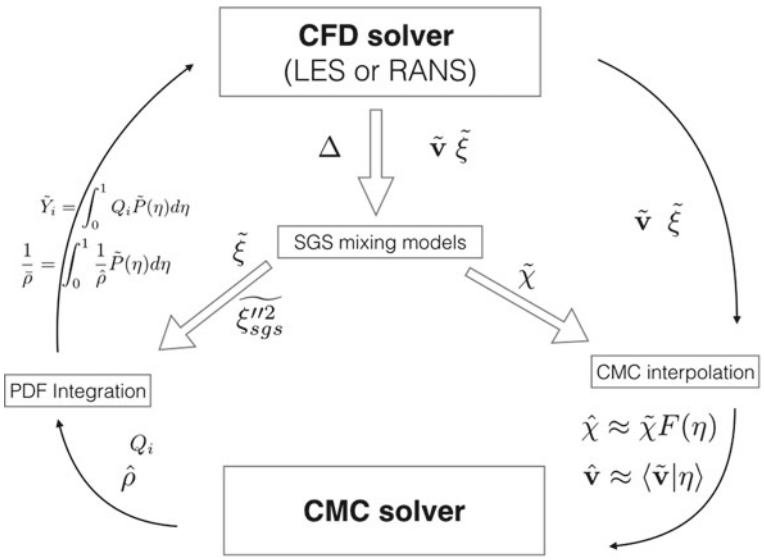

Fig. 9.1 Integration of CMC and CFD solvers (using LES notation)

The inverse of the filtered density $\bar{\rho}$ is then computed by using (9.32) at every cell and then fed back into the CFD solver (see Fig. 9.1). To obtain a relatively wide range of ξ instantaneously in a CMC cell, a relative large amount of LES (or unsteady RANS) cells are required. A typical mesh in a swirl burner will require 10 Million LES cells, and around 10^5 CMC cells (Garmory and Mastorakos 2015); which gives a ratio of LES to CMC cells of $N_{CMC}/N_{LES} \sim 100$. Assuming a scalar space discretisation of 100 points, LES-CMC simulations with N_{CMC}/N_{LES} ratios smaller than 100 will have similar cost as implicit-LES models, where sub-grid fluctuations of the chemical source term are neglected (Fureby 2009). In the lower limit of $N_{CMC}/N_{LES} \sim 1$, LES-CMC will be more expensive than alternative Eulerian LES-PDF approaches (Jones and Navarro-Martinez 2007).

9.3 Applications

9.3.1 Gaseous Flames

Early CMC implementations were limited to simple fully burning non-premixed jet flames (Devaud and Bray 2003; Fairweather and Woolley 2003; Kim and Huh 2002; Kim et al. 2000; Navarro-Martinez et al. 2005; Roomina and Bilger 1999, 2001), but auto-ignition and lifted flames soon followed in RANS (Kim et al. 2000; Patwardhan et al. 2009) and in LES (Navarro-Martinez and Kronenburg 2009; Stanković et al. 2011). The results showed how laboratory flames with simple hydrocarbon fuels could be simulated with moderate-size grids and only when premixed effects became important, agreement with experimental data deteriorated (Navarro-Martinez et al. 2011). The introduction of LES allowed to solve more complex swirl flames and bluff-body flows (Garmory and Mastorakos 2015; Navarro-Martinez and Kronenburg 2007; Zhang et al. 2016). Progressively more detailed chemistry was included, from direct and reduced methane mechanisms (Navarro-Martinez et al. 2005; Triantafyllidis et al. 2009), to large Dimethyl Ether mechanisms (Kronenburg et al. 2017), solving directly up to 124 species and in some cases up to 1000 s reactions (Løvås et al. 2011). CMC chemical solutions are always close to the manifold (unlike similar PDF transport simulations), which makes CMC perfectly suited for tabulation strategies or adaptive chemistry (Løvås et al. 2011). If a small Δ_{CMC} is used, local extinction events can be captured (Ayache et al. 2011; Garmory and Mastorakos 2011) and even flames with large extinction (such as Sandia F Garmory and Mastorakos (2011), Fig. 9.2) without the need of double-conditioning. However, grid resolution, discretisation scheme and scalar dissipation modelling proved to be important to capture these events (Garmory and Mastorakos 2013; Tyliszczak 2013).

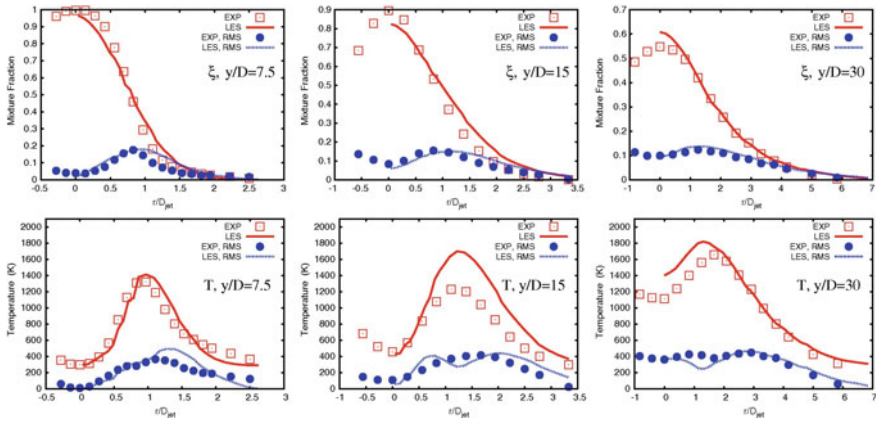

Fig. 9.2 Radial profiles of mixture fraction and temperature for a piloted jet flame (Sandia F). Figure from Garmory and Mastorakos (2011). Reprinted with permission from Elsevier

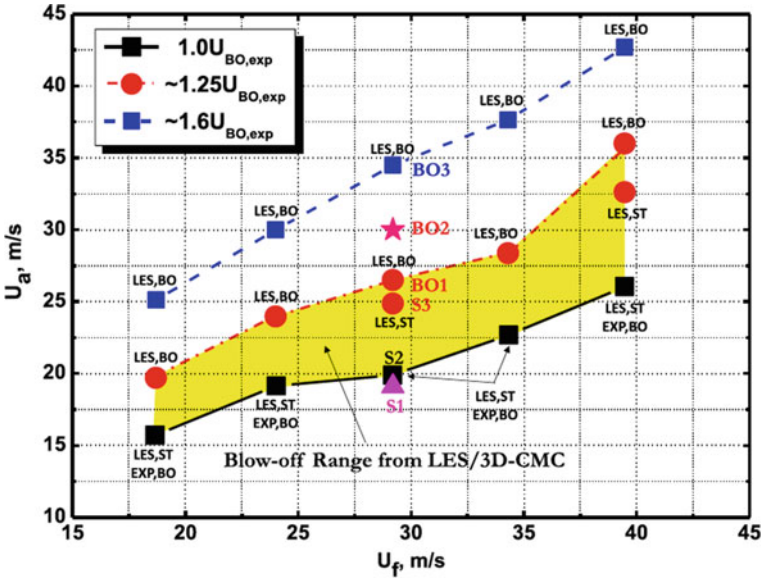

Fig. 9.3 Air velocity at blow-off as a function of the fuel jet velocity from experiments and LES-CMC. Figure from Zhang et al. (2016)

Recently, LES-CMC has been used to predict blow-out and global extinction on swirl flames (Zhang et al. 2016), reproducing trends from experimental data (Fig. 9.3). If the mixing field is well resolved and the CMC-mesh fine enough, LES-CMC can capture a wide range of flame phenomena and finite-rate effects.

9.3.2 Spray Flames

The mixture fraction in hydrocarbon combustion is based on the normalised carbon element concentration. In gaseous combustion, the mixture fraction is conserved. However in spray combustion, mixture fraction is no longer a passive scalar as fuel vapour is being introduced into the gas phase and there is a source term, $\dot{S}$, in the mixture fraction equation.

$$\rho\frac{\partial\xi}{\partial t}+\rho\mathbf{v}\cdot\nabla\xi=\nabla\cdot(\rho D\nabla\xi)+\dot{S}, \tag{9.39}$$

The mass evaporation introduces additional term in the CMC equations (9.30) The multiphase formulation (Bilger 2010; Mortensen and Bilger 2009) is

$$\begin{aligned}\frac{\partial Q_i}{\partial t}+\widehat{\mathbf{v}}\cdot\nabla Q_i=\frac{\widehat{\chi}}{2}\frac{\partial^2 Q_i}{\partial\eta^2}+\widehat{\dot{\omega}}_i+\nabla\cdot\widehat{D}_e\nabla Q_i \\ +e_Y+\left[\delta_{if}-Q_i-(1-\eta)\right]\frac{\partial Q_i}{\partial\eta}\hat{\dot{S}}+e_{SY},\end{aligned} \tag{9.40}$$

where $\delta_{kf}=1$ if the species consider is the fuel and 0 otherwise. An additional term appears that includes correlations between scalar and evaporation rate

$$e_{SY}=\frac{1}{\gamma}\frac{\partial}{\partial\eta}\left[(1-\eta)\gamma\left\langle Y''\dot{S}''|\eta\right\rangle\right] \tag{9.41}$$

although term is neglected in most studies (Borghesi et al. 2011; Giusti et al. 2016). The conditional scalar dissipation and scalar PDF are a priori different from the models explained in Sect. 9.2.2. In multiphase flows, the value of $\xi=1$ (or $\eta=1$) is not reached (only a maximum value η_{max}). However in most of the simulations, the AMC model (9.20) is still used, albeit derived with respect to a normalised scalar $\eta^*=\eta/\eta_{max}$ (Seo and Huh 2011). However, η_{max} is a function of position in non-homogenous flows (like spray flames) and the AMC model cannot reproduce the asymmetry of the scalar dissipation distribution. Zoby et al. (2011) proposed a different functional dependence to capture the asymmetry in the scalar dissipation

$$\hat{\chi}(\eta)=C\eta^2\ln\eta^2 \tag{9.42}$$

where C is a constant depending on the diffusion coefficient and relative flow velocity. The results showed good agreement with DNS data of droplet loading turbulent flows. Nevertheless, LES-CMC results of different spray flames (Giusti et al. 2016; Ukai et al. 2015) suggest that traditional gaseous closures can be used (see Fig. 9.4). Probably due to the small size of droplets, evaporation is fast compared to mixing timescales and these spray flames behave like conventional gaseous flames. In dilute sprays, LES-CMC approaches (often combined with a Lagrangian solver for the particles) give similar (if not better) performance than other models.

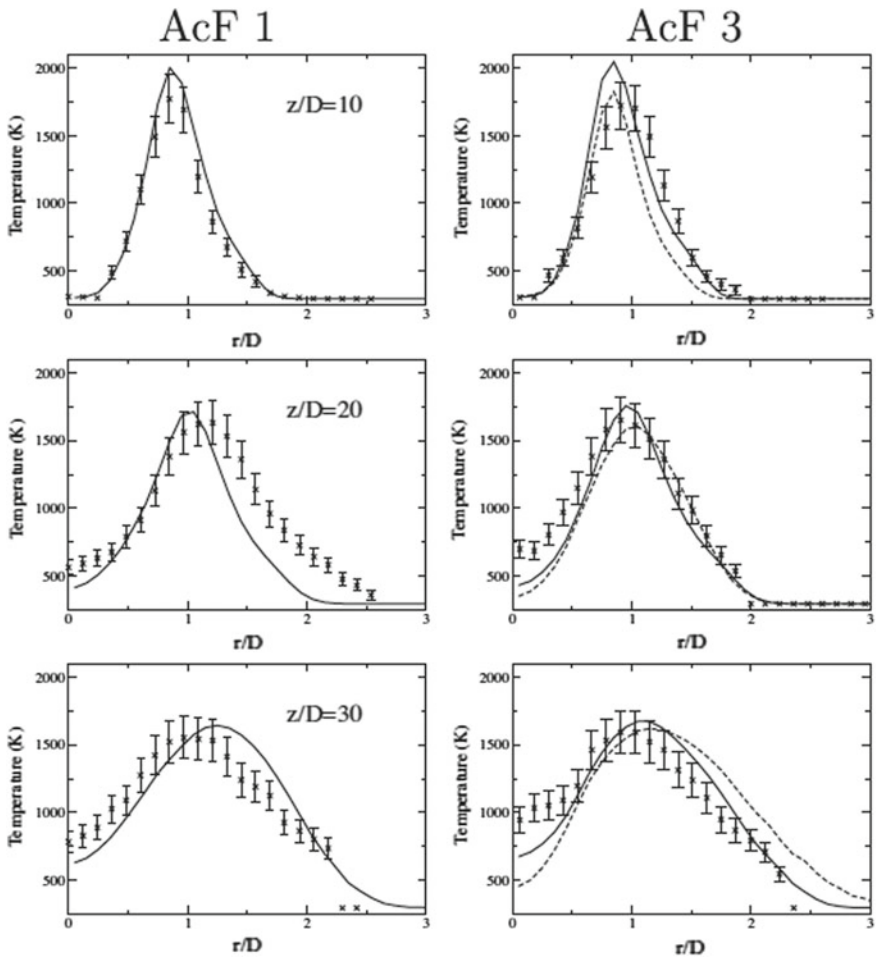

Fig. 9.4 Mean temperature profiles of two acetone spray flames. Lines, LES-CMC, symbols experiment with error bars. Figure from Ukai et al. (2015). Reprinted with permission from Elsevier

9.3.3 Differential Diffusion

The effects of differential diffusion can be included in the CMC equations by employing non-unity Lewis numbers. The difference of molecular diffusion between the mixture fraction, D_ξ, and the reactive scalar, D_i, introduces a new transport term in scalar space containing first derivatives in η. Although hydrogen combustion is prone to differential diffusion effects, most CMC simulations in the literature (Woolley and Fairweather 2009) are concerned with soot mass fractions. The LES formulation (Navarro-Martinez et al. 2011), including differential diffusion is (originally presented for RANS by Kronenburg et al. (2000))

$$\frac{\partial Q_i}{\partial t} + \widehat{\mathbf{v}} \cdot \nabla Q_i = \frac{D_i}{D_\xi}\left[\frac{\widehat{\chi}}{2}\frac{\partial^2 Q_i}{\partial \eta^2}\right] + \left(\frac{D_i}{D_\xi} - 1\right)\left[\widehat{M}\frac{\partial Q_i}{\partial \eta}\right] + \widehat{\omega}_i + e_Y, \tag{9.43}$$

where $M \equiv D_\xi \nabla \xi$, and $\tilde{M}$ is closed if sub-grid fluctuations of D_ξ are neglected. In RANS-CMC, differential diffusion effects on the turbulent transport term, e_Y, cannot be neglected. These contributions are assumed to be proportional to the conditional average of the differential diffusion variable, with a constant obtained from DNS (Kronenburg and Bilger 2001). In an alternative approach, Hewson et al. (2006) and Lignell et al. (2009), rearranged the diffusion term without the need to solve an additional equation (Kronenburg and Bilger 2001). In LES-CMC, e_Y is small compared to large-scale transport of the conditional variables and the ambiguity in modelling it is unlike to affect significantly the evolution of the conditional moments.

9.3.4 Internal Combustion Engines

Internal combustion engines are one of the most challenging flows to model. They include spray evaporation, flame ignition, unsteady detailed chemistry and variable pressure. Diesel engines, at low rpms, can be considered non-premixed combustion systems and therefore suitable for CMC modelling. The unsteady term in the conditional enthalpy equation in engines is non-zero and is approximated by

$$\left\langle \frac{\partial p}{\partial t} | \eta \right\rangle \approx \frac{\partial \langle p | \eta \rangle}{\partial t} \tag{9.44}$$

First applications of CMC at conditions relevant to diesel engines were performed by Wright et al. (2005) in RANS and by Bottone et al. (2012) in LES. The first engines simulation was performed by Paola et al. (2008) in unsteady RANS context and following the same methodology, CMC simulations have been performed in heavy-duty engines (Bolla et al. 2014; Wright et al. 2009). The ability of CMC to use complex chemistry, permits to model NO_x and soot emissions. Bolla et al. (2014) use a two-equation soot model with transport equations for conditional soot mass fraction and soot number density to predict emissions in a heavy-duty engine (see Fig. 9.5). The model reproduced quantitative trends and in some cases, peak soot concentrations.

9.4 Future Perspective and Conclusions

Conditional moment closure methods, in both RANS and LES variants, were developed mostly for non-premixed combustion and they have experienced considerable success. They have a wide range of applicability, from soot modelling to extinction

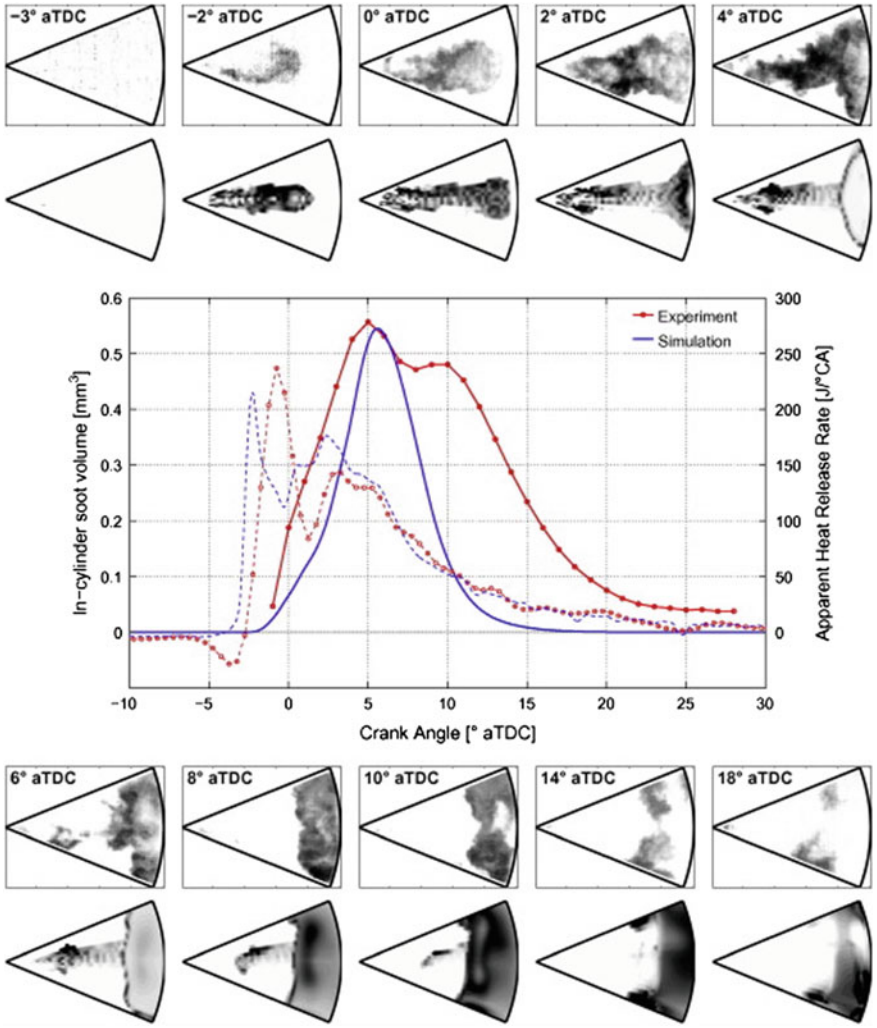

Fig. 9.5 In the centre evolution of soot volume (solid lines) and apparent heat release rate (dashed lines). Upper and lower spatial evolution of soot natural luminosity of experiment (upper row) and simulations (lower row). Figure from Bolla et al. (2014). Reprinted with permission from Elsevier

and ignition in engines. CMC solvers have been coupled to popular CFD software (OpenFOAM, StarCD, etc.) as well as myriad of academic in-house codes.

CMC can be extended to premixed combustion (not explained here) by selecting a reaction progress type variable. This can have applications in stratified combustion regimes and HCCI engines, albeit probably using conditioning on two variables. Conditioning on more than one scalar reduces the conditional fluctuations and therefore strengthens first-order closure hypothesis. Selecting an appropriate second

variable, extended CMC (or CMC-e) see Kronenburg and Kostka (2005); Ukai et al. (2015), permits to capture extinction. In the case of split injections, the second conditioning variable can be related to the 'age' or time between injections, see Shin and Richardson (2015) for details. However, there are major challenges from the theoretical viewpoint. In particular, the closure of the conditional cross-scalar dissipation model and how the model can be applied to different combustion regimes. MMC variants Klimenko and Pope (2003), simplified the scalar dissipation modelling and there is a growing trend to use Lagrangian-MMC approaches Cleary and Klimenko (2011) for non-premixed combustion.

The applications discussed in the paper have been in the context of low-Mach number flows, where the pressure solved is uncoupled from the equation of state. There are CMC formulations to compressible flows (Ciottoli 2013; Thornber et al. 2011), which can be of interest in the study of combustion instabilities. However, there have not been applications to high-speed combustion and this is still a fertile area of research,

Nevertheless, even with simplified formulations and uncertainties in sub-grid modelling, CMC has been able to reproduce finite-rate chemistry effects and turbulent-chemistry interactions in a myriad of laboratory flames and combustion engines. Due to its relatively low cost compared to more expensive PDF transport approaches, it allows a more detailed description of the chemical kinetics, including potentially large hydrocarbons. CMC development is going to be driven by the need of better prediction of pollutants in turbulent combustion systems. Its future lies in all types of non-premixed combustion systems, but in particular modelling of large combustion engines and aero-derived gas turbine combustors.

References

Ayache S, Mastorakos E (2011) Flow Turb Combust 88(1–2):207
Beguier C, Dekeyser I, Launder BE (1978) Phys Fluids 21(3):307
Bilger RW (1993) Phys Fluids A-Fluid Dyn 5:436
Bilger RW (2010) Combust Flame (2010)
Bilger RW (1993) Phys Fluids A 5:436
Bilger RW, Pope SB, Bray KNC, Driscoll J (2005) Proc Combust Inst 30(1):21
Bolla M, Farrace D, Wright YM, Boulouchos K (2014) Fuel 117:309
Borghesi G, Mastorakos E, Devaud CB, Bilger RW (2011) Combust Theor Model 15(5):725
Bottone F, Kronenburg A, Gosman D, Marquis A (2012) Flow Turb Combust 89(4):651
Branley N, Jones WP (2001) Combust Flame 127(1–2):1914
Bushe K, Steiner H (1999) Phys Fluids A 11:1896
Ciottoli PP (2013) Conditional moment for LES of compressible turbulent reactive flows. Sapienza University, Phd
Cleary MJ, Kent JH (2005) Combust Flame 143:357
Cleary MJ, Klimenko AY (2011) Phys Fluids 115102:1
Colucci P, Jaberi F, Givi P, Pope S (1998) Phys Fluids 10:499
De Paola G, Mastorakos E, Wright YM, Boulouchos K (2008) Combust Sci Technol 180(5):883
Devaud CB, Bray KNC (2003) Combust Flame 132(4):102
Devaud CB, Bray KNC (2003) Combust Flame 132:102

Fairweather A, Woolley R (2003) Combust Flame 133:393
Floyd J, Kempf AM, Kronenburg A, Ram RH (2009) Combust Theor Model 13(4):559
Fureby C (2009) Philosophical transactions. Ser A, Math Phys Eng Sci 367(1899):2957
Garmory A, Mastorakos E (2011) Proc Combust Inst 33:1673
Garmory A, Mastorakos E (2013) Int J Heat Fluid Flow 39:53
Garmory A, Mastorakos E (2015) Proc Combust Inst 35(2):1207
Girimaji SS (1992) Phys Fluids A 4:2529
Giusti A, Kotzagianni M, Mastorakos E (2016) Flow Turb Combust 97(4):1165
Hewson JC, Ricks AJ, Tieszen SR, Kerstein AR, Fox RO (2006) Conditional-moment closure with differential diffusion for soot evolution in fire. Tech Rep, Centre Turbulence Research
Jones WP, Navarro-Martinez S (2007) Combust Flame 150:170
Kim S, Huh Y (2002) Combust Flame 130:94
Kim S, Huh K, Fraser R (2000) Proc Combust Inst 28:185
Kim S, Huh K, Tao L (2000) Combust Flame 120:75
Klimenko AY, Bilger R (1999) Prog Energy Combust Sci 25:595
Klimenko AY, Pope SB (2003) Phys Fluids 15(7):1907
Klimenko AY (1990) Fluid Dyn 25:327
Klimenko AY (1995) Phys Fluids 7(2):446
Kronenburg A (2004) Phys Fluids 16(7):2640
Kronenburg A, Bilger RW, Kent JH (2000) Combust Flame 121:24
Kronenburg A, Bilger RW (2001) Combust Sci Technol 166(1):195
Kronenburg A, Kostka M (2005) Combust Flame 143(4):342
Kronenburg A, Mastorakos E (2010) The conditional moment closure method, vol 95. Springer Science & Business. Media, pp 91–114
Kronenburg A, Stein OT (2017) Flow Turb Combust 98(3):803
Kuo KK (1986) Principles of combustion. Wiley
Kuznetsov VR, Sabel'nikov VA (1990) Turbulent combustion. Taylor and Francis
Lignell D, Hewson J, Chen J (2009) Proc Combust Inst 32(1):1491
Løvås T, Navarro-Martinez S, Rigopoulos S (2011) Proc Combust Inst 863–889
Lu T, Law CK (2009) Prog Energy Combust Sci 35(2):192
Mastorakos E, Bilger R (1998) Phys Fluids 10:1246
Mortensen M, Bilger RW (2009) Combust Flame 156:62
Navarro-Martinez S, Kronenburg A (2007) Proc Combust Inst 31:1721
Navarro-Martinez S, Kronenburg A (2009) Proc Combust Inst 32:1509
Navarro-Martinez S, Kronenburg A (2011) Flow Turb Combust 87(2):377406
Navarro-Martinez S, Kronenburg A, di Mare F (2005) Flow Turb Combust 75:245
Navarro-Martinez S, Rigopoulos S (2011) Flow Turb Combust 89(2):311
O'Brien EE, Jiang TL (1991) Phys Fluids A 3:3121
Patwardhan SS, De S, Lakshmisha KN, Raghunandan BN (2009) Proc Combust Inst 32:1705
Peters N (1984) Prog Energy Combust Sci 10:319
Peters N (2000) Turbulent combustion. Cambridge University Press
Pitsch H (2006) Annu Rev Fluid Mech 38(1):453
Poinsot T, Veynante D (2001). Theoretical and numerical combustion. R.T. Edwards, Inc
Pope SB (2013) Proc Combust Inst 34(1):1
Roomina MR, Bilger RW (1999) Combust Theor Model 3:689
Roomina M, Bilger R (2001) Combust Flame 125:1176
Seo J, Huh KY (2011) Proc Combust Inst 33:2127
Shin DH, Richardson ES (2015) In: CD-Rom Proceedings. European Combustion Meeting, Hungary
Siwaborworn P, Kronenburg A (2013) Conservative implementation of LES-CMC for turbulent jet flames. Springer, Berlin Heidelberg, pp 159–173
Stanković I, Triantafyllidis A, Mastorakos E, Lacor C, Merci B (2011) Flow Turb Combust 86(2):689710

Swaminathan N, Bilger RW (2001) Combust Theor Model 5(2):241
Thornber B, Bilger RW, Masri AR, Hawkes ER (2011) J Comput Phys 230(20):7687
Triantafyllidis A, Mastorakos E (2009) Flow Turb Combust 84(3):481
Tyliszczak A (2013) Arch Mech 97–129
Ukai S, Kronenburg A, Stein OT (2015) Proc Combust Inst 35(2):1667
Woolley RM, Fairweather M (2009) Yunardi Fuel 88:393
Wright YM, Boulouchos K, Paola GD, Mastorakos E, Int SAE (2009) J Engines 2:714
Wright YM, DePaola G, Boulouchos K, Mastorakos E (2005) Combust Flame 143:402
Zhang H, Mastorakos E (2016) Flow Turb Combust 863–889
Zoby M, Navarro-Martinez S, Kronenburg A, Marquis AJ (2011) Int J Heat Fluid Flow 32(3):499

Chapter 10
Direct Numerical Simulation of Autoignition in Turbulent Non-premixed Combustion

Kedar G. Bhide and S. Sreedhara

Abstract Combustion in a CI engine is initiated by self-ignition of fuel–air mixture caused by high pressure and high temperature; a process known as autoignition. Autoignition is a challenging problem to simulate as the temperature increases from initial temperature to the adiabatic flame temperature in a very short duration. Numerical study of a turbulent flow using RANS/LES encounters a closure problem. Accuracy of closure models can be improved through experimental results, theoretical reasoning and direct numerical simulation (DNS) data. A review of DNS of autoignition in a turbulent non-premixed medium is presented in this chapter. As observed from DNS study, autoignition sites in a turbulent non-premixed medium are not randomly distributed but follow a pattern in the mixture fraction-scalar dissipation rate space. Turbulent flow is always three-dimensional in nature. 2D DNS of autoignition shows that ignition delay time increases with increase in initial turbulence intensity, which contradicts with the experimental observation. 3D DNS of autoignition resolves this conflict. The conflict is mainly due to the absence of vortex-stretching phenomenon in 2D DNS. Homogeneous charge compression ignition (HCCI) is being considered as one of the strategies toward improving performance of conventional CI engines. However, HCCI engines suffer from drawbacks like lack of control over combustion and limited operating regime. One of the modifications suggested in the HCCI technology to overcome these drawbacks is the use of stratification in the fuel–air mixture. Therefore, a few DNS studies on autoignition in the stratified medium have been discussed here. Further, discussion on the conditional moment closure (CMC) model and its validation using DNS data has been presented. Ignition delay time predicted by CMC was found to be in good agreement with DNS predictions.

Keywords DNS · Autoignition · CMC · HCCI · Charge stratification

K. G. Bhide · S. Sreedhara (✉)
IC Engines and Combustion Laboratory, Mechanical Engineering Department, Indian Institute of Technology Bombay, Mumbai 400076, India
e-mail: sreedhara.s@iitb.ac.in

© Springer Nature Singapore Pte Ltd. 2018

S. De et al. (eds.), *Modeling and Simulation of Turbulent Combustion*, Energy, Environment, and Sustainability, https://doi.org/10.1007/978-981-10-7410-3_10

Abbreviations

CFD	Computational Fluid Dynamics
CI	Compression Ignition
CMC	Conditional Moment Closure
DNS	Direct Numerical Simulation
HCCI	Homogeneous Charge Compression Ignition
HRR	Heat Release Rate
LES	Large Eddy Simulation
MR	Most Reactive
RANS	Reynolds-Averaged Navier–Stokes
SI	Spark Ignition
TDC	Top Dead Center
2D/3D	Two Dimensional/Three Dimensional

Nomenclature

c_P	Specific heat at constant pressure
D	Fickian diffusion coefficient
Da	Damköhler Number
$\mathrm{E_a}$	Activation energy of a reaction
h_r	Heat of reaction
Δh_α	Heat of formation of a species
H_F	Heat of combustion of fuel
N_S	Number of species
$Q(\eta; x, t)$	Conditional average of any scalar Y on $\xi = \eta$
R	Universal gas constant
T	Temperature
T_a	Activation temperature of a reaction (E_a/R)
T_{in}	Initial Temperature
u_{rms}	Root mean square value of velocity fluctuations
Y_i	Mass fraction of ith species
α, β	Indices of species
η	Sample space of ξ
θ	Excess temperature given by $(T - T_{in})c_P/h_r$
λ	Thermal Diffusivity
ξ	Mixture fraction (Eq. **2**)
ρ	Density
σ^2	Conditional variance of excess temperature θ
τ_{ign}	Ignition delay
τ_t	Integral timescale of turbulence
τ_0	Ignition delay in homogeneous mixture (or other reference timescale)
$\varphi_{\alpha\beta}$	Factor defined by Eq. **11**
χ	Scalar dissipation rate (Eq. 1)
$\dot{\omega}_i$	Chemical source term of ith species

Λ	Integral length scale of turbulence
Λ_k	Kolmogorov scale of turbulence
Λ_ξ	Integral scale of initial scalar distribution
$\mho$	Vortex locating index (Sect. 10.2.1)

10.1 Introduction

Combustion in practical devices like internal combustion engine, gas turbine takes place in a turbulent medium. Combustion in these devices can be initiated by (a) an external source, like in spark ignition (SI) engine or (b) self-ignition or autoignition, like in compression ignition (CI) engine. In CI engines, fuel is injected close to the top dead center (TDC) during compression stroke. Pressure and temperature of the air inside the cylinder at the time of injection is high (40–60 bar, 700–1000 K (Heywood 1988)). The fuel injected at this point through the injector atomises into smaller droplets and these droplets vaporize. Vaporized fuel mixes with surrounding hot and high pressure air. Due to high temperature and pressure, pockets of well-mixed fuel–air mixture undergo autoignition characterized by heat release which increases temperature and pressure in the chamber. This further facilitates vaporization of the incoming fuel (Heywood 1988). No external source is required to start the combustion. High temperature and pressure of air is sufficient to start the ignition once the fuel and air are mixed in the appropriate proportion. Nonlinear dependence of rate of reaction on temperature, through Arrhenius expression, is well-known. If the initial temperature, T_0, of fuel–air mixture is high enough to start a small reaction which generates heat, then this heat further increases the temperature of the mixture by a small amount. Increased temperature further accelerates the heat release. Temperature of the mixture increases rapidly after certain point in time and this process is known as autoignition (Mastorakos 2009). Ignition delay is an important parameter and is defined as the time between the start of injection and the start of combustion. Several definitions may be used to define the start of combustion, for example, the time of peak heat release. It is of the order of a *ms* in CI engines (Heywood 1988). Apart from CI engines, autoignition plays an important role in stabilizing turbulent jet flames with vitiated coflow as shown experimentally by Cabra et al. (2006).

Study of a perfectly mixed fuel–air mixture at initial temperature T_0 represents a zero dimensional study which ignores the effects of fluid dynamics on autoignition. Numerical (for example, Im et al. 2000) as well as experimental (for example, Fotache et al. 1997) studies help to understand fluid dynamic effects. Opposed jet flow configuration was generally used in many such studies. Fotache et al. (1997) in the experimental study of methane–air ignition observed that the temperature of the

air stream required for autoignition to occur, increased monotonically with increasing strain rate. Strain rate was calculated as the maximum gradient of axial velocity. Strain rate was considered as the inverse of characteristic flow timescale (Im et al. 2000). Strain rate was varied by varying fuel and oxidizer velocities. Im et al. (2000), in a numerical study, also observed that ignition delay increased with increasing strain rate. Beyond a certain value of the strain rate, called steady ignition limit, ignition did not occur. This dependence of ignition temperature or ignition delay on the strain rate is explained using a classical S-curve shown in Fig. 10.1 (Peters 2004). Ratio of characteristic flow timescale to the characteristic chemical timescale is known as Damköhler number (*Da*). As *Da* increases along the lower branch (increase in characteristic flow time), maximum temperature in the domain increases. At the critical point I, maximum temperature suddenly increases signifying a successful autoignition. Autoignition is not possible below this critical value Da_I. If one starts from higher branch and reduces *Da*, at the critical point E, maximum temperature suddenly drops indicating extinction of the flame. Im et al. (1999), in a numerical study, observed the influence of an unsteady velocity field on opposed jet diffusion flame. Scalar dissipation rate was proposed as another factor to represent the characteristic flow timescale. Scalar dissipation rate and strain rate were found to be correlated well with the change in imposed flow velocity. When an oscillating velocity field was imposed, the scalar dissipation rate was found to follow oscillating field better than the strain rate followed. Expression for scalar dissipation rate is given by Eq. (1), where λ denotes thermal diffusivity and ξ represents mixture fraction. Mixture fraction represents local fuel-oxidizer ratio and it changes from 0 in pure oxidizer to 1 in pure fuel. Transport equation of ξ does not contain a reaction term so it is defined appropriately based on the chemistry used in a study. For a single-step chemistry, ξ is defined as given by Eq. (2). $\beta = Y_F - r_{st}Y_{O,}$ where Y_F and Y_O are fuel and oxidizer mass fractions respectively. r_{st} is the ratio of mass of fuel to that of oxidizer in the stoichiometric mixture. High value of the scalar dissipation rate indicates high diffusive losses of species/temperature from a given location. Dimension of the scalar dissipation rate is s^{-1} and hence, local flow timescale can be taken to be low at the location of high scalar dissipation

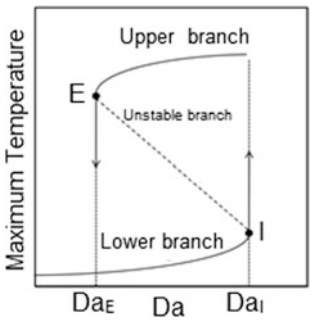

Fig. 10.1 S-curve showing a variation of maximum temperature in a well-stirred reactor with Damköhler number (Peters 2004)

rate. According to classical S-curve, autoignition may not be favored at such locations due to *Da* being smaller than the critical value, Da_I.

$$\chi = 2\lambda \left(\frac{\partial \xi}{\partial x}\right)\left(\frac{\partial \xi}{\partial x}\right) \tag{1}$$

$$\xi(x,t) = \frac{\beta(x,t) - \beta_{air}}{\beta_{fuel} - \beta_{air}} \tag{2}$$

As stated previously, combustion in practical devices takes place in a turbulent medium. In CI engines, turbulence affects atomization, vaporization, and mixing of fuel and air prior to the onset of autoignition. Experimental study by Mizutani et al. (1990) using shock tube demonstrated that turbulence promoted mixing of fuel–air and autoignition of column of cetane droplets occurred at 840 K and 10 bar that required a temperature of 1100 K to autoignite in the absence of turbulence. Ignition delay was also reduced with increase in turbulence intensity. However, still higher value of turbulence may inhibit autoignition by promoting heat loss from the igniting mixture. Therefore, the study of autoignition in a turbulent non-premixed medium becomes very important.

10.1.1 Numerical Modeling of Autoignition

Development of advanced CFD techniques along with upgraded computational facilities have allowed numerical study of not just autoignition but also of large number of turbulent reacting flows. Numerical approaches used for such studies and for turbulent flows in general are Reynolds-Averaged Navier–Stokes (RANS), large eddy simulation (LES), and direct numerical simulation (DNS). It is well known that details of the solution obtained at the end increase from RANS to DNS, but computational effort and grid resolution required also increase in the same order. RANS and LES suffer from closure problems where closure models are required for some of the terms in the governing equations. DNS approach tries to capture all the fluctuations of a variable at a point. Instantaneous, full set of Navier–Stokes equations are solved without using any closure models. Hence, DNS studies can be used to assess the accuracy of closure models used in the RANS/LES. Models used in the RANS/LES of non-premixed combustion have been discussed in the textbook by Poinsot and Veyante (2005).

Liñán and Crespo (1976) investigated autoignition in one-dimensional laminar mixing layer and introduced the concept of "most reactive mixture fraction", denoted as ξ_{MR}. This theory has been found to be valid under turbulent conditions also as seen from the DNS studies discussed in this chapter. The theory states that reaction starts at a location where mixture fraction ξ has attained the value of ξ_{MR}. It

may be understood qualitatively by using a single-step, second-order reaction. Rate of fuel consumption in such a reaction in terms of ξ is given by Eq. (3).

$$\dot{\omega}_F \propto \xi(1-\xi)\exp\left[\frac{-T_a}{T_{air}-\xi(T_{air}-T_F)}\right] \tag{3}$$

When T_{air} is equal to T_F, rate of fuel consumption reaches maximum at $\xi = 0.5$. When $T_{air} > T_F$, the exponential dependence of fuel consumption on temperature causes the peak to shift toward leaner and hotter ($\xi < 0.5$) mixtures. This value of ξ could be other than the stoichiometric mixture fraction ξ_{st}. Thus, the value of ξ_{MR}, where fuel consumption reaches maximum, is decided by T_a, T_{air}, and T_F in a second-order reaction.

10.2 Direct Numerical Simulation

As discussed in the previous section, DNS tries to capture all the fluctuations in a variable at a point. It requires a domain to be large enough to resolve large scales and a mesh to be fine enough to resolve smallest of the scales. In a domain of size L that has been discretized into N points in each direction, cell size becomes $\Delta x = L/N$. Domain length L should be greater than the integral scale $\bigwedge$ and the mesh size Δx should be smaller than the Kolmogorov scale $\bigwedge_k$. Combination of these restrictions leads to a criterion that determines the highest turbulent Reynolds number flow that can be solved using a given mesh size (Poinsot and Veyante 2005). It is given by Eq. (4). Re_T is defined based on $\bigwedge$ and u_{rms}. In addition to scales of turbulence, important length scales of combustion, such as flame thickness, should be resolved properly by the grid size used in a DNS study.

$$\mathrm{Re}_T < N^{4/3} \tag{4}$$

A mesh size of the order of microns is often used in DNS studies. Such a small mesh size takes the total number of grid points over a million even in a domain size of a few mm^3. Such a large number of grid points pose challenges to computation time as well as storage. DNS of real scale geometries is not yet possible due to these challenges. Therefore, DNS is usually carried out over a cubic domain where temperature, pressure, fuel distribution, and flow timescale are representative of practical devices. In addition to a small mesh size, DNS demands smaller time step to capture wide range of timescales. Explicit time stepping is often used in DNS and time step is decided by the conventional Courant–Friedrich–Lewy (CFL) number (Moin and Mahesh 1998). In a reacting flow, chemical timescales may be smaller than flow timescales. In such a scenario, fractional time stepping method may be used. A smaller time step for reaction terms and a larger time step for flow may be used in this technique (for example, Sreedhara and Lakshmisha 2000).

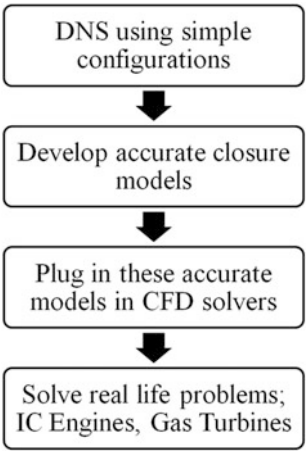

Fig. 10.2 Use of DNS in solving industrial problems like IC engines

Figure 10.2 shows the steps in developing new closure models using DNS and finally plugging these accurate closure models in commercial CFD packages to solve industrial problems. RANS simulations do not capture turbulent fluctuations and calculate only the averaged field. LES captures only large-scale fluctuations. Therefore, the effect of turbulent fluctuations and the effect of small-scale fluctuations need to be modeled in RANS and LES studies, respectively. This is known as a closure problem. Since DNS captures all scales of turbulent fluctuations, data obtained from the DNS may be used to assess the accuracy of existing closure models or to build new closure models. Assessment of accuracy of the CMC model has been discussed in Sect. 10.4 of this chapter.

10.2.1 DNS Studies of Autoignition

DNS studies of autoignition in a turbulent non-premixed medium have been reviewed in this section. Different configurations have been used by several authors. These configurations are provided in Table 10.1.

In an early two-dimensional (2D) DNS study, Mastorakos et al. (1997) simulated the autoignition of CH_4-air mixture using a single-step chemistry. This study revealed some of the fundamental aspects of autoignition in a turbulent medium, which have been confirmed by 3D DNS and using multistep chemistry in later studies. This study concluded that the autoignition in turbulent non-premixed medium occurs at a location where (a) mixture fraction has attained a value of most reactive mixture fraction and (b) conditional scalar dissipation rate is low. This aspect has been better explained by taking joint conditional mean of reaction rate conditioned on mixture fraction and scalar dissipation rate ($\langle \dot{\omega}_F | \xi, \chi \rangle$) by Sreedhara and Lakshmisha (2000) and is shown in Fig. 10.3a. It should be noted that the study

Table 10.1 Configurations considered in the DNS of autoignition

Author	Description
Mastorakos et al. (1997)	(a) Shearless mixing layer between fuel and air (b) Fuel slab surrounded by air on two sides
Sreedhara and Lakshmisha (2000, 2002a)	Parcels of relatively colder fuel dispersed randomly in the hot surrounding air
Yoo et al. (2011)	Fuel jet surrounded by highly heated coflow of air

of Sreedhara and Lakshmisha (2000) used a different configuration as shown in Table 10.1. In another study, Sreedhara and Lakshmisha (2002a) performed a 3D DNS of autoignition using single-step chemistry of *n*-Heptane–air. They observed that, similar to a 2D DNS, autoignition spots in a 3D DNS occur at a location where low conditional scalar dissipation rate and most reactive mixture fraction are jointly present. However, they also mentioned that for a multistep chemistry, it is not possible to have a unique value of ξ_{MR}. This was attributed to the different activation energies of different reactions which are active during the stages of combustion. Mastorakos et al. (1997) also observed that the turbulent flow ignited earlier than the laminar flow. It was proposed that since turbulence creates wide range of $\chi|\xi_{MR}$ (conditional scalar dissipation rate conditioned on most reactive mixture fraction), there exist some regions where $\chi_{turb}|\xi_{MR}$ is smaller than $\chi_{lam}|\xi_{MR}$. Such regions ignite earlier in turbulent flow. Partial premixing in the presence of turbulence also reduced the ignition delay. Partial premixing reduces $\partial\xi/\partial x$ and thus $\chi|\xi_{MR}$ which causes earlier ignition. A fuel slab of finite width surrounded by air on both sides showed earlier ignition compared to shearless mixing layer case in this study. Also, delay increased with increasing width of the slab. Lower width resulted in faster decay of $\chi|\xi_{MR}$ through faster mixing and ignited earlier. Mukhopadhyay and Abraham (2012) studied the autoignition of *n*-Heptane–air mixing layer using multistep chemistry capable of capturing two-stage ignition of *n*-Heptane. Two-stage autoignition of *n*-Heptane has been illustrated in Fig. 10.6. Autoignition in a turbulent medium was observed to occur earlier than in a laminar medium. Only high temperature autoignition was influenced by turbulence. Heat release from a low temperature ignition showed a weak negative correlation with the scalar dissipation rate, whereas high temperature autoignition was observed to occur at the location of low scalar dissipation rate. Yoo et al. (2011) studied the role of autoignition in stabilizing a lifted jet flame surrounded by hot coflow. Flame height showed a sawtooth variation with time characterized by a slow movement in the downstream direction and a sudden movement in the upstream direction. DNS data showed that sudden drop in the flame height occurs simultaneously with reducing scalar dissipation rate. Contours of OH showed igniting kernels near the exit of the jet. These kernels reduce the flame height. Kernels are eventually convected downstream by high axial jet velocity. This explains the sawtooth movement of the flame height.

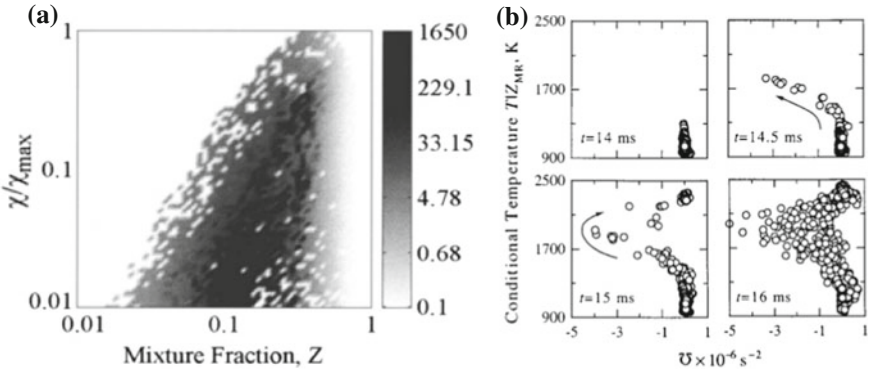

Fig. 10.3 **a** Joint conditional mean of reaction rate ($\langle \dot{\omega}_F | \xi, \chi \rangle$) at the instant of first appearance of autoignition spots **b** scatter plot of $T|\xi_{MR}$ and vortex location index $\mho$ at different times around first appearance of ignition spots. Both pictures are reprinted from Sreedhara and Lakshmisha (2000), by permission of the Combustion Institute

Sreedhara and Lakshmisha (2000, 2002a) further examined the location of autoignition spots relative to vortical structures. A new Index $\mho$ was defined that shows whether a location belongs to a vorticity dominated core ($\mho < 0$) or a strain-dominated tail ($\mho > 0$) regions. Temperature conditioned at most reactive mixture fraction is plotted as a function of $\mho$ in Fig. 10.3b. As shown in Fig. 10.3b, the reaction starts at 14.5 ms in the core region where strain rate is low (hence low χ). During vigorous burning stage, hot gases move toward the strain-dominated tail region (15 ms). The constant density simulation did not show such a movement of autoignition spots in T-$\mho$ plane. Autoignition occurred in core as well as in tail regions with equal probability when constant density was assumed. Therefore, density fluctuations were considered to be responsible for this movement of autoignition spots in T-$\mho$ plane. Krisman et al. (2017) recently studied the autoignition in a temporally evolving planar jet of *n*-Heptane in a stationary layer of air at high pressure using 3D DNS. Four-step chemistry capable of reproducing two-stage ignition of *n*-Heptane was used. Low temperature heat release was found to occur in strain-dominated regions of vortices. High temperature ignition was found to occur in the vorticity dominated core regions of vortices. Different criteria were used by Sreedhara and Lakshmisha (2000) and Krisman et al. (2017) to determine the local vortical structures in their respective studies.

In another 2D DNS study, Krisman et al. (2016) studied the two-stage ignition of dimethyl ether in a shearless mixing layer. Low temperature ignition was observed to occur at a location where mixture fraction is leaner than stoichiometric and the scalar dissipation rate is low. Strong negative correlation of heat release in the low temperature ignition with the scalar dissipation rate was observed. This low temperature ignition initiated a diffusively supported flame or deflagration, which traveled toward richer values of mixture fraction. This passage of diffusively supported flame was found to affect the high temperature ignition.

10.2.1.1 Influence of Turbulence Parameters on Ignition Delay

Im et al. (1998), Hilbert and Thevenin (2002), and Sreedhara and Lakshmisha (2000, 2002a) studied the influence of various turbulence parameters on autoignition in a turbulent non-premixed medium using DNS. These parameters include intensity of turbulence (u_{rms}), integral scale of turbulence ($\bigwedge$), integral timescale of turbulence ($\tau_t = \bigwedge/u_{rms}$) and integral scale of initial scalar distribution ($\wedge_\xi$). Im et al. (1998) performed 2D DNS of hydrogen–air mixing layer. Ignition delay for laminar case (τ_0) was used as a reference timescale. Three levels of turbulence were studied by changing $\bigwedge$ such that $\tau_t/\tau_0 \approx 0.3$, 1, and 3. For $\tau_t/\tau_0 \geq 1$, ignition delay (τ_{ign}) was found to be unaffected by change in τ_t. However, for $\tau_t/\tau_0 \approx 0.3$, increase in τ_{ign} was observed compared to previous two cases. Hilbert and Thevenin (2002) in a 2D DNS study changed $\bigwedge$ and u_{rms} simultaneously so that τ_t remained constant and τ_t/τ_0 was equal to 2. τ_{ign} was found to be independent of changes in $\bigwedge$ and u_{rms} in this study. Using 2D DNS, Sreedhara and Lakshmisha (Sreedhara and Lakshmisha 2000) studied the effect of $\wedge_\xi$, in addition to τ_t, on τ_{ign}. Change in τ_t was brought about by changing u_{rms}. All the cases considered in this study had $\tau_t/\tau_0 > 1$ (τ_0 represents ignition delay corresponding to a homogeneous mixture). Ignition delay was found to increase with decrease in τ_t when the ratio $\wedge_\xi/\bigwedge$ was greater than 1. However, it became independent of τ_t when the ratio $\wedge_\xi/\bigwedge$ was less than 1. This dependence was clearly explained based on the variation of $\chi|\xi_{MR}$ with time. When the ratio $\wedge_\xi/\bigwedge$ was greater than 1, faster turbulence (lower τ_t) resulted in higher value of $\chi|\xi_{MR}$ and thus delayed the ignition. When the ratio $\wedge_\xi/\bigwedge$ was less than 1, all curves showing variation of $\chi|\xi_{MR}$ with time nearly collapsed together resulting in similar values of τ_{ign} independent of τ_t. Sreedhara and Lakshmisha (2002a) in a 3D DNS study comprehensively studied the effect of turbulence parameters on τ_{ign}. When the ratio $\wedge_\xi/\bigwedge$ was less than 1 and τ_t/τ_0 was low, τ_{ign} decreased with faster turbulence. However, the effect of τ_t on τ_{ign} diminished with increasing τ_t/τ_0. However, when $\tau_t/\tau_0 \simeq 1$, the ratio $\wedge_\xi/\bigwedge > 1$ made effect of τ_t more pronounced compared to the case where $\wedge_\xi/\bigwedge < 1$. Based on this 3D study, influence of different parameters can be summarized as in Table 10.2. Two regimes of autoignition are possible (a) mixing controlled and (b) kinetics controlled (Sreedhara 2002). When the ratio τ_t/τ_0 was low, mixing of fuel with air controlled the rate of reaction. Faster turbulence facilitated this enhanced mixing and decreased the ignition delay. In kinetics controlled regime ($\tau_t/\tau_0 \approx 1$), mixing is not the rate limiting process. A few well-mixed spots were sufficient to start the ignition.

Table 10.2 Influence of decreasing τ_t on τ_{ign} based on 3D DNS

	$\tau_t > \tau_0$	$\tau_t < \tau_0$
$\wedge_\xi/\bigwedge < 1$	Largely unaffected	τ_{ign} decreases with decreasing τ_t
$\wedge_\xi/\bigwedge > 1$	τ_{ign} decreases with decreasing τ_t	Case not considered

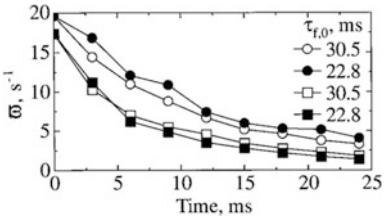

Fig. 10.4 Variation of ϖ with time in 2D (●, ○) and 3D (■, □) simulation. τ_t denoted by $\tau_{f,0}$ in this figure. Reprinted from Sreedhara and Lakshmisha (2002), by permission of the Combustion Institute

Effect of dimensionality (2D/3D) of DNS on the influence of τ_t on autoignition was also studied by Sreedhara and Lakshmisha (2002a). The 2D case ignited later than the 3D case for the same initial conditions. Also in 2D case, τ_{ign} increased with decreasing τ_t contrary to 3D cases discussed above. Increasing u_{rms} strengthens two opposing mechanisms (a) increased mixing of fuel–air promoting growth of ξ_{st} and (b) increased conditional scalar dissipation rate ($\chi|\xi_{st}$). A factor ϖ was proposed by Sreedhara and Lakshmisha (2002a) to determine relative strengths of these two effects. Lower value of ϖ favors earlier autoignition. Figure 10.4 shows a variation of ϖ with time in a 2D and a 3D DNS at two values of τ_t. Effect of decreasing τ_t on ϖ is opposite in a 2D and a 3D DNS. Also, value of ϖ in a 2D DNS is always higher than that in a 3D DNS. Therefore, the influence of decreasing τ_t is opposite in a 2D DNS and a 3D DNS. 3D turbulence promoted mixing due to the presence of vortex-stretching phenomenon in 3D turbulence, which is absent in 2D turbulence.

In spite of using different configurations as given in Table 10.1, several features of autoignition in a turbulent medium, such as autoignition spots originate at a mixture having most reactive mixture fraction and having low conditional scalar dissipation rate, remained the same. Effect of turbulence on ignition delay is also not influenced by the configuration of the problem. Ignition delay is mainly influenced by the regimes of autoignition, viz., mixing controlled regime or kinetics controlled regime.

10.3 Homogeneous Charge Compression Ignition Engine

Simultaneous reduction of NO_x and soot in conventional CI engines is a challenging goal. Higher temperatures promote formation of NO_x. In a conventional CI engine, a few well-mixed spots are present where temperature goes to high value and NO_x is formed. A few spots of fuel-rich mixtures may also exist where soot forms due to insufficient amount of oxidizer. Homogeneous charge compression ignition (HCCI) is being suggested as one of the strategies to overcome this problem (Yao et al. 2009). Fuel and air are well mixed, like in conventional SI

engine, before the combustion occurs in an HCCI engine. Because of premixing, formation of soot can be avoided. Also, lower equivalence ratio reduces NO_x emissions because of lower in-cylinder temperature. However, due to premixing of fuel–air, HCCI engine suffers from lack of control over combustion. Also, at higher loads, excessive pressure rise takes place which can damage the engine (Dec 2009). It may be noted that, if the fuel–air mixture is truly homogeneous, then the autoignition may be controlled solely by chemical kinetics. Since the kinetics is affected by pressure, temperature, and concentration of reactants, creating inhomogeneous mixture or stratification (in terms of local temperature and/or local equivalence ratio) may assist in controlling the combustion in an HCCI engine (Yao et al. 2009). Therefore, a few DNS studies on autoignition in a HCCI-like environment are discussed in the following section.

10.3.1 DNS of Combustion in HCCI Engines

Zeldovich (1980) identified two regimes of combustion in an inhomogeneous mixture (a) spontaneous ignition, where autoignition occurs successively at neighboring locations due to difference in autoignition delay time, which may appear like a propagating flame and (b) deflagration, where flame actually propagates in the mixture with reactive–diffusive balance. Zeldovich (1980) proposed that speed of this deflagration is inversely proportional to $|\nabla T|$. Possibility of deflagration in HCCI engine has been confirmed by experiments as well (for example, Kaiser et al. 2002). DNS studies of autoignition in HCCI-like environment also show this possibility of deflagration (Sankaran et al. 2005; Chen et al. 2006; Hawkes et al. 2006; Bansal and Im 2011). These studies highlight the importance of $|\nabla T|$ in determining the combustion regime. Therefore, it is of interest to study the factors which determine the regimes of combustion. Deflagration is characterized by a quantity called displacement speed given by Eq. (5), where ϕ is any reactive scalar (for example, one of the species mass fractions). Numerator in this equation is the sum of a diffusion and a reaction contribution to the propagation of the ϕ iso-contour. For deflagration in a purely premixed medium, balance between these two contributions should exist.

$$S_d = \frac{\nabla(\rho D_\phi \nabla \phi) + \dot{\omega}_\phi}{\rho |\nabla \phi|} \tag{5}$$

Figure 10.5 obtained by Chen et al. (2006), in a 2D DNS of ignition of inhomogeneous H_2-air mixture, shows this reactive–diffusive balance at different locations (A, B, and C) in the domain. Reaction term is almost of a constant magnitude (H_2 is being consumed). Contribution of diffusion is increasing from location A to location C with increase in local temperature gradient. At very high temperature gradient (location C), reaction and diffusion terms are balancing each

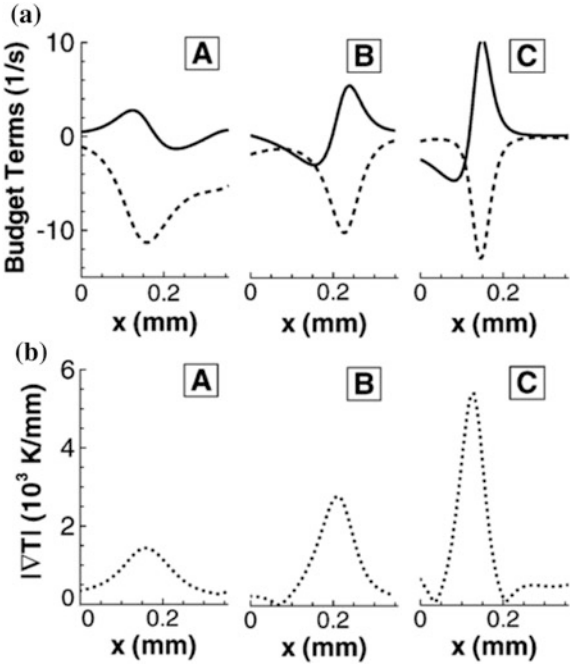

Fig. 10.5 **a** Structure of reaction–diffusion balance for H_2. Dashed line: Reaction, Solid line: Diffusion **b** local temperature gradient at different locations A, B, and C in the domain. Reprinted from Chen et al. (2006), by permission of Elsevier

other. Scatter plot of density weighted S_d, denoted by S_d^*, ($S_d^* = \rho S_d/\rho_0$), and $|\nabla T|$ in the same study (not shown here) confirms the inverse relation between S_d^* and $|\nabla T|$. Here, ρ_0 is a representative density of the reactants. However, S_d^* did not decrease indefinitely but attained a value close to the laminar flame speed at high $|\nabla T|$. Also at low $|\nabla T|$, S_d^* increased sharply (5–6 times the laminar flame speed) indicating spontaneous ignition. Therefore, the magnitude of S_d^* was established as a criterion to distinguish between these two regimes. Hawkes et al. (2006) investigated the effect of increase in fluctuations of initial temperature field. With increase in temperature fluctuations, deflagration mode became more prominent. This was due to availability of increased value of $|\nabla T|$ in the domain. In these studies (Sankaran et al. 2005; Chen et al. 2006; Hawkes et al. 2006) equivalence ratio was uniform in the domain and only temperature fluctuations were considered. Bansal and Im (2011) performed 2D DNS of H_2-air combustion wherein equivalence ratio fluctuations were also introduced. Two types of initial distributions were considered (a) uncorrelated temperature and equivalence ratio and (b) negatively correlated equivalence ratio and temperature. The case with uncorrelated field showed a deflagration mode whereas the case with negative correlation burned more homogeneously. Hence, it was concluded that combustion mode can be changed by changing initial correlation between temperature and equivalence ratio.

10.3.1.1 Heat Release Rate in HCCI Engine

As discussed previously, HCCI engine suffers from a drawback of excess pressure rise at higher loads. Pressure rise is controlled by the heat release rate during the combustion process. Therefore, heat release rate (HRR) in HCCI-like medium and factors influencing the HRR are discussed in this section. Introduction of stratification (temperature and/or equivalence ratio) extends the duration of HRR with lower peak values of HRR (Bansal and Im 2011; Yoo et al. 2011, 2013; Talei and Hawkes 2015). Due to the stratification, there are fewer sites which are about to autoignite at a given instant and this is responsible for prolonging the heat release. As discussed previously, Bansal and Im (2011) observed that the HRR profile in the negatively correlated temperature-equivalence ratio field was closer to the HRR observed in the homogeneous case. This was due to the absence of deflagration and hence homogeneous combustion occurred in the whole domain. Thus, the deflagration mode of combustion promotes smoothening of HRR.

Heavier hydrocarbons like *n*-Heptane show a two-stage ignition at lower initial temperatures. Also, there exists a negative temperature coefficient (NTC) regime where ignition delay increases with increase in initial temperature. Variation of ignition delay with temperature is shown in Fig. 10.6 for *n*-Heptane–air mixture. *n*-Heptane is used as a reference fuel to study autoignition and engine knock in CI engine, because the Cetane number of *n*-Heptane, approximately 56, is closer to that of commercially available diesel fuel (Curran et al. 1998). Yoo et al. (2011) studied the effect of temperature stratification on HRR at mean temperatures of 1008, 934, and 850 K (shown in Fig. 10.6).

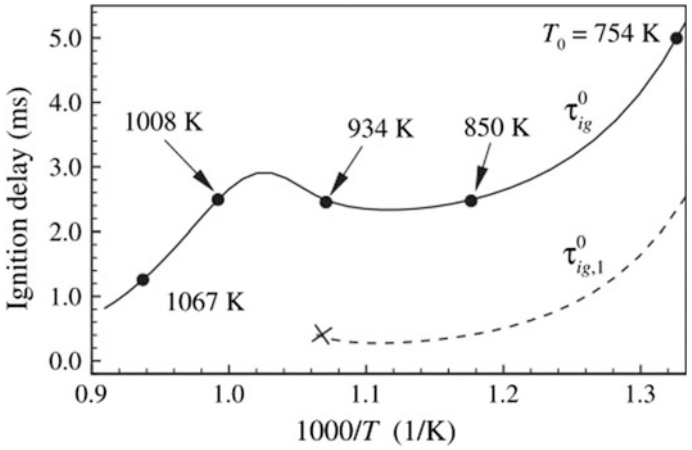

Fig. 10.6 Homogeneous ignition delay for *n*-Heptane–air mixture at constant volume and initial pressure of 40 bar as a function of initial temperature. Solid line: Stage two ignition delay, Dashed line: Stage one ignition delay. Reprinted from Yoo et al. (2011), by permission of Elsevier

For 1008 K case ignition delay decreased with increasing temperature stratification and an opposite trend was observed for 850 K case. 934 K case showed non-monotonic behavior. Also, the effect of stratification on 934 K, though a non-monotonic, was less pronounced compared to other two cases. Since the ignition delay is a function of initial temperature, a range of possible ignition delays exist in the domain based on the initial temperature distribution. It was shown that 1008 and 850 K case initially contained larger range of ignition delays. Since 934 K is located at the middle of NTC regime, it contained only a small range of ignition delays. This was the reason for less pronounced effect of stratification on 934 K case. Effect of stratification on low mean temperature case (754 K) was also not prominent because the turbulence could have homogenized the initial stratified field before the ignition occurred. The ratio τ_t/τ_0 was 0.5 in 754 K case. In another study, Yoo et al. (2013) investigated the effect of spark timing on combustion in a stratified medium using 2D DNS of *iso*-Octane-air mixture. Spark was provided in the form of high temperature zone at the center of the domain. Use of spark brought the ignition earlier. Pressure rise rate was smoother with earlier ignition. This was due to the deflagration wave started by the spark. However, the effect of spark timing on the pressure rise was not as noticeable as that observed with increase in temperature stratification. Yu and Bai (2013) investigated the effect of flow dimensionality (2D/3D) on the HRR in a stratified medium using DNS of H_2-air mixture. 3D case was found to ignite slightly later than 2D case and also heat release was more rapid in 3D case. As discussed in Sect. 10.2.1.1, in mixing controlled regime, 3D case brought about faster mixing of fuel–air. Temperature fluctuations in 3D case dropped faster than 2D case and hence the 2D case ignited earlier due to the presence few pockets having high temperature (Fig. 10b in Yu and Bai 2013). Stratified medium considered by Yu and Bai (2013) had uniform equivalence ratio and only temperature fluctuations were present. Also, due to better mixing in 3D case, heat release rate in the 3D case rises rapidly similar to that found in homogeneous combustion.

Talei and Hawkes (2015) performed 2D DNS of *n*-Heptane–air mixture with initial conditions like pressure, mean temperature, and mean equivalence ratio, almost same as those considered by Yoo et al. (2011). Talei and Hawkes (2015) considered stratification of initial equivalence ratio and maintained a negative correlation between initial temperature and equivalence ratio fields. Same reduced kinetic mechanism was used in both the studies. In all the cases considered by ignition occurred earlier with increasing temperature stratification. Equivalence ratio stratification was increased with temperature stratification by keeping their ratio constant. In the study by Yoo et al. (2011), the effect of increasing temperature stratification changed depending upon the mean initial temperature. Also, peak of heat release rate showed a non-monotonic behavior with increasing temperature stratification in the study by Talei and Hawkes (2015). Whereas, it decreased monotonically with increasing temperature stratification in the study by Yoo et al. (2011). Therefore, it can be said that an introduction of stratification in equivalence ratio along with temperature stratification changes the behavior of combustion in HCCI-like environment.

It may be noted from the above-reviewed publications that the stratification of temperature is a useful strategy in controlling the HRR in an HCCI engine. Temperature stratification promotes deflagration, which in turn, causes a smooth HRR in the domain. However, stratification of equivalence ratio along with that of temperature inhibits the deflagration mode of combustion. Temperature stratification inside combustion chamber is often created passively in an HCCI engine, resulting from mixing of bulk charge and boundary charge cooled by walls. Enhancing temperature stratification beyond naturally occurring stratification is a challenge (Dec 2009). Stratification of equivalence ratio may be controlled actively by controlling location and timing of injection of fuel.

10.4 Assessment of Conditional Moment Closure Model

Conditional moment closure (CMC) is one of the models proposed to capture turbulence–chemistry interaction without invoking any assumption on the flame structure. A discussion about CMC model and an assessment of its accuracy with DNS data has been presented in this section. The CMC model was independently proposed by Klimenko (1990) and Bilger (1993). It is well-known that variables like temperature, species mass fraction, fluctuate in time at a given location in a turbulent flow. CMC methodology assumes that these fluctuations can be associated with fluctuations of a single property, which is known as mixture fraction (ξ) in turbulent non-premixed combustion (Klimenko and Bilger 1999). The concept of CMC has been illustrated in Fig. 10.7. Figure 10.7 shows a scatter plot of a scalar Y and the mixture fraction ξ. Dashed line indicates an unconditional mean of Y. In CMC, mixture fraction space is divided into number of "bins" (or intervals) and the average of Y is calculated in that bin and is represented in Fig. 10.7 using hollow circles. It is called the conditional mean and denoted as $\langle Y|\xi=\eta\rangle$.It indicates the mean of values of Y subjected to the condition to the right of vertical line, i.e., $\xi = \eta$ is satisfied, where η is sample space of variable ξ. It may be clearly seen from Fig. 10.7 that the conditional fluctuations of Y are very small compared to unconditional fluctuations. In CMC, governing equations are solved for $\langle Y|\xi=\eta\rangle$.

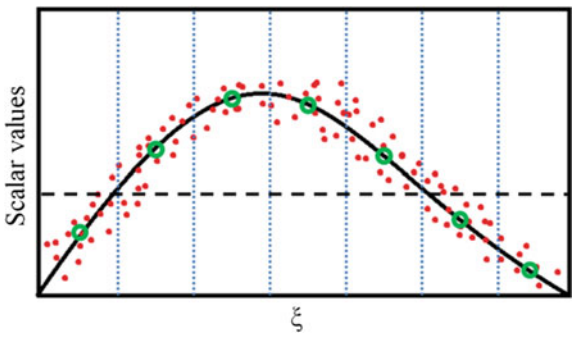

Fig. 10.7 Scatter plot (●) of a scalar Y and ξ. Solid line: Conditional mean of scalar Y conditioned on ξ, dashed line: Unconditional mean of scalar. ○ shows mean of respective bin

Variables calculated in the mixture fraction space are converted into variables in the physical space by using an appropriate probability density function of ξ. Discussion in this section closely follows Sreedhara (2002) and Sreedhara and Lakshmisha (2002a). CMC equations have been derived by Klimenko and Bilger (1999) in their review paper. In the next section, the CMC equations will be discussed.

10.4.1 CMC Equations

Governing equation of conditional mean of species mass fraction is given by Eq. (**6**). Q for any quantity is defined as $Q(\eta; x, t) = \langle Y|\eta\rangle$. In a spatially homogeneous and isotropic turbulence, advection terms vanish and momentum equations become zero after taking the average. Temperature is replaced by a suitably defined excess temperature $\theta = (T - T_{in})c_P/h_r$ where h_r is the heat of reaction. Governing equation of conditional mean of excess temperature is given by Eq. (**7**). Δh_α is the heat of formation of a species. In Eqs. (**6**)–(**7**), conditional mean of scalar dissipation rate ($\langle\chi|\eta\rangle$) and conditional mean of reaction rate ($\langle\dot{\omega}_\alpha|\eta\rangle$) require closure models. First, the model for reaction rate will be discussed.

$$\frac{\partial Q_\alpha}{\partial t} = \frac{1}{2}\langle\chi|\eta\rangle\frac{\partial^2 Q_\alpha}{\partial\eta^2} + \frac{1}{\rho}\langle\dot{\omega}_\alpha|\eta\rangle \quad (\alpha = 1, \ldots, N_S) \tag{6}$$

$$\frac{\partial Q_\theta}{\partial t} = \frac{1}{2}\langle\chi|\eta\rangle\frac{\partial^2 Q_\theta}{\partial\eta^2} + \frac{1}{\rho h_r}\frac{\partial Q_p}{\partial t} - \frac{1}{\rho h_r}\sum_{\alpha=1}^{N_S}\Delta h_\alpha\langle\dot{\omega}_\alpha|\eta\rangle \tag{7}$$

Closure of reaction rate can be expressed in terms truncated series approximation, as given by Mastorakos and Bilger (1998). It is given by Eq. (8). Here, $\Theta_0(\eta) = T_{in}^2(\eta)c_p/T_a H_F$ and H_F is the heat of combustion of fuel. Quantity σ^2 is conditional variance of temperature $\langle\theta''^2|\eta\rangle$ where $\theta'' = \theta - Q_\theta$. Additional governing equation for σ^2 is also given by Mastorakos and Bilger (1998) (not given here). Closure for conditional scalar dissipation rate has been given by Mell et al. (1994) and is given in Eq. (**9**).

$$\langle Y_\alpha Y_\beta \exp\frac{\theta}{\Theta_0(\eta)}|\eta\rangle = Q_\alpha Q_\beta\left[1 + \frac{\sigma^2}{2\Theta_0^2(\eta)}\right]\exp\frac{Q_\theta}{\Theta_0(\eta)} \tag{8}$$

$$\langle\chi|\eta\rangle = \chi_m \exp[-2\{erf^{-1}(2\eta - 1)\}^2] \tag{9}$$

Sreedhara and Lakshmisha (2002a) have given alternative closure models for reaction rate and scalar dissipation rate. Equation (8) involves assumption of small value of θ. However, this assumption breaks down during autoignition, especially during rapid heat release phase. Therefore, a new closure model was proposed which does not require this assumption. Instead, it assumes θ'' to be small which

holds good even during the rapid heat release phase. Final closure of reaction rate proposed by Sreedhara and Lakshmisha (2002a) is given in Eq. (**10**). Here $\Theta(\eta) = Q_T^2 c_P / T_a h_r$. Factor $\varphi_{\alpha\beta}$ has been introduced to take into account effects of species fluctuations and is given by Eq. (**11**). This factor was found to be important mainly when multistep chemistry was used. Model for $\varphi_{\alpha\beta}$ was also proposed by Sreedhara and Lakshmisha (2002b) (not given here). Equation (**9**) for conditional scalar dissipation rate assumes constant value of χ_m. However, based on DNS data of homogeneous decaying turbulence (Sreedhara and Lakshmisha 2000), it was observed that scalar dissipation rate decays with time (Fig. 6 in Sreedhara and Lakshmisha 2000, not shown here). This is true only for decaying turbulence. When the turbulence is externally forced, χ_m may remain constant. Therefore, $\chi_m = \chi_{m0}\exp(-2t/\tau_{t0})$ was proposed by Sreedhara and Lakshmisha (2002b). χ_{m0} and τ_{t0} are initial values of χ_m and integral timescale of the turbulence, respectively.

$$\langle Y_\alpha Y_\beta \exp\frac{\theta}{\Theta_0(\eta)} | \eta \rangle = \frac{Q_\alpha Q_\beta}{\varphi_{\alpha\beta}(\eta)} \left[1 + \frac{\varphi_{\alpha\beta}(\eta)\sigma^2}{2\Theta^2(\eta)} \right] \exp\left(\frac{-T_a}{Q_T} \right) \tag{10}$$

$$\varphi_{\alpha\beta}(\eta) = \frac{Q_\alpha Q_\beta}{\langle Y_\alpha Y_\beta | \eta \rangle} \tag{11}$$

10.4.2 Assessment of CMC Closure Models

Accuracy of CMC modeling was assessed by Sreedhara and Lakshmisha (2002b) using 3D DNS data related to autoignition of *n*-Heptane–air mixture. Single-step as well as four-step chemistry of *n*-Heptane–air was considered. Two types of CMC models, viz., CMC-I and CMC-II, were considered. $\langle \chi | \eta \rangle$ was modeled using Eq. (**9**) with χ_m being function of time in both the types of CMC.

(1) $\sigma^2 = 0$ and $\varphi_{\alpha\beta} = 1$ was used while calculating conditional reaction rate (CMC-I).
(2) σ^2 was obtained by solving its equation and model for $\varphi_{\alpha\beta}$ was used (CMC-II).

CMC-I ignores the effects of conditional temperature fluctuations and conditional species fluctuations.

Details of single-step and four-step chemistry used in Sreedhara and Lakshmisha (2002) are given in Tables 10.3, 10.4 and 10.5 for a quick reference. X and Y

Table 10.3 Single-step and four-step reaction mechanisms of *n*-C_7H_{16} -air

$n - C_7H_{16} + 11(O_2 + 3.76N_2) \rightarrow 8H_2O + 7CO_2 + 11 \times 3.76N_2 +$ Heat	(S1)
$n - C_7H_{16} \rightarrow X$	(R1)
$X + 11O_2 \rightarrow P$	(R2)
$n - C_7H_{16} + 2O_2 \leftrightarrows Y$	(R3F, R3B)
$Y + 9O_2 \rightarrow P$	(R4)

Table 10.4 Chemical kinetic parameters of reactions

Reaction	A (mm^3/mol.s or 1/s)	$T_a(K)$
S1	4.1×10^{14}	16000
R1	3.57×10^{8}	21650
R2	7.14×10^{13}	7220
R3F	1.07×10^{20}	21650
R3B	1.43×10^{21}	37285
R4	1.78×10^{15}	13230

Table 10.5 Heat of formation of species in the four-step mechanism

Species	n-C_7H_{16}	X	O_2	Y	P	N_2
Δh_α (MJ/kg)	−22.04	−7.92	0.0	−12.61	−10.42	0.0

represent the molecular groups ($3C_2H_4 + CH_3 + H$) and ($HO_2C_7H_{13}O + H_2O$), respectively. P represents final products ($7CO_2 + 8H_2O$). Heat of combustion for single-step mechanism was taken as 29.67 MJ/kg of fuel.

10.4.2.1 Single-Step Chemistry

Figure 10.8 shows comparison between evolution of conditional temperature (at $\eta = \xi_{MR}$) with time as predicted by DNS and CMC. Both CMC-I and CMC-II models successfully predict the evolution of conditional temperature. Also, initial value of Da had no effect on the accuracy of both these models. Even CMC-I predicted the correct variation of ignition delay with variation in initial integral timescale, i.e., decrease in ignition delay time with decrease in initial integral timescale of turbulence. However, CMC-I predicted an opposite trend (increase in ignition delay time with decrease in initial integral timescale of turbulence) to that observed in DNS when χ_m was kept constant. Also, deviation between CMC-I and CMC-II became prominent at higher initial values of χ_{m0}.

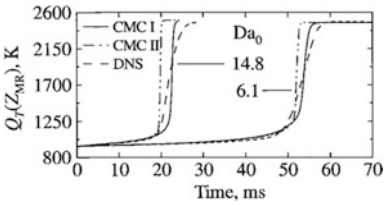

Fig. 10.8 Variation of conditionally averaged temperature with time at two different initial Da. Mixture fraction ξ denoted by Z in this figure. Reprinted from Sreedhara and Lakshmisha (2002), by permission of the Combustion Institute

10.4.2.2 Four-Step Chemistry

When multistep chemistry was used, CMC-I predictions deviated from the DNS data, whereas prediction of CMC-II was still in agreement with the DNS data. The value of the factor $\varphi_{\alpha\beta}$ was evaluated by comparing it against the data obtained from DNS. Its value was indeed found to be more than 1 for X-O pair when multistep chemistry was used. However, it was found to be 1 for single-step chemistry. Therefore, the effect of fluctuations in species mass fraction cannot be neglected in the problems involving multistep chemistry.

10.5 Conclusions

Several DNS studies of autoignition in a turbulent non-premixed medium were discussed in this chapter. Combustion in HCCI engine as an extension of conventional CI engines was also discussed. Finally, the use of DNS data in assessing the accuracy of closure models was presented. Major findings may be summarized as follows:

(1) Fluid dynamic effects on autoignition in laminar as well as in turbulent flows cannot be neglected. These effects become more important in turbulent medium where variables are fluctuating with time.
(2) DNS data has shown that autoignition in a turbulent non-premixed medium occurs when two conditions are jointly satisfied (i) mixture fraction attains a value of most reactive mixture fraction and (ii) conditional scalar dissipation rate is low. Also, with respect to fluid dynamic structures, autoignition spots appear at the vorticity dominated cores of vortices and combusting gases move toward the strain-dominated periphery.
(3) Most DNS studies on autoignition referred in this chapter relied on simplified chemistry and single-stage autoignition. However, few studies considering two-stage autoigntion using multistep chemistry were also discussed. Location of autoignition spots relative to local vortical structure was found to be similar in both types of studies.
(4) Two regimes of autoignition can be identified (i) mixing controlled and (ii) kinetics controlled. In the mixing controlled regime, rate of mixing controls the rate of reaction. Integral timescale is shorter than the characteristic ignition delay in this regime. In the kinetics controlled regime, integral timescale is longer than the characteristic ignition delay and a few well-mixed spots are sufficient to start combustion. Influence of integral timescale on ignition delay depends on these regimes of combustion.
(5) 2D DNS predicts an increase in ignition delay with decrease in integral timescale which contradicts experimental observations. 3D DNS settles this contradiction and predicts decrease in ignition delay with decrease in integral

timescale. The mechanism of vortex-stretching is responsible for this discrepancy between 2D and 3D DNS.

(6) Homogeneous charge compression ignition engine is an improvement over the conventional CI engine. Control of start of combustion in a truly homogeneous mixture of fuel–air is not possible and therefore the stratification is introduced in the mixture. DNS study of autoignition in HCCI-like medium reveals a possibility of the deflagration mode of combustion, which can smoothen the heat release rate. Correlation between initial equivalence ratio and temperature fields also affects the heat release rate.

(7) Data obtained from a DNS may be used to assess the accuracy of closure models used in RANS/LES. This application of DNS was demonstrated using study of the CMC model. If the right model for the scalar dissipation rate is used, first-order CMC can produce accurate results. However, with multistep chemistry, first-order CMC is inadequate.

Acknowledgements Most of these works were carried out by one of the authors, during his PhD, under the supervision of Prof. K. N. Lakshmisha, IISc, Bangalore.

References

Bansal G, Im HG (2011) Autoignition and front propagation in low temperature combustion engine environments. Combust Flame 158:2105–2112. https://doi.org/10.1016/j.combustflame.2011.03.019

Bilger RW (1993) Conditional moment closure for turbulent reacting flow. Phys Fluids A Fluid Dyn 5:436–444. https://doi.org/10.1063/1.858867

Cabra R, Myhrvold T, Chen J-Y et al (2006) Simultaneous laser raman-rayleigh-lif measurements and numerical modeling results of a lifted turbulent H_2/N_2 jet flame in a vitiated coflow. Combust Sci Technol 178:1001–1030. https://doi.org/10.1080/00102200500270106

Chen JH, Hawkes ER, Sankaran R et al (2006) Direct numerical simulation of ignition front propagation in a constant volume with temperature inhomogeneities: I fundamental analysis and diagnostics. Combust Flame 145:128–144. https://doi.org/10.1016/j.combustflame.2005.09.017

Curran HJ, Gaffuri P, Pitz WJ, Westbrook CK (1998) A comprehensive modeling study of n-Heptane oxidation. Combust Flame 114:149–177. https://doi.org/10.1002/kin.20036

Dec JE (2009) Advanced compression-ignition engines—understanding the in-cylinder processes. Proc Combust Inst 32 II:2727–2742. https://doi.org/10.1016/j.proci.2008.08.008

Fotache CG, Kreutz TG, Law CK (1997) Ignition of counterflowing methane versus heated air under reduced and elevated pressures. Combust Flame 108:442–470. https://doi.org/10.1016/S0010-2180(97)81404-6

Hawkes ER, Sankaran R, Pebay PP, Chen JH (2006) Direct numerical simulation of ignition front propagation in a constant volume with temperature inhomogeneities: II Parametric study. Combust Flame 145:145–159. https://doi.org/10.1016/j.combustflame.2005.09.018

Heywood JB (1988) Internal combustion engine fundamentals. Mcgraw Hill Education

Hilbert R, Thévenin D (2002) Autoignition of turbulent non-premixed flames investigated using direct numerical simulations. Combust Flame 128:22–37. https://doi.org/10.1016/S0010-2180(01)00330-3

Im HG, Chen JH, Law CK (1998) Ignition of hydrogen-air mixing layer in turbulent flows. Symp Combust 27:1047–1056. https://doi.org/10.1016/S0082-0784(98)80505-5

Im HG, Chen JH, Chen JY (1999) Chemical response of methane/air diffusion flames to unsteady strain rate. Combust Flame 118:204–212. https://doi.org/10.1016/S0010-2180(98)00153-9

Im HG, Raja L, Kee RJ, Petzold LR (2000) A numerical study of transient ignition in a counterflow nonpremixed methane-air flame using adaptive time integration. Combust Sci Technol 158:341–363. https://doi.org/10.1080/00102200008947340

Kaiser EW, Yang J, Culp T et al (2002) Homogeneous charge compression ignition engine-out emission-does flame propagation occur in homogeneous charge compression ignition? Int J Engine Res 3:185–195. https://doi.org/10.1243/146808702762230897

Klimenko AY (1990) Multicomponent diffusion of various admixtures in turbulent flow. Fluid Dyn 25:327–334. https://doi.org/10.1007/BF01049811

Klimenko A, Bilger RW (1999) Conditional moment closure for turbulent combustion. Prog Energy Combust Sci 25:595–688

Krisman A, Hawkes ER, Talei M et al (2016) A direct numerical simulation of cool-flame affected autoignition in diesel engine-relevant conditions. Proc Combust Inst 0:1–9. doi:https://doi.org/10.1016/j.proci.2016.08.043

Krisman A, Hawkes ER, Chen JH (2017) Two stage autoignition and edge flames in a high pressure turbulent jet. J Fluid Mech 824:5–41. https://doi.org/10.1017/jfm.2017.282

Liñán A, Crespo A (1976) An asymptotic analysis of unsteady diffusion flames for large activation energies. Combust Sci Technol 14:95–117. https://doi.org/10.1080/00102207608946750

Mastorakos E (2009) Ignition of turbulent non-premixed flames. Prog Energy Combust Sci 35:57–97. https://doi.org/10.1016/j.pecs.2008.07.002

Mastorakos E, Bilger RW (1998) Second-order conditional moment closure for the autoignition of turbulent flows. Phys Fluids 10:1246–1248. https://doi.org/10.1063/1.869652

Mastorakos E, Baritaud TA, Poinsot TJ (1997) Numerical simulations of autoignition in turbulent mixing flows. Combust Flame 109:198–223. https://doi.org/10.1016/S0010-2180(96)00149-6

Mell WE, Nilsen V, Kosály G, Riley JJ (1994) Investigation of closure models for nonpremixed turbulent reacting flows. Phys Fluids 6:1331–1358. https://doi.org/10.1063/1.868443

Mizutani Y, Kazuyoshi N, Jin Do C (1990) Effects of turbulent mixing on spray ignition. Proc Combust Inst 1455–1460

Moin P, Mahesh K (1998) Direct numerical simulation: a tool in turbulence research. Annu Rev Fluid Mech 30:539–578. https://doi.org/10.1146/annurev.fluid.30.1.539

Mukhopadhyay S, Abraham J (2012) Influence of turbulence on autoignition in stratified mixtures under compression ignition engine conditions. Proc Inst Mech Eng Part D J Automob Eng 227:748–760. https://doi.org/10.1177/0954407012459624

Peters N (2004) Turbulent combustion. Cambridge University Press

Poinsot TJ, Veyante D (2005) Theoretical and numerical combustion, 2nd ed. Edwards

Sankaran R, Im HG, Hawkes ER, Chen JH (2005) The effects of non-uniform temperature distribution on the ignition of a lean homogeneous hydrogen-air mixture. Proc Combust Inst 30:875–882. https://doi.org/10.1016/j.proci.2004.08.176

Sreedhara S (2002) Studies on autoignition in a turbulent nonpremixed medium using direct numerical simulations. PhD Thesis, Indian Institute of Science

Sreedhara S, Lakshmisha KN (2000) Direct numerical simulation of autoignition in a non-premixed, turbulent medium. Proc Combust Inst 28:25–33. https://doi.org/10.1016/S0082-0784(00)80191-5

Sreedhara S, Lakshmisha KN (2002a) Autoignition in a non-premixed medium: DNS studies on the effects of three-dimensional turbulence. Proc Combust Inst 29:2051–2059. https://doi.org/10.1016/S1540-7489(02)80250-4

Sreedhara S, Lakshmisha KN (2002b) Assessment of conditional moment closure models of autoignition using DNS data. Proc Combust Inst 29:2069–2077

Talei M, Hawkes ER (2015) Ignition in compositionally and thermally stratified n-heptane/air mixtures: a direct numerical simulation study. Proc Combust Inst 35:3027–3035. https://doi.org/10.1016/j.proci.2014.09.006

Yao M, Zheng Z, Liu H (2009) Progress and recent trends in homogeneous charge compression ignition (HCCI) engines. Prog Energy Combust Sci 35:398–437. https://doi.org/10.1016/j.pecs.2009.05.001

Yoo CS, Richardson ES, Sankaran R, Chen JH (2011a) A DNS study on the stabilization mechanism of a turbulent lifted ethylene jet flame in highly-heated coflow. Proc Combust Inst 33:1619–1627. https://doi.org/10.1016/j.proci.2010.06.147

Yoo CS, Lu T, Chen JH, Law CK (2011b) Direct numerical simulations of ignition of a lean n-heptane/air mixture with temperature inhomogeneities at constant volume: Parametric study. Combust Flame 158:1727–1741. https://doi.org/10.1016/j.combustflame.2011.01.025

Yoo CS, Luo Z, Lu T et al (2013) A DNS study of ignition characteristics of a lean iso-octane/air mixture under HCCI and SACI conditions. Proc Combust Inst 34:2985–2993. https://doi.org/10.1016/j.proci.2012.05.019

Yu R, Bai XS (2013) Direct numerical simulation of lean hydrogen/air auto-ignition in a constant volume enclosure. Combust Flame 160:1706–1716. https://doi.org/10.1016/j.combustflame.2013.03.025

Zeldovich YB (1980) Regime classification of an exothermic reaction with nonuniform initial conditions. Combust Flame 39:211–214. https://doi.org/10.1016/0010-2180(80)90017-6

Chapter 11
Soot Predictions in Higher Order Hydrocarbon Flames: Assessment of Semi-Empirical Models and Method of Moments

Rohit Saini and Ashoke De

Abstract Soot predictions in turbulent flames possess different challenge due to the multiscale interaction between turbulence, chemistry, and particle dynamics. In addition, the high intermittency associated with these processes complicates the modeling further. Also, the large number of reactions related to soot precursor (acetylene) and polycyclic aromatic hydrocarbons (PAH) impose additional constraints in the modeling. Moreover, the radiative heat transfer adds to the complexity as there exists a strong coupling (two way) between combustion and soot models. In the present study, soot formation in a highly sooty kerosene/air diffusion flame is numerically investigated using both the semi-empirical and detailed soot models, where the steady laminar flamelet model (SLFM) is invoked as turbulence–chemistry interaction model. A detailed kinetics is implemented, which is represented through POLIMI mechanism (Ranzi et al. Int J Chem Kinet, 46(9):512–542, 2014). Soot formation is modeled using two different approaches, i.e., semi-empirical two-equation models and quadrature methods of moments with first three moments are used and both the approaches consider various subprocesses such as nucleation, coagulation, surface growth, and oxidation. The radiation heat transfer is taken into account considering four fictitious gasses in conjunction with the weighted sum of gray gas (WSSGM) approach for modeling absorption coefficient. The experimental data and earlier published predictions from Young et al. (Proc Combust Inst 25(1):609–617, 1994) and Wen et al. (Combust Flame 135(3):323–340, 2003) respectively are used for assessment of different soot models. The centerline and radial soot volume fraction is reproduced satisfactorily by quadrature method of moments approach, while the strong dependence of combustion products is analyzed through soot–radiation interactions.

Keywords Kerosene flame · Semi-empirical soot models · Method of moment

R. Saini · A. De (✉)
Department of Aerospace Engineering, Indian Institute of Technology Kanpur, Kanpur 208016, India
e-mail: ashoke@iitk.ac.in

© Springer Nature Singapore Pte Ltd. 2018

S. De et al. (eds.), *Modeling and Simulation of Turbulent Combustion*, Energy, Environment, and Sustainability, https://doi.org/10.1007/978-981-10-7410-3_11

Nomenclature

ρ	Mixture density
T	Temperature
Z	Mixture fraction
t	Time
χ	Scalar dissipation rate
χ_{st}	Scalar dissipation rate at $Z = Z_{st}$
Z_{st}	Stoichiometric mixture fraction
$erfc^{-1}$	Inverse complementary error function
σ_t	Turbulent Prandtl number
ϕ	Representative scalar
a_λ	Absorption coefficient
G_λ	Incident radiation
λ	Wavelength
i	Radiation intensity
a_s	Characteristic strain rate
m_i	Mass of the particle
M	Concentration of "n" moment
N	Particle density function
μ_{eff}	Effective dynamic viscosity
n	Moment order

Abbreviations

PAH	Poly-cyclic aromatic hydrocarbons
PDF	Probability density function
DNS	Direct numerical simulation
LES	Large eddy simulation
SIMPLE	Semi-implicit method for pressure-linked equations
RANS	Reynolds-Averaged Navier–Stokes

11.1 Background and Objective

Soot is a potent threat to the environment and human health and these combustion-generated soot emissions should be avoided through optimization in the design of the combustion systems (Mahowald et al. 2011; Pöschl 2005). Above-mentioned issues pose a challenge to combustion designers that require a comprehensive understanding of combustion physics, especially soot formation, which is a complex phenomenon and remains poorly understood even today. The requirement of complete understanding of soot is synchronicity with the imposing stringent methods to reduce the pollution levels. The challenge in the accurate

quantitative estimation of soot formation still persists due to the involvement of a complex multi-physics phenomenon that includes fluid mechanics, thermodynamics, and heat transfer and multiphase flows (Turns 2000). Much progress has been made in the last two decades in formulating mathematical models that predict the concentration or mass of soot particles in the flames and validate the proposed mechanisms which in turn are helpful in better understanding soot characteristics and formation mechanisms (Appel et al. 2000; Zhang et al. 2009; Dworkin et al. 2011; Mueller et al. 2011). Nonetheless, it appears that there is still a disruption between the existing soot models and actual soot formation processes. This disruption gets magnified when it comes to soot formation from the combustion of higher order hydrocarbon fuels. This is primarily because of the increased challenges in numerical modeling due to alteration of soot formation contributing mechanisms such as inception, condensation, surface growth and coagulation which contribute to the destruction of soot particles, such as oxidation and fragmentation. Therefore, accurate and predictive modeling of these subprocesses is required in order to develop a better understanding of soot formation in the reacting systems.

The bridge of numerical modeling of turbulent flames has developed from Reynolds-Averaged Navier–Stokes (RANS) computations to large eddy simulation (LES) and toward direct numerical simulation (DNS) as well. In a similar fashion, the advances in soot modeling have progressed from one-step soot model (Khan and Greeves 1974), then to Hybrid Method of Moments (HMOM) (Mueller et al. 2009). Soot is commonly believed to be formed by coagulation of PAH species which grow by heterogeneous surface reaction with acetylene being the building block of this growth process. These reactions are frequently modeled by the so-called H-Abstraction-Carbon-Addition (HACA) mechanism proposed by Frenklach and Wang (Frenklach and Wang 1991). Brookes and Moss (1999) modeled soot field in pilot stabilized diffusion flame burning methane/air, under which soot inception rate of particles was considered to be proportional to the local concentration of acetylene and showed good agreement with the measurements at atmospheric pressure. Primarily to include soot formation in higher hydrocarbons, Hall et al. (1997) extended the soot inception rate in the previous model, which is based on the formation of two-ringed and three-ringed aromatics from acetylene, benzene, and phenyl radicals. Recently, Reddy et al. (2015, 2016) and Busupally and De (2016) explored empirical as well as semi-empirical soot models in Delft Flame III (Qamar et al. 2009) and turbulent lifted ethylene–air flame (Köhler et al. 2011) and achieved agreeable predictions as compared to experimental measurements and the published data as well. Lignell et al. (2007) performed two-dimensional DNS simulations combined with semi-empirical soot modeling in non-premixed turbulent counterflowing ethylene–air flame using acetylene as a soot precursor; later on Bisetti et al. (2012) performed DNS in heptane/air turbulent counterflow non-premixed flame using HMOM as soot model with soot inception rate, based on PAH molecules and their study has provided brief insights in the soot particle dynamics and particle size distributions. Further for brief insight of particle statistics, Method of Moment (MOM) approach was used by Frenklach (2002), which is based on the solution of the set of differential equations describing the

evolution of the statistical moments (M_n) of the particle size distribution function (PSDF) derived from Smoluchowski's equation. Pitch et al. (2000) performed computations using first two moments of the moment approach in conjunction with unsteady flamelet approach and obtained reasonable agreement with the experimental measurements. Furthermore, Lindstedt and Louloudi (2005) computed the same flame configuration with transported PDF methodology and found that the overall effect of increased number of moments is quite modest. From previous literature, three to six moments have been found sufficient in soot modeling of premixed (Appel et al. 2000) and non-premixed flames (Wang et al. 1996).

On the other hand, commercial fuels such as kerosene, diesel, etc., impose the biggest challenges in combustion modeling due to their complex chemical structure and involvement of a large number of reactions to represent the finite-rate chemistry effects. Several detailed mechanisms (Patterson et al. 2001; Honnet et al. 2009) of kerosene have been developed in the experimental studies using premixed systems. In the published literature (Lindstedt and Maurice 2000), the structure of the kerosene fuel is extensively described as n-decane/alkyl-substituted aromatic surrogate blends in order to capture the accurate premixed flame predictions. Rajeshirke et al. (2013) studied kerosene–air diffusion flame (similar in the present study) using semi-empirical soot modeling approach accounting both detailed as well as reduced chemical mechanisms and aimed at examining the effect of different soot precursors on the soot formation. A commonly encountered kerosene diffusion flame in realistic combustion environment is still persisted as a challenging field in terms of achieving the quantitative accuracy and computational efficiency. In the present study, an attempt has been made to quantify the soot predictions for sooty hydrocarbon turbulent flames (less to highly sooty) utilizing semi-empirical soot models and quadrature method of moments. The ability of methods of moments is to provide insight to soot particle distributions while comparing with the semi-empirical models and that becomes an advantage for this model, thereby leading to the motivation of the current study. Further, only three moments have been used to predict the soot statistics to retain the computation efficiency. The broad objective of the current work is to (i) investigate the effect of scalar quantities and species formation with two radiation approaches. (ii) investigate the soot formation using three different soot models in combination with different OH radical determination approaches. (iii) investigate the effect of the soot–radiation interaction with acceptable radiation approach. The results are compared with previously published experimental (Young et al. 1994) as well as the computational data (Wen et al. 2003) in order to explain the intermittencies in the soot formation.

11.2 Numerical Methods

The numerical approach used for solving the turbulence–chemistry interactions, radiation modeling, and soot models is described in the following section.

11.2.1 Steady Laminar Flamelet (SLFM) Approach

The SLFM (Peters 2000) model postulates that a turbulent flame is an ensemble of one-dimensional laminar flamelets obtained by statistical averaging and its internal structure is not altered by the turbulence. These laminar flamelets are parameterized by strain rate which is modeled through scalar dissipation. The governing equations of temperature and species mass fraction of the flamelet approach in mixture fraction space can be obtained from physical space by applying the coordinate transformation. For uniform diffusion (Le = 1), the flamelet equation can be written as

$$-\frac{1}{2}\rho\chi\frac{\partial^2 Y_i}{\partial Z^2}-\omega_i=0 \tag{11.1}$$

$$-\frac{1}{2}\rho\chi\left(\frac{\partial^2 T}{\partial Z^2}+\frac{1}{c_p}\frac{\partial c_p}{\partial Z}\frac{\partial T}{\partial Z}\right)+\frac{1}{c_p}\sum_{i=1}^{n}h_i\dot{\omega}_i=0, \tag{11.2}$$

where c_p and h_i are the specific isobaric heat capacity and the specific enthalpy of species i, respectively; $\dot{\omega}_i$ is the chemical species source term and is calculated with a chemistry reaction mechanism. The scalar dissipation rate and mixture fraction is used to convert mixture fraction space back to physical space. Scalar dissipation rate can be thought of as inverse of diffusion time scale and is written as

$$\chi=2D\left(\frac{\partial Z}{\partial y}\right)^2, \tag{11.3}$$

where D is the diffusion coefficient and χ is the function of the mixture fraction. The flamelets, therefore, can be parameterized by its value at stoichiometric mixture χ_{st} (Peters 1984), which is defined as

$$\chi_{st}=\frac{a_s\exp\left(-2[erfc^{-1}(2Z_{st})]^2\right)}{\pi} \tag{11.4}$$

The counterflow diffusion flamelet is used to determine characteristic strain rate "a_s" and is equivalent to the ratio of the relative speed of the fuel and oxidizer jets and the twice the distance between the jet nozzles.

The turbulent flame is modeled as an ensemble of discrete diffusion flamelets and for adiabatic systems, it is parameterized by Z and χ_{st}, where species mass fraction and temperature are determined from the β-PDF of Z and χ_{st} which is defined as

$$\overline{\phi}=\iint\phi(Z,\chi_{st})p(Z,\chi_{st})dZd\chi_{st}, \tag{11.5}$$

where φ represents species mass fractions and temperature.

For nonadiabatic systems, an additional dimension "mean enthalpy ($\overline{H}$)", in order to account heat losses, is added along with mean temperatures and density PDF tables. The evolution of the mixture fraction in the physical space is represented by the Favre-mean transport equations of mixture fraction (Z) and mixture fraction variance (Z'^2) as

$$\frac{\partial}{\partial t}(\rho\bar{Z}) + \frac{\partial}{\partial x}(\rho\vec{v}\bar{Z}) = \frac{\partial}{\partial x}\left(\frac{\mu_{eff}}{\sigma_t}\left(\frac{\partial\bar{Z}}{\partial x}\right)\right) \tag{11.6}$$

$$\frac{\partial}{\partial t}\left(\rho\overline{Z'^2}\right) + \frac{\partial}{\partial x}\left(\rho\vec{v}\overline{Z'^2}\right) = \frac{\partial}{\partial x}\left(\frac{\mu_{eff}}{\sigma_t}\left(\frac{\partial\overline{Z'^2}}{\partial x}\right)\right) + C_g\mu_t\left(\frac{\partial\overline{Z}}{\partial x}\right)^2 - C_d\rho\frac{\varepsilon}{k}\overline{Z'^2}, \tag{11.7}$$

where $Z' = Z - \overline{Z}$ and values of the constants σ_t, C_g and C_d are 0.85, 2.86 and 2.0, respectively.

11.2.2 Radiation Modeling

The medium is considered as optically thick for both the flames and radiation intensity is approximated by a Fourier's truncated series expansion in terms of spherical harmonics (P1 approximation) (Howell et al. 2010) given by the following equation:

$$-\nabla\left(\frac{1}{3a_\lambda}\nabla G\right) - a_\lambda(4\pi i_\lambda - G_\lambda) = 0 \tag{11.8}$$

In the above equation, Eq. (11.8), the first term represents the gradient of radiative heat flux and the amount of radiative heat source added to the energy equation is represented by the second term. The effective absorption coefficient (a_λ), which accounts for both for the absorbing (radiating) gas and soot mixture, is defined using Eq. (11.9):

$$a_\lambda = a_{absorbing\_gas} + a_{soot} \tag{11.9}$$

The weighted sum of gray gases (WSSG) model, consisting of four fictitious gasses in the non-gray medium, is used to calculate "$a_{absorbing\ gas}$" and further details regarding this approach can be found in Yadav et al. (2013). The effect of soot particles on radiative heat transfer is included using an averaged gray soot absorption coefficient, which is represented using Eq. (11.10):

$$a_{soot} = b_1\rho Y_{soot}[1 - b_T(T - 2000)], \tag{11.10}$$

where ρ is the soot density and Y_{soot} is the mass fraction of soot. The value of $b_1 = 1232.4$ m^3/kg and $b_T \approx 4.8 \times 10^{-4}$ K^{-1} are obtained from the Taylor–Foster approximation Taylor and Foster (1975) and Smith et al. (1982), respectively.

11.2.3 Soot Modeling

In the present work, two semi-empirical models, i.e., Brookes and Moss (1999) and an extension of it by Hall et al. (1997) are used in addition to Method of Moment (MOM) for modeling soot. The results from these soot modeling approaches are compared extensively for both the flames. In previously published works (Reddy et al. 2015, 2016; Busupally and De 2016), the use of above-mentioned semi-empirical models is studied extensively for modeling soot in "Delft Flame III" and "Lifted turbulent ethylene/air flame". In this work as well, we have used same modeling strategy with empirical models. Therefore, only a brief summary of those approaches is described here. The finer details of these semi-empirical approaches regarding handling of the various source terms are not explicitly explained here and taken from (Reddy et al. 2015, 2016; Busupally and De 2016). However, the details regarding the model are described in the following subsections.

11.2.3.1 Semi-Empirical Models

Soot yield is calculated from transport equations solved for normalized soot radical nuclei concentration, b^*_{nuc} and soot mass fraction Y_{soot} and are described as follows:

$$\frac{\partial}{\partial t}(\rho Y_{soot}) + \nabla \cdot \left(\rho \overrightarrow{\nu} Y_{soot}\right) = \nabla \cdot \left(\frac{\mu_t}{\sigma_{soot}} \nabla Y_{soot}\right) + \frac{dM}{dt} \tag{11.11}$$

$$\frac{\partial}{\partial t}\left(\rho b^*_{nuc.}\right) + \nabla \cdot \left(\rho \overrightarrow{\nu} b^*_{nuc.}\right) = \nabla \cdot \left(\frac{\mu_t}{\sigma_{soot}} \nabla b^*_{nuc.}\right) + \frac{1}{N_{norm}} \frac{dN}{dt}, \tag{11.12}$$

where M and N denotes soot mass concentration and soot particle number density, and these parameters are used to model inception, coagulation, growth and oxidation rates. For Moss–Brookes model, the inception rate is linearly dependent on the local concentration of the acetylene as shown in Eq. (11.13),

$$C_2H_2 \rightarrow 2C(s) + H_2 \tag{11.13}$$

whereas in the extended model by Reddy et al. (2015), inception rate considers the formation of two- and three-ringed aromatics from acetylene, benzene, and phenyl radicals, shown in Eqs. (11.14) and (11.15):

$$2C_2H_2 + C_6H_5 \rightleftharpoons C_{10}H_7 + H_2 \tag{11.14}$$

$$C_2H_2 + C_6H_6 + C_6H_5 \rightleftharpoons C_{14}H_{10} + H_2 + H \tag{11.15}$$

The oxidation due to O_2 and OH are used as suggested by Neoh et al. (1981) and Lee et al. (1962), respectively.

11.2.3.2 Method of Moments

In this section, we present the governing equations related to soot mass fractions using the method of moments approach Frenklach (2002). Notably in the current work, the soot size distribution is obtained using the first three moments only and the closure is achieved by logarithmic interpolation. The soot size distribution is defined using the concentration moment of the particle number density function for a given number of moments and recast as

$$M_n = \sum_{i=1}^{\infty} m_i^n N_i, \tag{11.16}$$

where M_n is the soot size distribution of nth moment and N_t represents the particle density of the size class "i". Accordingly, the total particle density is represented by $n = 0$ and total mass of the particles is defined by $n = 1$. Furthermore, the soot concentrations are also solved in the physical space and represented by the following transport equation as

$$\frac{\partial(\rho M_n)}{\partial t} + \nabla \cdot (\rho \overrightarrow{\nu} M_n) = \nabla \cdot \left(\frac{\mu_{eff.}}{\sigma_t} \nabla M_n \right) + S_n \tag{11.17}$$

The source term ("S_n") in Eq. (11.19) is the combination of the nucleation, coagulation, surface growth, and oxidation source term and related to soot statistics. This term can be written as follows:

$$\frac{dM_n}{dt} = S^{nuc.} + S^{coa.} + S^{surf.Growth+Oxid.} \tag{11.18}$$

The detailed discussion on the computations of these source terms is as follows:

Nucleation

Nucleation is usually known as a coagulation process between two precursor species for soot. The primary component which acts a building block for the formation of PAH molecules is considered to be soot precursor, i.e., acetylene Frenklach (2002). For the nth moment, the source term pertaining to nucleation is calculated as

$$S_n^{nuc.} = \gamma C_{nuc.} \sqrt{T} [X_p]^2 \tag{11.19}$$

In Eq. (11.19), the precursor species (molar concentration of acetylene in this case) is represented by $[X_p]$, γ is the sticking coefficient (Blanquart and Pitsch 2009) and C_{nuc}, is the constant. The γ is usually proportional to the fourth power of the mass of the precursor species.

Coagulation

In the present work, the underline assumption is a coalescent coagulation, which means the particles after the collision will remain a sphere with an increased diameter. The source term related to coagulation (for the $n = 0$th moment) in Eq. (11.18) is calculated as follows:

$$S_n^{coa.} = -0.5 \sum_{i=1}^{\infty} \sum_{j=1}^{\infty} \alpha_{i,j} N_i N_j \tag{11.20}$$

For higher moments, i.e., $n \geq 2$ is calculated using Eq. (11.21), as the coagulation process does not affect the total mass of the particle.

$$S_n^{coa.} = 0.5 \sum_{k=1}^{n-1} \left(\frac{n}{k}\right) \sum_{i=1}^{\infty} \sum_{j=1}^{\infty} m_i^k m_i^{n-k} \alpha_{i,j} N_i N_j \tag{11.21}$$

In the Eqs. (11.20) and (11.21), $\alpha_{i,j}$ is termed as the collision frequency. However, different coagulation regimes (continuum, free molecular and transition) do affect this term, and the nondimensional number (Knudsen number) is used to define the state of the coagulation process corresponding to respective regimes. Fixed initial distribution of soot particles is considered in a closed domain to estimate the coagulation process regime. Typically, the particles are initially mono-dispersed with the initial number density of 10^{18} m^{-3}, while the initial temperature is considered to be 1500 K. The particles are allowed to coagulate and the number density changed with time. The coagulation takes place in free molecular regime. The evolution of number density with time is depicted in Fig. 11.1 while the present data is also compared with earlier published results of Frenklach and Harris (1987).

Surface Growth and Oxidation

Typically, the soot formation due to nucleation is very small as compared to the overall soot formation and the dominant mode of the soot formation is primarily through surface growth. Simultaneously, the soot particles also lose mass due to oxidation either by O_2 or OH species. Primarily, the chemical kinetics controls the process of surface growth and oxidation and involves higher order of complexities. Thus, the reduced mechanisms are preferred in terms of computational efficiency to model these subprocesses. HACA mechanism is used to account surface growth and oxidation pathways. The moment source term corresponds to the surface

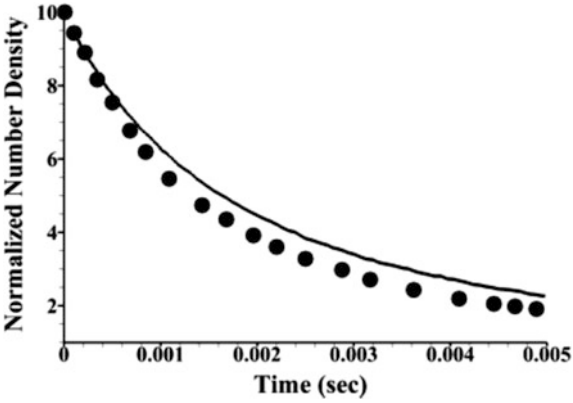

Fig. 11.1 Normalized number density versus time: line are predictions (Saini et al. 2017), symbols are published results of Frenklach and Harris (1987)

growth due to an addition of C_2H_2 species and oxidation due to O_2 or OH species is described as follows:

$$S = k_f[C_S^*] \sum_{k=0}^{n-1} (n,k)\Delta^{n-1} M_{k+2/3}, \tag{11.22}$$

where S is any source for the surface growth due to C_2H_2 or oxidation due to O_2 and OH. Δ represents the number of carbons atoms added or removed, and k_f is the reaction rate of growth or oxidation reaction.

Determination of OH Radical Concentration

The two approaches namely, equilibrium and instantaneous approach are used in the current study to calculate OH radical concentration. In the first approach, the concentration of the OH radicals and O radicals is calculated using Eq. (11.23) (Baulch et al. 1992; Westbrook and Dryer 1984) and Eq. (11.24) (Westenberg 1971).

$$[OH] = 2.129 \times 10^2 T^{-0.57} e^{-4595/T} [O_2]^{1/2} [H_2O]^{1/2} \tag{11.23}$$

$$[O] = 3.97 \times 10^5 T^{-1/2} e^{-31090} [O_2]^{1/2} \tag{11.24}$$

In the latter approach, instantaneous value of OH radical concentration from flamelet library is used.

11.3 Burner Details

The test case is a pre-vaporized turbulent kerosene flame (Young et al. 1994) with a confined configuration surrounded by borosilicate glass tube of the inside diameter of 155 mm. The vaporized kerosene is expelled from the electrically heated brass

Table 11.1 The boundary conditions at the inlet of the burner

	Mean velocity (m/sec)	Flow rate(g/min)	Temperature (K)	Reynolds number
Fuel	22.28	8.0	598	9500
Coflow	0.234	324	288	–

chamber into the burner through a nozzle of diameter of 1.5 mm. A small annular slot of 0.25 mm width, issuing hot mixture of ethylene and oxygen at the base of primary flame, is used to prevent liftoff and achieve stabilization of turbulent flame. In experiments (Young et al. 1994), time-averaged measurements of spatially resolved soot volume fraction are obtained for different chamber pressures ranging from 1 to 6.4 bar. However, present study is limited to the operating conditions correspond to 1 bar. Kerosene used in the experiments is a standard aviation grade having a C/H ratio of 0.51 and encompassing 14% H by mass and 20% aromatic content by volume. The inlet boundary conditions are listed in Table 11.1. The details of the experimental setup and boundary conditions are provided in published work of Young et al. (1994).

11.4 Computational Details

The present section discusses the numerical details along with the boundary conditions used in the current study.

Kerosene, being a jet fuel, is often represented by surrogates including a long chain aliphatic species and a cyclic compound. In the current work, kerosene is represented using a two-component surrogate fuel, containing 20% C_7H_8 described as the aromatic species and 80% $C_{10}H_{22}$ signifying the aliphatic species by volume. The C/H ratio of the surrogate mixture is 0.49, which is closer to that of the experimental value. Figure 11.2 illustrates the (a) axis-symmetric nonuniform grid and (b) computational domain with boundary conditions; where the axial and radial direction extends to 600 × 103 D, where D is the fuel jet diameter. Three nonuniform grids have been chosen for grid independence study; a coarse grid with 400 (axial) × 120 (radial), a medium grid with 600 (axial) × 180 (radial) cells, and a fine grid with 900 (axial) × 270 (radial) cells. Due to the confined configuration of the burner, the lateral boundary is modeled as no-slip with a fixed temperature of 600 K. A fully developed turbulent profile is applied at the inlet of the fuel jet and turbulence intensity is used at the inlet boundaries of the fuel and coflow. Since the current study has been performed with presumed-PDF-based model, which does not require a flame stabilizer. Therefore, in the current case, the pilot has not been used, which is also along the similar line with the published literature (Young et al. 1994; Peters 2000). However, it is noteworthy to mention

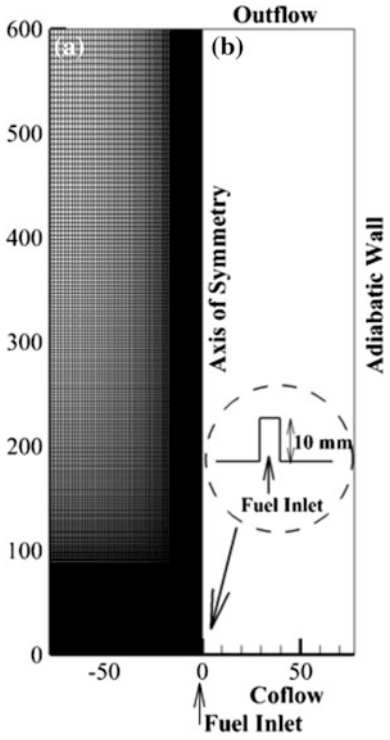

Fig. 11.2 Schematic of the **a** axisymmetric nonuniform grid, and **b** computational domain with imposed boundary conditions, respectively

that this will lead to minor discrepancies as the mean flow rate and power from pilot is less than 2.5% of the total flame power. The chemistry in this case is represented using a fairly detailed mechanism consisting of 121 species and 2613 reactions (Ranzi et al. 2014).

In this study, soot formation has been studied using two semi-empirical models along with Method of Moment (MOM) approach. The soot source terms including nucleation, coagulation, surface growth, and oxidation give an important insight of soot formation processes when coupled with soot–radiation interactions. Because of the symmetry of the burner, the present calculations are completed utilizing a two-dimensional axis-symmetric configuration. The mass, momentum, energy, and turbulence equations are solved using the Favre-averaged governing equations. The turbulence field is modeled using a two-equation standard $k-\varepsilon$ model with a rectification in the model constant ($C_{\varepsilon 1}$) to achieve correct jet spreading, as reported in the published literature (Pope 1978). The pressure–velocity coupling is achieved using SIMPLE algorithm and second-order upwind scheme is used to discretize all the convective fluxes. All computations carried out in the present work are performed using ANSYS FLUENT-16.0 (2015). The radiative heat transfer is modeled using WSSG model and non-gray behavior is invoked through a user-defined function (UDF) dependent on the four factious gasses and weight functions are

computed from Smith tables (Smith et al. 1982) as a function of H_2O and CO_2 partial pressures.

11.5 Results and Discussion

The current section presents the predictions of soot volume fraction in the sooty non-premixed turbulent flame. Initially, we report the grid independence study, followed by the soot results with inclusion of non-gray radiation and soot–turbulence interactions.

11.5.1 Grid-Independent Study

The centerline and radial profiles of mean mixture fraction and temperature with three different grids are compared along the combustor length and at two different radial locations, i.e., 100 and 300 mm from the fuel nozzle and are depicted in Fig. 11.3. The peak temperature along the centerline profile are captured by the medium and fine grids are 2097 K and 2098 K, respectively; however, coarser grid has failed in capturing the radial extent of the flame. The predictions of the scalar properties for the medium and fine grids are also found to be within the range of 1%. Therefore, the medium grid with 600 (axial) X 180 (radial) cells has been chosen for further calculations.

11.5.2 Structure of the Flame

The phenomenon of the reduction in the flame temperature with the inclusion of radiation models can be seen in the Fig. 11.4. The distribution shows good match of temperature, even in the close proximity of burner inlet, justifies our approximation of ignoring the pilot inlet. The inclusion of gray radiation reduces the centerline peak temperature from ~2110 to ~1850 K depicting the strong impact of flame–radiation interaction. The extinction scalar dissipation rate predicted in the current study is 18 s^{-1}, which is also in good agreement with the prediction of the Wen et al. (2003).

Further reduction in the centerline peak temperature by ~125 K is observed after invoking non-gray radiation approach and the flame length is reduced by ~70 D as compared to the gray radiation approach. The centerline temperature distribution in the vicinity of the fuel nozzle is in good agreement with the experimental measurements signifying the accurate capturing of the local flame extinction in the ignition dominating region. However, while progressing in the downstream region the width of the reaction zone is noticeably increased which can be ascribed to the

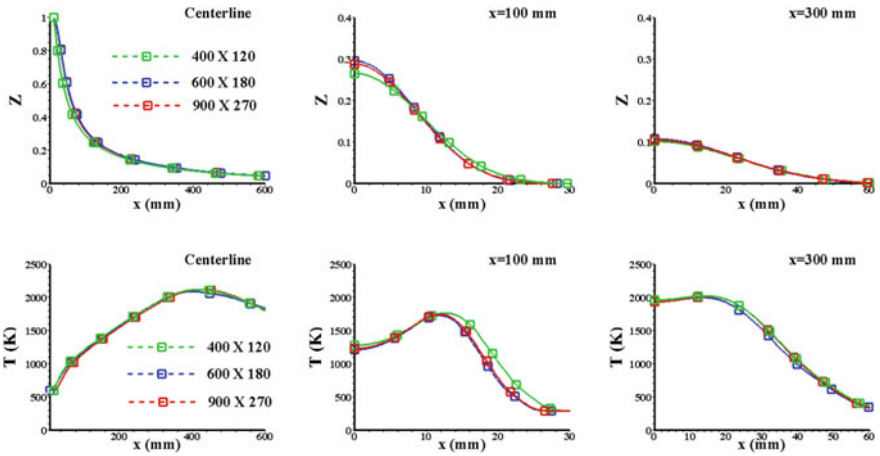

Fig. 11.3 Centerline and radial profiles of the mixture fraction and temperature with three different grids

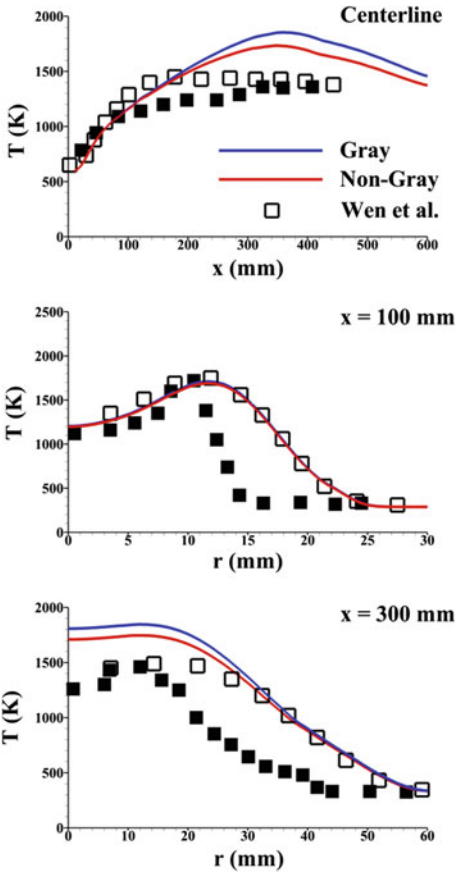

Fig. 11.4 Solid lines represent the centerline and radial profiles of the computed temperature; solid symbols are experimental measurements (Young et al. 1994) and hollow symbols correspond to Wen et al. (2003) predictions

excessive jet spreading caused by standard $k-\varepsilon$ turbulence model and is clearly visible in the radial distribution of temperature shown in Fig. 11.4.

This behavior of the temperature field is excessively observed from Fig. 11.4 in the radial profiles at the axial distances of 300 mm from the fuel jet inlet. The peak temperature predicted by radial profile at the axial distance of 100 mm is displaced by ~0.5 D in the downstream direction. The overpredicted radial temperature distribution at an axial distance of 300 mm could be inferred from the region of higher scalar dissipation rate. The non-gray radiation approach reduces the overpredicted temperature profile by ~100 K in the region close to the centerline of the combustor. The effect of radiation on the flame length is exhibited in Fig. 11.5, where the tip of the flame reaches 500 mm with gray radiation approach and further cut down to 400 mm with non-gray radiation approach. The overall trend followed by the predicted distribution is in fair agreement with the experimental measurements Young et al. (1994) and numerical data of Wen et al. (2003).

The centerline and radial distributions of the mean mixture fraction are reported in Fig. 11.6. The centerline distribution is in the excellent match with Wen et al. (2003) prediction and is well fitted within the maximum uncertainty (~5%) noted in the measurements. At the axial distance of 100 mm from the fuel nozzle, the radial distribution, shown in Fig. 11.6, depicts overprediction of ~16% in the peak mean mixture fraction indicating slower chemical kinetic rates in the vicinity of the fuel jet. In contrast, the peak mean mixture fraction in the radial profile at 300 mm

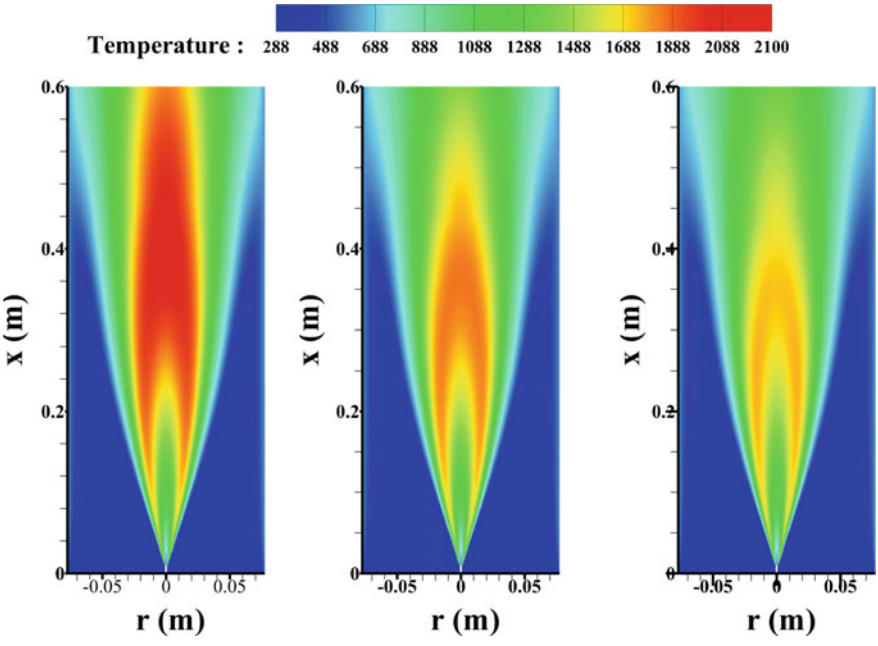

Fig. 11.5 Contours of the temperature field with no radiation, gray radiation, and non-gray radiation, respectively

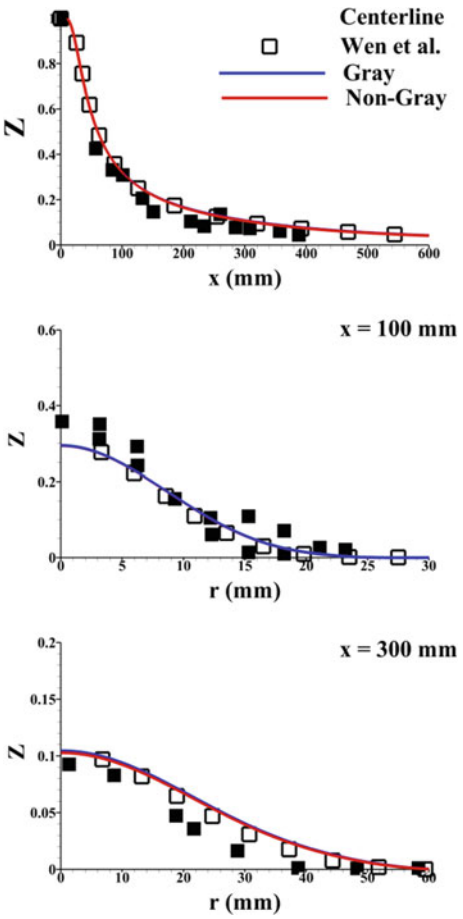

Fig. 11.6 Solid lines represent the centerline and radial profiles of the computed mean mixture fraction; solid symbols are experimental measurements (Young et al. 1994) and hollow symbols correspond to Wen et al. (2003) predictions

overpredicts by ~10%, showing improvement in the distribution while progressing downstream. The trend followed by both the radial distributions is in the good agreement with the measurements and lies within the above-mentioned uncertainty range. The variation of the mean mixture fraction is observed to be independent of radiation model approaches used in the current study.

Several experiments (Teini et al. 2012; Du et al. 1991) have been performed in order to understand soot oxidation and suppression of soot inception rate due to CO_2 reactivity in the reaction explained in Eq. (11.25). Figure 11.7 shows the computed centerline profiles of the CO, OH, H radicals' with and without inclusion of non-gray radiation approach.

$$CO + OH \rightleftharpoons CO_2 + H \tag{11.25}$$

The reduction of peak temperature due to inclusion of non-gray radiation is shown in Fig. 11.7 and after the peak region, the OH and H radicals reduced by

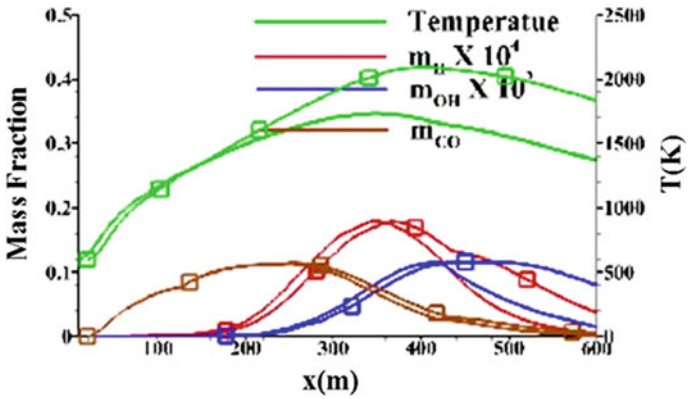

Fig. 11.7 Centerline distribution of mass fraction of H, OH, CO species, and temperature; lines with symbols are without radiation and lines with symbols are with non-gray radiation

factor of 2.5 and 1.2, respectively. This phenomenon leads to the destabilization of the above-mentioned reaction. The unbalance is occurred in the equilibrium of the reaction, due to inclusion of non-gray radiation will shift the equilibrium reaction toward left and attributes toward the increased chemical reactivity of CO_2 species, which will further cause the depression of soot formation through suppression of soot growth and soot oxidation due to reduction of OH radicals in the corresponding region.

11.5.3 Soot Predictions Without Radiation

The peak centerline soot by the MOM model using OH equilibrium approach is shown in Fig. 11.8a, which is overpredicted as compared to the peak experiment measurement (9.54 ppm) by a factor of 1.55 and the location of the peak value is predicted downstream by about 18 D. The overprediction in peak soot volume fraction of more than two folds is observed in the instantaneous approach shown in Fig. 11.8b. The steep rise in soot volume fraction is observed in 60–140 D and the location of the peak soot volume fraction is shifted downstream from the experimental peak value by approximately 10 D. Similar overprediction with the instantaneous approach is noticed in the radial distributions while progressing downstream. The centerline predictions, shown in Fig. 11.8a, depict the marginal underprediction in MBH (Moss–Brookes–Hall) model as compared to the MB (Moss–Brookes) model and can be accredited to the underprediction of the oxidizer species with the OH equilibrium approach. Whereas in the case of the OH instantaneous approach shown in Fig. 11.8b, centerline peak soot volume fraction with MBH model increases by factor of 4 as compared to the MB model.

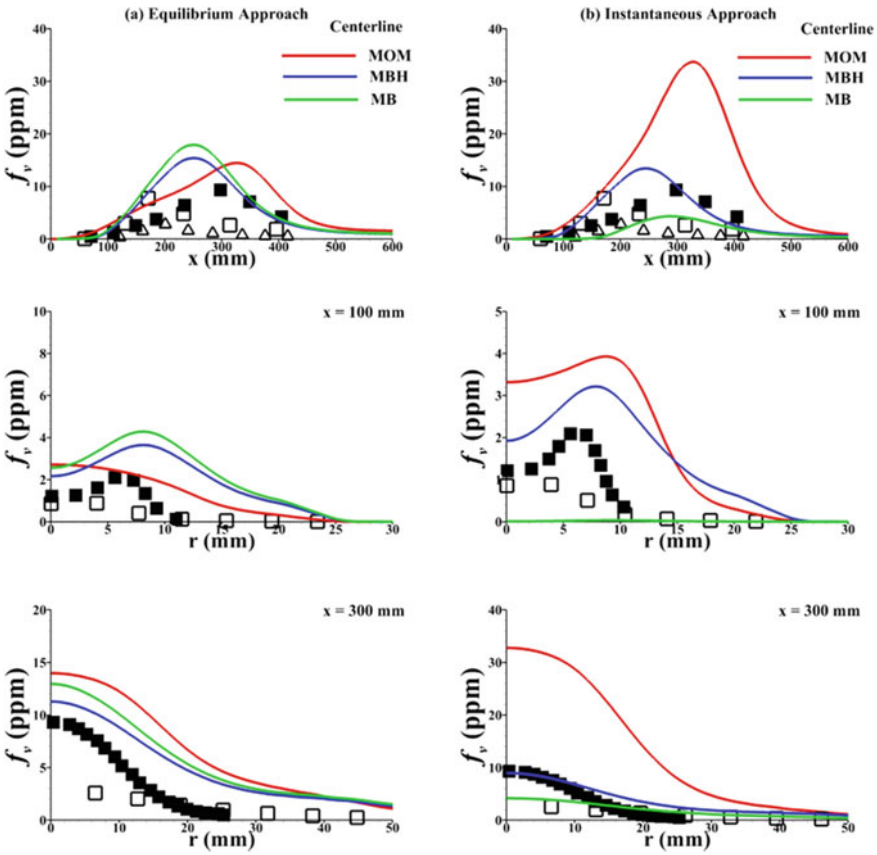

Fig. 11.8 Centerline and radial distribution of the soot volume fraction using **a** equilibrium approach and **b** instantaneous approach; solid symbols are experimental measurements (Young et al. 1994) and hollow symbols are predictions by Wen et al. (2003)

The overprediction in case of MOM model using OH instantaneous approach is due to the equivalent increase in the first moment, i.e., total mass of the soot particles shown in Fig. 11.9c, which can be attributed to the underprediction of OH radicals' concentration determined from the combustion model causing poor soot oxidation in case of instantaneous approach and indicating its sensitivity toward soot nucleation. The poor oxidation in the case of MBH model as compared to the MB model using OH instantaneous approach can be inferred from the oxidation source term, which reduced by an order of magnitude and is shown in Fig. 11.9b. However, the trend of reduction in MB model using OH instantaneous approach is similar with the observation of (Wen et al. 2003) and depicting inception rate in two- and three-ringed aromatics-based MBH model is increased by factor of 8 as compared to acetylene-based MB model as shown in Fig. 11.9a, b. The overall soot formation rate is found to be increased by an order of ~4.24 with MBH model.

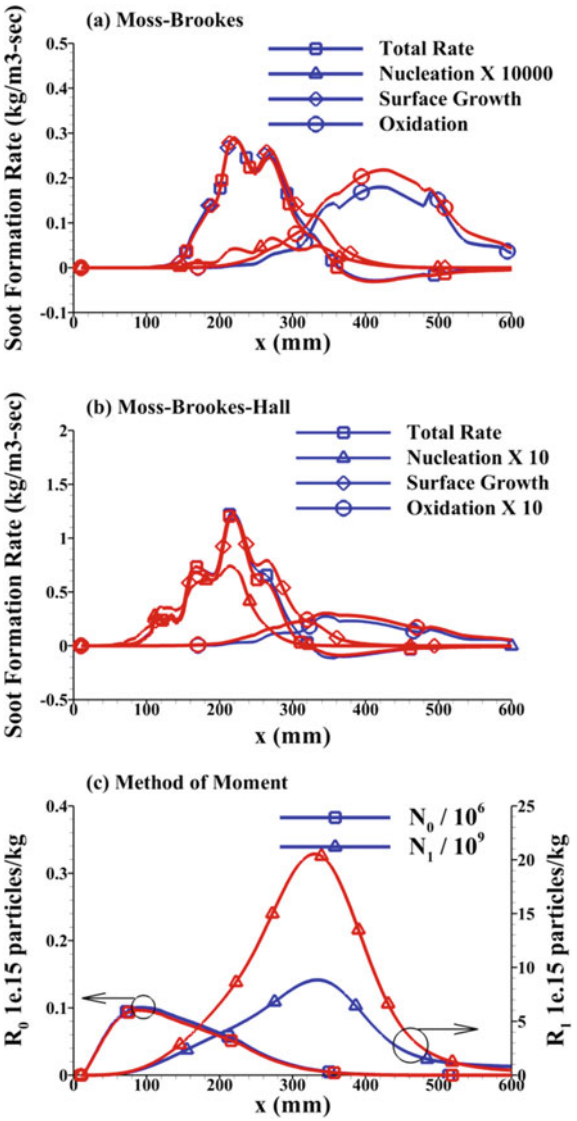

Fig. 11.9 Centerline distribution of the source terms involved in the evolution of soot formation; blue lines are with equilibrium approach and red lines signify instantaneous approach

11.5.4 Soot Predictions with Non-gray Radiation

Figure 11.10a depicts the axial and radial distribution of soot volume fraction with equilibrium approach. The peak of the axial distribution of MOM model with OH equilibrium approach is in excellent agreement with the experimental measurements but an overprediction by the factor of 1.33 is observed in the region between 65D to 165D, whereas similar overprediction has been observed for the case

without radiation (Fig. 11.8) as the factor of 1.15. It can be inferred from the radial distribution shown in Fig. 11.10a that the annular distribution of the soot volume fraction at 100 mm is overpredicted but nevertheless the trend observed is in reasonable agreement with the experimental measurements in the further downstream direction. In the case of instantaneous approach shown in Fig. 11.10b, the soot volume fraction reduces by approximately two folds with the inclusion of non-gray radiation; however, overprediction in the peak soot volume fraction is still persistent along the centerline distribution.

An upstream shift in the peak soot volume fraction value of about 28 and 10 D is observed with equilibrium approach and instantaneous approach, respectively, with the inclusion of the radiation. It can be seen in Fig. 11.10a that the increment of factor of 6 is observed in peak soot volume fraction with MBH model as compared to MB model under OH equilibrium approach. Noticeably, tremendous reduction in

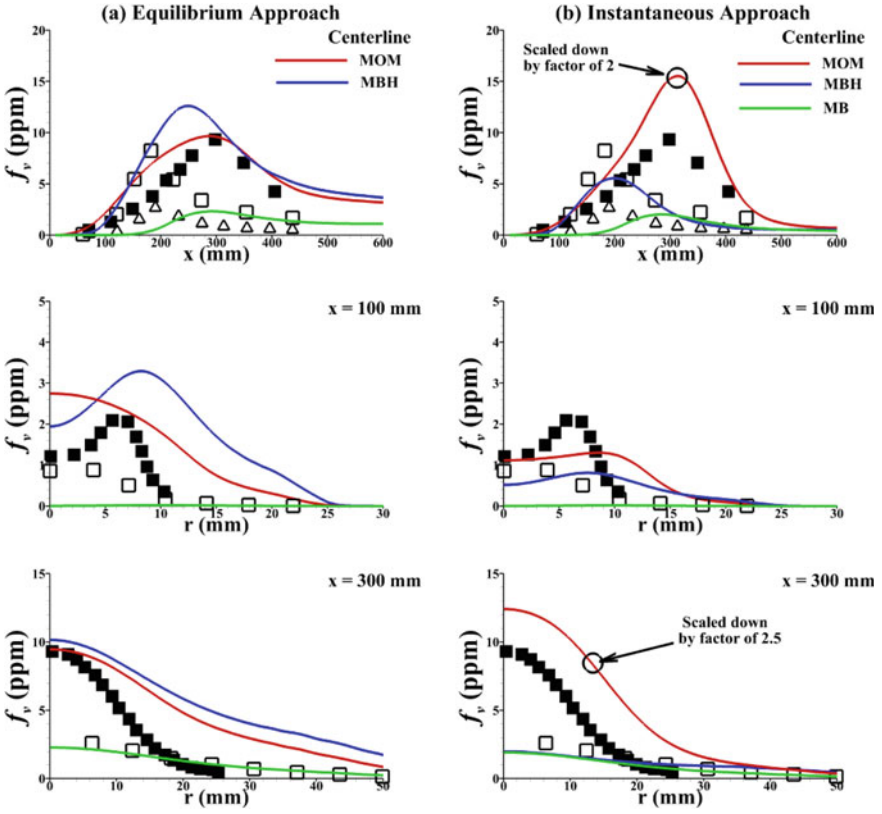

Fig. 11.10 Centerline and radial distribution of the soot volume fraction using **a** equilibrium approach and **b** instantaneous approach with inclusion of non-gray radiation approach; solid symbols are experimental measurements (Young et al. 1994) and hollow symbols are predictions of Wen et al. (2003)

soot volume fraction by the factor of 4 is noted with acetylene-based MB model after inclusion of radiation. With MBH model, a slight reduction in the peak value of the soot volume fraction is observed in the OH equilibrium approach whereas reduction with the OH instantaneous approach is noticed to be around factor of 2.5.

The reduction phenomenon of the peak soot volume fraction after invoking non-gray radiation is due to suppression of acetylene concentration (soot precursor species) due to change in temperature, which eventually reduces the surface growth of soot. Although, the reduction in temperature at the location of peak soot volume fractions could reduce the oxidation rate. Therefore, the growth and oxidation are two competing process where the non-gray radiation has direct impact. Since, the surface growth is the dominant factor in total soot yield, the decrease of oxidation rate is less than the decrease in the surface growth leading to a net reduction of the total soot yield. Interestingly, the trend of OH and H radicals, shown in Fig. 11.7, infers about the soot formation process in a descriptive manner. Soot oxidation starts at approximately x = 200 mm due to increase in OH radicals; similarly, with increase in H radicals, the soot formation continues to grow up to the axial distance of 350 mm. The increasing reactivity of CO_2 species affects the soot precursors such as acetylene and causes the suppression of soot inception rate leading to the reduction of soot formation in the end. Figure 11.11c shows moments associated with MOM model, and it is observed that the effect of radiation and different OH radical concentration approaches on the zeroth moment, i.e., total particle number density, is not significant, which is correct as the surface growth and oxidation will not change the number density. The peak of the first moment lies in the region of the maximum soot volume fraction and maximum temperature observed in the experimental measurements. The maximum difference in the first moment between the OH instantaneous approach and OH equilibrium approach is retained by a factor of 2.5, which is concurrent with the peak reduction of the soot volume fractions predicted by both the approaches.

The reason of tremendous reduction in MB model predictions with OH equilibrium approach is evident from the reduction of the nucleation rate and surface growth rate by the factor of 3 and 1.5, respectively, causing suppression of soot formation rate after inclusion of radiation. On associating this behavior with soot formation rates of OH equilibrium approach shown in Fig. 11.10a, b, the inclusion of radiation has reduced the overall soot formation rate by a factor of ~1.5 and soot oxidation rate is affected by the factor of 5.3. In the case of the OH instantaneous approach, the immense effect of radiation is noticed on the soot surface growth rate which drops down by a factor of 6 and overall soot formation rate reduces by a factor of 4. This reduction is continued despite underpredicted OH concentrations as the impact of reduction in C_2H_2 concentration is higher than the oxidation term due to OH.

The mean particle diameter along the centerline is shown in Fig. 11.12. The processes of soot evolution are congruent with the distribution of the mean particle diameters. The smaller particle diameters consisting up to 25 nm correspond to the maximum particle number density and is primarily responsible for soot production in the flame. Whereas larger particles occurring after the location of the peak soot volume fraction are present in the downstream section and remains un-oxidized.

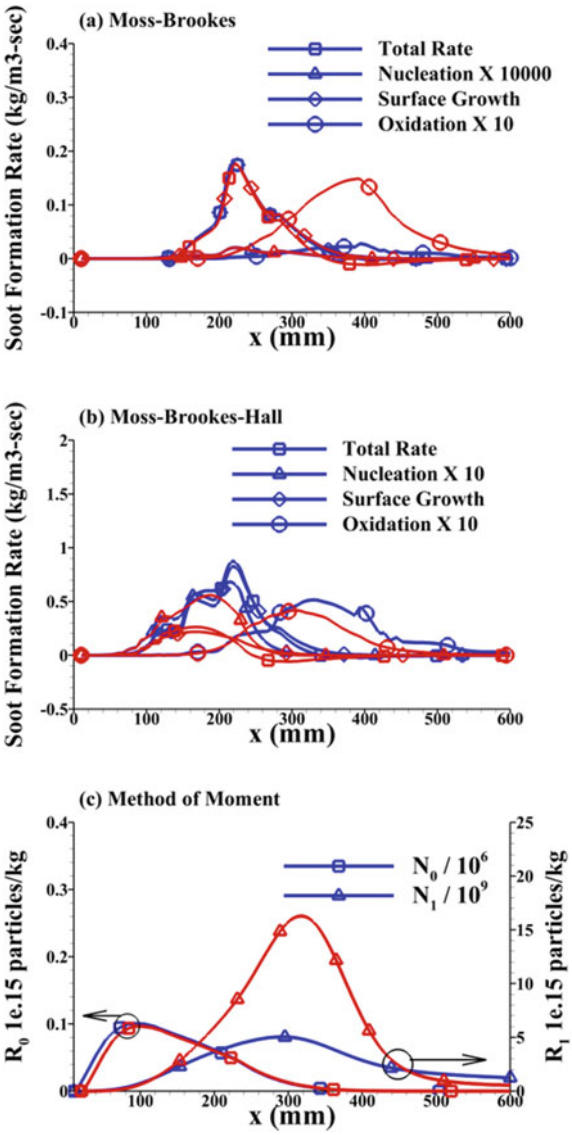

Fig. 11.11 Centerline distribution of the source terms involved in the evolution of soot formation with inclusion of non-gray radiation approach, blue lines are with equilibrium approach and red lines signify instantaneous approach

The maximum increase of 50 nm is observed in larger particle sizes with inclusion of soot–radiation interactions, however smaller particles sizes remains unaffected. Finally, the contours of soot volume fraction using semi-empirical soot models and method of moments with equilibrium approach and non-gray radiation model are shown in Fig. 11.13 and it can be clearly seen that global soot volume fraction in case of MB is underpredicted by one order of magnitude and MBH model

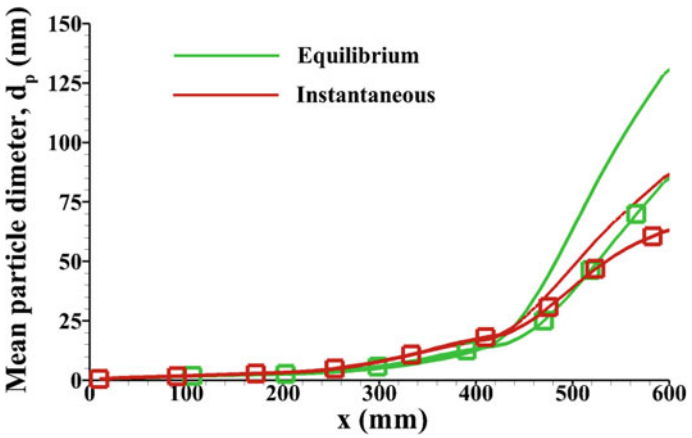

Fig. 11.12 Centerline distribution of mean particle diameter, d_p(nm) with different OH concentration approaches and lines without symbols are using non-gray radiation approach whereas lines with symbols are without inclusion of radiation

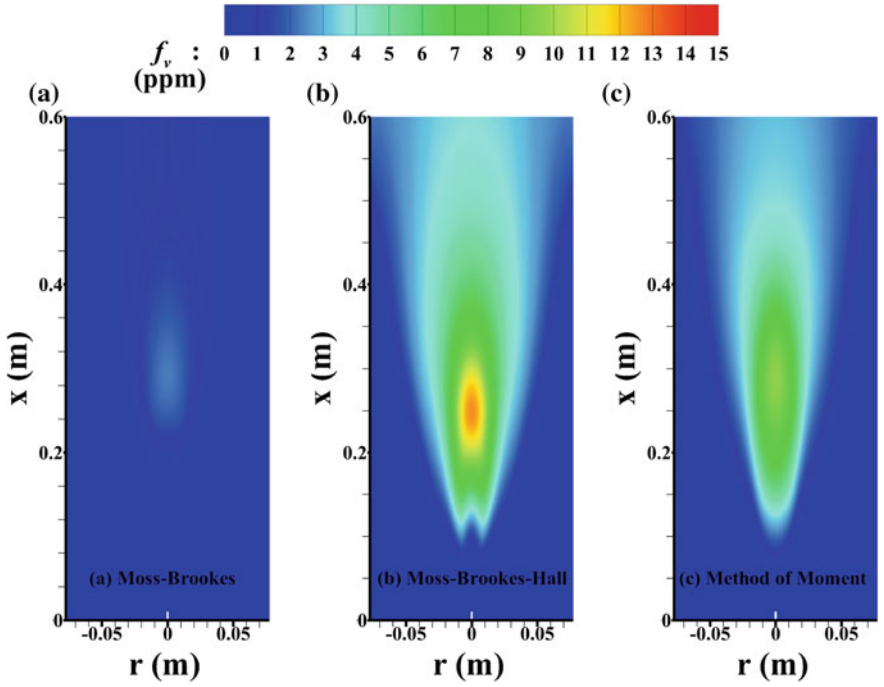

Fig. 11.13 Contours of the soot volume fraction where **a** Moss–Brookes model; **b** Moss–Brookes–Hall model; and **c** Method of Moment model using non-gray radiation and equilibrium OH concentration approach

overpredicts the soot levels close to the centerline whereas predictions from the MOM model are accurately predicting soot volume fraction and distribution of the axial and radial extents are in great match with the experimental measurements (Young et al. 1994). Similar observation with MOM has already been reported in the published literature for lower order hydrocarbon flames under atmospheric condition (Saini and De 2017).

11.6 Conclusion

This study presents an assessment of soot formation using two semi-empirical based models and method of moments for higher order hydrocarbon non-premixed turbulent jet flame at atmospheric condition. Acetylene is used as the primary soot precursor and two different OH concentration approaches are used to determine OH radicals' concentration. The non-gray radiation approach considering four fictitious gasses is invoked to consider radiative heat losses. Computational domain is consisting of the surrogate pre-vaporized kerosene–air turbulent flame (mixture of decane and toluene) inside a confined configuration operating at atmospheric pressure. The steady laminar flamelet model (SLFM) is used to model the turbulence–chemistry interactions and fairly detailed mechanism is used to include the effect of species concentration. The non-gray radiation approach shows strong effect when soot formation is coupled with flame temperature through soot–radiation interactions and soot volume fraction is observed to be sensitive to the surface growth rate. The effects of non-gray radiation must be included in order to capture the correct distributions of radiative heat loss. Method of moment coupled with soot–radiation interactions using OH equilibrium approach accurately predicts the peak value of soot volume fraction. The particle number density is found to be nearly constant with inclusion of radiation, whereas mass of the soot particles reduces under coupling of non-gray radiation and soot formation. The predictions using the equilibrium approach from the Moss–Brookes–Hall and Moss–Brookes model are reconstructed after inclusion of non-gray radiation approach, particularly due to the suppression of nucleation and surface growth rates and Method of Moment accurately captures spatial distribution of the soot volume fraction.

Acknowledgements Financial support for this research is provided through Aeronautical Research and Development Board (ARDB), India. Also, the authors would like to acknowledge the IITK computer center (https://www.iitk.ac.in/cc) for providing the support to perform the computation work, data analysis, and article preparation.

References

ANSYS Fluent (2015) 16.0 User's guide, Csnosburg, PA, USA

Appel J, Bockhorn H, Frenklach M (2000) Kinetic modeling of soot formation with detailed chemistry and physics: laminar premixed flames of C 2 hydrocarbons. Combust Flame 121 (1):122–136

Baulch DL, Cobos C, Cox RA, Esser C, Frank P, Just T, Warnatz J (1992) Evaluated kinetic data for combustion modelling. J Phys Chem Ref Data 21(3):411–734

Bisetti F, Blanquart G, Mueller ME, Pitsch H (2012) On the formation and early evolution of soot in turbulent nonpremixed flames. Combust Flame 159(1):317–335

Blanquart G, Pitsch H (2009) A joint volume-surface-hydrogen multi-variate model for soot formation. Combust generated fine carbonaceous particles, pp 437–463

Brookes SJ, Moss JB (1999) Predictions of soot and thermal radiation properties in confined turbulent jet diffusion flames. Combust Flame 116(4):486–503

Busupally MR, De A (2016) Numerical modeling of soot formation in a turbulent C2H4/air diffusion flame. Int J Spray Combust Dyn 8:67–85

Du DX, Axelbaum RL, Law CK (1991) The influence of carbon dioxide and oxygen as additives on soot formation in diffusion flames. Proc Combust Inst 23(1):1501–1507

Dworkin SB, Zhang Q, Thomson MJ, Slavinskaya NA, Riedel U (2011) Application of an enhanced PAH growth model to soot formation in a laminar coflow ethylene/air diffusion flame. Combust Flame 158(9):1682–1695

Frenklach M (2002a) Method of moments with interpolative closure. Chem Eng Sci 57(12):2229–2239

Frenklach M (2002b) Reaction mechanism of soot formation in flames. Phys Chem Phys 4 (11):2028–2037

Frenklach M, Harris SJ (1987) Aerosol dynamics modeling using the method of moments. J Colloid Interf Sci 118(1):252–261

Frenklach M, Wang H (1991) Detailed modeling of soot particle nucleation and growth. Proc Combust Inst 23(1):1559–1566

Hall RJ, Smooke MD, Colket MB (1997) Predictions of soot dynamics in opposed jet diffusion flames. Phys Chem Asp Combust Tribut Irvin Glassman 4:189–230

Honnet S, Seshadri K, Niemann U, Peters N (2009) A surrogate fuel for kerosene. Proc Combust Inst 32(1):485–492

Howell JR, Menguc MP, Siegel R (2010) Thermal radiation heat transfer. CRC press

Khan IM, Greeves G (1974) A method for calculating the formation and combustion of soot in diesel engines. Heat transfer in flames. Scripta (Chapter 25)

Köhler M, Geigle KP, Meier W, Crosland BM, Thomson KA, Smallwood GJ (2011) Sooting turbulent jet flame: characterization and quantitative soot measurements. Appl Phys B-Lasers Opt 104(2):409–425

Lee KB, Thring MW, Beer JM (1962) On the rate of combustion of soot in a laminar soot flame. Combust Flame 6:137–145

Lignell DO, Chen JH, Smith PJ, Lu T, Law CK (2007) The effect of flame structure on soot formation and transport in turbulent nonpremixed flames using direct numerical simulation. Combust Flame 151(1):2–28

Lindstedt RP, Louloudi SA (2005) Joint-scalar transported PDF modeling of soot formation and oxidation. Proc Combust Inst 30(1):775–783

Lindstedt RP, Maurice LQ (2000) Detailed chemical-kinetic model for aviation fuels. J Propuls Power 16(2):187–195

Mahowald N, Ward DS, Kloster S, Flanner MG, Heald CL, Heavens NG, Chuang PY (2011) Aerosol impacts on climate and biogeochemistry. Annu Rev Env Resour 36(1):45

Mueller ME, Blanquart G, Pitsch H (2009) Hybrid method of moments for modeling soot formation and growth. Combust Flame 156(6):1143–1155

Mueller ME, Blanquart G, Pitsch H (2011) Modeling the oxidation-induced fragmentation of soot aggregates in laminar flames. Proc Combust Inst 33(1):667–674
Neoh KG, Howard JB, Sarofim AF (1981) In: Siegla DC, Smith GW (eds) Particulate carbon formation during combustion. Plenum Press, New York, p 261
Patterson PM, Kyne AG, Pourkashanian M, Williams A, Wilson CW (2001) Combustion of kerosene in counterflow diffusion flames. J Propuls Power 17(2):453–460
Peters N (1984) Laminar diffusion flamelet models in non-premixed turbulent combustion. Prog Energy Combust 10(3):319–339
Peters N (2000) Turbulent combustion. Cambridge University Press
Pitsch H, Riesmeier E, Peters N (2000) Unsteady flamelet modeling of soot formation in turbulent diffusion flames. Combust Sci Technol 158(1):389–406
Pope SB (1978) An explanation of the turbulent round-jet/plane-jet anomaly. AIAA J 16(3):279–281
Pöschl U (2005) Atmospheric aerosols: composition, transformation, climate and health effects. Angew Chem Int Edition 44(46):7520–7540
Qamar NH, Alwahabi ZT, Chan QN, Nathan GJ, Roekaerts D, King KD (2009) Soot volume fraction in a piloted turbulent jet non-premixed flame of natural gas. Combust Flame 156 (7):1339–1347
Rajeshirke P, Nakod P, Yadav R, Orsino S (2013) Parametric study of Moss-Brookes (MB) and Moss-Brookes-Hall (MBH) model constants for prediction of soot formation in a turbulent Hydrocarbon flames. ASME Gas turbine India conference: V001T03A009
Ranzi E, Frassoldati A, Stagni A, Pelucchi M, Cuoci A, Faravelli T (2014) Reduced kinetic schemes of complex reaction systems: fossil and biomass-derived transportation fuels. Int J Chem Kinet 46(9):512–542
Reddy M, De A, Yadav R (2015) Effect of precursors and radiation on soot formation in turbulent diffusion flame. Fuel 148:58–72
Reddy BM, De A, Yadav R (2016) Numerical investigation of soot formation in turbulent diffusion flame with strong turbulence-chemistry interaction. ASME J Therm Sci Eng Appl 8 (1):011001
Saini R, De A (2017) Assessment of Soot formation in models in lifted ethylene/air turbulent diffusion flame. Therm Sc Eng Prog 3:49–61
Saini R, Reddy M, De A (2017) Soot formation in turbulence diffusion flames: effect of differential diffusion. Locomotive and rail road transportation (Technology, Challenges and Prospects). Springer, pp 193–216
Smith TF, Shen ZF, Friedman JN (1982) Evaluation of coefficients for the weighted sum of gray gases model. J Heat Trans 104(4):602–608
Taylor PB, Foster PJ (1975) Some gray gas weighting coefficients for CO2-H2O-soot mixtures. Int J Heat Mass Trans 18(11):1331–1332
Teini PD, Karwat DM, Atreya A (2012) The effect of CO2/H2O on the formation of soot particles in the homogeneous environment of a rapid compression facility. Combust Flame 159 (3):1090–1099
Stephen R Turns (2000) An introduction to combustion: concepts and applications. McGraw-Hill
Wang H, Du DX, Sung CJ, Law CK (1996) Experiments and numerical simulation on soot formation in opposed-jet ethylene diffusion flames. Proc Combust Inst 26(2):2359–2368
Wen Z, Yun S, Thomson MJ, Lightstone MF (2003) Modeling soot formation in turbulent kerosene/air jet diffusion flames. Combust Flame 135(3):323–340
Westbrook CK, Dryer FL (1984) Chemical kinetic modeling of hydrocarbon combustion. Prog Energy Combust 10(1):1–57
Westenberg AA (1971) Kinetics of NO and CO in lean, premixed hydrocarbon-air flames. Combust Sci Technol 4(1):59–64
Yadav R, Kushari A, Verma AK, Eswaran V (2013) Weighted sum of gray gas modeling for nongray radiation in combusting environment using the hybrid solution methodology. Numer Heat Trans Part B: Fund 64(2):174–197

Young KJ, Stewart CD, Moss JB (1994) Soot formation in turbulent nonpremixed kerosine-air flames burning at elevated pressure: experimental measurement. Proc Combust Inst 25(1):609–617

Zhang Q, Guo H, Liu F, Smallwood GJ, Thomson MJ (2009) Modeling of soot aggregate formation and size distribution in a laminar ethylene/air coflow diffusion flame with detailed PAH chemistry and an advanced sectional aerosol dynamics model. Proc Combust Inst 32 (1):761–768

Chapter 12
Modelling of Soot Formation in a Kerosene Spray Flame

Prakash Ghose, Amitava Datta, Ranjan Ganguly, Achintya Mukhopadhyay and Swarnendu Sen

Abstract Modelling the formation of soot in a kerosene spray flame is an important consideration in the design and development of gas turbine combustors. The aviation gas turbine engines run on kerosene-type jet fuels. Formation and emission of soot not only pollutes the environment but also augments the radiative heat flux from the flame, which may result in overheated liners and atomizers. Many complex processes are involved in the spray combustion in gas turbine combustors, which include turbulent transport of gas, formation of the fuel spray, droplet motion and evaporation, chemical reaction and thermal radiation in addition to pollutant formation. Each of these requires adequate modelling efforts for the right prediction of the overall process. In this chapter, a modelling technique for the prediction of spray flame and soot formation has been discussed in connection with the kerosene fuel. Considering the computational economy, we have restricted the discussion on RANS-based modelling, which is still popular in the industrial scale for the prediction of combustion phenomenon. Stochastic separated flow model is considered for the two-phase transport of the droplets formed in the atomized spray. The combustion of fuel follows the non-premixed flame mode, which has been modelled using the laminar flamelet model. The soot model is a semi-empirical one for which the model constants have been optimized for kerosene fuel. It is found that the optimized constants work well for kerosene in predicting the soot, which finally leads to good predictions of the liner wall temperature and exit gas temperature from the combustor. Different cases have been run with different air flow split into the combustor to analyse the effects using the developed model.

Keywords Spray combustion · Modelling · Flamelet model
Soot · Radiation

P. Ghose
School of Mechanical Engineering, KIIT University, Bhubaneswar, India

A. Datta (✉) · R. Ganguly
Department of Power Engineering, Jadavpur University, Kolkata, India
e-mail: amdatta_ju@yahoo.com

A. Mukhopadhyay · S. Sen
Department of Mechanical Engineering, Jadavpur University, Kolkata, India

© Springer Nature Singapore Pte Ltd. 2018

S. De et al. (eds.), *Modeling and Simulation of Turbulent Combustion*, Energy, Environment, and Sustainability, https://doi.org/10.1007/978-981-10-7410-3_12

Nomenclature

a_k	Weighting factor
C_{Drag}	Drag coefficient
c_p	Specific heat, J/kg-K
D	Diameter of the combustor, m
D	Diffusivity
d	Diameter, m
d_o	Mean droplet diameter, m
$d_{p_{soot}}$	Mean diameter of soot particle, m
ΔH_v	Latent heat of vapourization, J/kg
h , H	Enthalpy
h_c	Heat transfer coefficient, W/m^2-K
h_D	Mass transfer coefficient, m/s
I	Radiation intensity, W/m^2.sr
k	Turbulent kinetic energy, m^2/s^2
LS	Length scale
M	Soot mass concentration, kg/m^3
m	Mass, kg
$\dot{m}$	Mass flow rate, kg/s
N	Particle number density, 1/m^3
N_A	Avogadro number
p	Pressure, N/m^2
P	Probability density function
Re	Reynolds number
S	Source term
Sc	Schmidt number
T	Temperature, K
TI	Turbulent intensity
u, U	Velocity, m/s
$u^{'}$	Fluctuating velocity
w_i	Quadrature weight
X	Mole fraction
Y	Mass fraction
z	Path length

Greek Symbols

ε	Rate of dissipation of turbulent KE
κ	Absorption coefficient
λ	Thermal conductivity, W/m K
μ	Dynamic viscosity
μ_t	Eddy viscosity
ν	Kinematic viscosity, m^2/s
ξ	Mixture fraction

ξ'' Variance of mixture fraction
ρ Density, kg/m^3
σ Turbulent Prandtl number
ϕ Scalar variable
ϕ' Fluctuation of scalar variable
χ Scalar dissipation rate, s^{-1}
$\dot{\omega}$ Reaction rate
δ_{ij} Chroneker delta

Subscript

crit Critical
d Droplet
eff Effective
f Fuel
g Gas
i, j, k Coordinate direction
in Inlet
k kth species
l Liquid/fuel
rad Radiation
st Stoichiometric
ϕ Scalar variable
0 Reference value
w Wall
z In z-direction

Superscript

K kth species

12.1 Introduction

Study of combustion has a great practical relevance in various spheres of the society even today. Controlled combustion is an intricate phenomenon, as it includes various physical transports and complex chemical reactions together in a coupled manner. Today, there is a global interest towards the clean power generation addressing the concern towards sustainability. Therefore, tremendous efforts have been put up by the researchers to improve the combustion system that focus on reducing emissions, increasing combustion efficiency and lowering costs without forfeiting the reliability.

Gas turbine is a power generating device, which is used in aircraft and marine engines and also in stationary electrical power plants. Gas turbine combustor is a part of the gas turbine power plant, where chemical energy of the fuel is converted to thermal energy for its subsequent conversion to mechanical work in the turbine. The development of the aviation gas turbine engines saw a remarkable progress in the last century. Amongst the various components of the engines, combustors have experienced many important modifications. The major criteria, over which the developments in gas turbine combustor take place, are high combustion efficiency, stabilization of flame, ready reignition following flame extinction and reduced emission of the pollutants.

In the effort of development of the gas turbine combustor, modelling of combustion has a major role to play. A well-established model can reduce the extent of the cut and try experiments and thereby reduces the cost of development. The combustion chamber of a gas turbine experiences a highly turbulent and swirling flow situation along with the interaction of jets coming as primary, secondary, dilution and film cooling air. In recent times, many researchers have used the large eddy simulation (LES) as a modelling tool for the simulation of flow in a gas turbine to describe, e.g. the interaction of swirling jets, features of steady and transient combustion characteristics and global spray combustion behaviour including droplet dispersion and spray evaporation. However, the more involved simulation technique compels the chemical kinetics of reaction to be kept as simple, global form. Some researchers concluded that the large density gradient in reacting flow results in numerical instability in the application of LES in combustion. This along with the higher computational time and uncertainties in more complicated modelling issues, like soot formation, allows the industrial users to retain the RANS simulation for the use in gas turbine combustors.

The popular method of simulating flow in gas turbine, therefore, involves solving the Favre-averaged Navier–Stokes equations along with the standard two-equation turbulence models for their computational efficiency. Van Maele et al. (2003) compared the performance of different models in swirling combustion and prescribed realizable k-ε model to be a better option. Similar prescription was also forwarded by De et al. (2011) and Reis et al. (2014) in turbulent non-premixed flame applications. Eldrainy et al. (2011) found that the simulation results with realizable k-ε model in swirling flow agree well with those using LES model. Joung and Huh (2009) used the realizable k-ε model in commercial gas turbine combustor firing methane fuel.

Gas turbines used in transportation, like aviation and marine, use liquid fuels due to their high energy density and easy transportability. Burning of liquid fuel spray is inherently complicated as it involves many interconnecting processes, like atomization, dispersion and evaporation of spray and mixing of fuel vapour and air in addition to other physical and chemical phenomena observed in the process. The interaction between the dispersed liquid phase and the continuous gas phase can be simulated using stochastic separated flow model under the Eulerian–Lagrangian frame of reference (Tolpadi 1995; Datta and Som 1999). The evaporated fuel vapour burns in air as a turbulent non-premixed flame, which can either be

modelled by eddy dissipation model or by using the flamelet model. The flamelet model can consider detailed chemical kinetics of reaction through the solution of mixture fraction and its variance and a probability density function can be used to describe the interaction between turbulence and chemistry. However, non-premixed flames of liquid hydrocarbon fuels generally lead to the formation of soot, at least in the rich region of fuel, which enhances the radiative exchange of heat. Therefore, proper modelling of soot formation and coupling of it with radiative energy exchange also remain as additional challenges in the liquid fuel combustion process.

In this chapter, we have described a numerical model which can be used for the prediction of kerosene spray flame and can be applied in the combustor of a gas turbine. The model considers the prediction of soot and radiative heat transfer, which have significant relevance for the non-premixed type spray flame of hydrocarbon fuels.

12.2 Modelling of Liquid Fuel Spray Combustion

The flow inside a gas turbine combustor is highly turbulent due to the high velocity of air flow. In a turbulent flow, the variables fluctuate randomly in all the directions. The turbulent flows can be solved by averaging the fluctuating variables in the transport equation over a time interval long enough with respect to the time period of fluctuations. In the absence of significant density fluctuation, the density is considered as constant during the averaging of the transport equations. The time averaging of the variables is known as Reynolds averaging and the approach of solution of flow is known as Reynolds-Averaged Navier–Stokes (RANS) solution. In the combustion system, a wide range of fluctuating density occurs, which is guided by the fluctuations in local temperature and concentration of species. When the averaging of the transport equations is done with the consideration of fluctuating density, many additional terms are formed in the time-averaged transport equations. It increases the modelling difficulty to solve the equations through numerical methods. In order to eliminate the extra terms, a density weighted averaging method is adopted in all the transport equations. This technique of averaging is known as Favre averaging and the derived equations are called Favre-averaged equations.

12.2.1 Continuous Phase Modelling

It is well known that the instantaneous value of a variable (ϕ) in a turbulent flow field can be decomposed into the mean and fluctuating terms as

$$\phi = \bar{\phi} + \phi' \tag{12.1}$$

where $\bar{\phi}$ is the time-averaged mean and ϕ' is the fluctuating components. The density-weighted average (Favre average) of the variable is defined as,

$$\tilde{\phi} = \frac{\overline{\rho\phi}}{\bar{\rho}} \tag{12.2}$$

The Favre average decomposition form of a flow variable can be written as

$$\phi = \tilde{\phi} + \phi'' \tag{12.3}$$

The Favre-averaged governing equations for the transport processes are written in tensor notation as follows.

Conservation of overall mass (Continuity)

$$\frac{\partial}{\partial x_i}\left(\bar{\rho}\tilde{u}_i\right) = 0 \tag{12.4}$$

Conservation of momentum

$$\frac{\partial}{\partial x_i}\left(\bar{\rho}\tilde{u}_i\tilde{u}_j\right) = -\frac{\partial \bar{p}}{\partial x_i} + \frac{\partial}{\partial x_i}\left(\bar{\tau}_{ij} - \bar{\rho}\widetilde{u_i'' u_j''}\right) \tag{12.5}$$

Conservation of energy

$$\frac{\partial}{\partial x_i}\left(\bar{\rho}\tilde{u}_j\tilde{h}\right) = \frac{\partial}{\partial x_i}\left(\frac{\mu}{\sigma}\frac{\partial \tilde{h}}{\partial x_i} - \bar{\rho}\widetilde{h'' u_i''}\right) + S_{rad} \tag{12.6}$$

Conservation of species mass

$$\frac{\partial}{\partial x_i}\left(\bar{\rho}\tilde{u}_j\tilde{Y}_k\right) = \frac{\partial}{\partial x_i}\left(\frac{\mu}{Sc}\frac{\partial \tilde{Y}_k}{\partial x_i} - \bar{\rho}\widetilde{Y_k'' u_i''}\right) + \dot{\omega}_k \tag{12.7}$$

It can be observed that new terms have appeared in the above equations through the process of averaging. The new term in the conservation of momentum equation (Eq. 12.5) is $-\bar{\rho}\widetilde{u_i'' u_j''}$, which is known as the Reynolds stress or turbulent stress (τ_{ij}^t). The generalized form of Reynolds stresses is given, following Boussinesq hypothesis as,

$$\tau_{ij}^t = -\bar{\rho}\widetilde{u_i'' u_j''} = \mu_t\left(\frac{\partial \tilde{u}_i}{\partial x_j} + \frac{\partial \tilde{u}_j}{\partial x_i}\right) - \frac{2}{3}\bar{\rho}\tilde{k}\delta_{ij} \tag{12.8}$$

Here, i and j represents the directional vectors, $\tilde{k}$ is the density averaged turbulent kinetic energy, δ_{ij} is the Kronecker delta and μ_t is the turbulent viscosity (eddy viscosity).

Moreover, the terms $-\bar{\rho}\widetilde{h''u_i''}$ and $-\bar{\rho}\widetilde{Y_k''u_i''}$ in the time-averaged energy and species equations, respectively, which are also the turbulent fluxes, are unknown quantities and required to be approximated. These terms are modelled as $-\bar{\rho}\widetilde{h''u_j''} = \left(\frac{\mu_t}{\sigma_{ht}}\frac{\partial\tilde{h}}{\partial x_i}\right)$, and $-\bar{\rho}\widetilde{Y_k''u_i''} = \left(\frac{\mu_t}{Sc_t}\frac{\partial\tilde{Y}}{\partial x_i}\right)$ respectively where σ_{ht} is the turbulent Prandtl number and Sc_t is the turbulent Schmidt number. The eddy viscosity can be defined in terms of turbulent kinetic energy (k) and dissipation rate of turbulent kinetic energy (ε).

Two-equation k-ε models are popularly used for the closure of turbulent flow (Tolpadi 1995; Datta and Som 1999; Watanabe et al. 2010). Guo et al. (2001) applied different models such as standard k-ε model, RNG k-ε model, low Reynolds number k-ε model and the differential Reynolds stress model to a submerged jet. They strongly recommended the k-ε models due to their consistency to predict the results during oscillation because the rate of dissipation of vortices is slower with k-ε models. Karim et al. (2003) found that the standard k-ε model is often over-diffusive in predicting highly swirling flow and recommended the use of realizable k-ε model instead. The present chapter and the results described in it are based on the application of realizable k-ε model for the closure of turbulent quantities.

12.2.2 Dispersed Phase Flow Model

Eulerian–Lagrangian approach is a well-known method to solve the transport of a dispersed phase within a continuous or gas phase. In this approach, along with solving the continuous phase in Eulerian frame of reference, the discrete phase is solved in the Lagrangian frame. The exchanges of momentum, heat and mass in between the two phases occur at definite rates determined by the slip in velocity, temperature and concentration, respectively, at the interface. These exchange rates are used to compute the interphase source terms over the life time of the droplets. The interphase source terms so calculated are then used in the gas phase conservation equations as additional terms. The spray is considered to comprise of a finite number of droplet classes distributed over an initial dispersion angle based on the atomization law of the liquid fuel.

The trajectory of a droplet of the kth class is computed by evaluating the velocity and position of a representative droplet of the class along its motion. The velocity of the droplet is found out from the conservation of momentum equation considering only inertia and drag forces to be significant. The equation can then be written as

$$m_d(k)\frac{d\,u_{d_i}(k)}{dt} = \frac{\pi}{8}\bar{\rho}[d(k)]^2|u_i - u_{d_i}(k)|\,[u_i - u_{d_i}(k)]\,C_{drag} \tag{12.9}$$

where C_{drag} is the drag coefficient on the droplet, which is evaluated following the drag law (Morsi and Alexander 1972). The effect of gas phase turbulence on the droplet dispersion is simulated using a stochastic approach. Instantaneous gas phase velocity (u_i) around the droplet is obtained in the above equation by computing the fluctuating velocity following a discrete random walk model. The position of the droplet is obtained by integrating the velocity over short time ranges. If any droplet, in course of its motion, strikes the combustor wall, it is assumed to reflect from the wall following an elastic collision.

Evaporation of the liquid from the surface of the droplets takes place considering the vapour pressure on the droplet surface to be equal to the saturation pressure at the droplet temperature. A piecewise linear variation of the saturation pressure for the liquid fuel with temperature is considered for the evaluation. The mass transfer coefficient (h_D) is calculated from the Sherwood number correlation of Ranz and Marshall (1952a, b). The change in droplet mass of the kth class can therefore be accounted as

$$\frac{d\,m_d(k)}{dt} = \pi d(k)_d^2\, h_D\left(Y_{f_s} - Y_f\right) \tag{12.10}$$

where Y_{f_s} and Y_f are the mass fractions of the fuel vapour on the droplet surface and in the surrounding gas.

In order to find out the variation of temperature of the droplet, an energy balance across the droplet surface for the kth class is considered as

$$m_d(k)c_{d_p}\frac{dT_d}{dt} = \pi d(k)_d^2\, h_c\left(T - T_p\right) - \frac{dm_d(k)}{dt}\Delta H_v \tag{12.11}$$

The heat transfer coefficient (h_c) is found out from the Nusselt number correlation of Ranz and Marshall (1952a, b) and the radiation exchange with the gas phase is neglected. The second term on the right-hand side is the consumption of heat due to evaporation from the drop surface with ΔH_v indicating the enthalpy of vapourization.

The liquid phase conservation equations are solved for each of the droplet classes along their trajectories till each class gets completely evaporated. The interphase source terms for mass, momentum and energy, which are accordingly computed at different grid points depending upon the positions of the droplets, are used in the gas phase equations. These terms are to be additionally considered in Eqs. (12.4)–(12.7) as the interphase source terms.

12.2.3 Combustion Model

To simulate the turbulent combustion process, many computational models have been developed and adopted by different researchers. The concept of flamelet, introduced by Williams (1975), is considered as a well-established model for the non-premixed flames. In this model, the non-premixed flame is represented by an ensemble of thin laminar opposed flamelets, with one stream of oxidant and another stream of fuel. The scalar variables (temperature, concentrations) across the flamelets are expressed as functions of the local mixture fraction and scalar dissipation rate.

The relationship among the mass fraction of species with instantaneous mixture fraction can be generated at different scalar dissipation rate as follows:

$$\rho\frac{\partial Y_k}{\partial t}-\rho\frac{\chi}{2}\frac{\partial^2 Y_k}{\partial \xi^2}-\dot{\omega}_k=0 \tag{12.12}$$

On the other hand, the temperature can be expressed in the mixture fraction space using the equation

$$\rho\frac{\partial T}{\partial t}-\rho\frac{\chi}{2}\frac{\partial^2 T}{\partial \xi^2}-\frac{1}{c_p}\frac{\partial p}{\partial t}+\sum_{i=1}^{N}\frac{h_k}{c_p}\dot{\omega}_k=0 \tag{12.13}$$

The scalar dissipation rate (χ), in the above two equations, represents the straining of flame that signifies the departure of chemistry from the equilibrium state. Physically, the instantaneous scalar dissipation rate can be defined as

$$\chi=2D_\xi\left(\frac{\partial \xi}{\partial x_i}\right)^2 \tag{12.14}$$

where D_ξ is the mean diffusivity.

A reference scalar dissipation rate, called instantaneous stoichiometric scalar dissipation rate (χ_{st}), is set to differentiate the region where only the mixing calculation is to be considered from where the combustion calculations is performed. The stoichiometric scalar dissipation rate can be expressed as,

$$\chi_{st}=\frac{a_s\ \exp\left(-2[erfc^{-1}(2\xi_{st})]^2\right)}{\pi} \tag{12.15}$$

where a_s is the characteristic strain rate, ξ_{st} is the stoichiometric mixture fraction and $erfc^{-1}$ is the inverse complementary error function. The minimum value of scalar dissipation (χ_{ext}) at which the combustion process stops (flame quenching) is called extinction strain rate. However, as the stoichiometric scalar dissipation rate

(χ_{st}) tends to zero, the chemistry will be near equilibrium. Therefore, stoichiometric scalar dissipation rate (χ_{st}) measures the departure of flamelet from equilibrium.

The solution of the scalar equations generates a flamelet library, which is a collection of scalar variables as functions of mixture fraction, scalar dissipation rate and instantaneous enthalpy. The concept helps to transform the entire chemistry of reaction in terms of mixture fraction and scalar dissipation rate. Hence, the computational time gets considerably reduced even with detailed chemistry involving many species by avoiding the calculations of transport equations for every single species.

The flamelet model solves the Favre-averaged transport equations of mixture fraction and its variance in the gas phase using their respective conservation equations (Peters 2004; Versteeg and Malalasekera 2007). The steady-state transport equation Favre mean mixture fraction is expressed as

$$\frac{\partial}{\partial x_j}\left(\bar{\rho}\tilde{u}_j\tilde{\xi}\right) = \frac{\partial}{\partial x_j}\left(\frac{\mu_t}{Sc_\xi}\frac{\partial \xi}{\partial x_j}\right) + \dot{S}_\xi \tag{12.16}$$

where the first term on the RHS is the turbulent flux of mixture fraction ξ and the second term is the source term used in liquid fuel combustions due to interphase transport as referred in the previous section. The transport equation for the mixture fraction variance, ξ''^2, is expressed as

$$\frac{\partial}{\partial x_j}\left(\overline{\rho}\widetilde{u_j}\widetilde{\xi''^2}\right) = \frac{\partial}{\partial x_j}\left(\frac{\mu_t}{Sc_t}\frac{\partial \widetilde{\xi''^2}}{\partial x_j}\right) + C_{g1}\mu_t\left(\frac{\partial \widetilde{\xi''^2}}{\partial x_j}\right)^2 - \widetilde{\rho}\widetilde{\chi} \tag{12.17}$$

where C_{g1} is the model constant. The last two terms on the right-hand side of Eq. (12.7) are the generation rate of mean mixture fraction variance and the rate of destruction of mean mixture fraction variance, respectively. The mean scalar dissipation rate (χ), representing the departure from equilibrium due to stretch, can be evaluated through the decay of the mixture fraction fluctuations and its mean value as,

$$\tilde{\chi} = c_\chi \frac{\tilde{\varepsilon}}{\tilde{k}}\tilde{\xi''^2} \tag{12.18}$$

where c_χ is a constant having value 2.0 (Janicka and Peters 1982).

In the present formulation, an opposed laminar diffusion flame is simulated to generate the relationship among the various scalar variables (like species concentrations and temperature) with mixture fraction and scalar dissipation rate across the laminar flamelets. This has been accomplished by transforming the steady state scalar equations from the physical space to the mixture fraction space. The simulation considers a chemical kinetic model of kerosene ($C_{12}H_{23}$) combustion involving 17 species (such as $C_{12}H_{23}$, C_2H_2, CH, CO, CO_2, O_2, O, OH, H_2, H, H_2O, HO_2, NH, N, NO, N_2O, N_2) and 26 reactions (Kundu et al. 1998) to generate

the species source terms. The model considers nine flamelets, with scalar dissipation rates of 0.01 s^{-1}, 0.1 s^{-1}, and then 1–13 s^{-1} with an increment of 2 s^{-1}. The flame extinction occurs when the scalar dissipation rate is increased to higher values.

However to evaluate the mean values of the scalar variables, which are the functions of mean mixture fraction, a probability density function is used. The mathematical description of PDF has been clearly described in detail in (Evans et al. 2000). Pope (1991), Chen et al. (1989) gave the early contributions towards this method of solution. By this method, the reacted source term has been treated without any assumption of turbulent fluctuations (Pope 1985, 1994; Dopaza et al. 1994; Pope 2000). The concept of the probability density function in the model is explained with the help of Fig. 12.1. Mixture fraction is a fluctuating quantity that fluctuates with respect to time due to turbulence in the flow. If one wants to find out the probability for finding ξ within the range ξ_1–ξ_2 for a particular coordinate inside the computational domain it will be $\int_{\xi_1}^{\xi_2} P(\xi)\, d\xi$. Probability for finding ξ within the entire range (0–1) for this particular coordinates inside the computational domain is $\int_0^1 P(\xi) d\xi = 1$.

Since, the instantaneous scalar variables are function of instantaneous mixture fraction, the mixture fraction probability density function can be used to determine the mean quantity of any scalar variable by integrating the scalar variables jointly with the corresponding probability density function. Since Favre mean quantities are the required output in this work, the instantaneous probability density function ($P(\xi)$) is required to be converted to Favre PDF ($\tilde{P}(\xi)$) to calculate the Favre mean scalar variables within the flow field. The Favre PDF can be expressed as

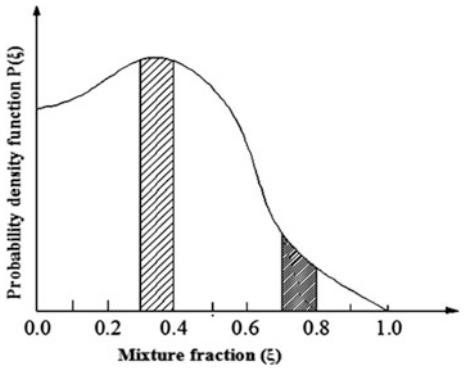

Fig. 12.1 A conceptual graph between PDF and mixture fraction

$$\tilde{P}(\xi) = \frac{\rho(\xi)}{\bar{\rho}} P(\xi) \tag{12.19}$$

The effect of turbulent fluctuation on the scalar variables has been accounted using a statistical distribution employing a joint probability density function (pdf) in mixture fraction, scalar dissipation rate and enthalpy, $\tilde{P}(\xi, \chi, H)$. The mean scalar variables have been evaluated as

$$\phi = \int_0^\infty \int_0^\infty \int_0^1 \phi(\xi, \chi, H)\, \tilde{P}(\xi, \chi, H)\, d\xi\, d\chi\, dH \tag{12.20}$$

The joint pdf has been expressed as $\tilde{P}(\xi)\ \tilde{P}(\chi)\tilde{P}(H)$ considering the variables to be statistically independent. The pdf for mixture fraction ($\tilde{P}(\xi)$) is presumed to be a beta function as

$$\tilde{P}(\xi) = \frac{\xi^{\alpha-1}\,(1-\xi)^{\beta-1}\,\Gamma(\alpha+\beta)}{\Gamma(\alpha)\,\Gamma(\beta)} \tag{12.21}$$

where parameters α and β are determined from the mean and variance of ξ (Versteeg and Malalasekera 2007). On the other hand, fluctuation in scalar dissipation rate is ignored and its pdf ($\tilde{P}(\chi)$) is taken as a delta function at the mean value. Further, the enthalpy fluctuations are assumed to be mainly due to mixture fraction fluctuations and independent of the enthalpy levels (Bray and Peters 1994). Therefore, the pdf in enthalpy is also taken as $\tilde{P}(H) = \delta\left(H - \tilde{H}\right)$. Eq. (12.20) is, therefore, reduced to $\phi = \int_0^1 \phi\left(\xi, \tilde{\chi}, \tilde{H}\right)\, \tilde{P}(\xi)\ d\xi$.

12.2.4 Radiation Model

Radiation inside the combustor is a volumetric phenomenon and the products such as carbon dioxide and water vapour also participates in radiative exchanges along with soot. P1 model (Siegel and Howell 1992) and DO (Discrete ordinate) (Fiveland 1982; Carlson and Lathrop 1993) models are the most frequently used radiation models in combustible flow calculations due to their capability to simulate the volumetric radiation along with the interaction of particulates in radiative heat transfer. The DO model is a finite volume approach of radiation model which was first introduced by Chandrashekhar (1950), which predicts better in the case of higher optical thickness.

Radiative heat transfer is important in the combustion of hydrocarbon fuels because of the active participation of the product components, like CO_2 and H_2O.

The radiative heat loss from the flames is particularly enhanced with soot formation due to the high emissivity of soot. The radiative heat exchange has been simulated by using discrete ordinate (DO) model (Modest 1993), with the radiative transfer equation solved for a finite number of angular directions ($\vec{s}_i, \quad i = 1, 2, 3 \ldots\ldots\ldots n$) throughout the span of 4π solid angle. In the radiation calculation, scattering is neglected as the soot particles are generally fine and remain well dispersed. The reduced form of the radiative heat transfer equation is given as

$$\frac{d\, I_i\,(r, \vec{s}_i)}{ds} = \kappa\, I_b\,(r) - \kappa\, I_i\,(r, \vec{s}_i) \tag{12.22}$$

where I_i is the radiation intensity in the ith direction, I_b is the radiation intensity of blackbody, r is the position vector, $\vec{s}_i$ is the direction vector in ith direction and κ is the combined absorptivity considering both the absorptivity of the gas phase (κ_{gas}) and soot (κ_{soot}).

Absorptivity of bulk gas has been evaluated by weighted sum grey gas model (wsggm) with the constant grey gas absorption coefficient (κ_k) for the participating gases ($k = 0, 1, 2, 3 \ldots K = k - 1$) along with suitable weighing factors (a_k) given as

$$\kappa_{gas} = -\frac{\ln\left[1 - \sum_{k=0}^{k-1} a_k\left(1 - e^{-\kappa_k p_k}\right)\right]}{z} \tag{12.23}$$

where p_i is the partial pressure of the participating gases and z is the path length. The weighing factor a_k is considered as a polynomial function of temperature and it is given as

$$a_k = \sum b_{k,j} T^j \tag{12.24}$$

The absorption coefficient contributed by soot (κ_k) is considered as a linear function of temperature and is given as (Sazhin and Sazhina 1996).

$$\kappa_{soot} = 1232.4 \rho_{soot}\left[1 + 4.8 \times 10^{-4}(T - 2000)\right] \tag{12.25}$$

The energy source term due to radiation can be evaluated as

$$S_{rad} = \nabla . \bar{q}_{rad} = \kappa\left(4\sigma T^4 - \sum_{i=1}^{N} w_i I_i\right) \tag{12.26}$$

where w_i is the quadrature weight associated with the direction i in the discrete ordinate method.

12.3 Modelling of Soot Formation

The formation of soot and the energy exchange due to radiation play significant roles in the prediction of spray combustion behaviour in the gas turbine. The gas temperature leaving the combustor and the temperature of different combustor parts (like combustor wall, fuel injector and primary air swirler) get affected by the soot distribution in the flame and the radiative energy exchange. Soot is formed during the combustion of hydrocarbon fuel at rich mixture condition and at high temperature. The precursor species, such as acetylene (C_2H_2), benzene (C_6H_6) and phenyl radical (C_6H_5), initiates the soot formation in the rich side of the flame. The nucleated precursors grow to become polycyclic aromatic hydrocarbons and finally give rise to young soot particles (Richter and Howard 2000; Mansurov 2005). Comprehensive reviews on soot formation have been given by Haynes and Wagner (1981), Glassman (1988), Frenklach (2002) and Mansurov (2005). Soot models can be broadly divided into three groups—empirical, semi-empirical and detailed model. All three types of models have been discussed by Kennedy (1997) for different fuels.

The early contribution towards the modelling of soot was given by Calcote and Manos (1983). In their model, they used a direct relation that predicts the soot with respect to the local equivalence ratio called threshold sooting index. This is a quick method and consumes less computation memory. Khan and Greeves (1974) proposed a one-step soot model based on empirical soot formation rate for diesel fuel. They, for the first time, considered the soot particle inception during combustion and expressed it as the function of temperature, pressure and equivalence ratio. Both the above models are based on a number of assumed constants, therefore are purely empirical models. Tesner et al. (1971) developed a two-equation soot model that includes some assumptive constants and predicts the nucleation rate. Consequently, soot was evaluated by solving the production and consumption of soot nuclei. Hiroyasu et al. (1983) proposed a soot model, which considered the soot formation process involving only two reactions steps. First step is the formation step, in which soot is linked directly to the fuel vapour molecules, while the second step considered the oxidation of soot. The rates of both the soot formation and oxidation are expressed in Arrhenius form. The net rate of change in soot mass is the difference between the rates of formation and oxidation.

These early models of soot formation are limited to the prediction of the final soot concentration without going into the actual physical and chemical processes. Nowadays, in order to understand the effects of the chemical and physical processes on soot formation, different semi-empirical models as well as detailed soot models incorporating multistep chemistry have been developed by various researchers. Most of the works on modelling of soot is done for lower hydrocarbon fuels, like methane. Brookes and Moss (1999), Sivathanu and Gore (1997), Kaplan et al. (1998), Mandal et al. (2009), Smooke et al. (1999) made significant contributions towards the modelling of soot formation for methane fuel. A few works towards predicting soot in kerosene fuel combustion have been found in the literature. Moss

and Aksit (2007) used a semi-empirical soot model in order to predict the soot in a laminar diffusion flame by using a surrogate kerosene fuel by modifying the model constants. Wen et al. (2003) and Watanabe et al. (2006) devoted their contributions towards the modelling of soot for the diffusion flame of surrogate kerosene fuel. However from the literature, it has been revealed that further research is required to predict the soot concentration with more accuracy for heavier hydrocarbon fuels.

Soot is an agglomerate of millions of carbon atoms along with few hydrogen and oxygen atoms. Formation of soot occurs under fuel rich circumstance at high temperature during combustion. Diffusion flame releases more soot than premixed flame due to the higher local equivalence ratio present in the flame. The formation soot occurs through various steps such as

1. Particle inception or Nucleation
2. Surface growth
3. Coagulation and Agglomeration
4. Soot oxidation

A schematic of the soot formation process can be shown as in Fig. 12.2.

During particle inception or nucleation process, young soot particles are first formed from the gas phase of the species. Various mechanisms for the inception of first soot particle have been proposed by different researchers (Tarek et al.; Calcote and Manos 1983), which considered polyacetylene (Moss and Aksit 2007) and polycyclic aromatic hydrocarbons (PAH) (Hall et al. 1997) as the incepted chemicals. On the other hand, acetylene (C_2H_2), benzene (C_6H_6) and phenyl (C_6H_5) are

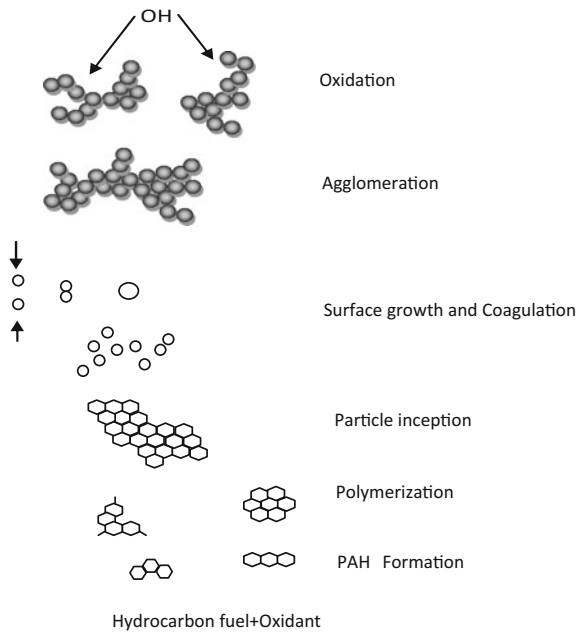

Fig. 12.2 Schematic of soot formation steps

considered as the precursors to evaluate the rate of soot inception in the computational modelling.

Although nucleation of soot particles contributes to determine the quantity of soot in flames, the major mass of soot is formed by the reaction between nucleated soot particles and gas phase species (Mansurov 2005). Most of the hydrocarbons (especially C_2H_2) react on the surface of the nucleated soot particles so that the particles grow up in size (Harris and Weiner 1983). Therefore, both in the acetylene model and PAH model (Moss and Aksit 2007) of soot formation only acetylene (C_2H_2) is used as surface growth species of soot.

Once the soot particles have been formed, they collide with each other and stick among themselves forming larger particles through a process called coagulation. However, this process is a physical phenomena and it depends upon the frequency of collision between the particles. Therefore after all, the rate of coagulation may be evaluated through a direct relationship with soot number density (number of soot particles per unit volume) multiplied with some proportionality constant.

In addition to the above processes, the oxidation of soot also occurs after its formation. O_2 and OH are the most active oxidizers that oxidized the soot inside the flame. The reaction mechanisms for oxidation of soot are given as

$$1/2O_2 + C(S) \rightarrow CO \tag{12.27}$$

$$OH + C(S) \rightarrow CO + H \tag{12.28}$$

12.3.1 Model Equations for Soot Formation

Brookes and Moss (1999) proposed a semi-empirical acetylene-based soot model that has been developed for lower hydrocarbon such as methane (CH_4). However, since the rate of soot formation is much slower than the rate of the combustion reactions, separate transport equations for soot mass fraction and nuclei concentration are solved. The transport equations are given as

$$\frac{\partial}{\partial x_i}\left(\bar{\rho}\tilde{u}_i\tilde{Y}_{soot}\right) = \frac{\partial}{\partial x_i}\left(\frac{\mu_t}{\sigma_{soot}}\frac{\partial \tilde{Y}_{soot}}{\partial x_j}\right) + \frac{dM}{dt} \tag{12.29}$$

$$\frac{\partial}{\partial x_i}\left(\bar{\rho}\tilde{u}_i\tilde{b}_{nuc}\right) = \frac{\partial}{\partial x_i}\left(\frac{\mu_t}{\sigma_{nuc}}\frac{\partial b_{nuc}}{\partial x_j}\right) + \frac{1}{N_{norm}}\frac{dN}{dt} \tag{12.30}$$

where $\tilde{Y}_{soot}$ is the soot mass fraction, M is the soot mass concentration, $\tilde{b}_{nuc}(=N/\rho N_{norm})$ is normalized radical nuclei concentration, N is soot number density (particles per cubic metre) and $N_{norm} = 10^{15}$ particles. σ_{soot} and σ_{nuc} are Prandtl number in soot mass fraction transport equation and nuclei transport equation respectively and their values are taken as 0.6.

The source term for number density (N) has been calculated by considering nucleation and coagulation of soot particles and is given as

$$\frac{dN}{dt} = \underbrace{C_\alpha N_A \left(\frac{X_{C_2H_2} P}{RT}\right) \exp\left(-\frac{T_\alpha}{T}\right)}_{Nucleation} - \underbrace{C_\beta \left(\frac{24\,RT}{\rho_{soot} N_A}\right)^{1/2} d_{p_{soot}}^{1/2} N^2}_{Coagulation} \tag{12.31}$$

The nucleation, surface growth and oxidation of soot are all accounted to evaluate the source term for mass concentration (M). The oxidation process has been modelled using the Fennimore-Jones model of soot oxidation. The overall equation of the source term of mass concentration is given as

$$\frac{dM}{dt} = \underbrace{C_\alpha M_p \left(\frac{X_{C_2H_2} P}{RT}\right) \exp\left(-\frac{T_\alpha}{T}\right)}_{Nucleation} + \underbrace{C_\gamma \left(\frac{X_{C_2H_2} P}{RT}\right) \exp\left(-\frac{T_\gamma}{T}\right) \left[(\pi N)^{1/3} \left(\frac{6M}{\rho_{soot}}\right)^{2/3}\right]^n}_{Surface\ Growth} - \underbrace{C_{oxid} C_\omega \eta_{coll} \left(\frac{X_{OH} P}{RT}\right) \sqrt{T} (\pi N)^{1/3} \left(\frac{6M}{\rho_{soot}}\right)^{2/3}}_{Oxidation} \tag{12.32}$$

12.3.2 Soot Model Optimization and Validation

In the present work, acetylene (C_2H_2) has been adopted as the precursor of soot, both in the nucleation and surface growth reactions. It has been found that the evaluation of C_2H_2 from the adopted chemical kinetics model results in a poor prediction of soot concentration. This may be the shortcoming of the kinetic model in evaluating acetylene. Therefore, we have evaluated acetylene concentration from the predicted data of Moss and Aksit (2007), showing the variation of C_2H_2 mol fraction with mixture fraction in the non-premixed combustion of kerosene surrogate fuel. The prediction was made from the simulation of one-dimensional, counterflow non-premixed flame using detailed chemistry for a model kerosene fuel.

A curve fitting exercise into the flamelet data of Moss and Aksit (2007), shown in Fig. 12.3, gives the following relations between C_2H_2 mol fraction ($X_{C_2H_2}$) and mixture fraction (ξ) in a kerosene flame

$$\text{For } 0 < \xi \le 0.17: X_{C_2H_2} = 4.9944\xi^3 - 1.5145\xi^2 + 0.1481\xi - 4.6065 \times 10^{-3}; \tag{12.33a}$$

$$\text{For } 0.17 < \xi \le 0.3: X_{C_2H_2} = 6.1369\xi^3 - 5.8333\xi^2 + 1.7998\xi - 0.1666; \tag{12.33b}$$

$$\text{For } 0.3 < \xi \leq 1: X_{C_2H_2} = -0.133\xi^4 + 0.3081\xi^3 - 0.2637\xi^2 + 0.08604\xi + 0.0053; \tag{12.33c}$$

The original model of Brookes and Moss (1999) was designed to predict the soot formation in non-premixed flames of methane fuel and the values for the model constants C_α, C_γ were prescribed as 54, 11700, respectively, for methane. Kerosene has a much higher tendency of forming soot than methane, which is evident in its lower smoke point. Therefore, the model constants of the source terms in Eqs. (12.31) and (12.32) are to be modified suitably for use with kerosene fuel ($C_{12}H_{23}$).

In order to optimize the model constants for kerosene, a validation study of the soot model has been separately done for an axisymmetric burner burning kerosene vapour. Study of soot formation in a similar burner for kerosene-vapour non-premixed flame burning in air was earlier conducted experimentally by Young et al. (1994) and computationally by Wen et al. (2003). The results are given in the work of Ghose et al. (2016), where the optimized constants of C_α, C_γ are prescribed as 648, 140, 400, respectively, with the constant for oxidation reaction C_{oxid} as 0.015.

In order to optimize the model constants in a kerosene non-premixed flame, a validation study of the soot model has been separately done for an axisymmetric burner. Study of soot formation in a similar burner for kerosene-vapour non-premixed flame burning in air was earlier conducted experimentally by Young et al. (1994) and computationally by Wen et al. (2003). The above-discussed models with modified constants along with the correlation established between mole fraction of precursor species and mixture fraction are used in the computation of soot. The physical model and the computational domain are schematically shown in Fig. 12.4.

Figure 12.5 shows the soot volume fraction distribution along the axial direction in the computational domain of Fig. 12.4. The predicted results of soot volume fraction from the model are compared with the experimental results of Young et al. in the figure. Moreover, Fig. 12.6 further illustrates such comparison in the radial

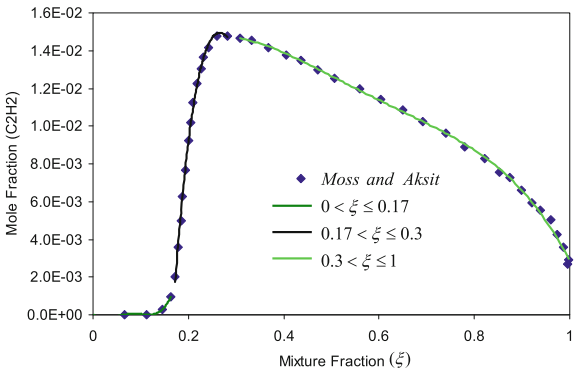

Fig. 12.3 Flamelet relationship for mole fraction of C_2H_2 and mean mixture fraction in non-premixed kerosene flame

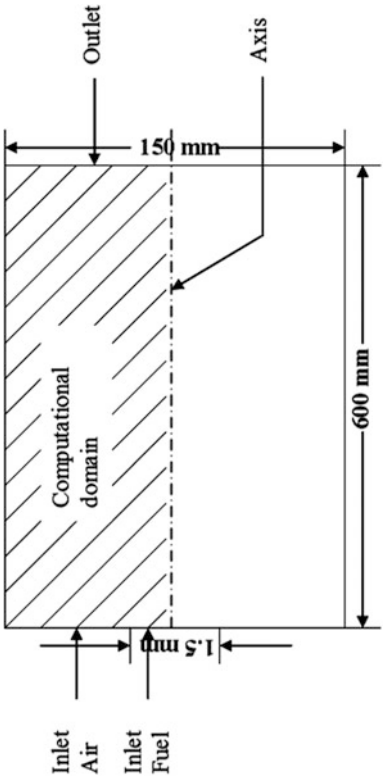

Fig. 12.4 Schematic of the physical geometry and computational domain for the validation of soot formation model

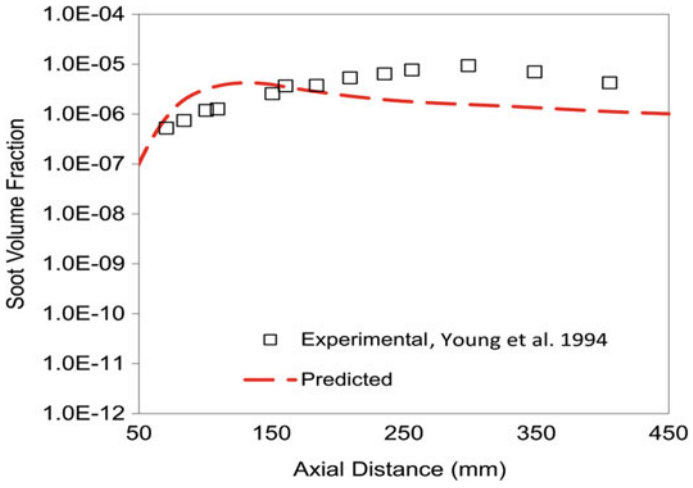

Fig. 12.5 Axial variation of soot volume fraction along the centreline of the kerosene jet flame

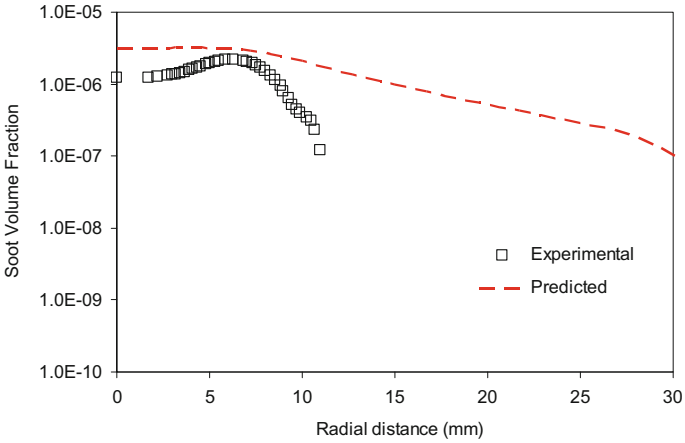

Fig. 12.6 Radial variation of soot volume fraction 100 mm above the inlet

direction at 100 mm above the inlet plane. The results show fairly good agreement with the optimized model constants for kerosene fuel, as mentioned earlier.

12.4 Physical Description and Operating Conditions of the Present Problem

The effects of air flow distribution on the performance of the combustor have been studied in a 3-D combustor geometry (Fig. 12.7) using the models described above. Three different air flow splits, with primary:secondary as 30:70, 40:60 and 50:50 have been considered in the analysis. The inlet plane of computation is considered

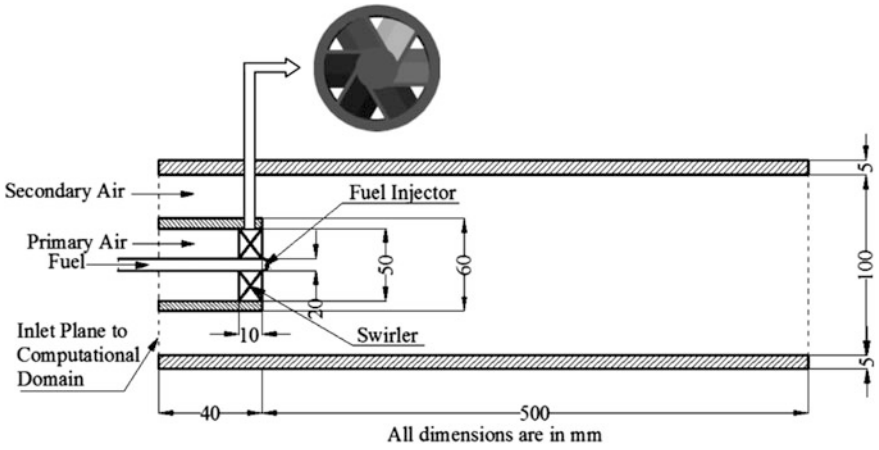

Fig. 12.7 Physical geometry of the combustor under study

at 40 mm upstream to the swirler plane. Experiments have also been carried out in an experimental test rig, which resemble the physical geometry of the present model.

The total air flow entering the combustor is split equally between the primary and secondary streams. The Reynolds number, corresponding to the average axial velocity of air in the combustor and combustor diameter ($\mathrm{Re_D} = 4\dot{m}_{air}/\pi D\mu$) is 26300, where $\dot{m}_{air}$ is the total mass flow rate of air (including primary and secondary), D is the combustor diameter and μ is the viscosity of air at inlet condition. Plug flow velocity distributions of air have been considered for the axial velocity at the entry to the combustor, both for the primary and secondary air. In addition, tangential velocity is imparted to the primary air at inlet for the constant angle vane swirler. Both primary and secondary airs are at room temperature (300 K) at the inlet. The turbulent intensity (*TI*) and the length scale (*LS*) at inlet planes are set as the boundary conditions of turbulent quantities.

No slip boundary condition is given on the wall with standard wall function for the turbulence calculation. A mixed (convection and radiation) boundary condition has been set to account the heat loss from the system to the atmosphere. A calculated value for heat transfer coefficient in between outer wall and atmosphere has been specified along with the emissivity for the wall surface material. Ambient temperature has been set at 300 K and the thickness of the wall is taken as 5 mm.

The density in the gas phase is computed using the equation of state for ideal gas law. The specific heat of the component species are evaluated considering polynomial variation with temperature. The mixing laws have been adopted for finding the properties of the gas mixture. Both turbulent Prandtl number and turbulent Schmidt number are considered as one.

For the discrete phase simulation, injection pressure and spray cone angle are given as measured from the experiments with the atomizer under use. The liquid is injected as 20 diameter classes of droplets sprayed within an initial spray cone angle of 36°. The dispersion angle of the spray is assumed to be 6°. The details of operating and simulating conditions for the simulation are given in Table 12.1.

The variables have been defined in the domain using a staggered grid arrangement. The discretization of the governing equations has been done using power law scheme while, the radiation model equation is discretized using second-order upwinding scheme. A pressure based solver is used in the simulation and the pressure-velocity coupling is solved with the SIMPLE algorithm. The geometry is meshed with unstructured hexahedral 324,394 elements. Ansys Fluent 13.0 is used to simulate the work.

Table 12.1 Operating and simulation conditions

Flow conditions	Primary air	Secondary air	Others
Mass flow rate (kg/s)	0.0124	0.018	–
Bulk velocity (m/s)	6.147	2.94	–
Temperature (K)	300	300	–
Swirl number	2.142	0.0	–
Air fuel ratio	–	–	110:1
Fuel flow rate (kg/s)			0.00036
Combustor pressure (atm)	–	–	1.0
Turbulent intensity (%)	4	4	–
Length scale	0.07D	0.07D	–
Liquid fuel temperature (K)	–	–	300
Spray cone angle (deg)	–	–	36
Injection pressure (bar)	–	–	5
Droplet class	–	–	20

12.5 Results and Discussion

The variations in temperature along the combustor wall (Fig. 12.8a) and in the exit gas (Fig. 12.8b) agree quite well with the measured values. A small discrepancy in the temperature prediction is noticed on the wall around the flame zone which may be attributed to the variation in radiative heat transfer from the flame. The predicted temperature distribution in the exhaust gas agrees very well with the experiments over the entire cross section of the combustor.

Figure 12.9a, b, c shows the mean temperature distributions in the vertical plane passing through the axis of the combustor for the three different air flow splits with superimposing velocity vectors. The highest temperature zones in the figures, adjacent to the fuel injector, depict the flame regions. It is clearly evident from the figures that the flame becomes shorter in size with the increase in the primary air. With increase of primary air flow through swirler, the tangential momentum in the inlet stream increases, and it creates a stronger central recirculation zone. With strong swirling motion, the mixing process intensifies in the flame zone. Since the rate of reactions is considered to be very fast, the overall combustion rate is controlled by the rates of physical processes. Therefore a short flame is generated. When the primary air fraction increases to 50% of the total flow rate, the central recirculation bubble is so strong that it breaks the flame bubble on the axis and the highest temperature flame zone is shifted away from axis (refer Fig. 12.9c). The flame becomes very short due to the increased rates of the physical processes.

Figure 12.10 compares the centreline temperature variations in the combustor for the three different air flow splits. It is seen that in all the cases, the temperature at the plane of the atomizer ($x = 0$) is somewhat high because of the incident radiation from the flame. The peak centreline temperature is the maximum for the 40:60 flow split case, though in the 30:70 flow split case the maximum temperature is reached at a further downstream location. In case of 50:50 air flow split, the maximum

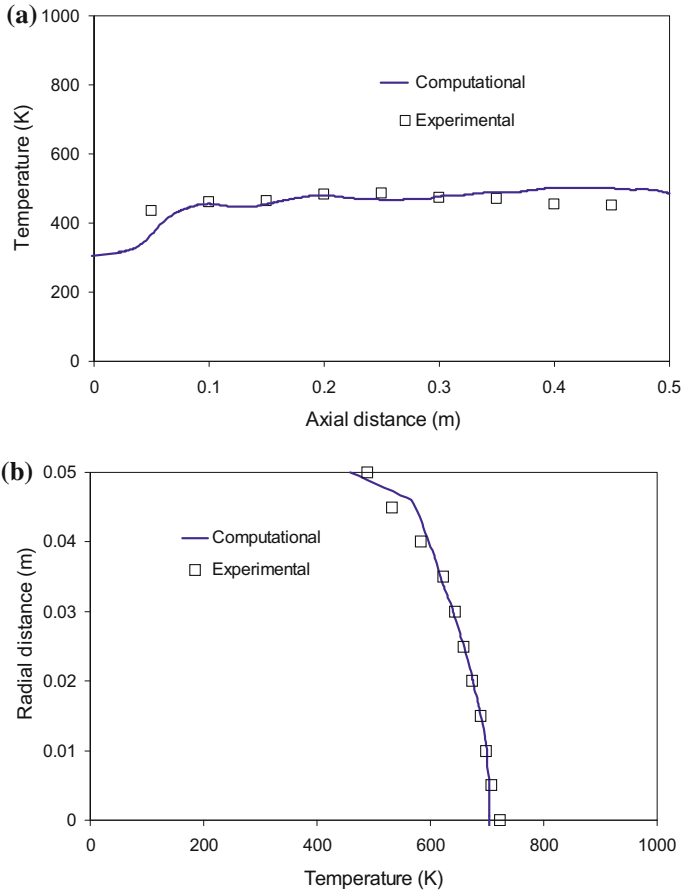

Fig. 12.8 Comparison of predicted and measured values of **a** wall temperature along the length of the combustor, **b** exit gas temperature across the radial direction

centreline temperature is much lower and occurs closer to the inlet plane. This variation in the centreline distributions can be clearly explained from the respective temperature contour plots. For the 30:70 and 40:60 air flow splits, the maximum temperature zones are located on the centreline. On the other hand, in the 50:50 case, the maximum temperature zone occurs in an annulus, which is away from the centre, and the peak centreline temperature is much less.

The variation in gas temperature at the combustor exit often has significance. In case of gas turbine, the more uniform exit gas temperature distribution is desirable for the health of the turbine. Figure 12.11 shows the radial variation of the gas temperature at the exit to the combustor for the three different air flow splits. In the case of 30:70 air flow split, the flame is longer and the maximum temperature in the combustor occurs closer to the exit plane. Therefore, the distance available to

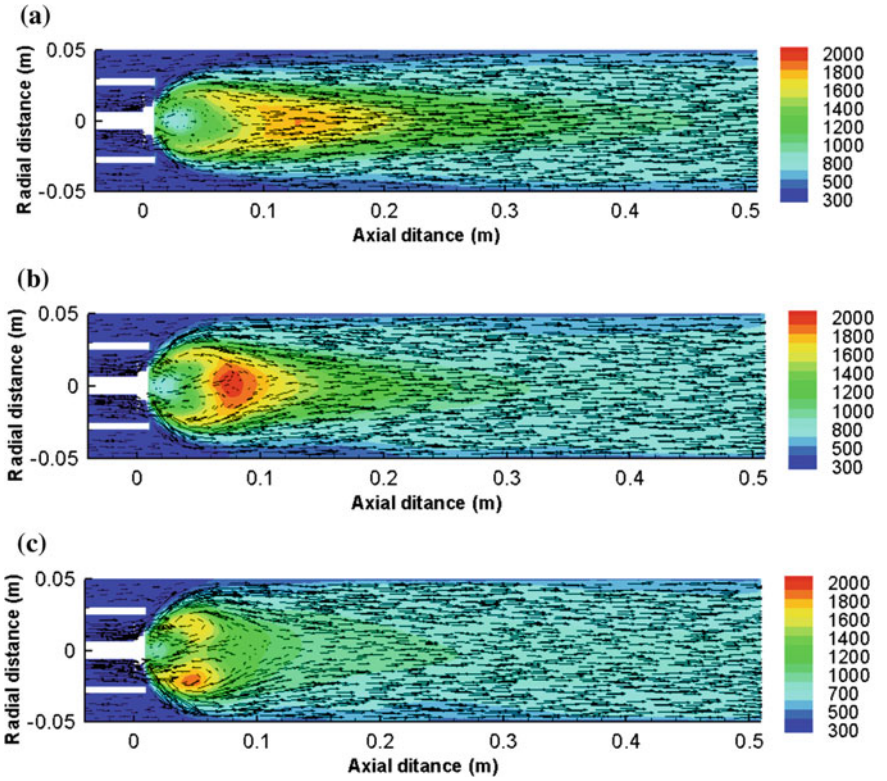

Fig. 12.9 Velocity vectors and Temperature distributions across the vertical plane through the combustor axis for three different air flow splits between primary and secondary streams **a** 30:70, **b** 40:60 and **c** 50:50

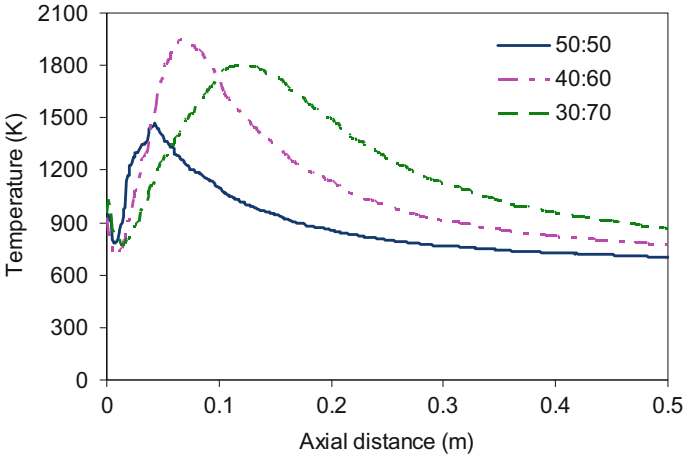

Fig. 12.10 Variation of centreline temperature along the length of the combustor for different air flow splits between primary and secondary streams

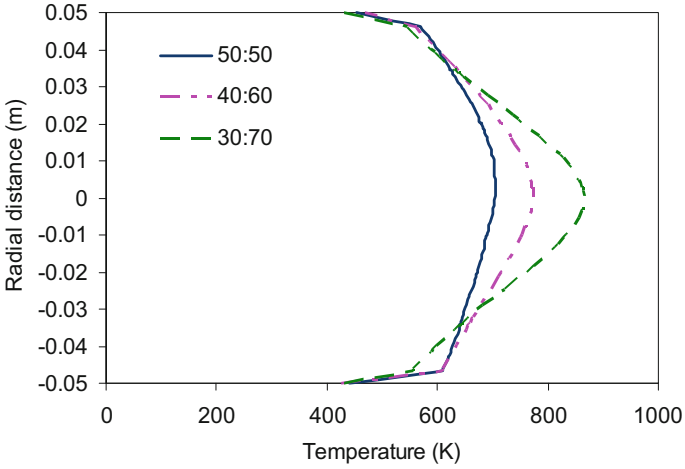

Fig. 12.11 Variation of exit gas temperature from the combustor at three different air flow splits between primary and secondary streams

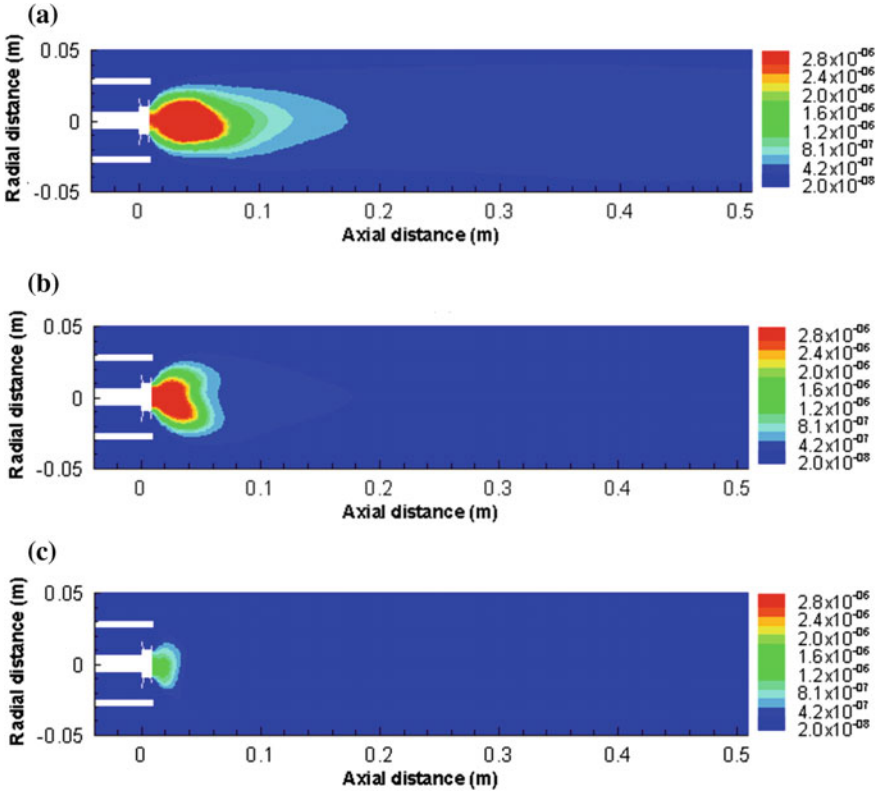

Fig. 12.12 Soot volume fraction across the vertical plane through the combustor axis for three different air flow splits between primary and secondary streams **a** 30:70, **b** 40:60 and **c** 50:50

transport the energy in the lateral direction becomes considerably shorter. As a result, greater non-uniformity in the temperature distribution prevails at the exit plane. When the primary to secondary air fraction increases to 50:50, the flame shortens in length and became wider. Therefore, a large distance available to transport the energy in the lateral direction, as a result exit temperature distribution became more uniform.

The soot distributions in the combustor are plotted in Fig. 12.12a, b, c for the three different air flow splits. When the primary air fraction is less a longer high temperature region is observed as shown in Fig. 12.9a. Soot precursor is an exponential function of temperature. Therefore, soot-laden zone is prolonged in this case. Moreover, due to fuel rich condition of mixture in flame region, maximum soot is also produced in this case. When primary air fraction increases and the ratio became 50:50, less amount of soot generated because fuel lean condition at flame region.

Figure 12.13 shows the variation of soot volume fraction on the centreline of the combustor for three different air flow splits. The peak soot volume fraction on the centreline is about five times higher in the 30:70 split case and more than four times higher in the 40:60 split case, compared to the 50:50 split case. Furthermore, it is seen from the soot contours that the concentration of soot near the fuel injector (x = 0) remains quite high. This results in the deposition of considerable soot on the atomizer body after continuous operation, which is also evident in the experiments. The higher soot volume fraction near the atomizer with lower primary air results in faster build-up of soot on the atomizer surface. When the soot build-up becomes large, the atomization quality of the fuel suffers and the combustion gets affected.

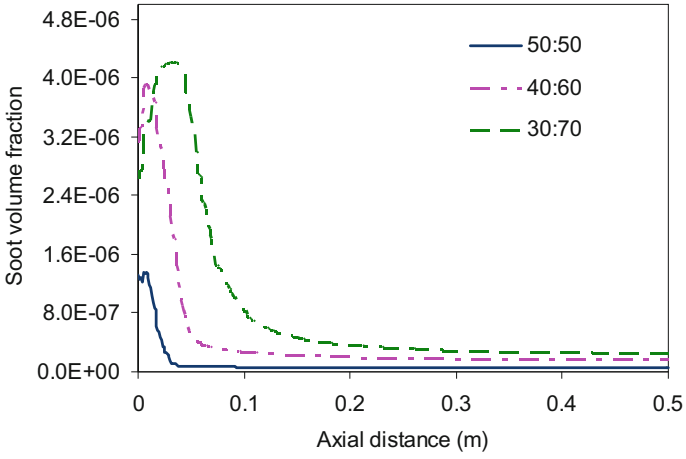

Fig. 12.13 Variation of soot volume fraction along the combustor centreline for three different air flow splits between primary and secondary streams

The soot-laden gas at high temperature causes increased radiation from the flame zone. The concentration of soot in the flame zone is dependent on the quantity of primary air supplied to the combustor. On the other hand, the secondary air, which enters along the outer wall of the combustor, helps to keep the wall surface cool. Therefore, the split between the primary and secondary air flow into the combustor will have an effect on the combustor wall and fuel injector surface temperatures.

It is clearly evident from Fig. 12.14a that the highest radiative flux on the wall is incident around the flame, close to the inlet to the combustor. This is caused by the high temperature of the flame and the high luminous radiation from the soot present in the flame zone. At the downstream location, the radiative flux on the wall is mostly from the participating gases in the flow. The maximum incident heat flux

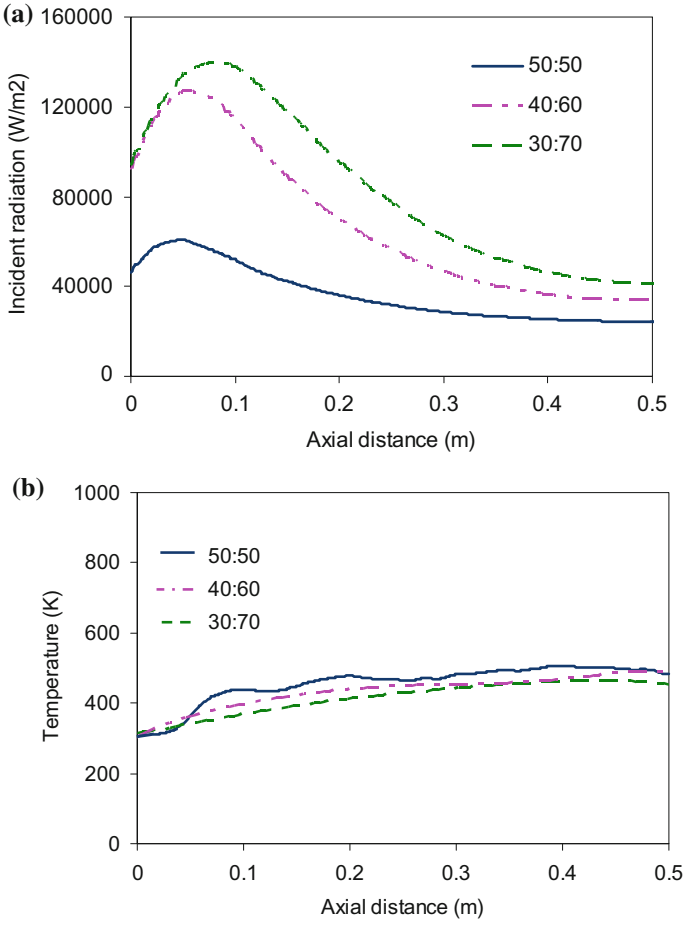

Fig. 12.14 Variation of **a** incident radiation, **b** outer wall temperature along the combustor length for three different air flow splits

due to radiation on the peripheral wall is achieved when the primary air flow is 30% of the total air flow. The soot volume fraction in the flame is much higher in this case, which is the prime reason of the increased radiative flux. The maximum incident radiation decreases by more than 50% when the primary air fraction is increased to 50% of the total flow. However, the peripheral wall of the combustor is cooled convectively by the flow of secondary air adjacent to the wall. The secondary air enters the combustor coaxially with the primary air flow and grazes along the wall, while exchanging energy with the high temperature core as well as with the combustor wall. When the primary air fraction is more, the fraction of the secondary air is less and it gives less convective cooling of the wall. Figure 12.14b shows the distribution of wall temperature along the length of the combustor. The wall temperature is seen to increase along the combustor length in all the three cases. However, the highest wall temperature is attained with the 50:50 air flow split and the lowest with 30:70 split. This is attributed to the fact that even with a much higher incident radiation in the 30:70 flow split case, the higher convective cooling due to increased secondary air flow keeps the wall at a lower temperature. On the contrary, though in the 50:50 case, the maximum radiative flux incident on the wall is low, but the wall temperature reaches a higher value as the secondary air flow adjacent to the wall is less.

An efficiency (η) term has been defined as the ratio of the total energy flow rate at the outlet to that at inlet. The calculated efficiency values have been listed in Table 12.2. It shows that as the swirl number is increased the combustor efficiency decreases.

It is also significant to study the incident heat flux and the surface temperature on the fuel injector considering the life of the injector. Figures 12.15 and 12.16 show the incident radiation flux and surface temperature on the swirler—injector assembly for the three different air flow splits. The incident radiation on the fuel injector is the highest for the case of lowest primary air fraction (Fig. 12.15a) due to increased radiation from the flame. This is attributed to the higher soot concentration in the flame in this case. The high incident radiation causes the fuel injector surface temperature to reach a value of nearly 1100 K in this case (Fig. 12.16a). The incident radiation flux on the injector surface reduces as the primary air fraction is increased (Fig. 12.15b and c). However, the surface temperature distributions on the injector (Fig. 12.16b and c) do not show a decrease in value for the corresponding cases. This may be attributed to the stronger convective heat transfer with the increase in primary air fraction due to back flow towards inlet plane. When the

Table 12.2 Combustor efficiency at different air split

Mass flow distribution primary:secondary	$\eta = \frac{\text{Total energy flow rate at combustor outlet}}{\text{Total energy flow rate at combustor inlet}}$
30:70	90.91%
40:60	90%
50:50	89.4%

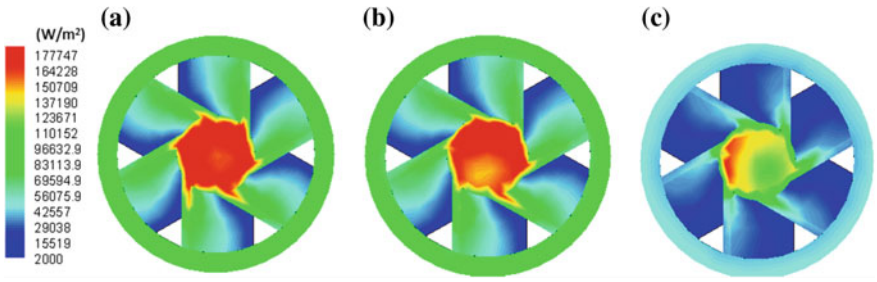

Fig. 12.15 Distributions of incident radiation on the swirler–injector planes for three different air flow splits between primary and secondary streams **a** 30:70, **b** 40:60 and **c** 50:50

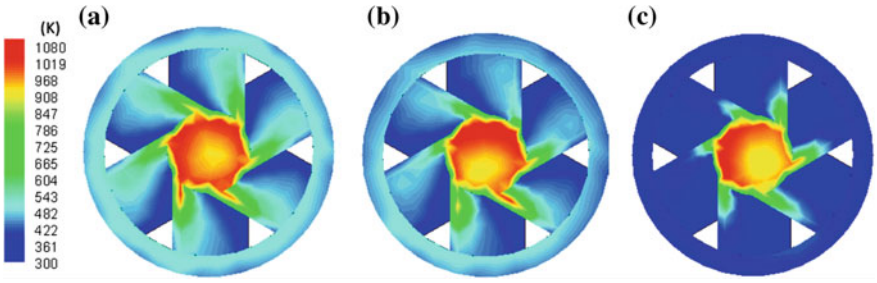

Fig. 12.16 Temperature distributions across the swirler–injector plane for three different air flow splits between primary and secondary streams **a** 30:70, **b** 40:60 and **c** 50:50

primary air flow rate increases, the central recirculation zone established on the combustor axis becomes more intensified. As a result, the high temperature gas from the downstream flows back with a higher velocity towards the injector. The resulting higher convective heat transfer offsets the lower incident radiative heat flux and maintains the injector nearly at the same high temperature for all the three cases. Thus, the fuel injector remains as the more critical component of the combustor and its material has to be selected properly to save it from failure.

12.6 Conclusion

This chapter explains the models for the simulation of spray combustion that can be used for gas turbine combustors. Soot formation and radiative exchange have been accounted in the model as they have important contributions in the non-premixed spray flames. Though, models involving LES and DNS are used in some of the research applications nowadays, we have resorted to RANS-based model considering their simplicity and applicability in complex cases used in practice. The turbulent transport has been modelled using realizable k-ε model. The combustion

is simulated using laminar flamelet model considering a chemical reaction mechanism for kerosene from the literature. The dispersed phase is simulated using Eulerian–Lagrangian approach considering stochastic effect of the turbulent gas phase flow. The interphase source terms need to be computed during the dispersed phase simulation and used in the simulation of the continuous phase. A semi-empirical soot model has been employed. Optimized empirical model constants have been used for the application in kerosene flame.

The comprehensive models have been used in a 3-D combustor with separate air entries as primary and secondary flows. The effects of different air flow split between the primary and secondary have been computed and the results are analysed. Some experiments in a combustor of the same geometry have also performed and the predicted results are compared with the experimental for some the liner and exit gas temperatures. The fuel injector is found to be a critical component showing very high temperature due to radiative and convective heat transfers from the flame.

Acknowledgements The authors gratefully acknowledge the funding support from the Gas Turbine Research Establishment (GTRE), Govt. of India under the GATET scheme (Grant No. GTRE/GATET/CA07/1012/026/11/001) to conduct the research whose results are presented here.

References

Bray KNC, Peters N (1994) Laminar flamelets in turbulent flames. In: Libby PA, Williams FA (eds) Turbulent reacting flows, chapter 2. Academic Press, London, pp 63–94

Brookes SJ, Moss JB (1999) Predictions of soot and thermal radiation properties in confined turbulent jet diffusion flames. Combust Flame 116:486–503

Calcote HF, Manos DM (1983) Effect of molecular structure on incipient soot formation. Combust Flame 49:289–304

Carlson BG, Lathrop KD (1993) Transport theory—the method of discrete ordinates. In: Greenspan H, Kelber CN, Okrent D (eds) Computing methods in reactor physics. Gorden and Breach, London, pp 165–266

Chandrashekhar S (1950) Radiative transfer. Clarendon, Oxford

Chen H, Chen S, Kraichnan RH (1989) Probability distribution of a stochastically advected scalar field. Phys Rev Lett 63(24):2657–2660

Datta A, Som SK (1999) Combustion and emission characteristics in a gas turbine combustor at different pressure and swirl conditions. Appl Therm Eng 19(9):949–967

De S, Lakshmisha KN, Bilger RW (2011) Modelling of nonreacting and reacting turbulent spray jets using a fully stochastic separated flow approach. Combust Flame 158:1992–2008

Dopazo C (1994) Recent developments in pdf methods. In: Libby PA, Williams FA (eds) Turbulent reactive flows, chapter 7. Academic Press, London, pp 375–474

Eldrainy Y, Saqr KM, Aly HS, Lazim TM, Jaafar MNM (2011) Large eddy simulation and preliminary modelling of the flow downstream a variable geometry swirler for gas turbine combustors. Int Comm Heat Mass Transf 38(8):1104–1109

Evans M, Hastings N, Peacock B (2000) Statistical distributions, 3rd edn. Wiley Series in Probability and Statistics. Wiley, New York

Fiveland WA (1982) A discrete-ordinates method for predicting radiative heat transfer in axisymmetric enclosure. ASME 82-HT-20

Frenklach M (2002) Reaction mechanism of soot formation in flames. Phys Chem Chem Phys 4:2028–2037
Ghose P, Patra J, Datta A, Mukhopadhyay A (2016) Prediction of soot and thermal radiation in a model gas turbine combustion burning kerosene fuel spray at different swirl levels. Combust Theor Model 20(3):457–485
Glassmann I (1988) Soot formation in combustion processes. In: Twenty-Second symposium (International) on combustion. The Combustion institute, pp 295–311
Guo B, Langrish TAG, Fletcher DF (2001) An assessment of turbulence models applied to the simulation of a two-dimensional submerged jet. Appl Math Model 25:635–653
Hall RJ, Smooke MD, Colket MB (1997) Predictions of soot dynamics in opposed jet flames. In: Dryer FL, Sawyer RF (eds) Physical and chemical aspects of combustion: a tribute to Irvine Glassman. Gordon & Breach, pp 189–230
Harris SJ, Weiner AM (1983) Surface growth of soot particles in premixed ethylene/air flames. Combust Sci Tech 31:155–167
Haynes BS, Wagner HG (1981) Soot formation. Prog Energy Combust Sci 7:229–273
Hiroyasu H, Kadota T, Arai M (1983) Development and use of a spray combustion modelling to predict diesel engine efficiency and pollutant emissions. Part 1: combustion modelling. Bull JSME 26(214):569–575
Janicka J, Peters N (1982) Prediction of turbulent jet diffusion flame lift-off using a pdf transport equation. In: Nineteenth Symposium (International) on combustion. The Combustion Institute, pp 367–374
Joung D, Huh KY (2009) Numerical simulation of non-reacting and reacting flows in a 5 MW commercial gas turbine combustor, ASME turbo expo 2009: power for land, sea, and air, Orlando, FL, 8–12 June
Kaplan CR, Patnaik G, Kailasanath K (1998) Universal relationships in sooting methane-air diffusion flames. Combust Sci Technol 13:39–65
Karim VM, Bart M, Erik D (2003) Comparative study of k-ε turbulence models in inert and reacting swirling flows. AIAA Paper No. 2003-3744
Kennedy IM (1997) Models of soot formation and oxidation. Prog Energy Combust Sci 23:95–132
Khan M, Greeves G (1974) A method for calculating the formation and combustion of soot in diesel engines. In: Afgan NH, Beer JM (eds) Heat transfer in flames, chapter 25. Scripta, Washington DC
Kundu KP, Penko PF, Yang SL (1998) Simplified Jet-A/Air combustion mechanisms for calculation of NO_x emissions, AIAA-98-3986
Mandal BK, Datta A, Sarkar A (2009) Transient development of flame and soot distribution in laminar diffusion flame with preheated air. ASME J Eng Gas Turbine Power 131, 031501-1
Mansurov ZA (2005) Soot formation in combustion processes. Combust Explo Shock Waves 41 (6):727–744
Modest MF (1993) Radiative heat transfer, 2nd edn. McGraw-Hill Inc., NY, USA
Morsi SA, Alexander AJ (1972) An investigation of particle trajectories in two phase flow system. J Fluid Mech 55(2):193–208
Moss JB, Aksit IM (2007) Modelling soot formation in a laminar diffusion flame burning a surrogate kerosene fuel. Proc Combust Inst 31:3139–3146
Peters N (2004) Turbulent combustion. Cambridge University Press, UK
Pope SB (1985) PDF methods for turbulent reactive flows. Prog Energy Combust Sci 11:119–192
Pope SB (1991) Combustion modelling using probability density function method, chapter 11. In: Oran ES, Boris JP (eds) Numerical approaches to combustion modelling. AIAA
Pope SB (1994) Stochastic Lagrangian models for turbulence. Annu Rev Fluid Mech 26:23–63
Pope SB (2000) Turbulent flow. Cambridge University Press, Cambridge
Ranz WE, Marshall WR Jr (1952a) Evaporation from drops. Part I. Chem Eng Prog 48(3):141–146
Ranz WE, Marshall WR Jr (1952b) Evaporation from drops. Part II. Chem Eng Prog 48(4):173–180
Reis LCBS, Carvalho JA Jr, Nascimento MAR, Rodrigues LO, Dias FLG, Sobrinho PM (2014) Numerical modelling of flow through an industrial burner orifice. Appl Therm Eng 67:201–213

Richter H, Howard JB (2000) Formation of polycyclic aromatic hydrocarbons and their growth to soot—a review of chemical reaction pathways. Prog Energy Combust Sci 26:565–608

Sazhin SS, Sazhina EM (1996) The effective-emissivity approximation for the thermal radiation transfer problem. Fuel 75(14):1646–1654

Siegel R, Howell JR (1992) Thermal radiation heat transfer. Hemisphere Publishing Corporation, Washington DC

Sivathanu YR, Gore JP (1997) Effects of gas-band radiation on soot kinetics in laminar methane/air diffusion flames. Combust Flame 110:256–263

Smooke MD, McEnally CS, Pfefferle LD, Hall RJ, Colket MB (1999) Computational and experimental study of soot formation in a coflow, laminar diffusion Flame. Combust Flame 117 (1–2):117–139

Tesner PA, Tsygankova LP, Guilazetdinov LP, Zuyev VP, Loshakova GV (1971) The formation of soot from aromatic hydrocarbons in diffusion flames of hydrocarbon-hydrogen mixtures. Combust Flame 17:279–285

Tolpadi AK (1995) Calculation of two phase flow in gas turbine combustor. ASME J Eng Gas Turbine Power 117(4):695–703

Van Maele K, Merci B, Dick E (2003) Comparative study of k-ε turbulence models in inert and reacting swirling flows. In: 33rd AIAA Fluid dynamics conference and exhibit, Oriando, FL, 23–26 June

Versteeg HK, Malalasekera W (2007) An introduction to computational fluid dynamics: the finite volume method, Second Edition. Pearson Education, Harlow, England

Watanabe H, Kurose R, Komori S, Pitsch H (2006) A numerical simulation of soot formation in spray flames. In: Proceedings of the summer program, center for turbulence research, pp 325–336

Watanabe H, Matsushita Y, Aoki H, Miura T (2010) Numerical simulation of emulsified fuel spray combustion with puffing and micro-explosion. Combust Flame 157:839–852

Wen Z, Yun S, Thomson MJ, Lightstone MF (2003) Modelling soot formation in turbulent kerosene/air jet diffusion flames. Combust Flame 135:323–340

Williams FA (1975) Description of turbulent diffusion flames, 1st edn. Plenum Press

Young KJ, Stewart CD, Moss JB (1994) Soot formation in turbulent nonpremixed kerosene-air flames burning at elevated pressure: experimental measurement. In: Symposium (International) on combustion, vol 25, pp 609–617

Part IV
Probability Density Function Methods

Chapter 13
Transported Probability Density Function Method for MILD Combustion

Ashoke De

Abstract Modeling of Moderate and Intense Low oxygen Dilution (MILD) combustion is a challenging task due to slow reaction rates. The present chapter aims at assessing the predictive capability of transport PDF-based combustion models for two burners (Delft-Jet-in-Hot-Coflow (DJHC) burner and Adelaide JHC burner), which mimics MILD combustion characteristics. In the present work, both the transported PDF approaches, i.e., Lagrangian PDF (LPDF) and multi-environment Eulerian PDF (MEPDF), are considered and assessed. For DJHC burner, both 2D and 3D calculations are reported for varying parameters. However, for Adelaide burner, only 2D computations are reported. In the context of LPDF calculations, different micro-mixing models are considered to investigate the effect of molecular diffusion. In the case of DJHC burner, all the models behave properly and predictions are observed to be in good agreement. However, the model discrepancies are noticed while comparing the species profiles, especially in the case of Adelaide burner. Also, the performance of the models is properly assessed by analyzing the profiles of minor species and RMS of scalar fields. Overall, the performances are improved with increasing O_2 content, i.e., higher Damkohler number range.

Keywords Transport PDF method · MILD combustion · JHC flames

Nomenclature

ρ	Mixture density
T	Temperature
Z	Mixture fraction
t	Time
P	Favre joint PDF of composition
u_i	Favre mean fluid velocity

Ashoke De (✉)
Department of Aerospace Engineering, Indian Institute of Technology Kanpur, Kanpur 208016, India
e-mail: ashoke@iitk.ac.in

© Springer Nature Singapore Pte Ltd. 2018

S. De et al. (eds.), *Modeling and Simulation of Turbulent Combustion*, Energy, Environment, and Sustainability, https://doi.org/10.1007/978-981-10-7410-3_13

S_k	Reaction of species k
ψ	Composition space vector
$u_i^{''}$	Fluid velocity fluctuation vector
J_{ik}	Molecular diffusion flux vector
$\theta_{m,mix}$	Micro-mixing
m^i	Mass of the particle
N_p	Total number of particle in a cell

Abbreviations

MILD	Moderate and Intense Low Oxygen Dilution
JHC	Jet-in-Hot Coflow
DJHC	Delft Jet-in-Hot Coflow
PDF	Probability Density Function
LPDF	Lagrangian PDF
MEPDF	Multi-environment Eulerian PDF
DQMOM	Direct Quadrature Method of Moments
IEM	Interaction-by-Exchange-with-the-Mean
CD	Coalescence Dispersion
EMST	Euclidean Minimum Spanning Tree
LES	Large Eddy Simulation
SIMPLE	Semi-Implicit Method for Pressure-Linked Equations
RANS	Reynolds-Averaged-Navier–Stokes

13.1 Background

To reduce pollutant emission and optimize the design, stringent laws have encouraged the combustion designer to work in this direction. In this context, the MILD (Moderate and Intense Low Oxygen Dilution) combustion has been gaining popularity as a promising alternative as it improves the thermal efficiency of combustion systems (combustor, furnaces, and burners) by lowering the level of pollutant emissions. One important feature of MILD combustion is the reactant temperature (inlet), which happens to be higher than the mixture's auto-ignition temperature. Usually, the recirculation of hot exhaust gases to the incoming cold air achieves this kind of reactant temperature at the inlet. The recirculation of the exhaust gas facilitates the combustion process in two ways: first, it improves the heat recovery at the inlet by raising the reactant temperature and second, it dilutes the mixture by reducing the oxygen concentration, thereby reducing the NO_x emissions. Some other important features of MILD combustion includes inherent flame stabilization, low turbulent fluctuations, barely visible or audible flame, smooth radiation flux, and uniform temperature field. This technique derives its

importance from the fact that it recovers the exhaust gas heat and depends on high recirculation ratios, thereby ensuring proper mixing of reactant (before any reaction could take place) streams with the flue gases. The concerns of industrial and environmental research groups in addition to the challenge of modeling these flames are the primary reason for gaining popularity of MILD combustion. That is why several experimental (Oldenhof et al. 2010a, b, 2012; Dally et al. 2002) and numerical (De et al. 2011, 2012; Kulkarni and Polifke 2012; Bhaya et al. 2014; Christo and Dally 2004, 2005; Kim et al. 2005; Frassoldati et al. 2010; Mardani et al. 2010, 2011; Aminian et al. 2012; Ihme and See 2011; Ihme et al. 2012; Dongre et al. 2014; De and Dongre 2015) studies have been conducted to address the issues related to this kind of combustion. In summary, MILD combustion is appeared to be an efficient technique and is of interest to the research community.

Turbulent non-premixed jet flames, particularly jet-in-hot-Coflow (JHC) flames have huge importance toward clean combustion techniques that includes excess enthalpy combustion, MILD combustion, and flameless combustion. In all of these, the presence of hot oxidizer stream, diluted with hot products, facilitates the reaction to take place. Noteworthy to mention that the DJHC and Adelaide JHC burners, considered herein, come under the same category.

The primary aim of DJHC burner was to study the basics of MILD combustion (Oldenhof et al. 2010a, b, 2012; De et al. 2011, 2012; Kulkarni and Polifke 2012; Bhaya et al. 2014; Dongre et al. 2014; De and Dongre 2015). Oldenhof et al. (2010a, b, 2012) studied these flames in details including the flame stabilization and lift-off height. With increasing coflow temperature and in addition of higher alkanes to the fuel as well, they reported that the lift-off height was reduced. However, there were no impacts on the lift-off height beyond a certain limit of the Reynolds number. Similarly, the Adelaide JHC flames were investigated using the temporally and spatially resolved measurements by Dally et al. (2002) and provided the detailed flame characteristics. The database of DJHC burner only provides the information about velocity, temperature, and turbulent quantities (Oldenhof et al. 2010a, b, 2012). However, on the other hand, the Adelaide JHC burner (Dally et al. 2002), does not provide any data on turbulent quantities and velocity profiles; but provides a detailed database in the context of major as well as minor species. Therefore, both the Delft and Adelaide JHC burners combinedly provide an extensive database which can be used for the numerical investigation to enlighten the fundamental understanding of combustion models in the MILD regime.

It is quite obvious to mention that both these JHC burners are subjected to different numerical studies. A previous study of DJHC flames by De et al. (2011) included RANS-based turbulence models like RKE (realizable k-ε), RNG (renormalization group k-ε), and SKE (standard k-ε) in conjunction with Eddy Dissipation Concept (EDC) combustion model. They reported that the modified SKE model showed an improved mean velocity profile but failed to predict the first-order statistics, such as Reynolds stresses, turbulent kinetic energy profiles, where a significant under-prediction was reported; while the RKE model improved the mean velocity profile but under-predicted the turbulent kinetic energy profiles for low Re. Also, the predicted mean temperature profile using EDC combustion model showed

an early ignition peak in the shear layer. Whereas, for high Reynolds number RKE model was found to perform better than SKE while the modified EDC model improved the temperature profiles. In another study, De et al. (2012) investigated the DJHC flames and reported similar results using both the LPDF and MEPDF models. The discrepancies in the results were primarily attributed to the inaccurate handling of turbulence-chemistry interaction in modeling these flames. Later on the studies by Kulkarni and Polifke (2012) investigated the same flames using Large Eddy Simulation (LES) in conjunction with tabulated chemistry as well as stochastic field combustion mode. The primary objective of their study was: (i) to investigate the sensitivity of lift-off height predictions due to Reynolds number and (ii) effect of entrainment on flame stabilization. Their study reported that for both low and high Reynolds numbers, the predicted temperature profile matched well close to the jet exit, but at the downstream region huge discrepancy between predictions and measurements was observed. However, the lift-off height was reasonably well predicted while comparing with measurements for different jet velocities and coflow mixtures. These results highlight the limitations of turbulence as well turbulence-chemistry interaction models but they form a foundation for more detailed studies using transported PDF methods for such flames. In another LES study, Bhaya et al. (2014) analyzed these flames using transported PDF combustion models. They found that the results from both the PDF models are in agreement with each other, while an early ignition was observed along with higher mean temperature. Very recently, De and Dongre (2015) investigated both these burners using different turbulent-chemistry interaction models and made a comprehensive assessment of the model predictions. They concluded that the transported PDF models provided the best results while compared with other models for JHC flames. Further, the final recommendation of their study was to delay the ignition, in turn, the reaction, by tuning the chemical time scale as required in the MILD combustion (De and Dongre 2015).

On the other hand, while considering the Adelaide burner, Christo and Dally (2005) studied the methane-hydrogen (CH_4–H_2) flames using different k-ε turbulence models along with the EDC combustion model with detailed chemistry. The assessment of turbulence model and turbulence-chemistry interaction model with various chemical mechanisms was the primary focus of their study, where they found the strong impact of the differential diffusion effects on the flame behavior. In another study, Christo and Dally (2004) reinvestigated the same flames using transported PDF approach (in RANS framework) by invoking various chemical mechanisms (Smooke 1991; Smith et al. 2010; Subramaniam and Pope 1998). There are several other numerical studies on these flames which include the studies of Kim et al. (2005), Frassoldati et al. (2010), Mardani et al. (2010, 2011), Aminian et al. (2012), Ihme and See (2011), Ihme et al. (2012). All of these studies primarily focused on the understanding of the flame structure and differential diffusion in the MILD regime for the different chemical mechanism (Kazakov and Frenklach 1994; Bowman et al. 1996; Bilger et al. 1990). Recently, Dongre et al. (2014) and De and Dongre (2015) investigated both these burners issuing JHC flames using the

transported PDF approach in order to assess the predictive capabilities of PDF models in the MILD combustion regime.

In turbulent combustion modeling, one of the important issues is the handshaking between the nonlinear interaction of fluid mixing and finite-rate chemistry and how it is handled in simulations. The commonly known transported PDF method or Lagrangian transported PDF (LPDF) method becomes useful in this regard when compared to other approaches. The primary advantage of transported PDF approach lies in the handling the chemical source term, which appears in a closed form in PDF transport equation. Therefore, there is no need for closure approximation related to reaction source term and the implementation of realistic combustion chemistry is much easier. Hence, the transported PDF methods are able to accurately describe the handshaking between the turbulence and chemistry. However, the biggest bottleneck of LPDF approach is the implementation along with the standard CFD techniques (like FVM, FEM) due to their high dimensionality, as the memory requirement increases with the increasing species. Thus, an alternative approach such as Monte Carlo algorithms that reduces the memory requirement is typically used (Pope 1985). However, as recommended by Pope (1985), each computational cell requires a large number of particles to minimize the statistical errors. As a result, on the other hand, the LPDF method becomes computationally demanding and time-consuming too. Therefore, the application of LPDF approach despite their accuracy is not feasible for large-scale industrial problems.

Contrarily, MEPDF methodology inherits the advantage of PDF transport method (closed form of reaction source terms); but at the same time becomes computationally feasible for the large-scale problem. A joint composition multi-environment Eulerian PDF (MEPDF) transport equation is approximated using a weighted discretization in composition space in conjunction with the IEM (interaction-by-exchange-with-mean) micro-mixing model plus the direct quadrature method of moments (DQMOM) (Fox 2003; Fan et al. 2004).

This approach was first proposed by Fox (2003) for multivariate cases and later on found to be a promising alternative to the LPDF method. In this method, two transport equations are primarily solved: one is for weights and another one for abscissa of quadrature points. The genesis of this approach was the population balance equation, where the bivariate PDF for particle size distribution was modeled using this method (Zucca et al. 2006; Marchisio and Fox 2005). Later on, this approach was extended for turbulent combustion, where a multi-environment presumed shape PDF (series of delta functions) is considered. Thus, the set of transport equations for the weights and abscissa of the quadrature points are obtained using the definition of this presumed shape PDF upon incorporating them into the joint composition PDF transport equation. The micro-mixing term is closed using the IEM model and the coupled method is commonly popular as DQMOM-IEM. Thus the resulting transport equations appear to be in closed form and look similar to the standard Eulerian scalar transport equations. Also, the theoretical description of the model suggests that the accuracy of the predictions improved with the increasing the number of environments. Another advantage of this model is that it does not produce statistical errors (Fox 2003). Using the MEPDF model, a few earlier

studies are also available in the literature (Tang et al. 2007; Liu and Fox 2005; Raman et al. 2006; Akroyd et al. 2010a, b; Jaishree and Haworth 2012; Yadav et al. 2013, 2014); however, none of these attempted to assess the performance of MEPDF model for jet-in-hot coflow flames.

It is quite well known that the reaction rates are comparatively slow in the MILD regime, and hence, the importance of molecular diffusion on flame characteristics is predominant. That is why, in particular, one has to encounter a great challenge in modeling MILD combustion using the commonly available/popular turbulence-chemistry interaction models. Notably, for infinitely fast chemistry, the steady flamelet model is preferred/more suitable, whereas the transport PDF models do have the closure of micro-mixing (molecular mixing) as a potential source of errors.

In the view of above discussion, it appears that there exists a gap to properly understand and to accurately model the nonlinear interaction between fluid mixing and finite-rate chemistry, especially in MILD combustion. Thus, the prime focus of the present study is to exploit the advantages of transported PDF modeling and assess the predictions by comparing the results with experimental data, obtained from other combustion models, in order to fill the gap between experimental and numerical findings and to accurately explain the turbulence-chemistry interaction as well as this model behavior in the context of MILD combustion.

13.2 Turbulence-Chemistry Interaction Models

In turbulent reacting flows, the relevant quantities are stochastics in nature and the probability distribution of such quantities is considered in transported PDF-based models, thereby making them more applicable for such flows. These are briefly discussed below.

13.2.1 Transported PDF Models

The building block of the transported PDF modeling is the joint composition PDF transport equation, which is recast as:

$$\frac{D(\rho f_\varphi)}{Dt} + \frac{\partial}{\partial \psi_k}\left[\rho S_k f_\varphi\right] = -\frac{\partial}{\partial x_i}\left[\rho \langle u_i'' | \psi \rangle f_\varphi\right] + \frac{\partial}{\partial \psi_k}\left[\rho \langle \frac{1}{\rho}\frac{\partial J_{i,k}}{\partial x_i} | \psi \rangle f_\varphi\right] \tag{13.1}$$

where f_ϕ is the single-point, joint probability density function (PDF) of species composition and enthalpy (Bhaya et al. 2014; Dongre et al. 2014; De and Dongre 2015; Pope 1985). On the left-hand side, the first term represents the total derivative of the PDF in physical space, while the transport in composition space due to chemical reactions is represented by the second term. Whereas on the right-hand side, the first and second terms denote the transport due to velocity fluctuation and

due to molecular mixing, respectively (Marchisio and Fox 2005; Tang et al. 2007). The LPDF method differs from the MEPDF owing to the approach adopted to discretize and solve Eq. (13.1). However, the literature by Marchisio and Fox (2005) and Tang et al. (2007) provided the detailed description on the transported PDF methods, while a comprehensive review on these approaches can be referred to the literature of Haworth (2010).

13.2.1.1 LPDF Method

In LPDF method (Marchisio and Fox 2005), usually the "notional" particles are used to model the turbulent reacting flow. The particles carry mass to satisfy the total mass of the control volume while their motion remains purely stochastic in the physical space. During calculation, the states of the particles are likely to change due to mixing, convection, and reaction.

The mass density function in the composition PDF formulation is recast as:

$$F^*_{\psi x}(\phi, z; t) \equiv \sum_{i=1}^{N_p} m^{(i)} \delta\left(\phi - \psi^{(i)}(t)\right) \delta\left(z - x^{(i)}(t)\right), \tag{13.2}$$

where the notional particles do not carry velocity and $\delta\left(z - x^{(i)}(t)\right)$, $\delta\left(\phi - \psi^{(i)}(t)\right)$ represent three-dimensional delta functions at the particle location and for the scalar, respectively. In Eq. (13.2), the F^* is represented as:

$$\langle F^*_{\psi x}(\phi, z; t)\rangle = \langle \rho(x,t)\rangle \tilde{f}_\psi(\phi; x, t) = \rho(\phi) f_\psi(\phi; x, t), \tag{13.3}$$

where $\tilde{f}_\psi(\phi, x; t)$ denotes the Favre PDF $\tilde{f}_\psi$, $f_\psi(\phi, x; t)$ represents the conventional PDF f_ψ and $\langle \rho \rangle$ is the mean mixture mass density.

For each notional particle, the position and composition at an infinitesimal time increment dt evolve as:

$$dx^*_i = \tilde{u}^*_i dt + dx^*_{i,\,turb} \quad (i = 1, 2, 3) \tag{13.4}$$

$$d\phi^*_m = S_m(\phi^*) dt + \theta^*_{m,\,mix} dt \quad (m = 1, 2, \ldots, N_\psi) \tag{13.5}$$

In this system, the ith particle has a mass $m^{(i)}$ and each particle is differed from each other by coordinates $x^{(i)}(t)$ and N_ψ scalar variables of $\psi^{(i)}(t)$. In the above system of equations, dx^*_{turb}, is usually modeled using a random-walk model, which is the representation of the particle position in physical space. This quantity is affected due to turbulent diffusion (turbulent velocity fluctuations) about the local mean velocity $\tilde{u}^*_i$. The increment in the composition is responsible due to the chemical source term (S_k) and molecular diffusion ($\theta^*_{m,\,mix}$: micro-mixing). In this approach, the modeling of micro-mixing term causes the largest source of modeling errors.

Thus, in the current study, we have invoked three different mixing models: IEM (Dopazo and O'Brien 1974), CD (Curl 1963), and EMST (Subramaniam and Pope 1998), in order to model the molecular mixing of the species in the PDF transport equation.

13.2.1.2 MEPDF Method

This method was first put forth by Fox and the detailed discussion along with the derivations of the MEPDF method can be found in his book (Tang et al. 2007). As noted earlier, the joint composition PDF transport equation (Eq. 1) is approximated to have a shape with a series of Delta functions with fixed or variable probability by taking the advantage of PDF approach. Thus, a series of N_e Delta functions represent the joint composition PDF equation as:

$$f_\psi(\phi; x, t) = \sum_{n=1}^{N_e} w_n(x,t) \prod_{\alpha=1}^{N_s} \delta[\phi_\alpha - \langle \psi_\alpha \rangle_n(x,t)], \tag{13.6}$$

where N_s denotes the number of species, N_e denotes the number of environments, w_n is the weight (or probability) of each environment, and $\langle \psi_\alpha \rangle_n$ represents the mean composition vector in the nth environment. The joint composition PDF Eq. (13.1) is transformed into the following set of equations using the definition of Eq. (13.6):

$$\frac{\partial \rho p_n}{\partial t} + \frac{\partial}{\partial x_i}(\rho u_i p_n) = \Gamma \nabla^2 p_n \tag{13.7}$$

$$\frac{\partial \rho \overrightarrow{s_n}}{\partial t} + \frac{\partial}{\partial x_i}(\rho u_i \overrightarrow{s_n}) = \Gamma \nabla^2 \overrightarrow{s_n} + C_\phi \frac{\varepsilon}{k}(\langle \phi_i \rangle - \langle \phi_i \rangle_n) + p_n S\left(\langle \overrightarrow{\phi_n} \rangle\right) + \overrightarrow{b_n}, \tag{13.8}$$

where $\overrightarrow{s_n} = p_n \overrightarrow{Y}_n$ or $p_n H_n$. In the above-mentioned transport equations, Eq. (13.7) denotes the probability of occurrence of nth environment while Eq. (13.8) represents the probability of either weighted species mass fraction or weighted enthalpy in each environment. The second term (micro-mixing) in Eq. (13.8) is closed by the IEM micro-mixing model, whereas the third term is the reaction source term and the fourth term is the correction term. The modeling assumption in MEPDF model is accounted using these two correction terms as:

$$\sum_{n=1}^{N_e} \langle \phi \rangle_n^{m_j - 1} b_n = \sum_{n=1}^{N_e} (m_j - 1) \langle \phi \rangle_n^{m_j - 2} p_n c_n \tag{9}$$

The set of these transport equations are solved for each environment using the finite volume discretization in Eulerian framework. For each environment, the reaction source term is evaluated using a stiff ODE solver and the source terms are tabulated using In Situ-Adaptive-Tabulation (ISAT) (Pope 1997) algorithm.

The absence of statistical errors provides an added advantage of this method while compared to LPDF method. However, the closed form reaction source term is solved in the Eulerian framework. For the earlier studies carried out by Tang et al. (2007), Liu and Fox (2005), Raman et al. (2006), Akroyd et al. (2010a, b), Jaishree and Haworth (2012), Yadav et al. (2013, 2014), and Bhaya et al. (2014), we can also highlight the fact that this method is computationally efficient.

However, in the MEPDF model, certain numerical aspects such as boundedness and singularity of the covariance matrix remain present as reported by Wang and Fox (2004). Generally, these are resolved using certain constraints, however, these constraints create another issue in the calculation of the correction terms, means the accurate representation of the moments of PDF equation (Eq. 13.1) is sacrificed. This leads to another possible source of errors in MEPDF method excluding the IEM closure. Further, it is reported by Jaishree and Haworth (2012) that the source terms in MEPDF model are ill-conditioned and particularly for multicomponent systems the realizability is violated. Also, it was mentioned that the ambiguities in the specification of MEPDF boundary condition along with their physical interpretation significantly reduces their accuracy.

13.3 Delft-Jet-in-Hot-Coflow (DJHC) Burner

This burner falls under the category of MILD combustion regime, and in this section, the predictions using the TPDF models are discussed.

13.3.1 Test Case Details and Numerical Setup

The DJHC burner comprises of a central fuel jet pipe with an internal diameter of 4.5 mm, surrounded by an outer tube of internal diameter 82.8 mm, which houses a secondary ring burner that generates a hot coflow to mimic MILD combustion (Oldenhof et al. 2010a, b, 2012). The partially premixed combustion mode is obtained in the secondary burner (Oldenhof et al. 2010a, b, 2012). Figure 13.1 depicts a schematic for the burner and the computational domain as well.

The results are reported from both 2D and 3D simulations, which are carried out in Fluent 13.0 (ANSYS fluent 13.0 user's guide 2010) and the details can be found in the literature (De et al. 2011, 2012; Kulkarni and Polifke 2012; Bhaya et al. 2014; Dongre et al. 2014; De and Dongre 2015). The fuel composition of the Dutch natural gas in the present formulation is 81% CH_4, 4% C_2H_6, and 15% N_2, whereas the hot coflow contains O_2 with a constant percentage of 7.6% (by mass) that corresponds to DJHC-I flame (Oldenhof et al. 2010a, b, 2012; De et al. 2011; De and Dongre 2015). For 2D calculations, the turbulence is modeled using RANS-based RKE turbulence model and the Reynolds number, based on the fuel jet, is 4100. The kinetics is handled by a reduced mechanism, DRM19 (Kazakov and Frenklach 1994), which is represented by 19 species and 84 reactions.

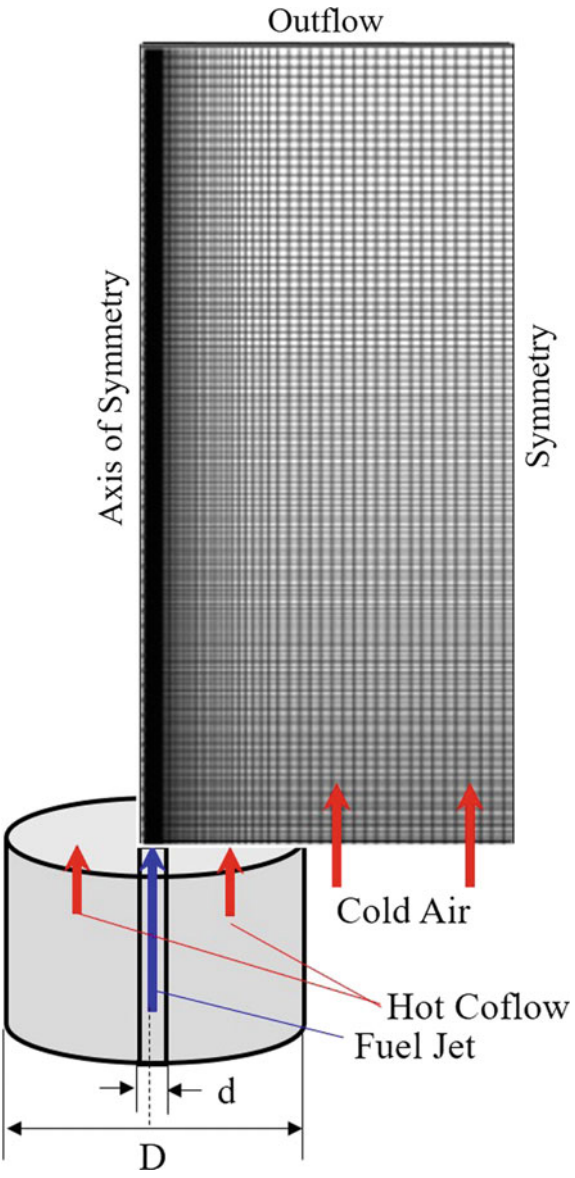

Fig. 13.1 Schematic of the computational domain with burner set up. **a** DJHC: d = 4.5 mm, D = 82.8 mm, **b** AHJC: 4.25 mm, D = 82.0 mm

For 3D simulations (LES), two different subgrid eddy viscosity models are used: one is Dynamic Smagorinsky model and other one is Dynamic Kinetic Energy Transport (KET) model. Since LES is computationally highly expensive, the chemistry is modeled using two different reduced mechanisms, ARM9 mechanism (nine species, five step Smith et al. 2010) and the SKEL mechanism (16 species, 41 reactions, James et al. 1999). In both 2D and 3D simulations, the mixing term in the LPDF model is approximated using three different mixing models namely CD,

EMST, and IEM, whereas for MEPDF it is IEM only with default mixing constant $C_{\varphi} = 2$. Particularly, the MEPDF calculations are performed with two environments whereas for the LPDF model, to reduce statistical errors, the computations are performed by taking 30 particles per cell. More details can be found in the literature (Bhaya et al. 2014; De and Dongre 2015). To properly assess the predictions against the measurements, the complete radial range of the measurements (−Ve to +Ve) is plotted together.

13.3.2 Discussion

Initially, we discuss the 2D results, followed by the 3D results. The simulated Re = 4100, and the oxygen concentration is 7.6% (by mass) for DJHC-I flame (Oldenhof et al. 2010a, b, 2012). After performing grid independence study, the grid with 180 × 125 (axial × radial) cells is chosen to perform the details simulations (De et al. 2011; De and Dongre 2015).

Figure 13.2 illustrates the radial profiles of mean axial velocity, turbulent kinetic energy, and mean temperature at three axial locations. There are no substantial

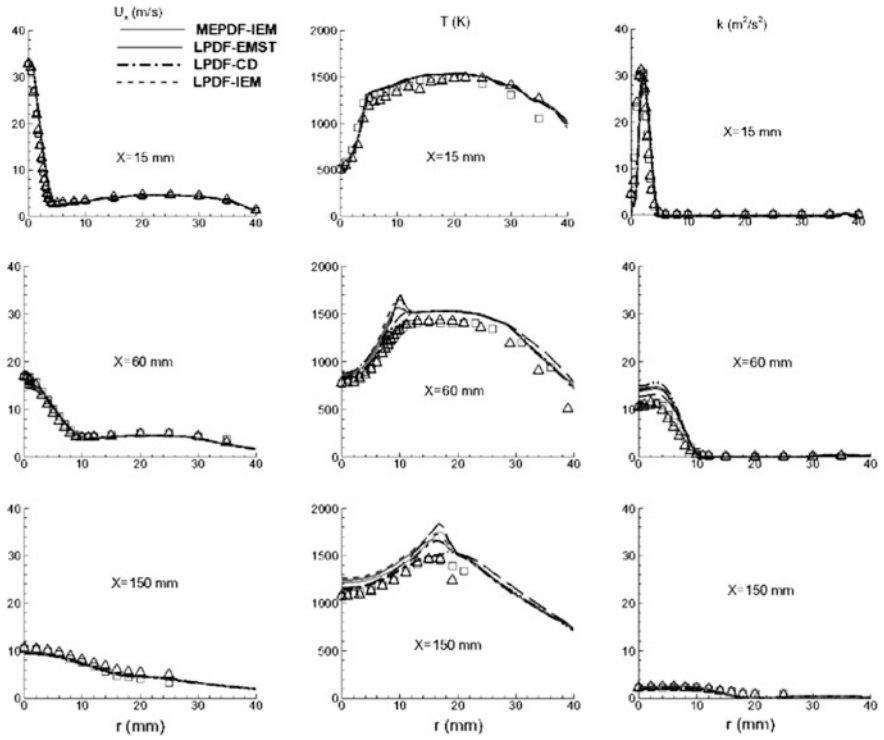

Fig. 13.2 Radial plots of mean axial velocity, mean temperature, and turbulent kinetic energy. Symbols (Δ: $0 \leq r \leq 40$, □: $-40 \leq r \leq 0$) represents measurements (Oldenhof et al. 2010a, b) and lines refer to predictions

differences observed while using different combustion models and mean profiles follow proper trends. However, turbulent kinetic energy profiles exhibit some glitches at the jet exit as well as the downstream, which is primarily due to the inaccuracies in the turbulence model (production and dissipation are not captured properly). The major differences among the model predictions can be observed from the temperature profile, i.e., $X = 60$ mm onwards. The peak temperature predicted by different mixing closure in LPDF models is: EMST = 1660 K, CD = 1655 K, and IEM = 1730 K; while the MEPDF model exhibits 1750 K, which is around 13% higher than the measurements (Oldenhof et al. 2010). It can be noticed while comparing the transported PDF predictions at $X = 150$ mm, that the peak temperature with EMST model is found to appear at $r = 10$ mm, whereas in case of CD it is $r = 12$ mm and with IEM it shifts to 8 mm radial locations. Further to add, the role of mixing models is found to be quite dominant at the difference in peak temperature amongst these models is more than 100 K. On the contrary, MEPDF model predicts the early ignition peaks at the axial location of $X = 60$ mm. Along with the mean profiles, the Reynolds stresses ($u'u'$) are plotted and shown in Fig. 13.3. It is quite clear form the figure that all the model under-predict the data initially, but capture well at the downstream locations. Hence, as noted earlier, these discrepancies can primarily be associated with the inaccuracies of the turbulence models.

To predict the lift-off height, the OH marker is used, and a threshold value of 1e-3 for the mean OH mass fraction is chosen to determine the lift-off height (Oldenhof et al. 2010a, b, 2012; Dally et al. 2002; De et al. 2011, 2012; Kulkarni and Polifke 2012; Bhaya et al. 2014). The flame lift-off height predicted by different models is as follows: MEPDF-IEM = 33 mm, LPDF-IEM = 36 mm, LPDF-EMST = 39 mm, and LPDF-CD = 40 mm. Although LPDF models produce better results compared to the MEPDF model, but all of them under-predict the value compared to the measurements which is close to 84 mm (Oldenhof et al. 2010).

Based on the mean quantities, it is very difficult to distinguish the differences among the model predictions. That is why the RMS of temperature is analyzed to quantify the same and depicted in Fig. 13.4. It is clearly observed that the RMS profiles are not accurately predicted by the MEPDF models. On the other hand, the measured temperature fluctuations are not provided as input BC for LPDF calculations and that is why all the LPDF models do not predict the RMS of temperature at the near exit locations; however, as we move downstream along the axis of symmetry, the profiles with LPDF models are significantly improved. Away from the centerline, they are under-predicted. Therefore, it is very much essential for LPDF models to provide temperature fluctuations along with mean temperature as the inflow boundary conditions to obtain better predictions.

Moving forward to the 3D calculations, the flow features for varying different physical parameters are discussed. Initially, the grid resolution is tested and details can be found in (Kulkarni and Polifke 2012; Bhaya et al. 2014). To investigate the impact of different eddy viscosity models, the predictions of mean velocity (U_x),

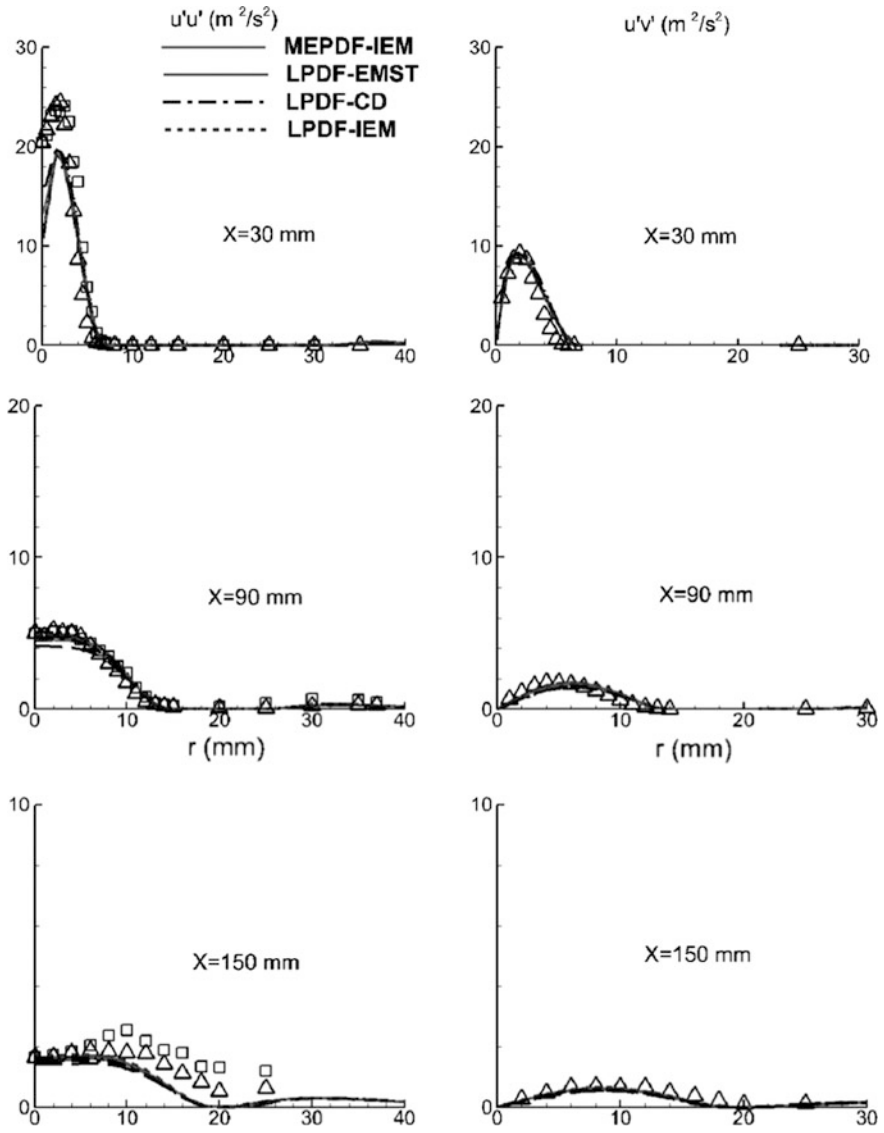

Fig. 13.3 Radial plots of Reynolds stresses (Symbols and lines refer to Fig. 13.2)

turbulent kinetic energy (k) and mean temperature (T) are reported in Fig. 13.5 using MEPDF model with SKEL mechanism. As observed, both the models exhibit similar behavior as: correctly predict the trend in the inner shear layer but under-predict along the centerline. Also, temperature profiles show the signature of early ignition which is not present in measurements. This difference can be better judged while comparing the TPDF models alongside. However, no substantial

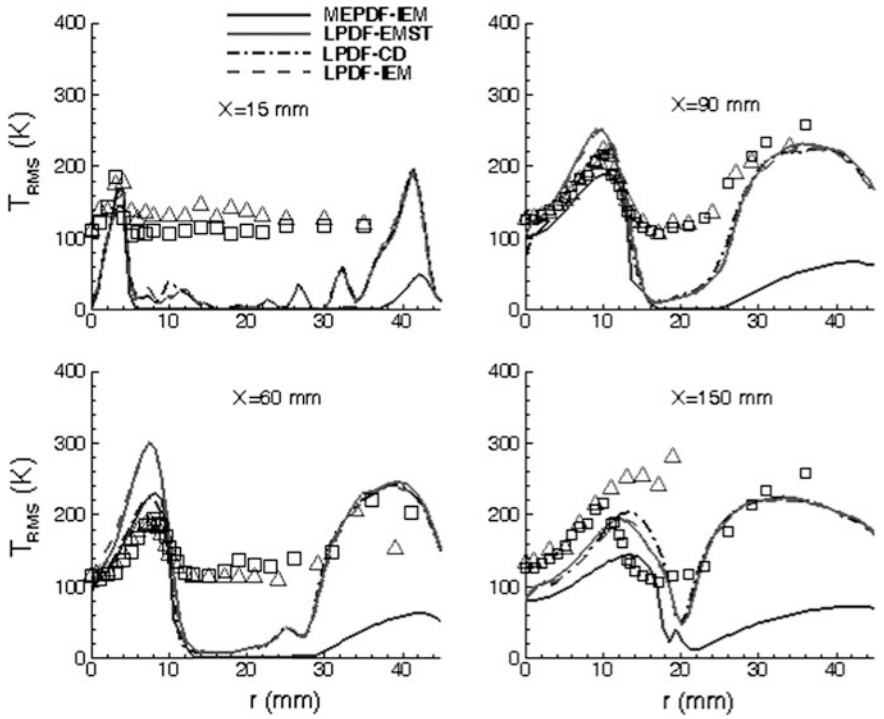

Fig. 13.4 Radial plots of RMS profiles of temperature (Symbols and lines refer to Fig. 13.2)

differences have led to carry forward the detailed calculation using Dynamic Smagorinsky model only. To quantify the impact of kinetics on the flame structure, the mean temperature plots are shown in Fig. 13.6 using Dynamic LES model with MEPDF approach. The differences among the mechanism are found to be negligible and the predictions are consistent with the previously published literature of Aminian et al. (2012). However, the lift-off height predictions do exhibit some differences such as: ARM9 predicts 44 mm and SKEL predicts it to be 49 mm. This is quite obvious, as the SKEL mechanism is the detailed one. Hence, the ignition phenomenon is slightly better captured as this occurs at the region in the domain where both the chemical and turbulent time scales are comparable. However, the variation in lift-off height distance is due to the overestimation of the mean temperature in that region, which is the result of the nature of the combustion model. Therefore, it is needed to investigate these variations in conjunction with LPDF models with LES, as discussed below. As the LES with LPDF calculations are expensive, the simulations are carried out using ARM9 mechanism only.

Figure 13.7 depicts the radial distribution of normal stress, shear stress and mean temperature using both MEPDF and LPDF methods using ARM9 mechanism. As observed, two combustion models produce similar results except some differences in

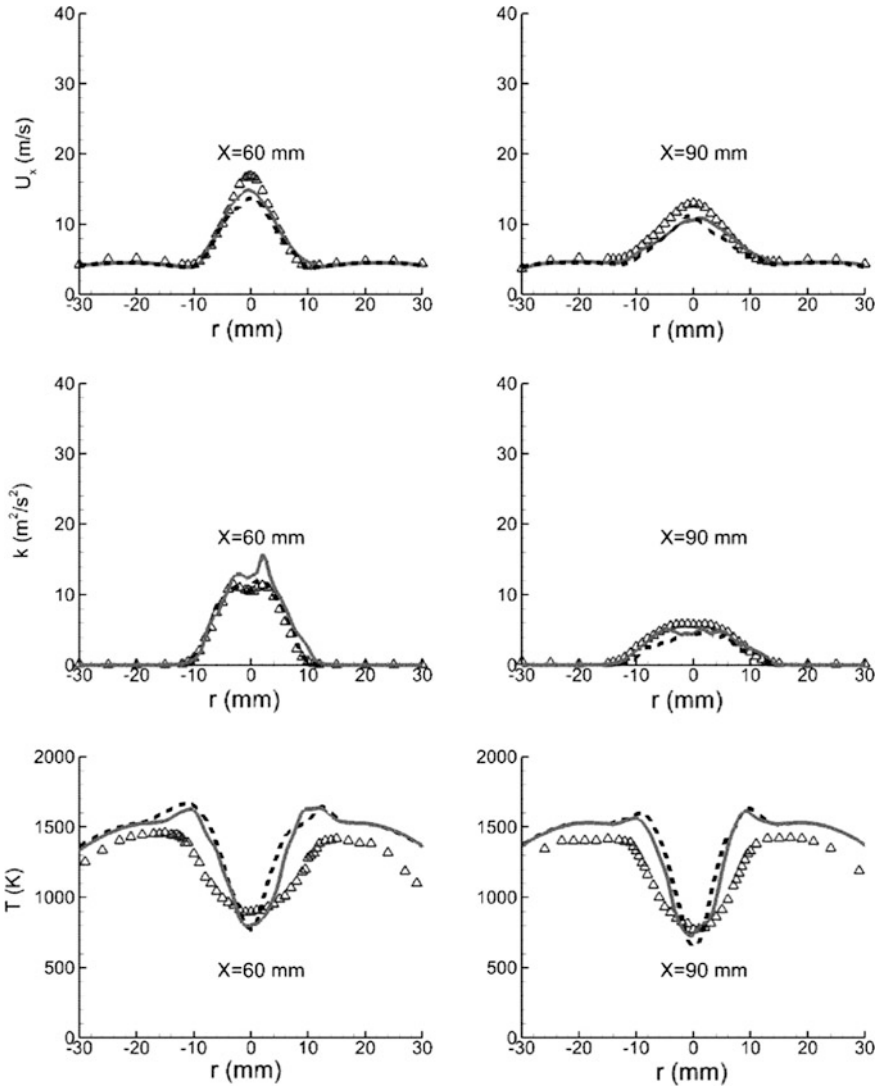

Fig. 13.5 LES + MEPDF with SKEL mechanism: radial plots of mean velocity (U_x), turbulent kinetic energy (k) and mean temperature (T). Δ: measurements (Oldenhof et al. 2010a; b), —: SKEL + Dynamic Cs, **- - -**: SKEL + KET

Reynolds stress components. Away from the centreline, the LPDF shows slightly better match compared to MEPDF model (Bhaya et al. 2014). However, the differences in mean temperature predictions are not significant; but the peak temperature using LPDF model is 16% higher than the measured value, i.e., 1698 K; whereas for the MEPDF model it is only 14% higher than the measured value, i.e., 1664 K.

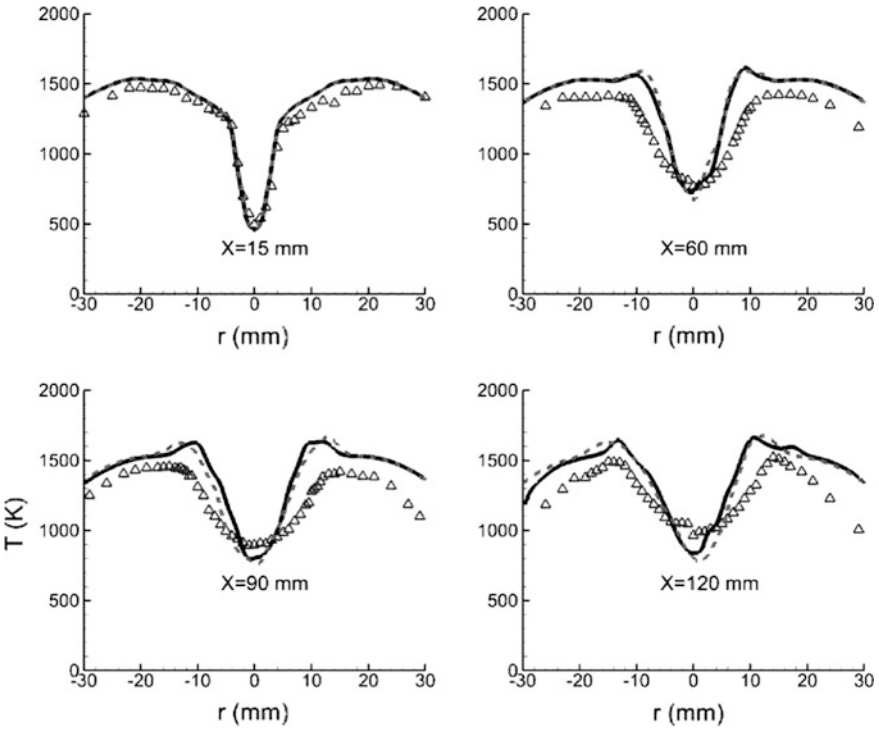

Fig. 13.6 LES + MEPDF with ARM9 and SKEL mechanism: radial plots of mean temperature. Δ: measurements (Oldenhof et al. 2010a, b), —: SKEL + MEPDF, - - -: ARM9 + MEPDF

Comparing the peak temperatures with the earlier published data, these predictions are on the slightly lower side. Noteworthy to mention that these flames are primarily kinetically controlled, that is why they are more sensitive to the fluctuations occurred at molecular level. Hence, the effect of micro-mixing is worth looking in the context of LPDF model.

Figure 13.8 depicts the radial plots of mean and rms fluctuations of the temperature at different axial locations. Although all the mixing models exhibit similar trend, the maximum peak temperature is predicted differently as: IEM—1698 K, CD—1587 K, and EMST—1588 K. Also, it is to be noted that the radial locations of the peak temperature are different for all these mixing models as reported in De et al. (2011), Kulkarni and Polifke (2012), Bhaya et al. (2014) and De and Dongre (2015). Moreover, the RMS of temperature is more or less predicted along the similar line by all of these models except minor differences due to their inherent definition of mixing of particles in the composition space. One important thing is to be noted that the lift-off height predictions are same for all of these mixing models and found to be 54 mm, which is quite better compared to the earlier predictions.

To assess the behavior of these models more conclusively in MILD regime, the comparison of scalar data (species profiles) is required. As the species data is not

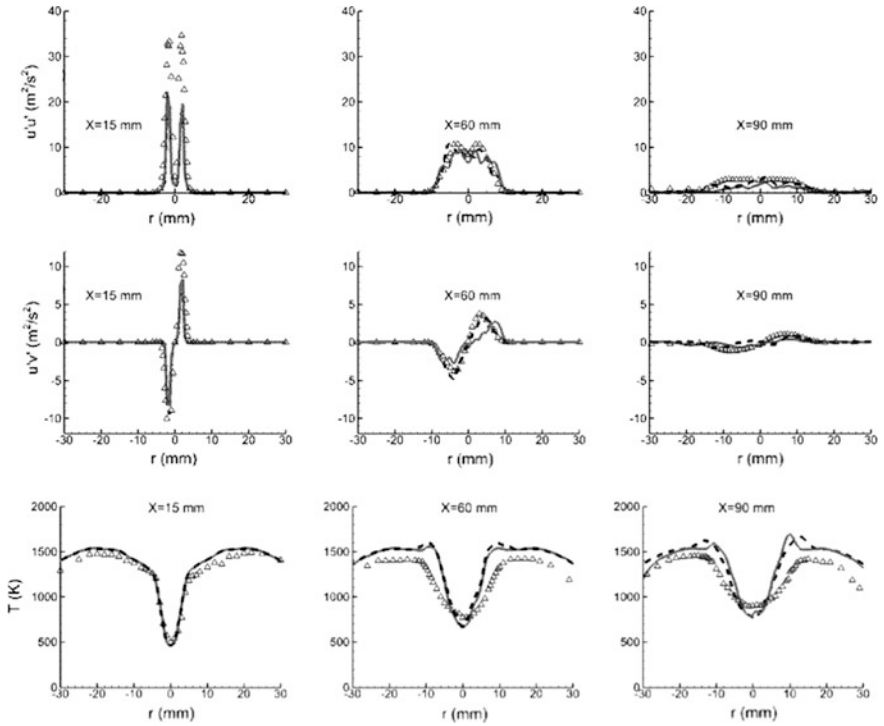

Fig. 13.7 LES with ARM9: radial plots of turbulent kinetic energy (k), Normal Stress (u′u′) and Reynolds shear stress (u′v′). Δ: measurements (Oldenhof et al. 2010a, b), —: ARM9 + LPDF, - - -: ARM9 + MEPDF

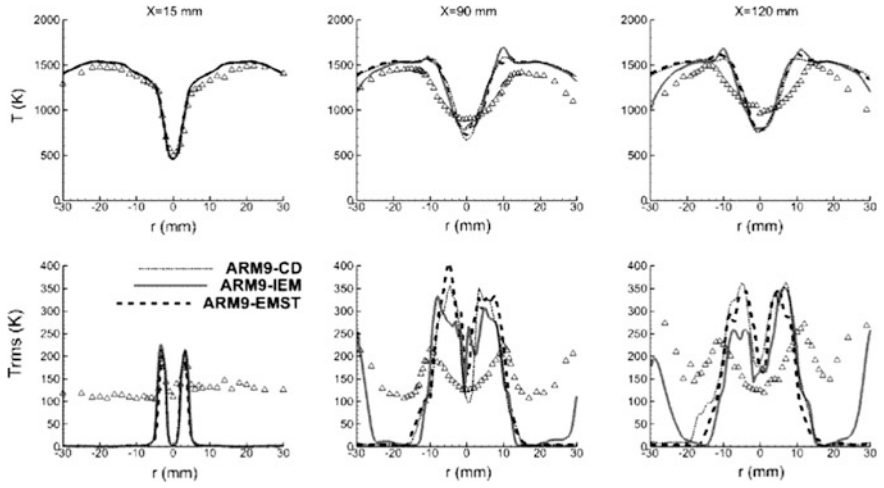

Fig. 13.8 LES + ARM9 mechanism: radial plots of the mean temperature (T) and its variance (Trms). Δ: experimental measurements (Oldenhof et al. 2010, b), —: ARM9 + IEM, …: ARM9 + CD, - - -: ARM9 + EMST

available from this particular burner (DJHC), the study has been extended for other burner, i.e., the Adelaide JHC burner and that database is quite exhaustive in nature, especially in terms of species data. This allows us to shed light in our understanding of the applicability of these models in the MILD regime.

13.4 Adelaide JHC Burner

In this section, we extend the discussion for Adelaide burner and assess the capability of different model predictions.

13.4.1 Test Case and Computational Details

The construction of this burner is also similar to the previous one, i.e., DJHC burner. But, the primary difference lies the cooling method, as described in De and Dongre (2015). The other difference between these two burners is the design of secondary burner. Further, the internal diameter of the fuel jet pipe is 4.25 mm, which is housed inside an outer annulus of internal diameter 82 mm, as shown in Fig. 13.1. More details can be found in the published literature (Dally et al. 2002; De and Dongre 2015).

Two different flames with different oxygen content in the hot coflow have been simulated, namely HM1 (3% O_2), and HM2 (6% O_2). In this case also, 2D simulations are carried out using RANS-based turbulence model, i.e., standard k-ε ($C_{\varepsilon 1} = 1.6$) model. In this case too, the chemistry is represented using DRM19 (Kazakov and Frenklach 1994) mechanism, while the Reynolds number is 10000 for all the flames simulated here. The mixing constant has been kept constant to the default value of $C_{\varphi} = 2$. The details of the boundary condition assignment and other relevant details can be found in De and Dongre (2015). To analyze the data, we have reported only two axial locations: one is close to the burner exit ($X = 60$ mm) and another is at the downstream ($X = 120$ mm).

Initially, the calculations are carried out with MEPDF method is plotted in Fig. 13.9 for HM1 flame, which appears to be extreme case with 3% O_2 content, making it more challenging to model. While looking at two major species data, i.e., CO_2 and H_2O, the predictions are way off from the measurements. This behavior has not been analyzed in DJHC burner as that burner does not provide the species data. Similarly, it was previously reported by Jaishree and Haworth (2012) the shortcomings of the MEPDF model to simulate pilot stabilized flames (De and Dongre 2015). Therefore, the MEPDF model has been discarded for detailed simulation in this burner, and the results are reported with LPDF models only. Also, after checking the statistical convergence, LPDF model data has been reported with 30 particles per cell. The details of this statistical convergence can be obtained from the literature (Bhaya et al. 2014; De and Dongre 2015)

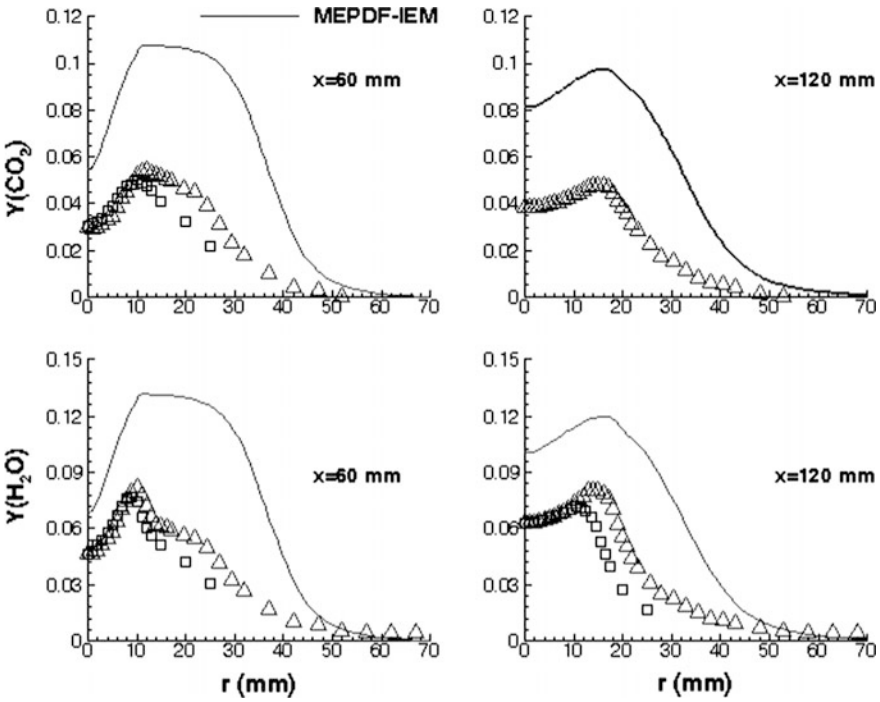

Fig. 13.9 Radial profiles of CO_2, and H_2O mass fraction for HM1 flame. Symbols (Δ: $0 \leq r \leq 70$, □: $-30 \leq r \leq 0$) represent measurements (Dally et al. 2002) and lines show predictions

The radial profiles of mean mixture fraction (for HM1, HM2 flames) are depicted in Fig. 13.10. All the models appear to predict the profile correctly without showing any significant differences. However, the major differences can be observed in the temperature profiles, shown in Fig. 13.11. Despite the fact that the PDF models incorporate the effects of temperature fluctuations in its formulations, none of them is able to accurately capture the centerline temperature. Among the models, LPDF with EMST mixing model appears to be the best. The peak temperature obtained for HM1 and HM2 flames are 1300 K and 1400 K, respectively with EMST model. For HM2 flame, the CD models show the lower peak temperature, i.e. 1160 K, compared to other two models and consistently under-predicted for both the flames. But, the predictions slightly improve as we move to higher O_2 content due to improvement in reaction rates, i.e., form HM1 to HM2 flame. These under-predictions can be associated with the lower reaction rate along the centerline, thereby over-predicting the O_2 profiles (Fig. 13.13).

Figure 13.12 illustrates the radial profiles of mean CH_4 and H_2 mass fraction for these two flames. The LPDF models capture the profiles accurately due to the well-defined boundary conditions for fuel and coflow streams. However, Fig. 13.13 exhibit some differences in O_2 profiles, which are over-predicted along the

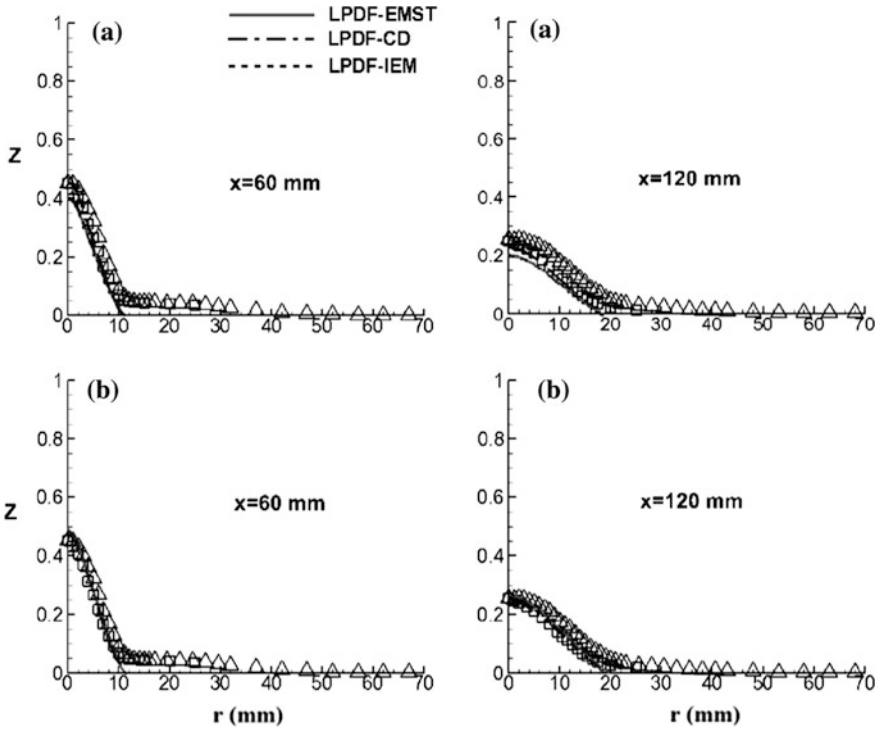

Fig. 13.10 **a** HM1, **b** HM2 flames: mean mixture fraction profiles. Symbols (Δ: $0 \leq r \leq 70$, □: $-30 \leq r \leq 0$) represent measurements (Dally et al. 2002) and lines show predictions

centerline in spite of proving exact boundary conditions at the inlet. These O_2 profiles indirectly have impact on the temperature profiles, as depicted in Fig. 13.10. This discrepancy may be associated with the reaction rate in modeling (turbulence-chemistry interaction) and cannot be quantified easily as we do not have any information about the flow field. Amongst the LPDF models, no substantial differences are observed, but the predictions improve as we move from HM1 to HM2. Previously published literature also reported the similar trends (Frassoldati et al. 2010; Mardani et al. 2010, 2011; De and Dongre 2015).

Figures 13.14 and 13.15 present the radial profiles of other species like CO_2, H_2O, OH, CO, mass fractions. All the LPDF models fairly capture the profiles, except LPDF-CD model which fails to capture the peak in CO_2 profile. Similarly, for H_2O the CD model shows under-prediction. Earlier published literatures have already reported that this kind of discrepancies is not due to kinetics (Frassoldati et al. 2010; Mardani et al. 2010, 2011; Dongre et al. 2014; De and Dongre 2015). Therefore, it can be asserted that the turbulent time scale along the centerline supersedes the scalar dissipation time scale, and hence, the reactants dissipate quickly and do have sufficient time to react along the centerline. This clearly shows up in the O_2 and temperature profiles (Figs. 13.11 and 13.13). Essentially, the

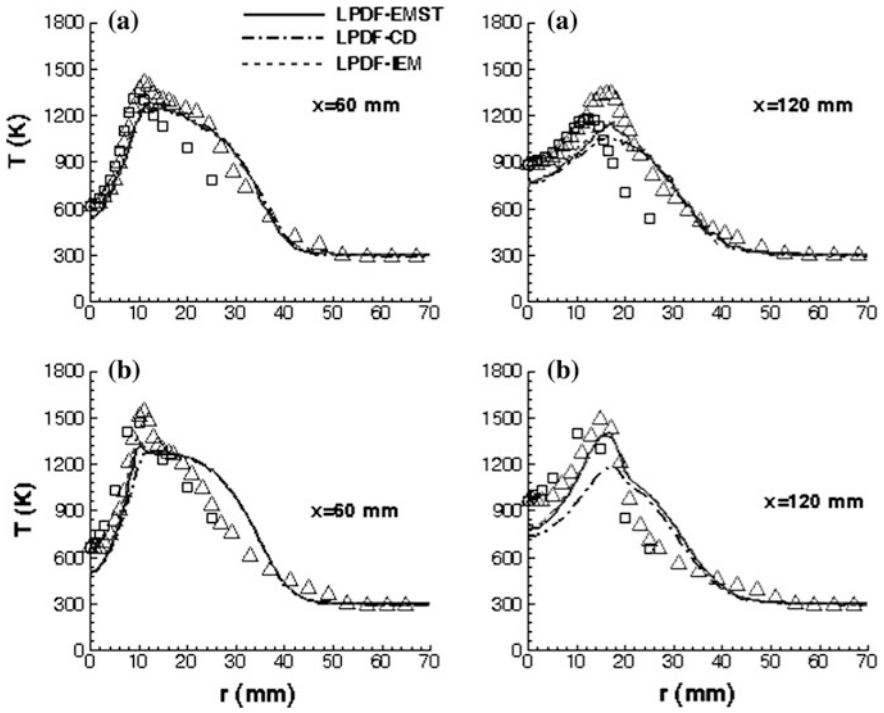

Fig. 13.11 **a** HM1, **b** HM2 flames: mean temperature profiles (Symbols and lines refer to Fig. 13.10)

combustion models fail to predict the species profiles correctly in this low Damkohler number range.

To have better understanding, we look at the minor species like OH and CO profiles in Fig. 13.15. For HM1 flame, none of the LPDF models is able to accurately capture the minor species, but they show improvement in the case of HM2 flame. In the case of CO, the profiles are well under-predicted along the shear layer for both the flames. While comparing different mixing models, LPDF-CD model shows significant differences from the others. Away from the centerline ($r > 20$ mm), the profiles are nicely captured. Comparing all the Figs. 13.13, 13.14, and 13.15), it can be noticed that the CO $\rightarrow$ CO_2 conversion is properly handled, thereby capturing the CO_2 profiles nicely; whereas OH $\rightarrow$ H_2O conversion does not appear to be proper along the centerline, resulting significant underestimation of H_2O and overestimation of O_2. This clearly signifies that there is strong coupling between turbulence-chemistry interaction models and chemical mechanism which requires more detailed and systematic investigation (De and Dongre 2015).

Apart from the mean data, the RMS of temperature and species profiles are also analyzed to have better understanding about these model behavior. Figures 13.16, 13.17 and 13.18 report all the RMS profiles for these scalar quantities. It is clearly

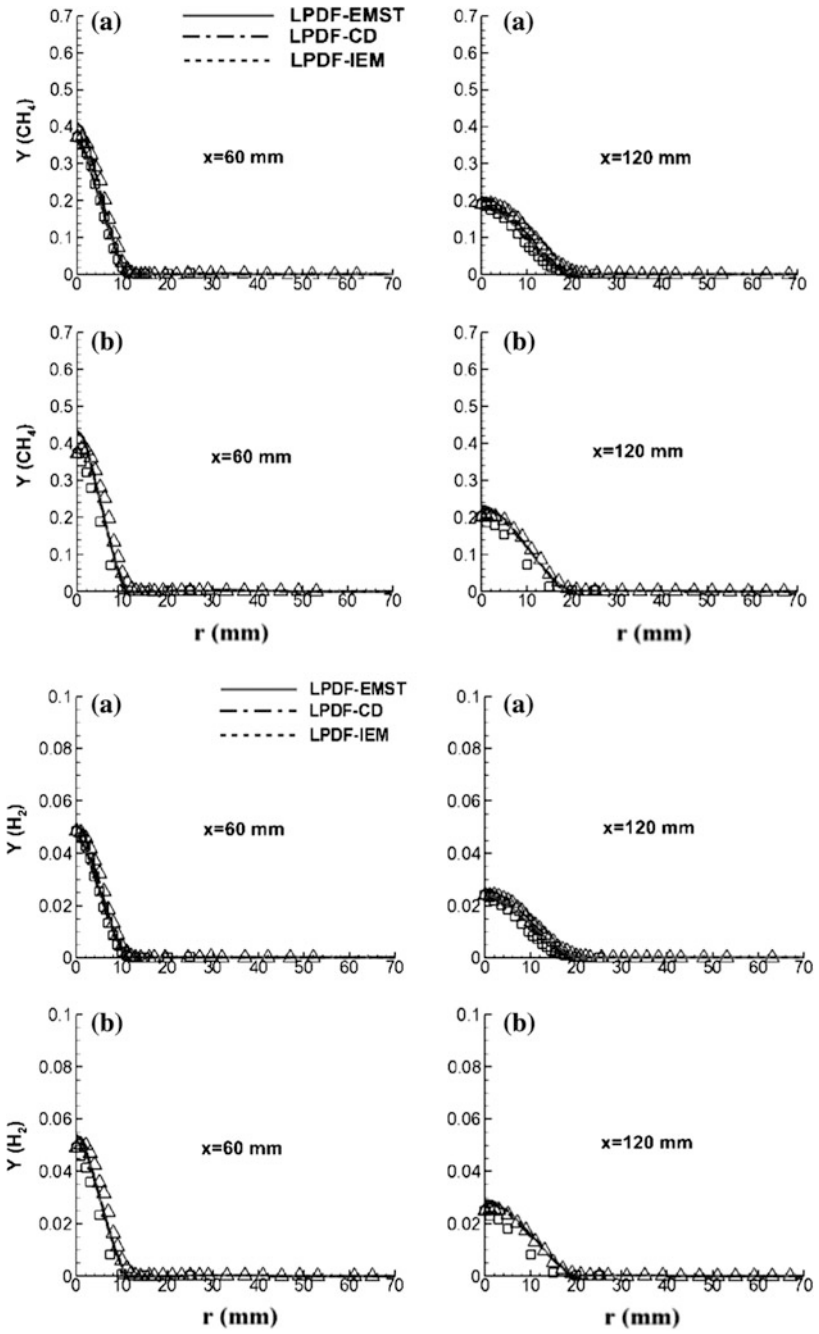

Fig. 13.12 **a** HM1, **b** HM2 flames: mean CH_4 and H_2 mass fraction profiles (Symbols and lines refer to Fig. 13.10)

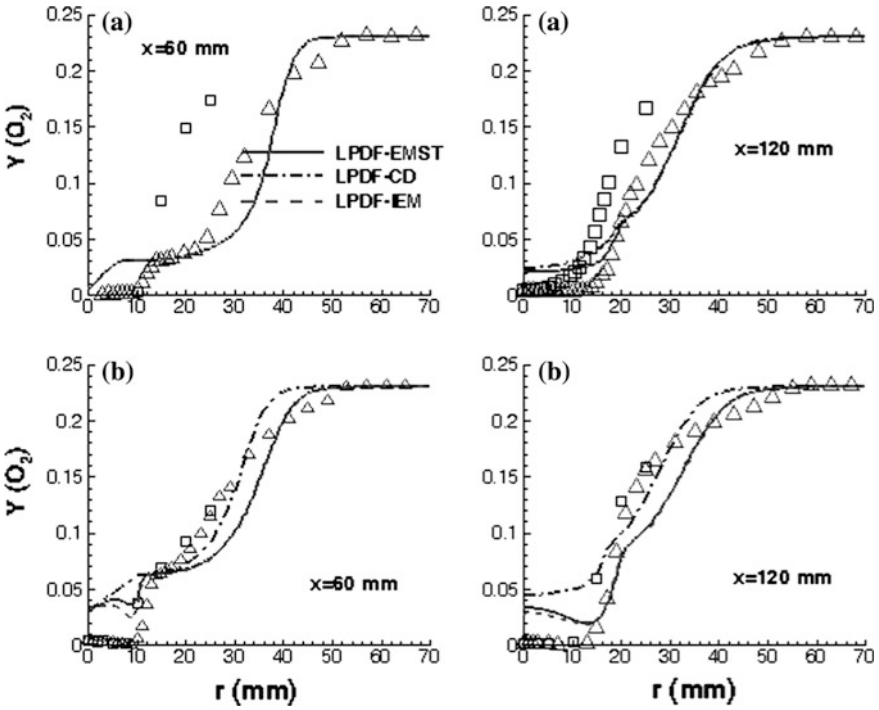

Fig. 13.13 **a** HM1, **b** HM2 flames: mean O_2 mass fraction profiles (Symbols and lines refer to Fig. 13.10)

evident that the LPDF-EMST model exhibits the best predictions among all the models for both the flames. Unlike the mean O_2 profiles (Fig. 13.12), the RMS profiles of O_2 are accurately predicted along the centerline throughout the domain. However, for HM1 flame, none of the models is able to predict the RMS profiles of CO and OH, as depicted in Fig. 13.18. As usual, the CD model behaves poorly and the EMST appears to be the best.

The observed discrepancies can be due to multiple reasons, but the lower reaction rates in MILD combustion make it more challenging to model. Also, one of the primary sources of errors in LPDF models is micro-mixing closure despite having the chemical source term in closure form. Second potential source of errors in Lagrangian PDF can come from the "notional particles": (a) due to particle tracking scheme, and (b) due to Monte Carlo methods. As noted earlier, the statistical source of errors are not present in the current simulation due to large number of particles, but bias errors (come from mean quantities) are not completely eliminated by averaging (De and Dongre 2015; Haworth 2010). For HM1 flame (3% O_2) happens to be the crude case for studying combustion models, but with increasing oxygen content the predictions improve as the reaction rate also increases, thereby increasing the Damkohler number. Means, we can obtain always better results at high

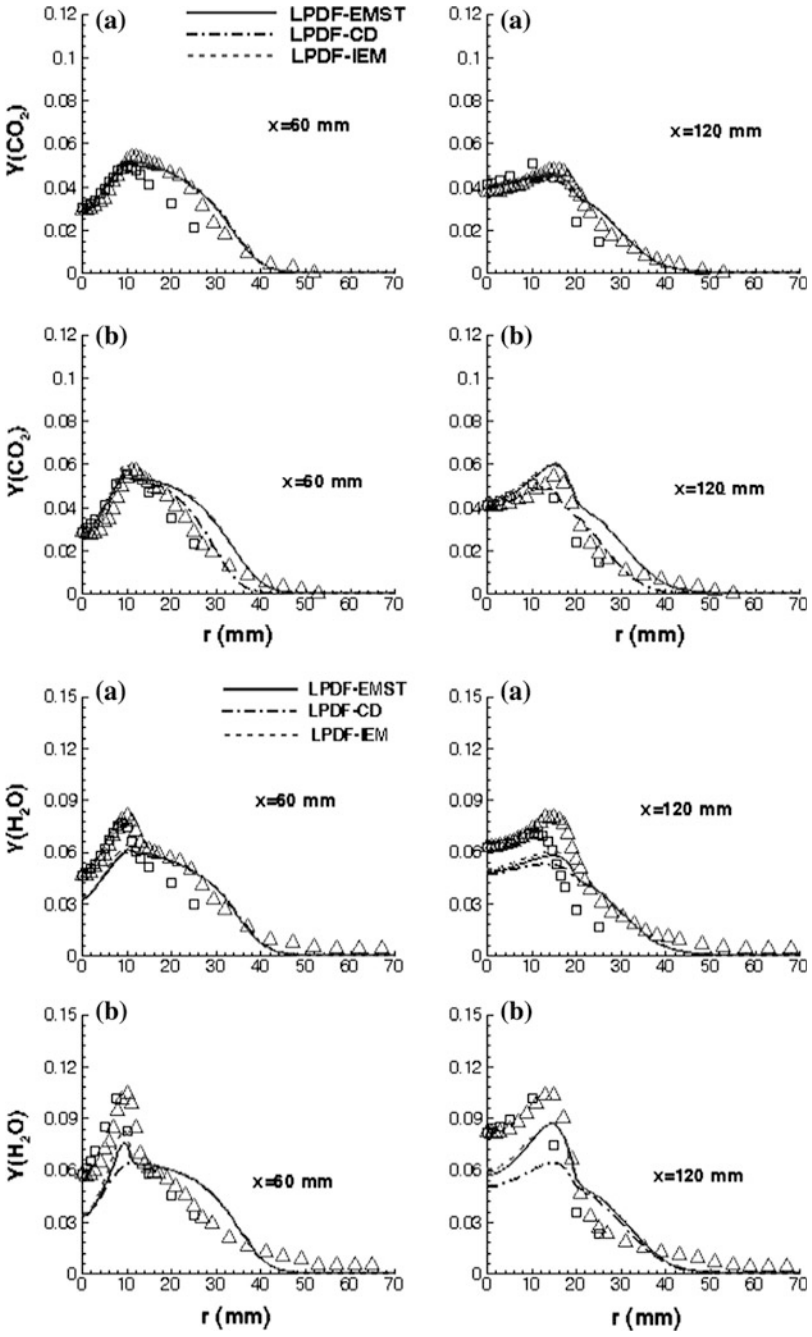

Fig. 13.14 **a** HM1, **b** HM2 flames: mean CO_2 and H_2O mass fraction profiles (Symbols and lines refer to Fig. 13.10)

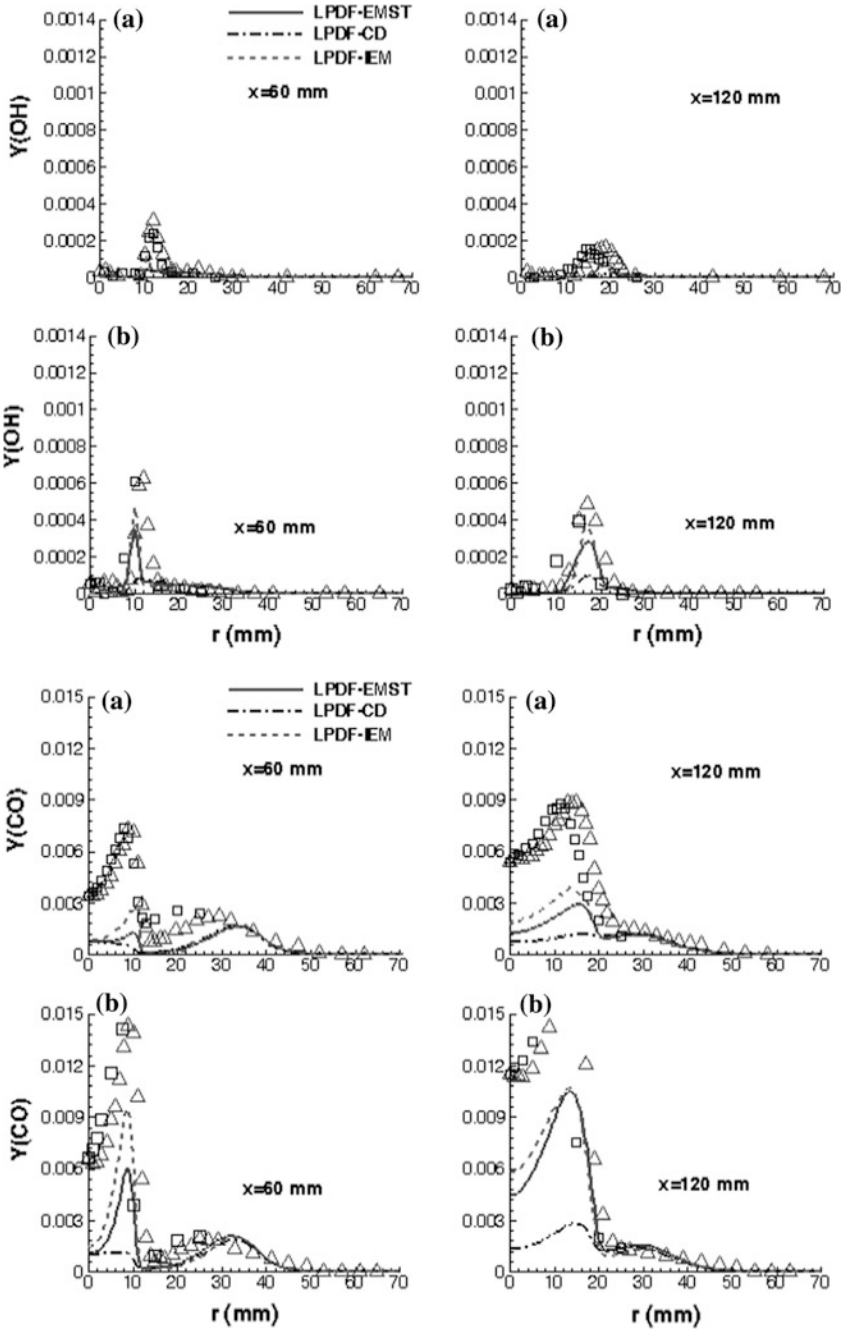

Fig. 13.15 **a** HM1, **b** HM2 flames: mean OH and CO mass fraction profiles (Symbols and lines refer to Fig. 13.10)

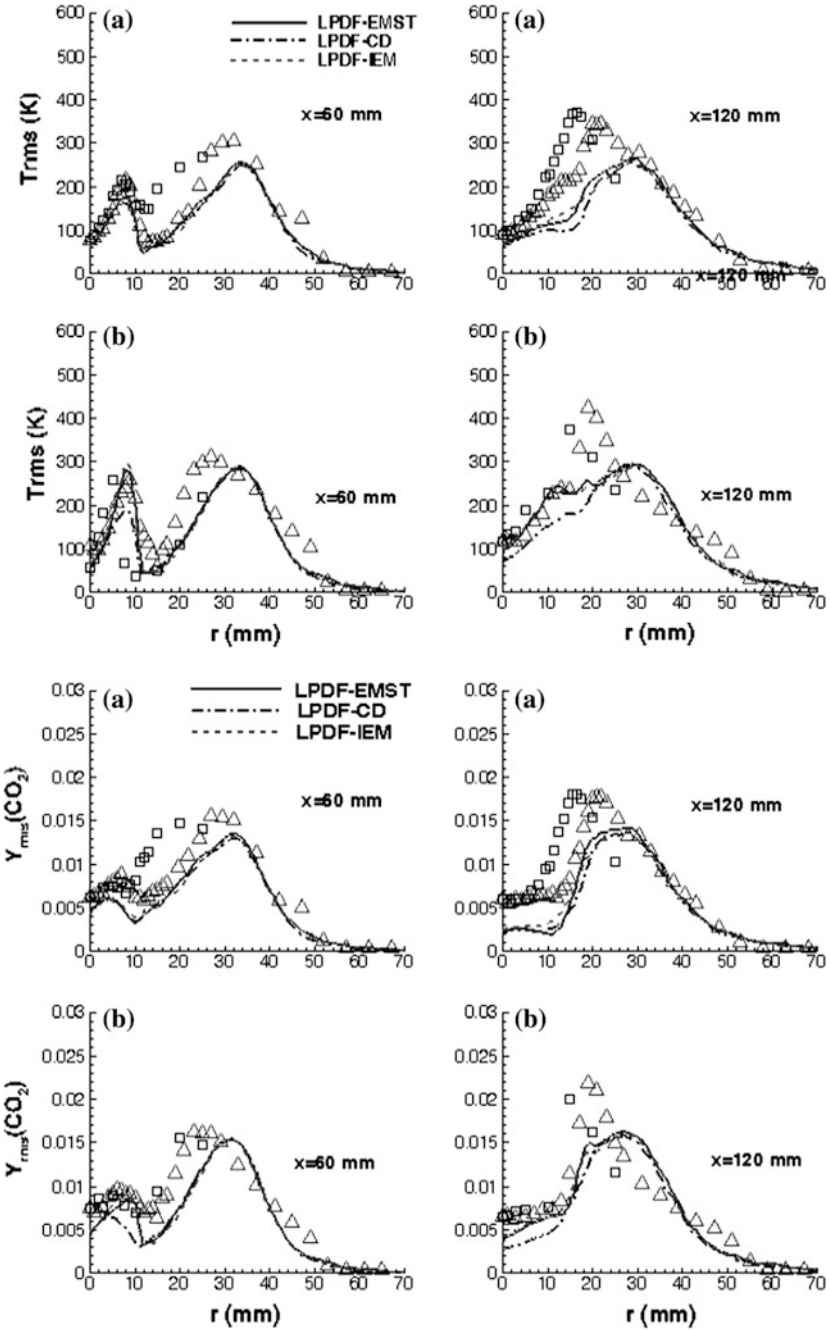

Fig. 13.16 **a** HM1, **b** HM2 flames: RMS of temperature and CO_2 mass fraction profiles (Symbols and lines refer to Fig. 13.10)

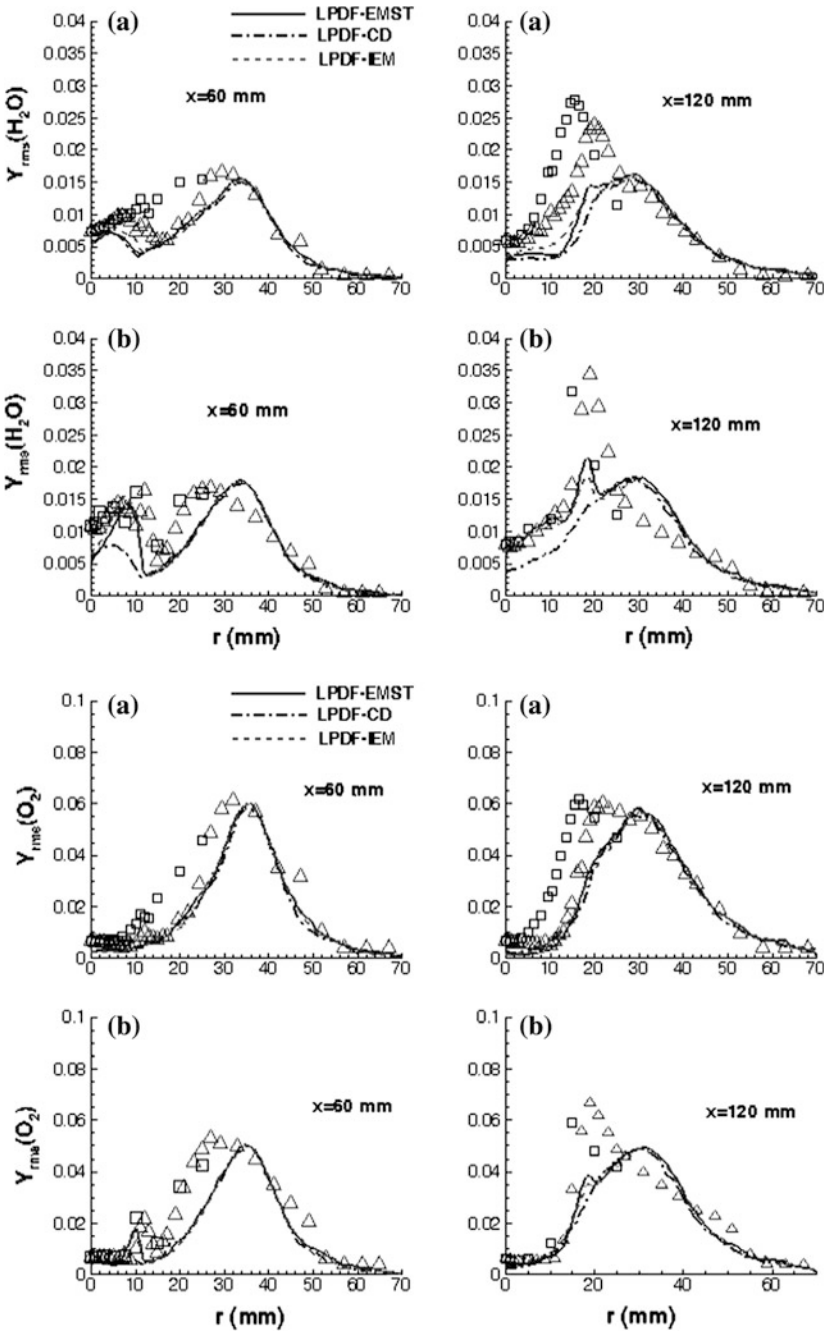

Fig. 13.17 **a** HM1, **b** HM2 flames: RMS of H_2O and O_2 mass fraction profiles (Symbols and lines refer to Fig. 13.10)

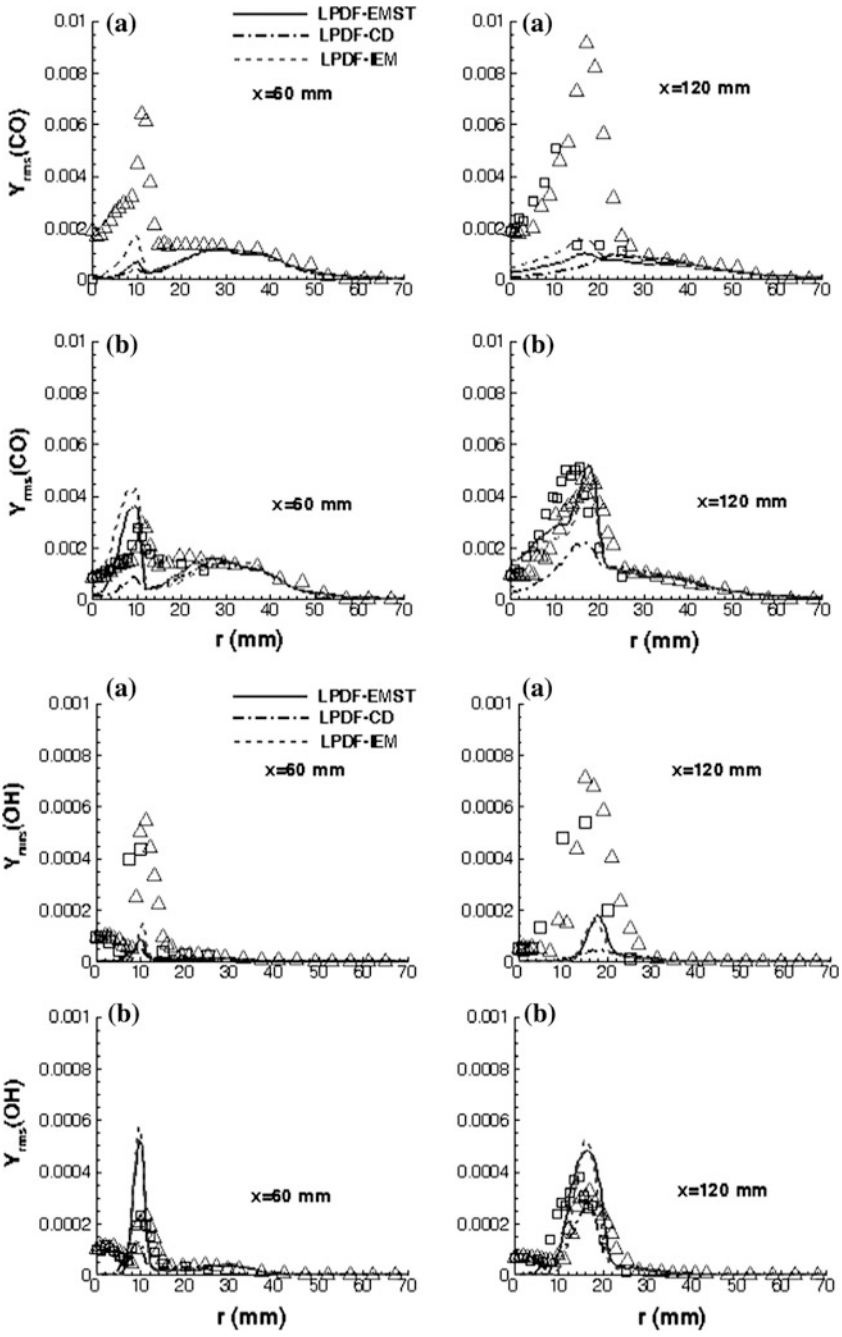

Fig. 13.18 **a** HM1, **b** HM2 flames: RMS of CO and OH mass fraction profiles (Symbols and lines refer to Fig. 13.10)

Damkohler number regime number irrespective of the chosen turbulence-chemistry interaction models (De and Dongre 2015). Overall, the transported PDF models perform better for both the burner and adequately capture the RMS profiles in the entire domain except the discrepancies observed mostly between the fuel jet and the hot coflow (shear layer). The predictions always improve with the increasing O_2 content in the hot coflow.

13.5 Conclusions

In this work, numerical investigation of two different burners mimicking MILD combustion has been analyzed using PDF transport-based turbulent-chemistry interaction models. Initially, the 2D investigation of DJHC-I flame (Re = 4100) has been carried out, followed by the 3D LES simulations, to assess the models based on the velocity and temperature statistics. In the case of 2D, all the models fairly capture the profiles at different axial locations except minor discrepancies in the temperature profiles. In case of 3D simulations, it is observed that the kinetics play a very minor role in the predictions. Also, it is observed that the LPDF results are better compared to the MEPDF results, especially in the case of EMST micro-mixing models. From both these 2D and 3D simulations, comparing the velocity and temperature statistics, it is noted that the information related to temperature fluctuations at the inlet boundary is very much essential for better predictions using LPDF models.

In the second part of the study, two Adelaide flames, namely HM1 and HM2 (Re = 10000), have been investigated for better understanding. While looking at the species profiles, it is quite evident that the MEPDF model absolutely fails to capture the species profiles. However, the different LPDF models exhibit similar behavior for mean statistics; but the differences is noticed when we look at the RMS profiles. Among the different LPDF models, the LPDF-EMST model predictions are found to be closer to the measurements. However, some minor discrepancies are still present the predictions as the LPDF models are also not free from errors. Overall, the predictions are found to be good and they are improved with increasing O_2 content. Still, the results can be improved in the presence of high fidelity turbulence model and needs detailed investigation in MILD combustion regime.

Acknowledgements Author appreciates the computational facilities available at IITK (http://www.iitk.ac.in/cc) to carry out this work.

References

ANSYS fluent 13.0 user's guide (2010) Canonsburg, PA, USA

Akroyd J, Smith AJ, McGlashan LR, Kraft M (2010a) Numerical investigation of DQMOM-IEM model as a turbulent reaction closure. Chem Eng Sci 65(6):1915–1924

Akroyd J, Smith AJ, McGlashan LR, Kraft M (2010b) Comparison of the stochastic fields method and DQMoM-IEM as turbulent reaction closures. Chem Eng Sci 65(20):5429–5441
Aminian J, Galletti C, Shahhosseini S, Tognotti L (2012) Numerical investigation of a MILD combustion burner: analysis of mixing field, chemical kinetics, and turbulence-chemistry interaction. Flow Turbul Combust 88:597–623
Bhaya R, De A, Yadav R (2014) Large Eddy simulation of MILD combustion using PDF based turbulence-chemistry interaction models. Combust Sci Technol 186:1138–1165
Bilger RW, Starner SH, Kee RJ (1990) On reduced mechanisms for methane-air combustion in non-premixed flames. Combust Flame 80:135–149
Bowman CT, Hanson RK, Davidson DF, Gardiner Jr WC, Lissianski V, Smith GP, Golde DM, Frenklach M, Goldenberg M (1996) GRI Mech. http://www.me.berkeley.edu/gri_mech/
Christo FC, Dally BB (2004) Application of transport PDF approach for modeling MILD combustion. In: 15th Australian Fluid Mechanics Conference, Sydney, Australia
Christo FC, Dally BB (2005) Modeling turbulent reacting jets issuing into a hot and diluted coflow. Combust Flame 142(1–2):117–129
Curl RL (1963) Dispersed phase mixing: 1. Theory and effects in simple reactors. AIChE J 9:175–181
Dally BB, Karpetis AN, Barlow RS (2002) Structure of turbulent non-premixed jet flames in a diluted hot coflow. Proc Combust Inst 29:1147–1154
De A, Dongre A (2015) Assessment of turbulence-chemistry interaction models in MILD combustion regime. Flow Turbul Combust 94:439–478
De A, Oldenhof E, Sathiah P, Roekaerts D (2011) Numerical simulation of Delft-Jet-in-Hot-Coflow (DJHC) flames using Eddy Dissipation Concept (EDC) model for turbulence-chemistry interaction. Flow Turbul Combust 87(4):537–567
De A, Dongre A, Yadav R (2012) Numerical investigation of Delft-Jet-in-Hot-Coflow (DJHC) burner using Probability Density Function (PDF) transport modeling. In: ASME Turbo Expo, San Antonio, Texas, ASME paper GT2013-95390
Dongre A, De A, Yadav R (2014) Numerical investigation of MILD combustion using multi-environment Eulerian probability density function modeling. Int J Spray Combust Dyn 6 (4):357–386
Dopazo C, O'Brien EE (1974) Functional formulation of non-isothermal turbulent reactive flows. Phys Fluids 17:1968–1975
Fan R, Marchisio DL, Fox RO (2004) Application of the direct quadrature method of moments to poly-disperse gas-solid fluidized bed. Powder Technol 139(1):7–20
Fox RO (2003) Computational models for turbulent reacting flows. Cambridge University Press
Frassoldati AF, Sharma P, Cuoci A, Faravelli T, Rangi E (2010) Kinetic and fluid dynamics modeling of methane/hydrogen jet flames in diluted coflow. Appl Thermal Eng 30:376–383
Haworth DC (2010) Progress in probability density function methods for turbulent reacting flows. Prog Energy Combust Sci 36:168–259
Ihme M, See YC (2011) LES flamelet modeling of three-stream MILD combustor: analysis of flame sensitivity to scalar inflow conditions. Proc Combust Inst 33:1309–1317
Ihme M, Zhang J, He G, Dally B (2012) LES of a Jet-in-Hot-Coflow burner operating in the oxygen-diluted combustion regime. Flow Turbul Combust 89:449–464
Jaishree J, Haworth DC (2012) Comparisons of Lagrangian and Eulerian PDF methods in simulations of non-premixed turbulent jet flames with moderate-to-strong turbulence-chemistry interactions. Combust Theory Model 16(3):435–463
James S, Anand MS, Razdan MK, Pope SB (1999) In situ detailed chemistry calculations in combustor flow analysis. ASME J Eng Gas Turbines Power 123:747–756
Kazakov A, Frenklach M (1994) Reduced reaction sets based on GRI-MECH 1.2. http://www.me.berkeley.edu/drm/
Kim SH, Huh KY, Dally BB (2005) Conditional moment closure modeling of turbulent non-premixed combustion in diluted hot coflow. Proc Combust Inst 30:751–757
Kulkarni RM, Polifke W (2012) LES of Delft-Jet-in-Hot-Coflow (DJHC) with tabulated chemistry and stochastic fields combustion model. Fuel Proc Technol 107:138–146

Liu Y, Fox RO (2005) CFD predictions for chemical processing in a confined impinging-jets reactor. AIChE J 52(2):731–744

Marchisio DL, Fox RO (2005) Solution of population balance equations using the direct quadrature method of moments. J Aerosol Sci 36(1):43–73

Mardani A, Tabejamaat S, Ghamari M (2010) Numerical study of influence of molecular diffusion in the Mild combustion regime. Combust Theory Model 14(5):747–774

Mardani A, Tabejamaat S, Ghamari M (2011) Numerical study of effect of turbulence on rate of reactions in the MILD combustion regime. Combust Theory Model 15(6):753–772

Oldenhof E, Tummers M, Van Veen EH, Roekaerts DJEM (2010a) Ignition kernel formation and lift-off behavior of jet-in-hot-coflow flames. Combust Flame 157:1167–1178

Oldenhof E, Tummers MJ, Van Veen EH, Roekaerts DJEM (2010b) Role of entrainment in the stabilization of jet-in-hot-coflow flames. Combust Flame 157(6):1167–1178

Oldenhof E, Tummers MJ, Van Veen EH, Roekaerts DJEM (2012) Transient response of the Delft jet-in-hot coflow flames. Combust Flame 159(2):697–706

Pope SB (1985) PDF methods for turbulent reactive flows. Prog Energy Combust Sci 11:119–192

Pope SB (1997) Computationally efficient implementation of combustion chemistry using in situ adaptive tabulation. Combust Theory Model 1:41–63

Raman V, Pitsch H, Fox RO (2006) Eulerian transported probability density function sub-filter model for large-eddy simulations of turbulent combustion. Combust Theory Model 10(3):439–458

Smith GP, Golden DM, Frenklach M, Moriarty NW, Eiteneer B, Goldenberg M, Bowman CT, Hanson RK, Song S, Gardiner Jr WC, Lissianski VV, Qin Z (2010) GRI Mech. http://www.me.berkeley.edu/gri_mech/

Smooke MD (1991) Reduced kinetics mechanisms and asymptotic approximation for methane-air flames. Springer

Subramaniam S, Pope SB (1998) A mixing model for turbulent reacting flows based on Euclidean minimum spanning trees. Combust Flame 115:487–514

Tang A, Zhao W, Bockelie M, Fox RO (2007) Multi-environment probability density function (MEPDF) method for modeling turbulent combustion using realistic chemical kinetics. Combust Theory Model 11(6):889–907

Wang L, Fox RO (2004) Comparison of micro-mixing models for CFD simulation of nano-particle formation. AIChE J 50(9):2217–2232

Yadav R, Kushari A, Eswaran E, Verma AK (2013) A numerical investigation of the Eulerian PDF transport approach for modeling of turbulent non-premixed pilot stabilized flames. Combust Flame 160(3):618–634

Yadav R, Kushari A, De A (2014) Modeling of turbulent lifted flames in vitiated co-flow using multi-environment Eulerian PDF transport approach. Int J Heat Mass Transf 77:230–246

Zucca A, Marchisio DL, Barresi AA, Fox RO (2006) Implementation of the population balance equation in CFD codes for modeling soot formation in turbulent flames. Chem Eng Sci 61 (1):87–95

Chapter 14
Large-Eddy Simulation of Nonpremixed Flames by Explicit Filtering

Joseph Mathew and Saugata Chakravorty

Abstract Large-eddy simulation (LES) provides improved predictions in applications which are controlled by dynamics of large-scale structures. Since flames are often anchored by recirculating flows or mixing layers, turbulent combustion is an application where the promise of LES is being realized. Following a brief introduction to LES, and its models for the turbulence, some combustion models are discussed. Two approaches are discussed in greater detail. First, the extension of an explicit filtering method, and second the filtered mass density function method (FMDF), which is analogous to the pdf methods for turbulent combustion. The performance of these methods was assessed by examining LES of flames developing from alternating fuel and oxidizer layers embedded in homogeneous, isotropic turbulent fields. Solutions with the explicit filtering method are not too different from reference DNS (direct numerical simulation), and improves with grid refinement. The FMDF solutions are noticeably better even on a coarse grid. Evolution of mean quantities, as well as pdfs follow those of the DNS very closely at all times, even though snapshots of the fields do not resemble each other.

Keywords Large eddy simulation · Explicit filtering · Filtered mass density function

---

The original version of this chapter was revised: Missed out author corrections have been incorporated. The erratum to this chapter is available at https://doi.org/10.1007/978-981-10-7410-3_21

J. Mathew (✉) · S. Chakravorty
Indian Institute of Science, Bangalore 560012, India
e-mail: joseph@iisc.ac.in

S. Chakravorty
e-mail: Saugata.Chakravorty@honeywell.com

S. Chakravorty
Honeywell, Bangalore, India

© Springer Nature Singapore Pte Ltd. 2018

S. De et al. (eds.), *Modeling and Simulation of Turbulent Combustion*, Energy, Environment, and Sustainability, https://doi.org/10.1007/978-981-10-7410-3_14

14.1 Introduction

A large-eddy simulation (LES) is an approximate description of a practical turbulent flow that is expected to be reliable and acceptably accurate. Typically, flows interact with their surroundings on a range of large scales, but the scale range present extends to the smallest scales at which fluid viscosity is most active. Most of the kinetic energy in a turbulent flow can be identified with a range of large scales whose dynamics determine the essential development of the flow. A simulation that captures the full range of motions, down to the Kolmogorov scale, is a direct numerical simulation (DNS). When an LES contains a substantial part of the kinetic energy of the flow, say 95%, a DNS would provide only small quantitative improvements with no qualitative differences. But, the computational effort for an LES is substantially less. At moderate Reynolds numbers, typical LES grids are at most one-hundredth that of DNS ones. LES for cold flows is now quite well-established (see, Sagaut (2006), for a comprehensive presentation from a decade ago).

It is useful to bear in mind that, most often, only time-averaged quantities are of interest in assessing practical designs. Such averages are obtained by solving Reynolds-averaged Navier–Stokes (RANS) equations. Turbulence models for RANS equations account for transport by turbulence fluctuations, but not that by large-scale structures. Owing to the special difficulties arising from strongly nonlinear reaction rate expressions for chemical source terms, much of the effort in reacting flow computations has been focused on improving reaction rate models for RANS. The shortcomings of RANS models for turbulent transport, which have been identified in non-reacting flows, have been largely ignored when computing reacting flows. It helps that RANS turbulence models are adequate for, say, round jets, or flows that separate from (even, rounded) corners which are common flame configurations. A parallel in LES for combustion is that even the simple models used for non-reacting flow LES have been deemed sufficient for reacting flow LES, because the solutions have been found to be more accurate. The improvement can be traced to LES providing more accurate predictions of scalar variance—a common input to combustion models; transport by large-scale structures is now computed and not (inadequately) modeled. Our studies have the aim of using a method that has been found to have good properties for non-reacting flow LES, and an LES combustion model that should also be an improvement.

In reactive flows, it may not be sufficient to compute a large-scale range alone. In typical applications of interest in engineering, certainly in combustors, flame thickness is small compared with integral length scales of turbulence, and any organized motions that may be present. Then, flame thickness is smaller than the smallest lengths that should be resolved for an LES of such flows when there is no reaction. Since reaction is a crucial process, some additional model ought be necessary to account for the effect of the flame on the evolution of the turbulent flow. We need not expect to resolve flame structure, but we ought to account for the wrinkling of the flame by a wide range of turbulent motions. Flame wrinkling creates much larger flame surface area. In turn, the rate of fuel consumption is much larger than that of a flame with smooth surfaces. Several approaches to LES of flames have been designed

with special models to address this expectation that small scales would be important, at least in the vicinity of flame surfaces A review of LES for combustion is available (Pitsch 2006). Such a comprehensive review is not the objective of this article. Instead, we present a recent study of combustion LES by two approaches, the filtered mass density function method (FMDF) and explicit filtering. The study reported here is limited to combustion occurring between alternating slabs of fuel and oxidizer in forced, homogeneous, isotropic turbulence. The same methods were applied to the Sandia D flame, but owing to limitations in computational facilities, the study is of limited value and has been omitted here. Although the flame length is about 70 diameters, our study was limited to the 20 diameter near field, allowing comparisons with measurements at 15 diameters only (Chakravorty 2010). Results of LES with pdf methods for Sandia flames have been discussed in a review (Haworth 2010).

Length scales allow us to define different types of computations and associated issues. Let η be the Kolmogorov length scale, L a large scale of the flow, say, the integral length scale or the jet diameter for a jet flame, l_f the flame thickness, and l_b the flame brush thickness. The flame brush arises due to wrinkling of the flame surface by the turbulence. In computations Δ is a representative grid spacing. In an LES, there would be a cutoff scale $l_c > \Delta \gg \eta$. In a DNS, $\Delta \approx \eta$; the smallest resolved scale should be smaller than length scale of the peak of the dissipation spectrum, so that viscous processes are represented and not modeled. In the combustion community, a more restrictive definition of DNS is also used: flame structure must also be resolved. Generally, l_f may be larger or smaller than η, but in an LES l_b should be larger than l_c—the larger scales of turbulence that create the flame brush should be represented in LES. l_c would lie somewhere in the inertial range. Generally, $l_f \ll l_c$ in an LES.

14.2 LES Models for Reacting and Non-reacting Flow

The need for LES models can be understood by considering the 1-d transport equation for $u(x,t)$,

$$\frac{\partial u}{\partial t} + \frac{\partial}{\partial x} f(u) = 0, \tag{14.1}$$

where $f(u)$ is a nonlinear function. An LES provides an approximation $\bar{u}(x,t)$ that contains a large-scale part of $u(x,t)$; $\bar{u} = G * u = \int G(x - x')\, u(x')\, \mathrm{d}x'$, where G is a low-pass, spatial filter. The evolution equation for $\bar{u}(x,t)$ can be obtained by applying the filter G to Eq. (14.1) to get

$$\frac{\partial \bar{u}}{\partial t} + G * \frac{\partial}{\partial x} f(u) = 0,$$

or, an equation in the original *form* with a remainder $\mathscr{R}$

$$\frac{\partial \bar{u}}{\partial t} + \frac{\partial}{\partial x} f(\bar{u}) = \mathscr{R},$$

$$\mathscr{R} = \frac{\partial f(\bar{u})}{\partial x} - G * \frac{\partial f(u)}{\partial x}.$$

$\mathscr{R} \equiv 0$ if $f(u)$ is linear. In nonlinear problems, since u is not known when solving for $\bar{u}$, $\mathscr{R}$ must be replaced with a model $\mathscr{R}_m(\bar{u})$ for closure.

For the Navier–Stokes equations for incompressible flow, the remainder appears in the filtered momentum equations only, and is, therefore, termed the subgrid-scale (SGS) stress τ_{sgs}. An eddy viscosity model, analogous to those for RANS computations, takes τ_{sgs} to be proportional to the strain rate tensor, and lets the coefficient be an eddy viscosity, dependent on grid spacing Δ and a velocity scale. This is the Smagorinsky SGS model (Sagaut 2006). A widely used improvement over the standard Smagorinsky model is a dynamic version that determines an overall coefficient from the solution itself; the SGS model is expected to have the same coefficient when estimated from the solution and a low-pass-filtered form of the same solution. Owing to the eddy viscosity form of the Smagorinsky model term, there is a dependence on large-scale content. As the grid is refined, this dependence causes the large-scale content of the solution to also change with grid refinement. Thus, LES with Smagorinsky SGS models may not converge monotonically with grid refinement. Detailed discussions of these and other models for non-reacting flow are available (Sagaut 2006).

It is helpful to take the governing equations for low-speed, reacting flow to be a low Mach number approximation of compressible flow. The necessary density variations are allowed, but omitting acoustic waves removes severe restrictions on time-steps. In dimensionless form, the low Mach number equations for mass, momentum and energy are

$$\frac{\partial \rho}{\partial t} + \nabla \cdot \rho \mathbf{u} = 0, \tag{14.2}$$

$$\rho \frac{\mathrm{D}\mathbf{u}}{\mathrm{D}t} = -\nabla p + \frac{1}{\mathrm{Re}} \nabla \cdot \tau, \tag{14.3}$$

$$\rho c_v \frac{\mathrm{D}}{\mathrm{D}t} T = -p \nabla \cdot \mathbf{u} - \frac{\gamma}{(\gamma - 1)\mathrm{RePr}} \nabla \cdot \mathbf{q} + \frac{\gamma}{(\gamma - 1)} H, \tag{14.4}$$

respectively. These equations contain velocity $\mathbf{u}$, density ρ, pressure p, temperature T, stress tensor τ, heat flux $\mathbf{q}$, specific heat at constant volume c_v, and specific heat ratio γ. All quantities are scaled with a reference velocity and length, or their values at a reference state. The Reynolds number Re and Prandtl number Pr are based on the reference scales and properties. H is the heat release due to combustion. The perfect gas equation of state is $p = \rho RT/M$; R is the universal gas constant and M is the molecular weight. Equation (14.3) is the momentum equation at first order; at the leading order we get $\nabla p^{(0)} = 0$. In closed systems, such as reacting flow in a closed box, $p^{(0)}$ increases in time due to heat release, and in open systems, like free jets, it remains constant. Composition changes are described by transport equations for mass fractions Y_α of each species α

$$\rho \frac{\mathrm{D}Y_\alpha}{\mathrm{D}t} = \frac{1}{\mathrm{ReSc}} \nabla \cdot \rho D \nabla Y_\alpha + \omega_\alpha. \tag{14.5}$$

Here ω_α is the reaction rate of species α, and Sc is the Schmidt number based on the reference values. In Eq. (14.5) the binary flux approximation $\mathbf{j}_\alpha = \rho D \nabla Y_\alpha$ has been used (with a common diffusion coefficient), but a more general treatment is possible.

14.2.1 Explicit Filtering Model

The explicit filtering model proposed by Mathew et al. (2003) was derived as an alternate, nearly equivalent implementation of the approximate deconvolution model (ADM) of Stolz and Adams (1999). The derivation offered a principle for LES: Integrate the governing equations for the flow under consideration without adding any model terms; use a numerical scheme whose spatial operations are performed with high-resolution formulas, and apply a high-resolution filter to transported fields after every time-step. For the model problem described by the 1-d transport equation, the explicit filtering method requires that Eq. (14.1) be integrated in time, and that after every timestep the field $u(x, t)$ be updated by filtering: $u(x, t) \leftarrow E * u(x, t)$, where E is a low-pass filter. The spatial derivative must be computed with a high-resolution discrete operation. Implicit (compact) difference formulas, or high-order explicit ones are suitable. Since these operators have flat transfer functions over a range of large scales, their effect on large scales do not change with grid refinement. Instead, as a grid is refined, the range of scales that are computed without numerical distortion increases and provides monotonic convergence to the DNS solution. For incompressible flow, the Navier–Stokes equations are integrated, and a spatial filter is applied to the velocity field in all three dimensions. Detailed discussions of this method are available (Mathew 2016). A further advantage of this approach is that it provides a uniform procedure for any set of governing equations. For example, the heuristic for incompressible flow that SGS stress can be taken to be proportional to SGS strain rate is not sufficient for compressible flow, let alone reacting flows which have different types of nonlinear terms. The explicit filtering model requires only that transported fields be filtered with a high-resolution filter. By construction, this model cannot be accurate if omitted small-scale parts can have any significant effect on large-scale dynamics. An LES model that attempts to incorporate such effects is discussed below.

14.2.2 Filtered Mass Density Function Method

The reaction rate term in Eq. (14.5) is of the form

$$\omega = \mathscr{A} T^a \prod_i (\rho Y_i)^{n_i} \exp(-E_a/RT),$$

and is a strongly nonlinear function of temperature T, density ρ, and species mass fractions Y. For multiple-step models, there are such terms for every substep that a given species participates in. E_a is the activation energy, and $\mathscr{A}$ is a constant.

The large-scale part of this term, which is needed for an LES, can differ significantly from the quantity obtained by merely taking large-scale parts of the variables as its arguments. There is no general heuristic to model the difference. The difficulty does not pertain to LES alone. Mean flow computations that solve RANS equations cannot obtain the needed mean reaction rate by inserting mean fields in reaction rate expressions; the differences may be of several orders of magnitude. So, functional models for effects of reaction rate terms have been proposed that are based on an understanding of its behavior, such as the eddy dissipation model, conditional moment closure, etc. Pdf methods were proposed because the reaction rate term could be treated exactly. Modeling effort gets transferred, and the hope is that the modeling is now easier. When the form of the pdf is assumed, it suffices to provide parameters such as means and variances. A more general method is to solve a transport equation for the pdf. A pdf method determines the joint probability $f(\psi; \mathbf{x}, t)\mathrm{d}\psi$ that a vector of random variables ϕ lies in ranges $\psi < \phi < \psi + \mathrm{d}\psi$ of its sample space at location $\mathbf{x}$ and time t.

When the composition vector ϕ comprises mass fractions of participating scalars Y_α ($\alpha = 1, 2, \ldots N$), and T, the reaction rate can be treated exactly, but nontrivial modeling is required for diffusion and convection. The extension to a joint pdf of composition and velocity allows convection to be treated exactly. The pdf approach has proved promising for RANS solutions. Pope (1990) reviewed the successes of these methods, and introduced the concept of a filtered density function as a formal extension of the pdf method to LES to treat the reaction rate term exactly, but indicated how much more difficult the approach would become. Later Colucci et al. (1998) derived an fdf method, applied it to simple shear flows and compared solutions to an LES without any modeling of the reaction rate term, taking a DNS as the reference. Jaberi et al. (1999) proposed the filtered mass density function (FMDF)

$$f_L(\psi; \mathbf{x}, t) = \int_{\mathbf{x}'} \rho(\mathbf{x}', t)\zeta[\psi, \phi(\mathbf{x}, t)]G(\mathbf{x}' - \mathbf{x})\mathrm{d}\mathbf{x}'$$

to handle variable density flows. Here, G is a low-pass filter and ζ is the fine-grained density.

It is useful to recall that the pdf method was developed to treat the strong nonlinearity of reaction rate terms exactly in mean flow computations which required finite-rate-chemistry models. The required mean quantities, whether reaction rate, or compositions followed readily as moments of the pdf. An LES is a specific realization of a flow. When the flow is stationary, each computed instant can be a sample; each point, line or plane of a field can be a sample when there are 1, 2, or 3 homogeneous directions, respectively. So the solution at an instant is either a sample or a set of samples, but is not a moment. LES equations require low-pass filtered reaction rates and not their expectations. Then, what is achieved by recourse to the FMDF? Implicitly, the FMDF method allows for subfilter content to be stochastic. Two ideas are relevant here: first, the function $\omega(\mathbf{x}, t)$ whose filtered form $\bar{\omega}(\mathbf{x}, t)$ with finite spectral support, as for any function restricted to a grid, is not unique. Second, when ω is a strongly nonlinear function, small-scale fluctuations of its arguments can cause large changes, albeit over small (subgrid-scale) regions, which can

nevertheless contribute to the large-scale solution—a small-scale fluctuation in temperature that increases formation of a species and heat release will spread and contribute to the large-scale part of the fields. Formally, the FMDF allows the large-scale part of the effect of such stochastic small-scale contributions to be incorporated via the FMDF (a pdf).

The transport equation for the FMDF is

$$\frac{\partial f_L}{\partial t} + \frac{\partial}{\partial x_i}\langle u_i|\psi\rangle f_L = \frac{\partial}{\partial \psi_\alpha}\left[\left\langle -\frac{1}{\hat{\rho}(\psi)}\frac{\partial}{\partial x_i}\left(\frac{\mu}{\mathrm{ReSc}}\frac{\partial \phi_\alpha}{\partial x_i}\right)\Big|\psi\right\rangle_F f_L\right] - \frac{\partial[\hat{\omega}(\psi)f_L]}{\partial \psi_\alpha}. \tag{14.6}$$

The second term on the rhs due to the reaction rate can now be computed exactly, but the second term on lhs due to advection and the first term on rhs due to diffusion needs modeling. Since $f_L(\phi; \mathbf{x}, t)$ has $N + 4$ dimensions, a direct solution of Eq. (14.6) soon becomes intractable as N increases. Instead a Monte Carlo scheme can be used that is stochastically equivalent. Developed previously for RANS pdf computations, the Lagrangian Monte Carlo method follows the evolution of a large number of representative Monte Carlo elements or particles which are translated short distances at the local fluid velocity. Each particle carries a composition vector which changes due to reaction. The effect of viscous diffusion is incorporated as a random-walk displacement of the particle position.

14.2.2.1 Lagrangian Monte Carlo Method for FMDF

Jaberi et al. (1999) split the second term on lhs of Eq. (14.6) into advection of f_L by the resolved (LES) velocity and an unresolved velocity difference that was modeled by a standard gradient diffusion term. Following the explicit filtering principle, here f_L is advected by the LES velocity without adding any terms for the difference. The first term on rhs of Eq. (14.6) was split into two components representing mixing in physical and composition spaces (Colucci et al. 1998). With these changes, the FMDF transport equation becomes

$$\begin{aligned}\frac{\partial f_L(\psi, \mathbf{x}, t)}{\partial t} &+ \frac{\partial}{\partial x_i}u_i(\mathbf{x}, t)f_L(\psi, \mathbf{x}, t) \\ &= \frac{\partial}{\partial x_i}\left[\frac{\mu}{\mathrm{ReSc}}\frac{\partial}{\partial x_i}\frac{f_L(\psi, \mathbf{x}, t)}{\tilde{\rho}(\mathbf{x}, t)}\right] - \frac{\partial}{\partial \psi_\alpha}\left[\hat{\omega}(\psi)f_L(\psi, \mathbf{x}, t)\right] \\ &\quad - \frac{\partial^2}{\partial \psi_\alpha \partial \psi_\beta}\left[\left\langle \frac{\mu}{\mathrm{ReSc}}\frac{\partial \phi_\alpha}{\partial x_i}\frac{\partial \phi_\beta}{\partial x_i}\Big|\psi\right\rangle_F f_L(\psi, \mathbf{x}, t)\right].\end{aligned} \tag{14.7}$$

A Lagrangian Monte Carlo solution of the above equation solves a stochastically equivalent system that provides the same FMDF. The FMDF is represented by a collection of Monte Carlo elements with attributes ϕ (composition), and $\mathbf{X}(t)$ (position). Displacements of the position vector follow

$$\mathrm{d}\mathbf{X}(t) = D_i(\mathbf{X}(t), t)\mathrm{d}t + E(\mathbf{X}(t), t)\mathrm{d}W_i(t), \tag{14.8}$$

where D_i and E are the drift and diffusion coefficients, respectively, and W_i satisfies a Wiener process. Coefficients D_i and E are obtained by comparing the Fokker–Plank equation corresponding to equation (14.8) with the spatial derivatives in Eq. (14.7).

Scalar composition changes due reaction and mixing in the composition space, represented by the third and fourth terms on rhs of Eq. (14.7), respectively. For the Linear Mean Square Estimation (LMSE) mixing model, the attribute ϕ_α of a Monte Carlo element evolves as

$$\frac{\mathrm{d}\phi_\alpha^n}{\mathrm{d}t} = \omega(\phi) - \Omega_m(\phi_\alpha^n - \tilde{\phi}_\alpha). \tag{14.9}$$

where LMSE model parameter Ω_m is the frequency of mixing within the subgrid. Once the FMDF is found, the mass fraction of species α is evaluated as

$$Y_\alpha(\mathbf{x}, t) = \int \psi_\alpha f(\psi; \mathbf{x}, t)\mathrm{d}\psi.$$

14.3 Numerical Methods and Simulations

Here, we discuss simulations with isotropic, homogeneous turbulence. Solutions are periodic in the three Cartesian coordinates. Uniformly spaced grids with a collocated arrangement was used for all variables. To reduce aliasing error, convection terms in Eq. (14.3) were obtained by taking its skew-symmetric form. All spatial derivatives were obtained using fourth-order, spectral-like, optimized compact differences (Lele 1992). Let f_i be a field variable at grid point i. The derivative f_i' was obtained from the implicit formula

$$\begin{aligned} &\beta f'_{i-2} + \alpha f'_{i-1} + f'_i + \alpha f'_{i+1} + \beta f'_{i+2} \\ &\qquad = a\frac{f_{i+1} - f_{i-1}}{2h} + b\frac{f_{i+2} - f_{i-2}}{4h} + c\frac{f_{i+3} - f_{i-3}}{6h}. \end{aligned} \tag{14.10}$$

Subscripts $i \pm 1$ denote neighboring locations on the grid. Spectral-like resolution was obtained by taking $a = 1.359865$, $b = 0.842596$, $c = 0.0209489$, $\alpha = 0.542341$, and $\beta = 0.069364$. Similarly, secondnd derivatives f_i'' were obtained from the formula

$$\begin{aligned} &\beta f''_{i-2} + \alpha f''_{i-1} + f''_i + \alpha f''_{i+1} + \beta f''_{i+2} \\ &\qquad = a\frac{f_{i+1} - 2f_i + f_{i-1}}{h^2} + b\frac{f_{i+2} - 2f_i + f_{i-2}}{4h^2} + c\frac{f_{i+3} - 2f_i + f_{i-3}}{9h^2}. \end{aligned} \tag{14.11}$$

with $a = 0.3921470$, $b = 1.470843$, $c = 0.097582$, $\alpha = 0.441666$, and $\beta = 0.038620$. The high-resolution filter applied to transported fields as SGS model was obtained from the implicit formula

$$\beta\hat{f}_{i-2} + \alpha\hat{f}_{i-1} + \hat{f}_i + \alpha\hat{f}_{i+1} + \beta\hat{f}_{i+2} = af_i + \frac{b}{2}(f_{i+1} + f_{i-1}) + \frac{c}{2}(f_{i+2} + f_{i-2}) + \frac{d}{2}(f_{i+3} + f_{i-3}) \tag{14.12}$$

with $a = (2 + 3\alpha)/4, b = (9 + 16\alpha + 10\beta)/16, c = (\alpha + 4\beta)/4$, and $d = (6\beta - 1)/16$. Taking $d = 0$ gives a one parameter family of filters. The effect of these choices for spatial operations can be appreciated by examining transfer (filter response) functions $T(k)$. For the first derivative, $T(k) = \tilde{k}(k)/k, (k \neq 0)$, where $\tilde{k}$ is the modified wavenumber and k is the wavenumber. For the second derivative $T(k) = \tilde{k}/k^2, (k \neq 0)$. In Fig. 14.1, all operations have flat transfer functions over a range of small k and then fall off smoothly toward the maximum wavenumber $k_{\max}$ that can be represented on the grid. Of course, $T(k)$ is not *exactly* unity for small k, but the difference is quite small for these schemes. This suffices for the explicit filtering method. Distortion of low wavenumber content by numerical operations is not significant. When the grid spacing is halved, $k_{\max}$ is doubled, and the range of k for which $T(k) \approx 1$ is also doubled. When low-order explicit formulas are used, $T(k)$ does not have a flat portion. Then, when the grid is refined, the distortion at a given low wavenumber reduces and in turn, this can affect the low wavenumber content in the solution. With the present formulas, on grid refinement low wavenumber content changes due to backscatter (decreasingly so), but not due to the discretization. Also, the cutoff wavenumber k_c (the beginning of the fall off) is smaller for the filter compared to those for derivative formulas. These formulas lead to pentadiagonal systems which require endpoint formulas in general. For periodic functions, endpoint formulas are not needed, and the system is solved by Cholesky decomposition.

The numerical scheme is an adaptation for variable density flows of the MAC scheme of Harlow and Welch (1965), and has been presented in detail in Chakravorty and Mathew (2004). It comprises an explicit integration of the momentum equation (14.3) for an intermediate velocity field, which is then corrected by solving a Poisson

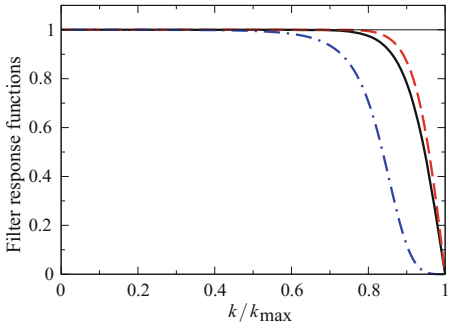

Fig. 14.1 Filtering of formulas. ——: first derivative; – – –: interpolation; – · – · –: explicit filter E

equation that enforces mass conservation (14.2). The energy equation (14.4) was accounted for by rearranging it to obtain $\nabla \cdot \mathbf{u}$ which is needed to advance density as per the continuity equation. The momentum was advanced by using the second-order Adams-Bashforth formula. For the solutions considered here which are periodic in all three directions, the Poisson equation could be solved directly by taking its Fourier transforms and then inverting the solution.

14.3.1 Monte Carlo Method for FMDF

The specific submodels used for the Monte Carlo part were the following. The parameters determining the spatial movement of Monte Carlo elements were E and $\mathbf{D}$. These were determined to be

$$E = \sqrt{\frac{1}{\rho}\frac{2\mu}{\mathrm{ReSc}}}, \qquad \mathbf{D} = \mathbf{u} + \frac{1}{\rho \mathrm{ReSc}}\nabla\mu. \tag{14.13}$$

The evolution of Eq. (14.8) was obtained from

$$\mathbf{X}(t + \Delta t) = \mathbf{X}(t) + \mathbf{D}(t)\Delta t + E(t)\sqrt{\Delta t}\xi(t), \tag{14.14}$$

where ξ are normal random numbers with zero mean and unit variance. The LMSE model for mixing has refinements that are a modification of Curl's model and aging (see Pope 1982, for details).

The FMDF suffices to determine all mass fractions and density/temperature, and the velocity field can be obtained from a standard grid-based solver. Then, the coupling between the flow and scalar fields is through the density. As a stochastic method, density from a Monte Carlo method exhibits significant spatial oscillations which affects the integration of the momentum equation. Colucci et al. (1998) suggests that density/temperature also be evaluated using a grid-based solver. Thus velocity, density and temperature are obtained from the finite difference LES solver and are inputs to the FMDF solver. Interpolation to Monte Carlo element location was by cubic splines. The LES solver accepts the filtered reaction rate from the FMDF solver. Around each finite difference grid points an ensemble domain is constructed. The mean over all Monte Carlo particles within an ensemble domain around each finite difference gridpoint provides the mean reaction rate at that point.

14.3.2 Validation

The finite difference solver was tested by simulating non-reacting, homogeneous, isotropic, decaying, and forced turbulence. DNS of decaying turbulence was

performed for a solution of period 2π on a grid of 64 points in each direction. Initial Reynolds number $\mathrm{Re}_\lambda = 35.4$, based on the turbulence kinetic energy and Taylor scale (0.42). Close quantitative agreement was obtained with the DIA solution of McComb and Shanmugasundaram (1984) of the evolution of turbulence kinetic energy and Taylor Reynolds number, as well as dissipation and skewness compared to other DNS. Details are available in Chakravorty (2010). Next, LES of forced, homogeneous, isotropic turbulence were obtained and compared against DNS. On a grid of 192^3 points on a box of side 2π, a stationary, resolved solution (DNS) was obtained with Taylor Reynolds number of about 80. LES were performed on grids of 32^3, 64^3, and 128^3 points, at four cutoff wavenumbers of the explicit filter $E(\alpha)$, obtained by changing filter parameter α. Figure 14.2 shows mean energy spectra from the LES and DNS, averaged over the duration $t = 15$ to 25. Observe that the LES spectra converge monotonically to the DNS as the grid is refined, by extending the spectral range as smaller scales are represented on the grid. Second, as filter cutoff wavenumber is increased, again there is a monotonic extension of the accurate range of the spectra. The integral length scale was less than one-sixth the period; upto one-third is considered sufficient for correlations to decay.

The FMDF part was examined by simulating mixing of a passive scalar in constant density, forced, homogeneous, isotropic turbulence, and comparing it with DNS and LES with explicit filtering. Since the Schmidt number $Sc = 0.7$, a grid that resolves the flow adequately for a DNS is suitable for scalar mixing. The initial velocity field was an instant from the simulation of forced turbulence mentioned above. The initial scalar field comprises two pairs of alternating slabs normal to one axis with $Z = 0$ and $Z = 1$; a tanh profile provided a smooth variation at slab boundaries. The grid for the DNS had 192^3 points. LES by explicit filtering was on grids of 32^3 and 64^3 points, while the FMDF computation was on the 32^3 grid.

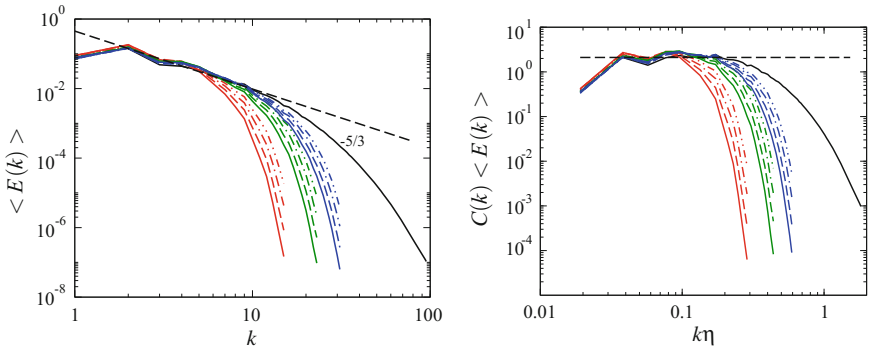

(a) Mean energy spectrum. (b) Kolmogorov-scaled spectrum.

Fig. 14.2 Mean kinetic energy spectrum. Black solid lines: DNS; red: LES-32; green: LES-48; blue: LES-64. ···: $\alpha = 0.6605$; – –:$\alpha = 0.6625$; – · –: $\alpha = 0.6640$; – · · –: $\alpha = 0.6650$. Kolmogorov-scaled compensated spectrum factor $C(k) =< \epsilon >^{-1/4} \nu^{-5/4}(k < \eta >)^{5/3}$; dissipation ϵ, viscosity ν, Kolmogorov length η

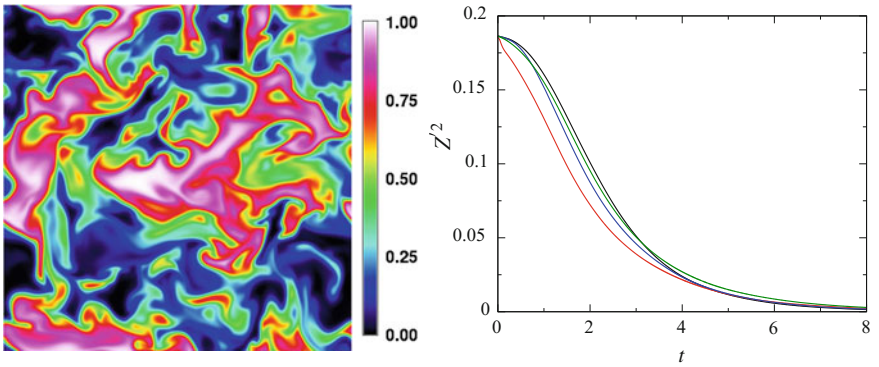

(a) Scalar field, $t = 2$ (b) Scalar variance evolution

Fig. 14.3 Scalar field at an instant and evolution of its variance. Black: DNS; red: LES 32^3 grid points; blue: LES on 64^3 grid; green: FMDF on 32^3 grid

Figure 14.3a is a snapshot of the scalar field from the DNS at $t = 2$ after scalar initialization. In Fig. 14.3b, differences in the scalar variance between LES on 32^3 points and the DNS are noticeable, but the 64^3 solution is much closer. The FMDF solution on 32^3 points is generally closer to the DNS than the 64^3 LES. More significant differences were observed in the evolution of the pdfs of the scalar $f_Z(Z)$. As the scalar slabs mix, the pdf evolves from slightly smeared δ functions at $Z = 0$ and 1, to a Gaussian. In the LES by explicit filtering, the mixing is far too rapid on the 32^3 grid, but improved on the 64^3 grid. The FMDF solution on 32^3 points remains much closer to the DNS. Here, and later, the label LES-EF will stand for LES by explicit filtering.

Qualitative differences can be observed in the evolution of scalar pdfs. The initial pdf has peaks at 0 and 1 due to uniform the scalar layers, with some spreading due to the smooth variation at the layer boundaries. As the field evolves these peaks broaden, disappear and becomes a Gaussian whose variance tends to zero as the scalar field becomes uniform. Figure 14.4a shows pdfs of the scalar at $t = 2$. Due to

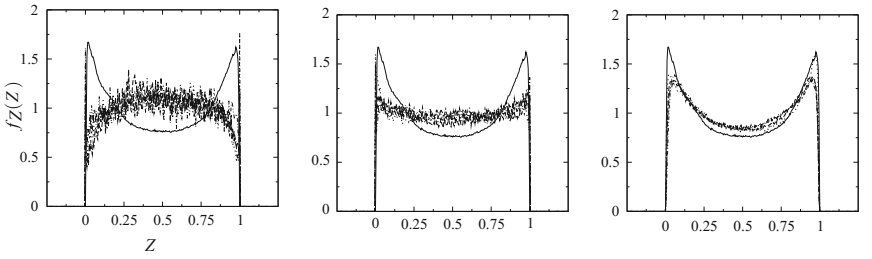

(a) LES-EF, 32^3 (b) LES-EF, 64^3 (c) LES-FMDF, 32^3

Fig. 14.4 Pdf of passive scalar at $t = 2$. Solid curve: DNS; broken curves LES. Data from LES with all four filters listed in Fig. 14.2 included

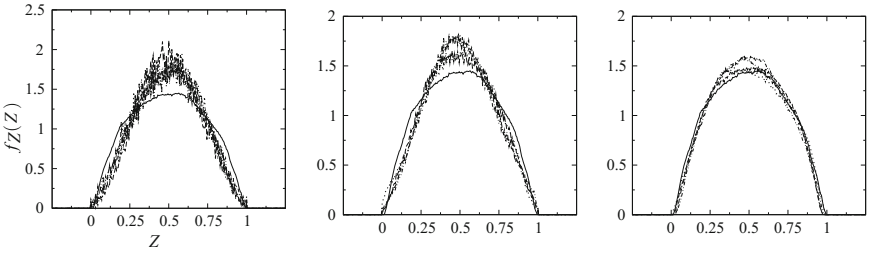

(a) LES-EF, 32^3 (b) LES-EF, 64^3 (c) LES-FMDF, 32^3

Fig. 14.5 Pdf of passive scalar at $t = 3$. Curves as in Fig. 14.4

very rapid initial mixing, on the 32^3 grid with explicit filtering the pdf is nearly uniform by $t = 1.6$ (not shown), and begins the approach to a Gaussian at $t = 2$ (Fig. 14.4b). The evolution is better (slower) on the 64^3 grid. The FMDF method follows the DNS much more closely (Fig. 14.4c). Figure 14.5 shows the pdfs at $t = 3$, when the peaks have disappeared. Between the two LES by explicit filtering, the solution clearly improves with grid refinement. (The pdf with the higher peaks in Fig. 14.5b are with smaller filter cutoff wavenumber.) Clearly, the FMDF solution is much closer to the the DNS. Although the overall evolution of solutions in LES by explicit filtering is not too different from the DNS, the mixing is definitely faster. The mixing improves with grid refinement and, consistently, with increasing filter cutoff. Remarkably, the FMDF solution follows the DNS pdf very closely even on the coarse grid. With these validations of the method, we can turn to reacting flow simulations.

14.4 LES of Nonpremixed Combustion

The initial condition is the same as that set up for the passive scalar mixing problem discussed above. Within the cube there were two pairs of slabs of fuel and oxidizer. The mixture fraction $Z = 1$ over the fuel slabs and zero over the oxidizer slabs. At the interfaces, Z has a sharp tanh profile. A single step, irreversible reaction and the Arrhenius rate equation

$$\omega_F = -\mathrm{Da}\rho^2 Y_F Y_O \exp(-Ze/T)$$

were specified. Heat release rate $H = -\mathrm{Ce}\omega_F$ in the energy Eq. (14.4). Two sets of simulations were performed. Setting the Zeldovich number $\mathrm{Ze} = 8$ allows significant finite-rate effects. For high heat release, Damkohler number $\mathrm{Da} = 100$ and $\mathrm{Ce} = 8$; the mean temperature rises by a factor of 5. For moderate heat release $\mathrm{Da} = 200$ and $\mathrm{Ce} = 4$, and the temperature rise is threefold. These parameters were chosen so that the reaction zone could be adequately resolved in the DNS. Oxidizer/fuel stoichiometric

ratio is one; mixture fraction at the stoichiometric condition is $Z_s = 0.5$. The velocity field and state was determined the conservation Eqs. (14.2), (14.3) and (14.4). All concentrations can be determined from mixture fraction and any one mass fraction; here, fuel mass fraction was chosen. Concentrations were determined from either transport Eq. (14.5) for mixture fraction and fuel mass fraction, or from the FMDF of these two scalars. LES were compared with a DNS on a 192^3 grid. For the Monte Carlo FMDF integration, 2,097,152 elements were taken. On the average, there are 64 elements in a cell of the 32^3 grid, and the minimum at any time does not fall below 32.

Figure 14.6a shows the evolution of the volume-averaged heat release rate over the course of the simulation. Initially, the reaction occurs over small regions at boundaries between layers of fuel and oxidizer where both are present due to the smooth initial conditions. For $t < 2$, although reactants are mixed by the turbulence, there is little reaction till the temperature can rise, and then there is a rapid rise to a maximum before fall off as available reactant levels decrease. Differences between the LES and DNS are always quite small. The explicit filtered solution leads the DNS, with the finer grid being closer. The FMDF solution on the 32^3 has the closest agreement over the entire duration. The distribution of heat release rate over a section (constant x) is shown in Fig. 14.6b. Contours of $Z = 0.5$ (stoichiometric value) are superposed. A close examination reveals that in some regions the contour passes through thin regions of high heat release. But, there are also broad regions of high and low levels of heat release through which the stoichiometric contour passes.

Heat release rate distributions for all three LES at $t \approx 3.4$ when the averaged rate is at a maximum are shown in Fig. 14.7. As can be expected with explicit filtering, structures have finer features as the grid is refined and one may expect these to tend to that found in the DNS. It is quite remarkable that the closer agreement of the FMDF solution should appear to have an even smoother structures than the 32^3 LES-EF.

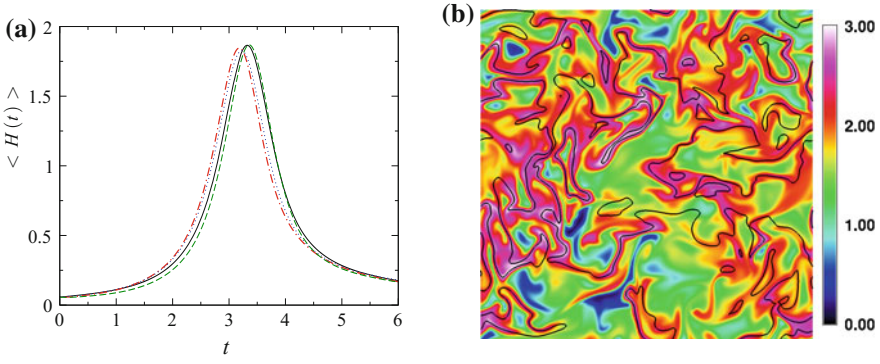

Fig. 14.6 Heat release rate. **a**: evolution of volume-averaged heat release rate. DNS (——), LES-EF 32^3 (– · – · –), LES-EF 64^3 (··· ···), FMDF 32^3 (– – –). **b** distribution at $t = 3.4$ in DNS; black curves are $Z = 0.5$

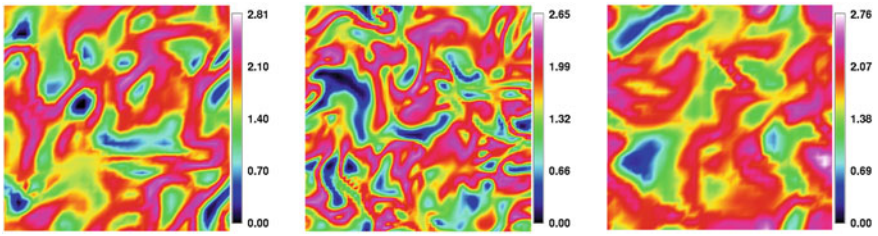

(a) LES-EF, 32^3 (b) LES-EF, 64^3 (c) FMDF, 32^3

Fig. 14.7 Heat release rate distributions at $t \approx 3.4$ (at maximum of average for each simulation)

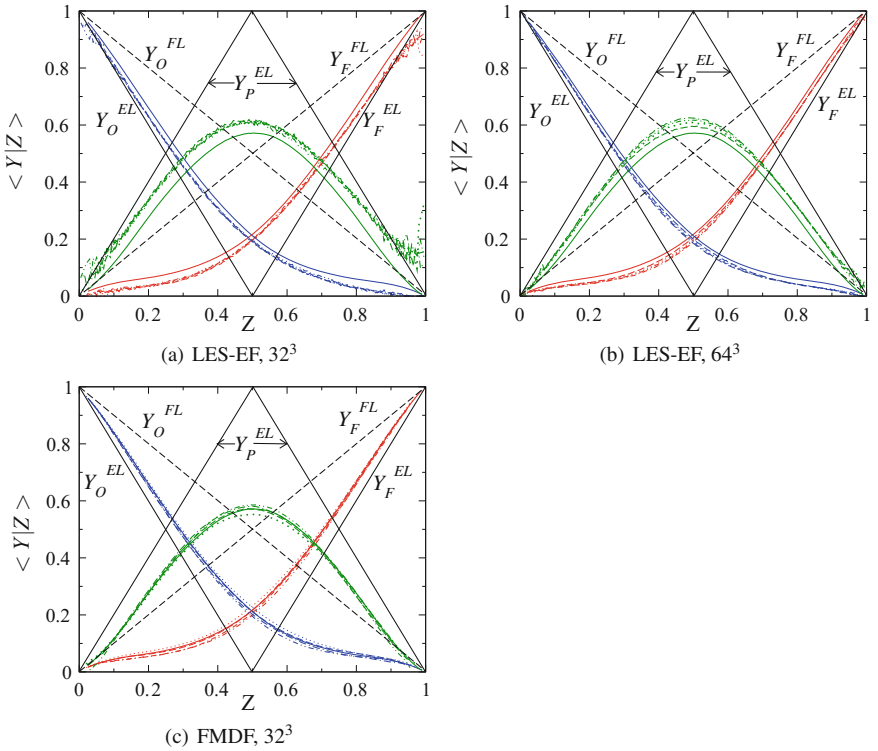

(a) LES-EF, 32^3 (b) LES-EF, 64^3

(c) FMDF, 32^3

Fig. 14.8 Mixture fraction-conditioned mean mass fractions of fuel $< Y_F|Z >$ (red), oxidiser $< Y_O|Z >$ (blue), and product $< Y_P|Z >$ (green). Solid curve: DNS, broken curves LES with all four filters listed in Fig. 14.2 caption. FL: frozen limit; EL: equilibrium limit

A useful global picture of the solutions realized by the different methods can be obtained by examining distributions of mass fractions conditioned on mixture fraction. In Fig. 14.8 the results are plotted along with lines for frozen and equilibrium limits. With explicit filtering, all distributions approach the DNS as the grid is refined. Remarkably, the FMDF agrees very closely with the DNS everywhere.

In each case, simulations with all four filters have been plotted. Only on the 64^3 grid does filter cutoff cause noticeable changes. With explicit filtering alone, there is excessive mixing by the large scales resulting in early, excess product formation. Grid refinement introduces smaller scales which modify the dynamics of large scales and reduce the excessive mixing.

Other analyses are available in Chakravorty (2010). Noting that the reaction rate expression has two factors—product of concentrations $Y_F Y_O$ obtained from the FMDF and $\rho^2 \exp(-Ze/T)$ which is obtained by solving the equations for the flow—the evolution and pdfs of these factors were examined. Even these separate factors follow the DNS when the FMDF solver is used. With explicit filtering the pdf of $Y_F Y_O$ has a smaller mean on the 32^3 grid and converges to the DNS on refinement. The other factor has a larger mean than in the DNS, and changing filter cutoff moves the mean significantly. The results of simulations for the moderate heat release case are qualitatively quite similar.

14.5 Summary

LES accounts for turbulent transport by large-scale motions. In practical combustors, it is now recognized that flame dynamics is affected by these large-scale processes. LES, even with simple models for the momentum transport, can provide better predictions than RANS because of improved predictions of scalar variance—an important input to combustion models. An emerging method for LES of non-reacting flow is the explicit filtering approach. We examined LES obtained by his approach and the FMDF method which accounts for the effects of strongly nonlinear reaction rate terms of finite-rate chemistry. As in other LES of non-reacting flow, the explicit filtering method found solutions that were not too different from DNS ones. Yet, the FMDF solutions, on a small grid, were still closer to the DNS. The agreement is on the overall progress of the reaction, the development of pdfs, on quantities obtained directly from the FMDF (concentrations) as well as those from the finite difference solver, and conditioned means. Thus, all quantities examined exhibit the same solution quality: explicit filtering solutions tend to the DNS with grid refinement from 32^3 to 64^3, but the FMDF solution on the 32^3 grid is always very close to the DNS. Accounting for subgrid fluctuations in computing the large-scale part of the reaction rate term seems to provide an improvement.

The methods for LES of combustion described above are unique in that the explicit filtering approach has been adopted for SGS modeling. A comprehensive summary of transported pdf methods and results for both RANS and LES was provided by Haworth (2010). The results were drawn from an examination of 39 studies of non-premixed, gaseous flames, published during 2000–2009, of which 9 are LES. All the LES used composition pdfs only, while the RANS studies include a few with velocity-composition and velocity-composition-frequency pdfs. All except one of the LES were performed using the Smagorinsky SGS model. An even broader view of the state of turbulent combustion modeling was presented by Pope (2013). Most

current methods were classified as being either flamelet-like or pdf-like, though there are notable exceptions. Unlike RANS/PDF, LES/PDF for reacting flows is less well understood. For example, it seems likely that simple, mixing models may be adequate for LES/PDF, but there have not been a sufficient variety of studies to make such assertions with confidence. A significant difficulty is the much larger computational cost compared to that for RANS/PDF, calling for special algorithms to make these simulations viable. Even among LES methods, costs increase progressively for LES with flamelets, LES/PDF with flamelets to LES with transported pdf (relative cost estimates are provided by Pope (2013)). Judicious choices will be needed for a given problem, especially for industrial applications.

Acknowledgements We acknowledge partial financial support through a grant from DRDO, Govt. of India (No. ERIP/ER/0601095/M/01/909) toward computing facilities and a Project Associateship for Dr. Chakravorty.

References

Chakravorty S (2010) On large eddy simulation of reacting flows using the explicit filtering method with a filtered mass density function. PhD thesis, Department of Aerospace Engineering, Indian Institute of Science

Chakravorty S, Mathew J (2004) A high resolution scheme for low mach number flows. Int J Numer Meth Fluids 46:245

Colucci PJ, Jaberi FA, Givi P, Pope SB (1998) Filtered density function for large eddy simulation of turbulent reacting flows. Phys Fluids 10(2):499

Harlow FH, Welch JE (1965) Numerical calculation of time-dependent viscous incompressible flow if fluid with free surface. Phys Fluids 8(12):2182

Haworth DC (2010) Progress in probability density function methods for turbulent reacting flows. Prog Energy Combust Sci 36(2):168–259. https://doi.org/10.1016/j.pecs.2009.09.003

Jaberi FA, Colucci PJ, James S, Givi P, Pope S (1999) Filtered mass density function for large-eddy simulation of turbulent reacting flows. J Fluid Mech 401:85

Lele SK (1992) Compact finite difference schemes with spectral-like resolution. J Comput Phys 103:16–42

Mathew J (2016) Explicit filtering for large eddy simulation as use of a spectral buffer. arXiv:1610.01738

Mathew J, Lechner R, Foysi H, Sesterhenn J, Friedrich R (2003) An explicit filtering method for large eddy simulation of compressible flows. Phys Fluids 15(8):2279–2289. https://doi.org/10.1063/1.1586271

McComb WD, Shanmugasundaram V (1984) Numerical calculation of decaying isotropic turbulence using the let theory. J Fluid Mech 143:95

Pitsch H (2006) Large-eddy simulation of turbulent combustion. Annu Rev Fluid Mech 38:453–482

Pope SB (1982) An improved turbulent mixing model. Combust Sci Technol 28:131

Pope SB (1990) Computations of turbulent combustion: Progress and challenges. In: Twenty-Third Symposium on Combustion, pp 591–612. https://doi.org/10.1016/S0082-0784(06)80307-3

Pope SB (2013) Small scales, many species and the manifold challenges of turbulent combustion. Proc Combust Inst 34(1):1–31. https://doi.org/10.1016/j.proci.2012.09.009

Sagaut P (2006) Large eddy simulation for incompressible flows, 3rd edn. Springer

Stolz S, Adams NA (1999) An approximate deconvolution procedure for large-eddy simulation. Phys Fluids 11(1999):1699–1701. https://doi.org/10.1063/1.869867

Chapter 15
Theory and Application of Multiple Mapping Conditioning for Turbulent Reactive Flows

Sanjeev Kumar Ghai, Santanu De, Konstantina Vogiatzaki and Matthew J. Cleary

Abstract This chapter presents the basic theory and conceptual evolution of the multiple mapping conditioning (MMC) framework, and presents recent applications for turbulent reactive flows. MMC was initially formulated as a method that integrates the probability density function (PDF) and conditional moment closure (CMC) models through a generalisation of mapping closure. MMC models utilise a *reference space*, whose PDF is prescribed a priori or which is simulated by some means such as a Markov diffusion process. The turbulent fluctuations of all scalars in this method are divided into *major* and *minor* groups, and the former are associated with the reference space via a mapping function. The reference space describes a low-dimensional manifold which can fluctuate in any given way, while the fluctuations of the (real) scalars are fully or partially confined relative to that reference space. The dimensionality of the reference space is usually small. For

Permanent affiliation is the University of Sydney. The contribution of MJC to this chapter was completed while he was a visiting research scholar at Princeton University from August 2017–January 2018.

S. K. Ghai · S. De (✉)
Department of Mechanical Engineering, Indian Institute of Technology Kanpur, Kanpur, India
e-mail: sde@iitk.ac.in

S. K. Ghai
e-mail: snjv@iitk.ac.in

K. Vogiatzaki
School of Computing, Engineering and Mathematics, University of Brighton, Brighton, UK
e-mail: K.Vogiatzaki@brighton.ac.uk

M. J. Cleary
School of Aerospace, Mechanical and Mechatronic Engineering, The University of Sydney, Sydney, Australia
e-mail: m.cleary@sydney.edu.au

M. J. Cleary
Department of Mechanical and Aerospace Engineering, Princeton University, Princeton, USA

© Springer Nature Singapore Pte Ltd. 2018

S. De et al. (eds.), *Modeling and Simulation of Turbulent Combustion*, Energy, Environment, and Sustainability, https://doi.org/10.1007/978-981-10-7410-3_15

example, in non-premixed combustion a reference space emulating the mixture fraction usually suffices. There are both *conditional* and *probabilistic* conceptualisations of MMC and both *deterministic* and *stochastic* mathematical formulations. In the past decade, an extension of probabilistic MMC has emerged that is known as *generalised MMC* that removes some of the formality of the original formulation and extends the type and usage of the reference variables. Generalised MMC is commonly associated, although not exclusively, with large eddy simulations (LES). This chapter reviews the conceptual and theoretical advances in MMC since its original formulation and also reviews some of the recently published applications of MMC in turbulent reactive flows.

Keywords MMC · Reactive flows · RANS · LES · PDF method Mixing model

Nomenclature

r_m	Characteristic scale in physical space
f_m	Characteristic scale in reference space
W_I	Chemical reaction rate
Q_α	Conditional expectation
$\mathbf{U}$	Conditional velocity
D	Diffusion coefficient
B_{kl}	Diffusion coefficient
$d_{x,i}^{p,q}$	Distance between particle in physical space
A_K	Drift coefficient
$\tilde{Z}_{LES}$	Filtered LES mixture fraction
X_I	Mapping function
Z	Mixture fraction
S_I^*	Mixing operator
MW	Molecular weight
n_s	Number of chemical species
n_m	Number of dimensions of manifold
$\mathrm{N_p}$	Number of particles
P_ξ	Pdf of reference space
P	Probability density function (PDF)
$\mathbf{Y}(x, t)$	Reactive scalar space
N_{ij}	Scalar dissipation
Y	Scalar, reactive scalar species mass fraction
T	Temperature
C_{min}	Timescale ratio
v	Velocity vector
w_p	Weight of particle p
w_I^*	Wiener processes

Greek symbols

ρ Density
τ_{min} Minor dissipation timescale
ξ Reference variable
τ_{ϕ} Scalar mixing timescale
ξ'' Subgrid fluctuation

15.1 Introduction

In the past few decades, several turbulent combustion models have been developed and demonstrated for both premixed and non-premixed turbulent flames (Veynante and Vervisch 2002). In most practical combustion systems, these two distinct areas are not encountered and combustion occurs under partially premixed conditions. The probability density function (PDF) method (Pope 1985) is one of the few models which, although initially developed for non-premixed combustion, is general enough in its formulation to be applicable to all combustion regimes (Pei et al. 2015; Brauner et al. 2016; Cao et al. 2007; Lindstedt and Vaos 2006). This is because the reaction rate term appears naturally in closed form, whereas in other combustion models some form of approximation is needed for the average or filtered reaction source. There is a caveat, however. The mixing term in the governing equation for the PDF is unclosed and not all of the mixing models which have been developed are applicable to all combustion regimes. Additionally, a disadvantage of the conventional PDF method is that the cost of computation is relatively large and for realistic systems involving hundreds of species, the application of PDF methods can become impractical. Addressing these issues is a motivation for the ongoing development of the multiple mapping conditioning models (Klimenko and Pope 2003).

Conditional moment closure (CMC) (Klimenko and Bilger 1999) is a well-known turbulent combustion model whereby the reaction rate closure is obtained by formulating the governing equations in terms of the conditional expectations of reactive scalars. In its simplest form, known as first-order CMC, the scalar quantities (species mass fraction and temperature) are assumed to fluctuate jointly with the fluctuation of one key quantity (normally the mixture fraction for non-premixed combustion) and the fluctuations around the conditional means are neglected. This model is computationally efficient relative to the PDF method while it lacks the ability to predict cases where the above assumption is invalid, for example, in partially premixed combustion where parameterisation by the mixture fraction breaks down. To address this extensions have been developed, like conditioning on multiple variables (Kronenburg 2004) or making second-order approximations to the conditional reaction rates (Mastorakos and Bilger 1998),

but these increase complexity by requiring closure of additional terms and they also increase the computational cost.

Since 2003 the multiple mapping conditioning (MMC) framework has emerged (Klimenko and Pope 2003). It may be seen as a logical extension of the conventional PDF method and conditional moment closure (CMC) through the generalisation of the mapping closure concept (Girimaji 1992; Pope 1991). MMC models utilise a *reference space*, whose PDF is either prescribed a priori or which is simulated by some means such as a Markov diffusion process. The turbulent fluctuations of all scalars in this method are divided into *major* and *minor* groups, and the former are associated with the reference space via a mapping function. For model simplicity and computational tractability, the dimensionality of the reference space is usually small. For example, in non-premixed combustion a reference space made of a single variable emulating the mixture fraction usually suffices. The reference space therefore describes a low-dimensional manifold which can fluctuate in any given way, while the fluctuations of the (real) scalars are fully or partially confined relative to that reference space. According to the MMC governing equations, the small-scale (micro) mixing occurs locally in the reference space, and provided that the reference space adequately describes the accessed composition space, the mixing will effectively be local in composition which is a desirable property. There are both *conditional* and *probabilistic* forms of MMC (Klimenko and Pope 2003; Klimenko 2005). The conditional form is associated with either a deterministic or stochastic computational implementation of the model and assumes that the minor scalars can fluctuate only jointly with the major scalars such that their conditional fluctuations are negligibly small. Probabilistic MMC is associated only with the stochastic form and allows the minor scalars to fluctuate relative to the major scalars, although these conditional fluctuations are still expected to be small. In this way, the MMC model becomes a full PDF model with MMC playing the role of a mixing model that is local in a reference space. In the past decade, an extension of probabilistic MMC has emerged that is known as generalised MMC (Klimenko 2005; Cleary and Klimenko 2009; Sundaram et al. 2016). This approach removes some of the formality of original MMC and extends the type and usage of the reference variables to incorporate non-Markov variables and variables that are used for purposes other than localisation of the mixing operation.

MMC adequately integrates the PDF and CMC approaches. It exploits the advantages of both the methods and reduces some of their complications. As a result, it is proving useful for modelling various combustion regimes including non-premixed atmospheric (Devaud et al. 2013; Ge et al. 2013; Straub et al. 2016; Varna et al. 2017; Vogiatzaki et al. 2011, 2015; Wandel and Lindstedt 2013) and high pressure engine-like conditions (Salehi et al. 2017), premixed combustion (Sundaram and Klimenko 2017), partially premixed combustion (Galindo et al. 2017) and aerosol nucleation (Neuber et al. 2017; Vo et al. 2017). This book chapter presents a review of MMC and the evolution in its conceptualisation. In the subsequent sections, a description of the basic concepts and theory will be presented including its different formulations. Results from the recent literature are reviewed. At the end of this chapter, conclusions are drawn. This work may be read

in conjunction with book chapter by Cleary and Klimenko (2011), in which case Sect. 15.2 of the present work may be skipped over, whereas the reviewed applications in Sect. 15.3 contain new research conducted since the earlier book chapter was published. The model derivations are not included here, and readers are directed towards the original publications, especially, those by Klimenko and co-workers (Klimenko and Pope 2003; Sundaram et al. 2016; Klimenko 2005, 2007, 2009a, b; Klimenko and Cleary 2010), if details of the derivations are sought after.

15.2 Concepts and Theory

In this section, we present the concepts underpinning MMC, starting with the governing equations for scalar transport and their joint PDF. We then introduce the idea of a reference space and review the mapping closure concept, which together provides closures to the MMC governing equations which are subsequently presented in both their deterministic and stochastic forms. Finally, the concepts and theory of generalised MMC are explored.

15.2.1 Scalar Transport Equations the MMC Concept

The transport equation for the n_s-dimensional reacting scalar space $Y(x,t) = (Y_1, Y_2, \ldots, Y_I, \ldots, Y_{n_s})$ is given by

$$\frac{\partial \rho Y_I}{\partial t} + \nabla.(\rho v Y_I) - \nabla.(\rho D \nabla Y_I) = w_I, \tag{15.1}$$

where $v = v(x,t)$ is the fluid velocity, D is the diffusion coefficient which for our present purposes is assumed to be equal for all species, ρ is the density, and w_I is the rate of production of species I. Both ρ and w_I are usually known functions of species mass fractions, Y_I, temperature (or enthalpy) and pressure.

In a turbulent flow, the stochastic distribution of the composition can be given by the one-time, one-point Favre joint PDF, $P_Y(y;x,t)$. In the limit of high Reynolds number, the PDF transport equation is

$$\frac{\partial \bar{\rho} P_Y}{\partial t} + \nabla.(\bar{\rho} u P_Y) + \frac{\partial W_I \bar{\rho} P_Y}{\partial y_I} + \frac{\partial^2 N_{IJ} \bar{\rho} P_Y}{\partial y_I y_J} = 0, \tag{15.2}$$

where the conditional expectations of velocity, production term, scalar dissipation and density are

$$u(y;x,t) \equiv \langle \rho v | Y = y \rangle / \rho_Y \tag{15.3}$$

$$W_I(y;x,t) \equiv \langle \rho w_I | Y = y \rangle / \rho_Y \tag{15.4}$$

$$N_{IJ}(y;x,t) \equiv \langle \rho D \frac{\partial Y_I}{\partial x_k} \frac{\partial Y_J}{\partial x_l} | Y = y \rangle / \rho_Y \tag{15.5}$$

and

$$\rho_Y(y;x,t) \equiv \langle \rho | Y = y \rangle \tag{15.6}$$

Here, the upper case subscripts *I, J,* and *K* run over n_s species and the lower case subscripts run over the orthogonal spatial dimensions. The lower case vector $\boldsymbol{y}$ is the sample space for $\boldsymbol{Y}$.

The above PDF is defined for the n_s-dimensional composition space, but in MMC the range of turbulent fluctuations is confined (fully or partially, depending on the interpretation of MMC that is taken) to a reduced n_m-dimensional manifold where $n_m < n_s$ corresponds to number of major species who subset is denoted $\boldsymbol{Y}^m$. The remaining subset of size $n_\alpha = n_s - n_m$ is referred to as the set of minor species denoted $\boldsymbol{Y}^\alpha$. Lower case Roman and Greek symbols are used to denote members of the major and minor species subsets, respectively. Major species are permitted to fluctuate in any physically realisable way, while the minor species are either (i) assumed to fluctuate jointly with the major species so that conditional fluctuations $\langle Y'_\alpha | Y^m = y^m \rangle = 0$, or (ii) have finite but (usually) small conditional fluctuations. In either interpretation the reduced PDF of the major species should satisfy the equation

$$\frac{\partial \bar{\rho} P_{Y_m}}{\partial t} + \nabla.(\bar{\rho} u P_{Y_m}) + \frac{\partial W_i \bar{\rho} P_{Y_m}}{\partial y_i} + \frac{\partial^2 N_{ij} \bar{\rho} P_{Y_m}}{\partial y_i y_j} = 0 \tag{15.7}$$

In the former interpretation, which is known as conditional MMC, the minor species are fully described by their conditional expectations $Q_\alpha(y^m;x,t) = \langle Y_\alpha | Y^m = y^m \rangle$ satisfying

$$\frac{\partial Q_\alpha}{\partial t} + u \nabla Q_\alpha + W_i \frac{\partial Q_\alpha}{\partial y_i} - N_{ij} \frac{\partial^2 Q_\alpha}{\partial y_i y_j} = W_\alpha \tag{15.8}$$

The full PDF is then approximated as

$$P_Y = P_{Y_m}.\delta(Q - y^\alpha) \tag{15.9}$$

In the latter interpretation, which is known as probabilistic MMC, the minor species fluctuations are not formally neglected but advantage is taken of the greater accuracy and lower computational cost that is afforded in the modelling by keeping the fluctuations of the minor species close to those of the major species.

The selection of the major species is nearly always case dependent. If the wrong or too few major species are chosen then the assumption that the conditional fluctuations of the minor species are small may be invalidated. If too many major species are chosen then the computational cost may be high. A broad definition is given to what may constitute a major species. It may be one of the key chemical species such as a product gas like carbon dioxide, or it may be a derived quantity like the mixture fraction which is useful in non-premixed combustion, the reaction progress variable which may be useful in premixed combustion or, even, combinations of the above and scalar dissipation which may be useful in partially premixed combustion (Kronenburg and Cleary 2008).

15.2.2 Reference Variables and Mapping Closure

Equations (15.7) and (15.8) contain conditional velocity $\boldsymbol{u}$ and the conditional scalar dissipation N_{ij} which are unclosed. The closure is achieved in MMC through the use of a reference space. Although the utilisation of a reference space is not a new idea in turbulent combustion modelling (Girimaji 1992, 1993; Pope 1991; Chen et al. 1989), MMC takes it a step further generalising the concept for both homogeneous and inhomogeneous flow conditions. In the original version of MMC formulated by Klimenko and Pope (2003), the reference space is linked to the major scalar space although it is stochastically independent of it to satisfy the independence and linearity principles, that is, required of good PDF mixing models (Subramaniam and Pope 1998). Generalised MMC (Klimenko 2005; Cleary and Klimenko 2009; Sundaram et al. 2016) broadens the concept further and allows additional reference variables that may be separate from the major species space but are useful quantities for emulating the turbulent distributions of the reactive scalars.

Mapping functions, $X_I(\boldsymbol{\xi}; x, t)$, provide a one-to-one transformation between the reference space, $\boldsymbol{\xi} = \left(\xi_1, \xi_2, \ldots, \xi_k, \ldots, \xi_{n_r}\right)$, and the reactive scalars, Y_I. Since mapping functions are the function of stochastic variables they are stochastic quantities themselves. They are characterised by a probability density function, P_X, which is a model for P_Y. The advantage is that, unlike the unclosed transport equation for P_Y given by Eq. (15.2), the transport equation for P_X is in closed form due to the known PDF of the reference space, P_ξ. This is the essence of mapping closure. P_ξ is known either because it is prescribed as in the original derivation of Klimenko and Pope (2003) or simulated independently of $\boldsymbol{Y}$ (Cleary and Klimenko 2009; Varna et al. 2017; Wandel and Lindstedt 2009).

Mapping functions are non-decreasing functions of their arguments at any given time. The general concept of a mapping function is explained by Vogiatzaki (2010) for a single reference variable, ξ, emulating a single major scalar, $Y = Z$ (i.e. the mixture fraction) in a non-premixed jet flame. Figure 15.1a shows the mapping functions (solid lines) in reference space, along with the standard Gaussian PDF of the reference space, P_ξ (dashed line). The black, green and red lines describe the evolution of mapping functions in reference space for rich, lean and shear layer

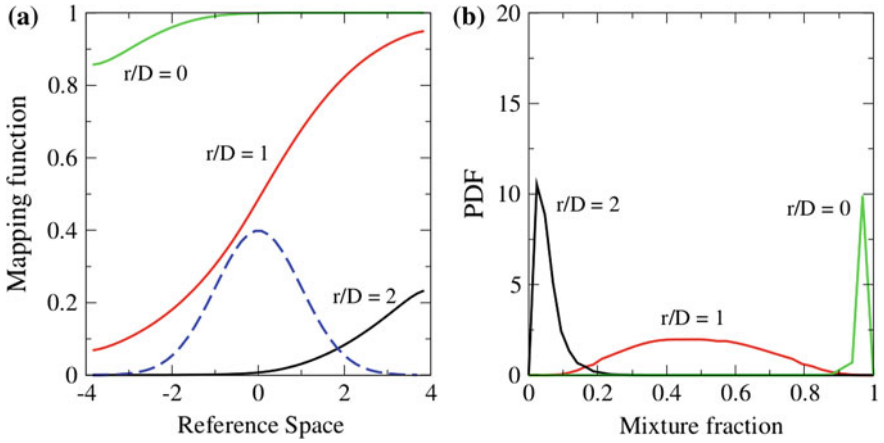

Fig. 15.1 **a** Mapping functions (solid lines) at different radial locations and the (static) reference variable Gaussian distribution (dashed line) over reference space. **b** Corresponding PDF's of mixture. Figure is from Vogiatzaki (2010)

regions, respectively. Figure 15.1b presents the corresponding mixture fraction PDFs, P_Z. In MMC, for each physical location, a mapping function is calculated that has as input the reference space and as output the range of the expected values of the species under consideration. Knowing both the reference space PDF and the values of the mapping function, the PDF of the physical scalar can then be calculated according to the mapping closure methodology.

15.2.3 Deterministic MMC

The deterministic form of the transport equation for the temporal and spatial evolution of the mapping functions $X_I(\boldsymbol{\xi}; x, t)$ is (Klimenko and Pope 2003)

$$\frac{\partial X_I}{\partial t} + U.\nabla X_I + A_k \frac{\partial X_I}{\partial \xi_k} - B_{kl} \frac{\partial^2 X_I}{\partial \xi_k \xi_l} = W_I, \tag{15.10}$$

where the subscript I represents all scalars (both major and minor) while k and l represent the major scalars only. This deterministic version of the model equations is associated only with the conditional perspective of MMC.

The above equation introduces the conditional (on reference space) velocity $U(\boldsymbol{\xi}; x, t)$, a drift coefficient $A_k(\boldsymbol{\xi}; x, t)$, a diffusion coefficient $B_{kl}(\boldsymbol{\xi}; x, t)$ and the conditional reaction rate $W_I = W_I(X(\boldsymbol{\xi}))$. The adjoint transport equation with the one-point, one-time joint PDF of the stochastic reference field is given by

$$\frac{\partial \bar{\rho} P_{\xi}}{\partial t} + \nabla.(\bar{\rho} U P_{\xi}) + \frac{\partial A_k \bar{\rho} P_{\xi}}{\partial \xi_k} + \frac{\partial^2 B_{kl} \bar{\rho} P_{\xi}}{\partial \xi_k \xi_l} = 0 \tag{15.11}$$

Equations (15.10) and (15.11) combined are formulated for compliance of the MMC model with Eq. (15.8) for the marginal PDF of the major species and Eq. (15.9) for the conditional expectation of minor species. A detailed examination of this compliance may be found in Klimenko and Pope (2003). Depending on the number of reference variables (for the present this is equal to the number of major scalars), MMC can be construed as a PDF or a CMC model. If $n_r = n_s$, then MMC becomes a complete joint PDF model; if $n_r < n_s$ then we have only n_r independent scalars whose evolution maps to the n_r-dimensional marginal PDF of the major scalars, while the remaining $n_s - n_r$ minor scalars are the dependent variables which are tackled through conditioning methods. It is, however, important to note that a single transport equation, Eq. (15.10), exists for all species, both major and minor. In deterministic MMC, the computational cost is directly linked to the number of reference variables. When a single reference variable such as mixture fraction is used, MMC is similar to first-order CMC although, as demonstrated below, it has a closed-form model for conditional scalar dissipation rate and the PDF of the mixture may be derived from the simulations rather than being an input quantity as it is in CMC. Likewise, the computational cost of MMC with a single reference variable will be comparable to that of first-order CMC. Moreover, by virtue of being expressed as a function of the independent joint Gaussian reference space, the deterministic MMC formulation presented above is valid for any number of reference variables, whereas specific CMC models need to be formulated as additional conditioning variables are added.

The coefficients U, A_k and B_{kl} are now described. They have to be specified consistently with the transport equation for P_{ξ}. Although other formulations are possible, we limit ourselves here to the version described in Klimenko and Pope (2003) corresponding to a jointly standard Gaussian distribution for P_{ξ} with zero mean and unity variance:

$$P_{\xi}(\boldsymbol{\xi}) = G(\xi_1) G(\xi_2) G(\xi_3) \ldots G\left(\xi_{n_r}\right), \tag{15.12}$$

$$G(\xi_k) = \frac{1}{\sqrt{2\pi}} exp\left(- \frac{\xi_k^2}{2} \right). \tag{15.13}$$

This distribution complies with Eq. (15.11) provided that (Klimenko and Pope 2003)

$$U(\boldsymbol{\xi}; x, t) = U^{(0)} + U_k^{(1)} \xi_k, \tag{15.14}$$

$$A_k(\boldsymbol{\xi}; x, t) = - \frac{\partial B_{kl}}{\partial \xi_l} + B_{kl} \xi_l + \frac{1}{\bar{\rho}} \nabla. \left(\bar{\rho} U_k^{(1)} \right). \tag{15.15}$$

The conditional velocity is linearly dependent on the reference space which is a common practice in conditional moment methods (Klimenko and Bilger 1999). Following mapping, closure convention B_{kl} is modelled independent of $\boldsymbol{\xi}$ leading to

$$U^{(0)} = \tilde{v} \tag{15.16}$$

$$U_k^{(1)} \langle \xi_k X_i \rangle = \widetilde{v' Y_i'} \tag{15.17}$$

$$B_{kl}(x,t) \langle \frac{\partial X_i}{\partial \xi_k} \frac{\partial X_j}{\partial \xi_k} \rangle = \tilde{N}_{ij}. \tag{15.18}$$

The quantities in angular brackets are average values obtained by convolution with P_ξ and $\tilde{N}_{ij}$ is the unconditional Favre-averaged scalar dissipation. Herein is the biggest advantage of using the mapping closure concept. Equations (15.16)–(15.18) show that the turbulence-chemistry interactions are closed using unconditional Favre-averaged quantities whereas external models for the conditional quantities are conventionally required to close the transport equation for the joint PDF and CMC.

15.2.4 Stochastic MMC

The solution to the Eq. (15.10) through a finite difference method, while practical for $n_r \sim 1$ (Devaud et al. 2013; Vogiatzaki et al. 2009), becomes computationally expensive for $n_r \gg 1$. The stochastic form of MMC can be derived based on the use of Lagrangian notional particles (Klimenko and Pope 2003):

$$dx^* = U\left(\boldsymbol{\xi}^*, x^*, t\right) dt, \tag{15.19}$$

$$d\xi_k^* = A_k^0\left(\boldsymbol{\xi}^*, x^*, t\right) + b_{kl}\left(\boldsymbol{\xi}^*, x^*, t\right) d\omega_l^*, \tag{15.20}$$

$$dX_I^* = \left(W_I^* + S_I^*\right) dt, \tag{15.21}$$

$$\langle S_I^* | \boldsymbol{\xi}^* = \boldsymbol{\xi}, x^* = x \rangle = 0. \tag{15.22}$$

In the above set of equations,

$$A_k^0 = A_k + \frac{2}{\tilde{P}_\xi} \frac{\partial B_{kl} P_\xi}{\partial \xi_l}, \tag{15.23}$$

$$b_{kl} b_{li} = 2B_{kl}. \tag{15.24}$$

Stochastic quantities that are associated with the evolution of notional particles are denoted by the asterisks. Equation (15.19) accounts for the transport in physical space, where the location of the particle is represented by x^* and $d\omega_i^*$ is the

increment of a Wiener process with zero mean and variance equal to dt. Equations (15.20) and (15.21) govern the transport in the reference space and composition space, respectively. W_I^* is the chemical source term and S_I^* is a mixing operator which simulates the conditional scalar dissipation. As stated in Eq. (15.22), the application of mixing does not alter the conditional expectations. The purpose of S_I^* is to keep the values of X_I^* close to its conditional mean value $\bar{X}_I^* = \langle X_I^* | \boldsymbol{\xi}^* = \boldsymbol{\xi}, x^* = x \rangle$. It is specific to MMC and ensures that mixing is local in both reference and physical spaces. It controls the dissipation of minor fluctuations and for this reason, may be referred to as the minor mixing operator (Sundaram et al. 2016). The dissipation of major fluctuations is simulated through Eq. (15.20) that is closed with Eqs. (15.23) and (15.24) which are linked to Favre mean quantities via Eq. (15.18). Under the conditional MMC perspective, fluctuations of X_I^* relative to $\bar{X}_I^*$ are constrained as much as possible and are treated as stochastic error whose impact on the conditional means diminishes with increasing number of notional particles. Under the conditional perspective, the stochastic formulation is equivalent to the deterministic formulation. The alternative probabilistic perspective treats the fluctuations as modelling quantities that allow P_X obtained by a solution to Eqs. (15.19)–(15.22) to emulate P_Y, even if the number of reference scalars is small. This latter view is especially relevant to the generalised form of MMC discussed below.

Mixing models are needed for the mixing operator, S_I^*. Since it controls only the minor fluctuations the choice of mixing model is not expected to have a significant impact on the results. Here, we present the modified Curl's model (Janicka et al. 1979) version of the minor mixing operator which has been most commonly used in practical stochastic MMC simulations. An overview of other mixing models may be found in Celis and da Silva (2015). The MMC-Curl mixing operator which involves an interaction between particles grouped into pairs (denoted by p and q) that are local in reference space and mixed over a time step duration of Δt (Straub et al. 2016):

$$X^{*,p}(t+\Delta t) = X^{*,p}(t) + \lambda\left(X^{p,q}(t) - X^{*,p}(t)\right)\frac{\Delta t}{\tau_\phi} \tag{15.25}$$

$$X^{*,q}(t+\Delta t) = X^{*,q}(t) + \lambda\left(X^{p,q}(t) - X^{*,q}(t)\right)\frac{\Delta t}{\tau_\phi} \tag{15.26}$$

In the above, $\lambda = 1 - exp\left[-\frac{w_p + w_q}{W}\frac{N}{2}\right] \approx \frac{w_p + w_q}{W}\frac{N}{2}$ where w_p, w_q and W are the weights of particles p and q and their sum, respectively. The number of particles per CFD cell is N. The quantity τ_ϕ is the scalar mixing timescale as found in conventional PDF methods (Pope 1985) and is here termed as the major dissipation timescale. As already stated, the particle pairs in MMC are not randomly selected but rather are selected such that they are local to each other in reference space. Therefore, all particles at a location (typically within one CFD cell) are sorted by their reference value and stored in an array. Two neighbouring particles within this

array are selected as a pair to be mixed. This mixing rule ensures localness in composition space. The mixing operator for the selected particle pair can now be written as

$$S_I^* = \frac{dX^{*,k}}{dt} \approx \lambda \frac{X^{p,q} - X^{*,k}}{\tau_{min}} \tag{15.27}$$

The minor mixing timescale, τ_{min}, controls the conditional fluctuations of scalars around the conditional mean. The timescales have the following relation

$$\tau_{min} = C_{min}.\tau_\phi \tag{15.28}$$

Wandel and Klimenko (2005) used the DNS study of Mitarai et al. (2003) for a homogeneous turbulent reacting flow with one-step irreversible chemistry to demonstrate how the ratio of the minor to major dissipation timescales controls the conditional fluctuations. A ratio of $O(100)$ yields rapid dissipation of the minor fluctuations and the model closely resembles first-order CMC. A ratio of 8 was identified to produce the correct level of conditional fluctuations in their homogeneous turbulence test case and recently Straub et al. (2016) corroborated that finding against data for the Sandia D–F laboratory flame series.

15.2.5 Generalised MMC

The term *generalised MMC* was first coined by Klimenko (2005) to name a form of MMC which relaxed some of the strictness implied by the original MMC model derived by Klimenko and Pope (2003), in particular by the dividing reference space into conditioning variables and non-conditioning variables. Conditioning reference variables emulate certain Lagrangian characteristics of turbulent flows and are used to localise the mixing in the space of the major species manifold. Non-conditioning reference variables assist the emulation of the turbulent quantities but are not used for localisation of mixing. Conditioning variables localise the mixing and imply a significant computational cost, whereas non-conditioning variables assist the simulations only and do not imply a major additional burden. As examples of generalised MMC, Klimenko (2005) suggested: (i) MMC with multiple dissipation-like non-conditioning variables whose purpose is to emulate a stochastic MMC diffusion coefficient, B_{kl}; (ii) MMC with velocity-like non-conditioning variables; and (iii) MMC with mixture fraction and dissipation-like reference variables obtained with the help of LES of the flow field.

Cleary and Kronenburg incorporated multiple dissipation-like reference variables in the deterministic context (Cleary and Kronenburg 2007). However, by its nature, the deterministic form of MMC implies conditioning must occur on all reference variables and that many dissipation-like variables were required to

emulate the spectrum of its fluctuations effectively at substantial computational cost. Generalised MMC is, therefore, best implemented in stochastic form.

Wandel and Lindstedt have developed and validated generalised MMC with velocity-like reference variables obtained from a stochastic binomial Langevin simulation (Wandel and Lindstedt 2013; Wandel and Lindstedt 2009; Wandel 2013). A comprehensive comparison of results for a turbulent mixing layer (Wandel and Lindstedt 2009) and the Sandia Flame E (Wandel and Lindstedt 2013) indicate good performance of the model.

Klimenko's initial model for MMC in the context of LES involved a single conditioning reference variable $\xi = \bar{\xi} + \xi''$, which emulates the stochastic mixture fraction, Z. Here $\bar{\xi} = \tilde{Z}_{LES}$ is the filtered LES mixture fraction field and ξ'' emulates the subfilter fluctuations of that mixture fraction that are modelled using multiple non-conditioning dissipation-like reference variables (similar to option (i) introduced above). This MMC-LES model would be suitable for a conventional stochastic Monte Carlo simulation, where there are many notional particles in each LES grid cell. Such an approach would come at a very large computational cost. An alternative much lower cost method based on a sparse stochastic implementation was subsequently developed (Cleary and Klimenko 2009, 2011; Cleary et al. 2009; Vo et al. 2017). In sparse methods, the number of notional particles to simulate the reacting scalar field is less than the number grid cells for the LES simulation of the flow field. At the larger scale separating mixing particles, the subgrid fluctuations ξ'' now play only a minor role and can be neglected. The model formulation remains much the same as Eqs. (15.19)–(15.22), except that Eq. (15.20) is replaced by.

$$d\xi_k^* = d\tilde{Z}_{LES}^* \tag{15.29}$$

For the mixing operation particles mix in pairs that are selected according to a minimisation of the square distance in an extended space comprised of ξ and x:

$$\hat{d}_{p,q}^2 = \sum_{i=1}^{3} \left(\sqrt{3} \frac{d_{x,i}^{p,q}}{r_m} \right) + \left(\frac{d_f^{p,q}}{f_m} \right) \tag{15.30}$$

Here, $d_{x,i}^{p,q}$ and $d_f^{p,q}$ are the distance between mixing particles in physical space and reference mixture fraction space, respectively, and r_m and f_m are characteristic scales in those spaces.

The advent of sparse methods and the use of non-Markov reference variables (i.e. in sparse MMC-LES the traced filtered mixture fraction from the LES replaces the stochastically modelled reference variable) has resulted in an extended interpretation of what constitutes generalised MMC. Here, we repeat verbatim the statements made in Cleary and Klimenko (2011):

The following three points summarise the essential features of a good generalised MMC model:

- *The conditioning reference variables should emulate as closely as possible the Lagrangian properties of the key major species to ensure accurate evaluation of conditional species expectations without compromising the independence of the reference space. This can be done with the assistance of non-conditioning reference variables.*
- *The surrogate mixing operator, S_I, should set the dissipation of minor fluctuations to correspond to the dissipation of physical conditional fluctuations. (Due to the independence of reference and composition scalar fields, minor fluctuations and conditional fluctuations are not the same thing but they are linked).*
- *The conditioning reference variables should be selected so that minor fluctuations are not too large. This ensures that scalar dissipation is predominantly modelled by diffusion in reference space (here, Eq. (15.20) or its replacement Eq. (15.29)) rather than by the surrogate mixing operator, S_I.*

Also to this effect, Sundaram et al. (2016) have list five propositions on the nature of generalised MMC.

15.3 Applications of MMC

Different versions of MMC have been used to simulate conditions ranging from non-premixed to premixed (including partially premixed) combustion regimes within the context of RANS and LES. In these models, a reference variable is used to imitate mixture fraction and/or progress variable. In deterministic MMC models, additional reference variables are used to imitate scalar dissipation and/or sensible enthalpy. A few examples, focusing particularly on the more recent cases, are reviewed in this section.

15.3.1 Deterministic MMC Applications

In deriving MMC for the first time Klimenko and Pope (2003) validated the deterministic version of the model against DNS data for the three stream mixing problem. Kronenburg and Cleary examined MMC for DNS cases of homogeneous, isotropic decaying turbulence using multiple reference variables (Kronenburg and Cleary (2008), Cleary and Kronenburg (2007a, b)); namely mixture fraction, normalised sensible enthalpy and scalar dissipation. The transient flame-phenomena, such as, extinction and reignition are captured to some extent. The first application of the deterministic MMC approach to laboratory jet diffusion flames with complex hydrocarbon chemistry is reported in Vogiatzaki et al. (2009a, b). A single reference variable was used to emulate the mixture fraction, and very good agreement with the experimental data may be observed. The most recent application of deterministic MMC is by Devaud et al. (2013) who implemented it into an LES

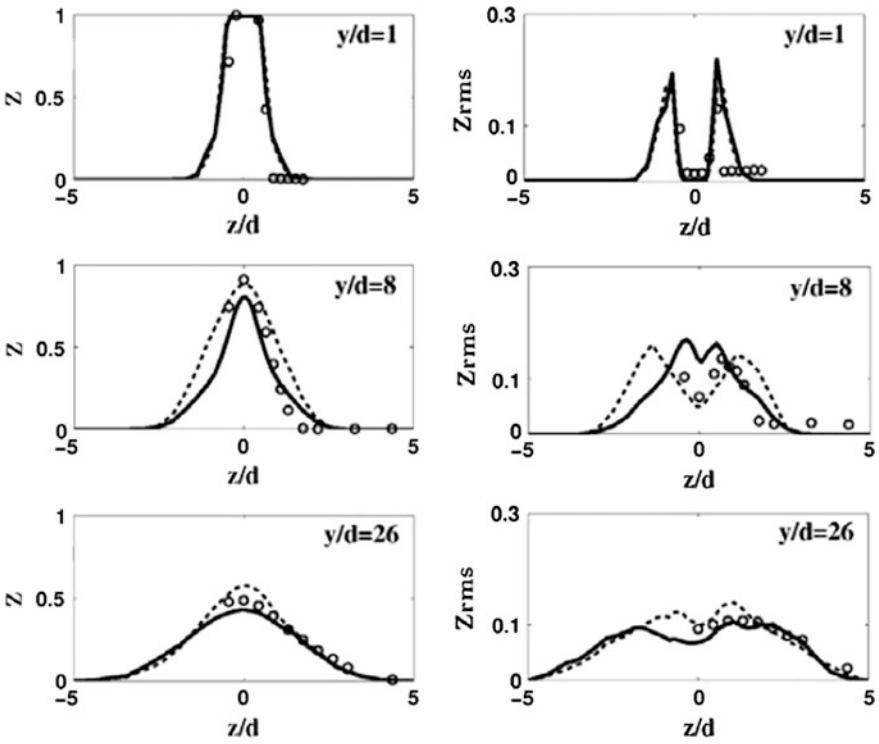

Fig. 15.2 Radial profile of mean mixture fraction and rms. Symbol represents experimental data, dashed lines LES solution and solid lines corresponds to MMC. Figure is from Devaud et al. (2013)

code to simulate a lifted jet diffusion flame in a vitiated coflow. They also used a single reference variable to emulate the subfilter distribution of mixture fraction. Figure 15.2 shows the time-averaged radial profiles of mixture fraction and its rms. There is overall good agreement with the experimental data.

15.3.2 Stochastic MMC Applications

As already mentioned, the first implementation of stochastic MMC was done by Wandel and Klimenko (2005) who validated it against the DNS data of Mitarai et al. (2003) for a homogeneous turbulent reacting flow with one-step irreversible chemistry. The first application to jet diffusion flames is reported in Vogiatzaki et al. (2011). The flame under consideration was the well-known Sandia flame D. In their formulation, they employed a single Markov reference variable mapped to the mixture fraction. Micro-mixing involved the interaction by exchange with the mean

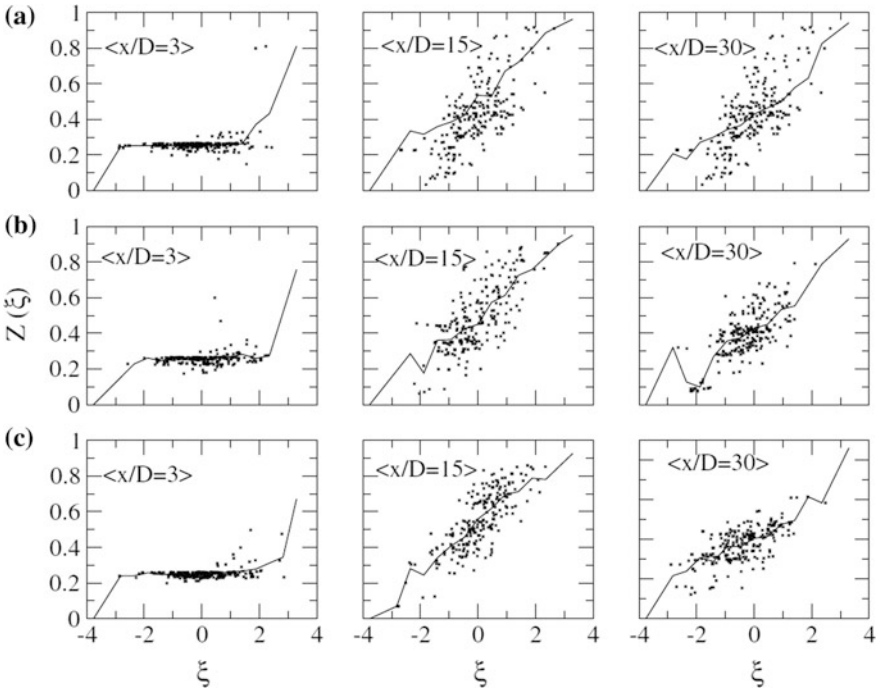

Fig. 15.3 Profiles of the mixture fraction at various axial locations over the reference space. **a** First row $\tau_{min} = \tau_D$ **b** Middle row $\tau_{min} = 0.7\tau_D$ **c** Bottom row $\tau_{min} = 0.5\tau_D$. Figure is from Vogiatzaki et al. (2011)

(IEM) mixing model (Dopazo and Obrien 1974). An additional minor dissipation timescale ($\tau_{\min}$) has been introduced within the MMC formulation that controls the fluctuations of the scalars around the conditional mean. Figure 15.3 shows the mixture fraction profiles in the reference space at different axial locations for three different minor timescales $\tau_{min} = \tau_D, 0.7\tau_D$ and $0.5\tau_D$, where τ_D is the physical dissipation timescale. It is evident that conditional fluctuations decrease with a decrease in the minor timescale. A similar observation can also be made for the reactive scalars, such as temperature and species mass fractions that are shown in Fig. 15.4. The MMC results with the three different values of τ_{min} are also compared with results from a conventional PDF-IEM simulations (i.e. without localisation of mixing in a reference space and, importantly, without the additional controlling parameter τ_{min}). While the MMC with $\tau_{min} = \tau_D$ produces reasonably accurate scatter plots the conventional PDF-IEM yields only very low levels of conditional fluctuations.

Subsequently, Vogiatzaki et al. (2015) investigated the sensitivity of stochastic MMC to different numbers of notional particles per grid cell and to different micro-mixing models. They tested $N_p =$ 20, 50 and 100 and both Curl's and IEM variants of MMC in RANS of Sandia Flame F. Figures 15.5 and 15.6 show scatter

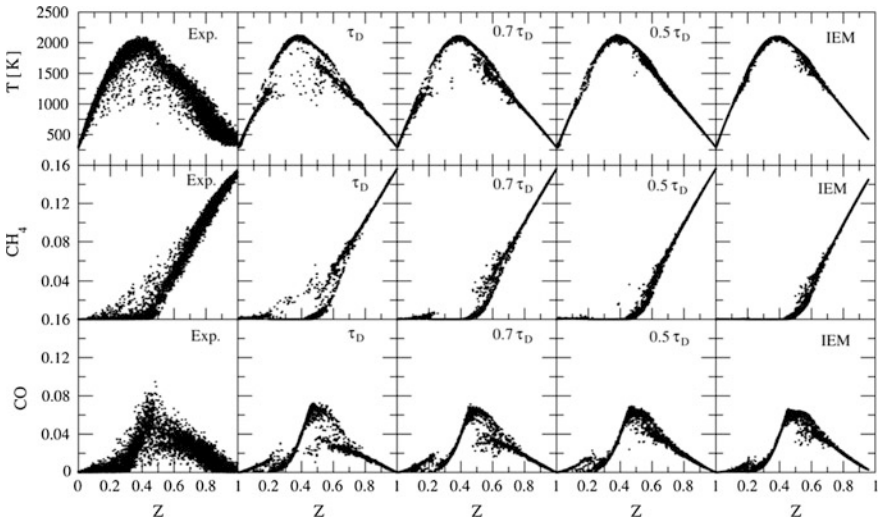

Fig. 15.4 Scatter plots of temperature, mixture fractions of CH_4, CO over the mixture fraction space at $x/D = 15$. Figure is from Vogiatzaki et al. (2011)

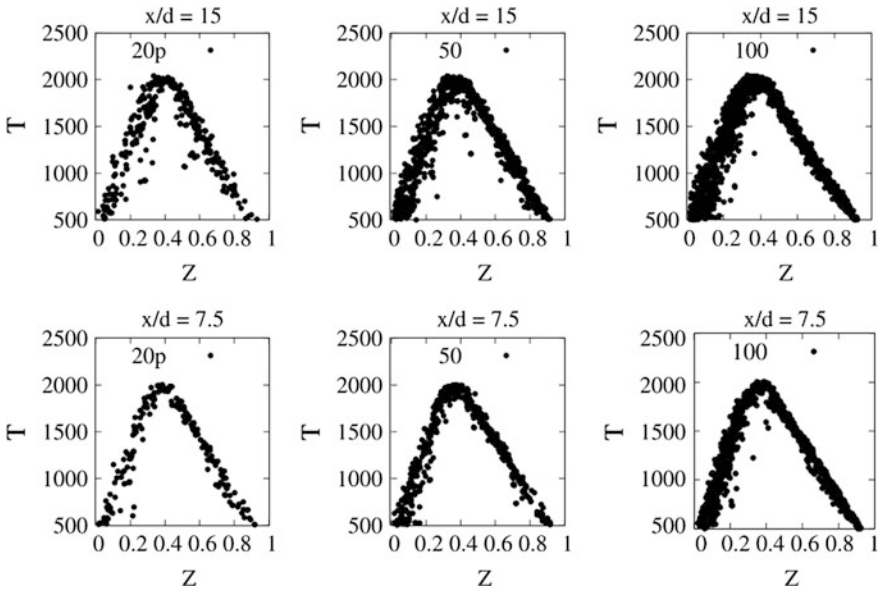

Fig. 15.5 Scatter plots of temperature over the mixture fraction space at $x/D = 7.5$ and 15 for MMC-IEM with three different particle number densities. Figure is from Vogiatzaki et al. (2015)

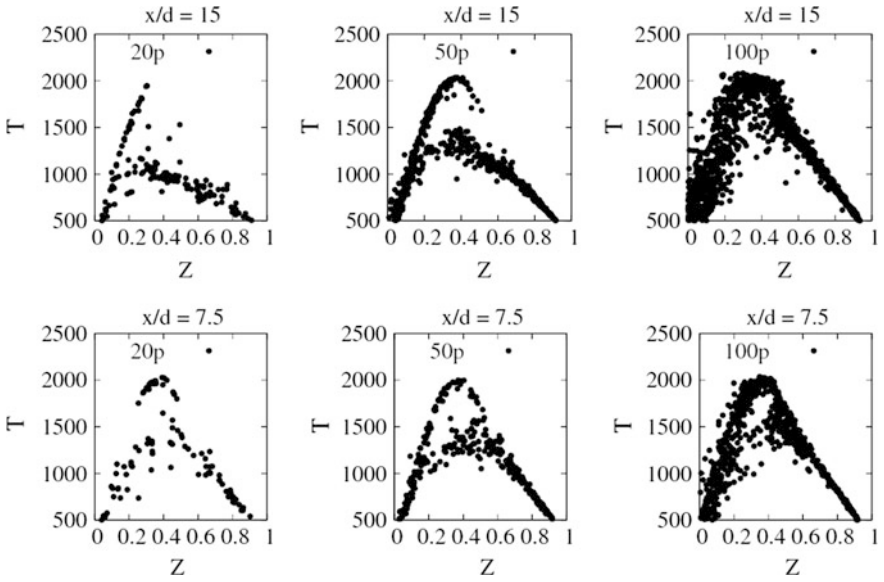

Fig. 15.6 Scatter plots of temperature over the mixture fraction space at $x/D = 7.5$ and 15 for PDF-IEM with three different particle number densities. Figure is from Vogiatzaki et al. (2015)

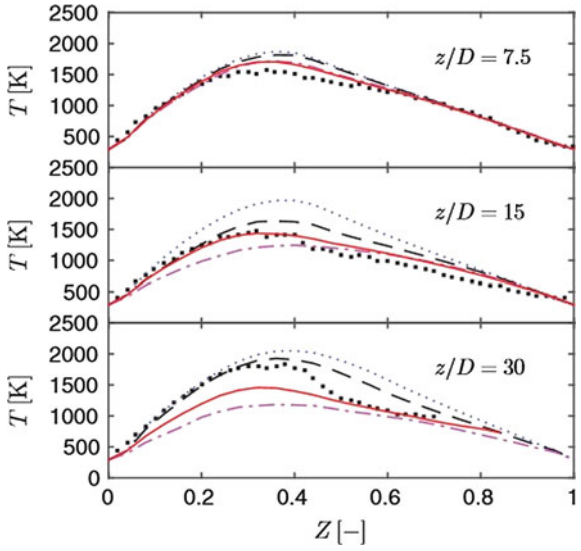

Fig. 15.7 Conditional temperature at different axial locations. Square symbols represent experimental data, red solid lines are PDF-Curls solutions, blue dotted lines are for MMC with $C_{min} = 0.25$, black dashed line for $C_{min} = 0.30$, pink dashed line for $C_{min} = 0.35$. Figure is from Straub et al. (2016)

plots of temperature versus mixture fraction for different N_p in both MMC-IEM and PDF-IEM simulations. The MMC method is noticeably less sensitive to a number of particles used per CFD cell with little difference in the results above $N_p = 50$ and even $N_p = 20$ is not much different.

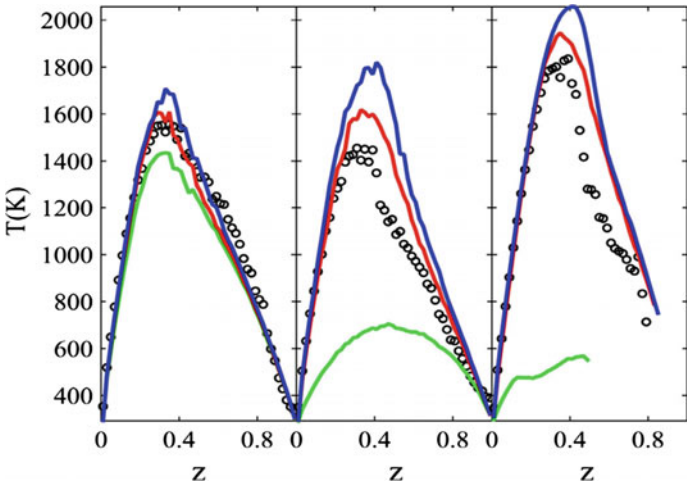

Fig. 15.8 Conditional temperature profiles at $x/D = 7.5$ (left), $x/D = 15$ (centre) and $x/D = 30$ (right). Blue, red and green lines correspond to target correlation parameters of $r_t = 0.948$, 0.935 and 0.912, respectively. Figure is from Varna et al. (2017)

Straub et al. (2016) also conducted stochastic MMC-RANS for Sandia Flame D-F to examine the effect of variation of the minor mixing timescale. Figure 15.7 represents the conditional temperature profiles of Sandia Flame F at three different axial locations. Results from a PDF-modified Curl's simulation are also included. $C_{\min} = 0.30$ gives the best agreement with the experimental data for Sandia Flame F and that value is close to that proposed by Wandel and Klimenko ($C_{\min} = 0.25$) for DNS of a homogenous reacting flow. Other values of $C_{\min}$ clearly show the underprediction ($C_{\min} = 0.35$) and overprediction ($C_{\min} = 0.25$) of conditional temperature (Wandel and Klimenko 2005). Readers should note that different definitions of $C_{\min}$ have been used in Straub et al. (2016) and Wandel and Klimenko (2005). Modified Curl's mixing model, which is known to overpredict the level of conditional fluctuations on account of the non-local nature of its mixing, fails to predict the flame reignition at $z/D = 30$.

Quite recently, Varna et al. (2017a, b) implemented a RANS-based stochastic MMC for the Sandia D–F series, where the static standard Gaussian reference variable proposed by Klimenko and Pope (2003) is replaced by a spatially and temporally evolving reference variable having the same mean and variance as the real mixture fraction while remaining stochastically independent of it. The adapted model is conceptually simpler than the original MMC formulation, but some terms are eliminated and the model does not directly account for the small-scale balance between diffusion and reaction. Consequently, the model overcomes the numerical instabilities found in the original formulation of MMC (Vogiatzaki et al. 2011). Figure 15.8 shows the conditional temperature profiles in Flame F for different values of the target correlation coefficient which corresponds to the correlation

between the reference and real mixture fractions and is linked to the ratio of the minor to major timescales.

15.3.3 Sparse MMC-LES Applications

Sparse MMC-LES is cost-effective in comparison to the conventional intensive stochastic simulations of the filtered density function. Using the Sandia flame series as a benchmark, Ge et al. (2013) demonstrated high-quality MMC-LES predictions are possible with as low as 1 Lagrangian particle per 27 Eulerian cells (1L/27E). Due to the significant reduction in the number of particles relative to intensive methods, sparse MMC-LES appears to be particularly useful in applications involving detailed chemical kinetics of complex fuels. Salehi et al. (2017) applied MMC-LES to the simulation of transient autoignition of n-dodecane under high pressure, engine relevant conditions. Figure 15.9 shows the change in vapour penetration length over time for a non-reacting case at 900 K for two threshold values of mixture fraction. The threshold value of mixture fraction ($Z_{th} = 0.1\%$) prescribed by engine combustion network (ECN) slightly overpredicts the penetration length after 0.5 ms. The other threshold value of mixture fraction used in simulations is more consistent with the experimental data. The ignition delay time and lift-off length for an autoigniting case are plotted in Fig. 15.10 for different values of the chamber ambient temperature and oxygen volume fraction. The ignition delay times and their trends with variations in the ambient conditions are satisfactorily predicted and the observed discrepancies are largely ascribed to the limitations of the available chemical mechanisms. While the results are less accurate, the lift of length trends are also predicted well. The results are comparable with the predictions of other turbulent combustion models as shown in Figs. 15.10d and f.

Sundaram et al. (2016) also tested the sparse MMC-LES method for a lifted flame series, specifically the case of a lifted hydrogen flame in a vitiated coflow and examined the sensitivity to the localisation parameter f_m in Eq. (15.30). The results

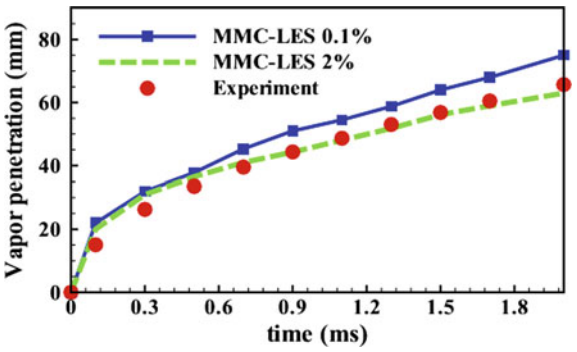

Fig. 15.9 Vapour penetration depth over time for two different definition of the vapour penetration length. Figure is from Salehi et al. (2017)

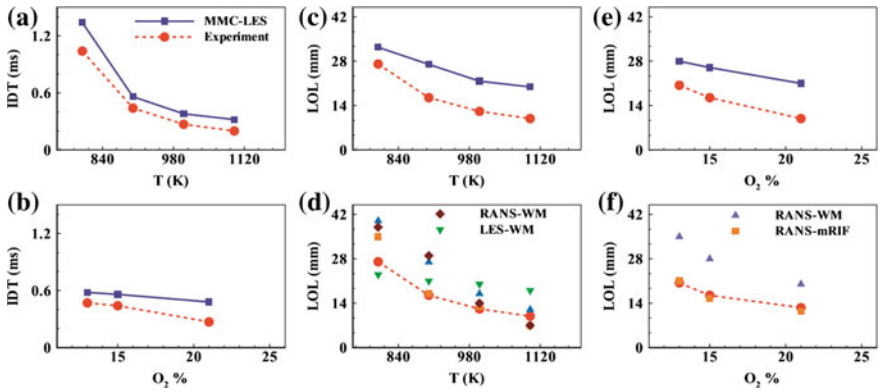

Fig. 15.10 Ignition delay time and lift-off length over ambient temperature and oxygen volume fraction (Salehi et al. 2017)

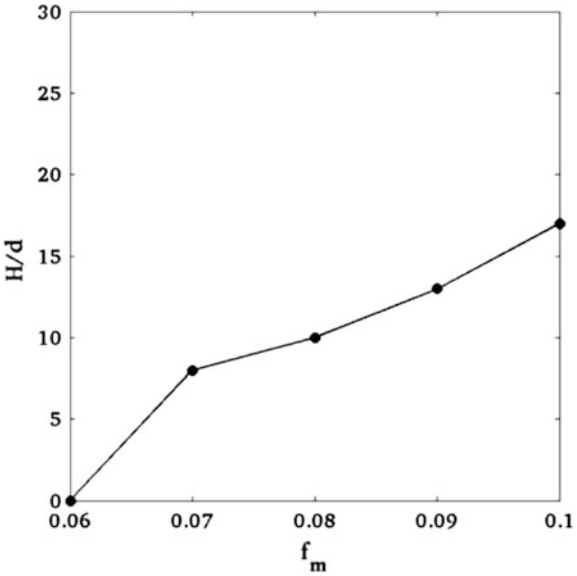

Fig. 15.11 Lift-off height variation with the change in localisation parameter f_m. Figure is from Sundaram et al. (2016)

are shown in Fig. 15.11 indicate that the lift-off height varies almost linearly with f_m and the $f_m = 0.08$ yields a good match with the experimentally observed lift-off value. This value of f_m is somewhat higher than the $f_m = 0.03$ that is suggested by previous studies of piloted jet flames (Ge et al. 2013).

Recently, Galindo et al. (2017) applied sparse MMC-LES to turbulent piloted flames with varying extent of inlet inhomogeneity exhibiting multimode combustion behaviour. The prevailing mode of combustion changes from premixed to non-premixed mode from the nozzle exit to downstream locations and also radially,

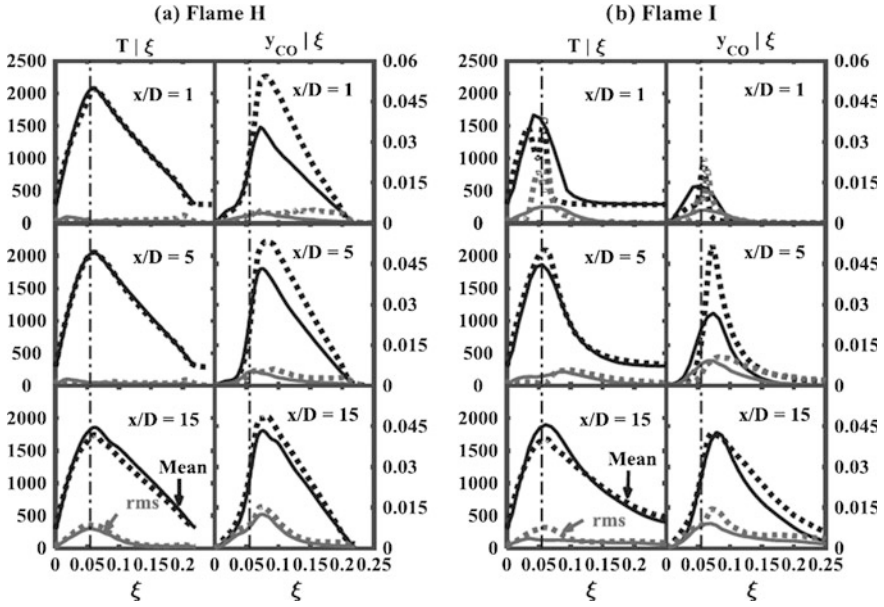

Fig. 15.12 Conditional mean and rms of temperature and CO mass fraction. **a** homogeneous inlet, **b** inhomogeneous inlet. Figure is from Galindo et al. (2017)

where a premixed flame was experimentally observed between the pilot and the main jet with a diffusion flame observed at greater radial locations. Using mixture fraction as the single reference variable, the modelling examined the extent to which the MMC-LES model is applicable to flames displaying the premixed flame-like structure close to the nozzle exit. The conditional profiles of mean and rms of temperature and CO mass fraction for both homogeneous (flame H) and inhomogeneous (flame I) inlet cases are shown below in Fig. 15.12. The conditional temperature statistics are very well predicted for the homogeneous case while the conditional mean of CO mass fractions is significantly underpredicted close to the nozzle exit but improves further downstream where good agreement with the data is observed. For the inhomogeneous inlet case, at $x/D = 1$, the model having only a mixture fraction like reference variable approached but could not completely capture the premixed flame structure. The accuracy of the predictions improves downstream where the combustion mode changes from premixed to non-premixed combustion.

In the past couple of years, some interesting applications of MMC-LES to particle and droplet synthesis processes in turbulent flows have been led by Kronenburg and co-workers (Neuber et al. 2017; Vo et al. 2017). Silica nanoparticle synthesis from silane in a temporal, counter-flowing, double shear layer is modelled using a reduced chemical mechanism of 23 species extending to a single solid state species (Vo et al. 2017). Differential diffusion is modelled in a simplified manner

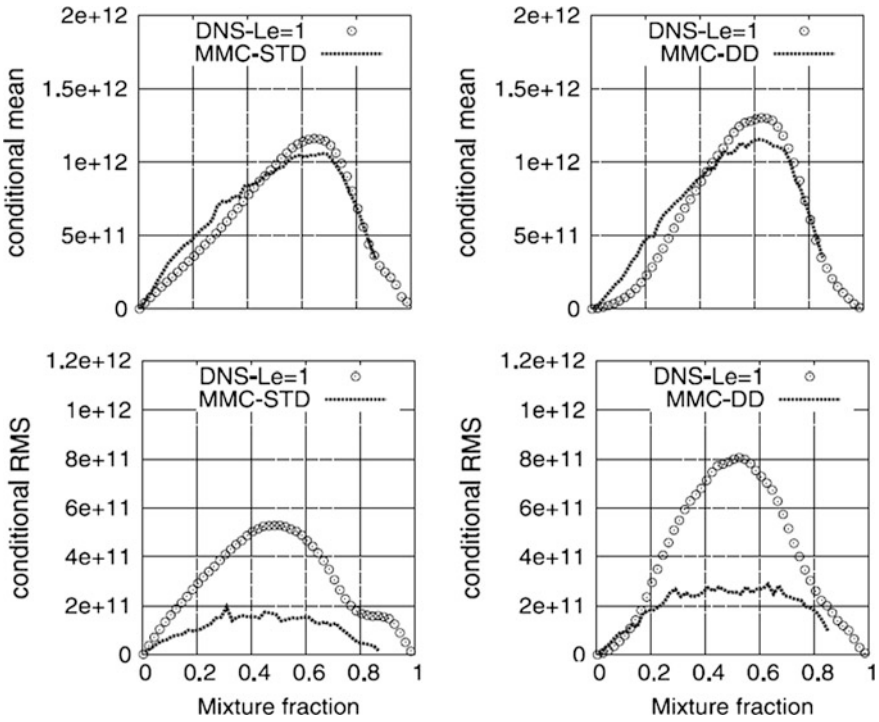

Fig. 15.13 Conditional mean and rms profiles for silica particle number density over mixture fraction. Left side represents results without differential diffusion and right side represents results with differential diffusion. Figure is from Vo et al. (2017)

through a diffusion coefficient weighted scaling of the mixing timescale for the solid silica species. Model predictions are compared to DNS data showing good agreement for the temporal evolution of the mixture fraction and the gaseous chemical species whose reactive timescales are short. The silica is a kinetically limited species with a much longer reaction timescale. As shown in Fig. 15.13 the conditional mean of silica particle number density is predicted quite well while the conditional rms is underpredicted by a large margin. The effects of differential diffusion are evident in both the DNS and MMC-LES with the latter correctly predicting the trend of increasing peak conditional silica number density when the effects of differential diffusion are included. The conditional rms trend is also predicted well when differential diffusion is added, although the quantitative disagreement with the DNS remains large.

Neuber et al. (2017) modelled nucleation and subsequent growth of dibutyl-phthalate (DBP) droplets in a turbulent jet. The droplet size distribution is accounted for by the inclusion of discrete droplet sections in the PDF definition such that the nonlinear interactions between turbulence and nucleation and growth

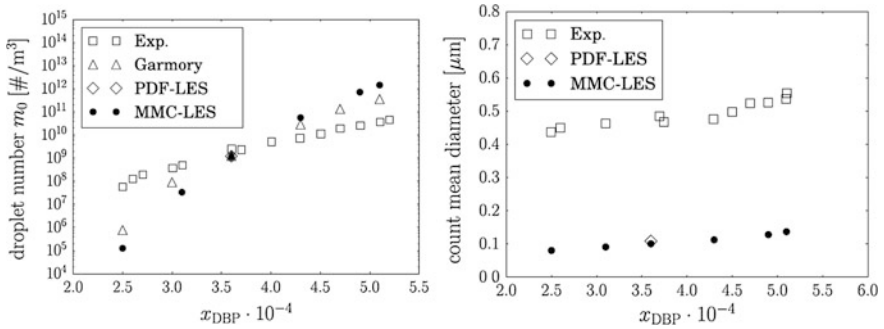

Fig. 15.14 Droplet number and count mean diameter over DBP loading. Exp (Gupta et al. 2011), Garmory and Mastorakos (2008), PDF-LES and MMC-LES (Neuber et al. 2017). Figure is from Neuber et al. (2017)

appear in the governing transport equations in closed form without need of additional filtering or modelling. Both sparse MMC-LES and conventional intensive LES-PDF simulations are compared to experimental data and are shown to produce almost identical results. On account of the sparse distribution of particles that is made possible by the localness of the mixing model, MMC-LES reduces the computational time by a factor of 9 in comparison to the LES-PDF simulations. Figure 15.14 shows the droplet number density and mean diameter at $x/D = 20$ for a range of dibutyl-phthalate (DBP) loadings. The droplet number predictions are quantitatively and qualitatively reasonable in comparison to the experimental data and are also consistent with the previous stochastic fields PDF simulations of Garmory and Mastorakos (2008). The droplet size predictions are significantly underpredicted by all reported models although it is mentioned that there are some reservations about the consistency of the experimental data.

15.3.4 MMC for Premixed Combustion

There are fundamental difficulties that are specific to the modelling of premixed flames using PDF-like methods. These are mainly due to the necessity of avoiding mixing across the flame front. Failure to properly account for localness of mixing in thin premixed flames leads to an inaccurate prediction of the flame propagation speed. Refining the grid in the region of the flame is possible but it comes at a very high-computational cost and consequently, alternative methods based on the artificial thickening of the flame to better match the computational grid have widespread popularity (Kuenne et al. 2011).

Following on from earlier work (Sundaram et al. 2015) on combustor modelling, Sundaram and Klimenko (2017) recently developed a general stochastic MMC approach for the premixed regime and explored the possibility of using different

types of reference variables whose job is to characterise the relative position of stochastic particles with respect to the flame front. These reference variables include the level set variable, a modified shadow position variable and a progress variable. The model which is finally suggested by the authors for further investigation combines the shadow position and progress variable in a two-stage mixing process that involves both intensive particle distributions (for flame front characterisation) and sparse particle distributions (for efficient computation of the detailed reactive species). Their simulation results for an idealised 1-D planar flame in the thin reaction zone regime with single step chemistry are shown in Fig. 15.15, where physical space is denoted by the symbol, x, the reference shadow position is denoted by the symbol, ξ, and the progress variable is denoted by ϕ. Figure 15.15a shows the mapping of the physical space with the reference space and it correctly produces very thin reaction zone in ξ space due to the localness of the first stage of mixing. Figures 15.15b and c show the progress variable in physical and reference spaces, respectively. In the physical space, significant scatter is observed while a thin flamelet-like solution is obtained in the reference space. By design, the model always produces the thin flame structure in reference space, whereas the degree of flame thickening in physical space is controlled in the model by a localisation parameter which can be adjusted to emulate the conditions that are observed in the real flame.

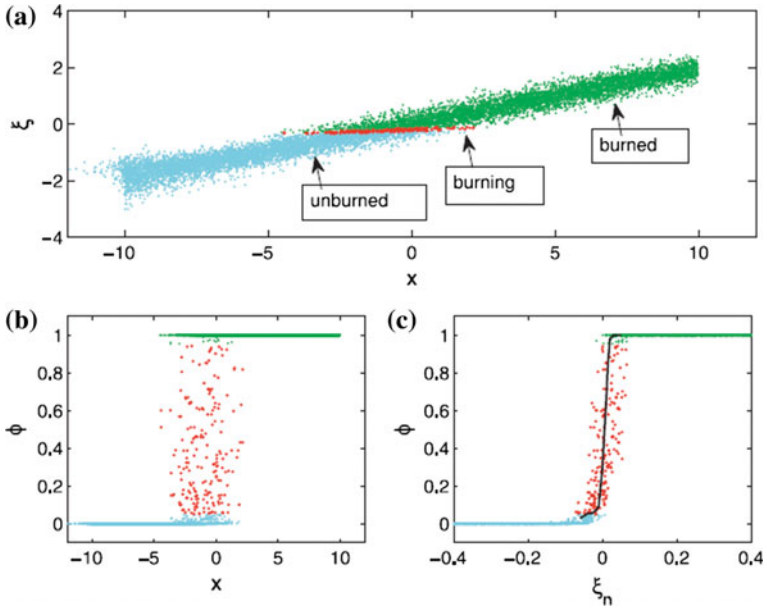

Fig. 15.15 Simulation result for 1-D planer flame with premixed MMC. **a** Mapping of reference space with physical space **b** particle distribution of progress variable in physical space and **c** particle distribution of progress variable in reference space. Figure is from Sundaram and Klimenko (2017)

15.4 Conclusions

This chapter provides an overview on the relatively new MMC approach to turbulent reacting flows. The basic concepts and theory of MMC along with recently published application are presented here in a condensed form. MMC is an attractive approach because it allows the coupling of different existing models into a single methodological framework through the use of a reference space and the concept of mapping functions. This allows the required extensibility for the modelling of certain terms which are otherwise complicated to close. The MMC model may be formulated both in deterministic and stochastic forms. In general, the deterministic framework of MMC is a natural extension of CMC while the stochastic MMC can be a complete joint PDF method. In the LES context, MMC has allowed the use of sparse distributions of notional Lagrangian particles which reduce cost and allow for, among other things, tractable computations of flames with complex chemistry. Within both the RANS and LES contexts, MMC has been demonstrated to be an accurate and computationally affordable approach. Model predictions are found to be sensitive to the minor dissipation timescale, and the literature suggests ways in which it can be formulated for accurate predictions of the conditional fluctuations. MMC is also proving useful for regimes other than non-premixed combustion and some recent applications to flames with inhomogeneous (partially premixed) inlets, premixed flames and particle and droplet synthesis have been reviewed here.

References

Brauner T, Jones WP, Marquis AJ (2016) LES of the cambridge stratified swirl burner using a sub-grid pdf approach. Flow Turbul Combust 96:965–985

Cao RR, Wang HF, Pope SB (2007) The effect of mixing models in PDF calculations of piloted jet flames. Proc Combust Inst 31:1543–1550

Celis C, da Silva LFF (2015) Lagrangian mixing models for turbulent combustion: review and prospects. Flow Turbul Combust 94:643–689

Chen HD, Chen SY, Kraichnan RH (1989) Probability-distribution of a stochastically advected scalar field. Phys Rev Lett 63:2657–2660

Cleary MJ, Klimenko AY (2009) A generalised multiple mapping conditioning approach for turbulent combustion. Flow Turbul Combust 82:477–491

Cleary MJ, Klimenko AY (2011) Multiple mapping conditioning: a new modelling framework for turbulent combustion. In: Echekki T, Mastorakos E (eds) Turbulent combustion modelling. advances, new trends and perspectives. Springer

Cleary M, Klimenko A (2011b) A detailed quantitative analysis of sparse-Lagrangian filtered density function simulations in constant and variable density reacting jet flows. Phys Fluids 23:115102

Cleary MJ, Kronenburg A (2007a) Multiple mapping conditioning. For extinction and reignition in turbulent diffusion flames. Proc Combust Inst 31:1497–1505

Cleary M, Kronenburg A (2007b) 'Hybrid' multiple mapping conditioning on passive and reactive scalars. Combust Flame 151:623–638

Cleary MJ, Klimenko AY, Janicka J, Pfitzner M (2009) A sparse-Lagrangian multiple mapping conditioning model for turbulent diffusion flames. Proc Combust Inst 32:1499–1507

Devaud CB, Stankovic I, Merci B (2013) Deterministic multiple mapping conditioning (MMC) applied to a turbulent flame in large eddy simulation (LES). Proc Combust Inst 34:1213–1221

Dopazo C, Obrien EE (1974) Approach to autoignition of a turbulent mixture. Acta Astronaut 1:1239–1266

Galindo S, Salehi F, Cleary MJ, Masri AR (2017) MMC-LES simulations of turbulent piloted flames with varying levels of inlet inhomogeneity. Proc Combust Inst 36:1759–1766

Garmory A, Mastorakos E (2008) Aerosol nucleation and growth in a turbulent jet using the stochastic fields method. Chem Eng Sci 63:4078–4089

Ge Y, Cleary MJ, Klimenko AY (2013) A comparative study of Sandia flame series (D-F) using sparse-Lagrangian MMC modelling. Proc Combust Inst 34:1325–1332

Girimaji SS (1992) A mapping closure for turbulent scalar mixing using a time-evolving reference field. Phys Fluids a-Fluid Dyn 4:2875–2886

Girimaji SS (1993) A study of multiscalar mixing. Phys Fluids a-Fluid Dyn 5:1802–1809

Gupta A, Ifeacho P, Schulz C, Wiggers H (2011) Synthesis of tailored WO3 and WOx ($2.9 < x < 3$) nanoparticles by adjusting the combustion conditions in a H2/O2/Ar premixed flame reactor. Proc Combust Inst 33:1883–1890

Janicka J, Kolbe W, Kollmann W (1979) Closure of the transport-equation for the probability density-function of turbulent scalar fields. J Non-Equilib Thermodyn 4:47–66

Klimenko AY (2005) Matching conditional moments in PDF modelling of nonpremixed combustion. Combust Flame 143:369–385

Klimenko A (2007) On simulating scalar transport by mixing between Lagrangian particles. Phys Fluids 19:031702

Klimenko A (2009a) Lagrangian particles with mixing. I. Simulating scalar transport. Phys Fluids 21:065101

Klimenko A (2009b) Lagrangian particles with mixing. II. Sparse-Lagrangian methods in application for turbulent reacting flows. Phys Fluids 21:065102

Klimenko AY, Bilger RW (1999) Conditional moment closure for turbulent combustion. Prog Energy Combust Sci 25:595–687

Klimenko A, Cleary MJ (2010) Convergence to a model in sparse-Lagrangian FDF simulations. Flow Turbul Combust 85:567–591

Klimenko AY, Pope SB (2003) The modeling of turbulent reactive flows based on multiple mapping conditioning. Phys Fluids 15:1907–1925

Kronenburg A (2004) Double conditioning of reactive scalar transport equations in turbulent nonpremixed flames. Phys Fluids 16:2640–2648

Kronenburg A, Cleary MJ (2008) Multiple mapping conditioning for flames with partial premixing. Combust Flame 155:215–231

Kuenne G, Ketelheun A, Janicka J (2011) LES modeling of premixed combustion using a thickened flame approach coupled with FGM tabulated chemistry. Combust Flame 158:1750–1767

Lindstedt RP, Vaos EM (2006) Transported PDF modeling of high-reynolds-number premixed turbulent flames. Combust Flame 145:495–511

Mastorakos E, Bilger R (1998) Second-order conditional moment closure for the autoignition of turbulent flows. Phys Fluids 10:1246–1248

Mitarai S, Riley JJ, Kosaly G (2003) A Lagrangian study of scalar diffusion in isotropic turbulence with chemical reaction. Phys Fluids 15:3856–3866

Neuber G, Kronenburg A, Stein OT, Cleary MJ (2017) MMC-LES modelling of droplet nucleation and growth in turbulent jets. Chem Eng Sci 167:204–218

Pei YJ, Hawkes ER, Kook S, Goldin GM, Lu TF (2015) Modelling n-dodecane spray and combustion with the transported probability density function method. Combust Flame 162:2006–2019

Pope SB (1985) Pdf methods for turbulent reactive flows. Prog Energy Combust Sci 11:119–192

Pope SB (1991) Mapping closures for turbulent mixing and reaction. Theoret Comput Fluid Dyn 2:255–270

Salehi F, Cleary MJ, Masri AR, Ge Y, Klimenko AY (2017) Sparse-Lagrangian MMC simulations of an n-dodecane jet at engine-relevant conditions. Proc Combust Inst 36:3577–3585

Straub C, De S, Kronenburg A, Vogiatzaki K (2016) The effect of timescale variation in multiple mapping conditioning mixing of PDF calculations for Sandia Flame series D–F. Combust Theory Modell, 1–19. https://doi.org/10.1080/13647830.2016.1191677

Subramaniam S, Pope SB (1998) A mixing model for turbulent reactive flows based on Euclidean minimum spanning trees. Combust Flame 115:487–514

Sundaram B, Klimenko AY (2017) A PDF approach to thin premixed flamelets using multiple mapping conditioning. Proc Combust Inst 36:1937–1945

Sundaram B, Klimenko A, Cleary M, Maas U (2015) Prediction of NO x in premixed high-pressure lean methane flames with a MMC-partially stirred reactor. Proc Combust Inst 35:1517–1525

Sundaram B, Klimenko AY, Cleary MJ, Ge YP (2016) A direct approach to generalised multiple mapping conditioning for selected turbulent diffusion flame cases. Combust Theor Model 20:735–764

Varna A, Cleary MJ, Hawkes ER (2017a) A multiple mapping conditioning mixing model with a mixture-fraction like reference variable. Part 2: RANS implementation and validation against a turbulent jet flame. Combustion and Flame (2017). https://doi.org/10.1016/j.combustflame.2017.03.017

Varna A, Cleary MJ, Hawkes ER (2017b) A multiple mapping conditioning mixing model with a mixture-fraction like reference variable. Part 1: Model derivation and ideal flow test cases. Combust Flame. https://doi.org/10.1016/j.combustflame.2017.03.016

Veynante D, Vervisch L (2002) Turbulent combustion modeling. Prog Energy Combust Sci 28:193–266

Vo S, Kronenburg A, Stein OT, Cleary MJ (2017a) Multiple mapping conditioning for silica nanoparticle nucleation in turbulent flows. Proc Combust Inst 36:1089–1097

Vo S, Stein OT, Kronenburg A, Cleary MJ (2017b) Assessment of mixing time scales for a sparse particle method. Combust Flame 179:280–299

Vogiatzaki K (2010) Stochastic and deterministic multiple mapping conditioning for jet flames, Imperial College London

Vogiatzaki K, Kronenburg A, Cleary MJ, Kent JH (2009a) Multiple mapping conditioning of turbulent jet diffusion flames. Proc Combust Inst 32:1679–1685

Vogiatzaki K, Cleary MJ, Kronenburg A, Kent JH (2009b) Modeling of scalar mixing in turbulent jet flames by multiple mapping conditioning. Phys Fluids 21

Vogiatzaki K, Kronenburg A, Navarro-Martinez S, Jones WP (2011) Stochastic multiple mapping conditioning for a piloted, turbulent jet diffusion flame. Proc Combust Inst 33:1523–1531

Vogiatzaki K, Navarro-Martinez S, De S, Kronenburg A (2015) Mixing modelling framework based on multiple mapping conditioning for the prediction of turbulent flame extinction. Flow Turbul Combust 95:501–517

Wandel AP (2013) Conditional dissipation of scalars in homogeneous turbulence: closure for MMC modelling. Combust Theor Model 17:707–748

Wandel AP, Klimenko AY (2005) Testing multiple mapping conditioning mixing for Monte Carlo probability density function simulations. Phys Fluids 17

Wandel AP, Lindstedt RP (2009) Hybrid binomial Langevin-multiple mapping conditioning modeling of a reacting mixing layer. Phys Fluids 21

Wandel AP, Lindstedt RP (2013) Hybrid multiple mapping conditioning modeling of local extinction. Proc Combust Inst 34:1365–1372

Part V
Recent Applications of Turbulent Combustion

Chapter 16
Recent Progress in Turbulent Combustion Modeling of Spray Flames Using Flamelet Models

Prithwish Kundu, Muhsin M. Ameen and Sibendu Som

Abstract The application of liquid fuels for a wide range of engineering applications has motivated the development of predictive CFD models for spray flames. The coupling of multiphase spray physics along with turbulence and complex chemistry of combustion poses a huge challenge to computational models in terms of accuracy and cost. The models need to accurately capture the spray breakup, evaporation, mixing and the accompanying chemistry along with turbulence chemistry interaction effects accurately in order to be predictive. Flamelet-type combustion models decouple the fluid flow from the chemistry and have significantly reduced computational costs. This framework can capture the effects of turbulence chemistry interactions and include large chemistry mechanisms without significantly increasing the computational costs. The flamelet concept also enables the a priori tabulation of flamelets which can further speed up computational models. The Eulerian-Lagrangian spray model coupled with the flamelet type combustion models have been used extensively to model spray flames in a wide range of applications like reciprocating engines, gas turbines and furnaces. This chapter discusses the theory and application of such modeling approaches in RANS and LES along with some latest flamelet solver developments which now enable the use of detailed chemistry mechanisms for higher hydrocarbon fuels without reduction.

Keywords Flamelet · Spray · Turbulence-chemistry interaction
Tabulation · Low temperature combustion

P. Kundu (✉) · M. M. Ameen · S. Som
Argonne National Laboratory, Lemont, IL, USA
e-mail: pkundu@anl.gov

© Springer Nature Singapore Pte Ltd. 2018

S. De et al. (eds.), *Modeling and Simulation of Turbulent Combustion*, Energy, Environment, and Sustainability, https://doi.org/10.1007/978-981-10-7410-3_16

16.1 Introduction

16.1.1 Non-premixed Spray Combustion

This chapter discusses the modeling challenges and approaches that have been developed to model spray flames. Combustion can be broadly classified based on the local flow conditions (laminar or turbulent) and the process in which the oxidizer is mixed with fuel (premixed or non-premixed) as shown in Fig. 16.1.

For most engineering applications, the demand for energy density and energy output are becoming increasingly higher. As a result, in order to burn more fuel within space and time constraints, higher mass flow rates of oxidizers and fuel are desired. Hence, most engineering devices operate under high Reynolds numbers, i.e., the turbulent flow regime. In these applications, the complex fuel chemistry gets coupled with the turbulent flow field and the resulting physics is significantly more challenging than laminar flames. Spark ignited engines, HCCI (Homogeneous Charge Compression Ignition) engines and some stationary gas turbines fall into the category of turbulent premixed combustion. These combustion regimes are characterized by a homogeneous fuel–air mixture ignited by an external or chemical source. These applications find a range of applications in the transportation sector. In premixed flames, the pressure fluctuations can lead to flame instabilities and devices need be designed carefully to address such issues. Non-premixed combustion, on the other hand, consists of separate fuel and oxidizer streams mixing together to form the reaction zone. Transport and diffusion play an important role in order to form a reacting mixture. Non-premixed flames are relatively simpler to implement and design as they do not encounter stability issues as the reaction rates

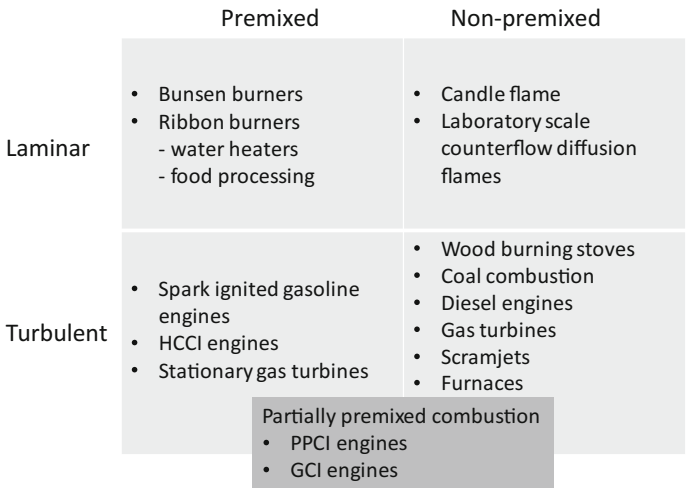

Fig. 16.1 Different regimes of combustion based on the applications

can be controlled through mixing. Liquid fuels have additional advantages in storage and handling. Liquid fuels do not need to be compressed like the gaseous fuels. This leads to a much higher energy density and simpler system design. Liquid fuels have thus found extensive applications in the automotive and aviation sectors over the past century. These types of flames do not need elaborate premixing mechanisms and other safety-related issues.

As a result of all these factors, non-premixed spray combustion has become an important area of research and its understanding is important for the engineering community. Compression ignition (CI) engines are characterized by high-thermal efficiencies, due to their higher compression ratios compared to SI engines, and thus dominate the heavy duty engine applications. Non-premixed combustion is also accompanied by significantly richer combustion regimes which lead to higher pollutant formation. Designing efficient combustion strategies along with lower emissions are the main challenges for the next generation non-premixed combustion systems. As a result, a large number of studies have been carried out to understand and model such processes. Novel combustion concepts like PPCI (Partially Premixed Compression Ignition) and GCI (Gasoline Compression Ignition) engines are some applications which are neither non-premixed nor premixed and these systems pose additional challenges in understanding and designing. This chapter focuses on modeling the turbulent non-premixed and partially premixed spray flames using the Flamelet approach (Peters 1984), the different modeling approaches, their evolution, advantages, and limitations. The latest trends in understanding and modeling combustion at low-temperature conditions are also discussed.

16.1.2 Modeling Challenges

16.1.2.1 Spray and Hydrocarbon Chemistry

Non-premixed flames can be ignited using an external energy source or autoignited if the oxidizer temperature exceeds a certain level. This temperature is determined by the activation energy barrier for the oxidation reactions at the given pressure conditions. Most CI engine applications feature autoignited spray flames and an overview of this process is discussed here and a schematic is shown in Fig. 16.2. This process consists of injection of the liquid fuel at a high velocity into an oxidizing domain. This liquid jet then undergoes spray breakup followed by evaporation to the gas phase. This is followed by the mixing of gas phase fuel and oxidizer. At this point, the gas phase fuel molecules start reacting with the oxidizer. Fossil fuels and biofuels are a mixture of complex long-chain hydrocarbons. These fuel molecules breakdown and form intermediate chemical species, which then follow a complex chemistry pathway to form saturated combustion products accompanied by heat release. While these chemical reactions proceed toward equilibrium, the chemical reactants are accompanied by continuous mixing with the

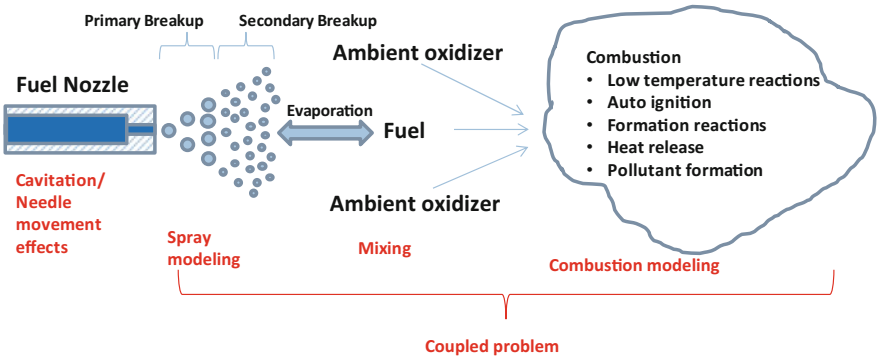

Fig. 16.2 Schematic of the main processes involved in spray combustion

ambient oxidizer. As a result, the chemical reactions do not occur at fixed chemical compositions and is a process that is highly coupled with the overall mixing process. Consider the combustion of hydrogen which is the simplest fuel molecule. The $H_2 + O_2$ fuel chemistry is represented by 9 species and 19 reactions by the detailed mechanisms (Conaire et al. 2004). However, the combustion of the simplest hydrocarbon fuel, CH_4 is accompanied by hundreds of species and reactions. The widely used GRI 3.0 mechanism has 53 species and 325 reactions (Smith et al. 2000). The chemistry becomes more complicated for larger fuel molecules. Oxidation of higher hydrocarbon fuels like n-dodecane ($C_{10}H_{26}$) (Sarathy et al. 2011a, b) and n-heptane (C_7H_{16}) involves tens of thousands of species and fifty thousand reactions occurring simultaneously (Mehl et al. 2011) As a result, it is extremely challenging to understand and model such processes. Modeling such a complex chemistry mechanism is not possible using the available computational resources. The process of mechanism reduction has been proposed by chemists and engineers to address this issue (Lu and Law 2005, 2008) A detailed chemistry mechanism with a few thousand species is reduced to a smaller mechanism which has the same ignition delay and laminar flame speeds as a detailed mechanism. However, these reduced mechanisms are applicable over limited ranges of equivalence ratios and pressures.

Fuels like diesel and gasoline are complex mixtures of long-chain hydrocarbons. It has still not been possible to estimate all the components of these fuels. A recent study (Pitz and Mueller 2011) showed the presence of about 5000 components in diesel fuel. It is almost impossible to determine the exact chemistry and the pathways that such a fuel will undergo. Due to these modeling challenges, the concept of a surrogate fuel is typically used to model diesel and gasoline type of fuels. A surrogate fuel is a simpler single component fuel molecule like n-heptane or n-dodecane that is used to mimic the average chemical and physical properties of the real fuel.

16.1.2.2 Turbulence-Chemistry Interaction and Stiff Chemistry

The complexity of chemistry is coupled with turbulent flows in typical spray flame applications. Turbulent flows encompass a very wide range of time and length scales. Small fluctuations in temperature fields can have a large impact on the chemistry. This is due to the fact that the Arrhenius reaction rates that are used to model reactions are strongly nonlinear in temperature. In order to have an accurate description of all the processes, it is essential to resolve the smallest time and length scales. This would mean resolving the flow up to the Kolmogorov scale. Such simulations, which are called as Direct Numerical Simulations (DNS), are extremely expensive and not feasible for practical applications which have very large domains sizes and Reynolds numbers. Large Eddy Simulations (LES) resolve the larger scales and use a subgrid model for the smaller unresolved scales. Reynolds-Averaged Navier–Stokes (RANS) methods represent the scalar variables as the sum of an ensemble mean and a fluctuating term. These fluctuation terms are then modeled using turbulence models based on the empirical relations. In these simulations, the local temperatures represent a mean value in RANS and a filtered value in LES. The chemistry source term for each species that is calculated based on this mean temperature will have a significant error introduced in them. This closure problem can significantly affect turbulent combustion simulations and has been a major focus of many studies. A range of Turbulence-Chemistry Interaction (TCI) models have been proposed for RANS and LES approaches. The chemical timescales of the different species can vary by orders of magnitude and can be a few orders of magnitude smaller than the fluid flow timescales. As a result, the system of equations that are required to solve a turbulent chemically reacting flow becomes very stiff and requires significantly lower time-steps to get an accurate solution.

The coupled complexities of turbulent flow, spray physics, and chemistry have made CFD models expensive. Industrial applications thus have to resort to lower fidelity models. This reduces the overall predictive capability of CFD models. Improvements in fuel surrogate and chemistry mechanisms have led to chemistry mechanisms with very large number of species. The cost of transporting a large number of species followed by evaluation of the chemistry using large mechanisms has a significant impact on CFD solvers. The computational cost increases as the cube of the number of species in a given reaction mechanism (Xu et al. 2016). The flamelet concept has a big impact on the CFD simulations and can simplify certain problems. This concept has been able to decouple chemistry from fluid flow calculations and remove the stiffness problem due to the large mechanisms. As a result, this method has been applied to a large number of spray flame and engine simulations. The presumed PDF approach allows to account for TCI effects at costs that are much lower than other methods. The flamelet models have been extensively applied and validated across gas jet flames as well as spray flames with a wide range of fuels.

16.2 The Flamelet Concept

Certain characteristics of non-premixed combustion can be utilized to make simplifications and modeling assumptions that drastically reduces the computational effort. Non-premixed flames are strongly related to the oxidizer–fuel mixing fields. The mixture fraction variable (Z) characterizes this mixing. In a two feed system, mixture fraction at any point is defined as fraction of mass originating from the fuel stream. It has also been defined in detail in Chap. 1. The chemistry can be reduced to a lower dimensional problem and expressed as a function of mixture fraction (Peters 1984). In the flamelet concept, the chemistry is solved in the mixture fraction space and the flow solver models the oxidizer–fuel mixing, i.e., the mixture fraction. The chemistry is then coupled to the flow solver at each time step based on the mixture fraction field. This effective decoupling of the chemistry from physical space to mixture fraction space can have significant benefits with respect to computational efficiency. The decoupling of fluid flow from the chemistry enables the use of very small time-steps in the chemistry solver and larger time-steps for the fluid flow solver. This eliminates the stiffness issues related with large chemistry mechanisms. Moreover, it can be assumed that the turbulent fluctuations in the composition space can be represented by a PDF distribution. Thus, TCI effects can also be integrated into this approach. The species transport equation is shown in Eq. 16.1. This equation represents the species conservation equation used to describe the evolution of species in a reacting flow in conservative form. The first term on the left-hand side $\frac{\partial Y_i}{\partial t}$ represents the net change in species concentration over a timestep. The second term represents the convection of the species mass fractions due to the flow velocity. The third term is the transport due to molecular diffusion. The term on the right-hand side $(\dot{\omega}_t)$ is the chemical source term due to chemical reactions.

$$\rho \frac{\partial Y_i}{\partial t} + \rho u_j \frac{\partial Y_i}{\partial x_j} - \frac{\partial}{\partial x_j}\left(\rho D_i \frac{\partial Z}{\partial x_j}\right) = \dot{\omega}_t \tag{16.1}$$

Consider a non-premixed flame. An infinitesimal area on the stoichiometric flame surface is shown in the schematic (Fig. 16.3).

The spatial coordinates are represented by X1, X2, and X3. X1 is perpendicular to the flame surface. Consider, a coordinate transformation from the physical space and time coordinates to mixture fraction.

$$\begin{aligned} &(t, x_1, x_2, x_3) \rightarrow (\tau, Z) \\ &\frac{\partial}{\partial t} = \frac{\partial}{\partial \tau}\frac{\partial \tau}{\partial t} + \frac{\partial Z}{\partial t}\frac{\partial}{\partial Z} \end{aligned} \tag{16.2}$$

where $\frac{\partial \tau}{\partial t} = 1$

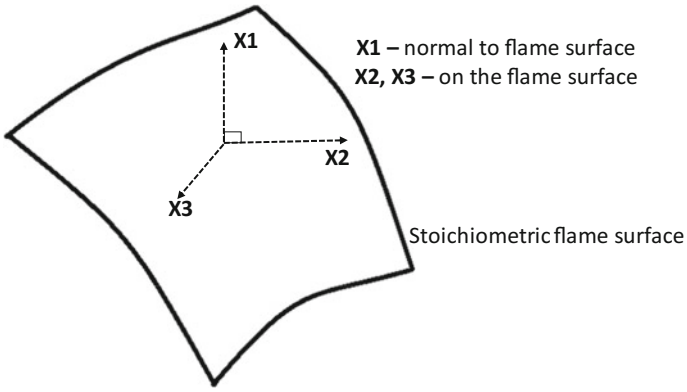

Fig. 16.3 Schematic of stoichiometric surface

$$\frac{\partial}{\partial x_j} = \frac{\partial Z}{\partial x_j}\frac{\partial}{\partial Z} \tag{16.3}$$

These transformations can now be substituted into the species transport equation

$$\rho\left(\frac{\partial Y_i}{\partial \tau} + \frac{\partial Y_i}{\partial Z}\frac{\partial Z}{\partial t}\right) + \rho u_j \frac{\partial Z}{\partial x_j}\frac{\partial Y_i}{\partial Z} - \frac{\partial}{\partial x_j}\left(\rho D \frac{\partial Z}{\partial x_j}\right)\frac{\partial Y_i}{\partial Z} - \rho D\left(\frac{\partial Z}{\partial x_j}\right)^2 \frac{\partial^2 Y_i}{\partial Z^2} = \dot{\omega}_\iota \tag{16.4}$$

After grouping terms and assuming that gradients in X2 and X3 direction can be neglected, we get the following equation (Peters 1984).

$$\rho\frac{\partial Y_i}{\partial \tau} = \rho D\left(\frac{\partial Z}{\partial x_j}\right)^2 \frac{\partial^2 Y_i}{\partial Z^2} + \dot{\omega}_\iota \tag{16.5}$$

Scalar dissipation rate is defined as $\chi = 2D\left(\frac{\partial Z}{\partial x_j}\right)^2$

$$\rho\frac{\partial Y_i}{\partial \tau} = \rho\frac{\chi}{2}\frac{\partial^2 Y_i}{\partial Z^2} + \dot{\omega}_\iota \tag{16.6}$$

This is the flamelet species equation. Similar coordinate transformation can be applied to the energy conservation equations.

$$\rho\frac{\partial T}{\partial t} - \rho\frac{\chi}{2}\frac{\partial^2 T}{\partial Z^2} - \rho\frac{\chi}{2C_p}\left[\sum_i\left(\frac{C_{pi}}{Le_i}\frac{\partial Y_i}{\partial Z} + \frac{\partial C_{p,i}}{\partial Z}\right)\right]\frac{\partial T}{\partial Z} = \frac{1}{C_p}\left(\frac{\partial P}{\partial t} - \sum_i \dot{\omega}_\iota h_i\right) \tag{16.7}$$

These set of Eqs. 16.6–16.7 are known as the flamelet equations. The flamelet equations are a representation of chemistry in the one-dimensional mixture fraction

space. The 1D counterflow diffusion flame is the basic representation of this concept. In Eq. (16.6), the first term on the left-hand side is the unsteady term which represents the net rate of change in species mass fraction. The first term on the right-hand side represents the transport of species due to the diffusion in mixture fraction space. The second term on the right-hand side represents the species source term which is the production or destruction of species due to chemical reactions. Thus, the net change in species mass fraction at any given mixture fraction is the result of competition between chemical reaction and diffusion. It should be noted that the flamelet equations presented here neglect the effects of radiation and fuel vaporization on the flame structure. Including these effects would lead to additional source terms in the RHS of Eqs. (16.6) and (16.7).

The concept of mixture fraction and flamelets can be used to represent 3D turbulent flames as well. Consider, a turbulent flame as shown in the schematic in Fig. 16.4. It shows the temperature and OH mass fraction contours at a given time instant. The black line represents the stoichiometric isoline. The magnified view of the flame is shown in (c). It can be observed that the largest gradients in the OH mass fraction occur in a direction that is perpendicular to the stoichiometric surface. The gradients parallel to the surface are minimal. Thus in a limiting case, as shown in (d) the turbulent flame can be viewed as a 1D laminar flame close to the stoichiometric surface. The entire flame can be represented as an ensemble of such 1D laminar flamelets which get wrinkled due to turbulence. It must be noted that

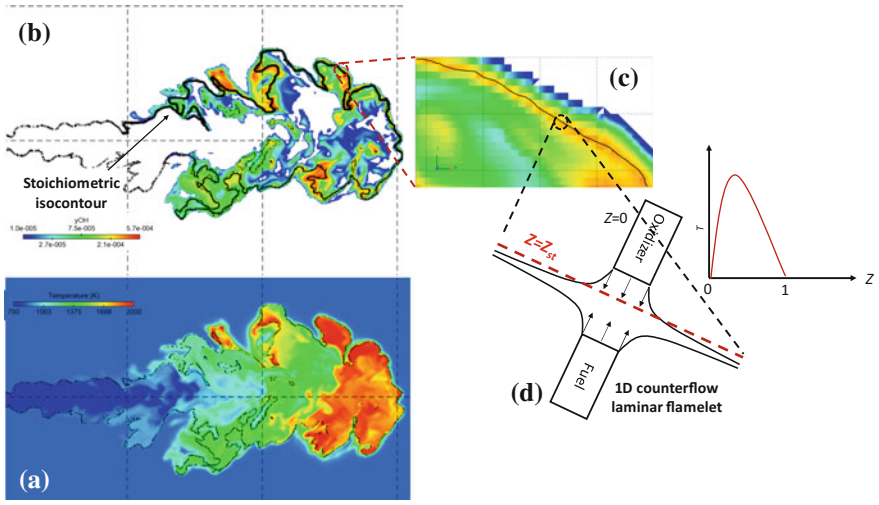

Fig. 16.4 The schematic shows the representation of 3D non-premixed flames within the flamelet concept. The temperature field of a typical non-premixed flame is shown in (**a**). The stoichiometric isoline is shown in (**b**) and (**c**) shows a magnified view of the flame with the stoichiometric isoline. The turbulent flame can be represented as a laminar diffusion flame at the infinitesimal limit and the effect of turbulence is to wrinkle these flamelets. Most of the scalar gradients can be observed in a direction perpendicular to the stoichiometric isoline as shown in (*d*)

each representative 1D flamelet will be subject to different flow conditions, i.e., χ. This term in the flamelet equations Eqs. (16.6–16.7) couples the flamelet equations to the local turbulent flow conditions.

The flamelet concept can be applied to gas jet flames as well as multiphase problems. The spray and evaporation models can be used to model the transition from the liquid phase to the gas phase. Mixture fraction transport equations can then be used to represent the gas phase fuel. The chemical reactions can then be solved in the mixture fraction space and species can be represented as functions of mixture fraction. The information from the flamelet space is then transferred to the physical space using mixture fraction. Thus, the chemistry can be coupled to the fluid flow calculations without solving for the actual species transport equations. Different modeling approaches can be devised based on the treatment of the flamelet equations and their coupling to the physical domain. These different families of flamelet models and their application to spray flames have been used extensively to model engine combustion and are discussed in the proceeding sections of this chapter.

16.2.1 Steady and Unsteady Flamelet Models

The chemistry in large Damkohler number problems can be assumed to be infinitely fast compared to the mixing timescale. Some simulations require the prediction of the quasi-steady-state operation and a time-accurate solution is not required. By substituting the unsteady term to 0 in the flamelet equations Eqs. (16.6–16.7) we get the steady flamelet equations shown below.

$$\rho\frac{\chi}{2}\frac{\partial^2 Y_i}{\partial Z^2} + \dot{\omega}_i = 0 \tag{16.8}$$

$$\rho\frac{\chi}{2}\frac{\partial^2 T}{\partial Z^2} + \rho\frac{\chi}{2C_p}\left[\sum_i\left(\frac{C_{pi}}{Le_i}\frac{\partial Y_i}{\partial Z} + \frac{\partial C_{p,i}}{\partial Z}\right)\right]\frac{\partial T}{\partial Z} = \frac{1}{C_p}\left(\sum_i \dot{\omega}_i h_i\right) \tag{16.9}$$

The independent variable Y_i is now only a function of mixture fraction (Z). These equations represent species and temperature profiles for a 1D non-premixed flame at steady state. The species equation show that the formation of chemical species is balanced by the diffusion in mixture fraction space. Higher scalar dissipation rates lead to higher diffusion and can extinguish the flame after a certain point. These types of models can be used to model flames that are governed by mixing and are stabilized based on the scalar dissipation. The steady model representation fails to describe unsteady flames found in many applications, where the overall process is influenced by the chemically unsteady behavior. The effect of finite rate chemistry and diffusion in Z space has a remarkable impact on the species profiles and the resulting flame shapes. The unsteady flamelet equations, on the other hand, are

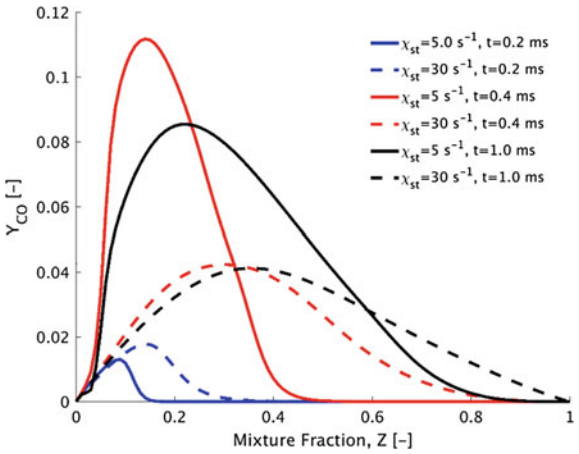

Fig. 16.5 Evolution of the mass fraction of CO as a function of Z from the solution of the flamelet equations for stoichiometric scalar dissipation rates of 5 and 30 s^{-1} for a counterflow diffusion flame

capable of representing finite rate chemistry effects along with the effects of scalar dissipation.

The scalar dissipation rate represents the influence of the external flow field on the local mixture fraction gradients and is given by:

$$\chi = 2D|\nabla Z|^2 \tag{16.10}$$

where D is the mixture diffusivity, and ∇Z is the gradient of mixture fraction in physical space. The functional dependence of scalar dissipation rate on mixture fraction is typically approximated using counterflow diffusion flame solutions (Peters 1984) as

$$\chi = \chi_{st} \frac{\exp\left[-2(erfc^{-1}(2Z))^2\right]}{\exp\left[-2(erfc^{-1}(2Z_{st}))^2\right]} \tag{16.11}$$

Here, *st* refers to the stoichiometric condition, χ_{st} refers to the scalar dissipation rate at the stoichiometric condition, and *erfc* is the complimentary error function. In the present work, the above functional dependence of scalar dissipation rate on mixture fraction is assumed. Other studies (Pitsch et al. 1998) have represented the scalar dissipation rates using natural logarithm profiles as well.

Solving Eqs. (16.6–16.7) using (16.11), the transient evolution of species mass fractions and temperature can be obtained for different values of χ_{st}. To demonstrate the nature of these solutions, the flamelet equations were solved for a counterflow diffusion flame with n-dodecane as the fuel and the oxidizer consisting of N_2 (71.98%), O_2 (16.41%), CO_2 (9.38%), and H_2O (2.23%). The temperature of the oxidizer was 900 K and the fuel was 386 K, and the pressure was 59.2 bar. These conditions correspond to the ECN Spray A setup (https://ecn.sandia.gov/). Figure 16.5 shows the transient evolution of the mass fraction of CO in the mixture

fraction space for $\chi_{st} = 5\ s^{-1}$ and $\chi_{st} = 30\ s^{-1}$. It can be seen that increasing χ_{st} leads to a more diffused profile with reduced peak values at later times. Similar behavior was observed for other species mass fractions as well.

16.2.2 Presumed PDF Approach in Flamelets

Flamelet-type models can be used to model the TCI term, which is represented by the Reynolds-averaged chemical source term in RANS and the filtered chemical source term in LES. The governing equations of RANS (LES) are used to numerically solve the Reynolds-averaged (filtered) flow and mixing fields and the flamelet solutions are then used to model the TCI term. For RANS, the mixing field is characterized by the Reynolds-averaged mixture fraction $\left(\widetilde{Z}\right)$, and the mixture fraction variance $\left(\widetilde{Z''^2}\right)$. For LES, the mixing field is characterized by the filtered mixture fraction $\left(\widetilde{Z}\right)$ and the subfilter mixture fraction variance $\left(\widetilde{Z''^2}\right)$. The governing equations for these quantities are discussed elsewhere (Kundu et al. 2014). The different flamelet approaches can be broadly classified into two types based on the means by which the flamelet solutions are coupled to the CFD solution—Representative interactive flamelet (RIF) models and tabulated models. The details of these two approaches are briefly described next.

16.2.3 Representative Interactive Flamelet (RIF) Model

In RIF models, the flamelet equations are solved during each time step as part of the CFD solution. The coupling between the flamelet solver and the CFD solver in RIF is schematically shown in Fig. 16.6. During each time step, the CFD solver provides the mixture fraction and scalar dissipation rate fields in each computational cell, which are then used as inputs to the flamelet solver. The solutions obtained from the flamelet solver are then integrated using presumed probability density functions (PDF) to obtain the Reynolds-averaged (filtered) species mass fractions.

Barths et al. (2000) introduced a multi-flamelet RIF model which has many advantages for jet flames. In this approach, multiple flamelets are transported and solved in order to account for the temporal and spatial variation of scalar dissipation in the computational domain. Multiple flamelets are sequentially injected into the computational domain along with the fuel. The flamelets are tracked with a marker probability equation for each flamelet (l) as shown below:

$$\frac{\partial\left(\bar{\rho}\widetilde{Z}_l\right)}{\partial t} + \frac{\partial\left(\bar{\rho}\widetilde{u}_i\widetilde{Z}_l\right)}{\partial x_l} = -\frac{\partial\left(\bar{\rho}\widetilde{u_l''Z_l''}\right)}{\partial x_l} + \overline{S}, \tag{16.12}$$

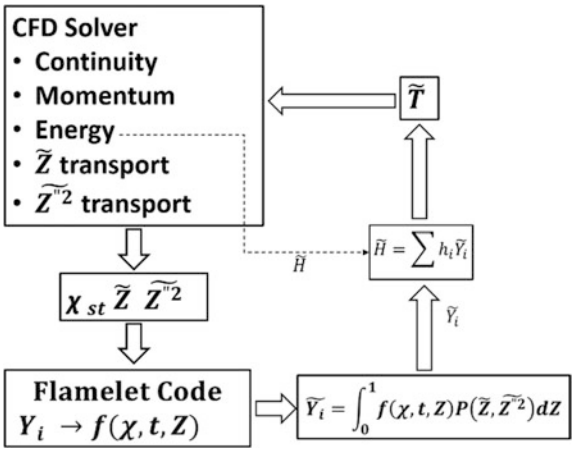

Fig. 16.6 Schematic of RIF model coupling with the CFD solver

where $\widetilde{u_l'' Z_l''}$ is typically approximated as $-D_t \frac{\partial \widetilde{Z}}{\partial x_i}$ based on the eddy diffusivity assumption. $\overline{S}$ is the mixture fraction source term which is obtained from the evaporation of the liquid fuel from the spray model. The markers also need to satisfy the condition that their sum is equal to the Reynolds-averaged (filtered) mixture fraction.

$$\widetilde{Z} = \sum_{l=1}^{n} \widetilde{Z}_l \tag{16.13}$$

The scalar dissipation rate for each flamelet is calculated as:

$$\widetilde{\chi_{st}}(l) = \frac{\int_{\widetilde{Z}}^{\widetilde{Z}_l} \bar{\rho} \widetilde{\chi_{st}^{\frac{3}{2}}} \widetilde{P}(Z_{st}) dv}{\int_{\widetilde{Z}}^{\widetilde{Z}_l} \bar{\rho} \widetilde{\chi_{st}^{\frac{1}{2}}} \widetilde{P}(Z_{st}) dv}, \tag{16.14}$$

where

$$\widetilde{\chi_{st}} = \widetilde{\chi} \frac{f(Z_{st})}{\int_0^1 f(Z) P(Z)\, dZ} \tag{16.15}$$

and

$$f(Z) = \exp\left[-2\left(erfc^{-1}(2Z)\right)^2 \right] \tag{16.16}$$

For RANS, $\widetilde{\chi}$ is the Reynolds-averaged scalar dissipation rate and is typically modeled as (Pitsch et al. 1998):

$$\widetilde{\chi} = C_\chi \frac{\tilde{\epsilon}}{\tilde{k}} \widetilde{Z''^2} \tag{16.17}$$

For LES, $\widetilde{\chi}$ is the filtered scalar dissipation rate and is typically modeled as (Tillou et al. 2014):

$$\widetilde{\chi} = \widetilde{\chi_{SGS}} + \widetilde{\chi_{res}} = \frac{D_t}{\Delta^2} \widetilde{Z''^2} + 2D \left| \nabla \widetilde{Z} \right|^2 \tag{16.18}$$

The flamelet equations Eqs. (16.6–16.7) are then solved during each CFD time step using the time-dependent stoichiometric scalar dissipation rates Eq. (16.7) for each flamelet to obtain the species mass fraction for flamelet l, $Y_{l,i}$. The effect of turbulence is modeled using a presumed PDF in the mixture fraction space.

$$\widetilde{Y}_{l,i}(x,t) = \int_0^1 Y_{l,i}(Z,t) P(Z;x,t)\, dZ \tag{16.19}$$

where $P(Z; x, t)$ is typically modeled using a beta PDF. The Reynolds-averaged (filtered) species mass fraction in each cell is then calculated as the weighted average of contributions from all n flamelets.

$$\widetilde{Y}_i = \sum_{l=1}^{n} \frac{Z_l}{Z} \widetilde{Y}_{l,i} \tag{16.20}$$

The use of RIF with multiple flamelets leads to a significantly improved prediction of the ignition and flame development phases especially in spray flames (Kundu et al. 2014). However, the computational expense of the multi-flamelet RIF approach has been found to be extremely high for two reasons:

- A large number of flamelets, typically 20–100, are required to accurately model the ignition and flame development, which necessitates the solution of 20–40 additional transport equations for these flamelets
- The integration with the presumed PDF during each time step for each flamelet Eq. (16.19) is extremely expensive when there is large number of CFD cells, especially for LES.

Due to these reasons, the more common approach to couple the flamelet solutions to the CFD solution is to use tabulated models which are explained next.

16.2.4 Tabulated Models

The alternative to the RIF models is the tabulated models, where the flamelet equations Eqs. (16.6–16.7) are solved a priori for different values of the

stoichiometric scalar dissipation rate, χ_{st}. These solutions are then integrated using presumed PDFs Eq. (16.19) and tabulated in low-dimensional manifolds. One of the most commonly employed tabulated model is the unsteady flamelet progress variable (UFPV) model (Ihme and See 2010) In the UFPV model, the flamelet solutions are pre-tabulated in terms of four variables—$\widetilde{Z}$, $\widetilde{Z''^2}$, χ_{st}, and C.

$$\widetilde{Y}_i = \widetilde{Y}_i\left(\widetilde{Z}, \widetilde{Z''^2}, \chi_{st}, C\right) \tag{16.21}$$

Here, C is the progress variable and represents the reaction progress and varies from 0 in the unreacted mixture and 1 in the fully burned mixture. Several definitions have been used to define C. Two of the most common definitions are:

$$C = \frac{T - T_u}{T_b - T_u} \tag{16.22}$$

$$C = Y_{CO} + Y_{CO_2} + Y_{H_2O} + Y_{H_2} \tag{16.23}$$

When used with RANS or LES, an additional transport equation needs to be solved for the Reynolds-averaged (filtered) progress variable, $\widetilde{C}$.

$$\frac{\partial \bar{\rho}\widetilde{C}}{\partial t} + \nabla \cdot \left(\bar{\rho}\tilde{v}\widetilde{C}\right) = \nabla \cdot \left(\bar{\rho}D_t \nabla \widetilde{C}\right) + \bar{\rho}\widetilde{\dot{\omega}_c} \tag{16.24}$$

Here, $\widetilde{\dot{\omega}_c}$ is the chemical source term of the progress variable which is obtained from the flamelet solution and is also pre-tabulated using the same four independent variables—$\widetilde{Z}$, $\widetilde{Z''^2}$, χ_{st}, and C. During the CFD simulation, in addition to the transport equations for density, momentum, and energy, three additional transport equations for $\widetilde{Z}$, $\widetilde{Z''^2}$, and $\widetilde{C}$ are solved and then the pre-tabulated flamelet solutions are accessed to obtain the species mass fractions and temperature in each computational cell. Several other tabulated models have also been proposed based on the concept of a progress variable to quantify the progress of the reactions including Flamelet Generated Manifold (FGM) models (Van Oijen et al. 2001) and Flame Prolongation of ILDM (FPI) models (Fiorina et al. 2003).

These tabulated models are significantly cheaper than the RIF model due to the need for a significantly smaller number of additional transport Eqs. (3 for tabulated models vs. 20–100 for RIF) and the use of pre-integrated tables which negates the need for the expensive integration using presumed PDFs. However, the nature of the solutions have been found to depend strongly on the choice of the definition of the progress variable (Ihme et al. 2012) Also, the use of a single progress variable to represent the progress of every chemical species from initial unburned to the final burned state can lead to large errors, especially for larger hydrocarbons.

16.2.5 Tabulated Flamelet Model (TFM)

Recently, the Tabulated Flamelet Model (TFM) approach for combustion modeling was developed (Ameen et al. 2016; Kundu et al. 2017a, b, c) specifically for spray flames. This model is a time-accurate tabulated version of the multi-flamelet RIF model, which attempts to combine the high accuracy of the RIF model and the low computational expense of the tabulated models. In the TFM approach, the pre-integrated flamelet solutions are tabulated in terms of four variables —t, χ_{st}, $\widetilde{Z''^2}$, $\widetilde{Z}$. Notice that the progress variable is now replaced using the physical time, t. Similar to the RIF model, multiple flamelets are transported to account for the temporal and spatial variation of the flamelet structure. Each flamelet in the computational domain has its own residence time and scalar dissipation rate. The residence time of a flamelet is given by the time elapsed since its injection into the domain. The contribution of flamelet l is obtained using the table lookup given by a four-dimensional linear interpolation:

$$\widetilde{Y}_{l,i} = \widetilde{Y}_{l,t}\left(\widetilde{Z}_l, \widetilde{Z''^2}, \widehat{\chi_{st}}(l), t_l\right) \tag{16.25}$$

The species mass fraction at each cell is then calculated as the weighted average of contributions from all flamelets as shown in Eq. (16.13). The coupling of TFM with the CFD solver is schematically shown in Fig. 16.7.

The use of residence time in the TFM approach leads to a significant reduction in errors associated with using a progress variable in other tabulated models. The use of pre-integrated low-manifold tables avoids the need to solve the flamelet

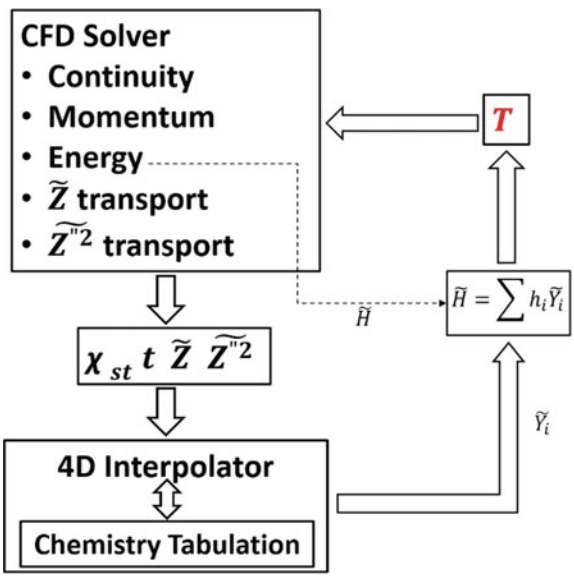

Fig. 16.7 Schematic of TFM coupling with the CFD code

equations and integrate the flamelet solutions during each time step as needed by the RIF model, leading to significantly lesser computational expense. In the rest of this chapter, the applicability of the TFM approach for RANS and LES of spray flames and optical engines will be demonstrated.

16.3 Engine Combustion

16.3.1 LES of Sprays Under IC Engine Conditions

For simulating sprays under IC engine conditions, RANS-based approaches have been traditionally preferred. These studies (Reitz and Rutland 1995; Lucchini et al. 2009; Som and Aggarwal 2010) have shown that the RANS approach, coupled with accurate turbulence, spray, and combustion models, can predict several global flow and combustion characteristics with reasonable accuracy. These characteristics include the penetration of the liquid phase (liquid length), vapor penetration, ignition delay and flame lift-off length. However, RANS approaches do not perform well in predicting the instantaneous structures during the transient development of the spray and flame. The accurate prediction of soot and NOx emissions in diesel engines are dependent on the transient nature of the reacting turbulent jet. Additionally, the large-scale structures present in the turbulent jet are likely to influence the mixing and subsequent soot and NOx formation mechanisms. Recently, LES has emerged as a powerful tool to study the mechanism of flame lift-off and the major factors affecting it as it can accurately resolve the large-scale mixing and transient effects.

Xue et al. (2013) compared the performance of RANS and LES approaches in predicting the instantaneous structure of a non-reacting spray. Figure 16.8 compares the instantaneous mixture fraction contours predicted by RANS and LES models with the experimental measurements for the ECN Spray H (https://ecn.sandia.gov/) at non-reacting conditions. The ECN Spray H experiment consists of an injection of n-heptane spray into a constant volume combustion chamber with optical access. For the RANS simulations, the RNG k-ε turbulence model was used, and for LES, the dynamic structure subgrid scale (SGS) model was used. A grid size of 62.5 μm was used for both RANS and LES. It can be seen that the RANS results show a smooth and diffused structure of the vapor jet with averaged flow structures. However, LES predictions show similar instantaneous flow structures and vapor penetrations as those measured experimentally.

Pei et al. (2015) performed LES and RANS simulations of the reacting ECN Spray A flame. ECN Spray A is similar to Spray H, but the fuel is n-dodecane instead of n-heptane. A perfectly stirred reactor (PSR) approach was used to model the turbulence-chemistry interaction. Figure 16.9 compares the temperature contours showing the transient flame development behavior predicted by these two approaches. The RANS simulations show the formation of a single dominant

ignition kernel at the leading edge of the jet, which propagates upstream before stabilizing at the flame lift-off location. In contrast, LES predicts the formation of multiple ignition kernels along the peripheries of the jet, which grow, merge and stabilize at the flame lift-off length. Even though the steady lift-off lengths predicted by RANS and LES are similar, the mechanism of flame stabilization is seen to be vastly different. The differences in the flame development, in turn, cause large differences in the pollutant predictions. Figure 16.10 compares the soot mass fraction distributions predicted by these two approaches with the experimentally measured soot luminosity. It can be seen that LES is able to predict the location and extent of the soot cloud accurately, whereas RANS predicts a smaller soot cloud at upstream locations as compared to the experiment.

The accuracy of LES in simulating spray flames is strongly dependent on four factors—subgrid model, spray model, grid size, and turbulent combustion model. Xue et al. (2013) studied the effects of the choice of SGS and spray models on the accuracy of LES. Two different SGS models were chosen—Smagorinsky model (Smagorinsky 1963), which is based on the eddy diffusivity hypothesis, and the dynamic structure (DS) model (Pomraning and Rutland 2002), which is not based on the eddy diffusivity hypothesis. Figure 16.11 shows the effect of the SGS model on the liquid and vapor penetrations for the non-reacting ECN Spray A. It is observed that the choice of the SGS model plays only a minor role on the predicted liquid and vapor penetrations. There are relatively large discrepancies in the liquid penetrations predictions and measurements. The reason for this is that the spray

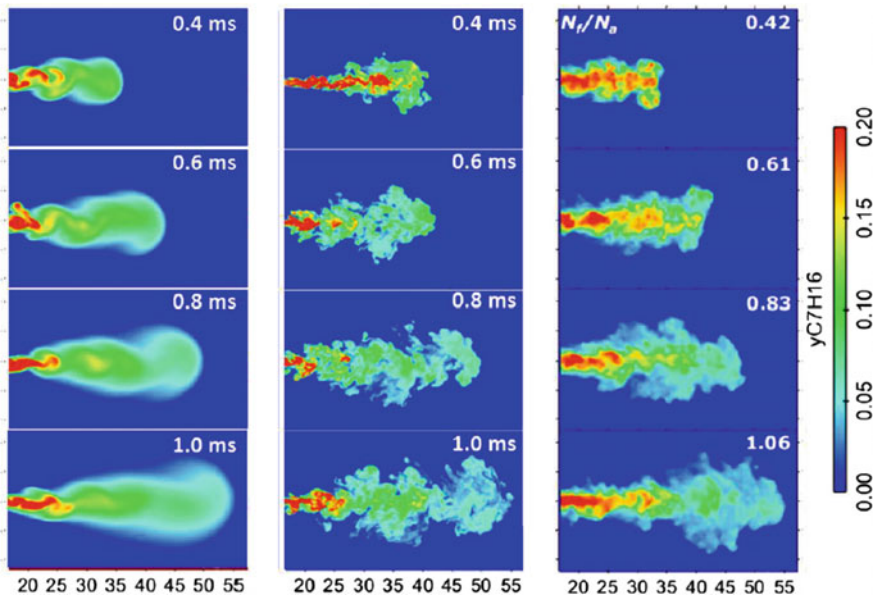

Fig. 16.8 Instantaneous mixture fraction distribution for Spray H from (left) RANS, (middle) LES, and (right) Experiment

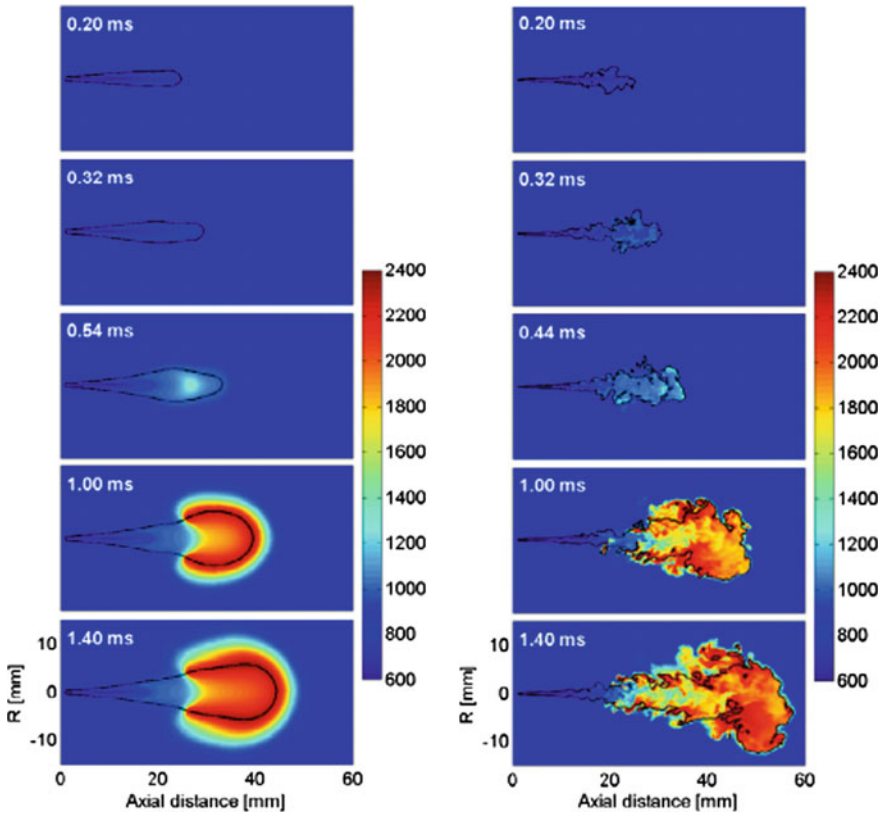

Fig. 16.9 Temporal evolution of temperature contours for (left) RANS and (right) LES of the ECN Spray A flame at the 900 K ambient temperature condition

model constants were tuned based on the RANS model simulations. In these simulations, the Kelvin–Helmholtz and the Rayleigh–Taylor models were used to predict the droplet breakup (Patterson and Reitz 1998) for the dispersed phase. The value of the Kelvin–Helmholtz constant, B_1, can strongly affect the liquid

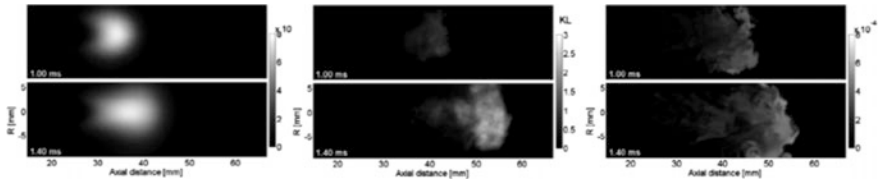

Fig. 16.10 Soot comparison from (left) RANS (mass fraction), (middle) Experiment (KLfactor), and (right) LES (mass fraction) at 1 and 1.4 ms for the ECN Spray A flame at 900 K ambient temperature condition

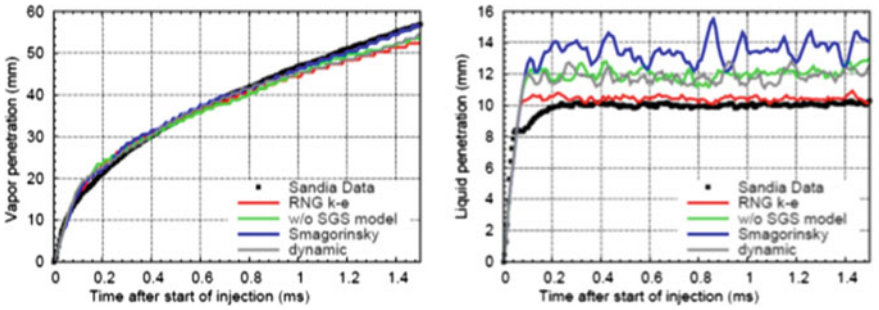

Fig. 16.11 Vapor and liquid penetrations for non-reacting Spray A predicted by different SGS models

penetration, as shown by Xue et al. (2013). Figure 16.12 shows the effect of B_1 on the liquid and vapor penetrations. It can be seen that the results with $B1 = 5$ are in better agreement with the experimental data for LES. On the other hand, the vapor penetration does not show much variation with the change of B_1. Thus, it is seen that better liquid penetration results can be obtained using LES models with the marginal tuning of the spray breakup constants without influencing the vapor penetration characteristics.

Figure 16.13 shows the effect of grid size on the liquid and vapor penetrations for the non-reacting ECN Spray A. The DS SGS model was used for all the simulations. It is observed that for very coarse grids (0.25 mm), LES is strongly dependent on the SGS models and is unable to resolve the global parameters accurately. With the use of finer grids, the LES results demonstrate the convergence of both liquid and vapor penetrations and show good agreement with experimental data for vapor penetration on 0.0625 mm grid or finer. Figure 16.14 compares the effect of grid size on the ignition delay and flame structure for reacting ECN Spray A flame. It is seen that using a 0.0625 mm grid leads to good predictions for the reacting cases as well. Quantitatively, the ignition delays match with the

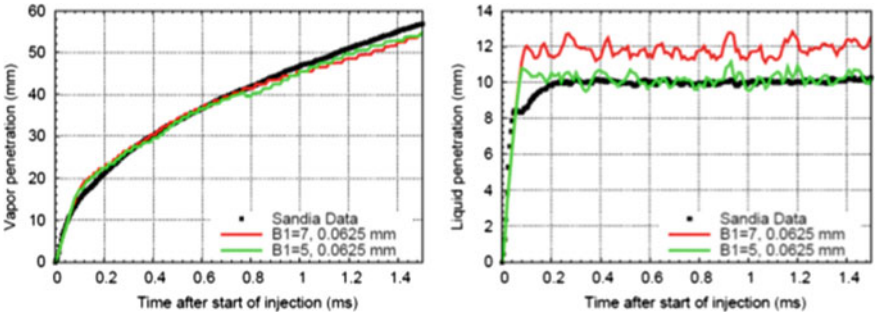

Fig. 16.12 Effects of spray breakup constant (B_1) on vapor and liquid penetrations for spray A predicted by the LES dynamic structure model

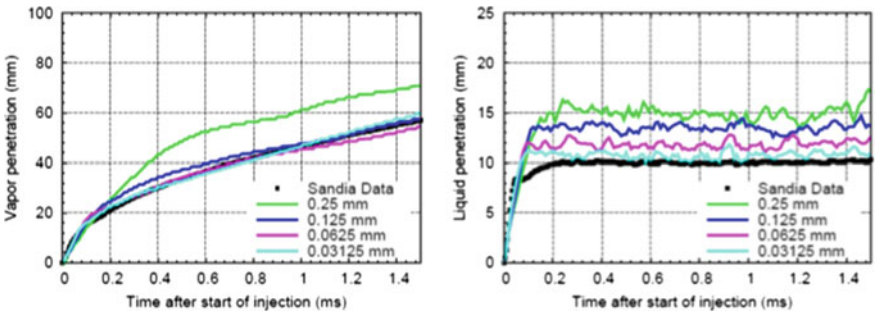

Fig. 16.13 Vapor and liquid penetrations for non-reacting ECN Spray A predicted by the LES dynamic structure model

experimental predictions at all temperatures except at the lower temperature of 800 K. The reason for this is due to the inadequate turbulent combustion model, which will be discussed in a later section.

The fourth major factor affecting the LES accuracy is the choice of the turbulent combustion model. As explained in an earlier section, the TFM model is a turbulent combustion model which combines the accuracy of the RIF model with the speedup of tabulated models. Figure 16.15 compares the ignition delay and lift-off lengths predicted by the TFM model with the homogeneous reactor model (HR-MZ) with multi-zoning to reduce computational expense, for the ECN Spray A flames. The traditional HR-MZ model consists of a transport equation for each species along with a source term calculated using the chemistry mechanism. For the ignition delay, it can be seen that the TFM model has less than 5% error with experiments for ambient temperatures of 900 K and above, and a 10% error for the 800 K case. The HR-MZ model, however, shows a much larger error at all ambient

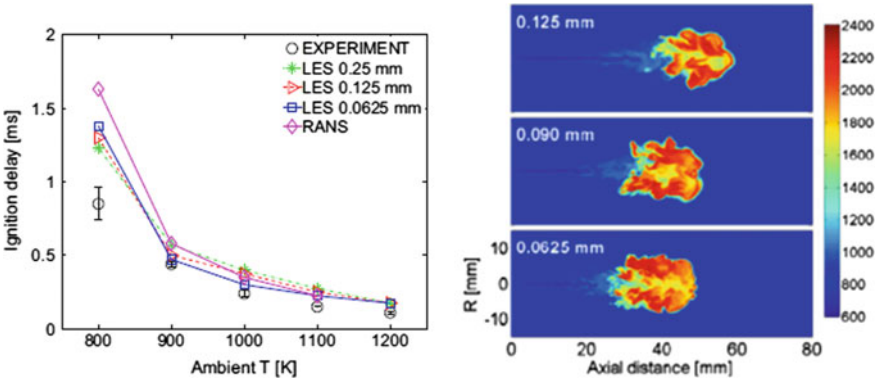

Fig. 16.14 (left) Comparison of predicted ignition delay with different LES grid sizes compared with experimental measurements. (right) Contours of temperature at 1 ms along the spray axis for different LES grid sizes. All Simulations are performed for ECN Spray A

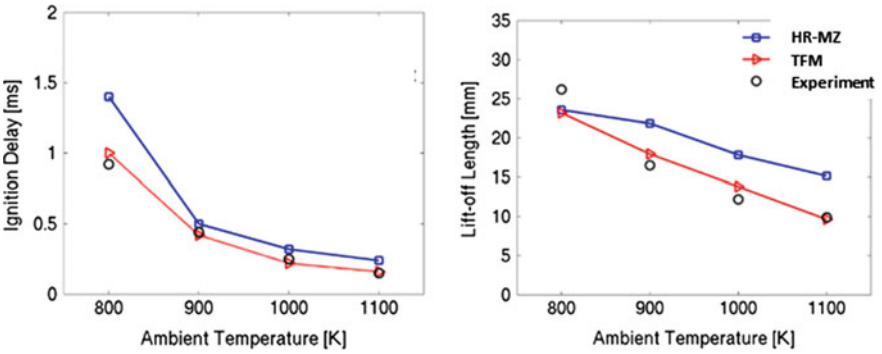

Fig. 16.15 Comparison of (left) ignition delay and (right) lift-off lengths for the TFM and HR-MZ models for LES of ECN Spray A at different ambient temperatures

temperatures, especially at 800 K. TFM model also shows good agreement for the lift-off length predictions at all ambient temperatures. Figure 16.16 compares the wall-clock time required to simulate 1 ms on 200 processors for the TFM and HR-MZ models. It can be seen that the TFM model demonstrates at least 1.5× speedup over the HR-MZ model for all ambient temperatures. Higher speedups are expected for larger chemistry mechanisms.

Figure 16.17 compares the temperature contours for the two turbulent combustion models at 1 ms for different ambient temperature cases. For both the models, the flame stabilization location is observed to move further upstream as the ambient temperature is increased. This is in agreement with experimental observations (https://ecn.sandia.gov/). It is also observed that the TFM model predicts lower peak temperatures than the HR-MZ model. This is along expected lines due to the inclusion of TCI through the use of presumed PDF for the mixture fraction. Another difference between the HR-MZ and the TFM models is that the TFM model predicts a weak flame at the upstream locations characterized by lower temperatures. This is due to the larger effect of TCI at these locations. The HR-MZ

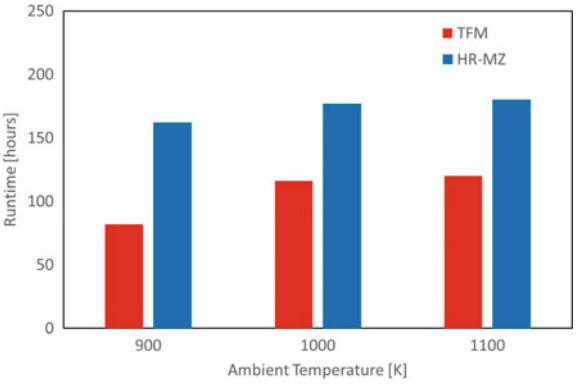

Fig. 16.16 Comparison of the computational time between the TFM and HR-MZ for various ambient temperature conditions. All the simulations were run on 200 processors

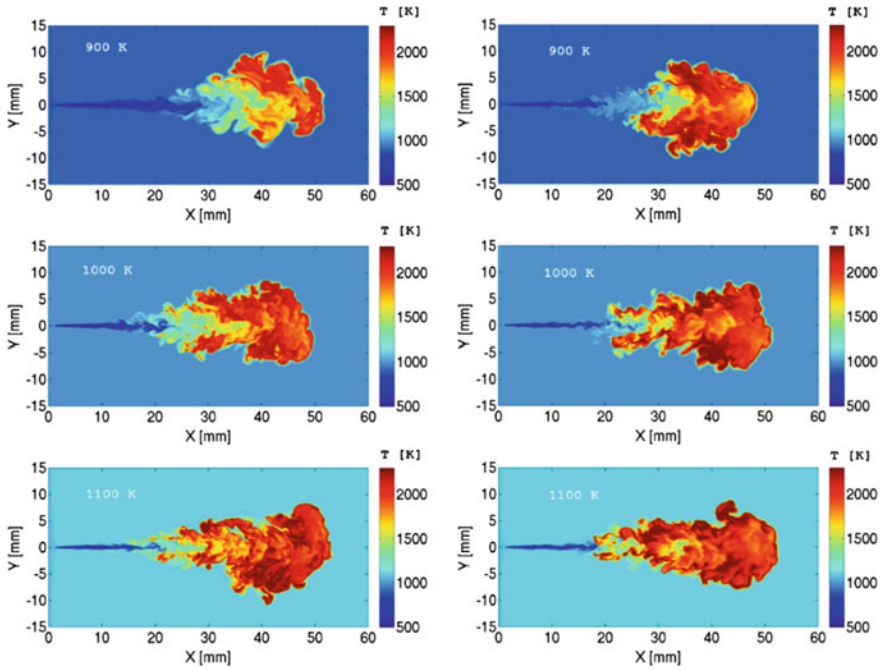

Fig. 16.17 Temperature contours at 1 ms for TFM (left) and HR-MZ (right) at different ambient temperatures

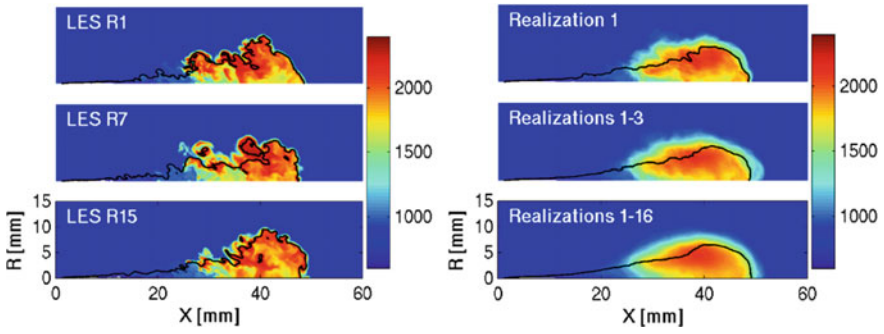

Fig. 16.18 (left) Temperature contours at 1 ms for three different realizations—R1, R7, and R15. (right) Contours of azimuthally averaged temperature at 1 ms averaged over different number of realization

model, however, predicts an equally strong flame all along the flame front, even near the flame stabilization location.

When LES is employed to make quantitative predictions, it is important to perform multiple realizations. LES is a statistical model of turbulence which can

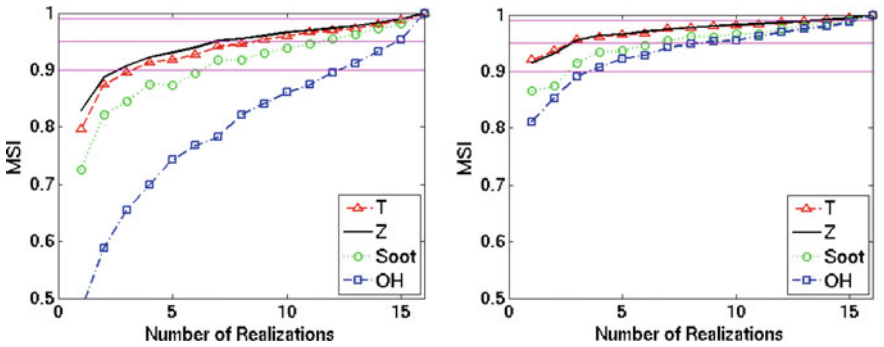

Fig. 16.19 Variation of MSI of temperature, mixture fraction, OH, and soot as a function of number of realizations for (left) no azimuthal averaging and (right) with azimuthal averaging

predict the correct statistics of the large scales of motion. Also, subgrid scale models for LES are derived in a statistical sense and are not exact unless some kind of statistical averaging is performed. For simulating spray flames, the most commonly employed means of performing multiple LES realizations is by perturbing a random seed in the spray models which influences the droplet initialization and turbulence-spray interaction (Ameen et al. 2016). Figure 16.18 shows the spatial distribution of temperature at 1 ms for three different LES realizations of the ECN Spray A flame. It is seen that there are noticeable differences in the flame structures for the different realizations. For instance, for realization R7, a separated flame surface is observed at an axial location of 40 mm and radial location of 10 mm, which is not observed for the other realizations. Pei et al. (2015) showed that the lift-off lengths for multiple realizations can vary by as much as 5 mm. Figure 16.18 also shows the statistically averaged temperature profiles obtained by averaging over 128 azimuthal planes and multiple realizations. Azimuthal averaging is valid here since the computational domain and boundary conditions are axisymmetric for this flame. It is observed that the differences between the mean temperature based on the 3 and 16 realizations are relatively small. Ameen et al. (2016) showed similar observations for a statistical mean of mixture fraction, OH mass fraction, and soot mass fraction.

The minimum number of realizations required to obtain self-similar profiles for the statistical averages can be quantified using relevance indices such as the magnitude similarity index (MSI). MSI is a number which ranges between 0 and 1 and quantifies the similarity in the spatial distributions of two scalar fields. Larger values of MSI denote stronger similarity and a value of 0.9 is considered to be a strong similarity. Figure 16.19 shows the variation of MSI with increasing number of LES realizations with and without azimuthal averaging. It is seen that the use of azimuthal averaging leads to a reduction in number of LES realizations to obtain statistical means from 13 to 3. It is also observed that quantities with short temporal and length scales like Y_{OH} and soot require more number of realizations than temperature or mixture fraction.

16.3.2 Low-Temperature Combustion

Traditional diesel engine combustion involves the injection of liquid fuels into high temperature and pressure conditions. The resulting flame is a typical diffusion flame, where the dynamics of spray evaporation and mixing play a dominant role. At these high temperatures, the chemical timescales are much smaller than fluid timescales and the chemistry can be assumed to be infinitely fast and mixing turns out to be the major rate-determining step. However, diesel combustion is typically subject to reactions occurring at higher equivalence ratios accompanied by the classical limitation of NOx-soot tradeoff. If the overall temperature of combustion is increased, the soot gets oxidized, however, this leads to an excess formation of NOx. The opposite trend is observed for lower temperatures. This can be represented on a regime diagram shown by equivalence ratio on the Y axis and temperature on the X-axis. As shown in Fig. 16.20, each point in the combusting domain can be represented in the equivalence ratio—temperature (ϕ-T) space. The soot peninsula and NOx islands represent the regions where formation reactions of these pollutants are very high.

Low-temperature combustion concepts in CI engine technologies aim to reduce the overall temperatures and equivalence ratios and shift the combustion in the ϕ-T space away from the soot and NOx forming regions. This reduces the pollutant formation drastically and retains the high-thermal efficiencies of CI engines. The HCCI concept involves the introduction of fuel into the cylinder at the intake stroke such that it forms a homogeneous mixture. The compression and subsequent autoignition ensure a much leaner combustion at lower temperatures. PPCI and GCI are low-temperature combustion concepts where the fuel is injected much before top dead center (TDC) such that the resulting fuel–air mixture is not homogeneous in composition and temperature. The ignition at low-temperature regimes are

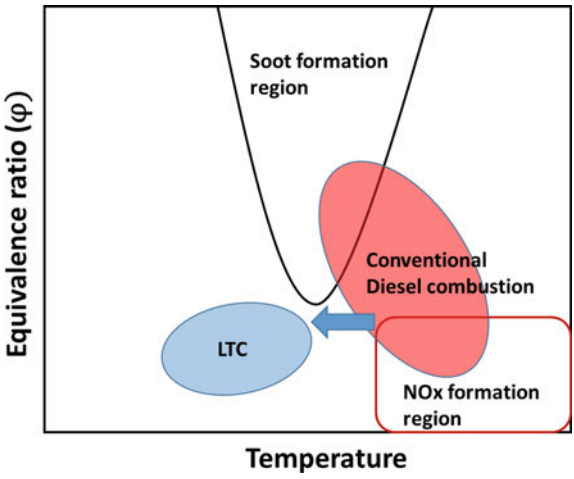

Fig. 16.20 Soot-NOx tradeoff in equivalence ratio —temperature space

controlled by chemical kinetics and the interactions with the turbulent flow field. Predicting the start of combustion under such conditions is challenging and depends on a number of competing factors. This is in contrast with traditional CI and SI engine technologies. In CI, the start of fuel injection and in SI the spark timing can be carefully controlled to control the start of combustion. As a result, designing LTC (low-temperature combustion) engines under varying load conditions and low load conditions is challenging and has prevented their practical application. This section outlines the role of TCI and chemical kinetics at low-temperature conditions.

Numerical methods have been used to understand combustion at LTC regimes. A number of fundamental studies using DNS have been carried out in the past to investigate autoignition processes at these LTC conditions. Numerical and experimental studies have shown flames to extinguish at higher scalar dissipation rates. DNS studies (Borghesi et al. 2013) of an n-heptane spray at 40 atm and 1000 K condition showed that at higher compositional stratification, the presence of high scalar dissipation rates leads to an increase in ignition delays. This is applicable for typical diesel combustion. However, at lower compositional gradients, an increase in scalar dissipation leads to the reduction in ignition delays (Mukhopadhyay and Abraham 2011). This was also observed in DNS of a Dimethyl Ether (DME) mixing layer problem (Minamoto and Chen 2016). It must be noted that such DNS studies are feasible for small domains and lower pressures. It is not feasible to carry out such simulations for low temperature, high-pressure conditions which are found in engines. Multiphase spray flame simulations at engine conditions using DNS is currently not within the reach of computational resources. The chemical kinetics at low-temperature conditions behave differently compared to high temperatures. Within a certain range of temperatures, the ignition delays of hydrocarbons reduce with increase in temperature. This is known as the negative temperature coefficient (NTC) regime. The chemical kinetics coupled with turbulence controls the ignition process and thus it becomes important to include these coupled effects in engine simulations. Flamelet models have proved to be a useful tool due to their relatively low cost and ability to include TCI effects along with high fidelity chemistry. LES at low-temperature conditions has been used to shed light on autoignition at high pressure and large timescale spray combustion problems.

The TFM method was used to simulate combustion of a single injection of liquid n-dodecane at 750 K ambient temperature condition. Some comparative studies are shown with the case with 900 K ambient temperature condition. The LES setup is similar to the one shown in the previous section. It consists of second-order accuracy discretization in space and first order in time. The jet penetration from simulations in validated against the available experimental data in Fig. 16.21.

The ignition process along with the formation of intermediate species with respect to time is shown in Fig. 16.22. The spray is injected at time $t = 0$. The maximum temperature in the domain is plotted against time. The first sign of temperature rise is the first stage ignition which is observed at 1.5 ms. Formaldehyde (CH_2O) is an important intermediate species and its formation marks the start

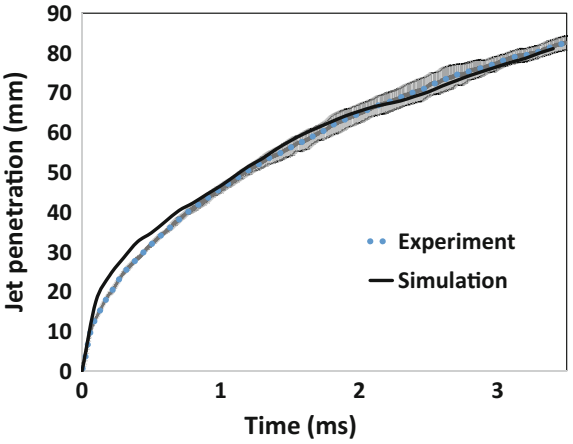

Fig. 16.21 Jet penetration vs time at low-temperature engine conditions. The LES results are compared with experimental data

of this process. The concentration of formaldehyde increases sharply and then reaches a quasi-steady state. Higher hydrocarbon fuels usually show this type of two-step ignition process. The first stage ignition, i.e., low-temperature heat release, is identified by the formation of intermediate species like CH_2O. These species subsequently get oxidized during the high-temperature heat release. High-temperature regions are characterized by the formation of OH radicals.

These processes can be visualized in the 3D domain as shown in Fig. 16.23. The formation of formaldehyde is observed in the core of the jet. As these mixtures get transported towards the periphery of the jet, the formaldehyde gets consumed with the formation of high-temperature regions at the jet periphery along with the formation of OH radicals.

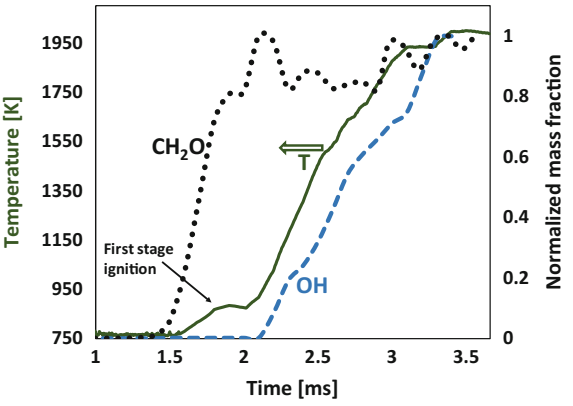

Fig. 16.22 Evolution of intermediate species (CH_2O), high temperature species (OH) and maximum temperature during the autoignition of an n-dodecane spray at 750 K ambient temperature conditions

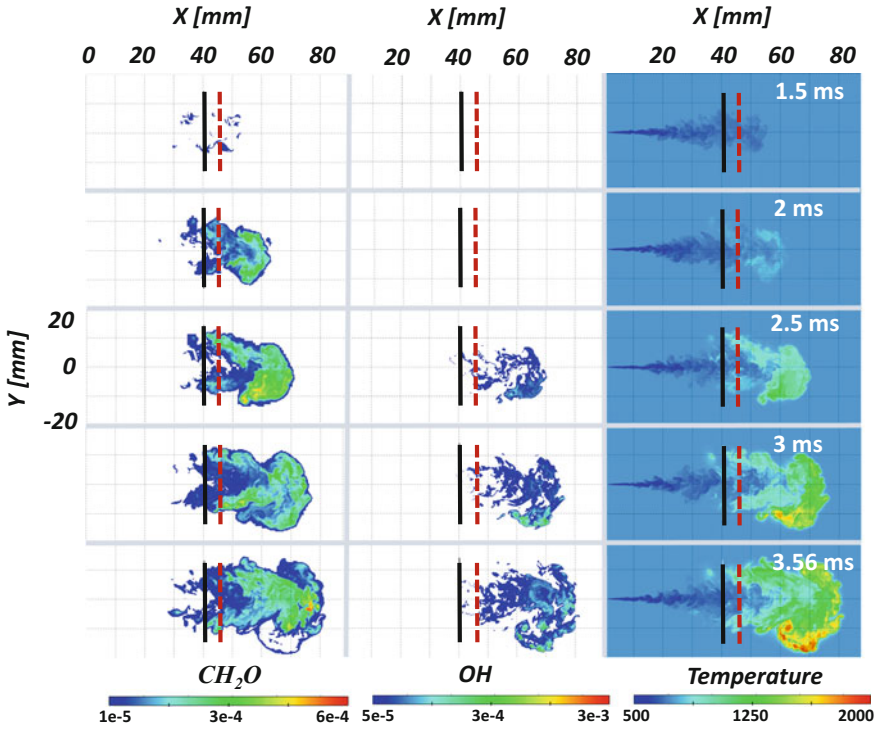

Fig. 16.23 Temporal evolution of CH_2O, OH mass fraction, and temperature contours at 750 K predicted by TFM. The vertical solid line represents the measured lift-off length from experiments using Injector1 and the dashed line represents the measured lift-off length from Injector 2

16.3.2.1 Role of Turbulence-Chemistry Interaction

The two-stage ignition process coupled with the effects of turbulent flow fields at lean conditions play an important role in how the flame ignites and stabilizes in LTC regimes. Homogeneous reactor combustion models that neglect TCI effects fail to predict ignition at such conditions. A one-dimensional study is carried out to understand this phenomenon. The unsteady flamelet equations are first solved with scalar dissipation rate (χ_{st}) equal to 0. Another set of flamelet equations are then solved with $\chi_{st} = 2\ s^{-1}$. The flamelets are subject to same boundary conditions as previously described for the spray flame at 750 K. The results are compared in Fig. 16.24. The case with $\chi_{st} = 0$ represents a homogeneous reactor. The temporal evolution of temperature in the mixture fraction space is shown from $Z = 0$ to $Z = Z_{st}$. This is the lean region. It can be observed that these lean regions ignite earlier for the case with finite scalar dissipation rate. At low temperatures, the

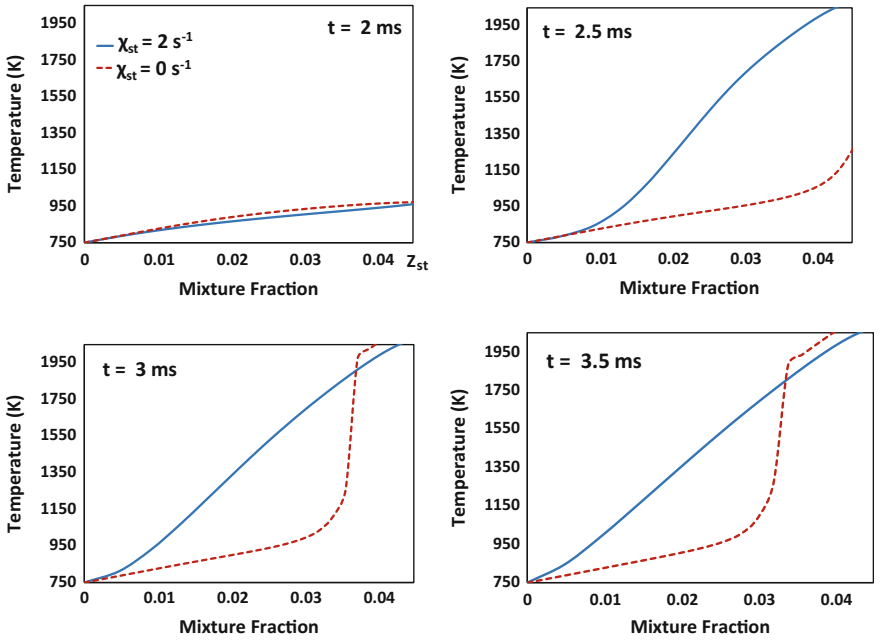

Fig. 16.24 Ignition of flamelets at 750 K for two conditions: (i) Stoichiometric scalar dissipation rate = 2 s^{-1} (solid line) (ii) homogeneous reactor assumption (dashed)

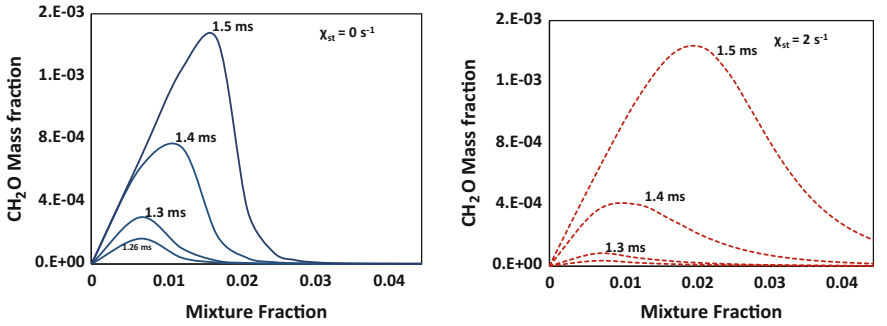

Fig. 16.25 CH_2O formation in mixture fraction space plotted for (i) homogeneous reactor case on left (i.e., 0 s^{-1}) and (ii) flamelet with stoichiometric scalar dissipation rate of 2 s^{-1}. The species profiles with scalar dissipation get broadened in the Z space due to diffusion leading to higher concentration of radicals and intermediate products in the near stoichiometric regions

ignition delays are substantially longer. As a result, the igniting spray flame is substantially leaner by the time ignition is observed.

In order to further understand this process, the species mass fractions are compared for this lean region for the two cases. Figure 16.25 shows the temporal evolution of CH_2O. In both cases, the formation of CH_2O is observed at mixture fractions lower than 0.01. The peak then moves toward the stoichiometric mixture fraction as time progresses. The homogeneous reactor case is characterized by higher CH_2O concentrations. At the corresponding time instant, the nonzero scalar dissipation rate case (Fig. 16.25 right) shows a diffused profile with lower peak values. As a result of diffusion, the radicals and intermediate species near the stoichiometric regions reach a higher value compared to the homogeneous reactor case. This enhances the ignition process and leads to the main ignition event which then propagates into the lean regions. It is observed that in absence of this diffusion, the main ignition does not take place in the lean regions. Hence, the homogeneous reactor case cannot predict any ignition for the spray flame at the 750 K condition.

Thus, at low-temperature combustion scenarios, scalar dissipation is observed to enhance autoignition. These effects along with the formation of radicals and intermediate species during the first stage of ignition need to be captured by the combustion model for high fidelity engine models that are used to design LTC engines.

16.3.3 Detailed Chemistry Mechanisms in CFD

As discussed in the previous sections, the autoignition and flame stabilization process is a result of some complex interactions between the turbulent flow field coupled with the formation of intermediate species and radicals. Detailed chemistry mechanisms are required to accurately predict these intermediates and the low-temperature heat release. The stiffness of large chemistry mechanisms has been a major hurdle toward predictive engine simulations. As a result, detailed chemistry mechanisms with a few thousand species need to be reduced based on the target conditions so that they can be accommodated within the available computational resources. The computational cost of simulations typically increases super-linearly with the number of species and reactions. The reduction of chemistry mechanisms is carried out by matching 0D ignition delays and flame speeds. The reduced mechanism is applicable over limited equivalence ratio, temperature, and pressure ranges. The reduction process does not ensure the preservation of the entire chemistry pathway. The ignition process and pollutants like soot are also dependent on these chemistry pathways and intermediate species. The flamelet methodology offers the distinct advantage of decoupling chemistry and fluid flow and can be used to address this issue.

Recent advances in Ordinary Differential Equation (ODE) solvers have tried to address this problem. To improve the computational efficiency, the traditional (Variable coefficient ODE) VODE solver can be replaced by the sparse stiff

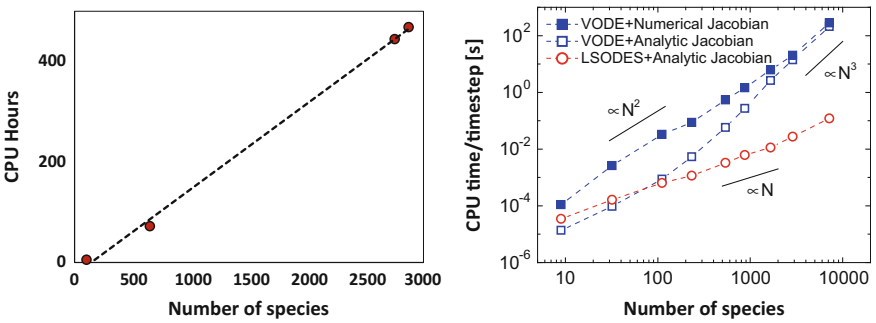

Fig. 16.26 (i) Computational cost for generating flamelet libraries as a function of species in the mechanism (left). (ii) CPU time per time step as a function of number of species in a mechanism for different chemistry solvers (right)

LSODES solver (Livermore Solver for ODEs in Sparse form) (Xu et al. 2016). The numerical Jacobian calculated at each time step is replaced by an analytical Jacobian which can be derived a priori for any given reaction mechanism. This reduces the computational cost for each time step significantly. Figure 16.26 shows the average CPU time per time step as a function of a number of species in a mechanism for 0D constant-pressure autoignition of stoichiometric mixtures at a pressure of 20 atm and initial temperature of 1000 K for different solvers. Different mechanisms for hydrogen (Li et al. 2004), ethylene (skeletal) (Luo et al. 2012), methane (Wang 2007), iso-octane (skeletal) (Lu and Law 2006), *n*-heptane (Mehl et al. 2011), iso-octane (Mehl et al. 2009), *n*-tetradecane (Westbrook et al. 2007), methyl decanoate (Herbinet et al. 2008), and *n*-icosane (Westbrook et al. 2007) are employed with number of species ranging from 9 to 7171. The setup with the traditional VODE solver and numerical Jacobian shows that the computational cost is approximately proportional to the square of the number of species for mechanisms with less than 2000 species. This cost decreases with the implementation of an analytical Jacobian. However, for mechanisms with more than 2000 species, due to the expensive LU decomposition, the use of analytical Jacobian does not gain much speedup and the computational cost is now proportional to the cube of the number of species as shown in Fig. 16.26. This is one of the main challenges in implementing highly detailed chemistry in CFD simulations. With the implementation of the LSODES solver along with analytical Jacobian, the computational cost is observed to be directly proportional to the number of species. This linear cost scaling is observed even for mechanisms with more than 10^3 species, thus making the implementation of such large detailed chemistry models realizable for high fidelity engine simulations when coupled with the flamelet solver.

It is also observed from Fig. 16.26 that the computational cost for generating the flamelet library with this framework is linearly proportional to the total number of species in the chemistry mechanism. This behavior is same as the linear behavior observed in the 0D simulations with the LSODES solver and analytical Jacobian. This shows that the computational cost with respect to a chemistry mechanism of

the flamelet library generator is strongly dependent on the chemistry solver and its numerical scheme. The cost of solving the diffusion part and PDF integration is relatively small and scales linearly with the total number of species.

16.3.3.1 Spray Flame Simulations with Detailed Chemistry

The improved flamelet chemistry solvers can be used to generate flamelet libraries to model the combustion in CFD using a flamelet model. The previously described spray flame problem is modeled using the detailed chemistry mechanism and validated against experimental data. The detailed n-dodecane chemistry with 2755 species is used for the CFD simulation and the results in Fig. 16.27 show a good match with the experimental observations.

16.3.3.2 Intermediate and High-Temperature Species

Formaldehyde is one of the intermediate species formed during the combustion of higher hydrocarbons. It indicates the first stage ignition, i.e., the cool flame region. Experimental work by Skeen et al. (2015) employed simultaneous Schlieren and formaldehyde PLIF imaging to investigate the low-temperature ignition events for the Spray A conditions. The experiments confirmed the formation of CH_2O in the cool flame region. The PLIF images show that the low-temperature reactions initiate at the periphery of the jet. These PLIF images were recorded for a single shot injection event. The comparisons between experiments and simulation are shown in Fig. 16.28 up to 490 μs which is approximately the start of the high-temperature ignition. Comparisons are made against a single LES realization as the experimental results consist of data from a single shot. The PLIF images are false color images obtained from the experiments. The CH_2O mass fraction contours from the simulations are colored using the same scale. At 140 μs the experiments do not detect

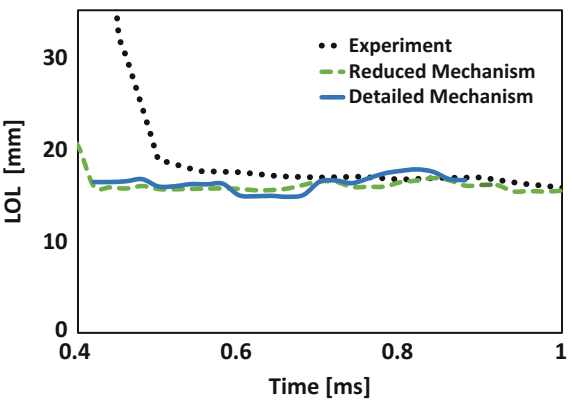

Fig. 16.27 Flame lift-off length evolution for the two mechanisms compared against experimental measurements

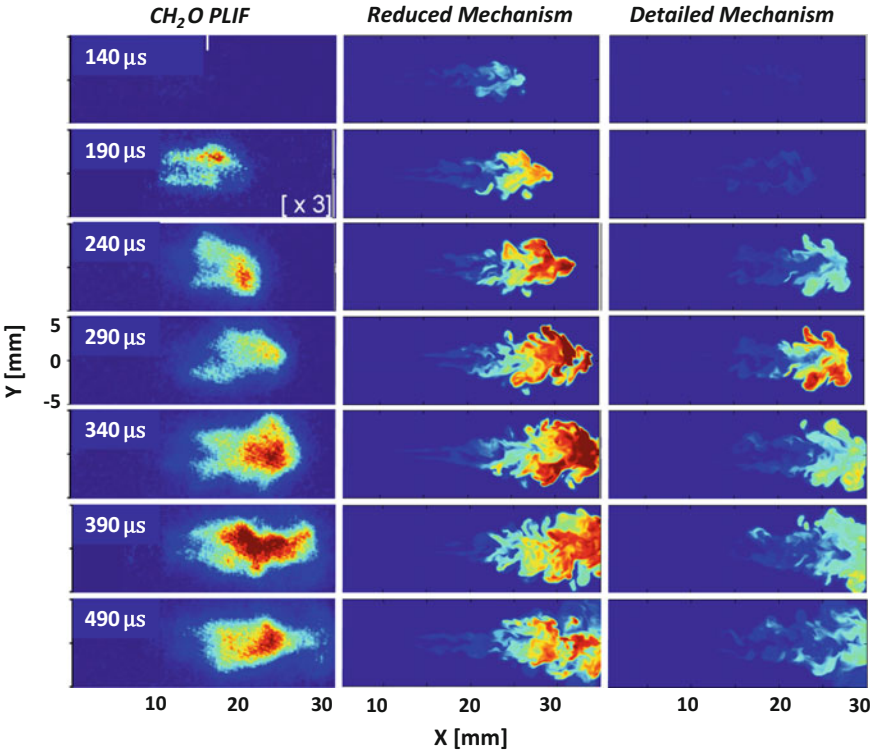

Fig. 16.28 Single shot CH_2O PLIF images from experiments are compared against model predictions from the reduced and detailed mechanisms at different times. The ambient conditions are for the baseline Spray A case with an ambient temperature of 900 K and 15% ambient O_2 concentration. The PLIF images are based on the false color images

any signal indicating the absence of the intermediate species. The detailed chemistry mechanism does not show any CH_2O formation at this time. The reduced mechanism, on the other hand, predicts formaldehyde formation at an earlier stage. As the jet penetrates, CH_2O gets transported toward the centerline. The cool flame regions, indicated by CH_2O formation, are observed to start at approximately 15 mm from the injector and extends up to 25 mm in the experiments at these conditions. Both mechanisms are able to predict this trend and the spread in the radial direction. However, as time progresses the PLIF images show that the high concentration CH_2O regions lie in the 15–25 mm range, while the CFD models predict the CH_2O regions a bit downstream of this location. This is due to the fact that the ignition delays predicted by the CFD models are slightly higher than the experimental results, and hence, the CH_2O formation regions are shifted downstream.

The high-temperature region is characterized by the formation of OH radicals. Recent developments have enabled experimentalists to qualitatively capture these

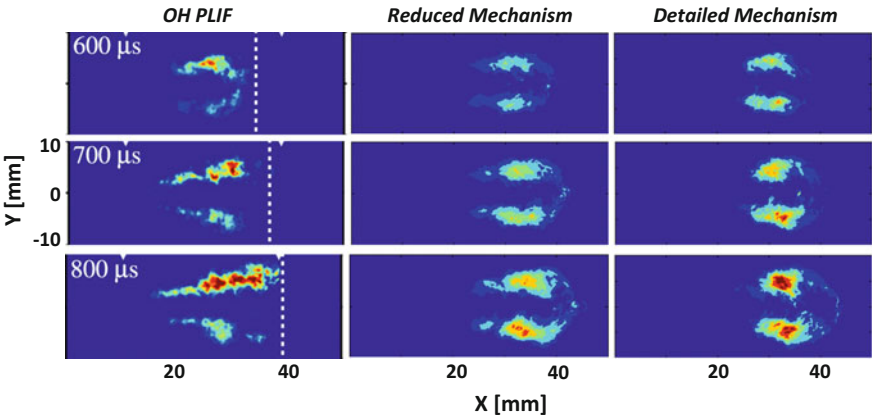

Fig. 16.29 Enseble averaged OH PLIF data at the baseline Spray A conditions (left) compared with the results from the detailed mechanism (center) and the reduced mechanism (right). The LES results are obtained by ensemble averaging over three realizations and azimuthal averaging over 128 planes

species at for spray flames at engine conditions. Maes et al. (2016) carried out PLIF of ground state OH for the Spray A conditions. Ensemble-averaged data from experiments is used to compare with the CFD models. Figure 16.29 shows the OH PLIF results at different time instances compared against the LES data. OH mass fraction contours are obtained from averaging over three LES realizations and 128 azimuthal planes. The OH PLIF is based on the false color images. The CFD results are colored with the same scale for both the reaction mechanisms. At 600 µs, a high concentration of OH is observed along the lateral edge of the jet. Both the reaction mechanisms are able to predict the OH formation but at a slightly upstream location between 25 and 30 mm axial distance from the nozzle. The detailed mechanism predicts higher peak concentrations of OH compared to the reduced mechanism. The simulations are able to predict the radial spread of the flame very close to the ones observed in the experiments. At 700 and 800 µs the PLIF images show a similar structure with high-temperature regions stabilizing at approximately 20 mm from the nozzle exit. OH is not observed in the head of the jet. The simulations also show very low concentrations of OH in the spray head region as seen in the experiments. The simulations are able to capture the high concentration regions on the edge, however, they do not show the truncated cone type structure at the base. The reduced mechanism predicts a relatively flatter flame shape.

The intermediate and high-temperature species prediction from these type of frameworks have been validated against latest experimental results. The two-step ignition process of higher hydrocarbons at LTC coupled with the effects of turbulent flow pose a challenge in predicting LTC engine combustion. The reduction of chemistry mechanisms has added to the list of uncertainties in engine combustion. The use of advanced chemistry solvers and the simplicity of the flamelet technique has now enabled the use of detailed chemical kinetics in engine

simulations. Moreover, it also includes the effect of TCI. The use of such modeling techniques has helped reduce the uncertainties and made engine combustion more predictive.

16.4 Summary

High fidelity modeling approaches are required to use CFD models as predictive tools in designing and optimizing engines, combustion concepts, and understanding pollutant formation mechanisms. Such approaches for spray combustion require large meshes along with accurate turbulence and chemical kinetics modeling. It has been shown that TCI effects coupled with chemical kinetics at high temperatures and pressures play a major role in the flame stabilization process. Capturing these physical processes are key towards building predictive models. However, the computational cost of such approaches has been proved to be a major bottleneck. The flamelet concept has enabled the decoupling of chemistry and fluid flow solvers thereby implementing elaborate chemistry mechanisms with high fidelity turbulence models and larger meshes. The reduction of chemistry to a lower dimensional manifold has also facilitated the a priori chemistry tabulation method which can improve computational speeds by orders of magnitude. Recent developments in stiff solvers coupled with flamelet modeling approaches have enabled the application of detailed chemistry mechanisms for engine conditions thereby reducing the uncertainties encountered in engine modeling. The flamelet approach for high pressure and temperature flames have been validated over a wide range of operating conditions and applications. Different types of flamelet models have been developed for such applications and discussed in this chapter. Advances in experimental methods have enabled model developers to directly validate the modeling approaches for spray flames over a large range of conditions. These include quantitative data like ignition delay, flame lift-off, jet penetration, and qualitative data for intermediate and high-temperature species. The flamelet modeling approach is observed to capture these features in lifted flames satisfactorily.

References

Ameen MM, Kundu P, Som S (2016) Novel tabulated combustion model approach for lifted spray flames with large eddy simulations. SAE Int J Engines 9

Ameen MM, Pei Y, Som S (2016) Computing statistical averages from large eddy simulation of spray flames. Report No. 2016-01-0585, SAE Technical Paper

Barths H, Hasse C, Bikas G, Peters N (2000) Simulation of combustion in direct injection diesel engines using a Eulerian particle flamelet model. Proc Combust Inst 28:1161–1168

Borghesi G, Mastorakos E, Cant RS (2013) Complex chemistry DNS of n-heptane spray autoignition at high pressure and intermediate temperature conditions. Combust Flame 160:1254–1275

Conaire MÓ, Curran HJ, Simmie JM, Pitz WJ, Westbrook CK (2004) A comprehensive modeling study of hydrogen oxidation. Int J Chem Kinet 36:603–622

Fiorina B, Baron R, Gicquel O, Thevenin D, Carpentier S, Darabiha N (2003) Modelling non-adiabatic partially premixed flames using flame-prolongation of ILDM. Combust Theor Model 7:449–470

Herbinet O, Pitz WJ, Westbrook CK (2008) Detailed chemical kinetic oxidation mechanism for a biodiesel surrogate. Combust Flame 154:507–528

Ihme M, See YC (2010) Prediction of autoignition in a lifted methane/air flame using an unsteady flamelet/progress variable model. Combust Flame 157:1850–1862

Ihme M, Shunn L, Zhang J (2012) Regularization of reaction progress variable for application to flamelet-based combustion models. J Comput Phys 231:7715–7721

Kundu P, Pei Y, Wang M, Mandhapati R, Som S (2014) Evaluation of turbulence-chemistry interaction under diesel engine conditions with multi-flamelet RIF model. Atomization Sprays 24

Kundu P, Ameen M, Unnikrishnan U, Som S (2017a) Implementation of a tabulated flamelet model for compression ignition engine applications, Report No. 2017-01-0564, SAE technical paper

Kundu P, Ameen MM, Som S (2017b) Importance of turbulence-chemistry interactions at low temperature engine conditions. Combust Flame 183:283–298

Kundu P, Echekki T, Pei Y, Som S (2017c) An equivalent dissipation rate model for capturing history effects in non-premixed flames. Combust Flame 176:202–212

Li J, Zhao Z, Kazakov A, Dryer FL (2004) An updated comprehensive kinetic model of hydrogen combustion. Int J Chem Kinet 36:566–575

Lu T, Law CK (2005) A directed relation graph method for mechanism reduction. Proc Combust Inst 30:1333–1341

Lu T, Law CK (2006) Linear time reduction of large kinetic mechanisms with directed relation graph: n-Heptane and iso-octane. Combust Flame 144:24–36

Lu T, Law CK (2008) Strategies for mechanism reduction for large hydrocarbons: n-heptane. Combust Flame 154:153–163

Lucchini T, d'Errico G, Ettorre D, Ferrari G (2009) Numerical investigation of non-reacting and reacting diesel sprays in constant-volume vessels. SAE Int J Fuels Lubr 2:966–975

Luo Z, Yoo CS, Richardson ES, Chen JH, Law CK, Lu T (2012) Chemical explosive mode analysis for a turbulent lifted ethylene jet flame in highly-heated coflow. Combust Flame 159:265–274

Maes N, Meijer M, Dam N, Somers B, Toda HB, Bruneaux G, Skeen SA, Pickett LM, Manin J (2016) Characterization of spray a flame structure for parametric variations in ECN constant-volume vessels using chemiluminescence and laser-induced fluorescence. Combust Flame 174:138–151

Mehl M, Curran H, Pitz W, Westbrook C (2009) Chemical kinetic modeling of component mixtures relevant to gasoline. In: European combustion meeting

Mehl M, Pitz WJ, Westbrook CK, Curran HJ (2011) Kinetic modeling of gasoline surrogate components and mixtures under engine conditions. Proc Combust Inst 33:193–200

Minamoto Y, Chen JH (2016) DNS of a turbulent lifted DME jet flame. Combust Flame 169:38–50

Mukhopadhyay S, Abraham J (2011) Influence of compositional stratification on autoignition in n-heptane/air mixtures. Combust Flame 158:1064–1075

Patterson MA, Reitz RD (1998) Modeling the effects of fuel spray characteristics on diesel engine combustion and emission, Report No. 980131, SAE technical paper

Pei Y, Som S, Pomraning E, Senecal PK, Skeen SA, Manin J, Pickett LM (2015) Large eddy simulation of a reacting spray flame with multiple realizations under compression ignition engine conditions. Combust Flame 162:4442–4455

Peters N (1984) Laminar diffusion flamelet models in non-premixed turbulent combustion. Prog Energy Combust Sci 10:319–339

Pitsch H, Chen M, Peters N (1998) Unsteady flamelet modeling of turbulent hydrogen-air diffusion flames. In: Symposium (international) on combustion; Elsevier, pp 1057–1064

Pitz WJ, Mueller CJ (2011) Recent progress in the development of diesel surrogate fuels. Prog Energy Combust Sci 37:330–350

Pomraning E, Rutland CJ (2002) Dynamic one-equation nonviscosity large-eddy simulation model. AIAA J 40:689–701

Reitz R, Rutland C (1995) Development and testing of diesel engine CFD models. Prog Energy Combust Sci 21:173–196

Sarathy S, Yeung C, Westbrook C, Pitz W, Mehl M, Thomson M (2011a) An experimental and kinetic modeling study of n-octane and 2-methylheptane in an opposed-flow diffusion flame. Combust Flame 158:1277–1287

Sarathy SM, Westbrook CK, Mehl M, Pitz WJ, Togbe C, Dagaut P, Wang H, Oehlschlaeger MA, Niemann U, Seshadri K (2011b) Comprehensive chemical kinetic modeling of the oxidation of 2-methylalkanes from C 7 to C 20. Combust Flame 158:2338–2357

Skeen SA, Manin J, Pickett LM (2015) Simultaneous formaldehyde PLIF and high-speed schlieren imaging for ignition visualization in high-pressure spray flames. Proc Combust Inst 35:3167–3174

Smagorinsky J (1963) General circulation experiments with the primitive equations: I. The basic experiment. Monthly Weather Rev 91:99–164

Smith GP, Golden DM, Frenklach M, Moriarty NW, Eiteneer B, Goldenberg M, Bowman CT, Hanson RK, Song S, Gardiner WJ (2000) GRI 3.0, Gas Research Institute, Chicago, IL. http://www.me.berkeley.edu/gri_mech

Som S, Aggarwal S (2010) Effects of primary breakup modeling on spray and combustion characteristics of compression ignition engines. Combust Flame 157:1179–1193

Tillou J, Michel J-B, Angelberger C, Veynante D (2014) Assessing LES models based on tabulated chemistry for the simulation of diesel spray combustion. Combust Flame 161:525–540

Van Oijen J, Lammers F, De Goey L (2001) Modeling of complex premixed burner systems by using flamelet-generated manifolds. Combust Flame 127:2124–2134

Wang H, You X, Joshi AV, Davis SG, Laskin A, Egolfopoulos F, Law CK (2007) USC Mech version II. High-temperature combustion reaction model of H_2/CO/C1-C_4 Compounds. http://ignis.usc.edu/USC_Mech_II.htm. Accessed May 2007. http://ignis.usc.edu/USC_Mech_II.htm

Westbrook C, Pitz W, Herbinet O, Silke E, Curran H (2007) A detailed chemical kinetic reaction mechanism for n-alkane hydrocarbons from n-octane to n-hexadecane. In: Proceedings of the Western States Section of The Combustion Institute

Xu C, Gao Y, Ren Z, Lu T (2016) A sparse stiff chemistry solver based on dynamic adaptive integration for efficient combustion simulations. Combust Flame 172:183–193

Xue Q, Som S, Senecal PK, Pomraning E (2013) Large eddy simulation of fuel-spray under non-reacting IC engine conditions. Atomization Sprays 23

Engine Combustion Network. https://ecn.sandia.gov/

Chapter 17
Numerical Simulation of Turbulent Combustion in Internal Combustion Engines

Xue-Song Bai

Abstract The combustion process in internal combustion engines can occur in multiple modes. In spark-ignition (SI) engines it is mainly a turbulent premixed flame propagation process; however, since the charge is at elevated temperature and pressure, it is possible to have autoignition in the unburned charge, which can lead to engine knock. In conventional Diesel engines, the combustion process is first started with the onset of ignition and followed by turbulent diffusion flames. In the development of modern compression ignition engines, the tendency is to use a mixed mode combustion in order to reduce soot and NOx emissions. Examples of such engine concepts are homogeneous charge compression ignition (HCCI), reactivity controlled compression ignition (RCCI), and partially premixed combustion (PPC) engines. To meet the challenge of high-performance numerical simulations in today's engine design it is necessary that the simulation models shall handle the different modes of combustion. In this chapter, the various combustion modes will be reviewed. Recent simulation results that reveal the finely detailed reaction zone structures in HCCI, RCCI, and PPC engines will be discussed. The challenges in the modeling of multiple modes combustion in internal combustion engine will be discussed in the frameworks of large-eddy simulation and Reynolds-averaged Navier–Stokes simulations. Finally, state-of-the-art models for the various combustion modes will be reviewed, focusing on the modeling of multimodes combustion problems.

Keywords Internal combustion engine · Homogeneous charge compression ignition · Partially premixed combustion · Low temperature combustion Numerical simulation

X.-S. Bai (✉)
Division of Fluid Mechanics, Department of Energy Sciences, Lund University, 221 00 Lund, Sweden
e-mail: Xue-Song.Bai@energy.lth.se

© Springer Nature Singapore Pte Ltd. 2018

S. De et al. (eds.), *Modeling and Simulation of Turbulent Combustion*, Energy, Environment, and Sustainability, https://doi.org/10.1007/978-981-10-7410-3_17

17.1 Introduction

Numerical simulation using Computational Fluid Dynamics (CFD) methods is widely used today to study in-cylinder flow and combustion process in internal combustion engines (ICE). Depending on the purpose of the simulations one can find different types of numerical simulations. One type of numerical simulation is aimed at gaining insight into the turbulent combustion physics in ICE; to do this, the numerical simulations are usually based on the so-called direct numerical simulation (DNS) approach. In DNS, the full set of transport equations is solved numerically using high-order accuracy numerical methods, considering molecular transport properties and relatively detailed chemical kinetic mechanisms (Chen 2011; Sankaran et al. 2005). DNS resolves all physical and chemical scales in the engine combustion process, which is computationally prohibitive at the moment. In a recent DNS of partially premixed combustion (PPC) of a n-heptane/iso-octane/air mixture in a $0.6 \times 0.6 \times 0.6$ mm constant volume domain, with 512^3 computational cells, 3.5 millions of CPU hours were required to simulate the combustion process of physical time about 0.26 ms (about 1.7 times of the integral time) (Zhang et al. 2015a), using the CURIE TN computer based in France at the Tres Grand Centre de Calcul (TGCC). Although DNS is not feasible for numerical simulations of multiple-cycle ICE combustion process with real engine geometry, it is powerful in exploring the fundamental details of ICE combustion process and outstanding findings have been obtained in recent years that can help understanding of the reaction zone structures of ICE combustion and guiding the development of simplified combustion models used for numerical simulations of practical engines.

The second type numerical simulations are aimed at studying the real engine combustion process for the development of new ICE. Today's ICE development is driven by the demands on the emission compliance, CO_2 emissions, performance, and cost-effectiveness, which has affected the development process of the combustion system in ICE industry. As an example, Persson et al. recently demonstrated a new design process (Persson et al. 2017), in which numerical simulations were heavily used in the development of the next-generation Volvo Cars diesel combustion system that was aimed at complying with Euro 6d including Real Driving Emissions (RDE). First, the requirements for the system were determined, after which key factors that affected the system performance were selected, such as the charge motion, combustion chamber geometry, and injector nozzle geometry. Based on the requirements, a robust charge motion with desired flow characteristics was defined. Numerical simulations were performed to optimize the combustion chamber geometry and spray system. The selected solutions were then verified by creating rapid prototype pistons for evaluation. With the aid of numerical simulations, the number of development loops for the engine can be reduced, resulting in a reduction of development cost and time.

To apply numerical simulations to ICE design the computation must be both reasonably accurate and computationally affordable. To do this, one has to rely on methods that employ certain averages or spatial filtering, through which the small-scales

of flow and reaction zone structures are removed, leaving the mean flow or large-scale flow motion and combustion phenomenon described by the governing equations to be resolved by coarse grid resolution. The well-known Reynolds-averaged Navier–Stokes (RANS) method is based on ensemble or time averages, whereas large-eddy simulation (LES) is based on the spatial filtering. RANS is used today in industrial engine design (Ge et al. 2010; Persson et al. 2017) due to its computational low cost; however, only the mean flow is simulated in RANS, while in many situations, large-scale unsteady turbulence structure is also of concern, e.g., when studying cyclic variation of ICE. In LES, the large-scale turbulent motion is simulated while only scales smaller than the spatial filter size are filtered away. Since the detailed turbulence structures in RANS and partly in LES are not simulated, the effect of small-scale turbulence structures on the mean or large-scale turbulence motion is included in the correlation terms in the RANS and LES governing equations. These terms need to be modeled to close the governing equations. The results of RANS and LES are essentially dictated by these models.

17.2 Challenges in Modeling of Turbulent Combustion in ICE

To describe the problem we consider the governing equations for RANS and LES. In general, the in-cylinder flow in ICE is at low Mach numbers during the compression and combustion strokes, after the intake valves are closed. Due to the piston motion, the flow is compressible and the thermodynamic conditions are transient. In ICE even the mean flow is unsteady: the piston is continuously reciprocating, which drives the flow to compress or expand. The Reynolds number is high thus the flow is turbulent. When the fuel is directly injected into the cylinder the problem involves liquid/gas two-phase flow. When the fuel/air mixture is ignited chemical reactions occur in the mixture, which often involves a large number of chemical species and elementary reactions.

In RANS, the mean flow can be computed by introducing cycle averages (also known as ensemble or phase averages), viz.,

$$\overline{Q}(\mathbf{x}, t) = \frac{1}{N_c} \sum_{i}^{N_c} Q_i(\mathbf{x}, t), \tag{17.1}$$

where $Q(\mathbf{x}, t)$ is a quantity describing the flow motion (e.g., velocity component) or thermodynamic property (e.g., density, temperature, or pressure) at point $\mathbf{x}$ and time t. N_c is the number of cycles used in the cycle average, and subscript i denotes the ith cycle. A quantity with overbar denotes the cycle averaged quantity. When applying cycle averages to the experimental data the cyclic variation of the mean flow is lumped into the turbulent fluctuation part (Heywood 1988), while in RANS the cyclic variation of the mean flow is not accounted.

In LES the governing equations are spatially filtered. The spatial filtering of a quantity $Q(\mathbf{y}, t)$ is defined as its convolution with a filter function, $G(\mathbf{y}; \Delta)$, viz.,

$$\overline{Q}(\mathbf{x}, t) = \int_{\Omega} Q(\mathbf{y}, t) G(\mathbf{x} - \mathbf{y}; \Delta(\mathbf{x}))\, d\mathbf{y}, \tag{17.2}$$

where the integration is defined over the entire flow domain Ω. Δ is the characteristic length of the spatial filter, which, in general, may vary with position. Here, the quantity with overbar denotes the spatial filtered quantity. Since the spatial filtering is local and based on the single cycle, cyclic variations of the mean flow are retained in the LES solution. Several authors have demonstrated the capability of using LES to study cyclic variations in spark-ignition (SI) engines (Haworth 1999; Vermorel et al. 2009). When using LES to simulate the cycle averaged mean flows the computational effort is rather high, since many cycles, e.g., at least 10 cycles, have to be simulated to obtain a reasonably converged mean field (Vermorel et al. 2009).

For reacting flows density weighted ensemble average or spatial filtering is used, i.e., $\tilde{Q}(\mathbf{x}, t) = \overline{\rho Q}/\overline{\rho}$, where ρ is the density of the local mixture, and the quantity with an over-tilde denotes the density weighted ensemble averaged or filtered quantity. Applying the density weighted ensemble average or spatial filtering to the governing equations of turbulent reactive flows results in the following averaged or filtered equation for RANS or LES, e.g., for the transport equation of species mass fraction, Y_k,

$$\frac{\partial \overline{\rho}\tilde{Y}_k}{\partial t} + \frac{\partial \overline{\rho}\tilde{u}_i\tilde{Y}_k}{\partial x_i} = \frac{\partial}{\partial x_i}\left(\overline{\rho}\tilde{u}_i\tilde{Y}_k - \widetilde{\overline{\rho}u_iY_k} - \frac{\partial \overline{J}_{k,i}}{\partial x_i}\right) + \overline{\rho}\tilde{\dot{\omega}}_k, \tag{17.3}$$

where u_i is the velocity component along the Cartesian coordinate x_i direction, $J_{k,i}$ is the molecular transport flux of species k along x_i direction, and $\dot{\omega}_k$ is the net formation rate of species k due to chemical reactions.

Although Eq. (17.3) in RANS and LES has the same form the quantities and terms in the equation have completely different physical meaning. In RANS, the turbulent scalar fluxes ($\overline{\rho}\tilde{u}_i\tilde{Y}_k - \widetilde{\overline{\rho}u_iY_k}$) and mean reaction rates $\tilde{\dot{\omega}}_k$ are from the contribution of the entire turbulence spectrum, while in LES the large-eddy motion is described by the filtered quantities ($\overline{\rho}, \tilde{u}_i, \tilde{Y}_k$) from the filtered governing equations, in which the effect of small sub-grid scale (SGS) motion is taken into account in the sub-grid scalar transport flux ($\overline{\rho}\tilde{u}_i\tilde{Y}_k - \widetilde{\overline{\rho}u_iY_k}$) and the spatially filtered chemical reaction rate $\tilde{\dot{\omega}}_k$. In RANS the turbulent scalar fluxes and mean reaction rate are independent of the grid cell size used in numerical simulations, while in LES the SGS scalar fluxes and the filtered reaction rate are not independent of the grid cell size. Since the filter size is proportional to the cell size, in LES when the filter size (cell size) decreases to the level that all flow and chemical reaction layer scales are resolved, the SGS scalar fluxes vanish and the filtered reaction rate is that of the unfiltered one; LES then becomes DNS.

The challenge in the modeling of turbulent combustion lies in the modeling of these turbulent transport fluxes and the averaged reaction rates. In RANS, various

models have been developed for the turbulent transport fluxes (and Reynolds stresses in the mean momentum equations). Very often two-equation $k-\epsilon$ models are used in ICE flow and combustion simulations (Reitz and Rutland 1995). In LES of ICE, a number of authors have modeled the sub-grid scalar fluxes and the sub-grid stresses (for the momentum equations) using the Smagorinsky model (Smagorinsky 1963), viz., for the scalar fluxes,

$$\overline{\rho}\tilde{u}_i\tilde{Y}_k - \overline{\rho}\widetilde{u_i Y_k} = \frac{\mu_{SGS}}{\sigma_{SGS}}\frac{\partial \tilde{Y}_k}{\partial x_i}, \tag{17.4}$$

where the sub-grid diffusion coefficient μ_{SGS} is modeled as $\mu_{SGS} = \overline{\rho}(C_s\Delta)^2 \mid \tilde{S}_{ij} \mid$, with $\tilde{S}_{ij}$ being the mean strain rate tensor and $\mid \tilde{S}_{ij} \mid = \sqrt{2\tilde{S}_{ij}\tilde{S}_{ij}}$. σ_{SGS} is the turbulent Schmidt/Prandtl number typically assigned the value of 1. The Smagorinsky constant C_s is often set a value of 0.17, which may, however, be different in different flow problems. This model constant can be determined dynamically by employing two different filtering operations, using a method known as the dynamic Smagorinsky model (Germano et al. 1991). A more complete review on the various SGS models used in ICE simulations has been given by Rutland (2011).

The mean reaction rate or the filtered reaction rate $\tilde{\omega}_k$ is the main challenge to model in RANS or LES. The combustion process is very different in different types of ICE, thus, specialized models for different types of engines have been developed. For example, for Diesel engines flamelet models based on the mixture fraction and scalar dissipation rate have been developed and widely used in engine combustion simulations (Felsch et al. 2007; Hasse et al. 1999; Mittal et al. 2012; Pitsch et al. 1996), whereas for spark-ignition engines, one can find ICE simulations using the coherent flame model (Marble and Broadwell 1977) based on a transport equation for flame surface density (Candel and Poinsot 1990), and level-set G-equations models (Peters 2000). Certainly, a longer list of specialized models exists and some of them will be discussed later in this chapter. A more comprehensive review on various models can be found in Reitz and Rutland (1995); Rutland (2011). These specialized models are valid for the combustion process for which the models were developed, while application of these specialized models to other types of combustion problems is often not acceptable. The idea of developing a specialized model for certain types of engines is to remove some of the unimportant physics details in the modeling to achieve the best efficiency of the simulation while retaining an acceptable accuracy of the simulation results.

From the model robustness point of view, a generalized model that is valid for multimodes combustion is most preferable, although such a model is often computationally expensive. General models are based on finite-rate chemistry coupling with the flow simulations, with the mean reaction rate or the filtered reaction rate $\tilde{\omega}_k$ explicitly modeled. Examples of models for $\tilde{\omega}_k$ are the partially stirred reactor model (PaSR), the eddy dissipation concept (EDC) model (Magnussen and Hjertager 1977), the effective time-scale model (Kong et al. 1995), and the transported probability density (PDF) models (Pope 1985), among others. Transported PDF models

have the advantage of directly closing the mean reaction rate terms, although the effect of molecular mixing on the evolution of the PDF requires further modeling. A challenge in the PDF models is the reduction of computational time and speedup of the computation.

In the remaining sections of this chapter, some specialized models for SI engines and Diesel engines will be reviewed briefly, followed by a presentation of the recent numerical simulations of low-temperature combustion engines, where multiple combustion modes exist and thus general models are often required to simulate these ICE combustion processes.

17.3 Numerical Simulation of Turbulent Combustion in Spark-Ignition Engines and Conventional Diesel Engines

Conventional SI engines and Diesel engines are the two types of engines dominating the market. Numerical simulations of the combustion process in these engines have a long history and successful experience, as demonstrated in the recent work of Persson et al. (2017). Extensive reviews on the numerical simulations and CFD models for SI engines and Diesel engines can be found in the literature, e.g., Reitz and Rutland (1995); Rutland (2011). In this section, a brief review on the CFD models often used in SI and Diesel engines is presented, aiming at bridging the discussion on the modeling of modern low-temperature combustion engines in Sect. 17.4.

17.3.1 Modeling of Turbulent Combustion in SI Engines

In spark-ignition (SI) engines the fuel is well mixed with the air before the initiation of combustion using a spark. The combustion process is mainly in the premixed flame mode. A premixed flame is characterized by the thin reaction layer that propagates into the unburned fuel/oxidizer mixture at a specific flame speed. In the reaction layer, the chemical reactions are initiated due to the heat and mass transfer from the burned hot products to the unburned colder mixture. The propagation speed of the reaction layer is, therefore, governed by both the molecular diffusion, turbulent transport, and chemical reactions. The essential key of modeling SI engine combustion is the modeling of the turbulent flame propagation speed in the engine. A large number of models have been developed for SI engine combustion simulations.

In SI engines, the propagation of turbulent premixed flames is at a high pressure and high temperature condition due to the piston compression. The thickness of the reaction zone becomes thinner with increasing compression ratio, while the laminar flame speed becomes larger with increasing compression ratio. The Kolmogorov micro length scale decreases with increasing compression ratio. The ratio

between the chemical time and the Kolmogorov time, known as the Karlovitz number, becomes smaller with increasing compression ratio,

$$Ka \sim Ka_0 r_c^{-2}, \tag{17.5}$$

where Ka_0 is the karlovitz number at atmospheric condition (before compression) and Ka is the Karlovitz number during the combustion stroke near the tope-dead-center (TDC). r_c is the compression ratio. In SI engines due to the high compression ratio the Karlovitz number is about 100 times smaller than that in atmospheric condition with the same turbulent large-eddy velocity and length scales. Thus, combustion processes in SI engines occur typically in low Karlovitz number combustion regimes, namely, the flamelet regimes and the thin reaction zones regime. The fundamental reaction zone structures in these regimes are similar to that of laminar flamelets (Peters 2000). The reaction zone in flamelet and thin-reaction zones regimes is not resolved in RANS and LES, which is in fact often treated as an interface separating the burned hot product and the unburned fuel/air mixture, e.g., in the well-known model of Bray–Libby–Moss (BML) (Bray et al. 1985). The thermochemical state across the flame is characterized using a reaction progress variable, defined as the normalized temperature, or mass fraction of the reactants or products. A governing equation for the mean progress variable ($\tilde{c}$) is derived from the temperature or species transport equation,

$$\frac{\partial \overline{\rho}\tilde{c}}{\partial t} + \frac{\partial \overline{\rho}\tilde{u}_i\tilde{c}}{\partial x_i} = \frac{\partial}{\partial x_i}\left(\frac{\mu_t}{\sigma_t}\frac{\partial \tilde{c}}{\partial x_i}\right) + \overline{\rho}\tilde{\dot{\omega}}_c, \tag{17.6}$$

where μ_t is turbulent eddy viscosity in RANS and SGS viscosity in LES. σ_t is the turbulent Schmidt number, which is on the order of unity. The mean reaction rate for the progress variable $\tilde{\dot{\omega}}_c$ is modeled in different ways in different models. In the BML model, $\tilde{\dot{\omega}}_c$ is modeled by employing a presumed PDF for the progress variable. A recent development in this framework is described in Dunstan et al. (2013), where modeling of the the scalar dissipation rate of the reaction progress variable is discussed and the mean reaction rate can be modeled using the scalar dissipation rate.

The coherent flame model (CFM) is based on the flame surface density (FSD) concept. The model was originally proposed by Marble and Broadwell for modeling turbulent diffusion flames (Marble and Broadwell 1977), and it later became popular for modeling of turbulent premixed flames, both in the RANS and LES frameworks. A transport equation for FSD was postulated in the earlier work of Marble and Broadwell (1977), while a more rigid derivation of the model was given later (Candel and Poinsot 1990; Pope 1988). The CFM model is also based on the assumption of flamelet combustion. In this model, the mean reaction rate is modeled to be proportional to FSD. A more recent development of this model is, for example, the extended coherent flame model (ECFM) of Colin et al. (2004) accounting for non-premixed flames, where in order to adapt the model to unmixed combustion for Diesel engine

application, a description of the mixing state had been added. It was represented by three mixing zones: a pure fuel zone, an air zone with possible residual gases, and a mixed zone in which the ECFM combustion model was applied. A mixing model was presented which allowed progressive mixing of the initially unmixed fuel and air.

Two models for SI flames that were developed based on the special treatment of the reaction zones are the thickened flame model (Colin et al. 2000) and the flamelet generated manifolds (FGM) (van Oijen et al. 2016). In the thickened flame model, the thin flamelet is numerically thickened by decreasing the reaction rates to allow for numerical resolution of the reaction layer. The numerical thickening is compensated by adjusting the diffusive transport terms to maintain the same laminar flame speed. The FGM model describes the flame front in a flame-adapted coordinate system, taking into account the effects of flame stretch in turbulent flames by resolving the detailed structure of flame stretch and curvature inside the flame front (van Oijen et al. 2016).

Another type of flamelet model for SI engine simulations is based on the level-set approach, e.g., the G-equation model (Peters 2000; Tan and Reitz 2006). In this model, the flame front is modeled as a thin layer propagation in the turbulent flow. The propagation of the reaction layer is modeled as a level-set function (G), whereas the local flame structure is expressed as a function of G. The mean flame quantities are calculated as an ensemble averages of premixed flamelets, through the G-function, see, e.g., Nilsson and Bai (2000). In the G-equation model, the level-set function G is usually converted to a distance function through a re-initialization procedure. The G-equation model has been applied to various flames, including flames with equivalence ratio stratification and local extinction (Carlsson et al. 2015; Nogenmyr et al. 2009). Tan and Reitz demonstrated the application of a G-equation model to SI engine simulations (Tan and Reitz 2006). They showed that the in-cylinder pressures and engine-out NOx emissions could be well replicated, in comparison with the experiments, at various ignition timing conditions.

Due to the elevated temperature and pressure environment in the engine cylinder, the flame propagation in SI engines can be complex, for example, the unburned mixture in front of the flames can be partially reactive (Martz et al. 2011; Pan et al. 2016), which results in an elevated flame speed, depending on the fuels. The propagation of premixed flames in SI engines can eventually trigger the onset of autoignition in the unburned fuel/air mixture, which can lead to engine knock. Owing to the inhomogeneity in the unburned charge, typically existing either in the species composition or in temperature, the ignition process appears as thin spontaneous ignition fronts propagating at a speed that can be much higher than the flame speed. At the ignition front, the initiation of the reactions is not due to transport of heat and mass from the hot combustion products, but rather it is due to the high initial temperature and pressure in the mixture that gives rise to autoignition of the mixture. The propagation speed of the reaction front is inversely proportional to the gradient of the ignition delay time in the mixture (Zeldovich 1980). For ideally homogeneous mixture, the propagation speed of the ignition front is infinity.

In order to model the ignition process finite-rate chemistry is required. Since the reactions occur simultaneously in the unburned mixture, not just in a thin layer, the filtered reaction rates are less sensitive to the filter size and grid cell size. A simple well-stirred reactor model (WSR), in which the spatial variations of the thermodynamic properties in the sub-grid scale are neglected, can be sufficient to model the mean rates. The challenge is however in how to reduce the computational burden required when using a full set of transport equations and large chemical kinetic mechanisms needed for complex fuels. Several authors have developed tabulation approaches to couple the ignition chemistry in CFD simulations (Joelsson et al. 2012; Knop et al. 2011; Lecocq et al. 2011). In these models, the mean source term in Eq. (17.6) is computed through lookup tables based on the ignition calculation in homogenous mixture with detailed chemical kinetic mechanisms.

17.3.2 Modeling of Turbulent Combustion in Diesel Engines

Conventional compression-ignition engines are known as Diesel engines. The flow physics is complex due to the direct injection of liquid fuels that undergo atomization, evaporation, and turbulent mixing before the combustion process. Modeling of spray atomization, breakup, and evaporation processes is crucially important for the predictive simulation of turbulent combustion in Diesel engines, and comprehensive models have been developed and applied in diesel engine combustion simulations, cf. e.g., Reitz (1987) and Reitz and Rutland (1995), and references therein.

The combustion process in Diesel engines contains multiple combustion modes (Dec 1997). When the fuel is injected through a nozzle to the engine cylinder, the fuel is atomized and vaporized in the proximity of the nozzle by interacting with the hot ambient air. Thereafter, the fuel vapor and air mixture is ignited at a location downstream the fuel jet. A diffusion flame is then established and stabilized downstream the fuel nozzle. The distance between the leading front of the flame and the fuel nozzle is known as the liftoff length. Soot emission is known to be closely correlated with the liftoff length, see, e.g., Jangi et al. (2013). A longer liftoff length gives rise to a more sufficient mixing of the ambient air to the center fuel jet, which can lower the equivalence ratio in front of the flame, and thus, the soot formation can be reduced. It is therefore important to properly capture the liftoff phenomenon in numerical simulations of Diesel engine combustion.

Depending on the ambient temperature, two mechanisms, autoignition and flame propagation coupled with the low-temperature ignition, can be used to explain the liftoff position and stabilization of diesel flames (Gong et al. 2014). When the ambient temperature is low, the liftoff position is an autoignition induced flame-front (AIIF); the flame is stabilized as a two-stage autoignition process. When the ambient temperature is high, the liftoff position shows a structure similar to the classic triple-flame with the low-temperature ignition upstream; hence, the flame is stabilized by the triple flame propagation coupled with the low-temperature ignition (Gong et al. 2014).

To capture the leading flame front position one may use a general model based on the finite-rate chemistry model, since the low-temperature chemistry in the region in front of the leading flame front needs to be captured. When using finite-rate chemistry the mean reaction rate requires a model. Some authors have used the simple WSR model. A more general approach is to use the transported PDF model to account for the interaction between turbulence and chemical reactions. A comprehensive review of the transported PDF model can be found in the review paper by Haworth (2010).

Finite-rate chemistry-based models are computationally time consuming. They have been used in exploring the fundamental diesel flame physics in constant volume combustion vessels (Jangi et al. 2013; Gong et al. 2014) and in experimental optical engine studies (Solsjo et al. 2013), while it is too time consuming to use in engine design simulations in industry. Specialized models are developed for Diesel engine combustion simulations. Two examples of these models are the representative interactive flamelet (RIF) model (Felsch et al. 2007; Hasse et al. 1999; Pitsch et al. 1996) and the conditional moment closure (CMC) model (Klimenko and Bilger 1999; Mastorakos and Bilger 1998; Swaminathan and Bilger 1999).

In the RIF model, a reactive scalar is assumed to be a function of mixture fraction. This model implies that the flame is affected by turbulence through its transport of mixture fraction, while the flame structure in the mixture fraction coordinate is essentially similar under different turbulent flow conditions. Turbulence can affect the flamelet structure through the mixing rate. A set of unsteady flamelet equations is derived from the transport equations of species mass fractions and energy, with mixture fraction as the independent variable and scalar dissipation rate at stoichiometric mixture fraction as an input parameter that represents the mixing rate in the equations. The set of flamelet equations is solved interactively with the flow equations; important flow field information, such as thermodynamic pressure, scalar dissipation rate, and density, is exchanged with the flow simulations at every time step. The the autoignition, combustion, and pollutant formation are all taken into account within a single RIF approach based on the detailed chemical kinetics. A recent evaluation of the RIF model and the finite-rate chemistry model with local well-stirred reactor, WSR, assumption within each CFD cell for diesel spray flames showed that, the RIF model and finite-rate chemistry model with WSR predicted the same ignition delay time, while the RIF model showed better capability in predicting the liftoff length than the well-stirred reactor model did (D'Errico et al. 2014).

In the CMC model, a set of governing equations is derived for the conditionally averaged quantities, e.g., species mass fractions conditioned on mixture fraction. Temporal and spatial variation of unconditionally averaged quantities can be obtained by integrating conditionally averaged values over the range of conserved scalar values after weighting with the local probability density function of the conserved scalar (Swaminathan and Bilger 1999). The CMC equations contain similar terms to that in the RIF equations, e.g., the diffusion term in the mixture fraction space with scalar dissipation rate as an input parameter. The CMC equations involve in addition an explicit term accounting for the convective fluxes in physical space.

This term disappears in homogeneous turbulence, thus, the resulting CMC equations are in a similar form to those of RIF (Swaminathan and Bilger 1999). The CMC model has been used to simulate spray autoignition (KIim and Huh 2002) and Diesel engine combustion with success (De Paola et al. 2008).

17.4 Numerical Simulation of Turbulent Combustion in LTC Engines

Low-temperature combustion (LTC) engine is a modern engine concept that was developed to comply with emission legislation and to improve the engine efficiency. Examples of such engine concept are homogeneous charge compression ignition (HCCI) (Najt and Foster 1983; Onishi et al. 1979), reactivity controlled compression ignition (RCCI) (Reitz and Ganesh 2015), and partially premixed combustion (PPC) engines (Kalghatgi et al. 2007; Manente et al. 2009). RCCI engine makes use of two different fuels with different reactivities, for example, gasoline (high octane number fuel, less easy to autoignite) and diesel (much easier to autoignite), to control the ignition timing and the heat release rate profiles to achieve optimal engine performance. Similar to Diesel engines, HCCI, and PPC are relying on a single fuel. The difference in these different engines is mainly in the injection timing of the fuel. In a Diesel engine, the fuel is injected late during the compression stroke near TDC to make use of the high pressure and high temperature environment to ignite the fuel once it is injected. In an HCCI engine the fuel is injected much earlier, very often during the intake stroke or early compression stroke to generate a more homogeneous fuel-lean mixture. In PPC engines, the injection timing of the fuel is in-between that of HCCI and Diesel engines.

17.4.1 Numerical Simulation of HCCI Engines

HCCI engine has been developed since the 1980s (Najt and Foster 1983; Onishi et al. 1979; Thring 1989). In HCCI engines, the fuel and air are premixed or nearly premixed since in direct injection HCCI engines the mixture will unavoidably have stratification in both composition and temperature. Nevertheless, the local mixture is under the fuel-lean condition and sometimes exhaust gas recirculation (EGR) is used to dilute the fuel/air mixture. The combustion temperature is therefore low, which results in low NOx emissions. The fuel-lean mixture is advantageous for suppression of soot formation in compression ignition engines. HCCI engines have higher engine efficiency than SI engines due to its higher compression ratio, and have lower soot and NOx emissions than Diesel engines due to the premixed fuel-lean mixture. A comprehensive review on HCCI engines has been given by Yao et al. (2009).

17.4.1.1 DNS of HCCI Combustion Process

An ideal HCCI with homogeneous composition and temperature in the engine cylinder would have a homogeneous ignition and the process would be dictated by the chemical kinetics. In practical HCCI engines, the composition and temperature are stratified and engine experiments have indicated the existence of distinct reaction fronts (Christensen et al. 1999). These reaction fronts propagate at a speed typically an order of magnitude higher than that found in SI engines. DNS of generic HCCI combustion processes has been carried out aiming at understanding the reaction zone structures, the propagation velocity of the reaction fronts, and factors that govern the pressure-rise rate and heat release rates, etc., under HCCI engine relevant conditions.

In a two-dimensional DNS (2D-DNS) study, Sankaran et al. (2005) studied the effect of the stratification of initial temperature fields on the initial ignition and subsequent heat release of lean fully premixed H_2/air ignition, and they found that both spontaneous ignition reaction fronts and premixed flame fronts can exist in the domain. Spontaneous ignition is dominant in the initial start of ignition, followed by a mixed mode of spontaneous ignition and premixed flame propagation, and in the end the remaining mixture is combusted in the mode of spontaneous ignition. The conclusion has been confirmed in other 2D-DNS (Chen et al. 2006; Zhang et al. 2016) and three-dimensional DNS (3D-DNS) (Yu and Bai 2013). In a recent 2D-DNS study of H_2/air HCCI combustion with both stratified composition and temperature, as well as different intensities of turbulence, Zhang et al. (2016) reported that the heat release rate profile in the HCCI cases shows an apparently slower rate of overall heat release than that in the corresponding ideal HCCI case (without any stratification). It further shows that higher turbulence intensity yields a retarded autoignition and a shorter combustion duration. A larger composition stratification leads to an earlier onset of ignition and prolonged combustion duration. The statistics of local displacement speed of the reaction front shows the peak of the local displacement velocity decreases as the combustion proceeds.

Figure 17.1 shows the temperature distribution in the H_2/air mixture under conditions similar to that of Zhang et al. (2016), with both composition and initial temperature stratification, but at a higher initial pressure. Due to the composition and temperature stratification the ignition of the mixture is nonhomogeneous in space. The reaction fronts (as indicated by the fronts of the high temperature zones) are strongly affected by turbulent eddies. At low turbulent rms velocity ($u'_{rms} = 0.2m/s$) the reaction fronts are more of circular shape whereas at a higher turbulent rms velocity ($u'_{rms} = 2m/s$) the they are highly distorted by the turbulence eddies. Turbulence is shown to prolong the ignition delay time and shorten the combustion duration (Yoo et al. 2011; Zhang et al. 2016), which is not primarily due to the direct interaction of turbulence eddies with the reaction fronts, but mainly owing to the effect of turbulence on the temperature field prior to the onset of ignition. With strong turbulence the composition and temperature stratification are reduced by eddy mixing. The local temperature maximum is therefore reduced, which results in a retarded ignition. A lower degree of thermal and composition stratification implies a faster propagation velocity of the reaction front, thereby, a shorter combustion duration.

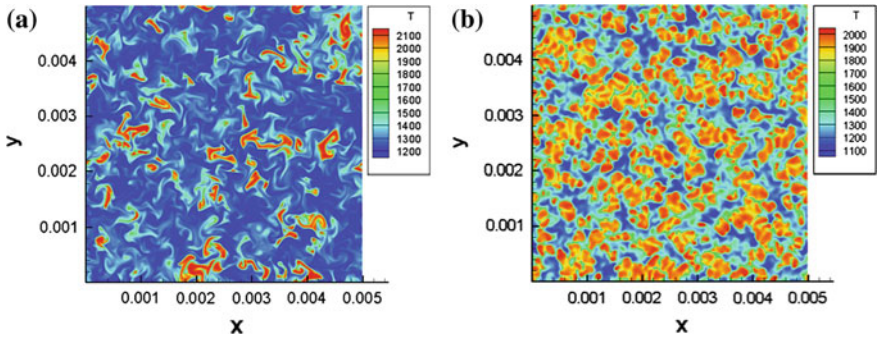

Fig. 17.1 Temperature distribution during the ignition stage in a H_2/air mixture with two different turbulent velocities, **a** $u'_{rms} = 0.2m/s$, **b** $u'_{rms} = 2m/s$. The initial temperature is $1175K$ with a temperature fluctuation of $\pm 15K$, the mean equivalence ratio is 0.67, with an equivalence ratio stratification of ± 0.05, the initial pressure is 118 bar. The domain has a dimension of 5×5 mm

Chen et al. (2006) developed a numerical diagnostics approach for analysis of the reaction front propagation in HCCI combustion. An indicator of front propagation due to deflagration or spontaneous ignition was proposed based on the local front displacement speed. The diagnostic approach was applied in studies of the effect of the initial temperature and turbulence field on HCCI combustion (Hawkes et al. 2006), and the effect of differential diffusion during auto-ignition of a hydrogen/air mixture (Bisetti et al. 2009).

The reaction front propagation in HCCI combustion is further studied in a H_2/air mixture in both two-dimensional and three-dimensionality configurations (Yu and Bai 2013). Compared with 2D-DNS, 3D-DNS predicted a delayed but more rapid heat release rate (15% higher in peak value). The difference is due to that, compared with 2D turbulence, 3D turbulence yields a faster heat transfer rate that leads to a more homogenous temperature field prior to the onset of ignition. The faster heat transfer rate in the 3D case is a consequence of one extra spatial dimension, which gives rise to both a higher value of initial velocity strain rate and an additional strain-self-amplification, which then leads to a faster production of temperature gradient and quicker mixing of the temperature field. It was also found that the higher 3D peak heat release rate is mainly due to the larger reaction front area in 3D-DNS, while the mean propagation speed of reaction fronts is similar in 3D and 2D.

17.4.1.2 Modeling of HCCI Combustion Process

The DNS results discussed in Sect. 17.4.1.1 indicate the co-existence of premixed flame fronts and spontaneous ignition fronts in HCCI combustion. The specialized models developed for the modeling of turbulent premixed flames in SI engines are generally not useful in modeling of HCCI engines. The paramount importance of chemical kinetics in HCCI combustion demands the use of finite-rate chemistry

models in simulation of HCCI combustion. The strong effect of turbulence mixing on the HCCI combustion process, especially on the composition and thermal stratification prior to the onset of ignition, requires a decent modeling of the turbulent mixing process, e.g., the modeling of the turbulent transport fluxes in Eq. (17.3). Although the HCCI reaction fronts are very thin, cf. Fig. 5 in Zhang et al. (2016), considerably thinner than the mesh size used in RANS and LES, it may, however, be not necessary to consider these thin reaction zone structures in the modeling of the mean reaction rate in RANS or the filtered reaction rate in LES, i.e., $\tilde{\omega}_k$ in Eq. (17.3). This is owing to that the prediction of the reaction front propagation depends mainly on the prediction of the onset of ignition, which depends on the temperature and composition field prior to the onset of ignition. These fields are much smoother than those after the onset of ignition. In practice, a simple PaSR model or WSR model is sufficient in modeling the $\tilde{\omega}_k$ term in RANS and LES. Furthermore, the relatively low ratio of the magnitude of diffusive transport terms to that of the reaction rates, cf. Chen et al. (2006) and Yu and Bhai (2013), implies that the unresolved gradient of composition or temperature across the thin reaction zone does not affect the propagation of the reaction fronts to an appreciate level.

A large number of HCCI engine simulations have been carried out using the so-called multi-zone model (Aceves et al. 2000; Babajimopoulos et al. 2015; Flowers et al. 2003), in which detailed chemical kinetic mechanisms are integrated in a small number of temperature zones. This type model has shown a low-computational cost and reasonably accurate prediction of HCCI engine combustion. More details about the multi-zone model will be given in Sect. 17.5.1.

Another type of HCCI engine combustion simulation is based on the tabulation approaches to couple the ignition chemistry in CFD simulations (Joelsson et al. 2012; Knop et al. 2011; Lecocq et al. 2011; Yu et al. 2006, 2007). In these models, the mean source term in Eq. (17.6) is computed through lookup tables based on the ignition calculation in homogenous mixture with detailed chemical kinetic mechanisms. An example of application of the tabulation approach to LES of HCCI engine combustion can be found in Yu et al. (2007).

17.4.2 Numerical Simulation of PPC Engines

The challenge in HCCI engine is its high sensitivity to engine operation conditions. The combustion process is highly sensitive to the temperature of the charge; at light load operation, unburned fuel, and CO emissions are cumbersome, and it is also difficult to ignite the mixture in cold-start. At heavy load the combustion heat release rate is high, which can give rise to high engine noise. To circumvent some of these drawbacks, other types of LTC combustion concepts have been developed for ICE. One of these is the concept of the partially premixed combustion (PPC) engine. PPC engine is a hybrid of the conventional Diesel engine (CDE) and HCCI engine. In PPC engines, the fuel is injected much earlier than that in Diesel engines but later than that in HCCI engines. Unlike CDE, in PPC engines there is a sufficiently long

time separation between the end of injection and the onset of autoignition, so that the fuel can sufficiently mix with the air. Unlike HCCI engines, the fuel stratification is large in PPC engines so that a slower heat release rate can be obtained.

Kalghatgi et al. (2007) showed that with highly reactive fuels such as diesel, a large amount of exhaust gas recirculation (EGR) or low compression ratio is needed to separate the end of the fuel injection and the start of combustion, and thus, high octane number fuel was suggested. Manente et al. (2009) examined the performance of a PPC engine with gasoline fuel and a rather high pressure-rise rate with a reduced engine efficiency was noticed. A way to ensure a desirable mixture for PPC is to split the fuel injection into different times. Hanson et al. (2009) investigated a heavy duty PPC engine with two injections of gasoline. They examined the effect of the fuel split between the first and the second injections and found that there was a tradeoff between emissions of NOx and soot, i.e., the reduction of NOx was accompanied by the increase of soot emission. Manente et al. (2010) investigated the use of ethanol as the fuel in PPC engines, and they found that the best engine performance could be achieved with the mass ratio of the fuel through the first injection and the second injection about 1. Although PPC engine showed a great potential in achieving a better tradeoff between engine efficiency and emissions the control of the fuel injection is not a trivial task. The combustion physics in PPC engines is relatively less understood; numerical simulations can play an important role in developing PPC engines.

17.4.2.1 DNS of PPC Engine Combustion Process

Zhang et al. (2015a, b) carried out DNS studies of PPC in a mixture of primary reference fuel (PRF70, with 70% iso-octane and 30% n-heptane on volume basis), air and EGR in a constant volume domain, under conditions relevant to PPC engines with two injections. The first injection of the fuel was assumed to mix with the air and EGR perfectly (representing the case of an early injection of the fuel in PPC engines), and the second injection was assumed to start later in the compression stroke (near TDC). The DNS results revealed the fundamental combustion process and the reaction zone structure in the PPC mixture of PRF70, air and EGR.

Figure 17.2 shows the reaction zone structures depicted by key species and the heat release rate at two points in time. A sequential combustion process is identified from the DNS results, which is the reason behind the slower heat release rate and the tradeoff between NOx emission and CO emission. The combustion process starts with the ignition of the mixture. The ignition process of the mixture in the fuel-lean region (where the fuel is from the first injection) converts the fuel to CO, which is subsequently oxidized to CO_2. This is similar to the HCCI combustion process. In this process, the heat release is typically rapid; the peak heat release rate depends on the homogeneity of the composition and temperature, as well as the equivalence ratio of the mixture. The latter can be controlled by the amount of fuel in the first injection. The ignition process of the fuel-rich mixtures (the fuel is mainly from the second injection) converts the fuel to combustion intermediates (mainly CO and H_2), which can not be oxidized further without mixing with the oxidiser in the fuel-lean

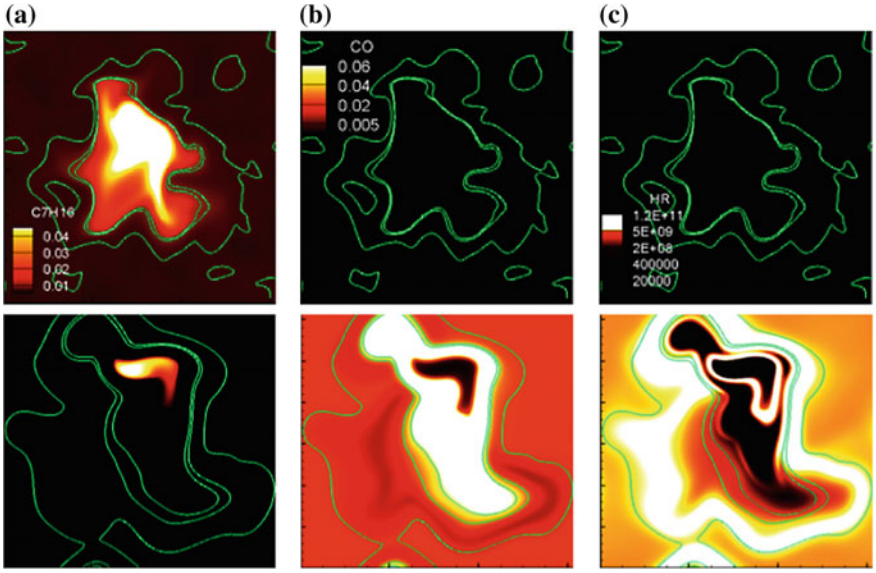

Fig. 17.2 Distributions of heat release rate (HR) and mass fractions of n-heptane and CO in a mixture of PRF70, air and EGR at two instances of time during PPC combustion process; **a** mass fraction of n-heptane, **b** mass fraction of CO, **c** heat release rate. Upper row: at 0.0317 ms; lower row: at 0.2 ms. The iso-lines correspond to the local equivalence ratio of 1.2 (the innermost line), 1 (the middle line), and 0.5 (the outermost line). The domain has a dimension of 0.614 mm × 0.614 mm × 0.614 mm. More details about the DNS results can be found in Zhang et al. (2015a, b)

region. Thus, the oxidation of the intermediate products in the fuel-rich region is in a diffusion flame mode, which is governed by turbulence mixing, and is typically much slower than that of the ignition process of HCCI.

Three distinctive regions are identified in PPC combustion (Zhang et al. 2012, 2015a, b), a lean nearly homogeneous charge region, a stoichiometric charge region and a fuel-rich charge region. NO formation is mainly during the combustion in the stoichiometric charge region due to the high combustion temperature. This implies that the interface between the first injection and the second injection should be decreased to reduce the NO emissions. The CO emission is mainly from the fuel-rich charge region where CO formed in the fuel-rich mixture undergoes oxidation reactions in the later stage of combustion, which is at the diffusion flame mode and dictated by the turbulence mixing process. The emission of CO increases with the mass of the fuel in the second injection.

Turbulence has a more important impact on PPC process than on the HCCI process. Similar to the HCCI process, increase in turbulence intensity leads to a rather significant increase in the peak heat release rate, owing to the faster mixing between the fuel-rich pocket and the fuel-lean mixture, which leads to more homogeneous mixture in the domain, thereby, a more rapid combustion process once it is started. Furthermore, with larger turbulence integral length or higher turbulence

intensity, thus a higher mixing rate, the CO oxidation process is enhanced and the emission of CO is reduced, however, at a cost of higher NO emission due to more complete combustion and thus higher temperature (Zhang et al. 2015b).

17.4.2.2 Modeling of PPC Engine Combustion Process

DNS results reported in Zhang et al. (2012, 2015a, b) indicate that the combustion process in PPC engines is at multiple modes. In the first stage, the combustion process is similar to that of HCCI, where the dominant mode is spontaneous autoignition of the mixture. Models developed for HCCI can be used to simulate the ignition process in PPC engines. The later stage of the PPC process is at the diffusion flame mode. Models developed for Diesel engine combustion are therefore usable for this stage of combustion. By coupling a multi-zone type of model and a flamelet type of model one can expect that a highly efficient, specialized model for PPC engines can be developed. This type of model is however complex to implement into CFD codes, and it is rarely reported in the literature.

Numerical simulations of PPC combustion has been carried out using a more general type of models, e.g., finite-rate chemistry (FRC) models. Solsjo et al. (2012) applied a FRC model based on the WSR to LES study of the mixing, ignition, and combustion processes in a laboratory engine operating under PPC conditions. It was shown that the model could capture the main features of PPC engine under conditions of different swirl numbers and injections. Jangi et al. (2017) compared two FRC models in RANS simulations of a methanol fuelled compression ignition engine that operated under both HCCI and PPC conditions. One was based on the Eulerian stochastic fields (ESF) PDF model and the other based on the WSR model. It was shown that the two model yielded similar results for the HCCI case with an earlier injection of methanol, whereas for the PPC case with later methanol injection the PDF model predicted an in-cylinder pressure profile in good agreement with the experiments, while the WSR model predicted a much slow ignition. In RANS simulation, the temperature field is smoothed, thus, the hot spot in the mixture prior to ignition is cooled, which results in a delayed onset of ignition with a WSR model. In PDF models, certain temperature fluctuations are incorporated into the simulations through the stochastic process, which leads to an earlier onset ignition. The LES-based WSR model allows for more realistic spatial variations of temperature and composition; thus, LES-WSR could predict more physical results in PPC engine simulations.

17.4.3 Numerical Simulation of RCCI Engines

Reactivity controlled compression ignition (RCCI) (Kokjohn et al. 2011; Reitz and Ganesh 2015) is another novel concept that can be used to circumvent the problems of control of HCCI ignition timing and heat release rate. In RCCI, a low reactivity

fuel (e.g., gasoline) is injected to the intake port together with the air supply and a homogeneous mixture of the low reactivity fuel and air is formed in the cylinder before the injection of a high reactivity fuel (e.g., diesel) to initiate the ignition. The ignition timing is therefore controlled by the injection of the high reactivity fuel, while the heat release rate is controlled by the mass split of the two fuels. The RCCI concept is very attractive for the application of alternative fuels in ICE. Natural gas and alcohols are examples of the attractive alternative fuels. These fuels have high octane numbers and they are difficult to use in compression ignition engines. One can improve the ignition property of these fuels by injecting another fuel (e.g., diesel) that is easy to ignite to initiate the ignition of high octane number fuels.

A number of investigations have been conducted on methanol/diesel RCCI engines to study its emission characteristics, e.g., Dempsey et al. (2013); Li et al. (2014); Masimalai (2014); Yao et al. (2008). With increasing methanol/diesel mass ratio the emission of soot and NOx was shown to decrease; however, the emission of unburned hydrocarbons and CO could increase due to the decreased combustion efficiency and increased fuel/air ratio in the methanol/air mixture (Masimalai 2014). It has been observed that the overall engine performance and emissions are rather sensitive to the intake temperature and the amount of EGR, due to their influence on the in-cylinder gas temperature prior to the onset of ignition. A high initial temperature in the methanol/air/EGR mixture could give rise to fast ignition in the methanol/air/EGR mixture in a way similar to HCCI engines, with rather high heat release rate and pressure-rise rate. A low initial temperature could delay the ignition of the high reactivity fuel, which can allow for more complete mixing of the high reactivity fuel with methanol/air/EGR before the onset of ignition, thus resulting in a rather different heat release profile (Hu et al. 2017). At low load and cold start, this could give rise to misfire (Yao et al. 2008). Some experimental studies have shown rather high pressure-rise rate and noise level of this type of dual fuel combustion at high methanol/diesel ratio, which could limit the amount of methanol to be used to substitute diesel in the engine (Popa et al. 2001).

17.4.3.1 DNS of RCCI Combustion Process

Hu et al. (2017) carried out two-dimensional and three-dimensional DNS studies of RCCI combustion with methanol and n-heptane as fuels in a constant volume domain with a dimensional of 14×12 mm (2D-DNS) and $14 \times 12 \times 2$ mm (3D-DNS). For the initial condition, methanol was assumed to have perfectly mixed with air and EGR, and the initial pressure was set to 42 bar. The EGR/air molar ratio was 1:1. The equivalence ratio of methanol/air/EGR mixture was 0.6. Gaseous n-heptane/air mixture was then injected, which initiated the ignition of the mixture. It was shown that the RCCI combustion can occur at different modes. The ignition of the mixture is at the mixing layer of the n-heptane jet; thereafter, the combustion process in the ambient methanol/air/EGR mixture can be at spontaneous ignition mode or premixed flame propagation mode. Finally, the combustion intermediate from the incomplete

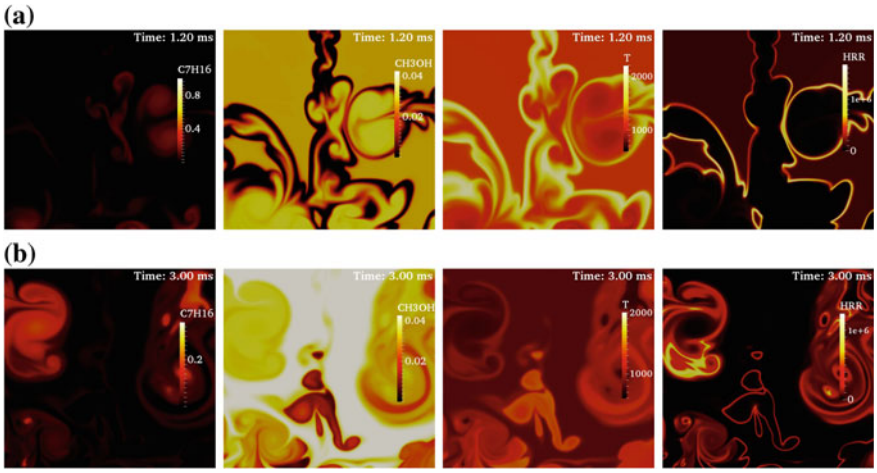

Fig. 17.3 Distributions of mass fractions of n-heptane (C7H16) and methanol (CH3OH), local temperature (T), and local heat release rate (HRR) during the combustion process of n-heptane, methanol, air, and EGR in a constant volume domain under conditions relevant to RCCI engines; **a** Initial temperature of 1000 K, **b** Initial temperature of 800 K. The initial pressure is 42 bar. The domain has a dimension of 14 × 12 mm. More details about the DNS results can be found in Hu et al. (2017)

oxidation of n-heptane can be burned in diffusion flame mode, by mixing with the remaining oxidizer in the ambient mixture.

Figure 17.3 shows the mass fractions of n-heptane and methanol, as well as local temperature and local heat release rate in the domain under two different initial temperature conditions, at the instance of time of peak overall heat release rate of the domain. At the initial temperature of 1000 K, the ignition occurs rather quickly, with the maximal heat release rate occurring at 1.2 ms. The highest temperature and the highest local heat release rate are found in the mixing layer between the n-heptane jet and the ambient mixture. In the ambient methanol/air/EGR mixture, the temperature and local heat release rate are also rather high, indicating that the mixture is undergoing autoignition, a process similar to that in HCCI engines. Due to the autoignition of the entire ambient mixture the peak overall heat release rate is rather high. The combustion mode in the low-initial temperature case (with initial temperature of 800 K) is different. The mixture ignites much later, which allows for a better mixing of n-heptane and the ambient methanol/air/EGR mixture. Due to the low-initial temperature, the ambient methanol/air/EGR mixture is combusted at a premixed flame mode.

Turbulence has an important effect on the RCCI process, in a way similar to that on the PPC process. Turbulence has an indirect effect on the ignition of the fuel/air mixture—by affecting the temperature and mixture fields prior to the onset of ignition. Turbulence has a more important impact on the later stage diffusion controlled combustion process, by controlling the mixing rate of the combustion intermediates

in the fuel-rich region with the oxygen in the fuel-lean region. Under low-initial temperature conditions, turbulence can directly affect the propagation of the premixed flame by wrinkling the flame front.

17.4.3.2 Modeling of RCCI Engine Combustion

Due to the existence of multiple modes in RCCI engine combustion, general models based on the finite-rate chemistry have been used in practical RCCI engine simulations, cf. Dempsey et al. 2013; Li et al. 2014. Li et al. (2014) used a KIVA 3V RANS code, where finite-rate chemistry was coupled with flow simulation using Chemkin solver to perform an optimization study of methanol/diesel RCCI engines. The mean reaction rate $\tilde{\omega}_k$ was modeled using the WSR model. This model has been used in HCCI and PPC engines simulations as discussed earlier. The results were shown to agree reasonably well with the engine in-cylinder pressure measurements and global heat release rate data. Such model is adequate for capturing the ignition process of RCCI, owing to the low sensitivity of the results to grid resolution. However, it is expected that the model is not accurate for simulation of the premixed flame propagation stage of RCCI combustion, which may occur at light load conditions. The model is also computationally demanding due to the direct solution of the species transport equations, especially when the chemical kinetic mechanism is large.

17.5 Speedup of Numerical Simulation Based on the Finite-Rate Chemistry

Combustion in ICE often involves multiple combustion modes, e.g., in SI engines turbulent premixed flames with possible autoignition, in Diesel engines starting with the onset of autoignition, ignition assisted premixed flame propagation at the leading front of the spray flame, and diffusion flames in the main part of the spray flame. In modern LTC engines, e.g., HCCI, PPC, and RCCI, spontaneous ignition and premixed flame propagation are frequently observed, and in the later stage of PPC and RCCI combustion, the process is at the diffusion controlled flame mode in which combustion intermediates such as CO and H_2 from the incomplete oxidation of the fuel in the fuel-rich region of the mixture is further continued. In most numerical simulations reported in the literature, finite-rate chemistry, FRC, coupling with the flow transport simulations has been frequently used. FRC has shown reasonable success in simulation of multiple mode combustion processes, especially in compression ignition engines. One main challenge in FRC models is the long computational time required due to the solution of a large number of species transport equations, specially due to the stiffness of the chemistry. Different approaches have been developed for efficiently coupling the chemistry with flow simulations, e.g., the computational singularity perturbation (CSP) approach (Lam and Goussis 1988), the intrinsic low-

dimension manifold (ILDM) approach (Maas and Pope 1992), the in situ adaptive tabulation (ISAT) (Pope 1997) approach, the direct relation graph (DRG) approach (Lu and Law 2005), and the dynamic adaptive chemistry (DAC) approach (Liang et al. 2009), among others. Details about these methods can be found in the above cited papers and references therein. In the remainder of this section, we will focus on two methods that are easy to implement and efficient in speeding up FRC simulations. The first is the multi-zone approach for HCCI engine simulations (Aceves et al. 2000) and the second is the chemistry coordinate mapping approach for multi-mode LTC engine simulations (Jangi and Bai 2012; Jangi et al. 2011).

17.5.1 Multi-zone Model

As discussed in Sect. 17.4.1.1 in HCCI the dominant process is the spontaneous ignition, although one can also find premixed flame propagation in the intermediate stage of HCCI combustion. When the ignition is the main process, in the transport equations for species mass fractions, the diffusive transport term is smaller than the chemical reaction rates. The chemical reaction rates depend on the local thermodynamic properties such as species mass fractions and temperature. In HCCI engines, if the composition stratification is small, the ignition process is dictated by the thermal stratification inside the cylinder.

The multi-zone model is based on the assumption that the HCCI combustion process depends only on the local temperature. In an engine cylinder with a stratified temperature field, the combustion process in different spatial locations in the cylinder would be the same if the temperature in these locations were the same. Based on this argument, one does not need to integrate the chemical reaction rates in each CFD cell in the cylinder but rather integrate the reaction rates for a number of different temperatures. The species and temperature evolutions in each temperature zone will be the same in the CFD cells that share the same temperature as that in the temperature zone.

Aceves et al. (2000) presented a multi-zone simulation of an HCCI engine. First, the KIVA code was run to simulate the temperature distribution inside the cylinder without combustion, based on which a number of temperature zones was selected. In each of the temperature zones, the evolutions of species and temperature were simulated using a detailed chemical kinetics code as the multi-zone solver (the HCT code; Hydrodynamics, Chemistry, and Transport). In each temperature zone the mass was conserved during the multi-zone ignition simulation, while the pressure in all temperature zones was kept the same. The volume of each temperature zone was therefore varied during ignition simulations. With only 10 temperature zones the predicted in-cylinder pressure evolution was already in satisfactory agreement with the experiments. The CO prediction is, however, less accurate. In practical engines, CO was typically not consumed completely in the lowest temperature regions of the combustion chamber. It diffuses back into the hotter gasses in the core of the combustion

chamber, where it is further oxidized. Thus, mixing of mass between the temperature zones should be taken into account in the prediction of the composition field.

The limitation of the original multi-zone method is that once the chemistry calculation begins, the detailed information from the CFD code is lost and there is no mixing between the zones. This is due to that the neighboring temperature zones are physically not always neighbors in space. The temperature zones interact one another only through the adjustment of pressure. Flowers et al. (2003) modified the multi-zone model to include the mixing effects, by introducing a coupled CFD/multi-zone model. Instead of a one-way mapping of the CFD temperature distribution onto the multi-zone chemical kinetics solver, their method proposed a two-way mapping of information back and forth throughout the cycle. In the coupled CFD/multi-zone model, one CFD time step is split into chemistry fractional steps and flow convection and diffusion fractional time steps. The chemistry solver is used in the temperature zones (the number of temperature zones is much fewer than the CFD cells) to integrate the chemical reaction source terms in the species transport equations, to obtain a factional change of species composition. The new species composition after the chemistry fractional step is then mapped back to the CFD cells. Thereafter, integration of the convection and diffusion terms is carried out in the CFD cells to complete the time step. Flowers et al. (2003) showed that, with mixing taken into account the prediction of CO was significantly improved.

Babajimopoulos et al. (2015) extended the coupled multi-zone model to HCCI engine simulation with stratification in both temperature and compositions. The multi-zones are extended into two-dimensional phase space, with temperature and a progress equivalence ratio as the coordinates. The proposed methodology showed a reduction of 90% of the computational time, while maintaining good agreement with the detailed solution.

Goldin et al. (2009) presented a cell agglomeration (CA) algorithm to speedup the numerical simulations coupled with detailed chemistry. Similar to the extended multi-zone model (Babajimopoulos et al. 2015; Flowers et al. 2003), the CA method is based on the fractional time-step integration of the flow transport terms and the chemical reaction rates. In the CA algorithm, the integration of the chemical reaction rates is done in the space of composition (N_s-dimension, N_s is the number of species in the mixture), temperature, and pressure. A uniform Cartesian mesh, in composition space was used to group computational cells with similar thermochemical composition, temperature and pressure at every reaction sub-time step. The new composition was mapped back to the CFD cells where the integration of the flow transport terms was carried out to complete the integration of one CFD time step. While the CA method is more general than the earlier multi-zone models, the large dimension of composition space is the challenge. Goldin et al. (2009) demonstrated the use of a subset of the composition space, e.g., with 11 dimensions (including T, N_2, O_2, CH_4, CO_2, H_2O, CO, OH, H_2, O and CH_2O) for two-dimensional methane/air premixed flame simulation, and a factor of three speedup rate of the simulations was achieved.

17.5.2 Multi-zone Chemistry Coordinate Mapping Method

Similar to that of the multi-zone model and the cell agglomeration method, the multi-zone chemistry coordinate mapping (CCM) approach is based also on the fractional step CFD method, in which the integration of the different terms of the governing equations within a CFD time step is split into several fractional time steps. In RANS and LES, even in DNS (Yu et al. 2012), the CFD time step determined by the CFL number is too large for the integration of the chemical reaction rates, due to the large span of time scales of chemistry. Thus, multiple small fractional sub-time steps are used within each CFD time step to integrate the stiff chemistry.

The time-consuming part of the numerical simulation is the integration of the chemical reaction rates. As shown earlier, the integration of chemical reaction rates can be done in low-dimension chemistry zones. Each zone corresponds to a number of different CFD cells in the physical domain, so integration of the chemical reaction rates and heat release rate is not performed in every CFD cell in the physical domain. The results in the chemistry zones are mapped back to the CFD cells in physical domain, and subsequently integrated to the flow transport terms in every CFD cell in the physical domain. This procedure decreases the computational cost significantly since it is possible to group physical cells into a much smaller number of chemistry zones.

It is clear that the key issue of this approach is the selection of the chemical phase space. The extended multi-zone model of Flower et al. (2003) used temperature as the phase space coordinate; the model of Babajimopoulos et al. (2015) used temperature and a progress equivalence ratio, while the CA algorithm of Goldin et al. (2009) used temperature and the mass fractions of a number of key species. In a series of DNS studies of H_2/air HCCI combustion, methane/air premixed flames, and CO/H_2/air premixed flames under constant volume conditions (all cases with initial homogeneous composition fields, relevant to conditions in HCCI and SI engines), Jangi et al. (2011) proposed a two-dimensional phase space, with the element mass fraction of H and temperature as the phase space coordinates. Temperature was used to characterize the reaction progress, whereas the H element mass fraction to characterize the differential diffusion effect in an initially premixed mixture. The method was referred to as the multi-zone chemistry coordinate mapping (CCM), since it involved a two-way mapping between the CFD cells in physical domain and the multi-zone cells in the chemistry phase space. The 2D DNS with CCM was shown to reduce the DNS CPU time by nearly 70% with nearly the same results as that obtained from the full DNS. For 3D simulations the speedup is much greater.

The CCM and its associated errors were evaluated in a DNS of autoignition of an n-heptane jet discharged into a hot atmosphere, and in a RANS of spray combustion in a constant volume combustion vessel (Jangi and Bai 2012). It was shown that a four-dimensional phase space, with temperature, mass fraction of H element, mass fraction of the fuel (n-heptane), and scalar dissipation rate of the element mass fraction of H as the phase space coordinates predicted satisfactory results. The CCM approach was shown to be suitable for numerical simulations of liquid n-heptane

spray combustion based on the RANS models. The transient processes of spray mixing with the ambient air, ignition of the mixture, and stabilization of the mixing controlled diffusion flames were well predicted by the RANS-CCM model. RANS-CCM replicated the same results as RANS with direct integration of the chemical reaction rates in the physical domain; the computational cost of RANS-CCM was, however, only 3–7% of that needed for RANS with the direct integration of chemistry.

The four-dimensional phase space was applied to study the effect of EGR on the structure and soot emissions in a diesel spray flame in a constant volume vessel (Jangi and Lucchini 2013), and the liftoff behavior of the spray flame of n-heptane in a Diesel engine (Solsjo et al. 2013), and the liftoff and flame structure of n-dodecane spray combustion in a constant volume combustion vessel (Gong et al. 2014). The results were promising in terms of accuracy and efficiency. Typically, a factor 30 speedup rate was achieved in these applications.

The CCM model was recently extended to couple with the particle-based transported PDF model that has the advantage to close the chemical reaction rates (Jangi et al. 2015). In this model, referred to as PDF-CCM, instead of identifying and clustering CFD cells into the CCM zones, the notional Lagrangian particles that were in similar thermodynamic states were identified and clustered into the phase-space zones. The method was applied to simulate methane/air lifted jet flames in vitiated coflow. The multiple modes combustion behavior at different ambient temperature conditions were well captured using PDF-CCM. Good agreement with experiments were observed while a speedup factor of 20 was reached in the simulations as compared with the original PDF model.

The PDF-CCM model has also been extended to the Eulerian stochastic field based PDF model (Jangi et al. 2015). The model is referred to as the ESF-CCM, in which the thermodynamic states of the discretized stochastic fields were mapped into a low-dimensional phase space. Integration of the chemical stiff ODEs was performed in the phase space and the results were mapped back to the physical domain. This method was shown to be able to speedup the original ESF-PDF model by a factor of 20 or more. The ESF-CCM model had shown good predictive potential in numerical simulation of various turbulent combustion processes, e.g., a lean premixed flame blowoff process (Hodzic et al. 2017) and n-dodecane spray combustion in a constant volume combustion vessel (Gong et al. 2014).

17.6 Concluding Remarks

Numerical simulations are expected to play a more important role in designing future internal combustion engines that are facing increasingly stringent emission legislations and demands on engine efficiency. New engines are also required to run with alternative renewable fuels to achieve fossil-fuel-free transportation and sustainable development. While computers are becoming more powerful with time numerical simulations for design purpose will rely on combustion models that are not only robust, accurate but also efficient. Specialized models such as RIF, CFM and FGM

shall be developed further to simulate wider flame problems. General models such as those employing detailed chemistry will be used in the future for combustion processes that involves multiple combustion modes. Certainly, it is very important to develop chemical kinetic mechanisms that are on one hand accurate enough to describe the problem and on other hand of moderate size and stiffness, suitable for CFD simulations. To use these finite-rate chemistry-based models improving the computational efficiency is crucial. Methods, such as ISAT, ILDM, DRG, and DAC are expected to be important in practical applications, while methods based on the multi-zone/CCM concept shall be further developed. These models showed a promising speedup property. Further development of these models is needed to have a consistent and optimal phase space, in order to achieve a well-balanced accuracy and efficiency.

Acknowledgements The author acknowledges the financial support from the Swedish Energy Agency through KC-FP and CeCOST.

References

Aceves SM, Flowers DL, Westbrook CK, Smith JR, Dibble RW, Christensen M, Pitz WJ, Johansson B (2000) A multi-zone model for prediction of HCCI combustion and emissions. SAE Technical Paper 2000-01-0327

Babajimopoulos A, Assanis DN, Flowers DL, Aceves SM, Hessel RP (2015) A fully coupled computational fluid dynamics and multi-zone model with detailed chemical kinetics for the simulation of premixed charge compression ignition engines. Int J Eng Res 6:497–512

Bisetti F, Chen JY, Chen JH, Hawkes ER (2009) Differential diffusion effects during the ignition of a thermally stratified premixed hydrogen-air mixture subject to turbulence. Proc Combust Inst 32:1465–1472

Bray KNC, Libby PA, Moss JB (1985) Unified modeling approach for premixed turbulent combustion-part I: general formulation. Combust Flame 61:87–102

Candel SM, Poinsot TJ (1990) Flame stretch and the balance equation for the flame area. Combust Sci Technol 70:1–15

Carlsson H, Nordstrm E, Bohlin A, Wu Y, Zhou B, Li ZS, Alden M, Bengtsson PE, Bai XS (2015) Numerical and experimental study of flame propagation and quenching of lean premixed turbulent low swirl flames at different Reynolds numbers. Combust Flame 162:2582–2591

Chen JH (2011) Petascale direct numerical simulation of turbulent combustion-fundamental insights towards predictive models. Proc Combust Inst 33:99–123

Chen JH, Hawkes ER, Sankaran R, Mason SD, Im HG (2006) Direct numerical simulation of ignition front propagation in a constant volume with temperature inhomogeneities: I. Fundamental analysis and diagnostics. Combust Flame 145:128–144

Christensen M, Johansson B, Franke A, Richter M, Alden M (1999) A study of the homogeneous charge compression ignition combustion process by chemiluminescence imaging, SAE Technical Paper 1999-01-3680

Colin O, Benkenida A (2004) The 3-Zones extended coherent flame model (ECFM3Z) for computing premixed/diffusion combustion. Oil Gas Sci Technol Rev IFP 59:593–609

Colin O, Ducros F, Veynante D, Poinsot T (2000) A thickened flame model for large eddy simulations of turbulent premixed combustion. Phys Fluids 12:1843

De Paola G, Mastorakos E, Wright YM, Boulouchos K (2008) Diesel Engine Simulations with Multi-Dimensional Conditional Moment Closure. Combust Sci Technol 180:883–899

Dec JE (1997) A conceptual model of DI diesel combustion based on laser-sheet imaging, SAE Technical Paper 970873

Dempsey AB, Walker NR, Reitz R (2013) Effect of piston bowl geometry on dual fuel reactivity controlled compression ignition (RCCI) in a light-duty engine operated with gasoline/diesel and methanol/diesel. SAE Int J Eng 6:78–100

D'Errico G, Lucchini T, Contino F, Jangi M, Bai XS (2014) Comparison of well-mixed and multiple representative interactive flamelet approaches for diesel spray combustion modelling. Combust Theor Modell 18:65–88

Dunstan TD, Minamoto Y, Chakraborty N, Swaminathan N (2013) Scalar dissipation rate modelling for Large Eddy Simulation of turbulent premixed flames. Proc Combust Inst 34:1193–1201

Felsch C, Luckhchoura V, Weber J, Peters N, Hasse C, Wiese W, Pischinger S, Kolbeck A, Adomeit P (2007) Applying representative interactive flamelets (RIF) with special emphasis on pollutant formation to simulate a DI diesel engine with roof-shaped combustion chamber and tumble charge motion, SAE Technical Paper 2007–01–0167

Flowers D, Aceves S, Martinez-Frias J, Hessel R, Dibble R (2003) Effect of mixing on hydrocarbon and carbon monoxide emissions prediction for iso-octane HCCI engine combustion using a multi-zone detailed kinetics solver. SAE Technical Paper 2003–01–1821

Ge HW, Shi Y, Reitz RD, Willems WW (2010) Engine development using multi-dimensional CFD and computer optimization, SAE Technical Paper 2010-01-0360

Germano M, Piomelli U, Moin P, Cabot WH (1991) A dynamic subgrid-scale eddy viscosity model. Phys Fluids A: Fluid Dyn 3(7):1760–1765

Goldin GM, Ren Z, Zahirovic S (2009) A cell agglomeration algorithm for accelerating detailed chemistry in CFD. Combust Theor Modell 13(4):721–739

Gong C, Jangi M, Bai XS (2014) Large eddy simulation of n-Dodecane spray combustion in a high pressure combustion vessel. Appl Energy 136:373–381

Hanson R, Splitter D, Reiz RD (2009) Operating a heavy-duty direct-injection compression-ignition engine with gasoline for low emissions. SAE Paper 2009-01-1442

Hasse C, Barths H, Peters N (1999) Modelling the effect of split injections in diesel engines using representative interactive flamelets, SAE Technical Paper 1999–01–3547

Hawkes ER, Sankaran R, Pebay PP, Chen JH (2006) Direct numerical simulation of ignition front propagation in a constant volume with temperature inhomogeneities II. Parametric study. Combust Flame 145:145–159

Haworth DC (1999) Large-eddy simulation of in-cylinder flows, Oil & Gas Science and Technology-Rev. IFP 54:175–185

Haworth DC (2010) Progress in probability density function methods for turbulent reacting flows. Prog Energy Combust Sci 36:168–259

Heywood JB (1988) Internal combustion engine fundamentals. McGraw Hill Book Company, New York

Hodzic E, Jangi M, Szasz RZ, Bai XS (2017) Large eddy simulation of bluff body flames close to blow-off using an Eulerian stochastic field method. Combust Flame 181:1–15

Hu SY, Gong C, Bai XS (2017) Dual fuel combustion of n-heptane/methanol-air-EGR mixtures. Energy Procedia 105:4943–4948

Jangi M, Bai XS (2012) Multidimensional chemistry coordinate mapping approach for combustion modelling with finite-rate chemistry. Combust Theor Model 16:1109–1132

Jangi M, Yu R, Bai XS (2011) A multi-zone chemistry mapping approach for direct numerical simulation of auto-ignition and flame propagation in a constant volume enclosure. Combust Theor Model 16(2):221–249

Jangi M, Zhao X, Haworth DC, Bai XS (2015) Stabilization and liftoff length of a non-premixed methane/air jet flame discharging into a high-temperature environment: An accelerated transported PDF method. Combust Flame 162(2):408–419

Jangi M, Lucchini T, Gong C, Bai XS (2015) Effects of fuel cetane number on the structure of diesel spray combustion: An accelerated Eulerian stochastic fields method. Combust Theor Modell 19:549–567

Jangi M, Li C, Shamun S, Tuner M, Bai XS (2017) Modelling of methanol combustion in a direct injection compression ignition engine using an accelerated stochastic fields method. Energy Procedia 105:1326–1331

Jangi M, Lucchini TG, D' Errico, Bai XS (2013) Effects of EGR on the structure and emissions of diesel combustion. Proc Combust Inst 34:3091–3098

Joelsson T, Yu R, Bai XS (2012) Large eddy simulation of turbulent combustion in a spark-assisted homogenous charge compression ignition engine. Combust Sci Technol 84:1051–1065

Kalghatgi G, Risberg P, Angstrom H (2007) Partially pre-mixed auto-ignition of gasoline to attain low smoke and low NOx at high load in a compression ignition engine and comparison with a diesel fuel. SAE Paper 2007-01-0006

KIim WT, Huh KY (2002) Numerical simulation of spray autoignition by the first-order conditional moment closure model. Proc Combust Inst 29(2002):569–576

Klimenko AY, Bilger RW (1999) Conditional moment closure for turbulent combustion. Prog Energy Combust Sci 25:595–687

Knop V, Michel JB, Colin O (2011) On the use of a tabulation approach to model auto-ignition during flame propagation in SI engines. Appl Energy 88:4968–4979

Kokjohn SL, Hanson RM, Splitter DA, Reitz RD (2011) Fuel reactivity controlled compression ignition (RCCI): a pathway to controlled high-efficiency clean combustion. Int J Eng Res 12:209–226

Kong SC, Han Z, Reitz RD (1995) The development and application of a diesel ignition and combustion model for multidimensional engine simulation, SAE Technical paper 950278. https://doi.org/10.4271/950278

Lam SH, Goussis DA (1988) Understanding complex chemical kinetics with computational singular perturbation. Proc Combust Inst 22:931–941

Lecocq G, Richard S, Michel JB, Vervisch L (2011) A new LES model coupling flame surface density and tabulated kinetics approaches to investigate knock and pre-ignition in piston engines. Proc Combust Inst 33:3105–3114

Li Y, Jia M, Hang Y, Liu Y, Xie M, Wang T et al (2014) Parametric study and optimization of a RCCI (reactivity controlled compression ignition) engine fueled with methanol and diesel. Energy 65:319–332

Liang L, Stevens JG, Farrell JT (2009) A dynamic adaptive chemistry scheme for reactive flow computations. Proc Combust Inst 32:527–534

Lu T, Law CK (2005) A directed relation graph method for mechanism reduction. Proc Combust Inst 30:1333–1341

Maas U, Pope SB (1992) Simplifying chemical kinetics: intrinsic low-dimensional manifolds in composition space. Combust Flame 88:239–264

Magnussen BF, Hjertager BH (1977) On mathematical modeling of turbulent combustion with special emphasis on soot formation and combustion. Symposium (International) on Combustion 16:719–729

Manente V, Johansson B, Tunestal P (2010) Characterization of partially premixed combustion with ethanol: EGR sweeps, low and maximum loads. J Eng Gas Turbines Power 132:082802

Manente V, Johansson B, Tunestal P (2009) Partially premixed combustion at high load using gasoline and ethanol, a comparison with diesel. SAE Technical Paper, 2009-01-0944

Marble FE, Broadwell JE (1977) The coherent flame model for turbulent chemical reactions, Project Squid, Technical Report TRW-9-PU

Martz JB, Kwak H, Im HG, Lavoie GA, Assanis DN (2011) Combustion regime of a reacting front propagating into an auto-igniting mixture. Proc Combust Inst 33:3001–3006

Masimalai SK (2014) Influence of methanol induction on performance, emission and combustion behavior of a methanol–diesel dual fuel engine, SAE Technical Paper 2014-01-1315

Mastorakos E, Bilger RW (1998) Second-order conditional moment closure for the autoignition of turbulent flows. Phys Fluids 10:1246

Mittal V, Cook DJ, Pitsch H (2012) An extended multi-regime flamelet model for IC engines. Combust Flame 159:2767–2776

Najt PM, Foster DE (1983) Compression ignited homogeneous charge combustion. SAE Technical paper 830264
Nilsson P, Bai XS (2000) Level-set flamelet library approach for premixed turbulent combustion. Experiment Thermal Fluid Sci 21:87–98
Nogenmyr KJ, Fureby C, Bai XS, Petersson P, Collin R, Linne M (2009) Large eddy simulation and laser diagnostic studies on a low swirl stratified premixed flame. Combust Flame 156:25–36
Onishi S, Jo SH, Shoda K, Jo PD, Kato S (1979) Active thermo-atmosphere combustion–a new combustion process for internal combustion engines. SAE Technical paper 790501
Pan J, Wei H, Shu G, Chen Z, Zhao P (2016) The role of low temperature chemistry in combustion mode development under elevated pressures. Combust Flame 174:179–193
Persson H, Babajimopoulos A, Helmantel A, Holst F, Stenmark E (2017) Development of the combustion system for volvo cars Euro6d VEA diesel engine, SAE Technical Paper 2017-01-0713. https://doi.org/10.4271/2017-01-0713
Peters N (2000) Turbulent combustion, Cambridge University Press
Pitsch H, Barths H, Peters N (1996) Three-dimensional modeling of NOx and soot formation in DI-diesel engines using detailed chemistry based on the interactive flamelet approach, SAE Technical Paper 962057
Popa MG, Megurescu N, Pana C, Racovitza A (2001) Results obtained by methanol fuelling diesel engine. SAE Technical Paper 2001-01-3748
Pope SB (1985) Pdf methods for turbulent reactive flows. Prog Energy Combust Sci 11:119–192
Pope SB (1988) The evolution of surfaces in turbulence. Int J Eng Sci 26:445–469
Pope SB (1997) Computationally efficient implementation of combustion chemistry using in situ adaptive tabulation. Combust Theor Modell 1:41–63
Reitz RD (1987) Modeling atomization processes in high-pressure vaporizing sprays. Atomizat Spray Technol 3:309–337
Reitz RD, Ganesh D (2015) Review of high efficiency and clean reactivity controlled compression ignition (RCCI) combustion in internal combustion engines. Prog Energy Combust Sci 46:12–71
Reitz RD, Rutland CJ (1995) Development and testing of diesel engine CFD models. Prog Energy Combust Sci 21:173–196
Rutland CJ (2011) Large-eddy simulations for internal combustion engines-a review. Int J Eng Res 12:421–451
Sankaran R, Im HG, Hawkes ER, Chen JH (2005) The effects of non-uniform temperature distribution on the ignition of a lean homogeneous hydrogen-air mixture. Proc Combust Inst 30:875–882
Smagorinsky J (1963) General circulation experiments with the primitive equations: I. The basic equations. Mon Weather Rev 91:99–164
Solsjo R, Jangi M, Chartier C, Andersson O, Bai XS (2013) Lift-off and stabilization of n-heptane combustion in a diesel engine with a multiple-nozzle injection. Proc Combust Inst 34:3031–3038
Solsjo R, Jangi M, Tuner M, Bai XS (2012) Large eddy simulation of partially premixed combustion in an internal combustion engine. SAE Technical Paper 2012-01-0139
Swaminathan N, Bilger RW (1999) Assessment of combustion submodels for turbulent non-premixed hydrocarbon flames. Combust Flame 116:519–545
Tan Z, Reitz RD (2006) An ignition and combustion model based on the level-set method for spark ignition engine multidimensional modeling. Combust Flame 145:1–15
Thring RH (1989) Homogeneous charge compression ignition (HCCI) engines. SAE Technical paper 892068
van Oijen JA, Donini A, Bastiaans RJM, ten Thije Boonkkamp JHM, de Goey LPH (2016) State-of-the-art in premixed combustion modeling using flamelet generated manifolds. Prog Energy Combust Sci 57(2016):30–74
Vermorel O, Richard S, Colin O, Angelberger C, Benkenida A, Veynante D (2009) Towards the understanding of cyclic variability in a spark ignited engine using multi-cycle LES. Combust Flame 156:1525–1541

Yao C, Cheung CS, Cheng C, Wang Y, Chan TL, Lee SC (2008) Effect of diesel/methanol compound combustion on diesel engine combustion and emissions. Energy Convers Manag 49:1696–1704

Yao M, Zheng Z, Liu H (2009) Progress and recent trends in homogeneous charge compression ignition (HCCI) engines. Prog Energy Combust Sci 35:398–437

Yoo CS, Lu T, Chen JH, Law CK (2011) Direct numerical simulations of ignition of a lean n-heptane/air mixture with temperature inhomogeneities at constant volume: parametric study. Combust Flame 158:1727–1741

Yu R, Bai XS (2013) Direct numerical simulation of lean hydrogen/air auto-ignition in a constant volume enclosure. Combust Flame 160:1706–1716

Yu R, Yu J, Bai XS (2012) An improved high-order scheme for DNS of low Mach number turbulent reacting flows based on stiff chemistry solver. J Comput Phys 231:5504–5521

Yu R, Bai XS, Lehtiniemi H, Ahmed SS, Mauss F, Richter M, Alden M, Hildingsson L, Johansson B, Hultqvist A (2006) Effect of turbulence and initial temperature inhomogeneity on homogeneous charge compression ignition combustion. SAE Technical Paper, 2006-01-3318

Yu R, Bai XS, Vressner A, Hultqvist A, Johansson B, Olofsson J, Seyfried H, Sjoholm JO, Richter M, Alden M (2007) Effect of turbulence on HCCI combustion. SAE Technical Paper, 2007-01-0183

Zeldovich YB (1980) Regime classification of an exothermic reaction with nonuniform initial conditions. Combust Flame 39:211–214

Zhang F, Yu R, Bai XS (2012) Detailed numerical simulation of syngas combustion under partially premixed combustion engine conditions. Int J Hydro Energy 37:17285–17293

Zhang F, Liu HF, Yu R, Yao M, Bai XS (2016) Direct numerical simulation of H_2/air combustion with composition stratification in a constant volume enclosure relevant to HCCI engines. Int J Hydrog Energy 41:13758–13770

Zhang F, Yu R, Bai XS (2015a) Direct numerical simulation of PRF70/air partially premixed combustion under IC engine conditions. Proc Combust Inst 35:2975–2982

Zhang F, Yu R, Bai XS (2015b) Effect of split fuel injection on heat release and pollutant emissions in partially premixed combustion of PRF70/air/EGR mixtures. Appl Energy 149:283–296

Chapter 18
Characterization of Turbulent Combustion Systems Using Dynamical Systems Theory

Sirshendu Mondal, Achintya Mukhopadhyay and Swarnendu Sen

Abstract Turbulent combustion which is ubiquitous in all real engines in power and propulsion industries has inspired the combustion community to a great extent in recent years. Turbulence being the most significant unresolved problem gets more complicated by the interaction with combustion as combustion involves a large number of chemical reactions occurring at different time scales. A researcher often focuses on some specialized problems of turbulent combustion as it has many different aspects to investigate. One such challenging aspect of turbulent combustion is combustion dynamics. Many such facets of combustion dynamics have been understood through modelling, simulation and experiments. The present chapter proposes a survey of combustion dynamics which has been addressed under the parlance of dynamical systems theory. More recently, combustion instability in turbulent combustors such as modern low-NO_x gas turbine has gained a lot of attention. The stable state is generally characterized by combustion noise which is generated by turbulent reactive flow. A transition occurs from combustion noise to combustion instability through a dynamical regime called intermittency. Combustion instability is, in general, detrimental for all combustion systems except pulse combustors where combustion instability is deliberately maintained for better performance. The dynamical transition in pulse combustor has also been analyzed both theoretically and experimentally. The analysis of a nonlinear analytical model using dynamical systems theory reveals the regime of limit cycle oscillations, Hopf bifurcation, period-doubling bifurcations and so on. A case study of numerical continuation in pulse combustor model will be explained in detail at the end of this chapter.

Keywords Combustion dynamics · Pulse combustor · Bifurcation analysis · Continuation method

S. Mondal (✉)
Indian Institute of Technology Madras, Chennai 600 036, India
e-mail: sirshendumondal13@gmail.com

A. Mukhopadhyay · S. Sen
Jadavpur Universty, Kolkata 700 032, India
e-mail: achintya.mukho@gmail.com

S. Sen
e-mail: sen.swarnendu@gmail.com

© Springer Nature Singapore Pte Ltd. 2018

S. De et al. (eds.), *Modeling and Simulation of Turbulent Combustion*, Energy, Environment, and Sustainability, https://doi.org/10.1007/978-981-10-7410-3_18

Nomenclature

A Combustor surface area (m^2)
A_e Combustor cross-sectional area (m^2)
$\mathscr{A}$ Pre-exponential factor (s^{-1})
B Pre-exponential factor (s^-1)
C_p Specific heat at constant pressure (J/kgK)
C_v Specific heat at constant volume (J/kgK)
D_Tp Diameter of tailpipe (m)
f Friction factor (dimensionless)
h Convective heat transfer coefficient (W/m^2K)
h_eff Effective heat transfer coefficient (W/m^2K)
L_{c_1} First characteristic length (V/A)
L_{c_2} Second characteristic length (V/A_e)
L_Tp Length of tailpipe (m)
$\dot{m}_i$ Mass flow rate at combustor inlet (kg/s)
$\dot{m}_e$ Mass flow rate at combustor exit (kg/s)
P Pressure (Pa)
P_0 Ambient pressure (Pa)
$\bar{P}$ P/P_0 (dimensionless)
P_e Pressure in tailpipe (bar)
$\bar{P}_e$ P_e/P_0 (dimensionless)
T Temperature (K)
T_a Activation temperature (K)
T_0 Ambient temperature (K)
$\bar{T}$ T/T_0 (dimensionless)
T_e Temperature in tailpipe (K)
$\bar{T}_e$ T_e/T_0 (dimensionless)
T_w Wall temperature (K)
$\bar{T}_w$ T_w/T_0 (dimensionless)
u Gas velocity in tailpipe (m/s)
V Volume of combustor (m^3)
$\bar{u}$ $u/(L_{C_2}/t\tau_f)$ (dimensionless)
v_0 Stoichiometric coefficient of oxygen
y_o Oxygen mass fraction (dimensionless)
y_f Fuel mass fraction (dimensionless)
$y_{f,i}$ Inlet fuel mass fraction (dimensionless)
Z_i $\dot{m}_i/V$ (kg/m^3s)
Z_e $\dot{m}_e/V$ (kg/m^3s)
γ Ratio of specific heats (dimensionless)
κ_p Planck mean absorption coefficient
ρ_0 Ambient density (kg/m^3)
σ Stefan–Boltzmann constant (W/m^2K^4)
τ_c Characteristic flow time (s)
τ_f Characteristic heat transfer time (s)

τ_h Characteristic chemical reaction time (s)
ω_f Fuel consumption rate (kg/m^{3}s)
Δh_c Heat of combustion (kJ/mol)

18.1 Introduction

Combustion takes place in turbulent flow field for most technical systems. In such systems, the main source of energy is fossil fuels. As the energy comes from other sources such as nuclear, solar and wind is less than 20% of total energy demand, the combustion of fossil fuel is a crucial technology for energy production at present. While combustion of a fossil fuel gives mechanical and electrical energy stored in its chemical bonds, it also produces pollutants such as oxides of nitrogen (NO_x), soot, unburned hydrocarbon (UHC) etc. On the other hand, there are stringent emission norms devised to enforce the clean combustion for the sake of our environment. Towards this, improvement of combustion efficiency and thereby enhancement of fuel economy are the key aspects of combustion research.

In practical systems, reactive flow becomes unstable due to the difference in density and gas expansion caused by the released heat from combustion. Such flow instability results in the transition to turbulence. The turbulence, in turn, enhances the mixing processes and thereby helps in improving combustion efficiency. Therefore, research in turbulent combustion has been most challenging as well as promising for the past few decades. In the introduction, we present the importance and complexities of turbulent flow, turbulent reactive flow and followed by the different aspects of turbulent combustion.

18.1.1 Turbulent Flows

According to Richard Feynman, turbulence is the most important unsolved problem in classical physics. As said earlier, in most practical applications the flow is turbulent. Therefore, to solve the engineering problems numerically, several turbulence models are developed. These models rely on closure hypothesis that solves the disparity between the number of unknowns and equations in a turbulent model. The basis of the closure lies in the fact that breaking up of large eddies happens—into smaller eddies—into even smaller eddies in the inertial range. This is known as eddy cascade hypothesis which thereby satisfies the Reynolds number independence in the large Reynolds number limit. The success in turbulence modelling inspires the engineers and scientists to implement the similar approaches for the turbulent combustion. This leads to the so-called turbulent combustion model to deal with the turbulent reactive flow.

On the other hand, experimental turbulent research has improved with the advancement of statistical techniques leading to better understanding of turbulent

problem. In the past few decades, we have observed the important developments in the ability to acquire and store a significant amount of data and in the application of new diagnostics tools such as particle image velocity (PIV), laser-induced fluorescence (LIF) and laser Doppler anemometry (LDA). A unified approach which allows us to analyse a turbulent flow in terms of both space and scale is wavelet transform (Farge 1992). Further, multi-dimensional, time-resolved measurements along with advanced data mining algorithms have improved the understanding turbulence as well as turbulent reactive flows.

Turbulence which is usually viewed as a stochastic phenomenon is best modelled through a probabilistic approach. Even then the flow may be highly sensitive to its boundary and initial conditions making the dynamics in phase space a strange attractor (Kadanoff 1983). The dynamics due to such nonlinearities present in a turbulent reactive flow will be discussed in the following sections.

18.1.2 Turbulent Reactive Flows

The scenario gets largely complicated when we implement the turbulence modelling approach in reactive flows. As fuel and oxidizer mix at the molecular level before they react, the reaction kinetics depend on the process of turbulent mixing. Further, such molecular mixing as well as heat conduction, diffusion of radicals etc., take place at the interface between small eddies. The whole process of mixing and diffusion which gets modified by the combustion is still a topic of investigation.

Combustion involves a large number of elementary chemical reactions. These reactions occurring on different time scales do not essentially interact with the time scales of inertial subrange (Peters 2000). The isothermal mixing is certainly different from the mixing with combustion. There is an increase of temperature due to heat release rate by combustion. This increase of temperature, in turn, affects the reaction rate as the combustion chemistry consisting of many chain branching and chain breaking reactions is very sensitive to temperature. Such feedback between heat release and combustion chemistry leads to the occurrence of ignition and extinction. Prior to ignition, reaction rate remains very low and depends on the Damköhler number which is the ratio of the residence time scale to the chemical time scale. As one increases the residence time by lowering the flow velocity, ignition point is approached leading to the situation where the heat release and the exothermic reaction rate set up a feedback loop, known as thermal runaway. In such a situation, the chemical time scales are small compared to all turbulent time scales. Therefore, they do not affect the inertial subrange. Furthermore, at the time of extinction, the chemistry becomes very slow and the mixing happens only in the scales of inertial subrange. Therefore, in the regimes of both fast and slow chemistry for most practical combustors, the scales of combustion can be separated from those of turbulence. Therefore, in most turbulent combustion models, scale separation is assumed.

It is well known that the flow is turbulent in almost all combustion devices. So, researchers who are interested in practical problems have been attracted to turbulent

combustion. Furthermore, the intricacies of turbulent combustion described above make it more exciting and challenging. When we think of turbulent reactive flow, it is roughly governed by Navier–Stokes equations along with chemical kinetic laws. In other words, there is a strong coupling between chemistry, transport phenomena and fluid dynamics in a problem of turbulent combustion. Therefore, different closures schemes are developed towards the understanding of turbulent transport and burning velocities.

Once a model is implemented in a numerical code, it needs to be validated against the experimental data and improved. The studies in experimental reacting flow are conducted for gaining a better fundamental understanding of different aspects of turbulent combustion. One such aspect is the interaction between chemical kinetics and hydrodynamics which can have significant effects on flame stability and pollutant formation in practical combustion systems. Another aspect, for example, is the dynamics of turbulent combustion which is the main focus of this chapter. By dynamics, we mean both temporal and spatiotemporal dynamics of a turbulent reactive flow.

18.1.3 Different Aspects of Turbulent Combustion

According to F. A. Williams, the topic of turbulent combustion is so huge that it can be compared with the story of defining the proverbial elephant (Buckmaster 1985). In other words, two random researchers working on turbulent combustion may define and characterize it from completely different point of views. Turbulent combustion is such a multifaceted topic that any review will be biased towards some aspects of the same. One such aspect is transport phenomena occurring in turbulent flames. This includes heat transfer, molecular diffusion, convection, turbulent transport etc. Further, to examine the formation of combustion products and pollutant species, one has to focus on the detailed chemical reaction schemes. Further, precise knowledge of chemistry is also mandatory for prediction of ignition, stabilization, extinction etc. On the other hand, for liquid fuel combustion, one needs to investigate the breakdown of liquid sheets, vaporization, turbulent mixing and droplet combustion. Radiative heat transfer should be one of the major focus while one is interested in studying soot formation and interaction with walls. Other aspect of turbulent combustion which is of practical importance is the dynamics or instabilities observed in practical turbulent combustors. The present chapter proposes a survey of combustion dynamics which has been addressed under the parlance of dynamical systems theory.

18.2 Combustion Dynamics

One of the most challenging areas in turbulent combustion research is combustion dynamics. The elementary dynamical processes related to turbulent combustion are

vortex rollup, coupling between flames and acoustics, dynamics of perturbed flame and the flame response to the variable strain. Among them, combustion instability due to the interactions between flame oscillation and acoustics in turbulent combustors such as modern low NO_x gas turbine has gained a lot of attention in recent times.

The occurrence of self-sustained large amplitude pressure oscillations produced due to a closed-loop interaction between the unsteady flame and the acoustic field of the confinement is known as combustion instability or thermoacoustic instability. The nonlinear analysis of such combustion instabilities sometimes focused on obtaining nonlinear describing function either experimentally or numerically (Noiray et al. 2008). The technique involves forcing the flame over all the possible ranges of frequencies and amplitudes, decoupling the flame from acoustics. However, dynamics of a forced system is different from that of a self-sustained systems (Pikovsky et al. 2003). On the other hand, the stability and the nature of the asymptotic state can be assessed from the time evolution of pressure inside a combustor. These linear (Trefethen and Embree 2005) and nonlinear (Burnley 1996) behaviour of the system can be systematically investigated using the tools from dynamical systems theory. In this section, we introduce thermoacoustic instability, traditional approach to study the phenomena followed by a short review on study of combustion dynamics in the framework of dynamical systems theory.

18.2.1 Thermoacoustic Instability

It is a dynamics phenomenon observed in most modern combustion systems such as aero engines, rocket motors, land-based gas turbines and so on. Thermoacoustic instability sets in primarily from a coupling of acoustic pressure oscillations in a confined space and unsteady release (due to turbulent fluctuations, coherent structures, equivalence ratio fluctuations, etc.). The pressure waves get amplified by the fluctuations in heat release rate. In other words, if the heat release rate fluctuates, pressure waves are generated due to the volumetric dilatation at the location of heat release. These waves, in turn, modulate the heat release rate fluctuations after reflection from the boundaries and the walls of the combustion chamber. Thus, a feedback loop is setup between acoustics and flame oscillations.

If the phase between the pressure oscillations established in the chamber and the fluctuations of heat release rate lies between $-90°$ and $90°$, a continuous growth in pressure and velocity oscillations may occur until the nonlinearities take over (Rayleigh 1878). Then the amplitude of pressure and velocity oscillations saturate (when the total energy losses from the combustion chamber balances the energy input through combustion) and an almost constant amplitude periodic oscillations are exhibited, known as thermoacoustic instability. During this saturated thermoacoustic instability, the amplitude pressure oscillations can go up to 120 dB in atmospheric flames and much more than that in rocket engines (Polifke 2004).

The occurrence of thermoacoustic instability is always undesirable except in pulse combustors which we discuss in the later part of this section. In general, this type of instability is a serious problem in the design and development of combustors. The high amplitude of pressure oscillations inside the combustor can induce structural damage to the combustor due to high heat transfer rate to the walls and can also lead to complete failure of the engine. As a consequence, it leads to huge revenue losses to gas turbine manufacturers (Nair and Sujith 2014). Therefore, predicting and controlling the onset of such oscillations require detailed investigation of inherent dynamics and the coupled interaction between acoustic field and the turbulent flame. The positive feedback loop which may result in thermoacoustic instability is closely related to the time scales of different processes.

There are different time scales involved in turbulent combustion. Those time scales are associated with the atomization and evaporation of the fuel, convection time scales, mixing time scales, chemical time scales, acoustic time scales, etc. In a sense, thermoacoustic instability is caused by the parity between these timescales (Polifke 2004). Further, the coherent structures in the reactive flow formed due to the characteristics of the flame holding devices or the geometry of the combustor can interact with the flame causing heat release rate fluctuations resulting in thermoacoustic instability (Lieuwen and Yang 2005). Unsteady combustion usually produces entropy waves in the flow field. These entropy waves when accelerated through the combustor exit or the turbine entrance can generate acoustic waves. Further, equivalence ratio fluctuations are also known to cause thermoacoustic instability (Lieuwen 2001). Thus, thermoacoustic instability can originate as a result of interaction between flame oscillations due to various flow features and the acoustic field. In almost all cases, this interaction is highly complicated and nonlinear due to the interplay between turbulence, the chemistry of the reaction.

18.2.2 Traditional Approach

Several studies in thermoacoustic instability considered the nonlinearities only in the gas dynamic process (Culick 1970, 1976, 1988, 1994). This was further substantiated by the fact that the acoustic pressure is less than 5% of the mean pressure and hence the nonlinearities in acoustic waves are not significant (Dowling 1997; Peracchio and Proscia 1999; Lieuwen 2002). However, it was shown that for lean premixed combustors, the nonlinearities in flame response is very significant (Lieuwen and Yang 2005; Preetham and Lieuwen 2004; Hosseini 2009). The studies included different simple thermoacoustic systems which are less complex compared to practical, say, gas turbine engine. However, such laboratory-scale systems are quite capable of capturing inherent dynamics and interactions leading to thermoacoustic instability.

Thermoacoustic instabilities have been studied in a prototypical thermoacoustic system, called Rijke tube, in order to avoid the complexities of the combustion process. A horizontal Rijke tube consists of a heated wire mesh positioned inside a horizontal duct through which a flow of air is established (Matveev and Culick

2003). The nonlinear nature of heat release rate has been established (Heckl 1985, 1988, 1990) and characterized (Matveev and Culick 2003). In a pioneering study, the non-normality of the thermoacoustic system was identified by Sujith and coworkers (Balasubramanian and Sujith 2008a, b). The effect of noise on the stability of a horizontal Rijke tube was also investigated (Waugh and Juniper 2011). They observed that under the influence of noise, a thermoacoustic system could become unstable even in the linearly stable regime. The effect of noise on the hysteresis characteristics of a horizontal Rijke tube was studied both experimentally and theoretically (Gopalakrishnan and Sujith 2015) and was shown that the width of the bistable region reduced as the noise intensity was increased. The presence of such nonlinear characteristics of thermoacoustic oscillations even in a prototypical system indicates the need for nonlinear analysis to understand thermoacoustic instability observed in practical systems with turbulent reactive flow. Even though a major share of the past research focused on linear stability analysis and identifying flame transfer functions to characterize thermoacoustic instability in different combustors, recently studying the nonlinear dynamics of thermoacoustic instability has gained lot of attention.

18.2.3 Dynamical Systems Theory Approach

A system that changes with time is called a dynamical system and is generally described through a set of differential equations. A branch of mathematics which deals with the time evolution of such systems is known as dynamical systems theory. The concepts and tools from dynamical systems theory are generally used to investigate and characterize the dynamical system even though one does not have the access to all the state variables of the system.

A thermoacoustic system can not only exhibit simple limit cycle oscillations but also could undergo a pitchfork and torus bifurcation and exhibit quasiperiodic oscillations (Jahnke and Culick 1994) which is characterized by the presence of two incommensurate dominant frequencies and their multiples. The possibility of chaotic oscillations was also identified by using numerical bifurcation analysis on models for premixed combustors (Sterling 1993; Lei and Turan 2009). Chaotic dynamics is also observed in experiments with lean gas turbine combustors (Fichera et al. 2001).

Recently, numerical continuation was used to investigate the bifurcation to thermoacoustic instability for a horizontal Rijke tube (Subramanian 2011) and it was shown interesting dynamical behavior such as co-existing multiple attractors, quasiperiodic behaviour and period-doubling route to chaos. In experiments, Kabiraj et al. (2012a, b, c) and Kabiraj and Sujith (2012) established routes to chaos in thermoacoustic system through bifurcation studies. In a ducted laminar premixed laminar combustor, they observed that apart from limit cycle oscillations thermoacoustic systems exhibited various complex dynamic states such as intermittency, frequency locked and chaotic states. They (Kabiraj et al. 2012a, b, c; Kabiraj and Sujith 2012) also observed both the Ruelle–Takens and the frequency locking quasiperiodic route

to chaos in their experiments. Later, detailed numerical investigations confirmed these findings (Kashinath et al. 2014, 2013).

Traditionally, the transition to thermoacoustic instability was thought of as a bifurcation from stable operation (steady state) to unstable operation (limit cycle) through a Hopf point (Lieuwen 2002; Kabiraj et al. 2012b). This simple description is valid for laminar systems. However, turbulent systems are complicated and a simple description of Hopf bifurcation may not be suitable for its description. Recent studies have been focussed on the transition from combustion noise to thermoacoustic instability for turbulent reactive flows from the viewpoint of dynamical system theory (Gotoda et al. 2011, 2012; Noiray and Schuermans 2013; Gotoda et al. 2014; Domen et al. 2015; Nair and Sujith 2014; Nair et al. 2014). Sujith and co-workers established that combustion noise is chaotic (Nair et al. 2014; Tony et al. 2015) and identified that the transition from combustion noise (chaotic dynamics) to thermoacoustic instability (periodic dynamics) happened through a dynamic regime called intermittency (Nair and Sujith 2014, 2015; Nair et al. 2014). The presence of intermittent dynamics was even exploited to obtain precursors for thermoacoustic instability (Nair et al. 2013, 2014; Nair and Sujith 2014). Nair et al. (2014) was able to quantitatively characterize the intermittency in the time series of acoustic pressure and was able to device a precursor to an impending thermoacoustic instability using Recurrence Quantification Analysis (RQA).

Later, Pawar et al. (2016) used RQA to characterize the dynamics of a laboratory spray combustor. They observed that transition to thermoacoustic instability happened through a regime of intermittency and that the intermittency is possibly of type II suggesting that the underlying bifurcation responsible for the intermittency is a subcritical Hopf bifurcation. The above observations exhibit the complex nature of oscillations in a combustor during different dynamic regimes. Especially, the chaotic nature of the oscillations during combustion noise is the result of underlying turbulent fluctuations in the flow field of the combustor. In the recent past, the interaction between pressure and heat release oscillations during the transition to thermoacoustic instability has been studied spatiotemporally (Mondal et al. 2017, 2016) in the framework of synchronization theory.

Having reviewed the studies focusing on the dynamics during the transition to thermoacoustic instability, we turn our attention to pulse combustor wherein, as said earlier, instability is preferred and maintained. In other words, whereas the primary focus of dynamical studies in gas turbine combustor is to suppress the instability, maintaining and controlling the oscillatory combustion is of prime concern in pulse combustor.

18.2.4 Pulse Combustor and Its Dynamics

Pulse combustor is the only air-breathing engine where combustion instability or the pressure pulsation is deliberately maintained. The pulsation or oscillation in pressure and velocity inside the combustor leads to higher efficiencies, higher heat transfer

rates and lower emission than corresponding steady combustors. Although, pulse combustors have been used for applications such as domestic heating and drying (Putnam et al. 1986), the feasibility of pressure gain combustion (Narayanaswami and Richards 1996) (i.e., combustion with a gain in total pressure unlike conventional gas turbine combustors where there is a fall in total pressure) with pulse combustors has enhanced the potential of its use as a propulsion device. In particular, due to lack of moving parts, pulse combustors are an attractive option for micro-propulsion devices (Geng et al. 2007). However, the dynamics of thermal pulse combustors are very sensitive to operating conditions. As the desirable performances are obtained only under specific dynamic behaviour, a proper understanding of the dynamics of thermal pulse combustor is crucial for its successful design.

The thermoacoustic oscillations in a pulse combustor correspond to limit cycle behaviour (Margolis 1994). A popular reduced order model of Richards et al. (1993) assumes a perfectly stirred reactor for the thermal pulse combustor and incorporates the coupling between the combustor dynamics and flow through the tailpipe. The route to chaos as a dynamical transition has been observed (Daw et al. 1995) in experiments with a laboratory-scale pulse combustor and also in the model of Richards et al. (1993). The work used residence time as the bifurcation parameter. Rhode et al. (1995), using the same model (Richards et al. 1993) extended the flammable range of flow time by controlling the chaos. They have used friction factor as the control variable. In another study, In et al. (1997) maintained (anti-control) chaos in the system that prevented the system from a transition to flame extinction, thereby they extended the flammable region. They, using the model of Richards et al. (1993), considered the residence time both as the bifurcating parameter and control parameter. Edwards et al. (2000, 2001) used nonlinear feedback control to extend the operation of pulse combustors to lean equivalence ratios and reduce levels of NO and unburned hydrocarbon (UHC) emission by intermittent injection of additional fuel.

Narayanaswami and Richards (1996) developed the concept of pressure gain combustion in gas turbine combustors using pulsed combustors. They extended the model of Richards et al. (1993) to include the expansion and backflow of the combustor gases into the inlet. In a companion paper, Gemmen (1996) compared the model predictions and experimental observations and obtained qualitative agreement. They also used a scale analysis to obtain the dimensions of pressure gain combustor. Tang et al. (1995) investigated the heat release timing in a non-premixed pulse combustor. Their studies indicated that the interaction between the complex flow and combustion processes causes the time delay needed to produce heat release oscillations that are nearly in phase with the pressure oscillations, thus assuring pulse combustion operation. Kushari et al. (1996) investigated the fuel effect on the dynamics of pulse combustors by comparing the amplitude and phase of oscillations for pulse combustors using methane, methane–carbon dioxide and methane–hydrogen–carbon dioxide fuel blends. They found that addition of hydrogen extends the rich flammability limit but decreases the amplitude of oscillations. Mukhopadhyay et al. (2008) investigated the effect of tailpipe friction on the dynamic characteristics of the pulse combustor for both self-sustained and forced oscillations. The results of experimental investigations reported in the literature suggest that wall temperature has a signicant

effect on the dynamic characteristics of the combustor. In the context of gas-less combustion of thermites, Margolis (1993) conducted a somewhat analogous study to investigate the route to chaos and presented results in terms of various qualitative and quantitative parameters. For further reading, we refer to the review articles of Mondal et al. (2015) and Meng et al. (2016).

18.3 Numerical Continuation of a Model Pulse Combustor: A Case Study

The direct time integration is computationally expensive. Further, the bifurcation points in the solution branch cannot be precisely traced through numerical integration. On the other hand, numerical continuation is an approach which is used to track the solution branches by smoothly varying one or more parameters and to accurately determine the bifurcation points (Strogatz 2014). Although bifurcation diagrams have been reported for different combustion systems in literature, such studies have mostly been limited to the stability analysis of steady states, referred to as fixed points in dynamical systems literature.

Benedetto et al. (2002) analyzed the stability of fixed points in a propane-fired, well-stirred reactor. They identified the effects of different operating parameters and found the existence of self-sustained oscillations in narrow regions close to extinction. They also studied the stability of fixed points for a coupled well-stirred reactors. Russo et al. (2005) extended the earlier study by considering the effect of blending hydrogen with propane in a well-stirred reactor. They found that the presence of hydrogen narrows down the region of self-sustained oscillations close to lean blowout. Petrova et al. (2008) also examined the stability of fixed points in perfectly stirred reactors and found the oscillatory behaviour near extinction. Garcia-Agreda et al. (2012) investigated the effect of adding hydrogen on the dynamic behaviour of lean-premixed combustion of pre-vaporized ethanol.

In conventional combustors, large pressure oscillations are generally considered undesirable and hence the focus is on the stability of fixed points. Only a few authors have studied the stability of periodic solutions, referred to as limit cycles in nonlinear dynamics (Jahnke and Culick 1994). On the other hand, in pulse combustors, the stable periodic solution is the desired state and stability of limit cycles needs to be carefully investigated. Hence, both birth of limit cycles from fixed points through Hopf bifurcation and transition from limit cycles to more complicated (possibly chaotic) dynamics are of interest. The existence of a large variety of dynamical states in thermal pulse combustors has been demonstrated by different researchers including the present group (Mukhopadhyay et al. 2008; Datta et al. 2009; Mondal et al. 2012, 2014). Mukhopadhyay et al. (2008), Datta et al. (2009) and Mondal et al. (2012) investigated the effects of different parameters on the nonlinear dynamics and possible transition to chaos in pulse combustors using a modified version of the perfectly stirred reactor model of Richards et al. (1993). It has been shown that as the tailpipe

friction factor is lowered, the system undergoes a transition from steady combustion through oscillating combustion to an intermittent combustion with chaotic characteristics before extinction (Bloom and Patterson 2009; Mukhopadhyay et al. 2008). Mondal et al. (2012) explored preheating and dilution of reactants as a mechanism for extending the periodic regime to higher reactant flow rates at which the flame extinguishes under unheated conditions. The focus of the present work (Mondal et al. 2016) is to systematically investigate the stability of both the fixed points and the limit cycles through identification of bifurcation points for different control parameters. The bifurcation points are identified from continuation of both steady states and limit cycles.

A pulse combustor consists of a combustion chamber and a tailpipe as shown schematically in Fig. 18.1. The coupling between the heat release rate inside the combustor and acoustics of the tailpipe is responsible for the self-sustained oscillations in pulse combustor. The present model is similar to that of Richards et al. (1993) and Datta et al. (2009). The major assumptions of the model are: (1) Perfectly Stirred Reactor (PSR) for the combustor; (2) plug flow in the tailpipe; (3) constant specific heat and ideal gas model for the reactant and product gases; and (4) single-step Arrhenius model for chemical kinetics and (5) convective and radiative heat loss to the wall. The original model of Richards et al. (1993) was subsequently modified by Datta et al. (2009) to include radiative heat loss from the flames, which introduces an additional nonlinearity.

This model which has been widely used in the literature to simulate the dynamics of pulse combustors is described in terms of four coupled nonlinear ordinary differential equations derived from conservation of mass, energy and fuel species in the combustor and from the conservation of momentum in the tailpipe. The model equations involve three characteristic times, flow time (τ_f), heat transfer time (τ_h) and chemical reaction time (τ_c), representing the flow rate, rate of heat transfer and rate of chemical reaction. Those are defined as follows.

$$\tau_f = \frac{\rho_0}{Z_i} \tag{18.1}$$

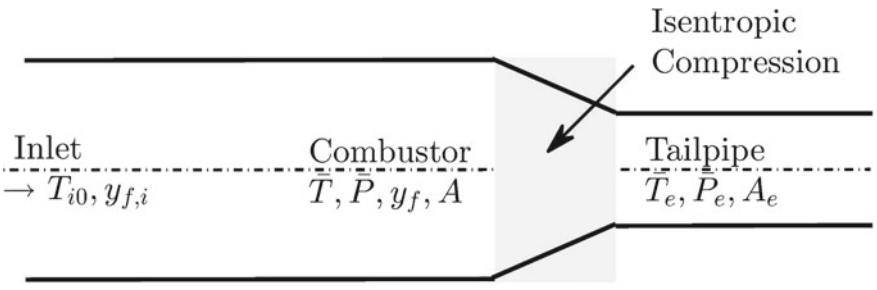

Fig. 18.1 Schematic of a pulse combustor consisting of a combustion zone and a tail pipe

$$\tau_h = \frac{L_{C_1}\rho_0 C_p T_0}{h_{eff} T_W} \tag{18.2}$$

$$\tau_c = \left[\frac{B\Delta h_c p^2}{C_p T_0 T^{3/2}} {y_f}^2 exp(-\frac{T_a}{T})\right]^{-1} \tag{18.3}$$

A single-step global Arrhenius kinetics (Eq. 18.4) is adopted for the derivation of chemical timescale, defined in Eq. 18.3.

$$\omega = -\mathscr{A}\nu_o T^{1/2}\rho^2 {y_f}^2 exp\left(-\frac{T_a}{T}\right) \tag{18.4}$$

where, the stoichiometric mixtures have been invoked at all times with the relation $y_o = \nu_o y_f$. The chemical timescale defined in Eq. 18.3 assumes perfect mixing of the reactants. The parameter h_{eff} in Eq. 18.2 reflects the effective heat transfer coefficient combining the convective and radiative heat losses. With an optically thin model, the effective heat transfer coefficient can be expressed as

$$h_{eff} = h + 4\kappa_p \sigma T_0^3 L_{c_1}(T_w^2 + T^2)(T_w + T) \tag{18.5}$$

Conservation of mass and energy equations for the combustor can be written as follows:

$$\frac{d\rho}{dt} = Z_i - Z_e \tag{18.6}$$

$$\frac{d}{dx}(\rho C_v T) = C_p(Z_i T_{i0} - Z_e T) - h_{eff} A(T - T_w) - {}_f\Delta h_c \tag{18.7}$$

Using ideal gas equation of state, the above equations lead to the following ordinary differential equations in terms of the timescales defined in Eqs. 18.1–18.3:

$$\frac{d\bar{T}}{dt} = \frac{\gamma\bar{T}}{\bar{P}}\left[\frac{\bar{Z}_i\bar{T}_{i0}}{\tau_f} + \frac{1}{\tau_h} + \frac{1}{\tau_c}\right] - \frac{\bar{T}^2}{\bar{P}}\left[\frac{Z_i}{\tau_f} + (\gamma - 1)\frac{Z_e}{\rho_0} + \frac{\gamma}{\bar{T_W}\tau_h}\right] \tag{18.8}$$

$$\frac{d\bar{P}}{dt} = \gamma\left[\frac{\bar{Z}_i\bar{T}_{i0}}{\tau_f} + \frac{1}{\tau_h} + \frac{1}{\tau_c}\right] - \gamma\bar{T}\left[\frac{Z_e}{\rho_0} + \frac{1}{\bar{T_W}\tau_h}\right] \tag{18.9}$$

Further, from the conservation of fuel species inside the combustor one can write the following:

$$\frac{d}{dt}(\rho y_f) = Z_i y_{f,i} - Z_e y_f + \omega_f \tag{18.10}$$

which, using the timescales defined in Eqs. 18.1–18.3, reduces to

$$\frac{dy_f}{dt} = \frac{\bar{Z}_i \bar{T}}{\bar{P}\tau_f}[y_{f,i} - y_f] - \frac{C_p T_0 \bar{T}}{\Delta h_c \bar{P} \tau_c} \tag{18.11}$$

The entire tailpipe is considered separately as a single control volume. Assuming plug flow, the momentum balance in the tailpipe can be expressed as

$$\frac{du}{dt} = \frac{1}{\rho_e V_{TP}}(P_e - P_0)A - \frac{F_f}{\rho_e V_{TP}} \tag{18.12}$$

In the above equation, F_f is the friction force given by $F_f = \frac{f}{4}\rho\frac{u}{2}\pi D_{TP} L_{TP}\frac{u}{|u|}$. The factor $\frac{u}{|u|}$ determines the direction of the friction force. After some algebraic manipulations, we obtain

$$\frac{d\bar{u}}{dt} = \frac{RT_{0f}\bar{T}_e}{L_{c_2} L_{TP} \bar{P}}(\bar{P}_e - 1) - \frac{f}{2}\frac{\bar{u}^3}{|\bar{u}|}\frac{L_{c_2}}{D_{TP}\tau_f} \tag{18.13}$$

Z_e is obtained from conservation of mass within the tailpipe as

$$Z_e = \frac{\bar{u}}{\tau_f}\frac{\bar{P}_e}{\bar{T}_e} \tag{18.14}$$

Finally, due to the short length of the nozzle connecting the combustor and the tailpipe, the flow in the nozzle is assumed isentropic. Thus, the pressure and the temperature in the tailpipe are related to the combustor variables through isentropic relations as

$$\bar{T}_e = \bar{T} - \frac{\bar{u}^2 L_{c_2}^2}{2C_p T_0 \tau_f^2} \tag{18.15}$$

and

$$\bar{P}_e = \bar{P}\left(\frac{\bar{T}_e}{\bar{T}}\right)^{\frac{\gamma}{\gamma-1}} \tag{18.16}$$

The bifurcation and stability analysis of the model (Eqs. 18.8, 18.9, 18.11 and 18.13) are performed using a MATLAB toolbox "MATCONT", which is a collection of numerical algorithms (Dhooge and Govaerts 2003; Mestrom 2002) implemented for the detection, continuation and identification of equilibrium points and limit cycles. We also present the results by integrating the model numerically to support the bifurcation results obtained from continuation method. The numerical integration is performed using the library function ODE45 (RK4) of commercial package, MATLAB.

For a set of ODEs, fixed points or equilibrium points are determined by setting all the time derivative equal to zero and solving the resulting set of algebraic equations (Jahnke and Culick 1994). The stability of the fixed points is determined by

examining the eigenvalues of the Jacobian matrix (evaluated at the fixed point) of the linearized system equivalent to the original system (Strogatz 2014). Further, stability analysis of limit cycles is required for pulse combustor which is expected to be operated in the oscillatory mode. For determining the stability of limit cycles, the first step is to construct Poincare maps which contain successive intersections of the trajectory with a specified plane. For limit cycles with period-1, which represents the dynamics of the pulse combustor in its desired state of operation, the trajectory always intersects any specified plane (transverse to the flow) at a single point. Thus, the Poincare map of a periodic (period-1) orbit is a fixed point. Now, the stability of the periodic orbits (or stability of the corresponding fixed points of the Poincare map) is determined by calculating the Floquet multipliers of the discretized system. Floquet multipliers of the periodic orbits are analogous to the eigenvalues of a steady state (Jahnke and Culick 1994). At the stability boundary, the real part of one of the eigenvalues is equal to zero and correspondingly one Floquet multiplier is equal to (+1). The periodic solution of the system is stable, if one of the Floquet multipliers equal to one, and all others Floquet multipliers are smaller than one (lying inside a unit circle of a complex plane). If at least one Floquet multiplier of a cycle lies outside a unit circle, the periodic solution of the system is unstable.

Using the model (Eqs. 18.8, 18.9, 18.11 and 18.13) mentioned above, we first evaluate the fixed points by varying the initial conditions. We end up with two different fixed points (there may be many more). Next, a stable fixed point (all eigenvalues having negative real parts) is selected as an initial point for continuation of steady state. For the present study, we examine the steady-state and limit cycle continuation for different bifurcation parameters, namely, tailpipe friction factor, wall temperature, heat transfer coefficient, inlet temperature and inlet fuel mass fraction.

The base set of parametric values given in Table 18.1 corresponds to those used by Datta et al. (2009) to obtain periodic solution. For all bifurcation parameters, the starting points correspond to such stable steady states obtained by altering one of the parameters from the base values while retaining the other parameters at their base

Table 18.1 Parameter values used in simulation

Parameter	Value	Parameter	Value
A	0.0167 m^2	κ_p	0.5
V	0.0001985 m^3	P_0	1×10^5 Pa
B	3.85×10^8 S^{-1}	T_a	50
C_p	1200 J/kgK	T_0	300 K
D_{TP}	0.0178 m	T_w	1140 K
L_{C_1}	0.0119 m	γ	1.27
L_{C_2}	0.7434 m	ρ_0	1.12 kg/m^3
L_{TP}	0.61 m	τ_f	0.027 s
$y_{f,i}$	0.06	h	120
$T_i 0$	300 k	f	0.03

Table 18.2 Eigenvalues of the system linearized about respective fixed points

Fixed points	Eigenvalues
$\bar{T} = 4.956001$	1021.9
$\bar{P} = 1.055721$	−152.8263
$y_f = 0.027355$	−2.0144e + 002 + 7.5374e + 002i
$\bar{u} = 4.793446$	−2.0144e + 002 − 7.5374e + 002i
$\bar{T} = 6.538749$	−1.4339e + 001 + 1.2093e + 003i
$\bar{P} = 1.072897$	−1.4339e + 001 − 1.2093e + 003i
$y_f = 0.011866$	−568.5047
$\bar{u} = 6.261388$	−461.4361

values. The parametric range of interest is obtained from previous numerical results of our group (Mukhopadhyay et al. 2008; Datta et al. 2009; Mondal et al. 2012). With the new set of parametric values, a few steady states are identified by changing the initial guesses of the state variables within physically relevant range and the stability of those steady states is checked. The fixed points and corresponding eigenvalues are shown in Table 18.2. The system is linearized about those fixed points and eigenvalues of the Jacobian matrix are calculated. Starting from a stable fixed point, continuation curve is drawn using MATCONT. The stable fixed point is chosen in such a way that changing one of the parameters can lead to periodic behaviour through direct integration of the model equations. In the following subsections, the results are presented for different bifurcation parameters individually.

18.3.1 Varying Tailpipe Friction Factor (f)

By integrating the above model numerically, Mukhopadhyay et al. (2008) obtained the transition from periodic oscillation ($f = 0.03$) to extinction through period doubling bifurcation ($f = 0.0285$) by lowering the tailpipe friction factor. In the present work, we present continuation of steady states and limit cycles by changing the friction factor (f). In Fig. 18.2, the solid (black) line represents the stable steady states whereas the dashed (red) line is the locus of unstable steady states.

On decreasing the friction factor, the temperature in the ignited steady state decreases and at $f = 0.032$, a Hopf bifurcation point arises (Fig. 18.2). As first (largest) Lyapunov exponent at this Hopf point is positive (1.79), there should be an unstable limit cycle. In the unstable branch (Fig. 18.2), two more Hopf points (at $f = -0.085$ and -0.014) and a limit point (at $f = -0.086$) arise. As these three bifurcation points arise at non-realistic value (negative) of friction factor, the dynamics at these points are not analyzed further. We examine the evolution of limit cycle from first Hopf point (at $f = 0.032$).

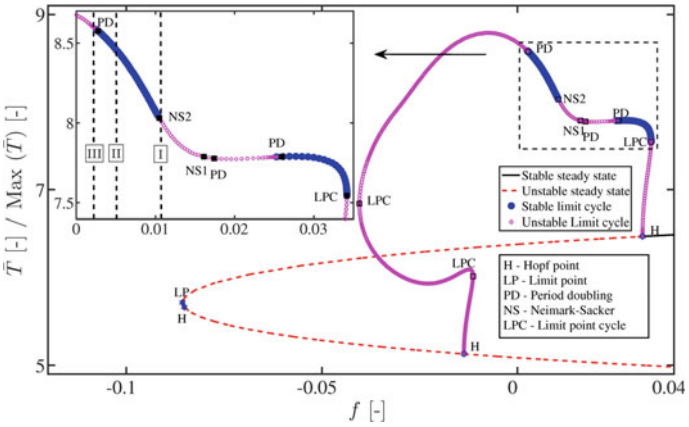

Fig. 18.2 Continuation of steady state and limit cycle varying tailpipe friction factor. Regimes of stable limit cycle are shown separately as inset. The values of friction factor at which the phase plots are shown in Fig. 18.3 are indicated as vertical dotted lines (I, II and III)

Continuation of limit cycle in terms of friction factor is shown in the same figure in terms of maximum dimensionless temperature. The branch of stable (unstable) limit cycle is marked with filled (open) circles. From Hopf point ($f = 0.032$), unstable limit cycle is evolved till limit point cycle (LPC) appears at $f = 0.034$ with a nonzero normal form coefficient and two multipliers having (approximately) unit values. Thus, the limit cycle manifold has a fold here and changes its stability. Stable limit cycle behaviour is found up to period-doubling bifurcation at $f = 0.026$ and the limit cycle remains unstable up to second Neimark–Sacker (NS2) point ($f = 0.01048$). In this unstable zone of limit cycle, a period-doubling bifurcation and a Neimark–Sacker (NS1) appear at $f = 0.017$ and $f = 0.016$ respectively. After NS2 point, second stable regime of limit cycle (with higher amplitude) appears up to another period-doubling bifurcation at $f = 0.0028$. Beyond that value, limit cycles become unstable and the branch of limit cycle terminates at another Hopf point ($f = -0.014$) in the unstable steady state branch.

On decreasing friction factor, pulsating behaviour (stable limit cycle) is regained after extinction (unstable limit cycle). Different stable zone in the continuation curve of limit cycle is presented as inset in Fig. 18.2. A significant contribution of the present work is the identification of periodic and quasiperiodic regimes at low values of friction factor much below the value of f for which flame extinction had been observed (Mukhopadhyay et al. 2008). This kind of analysis identifies alternative regions in parameter space where the desired system behaviour is obtained and thus improves the design process. A few parameters such as amplitude of oscillations, cycle-averaged heat transfer and cycle-averaged specific thrust are calculated and listed in Table 18.3. The amplitude of temperature oscillations is much higher at the lower range of f whereas higher heat flux value is obtained at higher range of f. Further, specific thrust at the tailpipe exit shows that, for propulsion application, a

Table 18.3 Comparison of performance parameters in different ranges (of limit cycle oscillations) of tailpipe friction factor

Parameters	$f = 0.026$ to 0.034	$f = 0.0028$ to 0.01048
Amplitude of temperature oscillations (peak to peak)	756.5–914.1 K	1230.9–1452 K
Cycle averaged heat transfer (flux)	74.9 kW/m^2	46.4–46.9 kW/m^2
Cycle averaged specific thrust (F/ṁ)	140 m/s	150–165 m/s

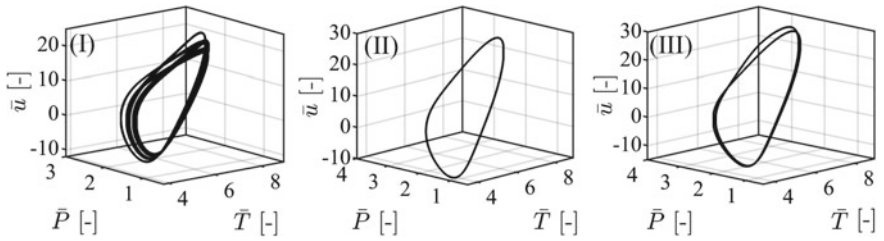

Fig. 18.3 Phase plots for (I) $f = 0.0105$, (II) $f = 0.005$, (III) $f = 0.002$, indicated in the bifurcation diagram (Fig. 18.2)

pulse combustor should be designed with lower friction factor. In short, depending upon the application, a designer can choose appropriate parametric values.

Phase plots are shown in support of transition between extinction and limit cycle behaviour (at $f = 0.0107$), second stable regime of limit cycle (at $f = 0.005$) and the period-doubling at $f = 0.002$ by integrating the model numerically in Fig. 18.3. Figure 18.3I–III corresponds to the values of indicated as dashed vertical line in Fig. 18.2 as I, II, and III respectively. With the decrease of friction factor, a different regime of periodic hot solution is achieved thorough aperiodic pulsation (Fig. 18.3a).

18.3.2 Varying Wall Temperature (T_w)

Datta et al. (2009) investigated the dynamics of pulse combustor using this model by numerical integration. They varied the wall temperature and got Hopf bifurcation at $T_w \approx 1161$ K and also got the steady combustion, limit cycle behaviour and period-doubling bifurcation ($T_w \approx 1090$ K). In the present work, a systematic study of nonlinear dynamics of pulse combustor model is done by varying wall temperature (T_w).

We show the bifurcation diagram in Fig. 18.4. On decreasing T_w, the temperature in the ignited steady state decreases and at $T_w = 1161.72$ K, a Hopf bifurcation point arises, validating the finding of Datta et al. (2009). At this Hopf point, an unsta-

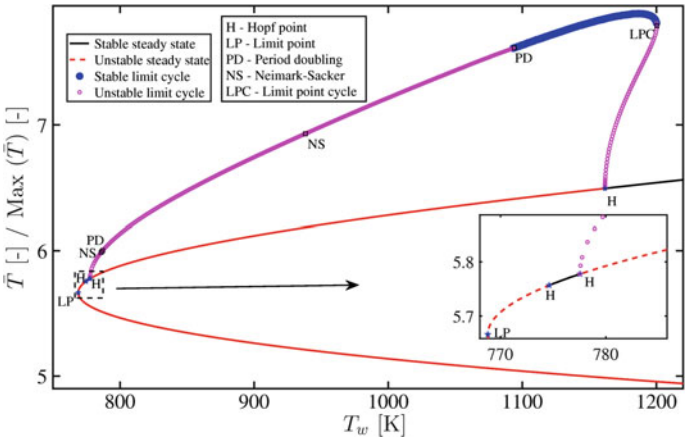

Fig. 18.4 Continuation of steady state and limit cycle varying wall temperature (T_w). A small regime of stable steady state is shown as inset

ble limit cycle should bifurcate as first Lyapunov exponent is positive (1.88). In the unstable branch, two more Hopf points (at $T_w = 777.54$ and 774.61 K) arise. A stable steady solution is achieved (inset of Fig. 18.4) between these points. At $T_w = 768.79$ K, a limit point (LP) arises where the unstable branch folds with positive normal form coefficient (thus the equilibrium manifold near LP looks like a parabola).

It may be noted that the bifurcations seen on unstable branches of the fixed point may not be observed in numerical simulations if there exists stable limit cycles for the same set of parameters. For these parametric ranges, the dynamics of the limit cycle would be more readily apparent from numerical simulations. To study the limit cycle behaviour, continuation of limit cycle has been performed starting from the Hopf point at $T_w = 1161.72$ K. The continuation curve of limit cycle is shown (Fig. 18.4) where a Limit Point Cycle (LPC) appears at $T_w = 1200.35$ K. The limit cycle manifold has a fold here. Floquet multipliers are displayed in MATCONT window in terms of modulus and arguments. As the modulus of one of the Floquet multipliers is greater than unity (indicating a multiplier lies outside of a unit circle in the complex plane), the periodic solution of the system gets unstable in between Hopf point ($T_w = 1161.72$ K) and limit point cycle ($T_w = 1200.35$ K). Two Neimark–Sacker (NS) points, which indicate torus bifurcation, appear at $T_w = 785.92$ K and at $T_w = 938.23$ K. Analysis of these bifurcation points (NS points), which are on the unstable branch of limit cycle continuation curve, is not the focus of the present study as the desired operating state for pulse combustor remains in the stable limit cycle regime.

In summary, stable limit cycle is found in between LPC at $T_w = 1200.35$ K and $T_w = 1094.01$ K (onset of period-doubling). With the present model, period-doubling bifurcation was achieved in the previous work (Datta et al. 2009) by numerical integration at almost same wall temperature. Unlike the case of friction factor,

for wall temperature, the range of T_w for which stable limit cycle is predicted by the current analysis is practically identical with the numerical simulations (Datta et al. 2009). However, the importance of this analysis as part of a design exercise is the complete identification of the ranges of wall temperature at which limit cycle behaviour can be expected.

18.3.3 Varying Convective Heat Transfer Coefficient (h)

In similar way, next, we present the bifurcation diagram varying convective heat transfer coefficient (h) in Fig. 18.5. On decreasing h, the temperature in ignited steady state decreases and at $h = 116.5\ \mathrm{W/m^2K}$, a Hopf bifurcation point arises (Fig. 18.5). There should exist an unstable limit cycle as the largest Lyapunov exponent at this Hopf point is positive (1.98). In the unstable branch, two more Hopf points (at $h =$ 199.9 and 200.6 $\mathrm{W/m^2K}$) arise between which stable solution is achieved. At $h =$ $206\ \mathrm{W/m^2K}$, a limit point (LP) arises where the unstable branch folds with nonzero normal form coefficient.

Starting from the Hopf point at $h = 116.5\ \mathrm{W/m^2K}$, continuation of limit cycle is also presented in Fig. 18.5. From Hopf point, the unstable limit cycle is evolved till limit point cycle (LPC) appears at $h = 108.96\ \mathrm{W/m^2K}$. The limit cycle manifold has a fold here and changes its stability. Stable limit cycle behaviour is found up to period-doubling bifurcation at $h = 129.6\ \mathrm{W/m^2K}$ and the limit cycle become and remain unstable for rest of the continuation. In unstable zone of limit cycle, two NS points appear at $h = 167.44$ and $198.5\ \mathrm{W/m^2K}$. As the oscillating behaviour is desirable in pulse combustor, we focus on stable steady state and its stability boundary. The stability margin (108.96–129.6 $\mathrm{W/m^2K}$) of limit cycle behaviour in terms of convective heat transfer coefficient is achieved. The complete range of convective

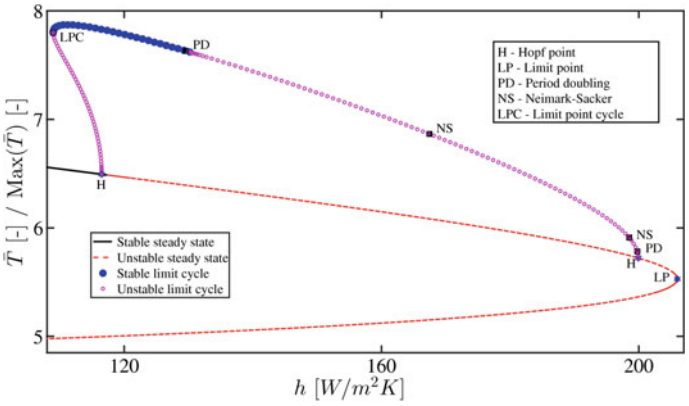

Fig. 18.5 Continuation of steady state and limit cycle varying heat transfer coefficient (h)

heat transfer coefficient at which limit cycle behaviour is obtained can be useful for the improved design and optimal operating condition of pulse combustor.

18.3.4 Varying Inlet Temperature ($\bar{T}_{i0}$)

Bifurcation diagram is next drawn by varying the dimensionless inlet temperature ($\bar{T}_{i0}$) in Fig. 18.6. In this figure, it is clear that multiplicity of steady state exists. On decreasing $\bar{T}_{i0}$, the temperature in ignited steady state decreases and at $\bar{T}_{i0} = 1.065$, a Hopf bifurcation point arises. At this Hopf point, the Lyapunov exponent is found positive (1.88). This causes an unstable limit cycle bifurcating from the equilibrium. Twofold bifurcation (LP) occurs at $\bar{T}_{i0} = 0.74$ and 2.96 with normal from the coefficient of opposite sign. This causes to form the parabolas of opposite direction in the continuation curve of steady state. After the second limit point, a branch of cold stable solution is achieved. Due to the higher inlet temperature, cold steady solutions show higher temperature.

Starting from the Hopf point at $\bar{T}_{i0} = 1.065$, continuation of limit cycle is also shown in Fig. 18.6. From the Hopf point, unstable limit cycle is evolved till limit point cycle (LPC) appears at $\bar{T}_{i0} = 1.08$. The limit cycle manifold has a fold here and changes its stability. Stable limit cycle behaviour is found up to period-doubling bifurcation at $\bar{T}_{i0} = 1.002$ and the limit cycle becomes and remains unstable for the rest of the continuation up to the Hopf point ($\bar{T}_{i0} = 0.7781$) in unstable steady-state branch. In the unstable zone of the limit cycle, two NS points appear at $\bar{T}_{i0} = 0.89$ and 0.78. The regime of periodic solution is achieved in between $\bar{T}_{i0} = 1.08$ and 1.002.

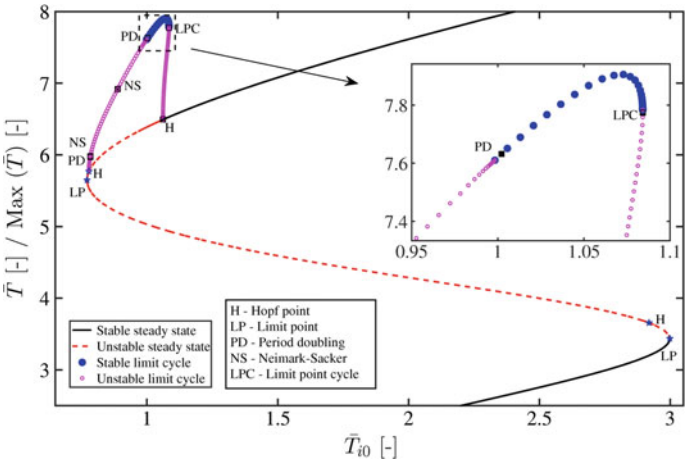

Fig. 18.6 Continuation of steady state and limit cycle varying dimensionless inlet temperature (T_{i0})

The knowledge of the complete range of inlet temperature giving rise to periodic solution can be useful for the optimal operating conditions for pulse combustor.

18.3.5 Varying Inlet Fuel Mass Fraction ($y_{f,i}$)

Lastly, we vary the inlet fuel mass fraction ($y_{f,i}$) to get the continuation curve for steady states and limit cycles (Fig. 18.7). Keeping similar steady state as initial point, bifurcation diagram is shown in Fig. 18.7. On decreasing $y_{f,i}$, the temperature in ignited steady state decreases and at $y_{f,i} = 0.0598$, a Hopf bifurcation point arises. As first Lyapunov exponent at this Hopf point is positive (1.96), there should exist an unstable limit cycle, bifurcating from the equilibrium. In the unstable branch, one more Hopf points (at $y_{f,i} = 0.0571$) and one limit point (at $y_{f,i} = 0.057$) arise. The largest Lyapunov coefficient at second Hopf point being negative (−82.2), a stable limit cycle should exist there.

Starting from the Hopf point at $y_{f,i} = 0.0598$, continuation of limit cycle is also shown in Fig. 18.7. From the Hopf point, unstable limit cycle is evolved till the limit point cycle (LPC) appeared at $y_{f,i} = 0.06$. The limit cycle manifold has a fold here and changes its stability. Stable limit cycle behaviour is found up to period-doubling bifurcation at $y_{f,i} = 0.05874$ and the limit cycle remains unstable beyond this value of inlet fuel mass fraction and closes at another Hopf point ($y_{f,i} = 0.0571$) in unsteady steady state branch. In this unstable branch of limit cycle, a period-doubling bifurcation appears at $y_{f,i} = 0.05731$. The regime of periodic solution is again achieved in between 0.06 and 0.05874 of inlet fuel mass fraction which in turn helps for the optimal operation of pulse combustor.

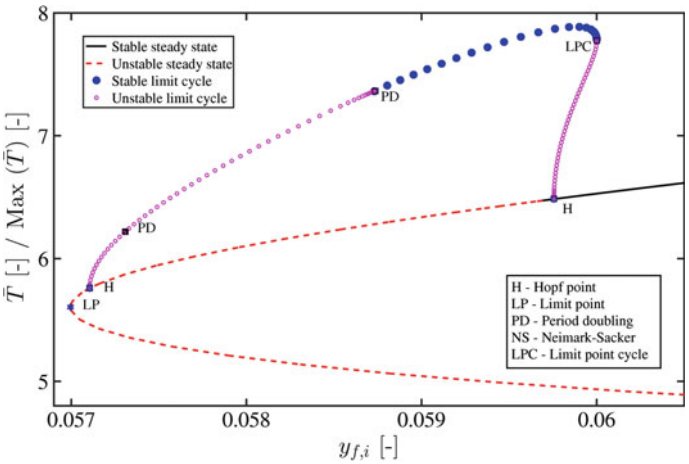

Fig. 18.7 Continuation of steady state and limit cycle varying inlet fuel mass fraction ($y_{f,i}$)

Summary

The present chapter discusses on one of the many aspects of turbulent combustion, known as combustion dynamics. Oscillatory combustion is popularly known as combustion instability or thermoacoustic instability. Oscillatory combustion which has several ruinous consequences for almost all practical combustors is only desirable and maintained in pulse combustor. A short review has been provided in the recent studies on combustion instability in the context of gas turbine as well as pulse combustor. In following sections, different dynamical states have been explored of a lumped model of thermal pulse combustor. While numerical integration of a system of differential equations is inappropriate for tracing solution branches in the presence of bifurcation, continuation method gives the complete dynamical scenario in a parametric axis. The stability boundaries of oscillatory behaviour for a model pulse combustor for different bifurcation parameters are analyzed. The mathematical model consists of four coupled nonlinear ordinary differential equations representing conservation of mass, energy and species in the combustor and momentum in the tailpipe. Continuation method was followed using MATCONT for identifying the stability and bifurcations of both fixed points and limit cycles for different bifurcation parameters.

The systematic analysis of the dynamics of the pulse combustor accurately determines the limits of parameters for which stable limit cycles can be obtained. This information is critical for optimal design and operation of pulse combustors. Apart from its importance in theoretical studies on dynamic characteristics of nonlinear systems, bifurcation analysis can be directly useful in correct and complete identification of feasible ranges of parameters for which the desired system behaviour can be expected. This can lead to improved design compared to that obtained using direct numerical simulations only. The present analysis identifies a range of lower friction factors for periodic behaviour which is difficult to obtain by direct integration. On the other hand, for other parameters, the ranges identified by bifurcation analysis and direct numerical simulations are almost identical. The direct simulations shown here and also reported in our earlier works corroborate the information obtained from the continuation analysis.

The dynamics as well as dynamical transition of turbulent combustion can be characterized in framework of dynamical systems theory. As hydrodynamic instability has direct effect on heat release rate oscillations exhibited in turbulent combustors, for the stability analysis of simple systems, hydrodynamics instability is bypassed by modelling the heat release rate oscillations. However, the present authors feel that modelling hydrodynamic instability would be more rigorous in the context of combustion instability analysis. Nevertheless, the routes for different dynamical transitions at the onset of combustion instability analyzed from simple model (as presented here) and simple experiments (for example, Rijke tube) can be helpful for the prediction and control of more complicated practical combustors with a certain range of operational parameters.

References

Balasubramanian K, Sujith R (2008a) Phys Fluids 20(4):044103
Balasubramanian K, Sujith R (2008b) J Fluid Mech 594:29–57
Bloom F, Patterson T (2009) Nonlinear Anal Real World Appl 10(5):3002–3017
Buckmaster JD (1985) The mathematics of combustion. SIAM
Burnley VS (1996)
Culick F (1988)
Culick F (1970) Combust Sci Technol 2(4):179–201
Culick F (1976) Acta Astronaut 3(9–10):735–757
Culick F (1994) AIAA J 32(1):146–169
Datta S, Mondal S, Mukhopadhyay A, Sanyal D, Sen S (2009) Combust Theory Model 13(1):17–38
Daw CS, Thomas JF, Richards GA, Narayanaswami LL (1995) Chaos Interdisc J Nonlinear Sci 5(4):662–670
Dhooge A, Govaerts W, Kuznetsov YA (2003) ACM Trans Math Softw (TOMS) 29(2):141–164
Di Benedetto A, Marra F, Russo G (2002) Combust Sci Technol 174(10):1–18
Domen S, Gotoda H, Kuriyama T, Okuno Y, Tachibana S (2015) Proc Combust Inst 35(3):3245–3253
Dowling AP (1997) J Fluid Mech 346:271–290
Edwards K, Finney C, Nguyen K, Daw C (2000) In: 2000 Technical meeting of the central states section of the combustion institute, pp 249–254
Edwards K, Nguyen K, Daw C (2001) In: Proceedings of the second joint meeting of the US sections of the combustion institute, vol 10, pp 3871–3889
Farge M (1992) Annu Rev Fluid Mech 24(1):395–458
Fichera A, Losenno C, Pagano A (2001) Appl Energy 70(2):179–191
Garcia-Agreda A, Di Sarli V, Di Benedetto A (2012) Int J Hydrogen Energy 37(8):6922–6932
Gemmen R (1996) J Eng Gas Turbines Power 118:469
Geng T, Zheng F, Kiker A, Kuznetsov A, Roberts W (2007) Exp Thermal Fluid Sci 31(7):641–647
Gopalakrishnan E, Sujith R (2015) J Fluid Mech 776:334–353
Gotoda H, Amano M, Miyano T, Ikawa T, Maki K, Tachibana S (2012) Chaos Interdisc J Nonlinear Sci 22(4):043128
Gotoda H, Nikimoto H, Miyano T, Tachibana S (2011) Chaos Interdisc J Nonlinear Sci 21(1):013124
Gotoda H, Shinoda Y, Kobayashi M, Okuno Y, Tachibana S (2014) Phys Rev E 89(2):022910
Heckl MA (1985) Heat sources in acoustic resonators. PhD thesis, University of Cambridge
Heckl MA (1988) J Sound Vib 124(1):117–133
Heckl MA (1990) Acta Acustica United Acustica 72(1):63–71
Hosseini S (2009) Non-linearities in the thermoacoustic response of a premixed swirl burner. PhD thesis
In V, Spano ML, Neff JD, Ditto WL, Daw CS, Edwards KD, Nguyen K (1997) Chaos Interdisc J Nonlinear Sci 7(4):605–613
Jahnke CC, Culick FE (1994) J Propul Power 10(4):508–517
Kabiraj L, Sujith R (2012) J Fluid Mech 713:376–397
Kabiraj L, Saurabh A, Wahi P, Sujith R (2012a) Chaos Interdisc J Nonlinear Sci 22(2):023129
Kabiraj L, Sujith R, Wahi P (2012b) J Eng Gas Turbines Power 134(3):031502
Kabiraj L, Sujith R, Wahi P (2012c) Fluid Dyn Res 44(3):031408
Kadanoff LP (1983) Phys Today 36:46–63
Kashinath K, Hemchandra S, Juniper MP (2013) Combust Flame 160(12):2856–2865
Kashinath K, Waugh IC, Juniper MP (2014) J Fluid Mech 761:399–430
Kushari A, Rosen L, Jagoda J et al (1996) In: Symposium (international) on combustion, vol 26. Elsevier, pp 3363–3368
Lei S, Turan A (2009) Combust Theory Model 13(3):541–557
Lieuwen TC, Yang V (2005) Progress in astronautics and aeronautics

Lieuwen T (2001) J Fluid Mech 435:289–303
Lieuwen TC (2002) J Propul Power 18(1):61–67
Margolis SB (1993) Combust Sci Technol 88(3–4):223–246
Margolis SB (1994) Combust Flame 99(2):311–322
Matveev KI, Culick F (2003) Combust Sci Technol 175(6):1059–1083
Meng X, de Jong W, Kudra T (2016) Renew Sustain Energy Rev 55:73–114
Mestrom W (2002) Master's thesis. Utrecht University, Utrecht, The Netherlands, Mathematical Institute
Mondal S, Mukhopadhyay A, Sen S (2012) Combust Theory Model 16(1):59–74
Mondal S, Mukhopadhyay A, Sen S (2014) Combust Sci Technol 186(2):139–152
Mondal S, Mukhopadhyay A, Sen S (2015) Pramana J Phys 84(3)
Mondal S, Mukhopadhyay A, Sen S (2016) Combust Theory Model 1–16
Mondal S, Unni VR, Sujith R (2016) In: Conference on nonlinear systems and dynamics IISER Kolkata, vol 16, 18
Mondal S, Unni VR, Sujith R (2017) J Fluid Mech 811:659–681
Mukhopadhyay A, Datta S, Sanyal D (2008) J Eng Gas Turbines Power 130(1):011507
Nair V, Sujith R (2014) J Fluid Mech 747:635–655
Nair V, Sujith R (2015) Combust Sci Technol 187(11):1821–1835
Nair V, Thampi G, Karuppusamy S, Gopalan S, Sujith R (2013) Int J Spray Combust Dyn 5(4):273–290
Nair V, Thampi G, Sujith R (2014) J Fluid Mech 756:470–487
Narayanaswami L, Richards G (1996) J Eng Gas Turbines Power 118:461
Noiray N, Schuermans B (2013) Int J Non-Linear Mech 50:152–163
Noiray N, Durox D, Schuller T, Candel S (2008) J Fluid Mech 615:139–167
Pawar SA, Vishnu R, Vadivukkarasan M, Panchagnula M, Sujith R (2016) J Eng Gas Turbines Power 138(4):041505
Peracchio A, Proscia W (1999) Trans-ASME J Eng Gas Turbine Power 121:415–421
Peters N (2000) Turbulent combustion. Cambridge University Press
Petrova MV, McGarry M, Wang H (2008) J Heat Transf 130(7):071201
Pikovsky A, Rosenblum M, Kurths J (2003) Synchronization: a universal concept in nonlinear sciences, vol 12. Cambridge University Press
Polifke W (2004) Advances in aeroacoustics and applications, 2004–05
Preetham P, Lieuwen T (2004) In: 40th AIAA/ASME/SAE/ASEE joint propulsion conference and exhibit, vol 4035
Putnam A, Belles F, Kentfield J (1986) Prog Energy Combust Sci 12(1):43–79
Rayleigh JWS (1878) Nature 18(455):319–321
Rhode M, Rollins R, Markworth A, Edwards K, Nguyen K, Daw C, Thomas J (1995) J Appl Phys 78(4):2224–2232
Richards G, Morris G, Shaw D, Keeley S, Welter M (1993) Combust Sci Technol 94(1–6):57–85
Russo G, Benedetto AD, Marra F (2005) Combust Sci Technol 177(2):413–434
Sterling JD (1993) Combust Sci Technol 89(1–4):167–179
Strogatz SH (2014) Nonlinear dynamics and chaos: with applications to physics, biology, chemistry, and engineering. Westview Press
Subramanian P (2011)
Tang Y, Waldherr G, Jagoda J, Zinn B (1995) Combust Flame 100(1–2):251–261
Tony J, Gopalakrishnan E, Sreelekha E, Sujith R (2015) Phys Rev E 92(6):062902
Trefethen LN, Embree M (2005) Spectra and pseudospectra: the behavior of nonnormal matrices and operators. Princeton University Press
Waugh IC, Juniper MP (2011) Int J Spray Combust Dyn 3(3):225–241

Chapter 19
On the Theory and Modelling of Flame Acceleration and Deflagration-to-Detonation Transition

V'yacheslav (Slava) B. Akkerman

Abstract Prevention of spontaneous premixed flame acceleration (FA) and deflagration (flame)-to-detonation transition(DDT) would avoid thousands of fatalities and injuries that occur every year in numerous disasters such asaccidental mining or power plants explosions. On the other hand, promotion of FA and DDT can be energeticallyefficientlyemployed in the emerging technologies such as pulse-detonation engines and micro-combustors. Fundamentally, the DDT applications range from terrestrial burning and inertial confined fusion to thermonuclearsupernovae and crystals of molecular/nano-magnets. In all these respects, the physical understanding andquantitative description of FA and DDT are critically needed from both practical and fundamental viewpoints.This need is addressed here, with a focus on combustion tubes/channels as the primary geometry. Specifically,various mechanisms of FA in pipes such as those due to (i) wall friction, (ii) in-built obstacles, and (iii) a fingerflame shape are described, with various stages of FA and DDT scenarios being simulated and quantified. Thelocus and timing of detonation initiation, triggered by an accelerating flame front, are prescribed.

Keywords Flame acceleration · Deflagration-to-detonation transition (DDT) Combustion tubes · Wall friction · Finger flames · Obstructed conduits

19.1 Introduction

There are two main self-supporting regimes of premixed burning: a *deflagration* (or "*flame*") and a *detonation*. Specifically, a deflagration is a slow, subsonic regime where the reaction propagates due to thermal conduction, transporting energy from the hot burnt matter to the cold fuel mixture. In contrast, a detonation is a fast,

V. (Slava) B. Akkerman (✉)
Department of Mechanical and Aerospace Engineering, West Virginia University, Morgantown, WV, USA
e-mail: Vyacheslav.Akkerman@mail.wvu.edu

© Springer Nature Singapore Pte Ltd. 2018

S. De et al. (eds.), *Modeling and Simulation of Turbulent Combustion*, Energy, Environment, and Sustainability, https://doi.org/10.1007/978-981-10-7410-3_19

supersonic process occurring due to shock waves, which compress the fuel mixture, thereby increasing its temperature and facilitating the reaction. As a result, the mechanisms of deflagration and detonation are conceptually different, and the detonation burning velocity generally exceeds that of a deflagration by three–four orders of magnitude. In spite of such a difference, a spontaneous deflagration-to-detonation transition (DDT) event has been widely encountered in various practical applications, thus inspiring a considerable interest, both from a fundamental science viewpoint and the practical perspectives, to elucidate and control the basic mechanisms of DDT.

The history of DDT studies exceeds 80 years. In particular, Shelkin originally devoted the DDT onset to turbulence and roughness at the combustor walls (Shelkin 1940). Zel'dovich classified the regimes of exothermal reactions with nonuniform initial conditions and proposed his renowned *gradient* mechanism of DDT, due to a localized thermal explosion induced by a thermal gradient (Zeldovich 1980). In fact, flame evolution creates a condition for detonation initiation through the gradients of reactivity (also known as the so-called "hot spots"). These hot spots may lead to spontaneous ignitions in the fresh gas. Then, the detonation may be triggered by the shock formation when velocity of such a spontaneous ignition wave overcomes the sound barrier. Also, Brailovsky and Sivashinsky devoted the DDT onset to the hydraulic resistance (viscous heating) (Brailovsky and Sivashinsky 2000). A detailed literature review on this subject can be found, for instance, in the recent review book (Clavin and Searby 2016).

Figure 19.1 illustrates, schematically, a general DDT scenario. Specifically, an initially slow deflagration (flame) front accelerates. Thus, it creates and pushes compression waves and eventually shock waves, which heat the fresh fuel mixture. As a result, an explosion occurs somewhere in the fresh gas ahead of the flame

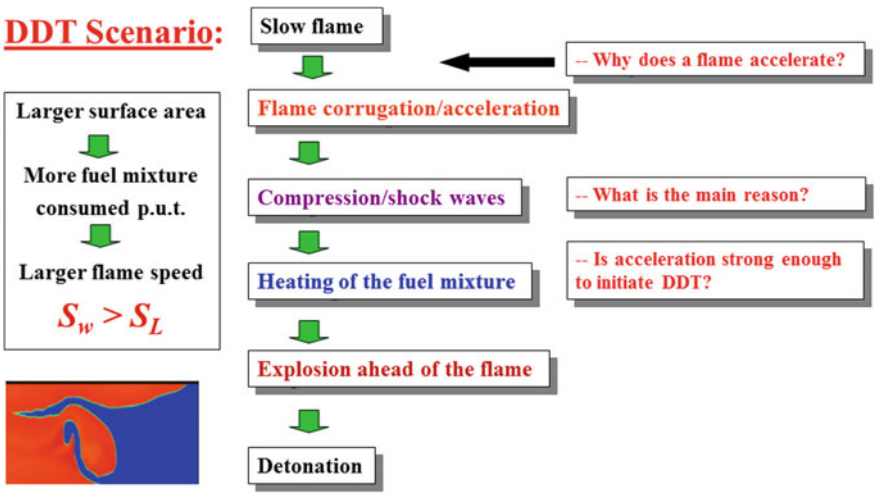

Fig. 19.1 Schematic of a DDT scenario

front, subsequently evolving the entire matter between the primary flame and the secondary explosion into a self-sustained detonation. While this scenario looks straightforward, to shed the light on its nature, one should, first, answer the primary question, namely *why does a flame accelerate?*

It is noted that flame acceleration is oftentimes devoted to a corrugation/distortion of the flame shape. Indeed, while the propagation velocity of a planar flame front, S_L, would not exceed several m/s, the majority of industrial and laboratory flames are usually corrugated. A curved flame has a larger surface area relative to a planar one involving the same mixture and under the same conditions; thus, it will consume more fuel per unit time and release more heat, thereby propagating more rapidly. Strictly speaking, corrugation of a flame front does not necessarily mean flame acceleration. In particular, a flame front, distorted due to the Darrieus–Landau (DL) combustion instability, was found to propagate steadily (Bychkov and Liberman 2000). Indeed, such a flame does not accelerate but propagates with a constant velocity (though the latter exceeds the speed of a respective planar flame front). Also, corrugated flames may oscillate, with a constant or near-constant average velocity, instead of acceleration (Akkerman et al. 2006a). However, in the majority of applications, a curved flame front yields a positive flame-flow feedback, thereby providing sustained flame acceleration. If acceleration occurs rapidly enough, it can make the DDT event feasible.

There are numerous causes of flame distortion such as turbulence, combustion instability, acoustics, wall friction, in-built arrays of obstacles, etc., as well as their interplay. Depending on a configuration, all these and other agents may compete or facilitate each other, thereby leading to no or weak or enormous flame acceleration. In this respect, the primary question above should be rephrased, in a more specific way, as follows: *what is the main reason for flame corrugation and acceleration?* Obviously, the answer depends on the configuration of a combustor as well as other circumstances. Then the subsequent question is: *for a particular, given setup—is flame acceleration strong enough to initiate and manage the DDT?* Partially, this question is addressed here. It is noted that the combustors with a large aspect ratio such as channels, pipes, gaps, or tunnels (the so-called "combustion tubes") appear the best candidates to manage the DDT. Among them, the combustion tubes with in-built arrays of obstacles provide extremely fast flame acceleration.

19.2 Motivation

On the one hand, sporadic flame acceleration and accidental gas and dust explosions are serious hazards to both workers and equipment in industries that generate, transport, or consume flammable gases or combustible dusts. This concerns, in part, the coal mining industry which has, historically, one of the highest occupational fatality and injury rates for employees. Although the mining fatality rate has decreased by two orders of magnitude since the 1800s, the recent mining accidents have shown that the current fire-safety bench-scale test methods do not provide an

acceptable level of prevention yet. In particular, modern coalmining machinery has significantly increased a portion of small-size coal dust collected in the intake/return airways, thus providing a substantial impact on a potential coal dust/methane explosion, fire, or DDT. Successful redesign of industrial safety tests will therefore require a deep understanding of flame acceleration and a DDT process—from fundamental principles to practical aspects.

On the other hand, often destructive and hazardous, rapid flame acceleration and detonation may also promote the efficiency of a combustor, as constructively employed, in particular, in pulse-detonation or rotation-detonation engines. As a consequence, there is a critical scientific need to elucidate and quantify the key factors that dictate a DDT process, especially in its late stages, with a particular focus on the effects of boundary conditions, combustion instabilities, turbulence, combustible/non-combustible dust impurities, and their interplay.

19.3 Background

The key parameters quantifying the flame evolution are the planar flame speed $S_L \approx (10^{-1}\sim10^{1})$ m/s, the actual velocity of a corrugated/turbulent flame with respect to the fuel mixture S_T, the thermal flame thickness estimated conventionally as $L_f \equiv D_{th}/S_L \approx (10^{-4}\sim10^{-6})$ m, where D_{th} is the thermal diffusivity of the fresh gas, the thermal expansion ratio $\Theta \equiv \rho_{fuel}/\rho_{burnt} \approx T_{burnt}/T_{fuel} \approx 5\sim10$, and the Lewis number defined as the thermal to mass diffusivities, $Le \equiv D_{th}/D_m \approx 0.2 \sim 2$. The (turbulent) flow is described by the root-mean-square (rms) velocity (turbulent intensity) U_{rms}, the integral turbulent length λ_I, and the characteristic hydrodynamic length scale R (say, a tube radius). Then, the dimensional analysis yields a Reynolds number associated with flame propagation in the form $\mathrm{Re} = S_L R/\nu = R/L_f Pr$, with the kinematic viscosity ν, the Prandtl number Pr; the turbulent Reynolds number $\mathrm{Re}_T = U_{rms}\lambda_I/S_L L_f$; and a characteristic flow Reynolds number given by the ratio $\mathrm{Re}_{flow} = (\Theta-1)\, S_T R/\nu = (\Theta-1)\, S_T R/S_L L_f\, Pr$.

While a flame is generally affected by an imposed turbulent flow, propagation of a curved flame also generates turbulence, sometimes quite strong, and it may also influence flame propagation. There is no an accurate way to distinguish the impacts of an imposed and flame-generated turbulent flows. Consequently, the turbulence parameters above are associated with those measured in the presence of a flame, and thus are a combination of imposed and flame-generated turbulences, with an intriguing, nonlinear coupling between them.

19.4 Flame Acceleration in "Combustion Tubes"

Spontaneous flame acceleration is exceptionally strong, in particular, in combustors with large aspect ratios such as slits, channels, tubes, and tunnels (Urtiev and Oppenheim 1966; Shepherd and Lee 1992; Roy et al. 2004; Bychkov et al. 2008; Tangirala et al. 2004; Ju and Maruta 2011); especially in obstructed conduits (Bychkov et al. 2008), where the flame speed can increase by several orders of magnitude and actually initiate a self-sustained detonation. The first qualitative explanation of the flame acceleration and DDT phenomena was proposed by Shelkin (1940), for the geometry of flame propagation in tubes. Specifically, wall friction and turbulence were suggested to play the dominant roles in the acceleration process. Namely, the combustible gas expands in the process of burning, which induces a flow in the fuel mixture. Being highly nonuniform due to wall friction, the induced flow thereby causes the flame front to become corrugated, hence increasing the fuel consumption rate and driving flame acceleration. Turbulence provides an additional distortion of the front and compensates the wall thermal losses. Although such acceleration of a premixed turbulent flame has been observed in various experiments (Roy et al. 2004; Kuznetsov et al. 2005; Johansen and Ciccarelli 2010), a quantitative understanding of this acceleration mechanism was limited until the recent studies (Kagan and Sivashinsky 2003; Ott et al. 2003; Gamezo et al. 2008) showing that even a laminar flame can accelerate in a tube, due to wall friction, while turbulence plays only a supplementary role in this scenario.

The constructive idea of Kagan and Sivashinsky (2003), Ott et al. (2003) has stimulated development of a laminar formulation for flame acceleration and DDT in tubes, supported by extensive computational simulations (Bychkov et al. 2005, 2007, 2010, 2012; Akkerman et al. 2006b, 2010; Bychkov and Akkerman 2006; Valiev et al. 2008, 2009, 2010, 2013) as well as the experimental data from the literature (Wu et al. 2007; Wu and Wang 2011; Dorofeev 2011). Two-dimensional (2D) channels and cylindrical tubes, unobstructed or obstructed, with various initial and boundary conditions, were considered. Three distinctive physical mechanisms of flame acceleration have been identified, as follows.

A. "Finger" Flame Acceleration: At the early stages of flame propagation from a closed channel/tube end, its front acquires a *"finger"*-like shape (Bychkov et al. 2007) and exhibits strong acceleration during a quite short time interval. This evolution is shown by the color snapshots in Fig. 19.2 below. At the initial, quasi-isobaric stage of combustion, the flame tip accelerates exponentially as (Bychkov et al. 2007; Valiev et al. 2013)

$$U_{tip}/S_L \propto \exp\left(\sigma_f S_L t/R\right), \tag{1}$$

where

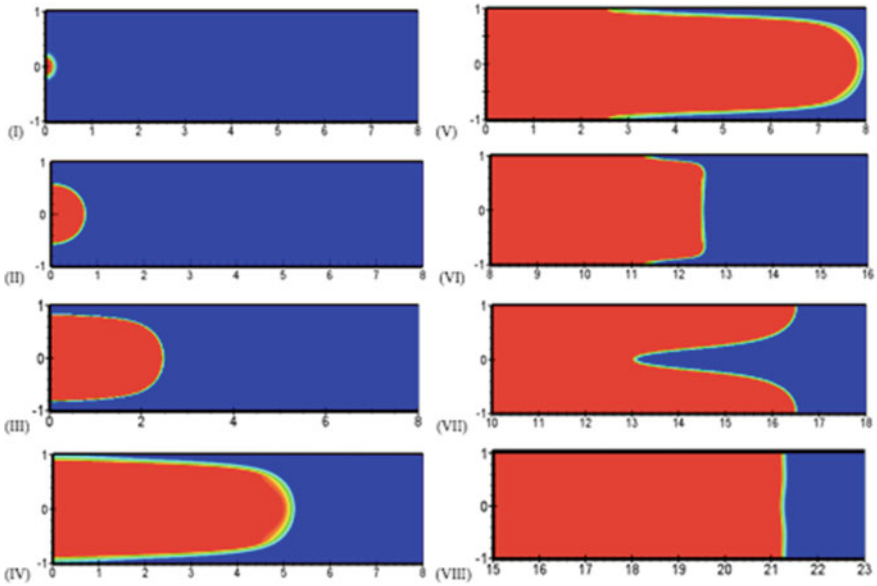

Fig. 19.2 Evolution of a finger flame front (Bychkov et al. 2007)

$$\sigma_{f,\,channel} = \Theta - 1, \quad \sigma_{f,\,tube} = 2\sqrt{\Theta(\Theta - 1)} \tag{2}$$

for a 2D channel and for a cylindrical tube, respectively. This acceleration mechanism is Reynolds-independent, and it is terminated as soon as a flame "skirt" contacts the side wall of a tube/channel. For fast flames, e.g., hydrogen–oxygen ones, even such a short finger flame acceleration can augment the flame velocity up to near-sonic values, with an important influence on the subsequent detonation initiation.

B. Flame Acceleration due to Wall Friction: The *Shelkin*-type mechanism of flame acceleration, associated with wall friction in smooth-wall tubes, Figs. 19.3–19.4, depends critically on the tube/channel radius, with the related initial exponential acceleration rate σ decreasing strongly with an increasing flame Reynolds number (Bychkov et al. 2005; Akkerman et al. 2006b)

$$S_T/S_L \propto \exp\left(\sigma_f S_L t/R\right), \tag{3}$$

where

$$\sigma_{f,\,channel} = \frac{(\mathrm{Re}-1)^2}{4\mathrm{Re}}\left(\sqrt{1+\frac{4\mathrm{Re}\Theta}{(\mathrm{Re}-1)^2}}-1\right)^2 \quad \rightarrow_{\mathrm{Re}>>1} \quad \frac{\Theta^2}{\mathrm{Re}}, \tag{4}$$

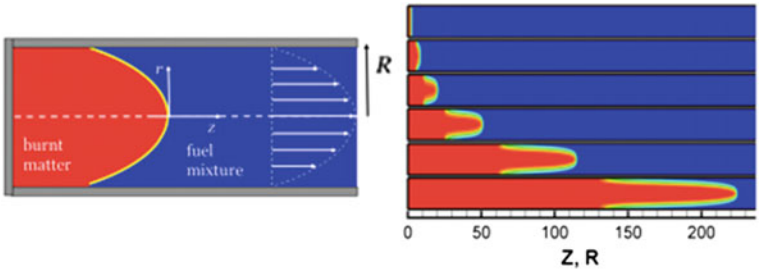

Fig. 19.3 The wall friction (Shelkin) scenario of flame acceleration in a smooth tube (Bychkov et al. 2005; Akkerman et al. 2006b)

$$\sigma_{f,tube} = \frac{\mathrm{Re}}{4}\left(\sqrt{1+\frac{8(\Theta-1)}{\mathrm{Re}}}-1\right)^2 \quad \rightarrow_{\mathrm{Re}>>1} \quad \frac{4(\Theta-1)^2}{\mathrm{Re}} \tag{5}$$

for a 2D channel and a cylindrical-axisymmetric tube, respectively.

So far, the consideration has been limited to equidiffusive ($Le = 1$) flames in adiabatic pipes. However, variations of the equivalence ratio modify the Lewis number Le thereby leading to various thermal-diffusive effects. For $Le > 1$ flames, the flame thickening has been found, which prevents a small-scale corrugation of the flame front, thereby mitigating acceleration, at least, at small Re. In contrast, $Le < 1$ flames may exhibit stronger corrugation, along with triggering of the diffusional-thermal instability and promotion of acceleration. The results of Fig. 19.5 justify all these expectations: indeed, we observe extremely unstable

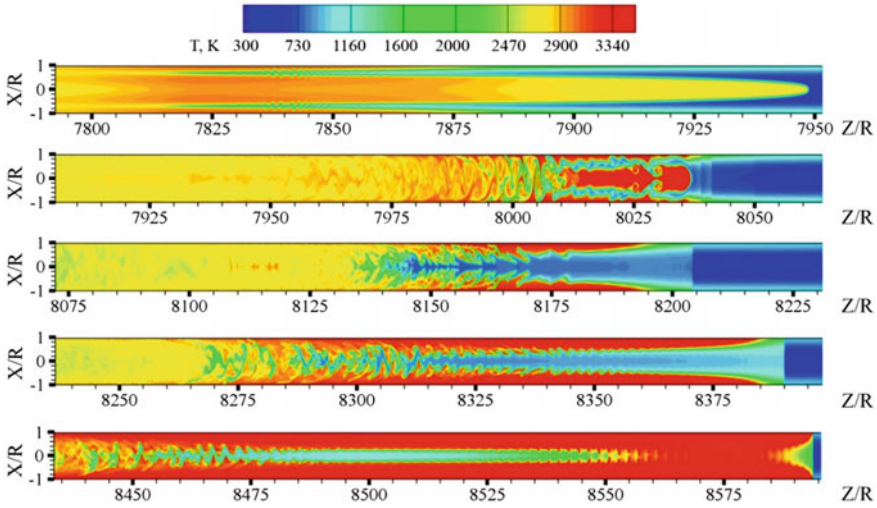

Fig. 19.4 The color temperature snapshots for shock formation and explosion triggering in a smooth tube (Valiev et al. 2009)

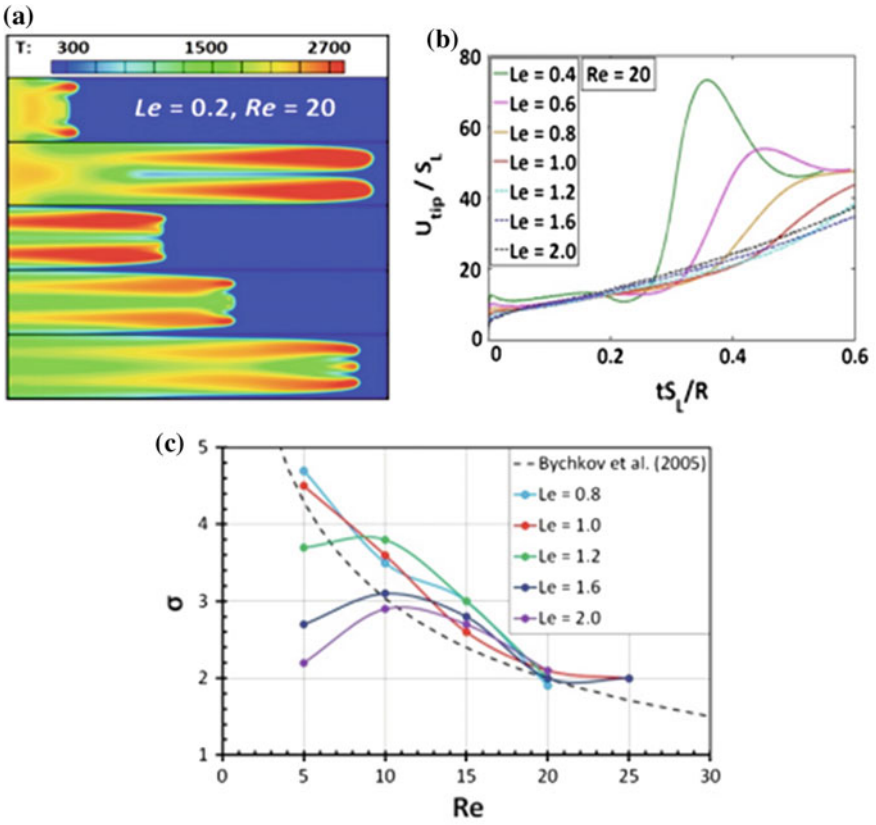

Fig. 19.5 Computational analysis of the influence of the Lewis number *Le* (thermal-diffusive effects) on flame acceleration due to wall friction: (a) color temperature snapshots; (b) the evolution of the scaled flame tip velocity U_{tip}/S_L; and (c) the exponential acceleration rate σ versus the Reynolds number associated with the flame propagation $Re = S_L R/\nu = R/L_f Pr$ (Bilgili et al. 2015)

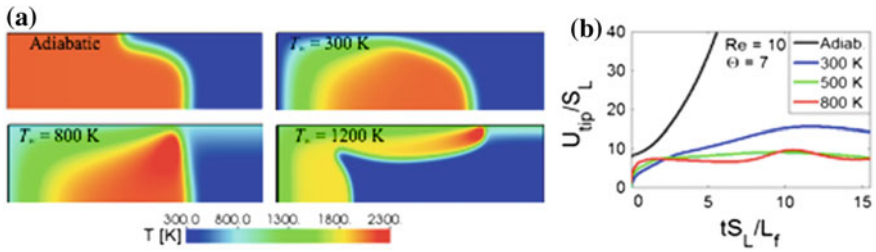

Fig. 19.6 Numerical simulation comparing combustion in channels with non-slip adiabatic and isothermal (cold, $T_w = 300$ K, and preheated, $T_w = 500$; 800; 1200 K) walls: the temperature snapshots [(**a**); upper half of a channel is shown] and the scaled flame tip velocity versus time (**b**) (Ugarte et al. 2015)

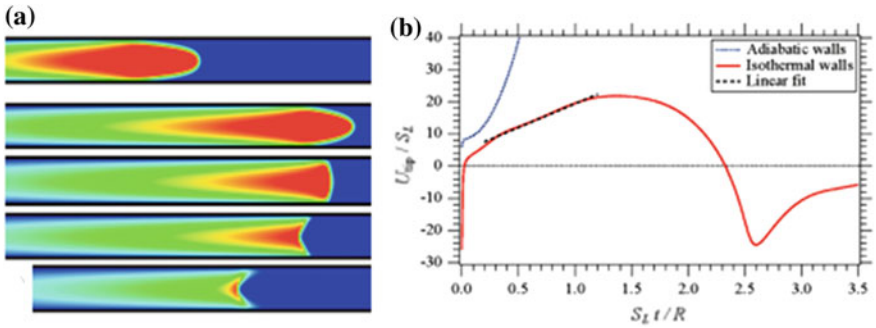

Fig. 19.7 Numerical simulation of flame propagation in an isothermal (T_w = 300 K) channel: the consecutive temperature snapshots (**a**) and the scaled flame tip velocity versus time (**b**) (Dion et al. 2015)

flames in Fig. 19.5a; moreover, smaller *Le* yields faster flame propagation, Fig. 19.5b. Finally, while σ generally decreases with Re, all the $Le > 1$ curves in Fig. 19.5c bent for the narrow channels, Re < 5∼10; see also (Bilgili et al. 2015) for more details.

Moreover, while the theories and simulations (Bychkov et al. 2005, 2007, 2010a, 2010b, 2012; Akkerman et al. 2006, 2010; Bychkov and Akkerman 2006; Valiev et al. 2008, 2009, 2010, 2013a, 2013b) employed adiabatic walls, it is recognized that wall heat losses can strongly influence the combustion process, especially in narrow tubes or channels. Figure 19.6 justifies this statement. For instance, Fig. 19.6b demonstrates exponential acceleration for adiabatic walls, in agreement with (Bychkov et al. 2005), but it shows near-linear acceleration for cold walls (T_w = 300 K) and steady or quasi-steady flame propagation in the case of preheated (T_w = 500 ∼ 800 K) walls (Ugarte et al. 2015). Moreover, a long-run simulation, Fig. 19.7, demonstrates a set of distinctive stages of flame propagation in a channel with isothermal, T_w = 300 K walls, namely, linear acceleration, its termination, flashback, and, finally, extinction (Dion et al. 2015). Keeping in mind that realistic combustor walls are neither adiabatic nor isothermal, these effects can potentially be a powerful tool to control the flame acceleration and DDT scenarios.

C. Fast Flame Acceleration in Obstructed Pipes: Finally, a novel physical mechanism explaining extremely fast flame acceleration in obstructed pipes has been subsequently revealed (Bychkov et al. 2008, 2010, 2012; Valiev et al. 2010). The new mechanism is based on delayed burning between the obstacles, creating a powerful jet-flow and thereby driving acceleration as illustrated in Fig. 19.8. This acceleration is extremely strong, as compared to unobstructed pipes, and independent of the Reynolds number, so the effect can be fruitfully utilized at industrial scales. Understanding of this mechanism thereby provides the guide for optimization of the obstacle shape while previously this task required tantalizing cut-and-try methods and costs.

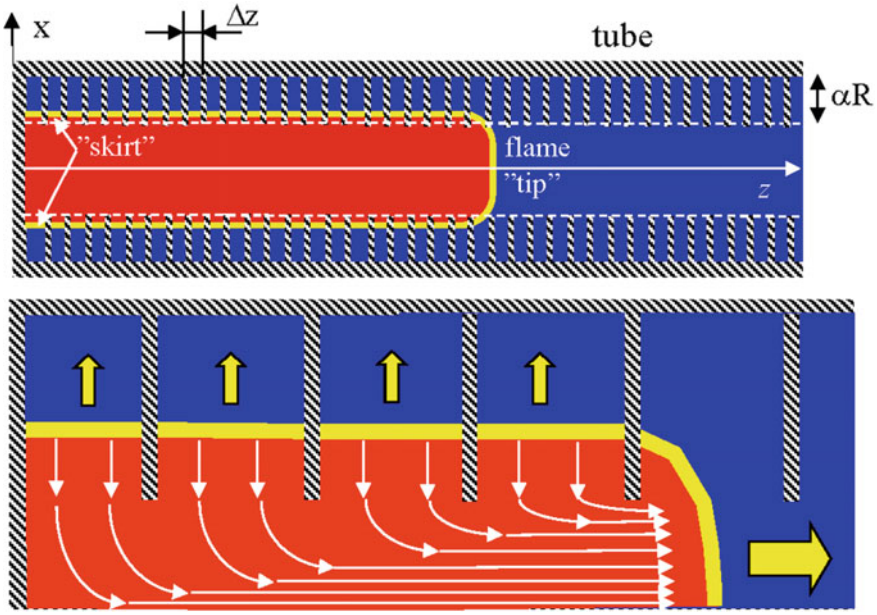

Fig. 19.8 Schematic of the physical mechanism of flame acceleration in obstructed pipes (Bychkov et al. 2008, 2010, 2012; Valiev et al. 2010)

For this obstacle-based acceleration, at a quasi-isobaric stage of the combustion process, the flame tip accelerates exponentially as (Valiev et al. 2010)

$$U_{tip}/S_L \propto \exp\left(\sigma_f S_L t/R\right), \tag{6}$$

with

$$\sigma_{f,\,channel} = \frac{\Theta - 1}{1 - \alpha}, \quad \sigma_{f,\,tube} = 2\frac{\Theta - 1}{1 - \alpha}\left(1 + \frac{1}{2(\Theta - 1)}\right), \tag{7}$$

for a 2D channel and a cylindrical tube, respectively. Here, α is the obstacles blockage ratio (see the illustration in Fig. 19.8). It is noted that the burning velocity is evaluated here by the flame tip velocity, i.e., the derivative of the flame tip position. Again, unlike unobstructed pipes, this acceleration is extremely strong and Reynolds-independent, so the effect can be fruitfully utilized at industrial scales (Figs. 19.9 and 19.10).

For all three mechanisms/configurations, we have described the evolution of the flame shape, velocity, acceleration rate, and the flow velocity profiles nearby the flame front, with the theories substantiated by the computational simulations of the hydrodynamics and combustion equations with an Arrhenius chemical kinetics.

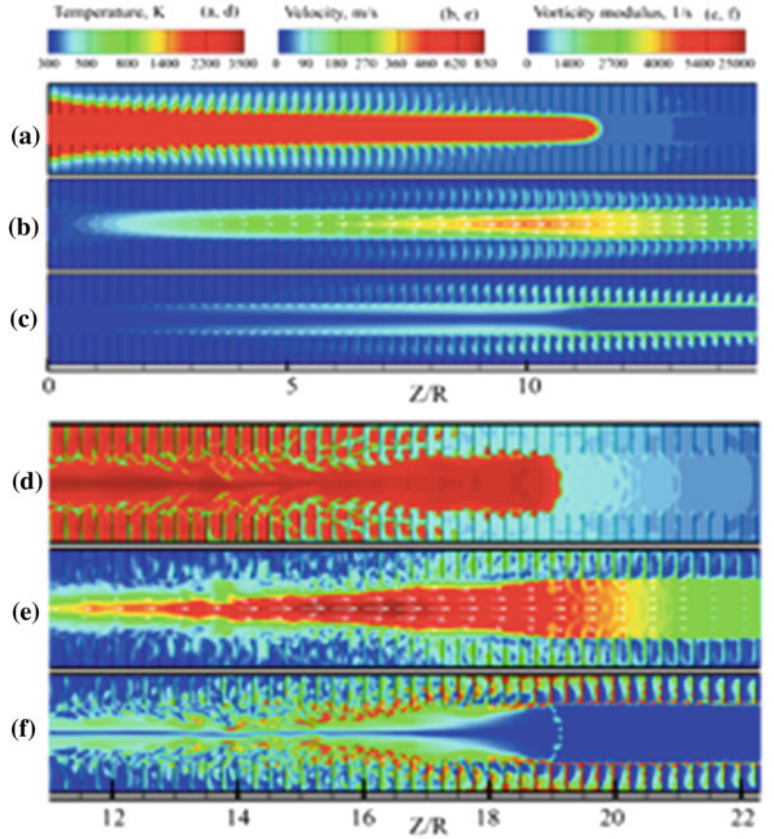

Fig. 19.9 Snapshots of temperature (a, d), velocity (b, e), and vorticity (c, f) at the initial (a–c) and developed (d–f) stages of burning in obstructed tubes (Valiev et al. 2010)

Then, we have also focused on the influence of gas compression at the developed stages of flame acceleration. Both geometries of channels and tubes with smooth walls and with obstacles have been considered. Specifically, accounting for small, but finite Mach numbers, we have shown that gas compression modifies the exponential regime into a slower one. The developed stages of flame acceleration with considerable gas compression have been studied using numerical modeling, which substantiated predictions of the analytical theory and shows moderation of the acceleration regime saturating eventually to steady or statistically steady fast flame propagation. The latter can be associated with the Chapman–Jouget (CJ) deflagration—an intriguing regime, where a flame propagates supersonically in a laboratory reference frame but subsonically with respect to the pushed fuel mixture, being thereby still not a detonation front but a flame (deflagration) front. Finally, the computational simulations demonstrate the possibility of the DDT event for the pipes both with smooth walls and with obstacles as shown in Figs. 19.11 and 19.12, respectively.

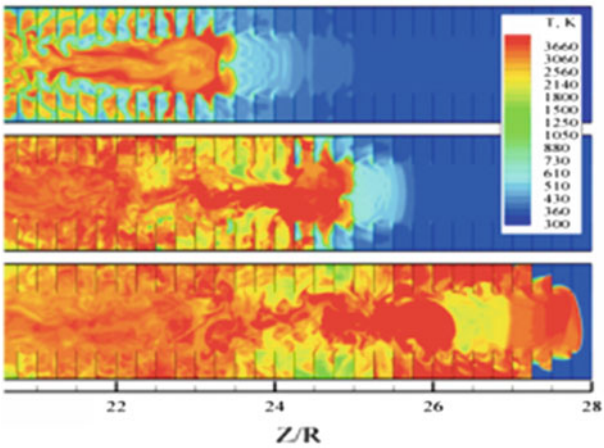

Fig. 19.10 The temperature snapshots at a developed stage of flame acceleration in obstructed tubes (Valiev et al. 2010)

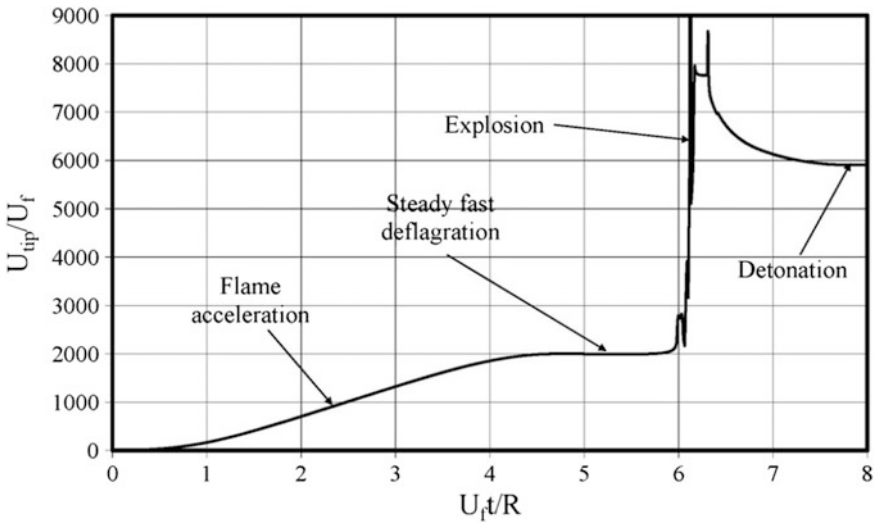

Fig. 19.11 Evolution of the flame tip velocity in the DDT process until a full detonation triggering (Valiev et al. 2009)

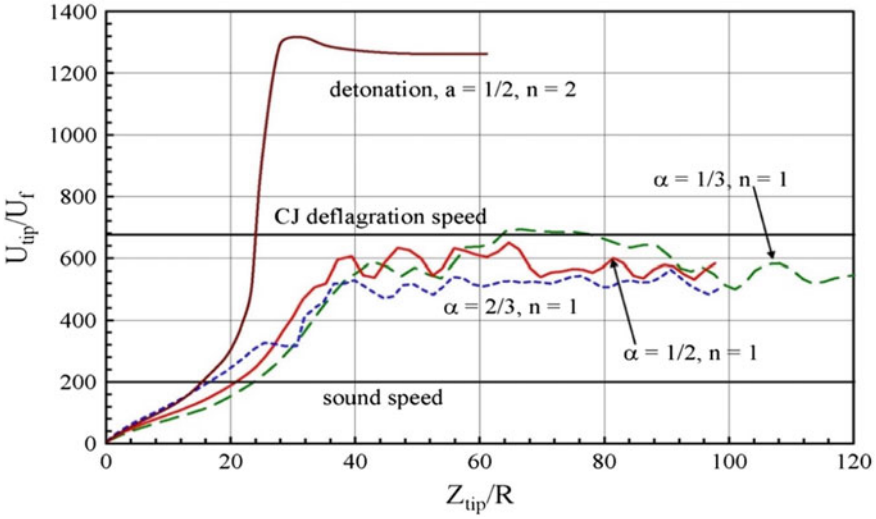

Fig. 19.12 Evolution of the flame tip velocity in obstructed pipe for $\Theta = 8$, $\alpha = 1/3; 1/2; 2/3$, $Ma = 5 \times 10^{-3}$ and different reaction orders with respect to density $n = 1; 2$ (Valiev et al. 2010)

19.5 Summary

In conclusion, the entire DDT scenario includes four distinctive stages, Figs. 19.11 and 19.12, namely (i) initial exponential acceleration in a quasi-incompressible state; (ii) moderation of the process because of gas compression, so the exponential acceleration state goes over to a slower one; (iii) eventual saturation to a steady, quasi-steady, or statistically steady high-speed flames correlated with the Chapman–Jouguet deflagration; and (iv) at this steady stage, heating of the fuel mixture leads to explosion ahead of the flame front, which develops into a self-supporting detonation. We have demonstrated that heating of the fuel mixture in smooth pipes occurs as a joint work of the shock waves generated by an accelerating flame and viscous heating by the walls (Valiev et al. 2008). Therefore, in smooth channels and tubes, the explosion conditions become preferential at the walls. In contrast, in obstructed pipes, the heating conditions depend strongly on the obstacles shape and spacing, see Fig. 19.11. Oftentimes, the explosion occurs at the obstacle edges reflecting the flame-generated shocks (Dorofeev 2011). The explosion condition is also sensitive to the chemical kinetics, see Fig. 19.12.

Acknowledgements This chapter is dedicated to deceased Prof. Vitaly Bychkov (1968-2015) of Umea University, Sweden, whose contributions to the field of flame acceleration and DDT are hard to be overestimated.

The author also thanks his collaborators—Professors Damir Valiev of Tsinghua University, China, Swetaprovo Chaudhuri of the Indian Institute of Science, Bangalore, India, and C.K. Law of Princeton University, USA—as well as his current and former students at West Virginia University, namely Orlando Ugarte, Sinan Demir, Berk Demirgok, Afeez Adebiyi, Jad Sadek, Serdar Bilgili, Anish Calaway, Frank Kronz, Ram Chalagalla, Swathi Shetty, Bugzy Idowu, Rawan Alkandari, Haley Morella, Torli Bush, Elizabeth Ridgeway, and Mandie Cathreno.

Finally, a financial support of the US National Science Foundation (NSF) through the CAREER Award No. 1554254 is recognized.

References

Akkerman V, Bychkov V, Petchenko A, Eriksson LE (2006a) Flame oscillations in tubes with nonslip at the walls. Combust Flame 145:675

Akkerman V, Bychkov V, Petchenko A, Eriksson LE (2006b) Accelerating flames in cylindrical tubes with nonslip at the walls. Combust Flame 145:206

Akkerman V, Law CK, Bychkov V, Eriksson LE (2010) Analysis of flame acceleration induced by wall friction in open tubes. Phys Fluids 22:053606

Bilgili S, Demirgok B, Valiev D, Bychkov V, Akkerman V (2015) Effect of Lewis number on the flame acceleration in channels. 9th US National Combustion Meeting, Cincinnati, OH, USA, May 17–20, 2015, Paper 3E08

Brailovsky I, Sivashinsky GI (2000) Hydraulic resistance as a mechanism for deflagration-to-detonation transition. Combust Flame 122:492

Bychkov V, Akkerman V (2006) Explosion triggering by an accelerating flame. Phys Rev E 73:066305

Bychkov VV, Liberman MA (2000) Dynamics and stability of premixed flames. Phys Rep 325:115

Bychkov V, Petchenko A, Akkerman V, Eriksson LE (2005) Theory and modeling of accelerating flames in tubes. Phys Rev E 72:046307

Bychkov V, Akkerman V, Fru G, Petchenko A, Eriksson LE (2007) Flame acceleration in the early stages of burning in tubes. Combust Flame 150:263

Bychkov V, Valiev D, Eriksson LE (2008) Physical mechanism of ultrafast flame acceleration. Phys Rev Lett 101:164501

Bychkov V, Akkerman V, Valiev D, Law CK (2010a) Role of compressibility in moderating flame acceleration in tubes. Phys Rev E 81:026309

Bychkov V, Akkerman V, Valiev D, Law CK (2010b) Influence of gas compression on flame acceleration in channels with obstacles. Combust Flame 157:2008

Bychkov V, Akkerman V, Valiev D, Law CK (2012) Gas compression moderates flame acceleration in deflagration-to-detonation transition. Combust Sci Technol 184:1066

Clavin P, Searby G (2016) Combustion waves and fronts in flows: flames, shocks, detonations, ablation fronts and explosion of stars, 1st ed. Cambridge University Press

Dion C, Demirgok B, Akkerman V, Valiev D, Bychkov V (2015) Acceleration and extinction of flames in channels with cold walls. 25th Internation Colloquium on the Dynamics of Explosions and Reactive Systems (ICDERS), Leeds, UK, Aug. 2–7, 2015, Paper 222

Dorofeev S (2011) Flame acceleration and explosion safety applications. Proc. Comb. Inst. 33:2161

Gamezo V, Ogawa T, Oran ES (2008) Flame acceleration and DDT in channels with obstacles: effect of obstacle spacing. Combust Flame 155:302

Johansen C, Ciccarelli G (2010) Numerical simulations of the flow field ahead of an accelerating flame in an obstructed channel. Combust. Theory Modell. 14:235

Ju Y, Maruta K (2011) Microscale combustion: technology development and fundamental research. Prog Energy Combust Sci 37:669

Kagan L, Sivashinsky G (2003) The transition from deflagration to detonation in thin channels. Combust Flame 134:389

Kuznetsov M, Alekseev V, Matsukov I, Dorofeev S (2005) DDT in a smooth tube filled with a hydrogen-oxygen mixture. Shock Waves 14:205

Ott J, Oran ES, Anderson J (2003) A mechanism for flame acceleration in narrow tubes. AIAA J 41:1391

Roy G, Frolov S, Borisov A, Netzer D (2004) Pulse-detonation propulsion: challenges, current status, and future perspective. Prog Energy Combust Sci 30:545

Shelkin KI (1940) Effect of nonuniform tube walls on the initiation and spreading of detonation in gases. J Exp Theor Phys 10:823

Shepherd JE, Lee JHS (1992) Major research topics in combustion. Springer-Verlag, VA

Tangirala V, Dean A, Chapin D, Pinard P, Varatharajan B (2004) Pulsed-detonation engine processes: experiments and simulations. Combust Sci Technol 176:1779

Ugarte O, Demirgok B, Valiev D, Akkerman V (2015) Combustion in micro-pipes: effect of preheated walls. 9th US National Combustion Meeting, Cincinnati, OH, USA, May 17–20, 2015, Paper 3E06

Urtiev P, Oppenheim K (1966) Experimental observation of the transition to detonation in an explosive gas. Proc. R. Soc. London A 295:13

Valiev D, Bychkov V, Akkerman V, Eriksson LE, Marklund M (2008) Heating of the fuel mixture due to viscous stress ahead of accelerating flames in deflagration-to-detonation transition. Phys Lett A 372:4850

Valiev D, Bychkov V, Akkerman V, Eriksson LE (2009) Different stages of flame acceleration from slow burning to Chapman-Jouguet deflagration. Phys Rev E 80:036317

Valiev D, Bychkov V, Akkerman V, Law CK, Eriksson LE (2010) Flame acceleration in channels with obstacles in the deflagration-to-detonation transition. Combust Flame 157:1012

Valiev D, Akkerman V, Kuznetsov M, Eriksson LE, Law CK, Bychkov V (2013a) Influence of gas compression on flame acceleration in the early stage of burning in tubes. Combust Flame 160:97

Valiev D, Bychkov V, Akkerman V, Eriksson LE, Law CK (2013b) Quasi-steady stages in the process of premixed flame acceleration in narrow channels. Phys Fluids 25:096101

Wu MH, Wang CY (2011) Reaction propagation modes in millimeter-scale tube for ethylene/oxygen mixtures. Proc Comb Inst 33:2287

Wu MH, Burke M, Son S, Yetter R (2007) Flame acceleration and the transition to detonation of stoichiometric ethylene/oxygen in microscale tubes. Proc Comb Inst 31:2429

Zeldovich YaB (1980) Regime classification of an exothermic reaction with nonuniform initial conditions. Combust Flame 39:211

Chapter 20
Combustion in Supersonic Flows and Scramjet Combustion Simulation

Vladimir A. Sabelnikov and Vladimir V. Vlasenko

Abstract The scramjet (supersonic combustion ramjet) is an air-breathing engine with the supersonic flow at the combustor entrance, i.e., with essentially lower deceleration of flow in the inlet with respect to common ramjet. The scramjet is designed for hypersonic flight of vehicle with Mach number large than 5 or 6, where the efficiency of a subsonic ramjet decreases, because the deceleration of high-speed flow to small subsonic speeds leads to extremely high temperature at the entrance to combustor, that, in its turn, generates a series of effects, deteriorating the performance of classical ramjet. The scramjet is characterized by strong coupling of all its elements. Supersonic core from the inlet to the nozzle, essential subsonic zones in thick boundary layers and high losses caused by strong shock waves, by viscous effects, by dissociation and radiation result in a situation, when positive thrust may be reached only on the basis of joint optimization of the whole flowpath. In comparison with experimental investigations, which remain very challenging to conduct in such flow conditions, computational fluid dynamics is an attractive complementary tool for the study supersonic reactive flow in the scramjet flowpath. Understanding and prediction of the flow structure are necessary for achieving the stable and efficient combustion, high thrust, and thermostable construction of the scramjet. The first half of the chapter addresses fundamentals of turbulent supersonic combustion: physics of combustion in supersonic flows with regard to scramjets, Navier–Stokes equations for multispecies reacting gas flow, kinetic schemes for simulation of scramjets, RANS/URANS, and LES approaches, the closure problems for turbulent fluxes. Particular attention is paid to the discussion of the difficulties when resolving closure problems for reaction rates. The contemporary models to account for turbulence-chemistry interactions (TCI) are shortly presented. The second half of the chapter focuses on partially stirred reactor (PaSR)

V. A. Sabelnikov (✉)
Department of Multi-Physics for Energetics, ONERA-The French Aerospace Laboratory - Palaiseau Center, Chemin de la Hunière - BP80100, 91123 Palaiseau, France
e-mail: vladimir.sabelnikov@onera.fr

V. A. Sabelnikov · V. V. Vlasenko
TsAGI, Zhukovsky, 140180 Moscow Region, Russia
e-mail: vlasenko.vv@yandex.ru

© Springer Nature Singapore Pte Ltd. 2018

S. De et al. (eds.), *Modeling and Simulation of Turbulent Combustion*, Energy, Environment, and Sustainability, https://doi.org/10.1007/978-981-10-7410-3_20

turbulent combustion models. Transported PaSR (TPaSR) and unsteady PaSR models are described in details, and experience of their application to simulation of experiments on supersonic combustion (within the framework of LES approach) is demonstrated. Finally, the problem of the selection of "correct" solution among multiple solutions of PaSR steady-state equations is considered.

Keywords Turbulent combustion · Turbulence-chemistry interaction Subgrid flow modeling · Subgrid combustion modelling · Partially stirred reactor · Scramjet · Dual mode ramjet

20.1 Introduction

20.1.1 Physics of Combustion in Supersonic Flows with Regard to Scramjets

Usual direct-flow air-breathing engine with subsonic combustion (ramjet, see Fig. 20.1) is one of the most attractive engines for supersonic aircraft. Its important advantages are extreme simplicity of construction (absence of moving parts) and growth of thrust with increase of the flight speed. For example, the thrust of an ideal ramjet (at zero angle of attack, with nozzle exit area F_{exit} equal to area of the inflowing streamtube F_∞, with ideal expansion in the nozzle up to static pressure of outer flow, $p_{exit} = p_\infty$, and in assumption of specific heat ratio $\gamma = const$) is expressed by formula (Bose 2012)

$$R_{id} \approx G_\infty (U_{exit} - U_\infty) = G_\infty U_\infty \cdot \left\{ \sqrt{\frac{(T_t)_{exit}}{(T_t)_\infty} \cdot \frac{1 - \left[p_\infty/(p_t)_{exit}\right]^{(\gamma-1)/\gamma}}{1 - \left[p_\infty/(p_t)_\infty\right]^{(\gamma-1)/\gamma}}} - 1 \right\}. \tag{20.1}$$

where $G_\infty = \rho_\infty U_\infty F_\infty$ is inflowing mass-flow rate of air, ρ is density, U is absolute value of velocity, T_t, and p_t stand for total temperature and total pressure, respectively.

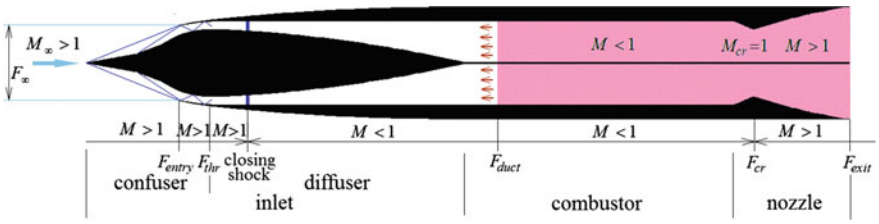

Fig. 20.1 Scheme of classical ramjet engine

In the range of flight Mach numbers $M_\infty = 3 \ldots 5$ ramjet is more effective than any other air-breathing engine (Segal 2009). However, at $M_\infty > 5$ its efficiency decreases, because the deceleration of high-speed flow to small subsonic speeds leads to extremely high temperature at the entrance to combustor $T_{entry} \approx T_\infty \left(1 + \frac{\gamma-1}{2} M_\infty^2\right)$. It generates a series of effects, deteriorating the performance of classical ramjet:

- restrictions caused by thermal stability of construction arise;
- the heat release q due to combustion decreases because of endothermic reactions of dissociation caused by the high temperature;
- the heat release relative to the flow enthalpy at the combustor entrance $Q = q/\left(C_p T_{entry}\right)$ (second Damköhler number (Annamalai and Puri 2006)) becomes low for production of sufficient thrust, C_p the heat capacity at constant pressure. Indeed, the ramjet thrust (20.1) is determined by growth of total temperature:

$$\frac{(T_t)_{nozzle}}{(T_t)_\infty} \approx \frac{T_{entry} + q/c_p}{T_{entry}} = 1 + Q; \tag{20.2}$$

- total pressure losses in the engine flowpath become too high that also leads to decrease of thrust (see (20.1)).

These problems lead to an idea of the direct-flow air-breathing engine with the supersonic flow at the combustor entrance (i.e., with essentially lower deceleration of flow in the inlet). Initially, it was assumed that flow in combustor will be entirely supersonic, and this concept of the engine became well known as scramjet ("supersonic combustion ramjet"). The scramjet concept had been proposed in fifties of twentieth century in Russia and in the USA. In 1957, Schetinkov had patented the scramjet that was projected as the main cruise engine for supersonic aerospace vehicle "Burya" (Schetinkov 1957; Sabelnikov and Penzin 2000; Prudnikov et al. 2008).

Very soon it became obvious that the scramjet is principally another class of air-breathing engines that requires solving other problems than in the case of a usual ramjet. Classical ramjet may be considered as a combination of three main elements —supersonic part of the inlet, duct with the subsonic flow (from closing shock in the inlet and up to the sonic section of the nozzle) and supersonic part of the nozzle. Each of these elements may be optimized separately; this fact resulted in the formation of three independent subdisciplines: aerodynamics of inlets, combustor processes, and aerodynamics of nozzles. To the contrary, the scramjet is characterized by strong coupling of all its elements. Supersonic "inviscid" core of the flow from inlet and up to nozzle, essential subsonic zones in thick boundary layers and high losses caused by strong shock waves, by viscous effects, by dissociation, and radiation result in situation, when positive thrust may be reached only on the basis of joint optimization of the whole flowpath.

To reach positive thrust, the hypersonic vehicle has to be sufficiently long. This statement is a direct consequence of the following unfavorable factors: (i) high-speed flow in the scramjet combustor, (ii) relatively low temperature at the combustor entrance at $M_\infty \leq 6$ (in comparison with flow decelerated to subsonic speed at the

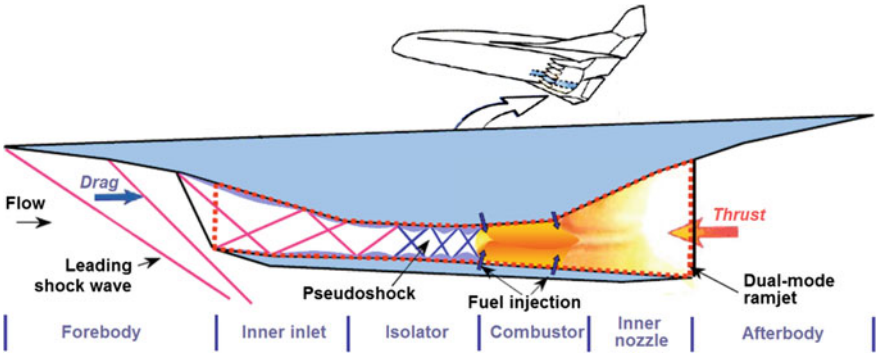

Fig. 20.2 Scheme of a vehicle with scramjet (taken from Internet, reworked)

same flight velocity) and, (iii) low efficiency of fuel/air turbulent mixing. It leads to problems with the weight of the engine, with construction cooling, etc. As a rule, integral schemes are considered, where the whole lower surface of the vehicle is used as elements of scramjet—see Fig. 20.2.

The leading surface of a vehicle is considered as compression ramp for the inlet, and the trailing surface—as expanding part of the supersonic nozzle. As a result of the large length of the compression surface, the thickness of turbulent boundary layer at the entrance to flowpath can be several tenths of percents of the duct cross-section. Therefore, characteristics of scramjet sufficiently depend on optimization of the duct flow structure. Strong nonlinear coupling among heat release, shock/rarefaction wave structures and boundary layers induces separations of boundary layers, which, in turn, change the flow structure.

For flight Mach numbers in the range $M_\infty = 4 \ldots 10$, the most often considered-in-the-literature concept is a dual-mode scramjet (see e.g., (Cockrell et al. 2002; Heiser and Pratt 1994; Curran and Murphy 2001)). For flight Mach number $M_\infty \leq 5 \ldots 6$ the combustion proceeds in the high-speed subsonic regime, and after acceleration to $M_\infty \geq 6 \ldots 7$ the supersonic combustion is realized. Change of the combustion mode can be achieved either by moving of the flowpath surfaces or by redistributing of the fuel injection region. At $M_\infty \leq 5 \ldots 6$ the flow temperature is not enough for the fuel autoignition, and combustion stabilization is reached using some artificial methods (temporary variation of duct geometry, temporary injection of compressed air, ignition by electrical discharge, etc.). At the end of combustor due to heat release the choking is realized. It results in compression wave that propagates upstream and finally stabilized before the region of heat release; downstream from this wave, subsonic flow is realized. The same situation is typical for a usual ramjet. However, in the usual ramjet the transition to subsonic flow regime is realized in normal shock wave; in dual-mode scramjet it takes place inside the prolonged structure with the interaction of shock and rarefaction waves with separated boundary layers that are called pseudo-shock (Matsuo et al. 1999). Pseudo-shock either can be located in isolator (prolonged slowly expanding part of the duct between the inlet and combustor) or can also

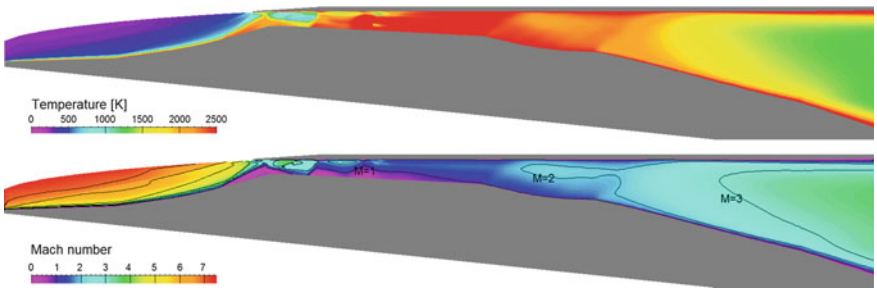

Fig. 20.3 Typical fields of temperature and Mach number at subsonic mode of dual-mode scramjet operation (TsAGI calculations in the frame of the HEXAFLY-INT European project (HEXAFLY-INT; Langener et al. 2013))

involve a part of the combustor. Combustion may start in the pseudo-shock structure or downstream, but it proceeds in mainly subsonic mode, Fig. 20.3. Contrary to a usual ramjet, where the thrust is mainly applied to diffuser part of the inlet, in scramjet the thrust is produced by expanding surfaces of the combustor and supersonic nozzle.

With the growth of the flight speed ($M_\infty \geq 6 \ldots 7$) the subsonic mode of combustion becomes ineffective (because of growth of losses in shock waves and the duct cooling losses), and transition to mainly supersonic combustion without the duct choking is performed, Fig. 20.4. At such flow speeds, the flow temperature at the isolator entrance is already enough for the fuel autoignition.

Here, it is appropriate to consider a question about differentiation of subsonic and supersonic modes of combustion. As one may note from the above text, combustion inside the duct or scramjet (or dual-mode scramjet at $M_\infty \geq 6 \ldots 7$) may be considered only as mainly supersonic; practically always it is possible to find zones, where combustion proceeds at subsonic velocities—near-wall regions of thick boundary layers, subsonic zones behind of strong shock waves, separation bubbles with recirculating flow, etc. Stabilization of combustion in high-speed flow

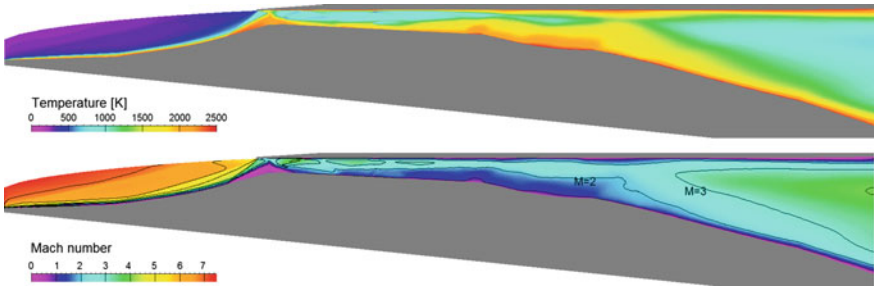

Fig. 20.4 Typical fields of temperature and Mach number at supersonic mode of dual-mode scramjet operation (TsAGI calculations in the frame of the HEXAFLY-INT European project (HEXAFLY-INT; Langener et al. 2013))

requires high temperature and a residence time of combustible mixture comparable with characteristic chemical time; that is why in the majority cases stabilization takes place in flow regions with reduced velocity. If this velocity is still supersonic, heat release due to combustion leads to the strong growth of temperature and reduction of speed, and it may induce the formation of strong shock waves with subsonic zones behind them even far from the combustor walls.

Clear differentiation of subsonic and supersonic modes of combustion may be given in inviscid one-dimensional (constant-area) stationary flow (Shapiro 1953). It is obvious that from the viewpoint of the flow energy balance the heat addition is analogous to execution of a work with respect to the flow; therefore, heat release is usually exhibited analogous to decrease of the cross-section area of the duct. In supersonic flow, the heat release in constant-area duct leads to deceleration of flow and to the growth of pressure; in subsonic flow the variations of flow parameters have an opposite sign.

In ducts with variable cross-section area and in the presence of viscid effects the situation becomes less obvious, because these factors also result in the variation of flow parameters. Moreover, flow in the duct cross-section is usually nonuniform (due to boundary layers, shock, and rarefaction waves, the interaction between them and other effects), and flow contains regions with both supersonic and subsonic flow. A possible approach is averaging of Mach number over the current cross-section area of the duct. This averaging may be accomplished in different ways; usually the safe solution is averaging over cross area section F with respect to convective flux of momentum (Sedov 1993):

$$\langle M \rangle = \frac{\int_F M \rho u^2 dF}{\int_F \rho u^2 dF}, \tag{20.3}$$

where u is longitudinal velocity (perpendicular to cross-section surface). If $\langle M \rangle > 1$, then one may claim that combustion proceeds in supersonic mode. However, such averaging can mislead the researcher. Indeed, if one will trace the gas volumes that entered the duct at the same time moments, then these volumes will cross the current cross-section in different time moments. Consequently, averaging (20.3) contains distributions from different time moments. As a result, a variation of $\langle M \rangle$ and of other averaged gas parameters along the duct can be inconsistent with real dynamics of these parameters along different streamlines. For example, we may have combustion in the thin subsonic near-wall region of boundary layers and the thick supersonic core of the flow without any combustion. Then, the averaging (20.3) will give $\langle M \rangle > 1$, although the combustion obviously proceeds in subsonic mode.

In fact, we may say confidently about the supersonic mode of combustion, only if in the places of combustion stabilization (i.e., in the places where the combustion starts in this duct) the flow is locally supersonic. In this case the stabilized flame is not affected by small disturbances produced downstream from the stabilization region. In the experiment, it may be checked easily by small variation of fuel

mass-flow rate that lead to a variation of heat release downstream from the place of flame stabilization. If this variation does not affect the flame in the place of its stabilization, then we may affirm that supersonic mode of combustion is realized. Here, it is important to point that combustion stabilization in high-speed chambers is often realized in the unsteady regime, with oscillations of flame zones along the duct. Unsteady effects may be caused not only by strongly turbulent character of the flow but also by local ignition and extinction, resulting in variation of flow structure.

Let there is a combustion in a high-speed chamber at some amount of relative heat release Q_0. The flow in an engine is directed from left to right. If flow core at the entrance is supersonic and Q_0 is sufficiently small (very lean mixture), than the supersonic character of the flow core is kept till the nozzle exit, and there are essential regions of combustion in supersonic flow. Let $x_{upstream}$ denotes the extreme left coordinate indicating the influence of heat release. Since in the general case the flow is unsteady, we assume that $x_{upstream}$ is an averaged value. Now let us start to increase gradually the relative heat release (e.g., by the growth of the fuel mass-flow rate). Increment of Q by small but finite value results in a displacement of flame (usually the flame is shifted upstream, i.e., $x_{upstream}$ decreases). Let us denote, the increment of $x_{upstream}$ by $\Delta x_{upstream}$. Within some range of Q $(Q_0 < Q < Q_{\max})$, $\Delta x_{upstream}$ will be varied slowly, because in the supersonic core the perturbations, caused by the addition of heat release, cannot reach the place, where the combustion starts. They can only propagate through the near-wall subsonic part of boundary layers, but this propagation is moderated by viscous damping. Perturbations lead to small variations of boundary layer thickness, to small shifts of shock wave structures in the duct and to slow variation of $\Delta x_{upstream}$. It will mean that have the supersonic mode of combustion is keeping.

But at some critical value $Q = Q_{\max}$, $\Delta x_{upstream}$ will increase abruptly, and flow structure will change considerably throughout. It will mean that somewhere downstream from the fuel injectors the heat release resulted in flow chocking. Surface with Mach number $M = 1$ was formed across the duct. Further addition of heat results in the formation of shock waves propagating upstream and changing the inflow boundary conditions. Usually, this process is accompanied with arising separations of boundary layers, the formation of pseudo-shock and regions with essentially subsonic zones of heat release. This is a transition to a subsonic mode of combustion.

At early stages of the scramjet idea development, it was assumed that the main fuel for high-speed aircraft will be hydrogen. However, later the projects of engines on liquid hydrocarbon fuel became widespread (Powell et al. 2001; Falempin and Serre 1999). Hydrocarbon fuels are much safe in operation, they are easy-controlled, and it leads to simpler and cheaper fuel system. Now, there are arguments for increasing the flight-speed upper limit for hydrocarbon-fueled aircraft to $M_\infty = 9 \ldots 10$ (Waltrup 2001). Hydrocarbon fuels require less volume for storage in comparison with hydrogen, that allows to decrease outer dimensions of vehicle by 8–15% (Townend 2001), raising its lift-drag ratio. Theoretical estimations allow

hoping that in the range of flight Mach number $M_\infty = 4 \ldots 10$ it is possible to reach the required characteristics of an engine with the fixed geometry of duct—without complex mechanical devices, providing the variable geometry of flowpath.

The supersonic inviscid core of the flow at the end of the inlet and thick turbulent boundary layers are typical peculiarities characteristic for scramjets, even in subsonic-mode operation. These peculiarities lead to new physical mechanisms of combustion. In supersonic flow, acoustic disturbances cannot propagate upstream; it complicates the formation of feedback between the end and the beginning of a duct. However, disturbances can propagate along subsonic parts of boundary layers or can form strong shock waves capable to propagate upstream. Formation of precombustion shock trains is a typical example of feedback establishment.

Interaction of strong shock waves with boundary layers (especially in the presence of heat release due to combustion) may lead to the formation of separation zones with slow recirculation motion of the gas. Such recirculation zones can work as stabilizers of combustion due to high temperature and long residence time of combustible mixture. Recirculation zones may also be produced by corners of the flowpath geometry. In stationary flow regime, combustion usually proceeds within outer mixing layers of recirculation zone, because its core is filled with hot combustion products. The exception is the case, when the fuel injector is placed inside the recirculation zone. Sometimes intermediate situations occur, when the fuel comes into the core of recirculation zone intermittently. Such situations result in oscillations of combustion zone within the duct.

In subsonic-flight air-breathing engines, combustion often proceeds within deflagration waves, stabilizing due to the upstream propagation of heat and reactants due to turbulent and molecular mixing. In scramjets, because of the high flow velocity, deflagration waves, once stabilized, have a small angle with respect to flow. Instead, other mechanisms of flame stabilization may occur. The growth of total enthalpy of flow (with an increase of flight Mach number) results in an increase of static temperature at the combustor entrance, sufficient for the autoignition (at flight Mach numbers $M_\infty \geq 6$). But it should be remembered that growth of entry temperature also leads to decrease of relative heat release $Q = q/(C_p T_{entry})$, i.e., to decrease of thrust efficiency of combustion. There are other physical mechanisms allowing to increase flow temperature without diminishing of Q. For example, shock waves, increasing the flow temperature, can also provoke the autoignition. Flow static temperature also grows in the turbulent shear layers due to the viscous dissipation of kinetic energy. This effect is especially important in engines with a high-speed core of the flow.

The high speed of flow leads to the growth of the mean strain rate in shear layers, i.e., to increase of turbulence production and, as a result, to a strong turbulence. The growth of Reynolds number also increases the range of length scales in turbulent motion. The laminar flames of finite dimensions can be completely extinguished in the strong turbulence because of a high stretch (e.g., (Poinsot and Veynante 2005) and references therein). Therefore, due to intensive mixing, the pockets of the mixture (with varying composition hot air + fuel) and hot combustion products are

formed. If it turns out that the ignition delay times (it should be stressed that the local delay times has to be considered) in some of these pockets become shorter with respect to the laminar flame residence time the local volume combustion in (micro) pockets will take place. This regime of turbulent combustion was put forward by Schetinkov (for premixed combustion) as early as in 1950th and was called by him as a microvolume model of turbulent premixed combustion (Schetinkov 1958, 1965). It should be stressed that species concentrations and temperature fluctuations are not negligible for microvolume burning, because of variation of compositions and temperature in individual microvolumes. Therefore, microvolume model of turbulent premixed combustion is principally different from Damköhler model of distributed combustion on Borghi diagram, e.g., (Poinsot and Veynante 2005): species concentrations and temperature fluctuations are neglected for distributed combustion, i.e., mean chemical source is calculated using mean temperature and species concentrations.

Interaction of all these factors results in very complex flow structure in the flowpath of a scramjet, though the duct geometry is relatively simple (in comparison with, e.g., turbojet engines). Understanding and prediction of this flow structure are necessary for achieving the stable and efficient combustion, high thrust and thermostable construction of the engine.

20.2 Key Equations

20.2.1 Navier–Stokes Equations for Multispecies Reacting Gas Flow

Flow in scramjet can usually be described by the model of viscous compressible multispecies perfect gas. This is an approximation that includes the following important assumptions:

1. All essential physical processes may be considered in the model of single-phase gaseous flow. This assumption works well, e.g., for hydrogen-fueled combustors. But hydrocarbon fuels, which are now considered as possible alternative to hydrogen, are usually stored in liquid phase, and injection is accompanied by evaporation of the fuel drops with possible combustion at the drop surfaces. These effects may be essential, if the evaporation length is comparable with characteristic length of fuel-air mixing and combustion. For high static temperatures of flow (about 1000 K), hydrocarbons evaporate rapidly (Barnett and Hibbard 1957), and assumption of gaseous combustion may be applied as approximate way of the flow consideration. It is necessary to note that this assumption also includes neglect of solid phase that is generated in hydrocarbon fuel combustion (soot particles).
2. Gas may be considered as continuous medium. It means that mean free path of gas molecules, λ, is considerably less than characteristic length scale L_{duct} of the

duct geometry (i.e., Knudsen number $Kn = \lambda / L_{duct} \ll 1$, (Laurendeau 2005)). In spite of considerable increase of the gas density after the gas compression in the inlet, this assumption theoretically can be violated for the smallest turbulent eddies, which characteristic length is determined by Kolmogorov length scale $\eta_K \sim L_{duct} / Re_{L_{duct}}^{3/4}$, $Re_{L_{duct}} = UL_{duct}/\nu$, U is characteristic mean velocity at the duct, ν laminar kinematic viscosity (Kolmogorov 1941). Rough estimation yields that the ratio $(L_{duct}/\eta_K) \approx Re_{L_{duct}}^{3/4}$ may reach $10^4 - 10^5$. However, usually it is assumed, that assumption $\lambda/\eta_K << 1$ works well (Wilcox 1998).

3. Gas is a mixture of N species, which are assumed to be perfect gases with common temperature T. It means that each species is described by Mendeleev–Clapeyron equation of state $p_k = \rho_k \frac{R_0}{W_k} T$ with the same temperature T, $R_0 = 8.314 J/(moleK)$ is the perfect gas constant, p_k and ρ_k are partial pressure and density of kth species. This assumption implies the neglect of forces of intermolecular interaction and large amount of particle collisions for the establishment of equal mean kinetic energy of different particles. Using Dalton law $p = \sum_{k=1}^{N} p_k$ and introducing mass fractions $Y_k = \rho_k / \rho$ ($\rho = \sum_{k=1}^{N} \rho_k$ is the density of the multispecies gas), we come to the following equation of state for the mixture of N species:

$$p = \rho R_0 T \sum_{k=1}^{N} \frac{Y_k}{W_k} = \rho \frac{R_0}{W} T, \quad \frac{1}{W} = \sum_{k=1}^{N} \frac{Y_k}{W_k}, \tag{20.4}$$

where W is the mean molecular weight of the mixture.

Navier–Stokes equations (NSE) for compressible multispecies gas (neglecting body forces, since they are is negligible for scramjet applications, and omitting the heat radiation flux) are (Poinsot and Veynante 2005):

$$\frac{\partial \rho}{\partial t} + \frac{\partial \rho u_i}{\partial x_i} = 0, \tag{20.5a}$$

$$\frac{\partial \rho u_i}{\partial t} + \frac{\partial \left(\rho u_j u_i + p\delta_{ij} - \tau_{ij} \right)}{\partial x_j} = 0, \tag{20.5b}$$

$$\frac{\partial \rho e_t}{\partial t} + \frac{\partial \left(\rho e_t u_i + p u_i - \tau_{ji} u_j + q_i \right)}{\partial x_i} = 0, \tag{20.5c}$$

$$\frac{\partial \rho Y_k}{\partial t} + \frac{\partial (\rho Y_k (u_i + V_{k,i}))}{\partial x_i} = \dot{w}_k, \tag{20.5d}$$

$$e_t = e + \frac{u_j u_j}{2}, \quad e = h - \frac{p}{\rho} = \sum_{k=1}^{N} Y_k h_k - \frac{p}{\rho}. \tag{20.5e}$$

Here and below the summation over repeated indices, that denote the spatial components of vectors and tensors, is assumed. The following notations are used in Eqs. (20.5a)–(20.5e): u_i is the ith component of the velocity vector $\mathbf{u}$, e_t is the total energy per unit mass of gas mixture, τ_{ij} is the viscous tensor, q_i is the ith component of molecular heat flux vector, $V_{k,i}$ is the ith component of the diffusion velocity vector $\mathbf{V}_k$ of species k, $\dot{w}_k$ is the reaction rate of species k, h, and h_k are the enthalpy of gas mixture and enthalpy for species k, respectively. Expressions for h and h_k are given by:

$$h_k(T) = h^o_{f,k} + h_{sk} = h^o_{f,k} + \int_{T_0}^{T} C_{pk}(T)\, dT, \tag{20.6}$$

$$h = \sum_{k=1}^{N} Y_k \left(h^o_{f,k} + h_{sk} \right) = \sum_{k=1}^{N} Y_k h^o_{f,k} + \sum_{k=1}^{N} Y_k h_{sk} = \sum_{k=1}^{N} Y_k h^o_{f,k} + h_s, \tag{20.7}$$

where $h^o_{f,k}$ stands for the formation enthalpies, $h_{sk} = \int_{T_0}^{T} C_{pk}(T)dT$ and $h_s = \sum_{k=1}^{N} Y_k h_{sk}$ are the sensible enthalpies of species k and of the mixture, respectively; C_{pk} the heat capacity at constant pressure of species k. Dependence of the enthalpy of species k upon temperature in the whole possible range of temperatures is rather complex and is usually approximated by polynomials of fifth (Kee et al. 1996; Burcat and Ruscic 2005) or even higher (Glushko 1978) order. However, the experience of numerical simulations of scramjets conducted in TsAGI, e.g., (HEXAFLY-INT; Frolov et al. 2015; Shiryaeva et al. 2014; Shiryaeva and Anisimov 2015), show that, for the description of temperature range $T = 300 \ldots 3000\ K$, which is typical for flows in scramjet, the approximation of h_k by quadratic polynomial

$$h_k(T) = h^o_{f,k} + \int_{T_0}^{T} C_{pk}(T)dT \approx a_k + b_k T + c_k T^2, \tag{20.8}$$

provides enough accuracy. This conclusion is very convenient in practical calculations, allowing reducing the task of determination of temperature from the given value of total energy of mixture to solution of quadratic equation.

The viscous tensor τ_{ij} (neglecting bulk viscosity), the molecular heat flux components q_i and the diffusion velocity components $V_{k,i}$ for species k are given by

$$\tau_{ij} = 2\mu S^D_{ij},\ S^D_{ij} = S_{ij} - \frac{1}{3} S_{kk}\delta_{ij},\ S_{ij} = \frac{1}{2}\left(\frac{\partial u_j}{\partial x_i} + \frac{\partial u_i}{\partial x_j} \right),\ \mu = \rho\nu \tag{20.9a}$$

$$q_i = -\kappa \frac{\partial T}{\partial x_i} + \rho \sum_{k=1}^{N} h_k Y_k V_{k,i},\ \kappa = \frac{\mu\, C_p}{Pr}, \tag{20.9b}$$

$$V_{k,i} = -D_k \frac{1}{Y_k}\frac{\partial Y_k}{\partial x_i},\ D_k = \frac{\nu}{Sc_k}, \tag{20.9c}$$

where κ and D_k are the thermal conductivity and the diffusion coefficient of species k, Pr, and Sc_k are the Prandtl and the Schmidt numbers, respectively. It should be noted that the diffusion processes involve binary diffusion coefficients D_{kj} (Poinsot and Veynante 2005; Ferziger and Kaper 1972). Simplified diffusion law (20.9c) is named as Fick's law. It is used in a majority of combustion numerical studies. It is good approximation for gaseous combustion in air, since mass fraction of fuel is usually small with respect to mass fraction of air. Therefore, the transport coefficients for all gas species may assumed to be close to the air transport coefficients (Poinsot and Veynante 2005; Ferziger and Kaper 1972): $Sc_k \approx 00.9$, $Pr \approx 0.7$. Molecular viscosity may be calculated using the well-known Sutherland formula (Rathakrishnan 2013).

Combustion of fuel in air includes many elementary reactions. In practical applications, reduced kinetic schemes are used that include only most important reactions with some approximations of reaction rates adjusted to provide good accuracy of the whole combustion process representation within given range of pressures, temperatures, and mixture compositions.

It is assumed that reactive flow comprises a chemical system of N species reacting through M elementary reactions (not confused with Mach number!). Equation of lth reaction can be represented as (Poinsot and Veynante 2005)

$$\sum_{k=1}^{N} \nu_{kl}^{f} X_k \rightleftarrows \sum_{k=1}^{N} \nu_{kl}^{r} X_k, \tag{20.10}$$

where X_k is a symbol for species k, ν_{kl}^{f} and ν_{kl}^{r} are the molar stoichiometric coefficients of kth species in lth forward and reverse reactions; $1 \le k \le N,\ 1 \le l \le M$. Then mass reaction rate $\dot{w}_k$ in the Eq. (20.5d) is expressed by the equation (Poinsot and Veynante 2005):

$$\dot{w}_k = W_k \sum_{l=1}^{M} \nu_{kl} \varpi_l, \tag{20.11}$$

where $\varpi_l = \varpi_{fl} - \varpi_{rl}$ is the progress rate of reaction l [mole $\cdot$ m^{-3} $\cdot$ s^{-1}] and $\nu_{kl} = \nu_{kl}^{r} - \nu_{kl}^{f}$; the rates of forward and reverse reactions ϖ_{fl} and ϖ_{rl} are written as:

$$\varpi_{fl} = K_{fl}(T) \prod_{k=1}^{N} [X_k]^{\nu_{kl}^{f}},\ \varpi_{rl} = K_{rl}(T) \prod_{k=1}^{N} [X_k]^{\nu_{kl}^{r}}, \tag{20.12}$$

where $[X_k] = \frac{\rho Y_k}{W_k} = \frac{\rho_k}{W_k}$ is molar concentration of kth species; the rate constants $K_{fl}(T)$, and $K_{rl}(T)$ are usually modeled using the empirical Arrhenius law:

$$K_{fl} = A_{fl} T^{\beta_l} \exp(-T_{al}/T). \tag{20.13}$$

The preexponential constant A_{fl}, the temperature exponent β_l and the activation temperature T_{al} (or equivalently the activation energy $E_{al} = RT_{al}$) are provided from experiments and in some cases from theoretical calculations. In majority of publications (see, e.g., (Westbrook and Dryer 1981; Davidenko et al. 2003; Li et al. 2004)) only approximations of forward reaction rate constants are given. Then reverse reaction rates constants $K_{rl}(T)$ are found from the expression $K_{rl}(T) = K_{fl}(T)/K_l^{eq}(T),$, where $K_l^{eq}(T)$ is the equilibrium constant of reaction k. Equilibrium constants are determined by thermodynamic properties of species. The readers are referred to the textbooks (e.g., (McAllister et al. 2011)) for details.

It should be noted that calculation of $K_{rl}(T)$ through $K_{fl}(T)$ and $K_l^{eq}(T)$ allows to increase the accuracy of kinetic scheme, because the accuracy of thermodynamic function approximations is considerably higher than the accuracy of reaction rate approximations (experimental data scatter for reaction rates is still very substantial, see, e.g., (Weydahl et al. 2011)). In the work (Vlasenko and Nozdrachev 2017), it is shown that the use of equilibrium constants allows avoiding numerical effects, related to the phenomena of nonphysical "dynamic" equilibrium described in the work (Shiryaeva 2010).

Among the elementary reactions proceeding in combustion process there are some reactions that require too large energy for the decomposition of stable particles or, inversely, include excessive release of energy due to formation of stable particles. Such reactions usually proceed with participation of additional particle M, adding deficient energy to system or removes excess energy from it. Typical example is the reaction $H_2 + M \rightleftarrows 2H + M$. Any particle contained in the mixture can play the role of such additional particle. In such cases, molar fraction of the additional particle is calculated by formula $[X_M] = \sum_{k=1}^{N} r_k [X_k]$, where the empirical coefficients r_k show the probability of participation of species k as additional particle. In the absence of information about these probabilities, one may take $r_k = 1$. If $r_k = 1$ for all species, then $[X_M] = \rho/W$, where W is molecular weight of the mixture.

20.2.2 Examples of Kinetic Schemes for Simulation of Scramjets

Now, let us consider several examples of kinetic schemes useful for scramjet applications. From the viewpoint of computational cost, the crucial factor is the quantity of chemical species N, because it determines the quantity of differential equations in the NSE (20.5a–20.5e). The quantity of operations in computation increases at least as N^2. The reason is stiffness of chemical kinetics differential

equations (Oran and Boris 2005) that result in the necessity to use implicit approximations and iterative methods. The typical approach is Newton method that required to invert Jacoby matrices of source terms, and their dimension is N^2. It leads to the situation, when the solution of differential equations for chemical species occupies the major part of computation time.

For the case of a hydrogen-fueled engine, the classical comprehensive kinetic mechanism is proposed by Jachimowski (Jachimowski 1988). It includes $M = 33$ reactions between $N = 13$ active species. However, reactions with participation of nitrogen become essential only in the case of flight Mach number $M_\infty > 12$. For dual-mode scramjets, nitrogen N_2 can be considered as inert species. It reduces the quantity of species to $N = 9$ (one of them is inert N_2) and the reactions number to $M = 20$. Among the modern kinetic mechanisms of hydrogen-air combustion, the one proposed by Conaire et al. (Conaire et al. 2004), with $M = 19$ reactions between the same $N = 9$ species, may be mentioned. It is important to note that there are more reduced kinetic mechanisms, but they cannot be considered as safe. Essential acceleration of computation (nearly 2 times) may be reached by excluding peroxides HO_2 and H_2O_2 from consideration, as it was made in the kinetic scheme (Davidenko et al. 2003). However, physically such removal should result in shortening the reaction time, and adjusting of reaction rate constants with the aim to get correct time of reaction has inevitably artificial character. Some simple kinetic mechanisms (e.g., (Moretti 1965)) do not include reactions of radical formation and require to introduce in computation some initial values of radical mass fractions. It introduces uncertainty in the task: the reaction development is changed with variation of the radical initial mass fractions.

The description of hydrocarbon fuels—air combustion is much more complex with regard to hydrogen-air combustion. The detailed kinetic mechanisms of these processes include hundreds and thousands of reactions between many tens of species even in the case of pure hydrocarbon fuels (practical aviation fuels, e.g., kerosene, are a complex mixture of multiple hydrocarbon species). For example, the detailed mechanism of ethylene (C_2H_4) oxidation contains 469 reactions between 71 species (Qin et al. 2000). Such mechanisms are inapplicable in practical calculations of high-speed flows. Several stages of the kinetic mechanism simplification are possible. Analysis of reaction rates and of the structures of reaction chains allows excluding insufficient reactions and species. As a result, the so-called skeletal mechanisms may be obtained, which are close in quality to detailed mechanisms. In the case with ethylene, the possible skeletal mechanism (Zambon and Chelliah 2007) consists of "only" 128 reactions between 31 species; it provides three times acceleration in the calculation in comparison with the detailed mechanism. But this quantity of reactants is still too high for practical tasks. Further reduction inevitably consists in transition to the introduction of global reactions—artificial summary stages replacing the chains of several reactions, with some approximation of reaction rate (often in non-Arrhenius form). Possible way of global reactions constructing is the well-known quasi-steady-state approximation for intermediate substances (Kuo 2005).

In many works (Edelman and Fortune 1969; Gokulakrishnan et al. 2006) two-stage approach is used. It consists of two partially superposed stages. At the first stage, oxidation of the hydrocarbon fuel to simple intermediate substances is considered. This stage is simulated approximately by one-sided (only forward) global reaction—for example,

$$C_nH_m + \frac{2n+m}{4}O_2 \rightarrow n\ CO + \frac{m}{2}H_2O \text{ or } C_nH_m + \frac{n}{2}O_2 \rightarrow n\ CO + \frac{m}{2}H_2.$$

The second stage consists of reactions in H-O-C system. This stage is described in details by real elementary reactions, including reactions of CO oxidation to CO_2 (3–4 elementary reactions) and reactions of hydrogen-air combustion mechanism described above. Such approach is described in (Westbrook and Dryer 1981). In the work (Gokulakrishnan et al. 2006), which is devoted to ethylene-air combustion, the global reaction $C_2H_4 + O_2 \rightarrow 2\ CH_2O$ is used; it is followed by a chain of reactions, describing oxidation of CH_2O, which in turn is followed by chains, describing H_2 and CO oxidation. This reduced kinetic mechanism includes 14 species, allowing to accelerate computation approximately 25 times.

In the reduced mechanisms, proposed in the work (Zambon and Chelliah 2007), ethylene-air combustion is described by 18 reactions between 19 species or by 15 reactions between 19 species, allowing to accelerate calculations 10 times in comparison with the detailed mechanism. All these reactions are two-sided but global (each reaction replaces a subset of real elementary reactions). Reaction rates for each reaction are obtained automatically on the basis of quasi-steady-state approximation. Authors show that the reduced mechanism allows describing the time dependence of the ethylene autoignition, the propagation speed of a laminar flame, and effects of extinction.

Combustion of complex aviation fuels may be considered in the same way by the introduction of the global reaction of complex fuel to simple species or by consideration of surrogate fuels, where real aviation fuel is replaced by a mixture of a small quantity of pure hydrocarbons. For example, Jet-A kerosene may be replaced by a surrogate mixture consisting of n-dodecane (molar fraction 40.4%), iso-octane (29.5%), 1, 3, 5-trimethylbenzene (7.3%), and n-propylbenzene (22.8%) (Dooley et al. 2012). After that, reduced mechanisms of these fuels combustion are applied.

One important property of hydrocarbon combustion at low initial temperatures is multistage autoignition (Vanhove et al. 2006). At the initial stage of hydrocarbon decomposition into more simple species, the subset of important reactions is changed with temperature, leading to the non-monotone behavior of the reaction time dependence upon temperature, see, e.g., Fig. 20.5.

To take this effect into account in reduced mechanisms, in the work (Basevich and Frolov 2006) it is proposed to use different formulas for the rate of the hydrocarbon partial oxidation, described by the global irreversible reaction

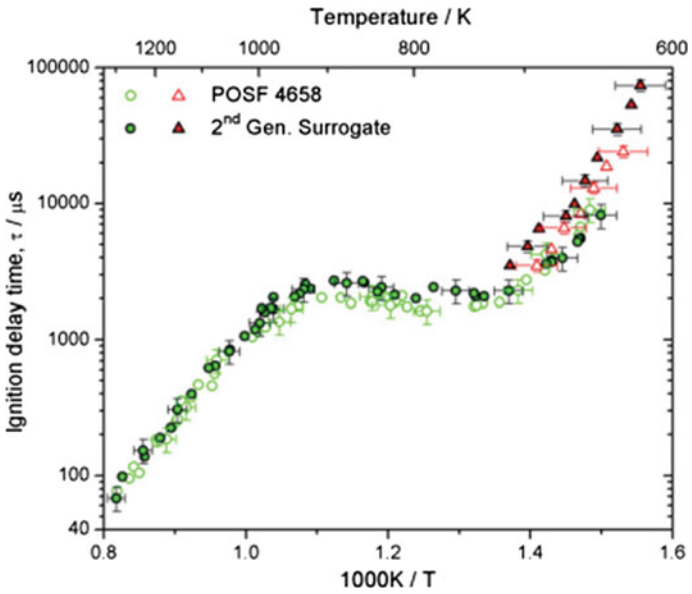

Fig. 20.5 Dependence of Jet-A/air ignition delay time upon temperature (Dooley et al. 2012)

$$C_nH_m + \frac{2n+m}{4}O_2 \rightarrow n\,CO + \frac{m}{2}H_2O.$$

At some critical temperature T_{cr}, one formula is replaced by another. Rate of the above global reaction is described by formula

$$\dot{w} = AT^{\beta}\left(\frac{\rho Y_{C_nH_m}}{W_{C_nH_m}}\right)\cdot\left(\frac{\rho Y_{O_2}}{W_{O_2}}\right)\exp\left(-E/T\right)$$

(it should be noted that for global reactions the reaction species exponents are not necessarily equal to the molar stoichiometric coefficients, e.g., (Poinsot and Veynante 2005)). For example, the following values of empirical constants may be used for propane C_3H_8:

$$T < 775\ K: \quad A = 1.956 \cdot 10^9\ \frac{\text{mole}}{\text{m}^3\,\text{sec}},\ \beta = 1,\ E = 20142\ K,$$
$$T > 775\ K: \quad A = 1.728 \cdot 10^9\ \frac{\text{mole}}{\text{m}^3\,\text{sec}},\ \beta = -0.2264,\ E = 22660\ K.$$

For propane/air combustion, authors of (Basevich and Frolov 2006) proposed to describe the second stage of combustion by following three global reactions:

(i) $2H_2 + O_2 \rightarrow 2H_2O$,
(ii) $2CO + O_2 \rightarrow 2CO_2$,
(iii) $CO + H_2O \rightleftarrows CO_2 + H_2$.

where the reactions (i) and (ii) are irreversible, and (iii) is reversible. This kinetic scheme was successfully used for simulation of propane combustion in high-speed combustors (Frolov et al. 2015); critical remarks on the restrictions of this model can be found in (Babushenko et al. 2015).

Finally, it is worth to note that there is an important way for crucial acceleration of chemical kinetics calculations within a numerical simulation of engine flows. This approach was proposed by Pope (1997) and is named ISAT (In Situ Adaptive Tabulation). The ISAT idea is based on the fact that in gas dynamic calculations the kinetics is calculated in millions of cells and hundreds of thousands times in each cell. In this situation, close conditions arise frequently. The idea is to solve chemical kinetics equations for the given conditions only one time and use the solution for all situations with close conditions. During the calculation, the conditions in cells and corresponding solution of the chemical equations are tabulated; if in some cell close conditions arise, the solution is taken from the table and applied. Such approach allows accelerating calculation more then 10 times and clears the way for using not only reduced but also detailed kinetic mechanisms. However, ISAT approach meets with a lot of serious problems: discretization of the ranges of parameters variation (with keeping enough accuracy of the reaction rates calculation), storage of huge data arrays, and a quick search of close conditions within these huge tables. There are analytical methods for the correct solution of these problems (Pope 1997).

20.3 Averaged and Filtered Conservation Equations

While the problem of laminar-turbulent transition is actual for flow around the outer compression surface of the high-speed propulsion system, the flow inside the duct of the high-speed engine has essentially turbulent character, with very high Reynolds number based on the characteristic size L_{duct} of the scramjet duct. Instability of flow and nonlinear interactions of growing perturbations lead to development of continuous spectrum of length and time scales—from largest turbulent eddies of scale comparable with L_{duct} till smallest eddies of the order of Kolmogorov length scale $\eta_K \sim L_{duct}/Re_{L_{duct}}^{3/4}$ (Kolmogorov 1941), that are subjected to essential influence of viscous dissipation. As it was mentioned above in the Sect. 20.2.1, the length ratio of largest to minimal eddies may reach $L_{duct}/\eta_K \sim 10^4 - 10^5$. All scales are important in the physics of turbulence (Kolmogorov 1941). Large eddies depend upon the geometry of duct and interact with the global flow, obtaining the kinetic energy from nonuniformity of global flow. This energy is partially transmitted from large eddies to smaller eddies and further. The smallest eddies of the order of Kolmogorov length scale η_K are equally important, because of the dissipation of

turbulence kinetic energy (TKE) into heat proceeds at these scales. The balance of production and dissipation of TKE determines the structure and properties of the turbulent flow. From the above considerations it follows, that the direct numerical simulation (DNS) of NSE (20.5a–20.5e), to describe all scales of turbulent motions, is hardly possible at very high Reynolds numbers $\mathrm{Re}_{L_{duct}}$ typical for flow in scramjet. Indeed, the resolution of all scales requires a computational grid with cells of the order η_K. This results in an extremely high quantity of mathematical operations. Crude estimation for the quantity of an algorithm working cycles for all computational cells during the characteristic time scale $T_{duct} \approx L_{duct}/U$ (U is characteristic mean velocity at the duct) yields $(L_{duct}/\eta_K)^3 \cdot (T_{duct}/\tau_K) \approx \mathrm{Re}_{L_{duct}}^{11/4}$, where $\tau_K \approx T_{duct}\mathrm{Re}_{L_{duct}}^{-1/2}$ is the Kolmogorov time scale (Kolmogorov 1941). And do not forget that each working cycle includes the solution of stiff chemical kinetics equations.

20.3.1 Reynolds Time Averaging Navier–Stokes Equations. RANS/URANS Equations

The most widespread approach to numerical simulation of the turbulent reacting flows in high-speed propulsion systems is based on an idea to perform averaging of NSE (20.5a–20.5e) with the aim to smooth the turbulent fluctuations of gas parameters and obtain the equations for mean primitive variables, RANS equations. This key idea was proposed by Reynolds at the end of XIX century (Reynolds 1894) for incompressible NSE. Reynolds himself considered time averaging instantaneous primitive variable $a(\mathbf{x}, t)$ over the time interval T that should be essentially higher that characteristic time of turbulent fluctuations τ_{turb}, but essentially lower than characteristic time of organized (nonstochastic) unsteady processes τ_{org}

$$\bar{a}(\mathbf{x}, t) = \frac{1}{T}\int_{t-T/2}^{t+T/2} a(\mathbf{x}, \tau)\, d\tau. \tag{20.14}$$

Reynolds time averaging (20.14) is applied to NSE (20.5a–20.5e), where all instantaneous primitive variables are represented as $a(\mathbf{x}, t) = \bar{a}(\mathbf{x}, t) + a'(\mathbf{x}, t)$, and a' stands for a turbulent fluctuations. Finally, the averaged equations are obtained using the rules (axioms) formulated by Reynolds (Reynolds 1894):

$$\bar{\bar{a}} = \bar{a}, \quad \overline{a'} = 0, \quad \overline{\bar{a}b} = \bar{a}\bar{b}, \quad \overline{ab'} = \overline{a'b'}, \quad \overline{\frac{\partial a}{\partial x}} = \frac{\partial \bar{a}}{\partial x}, \quad \overline{\frac{\partial a}{\partial t}} = \frac{\partial \bar{a}}{\partial t}. \tag{20.15}$$

The rules (20.15) follow strictly from the definition (20.14) for steady-in-the-average flow (when $\bar{a}$ do not depend on time, $\bar{a} = \bar{a}(\mathbf{x})$, and one can

take $\tau_{org} = \infty$, $T = \infty$), and approximately if the condition $\tau_{turb} \ll T \ll \tau_{org}$ is satisfied. In general case, the Reynolds rules for time averaging are not justified. The most questionable is commutation of the averaging operator with the time derivative: $\overline{\frac{\partial a}{\partial t}} = \frac{\partial \bar{a}}{\partial t}$. It is easy to check that $\overline{\frac{\partial a}{\partial t}} = \frac{\partial \bar{a}}{\partial t} + O\left(\frac{a'}{T}\right)$ (Wilcox 1998). But $\frac{\partial \bar{a}}{\partial t} = O\left(\frac{\Delta \bar{a}}{\tau_{org}}\right)$, where $\Delta \bar{a}$ is characteristic scale of the mean flow variation. Consequently, the addition $O\left(\frac{a'}{T}\right)$ may be neglected only at condition $\left|\frac{a'}{\Delta \bar{a}}\right| \ll \frac{T}{\tau_{org}}$. Taking into account $\frac{T}{\tau_{org}} \ll 1$, one may conclude that turbulent fluctuations should be at least two orders of value less than variations of mean turbulent flow. This condition is often violated in practice. Therefore, the approach based on the Reynolds time averaging (with the rules (20.15)) is accurate only for stationary-in-the-average turbulent flows ($\tau_{org} = \infty$). Nevertheless, Eqs. (20.14) and (20.15) are often used formally to obtain unsteady RANS (URANS) equations for primitive variables depending on time, $\bar{a}(\mathbf{x}, t)$. The above physical considerations show that the results obtained with the use of URANS have to be taken with caution. It should be stressed that URANS equations can be obtained directly using ensemble averaging (Poinsot and Veynante 2005; Wilcox 1998).

Usually, RANS is referred to the stationary in mean turbulent flows. Numerical solution of RANS equations may be obtained as a stationary limit of URANS equations solution, but this approach usually requires too large computation time and increases computational cost (numerical methods for URANS need an accurate approximation of unsteady terms). Instead, various methods of acceleration of time-marching procedure are used. Therefore, RANS numerical methods exploit the fact that a transient process of URANS solution has no physical sense, and the convergence to the stationary state may be accelerated and controlled by the numerical means (it is assumed that stationary solution is unique; multiple steady-state solutions are possible also, and arise in CFD practice).

As shown below the application of averaging to NSE results in arising unknown terms that contain double and triple correlations of fluctuations (e.g., $\overline{u_i' u_j'}$, $\overline{u_i' u_j' u_k'}$, etc.). Therefore, the closure problems of URANS/RANS equations arise: these correlations should be expressed through the characteristics of the mean flow. There are various ways of closure, but all of them are necessary based on empirical information (in particular, include empirical constants) and on some a priori physical assumptions about properties of turbulence. These closure methods are known as semi-empirical models of turbulence. These models can be based on the algebraic relations or can add partial differential equations to the system.

Reynolds approach has one essential and irremovable drawback: it uses averaging over the entire range of turbulent motions. However, it is quite obvious that large-scale turbulence is determined by the geometry and structure of the mean flow and therefore can not in principle be described in a universal manner. Since large-scale turbulence, which can not be described universally, is included in the averaging range, the constants (and sometimes the structure) of the semi-empirical model must vary from one flow to another. Thus, it is in principle impossible to

construct a universal semi-empirical model of turbulence. All currently known RANS-models of turbulence cannot describe the entire range of experimental data and require reconfiguration when considering new classes of tasks (see, e.g., (Troshin 2017)).

20.3.2 *Spatially Filtered Navier–Stokes Equations. LES Approach*

Search of ways for "more universal" description of turbulence had resulted in the formulation of approach that occupies an intermediate position between DNS and URANS/RANS approaches. This method, called LES (Large-Eddy Simulation), had been developed in works by Smagorinsky (1963), Lilly (Lilly 1967), Deardorf (1970, 1973) and others (e.g., the textbooks and reviews (Sagaut 2006; Garnier et al. 2009; Meyers et al. 2008; Rodi et al. 2013; Meneveau and Katz 2000; Pitsch 2006) and references therein). LES is based on the Kolmogorov's theory of the "universal equilibrium interval" at large Reynolds numbers $Re = u' L/\nu$ (Kolmogorov 1941) (see also (Poinsot and Veynante 2005)), where u' stands for the root mean square (rms) of velocity fluctuations and L is the integral length scale of turbulence (that is smaller than the characteristic linear scale of the global flow). Kolmogorov assumed that the statistical characteristics of vortices, whose length scales r are much smaller than L, are determined by the turbulent kinetic energy dissipation rate $\bar{\varepsilon}$, and by the kinematic viscosity ν. The turbulent kinetic energy dissipation rate ε is defined by the expression $\rho\varepsilon = \tau_{ij}\frac{\partial u_i}{\partial x_j}$. Strictly speaking, the definition of ε uses the velocity flctuations, but at large Reynolds numbers the input to ε from the mean velocities is negligibly small. The characteristic time scales of vortices from universal equilibrium interval are much shorter than the turbulence integral time scale $T_L = L/u'$. In LES, the turbulent large scales are explicitly calculated whereas the effects of smaller ones are modeled using subgrid closure models, discussed in the Sect. 20.4.2. Therefore, one may expect that LES is more accurate and reliable that URANS.

The existence of the universal equilibrium interval is confirmed by experiments. For example, in Fig. 20.6 the TKE spectra measured in experiments for a number of classical flows (Chapman 1979) are shown. The spectra are represented in the Kolmogorov's variables, i.e., $E(k) = \mathrm{v}_K^2 k_K^{-1} f(k/k_K)$, where k denotes wave number, $k_K = 2\pi/\eta_K$ is the Kolmogorov wave number, $\mathrm{v}_K = (\nu\bar{\varepsilon})^{1/4}$ is the Kolmogorov velocity scale (Kolmogorov 1941), $f(x)$ is a dimensionless function. It can be seen that the spectra of all turbulent flows for sufficiently large wave numbers k (i.e., for sufficiently small length scales, related with wave numbers k by expression $r \approx 2\pi/k$) are grouped with a small dispersion around one curve. At least for $r \leq 100\eta_K$ all spectra almost coincide.

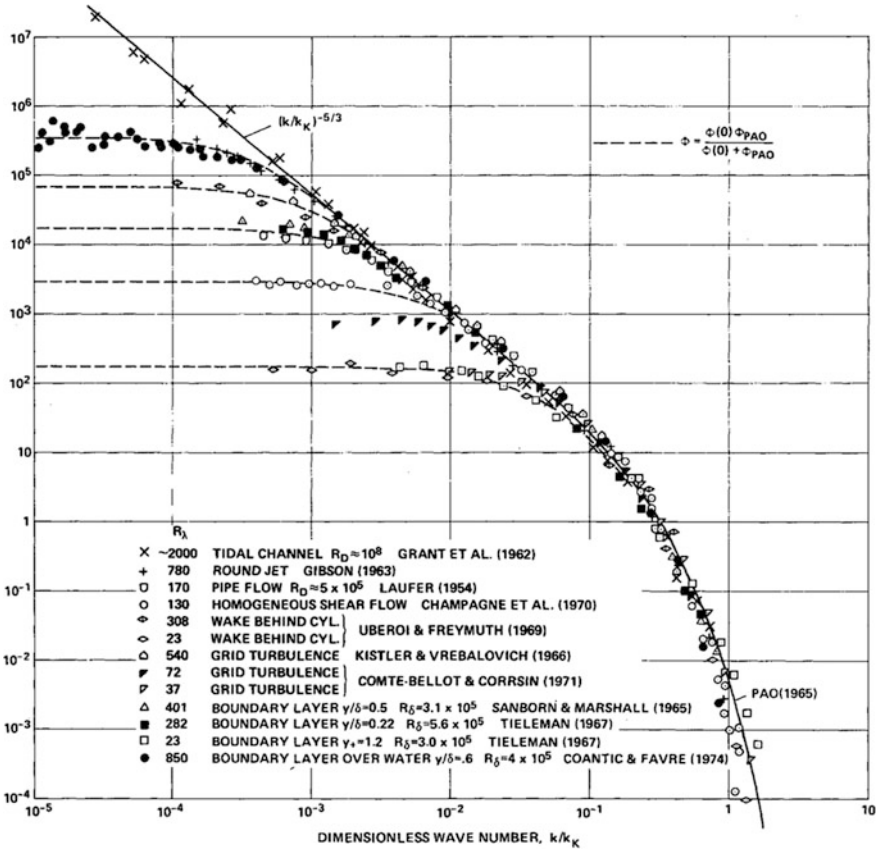

Fig. 20.6 Spectra of turbulence kinetic energy for various flows (Chapman 1979)

The idea of the LES methods is to average the turbulent flow not in time, as in RANS, but in space, by filtering out only small-scale fluctuations in the universal equilibrium range:

$$\bar{a}(\mathbf{x},t) = \int a(\mathbf{x}',t)\, G(\mathbf{x}',\mathbf{x},\Delta)\, d\mathbf{x}', \tag{20.16}$$

where $G(\mathbf{x}',\mathbf{x},\Delta)$ is spatial filter, Δ stands for the linear scale of the filter, which determines the scale of pulsations that will be filtered out. Usually, spatially symmetric filters are considered that have the form $G(\mathbf{x}',\mathbf{x},\Delta) = G(\delta x,\Delta)$, $\delta x = |\mathbf{x}' - \mathbf{x}|$. The linear scale of the filter Δ, theoretically, must be chosen in such a manner that Δ falls within the Kolmogorov inertial interval (subinterval of universal equilibrium interval), $L \gg \Delta \gg \eta_K$. Different types of spatial filters may be considered: box filters, Gaussian filters, Pade filters,

e.g., (Vasilyev and Lund 1997). The most widely used are box filters in physical and Fourier spaces, which have the following form in 1D case:

$$G(\delta x, \Delta) = \begin{cases} 1/\Delta, & \delta x \le \Delta/2, \\ 0, & \delta x > \Delta/2, \end{cases}, \tag{20.17}$$

$$G(\delta x, \Delta) = \frac{1}{\delta x}\sin\left(\pi\frac{\delta x}{\Delta}\right) = \int \Gamma(k)\cos(k\cdot\delta x)\,dk, \quad \Gamma(k) = \begin{cases} 1, & k \le \pi/\Delta, \\ 0, & k > \pi/\Delta. \end{cases}. \tag{20.18}$$

It is important to note that properties of spatial filtering (20.16) differ from properties of Reynolds averaging (20.15). For example, if the box filter (20.17) is used, in 1D case it is easy to show using Taylor series that

$$\begin{aligned} &\bar{\bar{a}} \approx \bar{a} + \frac{\Delta^2}{24}\overline{\frac{\partial^2 a}{\partial(\delta x)^2}}, \quad \overline{a'} \approx -\frac{\Delta^2}{24}\overline{\frac{\partial^2 a}{\partial(\delta x)^2}}, \\ &\overline{\bar{a}b} \approx \overline{\bar{a}}\,\overline{\bar{b}} + \frac{\Delta^2}{12}\left\{\frac{1}{2}\overline{\frac{\partial^2 a}{\partial(\delta x)^2}} + \overline{\frac{\partial a}{\partial(\delta x)}\frac{\partial b}{\partial(\delta x)}}\right\}, \\ &\overline{\frac{\partial a}{\partial x}} \approx \frac{\partial \bar{a}}{\partial x} - \overline{\frac{\partial^2 a}{\partial(\delta x)^2}}\cdot\frac{\Delta}{12}\frac{\partial\Delta}{\partial x}, \quad \overline{\frac{\partial a}{\partial t}} = \frac{\partial \bar{a}}{\partial t}. \end{aligned} \tag{20.19}$$

The general case of the nonuniform filter scale $\Delta \neq const$ are considered in (Vasilyev and Lund 1997; Ghosal and Moin 1995).

In the case of spatial filtration, eddies larger than the linear scale of the filter are reproduced directly in the calculation, and the contribution of small (subgrid-scale, SGS) eddies, whose size is smaller than the filter scale, is taken into account with the help of additional terms in the system of equations. These terms are approximated by semi-empirical models, which are very analogous to semi-empirical turbulence models in the RANS approach.

As Fig. 20.6 shows, grids for LES can be 100 times less detailed for each spatial direction than grids for DNS. This gives a savings of 10^6 times the number of cells compared to DNS. Thus, the LES method takes an intermediate place between DNS and RANS.

20.3.3 RANS, URANS, and LES for Compressible Reacting Flows

For high-speed reacting flows it is necessary to take into account the density fluctuations and other compressibility effects in turbulent flow (Friedrich 1993). In such tasks, the Reynolds averaging (20.14) or spatial filtration (20.17) results in too cumbersome equation system, with essential difficulties in closure. More effective

approach had been proposed by Favre (Favre 1965) (see also (Poinsot and Veynante 2005)): all primitive variables are decomposed into mean/resolved and fluctuation/unresolved (subgrid) components applying averaging (20.14) or spatial filter (20.16) such that $f = \tilde{f} + f''$, where $\tilde{f} = \overline{\rho f}/\bar{\rho}$ is the Favre (or density) mean/filtered variable.

Time-averaging/filtering the instantaneous NSE (20.5a–20.5e) leads to the equations, formally similar to the RANS equations

$$\frac{\partial \bar{\rho}}{\partial t} + \frac{\partial \bar{\rho}\tilde{u}_i}{\partial x_i} = 0, \tag{20.20a}$$

$$\frac{\partial \bar{\rho}\tilde{u}_i}{\partial t} + \frac{\partial\left(\bar{\rho}\tilde{u}_i\tilde{u}_j + \bar{p}\delta_{ij} - \bar{\tau}_{ij} + \overline{\tau_{ij}^t}\right)}{\partial x_j} = 0, \tag{20.20b}$$

$$\frac{\partial \bar{\rho}\tilde{e}_t}{\partial t} + \frac{\partial\left(\bar{\rho}\tilde{u}_i\tilde{e}_t + \overline{pu_i} - \overline{\tau_{ij}u_j} + \bar{q}_i + \overline{q_i^t} + \overline{q_{i,TKE}^t}\right)}{\partial x_i} = 0, \tag{20.20c}$$

$$\frac{\partial \bar{\rho}\widetilde{Y}_k}{\partial t} + \frac{\partial\left(\bar{\rho}\tilde{u}_i\widetilde{Y}_k + \bar{J}_{k,i} + \overline{j_{k,i}^t}\right)}{\partial x_i} = \bar{\dot{w}}_k, \tag{20.20d}$$

where

$$\bar{q}_i = -\kappa\overline{\frac{\partial T}{\partial x_i}} + \sum_{k=1}^{N}\overline{h_k j_{k,i}} = -\kappa\overline{\frac{\partial T}{\partial x_i}} - \sum_{k=1}^{N}\overline{\rho h_k D_k \frac{\partial Y_k}{\partial x_i}},\ \bar{J}_{k,i} = \overline{-\rho D_k \frac{\partial Y_k}{\partial x_i}}.$$

Averaged/filtered equation of state (20.4) contains additional term depending on the turbulent fluctuations, the correlation $(\widetilde{TY_k} - \widetilde{T}\widetilde{Y}_k)$

$$\bar{p} = \bar{\rho}R_0\widetilde{T}\sum_{k=1}^{N}\frac{\widetilde{Y}_k}{W_k} + \bar{\rho}R_0\sum_{k=1}^{N}\frac{1}{W_k}(\widetilde{TY_k} - \widetilde{T}\widetilde{Y}_k). \tag{20.21}$$

Unclosed filtered viscous tensor $\bar{\tau}_{ji}$, molecular fluxes $\bar{q}_i$ and $\bar{J}_{k,i}$ may be either neglected or modeled using mean parameters of gas substituted into Eqs. (20.9a)–(20.9c), i.e., $\mu \approx \mu(\widetilde{T})$, $D_i \approx D_i(\widetilde{T})$, $\kappa \approx \kappa(\widetilde{T})$. The unclosed turbulent fluxes of momentum $\overline{\tau_{ji}^t}$, energy $\overline{q_i^t}$ and species $\overline{j_{i,k}^t}$ are given by (see details in (Poinsot and Veynante 2005; Garnier et al. 2009; Pitsch 2006))

$$\overline{\tau_{ji}^t} = \overline{\rho u_j u_i} - \bar{\rho}\tilde{u}_j\tilde{u}_i = \bar{\rho}(\widetilde{u_i u_j} - \tilde{u}_i\tilde{u}_j), \tag{20.22}$$

$$\overline{q_i^t} = \bar{\rho}(\widetilde{h u_i} - \tilde{h}\,\tilde{u}_i), \tag{20.23}$$

$$\overline{j_{k,i}^t} = \bar{\rho}(\widetilde{Y_k u_i} - \tilde{Y}_k \tilde{u}_i), \quad \sum_{k=1}^{N} \overline{j_{k,i}^t} = 0, \tag{20.24}$$

and have to be modeled. Unclosed term $\overline{q_{i,TKE}^t}$ in energy Eq. (20.20c) contains the triple correlations and describes the turbulent diffusion of averaged/unresolved turbulent kinetic energy (TKE) $\tilde{k} = 0.5\,(\widetilde{u_j u_j} - \tilde{u}_j \tilde{u}_j)$. Usually $\overline{q_{i,TKE}^t}$ is neglected in comparison with other terms in the energy flux. Mean total energy $\tilde{e}_t$ contains TKE and the correlations $\widetilde{Y_k h_k} - \tilde{Y}_k \tilde{h}_k$:

$$\tilde{e}_t = \sum_{k=1}^{N} \tilde{Y}_k \tilde{h}_k + \sum_{k=1}^{N} (\widetilde{Y_k h_k} - \tilde{Y}_k \tilde{h}_k) - \frac{\bar{p}}{\bar{\rho}} + \frac{\tilde{u}_j \tilde{u}_j}{2} + \tilde{k}. \tag{20.25}$$

The turbulent fluxes (20.22)–(20.24), as well as TKE, can be represented as follows:

$$\widetilde{a\,u_i} - \tilde{a}\,\tilde{u}_i = \underbrace{(\widetilde{\tilde{a}\,\tilde{u}_i} - \tilde{a}\,\tilde{u}_i)}_{\text{Leonard flux}} + \underbrace{(\widetilde{a''\tilde{u}_i} + \widetilde{\tilde{a}\,u_i''})}_{\text{cross flux}} + \underbrace{\widetilde{a''u_i''}}_{\text{flux due to filtered motions}} \tag{20.26}$$

In the case of time averaging in URANS/RANS approach, Leonard flux, and cross flux are equal to zero. In LES approach, Leonard flux has value $O(\Delta^2)$ and cannot be neglected, but it can be calculated directly (e.g., (Poinsot and Veynante 2005; Garnier et al. 2009; Pitsch 2006)). Cross flux is equal to zero, if the box filter in physical space is applied. The rest term in (20.26) represents the contribution of turbulent motions that where filtered out. In URANS/RANS, this is total turbulent diffusive flux of physical parameter a (flux of jth momentum component, if $a = u_j$; flux of heat energy, if $a = h$; flux of mass of kth species, if $a = Y_k$). In the case of LES approach, $\widetilde{a'' u_i''}$ is flux due to subgrid-scale (SGS) eddies.

To close the Eqs. (20.20a–20.20d), the turbulent fluxes $\widetilde{u_i'' u_j''}$, $\widetilde{h'' u_j''}$, $\widetilde{Y_k'' u_j''}$, the correlations $\widetilde{Y_k'' h_k''}$ and $\widetilde{T'' Y_k''}$ and the averaged/filtered chemical source term $\bar{\dot{w}}_k$ must be modeled (through averaged/filtered quantities $\bar{\rho}$, $\tilde{u}_i$, $\widetilde{T}$, and $\widetilde{Y}_k$). Methods of closure will be considered in the next section (with an accent on high-speed propulsion systems).

20.4 The Closure Problems

20.4.1 URANS/RANS Closure Models for Turbulent Fluxes

Let us compare different classes of semi-empirical turbulence models for closing the URANS/RANS equations from the viewpoint of their applicability for describing

the flows in scramjets. Algebraic models (that use only algebraic relations to close the system of RANS equations, e.g., models (Prandtl 1925, 1942; Escudier 1965; Smith and Cebeci 1967; Baldwin and Lomax 1978)) are unsuitable for these goals, because they designed for a simple flow structure, require fine tuning for each class of flows, and do not take into account the dynamics of flow development. Differential turbulence models (which include one or more additional partial differential equations for describing the variation of various turbulence parameters in the flowfield) can be divided into two groups: models based on the Boussinesq hypothesis (the most well-known are described in (Jones and Launder 1972; Launder and Sharma 1974; Wilcox 1988; Menter 1994; Vieser et al. 2002; Langtry and Menter 2009; Spalart and Allmaras 1992; Allmaras and Johnson 2012)) and non-Boussinesq models (for example, (Launder et al. 1975; Speziale et al. 1991; Cécora et al. 2012; Rodi 1976; Menter et al. 2012)). Non-Boussinesq models potentially have the ability to describe fine details of the mean flow structure in rapidly developing flows with large parameter gradients. However, the non-Boussinesq models are more cumbersome, contain a large number of tuning constants and change noticeably the mathematical properties of the equations system being solved (for example, the diffusion terms with second derivatives disappear from the momentum equations, additional solution areas appear in the solution of the Riemann problem, e.g., (Nasr et al. 2009) and references therein.). Under conditions of multiscale flow with non-equilibrium chemical reactions (that leads to essentially nonlinear effects), the speed of computation, the simplicity and stability of the algorithm are more priority. From this viewpoint, nowadays the more safe choice for scramjet applications is the use of models based on the Boussinesq hypothesis.

This hypothesis postulates a similarity between the chaotic turbulent motion of gas volumes and the chaotic thermal motion of molecules. It implies the assumption that turbulent pulsations have the same properties as the thermal motion of molecules. Consequently, the Boussinesq hypothesis implicitly assumes that, as in the case of thermal motion of molecules, turbulent pulsations are small in comparison with the parameters of the mean flow, and that chaotic displacements of gas volumes are isotropically distributed along directions (which leads to the independence of the turbulent transport coefficients from the direction). The hypothesis of the smallness of turbulent pulsations makes it possible to neglect triple correlations of pulsations in comparison with the double correlations (and, consequently, to drop the flux $\overline{q^t_{i,\,TKE}}$ in the energy Eq. (20.20c)), and, in some cases, to neglect double correlations of pulsations in comparison with products of average values. In particular, the terms $\left(\widetilde{TY_k} - \widetilde{T}\widetilde{Y}_k\right)$ in the equation of state (20.21) are often dropped, i.e., it is assumed that $\bar{p} \approx \bar{\rho} R_0 \widetilde{T} \sum\limits_{k=1}^{N} \widetilde{Y}_k / W_k$.

It follows from the Boussinesq hypothesis that the functional structure of the closing relations for turbulent fluxes, Eqs. (20.21)–(20.23) should coincide with the structure of analogous expressions for molecular fluxes, Eqs. (20.9a)–(20.9c), with the replacement of the molecular transport coefficients by the turbulent transport coefficients:

$$\bar{\rho}\widetilde{u_i^{''}u_j^{''}} \approx \frac{2}{3}\bar{\rho}\tilde{k}\delta_{ij} - \mu_t\left(\frac{\partial\tilde{u}_j}{\partial x_i} + \frac{\partial\tilde{u}_i}{\partial x_j} - \frac{2}{3}\frac{\partial\tilde{u}_k}{\partial x_k}\cdot\delta_{ij}\right), \tag{20.27}$$

$$\bar{\rho}\widetilde{u_j^{''}h^{''}} \approx -\frac{\mu_t}{Pr_t}\frac{\widetilde{C}_p}{}\frac{\partial\widetilde{T}}{\partial x_i}, \tag{20.28}$$

$$\bar{\rho}\widetilde{u_j^{''}Y_k^{''}} \approx -\frac{\mu_t}{Sc_t}\frac{\partial\widetilde{Y}_k}{\partial x_i}, \tag{20.29}$$

where the coefficient of turbulent viscosity $\mu_t = \bar{\rho}\nu_t$ (ν_t stands for the kinematic turbulent viscosity) and the empirical constants (the turbulent Prandtl and Schmidt numbers, Pr_t and Sc_t) are introduced. The term $\frac{2}{3}\bar{\rho}\tilde{k}\delta_{ij}$ is sometimes called "turbulent pressure".

Just as the molecular viscosity in the molecular-kinetic theory is represented by the product of the mean free path of gas molecules and square root of mean molecule kinetic energy, one may assume that the turbulent viscosity should be expressed as $\mu_t \approx \bar{\rho}u^{'}l_{mix}$, where l_{mix} is the famous Prandtl "mixing length" (Prandtl 1925, 1942). Prandtl interpreted mixing length l_{mix} as the averaged length that the gas "mole" travels relative to the average flow until it loses its individuality as a result of mixing with the surrounding gas. It is natural to use $\sqrt{\tilde{k}}$ as an estimate of $u^{'}$. The nonclosed equation for TKE $\tilde{k}$ can be derived from the NSE (20.5b). For incompressible flow it reads, e.g., (Wilcox 1998):

$$\frac{\partial\bar{\rho}\tilde{k}}{\partial t} + \frac{\partial}{\partial x_i}\left[\bar{\rho}\,\tilde{k}\,\tilde{u}_i + \overline{p^{'}u_i^{''}} + \bar{\rho}\widetilde{k^{''}u_i^{''}} - \tilde{\mu}\frac{\partial\tilde{k}}{\partial x_i}\right] = \bar{\rho}\left(\widetilde{P} - \tilde{\varepsilon}_I\right), \tag{20.30}$$

where $k^{''} = u_i^{''}u_i^{''}/2$ is the instantaneous turbulent kinetic energy, $\widetilde{P} = \widetilde{u_i^{''}u_j^{''}}\frac{\partial\tilde{u}_i}{\partial x_j}$ is the rate of TKE production, and $\tilde{\varepsilon}_I = \frac{\tilde{\mu}}{\bar{\rho}}\widetilde{\frac{\partial u_i^{''}}{\partial x_j}\frac{\partial u_i^{''}}{\partial x_j}}$ is the rate of its dissipation in incompressible flow. The Favre averaging in the incompressible case coincides with Reynolds averaging and is kept here only for uniformity.

Kolmogorov (Kolmogorov 1942) was the first who developed a two-differential turbulence model (for incompressible flow). He closed Eq. (20.30) using the following closure relations for the turbulent flux $\overline{p^{'}u_i^{''}} + \bar{\rho}\widetilde{u_i^{''}k^{''}}$ and the dissipation of turbulent energy $\tilde{\varepsilon}_I$

$$\overline{p^{'}u_i^{''}} + \bar{\rho}\widetilde{u_i^{''}k^{''}} \approx -\frac{\mu_t}{Pr_t^k}\frac{\partial\tilde{k}}{\partial x_i}. \tag{20.31a}$$

$$\tilde{\varepsilon}_I \approx \omega\tilde{k},\ \omega \approx \sqrt{\tilde{k}}/L, \tag{20.31b}$$

where ω denotes the characteristic frequency of turbulence, for which he derived from NSE (20.5b) an additional differential equation. Then, using dimensional considerations $\mu_t \approx \bar{\rho}\sqrt{\tilde{k}}L \approx \bar{\rho}\tilde{k}/\omega$, yields (e.g., (Wilcox 1998)) for μ_t

$$\mu_t = C_\mu \bar{\rho}\frac{\tilde{k}^2}{\tilde{\varepsilon}_I}. \tag{20.32}$$

where C_μ is a model constant. Prandtl and Wieghardt (1947) used (independently of Kolmogorov) only Eq. (20.30) for TKE with closure (20.31a), as Kolmogorov did. The turbulence length scale was calculated by Prandtl from algebraic equation (e.g., for turbulent boundary layer the length scale is proportional to the distance from the wall).

It should be noted, that instead of the Kolmogorov ω-equation, one can consider directly the equation $\tilde{\varepsilon}_I$ (using the relation $\tilde{\varepsilon}_I \approx \omega\tilde{k}$). Thus, classes of semi-empirical turbulence models arise with two differential equations (for $\tilde{k}$ and for one more turbulence parameter)—classes k-ω (Wilcox 1988, 2008; Menter 1994; Vieser et al. 2002), k-ε (Jones and Launder 1972; Launder and Sharma 1974) and $k-L$ (Speziale 1987). Equation (20.32) also allows to derive the differential equation for the kinematic turbulent viscosity $\nu_t = \mu_t/\bar{\rho}$ from the equations $\tilde{k}$ and $\tilde{\varepsilon}_I$ (or from the equations for $\tilde{k}$ and ω). So, one more class of models with one differential equation for ν_t arises. This class includes the Secundov (Shur et al. 1995) and Spalart–Allmaras models (Spalart and Allmaras 1992; Allmaras and Johnson 2012). The Spalart–Allmaras model has gained wide popularity and has been applied to a wide range of tasks (including supersonic combustion (Karl et al. 2008)). However, a decrease in the number of differential equations reduces the number of the model degrees of freedom and leads to artificial modifications in the equation system (in particular, to the exclusion of TKE from formulas (20.24) and (20.27)).

Further development of semi-empirical turbulence models has shown that the parameter ω has certain advantages, since the asymptotic solution of quasi-equilibrium partial differential equation for ω demonstrates behavior close to the theoretical one in the vicinity of solid surfaces (Wilcox 1998). This allows to exclude nonuniversal near-wall modifications of the differential equation, which are introduced in the models of the class $k-\varepsilon$. Therefore, for the sake of brevity of presentation and simplicity, below only the models of the class $k-\omega$ will be considered. This, however, does not mean that the authors recommend this class of models as the optimal class for the solution of combustion problems.

To calibrate the models of turbulence (i.e., to determine the empirical constants of the model), experimental data, and DNS and LES calculations for classical flows (which fit into the paradigm of the Boussinesq hypothesis) are used. As a rule, the list of calibration tasks includes the decay of isotropic turbulence and various thin-layer flows (i.e., flows, where the parameters vary mainly in the plane perpendicular to the velocity vector): the equilibrium limit of the homogeneous shear

turbulence development, the logarithmic sublayer of the turbulent boundary layer, and others (Wilcox 1998; Johansson 2002).

Models of turbulence, based on equations like Eqs. (20.30)–(20.32), describe well the quasi-equilibrium thin-layer flows with a sufficiently weak turbulence. When describing flows that do not possess these properties, errors occur, which sometimes lead to an unstable development of the solution and to essentially nonphysical results. It is impossible to eliminate completely the errors within the framework of the Boussinesq hypothesis. But it is possible to moderate them, preventing their excessive growth and instability of the solution. For this purpose, additional corrections are introduced into the model. For example, in the Menter SST model (Menter 1994; Vieser et al. 2002), which belongs to the k-ω class, the restriction of the TKE production is introduced: in the equation for $\tilde{k}$ (20.30) P is replaced by $\min(P,\ 10\varepsilon_I)$. This helps to prevent an excessive nonphysical growth of the TKE in flow transition through the shock waves (which is important for the description of scramjet flows) and in the vicinity of the flow deceleration points.

By now, it is clear that within the framework of the Boussinesq hypothesis it is impossible to describe the near-wall turbulence and the free turbulence with the same set of constants. However, in ducts of air-breathing engines it is impossible to divide the flow into regions of the near-wall turbulence and the free turbulence. A possible solution of this problem is the use of blending functions $F(d_W)$ for a smooth interpolation between the sets of constants for wall turbulence and for free turbulence, depending upon the distance from the wall d_W. When $d_W \to 0$, $F(d_W) \to 1$; and when $d_W \to \infty$, $F(d_W) \to 0$. Then, the value of any empirical constant of the model can be determined by the formula $C = FC_1 + (1-F)C_2$, where C_1 is the value of the constant for a description of the near-wall flows, and C_2 is its value for free turbulence. This approach was first applied in the SST model (Menter 1994; Vieser et al. 2002), which is one of the most popular differential models of turbulence now. However, blending functions can also be implemented in other models—see, for example, (Babulin et al. 2016).

The equation for ω, which is used in the SST model, has the following form:

$$\frac{\partial \bar{\rho}\omega}{\partial t} + \frac{\partial}{\partial x_i}\left[\bar{\rho}\,\omega\,\tilde{u}_i - \left(\tilde{\mu} + \frac{\mu_t}{Pr_t^{\omega}}\right)\frac{\partial \tilde{k}}{\partial x_i}\right] = \bar{\rho}\,\frac{\omega}{\tilde{k}}\left(C_{\omega 1}\tilde{P} - C_{\omega 2}\tilde{k}\omega\right) + \min\left(10^{-10},\ CD\right), \tag{20.33}$$

where the term $CD = \frac{1-F}{Pr_{t2}^{\omega}}\frac{1}{\omega}\frac{\partial \omega}{\partial x_i}\frac{\partial \tilde{k}}{\partial x_i}$ is called "cross diffusion" and arises in derivation of the equation for ω from the equations for $\tilde{k}$ and for ε_I (Wilcox 1998). Cross-diffusion improves the quality of the model in description of the free turbulence. It should be noted that in Eq. (20.33) the hypothesis is used that the source terms are proportional to the production and dissipation of the TKE. This hypothesis is based on the assumption of a quasi-equilibrium state of turbulence.

The described above semi-empirical turbulence models are formulated for incompressible flows. Using crude assumptions about the isentropic nature of turbulent fluctuations and about the absence of the total enthalpy fluctuations (the so-called strong Reynolds analogy, e.g., (Smits and Dussauge 2006)), one can estimate the relative value of the density fluctuations: $\rho'/\bar{\rho} \sim \widetilde{M} \cdot M_t$, where $\widetilde{M} = \tilde{u}/\tilde{c}$ is the mean Mach number, and $M_t = \sqrt{2\tilde{k}}/\tilde{c}$ is the Mach number of turbulent fluctuations, c is the sound speed. From this relation, it is already easy to show that $\frac{\rho'/\bar{\rho}}{u'/\tilde{u}} = O\left(\widetilde{M}^2\right)$ and $\frac{\overline{\rho' u}}{\bar{\rho}\tilde{u}} = O\left(\widetilde{M}_t^2\right)$ (here u' denotes velocity fluctuations, but not velocity rms). Therefore, the relative magnitude of density fluctuations becomes closer to the magnitude of velocity fluctuations with an increase of the average Mach number (in free turbulence, e.g., in mixing layers and jets, the density fluctuations become noticeable at $\widetilde{M} \gtrsim 0.3$), and their contribution to the mean flow is determined by the turbulent Mach number M_t (in mixing layers it becomes essential when $M_t \gtrsim 0.2$). Therefore, in the description of the fuel injection into high-speed flow in a scramjet, the compressibility effects should be taken into account. In the boundary layers, the compressibility effects are less evident, since the turbulence production is concentrated mainly in the thin near-wall part of the boundary layer, where the average Mach number $\widetilde{M}$ is usually small. There is an opinion (Wilcox 1998) that in the non-separated boundary layers one can neglect the effects of compressibility up to external Mach number $\widetilde{M}_e = 5$. However, in separations of boundary layer (that are typical for flows in scramjet ducts), the mixing layer develops on the outer boundary of the separation zone around the streamline detached from the wall. This mixing layer determines the mass balance in the recirculation zone and, consequently, determines the size of this zone. In this free-turbulent flow the compressibility effects are significant.

The use of Favre averaging makes it possible to generalize semi-empirical turbulence models, developed for incompressible flows, to the case, when the compressibility effects are significant. Due to the fact that with Favre averaging the structure of turbulent flow equations does not change in comparison with an incompressible case, one can expect that turbulence models for compressible flows should have the same functional structure as models for incompressible flows. The compressibility effects can be taken into account by introducing corrections that depend on the turbulent Mach number M_t.

The most significant manifestation of compressibility effects is a decrease of the turbulent mixing efficiency. Numerous studies of high-speed mixing layers (Papamoschou and Roshko 1987; Goebel and Dutton 1990) show that the growth rate of the mixing layer depends on the so-called convective Mach number $M_{conv} = \frac{|\tilde{u}_1 - \tilde{u}_2|}{c_1 + c_2} \sim M_t$, where $\tilde{u}_1$, $\tilde{u}_2$ and c_1, c_2 stand for the mean velocities and sound speeds in the first and the second parallel flows, respectively. In the range $0.2 \lesssim M_{conv} \lesssim 1$, the mixing layer growth rate decreases monotonicaly 2.5–4 times (according to different experimental data), and after that it becomes constant. In the works of Zeman (1990) and Sarkar (1992, 1993) (see also (Lele 1994)), it was suggested that this effect is mainly associated with an increase of the TKE

dissipation rate in comparison with the incompressible flow. The increase of the dissipation can be taken into account in the TKE Eq. (20.30), for example, by replacing $\varepsilon_I \to (1+f(M_t))\cdot\varepsilon_I$, where

$$f(M_t) \approx \begin{cases} M_t^2, & M_t < 0.4, \\ 0.16, & M_t \geq 0.4 \end{cases}$$

However, there is an opinion that for large values of the turbulent Mach number, the decrease in the growth rate of turbulent mixing is caused not so much by the increase in the rate of TKE dissipation as by the increase in the turbulent stress tensor anisotropy, i.e., by its deviation from the formula (20.27) (Gomez and Girimaji 2013).

In flows with combustion, undoubtedly, additional effects appear that affect the behavior of turbulence. However, these effects have not yet been studied enough. For example, in the linear approximation (for small fluctuations) the pressure fluctuation can be represented as $p' = \rho' \frac{R_0}{W}\widetilde{T} + \bar{\rho}\frac{R_0}{W}T'' + \bar{\rho}R_0\widetilde{T}\sum_{k=1}^{N}\frac{Y_k''}{W_k}$. The standard model for the turbulent flux of TKE (20.31a and 20.31b) is based on the experimental data for cold air flows without essential variation of temperature and composition. Thus, in the model (20.31a and 20.31b) only the first component of pressure fluctuations are taken into account. In hot flows with chemical reactions, one can expect the appearance of the additional TKE fluxes associated with the work of pressure fluctuations due to temperature and concentration fluctuations. The additional term in the equation of state, Eq. (20.21) (containing $\widetilde{T''Y_k''}$) can also become significant. At the moment, there are no reliable models for describing such effects. Therefore, the turbulence model, which describes well the cold turbulent jet of air, can give noticeable errors in the description of a fuel jet with combustion. Some authors try to take this into account, changing the Prandtl and Schmidt turbulent numbers, Pr_t and Sc_t, e.g., (Shiryaeva et al. 2014; Shiryaeva and Anisimov 2015). Figure 20.7 shows the effect of these numbers on the cross-section profile of the near-wall jet of hydrogen in the classical experiment of Burrows and Kurkov (1973). According to the data of (Shiryaeva et al. 2014; Shiryaeva and Anisimov 2015), the influence of this effect may sometimes be more significant than the influence of turbulence on the average rates of chemical reactions. The methods for local determination of variable Prandtl and Schmidt numbers, based on the comparison of Boussinesq approximations for $\widetilde{h''^2}$ and $\widetilde{Y_k''^2}$ with the solution of partial differential equations for these quantities, are proposed in (Xiao et al. 2007; Molchanov 2011; Goldberg et al. 2011). Unfortunately, this is a rather cumbersome and expensive approach; moreover, it does not guarantee success in modeling real flows.

It should be added that the possibilities of turbulence modeling within the framework of the URANS/RANS approach are undoubtedly not exhausted. The semi-empirical models should be developed attracting deeper physical concepts for a well-founded description of various effects. A good example of such a model

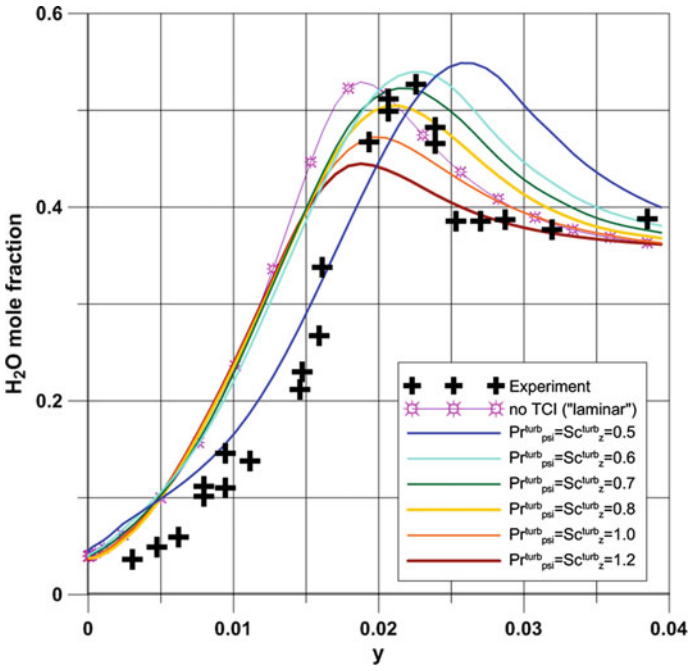

Fig. 20.7 Influence of Pr_t and Sc_t numbers on cross-section profile of the water vapor mass fraction (Shiryaeva and Anisimov 2015)

presents the work (Troshin 2017), where the new modifications of non-Boussinesq turbulence model are described. These modifications for the first time made it possible to describe the entire range of experimental data on classical turbulent mixing and jet layers.

20.4.2 LES Closure Models for Turbulent Fluxes

Despite the increased enthusiasm for the possibility of improving the quality of solving practical problems due to the transition from URANS/RANS to LES, the implementation of the LES method involves many difficulties, many of which have not yet been overcome. One of the main conditions for the correct operation of turbulent closures is the ability of the subgrid model to describe correctly the direct energy cascade from large eddies to small eddies (i.e., the transfer of the kinetic energy of resolved scales toward the subgrid scales). Because of turbulent chaos and due to loss of information about the geometry of the global flow, it can be hoped that small-scale velocity fluctuations are in the close-to-isotropy state. In this case, the average effect of the subgrid turbulence can be described by introducing an additional coefficient of the subgrid turbulent viscosity by analogy with the

molecular viscosity. Such subgrid-scale models (SGS models) constitute a wide class of turbulent closures for LES (a review of possible approaches and their mathematical justification can be found, for example, in (Berselli et al. 2006)). The simplest model of this class is the Smagorinsky model (Smagorinsky 1963), which is nothing but the classical Prandtl mixing length model, in which the mixing length is replaced by the grid spacing Δ:

$$\mu_t = C_S \bar{\rho}\, \Delta^2 \sqrt{2\widetilde{S}_{ij}\widetilde{S}_{ij}},\ \widetilde{S}_{ij} = \frac{1}{2}\left(\frac{\partial \tilde{u}_j}{\partial x_i} + \frac{\partial \tilde{u}_i}{\partial x_j} - \frac{2}{3}\frac{\partial \tilde{u}_k}{\partial x_k}\cdot \delta_{ij}\right) \tag{20.34}$$

where C_S is Smagorinsky's empirical constant, and $\widetilde{S}_{ij}$ is the space-filtered strain-rate tensor. Lilly (1967) had showed theoretically that the C_S value should be close to 0.18. However, this value had appeared to be overestimated, and it has to be adjusted during the transition from one class of flows to another. Usually, C_S is in the range 0.065 … 0.1.

One possible alternative is the dynamic SGS-models, first proposed by Ievlev (1990). In dynamic subgrid models of turbulence, it is assumed that the SGS model coefficients are invariant with respect to the linear scale of the spatial filter. In other words, it is assumed that the same subgrid model, without any change, can be used both for coarser and finer grid resolutions.

In the work by Ievlev (1990), for this purpose, it was proposed to perform a calculation on two grids. Germano (1991) had shown that, having a solution on a fine grid, one can obtain a solution on a coarse grid by means of an additional "test" spatial filtration and get an estimate of the turbulent stresses for it. Some part of these stresses, determining the interactions of the smoothed "test" velocity field with fluctuations of intermediate scale, can be calculated both explicitly and estimated using a subgrid model. Subsequently, the SGS model constants are chosen to provide a minimum difference between the turbulent stresses obtained explicitly on a fine grid and the turbulent stresses that the SGS model predicts for a coarser grid. Thus, the local instantaneous values of the SGS model constants are determined. The result is a subgrid model that does not require any experimental data for calibration.

Unfortunately, the system of equations for the SGS model constants is overdetermined, and the values of the constants have to be chosen to get a minimal deviation from the imposed conditions. There are also other bad properties of dynamic models: the equations for constants degenerate in some cases; the resulting values of constants demonstrate strong variation both in space and in time; negative values of the constants appear in places where it is physically impossible; and, as a consequence of the above deficiencies, the method can demonstrate an instable behavior. Despite the fact, that during last three decades many dynamic model variants have been proposed (e.g., (Singh and You 2013)), additional efforts are required to develop a reliable dynamic approach.

All SGS models unable to describe interactions leading to the local generation of the large eddies energy due to small-scale subgrid turbulence (the so-called reverse

energy cascade). This limits the grid spatial resolution from below: grid cells should fall within the inertial interval (i.e., $L \gg \Delta \gg \eta_K$), in which direct energy cascade prevails. However, in the turbulent boundary layers, as the wall is approached, the size of the largest vortices inevitably begins to decrease. The Reynolds number decreases, the range of scales is reduced, and, as a consequence, the inertial interval degenerates. The main generation of TKE occurs at scales comparable to the distance from the wall, and an inverse energy cascade appears locally. This phenomenon cannot be in principle described in terms of SGS models, where the subgrid turbulence performs purely dissipative functions.

Therefore, to simulate flows with boundary layers, the so-called hybrid RANS/LES approaches should be used. In this case, the near-wall region of the boundary layers is described by the RANS method, and the rest of the flow, where the grid resolution enters the inertial interval, is described by the LES method. The simplest version of this approach is the Balaras method (Piomelli and Balaras 2002), in which turbulent viscosity is calculated in two ways: according to the Prandtl model (Prandtl and Wieghardt 1947) and by the Smagorinsky formula. The final value of the turbulent viscosity is chosen as the smallest of these two values. Many other hybrid RANS/LES methods have been developed. The most popular now are the DES (Detached Eddy Simulation) method, proposed by Spalart with co-authors in (Spalart et al. 1997). In this method, a partial differential equation for turbulent viscosity is solved; in the near-wall regions it is converted to the equation of the Spalart–Allmaras RANS model, but far from the wall it describes the effects of subgrid turbulence. A survey of typical results of the DES method application is given in (Spalart 2009). In (Menter and Kuntz 2003), a variant of the DES method is described, that is based not on the differential equation for the kinematic turbulent viscosity ν_t, but on two-differential equations for the parameters $\tilde{k}$ and ω (far from the walls the parameter $\tilde{k}$ is treated as the subgrid TKE).

A feature of the LES method is that the contribution from the filtered small-scale turbulent motions is determined by the grid spacing Δ. In particular, Smagorinsky's formula shows that the subgrid viscosity has a value $O(\Delta^2)$. But the approximation errors of the used numerical method also depend on the grid spacing and can distort the description of the subgrid turbulence. In (Ghosal 1996) it was shown that the approximation errors of nonlinear terms in finite-difference schemes can significantly exceed the magnitude of the subgrid turbulent stresses. For finite-difference or finite-element schemes of the first accuracy order, these errors certainly exceed the contribution of subgrid turbulence, regardless of spatial resolution. In the case of second-order schemes, the contributions of the subgrid turbulence and of the approximation errors are comparable, and in order to eliminate distorting effects, it is necessary to carry out calculations on very detailed grids. Therefore, the natural choice for the LES method is the use of high accuracy schemes. It is worth to note that the second accuracy order schemes require placing 16–20 grid cells per the minimal resolved vortex size for an adequate description of turbulent eddies; the thirrd order schemes give the same result on grids containing 8–10 cells per the

vortex size; and the fourth order allow to take only 4–5 cells (Bosnyakov et al. 2015).

Recently, ILES (Implicit LES), developed in (Visbal and Rizzetta 2002; Visbal et al. 2003; Fureby and Grinstein 1999), has become very popular. The idea of the ILES method is that, under certain requirements, the dissipation of the numerical scheme used in the calculation can serve as a subgrid model of turbulence. In particular, the numerical viscosity of the secondnd accuracy order methods has the order of magnitude $O(\Delta^2)$, like the subgrid viscosity in the Smagorinsky model (20.34). Therefore, in principle it is possible to obtain an accurate description of the turbulent cascade without introducing a subgrid model of turbulence (i.e., solving NSE (20.5)) instead of LES Eqs. (20.20a–20.20d)). In an earlier version of this approach, called MILES (Monotonically Integrated LES), monotone schemes of the second order of accuracy were used (Fureby and Gri.nstein 1999). However, in (Visbal et al. 2003), instead of the subgrid model, the dissipative properties of schemes of a high order of accuracy were used. By now, many papers have appeared that report good results obtained by the ILES method in combination with schemes of high accuracy order—see, for example, (Lu and Liou 2010).

Nevertheless, the ILES method should be used with great care, because in real problems it is extremely difficult to predict the dissipative properties of the numerical method. Theoretical analysis of the ILES method (Grinstein et al. 2007; Grinstein and Fureby 2007) shows that even when high accuracy schemes are used, acceptable results are achieved only through the use of upwind flux corrections (that locally decreases the order of accuracy of the method). In (Lodato et al. 2013) it is reported that for high accuracy schemes, calculation by the conventional LES method in combination with a subgrid turbulence model gives a better prediction of turbulent stresses than ILES.

Computer resources, required by the LES method, even in tasks without combustion, are by 1–2 orders of magnitude larger than requirements of URANS/RANS methods. Since calculations of combustion require solving the system of stiff differential equations of chemical kinetics at each time step in each computational cell, the volume of computer resources increases significantly. Therefore, calculations of this class of flows require the use of supercomputers and always have a unique character, and it is unlikely that this situation would change radically in the foreseeable future. Although the first attempts to apply LES for modeling high-speed reactive flows date back to the end of the twentieth century (Thibaut and Candel 1998), the active use of LES to scramjet combustors started after 2000, e.g., (Berglund and Fureby 2007; Berglund et al. 2010; Fureby et al. 2011, 2015; Fulton et al. 2012; Laurence et al. 2013; Fureby 2008, 2012; Chapuis et al. 2013; ; Nordin-Bates et al. 2016; Moule et al. 2014a; Ingenito and Bruno 2009; Scherrer et al. 2016). It should be stressed that this list of the references is far from to be complete. Additional references can be found in the recent review (Gonzalez-Juez et al. 2017). The growth of supercomputer power, the development of parallel computing algorithms, the use of graphical processor units (GPU) had allowed to perform correct LES calculations on detailed grids for simulation of combustion in

high-speed chambers—see, e.g., (Berglund et al. 2010). LES study of the HyShot II combustor (Fureby et al. 2011; Fulton et al. 2012) produced a better agreement with experiment than 3D RANS equations, although some discrepancies remained. The LES method better reproduced the three-dimensional flow details, but was inferior to 3D RANS in describing the global effects of blockage of the flow by heat release (and, accordingly, in the prediction of the pressure distributions). It is obvious that in the coming decades the URANS/RANS and LES methods will coexist with each other in the calculations of the scramjet flows; LES data will be used to calibrate the URANS/RANS models, and LES calculations will be used to verify and refine the results obtained with the URANS/RANS approach.

20.4.3 Closure Problems for Reaction Rates

A particular attention must be paid developing the models for the averaged/filtered reaction rates $\bar{\dot{w}}_k$, Eq. (20.20d). According to relation (20.11), $\bar{\dot{w}}_k = W_k \sum_{l=1}^{M} \nu_{kl} \bar{\dot{\omega}}_l$, the problem reduces to modeling averaged/filtered rate of progress of reaction $\bar{\dot{\omega}}_l$. The rate of progress of reaction rate is given by Arrhenius law, which is a higly nonlinear exponential function of the temperature. The shocks and rarefactions waves in the high-speed supersonic flow result in the higher intensity temperature fluctuations compared to subsonic flames (e.g., (Jarrett et al. 1988)). Therefore, modeling finite-rate-chemistry effects in supersonic reactive flows needs a careful consideration of coupling chemistry and gasdynamics.

To illustrate the difficulties of averaging/filtering $\dot{\omega}$, let us consider (following (Poinsot and Veynante 2005)) a simple global irreversible reaction between fuel (F) and oxidizer (O) of the form:

$$F + sO \rightarrow (1+s)P. \tag{20.35}$$

It is assumed that the fuel mass reaction rate $\bar{\dot{w}}_F$ is given by (we remind, that for global reactions the reaction species exponents are not necessarily equal to the molar stoichiometric coefficients)

$$\dot{w}_F = -A_F \rho^2 Y_F Y_O \exp(-T_a/T). \tag{20.36}$$

Direct averaging/filtering (20.36) can not be done without knowledge of the joint probability density function of Y_F, Y_O, T and ρ, since the reaction rate is highly nonlinear function of the temperature. To see the difficulties modeling the averaged/filtered reaction rate $\bar{\dot{w}}_F$, let us expand the function $\exp(-T_a/T)$ as a Taylor series of the temperature fluctuation T'', assuming that the fluctuations T'' are small in comparison with the mean value $\widetilde{T}$. Dropping the details, that can be found in

(Poinsot and Veynante 2005), we present here the final result for the averaged/filtered reaction rate $\bar{\dot{w}}_F$ up to the second moments:

$$\bar{\dot{w}}_F = -A_F \bar{\rho}^2 \widetilde{T}^{\beta_F} \widetilde{Y}_F \widetilde{Y}_O \exp\left(-\frac{T_a}{T}\right) \times \left[1 + \frac{\widetilde{Y_F'' Y_O''}}{\widetilde{Y}_F \widetilde{Y}_O} + (P_1 + Q_1)\left(\frac{\widetilde{Y_F'' T''}}{\widetilde{Y}_F \widetilde{T}} + \frac{\widetilde{Y_O'' T''}}{\widetilde{Y}_O \widetilde{T}}\right) + (P_2 + Q_2 + P_1 Q_1)\frac{\widetilde{T''^2}}{\widetilde{T}^2} + \ldots\right]. \tag{20.37}$$

where

$$P_1 = \frac{T_a}{\widetilde{T}},\ Q_1 = \beta_F,\ P_2 = -\frac{T_a}{\widetilde{T}} + \left(\frac{T_a}{\widetilde{T}}\right)^2,\ Q_2 = \frac{(\beta_F - 1)(\beta_F - 2)}{2} \tag{20.38}$$

Equation (20.37) contains the following second moments: $\widetilde{Y_F'' Y_O''}$, $\widetilde{Y_F'' T''}$, $\widetilde{Y_O'' T''}$ and $\widetilde{T''^2}$. It should be stressed that usefulness of the Eq. (20.37) is limited by the fact that the coefficients P_1 and P_2 in (20.38) include the ratio of the activation temperature to the mean temperature, $T_a/\widetilde{T}$. This ratio is of order 10 for typical exothermic combustion reactions (Poinsot and Veynante 2005). Therefore, the Taylor series of the function $\exp(-T_a/T)$ diverges and (20.37) is not applicable.

This way of taking TCI into account is called the method of moments (Poinsot and Veynante 2005; Libby and Williams 1980). The simplest closure method consists in neglecting the dimensionless terms with the second moments in comparison with unity in brackets. This method is usually referred as the quasi-laminar approximation or no-model approach (see, e.g., (Annamalai and Puri 2006; Poinsot and Veynante 2005)). The turbulence-combustion interaction (TCI) is neglected in such an approach. The quasi-laminar approximation may be used for the practical cases where turbulent fluctuations of temperature and species are small. This may be realized in the high-speed reacting flows when chemical times are not negligible compared to flow times.

For these reasons, closure models for the reaction rates in turbulent combustion are not based on the Eqs. (20.37) and (20.38) but are derived from physical analysis of the instantaneous flame structure in turbulent flows. In other words, TCI models require take into account the processes that occur not only at the level of energy-containing eddies, but also at the Kolmogorov scale length η_K, e.g., (Poinsot and Veynante 2005; Kuznetsov and Sabelnikov 1990). The next section is devoted to the consideration of TCI models of this multiscale type.

Concluding this subsection let us give a list (not exhaustive) of TCI models, used in the context of RANS and LES (see also the recent review paper (Gonzalez-Juez et al. 2017)):

1. Flamelet progress variable (FPV) models, including G-equation, (Wang and Bai 2005), and flame surface density, (Hawkes and Cant 2000; Knikker and Veynante 2000), models, which are derived assuming that the reactions proceed in

the wrinkled by the turbulence flamelets (thin layers), separating the reactants from the products;
2. Probability density function models (PDF), (Givi), in which presumed PDFs or transported PDFs of species and temperature are used to calculate the averaged/filtered reaction rates;
3. Finite-rate chemistry (FRC) models, such as the Thickened Flame Model (TFM), (Charlette et al. 2002), Partially Stirred Reactor (PaSR) model, (Berglund et al. 2010; Fureby et al. 2015; Moule et al. 2014a; Ingenito and Bruno 2009), the Eddy Dissipation Concept (EDC) model, (Magnussen 1981), in which different mathematical and/or phenomenological models describing the turbulence-chemistry interactions are constructed;
4. Conditional moment closure (CMC) models, (Bilger 1993), in which the species equations are conditionally averaged on a one/few variables, neglecting by the species and temperature fluctuations with respect to the conditional species concentrations and temperature in the averaged/filtered reaction rates;
5. Linear Eddy (LEM) (Sankaran and Menon 2005) and one-dimensional turbulence (ODT) models (Kerstein 2009; Echekki et al. 2011) (LEM), using a grid-within-the-grid approach to solve 1D species equations with full resolution.

It is worth noting that the literature on TCI models is vast. In this regard, we refer the readers to a recent review (Gonzalez-Juez et al. 2017), which deals with the high-speed combustion. This review contains the results of a study of the comparisons between TCI models. It should be noticed, that the content of the review (Gonzalez-Juez et al. 2017) is limited by the analysis of the application of flamelets, TPDF and LEM models to high-speed-combustion problems.

20.5 LES-Transported PaSR Model: Multiphase Approach

20.5.1 Basic Physical Hypothesis of EDC, PaSR, and TPaSR Models

The EDC, PaSR and transported PaSR (TPaSR) models for simulation of turbulent combustion are applicable for high Reynolds $Re = u' L/\nu$ and moderate Damköhler $Da = T_L/\tau_c$ numbers, where τ_c denotes the characteristic chemical time scales. This regime of combustion is often observed in real combustion applications such as aero and power generation gas turbines, ramjet and scramjet engines, jet engines, and large-scale furnaces. The application of the EDC, PaSR, and TPaSR models for lower Re numbers, when combustion proceeds in the flamelet regime, is not straightforward.

The spatiotemporal distributions of velocity and scalar gradients have a profound impact on the spatiotemporal topology of the chemical reaction regions in turbulent flows, e.g., (Kuznetsov and Sabelnikov 1990). Batchelor and Townsend (1949),

studied experimentally local structure of the turbulent flow behind a grid (in non-reactive flow) and discovered that the turbulent fine structures, containing the most intensive velocity spatial derivatives (and, as consequence, most intensive molecular fluxes) are not uniformly distributed but concentrated in small isolated regions, whose volume is a small fraction of the total volume. The further experimental studies confirmed the results obtained in (Batchelor and Townsend 1949), and established that the intermittency increases with increasing *Re* number, e.g., (Kuznetsov and Sabelnikov 1990). Kuo and Corrsin, (1971), concluded from the experimental observations that the fine-structure regions consist of topological structures, such as vortex sheets, ribbons, and tubes folded in specific regions of the flow. More recently, DNS, e.g., (Woodward et al. 2001; Tanahashi et al. 2000; Tanahashi et al. 2008), provided support to this view, revealing how high-intensity vortices merge in complex shaped filaments that are embedded into sheets or arcs of low(er) intensity vorticity. The strong intermittent character of the local turbulence structure is dissimilar from the Kolmogorov (Kolmogorov 1941) (K41) turbulence theory, (Kolmogorov 1941; Kuznetsov and Sabelnikov 1990; Monin and Yaglom 1971; Tennekes and Lumley1972; Frisch 1995), in which the fine structures, and related quantities like dissipation, are distributed quasi-uniformly. The statistics of the fine structures in the K41 theory is determined only by the Kolmogorov length, $\eta_K = (\nu^3/\bar{\varepsilon})^{1/4}$, time $\tau_K = (\nu/\bar{\varepsilon})^{1/2}$ and velocity $\mathrm{v}_K = (\nu\bar{\varepsilon})^{1/4}$ scales, respectively, where ν denotes the molecular viscosity and $\bar{\varepsilon} \approx u^{'3}/L$ the mean dissipation.

A modified theory of local turbulence structure (the K62 theory) that incorporates the intermittency, was put forward in 1962 by Kolmogorov (1962), and Obukhov (1962) (see also (Kuznetsov and Sabelnikov 1990; Monin and Yaglom 1971; Tennekes and Lumley 1972; Frisch 1995; Landau and Lifshitz 1959; Tsinober 2013; Sreenivasan and Meneveau 1986, 1997; Tsinober 2009). The most important result of K62 theory is that the statistics of the small-scale turbulence is determined not just by η_K, τ_K and v_K (as was hypothesized in the K41 theory), but also by the integral scales, L and $T_L = L/u^{'}$. The interrelation of the Kolmogorov scale with larger scales can be illustrated by considering a slender region in a turbulent flow with dimensions L and η_K ($\ll L$). This slender region is then subjected to the stretch produced by the velocity gradient of larger vortices, $u^{'}/L$. Since the large-scale velocity fluctuations are correlated on a length of order L, the characteristic time scale of this stretch and, consequently of this slender region, will be of the order of integral time scale $L/u^{'}$ (it is instructive to compare the described picture of fine-scale structures with Burgers vortices (Batchelor 1967)).

DNS of planar flame propagation in homogeneous isotropic turbulence (at moderate *Re* and *Da* numbers), e.g., (Tanahashi et al. 2000, 2008), show a similar organization of the flow, with fine-structure vortices at the flame being essentially parallel to the flame, whereas those behind the flame are mostly perpendicular to the flame. Regions of high heat release and volumetric expansion are typically found to exist in tubular and sheet-like structures, distributed between the high and low-intensity vortical regions bracketing the flame.

Chomiak (1970, 1979), was the first who stressed, based on the intermittent character of high Reynolds turbulence, the importance of the fine structures for the description of the turbulent combustion. The ideas of Chomiak were later used in EDC (Magnussen 1981) and PaSR models of turbulent combustion, (Magnussen 2005; Gran and Magnussen 1996; Ertesvag and Magnussen 2000; Giacomazzi et al. 1999, 2000). It is worth noting that a first PaSR model was proposed as early as 1954 by Vulis (1961) (the book translated in English in 1961).

20.5.2 Assumptions Made in EDC Model

Here, for convenience of further references, a list of the main assumptions made by Magnussen in his paper on the RANS-EDC model (Fureby 2012) for the turbulent reacting flow, is given: (i) the fine structures, denoted by (*), are embedded in a surrounding structures, denoted by (^{0}), (ii) there is an exchange by mass and energy between the fine-structure regions and the surrounding fluid, the rate of exchange is proportional to a characteristic time scale τ^* of the order of Kolmogorov time scale, $\tau^* \approx \tau_K$, (iii) the fine structures are responsible for most of the molecular mixing, chemical reactions and heat release, (iv) the fluctuations of the thermochemical parameters with respect to the (conditional) averages in the fine structures and surroundings are neglected (similar to conditional moment closure (CMC) models), i.e., the (conditional) average chemical sources in the fine structures and surroundings are calculated as follows

$$\bar{\dot{w}}_i^* = \dot{w}_i^* = \dot{w}_i\left(Y_k^*, T^*\right),\ \dot{w}_i^0 = \dot{w}_i^0 = \dot{w}_i\left(Y_k^0, T^0\right), \tag{20.39}$$

(v) the chemical reactions take place only in the fine structures, i.e., $\dot{w}_i^0 = \dot{w}_i\left(Y_k^0, T^0\right) \approx 0$, then the mean chemical source is equal to

$$\bar{\dot{w}}_i = \gamma^* \bar{\dot{w}}_i^* + (1-\gamma^*)\bar{\dot{w}}_i^0 \approx \gamma^* \dot{w}_i\left(Y_k^*, T^*\right), \tag{20.40}$$

where γ^* is a volume fraction of the fine structures, (vi) the fine structures are locally considered as the steady Perfectly Stirred Reactors (PSR) without heat losses, (vii) at the PSR inlet the enthalpy and species are provided by the surrounding structures, i.e.,

$$h_{sk}^{inlet} = h_{sk}^0,\ Y_k^{inlet} = Y_k^0, \tag{20.41a}$$

(viii) at the PSR outlet the enthalpy and species coincide with the enthalpy and species in fine structures h_{sk}^* and Y_k^*, i.e.

$$h_{sk}^{outlet} = h_{sk}^{*},\ Y_k^{outlet} = Y_k^{*}. \tag{20.41b}$$

The same assumptions are used in PaSR model (Berglund et al. 2010; Vulis 1961). It is interesting to note that the assumption (iv) looks like the common no-model of TCI, but contrary to the last, (iv) is referred separately to the fine structures and surroundings.

As one can conclude from this list, the EDC model introduces only one characteristic time scale $\tau^* \approx \tau_K$. It is one of the important shortcomings of EDC model, because, from physical reasoning, the steady thermochemical parameters in the fine structures, considered as steady PSR, should depend at least on the second characteristic time, residence time τ_{res}, determined by convective flow effects (for stationary averaged flows). The PaSR model with two characteristic times τ_{res} and τ^* was analytically and numerically studied in (Sabelnikov and Figueira da Silva 2002) solving the probability density equation of a single reacting scalar, whose chemistry is described by an Arrhenius law. It was established that the key element of EDC model—the steady PSR, corresponds to a limit $\tau^*/\tau_{res} \to 0$. It is worth noting that the study (Sabelnikov and Figueira da Silva 2002) was conducted assuming only that the reactor is homogeneous, i.e., without neglecting the fluctuations of the thermochemical parameters.

Second shortcoming of EDC model is the assumption (vi) that the fine structures can be considered as a steady PSR, described by the algebraic equations. This assumption is quite restrictive, and not usable in the general case of no stationary flows, e.g., (Giacomazzi et al. 2000). In particular, using steady PSR does not permit to describe correctly transient phenomena such as ignition and extinction. Additional critical comments concerning the assumption (vi) can be found in (Giacomazzi et al. 2000).

20.5.3 TPaSR Model: Multiphase Approach for Subgrid Combustion Modeling

The LES-transported PaSR (LES-TPaSR) model for simulation of turbulent combustion was proposed in (Sabelnikov and Fureby 2013a, b). The present description of the TPaSR model is an updated version of the material from the papers (Sabelnikov and Fureby 2013a, b).

20.5.3.1 Subgrid Stress Tensor, Species Mass, and Heat Flux Vectors Closure

For the completeness and the convenience of the TPaSR model presentation, we describe shortly the closures for the subgrid stress tensor, species mass and heat fluxes used in (Sabelnikov and Fureby 2013a, b). With this aim let us rewrite the

filtered NSE (20.20a–20.20d) in the vector form, and replace the Eq. (20.20c) for the filtered total energy by the filtered equation for the sensible enthalpy

$$\frac{\partial \bar{\rho}}{\partial t} + \nabla \cdot (\bar{\rho}\tilde{\mathbf{u}}) = 0, \tag{20.42}$$

$$\frac{\partial \bar{\rho}\tilde{Y}_k}{\partial t} + \nabla \cdot (\bar{\rho}\tilde{\mathbf{u}}\widetilde{Y}_k) = \nabla \cdot (-\overline{\mathbf{j}_k} - \mathbf{j}_k^t) + \bar{\dot{w}}_k, \tag{20.43}$$

$$\frac{\partial \bar{\rho}\tilde{\mathbf{u}}}{\partial t} + \nabla \cdot (\bar{\rho}\tilde{\mathbf{u}} \otimes \tilde{\mathbf{u}}) = -\nabla \bar{p} + \nabla \cdot (\bar{\boldsymbol{\tau}} - \boldsymbol{\tau}^t), \tag{20.44}$$

$$\frac{\partial \bar{\rho}\tilde{h}_s}{\partial t} + \nabla \cdot (\bar{\rho}\tilde{\mathbf{u}}\tilde{h}_s) = \overline{\boldsymbol{\tau} : \nabla \mathbf{u}} + \overline{\frac{Dp}{Dt}} + \nabla \cdot (-\bar{\mathbf{q}} - \mathbf{q}^t) + \bar{\dot{\omega}}_T. \tag{20.45}$$

Here, $\boldsymbol{\tau}$ is the viscous stress tensor, Eq. (20.9a), $\boldsymbol{\tau} : \nabla \mathbf{u} = \rho\varepsilon = 2\mu S_{ij}^D S_{ij}^D$, $\frac{Dp}{Dt} = \frac{\partial p}{\partial t} + \mathbf{u} \cdot \nabla p$ and $\mathbf{q}$ are the molecular species mass and heat flux vectors; $\boldsymbol{\tau}^t = \bar{\rho}(\widetilde{\mathbf{u}\otimes\mathbf{u}} - \tilde{\mathbf{u}}\otimes\tilde{\mathbf{u}})$, $\mathbf{j}_k^t = \bar{\rho}(\widetilde{\mathbf{u}Y_k} - \tilde{\mathbf{u}}\widetilde{Y}_k)$ and $\mathbf{q}^t = \bar{\rho}(\widetilde{\mathbf{u}h_s} - \tilde{\mathbf{u}}\tilde{h}_s)$ are subgrid stress tensor, species mass and heat flux vectors, respectively, $\dot{\omega}_T = -\sum_{k=1}^{N} \dot{w}_k h_{f,k}^o$ is the heat release rate due to combustion (e.g., Poinsot and Veynante (2005)). It is assumed that $\overline{\frac{Dp}{Dt}} \approx \frac{\partial \bar{p}}{\partial t} + \tilde{\mathbf{u}} \cdot \nabla \bar{p}$, $\bar{\boldsymbol{\tau}} \approx 2\mu\left(\left(\frac{1}{2}\nabla\tilde{\mathbf{u}} + \nabla^T\tilde{\mathbf{u}}\right) - \frac{1}{3}(\nabla \cdot \tilde{\mathbf{u}})\mathbf{I}\right)$, $\bar{\mathbf{j}}_i \approx \bar{\rho} D_i \nabla \widetilde{Y}_i$, $\bar{\mathbf{q}} \approx -\kappa\nabla\widetilde{T} - \sum_{k=1}^{N} \tilde{h}_k \bar{\mathbf{j}}_k$ and $\bar{p} \approx \bar{\rho} R \widetilde{T}$ (disregarding the term $\widetilde{TY_k} - \widetilde{T}\widetilde{Y}_k$ in (20.21)), $\mu \approx \mu(\widetilde{T})$, $D_i \approx D_i(\widetilde{T})$, $\kappa \approx \kappa(\widetilde{T})$. The subgrid stress tensor and flux vectors are closed using the Mixed Model, proposed in (Bardina et al. 1980; Bardina 1983) (see also (Bensow and Fureby 2007)):

$$\boldsymbol{\tau}^t = \bar{\rho}(\widetilde{\tilde{\mathbf{u}}\otimes\tilde{\mathbf{u}}} - \tilde{\tilde{\mathbf{u}}}\otimes\tilde{\tilde{\mathbf{u}}}) - 2\mu_k\left(\left(\frac{1}{2}\nabla\tilde{\mathbf{u}} + \nabla\tilde{\mathbf{u}}^T\right) - \frac{1}{3}(\nabla \cdot \tilde{\mathbf{u}})\mathbf{I}\right), \tag{20.46}$$

$$\mathbf{j}_k^t = \bar{\rho}(\widetilde{\tilde{\mathbf{u}}\widetilde{Y}_k} - \tilde{\tilde{\mathbf{u}}}\tilde{\widetilde{Y}}_k) - (\mu_k/Sc_T)\nabla\widetilde{Y}_k, \tag{20.47}$$

$$\mathbf{q}^t = \bar{\rho}(\widetilde{\tilde{\mathbf{u}}\tilde{h}_s} - \tilde{\tilde{\mathbf{u}}}\tilde{\tilde{h}}_s) - (\mu_k/Pr_T)\nabla\tilde{h}_s, \tag{20.48}$$

where μ_k stands for the subgrid dynamical viscosity, it is calculated as $\mu_k = c_k\bar{\rho}\Delta u_\Delta^{'} = c_k\bar{\rho}\Delta k^{1/2} = \bar{\rho}\nu_k$, $\nu_k = c_k\Delta u_\Delta^{'} = c_k\Delta k^{1/2}$; c_k is a constant, $u_\Delta^{'}$ is the characteristic subgrid velocity fluctuations defined as $u_\Delta^{'} = \sqrt{k}$, where k denotes the subgrid kinetic energy. The subgrid kinetic energy k which can be found from an auxiliary equation, e.g., (Bensow and Fureby 2007), Sc_T and Pr_T are the turbulent Schmidt and Prandtl numbers. The wall-modeled LES is applied in the near-wall flow to reduce the computational cost (Fureby 2007).

20.5.3.2 A Multiphase Approach for Subgrid Combustion Modeling

The core of the LES-TPaSR model is the use of a multiphase analogy (e.g., (Drew 1983) for modeling the high-intensity fine-scale structures embedded in low-intensity background turbulence. The LES-TPaSR model keeps the assumptions (i)–(v) from the Magnussen RANS-EDC model (with a different expression for the rate of exchange), but the assumptions (vi)–(viii) are revised. Contrary to EDC and PaSR models, the thermochemical parameters in the fine structures $\left(Y_k^*, h_s^*\right)$ and surroundings $\left(Y_k^0, h_s^0\right)$ are governed by the partial differential equations, and therefore include the temporal and the convection effects. This explains why here the model is referred to as the Transported PaSR (TPaSR) model. It should be noted that in the original derivation (Sabelnikov and Fureby 2013a, b) the model was named as Extended PaSR (EPaSR) model, but, in our opinion, it is preferable to use the term Transported PaSR (TPaSR). If the temporal and subgrid convection effects, and the turbulent flux terms disregarded LES-TPaSR model is reduced to the LES-PaSR model, (Berglund et al. 2010). This limit case will be considered in the Sect. 20.5.7.

Let $\boldsymbol{\psi} = [Y_i, h_s]$, $1 \le i \le N$, is the composition space vector with $N+1$ components. The evolution of the nonfiltered vector components is governed by the local balance equations

$$\frac{\partial \rho \psi_i}{\partial t} + \nabla \cdot (\rho \mathbf{u} \psi_i) = \nabla \cdot \mathbf{k}_i + \dot{\omega}_i, \tag{20.49}$$

where $\psi_i = Y_i$, $\mathbf{k}_i = -\mathbf{j}_i$ and $\dot{\omega}_i = \dot{w}_i$ for $1 \le i \le N$, whereas $\psi_{N+1} = h_s$, $\mathbf{k}_{N+1} = -\mathbf{q}$, and $\dot{\omega}_{N+1} = \rho\varepsilon + \frac{\partial p}{\partial t} + \mathbf{u} \cdot \nabla p + \dot{\omega}_T$.

The instantaneous field equations for each phase are obtained with the aid of a phase function $I_\alpha(\mathbf{x}, t)$, which is defined as

$$I_\alpha(\mathbf{x}, t) = \begin{cases} 1 & \text{if } \mathbf{x} \text{ is inside of phase } \alpha \\ 0 & \text{otherwise} \end{cases}, \quad I_1 + I_2 = 1, \tag{20.50}$$

where indices $\alpha = 1$ in the fine structures (*) and $\alpha = 2$ in the surroundings (^{0}). The equations for each phase are obtained following the derivation given in (Drew 1983)

$$\frac{\partial (\rho_\alpha \psi_{i,\alpha} I_\alpha)}{\partial t} + \nabla \cdot (\rho_\alpha \mathbf{u}_\alpha \psi_{i,\alpha} I_\alpha) = \nabla \cdot (\mathbf{k}_{i,\alpha} I_\alpha) + \dot{\omega}_{i,\alpha} I_\alpha + M_{i,\alpha}, \quad \alpha = 1, 2, \tag{20.51}$$

$$M_{i,1} + M_{i,2} = 0. \tag{20.52}$$

Below the dependence of $\boldsymbol{\psi}$, ρ, ρ_α, $\psi_{i,\alpha}$ and I_α on $(\mathbf{x}, t)$ will usually be omitted for brevity. The term $M_{i,\alpha}$, the explicit form of which will be not needed here (can be found in (Drew 1983)), in the RHS of Eq. (20.51) refers to the mass $(1 \le i \le N)$

and energy $(i=N+1)$ exchange terms at the immaterial surface separating two phases (the fine structures and the surroundings). Summing up Eq. (20.51) over α results in the Eq. (20.49), as it should be, since

$$\begin{aligned} \rho &= \rho_1 I_1 + \rho_2 I_2, \quad \psi_i = \psi_{i,1} I_1 + \psi_{i,2} I_2, \\ \rho\psi_i &= \rho_1 \psi_{i,1} I_1 + \rho_2 \psi_{i,2} I_2, \quad \rho\,\mathbf{u}\psi_i = \rho_1 \mathbf{u}_1 \psi_{i,1} I_1 + \rho_2 \mathbf{u}_2 \psi_{i,2} I_2. \end{aligned} \tag{20.53}$$

Following the original derivation of LES-TPaSR model (Sabelnikov and Fureby 2013a, b), the velocity differences between the fine structures and surroundings are not taken into account, i.e., it is assumed below that $\mathbf{u} \approx \mathbf{u}_1 \approx \mathbf{u}_2$.

Filtering the Eq. (20.51) yields

$$\begin{aligned} &\frac{\partial(\gamma_\alpha(\bar{\rho}_\alpha)_\alpha(\tilde{\psi}_{i,\alpha})_\alpha)}{\partial t} + \nabla\cdot(\gamma_\alpha(\bar{\rho}_\alpha)_\alpha(\tilde{\psi}_{i,\alpha})_\alpha\tilde{\mathbf{u}}) \\ &= \nabla\cdot(\gamma_\alpha(-\bar{\mathbf{k}}_{i,\alpha})_\alpha - \gamma_\alpha \mathbf{b}^t_{i,\alpha}) + \gamma_\alpha(\bar{\dot{\omega}}_{i,\alpha})_\alpha + \overline{M}_{i,\alpha}, \end{aligned} \tag{20.54}$$

$$\overline{M}_{i,1} + \overline{M}_{i,2} = 0, \tag{20.55}$$

where $\gamma_\alpha = \overline{I}_\alpha$ is the filtered phase function, i.e., the volume fraction of phase α, $\gamma_1 + \gamma_2 = \overline{I}_1 + \overline{I}_2 = 1$. The Eq. (20.54) contains the conditionally filtered in the phase α: molecular species mass and heat flux vectors $(\bar{\mathbf{k}}_{i,\alpha})_\alpha$, subgrid flux term $\mathbf{b}^t_{i,\alpha}$, the thermochemical parameters $(\bar{\rho}_\alpha)_\alpha$, $(\tilde{\psi}_{i,\alpha})_\alpha$ and the reaction rates $(\bar{\dot{\omega}}_{i,\alpha})_\alpha$

$$\mathbf{b}^t_{i,\alpha} = \left(\overline{\rho_\alpha \psi_{i,\alpha} I_\alpha \mathbf{u}} - \gamma_\alpha(\bar{\rho}_\alpha)_\alpha(\tilde{\psi}_{i,\alpha})_\alpha\tilde{\mathbf{u}}\right)/\overline{I}_\alpha, \tag{20.56}$$

$$(\bar{\mathbf{k}}_{i,\alpha})_\alpha = \overline{\mathbf{k}_{i,\alpha} I_\alpha}/\overline{I}_\alpha,\ (\bar{\rho}_\alpha)_\alpha(\tilde{\psi}_{i,\alpha})_\alpha = \overline{\rho_\alpha \psi_{i,\alpha} I_\alpha}/\overline{I}_\alpha,\ (\bar{\dot{\omega}}_{i,\alpha})_\alpha = \overline{\dot{\omega}_{i,\alpha} I_\alpha}/\overline{I}_\alpha. \tag{20.57}$$

Filtering (20.53) yields the relations between the common filtered and the conditionally filtered parameters:

$$\bar{\psi}_i = \gamma_1(\bar{\psi}_{i,1})_1 + \gamma_2(\bar{\psi}_{i,2})_2, \tag{20.58}$$

$$\bar{\rho}\tilde{\psi}_i = \gamma_1(\bar{\rho}_1)_1(\tilde{\psi}_{i,1})_1 + \gamma_2(\bar{\rho}_2)_2(\tilde{\psi}_{i,2})_2. \tag{20.59}$$

$$\bar{\rho} = \gamma_1(\bar{\rho}_1)_1 + \gamma_2(\bar{\rho}_2)_2, \tag{20.60}$$

The sum over α of Eq. (20.54) results in LES Eqs. (20.43) and (20.45), taking into account the Eqs. (20.55)–(20.60). It is worth noting that for a box-filter, covering the cell volume ΔV, the volume fraction γ_α is given by

$$\gamma_\alpha = \overline{I}_\alpha = \frac{1}{\Delta V}\int_{\Delta V} I_\alpha(\mathbf{x}, t)\, dV = \Delta V_\alpha/\Delta V. \tag{20.61}$$

Let us return, for the simplicity writing, to the old notations, with (*) denoting the fine structures and (^{0}) the surroundings. Then the conditionally filtered characteristics are written as

$$\psi_i^* = (\tilde{\psi}_{i,1})_1 \text{ and } \psi_i^0 = (\tilde{\psi}_{i,2})_2. \tag{20.62}$$

Neglecting in the filtering chemical sources by subgrid fluctuations of the thermochemical parameters with respect to the conditionally filtered parameters (assumption (iv) in the Sect. 20.5.2), the Eqs. (20.54), (20.55), and (20.58)–(20.60) become

$$\frac{\partial(\gamma^*\rho^*\psi_i^*)}{\partial t} + \nabla\cdot(\gamma^*\rho^*\psi_i^*\tilde{\mathbf{u}}) = \nabla\cdot(\gamma^*(-\bar{\mathbf{k}}_i^* - \mathbf{b}_i^{t^*})) + \gamma^*\dot{w}_i\left(Y_k^*, T^*\right) + \overline{M}_i^*, \tag{20.63}$$

$$\frac{\partial(\gamma^0\rho^0\psi_i^0)}{\partial t} + \nabla\cdot(\gamma^0\rho^0\psi_i^0\tilde{\mathbf{u}}) = \nabla\cdot(\gamma^0(-\bar{\mathbf{k}}_i^0 - \mathbf{b}_i^{t0})) + \gamma^0\dot{w}_i\left(Y_k^0, T^0\right) + \overline{M}_i^0, \tag{20.64}$$

$$\overline{M}_i^* + \overline{M}_i^0 = 0, \tag{20.65}$$

$$\bar{\psi}_i = \gamma^*\psi_i^* + \gamma^0\psi_i^0 = \gamma^*\psi_i^* + (1-\gamma^*)\psi_i^0, \tag{20.66}$$

$$\bar{\rho}\tilde{\psi}_i = \gamma^*\rho^*\psi_i^* + \gamma^0\rho^0\psi_i^0 = \gamma^*\rho^*\psi_i^* + (1-\gamma^*)\rho^0\psi_i^0, \tag{20.67}$$

$$\bar{\rho} = \gamma^*\rho^* + \gamma^0\rho^0 = \gamma^*\rho^* + (1-\gamma^*)\rho^0, \tag{20.68}$$

We remind that Eqs. (20.63)–(20.68) are derived neglecting the subgrid fluctuations of the thermochemical parameters with respect to the conditionally filtered parameters (similarly to RANS-EDC model, Eqs. (20.39) and (20.40)). It should be stressed that this assumption is not applied to subgrid fluxes $\mathbf{b}_i^{t^*}$ and $\mathbf{b}_i^{t0}$, Eq. (20.56), because it would give zero subgrid fluxes. If, in addition to the assumption (iv) (the Sect. 20.5.2), the assumption (v) is added, then in Eq. (20.64) $\dot{w}_i\left(Y_k^0, T^0\right) \approx 0$. But, for the generality of the derivation, we will keep the term $\dot{w}_i\left(Y_k^0, T^0\right)$.

The filtered equation of state reads (disregarding the second term $\widetilde{TY_k} - \widetilde{T}\widetilde{Y}_k$ in (20.21))

$$\bar{p} = \gamma^* p^* + \gamma^0 p^0 \approx \bar{\rho} R_0 \widetilde{T} \sum_{k=1}^{N} \frac{\widetilde{Y}_k}{W_k}, \tag{20.69}$$

where

$$p^* = \rho^* R_0 T^* \sum_{k=1}^{N} \frac{Y_k^*}{W_k},\ p^0 = \gamma^0 \rho^0 R_0 T^0 \sum_{k=1}^{N} \frac{Y_k^0}{W_k}. \tag{20.70}$$

Neglecting (as it is assumed in Sabelnikov and Fureby 2013a, b) by the difference of the filtered pressures in the fine structures and surroundings, i.e. $p^* \approx p^0 \approx \bar{p}$, Eqs. (20.69) and (20.70) yield the expressions for the the densities ρ^* and ρ^0.

In practice, instead of the set of Eqs. (20.63) and (20.64), it is preferable to solve the equivalent set: the LES balance equations for $\tilde{\psi}_i$ (i.e., the sum of Eqs. (20.63) and (20.64)) and for ψ_i^*, (20.63)

$$\frac{\partial(\bar{\rho}\tilde{\psi}_i)}{\partial t} + \nabla \cdot (\bar{\rho}\,\tilde{\mathbf{u}}\tilde{\psi}_i) = \nabla \cdot (-\bar{\mathbf{k}}_i - \mathbf{b}_i^t) + \bar{\dot{w}}_i, \tag{20.71}$$

$$\frac{\partial(\gamma^* \rho^* \psi_i^*)}{\partial t} + \nabla \cdot (\gamma^* \rho^* \psi_i^* \tilde{\mathbf{u}}) = \nabla \cdot (\gamma^* (-\bar{\mathbf{k}}_i^* - \mathbf{b}_i^{t^*}) + \gamma^* \dot{w}_i(Y_k^*, T^*) + \overline{M}_i^*, \tag{20.72}$$

$$\bar{\dot{w}}_i = \gamma^* \dot{w}_i(Y_k^*, T^*) + (1-\gamma^*)\dot{w}_i(Y_k^0, T^0), \tag{20.73}$$

$$\psi_i^0 = \psi_i^* - \frac{\bar{\rho}}{\rho^0}\frac{(\psi_i^* - \tilde{\psi}_i)}{(1-\gamma^*)} = \frac{\bar{\rho}\tilde{\psi}_i - \gamma^* \rho^* \psi_i^*}{\bar{\rho} - \gamma^* \rho^*}. \tag{20.74}$$

where (20.74) follows from (20.67) and (20.68).

Below, for simplicity of the computational model, without loss of the basic physics, we will not differentiate between the subgrid fluxes in the fine structures and surroundings, i.e.,

$$\mathbf{b}_i^{t^*} \approx \mathbf{b}_i^{t0} \approx \mathbf{b}_i^t. \tag{20.75}$$

It is worth noting that neglecting subgrid fluctuations of the thermochemical parameters $\boldsymbol{\psi}$ with respect to the conditionally filtered parameters in the filtering chemical sources (assumption (iv) in the Sect. 20.5.2) is equivalent to the approximation of the filtered Reynolds and Favre PDFs of thermochemical parameters $f_R(\boldsymbol{\Phi}; \mathbf{x}, t)$ and $f_F(\boldsymbol{\Phi}; \mathbf{x}, t)$, respectively, by the singular probability density functions composed of two delta-functions

$$f_R(\boldsymbol{\Phi}; \mathbf{x}, t) = \gamma^* \delta(\boldsymbol{\Phi} - \boldsymbol{\psi}^*(\mathbf{x}, t)) + \gamma^0 \delta(\boldsymbol{\Phi} - \boldsymbol{\psi}^0(\mathbf{x}, t)), \tag{20.76}$$

$$\bar{\rho} f_F(\boldsymbol{\Phi}; \mathbf{x}, t) = \gamma^* \rho^* \delta(\boldsymbol{\Phi} - \boldsymbol{\psi}^*(\mathbf{x}, t)) + \gamma^0 \rho^0 \delta(\boldsymbol{\Phi} - \boldsymbol{\psi}^0(\mathbf{x}, t)), \tag{20.77}$$

where $\mathbf{\Phi}$ is the sample space variable corresponding to the random variable $\boldsymbol{\psi}(\mathbf{x},t)$, Eq. (20.53). It should be stressed that $\boldsymbol{\psi}^*(\mathbf{x},t)$ and $\boldsymbol{\psi}^0(\mathbf{x},t)$ in the Eqs. (20.76) and (20.77) are the conditional averages, Eq. (20.62), i.e., deterministic functions.

Indeed, by the formal definition, the filtered PDF is obtained by application the filtering to the fine-grained density (Gao and O'Brien 1993; Jaberi et al. 1999). The fine-grained density of thermochemical parameters for two-phase flow—fine structures and surroundings—reads (e.g., (Naud 2003))

$$\delta_R(\mathbf{\Phi}-\boldsymbol{\psi}) = I_1\delta(\boldsymbol{\psi}_1 I_1 - \mathbf{\Phi}) + I_2\delta(\boldsymbol{\psi}_2 I_2 - \mathbf{\Phi}), \tag{20.78}$$

Therefore the filtered Reynolds PDF is

$$f_R(\mathbf{\Phi};\mathbf{x},t) = \overline{\delta_R(\mathbf{\Phi}-\boldsymbol{\psi})} = \overline{I_1\delta(\boldsymbol{\psi}_1 I_1 - \mathbf{\Phi})} + \overline{I_2\delta(\boldsymbol{\psi}_2 I_2 - \mathbf{\Phi})} \tag{20.79}$$

It is seen, that if we neglect by subgrid fluctuations of the thermochemical parameters with respect to the conditionally filtered parameters, Eq. (20.79) reduces to (20.76).

Similarly, $f_F(\mathbf{\Phi};\mathbf{x},t)$, that is defined as follows (Jaberi et al. 1999),

$$\bar{\rho} f_F(\mathbf{\Phi};\mathbf{x},t) = \overline{\rho\delta_R(\mathbf{\Phi}-\boldsymbol{\psi})} = \overline{I_1\rho_1\delta(\boldsymbol{\psi}_1 I_1 - \mathbf{\Phi})} + \overline{I_2\rho_2\delta(\boldsymbol{\psi}_2 I_2 - \mathbf{\Phi})}, \tag{20.80}$$

reduces to Eq. (20.77), neglecting subgrid fluctuations of the thermochemical parameters with respect to the conditionally filtered parameters.

The Reynolds and Favre filtered values of an arbitrary function of the thermochemical parameters $Q(\boldsymbol{\psi})$ are found with the aid of the PDFs $f_R(\mathbf{\Phi};\mathbf{x},t)$ and $f_F(\mathbf{\Phi};\mathbf{x},t)$ as follows

$$\bar{Q} = \int_{\mathbf{\Phi}} Q(\mathbf{\Phi}) f_R(\mathbf{\Phi})\, d\mathbf{\Phi} = \gamma^* Q\left(\boldsymbol{\psi}^*\right) + \left(1-\gamma^*\right) Q\left(\boldsymbol{\psi}^0\right), \tag{20.81}$$

$$\begin{aligned} \bar{\rho}\widetilde{Q} &= \bar{\rho}\int_{\mathbf{\Phi}} Q(\mathbf{\Phi}) f_F(\mathbf{\Phi})\, d\mathbf{\Phi} = \int_{\mathbf{\Phi}} \rho Q(\mathbf{\Phi}) f_R(\mathbf{\Phi})\, d\mathbf{\Phi} \\ &= \gamma^*\rho^* Q\left(\boldsymbol{\psi}^*\right) + \left(1-\gamma^*\right)\rho^0 Q\left(\boldsymbol{\psi}^0\right), \end{aligned} \tag{20.82}$$

using Eqs. (20.76) and (20.77), respectively.

In particular cases $Q(\boldsymbol{\psi}) = \boldsymbol{\psi}$ Eqs. (20.81) and (20.82) reduce to Eqs. (20.66), (20.67).

It is worth noting that the results (20.81) and (20.82) can be obtained directly using the fine-grained Reynolds density, Eq. (20.78)

$$Q(\boldsymbol{\psi}) = \int_{\mathbf{\Phi}} Q(\mathbf{\Phi})\delta_R(\mathbf{\Phi}-\boldsymbol{\psi})\, d\mathbf{\Phi} = I_1 Q(\boldsymbol{\psi}^*) + I_2 Q\left(\boldsymbol{\psi}^0\right), \tag{20.83}$$

$$\rho Q(\boldsymbol{\psi}) = \int_{\boldsymbol{\Phi}} \rho Q(\boldsymbol{\Phi}) \delta_R(\boldsymbol{\Phi} - \boldsymbol{\psi})\, d\boldsymbol{\Phi} = I_1 \rho^* Q\left(\boldsymbol{\psi}^*\right) + I_2 \rho^0 Q\left(\boldsymbol{\psi}^0\right). \tag{20.84}$$

Filtering the Eqs. (20.83) and (20.84) yields the Eqs. (20.78) and (20.79), if we neglect by subgrid fluctuations of the thermochemical parameters with respect to the conditionally filtered parameters.

Summing up Eqs. (20.63) and (20.64) over the N species yields the continuity equations for the fine structures and surroundings, respectively

$$\frac{\partial(\gamma^* \rho^*)}{\partial t} + \nabla \cdot (\gamma^* \rho^* \tilde{\mathbf{u}}) = \dot{m}, \tag{20.85}$$

$$\frac{\partial(\gamma^0 \rho^0)}{\partial t} + \nabla \cdot (\gamma^0 \rho^0 \tilde{\mathbf{u}}) = -\dot{m}, \tag{20.86}$$

taking into account that $\sum_{i=1}^{N} \psi_i^* = \sum_{i=1}^{N} \psi_i^0 = 1$, $\sum_{i=1}^{N} \dot{w}_i = 0$. The sum of the Eqs. (20.85) and (20.86) must to give the global continuity Eq. (20.45), therefore

$$\dot{m} = \sum_{i=1}^{N} \overline{\mathrm{M}}_i^* = -\sum_{i=1}^{N} \overline{\mathrm{M}}_i^0, \tag{20.87}$$

where $\dot{m}$ stands for the exchange rate of mass between the fine structures and the surroundings. The origin of this exchange rate is the convection through the immaterial surface separating fine structures and surroundings.

20.5.4 Subgrid Modeling Exchange Terms

Let us begin from the modeling closure for $\dot{m}$, the exchange rate of mass between the fine structures and the surroundings. A closure for $\dot{m}$, proposed in (Sabelnikov and Fureby 2013a, b) is based on the assumption, that: (i) $\dot{m}$ depends on the volume fraction of the fine structures γ^*, $\dot{m}(\gamma^*)$, and (ii) in the case of a dynamic equilibrium state between the fine structures and the surroundings (the assumption of a dynamic equilibrium is implicitly used in PaSR models), γ^* reaches an equilibrium value γ_{eq}^* (which is defined in the Sect. 20.5.5.2), and $\dot{m}$ annuls, i.e., $\dot{m}(\gamma_{eq}^*) = 0$. Development of $\dot{m}$ in the vicinity of γ_{eq}^*, keeping only the linear term and using dimensional considerations yields

$$\dot{m} = -\bar{\rho}(\gamma^* - \gamma_{eq}^*)/\tau^*, \tag{20.88}$$

where τ^* denotes the fine structure residence time. It follows from (20.88) that if $\dot{m} > 0$, $\gamma^* < \gamma^*_{eq}$, the exchange rate of mass is directed from the surroundings to the fine structures. Otherwise, if $\dot{m} < 0$, $\gamma^* > \gamma^*_{eq}$, then the exchange rate of mass is directed from the fine structures to the surroundings. Equation (20.85) for γ^* becomes

$$\frac{\partial(\gamma^*\rho^*)}{\partial t} + \nabla\cdot(\gamma^*\rho^*\tilde{\mathbf{u}}) = -\frac{\bar{\rho}(\gamma^* - \gamma^*_{eq})}{\tau^*}. \tag{20.89}$$

Modeling the exchange terms $\overline{\mathrm{M}}_i^*$ and $\overline{\mathrm{M}}_i^0$ in Eqs. (20.63) and (20.64) needs more detailed analysis. One may conclude, based on the physical considerations, that $\overline{\mathrm{M}}_i^*$ and $\overline{\mathrm{M}}_i^0$ should contain two kinds of terms: (i) the first type of term, here denoted by $\overline{\Theta}_i^*$ and $\overline{\Theta}_i^0$, is due to the exchange rate of mass $\dot{m}$ between the fine structures and the surroundings, (ii) the second type of term, here denoted by $\overline{\Omega}_i^*$ and $\overline{\Omega}_i^0$, is due to molecular diffusion and thermal conductivity through the interface between the fine structures and surroundings. A necessity to include the second type of term follows from the consideration of the limiting case $\dot{m} = 0$, i.e., dynamic equilibrium state between the fine structures and the surroundings, when the exchange through the interface is only due to molecular diffusion. In the liming case $\psi_i^* = \psi_i^0$ the terms $\overline{\Omega}_i^*$ and $\overline{\Omega}_i^0$ should be equal to zero, since the molecular fluxes are absent. Summing these considerations the following closure for the exchange terms $\overline{\Theta}_i^*$ and $\overline{\Theta}_i^0$, $\overline{\Omega}_i^*$ and $\overline{\Omega}_i^0$ was proposed in (Sabelnikov and Fureby 2013a, b):

$$\overline{\Theta}_i^* = \frac{1}{2}(\dot{m} + |\dot{m}|)\psi_i^0 + \frac{1}{2}(\dot{m} - |\dot{m}|)\psi_i^*,\ \overline{\Theta}_i^0 = -\overline{\Theta}_i^*, \tag{20.90}$$

$$\overline{\Omega}_i^* = -\gamma^*\bar{\rho}(\psi_i^* - \psi_i^0)/\tau^*,\ \overline{\Omega}_i^0 = -\overline{\Omega}_i^*, \tag{20.91}$$

$$\overline{\mathrm{M}}_i^* = \overline{\Theta}_i^* + \overline{\Omega}_i^*,\ \overline{\mathrm{M}}_i^0 = \overline{\Theta}_i^0 + \overline{\Omega}_i^0, \tag{20.92}$$

The closure (20.90)–(20.92) satisfies Eq. (20.65) $\overline{\mathrm{M}}_i^* + \overline{\mathrm{M}}_i^0 = 0$ by construction (in fact, separately for both kinds of terms, i.e., $\overline{\Theta}_i^* + \overline{\Theta}_i^0 = \overline{\Omega}_i^* + \overline{\Omega}_i^0 = 0$, as has to be). The closure (20.90)–(20.92) does not contradict the underlying physics. Indeed, if $\dot{m} > 0$ (i.e., the mass exchange is directed from the surroundings to the fine structures, then (20.90) yields $\overline{\Theta}_i^* = \dot{m}\psi_i^0$ and $\overline{\Theta}_i^0 = -\overline{\Theta}_i^* = -\dot{m}\psi_i^0$. Similarly, if $\dot{m} < 0$ (i.e., the mass exchange is directed from the fine structures to the surroundings)), then (20.90) yields $\overline{\Theta}_i^* = \dot{m}\psi_i^*$ and $\overline{\Theta}_i^0 = -\overline{\Theta}_i^* = -\dot{m}\psi_i^*$.

Combining Eqs. (20.90) and (20.91) yields

$$\begin{aligned}&\overline{M}_i^* = \overline{\Theta}_i^* + \Omega_i^* = \frac{1}{2}(\dot{m} + |\dot{m}|)\psi_i^0 + \frac{1}{2}(\dot{m} - |\dot{m}|)\psi_i^* - \gamma^* \bar{\rho}\frac{(\psi_i^* - \psi_i^0)}{\tau^*},\\ &\overline{\mathrm{M}}_i^0 = -\overline{M}_i^*\end{aligned} \tag{20.93}$$

or in the equivalent form

$$\begin{aligned}&\overline{M}_i^* = \overline{\Theta}_i^* + \overline{\Omega}_i^* = \frac{1}{2}(\dot{m} + |\dot{m}|)\psi_i^0 + \frac{1}{2}(\dot{m} - |\dot{m}|)\psi_i^* - \gamma^* \frac{\bar{\rho}^2}{\rho^0}\frac{(\psi_i^* - \tilde{\psi}_i)}{\tau^*(1-\gamma^*)},\\ &\overline{\mathrm{M}}_i^0 = -\overline{M}_i^*.\end{aligned} \tag{20.94}$$

Here, the difference $\psi_i^0 - \psi_i^*$ is expressed through $\tilde{\psi}_i - \psi_i^*$ using (20.67) and (20.68):

$$\psi_i^* - \psi_i^0 = \frac{\bar{\rho}}{\rho^0}\frac{(\psi_i^* - \tilde{\psi}_i)}{(1-\gamma^*)},\ \rho^0(1-\gamma^*) = \bar{\rho} - \gamma^*\rho^*. \tag{20.95}$$

20.5.5 Subgrid Time and Equilibrium Volume Fraction of the Fine Structures

To finish the closure of the TPaSR model, we need to address the closures of two unknown characteristics: the exchange rate time τ^* and the equilibrium volume fraction of the fine structures γ_{eq}^*.

20.5.5.1 Subgrid Time Closure

We begin from the closure for the subgrid time τ^*. Here, an abridged version of the derivation is given. The readers are referred to the original papers (Sabelnikov and Fureby 2013a, b) where the complete derivation of the closure is presented. Based on the physical reasoning we assume that the subgrid time of the fine structures depends on its characteristic length scale ℓ_D, which has to be determined, and the Kolmogorov velocity, $\mathrm{v}_K = (\nu\varepsilon)^{1/4}$ (Kolmogorov 1941), i.e.,

$$\tau^* = \ell_D/\mathrm{v}_K. \tag{20.96}$$

Expression (20.96) is nothing, but the eddy turnover time of the eddies of the scale ℓ_D. If one assumes that ℓ_D in (20.96) is the Kolmogorov length scale η_K, then $\tau^* = \tau_K$, which is nothing but the fine structures residence time in EDC (Magnussen

1981) and FM (Giacomazzi et al. 2000) models. It should be stressed that the Magnussen assumption $\ell_D \approx \eta_K$ is based on the Kolmogorov (1941) hypothesis (Kolmogorov 1941) that the smallest fine structures are isotropic. However, this hypothesis is in the contradiction with the experimental data on the topology of the fine structures (discussed in the Sect. 20.5.1), which show that the fine structures are generally anisotropic (sheets, ribbons, and tubes) and therefore subjected to the stretch produced by larger vortices. Turning to the LES simulations, the characteristic subgrid velocity stretch can be estimated as $1/\tau_\Delta \approx u'_\Delta/\Delta$, where $\tau_\Delta \approx \Delta/u'_\Delta$ is the characteristic time scale of the subgrid velocity fluctuations $u'_\Delta \approx \sqrt{k}$ (k is the subgrid kinetic energy). Assuming that the characteristic length scale ℓ_D of the fine structures is controlled by molecular viscosity and the characteristic time scale of the subgrid velocity $\tau_\Delta \approx \Delta/u'_\Delta$ (similar to the theory of Burgers vortices (Batchelor 1967)) results in

$$\ell_D = \sqrt{\nu\tau_\Delta} = \eta_K\sqrt{\tau_\Delta/\tau_K} = \mathrm{v}_K\sqrt{\tau_K\tau_\Delta}, \tag{20.97}$$

expressing the molecular kinematic viscosity through Kolmogorov velocity and length scales, $\nu = \mathrm{v}_K\eta_K = (\mathrm{v}_K)^2\tau_K$.

It is worth noting that the relation for ℓ_D (20.97) is similar to the Taylor length scale $\lambda_T = (\nu L/u')^{1/2}$, introduced in the theory of isotropic turbulence, e.g., (Monin and Yaglom 1971; Frisch 1995), and defined by viscosity ν and the integral time scale L/u'. Therefore, the characteristic length scale ℓ_D can be considered as the dissipative length scale of the smallest resolved scales. Inserting the result (20.97) into Eq. (20.96) yields the desired relation for the subgrid time of the fine structures

$$\tau^* = \sqrt{\tau_K\tau_\Delta}. \tag{20.98}$$

The rate of dissipation $\bar{\varepsilon}$ entering into Kolmogorov time scale $\tau_K = (\nu/\bar{\varepsilon})^{1/2}$ is found from the expression $\varepsilon \approx \mathrm{v}'^3/L \approx (\mathrm{v}'_\Delta)^3/\Delta$. It is interesting to note that τ^* is equal to the geometrical mean of the Kolmogorov time and the time scale associated with the subgrid velocity stretch.

20.5.5.2 Equilibrium Volume Fraction of the Fine Structures

Here, two derivations of the expression for the equilibrium volume fraction of the fine structures γ^*_{eq} are presented. The first differs from the given in the original papers (Sabelnikov and Fureby 2013a; b) and is based on the use of the dimensional considerations and analysis of two limiting cases: (i) fast and (ii) slow chemistry in comparison with mixing rate. The second derivation reproduces the given originally in (Sabelnikov and Fureby 2013a; b).

Let us begin from the first derivation. We assume that γ_{eq}^{*} is determined by the following characteristics of the reacting fine structures τ_c, τ^{*}, τ_Δ, τ_K, Δ and η_K, where τ_c denotes the characteristic chemical time scale. From the dimensional considerations it follows

$$\gamma_{eq}^{*} = f\left(\tau_c/\tau^{*},\ \Delta/\eta_K, \tau_\Delta/\tau_K\right), \tag{20.99}$$

where $f(x, y, z)$ is unknown dimensionless function of the characteristic time and length scales ratios $x = \tau_c/\tau^{*}$, $y = \Delta/\eta_K$ and $z = \tau_\Delta/\tau_K$, respectively. It is worth noting that the parameters that characterize unsteady and convective effects are not present in (20.99), since we consider the equilibrium state of the fine structures ($\dot{m} = 0$). Neglecting intermittency yields $z = y^{2/3}$. Therefore, γ_{eq}^{*} depends only of x and y:

$$\gamma_{eq}^{*} = f(x, y). \tag{20.100}$$

There are two limiting cases for the ratio y, namely $y \gg 1$ and $y \approx 1$. The first case is indeed LES since $\Delta \gg \eta_K$, whereas the second case is indeed DNS since all scales are resolved, i.e., $\tau_\Delta \approx \tau_K$ and $\Delta \approx \eta_K$, and thus $\gamma_{eq}^{*} = f(1, 1) = 1$ irrespectively of x. Therefore, only the case $y \gg 1$ will be analyzed. We consider two limiting situations: (i) $x \ll 1$ (or $\tau_c \ll \tau^{*}$), which corresponds to fast chemistry, in which combustion is limited by mixing, and (ii) $x \gg 1$ (or $\tau_c \gg \tau^{*}$), which corresponds to slow chemistry, in which combustion is limited by the chemical reaction rate. In the first situation, ($x \ll 1$ or $\tau_c \ll \tau^{*}$), when combustion is limited by mixing, the product $\gamma_{eq}^{*}\bar{\omega}_i^{*}$ has to be of the order $1/\tau^{*}$, and taking into account that $\bar{\omega}_i^{*} \propto 1/\tau_c$ results in

$$\gamma_{eq}^{*} = f(x, y) \approx x,\ x \ll 1 \text{ and } y \gg 1. \tag{20.101}$$

In the second situation ($x \gg 1$ or $\tau_c \gg \tau^{*}$), when combustion is limited by the reaction rate, the product $\gamma_{eq}^{*}\bar{\omega}_i^{*}$ has to be of the order $1/\tau_c$. Thus, if we take into account that $\bar{\omega}_i^{*} \propto 1/\tau_c$, then

$$\gamma_{eq}^{*} = f(x, y) \approx 1,\ x \gg 1 \text{ and } y \gg 1. \tag{20.102}$$

In order to provide a reliable model for γ_{eq}^{*} for intermidiate values of ratios $x = \tau_c/\tau^{*}$ and $y = \Delta/\eta_K$, respecting the underlying cases and situations discussed above the following simple extrapolation for γ_{eq}^{*} might be proposed

$$\gamma_{eq}^{*} = (1 - F(y)) + \frac{x}{1+x} F(y) = \left(1 - F\left(\frac{\Delta}{\eta_K}\right)\right) + \frac{\tau_c}{\tau_c + \tau^*} F\left(\frac{\Delta}{\eta_K}\right), \qquad (20.103)$$

where a blending (monotonous) function $F(y)$ satisfies to $F(1) = 0$ and $F(\infty) = 1$. In the genuine LES $y \gg 1$, $(\Delta \gg \eta_K)$ and Eq. (20.103) reduces to

$$\gamma_{eq}^{*} = \frac{x}{1+x} = \frac{\tau_c}{\tau_c + \tau^*}. \qquad (20.104)$$

Now, we present shortly the derivation of the Eq. (20.104) proposed originally in (Sabelnikov and Fureby 2013a, b). Applying directly the definition (20.61) for the equilibrium fine-structure fraction for LES simulations yields $\gamma_{eq}^{*} = \Delta V^{*}/\Delta^3$, where ΔV^{*} and Δ^3 stands for the volume of the fine structures and the cell volume, respectively. Estimating ΔV^{*} as $\Delta V^{*} = \Delta^2 |\tilde{\mathbf{u}}| \tau_c$ and the cell volume Δ^3 as $\Delta^3 = \Delta^2 |\tilde{\mathbf{u}}| (\tau_c + \tau^*)$ (it is assumed that the sum $\tau_c + \tau^*$ represents the residence time in the LES cell) results in (20.104).

We mention here that an interesting approach to the estimation of the equilibrium volume fraction of the fine structures, based on the phenomenological fractal model (FM), was developed in (Giacomazzi et al. 1999, 2000).

It is worth noting that the characteristic chemical time scale should be representative of the overall chemical reaction, and therefore many options are available. The most simple estimation of τ_c is given by the common expression from the laminar flame theory, i.e., $\tau_c \approx \delta_u / s_u \approx \nu / s_u^2$, where δ_u and s_u are the laminar flame thickness and flame speeds, respectively.

20.5.6 LES-TPaSR Model Governing Equations

As all unknown terms in the Eqs. (20.63) and (20.64) for the fine structures and surroundings are modeled, we can summarize the equations for the LES-TPaSR model. Two LES-TPaSR equation sets are in order.

20.5.6.1 The First Set of Equations

The filtered continuity and momentum Eqs. (20.42) and (20.44), respectively, are solved together with the species equations, the energy equation for the fine structures and surroundings (20.63), (20.64) and the equation for the exchange rate of mass (20.89)

$$\frac{\partial\left(\gamma^*\rho^*Y_i^*\right)}{\partial t}+\nabla\cdot\left(\gamma^*\rho^*Y_i^*\tilde{\mathbf{u}}\right)$$
$$=\nabla\cdot\left(\gamma^*\left(-\bar{\mathbf{j}}_i^*-\mathbf{j}_i^t\right)\right)+\gamma^*\dot{w}_i\left(Y_k^*,T^*\right)+\overline{M}_i^*,\quad 1\le i\le N, \tag{20.105}$$

$$\frac{\partial\left(\gamma^*\rho^*h_s^*\right)}{\partial t}+\nabla\cdot\left(\gamma^*\rho^*h_s^*\tilde{\mathbf{u}}\right)=\gamma^*\dot{\omega}_{h_s}^*+\nabla\cdot\left(\gamma^*\left(-\bar{\mathbf{q}}^*-\mathbf{q}^t\right)\right)+\overline{M}_{h_s}^*, \tag{20.106}$$

$$\frac{\partial\left(\gamma^0\rho^0Y_i^0\right)}{\partial t}+\nabla\cdot\left(\gamma^0\rho^0Y_i^0\tilde{\mathbf{u}}\right)=\nabla\cdot\left(\gamma^0\left(-\bar{\mathbf{j}}_i^0-\mathbf{j}_i^t\right)\right)+\gamma^0\dot{w}_i\left(Y_k^0,T^0\right)+\overline{M}_i^0, \tag{20.107}$$

$$\frac{\partial\left(\gamma^0\rho^0h_s^0\right)}{\partial t}+\nabla\cdot\left(\gamma^0\rho^0h_s^0\tilde{\mathbf{u}}\right)=\gamma^0\dot{\omega}_{h_s}^0+\nabla\cdot\left(\gamma^*\left(-\bar{\mathbf{q}}^0-\mathbf{q}^t\right)\right)+\overline{M}_{h_s}^0, \tag{20.108}$$

$$\frac{\partial\left(\gamma^*\rho^*\right)}{\partial t}+\nabla\cdot\left(\gamma^*\rho^*\tilde{\mathbf{u}}\right)=\dot{m}=-\frac{\bar{\rho}\left(\gamma^*-\gamma_{eq}^*\right)}{\tau^*}, \tag{20.109}$$

$$\dot{\omega}_{h_s}^*=\bar{\rho}\tilde{\varepsilon}+\frac{\partial\bar{p}}{\partial t}+\tilde{\mathbf{u}}\cdot\nabla\bar{p}+\dot{\omega}_T^*,\ \dot{\omega}_T^*=\dot{\omega}_T\left(Y_k^*,T^*\right)=-\sum_{i=1}^{N}\dot{w}_i\left(Y_k^*,T^*\right)h_{f,i}^o, \tag{20.110}$$

$$\dot{\omega}_{h_s}^0=\bar{\rho}\tilde{\varepsilon}+\frac{\partial\bar{p}}{\partial t}+\tilde{\mathbf{u}}\cdot\nabla\bar{p}+\dot{\omega}_T^0,\ \dot{\omega}_T^0=\dot{\omega}_T\left(Y_k^0,T^0\right)=-\sum_{i=1}^{N}\dot{w}_i\left(Y_k^0,T^0\right)h_{f,i}^o, \tag{20.111}$$

$$\bar{p}\approx\bar{\rho}R_0\widetilde{T}\sum_{k=1}^{N}\frac{\widetilde{Y}_k}{W_k}=\rho^*T^*\sum_{k=1}^{N}\frac{Y_k^*}{W_k}=\rho^0T^0\sum_{k=1}^{N}\frac{Y_k^0}{W_k}. \tag{20.112}$$

The exchange terms are given by (20.93) and (20.94).

$$\begin{aligned}&\overline{M}_i^*=\overline{\Theta}_i^*+\overline{\Omega}_i^*=\frac{1}{2}\left(\dot{m}+|\dot{m}|\right)Y_i^0+\frac{1}{2}\left(\dot{m}-|\dot{m}|\right)Y_i^*-\frac{\gamma^*\bar{\rho}\left(Y_i^*-Y_i^0\right)}{\tau^*},\\&\overline{\mathrm{M}}_i^0=-\overline{M}_i^*,\end{aligned} \tag{20.113}$$

$$\begin{aligned}&\overline{M}_{h_s}^*=\overline{\Theta}_{h_s}^*+\overline{\Omega}_{h_s}^*=\frac{1}{2}\left(\dot{m}+|\dot{m}|\right)h_s^0+\frac{1}{2}\left(\dot{m}-|\dot{m}|\right)h_s^*-\frac{\gamma^*\bar{\rho}\left(h_s^*-h_s^0\right)}{\tau^*},\\&\overline{\mathrm{M}}_{h_s}^0=-\overline{M}_{h_s}^*.\end{aligned} \tag{20.114}$$

Then the filtered mass fractions $\tilde{Y}_i$ and sensible enthalpy $\tilde{h}_s$ are found using Eq. (20.67).

20.5.6.2 The Second Set of Equations

As was already said above, the equivalent set of the equations, more convenient in practice, solves the filtered species and the energy Eqs. (20.43) and (20.45) and the Eqs. (20.105) and (20.106) for the fine structures. The exchange terms in the

Eqs. (20.105) and (20.106) for the fine structures are rewritten using Y_i^* and $\widetilde{Y}_i$, h_s^* and $\tilde{h}_s$, Eq. (20.94)

$$\overline{M}_i^* = \overline{\Theta}_i^* + \overline{\Omega}_i^* = \frac{1}{2}(\dot{m}+|\dot{m}|)Y_i^0 + \frac{1}{2}(\dot{m}-|\dot{m}|)Y_i^* - \gamma^* \frac{\bar{\rho}^2}{\rho^0}\frac{(Y_i^* - \tilde{Y}_i)}{\tau^*(1-\gamma^*)}, \quad \overline{\mathrm{M}}_i^0 = -\overline{M}_i^*, \tag{20.115}$$

$$\overline{M}_{h_s}^* = \overline{\Theta}_{h_s}^* + \overline{\Omega}_{h_s}^* = \frac{1}{2}(\dot{m}+|\dot{m}|)h_s^0 + \frac{1}{2}(\dot{m}-|\dot{m}|)h_s^* - \gamma^* \frac{\bar{\rho}^2}{\rho^0}\frac{(h_s^* - \tilde{h}_s)}{\tau^*(1-\gamma^*)}, \quad \overline{\mathrm{M}}_{h_s}^0 = -\overline{M}_{h_s}^*. \tag{20.116}$$

where $\rho^0(1-\gamma^*) = \bar{\rho} - \gamma^*\rho^*$, Eq. (20.68).

For brevity, we do not write here the equations of the second set.

20.5.6.3 The Simplified LES-TPaSR Model

To avoid calculating the fine-structure and surroundings densities one may assume (without loss of physics) not to differentiate between ρ^* and ρ^0, i.e., to set $\rho^* \approx \rho^0 \approx \bar{\rho}$ (as it is assumed in (Sabelnikov and Fureby 2013a, b), and in the PaSR models cited above). Then, the LES-TPaSR model equations simplify essentially. The first set of the Eqs. (20.105)–(20.112) reduces to

$$\frac{\partial(\bar{\rho}\gamma^* Y_i^*)}{\partial t} + \nabla\cdot(\bar{\rho}\gamma^* Y_i^* \tilde{\mathbf{u}}) = \nabla\cdot(\gamma^*(-\vec{\mathbf{J}}_i^* - \mathbf{j}_i^t)) + \gamma^* \dot{w}_i(Y_k^*, T^*) + \overline{M}_i^*, \quad 1 \le i \le N, \tag{20.117}$$

$$\frac{\partial(\bar{\rho}\gamma^* h_s^*)}{\partial t} + \nabla\cdot(\bar{\rho}\gamma^* h_s^* \tilde{\mathbf{u}}) = \gamma^* \dot{\omega}_{h_s}^* + \nabla\cdot(\gamma^*(-\vec{\mathbf{q}}^* - \mathbf{q}^t)) + \overline{M}_{h_s}^*, \tag{20.118}$$

$$\frac{\partial(\bar{\rho}\gamma^0 Y_i^0)}{\partial t} + \nabla\cdot(\bar{\rho}\gamma^0 Y_i^0 \tilde{\mathbf{u}}) = \nabla\cdot(\gamma^0(-\vec{\mathbf{J}}_i^0 - \mathbf{j}_i^t)) + \gamma^0 \dot{w}_i(Y_k^0, T^0) + \overline{M}_i^0, \tag{20.119}$$

$$\frac{\partial(\bar{\rho}\gamma^0 h_s^0)}{\partial t} + \nabla\cdot(\bar{\rho}\gamma^0 h_s^0 \tilde{\mathbf{u}}) = \gamma^0 \dot{\omega}_{h_s}^0 + \nabla\cdot(\gamma^*(-\vec{\mathbf{q}}^0 - \mathbf{q}^t)) + \overline{M}_{h_s}^0, \tag{20.120}$$

$$\frac{\partial(\bar{\rho}\gamma^*)}{\partial t} + \nabla\cdot(\bar{\rho}\gamma^* \tilde{\mathbf{u}}) = \dot{m} = -\frac{\bar{\rho}(\gamma^* - \gamma_{eq}^*)}{\tau^*}, \tag{20.121}$$

$$\bar{p} \approx \bar{\rho} R_0 \widetilde{T} \sum_{k=1}^{N} \frac{\widetilde{Y}_k}{W_k}. \tag{20.122}$$

The second set includes the Eqs. (20.43) and (20.45), (20.117), and (20.118) and, for convenience of references, these equations are written here together

$$\frac{\partial \bar{\rho}\widetilde{Y}_i}{\partial t} + \nabla \cdot (\bar{\rho}\tilde{\mathbf{u}}\widetilde{Y}_i) = \nabla \cdot (-\overline{\mathbf{j}}_i - \mathbf{j}_i^t) + \bar{\dot{w}}_i, \quad 1 \le i \le N, \tag{20.123}$$

$$\frac{\partial \bar{\rho}\tilde{h}_s}{\partial t} + \nabla \cdot (\bar{\rho}\widetilde{Y}\tilde{h}_s) = \bar{\dot{\omega}}_{h_s} + \nabla \cdot (-\bar{\mathbf{q}} - \mathbf{q}^t), \tag{20.124}$$

$$\bar{\dot{\omega}}_{h_s} = \bar{\rho}\tilde{\varepsilon} + \frac{\partial \bar{p}}{\partial t} + \tilde{\mathbf{u}} \cdot \nabla \bar{p} + \bar{\dot{\omega}}_T, \ \bar{\dot{\omega}}_T = \gamma^* \dot{\omega}_T\left(Y_k^*, T^*\right) + \gamma^0 \dot{\omega}_T\left(Y_k^0, T^0\right) \tag{20.125}$$

$$\begin{aligned} &\frac{\partial\left(\bar{\rho}\gamma^* Y_i^*\right)}{\partial t} + \nabla \cdot (\bar{\rho}\gamma^* Y_i^* \tilde{\mathbf{u}}) \\ &= \nabla \cdot (\gamma^*(-\overline{\mathbf{j}}_i^* - \mathbf{j}_i^t)) + \gamma^* \dot{w}_i\left(Y_k^*, T^*\right) + \overline{M}_i^*, \quad 1 \le i \le N, \end{aligned} \tag{20.126}$$

$$\frac{\partial\left(\bar{\rho}\gamma^* h_s^*\right)}{\partial t} + \nabla \cdot (\bar{\rho}\gamma^* h_s^* \tilde{\mathbf{u}}) = \gamma^* \bar{\dot{\omega}}_{h_s}^* + \nabla \cdot (\gamma^*(-\bar{\mathbf{q}}^* - \mathbf{q}^t)) + \overline{M}_{h_s}^*, \tag{20.127}$$

$$\begin{aligned} &\overline{M}_i^* = \overline{\Theta}_i^* + \overline{\Omega}_i^* = \frac{1}{2}(\dot{m} + |\dot{m}|)Y_i^0 + \frac{1}{2}(\dot{m} - |\dot{m}|)Y_i^* - \gamma^* \bar{\rho}\frac{(Y_i^* - \tilde{Y}_i)}{\tau^*(1-\gamma^*)}, \\ &\overline{\mathrm{M}}_i^0 = -\overline{M}_i^*, \end{aligned} \tag{20.128}$$

$$\begin{aligned} &\overline{M}_{h_s}^* = \overline{\Theta}_{h_s}^* + \overline{\Omega}_{h_s}^* = \frac{1}{2}(\dot{m} + |\dot{m}|)h_s^0 + \frac{1}{2}(\dot{m} - |\dot{m}|)h_s^* - \gamma^* \bar{\rho}\frac{(h_s^* - \tilde{h}_s)}{\tau^*(1-\gamma^*)}, \\ &\overline{\mathrm{M}}_{h_s}^0 = -\overline{M}_{h_s}^*. \end{aligned} \tag{20.129}$$

20.5.7 Reduction of LES-TPaSR Model to LES-PaSR Model

It should be noted that the LES-TPaSR model, Eqs. (20.123)–(20.129), is reduced to the LES-PaSR model by assuming that the temporal, the convective and the turbulent flux terms in the Eqs. (20.126), (20.127) for fine structures characteristics Y_i^* and h_s^* can be neglected (it is worth noting that the same reduction can be done without the assumption $\rho^* \approx \rho^0 \approx \bar{\rho}$; it is omitted here). Then, the partial differential Eqs. (20.126) and (20.127) reduce to the algebraic equations relating the chemical sources in the fine structures with the exchange terms, namely

$$\gamma^* \dot{w}_i\left(Y_k^*, T^*\right) + \overline{M}_i^* = 0, \tag{20.130}$$

$$\gamma^*\left(\bar{\rho}\tilde{\varepsilon}+\frac{\partial\bar{p}}{\partial t}+\tilde{\mathbf{u}}\cdot\nabla\bar{p}+\dot{\omega}_T\left(Y_k^*,T^*\right)\right)+\overline{M}_{h_s}^*=0. \tag{20.131}$$

Summing up the Eqs. (20.130) over i yields the abridged Eq. (20.121)

$$\dot{m}=-\frac{\bar{\rho}(\gamma^*-\gamma_{eq}^*)}{\tau^*}=0, \tag{20.132}$$

and, consequently, $\gamma^*=\gamma_{eq}^*$ and $\overline{\Theta}_i^*=0$ in (20.90), $1\le i\le N+1$. The exchange terms (20.113), (20.114), (20.128), and (20.129) reduce to

$$\overline{\mathrm{M}}_i^*=\overline{\Omega}_i^*=-\gamma^*\bar{\rho}\frac{(Y_i^*-Y_i^0)}{\tau^*},\ \gamma^*=\gamma_{eq}^*,\ 1\le i\le N, \tag{20.133}$$

$$\overline{M}_{h_s}^*=\overline{\Omega}_{h_s}^*=-\gamma^*\bar{\rho}\frac{(h_s^*-h_s^0)}{\tau^*}, \tag{20.134}$$

for the first set of the equations, and

$$\overline{\mathrm{M}}_i^*=\overline{\Omega}_i^*=-\gamma^*\bar{\rho}\frac{(Y_i^*-\tilde{Y}_i)}{\tau^*(1-\gamma^*)},\ \gamma^*=\gamma_{eq}^*,\ 1\le i\le N, \tag{20.135}$$

$$\overline{M}_{h_s}^*=\overline{\Omega}_{h_s}^*=-\gamma^*\bar{\rho}\frac{(h_s^*-\tilde{h}_s)}{\tau^*(1-\gamma^*)}, \tag{20.136}$$

for the second set of the equations.

Combining Eqs. (20.133)–(20.136) with Eqs. (20.130), (20.131) yields the desired result for the first set

$$\dot{w}_i\left(Y_k^*,T^*\right)=\bar{\rho}\frac{(Y_i^*-Y_i^0)}{\tau^*},\ 1\le i\le N,\ \gamma^*=\gamma_{eq}^*, \tag{20.137}$$

$$\bar{\rho}\tilde{\varepsilon}+\frac{\partial\bar{p}}{\partial t}+\tilde{\mathbf{u}}\cdot\nabla\bar{p}+\dot{\omega}_T\left(Y_k^*,T^*\right)=\bar{\rho}\frac{(h_s^*-h_s^0)}{\tau^*}, \tag{20.138}$$

and for the second set

$$\dot{w}_i\left(Y_k^*,T^*\right)=\bar{\rho}\frac{(Y_i^*-\widetilde{Y}_i)}{\tau^*(1-\gamma^*)},\ 1\le i\le N,\ \gamma^*=\gamma_{eq}^*, \tag{20.139}$$

$$\bar{\rho}\tilde{\varepsilon}+\frac{\partial\bar{p}}{\partial t}+\tilde{\mathbf{u}}\cdot\nabla\bar{p}+\dot{\omega}_T\left(Y_k^*,T^*\right)=\bar{\rho}\frac{(h_s^*-\tilde{h}_s)}{\tau^*(1-\gamma^*)}. \tag{20.140}$$

Finally LES-PaSR model becomes (only the second set of the equations is written)

$$\frac{\partial \bar{\rho}\widetilde{Y}_i}{\partial t} + \nabla \cdot (\bar{\rho}\tilde{\mathbf{u}}\widetilde{Y}_i) = \nabla \cdot (-\overline{\mathbf{j}}_i - \mathbf{j}_i^t) + \bar{\dot{w}}_i, \quad 1 \le i \le N, \tag{20.141}$$

$$\frac{\partial \bar{\rho}\tilde{h}_s}{\partial t} + \nabla \cdot (\bar{\rho}\tilde{\mathbf{u}}\tilde{h}_s) = \bar{\boldsymbol{\tau}} \cdot \nabla \tilde{\mathbf{u}} + \frac{\partial \bar{p}}{\partial t} + \tilde{\mathbf{u}} \cdot \nabla \bar{p} + \nabla \cdot (-\bar{\mathbf{q}} - \mathbf{q}^t) - \sum_{i=1}^{N} \bar{\dot{w}}_i h_{f,i}^o, \tag{20.142}$$

$$\bar{\rho}\frac{(Y_i^* - \widetilde{Y}_i)}{\tau^*(1-\gamma^*)} = \dot{w}_i\left(Y_k^*, T^*\right), \ 1 \le i \le N, \ \gamma^* = \gamma_{eq}^*, \tag{20.143}$$

$$\bar{\rho}\frac{(h_s^* - \tilde{h}_s)}{\tau^*(1-\gamma^*)} = \bar{\rho}\tilde{\varepsilon} + \frac{\partial \bar{p}}{\partial t} + \tilde{\mathbf{u}} \cdot \nabla \bar{p} + \dot{\omega}_T\left(Y_k^*, T^*\right). \tag{20.144}$$

It is worth stressing that the temporal, the convective and the turbulent flux terms in the Eqs. (20.119) and (20.120) for the surroundings characteristics Y_i^0 and h_s^0 cannot be neglected. Indeed, if it is done, the temporal, the convective and the turbulent flux terms in Eqs. (20.123) and (20.124) for the filtered $\widetilde{Y}_i$ and $\tilde{h}_s$ should be neglected also (Eqs. (20.123) and (20.124) are the sum of Eqs. (20.119) and (20.120), (20.126) and (20.127)), but this is nonsense.

Let us return to the key assumption made to obtain the PaSR algebraic Eqs. (20.130), (20.131) from the differential Eqs. (20.126), (20.127): disregarding the temporal, the convective and the turbulent flux terms in LES-TPaSR equations. As a result of this procedure, the characteristic time and length scales connected with disregarded terms are excluded from the consideration, and multiscale character of the initial problem is lost. From the formal mathematical viewpoint disregarding the terms under discussion can be approved if τ^* is much smaller than the characteristic time scales connected with disregarded terms in the Eqs. (20.117) and (20.118). But in an opposite case (τ^* is much larger than the characteristic time scales connected with disregarded terms) the exchange terms can be neglected with respect to the temporal, the convective and the turbulent flux terms in LES-TPaSR equations. Therefore, the algebraic equations of PaSR model are not uniformly valid. Because of the singular character of the limiting procedure, the following problem arises: how to select a "correct" solution among multiple solutions of PaSR steady-state equations. The Sect. 20.7 is devoted to the discussion of this problem.

20.5.8 LES-TPaSR Model with Regard to Other LES Combustion Models

Let us compare briefly the theoretical formulations of LES-TPaSR model with the following LES combustion models: the LES-TFM, EDC, PaSR, and FPV family

models. The interested readers are referred to (Sabelnikov and Fureby 2013a, b; Fedina and Fureby 2010; Weller et al. 1998), where they may find the comparing predictions of these models with experimental data.

The filtered species equations in LES-TFM, EDC, PaSR, and TPaSR models are written as follows:

$$\frac{\partial(\bar{\rho}\widetilde{Y}_i)}{\partial t} + \nabla\cdot(\bar{\rho}\tilde{\mathbf{u}}\widetilde{Y}_i) = \nabla\cdot((\bar{\rho}D_i + \bar{\rho}D_k)\nabla\widetilde{Y}_i) + \bar{\dot{w}}_i, \tag{20.145}$$

whereas the LES-FPV family of models makes use of an equation for a progress variable, c, (and a mixture fraction equation if appropriate) such that:

$$\frac{\partial(\bar{\rho}\tilde{c})}{\partial t} + \nabla\cdot(\bar{\rho}\tilde{\mathbf{u}}\tilde{c}) = \nabla\cdot(\bar{\rho}D_k\nabla\tilde{c}) + \bar{\dot{w}}_c. \tag{20.146}$$

In the Eqs. (20.145) and (20.146), D_k is the subgrid diffusivity; $\bar{\dot{w}}_i$ and $\bar{\dot{w}}_c$ are the reaction rate terms.

For convenience of the comparison, the Table 20.1 summarizes the subgrid diffusivity D_k and chemical source $\bar{\dot{w}}_i$ for the indicated models. The following notations are used: Ξ, F and E stand for the flame wrinkling, flame thickening, and efficiency factors, respectively; $\gamma^*_{PaSR} = \gamma^*_{eq} = \tau_c/(\tau_c + \tau^*)$, γ^*_{TPaSR} and $\gamma^*_{EDC} = (\mathrm{v}_K/u'_\Delta)^3 = 1.02\,(\nu/\Delta u'_\Delta)^{3/4}$ (with $\varepsilon \approx (u'_\Delta)^3/\Delta$ for the Kolmogorov velocity $\mathrm{v}_K = (\nu\varepsilon)^{1/4}$) are the fine-structure volume fractions for the PaSR, TPaSR, and EDC models, respectively; $\delta_u \approx D/s_u$ is the laminar flame thickness. Additional information can be found in references (Sabelnikov and Fureby 2013a, b; Weller et al. 1998) and references therein.

It should be noted that the qualitative comparison between LES-TPaSR and LES-TFM, EDC, PaSR, and FPV family models presented in this subsection can be

Table 20.1 LES combustion model comparison

Model	Diffusivity	Reaction rate models	Flame wrinkling
FPV (Weller et al. 1998)	ν_k/Sc_T	$\rho_u s_u \Sigma = \rho_u s_u \Xi \lvert\nabla\tilde{c}\rvert$[a]	$\Sigma/\lvert\nabla\tilde{c}\rvert = \Xi^*$
TFM (Charlette et al. 2002)	$(FE-1)\,D_i$	$E/F\ \dot{w}_i(\bar{\rho}, \widetilde{Y}_k, \widetilde{T})$	$\sqrt{1+\min(\Delta/\delta_u, \Gamma u'/s_u)}$
PaSR (Berglund et al. 2010; Fedina and Fureby 2010)	ν_k/Sc_T	$\gamma^*_{PaSR}\dot{w}^*_i(Y^*_k, T^*)$	$\sqrt{\gamma^*_{PaSR}(1+D_k/D)}$
TPaSR	ν_k/Sc_T	$\gamma^*_{eq}\dot{w}^*_i(Y^*_k, T^*)$	$\sqrt{\gamma^*_{eq}(1+D_k/D)}$
EDC (Fureby 2012; Kolmogorov 1962)	ν_k/Sc_T	$\gamma^*_{EDC}\dot{w}^*_i(Y^*_k, T^*)$	$\sqrt{\gamma^*_{EDC}(1+D_k/D)}$

[a]Ξ is provided by a separate balance equation, (Ma et al. 2013), with an equilibrium value of $\Xi = 1 + 2\tilde{c}(\theta - 1)$, with $\theta = 1 + 0.62\,\mathrm{Re}_K(u'/s_u)^{1/2}$

considered only as approximate, because of additional assumptions. A detailed assessment of the cited here LES combustion models may be found in (Sabelnikov and Fureby 2013b), where predictions using the models listed in Table 20.1 are compared against the high Reynolds number turbulent lean-premixed bluff-body stabilized flame experimental database (Sabelnikov and Fureby 2013b).

The readers are referred to (Petrova et al. 2017), where the LES-TPaSR model is adapted to the RANS-TPaSR, and then applied to the numerical simulation of a backward-facing step premixed combustor.

20.6 Simulation of Supersonic Jet Flame with LES—UPASR Model

20.6.1 The LES—Unsteady PASR (UPASR) Model

The LES—unsteady PaSR (UPaSR) combustion model (Moule et al. 2014b) (see also (Moule et al. 2014a; Scherrer et al. 2016)) is situated between LES-TPaSR and LES-PaSR models. LES-UPaSR equations for the fine structures species concentrations Y_k^* and the sensible enthalpy h_s^* read

$$\bar{\rho}\frac{\partial Y_k^*}{\partial t}+\bar{\rho}\frac{Y_k^*-Y_k^0}{\tau^*}=\dot{w}_k\left(Y_k^*,T^*\right), \tag{20.147}$$

$$\bar{\rho}\frac{\partial h_s^*}{\partial t}+\bar{\rho}\frac{h_s^*-h_s^0}{\tau^*}=\bar{\rho}\tilde{\varepsilon}+\frac{\partial \bar{p}}{\partial t}+\tilde{\mathbf{u}}\cdot\nabla\bar{p}+\dot{\omega}_T\left(Y_k^*,T^*\right) \tag{20.148}$$

or in equivalent form

$$\bar{\rho}\frac{\partial Y_k^*}{\partial t}+\bar{\rho}\frac{\left(Y_k^*-\widetilde{Y}_k\right)}{\tau^*\left(1-\gamma^*\right)}=\dot{w}_k\left(Y_k^*,T^*\right), \tag{20.149}$$

$$\bar{\rho}\frac{\partial h_s^*}{\partial t}+\bar{\rho}\frac{\left(h_s^*-\tilde{h}_s\right)}{\tau^*\left(1-\gamma^*\right)}=\bar{\rho}\tilde{\varepsilon}+\frac{\partial \bar{p}}{\partial t}+\tilde{\mathbf{u}}\cdot\nabla\bar{p}+\dot{\omega}_T\left(Y_k^*,T^*\right). \tag{20.150}$$

The Eqs. (20.149) and (20.140) are solved together with the Eqs. (20.43) and (20.45). It is assumed that the fine structures fraction is equal to its equilibrium value $\gamma^*=\gamma_{eq}^*=\tau_c/(\tau_c+\tau^*)$, Eq. (20.104); the time derivative $\partial\gamma_{eq}^*/\partial t$ is neglected.

It is worth noting that using LES-UPaSR model, by its construction, the problem of the selection of "correct" solution between multiple solutions of PaSR steady-state equations does not arise (see Sect. 20.7), but at the same time it creates a new difficulty: UPaSR model equations are not Galilean invariant.

20.6.2 Simulation of Supersonic Hydrogen Jet Flame

LES-UPaSR model was used in (Moule et al. 2014b) for the numerical simulation of supersonic hydrogen jet flame in co-flow of air, experimentally studied by Cheng et al. (Cheng et al. 1994). Numerical results are obtained with the ONERA CFD code CEDRE. The readers are referred to (Scherrer et al. 2016; Jarrett et al. 1988; Moule et al. 2014b; Cheng et al. 1994) for the description of the experimental setup and associated data, and the results of the numerical simulation.

The most important result of the numerical simulation (Moule et al. 2014b) with regard to the combustion process is the conclusion that heat release is largely impacted by the supersonic jet structure through shock diamonds and associated pressure effects. Here, we limit ourselves by the brief description of the flame structure. Roughly, the flame consists of four regions: (i) the induction zone $(0 < X/D < 10)$, (ii) the auto-ignition zone $(10 < X/D < 18)$, (iii) the stabilization region $(18 < X/D < 26)$, where the flame anchors at the beginning of a shock diamond, and finally (iv) the end of combustion zone $(30 < X/D < 34)$ (X, and D denote longitudinal coordinate and the nozzle diameter, respectively).

The autoignition region is identified by an upstream peak in HO_2 radical formation in the middle of the jet (as seen in Fig. 20.8).

The flame stabilization region is significantly impacted by a shock diamond structure positioned at $X/D \approx 20$, Fig. 20.9.

It is seen, that the shock waves and heat release are strongly coupled in the stabilization region as well as downstream. One of the important results of the study (Moule et al. 2014b) is the discovery that the stabilization region is constituted

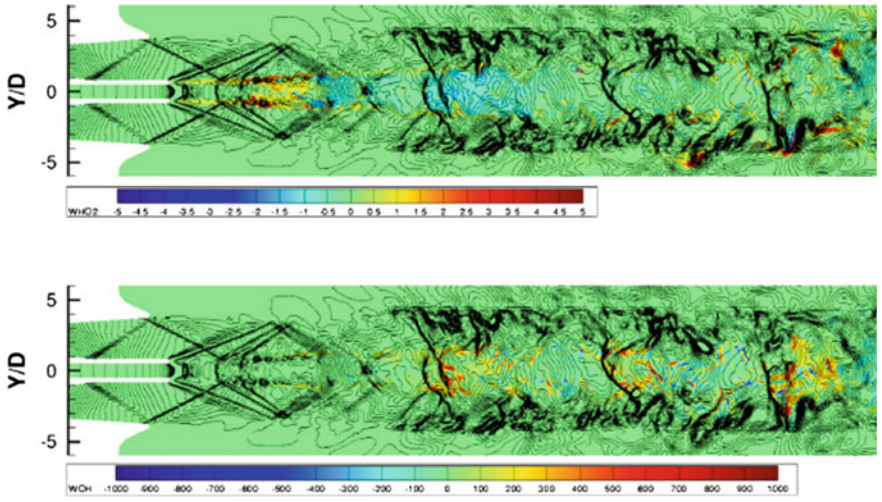

Fig. 20.8 Instantaneous fields of HO_2 (top) and OH (bottom) production rates $(\mathrm{kg} \cdot \mathrm{s}^{-1}\mathrm{m}^{-3})$ with pressure iso-lines [50–150 kPa]. This is Fig. 17 of (Moule et al. 2014b). It is reprinted with permission from Elsevier

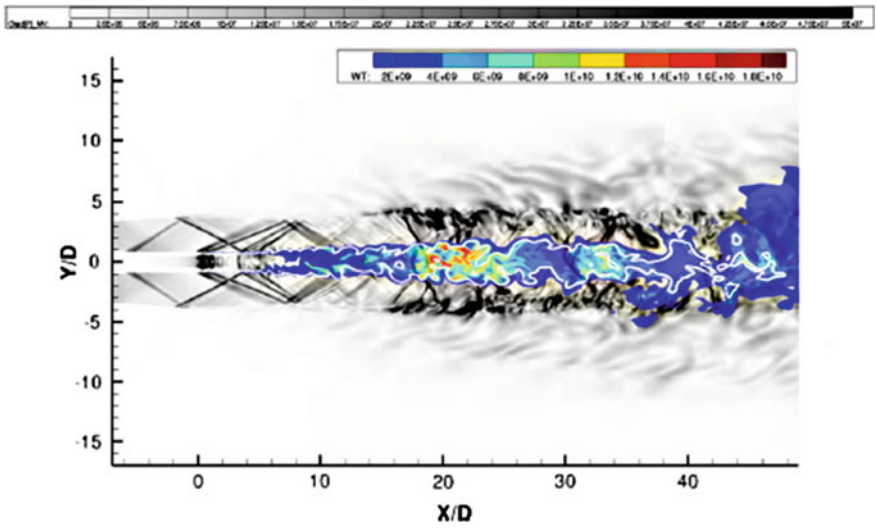

Fig. 20.9 Instantaneous fields of heat release $(\mathrm{W}\cdot\mathrm{m}^{-3})$ and pressure gradient $(\mathrm{Pa}\cdot\mathrm{m}^{-1})$ superimposed with the stoichiometric isoline (white). This is Fig. 24 of (Moule et al. 2014b). It is reprinted with permission from Elsevier

mainly of burning pockets of rich premixed reactants, similar to Schetinkov microvolume model of the turbulent combustion (Schetinkov 1958; Schetinkov 1965), contrary to standard non-premixed flames, where the heat release rate maxima closely follow the stoichiometric composition. It is demonstrated in Fig. 20.9, where the superposition of stoichiometric isoline (white curve), the pressure gradient, and heat release rate fields are presented.

The computational RANS-UPaSR model was also used (with ONERA computational fluid dynamics code CEDRE) to investigate a Mach 12 rectangular-to-elliptical-shape-transition scramjet engine developed and operated at the University of Queensland (Moule et al. 2014a).

20.7 Multiple Solutions in the PaSR Model

The main assumption of PaSR model, as was stated in the Sect. 20.5.1, is that the chemical reactions occur only in the fine structures that are locally considered as adiabatic steady Perfectly Stirred Reactors (PSR). At the PSR inlet the (sensible) enthalpy and mass fraction of kth species are provided by the surrounding structures, and given by Eq. (20.41a). At the PSR outlet the enthalpy and mass fraction of kth species coincide with the enthalpy and mass fraction of kth species h_{sk}^{*} and Y_k^{*} in PSR, and given by Eq. (20.41b). For simplicity of the exposition of multiple solutions problem, let us consider a simple global irreversible reaction between a fuel (F) and oxidizer (O) of the form $F + sO \rightarrow (1+s)P$, Eq. (20.35).

It is assumed that the species F, O, and P have the same molecular weights and the same constant heat capacity C_p. Equations (20.137) and (20.138) for fuel concentration Y_F^* and temperature T^* in fine structures considered as a steady PSR reduce to

$$\bar{\rho}(Y_F^* - Y_F^0) = \tau^* \dot{w}_F(Y_F^*, T^*),\ \dot{w}_F < 0, \tag{20.151}$$

$$\bar{\rho}C_p(T^* - T^0) = \tau^* \dot{w}_T(Y_F^*, T^*),\ \dot{w}_T = -Q\dot{w}_F > 0, \tag{20.152}$$

where $\dot{w}_F$ stands for the fuel reaction rate, Q is the heat of reaction. Y_F^*, Y_k^0, and $\widetilde{Y}_F$, T^*, T^0, and $\widetilde{T}$ are related by the expressions

$$\widetilde{Y}_F = \gamma^* Y_F^* + (1-\gamma^*)Y_F^0,\ \widetilde{T} = \gamma^* T^* + (1-\gamma^*)T^0, \tag{20.153}$$

$$\gamma^* = \gamma_{eq}^* = \tau_c/(\tau_c + \tau^*),$$

using Eq. (20.95), γ_{eq}^* is given by Eq. (20.104). Equations (20.151) and (20.152) can be rewritten in the equivalent form

$$\bar{\rho}(Y_F^* - \widetilde{Y}_F) = (1-\gamma^*)\tau^* \dot{w}_F(Y_F^*, T^*),\ \dot{w}_F < 0, \tag{20.154}$$

$$\bar{\rho}C_p(T^* - \widetilde{T}) = (1-\gamma^*)\tau^* \dot{w}_T(Y_F^*, T^*),\ \dot{w}_T = -Q\dot{w}_F > 0, \tag{20.155}$$

taking into account Eqs. (20.153). Summing Eqs. (20.152) and (20.151), multiplied by Q, yields

$$\bar{\rho}Q(Y_F^* - Y_F^0) + \bar{\rho}C_p(T^* - T^0) = 0, \tag{20.156}$$

$$Y_F^* = Y_F^0 + (T^0 - T^*)C_p/Q. \tag{20.157}$$

Equation (20.157) can be rewritten as

$$Y_F^{outlet} = Y_F^{inlet} + (T^{inlet} - T^{outlet})C_p/Q. \tag{20.158}$$

using Eqs. (20.41a) and (20.41b). Similarly, from Eqs. (20.154) and (20.155) follows

$$\bar{\rho}(Y_F^* - \widetilde{Y}_F) + \bar{\rho}C_p(T^* - \widetilde{T}) = 0, \tag{20.159}$$

$$Y_F^* = \widetilde{Y}_F + (\widetilde{T} - T^*)C_p/Q. \tag{20.160}$$

Equation (20.160) can be rewritten as

$$Y_F^{outlet} = \widetilde{Y}_F + \left(\widetilde{T} - T^{outlet}\right) C_p / Q, \tag{20.161}$$

using Eqs. (20.41a) and (20.41b). Combination of Eqs. (20.157) and (20.160) yields

$$\widetilde{Y}_F - Y_F^0 = \left(T^0 - \widetilde{T}\right) C_p / Q, \tag{20.162}$$

or

$$\widetilde{Y}_F - Y_F^{inlet} = \left(T^{inlet} - \widetilde{T}\right) C_p / Q. \tag{20.163}$$

taking into account that $Y_F^{inlet} = Y_F^0$, $Y_F^{outlet} = Y_F^*$, $T^{inlet} = T^0$, $T^{outlet} = T^*$, Eqs. (20.41a) and (20.41b).

Using Eqs. (20.157) or (20.160) in Eqs. (20.151), (20.155), we can obtain equation for T^* (temperature at the PSR outlet) as the only variable in two forms, respectively

$$(T^* - T^0)/\tau^* = \dot{w}_T(T^*)/\bar{\rho} C_p, \tag{20.164}$$

$$(T^* - \widetilde{T})/\tau'^* = \dot{w}_T(T^*)/\bar{\rho} C_p, \tag{20.165}$$

where

$$\tau'^* = (1 - \gamma^*)\tau^* = \tau^* Da^* / \left(1 + Da^*\right),\ Da^* = \tau^*/\tau_c, \tag{20.166}$$

Da^* is Damköhler number referred to the fine structures. The product $\tau'^* = (1 - \gamma^*)\tau^*$ can be interpreted as the modified fine structures residence time. The temperature in surroundings structures (temperature at the PSR inlet) T^0 and mean temperature $\widetilde{T}$ are the parameters in the Eqs. (20.164) and (20.165), respectively.

For determinacy let us consider Eq. (20.165). The right-hand side (RHS) of Eq. (20.165) is a heat production (HP) term, in which $\dot{w}_T(T^*)$ is given by the Arrhenius expression (highly nonlinear) for the chemical reaction rate, Eq. (20.36). The left-hand side (LHS) of Eq. (20.165) can be thought of as a heat transfer (HT) term (heat loses). It is well known that, in the general case, the solution of the algebraic nonlinear Eq. (20.165) is not unique (Zel'dovich et al. 1985) (see also the analysis conducted in (Sabelnikov and Figueira da Silva 2002)). Let us analyze qualitatively the solutions of Eq. (20.165) applying graphical method, following (Zel'dovich et al. 1985).

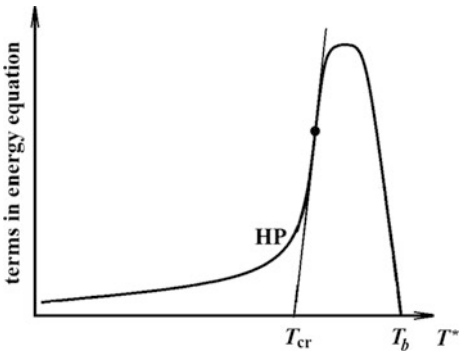

Fig. 20.10 Heat production (HP) curve and definition of critical temperature T_{cr}

The rate of heat production $\dot{w}_T(T^*)/\bar{\rho}C_p$ is plotted in Fig. 20.10, $T_b = \widetilde{T} + \left(Q/C_p\right)\widetilde{Y}_F$ is adiabatic flame temperature. It is assumed without loss of generality that the mixture in fine structures (in PSR) is lean, so the reaction ends at $Y_F^* = 0$, then (20.160) yields $T^* = T_b$.

In Fig. 20.10 T_{cr} is the intersection point of the temperature axis and the tangent to the heat production curve (HP) at the inflection point. The number of solutions of Eq. (20.165) depends on the ratio $\widetilde{T}/T_{cr}$.

20.7.1 The Case $\tilde{T}<T_{cr}$

Curves HP and HT for the case $\widetilde{T} < \widetilde{T}_{cr}$ are schematically shown in Fig. 20.11. Curve HP starts at practically negligible values at low temperatures, peaks close to the adiabatic flame temperature T_b, and drops to zero at T_b, because at least one of the reactants mass fractions F, O becomes zero at T_b. Curve HT is a straight-line with slope equal to $1/\tau'^*$. The slope increases with the decrease of τ'^*. The solutions of the Eq. (20.165) are the points of intersection of the curve HP with the heat loss lines HT. These heat loss curves may be located relative to the heat production

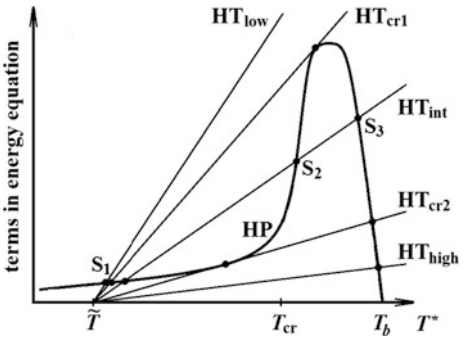

Fig. 20.11 Heat production (HP) and heat transfer (HT) curves for the case $\tilde{T} < T_{cr}$

curve in three ways (see Fig. 20.11): with three intersection points S_1, S_2, and S_3; with two intersection points S_1 and $S_2 = S_3$ (for $HT = HT_{cr1}$) or $S_1 = S_2$ and S_3 (for $HT = HT_{cr2}$); and with single intersection S_1 (for $HT < HT_{cr1}$) or S_3 (for $HT > HT_{cr1}$).

Single stationary solutions

1. Modified fine structures residence time $\tau^{'*}$ is larger than characteristic chemical time, then a single stationary regime is realized at a high temperature close to T_b. Here the reaction rate is not very high since the process takes place with almost complete burn up of the fuel. This situation is denoted by curve $HT_{high} > HT_{cr2}$. The PaSR operates at point S_3 at a temperature close to T_b. Hence, the amount of unburnt fuel escaping the PSR is very small and we achieve almost complete combustion.
2. Modified fine structures residence time $\tau^{'*}$ is smaller than characteristic chemical time, then a single stationary regime is realized at a low temperature close to $\widetilde{T}$. It is characterized by low heating of the mixture. The reaction proceeds slowly and burn–up is small. This situation corresponds to curve $HT_{low} < HT_{cr1}$. The PSR operates at the point S_1 at a temperature close to $\widetilde{T}$.

Three stationary solutions

3. Over a fairly wide range of intermediate modified fine structures residence time $\tau^{'*}$ the heat loss curve HT intersects the heat generation curve HR at three points.

   (i) The "cold" point S_3 (low temperature) corresponds to small heat generation and temperature increments.

   (ii) The "hot" point S_1 (high temperature) corresponds to a large heat generation and temperature increments.

   (iii) Point S_2 corresponds to the unstable solution (physically non-realizable), since small perturbation of $\tau^{'*}$ will make the system go to S_3 or to S_1.

Two stationary solutions

The heat loss line $HT = HT_{cr1}$ tangent to the heat production curve separates a single and three stationary solutions: there are two stationary solutions, S_1 and $S_2 = S_3$. The point $S_2 = S_3$ is unstable (blow-off of the PSR).

Analogous situation corresponds to the other loss line $HT = HT_{cr2}$ tangent to the heat production. In this case, $S_1 = S_2$ is unstable solution, while hot solution S_3 is stable.

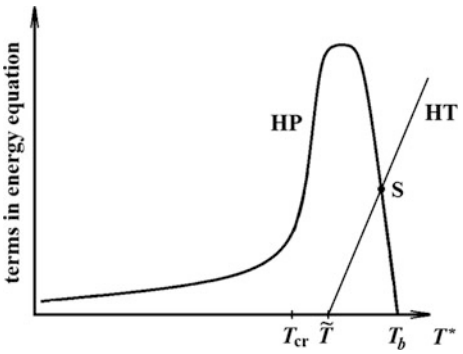

Fig. 20.12 Heat production (HP) and heat transfer (HT) curves for the case $\tilde{T} > T_{cr}$

20.7.2 The Case $\tilde{T}>T_{cr}$. Single Solution

Curves HP and HT for the case $\widetilde{T} > T_{cr}$ are schematically shown in Fig. 20.12. This case corresponds to the situation when the heat transfer HT is less than the heat generation. The PSR works in the high-temperature regime (the point S).

20.7.3 Solution Selection Problem

The above analysis of stationary solutions of PSR raises the question, what solution to select in the case of multiple (three) solutions ("cold" regime, point S_3, and "hot" regime, point S_1; point S_2 is unstable), using LES-PaSR, LES-EDC, RANS-PaSR, RANS-EDC turbulent combustion models (case of intermediate modified fine structures residence time with respect to the characteristic chemistry time).

It should be stressed that this problem does not arise when using TPaSR model, which consists of partial differential equations (PDEs). TPaSR model takes into account the whole history of the fine structures arriving to some point. Therefore, the content of the fine structures is completely defined by the initial and the boundary conditions. The problem of selection of solution (cold or hot) using PaSRs at the best of our knowledge is not discussed in the literature. It is worth noting that the solution selection difficulty is not resolved applying "unsteady" PaSR approach with fictitious time (e.g., (Lysenko 2014) and references therein). Indeed, this approach consists of, instead of the direct solution of algebraic Eq. (20.165), to look for the asymptotic solution (at $\tau \to \infty$) of the following "unsteady" equation for PSR describing the fine-scale structures (not confound with UPaSR model Eqs. (20.149) and (20.150)

$$\bar{\rho} C_p \frac{dT^*}{d\tau} = -\frac{(T^* - \widetilde{T})}{\tau'^*} + \frac{1}{\bar{\rho} C_p} \dot{w}_T(T^*), \tag{20.167}$$

with augmented "initial" conditions $T^*(\tau=0)$, here τ is fictitious time variable. The mean temperature $\widetilde{T}$ and the fine-scale structures fraction γ^* are the parameters. It should be stressed that the asymptotic solutions of Eq. (20.167) coincide with the solutions of the Eq. (20.165). Therefore, since the asymptotic solution of Eq. (20.167) depend on the choice of the initial condition for T^* at $\tau=0$, the. problem of selection of solution ("cold" or "hot") of algebraic Eq. (20.165) is substituted by the problem of the choice of the initial condition for T^*, solving Eq. (20.167): depending on $T^*(\tau=0)$ the "cold" or the "hot" solution of Eq. (20.165) is obtained.

20.8 Concluding Remarks

The scramjet is air-breathing engine with supersonic flow at the combustor entrance, i.e., with essentially lower deceleration of flow in the inlet with respect to common ramjet. Initially, it was assumed that flow in combustor will be entirely supersonic, and this concept of engine became well known as *scramjet* ("supersonic combustion ramjet"). The scramjet concept had been proposed in 50s of twentieth century in Russia and in USA. Very soon it became obvious that the scramjet is principally another class of air-breathing engines that requires to solves other problems than in the case of an usual ramjet. Classical ramjet may be considered as a combination of three main elements—supersonic part of the inlet, duct with the subsonic flow (from closing shock in the inlet and up to the sonic section of the nozzle) and supersonic part of the nozzle. Each of these elements may be optimized separately; this fact resulted in the formation of three independent subdisciplines—aerodynamics of inlets, the theory of combustor and aerodynamics of nozzles. To the contrary, the scramjet is characterized by strong coupling of all its elements. Supersonic core from the inlet to the nozzle, essential subsonic zones in thick boundary layers and high losses caused by strong shock waves, by viscous effects, by dissociation, and radiation result in a situation, when positive thrust may be reached only on the basis of joint optimization of the whole flowpath.

In comparison with experimental investigations, which remain very challenging to conduct in such flow conditions, computational fluid dynamics is an attractive complementary tool for the study supersonic reactive flow in the scramjet flowpath. Understanding and prediction of the flow structure are necessary for achieving the stable and efficient combustion, high thrust and thermostable construction of the scramjet.

The first half of the chapter focuses on the fundamentals of turbulent supersonic combustion. The physics of combustion in supersonic flows with regard to scramjets, Navier–Stokes equations for multispecies reacting gas flow, kinetic schemes for simulation of scramjets, RANS/URANS and LES approaches, the closure problems for turbulent fluxes are the main subjects addressed here. Special attention is paid to the discussion of the difficulties when formulating and deriving

the closure models for reaction rates. The second half of the chapter focuses on partially stirred reactor (PaSR) turbulent combustion models. Transported PaSR (TPaSR) and unsteady PaSR models are described in details, and experience of their application to simulation of experiments on supersonic combustion (within the framework of LES approach) is demonstrated. Finally, the selection of "correct" solution between multiple solutions of PaSR steady state equations is considered.

It is worth stressing that the physical and numerical modeling turbulent combustion in high-speed flows where turbulent mixing, shock, and rarefaction waves, compressibility effects and chemical kinetics processes are strongly coupled still remains a challenging issue.

The very important role, when tackling this issue, belongs to experimental databases that are used for the validation, improvements, and development of phenomenological TCI models for RANS, subgrid-scale models for LES, and reduced-kinetics models. Unfortunately, these are beyond the scope of this chapter.

Acknowledgements The first author (VAS) was financially supported by ONERA and by the Grant of the Ministry of Education and Science of the Russian Federation (Contract No. 14. G39.31.0001 of 13.02.2017). The second author (VVV) was supported by the Grant of the Ministry of Education and Science of the Russian Federation (Contract No. 14.G39.31.0001 of 13.02.2017).

References

Allmaras SR, Johnson FT (2012) Modifications and clarifications for the implementation of the Spalart-Allmaras turbulence model. In: Seventh international conference on computational fluid dynamics (ICCFD7), pp 1–11

Annamalai K, Puri IK (2006) Combustion science and engineering. CRC press

Babushenko DI, Kopchenov VI, Titova NS, Starik AM (2015) Prediction ability of reaction mechanisms for modeling of continuously rotating detonation in propane-air mixture. Combust Explos 8(1):164–172 (In Russian)

Babulin AA, Bosnyakov SM, Vlasenko VV, Engulatova MF, Matyash SV, Mikhailov SV (2016) Experience of validation and tuning of turbulence models as applied to the problem of boundary layer separation on a finite-width wedge. Comp Math Math Phys 56(6):1020–1033

Baldwin B, Lomax H (1978) Thin-layer approximation and algebraic model for separated turbulent flows. In: 16th aerospace sciences meeting, p 257

Bardina J (1983) Improved turbulence models based on large eddy simulation of homogeneous, incompressible turbulent flows. Ph.D. dissertation. Stanford University

Bardina J, Ferziger JH, Reynolds WC (1980) Improved subgrid scale models for large eddy simulation. AIAA paper, pp 80–1357

Barnett HC, Hibbard RR (1957) Basic considerations in the combustion of hydrocarbon fuels with air. NACA-TR-1300, p 273

Basevich VY, Frolov SM (2006) Global kinetic mechanisms for simulation of multi-stage self-ignition of hydrocarbons in reactive flows. Russian J Chem Phys 25(6):54–62

Batchelor GK (1967) An introduction to fluid dynamics. Cambridge Univ. Press

Batchelor GK, Townsend AA (1949) The nature of turbulent motion at large wave-numbers. Proc R Soc Lond A 199:238

Bensow R, Fureby C (2007) On the justification and extension of mixed models in LES. J Turb 8 (54):1

Berglund M, Fureby C (2007) LES of supersonic combustion in a scramjet engine model. Proc Combus Inst 31(2):2497–2504

Berglund M, Fedina E, Fureby C, Tegnér J, Sabelnikov V (2010) Finite rate chemistry large-eddy simulation of self-ignition in supersonic combustion ramjet. AIAA Journal 48(3):540–550

Berselli LC, Iliescu T, Layton WJ (2006) Mathematics of large eddy simulation of turbulent flows. Scientific computation, vol XVIII, p 348. Springer

Bilger RW (1993) Conditional moment closure for turbulent reacting flow. Phys Fluids A 5:436

Bosnyakov IS, Mikhaylov SV, Morozov AN, Podaruev VY, Troshin AI, Vlasenko VV, Garcia-Uceda A, Hirsch C (2015) Implementation of high-order discontinuous Galerkin method for solution of practical tasks in external aerodynamics and aeroacoustics. In: IDIHOM: industrialization of high-order methods-a top-down approach. Notes on numerical fluid mechanics and multidisciplinary design, vol 128, pp 337–379. Springer International Publishing

Bose T (2012) Airbreathing propulsion. Springer

Burcat A, Ruscic B (2005) Third millennium ideal gas and condensed phase thermochemical database for combustion with updates from active thermochemical tables. Argonne National Laboratory, Argonne, IL, p 417

Burrows MC, Kurkov AP (1973) Analytical and experimental study of supersonic combustion of hydrogen in a vitiated air stream. NASA TM X-2828

Chapman DR (1979) Computational aerodynamics development and outlook. AIAA Journal 17 (12):1293–1313

Chapuis M, Fedina E, Fureby C, Hannemann K, Karl S, Martinez Schramm J (2013) A computational study of the HyShot II combustor performance. Proc Combus Inst 34:2101–2109

Charlette F, Meneveau C, Veynante D (2002) A power-law flame wrinkling model for LES of premixed turbulent combustion. Part I: non-dynamic formulation and initial tests. Combust Flame 131:159

Cheng J, Wehrmeyer R, Pitz WJ, Jarrett O, Northam G (1994) Raman measurement of mixing and finite-rate chemistry in a supersonic hydrogen—air diffusion flame. Combust Flame 99:157–173

Chomiak J (1970) A possible propagation mechanism of turbulent flames at high Reynolds numbers. Combust Flame 15:319

Chomiak J (1979) Basic considerations in the turbulent flame propagation in premixed gases. Prog Energy Combust Sci 5:207

Cécora R-D, Eisfeld B, Probst A, Crippa S, Radespiel R (2012) Differential Reynolds stress modeling for aeronautics. In: 50th AIAA Aerospace Sciences Meeting including the New Horizons forum and aerospace exposition, p 465

Cockrell CE, Auslender AH, Guy RW, McClinton CR, Welch SS (2002) Technology roadmap for dual-mode scramjet propulsion to support space-access vision vehicle development. AIAA paper, 5188

Conaire MÓ, Curran HJ, Simmie JM, Pitz WJ, Westbrook CK (2004) A comprehensive modeling study of hydrogen oxidation. Int J Chem Kinet 36(11):603–622

Curran ET, Murphy SN (eds) (2001) Scramjet propulsion. In: Series progress in astronautics and aeronautics, vol 189, p 1324. AIAA

Davidenko D, Gökalp I, Dufour E, Magre P (2003) Numerical simulation of hydrogen supersonic combustion and validation of computational approach 12th AIAA international space planes and hypersonic systems and technologies, p 7033

Deardorff JW (1970) A numerical study of three-dimensional turbulent channel flow at large Reynolds numbers. J Fluid Mech 41:453–480

Deardorff JW (1973) The use of subgrid transport equations in a three-dimensional model of atmospheric turbulence. J Fluids Eng 9:429–438

Drew DA (1983) Mathematical modeling of two-phase §ow. Ann Rev Fluid Mech 15:261

Dooley S, Won SH, Heyne J, Farouk TI, Ju Y, Dryer FL, Kumar K, Hui X, Sung Ch-J, Wang H, Oehlschlaeger MA, Iyer V, Iyer S, Litzinger TA, Santoro RJ, Malewicki T, Brezinsky K (2012)

The experimental evaluation of a methodology for surrogate fuel formulation to emulate gas phase combustion kinetic phenomena. Combust Flame 159(4):1444–1466
Echekki T, Kerstein A, Sutherland J (2011) The one-dimensional-turbulence model. Turbul Combust Model 249–76
Edelman RB, Fortune OF (1969) A quasi-global chemical kinetic model for the finite rate combustion of hydrocarbon fuels with application to turbulent burning and mixing in hypersonic engines and nozzles. AIAA Paper, pp 69–86
Ertesvag IS, Magnussen BF (2000) The eddy dissipation turbulence energy cascade model. Combust Sci Tech 159:213
Escudier MP (1965) The distribution of the mixing length in turbulent flows near walls. Mechanical Engineering Department
Falempin F, Serre L (1999) The French PROMETHEE program-main goals and status in 1999. In: 9th International space planes and hypersonic systems and technologies conference, p 4814
Favre AJ (1965) The equations of compressible turbulent gases. Marceille University, Instutute de Mécanique Statistique de la Turbulence
Ferziger JH, Kaper HG (1972) Mathematical theory of transport processes in gases. North-Holland
Friedrich R (1993) Compressible turbulence. Space Course. TU Munich
Fedina E, Fureby C (2010) A comparative study of flamelet and finite rate chemistry LES for an axisymmetric dump combustor. J Turb 12(24)
Frolov SM, Zangiev AE, Semenov IV, Vlasenko VV, Voloshchenko OV, Nikolaev AA, Shiryaeva AA (2015) Simulation of flow in a high-speed combustor in two- and three-dimensional formulation. Combust Explos 8(1):126–135 (In Russian)
Frisch U (1995) Turbulence: the legacy of A.N. Kolmogorov. Cambridge. Cambridge University Press, New York
Fulton JA, Edwards JR, Hassan HA, Rockwell R, Goyne C, McDaniel J, Kouchi T (2012) Large-eddy/Reynolds-averaged Navier-Stokes simulations of a dual-mode scramjet combustor. AIAA paper 2012–115
Fureby C (2007) On LES and DES of wall bounded flows. Ercoftac Bulletin 72 (March)
Fureby C (2008) LES Modeling of combustion for propulsion applications. Phil Trans R Soc A 367:2957
Fureby C (2012) LES for supersonic combustion. AIAA paper, pp 2012–5979
Fureby C, Grinstein FF (1999) Monotonically integrated large eddy simulation. AIAA Journal 37 (5):544–556
Fureby C, Chapuis M, Fedina E, Karl S (2011) CFD analysis of the HyShot II scramjet combustor. Proc Combus Inst 33(2):2399–2405
Fureby C, Nordin-Bates K, Petterson K, Bresson A, Sabelnikov V (2015) A computational study of supersonic combustion in strut injector and hypermixer flow fields. Proc Combus Inst 35:2127–2135
Gao F, O'Brien EE (1993) A large-eddy simulation scheme for turbulent reacting flows. Phys Fluids A 5:1282–1284
Garnier E, Adams N, Sagaut P (2009) Large eddy simulation for compressible flows. Springer, Heidelberg
Germano M (1991) A dynamic subgrid-scale eddy viscosity model. Phys Fluids A 3(7)
Ghosal S (1996) An analysis of numerical errors in large-eddy simulations of turbulence. J Comput Phys 125:187–206
Ghosal S, Moin P (1995) The basic equations for the large eddy simulation of turbulent flows in complex geometry. J Comput Phys 118(1):4–37
Givi P Filtered density function for subgrid scale modeling of turbulent combustion. AIAA Journal 44:16
Glushko VP (ed) (1978–2004) Thermodynamic properties of individual substances, vol 6. Moscow, Nauka (In Russian)
Giacomazzi E, Bruno C, Favini B (1999) Fractal modeling of turbulent mixing. Combust Theory Model 3(4):637–655

Giacomazzi E, Bruno C, Favini B (2000) Fractal modeling of turbulent combustion. Combust Theory Model 4:391–412

Goebel S, Dutton J (1990) Velocity measurements of compressible turbulent mixing layers. In: 28th aerospace sciences meeting, p 709

Gokulakrishnan P, Pal S, Klassen M, Hamer A, Roby R, Kozaka O, Menon S (2006) Supersonic combustion simulation of cavity-stabilized hydrocarbon flames using ethylene reduced kinetic mechanism. In: Proceedings of the AIAA/ASME/SAE 42nd joint propulsion conference, pp 9–12. Sacramento, CA

Goldberg UC, Palaniswamy S, Batten P, Gupta V (2011) Variable turbulent Schmidt and Prandtl number modeling. Eng Appl Comput Fluid Mech 4(4):511–520

Gomez CA, Girimaji SS (2013) Toward second-moment closure modelling of compressible shear flows. J Fluid Mech 733:325–369

Gonzalez-Juez ED, Kerstein AR, Ranjan R, Menon S (2017) Advances and challenges in modeling high-speed turbulent combustion in propulsion systems. Prog Energy Combust Sci 60:26–67

Gran IR, Magnussen BF (1996) A numerical study of a bluff-body stabilized diffusion flame. Part 2. Influence of combustion modeling and finite-rate chemistry. Combust Sci Tech 119:191–217

Grinstein FF, Fureby C (2007) On flux-limiting-based implicit large eddy simulation. J Fluids Eng 129(12):1483–1492

Grinstein F, Margolin L, Rider W (eds) (2007) Implicit large eddy simulation. Cambridge University Press, New York, NY

Hawkes ER, Cant RS (2000) A flame surface density approach to large eddy simulation of premixed turbulent combustion. Proc Combust Inst 28:51

Heiser WH, Pratt DT (1994) Hypersonic airbreathing propulsion. AIAA education series. AIAA, Washington, DC

Ievlev VM (1990) Numerical simulation of turbulent flows. Moscow, Nauka. (In Russian)

Ingenito A, Bruno C (2009) Supersonic mixing and combustion: advance in LES modeling. Progress Propul Phys 1:515–530

Jachimowski CJ (1988) Analytical study of the hydrogen-air reaction mechanism with application to scramjet combustion (No. N-88-15846; NASA-TP-2791; L-16372; NAS-1.60: 2791). National Aeronautics and Space Administration, Hampton, VA (USA). Langley Research Center

Jaberi A, Colucci PJ, James S, Givi P, Pope SB (1999) Filtered mass density function for large eddy simulation of turbulent reacting flows. J Fluid Mech 401:85

Jarrett O, Cutler A, Antcliff R, Chitsomboon T, Dancey C, Wang J (1988) Measurements of temperature, density, and velocity in supersonic reacting flow for CFD code validation. In: 25th JANNAF combustion meeting, vol 1, pp 357–374

Johansson A (2002) Engineering turbulence models and their development, with emphasis on explicit algebraic Reynolds stress models theories of turbulence, p 253–300. Springer, Vienna

Jones WP, Launder BE (1972) The prediction of laminarization with a two-equation model of turbulence. Int J Heat Mass Trans 15(2):301–314

Karl S, Hannemann K, Mack A, Steelant J (2008) CFD analysis of the HyShot II scramjet experiments in the HEG shock tunnel. In: 15th AIAA international space planes and hypersonic systems and technologies conference. AIAA paper, pp 2008–2548

Kee RJ, Rupley FM, Meeks E, Miller JA (1996) CHEMKIN-III: A FORTRAN chemical kinetics package for the analysis of gas-phase chemical and plasma kinetics. Sandia national laboratories report SAND96-8216, p 162

Kerstein AR (2009) One-dimensional turbulence: stochastic simulation of multi-scale dynamics. Lect Notes Phys 756:291–333

Knikker R, Veynante D (2000) Experimental study of the filtered progress variable approach for LES of premixed combustion. In: Friedrich R, Rodi W (eds) Advances in LES of complex flows

Kolmogorov AN (1941) The local structure of turbulence in incompressible viscous fluid for very large Reynolds numbers. C.R. Acad Sci USSR 30:301–305

Kolmogorov AN (1942) Equations of turbulent motion of an incompressible fluid, Izvestiya AN SSSR.Ser. fiz 6(1–2):5.6–5.8
Kolmogorov AN (1962) A refinement of previous hypotheses concerning the local structure of turbulence in a viscous incompressible fluid at high Reynolds number. J Fluid Mech 13:82
Kuo YS, Corrsin S (1971) Experiments on internal intermittency and the structures distribution functions in fully turbulent fluid. J Fluid Mech 50:285
Kuo KK (2005) Principles of combustion. Wiley, New York
Kuznetsov VR, Sabelnikov VA (1990) Turbulence and combustion. Revised and augmented edition. Hemisphere publishing corporation. New York, Washington. Philadelphia, London
Langener T, Steelant J, Karl S, Hannemann K (2013) Design verification of a small scale scramjet combustion chamber. ISABE 2013. Korea, Busan, p 1655
Laurendeau NM (2005) Statistical thermodynamics: fundamentals and applications. Cambridge University Press
Landau LD, Lifshitz EM (1959) Fluid mechanics. Footnote on p 126. London, Pergamon
Langtry RB, Menter FR (2009) Correlation-based transition modeling for unstructured parallelized computational fluid dynamics codes. AIAA Journal 47(12):2894–2906
Launder BE, Sharma BI (1974) Application of the energy-dissipation model of turbulence to the calculation of flow near a spinning disc. Lett Heat Mass Trans 1(2):131–137
Launder BE, Reece GJ, Rodi W (1975) Progress in the development of a Reynolds-stress turbulence closure. J Fluid Mech 68(3):537–566
Laurence SJ, Karl S, Martinez Schramm J, Hannemann K (2013) Transient fluid combustion phenomena in a model scramjet. J Fluid Mech 722:85–120
Lele SK (1994) Compressibility effects on turbulence. Ann Rev Fluid Mech 26(1):211–254
Li J, Zhao Z, Kazakov A, Dryer FL (2004) An updated comprehensive kinetic model of hydrogen combustion. Int J Chem Kinet 36(10):566–575
Libby PA, Williams FA (eds) (1980) Turbulent reacting flows. In: Topics in applied physics, vol 44. Springer
Lilly DK (1967) The representation of small-scale turbulence in numerical simulation experiments. In: Proceedings of the IBM scientific computing symposium on environmental sciences, p 195–210. York-town Heights, USA
Lodato G, Castonguay P, Jameson A (2013) Discrete filter operators for large-eddy simulation using high-order spectral difference methods. Int J Numer Methods Fluids 72(2):231–258
Lu MH, Liou WW (2010) Application of a two-layer model for implicit large-eddy simulations using a high-order compact scheme. AIAA paper 2010–1101
Lysenko D (2014) On numerical simulation of turbulent flows and combustion. PhD thesis, NTNU
Ma T, Stein O, Chakraborty N, Kempf AM (2013) A-posteriori testing of algebraic flame surface density models for LES. Combus Theory Model 17(3):431–482
Magnussen BF (1981) On the structure of turbulence and a generalised eddy dissipation concept for chemical reactions in turbulent flow. In: 19th AIAA Sc. Meeting. St. Louis, USA
Magnussen BF (2005) The eddy dissipation concept. In: ECCOMAS thematic conference on computational combustion. Lisbon, Portugal
Matsuo K, Miyazato Y, Kim HD (1999) Shock train and pseudo-shock phenomena in internal gas flows. Prog Aerosp Sci 35(1):33–100
McAllister S, Chen JY, Fernandez-Pello AC (2011) Thermodynamics of combustion. In: Fundamentals of combustion processes, pp 15–47. Springer New York
Meneveau C, Katz J (2000) Scale-invariance and turbulence models for large-eddy simulation. Ann Rev Fluid Mech 32:1–32
Menter FR, Kuntz M (2003) A zonal SST-DES formulation DES Workshop, St Petersburg
Menter FR, Garbaruk AV, Egorov Y (2012) Explicit algebraic Reynolds stress models for anisotropic wall-bounded flows. In: Progress in flight physics. EDP sciences, vol 3, pp 89–104
Meyers J, Geurts BJ, Sagaut P (2008) Quality and reliability of large eddy simulations. Springer, Heidelberg
Moretti G (1965) A new technique for the numerical analysis of nonequilibrium flows. AIAA Journal 3(2):223–229

Menter FR (1994) Two-equation eddy-viscosity turbulence models for engineering applications. AIAA Journal 32(8):269–289
Molchanov AM (2011) Numerical simulation of supersonic chemically reacting turbulent jets. In: 20th AIAA computational fluid dynamics conference,pp 27–30 June 2011. Honolulu, Hawaii, AIAA Paper 2011–3211
Monin AS, Yaglom AM (1971) Statistical fluid mechanics: mechanics of turbulence, vol 2. MIT Press, Cambridge, MA, USA
Moule Y, Sabelnikov V, Mura A, Smart M (2014a) Computational fluid dynamics investigation of a Mach 12 scramjet engine. J Propul Power 30(2)
Moule Y, Sabelnikov V, Mura A (2014b) Highly resolved numerical simulation of combustion in supersonic hydrogen-air coflowing jets. Combust Flame 161:2647–2668
Nasr NB, Gerolymos GA, Vallet I (2009) The Riemann problem for reynolds-stress-transport in RANS and VLES. Comput Fluid Dyn 2008:723–729
Naud B (2003) PDF modeling of turbulent sprays and flames using a particle stochastic approach. Ph.D. thesis, Delft University of Technology
Nordin-Bates K, Fureby C, Karl S, Hannemann K (2016) Understanding scramjet combustion using LES of the HyShot II combustor. Proc Combus Inst 000:1–8
Obukhov AM (1962) Some specific features of atmospheric turbulence. J Fluid Mech 13:77
Oran ES, Boris JP (2005) Numerical simulation of reactive flow. Cambridge University Press
Prandtl L (1925) Bericht über Untersuchungen zur ausgebildeten Turbulenz. Z Angew Math Mech 5(2):136–139
Papamoschou D, Roshko A (1987) The compressible turbulent shear layer: an experimental study. J Fluid Mech 181:441–466
Petrova N, Sabelnikov V, Bertier N (2017) Numerical simulation of a backward-facing step combustor using RANS/extended partially stirred reactor model of turbulent combustion. In: Proceedings of EUCASS 2015, progress in propulsion physics, vol 11
Piomelli U, Balaras E (2002) Wall-layer models for large-eddy simulations. Annu Rev Fluid Mech 34:349–374
Pitsch H (2006) Large-eddy simulation of turbulent combustion. Annu Rev Fluid Mech 38:453–482
Poinsot T, Veynante D (2005) Theoretical and numerical combustion, 2nd edn. Edwards
Pope SB (1997) Computationally efficient implementation of combustion chemistry using in situ adaptive tabulation. Combust Theor Model 1(1):41–63
Powell OA et al (2001) Development of hydrocarbon-fueled scramjet engines: the hypersonic technology (HyTech) program. J Propul Power 17(6):1170–1176
Prandtl L (1942) Bemerkungen zur Theorie der freien Turbulenz. ZAMM J Appl Math Mech 22 (5):241, 243
Prandtl L, Wieghardt K (1947) Über ein neues Formelsystem für die ausgebildete Turbulenz. Vandenhoeck and Ruprecht
Prudnikov AG, Koroleva NS, Boev DA (2008) Faster than all winds. In: Memory of Yevgeny Sergeyevich Schetinkov. Engine No. 3 (57). http://engine.aviaport.ru/issues/57/ (In Russian)
Qin Z, Lissianski V, Yang H, Gardiner WC Jr, Davis SG, Wang H (2000) Combustion chemistry of propane: a case study of detailed reaction mechanism optimization. Proc Combust Inst 28 (2):663–1669
Rathakrishnan E (2013) Theoretical aerodynamics. Wiley
Reynolds O (1894) On the dynamical theory of incompressible viscous fluids and the determination of the criterion. Proc R Soc Lond 56(336–339):40–45
Rodi W, Constantinescu G, Stoesser T (2013) Large-eddy simulation in hydraulics. CRC Press, Hoboken
Rodi W (1976) A new algebraic relation for calculating Reynolds stresses. ZAMM, vol 56, p 219
Sabelnikov VA, Penzin VI (2000) Scramjet research and development in Russia. In: Curran ET, Murthy SNB (eds) Scramjet propulsion, Progress in astronautics and aeronautics, AIAA, vol 189, pp 223–368

Sagaut P (2006) Large eddy simulation for incompressible flows, an introduction, 3rd edn. Springer, Heidelberg
Sabelnikov V, Figueira da Silva LF (2002) Partially stirred reactor: study of the sensitivity of the Monte-Carlo simulation to the number of stochastic particles with the use of a semi-analytic, steady-state, solution to the PDF equation. Combust Flame 129:164–178
Sabelnikov V, Fureby C (2013a) LES Combustion modeling for high Re flames using a multi-phase analogy. Combust Flame 160(1):83–96
Sabelnikov V, Fureby C (2013b) Extended LES-PaSR model for simulation of turbulent combustion. Progress Propuls Phys 4:539–568. https://doi.org/10.1051/eucass/201304539
Sankaran V, Menon S (2005) Subgrid combustion modeling of 3D premixed flames in the thin-reaction-zone regime. Proc Combust Inst 38:575
Sarkar S (1992) The pressure-dilatation correlation in compressible flows. Phys Fluids A 4:2674, 2682
Sarkar S (1993) Turbulence modeling and simulation of high-speed flows. In: 2nd space course on low earth orbit transportation, vol 1. Munich University of Technology, October 11–22
Scherrer D, Dessornes O, Ferrier M, Vincent-Randonnier A, Moule Y, Sabelnikov V (2016) Research on supersonic combustion and scramjet combustors at ONERA, p 04. Aerospace Lab
Schetinkov ES (1957) Method of operation of the ramjet air-breathing engine. USSR Patent No. 471815
Schetinkov ES (1958) Calculation of flame velocity in turbulent stream. Symp (Int) Combust 7:583–589
Schetinkov ES (1965) Physics of gas combustion, Nauka, Moscow, in Russian (exists machinery translation en English: FTD-HT-23-496-48)
Sedov LI (1993) Similarity and dimensional methods in mechanics. CRC press
Segal C (2009) The scramjet engine: processes and characteristics. Cambridge University Press
Shapiro AH (1953) The dynamics and thermodynamics of compressible fluid flow, vol 1. Ronald Press, New York
Shiryaeva AA (2010) On the stationary state of a mixture of reacting gases. Russ J Phys Chem B 4 (3):413–422
Shiryaeva A, Anisimov K (2015) Development and application of numerical technology for simulation of different combustion types in high-speed viscous gas turbulent flows. In: 6th European conference for aeronautics and space sciences (EUCASS 2015), Kraków (Poland), 29 June–3 July 2015, 14 pages. Full text is available for participants at http://www.eucass2015.eu/detailed-programme/
Shiryaeva A, Vlasenko V, Anisimov K (2014) Development and application of numerical technology for simulation of different combustion types in high-speed viscous gas turbulent flows. In: 44th AIAA fluid dynamics conference. AIAA-2014-2097
Shur M, Strelets M, Zaikov L, Gulyaev A, KozIov V, Secundov A (1995) Comparative numerical testing of one-and two-equation turbulence models for flows with separation and reattachement. In: 33rd aerospace sciences meeting and exhibit, aerospace sciences meetings
Singh S, You D (2013) A dynamic global-coefficient mixed subgrid-scale model for large-eddy simulation of turbulent flows. Int J Heat Fluid Flow 42:94–104
Smagorinsky J (1963) General circulation experiments with the primitive equations: I. The basic experiment. Monthly weather review 91(3):99–164
Smith AMO, Cebeci T (1967) Numerical solution of the turbulent-boundary-layer equations. Douglas Aircraft Co. Inc. Long Beach Calif. Aircraft Div., No DAC-33735
Smits AJ, Dussauge JP (2006) Turbulent shear layers in supersonic flow. Springer Science and Business Media, p 417
Spalart PR (2009) Detached eddy simulation. Ann Rev Fluid Mech 41:181–202
Spalart PRA, Allmaras S (1992) A one-equation turbulence model for aerodynamic flows 30th aerospace sciences meeting and exhibit, p 439
Spalart PR, Jou W-H, Strelets M, Allmaras SR (1997) Comments on the feasibility of LES for wings, and on a hybrid RANS/LES approach. In: Liu C, Liu Z (eds) Advances in DNS/LES, pp 137–47. Greyden Press, Columbus

Speziale CG (1987) On nonlinear k-l and k-ε models of turbulence. J Fluid Mech 178:459–475
Speziale CG, Sarkar S, Gatski TB (1991) Modelling the pressure-strain correlation of turbulence: an invariant dynamical systems approach. J Fluid Mech 227:245–272
Sreenivasan KR, Antonia RA (1997) The phenomenology of small-scale turbulence. Ann Rev Fluid Mech 29:435
Sreenivasan KR, Meneveau C (1986) The fractal facets of turbulence. J Fluid Mech 173:356
Tanahashi M, Fujimura M, Miyauchi T (2000) Coherent fine scale eddies in turbulent premixed flames. Proc Combust Inst 28:5729
Tanahashi M, Sato M, Shimura M, Miyauchi T (2008) DNS and combined laser diagnostics of turbulent combustion. J Therm Sci Technol 3:391
Tennekes H, Lumley JL (1972) A first course of turbulence. MIT Press
Thibaut D, Candel S (1998) Numerical study of unsteady turbulent premixed combustion: application to flashback simulation. Combus Flame 113(1):53–65
Tsinober A (2009) An informal conceptual introduction to turbulence. Springer, Dordrecht, Heidelberg, New York, London
Tsinober A (2013) The essence of turbulence as a physical phenomenon. with emphasis on issues of paradigmatic nature. Springer, Dordrecht, Heidelberg, New York, London
Townend LH (2001) Domain of the scramjet. J Propul Power 17(6):1205–1213
Troshin AI (2017) Turbulence model taking into account the longitudinal flow inhomogeneity in mixing layers and jets. In: Progress in flight physics, EDP sciences, vol 9, pp 481–496
Vanhove G, Petit G, Minetti R (2006) Experimental study of the kinetic interactions in the low-temperature autoignition of hydrocarbon binary mixtures and a surrogate fuel. Combust Flame 145(3):521–532
Vasilyev OV, Lund TS (1997) A general theory of discrete filtering for LES in complex geometry. Ann Res Briefs 67–82
Vlasenko VV, Nozdrachev AY (2017) About necessity to use thermodynamic potentials in calculations with finite-rate chemical kinetics. Combust Explos 10(2):19–24. (In Russian)
Vieser W, Esch T, Menter F (2002) Heat transfer predictions using advanced two-equation turbulence models. CFX Validation Report 10/0602, AEA Technology, pp 1–69
Visbal MR, Rizzetta DP (2002) Large-eddy simulation on curvilinear grids using compact differencing and filtering schemes. J Fluids Eng 124(4):836–847
Visbal MR, Morgan PE, Rizzetta DP (2003) An implicit LES approach based on high-order compact differencing and filtering schemes. AIAA paper. 2003. T. 4098. C
Vulis LA (1961) Thermal rezhime of combustion, Chap. 3. McGraw-Hill, New York, NY. (Translation from the Russian edition: 1954. Teplovoy rezhim goreniya. Moscow Leningrad: Gosenergoizdat. p 288)
Waltrup PJ (2001) Upper bounds on the flight speed of hydrocarbon-fueled scramjet-powered vehicles. J Propul Power 17(6):1199–1204
Wang P, Bai XS (2005) Large eddy simulation of turbulent premixed flames using level-set G-equation. Proc Combust Inst 30:583
Weller HG, Tabor G, Gosman AD, Fureby C (1998) Application of a flame-wrinkling LES combustion model to a turbulent shear layer formed at a rearward facing step. Proc Combust Inst 27:899
Westbrook CK, Dryer FL (1981) Simplified reaction mechanisms for the oxidation of hydrocarbon fuels in flames combustion science and technology, 27(1–2):31–43
Weydahl T, Poyyapakkam M, Seljeskog M, Haugen NEL (2011) Assessment of existing H2/O2 chemical reaction mechanisms at reheat gas turbine conditions. Int J Hydr Energy 36 (18):12025–12034
Wilcox DC (1988) Reassessment of the scale-determining equation for advanced turbulence models. AIAA Journal 26(11):1299–1310
Wilcox DC (1998) Turbulence modeling for CFD, 2nd edn. DCW Industries
Wilcox DC (2008) Formulation of the k-ω turbulence model revisited. AIAA Journal 46 (11):2823–2838

Woodward PR, Porter DH, Sytine I, Anderson SE, Mirin AA, Curtis BC, Cohen RH, Dannevik WP, Dimits AM, Eliason DE, Winkler K-H, Hodson SW (2001) Very high resolution simulations of compressible turbulent flows. In: Ramos E, Cisneros G, Fernandez-Flores A, Santillan-Gonzalez A (eds) Computational fluid dynamics. 4th UNAM supercomputing conference proceedings, vol 3. World Scientific

Xiao X, Hassan HA, Baurle RA (2007) Modeling scramjet flows with variable turbulent Prandtl and Schmidt numbers. AIAA Journal 45(6):1415

Zambon AC, Chelliah HK (2007) Explicit reduced reaction models for ignition, flame propagation, and extinction of C2H4/CH4/H2 and air systems. Combust Flame 150(1):71–91

Zel'dovich YB, Barenblatt GI, Librovich VB, Makhviladze GM (1985) The mathematical theory of combustion and explosions, Chap. 1, paragraph 3. New York, Plenum

Zeman O (1990) Dilatation dissipation: the concept and application in modeling compressible mixing layers. Phys Fluids A 2(2):178–188

HEXAFLY-INT project site. http://www.esa.int/techresources/hexafly_int

Erratum to: Large-Eddy Simulation of Nonpremixed Flames by Explicit Filtering

Joseph Mathew and Saugata Chakravorty

Erratum to:
Chapter 14 in: S. De et al. (eds.), *Modeling and Simulation of Turbulent Combustion*, Energy, Environment, and Sustainability, https://doi.org/10.1007/978-981-10-7410-3_14

The original version of the book was inadvertently published missing out the corrections provided by author for all the figure axis labels in Chap. 14, which have been now incorporated. The erratum chapter and the book have been updated with the changes.

The updated online version of this chapter can be found at https://doi.org/10.1007/978-981-10-7410-3_14

© Springer Nature Singapore Pte Ltd. 2018

S. De et al. (eds.), *Modeling and Simulation of Turbulent Combustion*, Energy, Environment, and Sustainability, https://doi.org/10.1007/978-981-10-7410-3_21

Author Index

© Springer Nature Singapore Pte Ltd. 2018

S. De et al. (eds.), *Modeling and Simulation of Turbulent Combustion*, Energy, Environment, and Sustainability, https://doi.org/10.1007/978-981-10-7410-3